APPLICATIONS OF THE THERMOGRAVIMETRIC ANALYSIS IN THE STUDY OF FOSSIL FUELS

He Huang, Keyu Wang, Shaojie Wang, M. T. Klein and W.H. Calkins*
Dept of Chemical Engineering, University of Delaware, Newark, DE 19716

Key words: thermogravimetric analysis, fossil fuels, characterization

INTRODUCTION

Applications of thermal analysis in fossil fuel research date back as far as the techniques themselves. Thermogravimetry (TG) had been used by Somiya and Hirano in 1930 to determine the volatile yield of many coals (1). Advances in design of thermogravimetric analyzers (TGA) now allow experiments to be carried out simply and fast in high accuracy under various conditions from vacuum to high pressure (2-4). A TG method has been devised for the proximate analysis of coal with the results of the same precision and accuracy as BS and ASTM methods (5).

Thermogravimetric (TG) techniques have been used in our laboratory to characterize fossil fuel samples (6) and to study coal liquefaction kinetics, mechanisms, and processes (7-10). TGA has been providing sensitive, rapid, and reproducible measurements for those purposes. The various weight loss processes determined during the TG analysis reflect the physical and chemical structural changes during the conversion. Thermogravimetric analysis has other desirable features as well. First, only very small samples, usually about 30 mg, are required for each TG scan. Second, by suitable adjustments in the work-up procedures and the TG operating parameters, thermogravimetric analysis reveals important information concerning the reaction pathways. Besides, custom-built thermogravimetric techniques provide very flexible means and unique features for fossil fuel research (11-13).

Development and applications of the TG techniques in our laboratory are reported in this paper. These include 1). characterization of coal structure; 2). determining the liquefaction conversion and measuring the rate of the retrograde reactions occurring during coal liquefaction; 3). evaluating the thermal and catalyzed hydroprocessing of the coal-derived resids; and 4). determining the boiling range of liquid fuels. Various effects including the TG operating variables, such as heating rate, purge gas type (e.g. H_2 or N_2), gas flow rate, and modification of the TG sample pan as well as a method for the development of a custom built thermogravimetric system are also discussed in this paper.

EXPERIMENTAL

Apparatus. The Thermogravimetric Analyses (TGA) were performed with a Model 51 TGA (TA Instruments, New Castle, Delaware).

Procedures. An approximately 30-60 mg sample (e.g. coal, coal liquefaction residue, coal liquid, coal-derived resid, etc.) was loaded in a quartz pan and mounted in the instrument. Selected TG scans were processed using an 11-point smoothing filter of the Linear Regression & Error Analysis procedure (14). The program of manipulation of the TG operating variables was determined by the objectives of the particular experiment.

Materials Studied. Eight coals of rank from lignite to l.v. bituminous were obtained from the Argonne Premium Coal Sample bank. Analytical values of the these coals are given in the User's Handbook (15). Two 850°F distillation residue oils (resids), one derived from Wyodak subbituminous coal and another from Pittsburgh bituminous coal, were obtained from the Wilsonville Pilot Plant Runs 259 and 260, and prepared and composited by CONSOL Research. At room temperature, these two resids are solid and only partially soluble in tetralin.

RESULTS AND DISCUSSION

Coal Structure and Composition. A representative TG scan on the Illinois #6 coal is shown in Figure 1. In brief, two stages, i.e., 1) the heating rate at 10 °C/min to 950°C in nitrogen and hold for 7 min; and 2) the oxidation at 950°C, provided measures of Volatile Matter (VM), Fixed Carbon (FC), and Ash. Ash content measured by TGA is in close agreement with that determined by ASTM D3174. When a coal sample is bright to 110 °C in nitrogen and hold for 10 min, the weight loss is a measure of the moisture content (16).

The differential of the weight loss (DTG) curve highlights the various TG processes more clearly. The DTG curve for Illinois #6 shows a pattern which is more complex than many of the other Argonne coals. This becomes even more distinct and complex if the heating rate is slowed down to about 1 °C/min (6).

Thermogravimetric analyses were also run in a hydrogen atmosphere. This provided additional information regarding the structure of coal. (For safety reasons, hydrogen MUST be thoroughly displaced by nitrogen before air or oxygen is introduced.) DTG curves of the eight Argonne Premium Coals in nitrogen and in hydrogen show similar patterns. However,

the Volatile Matter yields at heating rates from 10 °C/min to 200 °C/min are consistently higher, and therefore the Fixed Carbon yields are lower, in hydrogen than in nitrogen. More importantly, the heating rate has a strong effect on the yields of Volatile Matter in either hydrogen or nitrogen. In hydrogen, the Volatile Matter yields decrease somewhat as the heating rate increases. This may be because the pyrolysis time is shorter at higher heating rate, providing less time for reaction with the molecular hydrogen to form more volatile products. However, in nitrogen, the Volatile Matter yields increase with increasing heating rate. This phenomenon may be because, at the low heating rates, the unquenched free radicals react to form more retrograde products (fixed carbon). This is consistent with the flash pyrolysis process, where the oil and gas product yields increase with increasing heating rate.

TGA provides an objective measure of coal rank. DTG curves scanned in 100 cm³(STP)/min nitrogen at 10 °C/min for the eight Argonne Premium Coals (which were dried in a vacuum oven with a nitrogen purge at 105 °C for 48 hours before use) are shown in Figure 2. These coals range ranking from lignite to l.v. bituminous. This plot clearly shows the gradual shift of peak temperature as the coal rank increases from Lignite to low volatile bituminous coal. However, the peak height increases to a maximum at about 81 wt% (daf) Carbon and then decreases as the rank increases.

Coal Liquefaction Studies. A Short-Contact-Time Batch Reactor (SCTBR) was used to run coal liquefaction. This reactor apparatus allows the heat up and quenching of the process stream to and from reaction temperature in about 0.3 seconds, respectively. The design and operation of such a SCTBR reactor system have been described in detail elsewhere (17,18). After a liquefaction run, the product mixture was filtered and the solid residue washed with fresh tetralin thoroughly, then rinsed with methylene chloride to remove residual tetralin, and dried in a vacuum oven with a nitrogen purge at about 105 °C for 48 hours. This resulted in the production of a liquid filtrate, which consisted mainly of tetralin and dissolved coal liquids, and a solid filter cake, of unconverted and/or partially converted solid coal residue.

During coal liquefaction, the coal liquids are extracted into the tetralin solvent. However, the mineral matter of the coal remains with the solid coal residue and is insoluble in tetralin, as proven by the TG scan on the liquid filtrate (8,19). Since the ash is not consumed during the liquefaction and remains in the solid, conversion to the tetralin-soluble oils can be derived based on an ash-balance (8,17):

$$Conversion = (1 - \frac{A_o}{A_s}) \times 100\% \qquad (1)$$

where A_o and A_s are the weight fractions of ash in the control sample and in the liquefaction residue, respectively. The control sample is the original coal which is processed exactly as a liquefaction residue except at ambient temperature. When the liquefaction is carried out in the presence of an inorganic catalyst, the conversion calculation must include an ash value corrected for the ash derived from the catalyst.

The thermal and catalyzed liquefaction conversions of Illinois #6 coal in tetralin at 390 °C are shown in Figure 3. In the thermal liquefaction, three distinct phases in the process were observed, i.e., a very rapid conversion followed by an induction period and then a slower liquefaction of the coal structure. The initial rapid conversion in the first minute is due to the physical extraction of a soluble fraction of the coal into the hot tetralin. This is followed by an induction period and then the slow conversion of the coal structure to liquid products. The induction period observed is actually a pseudo induction period. This induction period is a transition interval which is due to the simultaneous occurrence of two processes, a very rapid extraction and a relatively slower liquefaction of the coal structure. In fact, as the temperature increases, the induction period steadily becomes less pronounced as the rate of break down of the coal structure increases and becomes closer in reaction rate to the extraction step itself (10). That the induction period is not due to the build up of free radicals is also proven by ESR data (20,21). In the catalyzed liquefaction, the pseudo induction period is, as expected, diminished and the subsequent conversion is much faster for the catalyzed than the thermal liquefaction. More importantly, the retrograde process, leading to form tar, coke and char, is very significantly reduced in the presence of catalyst and hydrogen as is shown by the Fixed Carbon content in the residue as a function of liquefaction time (Figure 4). When the catalyzed liquefaction was run at higher temperature, the Fixed Carbon of the residue was even further reduced (Figure 5), suggesting that the precursors of the retrograde processes are being hydrogenated and stabilized during the catalyzed liquefaction. Liquid yields were thereby significantly improved (Figure 6).

DTG curves for partially converted coal liquefaction residues of Illinois #6 coal after liquefaction in tetralin at 390°C under 1000 psig nitrogen at selected contact times are

2

shown in Figure 7. The gradual disappearance of the two smaller peaks (one of them identified as FeS_2 conversion to FeS and S) clearly indicates that some chemical changes in the solid coal are taking place before the coal actually becomes liquid. In addition, the sensitivities of the production of VM in the residues to heating rate and to atmospheres of nitrogen and hydrogen are significantly changed as shown in Figures 8a and 8b for the unreacted original Illinois #6 coal and a liquefaction sample of Illinois #6 taken after 30 seconds at 390 °C, respectively. The profound changes shown in that short time suggests that even short exposure to donor solvent can significantly change the character of the coal before much actual liquefaction has taken place. This change may merely be the removal of a very unstable volatile fraction or actual stabilization by hydrogen transfer from the donor solvent.

Evaluating the thermal and catalyzed hydroprocessing of the coal-derived resids. The Short-Contact-Time Batch Reactor (SCTBR) was again used for the thermal and catalyzed hydroprocessing of the coal-derived resids. The resid reaction product workup procedure and determination of the thermal and catalyzed resid conversion have been described in detail elsewhere (8). The conversion of resid to tetralin soluble material was determined by relating the inorganic matter (ash) in the reacted resid with that of the un-reacted resid. Un-catalyzed conversion of tetralin-insoluble resids to tetralin soluble products in this study was very low (< 10 wt%) under coal liquefaction conditions (410 - 440 C, 1500 psig H_2, 2 - 5 of tetralin to resid ratio). But, up to 80 wt% (ash-free basis) was solubilized in tetralin using sulfided Ni/Mo on alumina catalyst at 434°C for 10 min. Hydroprocessing at liquefaction conditions (see above), and particularly in the presence of Ni/Mo on alumina catalyst, was effective for converting tetralin-insoluble to tetralin-soluble material, and for reducing the average molecular weight (8). Up to 50 wt% of the resid was already tetralin soluble even at room temperature. Therefore, the tetralin solubility cannot be used as a measure of the resid converted to low boiling fuels. The actual conversion of resid represents the portion of the resid which is broken down in the hyroprocessing to low molecular weight material boiling below 850 °F. For that reason, additional technique(s) is required for measuring the degree to which the resids is converted to lower boiling products (i.e. below 850 °F).

An analytical TGA method for boiling range measurement, SimDis TGA, has been developed for that purpose. This SimDis TGA technique requires a change in the conventional TGA sample pan. It was devised with a small aperture at the top of the pan. The fundamentals, methodology, and experimental details of the SimDis TGA technique have been reported in the Symposium on New Analytical Methods for Characterizing Fossil Fuels and Derived Products in Chicago in 1995 (22). The boiling point distribution of Wilsonville # 258 resid liquid sample, which was determined by the SimDis TGA technique, is shown in Figure 9. This resid sample was hydroprocessed in tetralin using sulfided molybdenum naphthenate catalyst at 403°C for 60 minutes. The fraction of the resid liquid boiled below 850 °F (i.e. 850 °F⁻) was 93.8 wt%, in which tetralin fraction was included. The following equation:

$$Conversion\ (850\ °F^-) = TSF \times (1 - \frac{850\ °F^+\ in\ tetralin}{RSF\ in\ tetralin}) \times 100\% \qquad (2)$$

was used to evaluate the resid conversion to 850 °F⁻ during the thermal and catalyzed hydroprocessing. In Equation 2, TSF (Tetralin Soluble Fraction) was determined by ash content in the solid residue (8); RSF (Resid Soluble Fraction) and 850 °F⁺ fractions in tetralin were determined by running the ramp and SimDis TGA methods (8,22) on the resid liquid products, respectively. Preliminary studies show that, for the illustrative sample in Figure 9, TSF (Tetralin Soluble Fraction) determined by ash content of the solid residue was 67.8 wt%; 850 °F⁺ fractions in tetralin determined by the ramp method was 8.62 wt%. Conversion of the Wilsonville #258 resid hydroprocessed under those conditions to 850 F⁻ was 19.0 wt%.

Determining boiling point distribution of liquid fuels. In addition to the SimDis TGA method, which is capable of measuring the boiling point up to 1000 °C and briefly described in previous section, a custom-built thermogravimetric apparatus for distillation of liquid fuels was also developed in our laboratory (23). As an example, boiling point distribution of a crude oil analyzed using the custom-built thermogravimetric apparatus is illustrated in Figure 10.

CONCLUSION

Thermogravimetric analysis (TGA) of coal and resid liquids and coal and resid solid residues, which were produced in coal liquefaction and coal-derived resid hydroprocessing in the SCTBR (Short-Contact-Time Batch Reactor) apparatus, provides a sensitive, rapid, and reproducible means of studying the kinetics and mechanisms of fossil fuel conversion

processes. SimDis TGA and the custom built thermogravimetric system for distillation provide unique means to characterize liquid fuels for the boiling point distribution.

Thermogravimetric Analysis (TGA) provides information concerning the various weight loss processes that can be a reflection of the physical and chemical structure of fossil fuel samples. More importantly, this technique is also capable of yielding TG scanning parameters, such as Volatile Matter, Fixed Carbon, Ash, etc. to be used to monitor the fossil fuel conversion processes. A significant example is to determine the onset and rate of the retrograde reactions during the coal liquefaction process.

REFERENCES

1. Somiya, T.; Hirano, S. *J. Chem. Soc. Ind. (Japan)* 1930, **33**, 737.
2. Schwartz, H.E.; Brownlee, R.G.; Bodusznynski, M.; Su, F. *Anal. Chem.* **1987, 59**, 1393.
3. Nie, X.; McClennen, W.H.; Liu, K.; and Meuzelaar, H.L.C. *ACS Fuel Chem Div Preprints* **38** (4), 1147 (1993).
4. Liu, K.; Jakab, E.; McClennen, W.H.; Meuzelaar, H.L.C. *ACS Fuel Chem Div Preprints* **38** (3), 823 (1993).
5. Ottaway, M. *Fuel* **1982, 61**, 713.
6. Huang, He; Wang, Keyu; Klein, M.T.; W.H. Calkins *ACS Fuel Chem Div Preprints* **40** (3), 465 (1995).
7. Huang, He; Wang, Keyu; Calkins, W.H.; Klein, M.T *ACS Fuel Chem Div Preprints* **39** (3), 741 - 746 (1994).
8. Huang, He; Calkins, W.H.; Klein, M.T. *I&EC Research* **33**, 2272-2279 (1994).
9. Huang, He; Wang, Keyu; Klein, M.T.; W.H. Calkins *Coal Science and Technology 24: Coal Science*, Eds J.A. Pajares and J.M.D. Tascon, Vol. II, p. 1207 (1995).
10. Huang, He; Wang, Keyu; Wang, Shaojie; Klein, M.T.; W.H. Calkins *ACS Fuel Chem Div Preprints* **40** (3), 550 (1995).
11. Massoth, F.E. Chem. Tech. 1972, May, 285.
12. Sears, J.T.; Maxfield, E.A.; Tamhankar, S.S. Ind. Eng. Chem. Fundam. 1982, 21, 474.
13. Dean, J.W.; Dadyburjor, D.B. Ind. Eng. Chem. Res. 1988, 27, 1754.
14. Wang, Keyu; Wang, Shaojie; Huang, He; Klein, M.T.; Calkins, W.H.; paper to be presented in the *Symp. on the Thermal Analytical Techniques*, March 24-29, 1996, in Mew Orleans.
15. Vorres, K.S. 'User's Handbook for the Argonne Premium Coal Sample Program' *ANL/PCSP-93/1*.
16. He Huang, D.M. Bodily, and V.J. Hucka *Proceedings 1993 International Conference on Coal Science* , 411-414.
17. Huang, He; Calkins, W.H.; Klein, M.T *Energy and Fuels* **8**, 1304-1309 (1994).
18. Huang, He; Fake, D.; Calkins, W.H.; Klein, M.T *Energy and Fuels* **8**, 1310-1315 (1994).
19. Calkins, W.H.; Huang, He; Klein, M.T. *Proceedings 1994 Pittsburgh Coal Conference* pps. 475-480.
20. Huang, He; Provine, W.D.; Jung, B.; Jacintha, M.A.; Rethwisch, D.G.; Calkins, W.H.; Klein, M.T.; Dybowski, C.R.; Scouten, C.G. *Proceedings of the International Conference on Coal Science*, **1993**, Ed. K.H. Michaelian, Vol. I, 266.
21. Provine, W.D.; Jung, B.; Jacintha, M.A.; Rethwisch, D.G.; Huang, He; Calkins, W.H.; Klein, M.T.; Scouten, C.G.; Dybowski, C.R. *Catalysis Today*, **1994**, Ed. D.B. Dadyburjor and J.W. Zondlo, Vol. **19**, No. *3*, 409.
22. Huang, He; Wang, Keyu; Wang, Shaojie; Klein, M.T.; W.H. Calkins *ACS Fuel Chem Div Preprints* **40** (3), 485 (1995).
23. Huang, He; Wang, Keyu; Wang, Shaojie; Klein, M.T.; W.H. Calkins paper to be presented in the *Symp. on the Thermal Analytical Techniques*, March 24-29, 1996, in Mew Orleans.
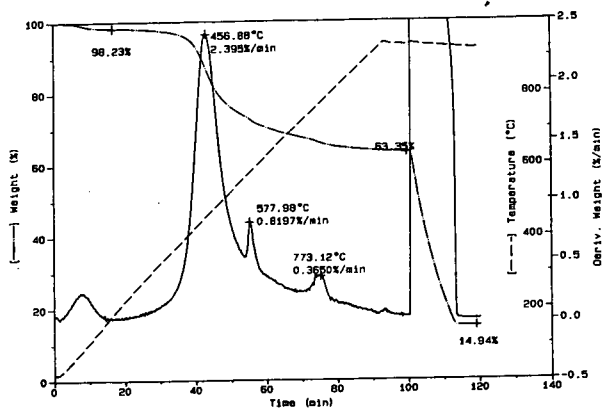
Figure 1 A TG scan of Illinois #6 coal at 10 C/min
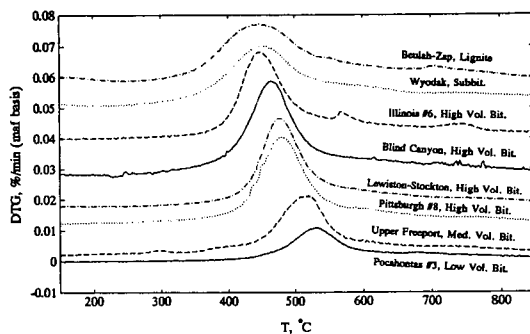

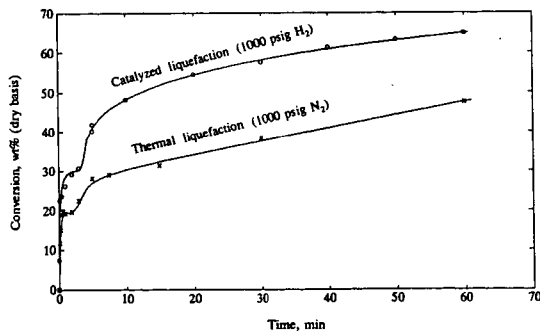Figure 2 DTG profiles of the eight Argonne coals

Figure 3   Conversion vs time of the thermal and catalyzed (about 0.9 wt % Mo of sulfided molybdenum naphthenate) liquefaction of Illinois #6
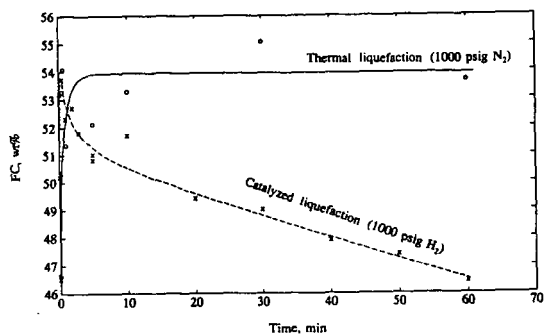
5

Figure 4 FC (Fixed Carbon) in the thermal (1000 psig N_2) and catalyzed (about 0.9 wt% Mo and 1000 psig H_2) liquefaction residues determined by TGA
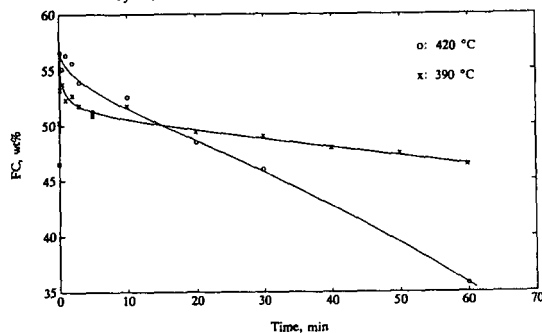

Figure 5 FC (Fixed Carbon) in the catalyzed (about 0.9 wt% Mo) liquefaction residues determined by TGA
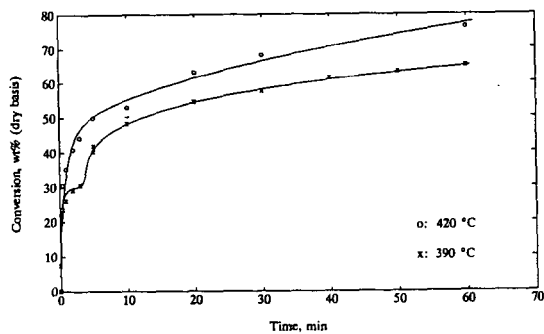

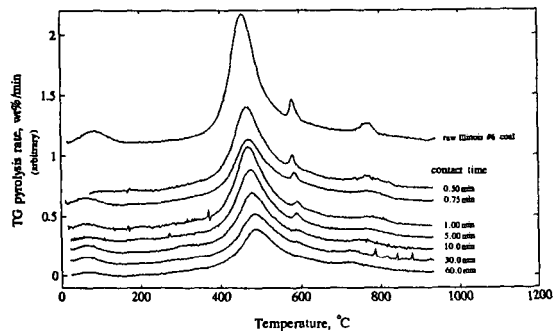Figure 6 Conversion of the Illinois #6 bituminous in catalyzed (about 0.9 wt% Mo) coal liquefaction under 1000 psig H_2

Figure 7 DTG profiles for the liquefaction residues of the Illinois #6 bituminous at the selected contact times
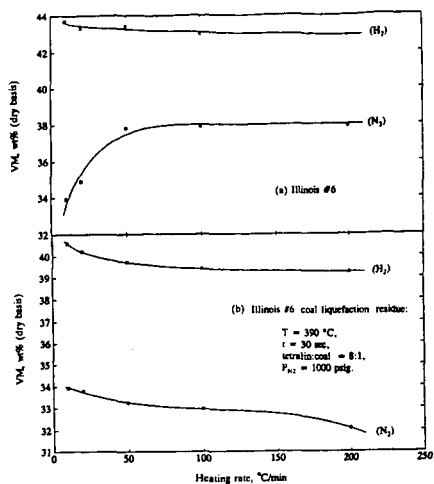
6

Figure 8 Effect of heating rate and type of purge gas on the VM yields of a). raw Illinois #6 coal and b). its liquefaction residue
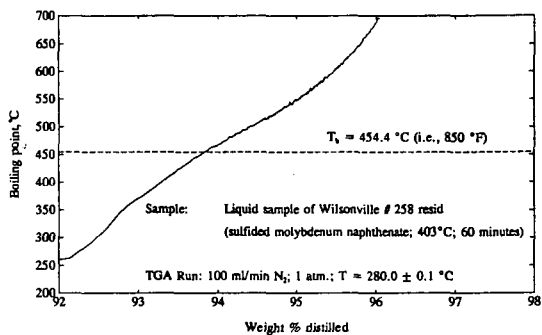

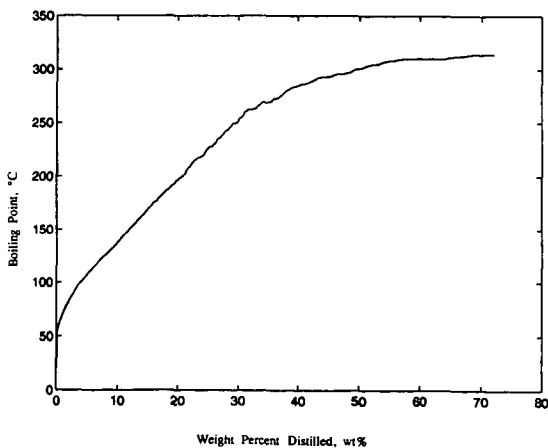Figure 9 Boiling point distribution of the hydroprocessed reisd liquid determined by SimDis TGA

Figure 10 Weight percent distilled vs boiling point of a filtered crude oil determined by a custom built TG for distillation

APPLICATION OF THERMAL ANALYSIS TECHNIQUES
IN ACTIVATED CARBON PRODUCTION

Gwen L. Donnals, Joseph A. DeBarr, Massoud Rostam-Abadi, Anthony A. Lizzio,
Todd A. Brady, Illinois State Geological Survey, Champaign, Illinois 61820

Keywords: thermal analysis, activated carbons

INTRODUCTION

Several current research programs at the Illinois State Geological Survey (ISGS) relate to the development of activated carbons from Illinois coal, fly ash, and scrap tires [1-5]. Preparation of activated carbons involves thermal processing steps that include preoxidation, pyrolysis and activation. Reaction time, temperature and gas composition during these processing steps ultimately determine the nature of the activated carbon produced. Thermal analysis plays a significant role in developing carbons by providing fundamental and engineering data that are useful in carbon production and characterization for process development.

EXPERIMENTAL

Thermal analysis instruments and their applications are useful for characterizing activated carbon precursors and intermediate and final products. Instruments available in the Thermal Analysis Laboratory at the ISGS include both atmospheric (Cahn TG-131) and high pressure (SRE Model TL-TGA 1900/600) thermogravimetric analyzers (TGA and PTGA). Evolved gases from a controlled fixed-bed thermal reactor are monitored by non-dispersive infrared CO and CO_2 analyzers (Rosemount model 880) and a quadrupole mass spectrometer (Fisons model MMPC300-D). All instruments are computer interfaced to allow data collection and rapid data reduction and analysis.

Proximate analysis is performed in the TGA to determine the amounts of moisture, volatile matter, fixed carbon and ash content in activated carbons. In a typical analysis, 50 mg of sample is heated in a platinum pan at 50°C/min to 950°C in N_2 flowing at 75 cc/min (STP). The temperature is held constant at 950°C for 10 minutes, then reduced to 750°C. Air is introduced at 750°C until the oxidation reaction is complete and no further weight loss is observed.

Activation studies are done in the TGA to determine appropriate conditions for activation of carbon samples in larger scale test facilities [6]. Reactivity is determined in the TGA using air at 380-500°C, CO_2 at 920-1000°C, or steam at 860-960°C. Typically, 2-10 mg of sample is heated in N_2 to a predetermined reaction temperature. Once the temperature and weight stabilize, appropriate reaction gas is substituted for the N_2 and weight loss is monitored as a function of time.

SO_2 removal efficiencies from simulated combustion flue gas by activated carbons is determined in the TGA [7]. In a typical run, 30-50 mg of sample is heated at 20°C/min in flowing N_2 to 360°C to remove surface impurities. The sample is then cooled to 120°C in N_2 and the gas stream is switched to a mixture of 5% O_2, 7% H_2O, balance N_2. Because at this temperature O_2 and H_2O are adsorbed onto the carbon, the sample weight is allowed to stabilize before SO_2 (2500 ppmv) is introduced into the TGA. Uptake of SO_2 is monitored for up to 60 h.

Methane adsorption capacities of activated carbons are determined using the PTGA [2]. The samples are degassed at 150°C for 3 h in N_2 prior to adsorption of methane. Adsorption of methane is done at 25°C at pressures of 0, 100, 200, 300, 400 and 500 psig. The rate of methane uptake and the adsorption capacity (g methane/g char) are recorded by a computerized data acquisition system.

The nature and extent of oxygen functional groups on the carbon surface are determined by temperature programmed desorption (TPD) [8]. TPD experiments are performed in a 2.5 cm ID stainless steel fixed-bed reactor system. In a typical run, 0.5 g of sample is heated at 5°C/min to 1000°C in N_2 flowing at 0.5 L/min. Temperature is held at 1000°C until evolved CO and CO_2 return to baseline concentrations, indicating complete desorption. Concentrations (ppm) of CO and CO_2, time and temperature are recorded by a computerized data acquisition system. The areas under the CO and CO_2 curves are converted to the amount of oxygen present on the carbon surface.

RESULTS AND DISCUSSION

Carbon production

Partial gasification during activation serves to develop surface area and porosity in char. The overall surface area and type of pore structure of the activated carbon may be controlled by the rate and

extent of gasification during activation. Chars may be activated with oxygen, steam, CO_2, or a mixture of these gases. At a given temperature, the relative rates of reaction for these gases range over several orders of magnitude, with O_2 > steam > CO_2. Thermogravimetry (TG) provides a method for directly monitoring both the rate and extent of activation as the reaction proceeds. This allows for good control of process conditions when preparing an activated carbon with characteristics needed for a particular application. Figure 1 shows the activation profile of a carbon prepared from a utility fly ash. Initial activation was done at 950°C in CO_2 for 1 hour, with a weight loss of only 5%. Surface areas of activated carbons, not corrected for ash content, generally increase monotonically during activation up to about 80% weight loss (conversion) [9]. After 1 h, the gas composition was changed to 50% steam/50% CO_2, which resulted in a total weight loss of 30% in 2 h. Using the data from Figure 1, a larger sample was prepared in a horizontal tube furnace that had surface area and adsorption properties similar to the sample prepared in the TGA.

Carbon Characterization

Carbons with a variety of surface areas and pore size distributions have been developed at the ISGS for various applications. One such application is the removal of contaminants from flue gas streams of waste incinerators [10]. STEAG, of Essen, Germany, has developed a process in which a bed of low surface area, low cost carbon is used to remove contaminants such as particulate matter, dioxins, furans, mercury, SO_2, other acid gases and heavy metals from flue gas. The ISGS was asked to prepare a low surface area, low cost activated carbon from Illinois coal for testing in the STEAG a/c/t™ process. Process variables, developed to prepare gram quantities of carbons in the laboratory, were used ultimately to prepare 500 pounds of activated carbon for tests in STEAG's pilot plant [11]. STEAG believes that the SO_2 adsorption behavior of a carbon is indicative of its ability to remove other contaminants from flue gas streams using their process [12]. Surface area and SO_2 adsorption behavior of the activated carbons prepared in each stage of scale up were used as guides to ensure that a carbon was produced with desired properties for the STEAG process. TG provided a rapid method for determining the relative rates of SO_2 adsorption and equilibrium SO_2 adsorption capacity of a carbon using only milligram quantities of sample. Figure 2 shows the kinetics of SO_2 adsorption in a simulated flue gas for the ISGS carbon and the carbon STEAG currently uses in their process (Herdofenkoks). Although the surface area of the Herdofenkoks was nearly three times that of the ISGS carbon, the initial rate of SO_2 adsorption was much greater for the ISGS carbon. This carbon has proven effective in STEAG's process during pilot plant tests.

TG has been used to study the effect of adsorption temperatures, gas compositions and carbon characteristics on SO_2 adsorption by carbons [13]. Figure 3 shows SO_2 adsorption by an air activated carbon heated to different temperatures in inert gas after activation. These carbons all had surface areas of about 300 m^2/g, suggesting that surface area is not a good indicator of SO_2 adsorption [13]. Corresponding TPD profiles for the air activated carbons show that as the parent carbon was heated to higher temperatures, less oxygen was present on the surface of the carbon (Figure 4). These results suggest that SO_2 capacity is inversely related to the amount of oxygen on the surface of the carbon. Similar data have been found for other carbons. These results were used to propose a new mechanism for SO_2 adsorption on activated carbons [14].

TG also permits rapid evaluation of the thermal regeneration of carbons, and may be used to predict the life cycle of adsorbents in different applications. Adsorption/desorption cycles were performed in the TGA to determine regenerative properties of an activated carbon prepared from Illinois coal by steam activation, followed by HNO_3-treatment and thermal desorption at 925°C [4]. After initial SO_2 adsorption, the carbon was regenerated in the TGA by heating to 360°C. Regeneration of the carbon in this manner resulted in a significant decrease in the SO_2 adsorbed in subsequent adsorption/desorption cycles (Figure 5). These results have been explained by the formation of stable oxygen complexes on the surface of the carbon that inhibit adsorption of SO_2 [4]. It is thought that regeneration of this carbon at higher temperatures would restore its original SO_2 capacity, but this remains to be determined.

Carbons prepared from different precursors such as coal, fly ash and tires may have different adsorption properties not only because of their structure, but also due to different composition. A significant portion of the carbonaceous material is lost during pyrolysis and activation, and non-volatile mineral matter present in the precursor is concentrated in the remaining carbon product. Proximate analysis of activated carbons can be done rapidly with TG to provide information on the moisture, volatile matter, fixed carbon, and mineral matter present in the carbon. Figure 6 shows proximate analyses for a fly ash carbon and three steam activated chars made from Illinois coal.

Activated carbon may be used for onboard methane storage in natural gas vehicles. This storage technology is less expensive, occupies less space and costs less to refuel than compressed natural gas storage, and may result in vehicles that are lighter and have much greater storage density at low

pressure (< 35 atm). Activated carbons that might be suitable for this application have been prepared at the ISGS from both Illinois coal and scrap tires [2]. Pressurized TGA allows methane adsorption isotherms to be measured for small quantities of sample as shown in Figure 7. Shown for comparison is the isotherm for a commercial activated carbon Calgon BPL. Activated carbons prepared from scrap tires exhibit a wide range of adsorption capacities. Methane adsorption capacities (g methane/g char) of some tire-derived carbons were within 10% of the BPL carbon.

SUMMARY

Thermal analysis techniques have been used at the ISGS as an aid in the development and characterization of carbon adsorbents. Promising adsorbents from fly ash, tires, and Illinois coals have been produced for various applications. Process conditions determined in the preparation of gram quantities of carbons were used as guides in the preparation of larger samples. TG techniques developed to characterize the carbon adsorbents included the measurement of the kinetics of SO_2 adsorption, the performance of rapid proximate analyses, and the determination of equilibrium methane adsorption capacities. Thermal regeneration of carbons was assessed by TG to predict the life cycle of carbon adsorbents in different applications. TPD was used to determine the nature of surface functional groups and their effect on a carbon's adsorption properties.

REFERENCES

1.   Lizzio, A.A. and Rostam-Abadi, M., "Production of Carbon Molecular Sieves from Illinois Coal," *Fuel Processing Technology*, 34, pp 97-122, 1993.
2.   Brady, T.A., "Adsorbent Carbons from Waste Tires for Natural Gas Storage," M.S. Thesis in Environmental Engineering in Civil Engineering, University of Illinois at Urbana-Champaign, 1996.
3.   Sun, J., Rood, M.J., Rostam-Abadi, M., Lizzio, A.A., "Natural Gas Storage with Activated Carbon from a Bituminous Coal," special issue of *Gas Separation and Purification*, in press.
4.   Lizzio, A.A., DeBarr, J.A., Donnals, G.L., Kruse, C.W., Rood, M.J., Gangwal, S.K., "Production and Use of Activated Char for Combined SO_2/NO_x Removal," Final Technical Report, Illinois Clean Coal Institute, Carterville, Illinois, 1995.
5.   DeBarr, J.A., Rapp, D.M., Rostam-Abadi, M., Lytle, J.M., Rood, M.J., "Valuable Products from Utility Fly Ash," First Quarterly Technical Report, Illinois Clean Coal Institute, Carterville, Illinois, 1995.
6.   Lizzio, A.A., DeBarr, J.A., Donnals, G.L., Kruse, C.W., Rood, M.J., Gangwal, S.K., "Production and Use of Activated Char for Combined SO_2/NO_x Removal," Third Quarterly Technical Report, Illinois Clean Coal Institute, Carterville, Illinois, 1994.
7.   DeBarr, J.A., Lizzio, A.A., Daley, M.A., "Adsorption of SO_2 on Bituminous Coal Char and Activated Carbon Fibers from Phenol Formaldehyde," ACS preprints, Fuel Chemistry Division, 1996.
8.   DeBarr, J.A., Lizzio, A.A, "New Insights on the Mechanism of SO_2 Removal by Carbon," Proceedings of the 22nd Biennial Conference on Carbon, San Diego, CA, July 1995.
9.   Lizzio, A.A and Radovic, L.R., "On the Usefulness of Total Surface Area for Predicting Carbon Gasification Reactivity Profiles", 19th Biennial Conference on Carbon, University Park, PA, 1989.
10.   Brueggendick, H. And Pohl, F.G., "Operating Experience with STEAG's Activated Carbon Process-a/c/t™ in European Waste Incineration Plants," Proceedings of Tenth Annual International Pittsburgh Coal Conference, Pittsburgh, PA, 1993.
11.   Lizzio, A.A., DeBarr, J.A., Kruse, C.W., "Development of Low Surface Area Char for Cleanup of Incinerator Flue Gas," Proceedings of the 22nd Biennial Conference on Carbon, San Diego, CA, July 1995.
12.   Rummenhol, V., Presentation to Illinois Coal Development Board, Illinois Clean Coal Institute and Illinois State Geological Survey, Champaign, IL, March 2, 1994.
13.   DeBarr, J.A., "The Role of Free Sites in the Removal of SO_2 from Simulated Flue Gases by Activated Char," M.S. Thesis in Environmental Science, University of Illinois at Urbana-Champaign, 1995.
14.   Lizzio, A.A., DeBarr, J.A., "The Mechanism of SO_2 Removal by Carbon," ACS preprints, Fuel Chemistry Division, 1996.
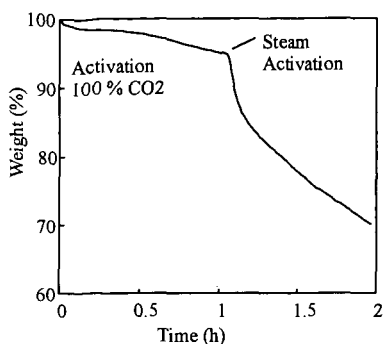
Figure 1. Activation profile of carbon prepared from a utility flyash.
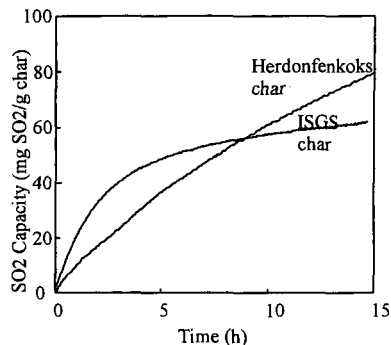
Figure 2. SO2 adsorption of ISGS and Herdonfenkoks chars.
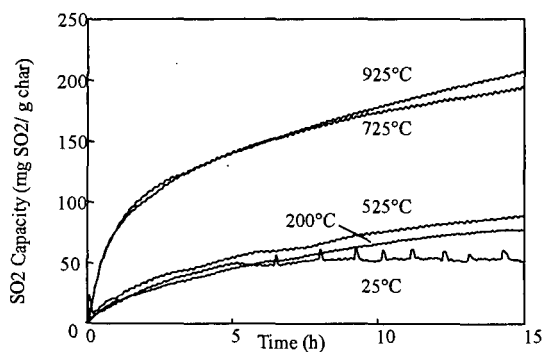

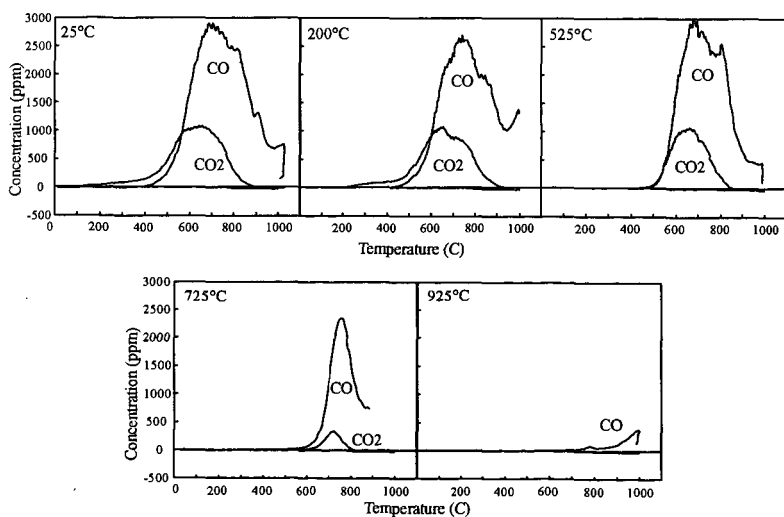Figure 3. SO2 adsorption profiles of air activated carbons heated to different temperatures.

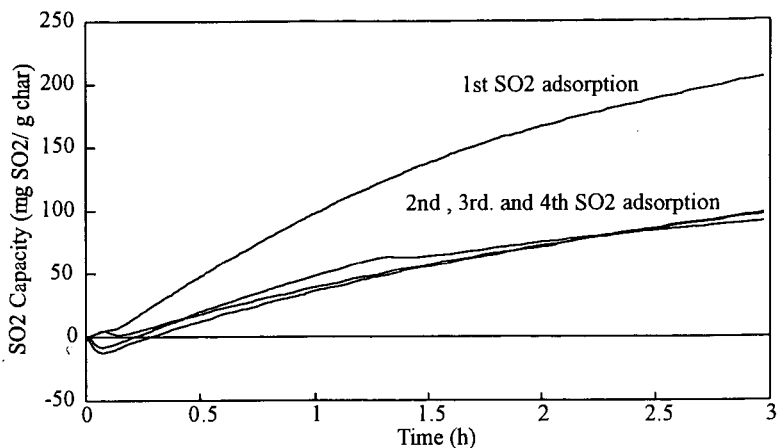Figure 4. TPD profiles of air activated carbons heated to different temperatures.

Figure 5. Thermal regeneration of nitric acid treated IBC-102 char.
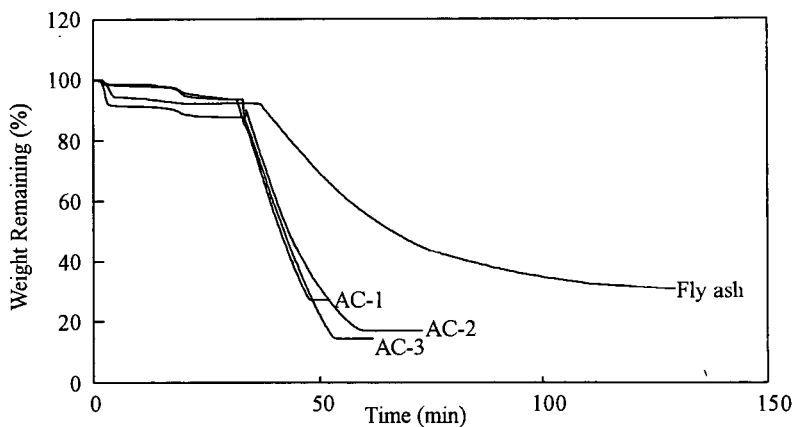

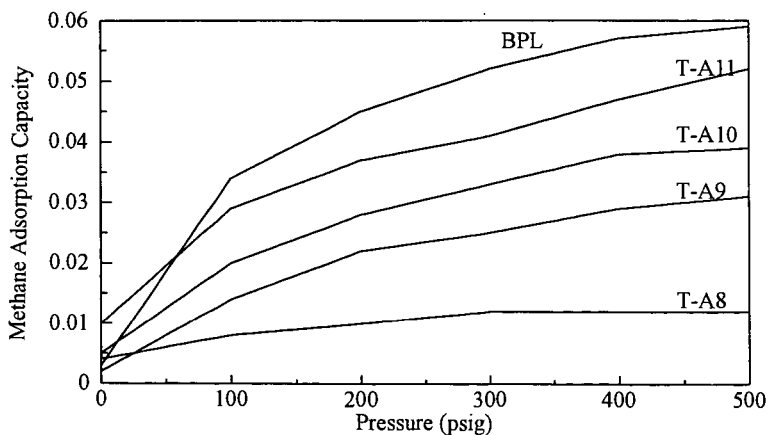Figure 6. Proximate analysis of activated carbons.

Figure 7. Methane adsorption capacity for carbons (g methane/g char at 298K).

AN EXAMINATION OF BURNING PROFILES AS A TOOL

TO PREDICT THE COMBUSTION BEHAVIOR OF COALS

Sarma V. Pisupati

Energy and Fuels Research Center
The Pennsylvania State University
C211 Coal Utilization Laboratory
University Park PA 16802

Keywords: Burning profiles, Combustion behavior, DTGA

Introduction

Thermal analytical techniques such as thermogravimetric analyzer (TGA) have been used extensively in characterizing the thermal behavior of coals. Intrinsic reactivity (expressed as instantaneous, average and time required for 50% burnoff (τ_{50})), volatiles release profiles and burning profiles are common parameters used to predict combustion behavior in a large combustion system. The burning profile provides information on the combustion rate including intensity of reaction, heat release rate and residence time requirements for a fuel compared to those of a fuel with known combustion characteristics. The technique for determining the burning profile was developed by Babcock and Wilcox as a method for evaluating fuels to select the optimum boiler design (Wagoner and Duzy, 1967). The technique has been modified by others (Cumming, 1984; Cumming and McLaughlin, 1982; Morgan et al., 1986, 1987; Smith et al., 1981) to characterize the combustion behavior of coals in a laboratory. However, information on the validity of these profiles to industrial scale and utility boilers is scarce.

Penn State Energy and Fuels Research center evaluated combustion behavior of coals in various devices ranging from drop tube reactor to an industrial scale boiler. This paper summarizes the observations, and discusses the applicability of the data from the profiles to predict the combustion behavior.

What is a Burning Profile ?

A burning profile is a plot of the rate at which a solid fuel sample changes weight as a function of temperature, when heated at a constant rate. Cumming and McLaughlin (1982) used four characteristic temperatures to interpret a burning profile; 1) the first initiation temperature where the weight first begins to fall (IT_{VM}); 2) the second initiation temperature where the rate of weight loss accelerates due to the onset of combustion of char (IT_{FC}); 3) the peak temperature (PT) where the rate of weight loss is a maximum; and 4) the burnout temperature, where the weight becomes constant at the completion of burning (BT). Cumming (1984) later proposed in lieu of the above four characteristic temperatures, a weighted mean apparent activation energy value which correlated well with the PT. These characteristic temperatures as proposed by Cunning and McLaughlin (1982) have been used with minor modifications by Morgan et. al. (1986, 1987) to interpret burning profiles.

Literature Review

Wagoner and Winegartner (1973) reported a successful combustion evaluation of fluid coke from a California crude and a delayed coke derived from a Louisiana crude oil with respect to a reference combustion profile of Pocahontas coal. These profiles were reported to predict the performance of these fuels in an industrial boiler. Smith et al. (1981) later evaluated the relative ease of combustion of sixty-six coals ranging in rank from lignite to low-volatile bituminous and with low mineral matter contents. The activation energies obtained varied from 4 KJ mol $^{-1}$ in the high temperature, diffusion controlled zone to 290 KJ mol $^{-1}$ in the chemical reaction controlled, low-temperature zone.

Morgan et al.(1986) correlated the BTs from the burning profiles to predict burnout values based on a model that uses data on oxidation rates of chars prepared in an entrained flow reactor and coal properties. Nine coals were ranked based on their performance in a pilot scale pulverized coal combustor and the ranking correlated well with the characteristic temperatures from the burning profiles of the coals. Superior burnout has been reported with coals having low burnout temperatures.

Wagoner and Winegartner (1973) reported that the Pocahontas coal with a volatile matter content of 14-16.5% and a Bureau of Mines char with a 5% volatile matter should have identical combustion characteristics based on their burning profiles. But, Demeter et al. (1973) found that in a 500 lb/hr experimental coal combustor the Pocahontas coal burnt with out any auxiliary fuel or

preheat of the primary air whereas the Bureau of Mines char needed preheat or auxiliary fuel to burn successfully .

Experimental

In this study combustion behavior of coals as evaluated in a drop tube reactor, a research boiler generating 1,000 lb/h steam and a 15,000 lb/h (steam) industrial scale demonstration boiler is reported. For coals tested in these devices, burning profiles were obtained in a Perkin Elmer TGA.

The experimental variables in the TGA which were found to affect the rate of burning and hence the burning profile included heating rate, sample weight, shape and material of construction of the sample pan and the heat capacity of the pan. Although the experimental conditions originally employed by Wagoner and Duzy (1967) allow the combustion rate to be limited by the diffusion rate of oxygen, as shown by Smith et al. (1981), and the temperature of the sample may not have been representative of the temperature of the burning fuel, the burning profile data obtained in the TGA seemed to produce consistent results in the evaluation of the relative combustion performance of unknown fuels with different equipment in different laboratories.

The results during optimization of test conditions indicated a good reproducibility of characteristic temperatures (± 1.8°C). The effect of heating was determined using an Upper Freeport seam coal for heating rates of 5, 10, 15, and 20°C min^{-1} and a sample weight of 5 mg. The results are shown in Table 1. It is seen from the results that as the heating rate was increased the characteristic temperatures proportionately increased which did not change the relative ranking of a coal. At higher heating rates some low rank coals ignited and therefore, led to uncontrolled temperature of the sample. Hence, a heating rate of 10°C min^{-1} was used in this study. The effect of sample amount was not as significant as that of heating rate and a sample size of 5 mg was used.

Table 1. Effect of Heating Rate on Characteristic Temperatures

Heating Rate	5°C/min	10°C/min	15°C/min	20°C/min
Initial Temperature (IT)	325.6	337.5	350.0	347.0
Peak Temperature (PT)	494.1	505.1	522.6	618.3
Burnout Temperature (BT)	542.0	616.0	618.3	630.0

The following characteristic temperatures as defined in earlier work (Pisupati et al., 1991 and Pisupati and Scaroni, 1993) were obtained for each sample. The Initial Temperature (IT), is defined as the temperature at which the rate of weight loss exceeded 0.1% min^{-1} after the initial moisture loss peak. The Peak Temperature (PT) is defined as the temperature at which the rate of weight loss was maximum and the Burnout Temperature (BT) is the temperature at which the rate of weight loss decreased to 1.0 % min^{-1}.

Results and Discussion

In an earlier study conducted in the laboratory, a set of five fresh and companion crop coals was used to investigate the influence of natural weathering (in-situ) and low-temperature oxidation on the combustion behavior of the coals. In the study a fresh coal sample was oxidized in the laboratory for 2 hours, and for 72 hours in stagnant air to oxidize the coal to a similar level to that of the naturally weathered crop coal. Combustion behavior of the suite of coals was determined in the laboratory by obtaining burning profiles and the combustion efficiency in a drop tube reactor. The characteristic temperatures were derived from the burning profiles. Figure 1 shows the profiles for the Fort Palmer fresh and crop coals. Analogous profiles were obtained for other samples. The initial negative weight change in the burning profiles is due to the loss of moisture. The second positive peak at around 300°C for the fresh coal samples is attributed to the adsorption of oxygen, and represents a weight gain of about 3%. Adsorption of oxygen by the significantly oxidized crop coals was not apparent and these coals had lower initial temperatures (approximately 20-115°C less) than the corresponding fresh coals. This can be explained as follows. Desorption of the preoxidized oxygen in the crop coals creates unoccupied sites for further oxygen adsorption and subsequent desorption, thereby initiating significant weight loss at much lower temperatures.

For these oxidized coals, it was observed that there were two distinct peaks The lower peak is attributed to the decomposition of the carbon-oxygen complex and to the devolatilization of the coal. The height of this peak for the crop coals was proportional to the degree of oxidation. These profiles indicated that combustion is expected to be complete for the crop coals at lower temperatures than for their companions for otherwise the same operating conditions.
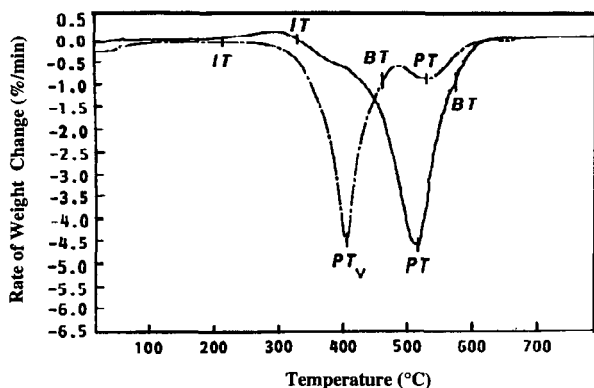
Figure 1. Burning Profiles for the Fort Palmer Fresh (———) and Crop (- - -)Coals

The combustion efficiencies were conducted in a vertical, electrically heated drop tube reactor (DTR). Details of the reactor can be seen elsewhere (Pisupati and Scaroni, 1993). A relatively low combustion temperature of 1,300°C was used to accentuate the differences in combustion efficiencies. A coal feed rate of 0.33 g min $^{-1}$ and a total combustion air of 4 l min $^{-1}$, which corresponds to an excess air of 25%, was used. The results from the combustion studies in the drop tube reactor were consistent with observations from the burning profiles. Figure 2 shows a correlation between the burning profile data and the combustion efficiency determined in the DTR. The figure indicates that the lower the initial temperature, the higher the combustion efficiency.
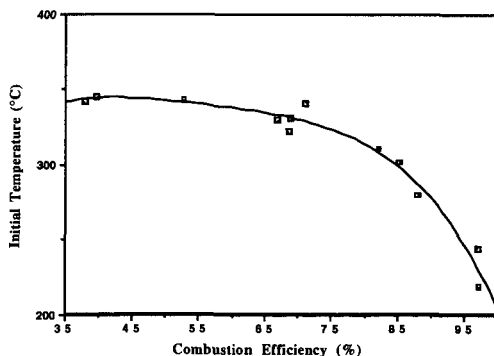
Figure 2. Initial temperatures (IT$_{bp}$) Obtained from Burning Profiles as a Function of Combustion Efficiency Determined in the DTR.

In another study, combustion behavior of two Pennsylvania bituminous coals, an Indonesian subbitminous coal, and blends of PA and Indonesian coals was determined in a research boiler. Burning profiles were obtained for these coals and blends in the TGA prior to the combustion tests in the boiler. The compositional analysis of the coals is provided in Table 2.

The combustion tests were conducted in a 1,000 lb steam /h water tube research boiler with a maximum thermal input of 2 million Btu/h. The boiler is a standard Cleaver Brooks "A-frame" water tube boiler. The combustion chamber is 3 ft wide, 3 ft high and 7 ft long. To promote evaporation and ignition of difficult-to-burn fuels, a ceramic quarl extends the length of the combustion chamber by two feet. The quarl and the boiler are preheated by burning natural gas prior to introducing of the test fuel until the surface temperature was approximately 900°F. The

15

Table 2. Proximate Analysis (wt.%, d.b.)

	100% PA	80% PA - 20% Indonesian	50%PA - 50% Indonesian	100% Indonesian	100% Upper Freeport (PA)
Volatile Matter	20.47	25.17	32.74	46.20	31.89
Fixed Carbon	67.19	64.70	60.13	52.14	61.61
Ash	12.34	10.13	7.13	1.66	6.50
Moisture (as-fired)	1.69	7.46	12.73	21.44	7.14
H.H.V.(Btu/lb as fired)	13,680	12,679	11,617	10,098	13,680

preheated quarl acts as a source of radiant heat to help support the flame. Pulverized coal was fed from a two foot diameter hopper to an eductor via a 1.5-inch diameter screw feeder. The pulverized coal was entrained by dense phase transport ($\approx$1 lb of air/lb of coal) into an annular section and then through a swirler. The feed rate of pulverized coal was monitored by load cells. Slowly, the coal firing rate was increased while reducing simultaneously the natural gas rate until the desired load was obtained on coal. A thermal input of approximately 1.6 MBTU/h was held constant throughout the testing. The combustion gases, at the end of the radiant section, are split into two convective passes, one on each side of the radiant combustion chamber. The gases exiting the convective section are cooled to below 500°F in an economizer located on top of the combustion chamber and then pass into a baghouse. The products of combustion (O_2, CO_2, CO, NO_x and SO_2) are monitored at the economizer outlet with a series of on-line gas analyzers. The ash samples were collected and analyzed for moisture and unburnt carbon to calculate the carbon burnout using the ash tracer technique as follows:

$$\text{Combustion Efficiency (\%)} \;=\; \left[1 - \frac{A_c\left(100 - A_r\right)}{A_r\left(100 - A_c\right)}\right] \times 100$$

where, A_c = wt. percent ash in the coal, and A_r = wt. percent ash in the residue

Figure 3 shows a correlation between the Initial temperatures (from the burning profiles in a TGA) and the combustion efficiencies determined in the boiler. The plot shows a good correlation between the burning profile data and the combustion efficiencies as determined in the boiler. However, the flue gas oxygen levels were 5.5 and 5.9% for the Indonesian and PA coals, whereas for the Upper Freeport coal the boiler oxygen level was 6.5% and therefore, the combustion efficiency was slightly higher than expected from the interpolation. This underscores the importance of the operating conditions and sample characteristics.

Two bituminous coals were fired in a 15,000 lb/h industrial scale, demonstration boiler as micronized coals (80% passing through US standard 325 mesh instead of 80% passing 200 mesh). The boiler is a D-type package boiler designed for fuel oil. The boiler and auxiliaries are adapted with minor modifications to burn coal and coal-water slurry fuels. Details of the boiler can be found elsewhere (Pisupati et al., 1993). The combustion efficiency data obtained in the demonstration boiler is shown on Figure 3 as open diamonds. The combustion efficiency obtained for both coals was varying from 90 to 95% depending on the operating conditions such as excess air and fuel firing rate etc. The data plotted were for the conditions when the boiler oxygen was 3.2% and the firing rate was 14.8 MMBtu/h for both coals. The initial, peak, and the burnout temperatures for the Brookville bituminous coal were 310.8, 492.4 and 555°C, respectively. The initial, peak, and the burnout temperatures for the Kentucky bituminous coal were 313.8, 508.8 and 577.5°C, respectively. Very close initial temperatures reflected in close combustion efficiencies in the boiler under identical conditions. This also shows that the initial temepratures correlate well with the combustion efficiency. This probably is due to the earlier decomposition and thereby causing physical and chemical structural changes of the residual char earlier and hence a change in the reactivity.

Combustion Studies of blends of coals

One of the puzzling questions has been whether the characteristic temperatures obtained from burning profile hold good for blends of coals. Cumming (1989) has reported that the burning profile of a blend of coals of different rank (bituminous and anthracite) indicates that the fuels burn without interaction. Similar observations were made at this laboratory with bituminous and anthracite blends. However, blends of bituminous and lower lank coals indicated a linear correlation. Artos and Scaroni (1993) have shown that when a bituminous coal is blended with a subbituminous coal, the initial temperatures (IT) were proportionately lower with increasing

16

percent of a subbituminous coal. The study also showed a linear increase in the combustion efficiency in the DTR with the addition of the subbituminous coal.
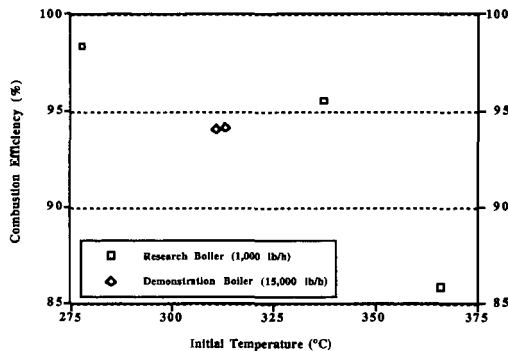
Figure 3. **Correlation between the Initial Temperatures and the Combustion Efficiencies obtained in the 1,000 lb/h Research Boiler and in the 15,000 lb/h Demonstration Boiler.**

In this study, an Indonesian subbituminous coal was blended with a Pennsylvania bituminous coal and the burning profiles and combustion behavior was determined in the TGA and the Research Boiler, respectively. The burning profiles are shown in Figure 4 for the Indonesian coal and blends with PA coal in various proportions. It can be clearly seen that there is a clear progressive increase in the characteristic temperatures with the increase in the proportion of the PA coal. This study confirms the observations of Artos and Scaroni (1993). The difference between the IT and the BT for the blends is higher indicating the initial decomposition starts at a lower temperature corresponding that of the lower rank coal in the blend and the combustion is not complete until the component with lower reactivity is burned. This suggests that there possibly is no influence of one coal on the other in a TGA. However, since there is a good correlation between the initial temperature and the combustion efficiency it may be concluded that blending coal which decomposes at lower temperature with less reactive coal, the former influences the combustion behavior of the latter in a boiler with self sustaining flame.
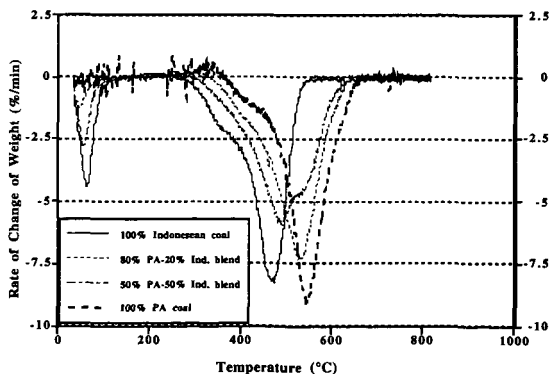
Figure 4. **Burning Profiles of Pennsylvania Bituminous Coal Blends**

Figure 5 shows a correlation between the initial temperature and the combustion efficiency obtained in the 1,000 lb/h research boiler for the coals and coal blends.

Summary

Burning profiles of a suite of coals ranging from fresh coals to severely weathered coals, and subbituminous coals and bituminous coals were obtained. Combustion efficiencies were also determined in a Drop tube reactor, 1,000 lb/h research boiler, and a 15,000 lb/h industrial scale demonstration boiler. A good correlation was obtained between the initial temperature and the

17

combustion efficiency obtained under identical conditions was observed. A burning profile appears to be a good tool for evaluation of the relative combustion characteristics of fuels at a laboratory scale, when it is difficult, or there is not enough fuel, to test fire in a large installation.
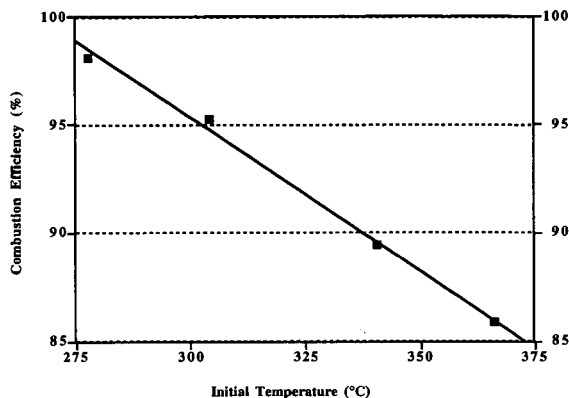

Figure 5. Correlation Between the Initial Temperatures and the Combustion Efficiencies Obtained in the Research Boiler

Because various investigators employed experimental conditions that were different from those originally proposed by Wagoner and Winegartner (1973), yet still obtained reproducible and interpretable results, it can be concluded that any laboratory using the technique of determining burning profiles to characterize the combustion behavior of coals can use their own reference standard conditions as long as all the samples (both the reference and unknown fuel) are tested under those standard conditions to obtain interpretable and meaningful data. However, it is not yet clear whether these profiles could predict the combustion efficiency of coal-water slurry fuels. The data generated under identical conditions may predict the combustion behavior of an unknown fuel under similar conditions. Those conditions may not be the optimum conditions for the fuel.

Acknowledgments

References

Artos, V. and Scaroni, A. W., (1993) Fuel, 72, 927.

Cumming, J. W. and Mc Laughlin, J. (1982) Thermochemica Acta, 57, 253.

Cumming, J. W. (1984) Fuel, 63, 1436.

Cumming, J. W. Thermochemica. Acta, 1989, 155, 151

Demeter, J. J., McCann, C. R. and Bienstock, D. (1973) ASME Paper No 73-WA/Fu2, presented at the Winter Annual Meeting, ASME, New Orleans, LA.

Morgan, P. A., Robertson, S. D. and Unsworth, J. F., Fuel, 1986, 65, 1546.

Morgan, P. A., Robertson, S. D. and Unsworth, J. F., Fuel, 1987, 66, 210.

Pisupati, S. V., Scaroni, A. W. and Stoessner, R, (1991) Fuel Processing Tech., 72, 779.

Pisupati, S. V., Britton, S. A., Miller, B. G. and Scaroni, A. W.(1993) Proceedings of the 18th International Technical Conference on Coal Utilization and Fuel Systems, Coal and Slurry Technology Association, April 26-29, Clearwater, Florida, FL, pp. 349 - 360.

Pisupati, S. V. and Scaroni, A. W., (1993) Fuel, 72, 779.

Smith, S. E., Neavel, R. C., Hippo, E. J. and Miller, R. N. (1981) Fuel, 60, 462.

Wagoner, C.L.and Duzy, A. F., ASME Paper 67-WA/FU-4, Winter Annual Meeting and Energy Systems Exposition, American Society of Mechanical Engineers, Pittsburgh, 1967.

Wagoner, C. L. and Winegartner, E. C. Trans ASME Ser. A, J. Eng. Power, 1973, 95, 119.

EFFECT OF PRESSURE ON PREPARATION OF SO_2 SORBENT FROM LEONARDITE AND ON SO_2 ADSORPTION BY LIMESTONE AND DOLOMITE AS DETERMINED FROM PRESSURE THERMOGRAVIMETRIC ANALYSIS

R.C. Timpe, R.W. Kulas, and B.C. Young
University of North Dakota Energy and Environmental Research Center
15 North 23rd Street
Grand Forks, North Dakota 58203

Keywords: Pressure TGA, SO_2 adsorption, limestone

ABSTRACT

Control of SO_2 with limestone or dolomite is state-of-the-art at the present time, but activated carbon in the form of low-rank coal char also has some promise. A process for production of the sorbent includes selection of temperature regime, pressure, activation gas, residence time, and additive. The effect of pressure on the behavior of sorbent during SO_2 removal from flue gas or during production of sorbent carbon is the parameter least found in the literature. Pressure thermogravimetric analysis (pTGA) provides a simple means of studying this effect.

In this study, a fully calcined and a partially calcined dolomite and limestone were tested for SO_2 sorbent characteristics under pTGA at 840°C at 160 psig. The stones were characterized by capacity and rate of sorption of SO_2.

A leonardite was carbonized at 480°C and activated at 800°C under nitrogen at ambient, 150, 300, and 450 psig. Each char was then exposed to a flowing gas mixture containing argon and SO_2. The char produced at lower pressures adsorbed more SO_2 than those produced at successively higher pressures as determined by TGA and confirmed by American Society for Testing and Materials (ASTM) total sulfur measurements.

INTRODUCTION

Combustion of coal provided approximately 55% of the available electric power in the United States in 1993 with the burning of approximately 814,000 tons (1) of coal. As the demand for electricity increases, the demand for coal will also increase, resulting in accelerated depletion of our coal supplies. At present, the quality of the coal mined to produce this electricity, in terms of pollutants such as sulfur, nitrogen, and heavy metals liberated to the environment, is relatively clean compared to much of the remaining minable coal reserves. Government, utilities, and researchers have been aware of the potential environmental consequences of burning "dirtier" coal for more than three decades and have been attempting to deal with the problem through application of known technology and development of newer, more efficient, less costly methods of emission control. Both precombustion and postcombustion methods have been attempted as means to remove potential pollutants from coal before they enter the environment. Industrially, precombustion cleaning of bituminous coal by physical means, e.g., float-sink, froth floatation, magnetic separation, has met with mild success, while cleaning by chemical means, e.g., molten caustic leaching, has been generally discounted as being too costly. Similarly, physical or chemical cleaning of low-rank coal results in excessive cost for the product.

For lack of economically and technically feasible precombustion cleaning methods, most environmental protection from the emissions from coal combustion is currently done by cleaning stack gas from the utility. Sorbents such as limestone ($CaCO_3$) and dolomite ($CaCO_3-MgCO_3$) are commonly used for scrubbing SO_2 from the gas. Well-known processes such as those of Pure Air's Advanced Scrubber, Chiyoda's CT-121 Scrubber, S-H-U wet limestone scrubber, LIFAC sorbent injection system, Bechtel's Confined Zone Dispersion Process, AirPol Gas Suspension Adsorption Process, the Babcock and Wilcox LIMB Process, and Consolidation Coal's Coolside Process all make use of limestone in either the raw or calcined form as the sorbent for SO_2 emissions (2). Factors concerning the cleaning efficiency of the stones include partial pressure of SO_2, contact time, degree of calcination, surface area, temperature, and surface incidence of inert material. Each of these factors can be studied using thermal analysis techniques. Pressure thermogravimetric analysis is particularly useful for these studies since it allows the determination of the effect of all of these factors.

Similarly, preparation of sorbents such as activated carbon is affected by each of the properties above.

EXPERIMENTAL

Prior to testing, the dolomite and limestone samples were crushed in a hammer mill and then further reduced in size on a Braun mill. The samples were reconstituted by recombining sieve fractions and mixing thoroughly.

Two tests were performed on each of the two $CaCO_3$-based samples using the pressure thermogravimetric analyzer (pTGA). The test methods used to determine SO_2 uptake from a mixed gas stream by each sample were as follows:

The samples were crushed in mortar and pestle to pass 20-mesh screen (0.84 mm = 840 μm). The samples were classified into four size fractions by sieving. Class sizes were 250-840 μm, 150-250 μm, 75-150 μm and < 75 μm. To obtain test results which would represent sorption results characteristic of the bulk material, size fractions were recombined prior to pTGA testing.

Method 1. Approximately 20 mg of crushed reconstituted sample was loaded onto the sample pan of an SRE 1990/600 pTGA. The cover was replaced, and the sample chamber was pressurized to 160 psig with N_2 and the gas flow adjusted to nominally 100 mL/min. Heatup was approximately 100°C/min to 840°C, and the sample was calcined at that temperature for up to 150 minutes. Nitrogen flow was then replaced by a synthetic sulfated combustion gas mixture containing 13% CO_2, 3.5% O_2, and 0.25% SO_2 (balance N_2), and flow was continued for at least 60 minutes. The tests were terminated and the system cooled down under flowing N_2.

Method 2. Approximately 20 mg of crushed reconstituted sample was loaded onto the sample pan of the SRE 1990/600 pTGA. The cover was replaced, and the sample chamber was pressurized to 160 psig with a gas mixture containing 13% CO_2 and 3.5% O_2 (balance N_2) and the gas flow adjusted to nominally 100 mL/min. Heatup was approximately 100°C/min to 840°C, and the sample was held at that temperature for up to 90 minutes (for half-calcination). The synthetic sulfated combustion gas mixture containing 13% CO_2, 3.5% O_2, and 0.25% SO_2 (balance N_2) was then introduced, and the tests were completed as in Method 1.

The effect of pressure on the sorption capacity of activated char prepared from a North Dakota leonardite was studied. The sample was carbonized at 480°C under N_2 at each of four pressures: 450 psig, 300 psig, 150 psig, and ambient pressure. Each sample was activated under N_2 at 800°C at its respective pressure. The resulting activated char was tested for SO_2 adsorption capacity. Each sample analyzed for SO_2 capacity was then analyzed for total sulfur content.

RESULTS AND DISCUSSION

The results of sieving the crushed dolomite and limestone samples are shown in Table 1. Over 75% of the limestone consisted of particles less than 75 microns in size compared with ~57% of the dolomite under the same crushing conditions.

From the results of the sieve fractions, it can be assumed that the limestone would have greater surface area, although not measured in this study, than that of the dolomite since it has a much larger fines fraction. Therefore, the former should have the greater capacity for SO_2 adsorption than the latter. However, from the results of SO_2 uptake in Table 2, it appears that that is not true. In addition, the rate of uptake of SO_2 should also be more rapid on that with the larger surface area, but instead the rates are nearly the same for the fully calcined samples and are identical for the half-calcined samples. If the difference between rates and capacities of the two samples were consistent, differential decrepitation of the materials might explain the apparent contradiction. However, this does not appear to be the case since the rates of uptake are the same while the capacities differ. The presence of the $MgCO_3$ in the dolomite may be the best explanation for the higher sorptive capacity of the dolomite. Assuming limestone to be $CaCO_3$ and dolomite to be $CaCO_3$-$MgCO_3$, there are more metal ions per unit mass in dolomite than in limestone resulting in the potential for more available SO_2 receptor sites. The presence of the $MgCO_3$ may catalyze the calcination and thus activate the surface more effectively. Additional data are needed to confirm this as a reason for the observed difference in SO_2 sorption between the dolomite and the limestone samples.

The SO_2 adsorbed on the activated char shown in Table 3 indicates that preparation of activated char from leonardite under pressure results in decreased activity toward SO_2. This is supported by the total sulfur measurements made on the residual activated char after it has adsorbed the SO_2. The decrease in SO_2 adsorption results from the loss of active sites on the char. The apparent pressure dependence may be due to heavy tar formation at the openings of pores resulting in a loss in total surface area and, consequently, the loss of active sites for SO_2 sorption.

CONCLUSIONS

- Both the fully calcined and half calcined dolomites tested were better SO_2 sorbers than the corresponding calcined forms of the limestone tested.

- Although their capacities for SO_2 differed, the rates at which the dolomite and limestone adsorbed were similar for the fully calcined forms and identical for the half-calcined forms.

- Crushing the stones resulted in a significantly different distribution of size fractions.

- Activated char produced from North Dakota leonardite under increased pressure had lower activity toward SO_2 than that produced at ambient pressure, probably because of pore plugging by tar unable to boil away.

REFERENCES

1. *Keystone Coal Industry Manual*; Mining Information Services, Robert Dimond, Publishing Director, 1995, p S-2.

2. U.S. Department of Energy (DOE). "Clean Coal Technology: The Investment Pays Off," Report No. DOE/FE-0291 (Revised), July 1995.

ACKNOWLEDGMENTS

TABLE 1
Sieve Fractions from Limestones and Dolomite

	Particle Size, μm				
	250–840	150–250	125–150	75–125	<75
Dolomite	0.1	0.7	10.3	31.4	56.8
Limestone	0.1	0.4	3.3	19.5	75.5

TABLE 2
Comparison of Fully Calcined and Half-Calcined Limestone
and Dolomite Toward SO_2 Adsorption

Abbr.	Calcination wt%	Ads. Total wt%	Ads. CO_2 wt%	Ads. SO_2 wt%	SO_2 Ads. CO_2 Eq. wt%	Ads. SO_2 %/min.
Fully Calc.						
Dolo.	−40.9	34.4	20.4	14.0	15.0	0.22
Lime	−32.6	39.5	31.0	8.5	8.0	0.19
Half-Calc.						
Dolo.	−8.3	11.6	--	11.6	14.2	0.16
Lime	2.2	10.5	--	10.5	10.3	0.16

TABLE 3
Effect of Pressure on SO_2 Sorption by Activated Char
Prepared from North Dakota Lignite

pTGA, psig	SO_2 Adsorbed on Activated Char, wt%	Total S in Spent Char, wt%
450	7.4	4.8
300	7.3	4.7
150	8.1	5.2
Ambient	8.7	6.0

RATES OF PYROLYSIS AND COMBUSTION OF BARK
BY THERMOGRAVIMETRIC ANALYSIS

Wei-Yin Chen
Department of Chemical Engineering, Anderson Hall
University of Mississippi, University, MS 38677

Wood supplies approximately 3 percent of the U.S. energy consumption (Schreuder and Tillman, 1980). Bark represents about 10-15% of the weight of the trunk cut in the forest. Wood combustion phenomena has been extensively reviewed (e.g., Tillman et al., 1981). Recent technological development is reflected in an article by Barsin et al. (1988), and a report published by the Electric Power Research Institute (Johnston et al., 1993). Fundamental understanding of wood pyrolysis has also grown substantially in the last two decades. Shafizadeh (1982) reviewed the wood pyrolysis and combustion kinetics based on weight loss profiles. About the same time, Hajaligol et al. (1982) reported the kinetics of the individual product species for rapid pyrolysis of cellulose. Boroson et al. (1989) observed that heterogeneous cracking of wood pyrolysis tars takes place over flesh wood char surface. Pyrolysis kinetics of different lignocellulosic materials have been investigated by Bilbao et al. (1989, 1990). Heat and mass transfer limitations are inevitable during burning of large particles, and have been the target of a number of modeling efforts (e.g., Kanury, 1972; Maa and Bailie, 1973; Chan et al., 1985; Ragland et al., 1988; Bilbao et al., 1993).

Due to its lower physical strength and less uniform structure than interior wood, bark is usually burned along with wood waste as a fuel, particularly by sawmills and pulp mills. Bark has the heating value of 8,000 to 10,000 Btu/lb, which is higher than that of wood (Wegner, 1991). The objective of this paper is to experimentally acquire information about the bark kinetics during pyrolysis and combustion conditions. A kinetic model is also developed for the comparison.

EXPERIMENTAL

Since weight loss is used as a measure of bark conversion in the present study, the design of experiments has some salient features of a thermal balance, Figure 1. The center piece of the reactor is a cylindrical sample basket of dimension 1 in × 2 in length, which is made of 40 mesh stainless steel screen. The reactor vessel is an alumina tube with inside diameter of 2.5 in, which is heated to the desired temperature by a Thermcraft furnace model 23-18-1ZH with dimensions 3 in × 18 in long. The reactor is equipped with a distributor at about 6 in from the bottom end of the furnace, and a fluidized sand bed serving as a heat source of the gas stream.

Samples of pine bark, cut into 10mm spheres, were dried at 105°C for 24 hours before the experiment. Nitrogen and air were used as the fluidizing gas during pyrolysis and combustion, respectively. To begin a run, the sample basket containing a single particle of bark is lowering into the preheated fluidized sand bed. After a predetermined period of time, the basket was raised to a water-jacketed, reversed-nitrogen flow section for rapid quenching. Sample weight before and after the experiment were recorded. The ultimate analysis of the bark sample is shown in Table 1.

Experiments were conducted at sand temperatures 750, 800 and 850°C for pyrolysis; and 500, 600, 700 and 800°C for combustion. To achieve these temperatures, the furnace was set 90°C higher than the desired sand temperature. The gas flowrate, 15,000 ml/min, was chosen to ensure that it was three times higher than the theoretical air required at highest burning rate.

KINETIC MODEL

The bark combustion model under consideration contains three major components: bark pyrolysis, char combustion, and heat transfer.

During pyrolysis, the organic portion of the bark converts to volatiles and solid char, i.e.,

$$\text{Bark} + \text{heat} \rightarrow \underset{(V)}{\text{Volatiles}} + \underset{(1-V)}{\text{Char}} \tag{1}$$

Here, the fraction of weight loss, V, is used as an index of bark conversion. The volatile compounds include the gaseous species and tarry species disengaged from the char. Similar to a number of coal pyrolysis studies (e.g., Howard, 1981), bark pyrolysis is treated as a first order reaction in the following form

$$\frac{dV}{dt} = k_1(V_\infty - V) \tag{2}$$

where V_∞ is the final volatile yield as time approaches infinity. The pyrolysis rate constant k_1 is assumed to follow the Arrhenius law

$$k_1 = k_{10} e^{-\frac{E_1}{RT_P}} \tag{3}$$

where T_p is particle temperature, and E_1 is the pyrolysis activation energy.

Similar to coal pyrolysis (Howard, 1988), we observed temperature dependence of V_∞ during regression. Niksa (1988) proposed that phase equilibrium determines partitioning of tar in the gas and condensed phase, and the final volatile yield in the gas phase, V_∞, depends on temperature as follows:

$$V_\infty(T_p) - V_{10} e^{-\frac{E_3}{T_p}} \tag{4}$$

where V_{10} and E_3 are adjustable parameters.

In the presence of oxygen, oxidation of the organics in the char contributes to additional weight loss

$$\begin{array}{l} Char \cdot O_2 \rightarrow CO_2 \cdot H_2 O \\ (W) \end{array} \tag{5}$$

Assuming char combustion is first order with respect to oxygen concentration and the weight of char, we obtain

$$\frac{dW}{dt} - -k_1(V_\infty - V) - k_2' W(O_2) \tag{6}$$

Since oxygen was continuously fed into the combustor at a rate four times that required for burning the volatile carbon, oxygen concentration is assumed to be constant during the combustion. Thus, we can combine k_2' and the oxygen concentration as a new constant k_2 and Eq. 6 becomes

$$\frac{dW}{dt} - -k_1(V_\infty - V) - k_2 W \tag{7}$$

Assuming that the combustion rate constant, k_2, follows the Arrhenius law,

$$k_2 - k_{20} e^{-\frac{E_2}{RT_p}} \tag{8}$$

Mass transfer limitations, such as oxygen diffusion into the char, are usually involved in combustion of particles of 1 cm in diameter, thus the rate measured based on Eqs. 7 and 8 should be considered effective or global reaction rate (Carberry, 1976).

Combustion of volatiles generated in bark pyrolysis will also take place outside bark particles at the same time,

$$Volatiles \cdot O_2 \rightarrow H_2 O \cdot CO_2 \tag{9}$$

However, since this reaction does not contribute to the weight loss and it is not included in the present model. Weight loss measurements indicate that devolatilization of bark particles takes place almost instantaneously at 800°C. However, at 500°C, devolatilization does not start until at about 20 s. These observations imply that heat transfer is a limiting factor in the range of our investigation, and an equation governing the temperature variation of the particle is required. Based on the published value of thermal conductivity of cellulosic materials, $0.12 \ W.m^{-1}.K^{-1}$ (Reed, 1983), the estimated Nusselt number of heat transfer for a bark particle gives values in the range 0.8 to 1.8. Since this is not a large number, we assume that the temperature is uniform inside a bark particle during pyrolysis and combustion. It should be mentioned that there is evidently a radial temperature profile and diffusion limitations of volatiles inside the wood particles with diameter 56 mm (Bilbao et al., 1993). Energy balance yields

$$\rho_p V_p C_p \frac{dT_p}{dt} \cdot Ah(T - T_p) \cdot \varepsilon A\sigma(T_w^4 - T_p^4) \cdot \Delta H_p r_p W_{p0} \cdot \Delta H_o r_o W_{p0} \tag{10}$$

Equation 10 states that temperature rise of a bark particle is governed by convective heat transfer, radiative heat transfer, heat of pyrolysis, and heat of combustion. We assume that the heat of volatiles combustion is carried away by gas, and is not included in this equation. Our calculation reveals that convection contributes to less than 20% of radiative heat transfer. Furthermore, experiments indicate that char combustion is much slower than pyrolysis, and char combustion does not contribute significant weight loss and temperature rise during the heat-up period. Thus, the first and the fourth terms on the right hand side of Eq. 10 are eliminated in the regression process, i.e.,

$$\rho_p V_p C_p \frac{dT_p}{dt} = \varepsilon A \sigma (T_w^4 - T_p^4) + \Delta H_p r_p W_{po}$$

(11)

Again, due to the fact that significant char combustion does not take place during the heat-up period, the bark particle external surface area, A, in Eq. 11 is assumed to be a constant during the combustion process. The published value for heat capacity of bark, C_p, is 0.327cal/g.°C (Reed, 1983), and the nominal density of bark particle, ρ_p, was experimentally determined, 0.42kg/dm³.

The model discussed above has three dynamic equations, Eqs. 2, 7 and 11. Equations 3, 4 and 8 are also required for the integration of the three dynamic equations. The seven parameters, k_{10}, E_1, k_{20}, E_2, V_{10}, E_3 and ΔH_p are recovered from regression through comparison of the model with the data obtained from pyrolysis and combustion experiments. The optimization has been achieved by resorting to BCONF/DBCONF, a subroutine in the International Mathematical and Statistical Library which minimizes a multi-variable function subject to bounds on the variables using a quasi-Newton method and a finite-difference gradient. The integration of the large sets of differential equations has been carried out on a Cray X-MP2/216 supercomputer with LSODE, a software package based on Gear's method for solving stiff differential equations (Hindmarsh, 1982).

RESULTS AND DISCUSSION

The optimization procedure resulted in the following values of the seven system parameters:

k_{10} = 1,557 s⁻¹ E_1 = 37,333 J/mol
k_{20} = 0.295 s⁻¹ E_2 = 22,028 J/mol
V_{10} = 0.862 E_3 = 228 K
ΔH_p = 434 J/g of dry bark

The value of final volatile yield, V_{10}, is in good accord with the reported volatile matter for cedar bark, 0.869, moisture and ash free basis (Tillman et al., 1981). The heat of pyrolysis, ΔH_p, is somewhat higher than that reported for cellulose, 274 J/g (Bilbao et al., 1993), and that for cottonwood, 268 J/g (Pan, 1993). This discrepancy may be caused by the high heating rate, or the assumptions used in the present study. It has been demonstrated that high temperatures favor decomposition to volatiles, which require heat, while low temperatures favor char formation, which release heat (Shafizadeh and DeGroot, 1976). Bilbao et al. and Pan obtained their values through DSC analysis with a heating rate below 20 °C/min, and the heating rate in the present study is above 400°C/min. The activation energy of bark pyrolysis is consistent with those found by other researchers: 24,208 J/mol between 290 and 400°C (Bilbao et al., 1993) and 52,900 J/mol above 325°C for pine wood (Bilbao et al., 1991).

The experimental data in general are in good accord with the predictions of the model. Only part of our results are presented below. Figures 2 presents the comparisons of pyrolysis and combustion results from experiments at the sand temperatures 800°C. The predicted temperature profiles of bark particle during heating are also included in this Figure. Slower rise in temperature between 170 to 230°C indicates endothermic reaction of pyrolysis in this temperature range, which is somewhat narrower than that reported by Wegner, 100 to 450°C (1991). Note that char combustion does not contribute significant weight loss in the first 20s, while pyrolysis is essentially complete during this time. This observation is consistent with the assumption that heat of combustion of char does not play an important role during the heat-up period.

Figures 3 demonstrates the weight loss profiles during combustion at 600°C sand temperature. The data generally conform well with the model predictions. However, at 500°C, the pyrolysis is slower in the experiment than predicted by the model. This illustrates the limitations of the present phenomenological model. Bark is a complex material and its decomposition products contain numerous compounds, while the present model uses weight loss as an index of reaction conversion. The assumptions associated with heat transfer can also cause discrepancies. Furthermore, from thermodynamic principles and collision theory, both the frequency factor and the activation energy can be functions of temperature (Zellner, 1984).

Fragmentation of bark particles and volatiles ignition during combustion may be important to the future developments of phenomenological model. We observed fragmentation of bark particles at temperatures 600°C and above. Each bark particle breaks into 2 to 6 pieces along its geological planes after 15 to 25 seconds in the furnace, and higher temperatures cause more vigorous fragmentation. Fragmentation results in increase in larger surface areas and therefore reduced transfer limitations. Furnace temperature also affects ignition of volatiles. At 800 and 700°C, flame starts at about 2 s after the bark particle is lowered into the furnace. At 600°C, flame was observed at about 5s. At 500°C, ignition was delayed to 19s.

CONCLUSIONS

Bark from pine has been investigated in both pyrolysis and combustion environments. The experimental data are in good accord with a kinetic model which includes three dynamic equations: bark pyrolysis, char combustion, and heat transfer to the bark particle. Three of the seven parameters, final volatile yield, heat of pyrolysis, and activation energy of bark pyrolysis, are in good agreement with published values for similar species. These results suggest that the model is capable

of depicting the weight loss profiles in a furnace with a temperature in the range 500 to 850 °C.

Experiments also reveal that volatiles evolution and char combustion take place during two different periods of time during the thermal process. Furthermore, fragmentation of bark particles was also observed at temperatures above 600°C.

LITERATURE CITED

Barsin, J.A., J. Pottera, and G. Stewart, "Conversion of A Recovery Boiler to Bark Burning," Tappi Journal, 71, 107-113 (1988).

Bilbao, R., A. Millera, and J. Arauzo, "Thermal Decomposition of Lignocellulosic Materials: Influence of the Chemical Composition," Thermochimica, 143, 149-159 (1989).

Bilbao, R., A. Millera, and J. Arauzo, "Kinetics of Weight Loss by Thermal Decomposition of Different Lignocellulosic Materials: Relation between the Results Obtained from Isothermal and Dynamic Experiments," Thermochimica, 165, 103-112 (1990).

Bilbao, R., M.B. Murillo, and A. Millera, "Thermal Decomposition of Lignocellulosic Materials: Comparison of the Results Obtained in Different Experimental Systems," Thermochimica Acta, 190, 163-173 (1991).

Bilbao, R., A. Millera, and M.B. Murillo, "Temperature Profiles and Weight Loss in the Thermal Decomposition of Large Spherical Wood Particles," Ind. Eng. Chem. Res., 32(9), 1811-1817 (1993).

Bird, R.B., W.E. Stewart, and E.N. Lightfoot, "Transport Phenomena," John Wiley & Sons, New York, P.409, 1960.

Boroson, M.L., J.B. Howard, J.P. Longwell, and W.A. Peters, "Heterogeneous Cracking of Wood Pyrolysis Tars over Fresh Wood Char Surfaces," Energy & Fuels, 3, 735-740 (1989).

Carberry, J.J., "Chemical and Catalytic Reaction Engineering," McGraw-Hill, New York, p.205, 1976.

Chan, W.C.R., M. Kelbon, and B. Krieger, "Modeling and Experimental Verification of Physical and Chemical Processes during Pyrolysis of a Large Biomass Particle," Fuel, 64, 1505-1513 (1985).

Gray, R.L., and R.A. Parham, "A Good Look at Wood's Structure," Chemtech, 4, 232-238 (1982).

Hajaligol, M.R., J.B. Howard, J.P. Longwell, and W.A. Peter, "Product Compositions and Kinetics for Rapid Pyrolysis of Cellulose," Ind. Eng. Chem. Proc. Des. Dev., 21, 457-465 (1982).

Hindmarsh, A.C., "ODEPACK, A Systematized Collection of ODE Solvers," Report UCRL-88007, Lawrence Livermore National Laboratory, August (1982).

Howard, J.B., "Fundamentals of Coal Pyrolysis and Hydropyrolysis" in "Chemistry of Coal Utilization," second supplementary volume, edited by Elliott, M. A.,, Wiley Interscience, New York, pp.688-785, 1981.

Johnston, S.A., J.G. Cleland, R.S. Truesdale, T.C. Clark, W.D. Stancil, L.D. Ostlie, and B. Weigel, "Whole Tree Energy™ Design - Volume 1: Engineering and Economic Evaluation," Final Report submitted to the Electric Power Research Institute, Report TR-101564 under Project 2612-15, Palo Alto, CA, December, 1993.

Kanury, A.M. "Rate of Burning Wood: A Simple Thermal Model," Combustion Science and Technology, 5, 135-146 (1972).

Maa, P.S., and R.C. Bailie, "Influence of Particle Sizes and Environmental Conditions on High Temperature Pyrolysis of Cellulosic Material - I. Theoretical," Combustion Science and Technology, 7, 257-269 (1973).

Niksa, S., "Rapid Coal Devolatilization as an Equilibrium Flash Distillation," AIChE J., 34, 790-802 (1988).

Pan, W.P.,Western Kentucky University, Personal Communication, September 29, 1993.

Ragland, K.W., J.C. Boerger, and A.J. Baker, "A Model of Chunkwood Combustion," Forest Products Journal, 38(2), 27-32 (1988).

Reed, R.J., North American Combustion Handbook, second edition, North American Mfg. Co, Cleveland, Ohio, 1983.

Schreuder, G.F., and D.A. Tillman, "Wood Fuels Consumption Methodology and 1978 Results," in "Progress in Biomass Conversion," Vol. 2, K.V. Sarkanen and D.A. Tillman eds., pp.60-88, Academic Press, New York, 1980.

Shafizadeh, F., "Introduction to Pyrolysis of Biomass," Journal of Analytical and Applied Pyrolysis, 3, 283-305, 1982.

Shafizadeh, F., and W.F. Degrade, "Thermal Analysis of Forest Fuels," in "Fuels and Energy from Renewable Resources," D.A. Tillman et al. ed., pp.93-114, 1977.

Tillman, D.A., A.J. Rossi, and W.D. Kitto, "Wood Combustion - Principles, Processes, and Economics," Academic Press, New York, 1981.

Wegner, T.H., "Wood" in "Encyclopedia of Polymer Science and Technology, edited by J. I. Kroschwitz, second edition, John Wiley & Sons, New York, 17, pp. 843-887, 1991.

Zellner, R., "Bimolecular Reaction Rate Coefficients," in "Combustion Chemistry," W.C. Gardiner ed., Springer-Verlag, New York, pp.129-134, 1984.

TABLE 1. Ultimate Analysis of Bark (Report by Huffman Laboratory)

dry-loss, %	4.92
ash, %	4.08
carbon, %	51.20
hydrogen, %	5.66
oxygen, %	40.67
nitrogen, %	0.21
sulphur, %	0.02

The sample was ground prior to analysis. Moisture was determined by loss on drying in air at 105°C to a constant weight and is on an as received basis. All other results are on a dried sample basis by weight.
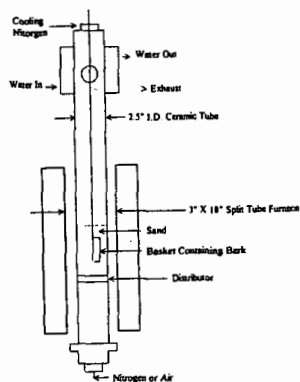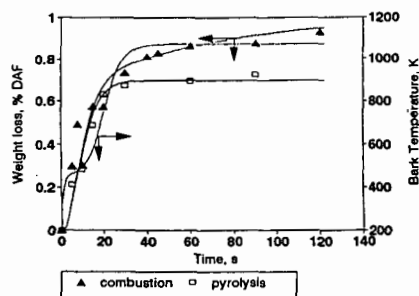

Figure 1. Experimental apparatus

Figure 2. Experimentally observed and model predicted weight loss of bark during pyrolysis at 800°C sand temperature. Predicted bark particle temperature is also shown.
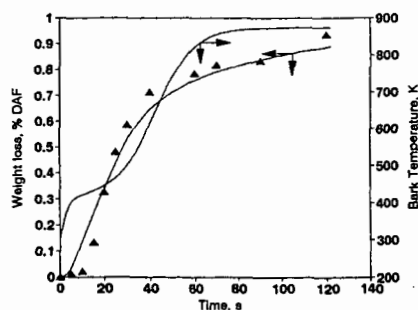

Figure 3. Experimentally observed and model predicted weight loss of bark during combustion at 600°C wall temperature. Predicted bark particle temperature is also shown.

A NOVEL SMOOTHING ROUTINE FOR THE DATA PROCESSING IN THERMOGRAVIMETRIC ANALYSIS

Keyu Wang, Shaojie Wang, He Huang, M. T. Klein and W.H. Calkins*
Dept of Chemical Engineering, University of Delaware, Newark, DE 19716

Key words: smoothing, differentiation, thermogravimetric analysis

INTRODUCTION

Thermogravimetric (TG) techniques have been used in characterizing fossil fuels (1-4) and in studying coal liquefaction kinetics, mechanisms, and processes (5,6). The TG techniques have been providing sensitive, rapid, and reproducible measurements for those purposes.

The primary output of thermogravimetric analysis (TGA) is in the form of a three-column matrix of time, temperature, and mass (or mass%). The first derivative of the TG (i.e. DTG) is capable of revealing fine details of the processes occurring more clearly for sample characterization (2,7) and/or as an input variable for further analysis, for example, in the SimDis (Simulated Distillation) TG technique (8).

There always is a limitation on the sensitivity of the TGA instrument. This is particularly true for those analyses run at either very low heating rates or very slow DTG decay experiments, where small changes in mass occur. Therefore, smoothing and filtering of these large data sets to obtain noise-free DTG curves are crucial in those TGA applications.

Several methods have been developed for smoothing and differentiation of experimental data (9-15). The objective of this paper is to present a novel and specific method for smoothing and differentiation of thermogravimetric data. The principle of the method is based on the characteristics of the TG data (e.g. time vs. mass). Linear regression and error analysis are used in the smoothing and filtering routine. The computer program required is simple and effective. The method used in the program promises auto-convergence. The reported technique in this paper could also be applied to other analytical instrumentation.

EXPERIMENTAL

The thermogravimetric analyzer (TGA) was a Model 51 TGA (TA Instruments, New Castle, Delaware). The program of manipulation of the TG variables, such as heating rate, type of purge gas and its flow rate, and final (or step) temperature, was determined by the objectives of the particular experiment. The output matrix of a TG scan (time, temperature, mass) was recorded by computer. The digitized data were then transferred into DOS (ASCII) format using a program provided by TA Instruments. The ASCII format data were loaded into MATLAB (The MathWorks, Inc.) and processed using a MATLAB routine.

METHOD OF SMOOTHING AND DIFFERENTIATION

The General Problem. The random errors which, regardless of their source, are characterized as noise are always present in the TGA measurements. This background noise reduces signal-to-noise ratio, resulting in decreasing sensitivity. This is particularly true when the DTG is the objective result of a TG scan. Figures 1 and 2 show the DTG plots for TG scans run at a very low heating rate (1°C/min) and a very slow DTG decay, respectively. These DTG plots were obtained from numerical differentiation of the original TG data. As shown in Figures 1 and 2, it is necessary for the investigator to remove the noise as much as possible without, at the same time, distorting the experimental data, especially for those processes where small changes in mass occur. Smoothing and filtering of these thermogravimetric data to obtain the noise-free differentiation (DTG curve), therefore, are required in the TGA applications.

The Characteristics of the TG Data (time vs. mass). A TG curve of the Illinois #6 coal at a heating rate of 1 °C/min in 100 cm^3(STP)/min nitrogen is shown in Figure 3. Thirty one data points of (t,w) taken from Figure 3 are plotted in Figure 4. The plot shows a very good linearity between the mass and time. In general, this is always true for a certain short time interval of a TG scan. It is this characteristic that is used to develop a method for smoothing and differentiation of the TG data.

Smoothing and Differentiation by Linear Regression and Error Analysis. One of the simplest ways to smooth fluctuating data is by a n-point (n=2k+1; k=1,2,3,...)moving average procedure. In this method, a fixed odd number (2k+1) of data points are taken to obtain the average for the center point, (k+1)th point, of the group. To move on, the first point in the group is dropped, the next point at the end of the group added, and the process is repeated. In statistics, noises in the data file are not filtered by this simple average procedure.

27

Consider a group of n (for example, n = 11) points of (t, m) taken from a TG file and plotted in Figure 5. Based on the characteristics of the TG data discussed in the previous section, a linear regression can be performed in this group by

$$m = a + b \times t \tag{1}$$

and represented by the solid line in Figure 5. The obtained linear regression parameters (i.e., a and b) can be used to estimate the m (mass) at each t (time) in the group. The errors (e) between the linear regression ($m_{cal.}(i)$) and experimental data ($m_{exp.}(i)$) in the group are defined as

$$e(i) = m_{cal.}(i) - m_{exp.}(i) \tag{2}$$

The statistical parameters of the errors for this group, e.g. mean (e_{mean}) and standard derivation (e_{std}) of the errors, are calculated by:

$$e_{mean} = \frac{\sum_{i=1}^{i=n} e(i)}{n} \qquad (e.g. \ n = 11) \tag{3}$$

$$e_{std} = \frac{\sqrt{\sum_{i=1}^{i=n} (e(i) - e_{mean})^2}}{n - 1}$$

To eliminate the noise from this group, standard deviation of the errors can be used as a criterion to define the filter range. This is plotted as dashed-lines in Figure 5. In detail, if the experimental data point locates outside the filter range, i.e. $e_i > e_{std}$, it is considered as a noise in the group. To filter this noisy point, it is replaced by an estimated value of $m_{cal.}(i)$ using the linear regression. This filter procedure can be used on each point in the group and a new data set can be formed. This new data set is plotted in Figure 6. The points with "x" in Figure 6 represent the filtered data. Linear regression can be again carried out in this new data group, followed with upgraded error analysis and filtering process. The linear regression, error analysis and the filter procedure are repeated until the standard deviation of the errors is below a predetermined value of $e_{std, o}$. In this study, a relative standard deviation of the errors, re_{std}, rather than e_{std}, has been used for evaluating the calculations. This relative standard deviation of the errors is defined as e_{std} times the absolute value of the slope (DTG) of the linear regression, i.e.,

$$re_{std} = abs(b) \times e_{std} \tag{4}$$

This relative standard deviation of the errors used as a criterion to evaluate calculations can insure the precision of very slow process (i.e., very low DTG scan). It has been found that $re_{std,o}$ set at 10^{-5} gives very satisfactory results. The final regression results are used to estimate the smoothed mass and differentiation for the center point of $t_{(k+1)}$, i.e.,

$$m_{k+1} = a + b \times t_{k+1} \tag{5}$$

Since the standard deviation of the errors constantly decreases with iterations, the computation method used in the program promises auto-convergence.

For a TG analysis, the n-point smoothing, filtering and differentiation routine has been moved in the data file similarly as the moving average method which has been described earlier. A scheme of the computation routine is illustrated in Figure 7. For the "end-points" (i.e., either the initial or the final k points in the data file), a different method has to be used to evaluate them. One of the simplest ways to handle this "end-points" problem is to throw them away, since these end-points usually are not important or not of interest. In this study, the end-points have been simply assigned by their original values. If the "end-points" become important, a much more sophisticated method developed by Leach et al. (10) could be used.

APPLICATIONS
SimDis TGA. A SimDis TGA method for determining the boiling point distribution of liquid fuels is reported elsewhere (8). Original DTG plot for a petroleum sample,light paraffinic vacuum distillate,is shown in Figure 2. To transfer the DTG decay into boiling point distribution, it is necessary to smooth the noisy DTG data. The results of n = 0- (i.e., original), 3-, 5-, 7-, 9-, and 11-point smoothing and filtering are illustrated in Figure 8. The

more the data points used for smoothing and filtering, the smoother the DTG curve. However, at the same time, the more CPU or the longer computing time are required. More importantly, a large data number n used in smoothing increases the risk of distorting the experimental data. Eleven-point smoothing and filtering has been found to give the optimized results for the cases studied thus far. Figures 9a and 9b show the comparison plot (i.e., a plot including both smoothed results and original experimental data) and 11-point smoothing plot, respectively. The results indicate the smoothing and filtering method used in this study is very effective.

    Characterization of coal structure. A representative TG scan on the Argonne Premium Illinois #6 bituminous coal, which was dried in a vacuum oven with a nitrogen purge at 105 °C for 48 hours before use, is shown in Figure 10. The two phases, i.e., 1) the heating rate to 950°C in nitrogen and hold for 7 min; and 2) the oxidation at 950°C, provided measures of VM, FC, and Ash, respectively. The differential of the weight loss (DTG) curve highlights the various TG processes more clearly. This becomes even more distinct and complex if the heating rate is slowed down to about 1 °C/min (2). However, the original DTG plot for this low heating rate shown in Figure 1 is so noisy that the processes involved in the TG scan could not be distinguished. The comparison plot and the 11-point smoothing results for this low heating rate scan are shown in Figures 11a and 11b, respectively. The processes involved in the TG pyrolysis of the coal at this low heating rate, as shown in Figure 11b, are very clearly distinguished. The low temperature peak represents the loss of residual moisture below 200 °C. The main Volatile Matter peak starts at 350-400 °C and actually consists of three or perhaps four individual weight loss processes. The large peak is broad and probably consists of a number of pyrolysis processes. The well defined peak at 571 °C is tentatively identified as due to pyrite decomposition to pyrrhotite and sulfur because this peak is absent in coals containing little or no pyrite. Also, the decomposition temperature corresponds closely to that reported for pyrite (16). Two other small peaks are not yet identified but are fairly broad. They disappear gradually during coal liquefaction (5).

    With this smoothing and filtered method, the sole function of the computation is to act as a filter to smooth the noise fluctuations and hopefully to introduce no distortions into the experimental data. The problem of distortion is quite difficult to assess. In Figures 1 and 2, there are small fluctuations in the raw data. Are these fluctuations real, or, as is more likely, are they just noise? The question can not be simply answered by taking just the data from a single run. However, if two or three runs were taken, they gave the same results or, more characteristically, in same patterns. These indicated that the fluctuations are due to the noise, since the random errors will not recur in <u>exactly</u> the same place in different runs. The results of duplicate tests on all samples inspected in this study suggest that the fluctuations are truly due to noise.

CONCLUSION

    For a certain short interval of a TG scan, the correlation between the mass and time is linear. A smoothing and filtering routine based on the use of linear regression and error analysis has been developed and successfully applied in the thermogravimetric data processing. This method provides a filter to smooth the noise fluctuations and, at the same time, to introduce no distortions into the TGA experimental data. The computer program required is quite simple and effective. The method used in the program promises auto-convergence.

REFERENCES

1.   Ottaway, M. *FUEL* **1982, 61**, 713.
2.   He Huang, Keyu Wang, M.T. Klein, and W.H. Calkins *ACS Fuel Chem Div Preprints* **40** (3), 465 (1995).
3.   He Huang, Keyu Wang, W.H. Calkins and M.T. Klein *ACS Fuel Chem Div Preprints* **39** (3), 741 - 746 (1994).
4.   He Huang, W.H. Calkins and M.T. Klein *I&EC Research* **33**, 2272-2279 (1994).
5.   He Huang, Keyu Wang, M.T. Klein, and W.H. Calkins *ACS Fuel Chem Div Preprints* **40** (3), 550 (1995).
6.   He Huang, Keyu Wang, M.T. Klein, and W.H. Calkins *Coal Science and Technology 24: Coal Science*, Eds J.A. Pajares and J.M.D. Tascon, Vol. II, p. 1207 (1995).
7.   He Huang, D.M. Bodily, and V.J. Hucka *Proceedings 1993 International Conference*

on Coal Science pp 411-414.

8.   He Huang, Keyu Wang, M.T. Klein, and W.H. Calkins   *ACS Fuel Chem Div Preprints* **40** (3), 485 (1995).
9.   Whitaker, S.; Pigford, R.L. *Ind. Eng. Chem.* **52**, 185 (1960).
10.   Leach, R.A.; Carter, C.A.; Harris, J.M. *Anal. Chem.* **56**, pp. 2304-2307 (1984)
11.   Baedecker, P.A. *Anal. Chem.* **57**, pp. 1477-1479 (1985)
12.   Khan, A. *Anal. Chem.* **60**, pp. 369-371 (1988)
13.   Guest, P.G. *Numerical Methods of Curve Fitting* University Press, Cambridge, England (1961).
14.   Hamming R.W. *Numerical Methods for Scientists and Engineers* McGraw-Hill Book Co., New York (1962).
15.   Ralston, A. *A First Course in Numerical Analysis* McGraw-Hill Book Co., New York (1965).
16.   Luganov, V.A.; Schebalin, V.I. *Can. Metall. Q.* **1982**, 21, 157.
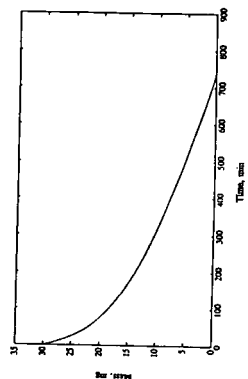
Figure 3 TG curve of Illinois #6 coal pyrolysis at 1 C/min (only volatile portion)
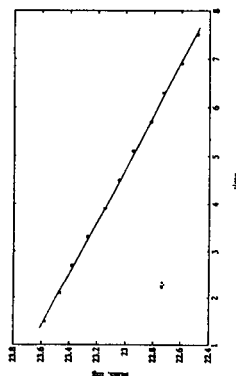
Figure 6 Mass vs time for a filtered n-point group
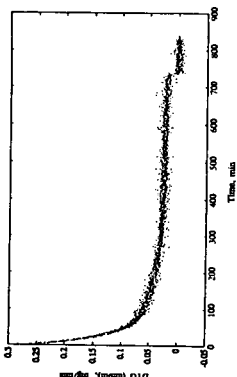
Figure 2 DTG decay of a SimDis TGA scan on a liquid fuel
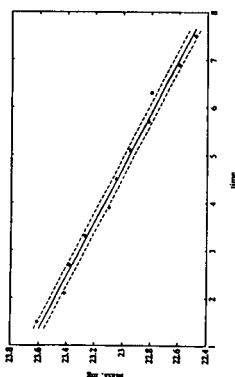
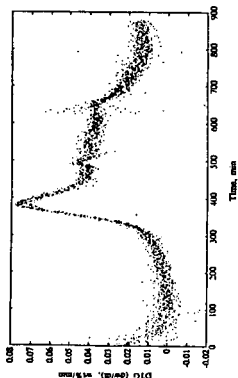Figure 5 Mass vs time for a n-point group
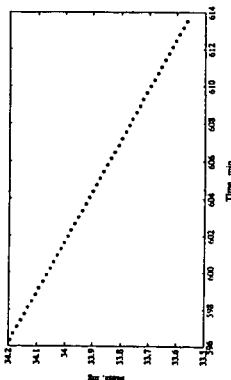
Figure 1 DTG of Illinois #6 coal pyrolysis at 1 C/min

Figure 4 Characteristic of mass vs time in a TG scan (Thirty-one data points taken from Figure 3)
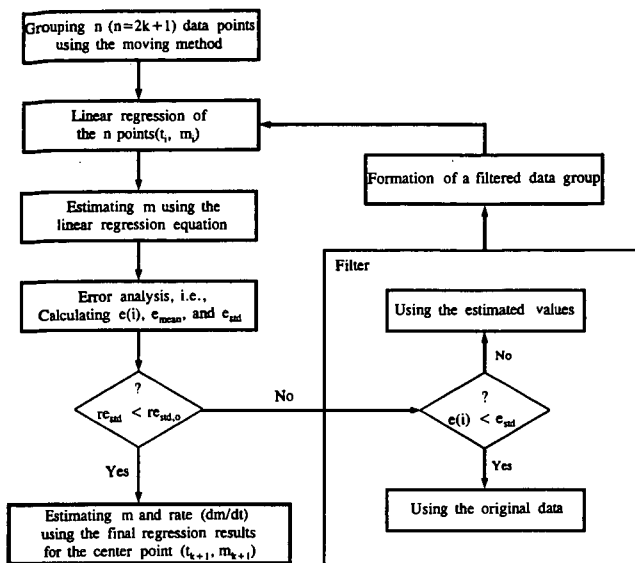
Grouping n (n=2k+1) data points using the moving method

Linear regression of the n points(t$_i$, m$_i$)

Estimating m using the linear regression equation

Formation of a filtered data group

Error analysis, i.e., Calculating e(i), e$_{mean}$, and e$_{std}$

Filter

Using the estimated values

? re$_{std}$ < re$_{std,o}$

No

? e(i) < e$_{std}$

No

Yes

Yes

Estimating m and rate (dm/dt) using the final regression results for the center point (t$_{k+1}$, m$_{k+1}$)

Using the original data

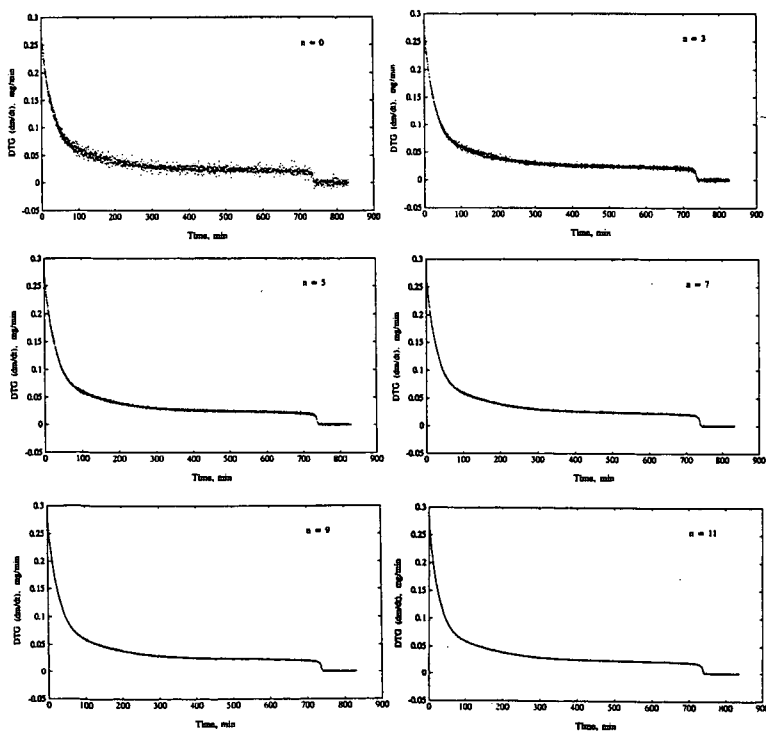Figure 7 Flow-sheet of the n-point smoothing and filtering procedure

Figure 8 The results of n = 0-, 3-, 5-, 7-, 9-, 11-point smoothing and filtering
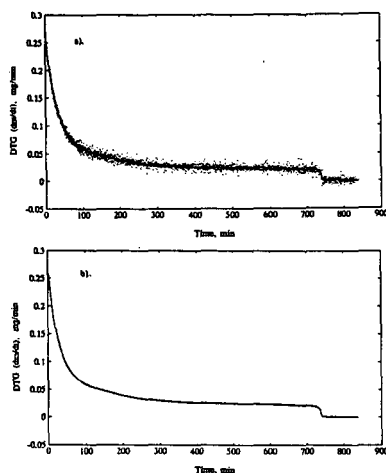
31

Figure 9 Visualization of n-point smoothing and filtering of the DTG at very slow heating rate shown in Figure 1: a). comparison plot; b). 11-point smoothing and filtering plot
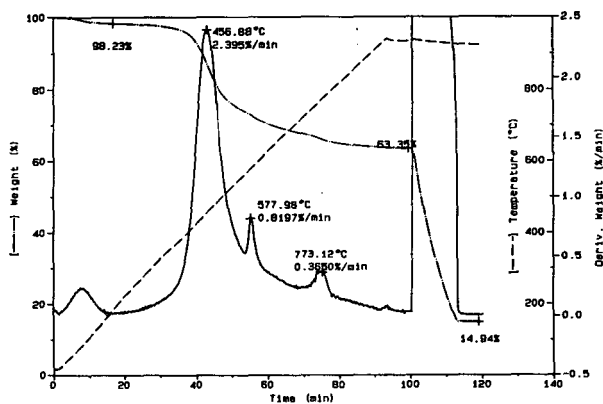

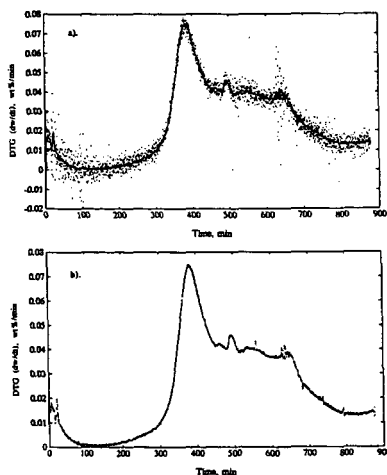
Figure 10 A TG scan of Illinois #6 coal at 10 C/min

Figure 11 Visualization of n-point smoothing and filtering of the DTG decay shown in Figure 2: a). comparison plot; b). 11-point smoothing and filtering plot

32

ENERGY STORAGE MATERIALS AND COATINGS.
DSC AND FLAMMABILITY STUDIES

Michael W. Babich and Ramazan Benrashid
Department of Chemistry
Florida Institute of Technology
150 West University Blvd.
Melbourne, Florida 32901-6988

Keywords: Energy Storage Materials, Phase Change Materials, Flammability

Introduction

For many years investigations into the thermal and moisture storage properties of materials undergoing reversible phase changes in the temperature range of interest for that particular application have been conducted. The prototypical material is, of course, water at O°C or 100°C. The interest in these materials has arisen largely from the need to conserve fossil fuels and cut energy costs. Both reasons are still valid. (1-2)

These materials have been called phase change materials, (PCM's), Energy Storage Materials (ESM's) or enthalpy storage materials in the literature, and these terms are used interchangeably for the most part. They have been incorporated into a wide variety of components used in construction and fabrication of everything from buildings to packaging materials to space suits.

Interest has existed in phase change materials for thermal storage since the late 1940's largely due to the pioneering studies of M. Telkes using Glauber's Salt. (3,4) These studies set the tone and path for work to follow even through thermal storage using this salt was never widely commercially successful. The primary disadvantage of Glauber's Salt is phae segregation upon melting. Work prior to the latest ESM materials was reviewed by Lane in 1987. (5) The early work concentrated heavily on melting of salt hydrates and gave quite mixed results. Non-segregating hydrates (those with congruent melting) such as $MgCl_2 \cdot 6H_2O$ at 117° gave the best results, but are not always available for the temperature range of interest. Table 1 shows a selection of these types of materials which have been used commercially and their temperatures of transition.

One of the most novel approaches developed was to use the solid-solid transition in polyalcohols the temperature of which can be somewbat adjusted by blending. These materials include pentaerythritol and neopentyl glycol (6,7). These transitions have been studied from 25° to 140°C. The lower temperature cases have not proven very useful as yet in any actual application.

Our area of primary interest, of course, has been in the application of phase change materials for thermal storage. PCM's have been used supplementally in both passive heating and cooling applications. These PCM's incorporated into construction materials can function to limit the temperature variation in a commercial or residential structure over a twenty four hour cycle by releasing heat during cooler periods and absorbing heat during warmer periods. Energy savings of 30 - 70% have been projected and up to 90% of annual sensible cooling could be shifted to off-peak hours. Further, coupling enthalpy storage with moisture storage has been shown to control humidity as well.

Desired Properties

Lane has listed some of the following properties for phase change materials. (5) This list was modified by Babich and Hwang and is shown in Table 2. (8-9)

How the importance of the properties on this list are weighted depends entirely on the application intended. The optimum set of properties can be determined for each situation. The choice may be economics driven in one case or application driven in another. It is for this reason that we strongly feel no one material is likely to solve every problem. Instead a range of good phase change candidates must be available to fit the very many possible uses for these materials.

Methods of Study

These ESM materials have been evaluated by a wide variety of methods, but the most successfully used thus far is differential scanning calorimetry (DSC). This method works well for both neat and adsorbed materials and for both heating and coating cycles. It has also been successfully demonstrated that the small sample size used in these studies gives totally reproducible results in large scale tests. (9) An actual DSC curve for undecylenic acid is shown in Figure 1.

From these curves one may readily obtain the heat of fusion or freezing and also the range of melting or freezing. Supercooling, if present, is obvious in these studies and the shape (width) of the transition is easily seen. These factors make this technique the method of choice. Differential Thermal Analysis (DTA) has also been used is some of the earlier work with some success. Actual bulk studies have been carried out utilizing structures ranging from passive test boxes to full scale room testing. These investigations have been described in detail in other work (10) In tests conducted at the Florida Solar Energy Center (FSEC) it has been shown conclusively that bulk tests agree very nicely with DSC studies conducted by Babich et al. (11)

The Current Situation

PCM's have now been developed which can be added to building materials e.g. wallboard, and which will contribute significantly to reduction of heating and cooling costs. There are three schools of thought with overlapping classes of compounds which presently represent the main efforts in low temperature thermal storage via energy storage materials. These areas can be subdivided by the approaches followed into the area of fatty acids and specificly blended mixtures thereof pioneered by Shapiro and coworkers, the long chain hydrocarbons developed by Salyer and coworkers and the more broad based search for new materials or the coating of older ones for specific uses by Babich et al.

Section I: Fatty Acids

Low melting fatty acids and blends of fatty acids have been considered as PCM's for several years. They have good properties in many respects. They are low-volatility, low melting, high boiling, low melting, organic materials which are readily imbibed by construction materials like gypsum wallboard. Further, many examples like coconut oil are very inexpensive making them very attractive as PCM's. Research by Shapiro and others has

been largely driven by economic considerations as well as properties (12-14). Some of the fatty acids and fatty acid mixtures studied early on are shown along with their thermal characteristics in table 3. Many of these mixtures are commercially available.

These materials are imbibed well into wallboard at very easily reproduced rates and with readily measured masses as shown in Figure 2. Further, they tend to be reasonably chemically stable and remain strongly absorbed indefinitely through many thermal cycles. They have normally been studied in the range of 20-30% absorption by mass. For these materials supercooling is not a problem at the rate of temperature change in normal structures. Actual room size structures using wallboard imbibed with fatty acid have been constructed and function well thermally.

The real drawbacks to the use these materials lay in two main areas. First they are asthetically unappealing. They have odors which were not very evident in lab scale testing but become very strong in large scale testing precluding their use in many structures. They also discolor the wallboard slightly which can be overcome by painting. They contribute both to flame spread and smoke production in flammability tests as shown in Tables 3. (15,16) It has been stated that fatty acids may exhibit corrosivity in some applications though this has not been conclusively demonstrated, and also that they may promote mold growth.

Section 2: Long Chain Hydrocarbons

Low melting long chain hydrocarbons (sometimes called hydrocarbon waxes) have also been effectively utilized as PCM's absorbed into wallboard(17-19). They, like the fatty acids, also have good properties in several respects. These are also low volatility, high boiling, low melting organic materials which can be imbibed effectively by wallboard. A group of these materials studied and their thermal characteristics are shown in Table 5. Some of these are also available at very low cost. Witco Chemical Company for example can provide a predominantly n-octodecane (K-18) at ~$0.50/lb/as apposed to 99% pure n-octedecane at ~$10.00/lb. These hydrocarbons have also been effectively encapsulated and pelletized. (19)

These are used at approximately the same loading, 20-30% by mass, as the fatty acids and mixtures. The thermal characteristics are similar. These materials are chemically quite stable though some breakdown over extended times has been noticed. (20). Supercooling is also no problem in these materials at normal ambient thermal cycling rates.

Drawbacks, however, in these materials are quite similar to some of the fatty acids. The chief problem is once again flammability and smoke production. Again epoxy coatings can be effective reducing flammability in some cases to that of untreated wallboard. These PCM's do not support mold growth.

Section 3. Other Materials and Integrated Approaches.

Babich et. al. have taken the approach of ESM's tailored to specific purposes and/or controlling the disadvantages of materials discussed in sections 1 and 2. (8, 9, 11, 20) Many materials have been studied including inorganic materials and silicone waxes some of which show great promise. Work in the area of new materials is in its infancy and is just beginning to yield good results. Further coupling of PCM's with moisture storage coatings may be of even greater utility. (21) These workers have reexamined several organic PCM's and investigated several new ones as shown in Table 5. Many of these, especially hexadecane, 1-dodecanol and allyl palmitate work exceeding well. (9) Unfortunately, allyl palmitate is too expensive for routine commercial use unless a newer, less expensive source can be found.

Babich et al have also clearly demonstrated and discussed at length the effectiveness of coatings of epoxy paints with aluminum and magnesium hydroxides for control of flammability. (22,23) Rate of flame spread, rate of heat release and onset of smoke production have been greatly retarded. In many cases the treated material is as good as untreated wallboard. ASTM and NBS approved tests have been used and sample results are shown in Table 4 and Figure 3. In this figure the amount of control the coating yields is most obvious. The incremental cost increase for this method is very small as most commercial wallboard will have to be painted anyway. These coatings could be applied as the primer by wallboard manufacturers or in the structure after construction. Additionally this method may be successfully coupled with any of the materials discussed previously.

Also a method has been developed with tremendous potential to couple ESM's with moisture storage systems. (21, 24) This approach, if further developed, could lead to new combinations of materials which will accomplish thermal storage with humidity control and be fire retardant as well. New congruent melting, salt hydrates are also currently under investigation both for ESM use and in coatings combining moisture exchange with ESM properties. Other dessicant materials are also being tested for use in coatings.

Summary

Tremendous potential exists in the area of ESM's for energy storage and in the area of moisture storage materials coupled with the ESM's. The efficacy of ESM materials for energy storage has clearly been demonstrated as has the utility of moisture storage agents for humidity control. The effectiveness of coatings in reduction of rate of flame spread, onset of smoke production and rate of heat release is indisputible. DSC is clearly the method of choice for preliminary studies of these systems.

References

1. J. Paris, M. Falardeau and C. Villeneuve, "Thermal Storage by Latent Heat: A Viable Option for Energy Conservation in Buildings," Energy Sources, 15, 85-93 (1993).
2. D. W. Hawes, D. Feldman and D. Banu, "Latent Heat Storage in Building Materials," Energy and Building, 20, 77-86 (1993).
3. M. Telkes, U. S. Patent 3,986,969 (1976).
4. M. Telkes, "Nucleation of Supersaturated Inorganic Salt Solutions," Ind. Eng. Chem., 46, 1308 (1952).
5. G. A. Lane, "Phase-Change Thermal Storage Materials" in The Handbook of Applied Thermal Design, E. C. Guyer, ed. McGraw-Hill, New York (1987).
6. D. Chandra, C. S. Barrett and D. K. Benson, "Adjustment of Solid-Solid Phase Transition Temperature of Polyalcohols by the Use of Dopants," in Advanced in X-ray Analysis, vol. 29, ed. E. S. Barrett, Plenum, 350-313 (1986).
7. D. Chandra, J. Helms, and A. Mojumdar, J. Electrochem Soc., 141, 1921-1927 (1994).
8. M. W. Babich, S. Hwang and R. D. Mounts, "The Search for Novel Energy Storage Materials Using Differential Scanning Calorimetry," Thermochim. Acta, 210, 83-88 (1992).

9. M. W. Babich, S. Hwang and R. D. Mounts, "DSC Studies of New Energy Storage Materials. Part 2. New Materials and Bulk Studies," Thermochim Acta, 226, 163-168 (1993).

10. A. F. Rudd, "Phase-Change Material Wallboard for Distributed Thermal Storage in Buildings," ASHRAE Transactions, 99, Pt. 2, 339-346 (1993)

11. M. W. Babich S. Hwang and R. D. Mounts, "The Thermal Analysis of Energy Storage Materials by Differential Scanning Calorimetry," Thermochim. Acta, 210, 77-82 (1992).

12. M. Shapiro, D. Feldman, D. Hawes and D. Banu. "P.C.M. thermal storage in drywall using organic phase-change material." Passive Solar Journal 4(4): 419-438, (1987).

13. M. Shapiro and D. Feldman, "A Family of Thermal Ballast Building Bricks and Blocks," Proc. Ninth Biennial Congress ISES, Montreal, Canada, p. 853, June 23-39 (1985).

14. D. Feldman, M. Shapiro, D. Banu and C. J. Fuhs, Sol. Energy Mater., 28(3-4) 201-216 (1989)

15. M. W. Babich, R. Benrashid and R. D. Mounts, "DSC Studies of New Energy Storage Materials, Part 3,. Thermal and Flammability Studies," Thermochim. Acta, 243, 293-200 (1994).

16. M. W. Babich, R. Benrashid and R. D. Mounts, "New Energy Storage Materials: Thermal and Flammability Studies," Proceedings of the 22nd North American Thermal Analysis Society Conference, Denver, Colorado, 653-658 (1993).

17. I. O. Salyer, A. K. Sircar and R. P. Chartoff, "Advanced Phase Change Materials for Passive Solar Storage Application," Proceedings of the Solar Buildings Conference, Wash. D.C., March 18-20 (1985).

18. I. O. Salyer, A. K. Sircar, R. P. Chartoff and D. E. Miller, "Advanced Phase Change Materials for Passive Solar Storage Applications." Proceedings of the 20th Intersociety Energy Conversion, Engineering Conference, Miami Beach, Florida, August 18-23 (1985).

19. I. O. Salyer and A. K. Sircar, "Development of Phase Change Technology for Heating and Cooling of Residential Buildings and other Applications," Proceedings of the 28th Intersociety Energy Conversion Engineering Conference, Atlanta, Georgia (1993).

20. S. Hwang, M. S. Thesis, Florida Institute of Technology (1991).

21. A. F. Rudd, "Development of Moisture Storage Coatings for Enthalpy Storage Wallboard," ASHRAE Transactions, 100, 3744-3751 (1994).

22. M. W. Babich and R. Benrashid, "Energy Storage Materials Thermal and Flammability Studies," Proceedings of the 23rd North American Thermal Analysis Society Conference, 254-259 (1994).

23. M. W. Babich and R. Benrashid, "DSC and Flammability Studies of Organic and Inorganic Energy Storage Materials," Thermochim Acta, In press (1995).

24. A. Kamel, M. Swami, S. Chandra and P. Fairey, "An Experimental Study of Building-Integrated Off-Peak Cooling Using Thermal and Moisture ("Enthalpy") Storage Systems," ASHRAE Transactions, 97, Part 2, 240-244, (1991).

Material Examples of Use	Transition Temp. °C	Heat of Fusion (J/g)	
CaCl₂ • 6H₂O - CaBr₂ • H₂O - KBr	15-34°C	121	Heat sink in heat pumps
CaCl₂ • 6 H₂O	27°	192	Passive solar panels Central solar Heat
Glauber's Salt	32°	251	Greenhouse heating
MgCl₂ · Mg(NO₃)₂ • 6H₂O	58°	134	Hot water heating
Na₂C₂H₃O₂ • 3H₂O	58°	225	Railway heating
Mg(NO₃)₂ • 6H₂O	89°	163	Dishwashing systems
NH₄Al(SO₄)₂ • 12H₂O	95°	267	Water Heating
MgCl₂ • 6H₂O	114°	167	Absorption AC

Table 1.   Examples of Available Phase Change Materials - Salt Hydrates

Class	Specific Property
Thermal	Suitable phase transition temperature
	Reasonable phase transition range
	Large latent heat of transition
	High boiling point
Physical	Favorable type of phase transition
	Low vapor pressure
	High reproducibility
	Little change in volume
Chemical	Compatible with construction material
	Long term stability of materials
	Non-toxic
	Non-corrosive
	No additional fire hazard
	Low smoke production in fires
	No sensory irritation
	Good aesthetic qualities
Kinetic	No supercooling
	Sufficient crystallization rate
Economic	Cost
	Availability in marketplace

Table 2.   Desirable Properties for Phase Change Materials

Material	mp (°C)	ΔHm (j/g)	fp (°C)	−ΔHf (j/g)
EM625 Coconut Acid	25.0	107.1	15.8	110.1
EM626 Coconut Acid	25.4	119.1	17.6	119.6
EM627 Coconut Acid	30.0	117.2	26.2	147.1
EM659 Capric Acid	28.8	147.4	23.2	140.7
EM651 Lauric Acid	42.0	132.9	37.9	134.5
EM Methylpalmitate	26.8	104.3	20.0	94.1
EK Capric Acid	31.0	128.6	27.1	125.8
EK Lauric Acid	42.5	128.6	38.1	131.5
EK Methylpalmilate	28.8	163.2	23.3	160.9
EK Methylstearate	37.0	160.7	32.2	159.5
SG Undecylenic Acid	24.4	143.5	19.4	144.2
Capric Acid / Lauric Acid Ratio				
1/0	28.6	147.4	23.2	140.7
9/1	25.6	71.7	18.2	38.1
7/3	17.7	60.2	13.1	51:1
5/5	19.7	55.5	15.5	40.8
3/7	20.5	123.8	26.9	62.6
1/9	37.4	125.7	33.4	118.9
0/1	42.0	132.9	37.9	134.5

Table 3. Thermal Results for Fatty Acids and Fatty Acid Mixtures
EM = Emery Chemical Co., EK = Eastman Kodak Chemical Co..
SG = Sigma Chemical Co.

Samples	# of Sample	D90	D240	D475	Dc	Corrected Dm	Dm/Wt	Weight G	Sample Weight
α-Cellulose	5	5.4	92	158.6	8.9	195	71.5	1.95	2.7
Wallboard	3	1.4	19.5	35.3	0.8	35.4	0.8	6.3	49.2
FR Wallboard	3	0.8	16.2	38.2	0.2	37.8	0.7	6.1	55.7
S1	3	25.9	241.3	505.3	0.6	505.3	8.1	15.1	63.3
S1 Epoxy	3	2.3	101.6	390.5	4.5	477.8	3.0	12.6	70.4
S1 Al(OH)3	3	0.7	36.0	60.5	5.7	497.6	7.3	10.5	68.20
S1 Mg(OH)2	3	0.4	15.1	38.0	4.4	505	7.2	22.9	70.2
S2	3	27.7	237.8	496.8	31.5	479.7	7.8	13.2	59.7
S2F	3	25.9	219.5	466.2	31.3	463.7	7.5	10	62
S2 Epoxy	3	5.4	26.7	325	32	486.3	8.1	9.8	58.6
S2F Epoxy	3	3.3	24.9	376.8	29	480.7	7.2	10.9	65.4
S2 Al(OH)3	3	2.3	17.4	261	55	473.9	8	11.0	59.2
S2 Mg(OH)2	3	2.7	23.5	392	73.5	458.6	8	11.8	57.7
SFS2 Al(OH)3	3	3.3	11.5	252.5	31	463.2	7.1	10.9	65.3
SFS2 Mg(OH)2	3	0.9	10.7	248.4	27	390	6.1	12.2	64.5
S3	3	22.4	180.5	435	9.5	494	8.7	10.8	56.9
S3 Epoxy	3	25.8	160	489.5	5.8	496.9	8.1	9.3	61.5
S3 Al(OH)3	3	7.4	128.5	418.3	6.9	501.7	8	10.2	62.5
S3 Mg(OH)2	3	0.9	113.2	329.7	8.9	467.9	7.9	11.4	63.4
S4	3	10.4	104.6	499	13.3	487.6	8.6	12.4	56.9
S4 Epoxy	3	12.3	59.5	205.7	5	498.3	9.2	12.6	54.2
S4 Al(OH)3	3	15.5	59.2	201.5	4.2	494.7	9.3	11.7	53.6
S4 Mg(OH)3	3	0.6	13.1	121.1	2.5	427	7.6	10	56.6

S1=Hexadecane
S2=1-Dodecanol
S3=Undecylenic acid
S4=Coc-nut oil

Table 4. Results from Flame Spread Test.

Material	mp °C	ΔHm (j/g)	fp °C	ΔHf(j/g)
n-Hexadecane b	20.0	216	10.4	220
n-Octadecane a	28.4	200	17.9	200
1-Dodecanol b	23.8	184	17.5	190
n-Heptadecane b	22.6	164	19.0	165
Allylpalmitate d	22.6	173	16.2	125
Undecylenic Acid e	24.8	141	18.1	143
1-Nonadecane b	23.2	131	20.1	134
1-Iodohexadecane b	22.2	131	8.6	132
n-Octadecylacrylate c	25.7	115	22.1	99
Diphenyl ether b	27.2	97	-8.2	61
Diphenylmethane b	24.4	86	-3.3	75
Chlorobenzothiazole b	18.8	65		
3-Iodoaniline b	22.5	64		
Polytetrahydrofuran b	17.5	59	0.1	76.4
Trimethylcyclohexene b	24.1	47		
Phorone	25.8	124	11.2	3.7

Table 5. Thermal Results for New Enthalpy Storage Materials
*Average of three measurements. Average standard
deviation for mp and fp = 0.3°. Average standard
deviation for H = 4 j/g. (a) Mainstream Engineering
Co., (b) Aldrich Chemical Co., (c) Scientific
Polymer Products, Inc., (d) Dajac Laboratories, Inc.
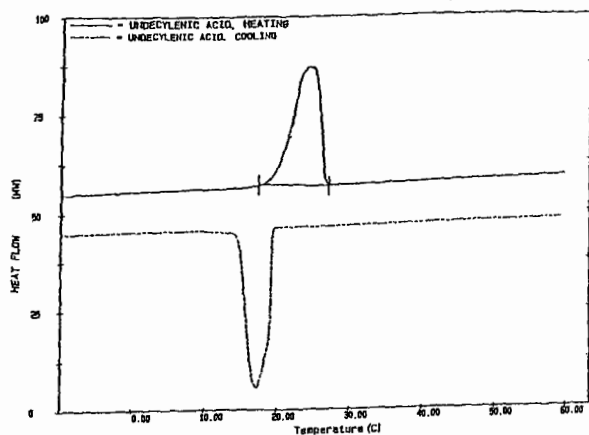(e) Sigma Chemical Co.

Figure 1. Sample DSC Curve for Undecylenic Acid
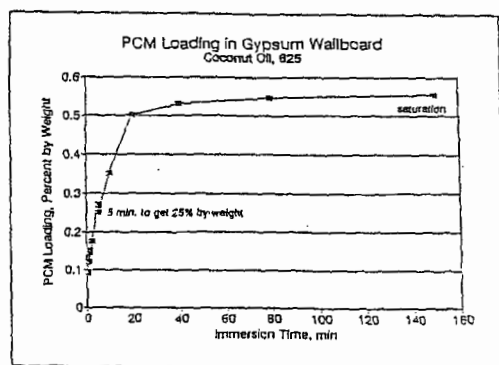(Heating and Cooling Curves)
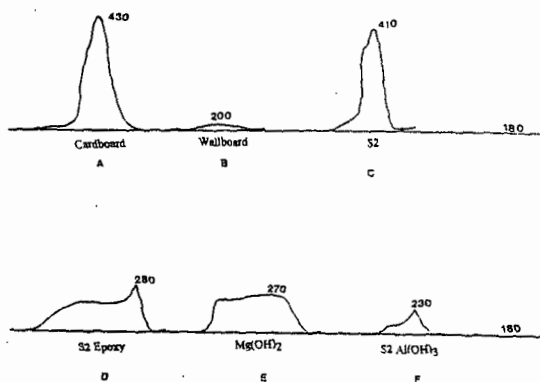

Figure 2. Sample ESM Loading in Gypsum Wallboard

Figure 3. Comparison of maximum temperature in stack NBS
Radiant Panel Tests for cardboard (A), wallboard (B)
wallboard treated with 1-icdecanol S2 (C), epoxy
coated S2 (D), Mg(OH)$_2$/epoxy coated S2 (E), and
Al(OH)$_3$/epoxy coated S2 (F).

37

ANALYSIS OF ASPHALT-BASED ROOF SYSTEMS USING THERMAL ANALYSIS

Ralph M. Paroli and Ana H. Delgado

Institute for Research in Construction,
National Research Council of Canada
Ottawa, Ontario, Canada K1A 0R6

Keywords: Thermal analysis, roof membrane, asphalt, modified bitumen

INTRODUCTION

Asphalt has been used in the construction of roads and houses for thousands of years. The properties of asphalt has rendered it quite useful in roofing and waterproofing applications. The most popular use of asphalt in industrial roofing is in the form of a built-up roof or modified-bituminous sheet. This type of roof consists of asphalt, reinforcement and aggregate which is used to protect the asphalt from ultraviolet rays. All materials have their weaknesses and asphalt is no exception. A good asphalt (e.g., low asphaltene content) must be used to ensure the quality and low-temperature performance of roofing asphalts. Polymer additives can be added.

The criteria for choosing a polymer additive are: (a) the viscosity of the asphalt should not be significantly altered (b) It must be sufficiently compatible with the asphalt so as to avoid any phase separation during application (even at high temperatures). (c) It must improve some of the mechanical properties of the asphalt such as resistance to permanent deformation, fracture and high-temperature. In low-temperature environments, the polymer must be able to enhance the low-temperature flexibility and lower the glass-transition temperature (T_g) of the asphalt. Two commonly used polymer additives are styrene-butadiene-styrene block copolymer (SBS) and atactic polypropylene (APP). The exact amount of polymer added depends on the polymer and desired property. For example, 10-15% of SBS is sufficient to yield a continuous phase in the asphalt.

Roofing membranes have been used for many years. In the past, the testing of various roofing materials was simple because of the accumulated experience and also because of the lack of variety. Today, with the variety of additives, it is quite difficult to compare them solely on the basis of mechanical properties. This is especially true since the mechanical properties of these materials are not only related to macroscopic behaviour but also at the molecular level which is controlled by chemical composition and molecular arrangement.

Thermal analysis is a technique that can provide some insight as to why some roofing materials do not perform properly. In the past seven years, quite a few papers have been published using these techniques for roofing (see references 1-10 and references therein). Thermogravimetry (TG) can be used to monitor weight loss due to weathering and/or aging. Dynamic mechanical analysis (DMA) can be used routinely to determine the glass transition temperature. Together, DMA and TG can provide a measure of the degradative factors which can lead to the correlation between accelerated weathering and actual field performance. The objective of this study is to demonstrate the utility of TG and DMA in establishing the durability of modified-bituminous roof membranes.

EXPERIMENTAL

Composition of Modified Bitumen Membranes.

Four commercially-available, polymer-modified bituminous roofing membranes were obtained and labelled as SBS1, SBS2, SBS3 and APP1. A typical composition for the roofing membrane samples used in this study is given in Table I. The quantities will vary from product to product. It should be noted that the granules, reinforcement and

polyethylene account for between 36 and 40% of the total weight of a cap sheet but are excluded from the percentages listed in Table I.

Sample Preparation

Each material was cut into seven pieces of about 150 x 250 mm. One piece was used as a control, three were placed in an air-circulating oven preheated at 80 °C, and the remaining three were placed in an air-circulating oven set at 100 °C, for heat-aging. One piece of each material was removed from the oven, after 1, 7, and 28 days. Specimens were cut out for tensile testing and thermal analyses.

Thermogravimetry (TG)

The weight-loss of each roofing sample was monitored by thermogravimetric analysis using a Seiko Instruments Inc. STA 320 interfaced to a HP-900 Workstation. A piece of approximately 20 mg of sample was cut without including granules. The analyses were carried out at temperatures between 20 °C and 600 °C using a nitrogen gas flow of 150 mL min^{-1} and from 600 °C to 1000 °C under air. The scanning rate was 20 °C min^{-1}. Throughout this study the derivative TG (DTG) curve was used as it provided the desired quantitative data (see Fig. 1). The data are tabulated in Table II as a function of heat-aging temperature and exposure-time.

Dynamic Mechanical Analysis (DMA)

The glass transition temperature of the membranes was obtained using a Rheometrics RSA II (software version 3.0.1) dynamic mechanical analyzer equipped with a mechanical cooling device. The following experimental profile was used for this study:

Geometry:	3-point bending
Sample width:	8 - 10.5 mm
Sample thickness	3.5 - 4.0 mm
Sample length	48.00 mm
Sweep type	Temp. steps
Frequency:	1 Hz (6.28 rad/sec)
Temperature Range:	-100 °C to +30 °C
Heating Rate:	2.0 °C/min
Soak Time:	2.0 min
Strain:	2×10^{-2} %

Typical DMA curves are shown in Fig. 2. The glass transition temperature, T_g, (α-transition values) was obtained from the average of at least two and no more than four specimens from the same sample. The values are reported as the maximum in the loss modulus (E") vs temperature curve. It is also possible to use the maximum of the tanδ peak vs temperature curve, however, it was found that the E" curve gave a better correlation with traditional mechanical data (e.g., tensile and elongation). The glass transition temperatures of the various samples are summarized in Table III.

RESULTS AND DISCUSSION

Three SBS (styrene butadiene styrene) modified membranes and one APP (atactic polypropylene) modified membrane were selected. The granules on the SBS modified membranes should be taken into account during analysis because they account for approximately one-third of the total weight and are not affected by high temperatures. Their presence minimizes the weight loss detected during the actual experiment. For this reason, the granules were removed from the SBS samples prior to testing. The APP modified membrane did not contain granules.

The results of the TG show that the polymer-modified bitumens are not affected by short term exposure to temperatures of 80 and 100 °C. But two samples show a large loss of weight after being heated in an oven for

28 days at 100 °C. The weight loss for SBS1 and SBS2, as determined by TG, is much less after 28 days of heating at 100 °C than it was at 7 days. Thus, weight was lost in the oven during the aging. This demonstrates that this technique can be useful in determining the relative stability of modified bituminous membranes. It is likely that changing the conditioning by heating the membrane in an oven for six months at 80 °C would provide a better reading on the long term durability of these membranes. In the field, loss of protective granules, which is a problem, will also expose the bitumen to UV radiation and accelerate the overall rate of deterioration of the membrane.

Generally, the glass transition temperature of control SBS modified membranes is in the -48 to -50 °C range. Heat aging, however, gradually raises the T_g to around -30 °C. On the other hand, the APP modified sample appears to be unaffected by heating as its T_g remains constant at -30 °C. Most samples also showed a another transition around -15 °C. While the component responsible for this transition is still unknown; its existence, however, might indicate that installing SBS-modified membranes in sub-zero temperature, using hot asphalt, as specified by the manufacturers could cause problems. It should be noted that all manufacturers call for their membranes to be unrolled and allowed to relax prior to installation.

CONCLUSIONS

The modified bituminous membranes, because of their low softening temperature and their complex chemical composition, provide results that are more difficult to interpret than the previously published EPDM and PVC membranes. The results, nevertheless, appear to be quite reliable when compared to the performance of these membranes in the field.

The results have shown that APP-modified material had a warmer glass transition temperature than the SBS-modified. The APP-modified bitumen, however, was more heat resistant than the SBS-modified ones.

The heating-aging temperature of 100 °C is not recommended because of the low softening point of the asphalt. A heat-aging temperature of 80 °C for six months could be preferable to assess the relative durability.

Loss of weight resulting from heat-aging affects the performance of modified bituminous membranes and appears to be an important factor in determining service-life. Little weight loss (~5%) after aging/weathering is indicative of stability to the aging program.

REFERENCES

1. C. G. Cash, Single Ply Roofing Technology: ASTM STP 790, pp. 55-64, (1982).

2. D. Backenstow and P. Flueler, Proceedings, 9th Conference on Roofing Technology, National Roofing Contractors Association, Rosemont, IL, pp. 54-68, April 1987.

3. R. M. Paroli, O. Dutt, A. H. Delgado, M. Mech, Thermochimica Acta, 182, 303-317, (1991).

4. G. D. Gaddy, W. J. Rossiter, Jr., R. K. Eby, Proceedings, 1991 International Symposium on Roofing Technology, pp. 502-507, 1991, F. Kocich, editor, National Roofing Contractors Association, Rosemont, IL.

5. G. D. Gaddy, W. J. Rossiter, Jr., R. K. Eby, ASTM STP 1136, 168-175, (1991).

6. R. M. Paroli, O. Dutt, A. H. Delgado, H. K. Stenman, Journal of Materials in Civil Engineering 5(1), 83-95, (1993).

7. K. Oba, and F. Björk, Polymer Testing, 12, 35-56 (1993).

8. J. J. Penn, R. M. Paroli, Thermochimica Acta, 226, 77-84 (1993).

9. I. S. Rodriguez, O. Dutt, R. M. Paroli, N.P. Mailvaganam, Materials and Structures, 26(160), 355-361 (1993).

10. "Thermal Analysis Testing of Roofing Membrane Materials: Interim Report of the Thermal Analysis Task Group", *Conseil International du Batiment pour la Recherche l'Etude et la Documentation (CIB) W.83 and Réunion Internationale des Laboratoires d'Essai et de Recherche sur les Matériaux et les Constructions (RILEM) 120-MRS Joint Committee on Membrane Roofing Systems*, September 1993.

11. K. Oba, Flat roofs: Investigation of heat welding Techniques for polymer-modified bituminous roofing membranes. Dissertation, Royal Institute of Technology. Sweden (1994).

12. R. M. Paroli, O. Dutt, T. L. Smith, B. J. Whelan, Roofing Research and Standards Development: Volume 3, ASTM STP 1224, Thomas J. Wallace and Walter J. Rossiter, Jr., Eds., American Society for Testing and Materials, Philadelphia, 1994, pp.139-147.

Table I   Typical matrix composition of SBS modified membranes

Ingredients	% by weight	Function
Bitumen	66 - 74	Waterproofing agent
Rubber modifier	11 - 16	Imparts elastomeric properties
Filler	11 - 18	Provides rigidity

Table II   TG data for modified bituminous membranes

Heating Schedule		Weight Loss (%)			
Temp (°C)	Days	SBS1	SBS2	SBS3	SBS4
unheated		71.8	78.4	55.5	78.2
80	1	69.1	80.6	57.3	78.8
80	7	71.6	71.9	54.8	78.8
80	28	70.3	70.8	55.3	77.0
100	1	70.3	74.8	57.6	74.0
100	7	69.2	73.0	55.1	75.9
100	28	36.3	29.9	52.1	73.8

Table III   Glass Transition Temperature (T_g) of Modified Bitumens

Heating Schedule		Tg (°C) for Samples			
Temp (°C)	Days	SBS1	SBS2	SBS3	APP1
Unheated		-50	-50	-48	-30
80	1	-50	-50	-46	-30
80	7	-40	-50	-46	-30
80	28	-40	-48	-50	-30
100	1	-40	-40	-50	-30
100	7	-40	-40	-48	-30
100	28	-30	-30	-30	-30

Figure 1. Typical TG/DTG curves for a polymer-modified bitumen roof
membrane.
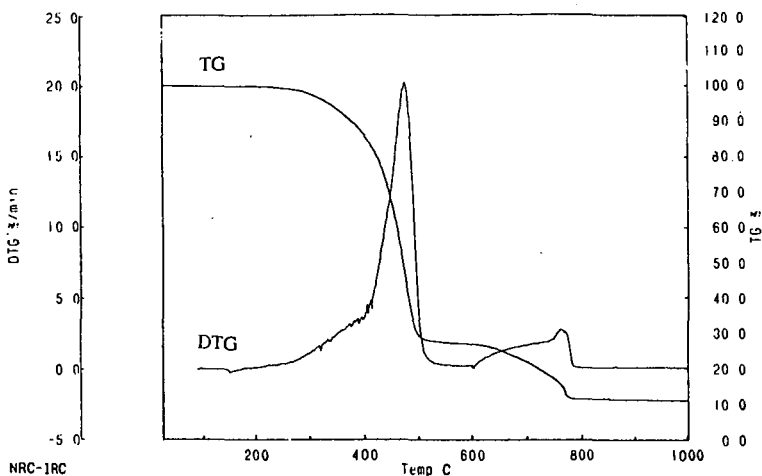
Figure 2. Typical DMA curves for a polymer-modified bitumen roof
membrane.
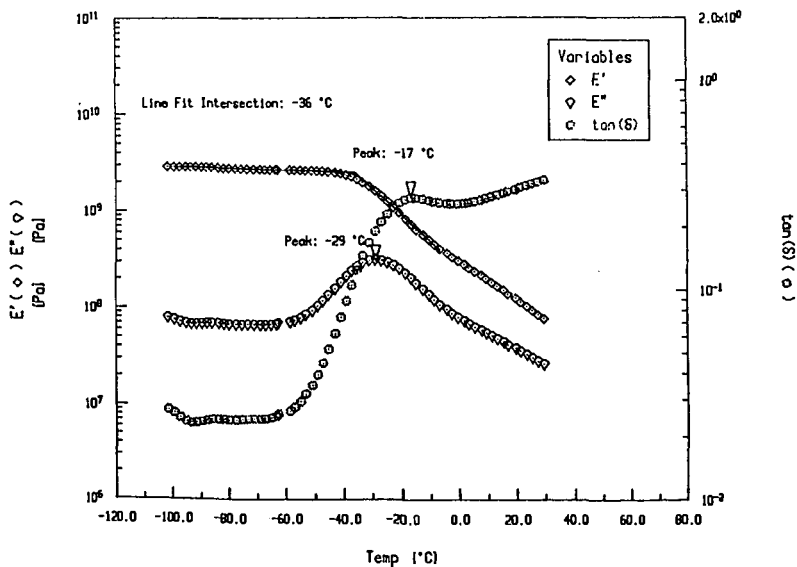
USE OF TG-FTIR ANALYSIS FOR THE CHARACTERIZATION
OF FUELS AND RESOURCES

Michael A. Serio, Rosemary Bassilakis and Peter R. Solomon

Advanced Fuel Research, Inc.
87 Church Street
East Hartford, CT 06108

Keywords: Thermal Analysis, FT-IR, Fuels

ABSTRACT

Thermogravimetric (TG) analysis combined with Fourier Transform Infrared (FT-IR) analysis of evolved products has proven to be a powerful technique for characterization of coal, source rock, heavy hydrocarbons, biomass, waste materials, and plastics. The TG-FTIR method can be used to determine the resource potential of a material, i.e., the types of products a material is likely to produce when subjected to processing by pyrolysis or combustion. It can also provide kinetic information for model validation or extrapolation and can provide the equivalent information to proximate and ultimate analysis. In addition, TG-FTIR analysis can be used to characterize the adsorbent potential and combustion reactivity of solids. The TG-FTIR method can provide this information in a more rapid, reproducible, and inexpensive way when compared to most other types of laboratory characterization methods such as drop tube reactors. This paper reviews the application of TG-FTIR analysis to hydrocarbon fuels and resources.

INTRODUCTION

Thermogravimetric analysis (TGA) has been employed in coal science to perform a number of characterizations including: proximate analysis,[1] kinetics of weight loss,[2] char reactivity,[3-6] and gas adsorption measurements.[7] A complementary technique, evolved product analysis, has been employed to study pyrolysis product distributions and kinetics,[8-11] functional group compositions,[10,12,13] and temperature programmed desorption.[14-15] A TG-FTIR instrument combines TGA with evolved product analysis by Fourier Transform Infrared (FT-IR) spectroscopy. FT-IR analysis of evolved products has advantages over mass spectroscopy in allowing analysis of very heavy products, and over gas chromatography in speed.

TG-FTIR instruments are available from several instrument manufacturers, including On-Line Technologies, Inc. (On-Line), an affiliate of Advanced Fuel Research, Inc. (AFR). In addition, Bio-Rad and Perkin-Elmer, among others, offer a TG-FTIR instrument. One of the differences among these instruments is the method used to analyze and quantitate the heavy liquid products from pyrolysis of the sample, which form an aerosol upon subsequent cooling prior to entry into the multi-pass FT-IR cell. These instruments have primarily been used for the analysis of polymers, pharmaceuticals, minerals, etc., including a limited amount of work done at AFR.[17,36,37] Nearly all of the work on the application of TG-FTIR to hydrocarbon fuels and resources has been done at AFR or its collaborators. Consequently, the scope of this review will be limited to this body of work.

The application of TG-FTIR to coal analysis at AFR has been described in several publications.[16-25] To analyze coal, a sequence of drying, pyrolysis and combustion is employed to obtain: proximate analysis, volatiles composition, volatiles kinetics, and relative char reactivity. By using several different heating rates, kinetic rate constants for volatiles evolution have been obtained.[17,21] TG-FTIR analysis has also been used at AFR to characterize other hydrocarbon materials such as modified coal samples,[26-28] coal liquefaction resids,[29] petroleum source rocks,[30] lubricants,[31] biomass,[32,33] waste tires,[34,35] and polymers.[17,36,37] This paper will briefly review the use of the TG-FTIR technique at AFR for the characterization of hydrocarbon fuels and resources.

EXPERIMENTAL

Apparatus - A schematic of the AFR TG-FTIR instrument is presented in Fig. 1. Its components are as follows: a DuPont™ 951 TGA; a hardware interface (including a furnace power supply); an Infrared Analysis 16 pass gas cell with transfer optics; a Bomem 110 FT-IR; (Resolution: 4 cm⁻¹, Detector: MCT). A helium sweep gas (250 cc/sec) is employed to bring evolved products from the TGA directly into the gas cell. A window purge of 700 cc/sec is employed at each end of the cell. The system is operated at atmospheric pressure. This instrument package is available commercially as the *TG/plus* from On-Line Technologies, Inc. (East Hartford, CT).

The most difficult volatiles to analyze are the heavy decomposition products which condense at room temperature, such as tars from coal. In the *TG/plus*, the high conductivity helium sweep gas and the rapid cooling cause these products to form an aerosol which is fine enough to follow the gas through the analysis cell. The cell is connected without restrictions to the sample area. The aerosol is also fine enough that there is only a little scattering of the infrared beam and it is thus attenuated almost as though the tar was in the gas phase, as shown in Fig. 2. Based on the aerosol's Rayleigh scattering of infrared radiation, the diameter of the aerosol droplets in this case is less than 1.0 μm. As indicated above, the

43

technique for analysis of the heavy liquid aerosols is one of principal features that differentiate the various commercial TG-FTIR instruments.

Procedure - As an example of the analysis procedure, the pyrolysis and oxidation of a lignite is described. More detail can be found in Refs. 16 and 17. Figure 3a illustrates the weight loss from this sample and the temperature history. A 35 mg sample of Zap lignite, loaded in the sample basket of the DuPont™ 951, is taken on a 30 °C/min temperature excursion in the helium sweep gas, first to 150 °C to dry for 240 sec, then at 30 °C/min to 900°C for pyrolysis. Upon reaching 900 °C, the sample is immediately cooled to 250 °C over a twenty minute period. After cooling, a small flow of O_2 (0.3 cc/sec) is added to the helium sweep gas at the 57 minute mark and the temperature is ramped to 700 °C at 30 °C/min (or as high as 1000 °C) for oxidation.

During this excursion, infrared spectra are obtained once every thirty seconds. As shown in Fig. 2, the spectra show absorption bands for CO, CO_2, CH_4, H_2O, SO_2, COS, C_2H_4, and NH_3. The spectra above 250 °C also show aliphatic, aromatic, hydroxyl, carbonyl and ether bands from tar. The evolution of gases derived from the IR absorbance spectra are obtained by a quantitative analysis program which employs a database of integration regions and calibration spectra for different compounds [16,17]. The routine employs regions of each calibration spectrum which permit the best quantitation with the least interferences. The routine is fast enough to allow the product analysis to be displayed on the computer screen during the actual experiment.

Figure 3b illustrates the integral of the evolution curves to obtain the cumulative evolved product amounts. Because the data are quantitative, the sum of these curves match the weight loss as determined by the TGA balance. Discrepancies occur in this match because of missing components such as H_2 which cannot be seen by IR. Also, when O_2 is introduced, the balance shows a net gain in weight due to O_2 chemisorption.

The TG-FTIR system provides all of the usual capabilities of a TGA for measurement of char reactivity or surface characterization by Temperature Programmed Desorption (TPD) with the additional advantage of measurement of the evolved products. A non-isothermal reactivity test developed at AFR using a conventional TGA system[3-5] was later adapted to the TG-FTIR.[38] Studies of coal chars using TPD have also been made in this apparatus.[24]

RESULTS AND DISCUSSION

Examples of analyses done with the TG-FTIR apparatus will be presented in detail for coal samples and selected examples will be given for lignin and polymers. The coal data included in this paper is primarily from samples from the Argonne Premium sample bank, which have been extensively characterized using this technique.[18,19,21,24-26] Other characterizations of the Argonne samples have been summarized by Vorres.[39]

Measurement of Char Properties - The results from the application of the TG-FTIR instrument to measurements of the critical temperature (T_{cr}) (an index of reactivity that defines the temperature at which a small but measurable rate of weight loss occurs) and the oxygen chemisorption capacity (OCC) for the Argonne Premium coals are shown in Fig. 4. As expected, the values of T_{cr} decrease with decreasing rank (increased oxygen content) which indicates that lower rank coals are more reactive. This variation in reactivity with rank is primarily due to mineral contributions to reactivity.[3-5] The measurements of oxygen chemisorption capacity (OCC), which are related to the active site concentration, are inversely related to T_{cr} and are also shown in Fig. 4. In our work, we have found that the value of T_{cr} is a more useful correlative parameter for reactivity than the OCC.[38]

Measurement of Volatile Product Evolution - The TG-FTIR system has been used to conduct programmed pyrolysis experiments on the Argonne premium coals over a range of heating rates (3, 30, 50, 100 °C/min).[18,19,21,24-26] The changes in the positions of the evolution curves with temperature for the various volatile components can be used to define the kinetic parameters. An example is shown in Fig. 5 where the temperature for the maximum tar evolution rate is plotted for the eight Argonne coals at two different heating rates. Similarly, the changes in the integrated amounts of each volatile product can be used to characterize the coal functional group composition, as shown in Fig. 6 for the evolution of NH_3.

An example of results from TG-FTIR analysis of eight lignin samples is shown in Fig. 7. This plot shows a summary of the gas, tar and char yields for a study where high tar yields were desired to allow subsequent processing of lignin into carbon materials.[32] The tar yields from the eight lignin samples varied from ~10 wt% for the H_2SO_4 lignin to >50 wt.% for the Iotech lignin. Another feature of the use of TG-FTIR for the analysis of hydrocarbon materials is the ability to conduct an on-line spectroscopic analysis of the heavy liquid products. An example is shown in Fig. 8, which compares the spectrum obtained at the temperature of the maximum evolution rate for six polymers. The slope of the baseline indicates the degree of scattering and hence the size of the tar aerosols, as discussed above. This is a characteristic of the material which depends on the molecular weight distributions of the oligomers formed, the viscosity, and surface tension. Since the tar aerosol droplets are components of smoke and, ultimately of soot, the technique has the potential to provide information which correlates with these important combustion properties of polymers. Figure 8 indicates that the TG-FTIR method reveals

significant differences in the tar structure and in the size of the tar aerosols between these different polymers.

Relationships between Kinetic Rates of Different Volatile Species - It has been found that some pools in the different volatile species have peak evolution rates at the same temperature and those peaks have the same shifts when the heating rate changes. The Utah Blind Canyon coal provides a good example of this phenomenon[19,24]. The TG-FTIR measurements indicate that the tar evolution, the CO_2-Loose, CO-Loose, and the H_2O-Loose pools all show very close peak evolution rate temperatures, at about 480 °C for 30 °C/min., at about 519 °C for 100 °C/min. and at about 430 °C for 3 °C/min. runs. This feature implies that these volatile pools can be fit with the same kinetic parameters. This may also imply that there is some common evolution chemistry.

Modeling of Devolatilization Processes - The kinetic parameters for the functional group pools from the eight Argonne premium coals and some additional coals have been determined using a set of rules that were developed to allow a systematic method of establishing the rank variations (e.g., the frequency factors were fixed at values of less than 10^{15}/sec. and only the activation energies were allowed to vary with rank)[21]. The kinetic and compositional parameters obtained from TG-FTIR analysis are used along with other characterization information to calibrate our Functional Group - Depolymerization, Vaporization, Crosslinking (FG-DVC) model of coal devolatilization.[21] A typical comparison of theory and TG-FTIR data is shown in Figs. 9 and 10. Figure 9 shows a comparision of theory and experiment for the weight loss and major volatile species for pyrolysis of a Consol #2 coal at 30 °C/min. Figure 10 shows a comparison of FG-DVC model predictions and experimental data for the tar evolution rate at 30 °C/min. from all eight Argonne Premium Coals. The agreement between the theory and experiment is generally quite good except for species where mineral contributions are important in Fig. 9 (CO_2, H_2O). The kinetic parameters obtained from the TG-FTIR method extrapolate well to very low heating rates, as in natural maturation processes,[20,28] as well as to the high heating rates of importance in most coal gasification and combustion processes.[18,21] Other versions of the FG-DVC model have been developed for lignin[33] and phenol-formaldehyde[36] using the same approach.

CONCLUSIONS

Thermogravimetric (TG) analysis combined with Fourier Transform Infrared (FT-IR) analysis of evolved products has proven to be a powerful technique for characterization of coal, source rock, heavy hydrocarbons, biomass, waste materials, and plastics. The TG-FTIR method can be used to determine the resource potential of a material, i.e., the types of products a material is likely to produce when subjected to processing by pyrolysis, or combustion. It can also provide kinetic information for model validation or extrapolation and can provide the equivalent information to proximate and ultimate analysis. In addition, TG-FTIR analysis can be used to characterize the adsorbent potential and combustion reactivity of solids.

ACKNOWLEDGEMENTS

REFERENCES

1. Ottaway, W., Fuel, **61**, 713 (1982).
2. Ciuryla, V.T., Weimer, R.F., Bivans, A., and Motika, S.A., Fuel, 58, 748 (1979).
3. Solomon, P.R., Serio, M.A., and Heninger, S.G., ACS Div. of Fuel Chem. Preprints, **31**, (3), 200 (1986).
4. Best, P.E., Solomon, P.R., Serio, M.A., Suuberg, E.M., Mott, W.R, Jr., and Bassilakis, R., ACS Div. of Fuel Chem. Preprints, **32**, (4), 138 (1987).
5. Serio, M.A., Solomon, P.R., Bassilakis, R., and Suuberg, E.M., ACS Div. of Fuel Chem. Preprints, **34**, (1), 9 (1989).
6. Mahajan, O.P., Yarzab, R., and Walker, Jr., P.L., Fuel, **57**, 643 (1978).
7. Suuberg, E.M., Calo, J.M., and Wojtowicz, W., ACS Div. of Fuel Chem. Preprints, **31**, (3), 186 (1986).
8. Winans, R.E., McBeth, R.L., and Neill, P.H., ACS Div. of Fuel Chem. Preprints, **33**, (3), 85 (1988).
9. Chakravarty, T., Windig, W., Hill, G.R., and Meuzelaar, H.L.C., Energy & Fuels, **2**, (4), 400 (1988).
10. Solomon, P.R. and Hamblen, D.G., Progress in Energy and Combustion Science, 9, 323 (1983).
11. Burnham, A.K., Oh, M.S., Crawford, R.W., and Samoun, A.M., Energy & Fuels, **3**, 42 (1989).
12. Attar, A. and Hendrickson, G.G., Coal Structure, (R.A. Meyers, Ed.), Academic Press, NY, **5**, 131 (1982).
13. LaCount, R.B., Anderson, R.R., Friedman, S., and Blaustein, B.D., Fuel, **66**, 873 (1987).
14. Hall, P.J. and Calo, J.M., Energy & Fuels, **3**, 370 (1989).
15. Zhang, Z.G., Kyotani, T., and Tomita, A., Energy & Fuels, **3**, 566 (1989).
16. Carangelo, R.M., Solomon, P.R., and Gerson, D.G., Fuel, **66**, 960 (1987).
17. Carangelo, R.M., Solomon, P.R., Bassilakis, R., Gravel, D., Baillargeon, M., Baudais, F., and Vail,

G., American Laboratory, p. 51, (1990).

18. Serio, M.A., Solomon, P.R., Charpenay, S., Yu, Z.Z., and Bassilakis, R., ACS Div. of Fuel Chem. Preprints, 35, (3), 808 (1990).
19. Solomon, P.R., Serio, M.A., Carangelo, R.M., Bassilakis, R., Gravel, D., Baillargeon, M., Baudais, F., and Vail, G., Energy & Fuels, 4, (3), 319 (1990).
20. Solomon, P.R., Serio, M.A., Carangelo, R.M., Bassilakis, R., Yu, Z.Z., Charpenay, S., and Whelan, J., Journal of Analytical and Applied Pyrolysis, 19, 1 (1991).
21. Solomon, P.R., Hamblen, D.G., Serio, M.A., Yu, Z.Z., and Charpenay, S., Fuel, 72, (4), 489 (1993).
22. Solomon, P.R., Serio, M.A., and Suuberg, E.M., Progress in Energy and Combustion Science, 18, pp 133-220 (1992).
23. Solomon, P.R., Serio, M.A., Carangelo, R.M., and Bassilakis, R., ACS Div. of Fuel Chem. Preprints, 35, (2), 334 (1990).
24. Carangelo, R.M., Serio, M.A., Solomon, P.R., Charpenay, S., Yu, Z.Z., and Bassilakis, R., ACS Div. of Fuel Chem. Preprints, 36 (2), 796 (1991).
25. Bassilakis, R., Zhao, Y., Solomon, P.R. and Serio, M.A., Energy & Fuels, 7, 710 (1993).
26. Serio, M.A., Kroo, E., Charpenay, S., and Solomon, P.R., ACS Div. of Fuel Chem. Preprints, 37, (4), 1681 (1992).
27. Serio, M.A., Kroo, E., Teng., H., Solomon, P.R., ACS Div. of Fuel Chem. , Preprints, 38, (2), 577 (1993).
28. Charpenay, S., Serio, M.A., Bassilakis, R., and Solomon, P.R., "Influence of Maturation on the Pyrolysis Products from Coal and Kerogens, Part I: Experimental," Accepted in Energy & Fuels, (October 1995).
29. Teng, H., Serio, M.A., Bassilakis, R., Knight, K.S., Bates, S.C., and Solomon, P.R., ACS Div. of Fuel Chem. Preprints, 37, (4), 1903 (1992).
30. Whelan, J.K., Solomon, P.R., Deshpande, G.V., and Carangelo, R.M., Energy and Fuels, 2, 65 (1988).
31. Bonanno, A.S., Bassilakis, R., and Serio, M.A., "TG-FTIR methods for the Evaluation of Lubricant Contamination," to be presented at ACS New Orleans meeting, March, 1996.
32. Serio, M.A., Kroo, E., Bassilakis, R., Solomon, P.R., and Malhotra, R., ACS Div. of Fuel Chem. Preprints, 36, (3), 1110 (1991).
33. Serio, M.A., Charpenay, S., Bassilakis, R., and Solomon, P.R., Journal of Biomass & Bioenergy, 7, (1-6), 104 (1994).
34. Teng, H., Serio, M.A., Bassilakis, R., Morrison, P.W., Jr., and Solomon, P.R., ACS Div of Fuel Chemistry Preprints, 37, (2), 533 (1992).
35. Teng,H., Serio, M.A., Wojtowicz, M.A., Bassilakis, R., and Solomon, P.R., Industrial & Engineering Chemistry Research, 34, 3102 (1995).
36. Serio, M.A., Charpenay, S., Bassilakis, R., and Solomon, P.R., ACS Div. of Fuel Chem. Preprints, 36, (2), 664 (1991).
37. Serio, M.A., Bassilakis, R., McMillen, D.F., Satyam, A., and Malhotra, R., Intl. Conf. on Coal Science, Alberta, Canada, II (163) (1993).
38. Serio, M.A., Solomon, P.R., Yang, Y.P., and Suuberg, E.M., "The Use of TG-FTIR Analysis to Determine Char Combustion Properties", presented at the AIChE Annual Meeting, Chicago, Ill, (Nov. 11-16, 1990).
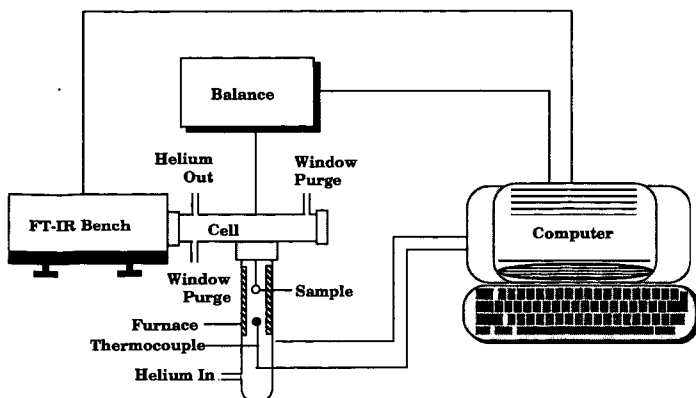39. Vorres, K.S., Energy & Fuels, 4, 420 (1990).

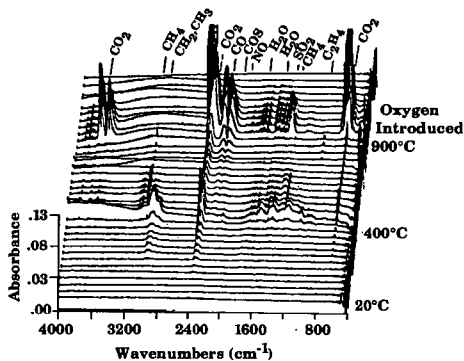**Figure 1.** Schematic diagram of the standard TG/FT-IR instrument.

Figure 2. Spectra from TG/FT-IR of coal. Heating rate is $0.5°C/s^{-1}$ from 20 to 900°C. The remaining char is then burned at 700°C.
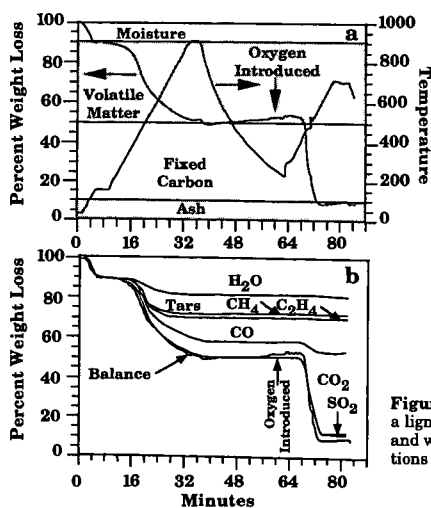

Figure 3. TG/FT-IR analysis of a lignite. a) Temperature history and weight loss; b) Species contributions to weight loss.

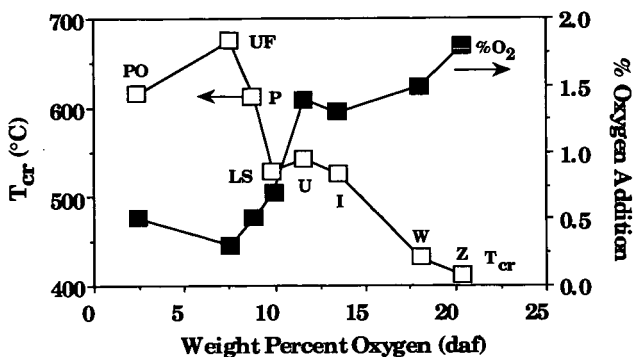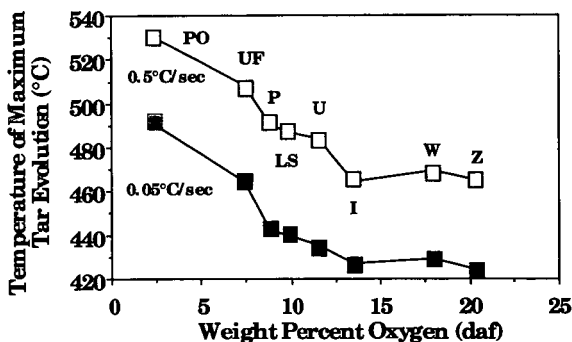**Figure 4.** Rank variation of T_{cr} and oxygen chemisorption.
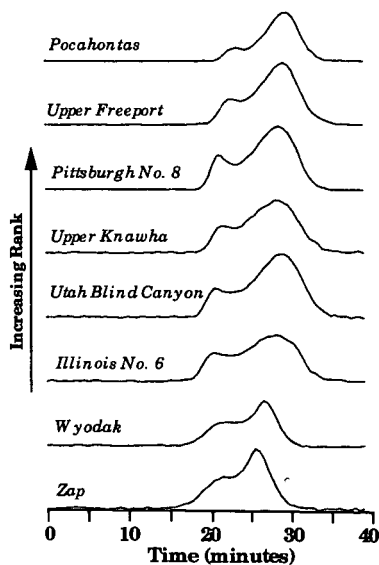

Figure 5. Rank variation of tar evolution temperature.

Figure 6. Evolution of NH_3 from programmed pyrolysis (30°C/min) of the Argonne premium coals.
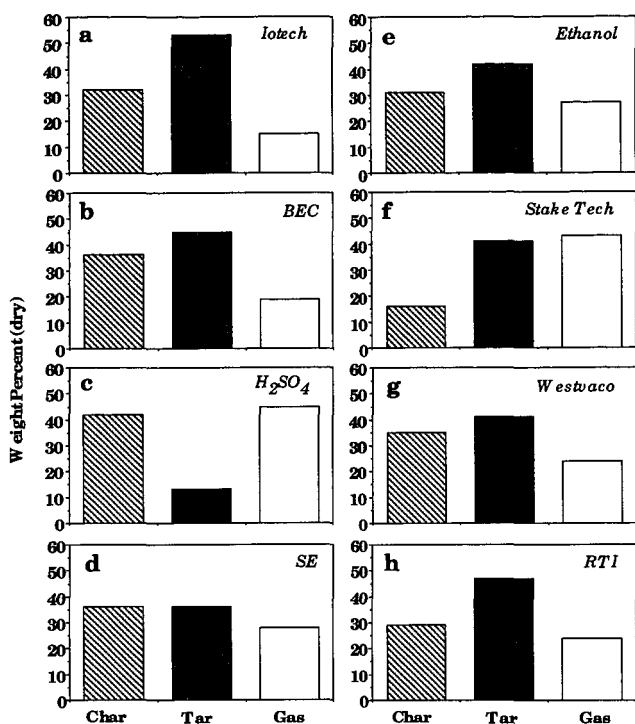
Figure 7. Comparison of char, tar and gas yields from programmed pyrolysis of eight lignins.
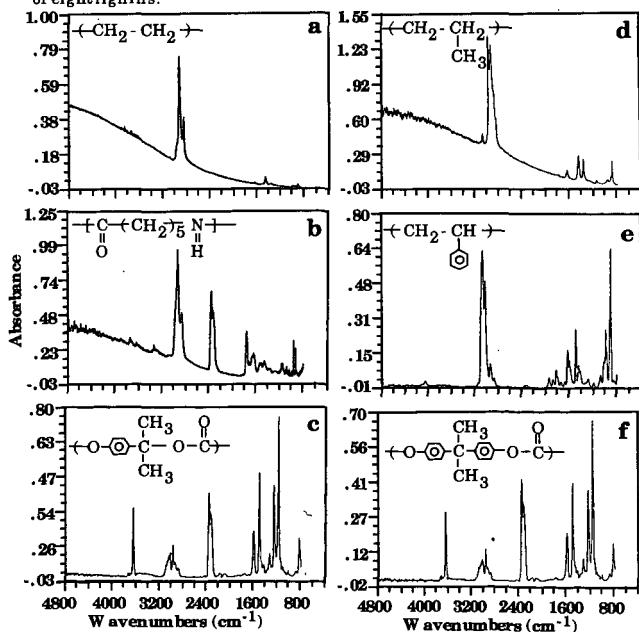
Figure 8. Comparison of IR spectra at peak temperature in tar evolution profile from TG/FT-IR analysis of several polymers. a) Polyethylene (PE); b) Nylon; c) Lexan (standard); d) Polypropylene (PP); e) Polystyrene (PS); f) Lexan (flame retardant).
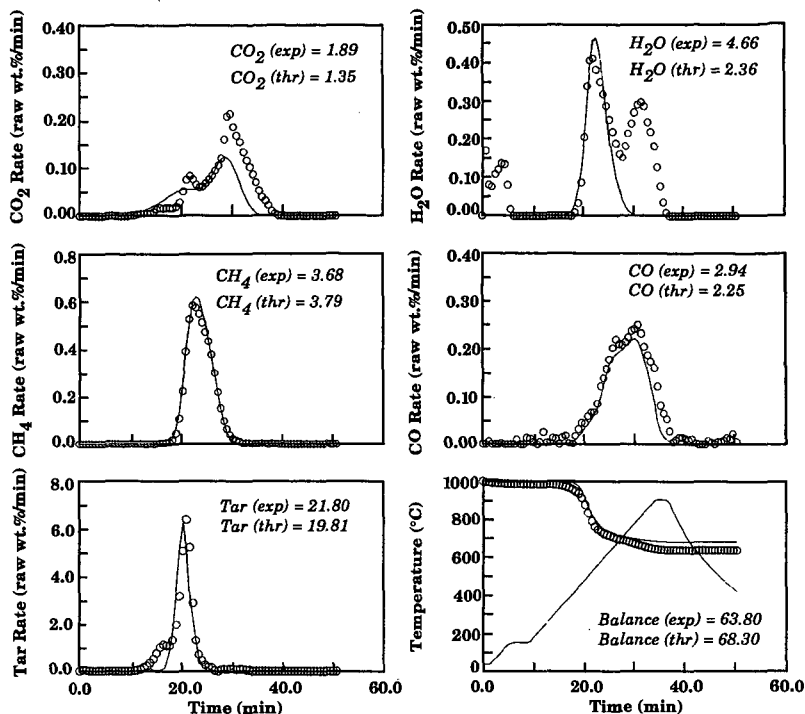
Figure 9. Comparison of TG/FT-IR data and FG-DVC model predictions for CONSOL #2 coal, pyrolyzed at 30°C/min.
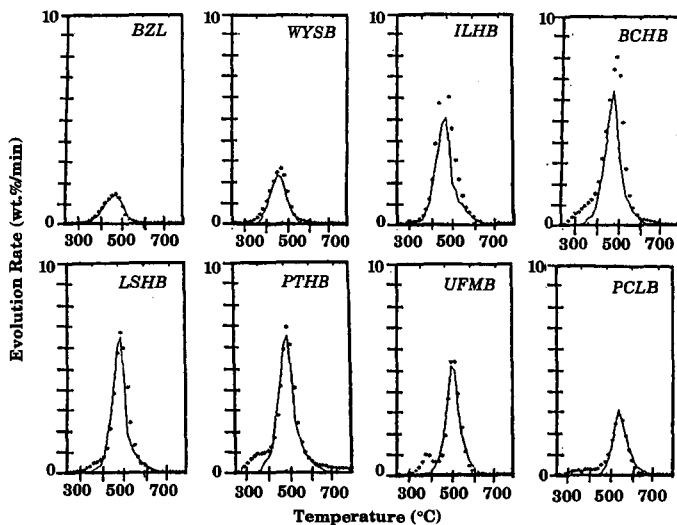
Figure 10. Comparison of measured and predicted tar evolution from pyrolysis of the eight Argonne premium coals.

A STUDY OF ON-LINE ANALYSIS OF CHLORINE DURING COAL COMBUSTION

John Napier, Jenny Heidbrink, Jennifer Keene, Hanxu Li, Wei-Ping Pan, and John T. Riley
Department of Chemistry and Materials Characterization Center
Western Kentucky University
Bowling Green, KY 42101

ABSTRACT

The behavior of chlorine during the combustion of coal was studied using TG-FTIR and TG-MS systems. Parameters of the coal samples studied included variations in chlorine content, rank, and mesh size. The identification of evolved gases at different temperatures indicated three mechanisms of HCl release. The first evolution of HCl was due to thermal effects, and corresponds to the release of HCl absorbed on pore walls of the coal. The second evolution of HCl is a function of coal rank, and represents a more tightly bound chlorine associated with the hydrated coal matrix. The third evolution of HCl is a result of inorganic chlorides in the coal.

INTRODUCTION

The presence of chlorine in coal is a concern for end users of coal. This concern, if the chlorine in coals causes corrosion, has tremendous impact on the marketability of the coal. The extent of boiler corrosion due to chlorine may not be directly related to the amount of chlorine in the coal. However, it may be related to how the chlorine occurs in the coal or to other factors. During the combustion of coals of various types, the mechanisms of the release of chlorine species are influenced by many factors, such as the forms of chlorine in the coal, coal rank, and experimental conditions.

The main forms of chlorine present in coal that have been proposed are:[1]
- inorganic chlorides
- chlorine ions in brine and other water associated with the coal.

Edgecomb[2] examined the release of chlorine as HCl in the heating of twenty-nine British coals (0.2-1.0% Cl) in dry air at 200°C for twenty-four hours. His studies showed that more than half of the chlorine is liberated as HCl at this temperature. However, Daybell suggested that chlorine in some British coals give off 97% of their chlorine as HCl in oxygen-free nitrogen at 258°C.[3] Gibb observed that most of the chlorine in British coals evolved under mild conditions.[4] Several Illinois coals were studied by Hackley and Chou using a high temperature furnace-quadrupole gas analyzer (HF-QGA) technique. They determined that the evolution of HCl from their coals began around 250°C, peaked at 495°C, and leveled off close to 600°C.[5] Muchmore and coworkers investigated chlorine removal from an Illinois high-chlorine coal with thermal treatment followed by analysis using an electrode technique. It was concluded that 84.3% of the total chlorine in the coal was removed by preheating in nitrogen at a lower temperature prior to a six minute reaction at 385°C.[6]

These studies, reporting different coals having different chlorine release temperatures under different conditions, may provide some insight into the question concerning boiler corrosion and chlorine content. In the work reported in this paper the behavior of chlorine during combustion is investigated using relatively new techniques. The effect of chlorine content as well as rank and mesh size of coal on the evolution of chlorine species was investigated.

EXPERIMENTAL

This study used ten coal samples ranging in chlorine content (0.03-0.88%), mesh sizes (400, 200, and 60 mesh), and chemical composition as listed in Table 1. Combustion of the samples took place in an air atmosphere under either of two heating methods. The dynamic heating method, a steady increase in temperature with time, enables a view of the complete combustion process. The second, an isothermal heating method, allowed for the isolation and separation of HCl emission mechanisms. The isothermal method consists of steadily heating the sample to a certain temperature, holding at the temperature for a designated amount of time, followed by a continuation of the temperature increase.

Analyses of the combustion process and evolved gases were obtained utilizing TG-FTIR and TG-MS systems. The thermogravimetric (TG) studies gave combustion profiles in terms of weight loss and rate of weight loss and were done with either a DuPont 951 or a TA Hi-Res TGA 2950 thermogravimetric analyzer. By coupling the instruments with a VG Thermolab Quadrupole Mass Spectrometer (MS) one can identify and quantify evolved gases by their molecular weights. Interfacing a TG with a Perkin

Elmer 1650 Fourier Transform Infrared Spectrometer (FTIR) allows one to confirm the identified gases and distinguish between gases of the same molecular weights.

RESULTS AND DISCUSSION

Figure 1 is a typical thermogram showing the analysis of the combustion of a coal sample using the dynamic heating method. One can follow the transitions through the combustion process by noticing changes in both the TG curve showing weight loss and the DTG curve showing rate of weight loss. Points of interest on the DTG curve are the changes in weight loss rate at 300°C, 400°C, and 447°C. The region containing these points in order show: (1) a devolatilization zone, (2) an overlapping weight loss due to the initial combustion of the fixed carbon at the 400°C inflection point, and (3) a weight loss, due to combustion, with a maximum at 447°C (DTG peak maximum).

Mass spectroscopic profiles given in Figure 2 show the evolution of SO_2 (64), H_2O (18), CO_2 (44), HCl (36), and either acetic acid (60) or COS (60) during dynamic heating. The peak maximum for rate of weight loss in the TG curve corresponds to the peak maxima of CO_2 and SO_2 emissions at 447°C. The $m/z = 60$ peak follows the HCl and water curves by 10°C. FTIR on-line analysis shows the first peak in the $m/z = 60$ curve to be due to the evolution of acetic acid while the second peak is due to COS. The emission of HCl and H_2O begins at 200°C, peaks at 300°C, and subsides. Their second peaks appear at 400°C with a maximum at 440°C before leveling off around 500°C. This indicates two mechanisms of chlorine release involving water. Expansion of the HCl curve shows a small third peak occurring at 700-800°C.

Employment of the isothermal heating method revealed HCl and water emissions as the temperature approached 300°C, as illustrated in Figure 3. At that point (30 min, 300°C) the temperature was held constant for one hour with no emissions occurring. Continuation of the temperature increase produced the second emission of HCl and water confirming two separate mechanisms, thus illustrating two different structures of chlorine bonding in the coal.

The first HCl peak is due to thermal effects and consistently peaks around 300°C for all coals. Due to the greater amount of energy needed to break the bonds, the second peak represents a more tightly bound chlorine released during the oxidation of the coal. The second peak is a function of coal rank due to its direct relationship with coal DTG maxima as is illustrated in Figure 4. DTG analyses of the coals indicate higher ranking coals having higher maximum rates of combustion. The higher temperature DTG peaks and higher ranking coals correspond to higher temperature maxima for the second HCl emissions.

A quantitative study of the evolution of HCl and SO_2 versus the content of the chlorine and sulfur in the coal was obtained by integrating the area under the HCl peaks in the mass spectra. A good agreement ($R^2 = 0.997$ for chloride and $R^2 = 0.942$ for sulfur) was obtained between the chlorine content and the total amount of HCl evolved, as is illustrated in Figure 5. This figure also provides evidence that most of chlorine in coal is released in the form of HCl during combustion. The slightly lower coefficient obtained for the sulfur is due to the limitation of TG systems. The TG system can only be heated to 1000°C. According to ASTM Method D 4239, the coal should be heated to 1400°C to identify the sulfate species. Thus, the temperature difference may cause the slightly lower correlation coefficient.

Mesh size also played a role in determining the temperature of HCl evolution. The smaller mesh coal produced emissions at a lower temperature. Smaller particle size, such as 400 mesh, has a higher surface-to-volume ratio allowing less hindrance to the devolatilization of the chlorine attached to the coal pores and surface.

CONCLUSIONS

Thermal analytical techniques reveal there are three HCl evolution peaks, indicating three different types of chlorine bonding to the coal. The first HCl evolution peak, due to thermal effects, is the release of HCl normally absorbed on pore walls. The second peak, a function of the coal rank, represents a more tightly bound chlorine associated with the hydrated coal matrix. A third peak is a result of inorganic chlorides in the coal.

Thermal analytical and mass spectral data indicate a good correlation between chlorine content in the coal and the total amount of HCl evolved. Results also show the smaller particle sizes of the coal cause HCl evolution to occur at a lower temperature.

ACKNOWLEDGEMENTS

REFERENCES

1.   Sloss, L.L. "Halogen Emissions from Coal Combustion," IEACR/45, IEA Coal   Research, London, February, 1992.

2.   Edgecomb, L.J. Fuel, 1956, 35, 38.

3.   Daybell, G. N. Fuel, 1958, 37, 283.

4.   Gibb, W. H. "The Nature of Chlorine in Coal and Its Materials for Coal Conversion System," (Eds. Meadowcroft, D. B. and Manning, M. I.), Applied Science Pub., London, UK, Ch. 2, 1982, 25-45.

5.   Chou, C.L.; Hackley, K.C.; Cao, J.; More, D.M.; Xu, J.; Rech, R.R.; Pan, W.-P.;Upchurch, M.L.; Cao, H.B. "Behavior of Sulfur and Chlorine in Coal During Combustion and Boiler Corrosion," Illinois Clean Coal Institute, Final Technical Report, Carterville, IL, August, 1993.

6.   Muchmore, C. B.; Hesketh, H. E.; Chen, H.L. "Thermal Treatment for Chlorine Removal From Coal," Center for Research on Sulfur in Coal," Technical Report, Carterville, IL, July 1992.

Table 1. Ultimate Analysis Data (Dry Basis) for Coals Studied

Coal	Cl	C	H	O	N	S	Ash
A	0.88	79.75	5.37	8.20	1.55	0.94	3.23
B	0.39	63.95	4.21	6.31	1.29	1.31	22.24
C	0.38	70.34	4.25	6.55	1.54	1.02	16.10
D	0.26	75.40	4.92	6.70	1.50	2.94	8.17
E	0.16	72.29	4.99	7.13	1.27	4.47	9.71
F	0.20	86.71	4.23	2.17	1.27	0.66	4.77
G	0.13	66.20	4.21	7.10	1.25	0.71	19.84
H	0.04	65.85	4.36	18.19	1.25	0.80	9.72
I	0.03	68.43	4.88	16.24	1.02	0.63	8.77
J	0.03	76.89	5.49	10.76	1.50	0.62	4.71

Sample: COAL 33501 P=5*10-5
Size: 20.4490 mg
Method: COAL
Comment: IT=100C HT=15V MV=1632 MSFILE=ICCI607 70EV HT TEST

TGA

File: C:ICCI607
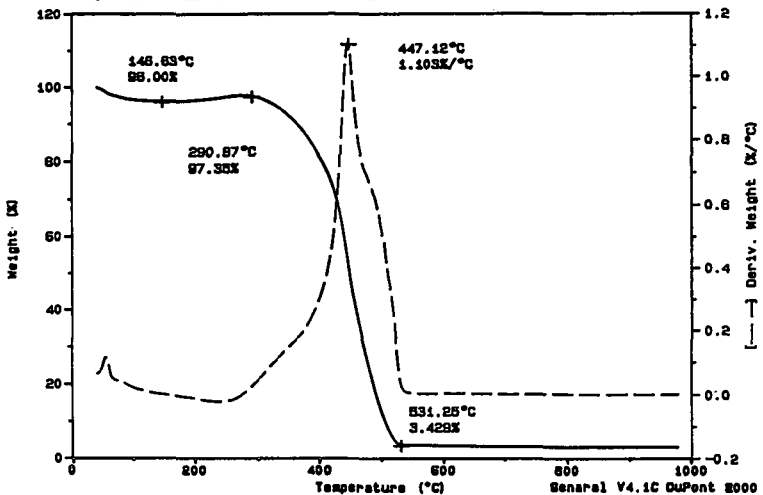Operator: PAN   10C/MIN TO 990
Run Date: 25-Mar-95 02:55

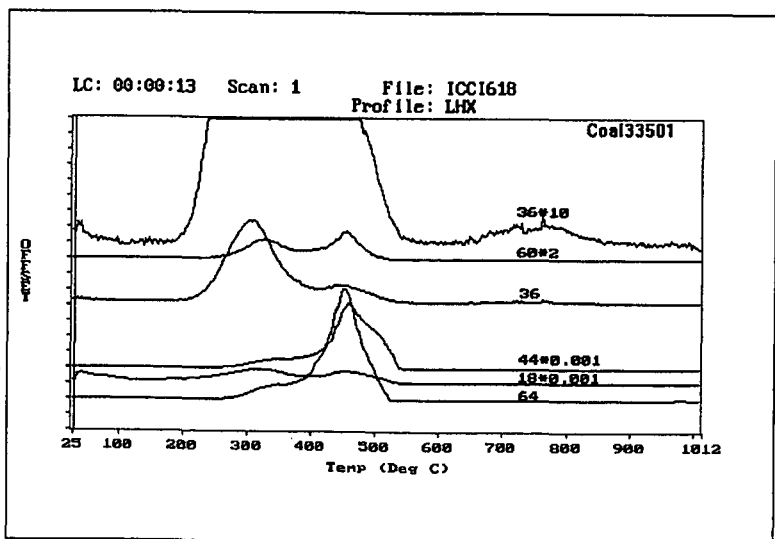**Figure 1.   TG curve for the combustion of coal A in air.**

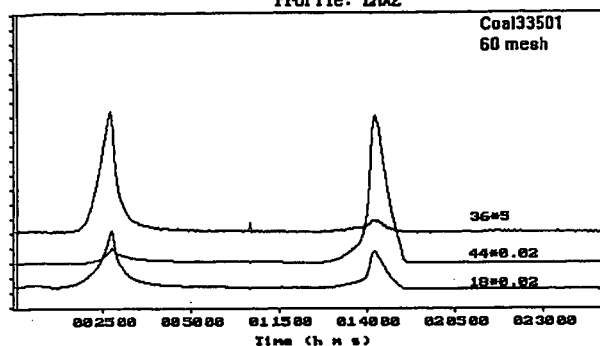**Figure 2.   Mass spectrometric evolved gas profiles for the combustion of coal A.**

54

Figure 3.   Mass spectrometric evolved gas profiles for combustion
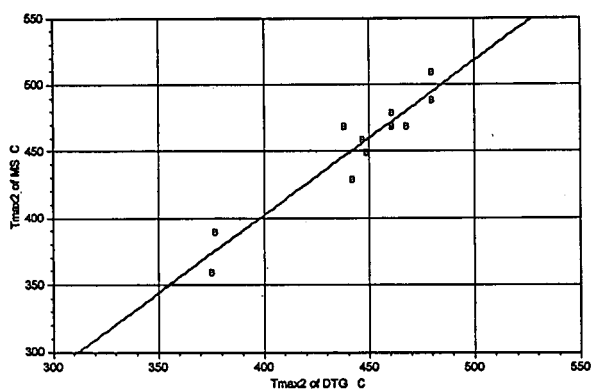   of coal A under isothermal conditions.

Figure 4. T_{max2} values from DTG curves versus T_{max2} values
            from mass spectra.
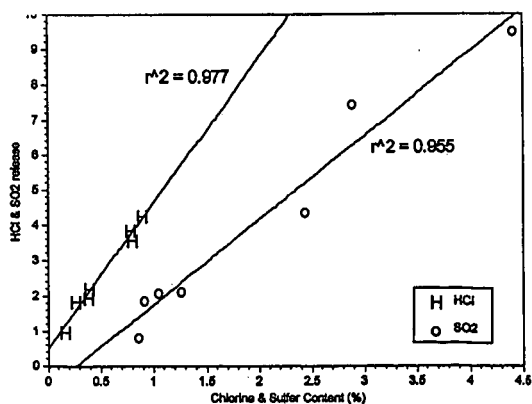
Figure 5.   HCl and SO_2 release versus chlorine and sulfur
            content in coals.

TG/MS STUDY OF ORGANIC COMPOUNDS EVOLVED DURING THE CO-FIRING OF COAL AND REFUSE DERIVED FUELS

Shobha Purushothama, Richard Lu, Xiaodong Yang, John Hyatt,
Wei-Ping Pan, John T. Riley, and William G. Lloyd
Department of Chemistry and Materials Characterization Center
Western Kentucky University
Bowling Green, KY 42101

Key words: Evolved gas analysis, coal and RDF, co-firing

INTRODUCTION

The Environmental Protection Agency reported that the total municipal solid waste (MSW) produced in the U.S. increased from 179 million tons in 1988 to 195 million tons in 1990.[1] It is predicted that the country will produce about 216 million tons of garbage in the year 2000.[2] Waste-to-energy conversion of MSW appears to be most attractive because of the energy recovered, economic value of the recycled materials, and the cost saving derived from reduced landfill usage. However, extra care needs to be taken in burning MSW or Refuse Derived Fuel (RDF) to optimize the operating conditions of a combustor so that the combustion takes place in an environmentally acceptable manner. For instance, polychlorinated dibenzodioxins (PCDDs) and polychlorinated dibenzofurans (PCDFs) have been found in the precipitator fly ash and flue gas of a number of incinerator facilities in the United States and Europe. Though the amount of PCDDs and PCDFs is only in the parts-per-billion to parts-per-trillion range, these chlorinated organics exhibit very high toxicity (LD_{50} < 10 μg/Kg) and 2,3,7,8-tetrachlorodibenzodioxin has been found to be acnegenic, carcinogenic, and teratogenic. This has slowed or even stopped the construction and operation of waste-to-energy plants. In previous work,[3] the study of single materials has given us a good understanding of the characteristics and thermal behavior of these materials, their relative thermal stability and temperature relationships, their decomposition products and the evolution profiles of different gaseous products. The formation of molecular chlorine during combustion processes could be a key step for the formation of chlorinated organic compounds. The production of phenol and furan during the combustion of newspaper and cellulose could provide the important precursors for the formation of polychlorinated dibenzodioxin (PCDD) and polychlorinated dibenzofuran (PCDF).

EXPERIMENTAL

Materials used in this study include two coal samples (92073 - a KY #9 coal and 90003 - an IL #6 coal), PVC (OxyChem Corporation), cellulose (Whatman Corporation), and newspaper. The TG/MS system consists of a DuPont Instruments Model 951 Thermogravimetric Analyzer interfaced with a VG Thermolab Mass Spectrometer. The detection range of the TG/MS system is 1-300 atomic mass units (amu). Electron impact ionization energy is 70 eV. A sample size of ~20 mg was heated in air (50 mL/min) at a slow heating rate of 10°C/min to 700°C and a fast heating rate of 100°C/min to 900°C then held at the maximum temperature for five minutes. The MS system can automatically sample the gases evolved from the TG system, analyze them with its quadrupole analyzer, and save the spectra. The detailed experimental conditions are discussed in Lu's thesis.[4]
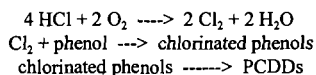
RESULTS AND DISCUSSION

Comparing the TG curves for the five raw materials (coals 92073 and 90003, PVC, cellulose, and newspaper) shows that the coals have a higher decomposition temperature and slower weight loss rates compared to the other materials. PVC, newspaper and cellulose show three distinct weight loss stages. At the fast heating rate similar results were obtained except that the weight loss shifts to higher temperatures (T $_{max}$) and the rate of maximum weight loss (R_{max}) increases. This indicates that the decomposition reactions of fuels occur much faster and at higher temperatures as the heating rate increases. The decomposition at the slow heating rate was studied in order to understand the mechanism of each stage. The study at the fast heating rate was done to approach the firing conditions of an atmospheric fluidized bed combustor (AFBC) unit. The heating rates in an AFBC system are much faster than those of the TGA experiments. Thus it is expected that the decomposition reactions occur at higher T_{max} and R_{max} values in the AFBC systems.

The evolved gases were identified using two analytical systems, TG/FTIR and TG/MS. The TG/FTIR system can be used to identify compounds with different functional groups and similar masses. The TG/MS can be used to identify species such as Cl_2, O_2, and N_2 which cannot be detected using FTIR techniques. The results show that at a fast heating rate the decomposition reactions are

compressed into a narrow time range. Hence the decomposition stages cannot be separated as is done with the slow heating rate. The FTIR data indicate that more hydrocarbons are produced at fast heating rates whereas more oxidation products are obtained at slow heating rates. Mass spectrometric results indicate that chlorine molecules are produced concurrently with HCl during the decomposition of PVC. The ratio of HCl/Cl_2 produced is around 150. This suggests that some of the abundant HCl could undergo a thermal Deacon reaction. This reaction is favored up to 600°C at atmospheric pressures. The Deacon reaction (given below) could provide a plausible starting point for the formation of chlorinated dioxins from the combustion of chlorine rich fuel mixtures.[4] The suggested mechanism is as follows:

$$4 \, HCl + 2 \, O_2 \; \text{----}\!> \; 2 \, Cl_2 + 2 \, H_2O$$
$$Cl_2 + phenol \; \text{--->} \; chlorinated \; phenols$$
$$chlorinated \; phenols \; \text{------}\!> \; PCDDs$$

The study of single materials gives a good understanding of the characteristics and thermal behavior of these compounds, their relative thermal stability, and the evolution profiles of different gaseous decomposition products. This will help in the analysis of thermal decomposition products of blends and in the evaluation of their combustion kinetics and interactive mechanisms.

A series of experiments on blends (containing different amounts of coal, PVC, newspaper and cellulose) was conducted at both heating rates. PVC, which is a major source of chlorine, accounts for only 1% of MSW. A greater amount was used in these studies to investigate the conditions and mechanism for the formation of the chlorinated species. At a slow heating rate it is possible to evaluate kinetic and dynamic changes occurring during combustion. The studies at a fast heating rate will provide a better picture of combustion performance in an AFBC system.

The blends used in this study were manually prepared and labeled as follows:

> Blend 1: 03PVC is a mixture of coal 90003 and PVC (50% each);
> Blend 2: 03NEW is a mixture of coal 90003 and newspaper (50% each);
> Blend 3: 03Cell is a mixture of coal 90003 and cellulose (50% each);
> Blend 4: 03PN is a mixture of coal 90003 (50%), PVC (25%), and newspaper (25%);
> Blend 5: 035122 is a mixture of coal 90003 (50%), PVC (10%), newspaper (20%), and cellulose (20%);
> Blend 6: 73PVC is a mixture of coal 92073 and PVC (50% each);
> Blend 7: 73NEW is a mixture of coal 92073 and newspaper (50% each);
> Blend 8: 73Cell is a mixture of coal 92073 and cellulose (50% each);
> Blend 9: 73PN is a mixture of coal 92073 (50%), PVC (25%), and newspaper (25%);
> Blend 10: 735122 is a mixture of coal 92073 (50%), PVC (10%), newspaper (20%), and cellulose (20%).

1.   TG/DTG Results

Table 1 is a summary of the TG/DTG results at both heating rates for all the blends. It can be seen that the maximum rates of major weight loss (R_{max}) at the fast heating rate are much higher than those at the slow heating rate. For example, decomposition increases from 10%/min to 62%/min for blend #35122. This indicates that the decomposition reactions of fuels occur at a faster reaction rate as the heating rate increases. Since the heating rates in an AFBC system are much faster than those in TGA experiments it can be expected that decomposition reactions will occur at greater R_{max} in AFBC systems.

On comparison with data for single materials, there is an important difference. For most blends, the combustion profiles are compressed into a continuous stage of weight loss at the fast heating rate. This means that the different decomposition stages for most blends can be separated from each other only at a slow heating rate. It is difficult to distinguish each decomposition stage in the combustion profiles at the fast heating rate, except for the moisture loss stage. Unlike those at the slow heating rate, the profiles of decomposition reactions for most blends display only one continuous weight loss at the fast heating rate. Also, the T_{max} in the compressed profiles are in between the two T_{max} values at the slow heating rate. For example, T_{max} for H73PN is 344°C but T_{max} for 73PN is 336°C and 432°C.

Figure 1 is a comparison of TG curves for blend 035122 and its components, coal 90003, PVC, cellulose, and newspaper, at the slow heating rate. The blend has a much lower decomposition temperature than the coal because of mixing with the easily decomposing components, (with high

volatile matter content), newspaper, cellulose, and PVC. This indicates that there are some mutual chemical interactions among the components during the combustion process. For the blend curve, the first weight loss is due to moisture. The second weight loss comes from the decomposition of PVC, newspaper and cellulose. The third weight loss is due to combustion of coal and carbon residues from PVC. It is possible that the combustion of newspaper, cellulose and PVC induce the shift of the coal combustion to a much lower temperature. The temperature at 50% weight loss ($T_{1/2}$) for coal is about 500°C and 370°C for the blends.

At the fast heating rate, the same trend is observed, the blend decomposes at much lower temperatures than the coal ($T_{1/2}$ for coal is ~750°C and ~450°C for blend). Compared with the blend curve at the slow heating rate the combustion profile of the blend becomes more continuous so that the second and third weight losses, which were clearly seen previously, cannot be definitely separated, indicating that combustion behavior is different at different heating rates.

2.   Mass Spectrometry Results

Table 2 summarizes the tentative identification of some peaks in the MS spectra of blends 1 to 10 at the slow and fast (with a prefix "H-") heating rates. The compounds in bold type are also detected by the gas trap and GC/MS techniques. It is difficult to clearly interpret the complicated spectra obtained from the combustion of all the blends and attention was given to the sulfur and chlorine species in the evolved gases.

Figure 2 shows some mass profiles at the slow heating rate for blend 9(73PN). There are two major decomposition stages shown in this figure. The first stage occurs around 300°C. In this stage, HCl (36 and 38) and chlorine (70, 72 and 74) from PVC, furan (68) and furfural (96) from newspaper are major products. The second stage is at around 340°C. In this stage, larger molecules, toluene (92), methyl thiophene (98), xylene (106), chlorobenzene (112), and naphthalene (128) start evolving, which indicates that the coal begins to decompose. Phenol is also identified from the decomposition of newspaper. These two stages correspond to the second weight loss in the TGA curve.

There are similar results in Figure 3 (blend 5, file 035122). The peaks 60 (carbonyl sulfide) and 64 (sulfur dioxide) display the same changes as observed in coal 92073, i.e., sulfur dioxide has three decomposition phases and carbonyl sulfide has only two. In the profiles for HCl and molecular chlorine there are some differences. The HCl and molecular chlorine show two peaks at about 300°C and 340°C. The first peak may be attributed to the decomposition of PVC. The second peak is due to the decomposition of coal 90003 (high chlorine, low sulfur) and newspaper. An important fact is that molecular chlorine, phenol and furan are released at the same temperature range. This indicates that there is some possibility for the formation of chlorophenol at this temperature. However, it is difficult to identify chlorophenol from TG/MS studies due to two reasons. First, the amount of phenol ($m/z = 94$) present in the gas phase is very small. Secondly, chlorophenol has the same mass, 128, as naphthalene. These two species cannot be distinguished from each other in the TG/MS system. This problem can be resolved using a separation system. In tubular furnace studies more sample can be loaded, increasing the amount of phenol produced. Also the GC/MS system can separate the components prior to identification. The results from 10 grams of blend sample show that naphthalene is a major product and small amounts of chlorophenol is also identified. The results using 100 mg phenol as sample and 0.5% chlorine in nitrogen as purge gas and the same heating rate show that mono-, di-, and tri-chlorophenols can be formed. This indicates that during co-firing coal with MSW, either the amount of phenol produced is too small to form chlorophenol, or the amount of the produced chlorophenol is too small to be detected by the TG/MS system.

Comparison of the evolved gases at slow and fast heating rates show trends very similar to those of the individual raw materials. More hydrocarbons and chlorinated species are formed during the same time span at the fast heating rate whereas they evolve at different times at the slow heating rate.

CONCLUSIONS

*   The TG/FTIR/MS system was used to identify molecular chlorine, furan, phenol and other aromatic compounds, along with HCl, CO, CO_2, and H_2O in the gaseous products of the combustion of coal, PVC resin, newspaper, and cellulose in air. This is a significant finding that will lead us to study this combustion step further to look for the formation of chlorinated organic compounds.
*   The TG/MS techniques allow the study of reaction pathways for the formation of gaseous products during combustion.

REFERENCES

1. Steuteville, R. "What is New in the Waste Stream," *Biorecycle*, **1992**, *33*, 10.

2. Dichristina, M. "How We Can Win the War Against Garbage," *Popular Science*, **1990**, *237(10)*, 57.

3. Lu, H.; Purushothama. S.; Yang, X.; Pan, W.P.; Flynn, J.; Gill, P. "Co-firing High *Sulfur Coal with Refuse Derived Fuel*," Proceedings 24th NATAS Conference, **1995**, 414-417.

4. Lu, H. "A Study of Combustion of Coal with RDF Using Thermal Analytical Techniques," M.S. Thesis, Western Kentucky University, **1995**.

Table 1. Summary of TG/DTG Results for Blends

Sample	$\Delta W_2(\%)$	T_{max}	R_{max}	$\Delta W_3(\%)$	T_{max}	R_{max}
03PVC	30	307	6	64	457	6
H03PVC	42	354	71	55	435	32
03New	30	340	19	59	463	8
H03New	93	349	41			
03Cell	43	341	17	48	442	18
H03Cell	92	361	67			
03PN	27	302	7	64	419	13
H03PN	94	345	81			
035122	49	300	10	44	444	7
H035122	51	324	62	39	595	13
73PVC	37	306	7	51	437	5
H73PVC	82	347	57			
73New	51	337	33	24	444	14
H73New	73	374	99			
73Cell	53	346	23	30	423	19
H73Cell	82	383	99			
73PN	52	336	31	29	432	12
H73PN	85	344	98			
735122	40	300	6	42	418	8
H735122	49	331	70	43	538	12

Note: R_{max} is maximum rate of weight loss, %/min; T_{max} is the temperature at R_{max}, °C; ΔW is the weight loss.

Table 2. Tentative Parent Structures of MS Peaks for Coal 92073 Blends

Name	B6	HB6	B8	HB8	B9	HB9	B10	HB10
dimethylnaphthalene		156						
vinylnaphthalene		154						
acenaphthene			154					
biphenyl			154					
methylbenzothiophene	148			148	148	148		
dichlorobenzene	146			146	146	146		
indan-1,3-dione	146			146	146	146		
methylnaphthalene		142		142	142	142		
decene		140		140	140	140		
ethylxylene		134	134		134	134	134	
tetrahydronaphthalene	132			132	132	132		
naphthalene		128	128		128	128	128	
chlorotoluene	126	126		126	126	126		
propylbenzene	120	120		120	120	120	120	
ethylmethylbenzene	120	120		120	120	120	120	
trimethylbenzene	120	120		120	120	120	120	
indene		116	116				116	116
chlorobenzene	112	112		112	112		112	112
octene	112	112		112	112		112	112
xylene	106	106	106	106	106		106	106
ethylbenzene	106	106	106	106	106		106	
3-methyl-2-furanone	98	98	98	98	98		98	98
methylthiophene	98	98	98	98	98		98	98
furfural	96	96	96	96	96		96	96
phenol	94	94	94		94		94	94
toluene	92	92	92	92	92		92	92
thiophene	84	84	84	84	84		84	84
benzene	78	78	78	78	78		78	78
furan/1,3-pentadiene	68	68	68	68	68		68	68
SO_2/1,3-pentadiyne	64	64	64	64	64		64	64

"H-" prefix means the fast heating rate was used. "B + number" means the blend + number. The compounds in bold type indicate those also detected by the GC/MS system.

COMPARISON FOR BLEND AND ITS COMPONENT TGA CURVES
Files: 035122.018   90003.006   PVC.002   NEWSPAPER.020   CELLULOSE.003
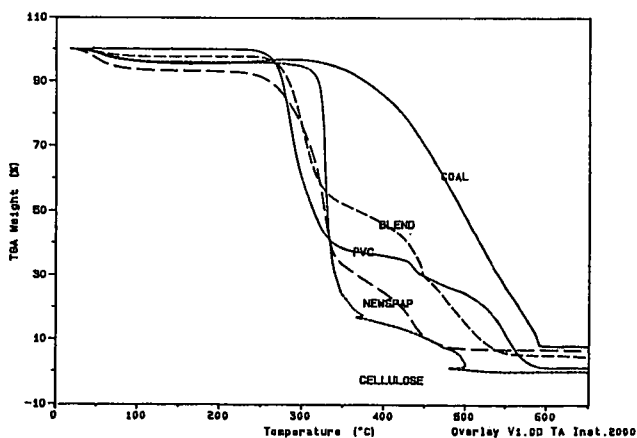
Figure 1. TG Curves for blend 035122 and the four components of the blend.
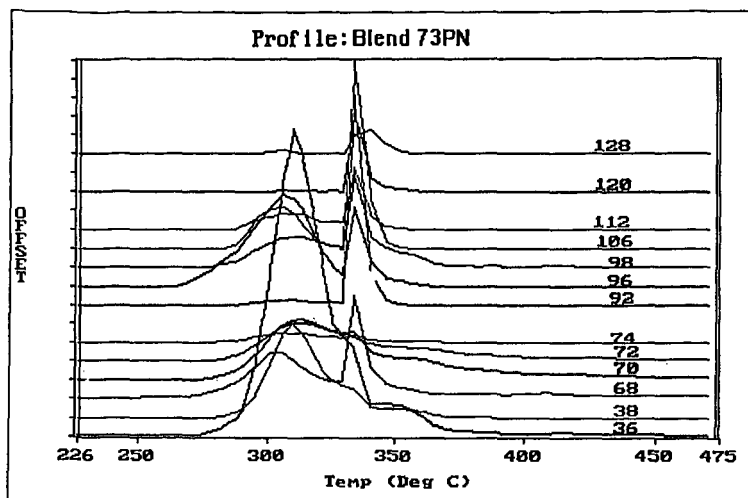
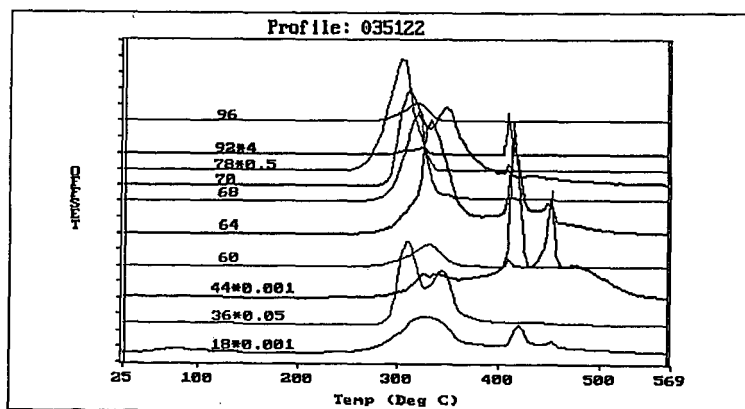Figure 2. Profiles of m/z values for combustion products of
blend 9(73PN).

Figure 3. Profiles of m/z values for combustion products
of blend 5(035122).

TG-FTIR METHODS FOR THE EVALUATION OF LUBRICANT CONTAMINATION

Anthony S. Bonanno, Rosemary Bassilakis and Michael A. Serio

Advanced Fuel Research, Inc.
87 Church Street
East Hartford, CT 06108

ABSTRACT

A typical Air Force base will produce several thousand gallons per year of used turbine engine lubricants (1-5). The potential for contamination of the collected lubricants, particularly with halogenated compounds such as degreasing solvents and other fluids, reduces the effectiveness of a previously developed reclamation process. In this project, the feasibility of using two different thermal/FT-IR analysis methods in combination with advanced data analysis techniques to detect contamination in used turbine engine lubricants was investigated. The first method, TG/FT-IR combined with advanced data analysis routines, was shown to be capable of detecting the presence of several different types of contaminants in synthetic lubricants at concentrations of about 5%. It was demonstrated that data analysis routines based on factor analysis (SIMCA) and neural networks could be used for identifying the presence of a contaminant. The second method, TG/secondary oxidation/FT-IR, was developed specifically for detecting trace levels of chlorinated contaminants in lubricants. Optimization of this method using existing instrumentation led to a detection limit of about 300 ppm (w/w) organic chlorine in the lubricant. Further improvements in hardware and software components could lead to detection limits of <10 ppm. This instrumentation could also be used to characterize used motor oils, cooking oils or pyrolysis oils.

INTRODUCTION

The Dalton Process is a proprietary process for reclaiming synthetic ester based turbine lubricants (MIL-L-7808 and MIL-L-23699) for reuse (1,3,4). Under controlled collection of the used lubricants, this process has been shown to give as high as 95% yield of virgin lubricant (4). However, contamination of the used lubricants greatly reduces the yield of the reclamation process, and since supervised collection of used lubricants is not feasible, methods are required to rapidly determine the presence of unacceptable levels of contamination. Likely contaminants are volatile hydrocarbons in the form of kerosene type turbine fuels, domestic paraffins, petroleum naphthas, and chlorinated degreasing agents such as trichloroethylene. Previously used methods of identifying contaminated lubricant samples involved classifying the samples on the basis of appearance and odor (normal or abnormal), and subjecting the samples to a series of analytical tests in order to determine parameters such as volatile contaminant content, volatile hydrocarbon content, mineral oil content, and foaming propensity (3). The results of these analyses were used to specify whether a used lubricant sample was suitable for reclamation. A more rapid and objective method of classifying used lubricants and related materials is needed. Thermogravimetric (TG) analysis combined with Fourier Transform Infrared (FT-IR) analysis of evolved products has been used at Advanced Fuel Research, Inc. (AFR) and elsewhere for characterization of a variety of hydrocarbon materials (6,7). The objective of the current study was to investigate the application of TG-FTIR methods for the evaluation of lubricant contamination.

The successful development of a TG-FTIR based lubricant evaluation instrument would allow non-technical Air Force personnel to rapidly and reproducibly determine whether used lubricants are suitable for reclamation or reuse. This type of instrumentation would also find several uses in the commercial sector. These include analysis of used motor oils and of oils produced from post-consumer plastics. The processing of corn oil and cotton seed oil often results in the contamination of residual "soapstock" with chlorinated hydrocarbons, which prevents recovery of the useable oil through acidulation. The recovery of useable motor oil by supercritical fluid extraction is currently being evaluated. The value of the recovered oil is directly related to the amount of residual organochlorine in the extract.

EXPERIMENTAL

Sample Selection and Preparation

The Air Force provided two types of synthetic turbine lubricants (MIL-L-7808 and MIL-L-23699) from two different sources (Mobil and Hatco). The contaminants of primary interest were halogenated compounds, therefore, three chlorinated compounds were selected as representative contaminants for this work: trichloroethylene (TCE), dichloromethane, and *ortho*-dichlorobenzene (o-DCB). Other contaminants of interest included fluids that could routinely be found at an Air Force base and could potentially contaminate the used lubricants. A set of representative fluids was collected from commercial sources. These included methanol, motor oil (Castrol GTX 10W30), hydraulic jack oil (Gold Eagle),

brake fluid (Prestone), turbine fuel (Jet A), diffusion pump silicone oil, and Dow-Corning silicone oil (DC-200). The primary constituents of these fluids are given in Table 1.

Table 1. List of the lubricants and contaminants analyzed.

Type of Fluid	Primary Constituents
MIL-L-7808, MIL-L-23699	polyol esters
motor oil, hydraulic oil	mineral oils
brake fluid	polyalkylene glycol ethers
turbine fuel (Jet A)	aliphatic hydrocarbons
diffusion pump oil	poly(dimethyl/diphenyl siloxane)
DC-200 silicone oil	polydimethylsiloxane

A preliminary spectral analysis revealed that the MIL-L-7808 and MIL-L-23699 lubricants were quite similar. Consequently, further study was limited to the Mobil MIL-L-23699 lubricant. The samples analyzed included the pure lubricant, the pure "contaminants," and the lubricant spiked with a known amount of a given contaminant. The spiked samples were prepared by pipetting the required volume of the contaminant into a graduated cylinder and topping off with the lubricant. In order to minimize errors due to loss of volatile components, each sample was prepared immediately prior to analysis.

Lubricant Analysis Studies

TG/FT-IR Instrument - The combined thermal/FT-IR analysis technique is an extension of the TG/FT-IR (thermogravimetric analysis with FT-IR analysis of the evolved species) instrumentation developed by AFR and sold commercially by Bomem, Inc. as the *"TG/Plus"*. The details of the TG/FT-IR method and instrumentation have been described previously in the literature (6-8), but a brief description will be given here. The apparatus, illustrated schematically in Figure 1, consists of a sample pan suspended from a balance within a furnace. As the sample is heated, the evolving volatile products are carried out of the furnace by an inert gas stream directly into a 5-cm diameter multi-pass gas cell (heated to 150 °C) for analysis by FT-IR. Spectra are obtained at specified time intervals in order to quantitatively determine the evolution rate and composition of the evolved products. The sample can be subjected to programmed temperature ramp rates between 3 °C/min and 100 °C/sec, with a temperature range of 20 to 1000 °C. The system monitors the time dependent evolution of specific gases, the heavy liquid evolution rate and its infrared spectrum with identifiable bands from the functional groups, the mass loss during the run, and the mass of the non-volatile residue remaining at the end of the run. An analysis of C, H, N and S in the residue can be obtained at the end of the pyrolysis experiment by introducing oxygen and analyzing the combustion products.

TG/FT-IR analysis of lubricant samples - Two specific problems were encountered during the initial TG/FT-IR analysis of the synthetic lubricant samples (9). It was found that the lubricant samples volatilized very rapidly, thus resulting in a high concentration of aerosol in the FT-IR gas cell. The high aerosol concentration resulted in significant scattering, and therefore the spectra appeared to be distorted. Additionally, the sample condensed on the quartz tube between the furnace and the flow cell, and then revolatilized as the furnace reached a higher temperature. This limited the ability to correlate between the FT-IR data and the TG balance data. A method was developed that would result in slower evolution of the sample in order to improve the results. The lubricant was adsorbed onto pre-pyrolyzed sand and was crimped in a stainless steel boat. This was found to significantly slow the rate of evolution of the lubricant, and also limited the condensation of evolved products.

Using this sample introduction method, several samples were run in the standard TG/FT-IR mode using a temperature profile with a ramp rate of 30°C/min and a sample size of about 10 mg. The samples included the Mobil 23699 lubricant, the contaminants listed in Table 1, and the lubricant spiked with the contaminants (usually at a concentration of 5%). The spectra obtained during the runs were then converted to a format compatible with Spectra Calc data processing software (Galactic Industries, Salem, NH) for further analysis.

TG/secondary oxidation/FT-IR analysis of lubricant samples - TG/FT-IR with secondary oxidation or pyrolysis allows the evolved species to be oxidized or further pyrolyzed before passing into the FT-IR gas cell. The secondary oxidization unit consists of a quartz tube through which the evolved species flow prior to entering the gas cell. The tube houses a resistive platinum element which is used to heat the evolved species to 800-900 °C. A 15 mL/min flow of preheated gas is introduced just prior to the heater; helium is used for the secondary pyrolysis mode, and oxygen is used for the secondary oxidation mode.

RESULTS AND DISCUSSION

Detection of General Contamination in Synthetic Lubricants

SIMCA analysis for contaminants - In the development of a methodology to detect contamination in used turbine engine lubricants, the data analysis routine must be designed to answer specific questions. If specific contaminants are likely to be encountered, for example, silicone oil, then one could ask "Is there any silicone oil in the lubricant?" Then a spectral analysis routine could be developed to look for the IR bands characteristic of silicone. The question being asked in this case is more general; "Is there anything out of the ordinary in the lubricant?" In this case the spectral analysis routine must be more general, and should be capable of not only identifying IR bands that do not arise from the lubricant, but also differences in the relative intensities of bands that might also indicate the presence of a contaminant. A discriminant analysis technique based on principal components analysis (PCA) was applied to the data obtained in order to detect the presence of an unspecified contaminant.

Several studies have employed PCA, also known as factor analysis, in the development of discriminant algorithms. Although PCA and its applications have been thoroughly described in the literature (10,11), a brief discussion will be given with an emphasis on its role in discriminant analysis techniques. PCA involves decomposing the original data matrix of n spectra by m measurements (or wavelengths) into a matrix of scores, and a matrix of factors, as given by: $X = SF + E$; where X is the mean-centered data matrix, S is the n by a matrix of scores, F is the a by m matrix of factors, and the decomposition was carried out to a factors. E is an n by m matrix that contains the residual values for each spectrum at each measurement. The factors are linear combinations of the original measurements and are chosen sequentially to represent the directions of maximum variance in the data set. Each spectrum in the data matrix has a set of scores that indicate the amount of each factor required to represent the initial spectrum. Although the decomposition can be carried out to use all of the degrees of freedom available, usually the significant variance in the data set can be represented by a smaller number of factors, and any further factors represent only random variations (noise). After decomposition, each of the n spectra in the training set can be described by the set of a scores instead of m measurements (usually with $a<<m$). This not only reduces the dimensionality of the data set, but also improves the quality of the data since some of the noise is excluded from the primary set of factors.

Malinowski has discussed the determination of the optimum number of factors, a, that are needed to accurately represent the data matrix (12,13). He showed that, for a data matrix that is factor analyzable, there exists a primary set of factors that consists of a mixture of meaningful information and error, and a secondary set of factors that consists of pure error, or noise. Since it is the primary set that is of use in chemical analysis, rejection of the secondary set of factors will actually lead to an improvement of the raw data set. The problem lies in deciding where to separate the factors into primary and secondary sets. For multivariate quantitative calibration (e.g., partial least squares), the dependent variables can be used to monitor the progress of the decomposition. PCA decomposition, however, does not rely on dependent variables; the factors are selected solely on the basis of the variance within the data matrix. Malinowski derived several indicator functions which monitor the error via the eigenvalues associated with the factors (13). The eigenvalues give a measure of the amount of variance represented by each factor. The number of primary factors can be determined by starting with the least significant factor, and working backwards, until the point where the eigenvalues begin to represent more than the known experimental error. The factors beyond this point can be taken to be members of the primary set.

Once the training set data matrix has been decomposed by PCA, the scores can be used to develop a discriminant algorithm, similar to the way in which individual absorbance values can be used. Factorial discriminant analysis (FDA), which uses linear discriminating functions, has been demonstrated for several applications using NIR and mid-IR spectra (14-16). FDA uses the primary set of factors to define the space occupied by the training set. An alternative method, called soft independent modeling of class analogy (SIMCA), employs the information contained in the secondary set of factors (17). In SIMCA, the spectrum is reconstructed using the primary set of factors, and the residual spectrum is computed as the difference between the original and the reconstructed spectra. This is identical to computing the residual spectrum using the secondary set of factors but eliminates roundoff errors that can result from the small values in the secondary factors. The residual variance for a given spectrum is then computed as the sum of the squares of the values in the residual spectrum. An F-test can then be used to compare the residual variance for an unknown to the residual variances for the training set in order to statistically determine if the unknown is significantly different from the training set. Although FDA and SIMCA both employ PCA, the basic concept of the two techniques is quite different. FDA compares samples in a space that represents the significant variance of the training set, while SIMCA compares in the remaining orthogonal space. Van der Voet *et al.* have described these two spaces as inside-model space (IMS) and outside-model space (OMS), respectively (18). Both methods have certain merits, but the two are certainly suited to different types of applications. For example, FDA is best suited to an application that would discriminate against known sources of variation. This allows the PCA to accurately represent the space in which the variations will occur. SIMCA however is more suited to identify variations that are quite different from the inherent variance of the training set. The work of Gemperline *et al.* provides a

good example of this (19). Using SIMCA they successfully discriminated adulterated pharmaceutical raw materials from training sets of pure materials based on NIR reflectance spectra.

The data that are obtained during a TG/FT-IR run differ somewhat from the data typically used in discriminant analysis. FT-IR spectra are measured as the components of the sample evolve, and therefore spectra obtained during the run can vary widely. Therefore, discriminant analysis in the IMS will not be very useful since the variations in the factor space for an uncontaminated sample will be quite large. However, if the primary factors accurately represent the species evolving from the uncontaminated lubricant, then the presence of contaminants in a lubricant should result in evolving species that spectrally fall outside of the IMS defined for the uncontaminated lubricant. In this case, a discriminant analysis routine that analyzes the OMS (such as SIMCA) should be capable of detecting the presence of a contaminant. It is important to note that this approach requires that the contaminant produces evolving species that are spectrally different from the species evolving from the uncontaminated lubricant. The magnitude of required spectral difference is dependent upon the implementation of the discriminant algorithm, and spectral pretreatment will be particularly important.

SIMCA was evaluated as a method of detecting contamination in used synthetic lubricants on the basis of the data collected during a standard TG/FT-IR analysis (no postoxidizer). The spectra obtained during a run of an uncontaminated lubricant were used as the training set. First derivative spectra were used in order to eliminate the effects of baseline variations resulting from scattering. After selection of the spectral region of interest, the mean-centered training set was decomposed, and the number of factors in the primary set was determined using Malinowski's IND function (13). The residual variance was then computed for each spectrum in the training set and for all the spectra obtained from the runs of all the other samples, including the uncontaminated lubricant, various pure contaminants, and various "contaminated" lubricants. The residual variance for each spectrum, and the residual variance for the training set, were then used to compute the F-statistic using the approach outlined by Gemperline et al., (19). Gemperline classified samples as members if F was below the 95% level, as non-members if F was above the 99% level, and as undecided if F was between the 95% and 99% levels.

An example of the results of the factor analysis is shown in Figure 2. Figure 2a shows a plot of the spectra obtained for an uncontaminated lubricant and the residual spectra that result from projecting the spectra onto the primary set of factors. In Figure 2b, the spectra and residual spectra are shown for a lubricant sample contaminated with 5% polydimethylsiloxane. The large features present in the residuals result from spectral features due to the contaminant. Since these features are of larger magnitude than can be attributed to noise, this sample is identified as containing a contaminant. Several spectral regions were used to develop discriminant analysis routines, and the best general results were obtained using a region containing 4000-2450 and 2250-890 cm^{-1}. The 2450-2250 cm^{-1} region was excluded in order to reduce the effects of variable CO_2 evolution profiles, and the region below 890 cm^{-1} was excluded due to the presence of large noise spikes. These two regions were found to adversely affect the performance of the discriminant routines.

In Figure 3, the F-values are plotted for lubricant samples contaminated with several fluids. The samples with 5% silicone (PDMS) oil and 5% brake fluid are easily identified as contaminated, but the samples with 5% jet fuel, 5% motor oil, and 5% hydraulic oil all fell in the region where no decision can be made. This can be explained by the fact that the silicone oil and the brake fluid both have unique spectral bands that result in significant contributions to the residual spectrum, while the spectra of the other samples only exhibit bands due to C-H vibrational modes which are also present in the lubricant. Since these samples are only present at a concentration of 5% the contribution to the residual spectrum is small. This is verified by the fact that the sample with 30% hydraulic oil is identified as contaminated. In future work, additional spectral pretreatment methods will be investigated in order to magnify the spectral differences between the lubricant and these types of contaminants. It has been demonstrated by Hasenoerhl et al. (20) that pretreatment routines such as variance scaling and feature weighting can vastly improve the performance of PCA-based discriminant analysis routines.

The F-values were also plotted for another uncontaminated lubricant sample and samples contaminated with 5% methanol, 5% dichloromethane, and 5% trichloroethylene (TCE) (9). The discriminant analysis routine performed well for the uncontaminated sample and the methanol-contaminated sample. The two samples contaminated with chlorinated species were not detected as contaminated. This is due in part to the fact that the spectral region characteristic of C-Cl vibrational modes was excluded in order to limit the contribution of extraneous noise spikes. Results from analyses including this spectral region are poor due to the presence of these noise spikes, but do indicate that chlorinated contaminants can be detected at relatively high concentrations. As discussed below, much more sensitive detection of chlorinated contaminants can be achieved by using secondary oxidation to convert organic chlorine to HCl.

Artificial neural network analysis for contaminants - In the past decade, significant effort has been made to develop computing strategies that simulate biological systems. The resulting artificial neural networks (ANN) are grossly simple in comparison to biological networks, but are well suited for performing tasks such as pattern recognition, cost minimization, etc. (21). A typical ANN is made up

of three layers of processing units (nodes) and weighted connections between the layers of nodes. The input data is introduced at the input layer and is fed to the hidden layer through the weighted connections. Each node of the hidden layer sums its inputs and then applies an activation function to compute its output. The outputs of the hidden layer are then processed by the output layer, and their outputs are given as the output of the ANN. The function of the network is determined by the activation functions applied by the nodes and by the weights of the connections between the nodes. The weights can be strong or weak, and positive (excitatory) or negative (inhibitory). Typical activation functions are linear, step, and sigmoidal. Once the configuration of the ANN is defined for a given application, and the appropriate activation functions are selected, a network must be trained to perform the desired task. This is analogous to "learning" in a biological system. The usual method involves introducing training data to the ANN and comparing the output of the network to the correct or desired output. The error is then propagated back through the network in order to adjust the weights. This process is repeated until the error level falls below an acceptable level.

Recent applications of ANN technology to infrared spectral data fall into two primary classes: 1) multivariate quantitative analysis, and 2) classification. The primary advantage of ANNs for the development of quantitative models lies in the inherent capability to model nonlinearity. Classification networks applied to spectral data take advantage of the capability of ANNs to handle complex pattern recognition problems. Expert systems have been developed which employ ANNs to determine the functional groups present in a compound on the basis of its infrared spectrum (22). More specific classification networks have also been developed. Examples include sorting plastics encountered at a recycling plant based on their infrared spectra (23), and classifying woods as either hardwoods or softwoods on the basis of their FT-Raman spectra (24). These results are very promising and are indicative of the potential of using ANNs with spectral data to develop powerful classification techniques.

In order to investigate the potential of using a classification network to detect the presence of contaminants in synthetic lubricants, several networks were trained to recognize the presence of chlorinated solvents in the evolved species from a TG/FT-IR run. Training of the networks involved presenting examples of spectra from uncontaminated and contaminated runs. In order to provide a more general set of "contaminated" spectra, library spectra of dichloromethane and trichloroethylene (TCE) were added to the spectra obtained from the uncontaminated run.

Networks were developed and trained using the NeuralWorks ANN development package (NeuralWare, Pittsburgh, PA) in conjunction with custom C routines for data preprocessing and presentation. The network was trained using spectra from a TG/FT-IR run for an uncontaminated sample and spectra from the same run artificially spiked with library spectra. This was accomplished by writing a C program that presented either a spiked or unspiked spectrum to the network during training. The program was interfaced directly to the ANN development software in order to allow computation of new spiked spectra on the fly during training. At the beginning of each presentation, the program randomly chooses to present either a spiked or unspiked spectrum. If a spiked spectrum is to be presented, then a random fraction of a library spectrum is added to a randomly selected spectrum from the TG/FT-IR run. This presentation method allowed the training data to represent a large range of potential contamination conditions. Before presentation to the network, spectra were preprocessed with a Fourier filter routine to remove low frequency baseline variations and some of the high frequency noise, and the spectra were then normalized to unit vector length in order to give all spectra equal importance.

Figure 4 shows the prediction results from a network trained as described above. A network output of 1.0 indicates the evolution of a contaminant, and an output of -1.0 indicates that no contaminant is evolving. Figure 4a is the result for an uncontaminated lubricant run. While this result shows excellent prediction, this is the same data used to train the network, and therefore does not significantly demonstrate generalization. In Figure 4b, the result is shown for a TG/FT-IR run of a lubricant contaminated with TCE. The TCE evolving from 1-8 minutes is clearly identified as a contaminant, and the remainder of the run is accurately identified as uncontaminated. This result clearly demonstrates both the ability of the network to detect contamination and the ability of the network to generalize, i.e., accurately predict the uncontaminated portion of the run. The plot shown in Figure 4c shows the result for a TG/FT-IR run of a lubricant contaminated with dichloromethane. While the network clearly identified the contaminant evolving from 1-10 minutes, it did not successfully predict the absence of contaminant during the later part of the run (~45-70 minutes). This indicates that the network may produce false positives in the prediction of contamination.

Continuation of ANN development in future work will address the problem observed in Figure 4c. Further investigation of preprocessing routines should provide a solution to this problem. Additionally, other ANN architectures will be investigated. While the networks developed to date do not perform as well as desired, the results discussed above are promising, and indicate that further investigation may provide a powerful methodology for detecting contamination in synthetic lubricants.

Detection of Trace Chlorinated Contaminants in Synthetic Lubricants

While TG/FT-IR combined with the data analysis methods discussed above is well suited to identifying general contamination at relatively high concentrations, the detection of trace level contamination by chlorinated species is better accomplished using TG/FT-IR with secondary oxidation to convert the evolving organic chlorine to HCl. There are several factors that lead to greatly improved sensitivity for the detection of chlorinated species. Since the evolving species are converted to the gaseous combustion products (H_2O, CO_2, HCl), the quantitative analysis software can be vastly simplified. HCl can easily be measured by FT-IR in the presence of high concentrations of CO_2 and H_2O, since there is little spectral interference. Additionally, conversion of the evolving species to gaseous products eliminates the formation of aerosols in the gas cell, and therefore much larger samples of lubricant can be analyzed. This also allows for the use of a longer residence time in the gas cell and a faster temperature ramp in the furnace since there is less risk of condensation of heavy products on the gas cell mirrors and windows.

Two sets of samples contaminated with chlorinated compounds were run using the TG/FT-IR method with secondary oxidation. The first two samples were spiked with o-DCB and TCE, respectively, and ~45 mg samples were analyzed. The resulting spectra from the o-DCB contaminated sample are given in Figure 5. The spectra from this run shows the HCl evolving from 2-6 minutes into the run, along with high concentrations of H_2O evolving throughout the run. It is clear from the spectra that the relatively strong H_2O bands (4000-3000 cm^{-1}) will not obscure the weaker HCl bands between 3000 and 2600 cm^{-1}. As shown in Table 2, the measured HCl concentration agrees well with the expected concentration for the sample spiked with o-DCB, but is somewhat low for the sample spiked with TCE. It is believed that the bias observed for the TCE sample is a result of volatilization of the TCE during sample preparation.

Two ~200 mg samples contaminated with 1.3% and 0.13% o-DCB, respectively, were also run in order to increase the sensitivity of the method, and the quantitative analysis results are also summarized in Table 2. In the case of the ~200 mg samples, incomplete oxidation of the evolving lubricant led to the formation of significant amounts of methane, which can interfere with the quantitation of HCl. (Further tuning of the secondary oxidizer should allow for complete oxidation of samples of this size.) However, the HCl was still observed evolving from 2-6 minutes during the run (as was the case with the smaller samples), before the methane evolution becomes significant. It should be noted that a bias was observed for the 1.3% o-DCB sample, and it is believed that this is a result of an error in the preparation of the sample. The HCl concentration measured for the 0.13% o-DCB sample agrees well with the expected concentration of 0.065% HCl. This corresponds to 620 ppm (w/w) organic chlorine in the lubricant sample, and on the basis of the signal-to-noise ratio in the spectra, indicates a detection limit of about 300 ppm (w/w). On the basis of these results and projections of the gain that can be achieved with additional improvements the lower detection limit for organic chlorine in synthetic lubricant samples could be reduced to less than 10 ppm (9).

Table 2. Summary of the quantitative analysis results for the TG/secondary oxidation/FT-IR analysis of lubricant samples spiked with chlorinated contaminants.

contaminant	sample size (mg)	Cl conc. (wt %)	HCl conc. (wt %)	measured HCl (wt %)
0.65 wt% o-DCB	41.2	0.31	0.33	0.35
0.65 wt% TCE	46.9	0.53	0.54	0.37
1.3 wt% o-DCB	198.5	0.62	0.65	0.35
0.13 wt% o-DCB	208.2	0.062	0.065	0.059

SUMMARY AND CONCLUSIONS

In this work, the feasibility of using two novel thermal/FT-IR analysis methods in combination with advanced data analysis techniques to detect contamination in used turbine engine lubricants was demonstrated. The first method, TG/FT-IR combined with advanced data analysis routines, was shown to be capable of detecting the presence of different types of contaminants in synthetic lubricants at concentrations of about 5%, and this sensitivity could probably be increased to about 1% with software and hardware improvements. It was demonstrated that data analysis routines based on factor analysis (SIMCA) and neural networks could be used for identifying the presence of a contaminant. The second method, TG/secondary oxidation/FT-IR, was developed specifically for detecting trace levels of chlorinated contaminants in lubricants. Optimization of this technique using existing instrumentation led to a detection limit of about 300 ppm (w/w) organic chlorine in the lubricant. Further improvements in the hardware and software components could lead to detection limits of <10 ppm.

ACKNOWLEDGEMENTS

REFERENCES

1. Micallef, R.A., Squires, A.T.B.P., Technical Report AFWAL-TR-87-2067, Wright-Patterson AFB OH (November 1987).
2. Yoast, K.L., "Conservation of Petroleum Wastes at Red River Army Depot," Final Report No. USAMC-02-08-73-023, U.S. Army Material Command, Alexandria VA (March 1974).
3. Micallef, R.A., Squires, A.T.B.P., "Characterization of Used MIL-L-7808 Lubricants," Technical Report AFWAL-TR-85-2017, Wright-Patterson AFB OH (May 1985).
4. Micallef, R.A., Squires, A.T.B.P., "Reclamation of Synthetic Turbine Engine Lubricants," Technical Report AFWAL-TR-81-2072, Wright-Patterson AFB OH (August 1981).
5. Saba, C.S., Smith, H.A., Keller, M.A., Jain, V.K., Kauffman, R.E., "Lubricants Performance and Evaluation," Technical Report AFWAL-TR-87-2025, (June 1987).
6. Carangelo, R.M. Solomon, P.R., and D.G. Gerson, Fuel, 66, 960, (1987).
7. Whelan, J.K., Solomon, P.R., Deshpande, G.V., and Carangelo, R.M., Energy and Fuel, 2, 65, (1988).
8. Solomon, P.R., Serio, M.A., Carangelo, R.M., Bassilakis, R., Gravel, D., Baillargeon, M., Baudais, F., and Vail, G., Energy & Fuels, 4, (3), 319, (1990).
9. Serio, M.A., Bonanno, A.S., Bassilakis, R., Kroo, E., and Solomon, P.R., Final Report AFWAL-TR-93-2119 (November, 1993).
10. Malinowski, E.R., Howery, D.G., Factor Analysis in Chemistry, John Wiley & Sons, New York, 1980.
11. Jolliffe, I.T., Principal Components Analysis, Springer-Verlag, New York, 1986.
12. Malinowski, E.R., Anal. Chem., 49, 606 (1977).
13. Malinowski, E.R., Anal. Chem., 49, 612 (1977).
14. Devaux, M.F., Bertrand, D., Robert, P., Qannari, M., Appl. Spec., 42, 1015 (1988).
15. Devaux, M.F., Bertrand, D., Robert, P., Qannari, M., Appl. Spec., 42, 1020 (1988).
16. Downey, G., Robert, P., Bertrand, D., Kelly, P.M., Appl. Spec., 44, 150 (1990).
17. Wold, S., Sjostrom, M., in Chemometrics: Theory and Application, Ed. by B.R. Kowalski, American Chemical Society, Washington D.C., pp. 242-282 (1977).
18. Van Der Voet, H., Coenegracht, P.M.J., Hemel, J.B., Anal. Chim. Acta, 192, 63 (1987).
19. Gemperline, P.J., Webber, L.D., Cox, F.O., Anal. Chem., 61, 138 (1989).
20. Hasenoehrl, E.J., Perkins, J.H., Griffiths, P.R., Anal. Chem., 64, 656 (1992).
21. Kohonen, T., Neural Networks, 1, 3, (1988).
22. Wythoff, B.J., Levine, S.P., Tomellini, S.A., Anal. Chem., 62, 2702, (1990).
23. Alam, M.K., Stanton, S.L., Energy and the Environment, August, 4 (1992).
24. Personal communication with P.R. Griffiths, University of Idaho, October, 1993.
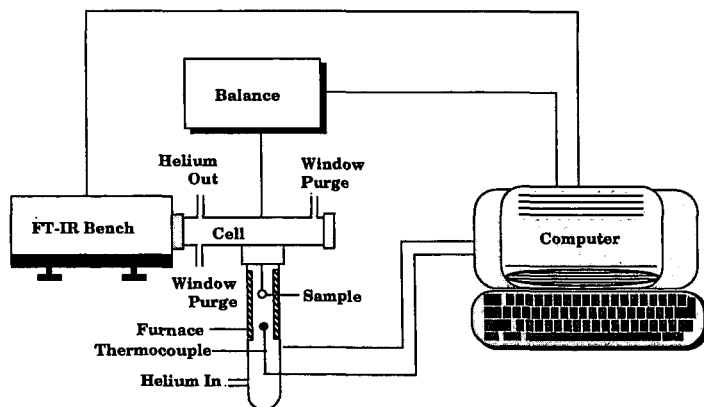
Figure 1. Schematic diagram of the standard TG/FT-IR instrument. The sample is suspended from a balance in the furnace, and, as the sample is pyrolyzed, the evolving species are swept into the FT-IR gas cell. The instrument was modified to include an oxidation zone before the gas cell.

Raw Spectra

Spectral Residuals
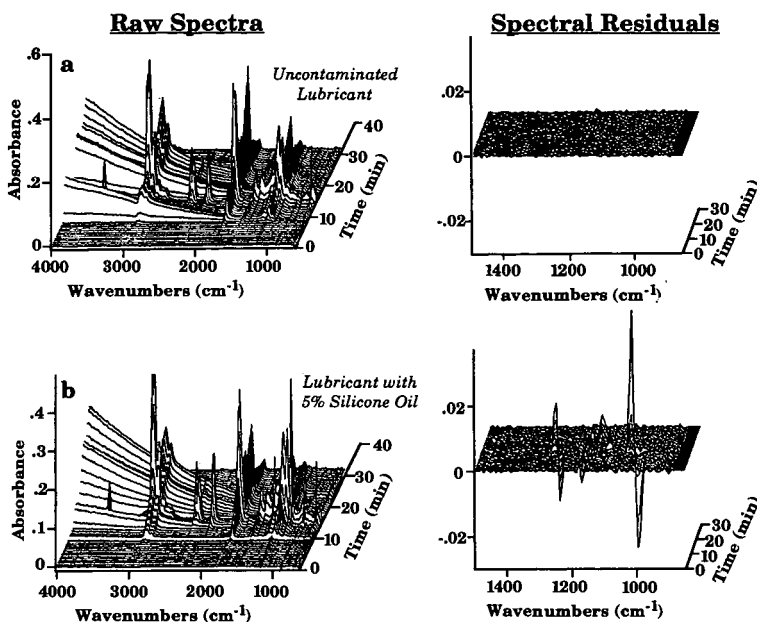
Figure 2. Examples of SIMCA analysis for TG/FT-IR runs of a) uncontaminated lubricant and b) lubricant with 5% polydimethyl siloxane. The raw spectra from the run are shown on the left, and the residual spectra resulting from projection onto the primary factors are shown on the right (note the expanded scale).
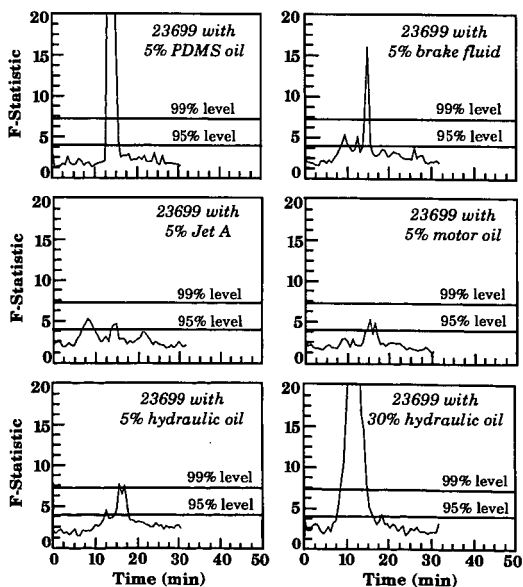

Figure 3. Results of SIMCA analysis for contamination in used synthetic lubricants. The F-values are plotted versus time for TG/FT-IR runs of lubricant samples contaminated with various fluids likely to be encountered at an Air Force base.
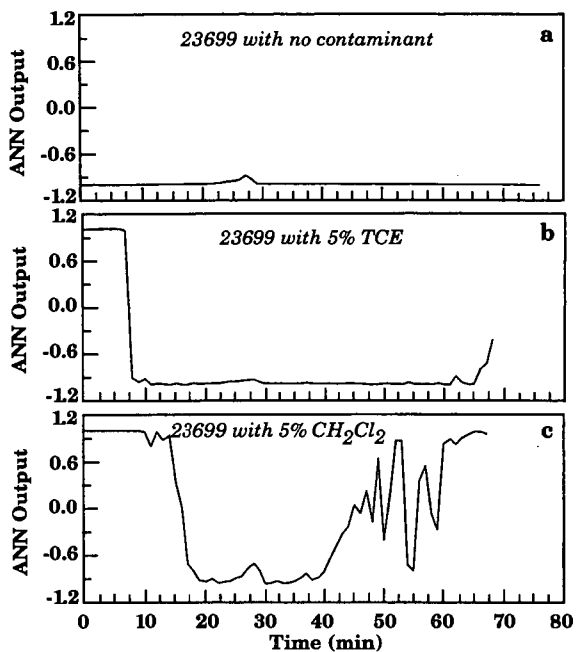
Figure 4. Neural network based prediction of chlorinated contaminants evolving during TG/FT-IR runs. A value of 1.0 indicates the presence of contaminant and -1.0 indicates the absence of contaminant. a) uncontaminated Mobil 23699; b) trichloroethylene contaminated Mobil 23699; c) dichloromethane contaminated Mobil 23699.
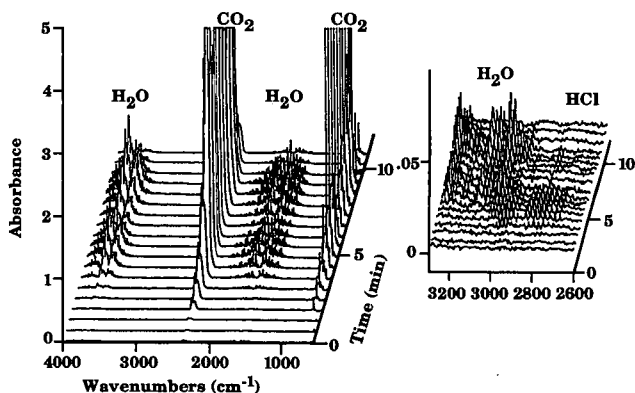
Figure 5. Spectra obtained during TG/secondary oxidation/FT-IR analysis of a 41.2 mg sample of lubricant spiked with 0.63% o-DCB. The scale is expanded in the plot on the right to show the evolution of HCl.

CHARACTERIZATION OF ACIDIC PROPERTIES OF MICROPOROUS AND MESOPOROUS ZEOLITE CATALYSTS USING TGA AND DSC

Chunshan SONG, Wei-Chuan LAI, Andrew D. SCHMITZ, and Kondam Madhusudan REDDY

Fuel Science Program, Department of Materials Science and Engineering, Pennsylvania State University 209 Academic Projects Building, University Park, PA 16802-2303

ABSTRACT

Thermal gravimetric analysis (TGA) and differential scanning calorimetry (DSC) were applied for characterizing the acidic properties of microporous and mesoporous zeolite catalysts through temperature-programmed desorption (TPD) of n-butylamine (n-BA) as a base probe molecule. A flow system was designed with heating and evacuation capability for preparing the n-BA adsorbed sample. In the TGA, n-BA desorption at different temperatures represents the interaction with surface acidic sites of different strength. The acid sites corresponding to base desorption at 100-240°C, 240-340°C, and 340-500°C, were classified as weak, intermediate, and strong acid sites, respectively. DSC indicates the endothermic nature of the differential thermogravimetric peaks (observed from TGA) in the above temperature regimes, confirming the TPD data. The microporous zeolites examined include three proton-form mordenites, three proton-form and metal-ion exchanged Y-zeolites, and four noble metal catalysts supported on mordenite and Y-zeolite. Four mesoporous zeolites were synthesized and examined by the same TPD method. Both the total acidity (mmol/g) and acid strength distribution depend on the zeolite type, Si/Al ratio, and metal loading. Ni and La ion-exchange decreased the strong acid sites. Pt and Pd loading on an HY decreased the strong acid sites but their loading on an H-mordenite had little effect on its strong acid sites. Mesoporous zeolites showed lower acidity and lower fraction of strong acid sites compared to HY and H-mordenites. However, the acidity of mesoporous zeolites strongly depends on the aluminum source compounds used in the hydrothermal synthesis of the zeolites.

INTRODUCTION

Recently, we have initiated a major effort in exploring microporous and mesoporous zeolite catalysts for conversion of polycyclic hydrocarbons related to fuel processing and shape-selective catalysis [Song and Kirby, 1994; Song and Moffatt, 1994; Schmitz and Song, 1994, 1995; Lai and Song, 1995; Reddy and Song, 1995a,b,c; Lai et al., 1995; Schmitz et al., 1995]. For a wide range of fuel processing reactions and shape-selective reactions, zeolite acidity is a key factor affecting activity and selectivity. In the present work, we attempt to characterize the acidic properties of mesoporous and microporous zeolites using thermogravimetric analysis (TGA) and differential scanning calorimetry (DSC).

Base molecules adsorb on Bronsted and Lewis acidic sites of solid surface, and can be removed by thermal desorption at elevated temperatures. The desorption temperature depends on the strength of the interaction between the base and the surface acidic sites. A widely used technique for characterizing the acidity of solid surface is temperature-programmed desorption of a base (e.g., ammonia) using thermal conductivity detector [Fernandes et al., 1994; Hunger and Szombathely, 1994]. However, acidity characterization can also be carried out using several other techniques, including infrared spectroscopy [Cannings, 1968; Lefrancois and Malbois, 1971; Ward, 1976; Makarova et al., 1994], nuclear magnetic resonance [Brunner et al., 1994], TGA [Ghosh and Curthoys, 1984], and calorimetry [Chen et al., 1992; Cardona-Martinez and Dumesic, 1992; Parrillo et al., 1994].

In this paper, we report acidity characterization of zeolites by temperature-programmed desorption of n-butylamine (n-BA) using TGA and DSC as detector. There are two advantages of using n-BA with TGA detection. The first one is that, compared to NH3, n-BA is closer in size and length to hydrocarbon molecules, and the acid sites detected by n-BA desorption may be practically more useful. The second is that using a higher-molecular-weight base (relative to NH3) can enhance the sensitivity of the TPD conducted on TGA, since TGA is not as sensitive as TCD. However, these advantages do not come without problems. Possible problems are n-BA decomposition at high temperatures [Ghosh and Curthoys, 1984] and likely slower diffusion compared to that of ammonia. Nonetheless, n-BA has been found to be a useful probe molecule for acidity characterization of zeolites.

EXPERIMENTAL

Microporous Zeolites

The microporous zeolites examined in this work include three hydrogen mordenites (HML8, HM20A, and HM30A), two noble metal loaded mordenites (Pt/HM30A and Pd/HM30A), and two sets of Y zeolite-based catalysts: the first set includes a hydrogen Y zeolite (HY-1 with SiO_2/Al_2O_3 molar ratio of 4.8) and two metal ion-exchanged Y zeolites (LaHY and NiHY); the second set includes another hydrogen Y-zeolite (HY-2 with SiO_2/Al_2O_3 molar ratio of 5.0) and two noble metal-loaded Y-zeolites (Pt/HY and Pd/HY). The three H-mordenites (HML8, HM20A, and HM30A) with different SiO_2/Al_2O_3 molar ratios (17, 21, and 38, respectively) were prepared by heat treatment of three commercial ammonium mordenite samples [Lai and Song, 1995; Schmitz et al., 1995]. The noble metal-loaded zeolites (Pt/HM30A, Pd/HM30A, Pt/HY, Pd/HY) were prepared by incipient wetness impregnation from aqueous solution of platinum and palladium salts: aqueous H_2PtCl_6 solution and aqueous $PdCl_2$ dissolved in hydrochloric acid (H_2PdCl_4). The noble metal loading on the support was nominally 6 wt%. The metal-loaded catalysts were calcined in air at 450 °C for 2 h after being dried in a vacuum oven. The three Y zeolites (HY, LaHY, and NiHY) were prepared according to the procedures described elsewhere [Song and Moffatt, 1994]. More details on the preparation and properties of the catalysts are described elsewhere [Song et al., 1991; Schmitz and Song, 1995].

Mesoporous Zeolites

The mesoporous materials were synthesized according to the procedure described elsewhere [Reddy and Song, 1995b]. Briefly, the mesoporous zeolites were synthesized from a mixture of reactants with the following composition: $50SiO_2$-xAl_2O_3-$4.32Na_2O$-$2.19(TMA)_2O$-$15.62(CTMA)Br$-$3165H_2O$; where $x=1.0$ and 2.0. The organic template from the as-synthesized solids was removed by calcining the samples in a tubular furnace at 550 °C for one hour in

nitrogen and 6 hours in air flow. The calcined samples were ion-exchanged with ammonium nitrate (0.5M) at 90°C. The protonated form was then obtained by calcining these ammonium ion-exchanged samples at 480 °C for 3 hours. More details for synthesis and spectroscopic characterization may be found elsewhere [Reddy and Song, 1995b].

TGA and DSC of Base-Saturated Samples
The acidity of catalysts were characterized by the temperature-programmed desorption of a base using thermogravimetric analysis (TGA) in combination with differential scanning calorimetry (DSC). n-Butylamine (n-BA) was chosen as the base for adsorption-desorption study; it was obtained from Aldrich Chemical Company and was used as received with a purity of 99+%.

For the preparation of n-BA adsorbed samples, we have designed a flow system with heating and evacuation capability, where a given zeolite was degassed in vacuo at 400°C, cooled to room temperature, and then exposed to n-BA vapor in flowing ultra-high purity nitrogen for 1 hour; N_2 with a flow rate of about 100 cm^3/min was used as a carrier gas. The base-saturated catalyst was then transferred to TGA or DSC for analysis.

The desorption experiments were carried out with base-saturated catalyst contained in an uncovered alumina crucible using Mettler TG50 thermogravimetric balance. Samples of about 10 mg were used in each measurement and a purge gas (N_2) flow of 200 cm^3/min at room temperature was used. Before the thermal analysis was started, the base-saturated sample was kept at 30 °C for 30 minutes with purge flow to remove physisorbed n-BA. The desorption temperature was programmed from 30 to 600 °C at a heating rate of 10 °C/min, and the decrease in weight with increasing temperature was monitored. TGA and DTG (differential thermogravimetry) data were then obtained.

The desorption was also carried out in a differential scanning calorimeter using Mettler Model DSC 27HP. About 7.5 mg of each of the catalysts was placed in an uncovered standard aluminum crucible (40 mL), and was heated from 30 to 600 °C at a rate of 10 °C/min with an initial isothermal time of 30 min. The system was continuously purged with 100 cm^3/min of N_2.

RESULTS AND DISCUSSION

Figure 1 shows the TGA and DSC profiles of temperature-programmed desorption of n-BA from HY (HY-1). DSC curve shows only endothermic peaks: a low-temperature peak near 100 °C, a shallow peak near 200 °C, a large peak at 405 °C, and a shoulder near 440 °C. DTG shows similar results except that the peak near 100 °C is not as clear as that in DSC. It can be seen that for HY the results from DTG compared fairly well with that from DSC. The peak near 100 °C may be due to the desorption of physisorbed n-BA, and n-BA adsorbed on weak acid sites. As another possible contributing factor, trace amount of water might have re-adsorbed on the base-covered catalyst. However, prior to n-BA adsorption, the previously calcined catalysts were further thermally pretreated in situ under vacuum to remove moisture, then covered and saturated with base in situ, and transferred to TGA in a closed vial. Thus only the base-saturated sample is exposed to air during sample unloading from the adsorption apparatus and loading into the TGA cell. On the other hand, the high-temperature peaks above ca. 300 °C are attributed to n-BA desorption from acid sites. Stronger acid sites desorb the base (n-BA) at higher temperatures. Therefore, the n-BA desorption at different temperatures corresponds to the surface acidic sites with different acid strength.

The surface acidic sites corresponding to TGA-derived weight loss due to base desorption at 100-240°C, 240-340°C, and 340-500°C, were classified as weak, intermediate, and strong acid sites, respectively. DSC indicates the endothermic nature of the differential thermogravimetric (DTG) peaks, confirming the TPD data obtained using TGA. It was assumed that the weight loss below 100 °C (about 1-1.5 weight % of the saturated catalysts) was due to the desorption of physisorbed base, and thus only the amount of n-BA desorbed above 100 °C was considered in the calculation of acidity. The low temperature range of 100-240°C was chosen to represent weak acid sites based on the report of Ghosh and Curthoys [1984]. The temperature limit was set at 500 °C because it was suggested that the weight loss above 500 °C may also be due to the dehydroxylation of the catalysts [Ghosh and Curthoys, 1984].

Acidic Characteristics of Microporous Zeolites
The DSC and TGA curves of n-BA desorption are presented in Figure 2 for HY (HY-1) and metal-ion exchanged Y zeolites (and HM20A), and in Figure 3 for mordenites and noble metal-loaded mordenite catalysts. On the basis of Figures 2 and 3, the weight losses (due to n-BA desorption) from Y-zeolite catalysts are greater than those for the mordenites at all temperatures, indicating that the Y-zeolites have both more acid sites and higher acid strength than the mordenites.

Among the three Y-zeolites (HY, LaHY, NiHY), LaHY has slightly more weak sites than the other two, but it has fewer strong sites than HY. HY has more strong acid sites judged from the enormous endothermic heat flow (Figure 2, right) and sharp weight loss (Figure 2, left) in the 340-500 °C range. NiHY has similar amount of weaker sites but much fewer strong sites than HY and LaHY (Figure 2, left). Among the mordenite based catalysts, HML8 only possesses a small number of weak sites, in fact the least among the eight catalysts; however, it has similar amount of strong sites as HM30A has, although they have different SiO_2/Al_2O_3 ratio.

We also compared two sets of metal-loaded Y-zeolites prepared by impregnation. Their n-BA TPD profiles are presented in Figure 4. The metal loaded Y zeolites (Pt/HY, Pd/HY) give almost linear weight loss curves, devoid of the rapid weight loss at 340-500°C which is apparent with HY (HY-2, Figure 4, left). One explanation for this behavior is that the metal particles preferentially attach to the support at strong acid centers. Metal-support interactions of this nature may explain why Group VIII metals on acidic zeolites, especially on HY, are known to be electron-deficient [Stanislaus and Cooper, 1994]. A second possibility is that metal particles prevent n-BA from diffusing onto strong acid sites by blocking the channel.

Pd/HM38 (identical to Pd/HM30A in Figure 3) and Pt/HM38 (identical to Pt/HM30A in Figure 3) give TPD profiles that are similar to each other. In this case, the presence of metal does not significantly impede diffusion of n-BA. It is possible that a significant portion of the metals reside in the mordenite side-pocket channels (dimension 2.9 x 5.7 Å) that run perpendicular to the main channels. The two noble metal loaded mordenites have quite similar acidity, and they possess fewer strong sites than HM30A.

Tables 1-3 summarize the acidity of the microporous zeolite catalysts determined from the amount of n-BA desorbed (from the TGA measurements) at three temperature ranges (100-240, 240-340, and 340-500 °C). From Tables 1 and 2, the total acidity of the catalysts decrease in the following order: HY > LaHY > NiHY > Pt/HY ≈ Pd/HY > HM20A >
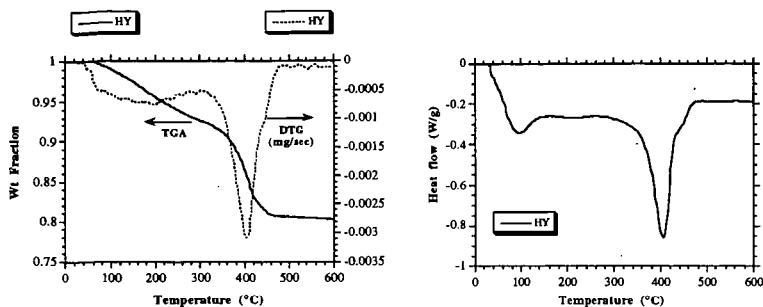
72

Figure 1. Temperature-programmed desorption of n-BA from HY zeolite (HY-1) conducted on TGA (left) and DSC (right).
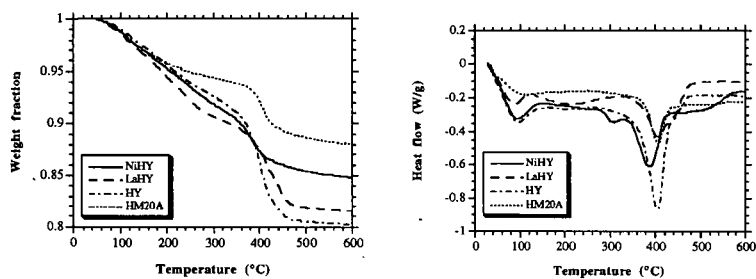

Figure 2. Temperature-programmed desorption of n-BA from proton-form zeolite catalysts conducted on TGA (left) and DSC (right).
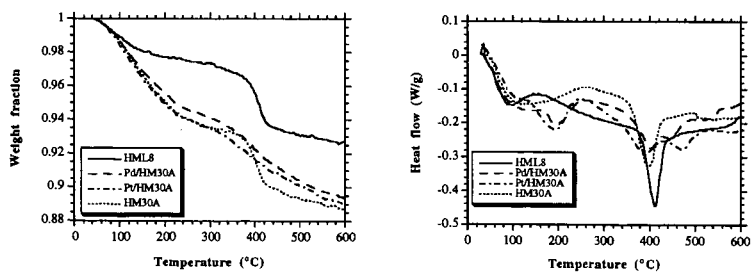

Figure 3. Temperature-programmed desorption of n-BA from mordenite-based catalysts conducted on TGA (left) and DSC (right).

HM30A > Pd/HM30A ≈ Pt/HM30A > HML8. Table 3 shows that the reproducibility of the TPD data is reasonably good.

Table 1. Acidity of Y-Zeolites from n-BA TPD (Acidity Unit: mmol/g)

Cat ID	HY (1)	LaHY	NiHY	HY (2)	Pt/HY	Pd/HY
Alt No.	HY-1	LaHY-1	NiHY-1	HY-2	Pt/HY-2	Pd/HY-2
T range, °C						
100 - 240	0.79	0.97	0.76	0.88	0.63	0.60
240 - 340	0.49	0.48	0.51	0.52	0.49	0.44
340 - 500	1.85	1.32	0.84	1.50	0.63	0.66
Total, mmol/g	3.12	2.77	2.11	2.90	1.75	1.71

Table 2. Acidity of Mordenites from n-BA TPD (Acidity Unit: mmol/g).

Cat ID	HML8	HM20A	HM30A	Pt/HM30A	Pd/HM30A
Alt No.	HM17 AS+WL	HM21 AS+WL	HM38 AS+WL	Pt/HM38	Pd/HM38
T range, °C					
100 - 240	0.19	0.56	0.75	0.68	0.62
240 - 340	0.10	0.17	0.15	0.18	0.17
340 - 500	0.57	0.80	0.61	0.44	0.51
Total, mmol/g	0.86	1.53	1.51	1.30	1.29

Table 3. Reproducibility of the Acidity Data (mmol/g) from n-BA TPD on TGA

Cat ID	HML8	HML8	HM20A	HM20A	HM30A	HM30A
Alt No.	HM17 WL	HM17 AS	HM21 WL	HM21 AS	HM38 WL	HM38 AS
T range, °C						
100 - 240	0.20	0.19	0.56	0.56	0.69	0.81
240 - 340	0.09	0.10	0.16	0.18	0.13	0.16
340 - 500	0.56	0.57	0.82	0.78	0.63	0.59
Total, mmol/g	0.86	0.86	1.54	1.52	1.45	1.56

Acid Characteristics of Mesoporous Zeolites

Mesoporous molecular sieves of MCM-41 type represent a new family of crystalline materials, and their synthesis has been made possible recently by Mobil researchers [Kresge et al., 1992; Beck et al., 1992]. The mesoporous zeolites (aluminosilicates) of MCM-41 type are of particular interest, because their uniform pores can be tuned in the range of 15 to 100 Å. Several research groups have reported the synthesis of mesoporous zeolites [Chen et al., 1993a,b; Corma et al., 1994; Borade and Clearfield, 1995; Reddy and Song, 1995a,b,c].

We have synthesized mesoporous zeolites, and found that the catalytic properties of the MCM-41 zeolites depend on the type of Al source compounds used for their synthesis [Reddy and Song, 1995b]. Here we compare the acidic properties of MCM-41 type mesoporous zeolites synthesized using alumina (pseudo boemite), Al sulfate, Al isopropoxide, and sodium aluminate.

Figure 5 and Table 4 show the TGA results for TPD of n-BA from the mesoporous zeolites synthesized with feed SiO_2/Al_2O_3 molar ratio of 50 using four different Al source compounds. From the weight losses due to n-butylamine desorption, it is clear that MCM-41 samples prepared with aluminum isopropoxide and aluminum sulfate adsorbed more n-BA (about 18 wt%), whereas the sample prepared with pseudo boehmite adsorbed less n-butylamine (about 10 wt%). These results indicate that first two samples adsorbed more base, hence they are more acidic than the last one, which confirms that aluminum incorporation is better for the first two samples. The better Al incorporation was also verified by solid-state NMR and XRD, as reported elsewhere (Song and Reddy, 1995b). The highest amount of n-BA was desorbed from the mesoporous zeolite prepared from sodium aluminate, in both the 100-240°C and the 340-500°C ranges. It seems that this mesoporous zeolite has the highest acidity among the four samples (synthesized with SiO_2/Al_2O_3 molar ratio of 50) examined.

Table 4. Acidity of Mesoporous Zeolites Determined from Desorption of *n*-Butylamine

n-Butylamine Desorption Temperature (°C)	Acid Strength	Acidity (mmol/g) of MCM-41			
		PB2(44)[a]	AS2(87)[a]	AI2(47)[a]	SA2(49)[a]
100-240	Weak[b]	0.81[b]	1.27[b]	0.84[b]	1.84[b]
240-340	Intermediate	0.06	0.17	0.25	0.16
340-500	Strong	0.10	0.29	0.32	0.42
Total acidity		0.97	1.73	1.41	2.42

[a] Values in the parentheses indicate SiO_2/Al_2O_3 molar ratios of the samples synthesized using PB (pseudo boehmite), AS (Al sulfate), AI (Al isopropoxide) and SA (sodium aluminate).

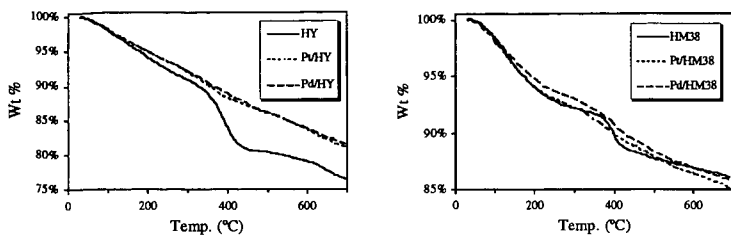[b] A portion of the n-BA desorbed at 100-240°C may be due to physical adsorption.

74

Figure 4. TGA-derived n-BA TPD from Pt- and Pd-loaded Y-zeolite (left, HY-2) and Pt- and Pd-loaded mordenite catalysts (right).
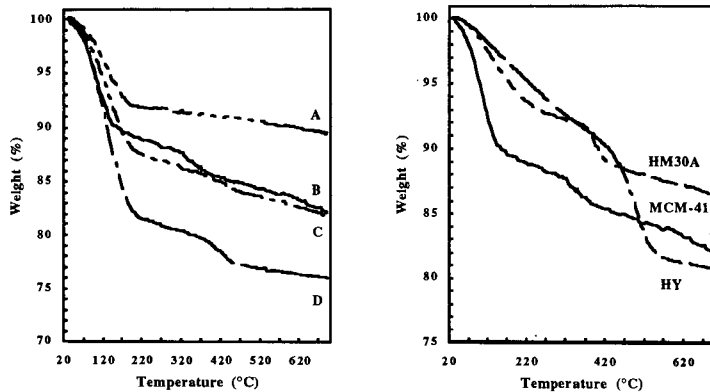

Figure 5 (Left). n-BA TPD from MCM-41 prepared using (A) pseudo boemite, (B) Al isopropoxide, (C) Al sulfate, and (D) solidium aluminate.

Figure 6 (Right). Comparison of n-BA TPD from MCM-41 prepared from Al isopropoxide and H-Y (HY) and H-mordenite (HM30A).
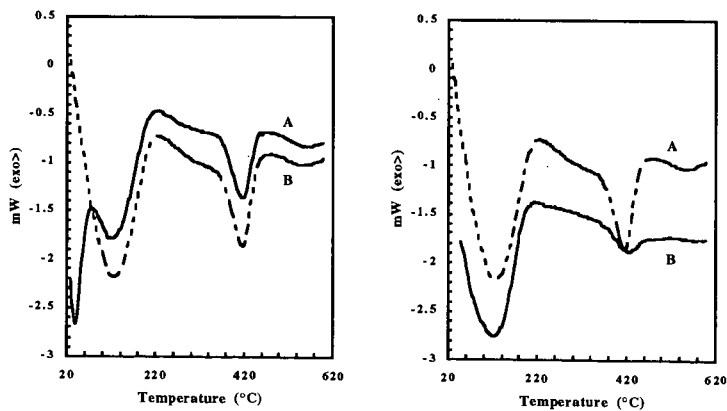

Figure 7 (Left). DSC for n-BA desorption from MCM-41 prepared from sodium aluminate ($SiO_2/Al_2O_3= 25$) without (A) and with (B) initial N_2 flushing at room temperature for 30 min (DSC run started after the N_2 flusing).

Figure 8 (Right). DSC profiles of n-BA desorption from MCM-41 prepared from sodium aluminate with SiO_2/Al_2O_3 ratio of 25 (A) and 50 (B).

Figure 6 compares the n-BA TPD profile of a proton-form mesoporous zeolite (synthesized using Al isopropoxide with feed SiO_2/Al_2O_3 molar ratio of 50) with those of a H-Y zeolite (HY) and a H-mordenite (HM30A). Our preliminary TPD results indicate that compared to a hydrogen Y-zeolite (SiO_2/Al_2O_3: 5) and a hydrogen mordenite (SiO_2/Al_2O_3: 38), there are less number of strong acid sites in the MCM-41 samples. In terms of the relative amount of n-butylamine desorption in the temperature range of 340-500°C, the qualitative order of acidity is HY > HM > protonated MCM-41. From Figure 6, it appears that the amount of the n-BA desorbed from MCM-41 below 200 °C is much higher than that from either HY or HM. The higher amount of low temperature desorption compared to mordenite could be due to several factors: 1) larger number of acid sites with low acid strength, 2) larger pore volume and larger sorption capacity which lead to more n-BA physical adsorption, and 3) the easier out-of-pore diffusion of n-BA from mesopores which are not readily available in microporous zeolites.

On the basis of the above discussion, a question that arises is whether all the n-BA desorption at 100-240°C is really due to weak acid sites in the case of mesoporous zeolites. Figure 7 shows DSC profiles of a mesoporous zeolite (synthesized using sodium aluminate with feed SiO_2/Al_2O_3 molar ratio of 25) with and without initial N_2 flushing (purge flow). The initial N_2 flushing affects the n-BA desorption at low temperatures (<220°C), but does not affect the n-BA desorption at high temperatures. Figure 8 shows DSC profiles of two mesoporous zeolites (synthesized using sodium aluminate with feed SiO_2/Al_2O_3 molar ratios of 25 and 50). Since the acidity of zeolites is associated with Al in tetrahedral coordination, the zeolite with higher Si/Al ratio should have lower acidity. As shown in Figure 8, increasing Si/Al ratio decreased the high-temperature DSC peak, as expected. However, the effect of Si/Al ratio on the low-temperature peak appears to be significantly less compared to that on the high-temperature DSC peak. These results suggest that the low-temperature DSC peak with the mesoporous zeolites is partly due to physical sorption.

Summary

TGA and DSC are useful techniques for characterizing acidic properties of microporous and mesoporous zeolites by temperature-programmed desorption of n-BA. The desorption of n-BA at different temperatures represents its interaction with surface acidic sites of different acid strength. Base desorption at 100-240°C, 240-340°C, and 340-500°C, was classified as weak, intermediate, and strong acid sites, respectively. DSC indicates the endothermic nature of the DTG peaks (observed from TGA) in the above temperature regimes, confirming the TPD data. However, desorption of physisorbed n-BA may also contribute to the peak in the 100-240°C range.

For the microporous zeolites (Y and mordenites) examined, both the total acidity (mmol/g) and acid strength distribution depend on the zeolite type, Si/Al ratio, and metal loading. Among the three proton-form mordenites, no linear correlation between their acidity and their Si/Al ratio was observed. Ni and La ion-exchange of HY decreased the strong acid sites. Pt and Pd loading by impregnation on HY decreased the strong acid sites but their loading on an H-mordenite had little effect on its strong acid sites.

Mesoporous zeolite samples of MCM-41 type prepared using different aluminum sources do show acidity in their proton-form. Mesoporous zeolites show lower acidity and lower fraction of strong acid sites compared to HY and H-mordenites. However, the acidity of mesoporous zeolites strongly depends on the aluminum source compounds used in the hydrothermal synthesis of the zeolites. The acidity measured by n-BA desorption at 240-500°C decreases with respect to the Al source in the following order: sodium aluminate > Al isopropoxide > Al sulfate > pseudo boemite.

REFERENCES

Beck, J. S.; Vartuli, J. C.; Roth, W. J.; Leonowicz, M. E.; Kresge, C. T.; Schmitt, K. D.; Chu, C. T. W.; Olson, D. H.; Sheppard, E. W.; McCullen, S. B.; Higgins, J. B.; Schlenker, J. C., J. Am. Chem. Soc., 1992, 114, 10834.
Borade, R. B.; Clearfield, A., Catalysis Letters, 1995, 31, 267.
Brunner, E.; Beck, K.; Koch, M.; Pfeifer, H.; Staudte, B.; Zscherpel, D. Stud. Surf. Sci. Catal., 1994, 84, 357.
Cannings, F.R., J. Phys. Chem., 1968, 72, 4691.
Cardona-Martinez, N.; Dumesic, J.A., Adv. Catal., 1992, 38, 149.
Chen, C.-Y.; Burkett, S. L.; Li, H.-X; Davis, M., Microporous Mater. 1993, 2, 17.
Chen, C.-Y.; Li, H.-X; Davis, M., Microporous Mater. 1993, 2, 27.
Chen, D.T.; Sgarma, S.B., Filimonov, I.; Dumesic, J.A., Catal. Lett., 1992, 12, 201.
Corma, A.; Fornes, V.; Navarro, M. T.; Perez-Pariente, J.; J. Catal. 1994, 148, 569.
Fernandes, L. F.; Bartl, P.E.; Monteiro, J.L.F.; da Silva, J. G.; de Menezes, S.C.; Cardoso, M.J., Zeolites, 1994, 14, 533.
Ghosh, A. K.; Curthoys, G., J. Phys. Chem., 1984, 88, 1130.
Hunger, B.; Szombathely, M.V. Stud. Surf. Sci. Catal., 1994, 84, 669.
Kresge, C. T.; Leonowicz, M. E.; Roth, W. J.; Vartuli, J. C.; Beck, J. S., Nature, 1992, 359, 710.
Makarova, M.A.; Garforth, A.; Zholobenko, V.; Dwyer, J.; Earl, G.J.; Rawlence, D., Stud. Surf. Sci. Catal., 1994, 84, 365.
Lai, W.-C., ; Song, C., van Duin, A.; de Leeuw, and J.W., Am. Chem. Soc. Div. Fuel Chem. Prepr., 1995, 40 (4), 1007.
Lai, W.-C., ; Song, C., Am. Chem. Soc. Div. Fuel Chem. Prepr., 1995, 40 (4), 1018.
Lefrancois, M.; Malbois, G., J. Catal., 1971, 20, 350.
Parrillo, D.J.; Biaglow, A.; Gorte, R.J.; White, D. Stud. Surf. Sci. Catal., 1994, 84, 701.
Reddy, K.M.; Song, C., Am. Chem. Soc. Div. Fuel Chem. Prepr., 1995a, 40 (4), 1003.
Reddy, K.M.; Song, C., Catalysis Letters, accepted for publication, 1995b.
Reddy, K.M.; Song, C., Catalysis Today, accepted for publication, 1995c.
Schmitz, A.D.; Song, C., Am. Chem. Soc. Div. Fuel Chem. Prepr., 1994, 39 (4), 986.
Schmitz, A.D.; Song, C., Am. Chem. Soc. Div. Fuel Chem. Prepr., 1995, 40 (4), 918.
Schmitz, A.D.; Bowers, G.; Song, C., Am. Chem. Soc. Div. Fuel Chem. Prepr., 1995, 40 (4), 930.
Song, C.; Kirby, S., Microporous Materials, Elsevier, 1994, 2 (5), 467.
Song, C.; Moffatt, K., Microporous Materials, Elsevier, 1994, 2 (5), 459.
Stanislaus, A.; Cooper, B.H., Catal. Rev.-Sci. Eng., 1994, 36, 75.
Ward, J.W. in "Zeolite Chemistry and Catalysis", ACS Monograph 171, J.A. Rabo Ed., ACS:Washington D.C., 1976, Chap. 3, pp. 118-284.

THERMAL STUDIES OF METAL PROMOTED SULFATED ZIRCONIA

Melody Bi, Hanxu Li, Wei-Ping Pan, William G. Lloyd, and Burtron H. Davis*
Department of Chemistry and Materials Characterization Center, Western Kentucky University,
Bowling Green, KY 42101, *Center for Applied Energy Research, University of Kentucky,
Lexington, KY 40506

ABSTRACT

SO_4^{2-}-ZrO_2 is considered to be a superacid catalyst. The metal promotion on sulfated zirconia has been shown to enhance the stabilities of the catalysts. The activation of these catalysts involves complex chemical changes. In the present investigation, a simultaneous TG/MS technique was utilized to investigate the weight loss and to monitor the chemical compounds that evolve under controlled heating in different environments. Some insight of the activation mechanism of the catalysts was thus obtained. The evolution of HCl and Cl_2 were well identified according to the mass ratio of Cl isotopes. The evolution of SO_2 and SO showed a continuum beyond 900°C which corresponds to the TG results. This indicated SO_4^{2-} is present in the solid in a variety of structures. The samples were also analyzed in STD (TGA-DTA). The results show so far sulfate ion is the most efficient species to retard the phase transformation process of zirconia.

INTRODUCTION

Solid oxide catalysts have been widely used in petroleum refineries for skeletal isomerization of n-paraffins and to isomeric alkanes to produce oxygenates, which are important components of automobile fuels. Among the solid oxide catalysts, zirconium oxide (ZrO_2) is claimed to be the only oxide catalyst that has acidic, oxidizing and reducing properties. The discovery by Tanabe and Hattori of the superacidic properties of sulfuric acid treated zirconium oxide (ZrO_2/SO_4^{2-}), the acidity of which was estimated to be as high as $H_0 < -14.5$ by the adsorbed Hammett base technique, has given a new impulse to solid catalysis.[1] Sulfated zirconia was obtained by immersing hydrous ZrO_2 catalyst powders in a sulfuric acid solution. Such sulfated zirconia catalysts have exhibited superacidic properties and show high activity for isomerization of hydrocarbons.[2-4] It was suggested that the superacid sites are generated by the interaction between the oxide and sulfate ions, and the presence of sulfate ion somehow inhibits the recrystallization of ZrO_2, therefore the sulfated zirconia retained a much greater fraction of the initial surface area than the unsulfated catalysts.[5] The addition of platinum to a sulfated zirconia catalyst has been shown to enhance the stability of the catalyst for the isomerization of butane and pentane at low temperatures, though the state of platinum in this type of platinum impregnated zirconia catalysts is still a matter of controversy.[6] Recently, another class of solid superacid catalysts--sulfated zirconia oxide, containing Fe and Mn, have been shown to be active for the skeletal isomerization of n-butane at room temperature.[7-9] Kinetic results indicated that this class of catalysts was about three orders of magnitude more active than a sulfated ZrO_2. Though extensive characterization studies have been carried out on the sulfate modified zirconia, less has been reported for the metal promoted sulfated zirconia. Commonly, these catalysts are activated at temperatures in the region of 600-725°C in air prior to use as catalysts for various reactions. The activation of these catalysts involves complex chemical changes. In the present investigation, simultaneous TG/MS and TG/DTA techniques were utilized to investigate the weight loss and the phase transformation of the solid and to monitor the chemical compounds that evolve under controlled heating in different environments.

EXPERIMENTAL

Zirconia was prepared by rapidly precipitating from a 0.3M solution prepared from anhydrous $ZrCl_4$ with an excess amount of NH_4OH to a final pH of 10.5. The resulting precipitate was washed thoroughly with deionized water until a negative test was obtained for the presence of chloride ions in the wash. The dried hydroxide gel was sulfated by immersing the powder in 0.5M H_2SO_4 and stirring for 2 hours. The precipitate was collected by filtration without further washing, and dried. Pt-SO_4^{2-}-ZrO_2 was obtained by impregnating sulfated zirconia powders with an aqueous solution of H_2PtCl_6. The Fe/Mn promoted sulfated zirconia were prepared by dissolving appropriate amounts of Fe(III) and Mn(II) nitrate/sulfate salts in the amount of water needed to prepare a catalyst containing the desired amount of Fe and Mn using an incipient wetness impregnation technique. All catalysts, after impregnation, were dried at 120°C overnight and stored in a desiccator until used for thermal analysis. The samples thus prepared used in the present analysis include 1%(5%)Pt-SO_4^{2-}-ZrO_2 and 2%Fe/0.5%Mn (sulfate salt/nitrate salt)-SO_4^{2-}-ZrO_2.

The samples were analyzed in a TA TGA 2950 instrument which was coupled to a VG Mass Spectrometer (from ThermoLab), Figure 1. The MS spectrometer allows the determination of multiple gas components in the mass range of 1-300amu. It has a specially designed flexible capillary tube with a fused silica liner, which is heated to 170°C to avoid condensation of evolved gasses. It requires 60 milliseconds for gas transfer from the TGA to the MS. The mass spectrometer has a Nier type enclosed ion source, a triple mass filter, and two detectors (a Faraday cup and a secondary emission multiplier). The TG-MS system has an operating temperature range to 900°C. Data from the mass spectrometer was acquired using a log histogram mode scan (LHG) in which the intensities of all peaks in a specified mass range were monitored and stored repeatedly during the temperature program. A data conversion program was used to display the intensities of the desired ions as a function of temperature. The runs were conducted separately in a purge gas of helium or air at a flow rate of 50 ml/min. Heating rates were 20°C/min. The samples were also analyzed in a TA SDT 2960 instrument, which is an analysis module that is capable of performing both thermogravimetric analysis (TGA) and differential thermal analysis (DTA) at the same time in a temperature range from room temperature to 1500°C in a controlled atmosphere. While the physical measurement of weight loss is obtained by TGA, in the meantime, the thermal events occurring to the samples are recorded by DTA. An upward peak represents for an exothermic event while a downward peak represent for an endothermic event on a DTA curve. Platinum crucibles were used as sample holders, and Al_2O_3 was used as the reference material.

RESULT AND DISCUSSION

When 1%(5%)Pt-SO_4^{2-}-ZrO_2 samples were heated in helium, two major weight loss regions are seen on TG curve, see Figure 2, curve (a), (b). According to the MS data, Figure 3, the first weight loss region is between room temperature to 620°C, which corresponds to the loss of water, carbon dioxide, hydrogen chloride and chlorine. The identification of HCl and Cl_2 is based upon the molar mass of the compounds as well as the mass ratio of the Cl isotopes. In the case of HCl evolved from 5%Pt-SO_4^{2-}-ZrO_2 sample, the ratio of peak area integration of HCl(38)/HCl(36) is around 1:3, which meet very well with the theoretical data. The integration of Cl_2 peak area didn't give a good agreement with theoretical isotope ratio. This is because when only trace amount of chlorine is released from the sample, the magnitude of noise is comparable to the Cl_2 profile. In that case, the integration can not be precise to give the real isotope mass ratios. However, the trend does agree with that isotope peaks Cl(70)>Cl(72)>Cl(74). Water is lost during this temperature range. The long tail of water peak profile indicated most of water is present as adsorbate on the surface area, whereas some water exists in the deeper pores within the solid. The evolution of carbon dioxide at different temperature ranges is due to the coordination between carbon dioxide, which is a Lewis acid, and zirconia, which is a Lewis base, during sample preparation. The variation of weight loss at this temperature region depend upon the drying condition of the catalyst sample as well as the amount of sulfuric acid adsorbed on the sample. The second weight loss region is from 620°C to a temperature beyond 900°C, which corresponds to the decomposition of sulfate ion to give off sulfur oxides as well as a continuous evolution of HCl (MS data). The peak profiles of sulfur oxides show a continuum beyond 900°C since the profiles of SO_2 and SO didn't go back to the base line level. This can be evidenced by TG data which shows that the TG curve doesn't level off at this point. The results indicated that there could be different types of sulfate in zirconia. The evolution profile of HCl also shows 3 peak maxima which indicated several forms of bonding between Cl and zirconia. Thus, in the inert gas the heating events can be described as occurring in two temperature regions:

$$\text{Region I } (<620°C)$$
$$ZrO(OH)_2 \cdot H_2PtCl_6 \longrightarrow 2HCl + Pt + H_2O + ZrO_2 + 2Cl_2$$
$$\text{Region II } (>620°C)$$
$$SO_4^{2-}\text{-}ZrO_2 \longrightarrow ZrO_2 + SO_2 + SO + O_2$$
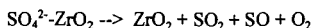
The evolution of oxygen coincides with the evolution of sulfur oxides as shown on the MS data and suggests that SO_3 might form prior to the evolution of SO_2 and SO. However, SO_3 was not identified by mass spectrometry. The results obtained when pretreating gas was air are similar to those of the runs in helium; however, when air is used it is not possible to measure the evolution of oxygen.

When 2%Fe/0.5%Mn(sulfate salt/nitrate salt)-SO_4^{2-}-ZrO_2 samples were heated in helium to 900°C, there was also two major weight loss regions on the TG curve at the same temperature region as it for platinum sulfated zirconia. (see Figure 2, curve (c), (d). For Fe and Mn nitrate salt treated sulfated zirconia, the first major weight loss includes the decomposition of nitrate ion at around 300°C in addition to the other gas species as mentioned above for platinum sulfated zirconia sample (see Figure 4). Integration of peak area shows NO:NO_2 is 5:1, which agree with the fraction of nitrate ion that

evolves containing more NO than NO_2. Therefore, the heating events for this sample below 620°C can be described as follows:

Region I (<620°C)

$$ZrO(OH)_2 \circ Fe(NO_3)_2/Mn(NO_3)_2 \longrightarrow ZrO_2 + Fe_2O_3 + MnO + 2NO_2 + 2NO + H_2O$$
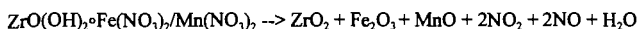
The second major weight loss can be attributed to the decomposition of sulfate ion as seen in other sulfated zirconia samples in the second temperature region.

As for Fe/Mn sulfate salt treated sulfated zirconia, the result is similar to that of the platinum sulfated zirconia samples. It was shown that the existence of different metals or metal oxides does not affect the decomposition temperature of sulfate ion. Also, the results obtained when the pretreating gas was air are similar to those of the runs in helium, which indicate oxygen doesn't have any significant effect on the activation process.

When the platinum sulfated zirconia is analyzed in SDT at an air environment, we could see clearly the endothermic peak on DTA curve corresponding to the loss of gas species as water, carbon dioxide, hydrogen chloride and chlorine. There is a distinct exothermic peak on DTA curve occuring at 648 °C which corresponds to the phase transformation of the solid from amorphous state to crystallite state. As a matter of fact, this exothermic event overlaps with an endothermic event which corresponds to the decomposition of the sulfate ion. Therefore, when heating the sample in air or an inert gas, the exothermic event is the result of an exothermic and an endothermic event so that the shape of the trace will depend upon the heat balance for these two events. For zirconia alone, this exotherm occurs at 450°C under the same heating condition, while in the presence of sulfate ion, the phase transformation process is retarded to a much higher temperature. It was found for sulfated zirconia samples, this exotherm occurs at 622 °C under the same heating conditions. This indicates that the existence of metals on the sulfated zirconia doesn't have any significant effect on this exothermic event. When anions other than sulfate ion were used to treat sulfated zirconia, this exotherm occurs at 533°C for molybdate zirconia, 527°C for dichromate zirconia and 465°C for tungstate zirconia.[10] It is found that sulfate ion is so far the most efficient species to retard phase transformation of the catalyst, thus permitting a high surface area to be maintained through a higher temperature range.

CONCLUSION

When catalyst samples of $1\%(5\%)Pt-SO_4^{2-}-ZrO_2$ and $2\%Fe/0.5\%Mn$ (sulfate salt/nitrate salt)-SO_4^{2-}-ZrO_2 were heated in air or inert gas, online analysis by TG-MS shows different gas species evolved during different temperature regions. HCl and Cl_2 were identified even in trace amounts according to their isotope mass ratios. The existence of metals or metal oxides on the sulfated zirconia does not affect the decomposition of sulfate ion; neither does it affect significantly the phase transformation of the solid in air or inert gas environment. Sulfate ion was found so far to be the most efficient species to retard the phase transformation process of zirconia.

ACKNOWLEDGEMENT

REFERENCES

1.   Tanabe, K. and Hattori, H. *Chem.Lett.*, **1976**, 625.

2.   Hini, M. and Arata, K. *J.Chem. Soc., Chem. Commun.*, **1980**, 851.

3.   Arata, K.; Hino, M.; and Yamagata, N. *Bull. Chem. Soc. Jpn.*, **1990**, 63, 244.

4.   Wen, M. Y.; Wender, I.; and Tierney, J.W. *Energy Fuels*, **1990**, 4, 372.

5.   Scurrell, M. S. *Appl. Catal.*, **1987**, 34, 109.

6.   Hosi, T.; Shimidzu, T.; Itoh, S.; Baba, S.; Takaoka, H. *Prepr.-Am. Chem. Soc., Div. Pet. Chem.* **1988,** 33(1), 562.

7.   Hollstein, E.J.; Wei, J.T.; and Hsu, C.Y. US patents 4, 918, 041, 1990, and 4, 956, 519, 1990.

8. Hsu, C.Y.; Patel, V.K.; Vahlsing, D.H.; Wei, J.T.; and Myers, Jr., H.K. US Patents 5, 019, 617, 1991.

9. Lin, C.H. and Hsu, C.Y. *J. Chem. Coc., Chem. Commun.*, **1992**, 20, 1479.

10. Bi, M.; Li, H.; Pan, W.P.; Lloyd, W.G.; and Davis, B.H. North American Thermal Analysis Society Conference, **1995**, #76, 350.
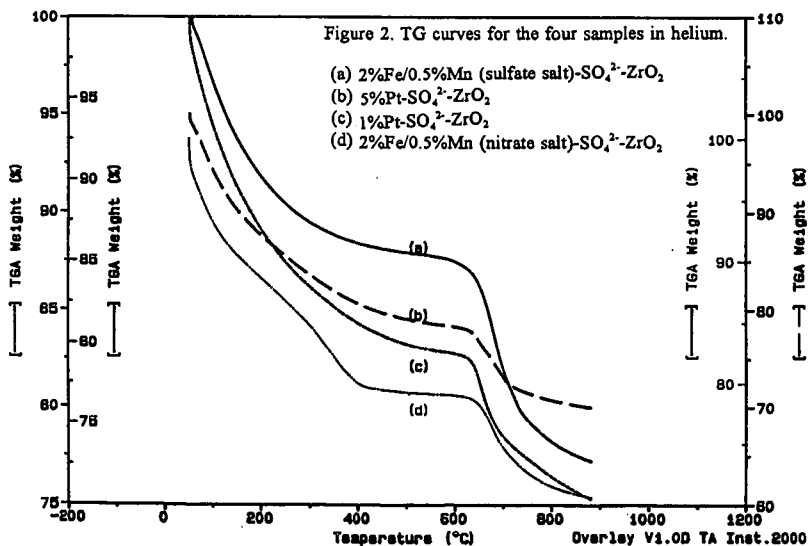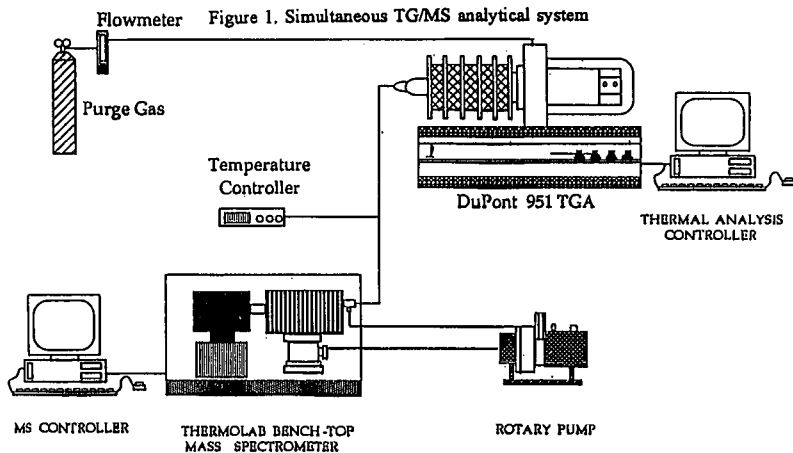
Flowmeter   Figure 1. Simultaneous TG/MS analytical system

Purge Gas

Temperature Controller

DuPont 951 TGA

THERMAL ANALYSIS CONTROLLER

MS CONTROLLER

THERMOLAB BENCH-TOP MASS SPECTROMETER

ROTARY PUMP

Figure 2. TG curves for the four samples in helium.

(a) 2%Fe/0.5%Mn (sulfate salt)-SO_4^{2-}-ZrO_2
(b) 5%Pt-SO_4^{2-}-ZrO_2
(c) 1%Pt-SO_4^{2-}-ZrO_2
(d) 2%Fe/0.5%Mn (nitrate salt)-SO_4^{2-}-ZrO_2

TGA Weight (%)

TGA Weight (%)

TGA Weight (%)

TGA Weight (%)

Temperature (°C)   Overlay V1.0D TA Inst.2000

80

Figure 3. The MS data for 5%Pt-SO_4^{2-}-ZrO_3 sample in helium.
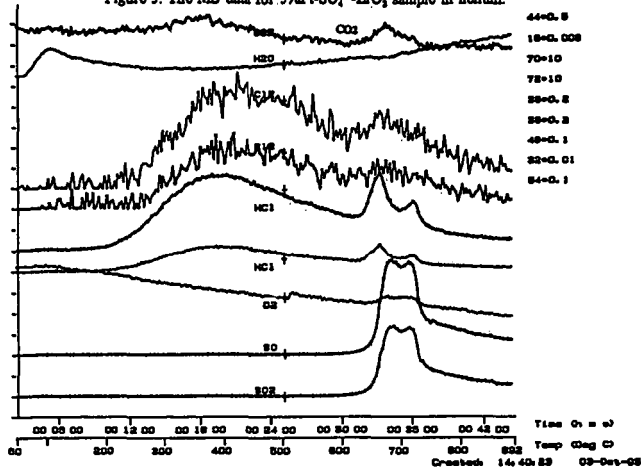
Figure 4. The MS data for 2%Fe/0.5%Mn (nitrate salt)-SO_4^{2-}-ZrO_3 sample in helium.
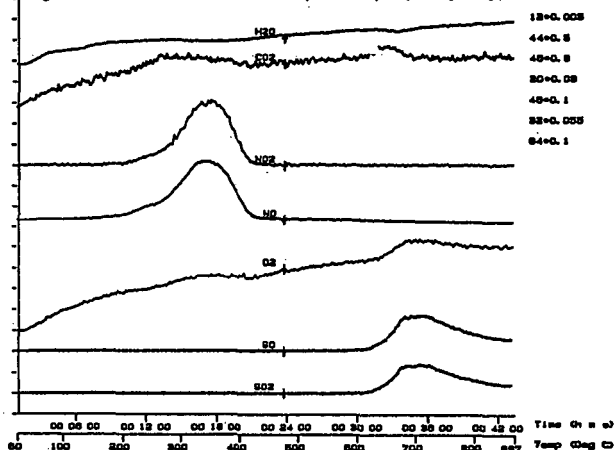
Figure 5. The SDT data for 1%Pt-SO_4^{2-}-ZrO_3 sample in air.

81
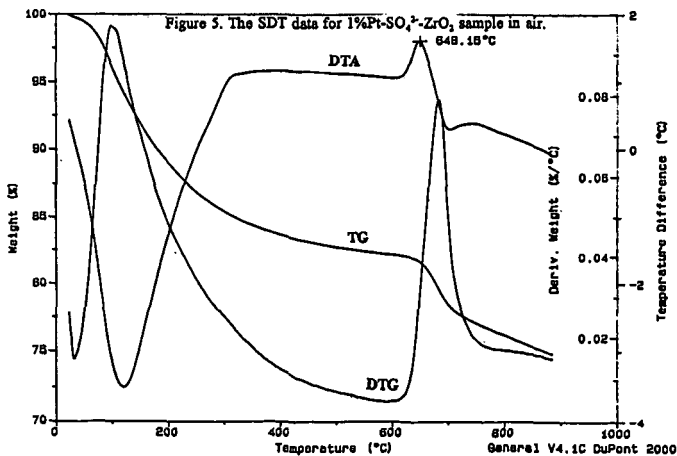
MEASUREMENTS OF VAPOR PRESSURES OF HETEROATOM-CONTAINING PAH AND COAL-TAR MODEL MIXTURES

V. Oja and E.M. Suuberg
Division of Engineering
Brown University
Providence, RI 02912

Keywords: Coal Tar, Vapor Pressures, Polycyclic Aromatic Hydrocarbons

INTRODUCTION

This paper presents the results of measurements of the vapor pressures of large polycyclic aromatic hydrocarbons (PAH), including those containing heteroatoms, and some mixtures of these compounds. The work was motivated by the lack of vapor pressure data on coal tars, which tend to have a highly aromatic nature and which also contain significant numbers of heteroatoms. Relatively few data are available on the vapor pressures of large polycyclics containing heteroatoms. Knowledge of coal tar vapor pressures is important in predicting the pyrolysis behavior of coals, since most advanced models of coal pyrolysis utilize an evaporation step to describe the loss of tar from the particles [1-8].

There have been some efforts made at characterizing vapor pressures of coal *liquids*, as opposed to coal tars [9]. For the most part, that work was concerned with relatively lighter compounds than are of interest in pyrolysis (typically, four fused aromatic rings or less, with molecular weights of about 300 or less). Primary coal tars exhibit molecular weights that are well over 1000 [1,6]. In addition, there is a tendency in liquefaction to reduce the heteroatom content of the coal liquids, so the important role of heteroatoms in determining properties of coal tars might not be well modeled by coal liquids. The predictive methods seen to work reasonably well with hydrocarbon model compounds for coal liquids were often noted to work more poorly in heteroatomic systems [9].

There is little hope of characterizing materials as complex as coal tars in very great detail. There is strong incentive to keep the amount of data needed for prediction of vapor pressures of such mixtures to an absolute minimum. This issue has historically been addressed by the use of correlations based upon molecular weight distributions alone [1-8,10,11], since molecular weight and temperature are the two most important variables in determining vapor pressures. These correlations have been of one particular form, obtained from the Clausius-Clapeyron equation, assuming that the heat of vaporization is a function of the molecular weight and not a function of temperature. The resulting form of correlation developed by Suuberg et al. [10] is :

$$P = \alpha \, \exp\left(-\beta \, \frac{M^\gamma}{T} \right)$$

This is the simplest expression which appears to be consistent with the known thermodynamics of the situation and is used because of the lack of detailed chemical structure and vapor pressure data on coal tar. It should also be noted, consistent with this approach, that it has been shown possible to correlate molecular weight of coal liquids using only boiling point information, at least up to about 400 molecular weight [9].

Several workers have employed such a correlation, and values of the constants they have obtained by fitting the data to literature data on aromatic hydrocarbons are shown below:

	α	β	γ
Suuberg et al.[10]	1.23×10^5	236	0.654
Suuberg et al.[11]	5765	255	0.586
Niksa [3]	70.1	1.6	1.0
Niksa and Kerstein [4]	3.0×10^5	200	0.6
Fletcher et al. [5]	87060	299	0.59
Oh et al. [8]	6.23×10^5	561	0.474

In this expression, P is in atmospheres, T is in K, and M is in daltons. Comparisons of the predictions of several of these models have been offered elsewhere [5]. Wide variations were noted in the predictions, and there is a concern about adequacy of predictions of the vapor pressures under pyrolysis conditions. Nevertheless, it is clear that there is a general convergence of most of the values of α, β, and γ in the literature. A comparison of the predictions of boiling point with molecular weight is shown in Figure 1, for various models. The results of Tsonopoulos et al. [9] and Fletcher et al. [5] are seen to be in good agreement, but this is not surprising, since they involved regression of many of the same data on coal liquids. For reference, the measured

properties of anthracene are indicated.

Most of the experimental data in the literature on what might be considered model compounds for coal tars have been measured in a pressure range from 10^{-4} to 10 torr. A problem arises in extrapolating existing experimental data out of the temperature range in which it was obtained. Measurements of vapor pressures of high molecular weight materials requires high temperatures to obtain conveniently measurable pressures, but high temperatures cannot be employed because of the concern about thermal decomposition during measurement. This, then, requires the use of moderate temperatures (<300°C) and sensitive, indirect vapor pressure measurement techniques. Yet it is the high temperature range (>300°C) that is of practical interest for coal tars, since these materials are formed at those high temperatures. Thus the extrapolation to high temperatures is of great importance. Significant concerns arise because many of the measurements must be performed with the compounds of interest in the solid phase, as opposed to the liquid phase in which they might exist at the high temperatures of practical interest. Thus the measurements are being conducted under *sublimation* conditions, whereas in practice, true evaporation will be occurring. This makes the prediction of changes in vapor pressure with temperature very difficult. Not only is a correction required to correct for sublimation as opposed to evaporation (involving an enthalpy of fusion), but the enthalpy of evaporation itself is a decreasing function of temperature.

In sublimation work, it is not uncommon to find that the Clausius-Clapeyron equation, with a constant $\Delta H_{sublimation}$, fits vapor pressure data reasonably well, i.e., $d\,[\ln P^\circ]/\,d\,[1/T] = -\Delta H_{subl}/R$. The difficulty in developing reliable correlations of ΔH_{subl} with molecular weight is evident from the data of Figure 2, which shows data for high molecular weight aromatic hydrocarbons (a few containing heteroatoms). The poor correlation might be in part attributable to the difficulty of performing measurements by the indirect methods required. However, part of the difficulty might also be understood in terms of the enthalpy of sublimation consisting of contributions from the enthalpies of vaporization and fusion [12]. The enthalpies of vaporization of many compounds can be reasonably estimated by any number of means. The enthalpy of fusion, on the other hand, is very difficult to correlate with other properties [12]. For high molecular weight materials, the enthalpies of fusion can become comparable in magnitude to the enthalpies of vaporization. In this work, we are addressing this issue specifically, and will report on it separately.

EXPERIMENTAL

The vapor pressures of actual coal tars and model "tars", consisting of mixtures of PAH, are measured, using a molecular effusion/TGA technique. The various so-called "effusion" methods are based on the molecular effusion of a vapor from a surface, or through an orifice [13]. Of these methods, that which has been selected for use here is the Knudsen method [14,15], in which a substance of interest effuses through a small pinhole, of known area, in an otherwise sealed container or cell. The Knudsen method is used for the measurement of low vapor pressures in the range from 1 to 10^{-6} torr, under molecular flow conditions. This ideally requires that pressures inside and outside the sample cell are low enough that the frequency of collisions of vapor molecules with gas phase species are low in comparison with the frequency of collisions with the cell. The measurement of vapor pressure involves determining the rate of loss of molecules of the evaporating substance from the effusion cell under these conditions. Measurements are made under isothermal conditions, with weight loss from the cell being recorded as a function of time, generally in a TGA-type apparatus.

The basic theory of the effusion method has been often reviewed in the literature [14-16]. The theory of method is actually based upon the basic kinetic theory of gases. From these classical results, Knudsen derived an expression for the slow isothermal flow out of a cell with a small hole in it. The vapor pressure of a material in the cell can be calculated from Knudsen's original effusion rate result :

$$P_1 - P_2 = \frac{G}{t}\,\frac{w_1 + w_2}{\sqrt{\rho}}$$

where P_1 is the pressure of saturated vapor inside the cell, P_2 is the pressure outside of the effusion cell, w_1 is the resistance of hole in the cell, w_2 is the resistance of cell containing the sample, G is the mass lost by effusion, t is the effusion time, ρ is the density of the vapor at the temperature of experiment. The relation simplifies upon applying several simplifying assumptions, including the ideal gas law, that the pinhole leak is the main flow resistance, and assuming $P_1 \gg P_2$, yielding:

$$P = \frac{m}{t\,A_0}\left(\frac{2\pi R T}{M}\right)^{1/2}$$

83

The above result is called the ideal Knudsen equation, in which P is the desired vapor pressure, m the mass loss during the effusion time interval , A_0 is orifice area, M the substance molecular weight , t the effusion time, and T the absolute temperature of the experiment. It is further assumed when applying this equation to the effusion process that the equilibrium vapor pressure of the effusing species obtains within the cell, that the orifice walls do not intercept and return into the cell an appreciable fraction of molecular current entering the hole, that there is no back flux into the orifice exit and the number of intermolecular collisions in the vapor phase occurring within the orifice is negligible.

In our implementation, the mass loss rate was continuously recorded, using a Cahn 2000 recording electrobalance. The cell containing the pinhole leak was suspended on one arm of the balance, which has nominal sensitivity in the μg level. The backpressure in the TGA system was maintained at 10^{-7} torr, which has been noted to be sufficient so as to provide accuracy in the 10^{-6} torr range of vapor pressures. The cell itself was maintained inside of a black capsule within the TGA, and was in close proximity to a thermocouple within the capsule. This was necessary in order to achieve the 0.1°K accuracy in temperature measurement required in vapor pressure work at low temperatures.

RESULTS AND DISCUSSION

Variation of Vapor Pressure with Temperature
Typical results are shown in Figure 3, for anthracene between 47 and 75 °C. The anthracene was of 99+% purity, purchased from Sigma Chemical Company, and used without further purification. Comparison is shown with other sources of data on this compound [17-21]. Again, the spread of the data is indicative of the difficulty in performing such measurements, on even relatively "easy" low molecular weight aromatics. The other feature which is clear from Fig. 3 is that the assumption that the enthalpy of sublimation is reasonable. Our results provide an enthalpy of sublimation of 101.6 kJ/mol. By way of comparison, the enthalpy of vaporization of anthracene, at its normal boiling point of 340 °C, is 56.5 kJ/mol [12]. The melting point of anthracene is 216°C, so our experiments were performed much below the melting point. This is, again, very clear indication of the danger in blindly extrapolating vapor pressure data over a wide range of temperatures. The actual extrapolation is shown in Figure 4. It is seen that the extrapolation leads to a reasonable prediction of the first reported point in the liquid region, since this was very close to the melting point of the anthracene. As one extrapolates into the liquid region, the comparison becomes progressively poorer, because $\Delta H_{subl} \neq \Delta H_{vap}$. If one considers the earlier suggested correction of the enthalpy of sublimation to the enthalpy of vaporization, the enthalpy of fusion would be around 45 kJ/mol. The ratio of the enthalpy of fusion to the enthalpy of vaporization is roughly 0.8, which is quite close to the the same ratio for n-dodecane (0.84 [12]), the normal alkane with a molecular weight closest to that of anthracene.

Mixture Models
It is unclear what mixture models can be used to describe vapor-liquid equilibrium for tars, which are obviously multicomponent mixtures. Typically, the most common assumption is Raoult's Law, in which the tar mixture is assumed ideal. There have been no attempts to establish how reasonable this assumption might be.   Nearly ideal mixing behavior was seen for aromatic hydrocarbon mixtures (e.g. anthracene and perylene). An example of how a simple mixture model might badly fail is provided in Figure 5, for a mixture of phenanthridine and 1-hydroxypyrene. Aromatics containing such functional groups would be expected in coal tars. It would be anticipated that there would be strong acid-base interaction in this case, and this is clearly shown by the fact that the vapor pressure is far lower than predicted by Raoult's Law. Clearly more work is needed to establish how closely Raoult's Law might be followed in real tars.

ACKNOWLEDGMENT

REFERENCES
1. Suuberg, E.M., in *Chemistry of Coal Conversion* (R. Schlosberg, Ed.), Plenum, 1985.
2. Unger, P.E., Suuberg, E.M., *18th Symp. (Int.) on Comb.*, The Comb. Inst., p. 1203, 1981.
3. Niksa, S. *AIChE J, 34,* 790 (1988).
4. Niksa, S. and Kerstein, A., *Energy Fuels, 5,* 647 (1991).
5. Fletcher,T., Kerstein,A. , Pugmire, R., Solum, M., Grant, D. *Energy Fuels, 6,* 414 (1992).
6. Solomon, P.R., Serio, M.A., and Suuberg, E.M., *Prog. Energy Comb. Sci., 18,* 133 (1992).
7. Solomon, P.R., Hamblen, D.G., Carangelo, R.M., Serio, M.A., Deshpande, G.V., *Energy Fuels, 2,* 405 (1988).
8. Oh, M.S., Peters, W.A., and Howard, J.B., *AIChEJ, 35,* 776 (1989).
9. Tsonopoulos, C., Heidman, J., and Hwang, S.-C., *Thermodynamic and Transport Properties of Coal Liquids,* Wiley, 1986.
10. Suuberg, E.M., Peters, W.A. and Howard, J.B., *17th Symp. (Int.) on Comb.,* The

Combustion Institute, p. 117, 1979.

11. Suuberg,E.M., Unger, P.E., and Lilly, W.D., *Fuel, 64*, 956 (1985).

12. Reid, R.C., Prausnitz, J.M., and Poling, B., *The Properties of Gases and Liquids*, 4th Ed. McGraw-Hill, 1987.

13. Dushman, S., *Scientific Foundations of Vacuum Technique*, Wiley, 2nd edition, 1962.

14. Knudsen, M., *Ann. Physik., 28*, 999, 1909.

15. Knudsen, M., *Ann. Physik., 29*, 179, 1909.

16. Hollahan, J., *J. Chem. Educ., 39*, 23, 1962.

17. Hansen, P.C and Eckert, C. A., *J. Chem. Eng. Data, 31*, 1 (1986)

18. DeKruif, C.G.,*J. Chem. Thermodynamics, 12*, 243 (1980).

19. Kelley,J.D.and Rice, F.O.,*J. Phys. Chem., 68*, 3794 (1964).

20. Macknick, A.B. and Prausnitz, J.M., *J. Chem. Eng. Data, 24*, 176 (1979).

21. Sonnefeld,W.J., *Anal. Chem., 55*, 275 (1983).
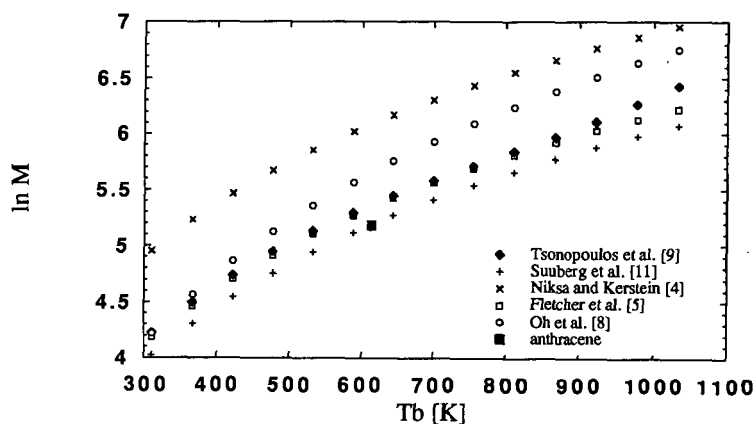
Figure 1. Predicted variation of boiling point with molecular weight, for low molecular weight aromatics.
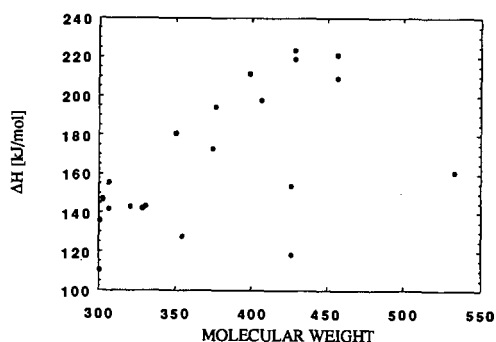
Figure 2. Variation of enthalpies of sublimation with molecular weight of aromatics. Data from *Handbook of the Thermodynamics of Organic Compounds*, by R.M. Stephenson and S. Malanowski, Elsevier, 1987.
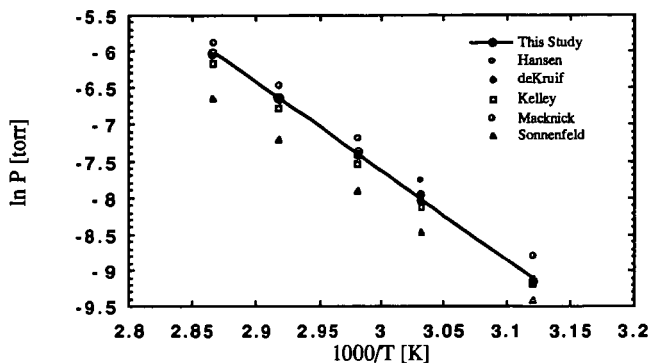
Figure 3. Vapor pressures of solid anthracene, from this study and the literature.
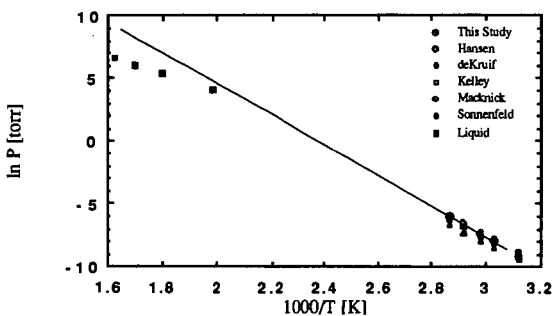
Figure 4. Vapor pressures of solid and liquid anthracene. Liquid data from Stephenson and Malanowski.
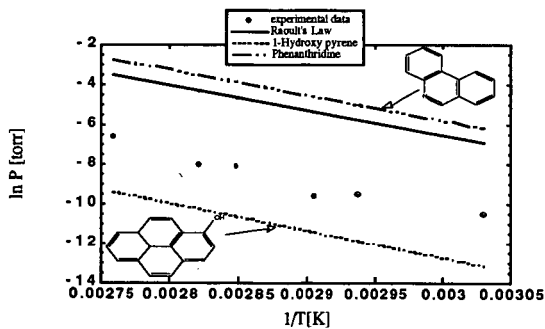
Figure 5. Vapor pressures of 1-hydroxypyrene, phenanthridine, and a mixture of 54 mol% 1-hydroxypyrene, 46% phenanthridine. The Raoult's Law prediction for the mixture is also shown.

DISTILLATION OF LIQUID FUELS BY THERMOGRAVIMETRY

He Huang, Keyu Wang, Shaojie Wang, M. T. Klein and W.H. Calkins*
Dept of Chemical Engineering, University of Delaware, Newark, DE 19716

Key words: thermogravimetric analysis, distillation, liquid fuels

INTRODUCTION

The most widely used separation technique in the petroleum industry and other liquid fuel production processes as well as in much of the chemical industry is distillation. To design and operate an appropriate commercial and laboratory distillation unit requires a knowledge of the boiling point distribution of the materials to be separated. In recognition of these needs, the ASTM developed the distillation procedures of D86, D216, D447, D850, and D1078. They are widely used in laboratories for the purposes of sample characterization, product and quality control, and distillation column design. However, the significant drawbacks of these ASTM methods include 1). close monitoring of the distillation is required. This is particularly difficult for those samples which are very toxic and/or cause any other safety problems; 2). the sample under test must be transparent and free of separated water (1); and 3). results obtained by these methods are not particularly precise. This motivated the development of a novel automatic distillation system based on the use of a custom-built thermogravimetric apparatus.

Thermogravimetry (TG) can be used to determine variation in mass as a function of temperature and/or time. Thus, thermogravimetric techniques, in principle, could be used in study of any physical and chemical processes where changes in mass are function of temperature and/or time. Hence, either commercial or custom-built thermogravimetric apparatus provides flexible means and unique features for study of various physical processes and chemical reactions. In the state-of-the-art custom-built thermogravimetric system, a computer is generally used for data acquisition of time, temperature and mass.

Massoth and Cowley (2) utilized a stirred flow thermogravimetric reactor for catalyst studies of hydrogenation of 1-butene under steady-state conditions. Sears et al. (3) reported a pressurized thermogravimetric equipment for use in oxidizing atmospheres at high temperatures. Dean and Dadyburjor (4) used a continuous thermogravimetric technique, combined with a pulse microreactor and on-line gas chromatograph, to study deactivation of cracking catalysts by coking.

In this paper, design and operation of a custom-built thermogravimetric apparatus for the distillation of liquid fuels are reported. Using a sensitive balance with scale of 0.001 g and ASTM distillation glassware, several petroleum and petroleum-derived samples have been analyzed by the thermogravimetric distillation method. When the ASTM distillation glassware is replaced by a micro-scale unit, sample size could be reduced from 100 g to 5-10 g. A computer program has been developed to transfer the data into a distillation plot, e.g. Weight Percent Distilled vs. Boiling Point. It also generate a report on the characteristic distillation parameters, such as, IBP (Initial Boiling Point), FBP (Final Boiling Point), and boiling point at 50 wt% distilled. Comparison of the boiling point distributions determined by TG (thermogravimetry) with those by SimDis GC (Simulated-Distillation Gas Chromatography) on two liquid fuel samples (i.e. a decanted oil and a filtered crude oil) are also discussed in this paper.

EXPERIMENTAL

Apparatus. A schematic diagram of the thermogravimetric apparatus for distillation is shown in Figure 1. A K-type thermocouple was used to measure the boiling temperature. The thermocouple was supported by a tight bevel-seal (Kontes, Vineland, New Jersey) with the thermocouple vertical and centered in the tube of the distillation head and in such a position that the thermocouple end-point (i.e. thermocouple joint) is level with the lowest point of junction between head tube and head neck (see Figure 1). The signal from the thermocouple was first processed by a DIN Rail Thermocouple Transmitter (MCR-TC Series, Omega Engineering, Inc.). A Mettler PK300 Balance with precision of 0.001 g was used to monitor the mass change in the distillate receiver. A Mettler GC47 D/A Converter was used to transfer the digital signals from the balance to analog signals for data acquisition. Asystant+ data acquisition system with DT2805 A/D board (Asyst Software Technologies, Inc.) was installed in a IBM computer and used for data acquisition. Both temperature and mass signals were sampled at 1 Hz. A ASTM distillation head and 250-ml flask (Kontes) and an electric heater were used for distillation.

Distillation. For each distillation, about 100-g liquid fuel was transferred into the distillation flask. Both the empty flask (W_{flask}) and initial distilland liquid fuel ($W_{initial}$) were weighed using the balance. Adjust the electric heater referring to the instructions given in ASTM D1078 and record the temperature and distillate mass by the computer. After the

condenser tube has drained, the total mass of distillate weighed by the balance was recorded as recovery ($W_{recovery}$). Cooling the distillation flask to room temperature, the distillate left plus the flask ($W_{left+flask}$) was weighed by the balance. The amount of residue ($W_{residue}$) was obtained by the subtraction of W_{flask} from $W_{left+flask}$. The amount of distillation loss (W_{loss}), due to surface wetting, was estimated by subtracting $W_{initial}$ and the sum of $W_{recovery}$ and $W_{residue}$.

Cleaning System. The apparatus system is cleaned in place by a series of suitable low-boiling solvent distillation. The number of cleaning distillations and type of solvent used are selected based on the distilland being studied. The effectiveness of cleaning can be monitored by analysis of the distillate streams (e.g. by GC analysis). After cleaning, the distillation glassware are placed into an oven and the temperature set above the boiling point of the solvent used.

Data Processing. The collected mass data were processed using an 11-point smoothing filter of the Linear Regression & Error Analysis procedure (5).

Materials Studied. A decanted oil and a filtered crude oil, together with seven other liquid fuels (designated as Samples A, B, C, etc.), have been studied using the thermogravimetric distillation apparatus. Pure organic compounds from low boiling point to high boiling point, such as methylene chloride (99.9+%), tetralin (1,2,3,4-tetrohydronaphthalene, 99%), and 1-methylnaphthalene (98%) from Aldrich Chemical Co., have been used for testing and calibrating the apparatus.

RESULTS AND DISCUSSION

Calibration of the Apparatus System Using Pure Organic Compounds. Several pure organic compounds have been used to test and calibrate the thermogravimetric apparatus. In theory, transfer time of distillate through the condenser, as a delay effect, should be corrected for accurately determining the boiling point distribution (i.e. Weight Percent Distilled vs Boiling Point) and characteristic distillation parameters, such as Initial Boiling Point (IBP), Final Boiling Point (FBP) (or Decomposition Point, DP). Results of the tetralin distillation using the TG method are shown in Figure 2. Surprisingly, there was no distillate-transfer time observed (see Figure 2). The dashed-line in Figure 2 defines the time required by the distillate being transferred through the condenser. The results shown in Figure 2 indicate no delay effect, i.e. as soon as the temperature reaches the tetralin boiling point, the first drop of tetralin falls into the distillate receiver. The same results were obtained in distillations of methylene chloride and 1-methylnaphthalene. The reason of these phenomena may be due to that the condenser surface was wetted by the vapor of the sample before its boiling point was reached. The Weight Percent Distilled vs. Boiling Point for the tetralin is shown in Figure 3. That the boiling point was increased after 95 wt% distilled is apparently due to impurities in the tetralin. The results of duplicate tetralin distillations are summarized in Table I. Weight percent distillation recoveries, residues, and losses, plus the boiling points observed, together with the literature value (6), are also given in Table I.

Distillation of Liquid Fuels. Plots of the Weight Percent Distilled vs. Boiling Point for the seven liquid fuels using the TG method are shown in Figures 4-10. Based on ASTM definition (7), the IBP (Initial Boiling Point) is the temperature detected as the first drop of condensate falls into the distillate receiver. Thus, in this TG method, the Initial Boiling Point was the temperature recorded at which the distillate mass is above zero. The mass of the first drop of the distillate recorded for these liquid fuels was in the range of 0.005 to 0.02 g. The Final Boiling Point (FBP) (i.e., the end point or decomposition point) was the maximum temperature recorded during the test. If no residue was left in the distillation flask, the dry point, instead of FBP, was reported. Characteristic distillation parameters (e.g. IBP, FBP, BP @50 wt%), together with the weight percent distillation recoveries, residues, and losses, of the seven liquid fuels are summarized in Table II.

The first derivative of TG distillation (i.e. d(wt%)/dt) vs boiling point for Sample A is shown in Figure 11. This plot indicates the density function of distillate against boiling point. It can be used as additional information for characterizing the boiling property of liquid fuels.

Comparison of TG Distillation with SimDis GC. Plots of the Weight Percent Distilled vs. Boiling Point using the TG method (solid line) and SimDis GC technique (dashed line) for a filtered crude petroleum and a decanted oil are shown in Figures 12 and 13. The results show significant differences. It is more evidenced when the characteristic distillation parameters (e.g. IBC, FBP, BP @50 wt%) of the two samples determined by the both methods are summarized in Table III. These deviations of the SimDis GC method from the distillation may be resulted by the interactions between the tested sample and the selected column packing and by the differences in properties and distillation characteristics between the calibration standards and tested samples. The weight percent distillation recoveries, residues, and losses are also included in Table III. Compared to the SimDis GC

method, the TG technique, when operated under atmospheric pressure, is limited to measuring the boiling point up to about 380 °C.

CONCLUSION

The custom built thermogravimetric apparatus for distillation provides an accurate, convenient, and simple determination of boiling point distribution of liquid fuels. It has potential as a modified method to replace the widely used ASTM distillation methods. Boiling point distributions of two oil samples determined by the thermogravimetric method and SimDis GC technique show significant differences. These deviations of the SimDis GC method from distillation may be due to sample-GC column packing interactions and differences between the calibration standards and tested samples.

ACKNOWLEDGMENTS

REFERENCES

1. Distillation of Industrial Aromatic Hydrocarbons and Related Materials *ASTM D 850*, 1991.
2. Massoth, F.E. *Chem. Tech.* 1972, May, 285.
3. Sears, J.T.; Maxfield, E.A.; Tamhankar, S.S. *Ind. Eng. Chem. Fundam.* 1982, 21, 474.
4. Dean, J.W.; Dadyburjor, D.B. *Ind. Eng. Chem. Res.* 1988, 27, 1754.
5. Wang, Keyu; Wang, Shaojie; Huang, He; Klein, M.T.; Calkins, W.H.; paper to be presented in the *Symp. on the Thermal Analytical Techniques*, March 24-29, 1996, in Mew Orleans.
6. Lide, D.R. *CRC Handbook of Chemistry and Physics*, 72nd ed.; CRC Press, Inc., Boca Raton, FL, 1991.
7. Distillation of Petroleum Products *ASTM D 86*, 1990.

Table I Results of tetralin distillation

Distillation Run No.	Boiling Point °C	Recovery wt%	Residue wt%	Loss wt%
1	207.8	98.7%	0.7%	0.6%
2	207.7	99.1%	0.5%	0.4%
3	207.8	98.9%	0.5%	0.6%
Literature value	207.6	-	-	-

Table II Results of the seven liquid fuel distillations

Sample	IBP °C	BP @50wt% °C	FBP °C	Recovery wt%	Residue wt%	Loss wt%
A	206.1	278.5	316.4	95.3%	3.2%	1.5%
B	169.4	285.6	334.9	90.5%	8.6%	0.9%
C	84.3	285.6	346.2	89.7%	9.8%	0.5%
D	194.1	272.7	350.8	96.1%	3.5%	0.4%
E	105.1	365.7	378.2	59.9%	35.1%	5.0%
F	209.6	342.0	353.8	71.9%	23.3%	4.8%
G	198.1	280.6	348.5	95.5%	3.9%	0.6%

Table III Comparison of SimDis GC with TG

Distillation Method	IBP °C	BP @40wt% °C	BP @50wt% °C	FBP °C	Recovery wt%	Residue wt%	Loss wt%
Sample: Crude oil							
TG (1st)	56.3	-	301.5	314.7	71.9%	22.0%	6.1%
TG (2nd)	55.8	-	297.6	314.9	72.6%	21.1%	6.3%
SimDis GC	95.6	-	431.1	720.0	91.0%	-	-
Sample: Decanted oil							
TG (1st)	244.1	363.7	-	364.6	42.5%	50.2%	7.3%
TG (2nd)	244.9	368.7	-	373.6	46.8%	45.5%	7.7%
SimDis GC	215.6	383.9	-	705.0	99.5%	-	-
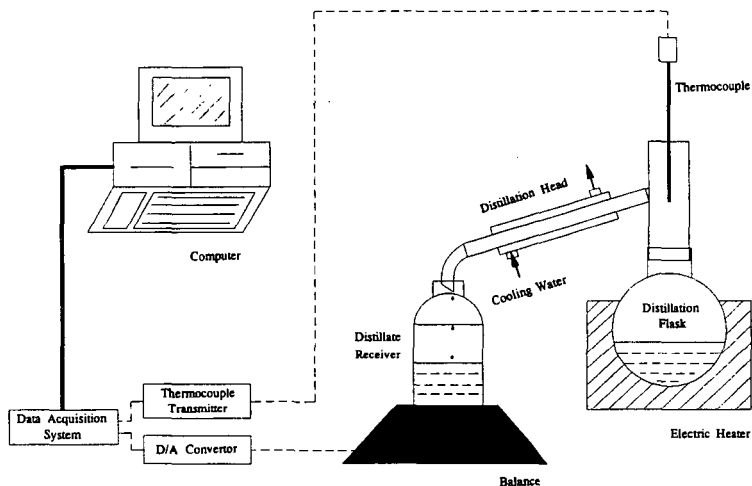
Figure 1 Schematic diagram of a custom built TG for distillation
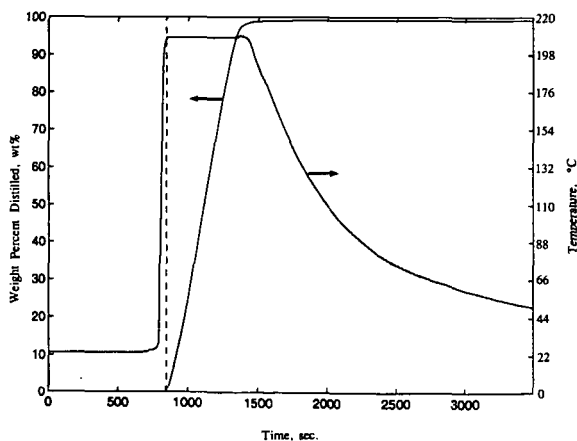
Figure 2 Temperature-mass-time plot for tetralin distillation
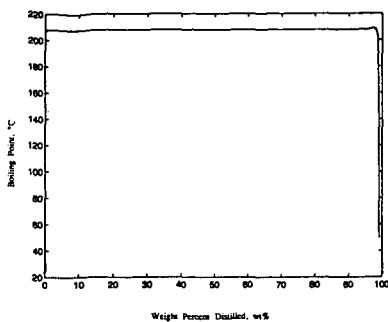
Figure 3 wt% vs T_b of tetralin
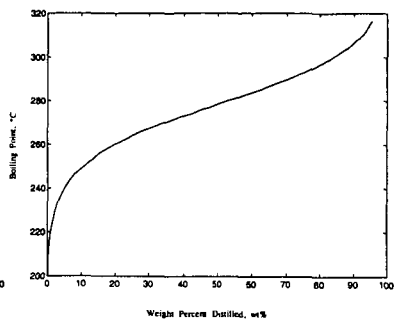
Figure 4 wt% vs T_b of Sample A
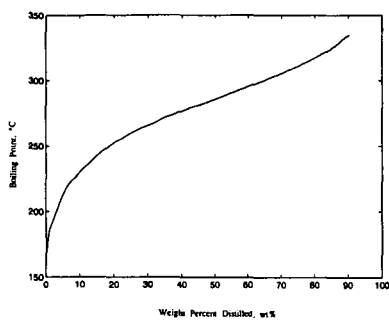
Figure 5 wt% vs T_b of Sample B
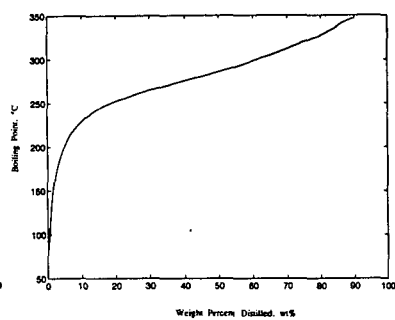
Figure 6 wt% vs T_b of Sample C
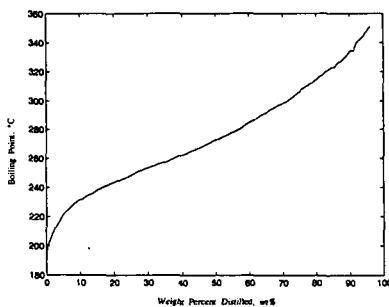
Figure 7 wt% vs T_b of Sample D
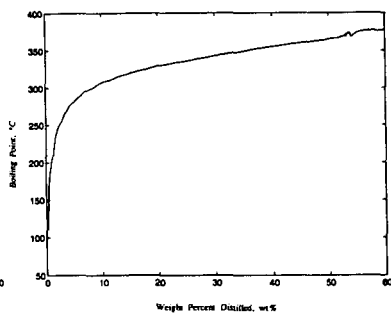
Figure 8 wt% vs T_b of Sample E
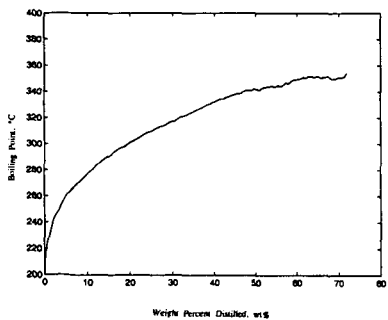
Figure 9 wt% vs T_b of Sample F
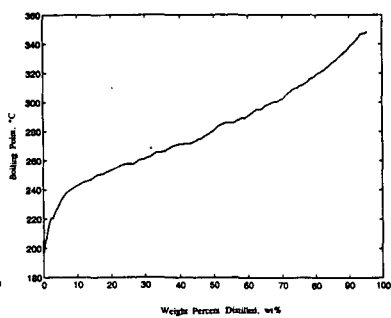
Figure 10 wt% vs T_b of Sample G

91
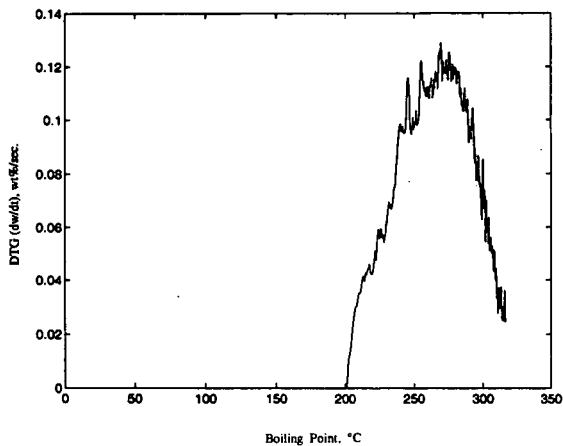
Figure 11 DTG vs T_b of Sample A
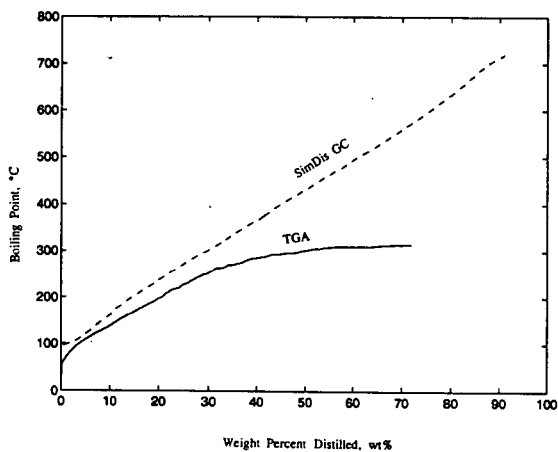
Figure 12 wt% vs T_b of a crude oil determined by TG and SimDis GC
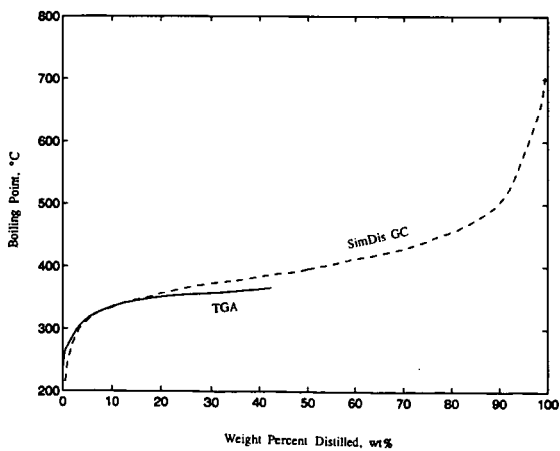
Figure 13 wt% vs T_b of a decanted oil determined by TG and SimDis GC

THE USE OF STEP SCAN FT-IR/PAS FOR THE STUDY OF STRUCTURAL CHANGES IN COAL AND CHAR PARTICLES DURING GASIFICATION

Osamu Yamada, Hajime Yasuda, Yasushi Soneda, Mitsuo Kobayashi,
Mitsunori Makino, and Mamoru Kaiho
National Institute for Resources and Environment
16-3 Onogawa, Tsukuba, Ibaraki 305 JAPAN

INTRODUCTION

To understand the reactions occur during coal gasification, it is essential to investigate reactivity and structural changes in coal and char. As coal and char are solid which hardly dissolve into most of solvents, variety of applicable methods for analyses is limited. An FT-IR spectroscopy is a promising method to detect the status of various kinds of functional groups and their chemical and physical changes. Recently, FT-IR photoacoustic spectroscopy(FT-IR/PAS) of coal has been intensively studied.[1] Depth profiling analyses using FT-IR/PAS is also discussed focusing on the technique to avoid a saturation of the photoacoustic signal.[2-4] In this paper, a step scan FT-IR/PAS with a phase modulation was applied to depth profiling of coal particles whose surfaces were treated by oxidation and ion-irradiation to elucidate a sampling depth. Depth profile of gasification char particles obtained from HYCOL entrained flow type gasifier were analyzed by step scan FT-IR/PAS.

EXPERIMENTAL

Preparation of oxidized coal samples

20g of Miike coal(C: 82.2%, daf; H: 6.2%, daf; N: 1.0%, daf; ash: 7.7%, dry, 24~60mesh) was placed in a glass-made, constant volume closed reactor equipped with a circulator, and was dried at 150ºC under vacuum for 3 weeks. Oxidation reaction was initiated by introducing oxygen from the reservoir to the reactor maintained at 100ºC. Pressure drop was monitored by pressure gauge(Balzers APG010) to calculate the amount of oxygen absorbed into coal.

Taiheiyo coal(C: 74.6%, daf; H: 6.6%, daf; N: 1.4%, daf; ash: 12.9%, dry; particles of 2~5mm) was held in a stainless steel wire mesh and oxidized in a air stream heated up to 300ºC for 1h.

Oxidized coal samples were used for FT-IR/PAS analyses without further pulverization. After IR analyses, each sample is mixed with phenol resin, solidified and polished to make a cross sectional observation by a microscope using reflected light with an oil immersion method.

Preparation of ion-irradiated coal

Taiheiyo coal(60~100mesh) was dried under vacuum(~10⁻⁴torr) at 170ºC for 3 weeks. 4g of the dried coal was exposed to irradiation of argon ion with energy of 100keV for 4h using 200keV ion implanter(B) at Ion Engineering Center Corporation(Osaka, Japan).

Gasification Char

Chars were produced from Taiheiyo coal and Muswellbrook coal(C:80.3, daf, H:5.5, daf, N:1.7, daf, ash 11.7%, dry) during the operation of HYCOL gasifier (Chiba, Japan)[5].

FT-IR measurement

A Biorad FTS-60A/896 step scan FT-IR spectrometer was used for all spectral measurements. Spectra were recorded at resolution of 8cm⁻¹ using an MTEC model 100 photoacoustic cell with its accompanying preamplifier/power supply. Helium was used as the carrier gas in the PA cell. Stanford Research Systems SR510 lock-in amplifier was used when phase modulation was applied. Step scan speed/phase modulation frequency of 10/100Hz and 50/400Hz was used for the FT-IR measurement.

RESULTS AND DISCUSSION

Step scan FT-IR/PAS with a phase modulation

FT-IR/PAS has been in use for about ten years.[2] Many photoacoustic applications involve the study of the spectra for layered and heterogeneous samples with varying interferometer scanning velocity, to probe deeper into them

as the velocity is reduced. The main advantage of step scan interferometry for PAS is that a single modulation frequency can be applied over the entire spectral range to generate the PA signal. Step scan data collection for depth profiling experiments produces a constant sampling depth across the spectrum for each frequency used.[4] Spectrum obtained without phase modulation is quite photoacoustically saturated, but the phase modulated spectra are not. Among the vector component of PA signals, in-phase(0°) component carries response of deep layer and quadrature(90°) component takes signal of surface layer. In principle, by changing the phase angle of the lock-in amplifier, it should be possible to probe different depths of the sample with the same depth for all infrared frequencies in the spectrum.

Oxidized coal

Results of oxidation of Miike coal is summarized in Table 1. Main product in gaseous phase was water. Approximately one half of total amount of oxygen reacted($O_2 react$) was consumed to form H_2O, CO and CO_2 . Oxidized coal samples which gained 0.54~2.36%(initial coal weight basis) of oxygen was consequently obtained. Photoacoustic spectra recorded at 2.5kHz(rapid scan) were shown in Figure 4. PA spectrum of unoxidized(dried) Miike coal recorded at the same FT-IR settings was used for reference.

Absorption peak at around 1700cm-1, attributable to carbonyl group, increased by oxidation. Broad peak reflects various kinds of carbonyl entities. Shoulder peak observed at higher than 1700cm-1 is attributed to ester or carboxylic acid. Small peaks detected at 1540cm-1 may be attributed to carboxylic ion. Besides, peaks at 2800~3050cm-1 decreased with oxidation indicating that reaction of dehydrogenation from mainly aliphatic compounds proceeded. Absorption increased around 3400cm-1 can be attributed to formation of hydroxyl group. PA spectra obtained here seems to be quite similar to those acquired by diffuse reflectance FT-IR spectroscopy[6] except OH region.

Depth profiling analyses of a series of oxidized coal samples was performed by using step scan mode(step speed/phase modulation frequency = 50Hz/400Hz). Figure 2 illustrate step scan FT-IR/PA spectra of oxidized Miike coal which are measured and phase-separated with phase angles of 45° and 0° respectively. PA spectrum of unoxidized Miike coal was used for background correction. In the layer near surface detected with phase angle of 45°(A), absorption at 1700cm-1 and 1100cm-1 increased indicating the formation of oxygen containing functional groups such as C=O and C-O with increase in the amount of oxygen reacted with coal. On the other hand, peaks at 2800~3050cm-1 did not show a definite increase nor decrease with series of oxidation conditions. Similar tendency of the intensity changes in peaks was observed when phase angle was decreased to 0° to obtain the signals from deeper layer as shown in Figure 2(B).

It is assumed that oxygen containing functional groups formed by oxidation uniformly distributes in oxidized layer, but dehydrogenation reaction takes place mainly in the surface layer. Other interpretation may be that aliphatic compounds decomposed and released by oxidation moves inside coal particle with certain mobility.

Michaelian utilize an FT-IR spectrometer with STop-and-Go mode for depth profiling of oxidized coal and estimated the thickness of oxidized layer at ~12μm corresponding to the modulation frequency of 200Hz.[3] This estimation, however, involves some assumption. Measurement of actual sampling depth is required. Oxidized Miike coal samples were used for cross-sectional observation by microscope with reflected lights. No obvious oxidation layer could be seen by microscope observation, possibly due to the mild oxidation conditions. Taiheiyo coal oxidized at 300°C was used for estimation of sampling depth of step scan FT-IR/PAS measurement. Figure 3 shows depth profiling PA spectra of oxidized Taiheiyo coal with various modulation frequencies and phase angles. PA spectra of unoxidized Taiheiyo coal was used for back ground correction to compare the changes in peaks before and after oxidation. When modulation frequency of 400Hz and phase angle of 90° were selected, the vicinity of coal surface should be detected. Considerable decrease in peaks at 2800~3050cm-1 attributed to CH stretching band was observed. Decreasing phase angle from 90° to 0° to obtain the signals of deeper layer, a peak at around 1700cm-1 attributed to C=O band increased. When modulation frequency is switched to 100Hz, infrared beam is expected to penetrate into deeper layer of coal particle. Applying the phase angle

of 90~45°, decrease in CH peaks was observed, while difference between PAS spectra of oxidized and unoxidized samples scarcely be detected with a phase angle of 0°. This indicates that changes in functional groups caused by oxidation occur only in the vicinity of coal surface.

Oxidized Taiheiyo coal samples were used for cross-sectional observation by microscope with reflective lights. 5~10μm of bright rim was observed on the edge of coal particles. Unoxidized coal did not show this kind of rim. Thus, actual sampling depth of the spectrometer is estimated to around 10μm.

Ion-irradiated coal

Step scan FT-IR/PA spectra of ion irradiated coal measured with various modulation frequencies and phase angles are shown in Figure 4. PA spectra of untreated Taiheiyo coal obtained at the same FT-IR settings are used as background. In the spectra recorded with 400Hz of modulation frequency, peaks at 2800~3050cm-1 and 1700cm-1 obviously decreased indicating dehydrogenation and decarbonylation occurred during ion irradiation. On the other hand, changes in functional groups is scarcely detected when modulation frequency is set to 100Hz with a phase angle of 45° and below. According to the results of ion irradiation on metal surface, layer with a thickness of 1μm should be treated. Effects of ion irradiation on coal may be different and penetration depth is expected to deeper than 1μm in the case of coal. The spectra of ion treated coal seems to be consistent with the estimation from the oxidation experiment and microscopic observation of Taiheiyo coal.

Gasification char

A Taiheiyo coal char and a Muswellbrook coal char produced by HYCOL entrained flow gasifier are used for the IR measurement. No obvious absorbance peaks could be detected on the surface by the conventional FT-IR spectroscopy. In Figure 5, depth profiling FT-IR/PA spectra are shown. For better baseline correction, spectra of the char collected at the same time in different two places (cyclones CY-301 and 302) during the operation of HYCOL gasifier are mutually compared. Using step scan speed as slow as 10Hz to allow IR beam to penetrate deeply inside char, peaks at 2900cm-1, attributed to CH, and broad peaks centered at 1700 and 3400cm-1 could be clearly detected. These peaks directly indicate that some organic part including oxygen containing functional groups still remain inside the char particle after being processed at high temperature up to 1600°C. Two kinds of chars showed different depth profile. It is reported that almost all Taiheiyo char is categorized as network or Lacy type and Muswellbrook chars are mainly thick and thin walled balloon type[5]. Depth profile may reflect the difference of morphology of respective chars.

CONCLUSIONS

Step scan FT-IR/photoacoustic spectroscopy (PAS) was used for depth profiling of coal and gasification char particles. Phase modulation on the interferometer and phase separation at the detector, by a lock-in amplifier, and a variety of modulation frequencies and phase angles were used. The results showed considerably different spectra with depth of the coal. Sampling depth was estimated to ca 10μm by comparing the depth profiling spectra and cross-sectional microscopic observation of oxidized coal. Depth profiling of char obtained from HYCOL gasifier indicated the existence of an organic structure inside char particle. Considering that no obvious absorbance peaks could be detected by the conventional FT-IR spectroscopy, the use of step scan FT-IR/PAS is concluded to be a promising method for the analyses of even high temperature gasification chars as well as coals.

REFERENCES
1)   D. W. Vidrine, 'Fourier Transform Infrared Spectroscopy', (Ed. J. R. Ferraro and L. J. Basile) Vol. 3, Academic Press, N.Y., (1982).
2)   D. W. Vidrine, Appl. Spectrosc., 1980, 34, 314.

3) K. H. Michaelian, Appl. Spectrosc., 1989, 43, 214 ; 1991, 45, 302.
4) R. M. Dittmar, J. L. Chao, and R. A. Palmer, Appl. Spectrosc., 1991, 45, 1104.
5) Matsuoka, H., Muramatsu, T., Nakanouchi, T., Sano, K., Fukushima, S., Tsujiguchi, S., and Koyama, S., Proc. 11th Annual International Pittsburgh Coal Canference, 1994, 2, 1316.
6) O. Yamada, Journal of NIRE, 1993, 2, 513.

Table 1   Results of oxidation of Miike coal [a]

Run	Time	O_2react [b]	Gaseous products / mmol					Analyses of oxidized coal		
	/ h	/ mmol	H_2O	CO	CO_2	CH_4	C_{2+}	O_2abs[c] /wt%	C%[d]	H%[d]
1	26	5.62	3.42	0.16	0.46	~ 0	~ 0	0.54	81.5	6.20
2	51	10.54	4.55	0.35	1.11	~ 0	~ 0	1.07	81.2	6.17
3	124	17.69	10.23	0.63	1.66	0.01	~ 0	1.79	80.6	6.08
4	384	25.17	15.14	0.99	2.63	0.01	~ 0	2.36	79.9	6.02

a) 20g of coal was used. Reaction temp: 100°C   b) The amount of oxygen reacted with 20g of coal.
c) The amount of oxygen absorbed in coal.   d) Ultimate analysis data, daf basis.
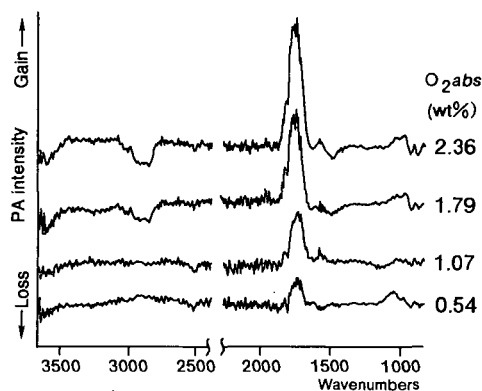
Figure 1   Photoacoustic spectra of oxidized Miike coal recorded at 2.5kHz(rapid scan mode). Spectrum of unoxidized Miike coal is used as background.
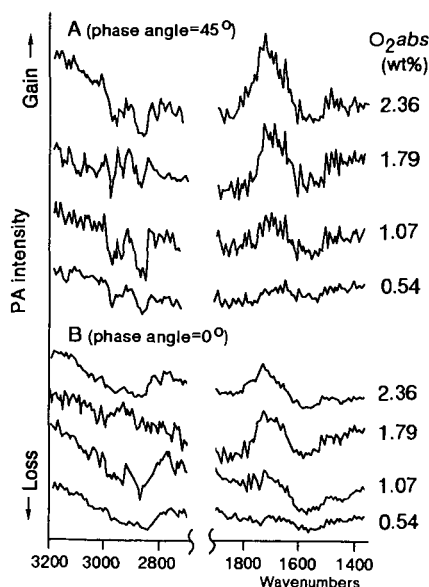
Figure 2   Step scan FT-IR/PA spectra of oxidized Miike coal measured with step scan/phase modulation freq.= 50/400Hz. Spectrum of unoxidized Miike coal is used as background.
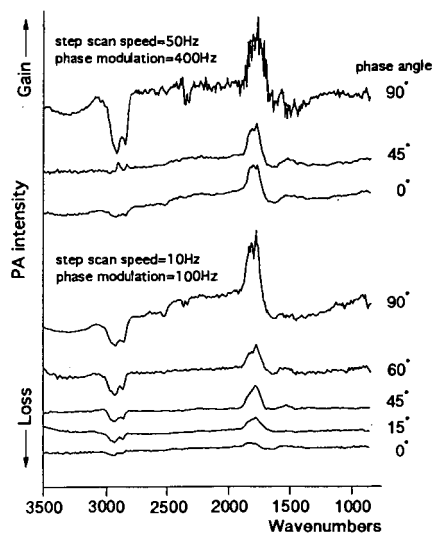
Figure 3 Depth profiling FT-IR/PA spectra of oxidized Taiheiyo coal. Spectrum of unoxidized Taiheiyo coal is used as background.
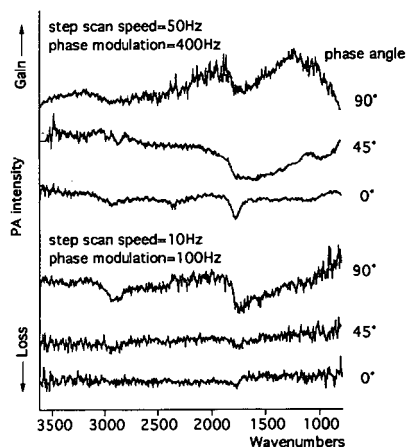
Figure 4 Depth profiling FT-IR/PA spectra of ion-irradiated Taiheiyo coal. Spectrum of untreated coal is used as background.
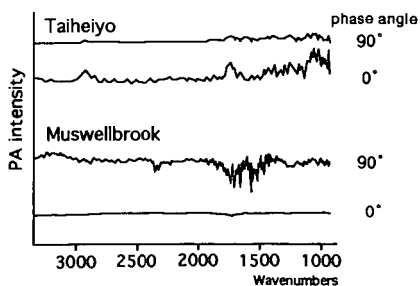
Figure 5 Depth profiling FT-IR/PA spectra of gasification chars obtained from HYCOL gasifier measured with step scan/phase modulation freq.= 10/100Hz.

THE EFFECT OF CHAR "AGE" ON GASIFICATION REACTIVITY

L. Zhang, J.M. Calo, and W. Lu
Chemical Engineering Program
Division of Engineering
Brown University
Providence, Rhode Island 02912, U.S.A.

Keywords: Reactivity; char "age"; thermal desorption methods.

INTRODUCTION

It is well known that, *ceteris paribus,* the overall gasification rate decreases with increasing pyrolysis severity [e.g., 1-7]. This effect can be attributed to various sources, including the loss of heteroatoms and annealing processes. All these types of processes affect the active site density of a char which is an important factor in determining its reactivity. In the current communication, we investigate the relationship between populations of oxygen surface complexes, which form on these sites, and char reactivity as a function of char "age."

EXPERIMENTAL

The char samples used in the current experiments were produced from Wyodak subbituminous coal samples obtained from the Argonne Premium Coal Sample Bank [8], and a phenol-formaldehyde resin synthesized in our laboratory. The latter material was used as a prototype of a non-mineral matter containing char.

Char samples were produced in a tube furnace in flowing ultrahigh purity helium at various ultimate temperatures for two hours. Variation in char "age" was achieved by pyrolyzing samples at temperatures of 900, 950, 1000°C for resin char, and 1000, 1050, and 1100°C for Wyodak char, respectively, for two hours.

All the oxidation and thermal desorption experiments were carried out in the TPD-MS/TGA apparatus. For gasification, the samples were exposed to one atmosphere of carbon dioxide at a selected temperature to a desired burn-off. The thermal desorptions were all carried out at a heating rate of 50K/min to 1200°C in ultrahigh purity helium carrier gas [9].

RESULTS AND DISCUSSION

Reactivities. As expected, the reactivities of the resin and Wyodak coal char samples all decrease monotonically with increasing pyrolysis temperature; i.e., the "younger" chars are more reactive than the "older" chars. Apparent activation energies, determined from Arrhenius plots, are presented in Table I. As shown, these values are well within the range reported by other workers (e.g., [6,7]) for different types of chars and carbons. These results suggest that the apparent activation energies of the "younger" chars are less than for the "older" chars, but only slightly so; certainly not enough to explain the significant differences in observed reactivities.

TPD Spectra. CO TPD spectra from CO_2-gasified Wyodak coal char samples as a function of pyrolysis temperature are presented in Figure 1. As shown, the broad desorption peak is centered at about 950°C. The total amount of oxygen surface complexes decreases with char "age", but not homogeneously over the entire TPD spectrum. That is, the higher temperature surface complexes fall off more rapidly with "age" than the lower temperature complexes. In fact, the low temperature complex population in Figure 1 is practically invariant with char "age."

Figure 2 presents the corresponding data for resin the char samples. The same qualitative behavior is readily apparent, although the desorption is peaked at a higher temperature of about 1010°C. In addition, the total amount of oxygen surface complexes is about a factor of three or so less than for the Wyodak coal char samples. Just as for the Wyodak coal char, the "younger" char samples exhibit a greater amount of CO evolution than the "older" char samples, and the decrease in the population of oxygen surface complexes is not homogeneous over the entire TPD spectrum; the higher temperature population falls off more rapidly than that at lower temperatures. However, somewhat larger differences are apparent in the low temperature region than in the corresponding Wyodak coal char spectra.

Distributions of Desorption Activation Energies. The observation that the population of oxygen surface complexes does not decrease evenly over the entire TPD spectrum suggests that the char surface exhibits a distribution of desorption activation energies. Du *et al.* [10] and Calo and Hall [11] developed distributed activation energy models for the desorption of oxygen surface complexes from carbons following O_2 and CO_2 gasification. In the current work, the distribution of desorption activation energies was calculated using the method described by Calo and Hall [11]. The relationship between the instantaneous CO desorption rate and the distribution of desorption activation energies can be expressed as:

$$d[CO]/dt = [C-O]_o S(E^*) dE^*/dt \qquad [1]$$

where E^* is the local desorption activation energy, as approximated by an instantaneous step at energy E^*, $S(E^*)$ is the desorption activation energy probability density function, $d[CO]/dt$ is the desorption rate of oxygen surface complexes as CO during TPD, and $[C-O]_o$ is the total initial (i.e.

prior to the initiation of desorption) amount of CO-evolving oxygen surface complexes on the surface. Based on the classical work of Redhead [12], the parameters are related by:

$$E*/RT = \ln [\upsilon_0 T/\beta] -3.64 \tag{2}$$

which holds for for $10^8 < \upsilon_0/\beta < 10^{13}$ (K^{-1}), where υ_0 is the pre-exponential factor for the desorption rate constant, T is the temperature, and β is the heating rate. Since a TPD experiment gives the instantaneous desorption rate directly, and $dE*/dt$ can be obtained from Eq. [2], the distribution of desorption activation energies, $[C-O]_oS(E)*$, can be determined from Eq. [1].

The value of the pre-exponential factor, υ_0, was assumed to be constant. A series of TPD runs was performed at various heating rates from 25K/min to 100K/min for the same oxidized char samples. It was determined that a value of $\upsilon_0 = 10^{10}$ min^{-1} yielded the best fit in that it produced essentially the same energetic distribution for all the heating rates. This proved to be the best value for both resin and Wyodak char. Consequently, this value was used for the determination of the distributions of desorption activation energies.

Figure 3 presents a comparison of desorption activation energy distributions determined for Wyodak coal char pyrolyzed at various temperatures. As shown, as the pyrolysis temperature decreases, the desorption activation energy distribution of the char also changes. A similar trend was also found for resin char, as shown in Figure 4. In comparison to the Wyodak coal char distributions, the energetic distributions for resin char samples are shifted to higher energies. It is noted that mineral matter (most probably calcium) in the Wyodak coal char plays a significant role in determining the population of the low temperature surface complexes which turn over most rapidly during gasification. The absolute amount of the low temperature oxygen surface complexes is considerably greater for Wyodak coal char than for resin char, which contains no mineral matter. Therefore the mineral matter in the Wyodak coal char preferentially catalyzes the formation of low desorption activation energy surface complexes. This represents the basis of the catalytic effect in this char. This is the principal reason that the reactivity of Wyodak coal char is significantly greater than that for resin char even at lower gasification temperatures.

Mean Desorption Activation Energies and Active Site Concentrations. Two important parameters that can be used to characterize reactivity are the apparent mean concentration of active sites and the average desorption activation energy. For conditions where the gasification rate is desorption rate-controlled, the reactivity can be correlated using the distribution of desorption activation energies. This is accomplished by integrating the desorption rate over the entire distribution:

$$r = \int_0^\infty \upsilon_0 \exp(-E*/RT) [C-O]_oS(E*)dE* \tag{3}$$

In order to address the issue of the rate-controlling step in the current work, the following types of experiments were performed. Following gasification, samples were rapidly quenched to room temperature in either pure helium or CO_2. This was done to assess whether or not the surface was saturated with oxygen surface complexes at gasification conditions. It was reasoned that if the gasification reaction was not controlled by the desorption step, unoccupied active sites would exist which by cooling in the reactant would form additional oxygen surface complexes as the temperature decreased. Consequently, the resultant TPD spectra would differ from those obtained following rapid quenching in helium. From such experiments it was found that gasification of both resin and Wyodak coal char in one atmosphere of CO_2 is desorption rate-controlled under the current experimental conditions [13].

Equating the gasification rate expression for a single mean activation energy, E_d, with that described by a continuous distribution, as in Eq. [3], yields:

$$C_t \exp(-E_d/RT) = \int_0^\infty \exp(-E*/RT) [C-O]_oS(E*)dE* \tag{4}$$

Figures 5 and 6 present the apparent mean active site concentration, C_t, calculated from Eq. [4], as a function of pyrolysis temperature for Wyodak coal char and resin char, respectively. These plots show that the mean active site concentration decreases as the pyrolysis temperature of the char samples increases. This result means that a "younger" char effectively has more active sites than an "older" char on a per unit mass basis. A similar conclusion has been reported by other workers (e.g.,[3,6,7]) Since gasification occurs at active sites on which oxygen surface complexes are formed, a char with a higher active site concentration at low desorption activation energies will exhibit a greater reaction rate.

The mean desorption activation energies determined from Eq. [4] are presented in Table I. As shown, they are almost constant with "age" for both resin and Wyodak coal chars. These values of mean desorption activation energies are similar to the apparent values determined from the reactivity measurements. They are also quite close to that reported for CO_2 gasification of a PVC char by Hüttinger and Nill [14]. It is clear that there is relatively little effect of char "age" on the mean desorption activation energy. Rather, the reactivity is controlled primarily by the active site

99

concentration, especially at the lower activation energies in the distribution. In a way, this is similar to the catalytic effect of metals and mineral matter on carbon gasification. That is, the catalytic effect in carbon gasification is predominantly an increase in the number of effective sites rather than the more typical catalytic effect of decreasing the effective activation energy.

SUMMARY· AND CONCLUSIONS
The objective of this work was to explore the relationship among char "age", CO_2 reactivity, and thermal desorption techniques. The results indicate that the major influence of char "age" for the samples investigated is the concentration of active carbon sites, which is greater for the "younger" chars than for the "older" chars. There is little apparent effect of char "age" on the mean desorption activation energy. Comparisons of the apparent activation energies from reactivity measurements with those obtained from analysis of the desorption activation energy distributions show reasonably good agreement, which suggests that reactivities of both chars in one atmosphere of CO_2 at the temperatures investigated are desorption rate-controlled.

It was determined that both chars exhibit energetically heterogeneous surfaces for all the samples examined. For these chars, the distribution of desorption activation energies can be determined from TPD desorption spectra. Prediction/correlation of reactivities from the desorption activation energy distribution was shown to be feasible for the carbon-CO_2 reaction operating under desorption rate-controlled conditions for both resin and Wyodak coal char over the range of char "ages" investigated.

It is noted that we have found very similar behavior for steam-gasified chars as a function of char "age" [15].

REFERENCES
1. Jenkins,R.G., Nandi,S.P., Walker,Jr P.L. *Fuel* **52**, 288 (1973).
2. Johnson, J.L., *Kinetics of Coal Gasification*, Wiley, NY, 1979.
3. Suuberg, E.M., M. Wójtowicz, and J.M. Calo, *Carbon* **27**, 431 (1989).
4. Radovic, L.R., Walker,Jr., P.L., Jenkins,R.G., *Fuel* **62**, 849 (1983).
5. Miura, K. and Hashimoto, K., and Silveston, P.L., *Fuel* **68**, 1461 (1989).
6. Calemma, . and Radovic, L.R., *Fuel* **70**, 1027 (1991).
7. Rodriguez-Mirasol, J., Cordero, T., and Rodriguez, J.J., *Carbon* **31**, 1, 53, (1993).
8. Vorres, K.S., Users Handbook for the Argonne Premium Coal Samples, ANL/PCSP-93/1, DOE, Argonne, Il, 1993.
9. Zhang, L., *Ph.D. Dissertation*, Division of Engineering, Brown University, 1995.
10. Du, Z., A.F. Sarofim, and J.P. Longwell, *Energy & Fuels* **4**, 296 (1990).
11. Calo, J.M. and P.J. Hall, in *Fundamental Issues in the Control of Carbon Gasification Reactivity*, J. Lahaye and P. Ehrburger, eds, NATO ASI Series, Series E: Applied Sciences, Vol. 192, p. 329, Kluwer Academic Publishers, Dordrecht, 1991.
12. Redhead, P.A., *Vacuum* **12**, 203 (1962).
13. Zhang, L., *Ph.D. Dissertation*, Division of Engineering, Brown University, 1995.
14. Hüttinger, K. and Nill, J.S., *Carbon* **28**, 4, 457, (1990).
15. Calo, J.M. and W. Lu, *Proc. Carbon '95*, University of California, San Diego, p. 546, 1995.

Table I. **Mean activation energies as a function of char "age" for Wyodak coal and resin chars, as determined from reactivities and distributions of desorption activation energies.**

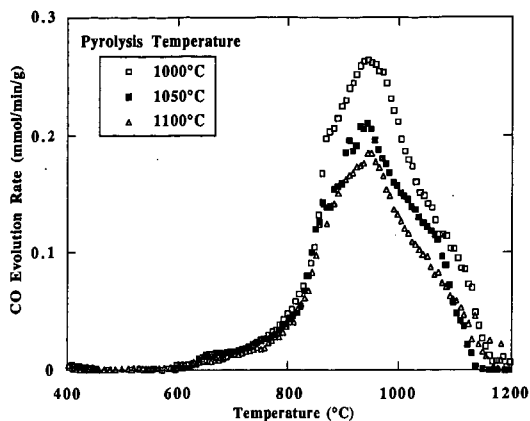| Wyodak Coal Char			Resin Char		
Pyrolysis Temperature (°C)	Mean Activation Energy (kJ/mol) (Reactivity)	Mean Activation Energy (kJ/mol) (Desorption)	Pyrolysis Temperature (°C)	Mean Activation Energy (kJ/mol) (Reactivity)	Mean Activation Energy (kJ/mol) (Desorption)
1000	214	211	900	195	234
1050	233	212	950	207	237
1100	243	212	1000	230	238

Figure 1. The effect of pyrolysis temperature on CO TPD spectra (50K/min) of Wyodak coal char gasified in 1 atm of CO_2 at 825°C to 20% burn-off.
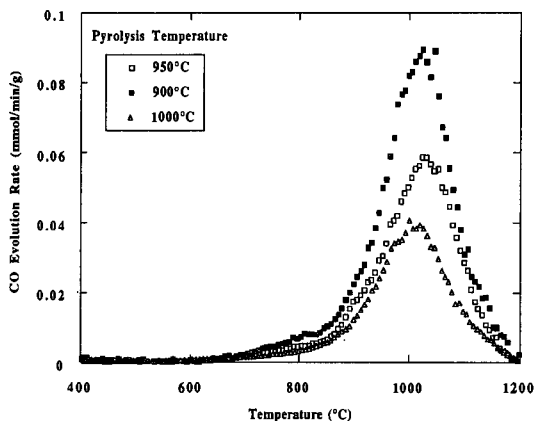

Figure 2. The effect of pyrolysis temperature on CO TPD spectra (50K/min) of resin char gasified in 1 atm of CO_2 at 890°C to 5% burn-off.
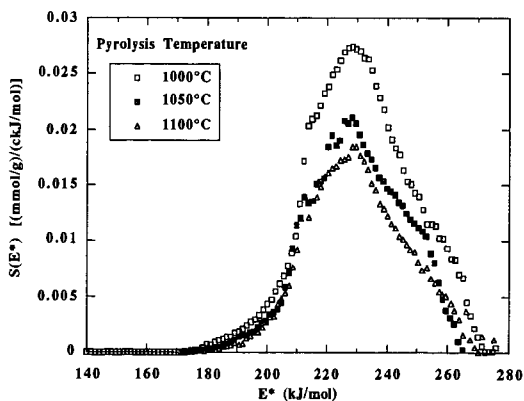

Figure 3. Comparison of desorption activation energy distributions for Wyodak char pyrolyzed at various temperatures and gasified in 1 atm of CO_2 at 825°C to 20% burn-off.
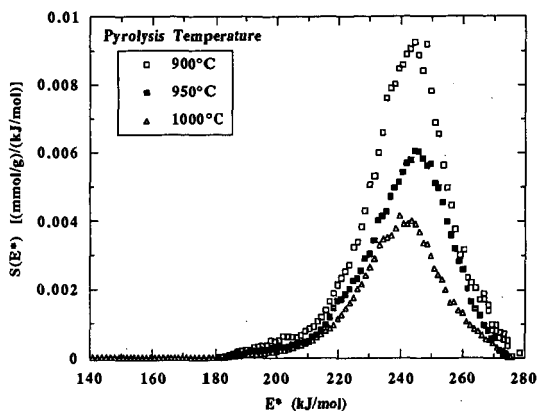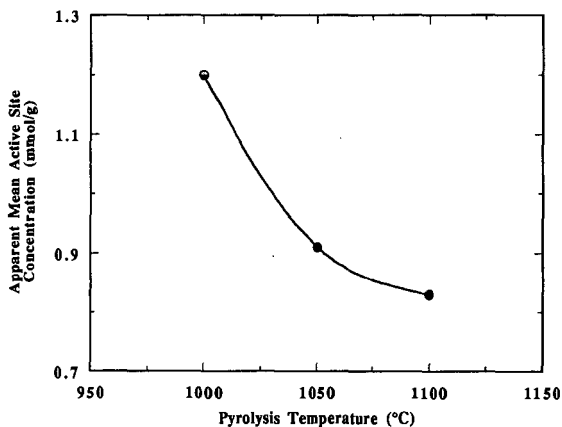
Figure 4. Comparison of desorption activation energy distributions for resin char pyrolyzed at various temperatures and gasified in 1 atm of CO_2 at 890°C to 5% burn-off.

Figure 5. Apparent mean active site concentration as a function of pyrolysis temperature for Wyodak char gasified in 1 atm of CO_2 at 825°C to 20% burn-off.
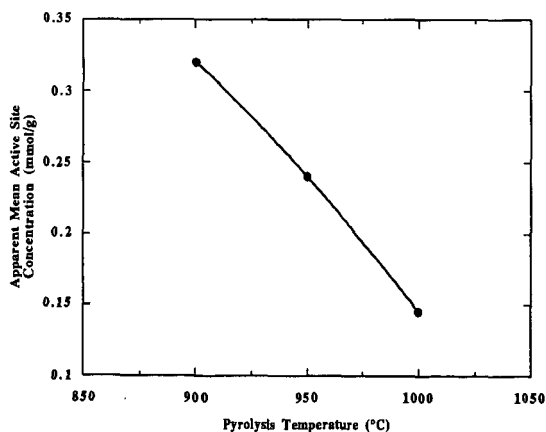
Figure 6. Apparent mean active site concentration as a function of pyrolysis temperature for resin char gasified in 1 atm of CO_2 at 890°C to 5% burn-off.

THE ROLE OF CARBONIZATION IN THE EVOLUTION
OF COAL CHAR GASIFICATION REACTIVITY

Osvalda Senneca, Paola Russo, Piero Salatino
Dipartimento di Ingegneria Chimica - Università *Federico II* di Napoli
Istituto di Ricerche sulla Combustione - C.N.R.
Piazzale V. Tecchio - 80125 Napoli (Italy)

Keywords: carbon gasification, annealing, reactivity.

INTRODUCTION

The relevance of thermal annealing of coals to the physico-chemical properties of the residual coke or char has been often addressed in the literature. The emphasis is most frequently on the structural modifications induced by carbonization in relation to mechanical properties. More limited and sparse information is available on the influence of the severity of pyrolysis and of carbonization conditions on the reactivity of chars in the context of coal gasification.

Thermal annealing affects char gasification along two paths: on one side it induces reordering of the turbostratic structure of coals, on the other side it affects the activity and distribution of mineral inclusions. Both processes lead to char deactivation, their relative importance being dependent on the nature of the parent coal.

In this paper the effect of thermal annealing on the reactivity of char from bituminous coal in carbon dioxide atmospheres is investigated. Experimental results are interpreted in the light of a simple reaction model.

MODEL DEVELOPMENT

The effect of thermal annealing on the reactivity of chars with carbon dioxide is afforded in a simplified manner. The detail of the individual processes that occur during thermal annealing is not considered: the whole spectrum of phenomena, including catalyst deactivation and carbon structure reordering, is lumped into a single deactivation step.

It is assumed that before thermal annealing only carbon of type A is present. Along heat treatment carbon A transforms into a less reactive carbon, B. This is at the origin of deactivation. The two types of carbon, A and B, may be thought as differing by degree of graphitization, catalytic activity or pore structure.

The kinetic model is based on a triangular network of reactions:

Gaseous products
(1)   (3)
Annealing (2)
Untreated char, A   Heat treated char, B
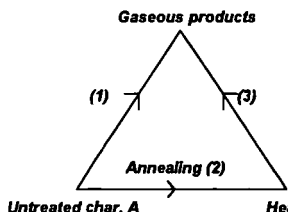
(1) the heterogeneous reaction of char A;
(2) thermal annealing transforming A into B;
(3) the heterogeneous reaction of char B. This reaction is slower than reaction (1).

The following simplifying hypotheses are made:
i. all reactions are irreversible;
ii. all reactions are activated by temperature according to an Arrhenius type expression;
iii. the kinetics of reactions (1) and (3) is first order with respect to the mass of A and B respectively;
iv. the kinetics of reactions (1) and (3) is first order with respect to the concentration of the gaseous reactant (CO_2);
v. the annealing process (2) is influenced neither by the gaseous atmosphere, nor by pressure;
vi. the annealing process (2) is irreversible;
vii. the kinetics of the annealing process (2) is first order with respect to the mass of A.

At a given temperature mass balances for chars of type A and B are as follows:

$$1) -\frac{dm_A}{dt} = m_A \cdot k_A \cdot p_{CO2} + k_{A \to B} \cdot m_A$$

$$2) -\frac{dm_B}{dt} = m_B \cdot k_B \cdot p_{CO2} - k_{A \to B} \cdot m_A$$

Initial conditions:
t=0
$$m_{A0} + m_{B0} = w_0$$
$$m_{A0} = w_0 \cdot \exp(-k_{A \to B} \cdot t_{HT})$$

where m_A, m_B are the mass of type A and type B char, w_0 is the initial total mass of char, k_A, k_B are the rate constants for the heterogeneous reaction of type A and B char respectively, p_{co2} is carbon dioxide partial pressure, and $k_{A \to B}$ is the rate constant for the annealing reaction .

Initial conditions take into account the possibility that heat treatment under inert atmosphere occurred for a time tHT, prior to gasification.

The reaction rate at zero carbon burn-off, expressed as the rate of change of carbon conversion degree, f, is given by:

$$3) \quad \left[-\frac{df}{dt}\right]_0 = k_A \cdot p_{CO2} \cdot \exp(-k_{A \to B} \cdot t_{HT}) + k_B \cdot p_{CO2} \cdot (1 - \exp(-k_{A \to B} \cdot t_{HT}))$$

At higher burn-off, solution of the system of equations (1)+(2), with the assigned initial conditions, yields the following expression for the instantaneous carbon gasification rate:

$$4) \quad \left[-\frac{df}{dt}\right]_r = k_B \cdot p_{CO_2} \cdot \left(1 - \frac{m_{A0}}{w_0} + \frac{m_{A0}}{w_0} \cfrac{1}{1 + \cfrac{k_A \cdot p_{CO_2}}{k_{A \to B}} - \cfrac{k_B \cdot p_{CO_2}}{k_{A \to B}}}\right) \cdot \exp(-k_B \cdot p_{CO_2} \cdot t) +$$

$$+ \frac{m_{A0}}{w_0} \cdot \left(k_A \cdot p_{CO_2} + k_{A \to B}\right) \cdot \left(1 - \cfrac{1}{1 + \cfrac{k_A \cdot p_{CO_2}}{k_{A \to B}} - \cfrac{k_B \cdot p_{CO_2}}{k_{A \to B}}}\right) \cdot \exp((k_A p_{CO_2} + k_{A \to B}) \cdot t)$$

It can be noted that the reaction rate at any burn-off is a function of the duration of heat pre-treatment (tHT) and is parametric in the value of the three kinetic constants, k_A, k_B and $k_{A \to B}$.

The basic approach of the proposed model resembles that of a former one by Nagle and Strickland-Constable (NSC) (8). Formulated in 1961 to describe the oxidation of pyro-graphite at high flow rates, pressures of 0.2 atm, temperatures comprised between 1050 and 1700°C, the NSC model took after the theory of Blyholder, Bindford and Eyring (9) and assumed that two sites are present on the carbon surface, namely A, a more reactive one, and B, a less reactive one. Two heterogeneous reactions and one reaction of annealing were also considered, but their network differed from the one proposed in the present work. In particular the mass fraction of A was treated under a pseudo-steady state approximation.

EXPERIMENTAL

Experimental work has been focused on the gasification of chars with carbon dioxide. It has been directed to the evaluation of model parameters (kinetic constants for reactions (1), (2), and (3)), and to comparison with model predictions.
Samples of South African (SA) coal, ground and sieved to the size range of 75-125 µm, have been carbonized in inert atmosphere at 900°C for different times, comprised between 1 and 300 min. Heat treated chars have, then, been checked for reactivity with CO_2 under standard conditions.
Heat treatment was performed isothermally in a PL-TG1000M thermobalance after heating up the sample at a rate of 999°C/min. The thermobalance operated at atmospheric pressure with a 50 ml/min flow of nitrogen.
Standard reactivity tests were carried out isothermally in the thermogravimetric apparatus at 900°C and atmospheric pressure, with a 50 ml/min flow of carbon dioxide. Reaction rates have been expressed as rate of change of carbon conversion degree throughout the paper.

RESULTS

Experimental results
The dependence of the instantaneous reaction rate df/dt on carbon burn-off, f is shown in figure 1. Data are relative to SA coal heat treated at 900°C for different tHT. Notably, reaction rate corresponding to different tHT converge at f>0.55. The interpretation of these curves is deferred until *Model results and validation*.
The effect of tHT on char reactivity at 0% burn-off is reported in figure 2 for char heat treated at 900°C for tHT comprised between 1 and 300 min. Reaction rates at 0% burn-off have been evaluated from df/dt versus f curves of figure 1 by linear extrapolation of data up to 10% burn-off. A non linear decrease of initial char reactivity with duration of heat treatment is observed.

Evaluation of model parameters

Model parameters have been evaluated from reactivities of samples heat treated at 900°C for different tHT.

The reaction rate constants of the heterogeneous reactions of type A and B char have been evaluated from df/dt versus f curves of samples heat treated for 1 and 300 min respectively (fig.1). The rate constant k_A has been assumed equal to the extrapolation to 0% burn-off of the first curve, using data points corresponding to 0<f<0.1; the rate constant k_B, instead, has been based on the extrapolation to 0% burn-off of the second curve, using data points corresponding to f >0.65.

The annealing constant has been evaluated from instantaneous reaction rates at 0% burn-off of samples heat-treated for different tHT (fig.2). On the basis of equation (3) of the model, once the rate constants k_A and k_B are known, regression analysis of data in figure 2 yields the annealing constant $k_{A \to B}$. Accordingly, $k_{A \to B}$ turns out to be about 0.02 min^{-1}. The best fit curve through the data is reported in fig. 2.

Model results and validation

Figure 1 compares computed profiles of gasification rate versus burn-off with those obtained in experiments using different tHT. Fair agreement of model prediction with experimental data is observed. It can be noted that at f<0.55 reaction rates are higher and fall off quicker, the shorter the heat-treatment, while at f>0.55 curves corresponding to different tHT converge, and reactivity appears no longer influenced by the duration of heat-treatment.

The convergence of curves relative to different tHT can be explained considering that in the first stage both annealing of carbon A, and char oxidation are active at the same time, whereas, once carbon A is depleted, oxidation of carbon B remains the main process active.

Notably, the occurrence of gradual transition from the reactivity of char A to that of char B, rather than a stepwise drop of reaction rate, is a consequence of the fact that the time scale over which annealing takes place at 900°C is comparable with those of the heterogeneous reactions 1) and 3). On the contrary, the pseudo-steady state approximation invoked by the NSC model implied that a stationary value of mass fraction of A was reached over a time scale much shorter than that of the gasification reaction.

On account of the closeness of annealing and gasification time scales at temperatures around 900°C, it can be argued whether annealing is the key factor for the evolution of char reactivity throughout conversion.

DISCUSSION

A rough order of magnitude evaluation of the time scale of the annealing process as compared with those of reactions with oxygen and carbon dioxide over a wide range of temperatures will be attempted in the following.

A kinetic constant of annealing of 0.02 min^{-1} has been evaluated at 900°C in this work. Accordingly the time required to transform the 95% of mass A into B would be approximately 140 min. Estimates of time scales of annealing at different temperatures are directly or indirectly provided in a number of papers (1,3,7). All these points have been located in the diagram of figure 3, reporting the process time scale versus reciprocal absolute temperature.

The solid line in figure 3 has been simply obtained by extrapolation to different temperatures of the annealing time evaluated in the present work at 900°C. The activation energy value of 97000 cal/mol has been used in the extrapolation. This value is that suggested by NSC and lies within the broad range of activation energies for annealing proposed in the literature (between 20000 (2) and 200000 (9) cal/mol).

The analysis is pursued further by comparing the time scale of annealing with those of the C-O_2 and C-CO_2 reactions.

In figure 3 a characteristic time of reaction, defined as the inverse of the reaction rate $(df/dt)_{f=0}$, is also plotted as a function of 1/T. Plots are relative to heterogeneous gasification of SA char with carbon dioxide and with oxygen in air, and have been obtained from extrapolation of experimental data at 1173K (10) and 693K (11) respectively. Activation energies suggested by Salatino et al. (10) and D'Amore et. al (11) (45000 cal/mol for reaction with carbon dioxide and 29000 cal/mol for reaction with oxygen) have been assumed.

The limitations of the comparison afforded in figure 3 lie, on one side, in the considerable uncertainty as regards the activation energy of annealing, and, on the other side, in the inadequacy of extrapolations of intrinsic kinetic data to temperatures where diffusion resistances may be relevant. Being aware of all the above approximations, it can be speculated that: at temperatures lower than 1173 K the rate of annealing is lower than the rate of reaction with both CO_2 and O_2. At about 1800K the time of annealing and the time of reaction with oxygen are comparable, as Davis et al. (7) found experimentally, and both are shorter than the time of reaction with carbon dioxide. At temperatures typical of entrained coal gasification processes (>1800K) the time scale of thermal annealing should be shorter than the time-scale of both gasification reactions considered: under these conditions, neglecting annealing when estimating reaction rates for entrained coal gasification processes may lead to serious overestimation.

CONCLUSIONS

A very simple approach has been undertaken to clarify the interactions between annealing and gasification reactions. A model based on a triangular network of reactions shows some ability to match experimental reactivity profiles over the entire range of carbon burn-offs.

A pronounced effect of the heat treatment of coal on the reactivity of its char towards CO_2 has been observed at the temperature of 900°C. Under the experimental conditions investigated thermal annealing occurs over time scales comparable with those of gasification reactions.

REFERENCES

1) Blake, J.H., Bopp, G.R., Jones, J.F., Miller, M.G., Tambo, W., *Fuel* **46** 115-125 (1967);
2) Blackwood, J.D., Cullis, B.D., McCarthy, D.J., *Aust. J. Chem.* **20** 1561-70 (1967);
3) Radovic, L.R., Walker, P.L. jr., Jenkins, R.G., *Fuel* **62** 849-56 (1983);
4) Kasaoka, S., Sakata,Y. and Shimada, *Fuel* **66** 697-701 (1987);
5) Sahu, R., Levendis, Y.A., Flagan, R.C., *Fuel* **67** 275-283 (1988);
6) Marsh, H., Diez, M.A., Kuo, K., in *Fundamental Issues in Control of Carbon Gasification Reactivity*, (J. Lahaye and P. Ehrburger, Eds), Kluwer Academic, Dordrecht, pp 205-220 (1991);
7) Davis K.A., Hurt, R.H., Yang, N.Y.C, Headley, T.J., *Combust. Flame* **100** 31-40 (1995);
8) Nagle, J., Strickland-Constable, R.F., *Proc. of Fifth Conf. Carbon*, Vol. 1, Pergamon Press, New York, pp 154-164 (1963);
9) Blyholder, G., Binford, J.S. jr., Eyring, H., *J. Phys. Chem.* **62**, 263-267 (1958);
10) Salatino, P., Senneca, O., Masi, S., A kinetic similarity analysis of the gasification of a coal char by oxygen and carbon dioxide, submitted for publication;
11) D'Amore, M., Masi, S., Salatino, P., *Combust.Sci.Tech.*, **63,** 63-73 (1989).
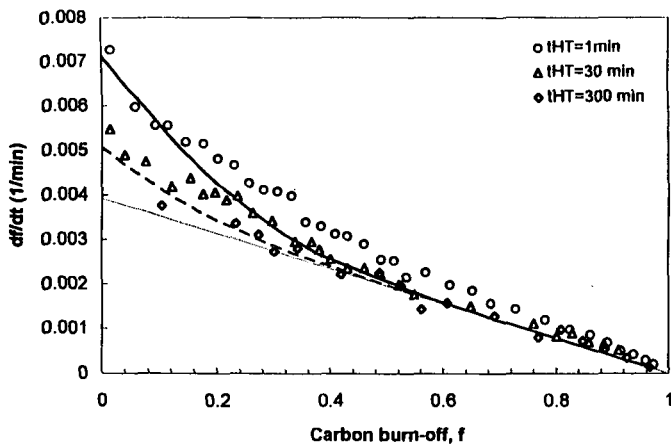
Fig.1 Reaction rate of SA char versus burn-off for HTT=900C and different tHTs.
Lines represent model results
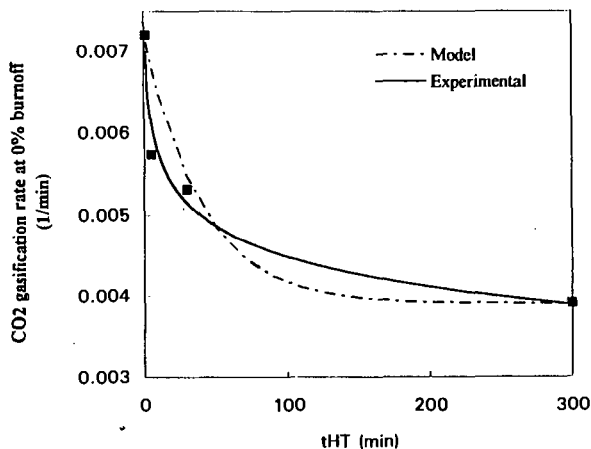
Fig. 2 Effect of tHT on reactivity at 0 % burn-off of SA char treated at 900C
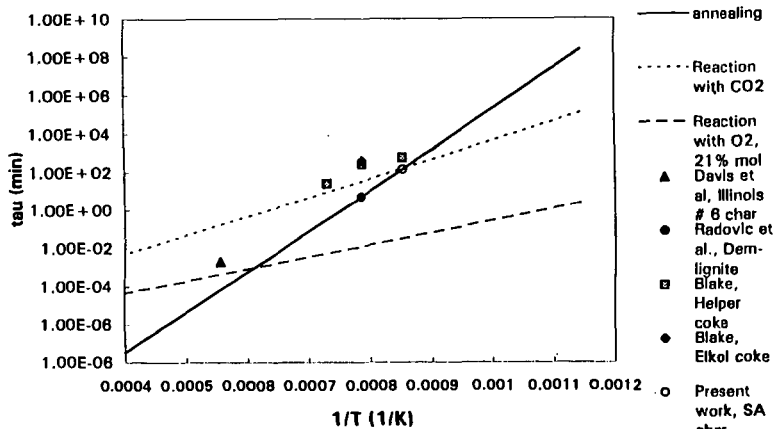
Fig. 3 Characteristic times and comparison of experimental data from different authors.

THE MECHANISM OF OXIDATION OF FULLERENES WITH MOLECULAR OXYGEN

M. Wohlers, A. Bauer, Th. Belz,Th. Rühle,Th. Schedel-Niedrig, R. Schlögl
Fritz Haber Institut der Max Planck Gesellschaft
Faradayweg 4-6, D-14195 Berlin, FAX -4930-8413-4401

INTRODUCTION

The novel allotrope of carbon, fullerene is a molecular analogue to the other form of sp^2 hybridised carbon, graphite. In our general attempt to understand the carbon-oxygen reaction at an atomic level we use fullerenes as reference compounds in oxidation studies as they will not exhibit influences of electronic defects on the reactivity. The van der Waals crystals of C_{60} and of C_{70} can be prepared by slow sublimation with single crystalline quality and in absence of any detectable phase impurity due to the molecular separation procedures for the sublimation precursors. It is equally convenient to work on thin films of fullerenes on e.g. silicon (100) surfaces, on large single crystals and on sublimed powder.

Solid fullerenes are air-sensitive materials. They degrade quickly within minutes into a stage of reduced solubility and become eventually fully polymerised upon air/sunlight exposure at 300 K(1). This property is reminiscent on coal degradation, a process in which a variety of gases are released at low rates. We first investigate this initial step of reactivity of fullerenes with air using temperature-programmed methods.

Upon thermal treatment gasification sets in at 573 K with a steep increase in rate at 720 K (2). We will investigate the steps of oxygen activation and fullerene attack in this window of low reactivity by FT-IR , by X-ray absorption spectroscopy and by XPS.

The pattern of gasification in temperature-programmed TG-MS experiments will be compared for the C_{60} fullerene and several other carbon materials in order to evaluate on the validity of the fullerene oxidation as model for the graphite oxidation reaction.

Intercalation of oxygen into the octahedral voids of C_{60} crystals was found to proceed without oxygen dissociation at 300 K (3). The process was described as being reversible at 300 K. Polymerisation of C_{60} at 300 K was observed to proceed to 80% in seven days under oxygen containing 2.6 % ozone (4). Photo-oxidation at 300 K was investigated with a thin film of C_{60}. An intermediate di-carbonyl structure of a fullerene dioxide was suggested based upon an IR absorption at 1750 cm-1. A second broad absorption at 1000 cm-1 remained largely unexplained (5).

High-temperature oxidation of C_{60} was found to begin at 525 K. IR bands at 1780 cm-1 were assigned to cyclic anhydrides, a second feature at 1590 cm-1 to isolated C=C double bonds. Additional discrete peaks at 1102 cm-1, 1037 cm-1 and 958 cm-1 which are superimposed on a broad intense background remained unassigned (6). The possible presence of the fullerene monoxide as epoxide structure can be ruled out on the basis of the absence of its single intense fingerprint peak at 867 cm-1. The reactivity of fullerenes and graphitic carbons against oxidation in air was studied with kinetic methods (7). Several batches of C_{60} showed different quantitative reaction behaviour but produced all a mixture of CO and CO_2 in a two-peak reaction profile centred around 730 K. A significant weight uptake in oxygen of 0.73 mole oxygen per mole fullerene was detected at lower temperature than the reaction onset occurred. Intercalation of CO_2 during attempts to determine the surface area was observed whereas dinitrogen did not intercalate. We have previously studied the interaction of oxygen with fullerenes using a variety of methods. The correlation of these data with kinetic observations is described in a recent review paper (8).The present work contains new results which are based upon the observation that the pre-history of the material plays an essential role in its gas-solid interface chemistry. Contrary to the basic expectations, the defect structure of the molecular crystal controls the intercalation of gases into the void system of the crystal and pre-determines the low-temperature reaction to oxygen-adduct precursors and controls the degradation of the molecular crystal by oxidative polymerisation. For this reason, even air-exposure for minutes causes irreversible damage to a fullerene crystal and generates an ill-defined initial status for a reaction experiment. All sample preparation and fullerene manipulation was carried out with freshly sublimed material in a glove box with a controlled level of less than 1.0 ppm of oxygenate contamination. This treatment gave quantitatively reproducible data with no differences in characteristic parameters between sample batches and minimised the weight uptake prior to oxidation. In this way characteristic differences between C_{60} and C_{70} became apparent as the different fullerene structures cause differences in reactivity which are smaller, however, than the spread in properties due to ill-defined materials. The air-induced degradation destroys the molecular nature of the fullerene crystal first before more obvious effects like the accumulation of oxides can be detected spectroscopically.

RESULTS
INTERCALATION OF OXYGEN

Clean fullerenes were transferred in a TDS apparatus and exposed in-situ for 24 h to synthetic air at ambient pressure. The results of the following TDS are shown in Figure 1 for the two fullerenes. The

two experiments first show that both fullerenes can intercalate a large amount of Ar during storage at 300 K. They further intercalate oxygen which replaces partly the Ar during exposure to air at 300 K. Furthermore, the oxygen reacts with the carbon skeleton under formation of labile C-O
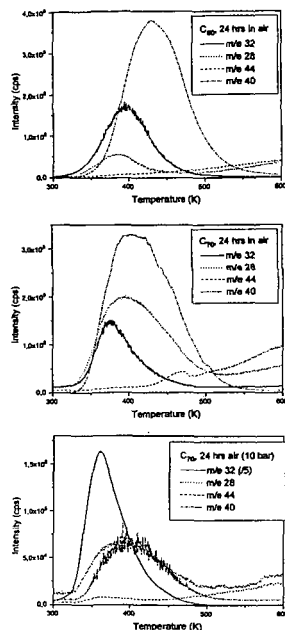

Figure 1. TDS profiles of fullerenes stored under Ar after exposure to air at 300 K and ambient pressure. The linear heating rate was 0.27 K/s. Desorption occurred into UHV. The sample size was with 10 mg identical for both experiments. The experiments were halted at 623 K due to beginning sublimation . The absence of nitrogen under the m/e 28 peak was checked with the absence of an m/e 14 peak. The high pressure experiment (bottom plot) was carried out with a different sample holder and a different sample mass. Note the reduced scale for the m/e 32 peak.

groups or even under formation and intercalation of CO as can be seen from the m/e 28 traces. This reactivity is quite different for the two fullerenes with C_{60} being more stable, as expected from its more „aromatic" and highly symmetric valence electronic structure. Above 450 K both fullerenes react in a thermally activated form with oxygen which was not evolved at 400 K /380 K respectively. This oxygen seems to be present in a more strongly bound and already activated form(epoxide) converting into gasification products at temperatures well below the literature values of gasification activity (2,6,8). The shapes of the desorption profiles indicate different reaction orders caused by the different relevance of bulk diffusion terms on the overall process. The spherical symmetry of C_{60} giving rise to isotropic gas diffusion is more suitable to enclose all gases irrespective of their chemical nature (Ar and di-oxygen), for the uniaxially elongated C_{70} molecule the gas diffusion in its solid is anisotropic but the chemical interaction seems less efficient as evidenced by the lower initial desorption temperature.

The fact that the noble gas desorbs at higher temperatures than the di-oxygen can be accounted for by the different location in the crystal. The oxygen is intercalated in an outer shell of each crystal, the Ar evolves from the inner core. In addition, it has to penetrate the damaged regions of the fullerene crystals which occur as consequence of the partial gasification. As the precursor to the gasification is molecularily disperse, this reaction is not topotactic and attacks every molecule within the shell of intercalation. A large number of partly oxidised molecules with dangling bonds and reactive C=C fragments will remain which can stabilise themselves by polymerisation into a three-dimensional network of non-planar basic structural units. In the presence of oxygen these defective fullerenes are activated precursor structures for enhanced gasification.

Raising the total pressure of air to 10 bars causes the reaction front to move deeper into each crystal This is illustrated for C_{70} where the di-oxygen desorption occurs at the same position but with a much higher intensity than after exposure at one bar. The „noise" on the Ar trace indicates the eruptions of the gas protruding through the now dense solid-solid reaction interface between oxidised and intact fullerene. It is noted that the fraction of di-oxygen which is activated to cause gasification is not changed by the total pressure which only increased the abundance of molecular oxygen intercalated.

In all these experiments the evolution of CO_2 is low but begins exactly with the evolution of di-oxygen. This indicates that only few fullerene molecules are more deeply oxidised than to the carbonyl stage. The fact that in all experiments a rise in the CO_2 partial pressure above 500 K is observed, indicates that a second process of oxidation requiring a higher thermal activation occurs and that a significant amount of oxygen which does not recombine to di-oxygen, resides within the fullerene crystals. It was verified that this sequence of events is independent of the optimised low heating rate.

The observation that C_{60} holds gas molecules more strongly than C_{70} was verified in a static experiment proving the ability of the system to intercalate molecular CO in the same way as molecular oxygen. Ar-loaded fullerenes were degassed with He at 573 K in-situ in a high pressure DRIFTS cell and exposed to 5 bar CO at 400 K for 1h. Both intercalated species show a red shift (2125 cm-1) to the gas phase (2170.21 cm-1) and C_{60} an extra shift of 5% which is in the expected order of magnitude according to the TDS experiments. This experiment is a chemical probe for the overall weak bonding interaction between fullerene host and diatomic guest molecules.

ELECTRONIC STRUCTURE OF OXO-INTERMEDIATES

Photoemission and photoabsorption with tuneable excitation wavelengths were used to study the chemical bonding of the intermediates causing the CO emission at 370-400 K and the enhanced CO_2 emission at 570 K. The valence band electronic structure of both fullerenes is characterised by a sequence of well-resolved molecular states which were probed with 100 eV excitation energy to
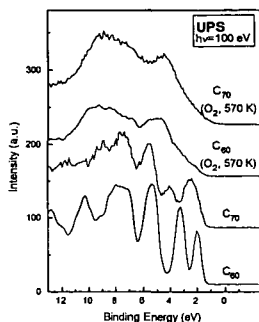
Figure 2: Valence band spectra of fullerene films in their pristine state and after oxidation at 570 K in 500 mbar oxygen (in-situ experiments). The data were recorded at the SX700 1 beamline at the BESSY synchrotron. The Fermi edge was calibrated with a gold sample.

ensure a minimum cross section modulation of σ and π states. This situation is not drastically altered upon intercalation of oxygen at 300 K and heating up to 400 K where already significant chemical reactivity was detected by the bulk-sensitive TDS technique. This implies that the average surface structure is containing up to 400 K still a large abundance of intact fullerene molecules. As can be seen in Figure 2, the surface undergoes complete restructuring upon heating to 570 K and transforms into a polymer structure with extended electronic states characterised by a resonance at 4.6 eV and a broad band around 9.5 eV. These peaks are not those of graphite (2.8 eV and 7.5 eV) but belong to oxygenated (O2p emission at 4.6 eV) partly unsaturated carbon-carbon bond systems. The corresponding C 1s XPS data show three structures at 285. 6 eV for the carbon-carbon skeleton (not graphitic, would be at 284.6 eV) and at 287.1 eV and 289.2 eV for oxygen-carbon single and double bonds. This classifies the chemical reaction leading to CO emission as a process creating mainly defective molecules such as holey fullerene cages with some oxygen functionalities at the empty co-ordination sites. Further thermal treatment is required to remove the C-O functions under CO_2 evolution and to create free carbon co-ordination sites which are saturated by homo-polymerisation with either intact molecules (they act as electrophilic unsaturated entities) or with neighbouring damaged cages. The abundance of oxygen functionalities is larger on C_{70} than on C_{60} although both species give rise to exactly the same spectral positions indicating the close similarity of the chemical bonding.

The modified reactivity of oxygen at different temperatures should be reflected in different chemical bonding of the oxygen precursors which must be present in a more reactive form at 370 K than at 570 K. X-ray absorption spectroscopy is well-suited to prove this as it is element-specific and offers high chemical selectivity. The discrimination of the chemical structure of the oxygen precursors at the two temperatures is shown in Figure 3. At 370 K a species with oxygen single bonds well-compatible with an epoxide (but no peroxide) or an ether structure is detected. The characteristic feature for this is the low intensity of the π* resonance indicating the hybridisation/occupation of these states. At 570 K the oxygen is bonded via double bonds as can be seen from the now prominent π* resonance at 532 eV.
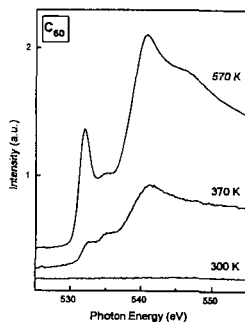
Figure 3: X-ray absorption spectra at the O 1s edge of C_{60} films oxidised at 370 K and 570 K in 500 mbar oxygen for 10 h each. The absence of any detectable oxygen after exposure of the film at 300 K indicates that the chemical bonding of intercalated molecular oxygen was too weak to prevent desorption of the surface-near layers in the UHV of the spectroscopy experiment.

DYNAMICS OF THE OXIDATION

In-situ DRIFTS spectroscopy was used to investigate the participation of the two oxo-intermediates in steady state reaction. The lowest possible temperature at which steady state conversion occurred with both fullerenes was 570 K. At this temperature the samples were exposed to 250 ml/min synthetic air and spectra were recorded as difference spectra to the initial state. In previous experiments it was shown that also at 470 K the formation of additional IR absorptions around 750 cm-1 and 1000 cm-1 occurred which is in agreement with the formation of carbon-oxygen insertion precursor compounds. The data in Figure 4 provide clear evidence for the formation of several oxygen-containing intermediates which are present under steady state oxidation. The low temperature was chosen to allow sufficient data to be accumulated for verification of the steady state. The spectra indicate the same functional groups to be formed than detected in a recent study of oxidised carbon blacks (9). The spectral quality is, however, much better in the present case due to the detection of in-situ spectra (without intermitting the oxidation process and without dilution of the carbon materials).

We observe a split carbonyl band around 1750 cm-1 indicating the presence of other C=O groups besides the cyclic anhydrides for which the high frequency of the absorption is characteristic. The 1580 cm-1 band for isolated double bonds is very prominent and occurs in both fullerenes with the
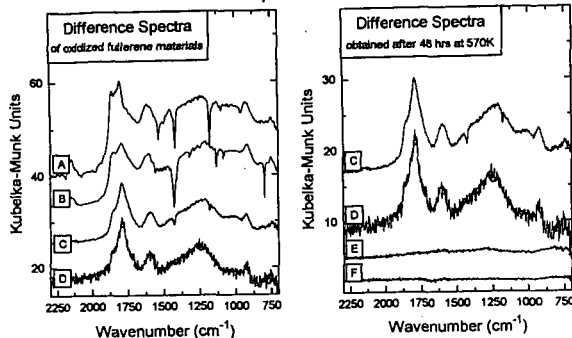
Figure 4: DRIFTS spectra of several fullerene and carbon materials during in-situ oxidation at 570 K. The left panel reports difference spectra after 20 h on stream, the right panel after 48 h oxidation. The burn-off was after 48 h below 10%. Samples were: $A=C_{60}$, $B=C_{70}$, C=fullerene black raw, D= fullerene black after extraction of solubles with toluene, E= activated carbon Norit A, F= graphitic electrode deposit (nanotubes).

same intensity irrespective of the quite different initial electronic structure. The negative sharp bands arise from the loss of molecular fullerene abundance in the gasifying samples. We note that in the non-extracted fullerene black the molecular fullerenes are oxidised preferentially over the other carbon as the bands of C_{60} occur as negative pattern. The molecular bands are superimposed on a broad structure peaking at 1000 cm-1, which was observed in all oxidation studies of fullerenes (6,8) and with oxidised carbon blacks (9). C-O single bond features and the fingerprints of C-C overlap here with high frequency aromatic substitution bands. Such bands occur further at lower frequencies of about 900 cm-1 and 750 cm-1. All these features were also detected in the carbon black oxidation study (9) and are discussed there with respect to the previous literature. The perfect agreement of the spectral features between all materials with nominally only sp^2 bonding clearly reveals that the reaction mechanism detected in detail for the model compounds of fullerenes should qualitatively apply for planar sp^2 carbon materials.

GASIFICATION OF FULLERENES

Temperature-programmed gasification data were obtained from TG-MS experiments in synthetic air (250 ml/min, 5K/min heating ramp). The results for C_{60} are displayed in Figure 5.
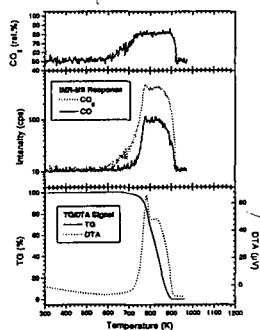
Figure 5: Combined TG-MS gasification experiment of 2.5 mg C_{60} in synthetic air. A horizontal sample pan with a specially directed gas supply and a high throughput ensured the absence of mass transport limitations. A special mass-spectrometer of the IMR-MS type allows to monitor the selectivity without interference with detection of molecular nitrogen and without fragmentation overlap. Note the log ordinate in the MS response plot. The weight uptake before gasification is low due to the high crystal quality of the material which was not air-exposed prior to the gasification experiment.

The gas evolution curve indicates the onset of gasification at 570 K in agreement with the data of Figure 1 (2,6). The selectivity changes in the initial stages of low-temperature oxidation which are dominated by the reaction of precursor compounds. Their abundance is with high-quality crystals so low that the weight uptake of less than 2% between 470 K and 570K is not visible in the overall weight change pattern. Contrary to the reaction pattern for all planar carbon samples which gasified under our experimental conditions all in a double-peak fashion with a slower initial rate and an accelerated second main reaction, the C_{60} fullerene gasifies also in a two-step sequence (7) but with an accelerated initial event. This is taken as indication for the action of the accumulated precursor compounds which leave a large number of defective fullerene molecules after cage-opening oxidation steps. The DTG curve (not shown) reveals that about 20 % of the total mass burns with the accelerated rate. This amount of material coincides with the number of molecules in the skin of oxygen penetration under ambient pressure which was shown to exist in the data of Figure 1.

THE REACTION MECHANISM

The observations indicated above and results from kinetic experiments (2,8) can be combined in a sequence of events for the fullerene oxidation. It is pointed out that no qualitative difference was found for the two molecular fullerenes and the DRIFTS data indicated that the mechanism should also apply for other sp^2 carbon materials. A schematic representation is given in Figure 6, for energetic details see ref. (8).

111

Figure flowchart labels (left side):

intercalate

fullerene oxide — epoxide

low

T — high — pO_2 — low

high

oxygen insertion   cage opening + CO

CO_2 + ring opening   polymer

pO_2 — low

high

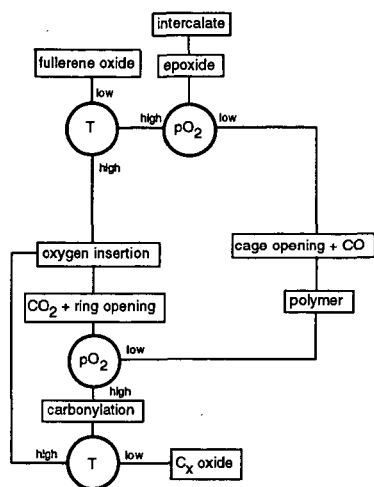carbonylation

high — T — low — C_x oxide

Figure 6: Schematic diagram of the sequence of events in fullerene oxidation: The end products besides CO and CO_2 are fullerene oxides, a homopolymer and carbon oxides with defective fullerene structures. The control variables are oxygen partial pressure and temperature.

The reaction starts with an intercalation of molecular oxygen into the van der Waals gaps of the molecular solids. With little thermal activation dissociation occurs and labile epoxides are formed besides activated atomic oxygen which will react with other electrophilic centres on the fullerene molecules. As long as the temperature is kept low (370 K) and the oxygen partial pressure remains present, the epoxides will be retained as fullerene oxides (epoxide or oxygen insertion compound). These materials are, however, not stable and will eventually react under ring opening and CO evolution to a defective fullerene molecule. Stabilisation of this state will occur at low oxygen pressures by homo-polymerisation. At higher partial pressures oxygen will be inserted in the form of e.g. cyclic anhydrides. Above 470 K these structures will evolve CO_2 and cause ring opening in the already attacked fullerene molecule. Should the oxygen partial pressure be low again (e.g. in TDS experiments, or during thermal processing), stabilisation by polymerisation will occur. At still sufficient partial pressures of oxygen carbonylation of the defective structure (5) will follow which remains as metastable product up to 570 K but which gasifies readily at higher temperatures entering a reaction loop ending with complete combustion (6). The reaction product of a polymer will not occur frequently with planar carbons (pinning defect) but the other products as well as the control variables do also occur with conventional carbon materials. The non-planar bonding geometry of the fullerene surface leads to an accumulation of the metastable intermediate products of carbon oxidation as they are formed at lower temperatures than on planar surfaces. For this reason it was possible to observe these intermediates in convenient abundance (9) for spectroscopic characterisation. At higher temperatures of above 700 K where gasification rates become significant for all carbon materials (7) the abundance of the intermediates will be much reduced also for fullerene carbon. Their ease of formation may, however, affect the overall kinetics detectable in macroscopic gasification experiments (7) as illustrated with Figure 5. The relevance of molecular intercalation of oxygen in graphitic carbon and the eventual localisation in between graphene galleries or at defect sites is currently under study. The higher temperatures required for intercalation in graphitic carbon than for fullerene carbon renders any detection with structural methods difficult as can be estimated from the localisation (10) of the extra oxygen in C_{60}.

In conclusion, the different topologies of curved fullerenes and planar sp^2 carbon cause a different abundance of oxo-intermediate compounds at low reaction temperatures. The higher chemical energy of the curved fullerenes allows for a lower activation energy for intermediate formation as well as the total „internal" surface of the fullerene crystal reacts as compared to the low abundance of reactive prismatic surfaces in planar carbon. High quality spectra were accessible for the intermediates allowing to observe some atomistic details of the carbon oxidation process.

ACKNOWLEDGEMENT

REFERENCES

(1) R. Taylor, J.P. Parsons, A.G. Avent, S.P. Rannard, T.J. Dennis, J.P. Hare, H.W. Kroto, D.R.M. Walton, *Nature, 351,* (1991) 277

(2) H. Werner, M. Wohlers, D. Bublak, J. Blöcker, R. Schlögl, *J. Full. Sci. Technol., 1,* (1993), 457

(3) R.A. Assink, J.E. Schirber, D.A. Loy, B. Morosin, G.A. Carlson, *J.Mater. Res.,7,* (1992), 2136

(4) D. Heyman, L.P.F. Chibante, *Chem. Phys. Lett.,* (1993), 207

(5) C. Taliani, G. Ruani, R. Zamboni, R. Danielli, S. Rossini, V.N. Denisov, V.M. Burlakov, F. Negri, *J. Chem. Soc., Chem. Commun.,* (1993), 220

(6) A.M. Vassallo, L.S.K. Pang, P.A. Cole-Clarke, M.A. Wilson, *J. Am. Chem. Soc., 113* (1991), 1103

(7) I.M.K. Ismail, S.L. Rodgers, *Carbon, 30,* (1992), 229

(8) M. Wohlers, A. Bauer, Th. Rühle, F. Neitzel, H. Werner, R. Schlögl, *J. Full. Sci. Technol.,* (1996), in press

(9) P.E. Fanning, M.A. Vannice, *Carbon,31* , (1993), 721

(10) W. Bensch, H. Werner, H. Bartl, R. Schlögl, *J. Chem. Soc., Faraday Trans., 90,* (1994), 2791

PURIFICATION OF CARBON NANOTUBES FROM CATHODE DEPOSIT BY MEANS OF DIFFERENT OXIDATION RATES

F. Ikazaki, K. Uchida, S. Ohshima, Y. Kuriki, K. Yase, S. Yoda and M. Yumura
National Institute of Materials and Chemical Research
1-1 Higashi, Tsukuba, Ibaraki 305 JAPAN

Abstract
Two purification methods of nanotubes from a cathode deposit by an arc plasma were conducted by means of different oxidation rates of various graphites. One was chemical and the other physical method. Both could purify nanotubes at their optimum conditions. In the former, the catalytic oxidation was used of graphite materials by copper. Copper supported graphite was prepared by the intercalation of copper chloride and by the reduction to metal copper. The catalytic oxidation decomposed the graphite at 773 K and less. The temperature was significantly lower than the oxidation temperature former reported of graphite, which enabled purification. In the latter, dispersion, comminution and filtration of a cathode deposit in ethanol were used to separate coarse graphite. The rate of weight loss by oxidation increased with the decrease of size of the graphite. Nanotubes were more slowly oxidized from the edges than the graphite of the same size. This could purify nanotubes.

1. Introduction

Carbon nanotubes were first observed by Iijima[1] in cathode deposits produced by an arc plasma method. They are completely novel carbon materials which have the property of either metal or semi-conductor according to the diameter and helical pitch[2]. Carbon nanotubes are also expected to have about two order higher fracture strength than that of commercial carbon fibers due to few defects in carbon crystal structures. Other carbon materials like graphite and amorphous carbon existed together with carbon nanotubes in the cathode deposit. Different from C60, carbon nanotubes are not dissolved in any organic solvent. Carbon nanotubes have to be purified from these carbon materials not only to analyze the properties but also to utilize the unique properties for industrial applications

Some methods[3]-[6] were proposed for the purification. These methods were based on oxidation methods. But carbon nanotubes and other carbon materials in cathode deposits are not considered that they have much different oxidation rates. Some process was inevitable to enlarge the difference of oxidation rates between carbon nanotubes and the other carbon materials before oxidation. Two such methods were developed in our group; one was chemical,the other physical method.

2. Experimental procedure

2.1 Sample

In chemical method, graphite powder(Nippon Carbon Co., SAD-4) was used for a model graphite. The diameter ranges from #100 to #325(about 44-149μm). Crude nanotubes, i.e. as-prepared cathode deposits were purchased from Shinku Yakin Co. or were prepared by an arc plasma in our laboratory. The weight percentage of nanotubes contained in the cathode deposit was not known.

2.2 Basic idea of both methods and procedures

Chemical method The chemical method is based on the concept that graphite intercalation compounds(GIC) are not synthesized in the case of carbon nanotubes because of the rigid structure of carbon nanotubes. Some metals like copper, molybdenum and so on catalytically oxidize graphite[7] at a rather low temperature. When graphite materials in cathode deposits intercalate such metal, for instance copper, carbon nanotubes are expected to be purified at a rather lower temperature. **Fig.1** is the procedure of chemical purification method. In our experiment copper was selected as a catalyst. Copper chloride-intercalated graphite(CuCl2-GIC) was prepared, followed by the reduction of chloride to metal copper, because copper-intercalated graphite was not obtained directly and chloride-intercalated graphite was stable in the air. Copper chloride-intercalated graphite was reduced either by gas phase containing hydrogen at 773 K for 1 hour or by metal lithium in THF containing naphthalene at room temperature for 1 week. Thus prepared graphite is hereafter called as copper supported graphite.

Physical method Basic idea is that the apparent oxidation rate of carbon material depends on the diameter of the material. There were various kinds of carbon materials in as-prepared cathode deposits, some of which were rather coarse graphite particles with lower oxidation rate than carbon nanotubes. Only very small portion of existing carbon nanotubes would survive when the as-prepared cathode deposits containing carbon nanotubes,amorphous carbon and graphite materials, were oxidized all together. Separation process is necessary of rather coarse carbon materials, i.e. coarse graphite from the as-prepared cathode deposit before oxidation process. Schematic procedure of the physical method is shown in **Fig.2**. Dispersion in methanol, classification by centrifugal forces and comminution in methanol of

cathode deposits were utilized to separate graphite particles with larger Stokes' diameter than carbon nanotubes. Then purified carbon nanotubes would be obtained by higher oxidation rate of the cathode deposits with equal and smaller Stokes' diameter than carbon nanotubes.

2.3 Characterization

Particle size distribution was measured by centrifugal settling photoextinction method(Shimadzu SA-CP3).

Thermogravimetric analyzer(Shinku rikou, TGD 9600) measured the oxidation rate of the cathode deposits remaining in each separation step in the physical method and of graphite and copper supported graphite in the chemical method. The sample weight was usually ca. 10 mg, but was ca. 2 mg in the case of the cathode deposit remaining in each separation step in the physical method. Temperature was raised at a rate of 10 K/m.

SEM(Hitachi, S-800 with EDX) was used for observation and element analysis of cathode deposits and of purified carbon nanotubes.

XRD(Philips PW1800) was used to measure the crystal structure of cathode deposit ,graphite,copper chloride-intercalated graphite and copper supported graphite.

Oxidation was also conducted with Thermogravimetric analyzer.

3. Results and discussions

3.1 Chemical method

Copper chloride-intercalated graphite(CuCl2-GIC) and copper supported graphite were identified by XRD profiles as shown in **Fig.3**. Oxidation rate measured by Thermogravimetry (TG.) is depicted in **Fig.4**. Copper supported graphite was oxidized at a considerable rate at the low temperature of 673 K.

Copper particles in the cathode deposits after the reduction by hydrogen seemed a little larger than those by metal lithium. The reduction by metal lithium was therefore considered better for the purification of crude nanotubes.

Oxidation was examined from 673 to 873 K   **Fig.5** shows the photographs at the oxidation temperature of 773 K. Even at the low temperature of 673 K carbon nanotubes could also be purified. The temperature was ca. 350 K lower than that of Ebbesen's method. The chemical method needs some reagents and takes time, but is very easy to be conducted.

3.2 Physical method

Figs 6 and 7 show the particle size distribution and oxidation rate of as-prepared cathode deposit and the cathode deposit remaining in each separation step. Apparent oxidation rate increased with the decrease of the particle size distribution of the remaining cathode deposit. The apparent activation energy also decreased with the decrease of the particle size distribution.

Purified carbon nanotubes are shown in **Fig.8**, which shows this method could separate graphite from the as-prepared cathode deposit. The oxidation temperature of 823 K. The temperature was about 200 K lower than that of Ebbesen's method. One of the defects in this method is rather tedious and needs skill.

4. Conclusion

Two purification methods were proposed of carbon nanotubes from as-prepared cathode deposits;one was chemical, the other physical method. Followings are the results induced.
(1) Both methods purified carbon nanotubes from as-prepared cathode deposit.
(2) The oxidation temperature was greatly lower than that of Ebbesen's method; ca. 350 K in chemical method and 200 K in physical method.
(3) Any process was inevitable to enlarge the difference of oxidation rate between carbon nanotubes and the other carbon materials containing in as-prepared cathode deposit.
(4) Optimization of the two methods is still necessary according to the varying property of as-prepared cathode deposit.

Literature cited

1) Iijima S.; Nature,**354**,56(1991)
2) Tanaka K., Satoh T., Yamabe T., Okahara K., Uchida K.,Yumura M.,Niino H., Ohshima S., Kuriki Y., Yase K. and Ikazaki F.; Chem. Phys. Letters, **223**,65(1994)
3) Ebbesen T.W., Ajayan P.M., Hiura H. and Tanigaki K.; Nature,**367**,519(1994)
4) Uchida K., Yumura M., Ohshima S., Kuriki Y., Yase K. and Ikazaki F.; Chemical Engineer(In Japanese),**39**,896(1994)
5)Takarada Y., Morishita K., Yumura M. and Uchida K.; Proc. of 8th Fullerene symposium,p253(1995, Kyoto)
6) Ikazaki F., Ohshima S., Uchida K., Kuriki Y., Hayakawa H., Yumura M., Takahashi K. and Tojima K.; Carbon,**32**,1539(1994)
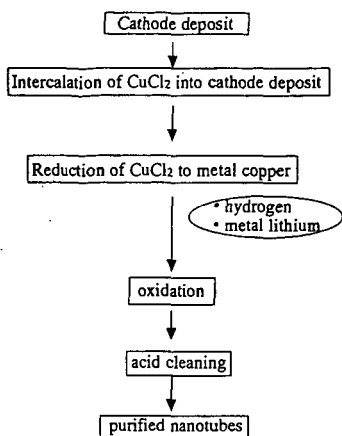7) Baker R.T.K.; Carbon,**24**,715(1986)
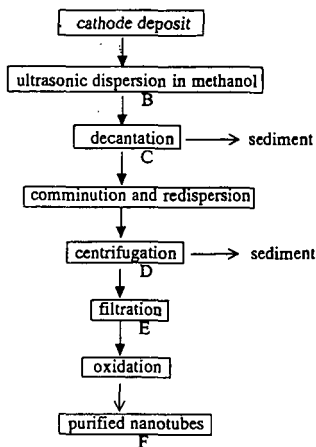
Fig.1 Procedure of chemical method
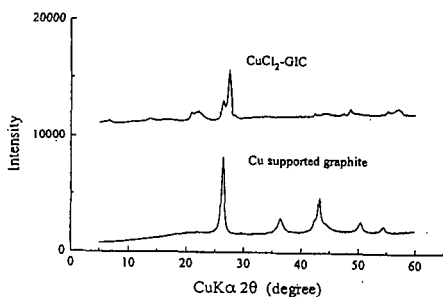
Fig.2 Procedure of physical method

Fig.3 XRD profiles of CuCl$_2$-intercalated graphite and Cu supported graphite
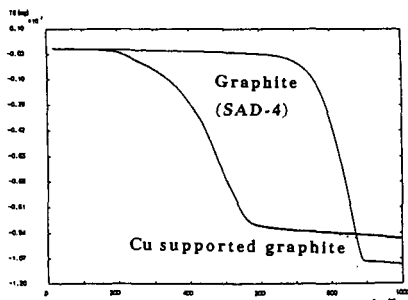

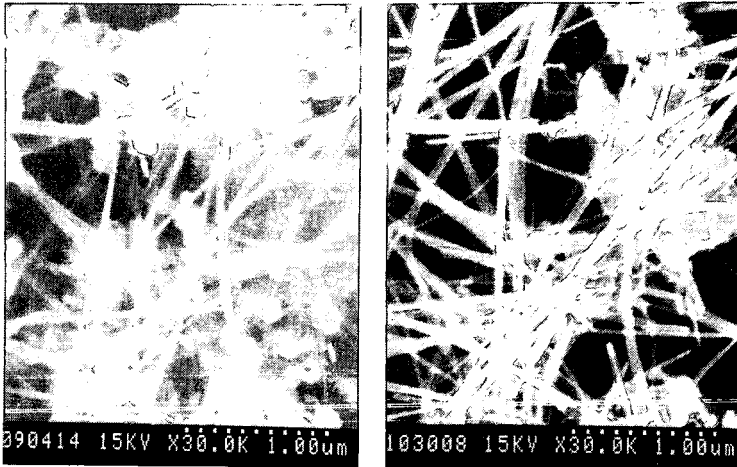Fig.4 TG analysis of graphite(SAD-4) and Cu supported graphite

Fig.5 SEM photographs at the same position of cathode deposit at the oxidation
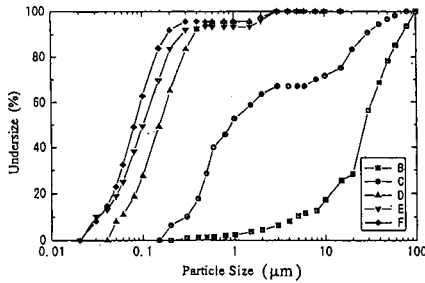temperature of 773 K (left; 773 K 1h, right 773 K 3h in Chemical method)

Fig.6 Particle size distribution of cathode deposit remaining in each separation step
of physical method(Symbols(B-F) correspond to the symbols in Fig.2)
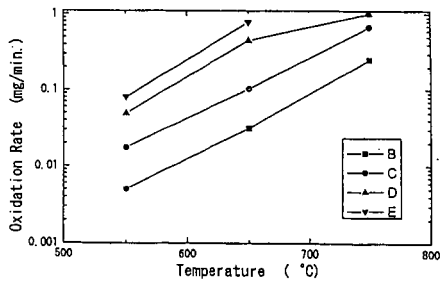
Fig.7 Oxidation rate of cathode deposit remaining in each separation step
of physical method(Symbols(B-E) correspond to the symbols in Fig.2)
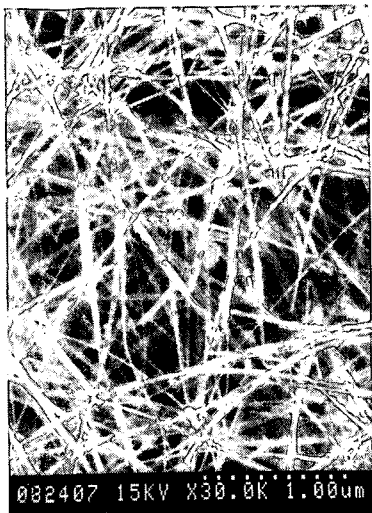
Fig.8 SEM photograph of cathode deposit after physical purification method

082407 15KV X30.0K 1.00um

GASIFICATION OF CARBON NANOTUBE-CONTAINING MATERIAL

K. Morishita and T. Takarada

Faculty of Engineering, Gunma University
1-5-1, Tenjin-cho, Kiryu, Gunma, Japan 376

Introduction

Carbon nanotubes synthesized using arc discharge evaporation method always include graphitic carbon, amorphous carbon and carbon nanoparticles. The purification step is needed to precisely characterize the physical and chemical properties of nanotubes and to study the application of those. Recently, the purification of nanotubes by the gasification with oxygen[1, 2] or carbon dioxide[3] was carried out. However, few studies on the mechanisms of gasification of carbon nanotube-containing materials have been reported. In this study, the gasification behaviors of nanotube-containing materials and nanotubes were investigated by fixed point observation techniques with scanning electron microscope (SEM) and transmission electron microscope (TEM).

Experimental

Materials

Samples synthesized by arc-discharge evaporation method (Vacuum Metallurgical Co., ltd., Type-3) in National Institute of Materials and Chemical Research were used. The conditions of synthesis were DC voltage of 18V and He pressure of 500 Torr. An inner black core of the cathode product was picked up. Then, the core was crushed and dispersed in methanol with the use of a sonicator. The sample recovered as a float was used as raw materials in this study.

Gasification

The gasifiation of sample was carried out in a thermo-balance (Shinku Riko; TGD-7000). After evacuation and substitution with N_2 gas, sample was heated up to a desired temperature with N_2 flow. Then, reaction gas was introduced into the reactor and the gasification of sample was initiated. The experimental conditions were as follows : oxygen (1, 10vol%) 773K, 823K, 1023K, 1073K; carbon dioxide (100vol%) 1173K.

SEM and TEM observations

A series of SEM observation and gasification of sample was carried out as follows. The raw materials put on Si wafer was observed with SEM and then set in the thermo-balance. After the sample was gasified for a desired reaction time, the area selected by the previous observation was observed with SEM, again. These procedures were repeated several times. The SEM used was JEOL JSM-5300. In the case of TEM observation, sample was put on copper grid (400mesh). A series of TEM observation and gasification of sample was essenntially similar to the case with SEM mentioned above. TEM observations were carried out using JEOL 1200EX at ACCV of 100kV. In these experiments, more than 10 fields were observed and more than 50 photograghs were taken for each sample. It is very important to observe many fields because microscopic observations are apt to give prejudiced informations.

Results & Discussions

Reactivity

Nanotube-containing materials were gasified in a thermo-balance. Figure 1 shows the gasification profiles obtained under various conditions. The reactivity of sample toward oxygen was so high that about 90wt% of sample was gasified in 5min at conditions of 1023K and 10vol% of oxygen. The activation energy for oxygen gasification was estimated as about 140kJ/mol. The gasification profile of sample in carbon dioxide was somewhat peculiar. The conversion was smoothly increased up to around 70wt%, and the gasification was seemed to be

saturated after that.

Gasification behaviors of nanotube-containing materials

A series of SEM observation and gasification of sample was repeated several times. Figure 2 shows the SEM photographs of raw material and the samples partially gasified. The gasification temperature was 1023K. Besides carbon nanotubes, many large lumps of carbon and many carbon nanoparticles were observed in the raw material. As the reaction progressed, other carbonaceous materials were gradually consumed and only carbon nanotubes were remained at 5min of reaction time. This is due to the difference in the reactivity between carbon nanotubes and other carbon materials. In the course of gasification, many tubes were newly appeared from lumps of carbon materials. Careful observations revealed that not only other carbonaceous materials but also carbon nanotubes were damaged by oxygen gasification. Figure 3 shows the results obtained at 823K. The total conversion was about 90wt%. No remarkable difference in the gasification rate between other carbon materials and nanotubes was observed. Therefore, considerable amount of other carbon materials were remained in the sample gasified. It may safely be said that it is better for the efficient recovery of nanotubes to gasify raw material with oxygen at a high temperature such as 1023K than at a low temperature of 823K. In the case of CO_2 gasification at 1173K, as the reaction progressed, large lumps of carbonaceous materials were gradually gasified just like the case of oxygen gasification. A number of carbon nanoparticles, however, were remained in the sample. Further purification step will be needed.

Gasification behaviors of nanotubes and nanoparticles

To clarify the gasification behaviors of nanotubes and nanoparticles, a series of TEM observation and gasification of sample was repeated several times. The gasification temperature was 1023K. A wide variety of gasification manners of carbon nanotubes were observed. It was often recognized that the gasification of nanotube was initiated from the cracks, defects and strains in nanotubes. Other typical gasification manner was shown in Figure 4. It can be seen that nanotube was gasified from the tip of the tube. This gasification manner was often observed in this study and reported by Tsang et al.[3]. The diameter of tube was reduced from 18nm to 11nm near the tip (point-A) and from 20nm to 15nm at point-B in 5 seconds. From these results, the gasification rate of carbon nanotube is able to be measured directly. A carefull observation showed that the tip angle of closed layer near the cap was enlarged as shown at point-C. Figure 5 shows the gasification manners of tubes and particles. In this field, many nanoparticles were observed as shown in Figure 5a. At 5sec of gasification time, some nanoparticles were considerably damaged and outer layers of some nanotubes were stripped off. Finally, almost all the nanoparticles were gasified at 10sec. The gasification rate of the irregular-shaped particles was higher than that of smooth-faced particles.

Similar experiments were carried out at 823K. The results obtained were shown in Figures 6 and 7. As the reaction progressed, the outer layers were transformed to amorphous and the spacing of the lattice was enlarged (Fig. 6). It was commonly observed that relatively thin tubes just as pointed by arrow in Figure 6 were swelled by the oxidation. The pitting formation by the oxygen gasification was sometimes recognized on the cylindrical outer surface of tubes (Figure 7). As a whole, no obvious difference in the gasification rate between nanotubes and nanoparticles was recognized at 873K. This is consistent with the results obtained with SEM observations.

Conclusions

The gasification behaviors of carbon nanotube-containing materials were clarified by SEM and TEM observations. The gasification rates of other carbonaceous materials were higher than those of nanotubes at 1023K. A wide variety of gasification manners of nanotubes were observed. The gasification manner of nanotubes strongly depended on the gasification temperature.

References

1. P. M. Ajayn et al., *Nature*, **362**, 522 (1993)
2. T. W. Ebbesen et al., *ibid.*, **367**, 519 (1994)
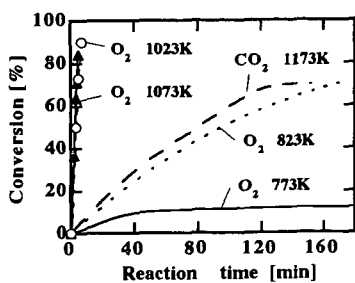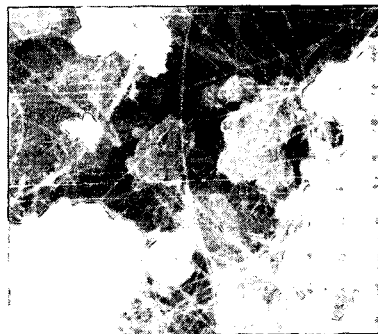3. S. C. Tsang et al., *ibid.*, **362**, 520 (1993)
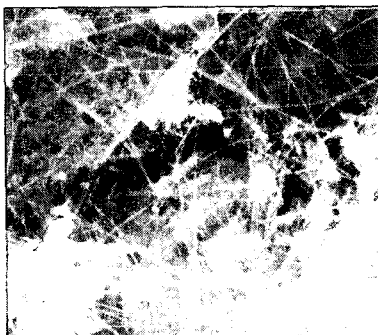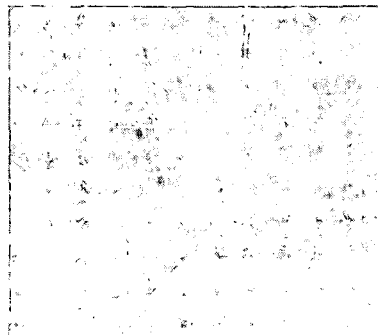
Fig. 1　Reaction profiles of samples

(a)

(b)

(c)

(d)

(e)

1um

Fig. 2　SEM images of samples before and after O_2 gasification at 1023K

(a)　raw material

(b)　reaction time　0.5 min
(d)　reaction time　3 min

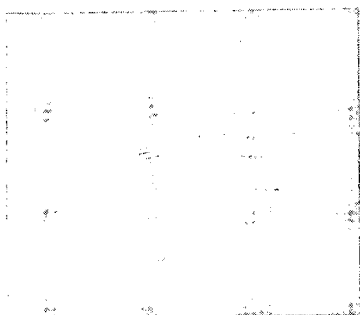(c)　reaction time　1 min
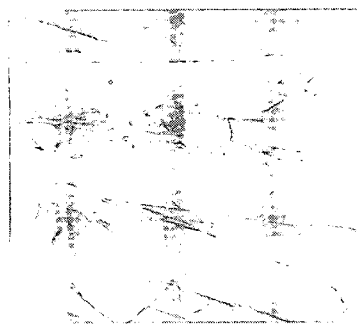(e)　reaction time　5 min
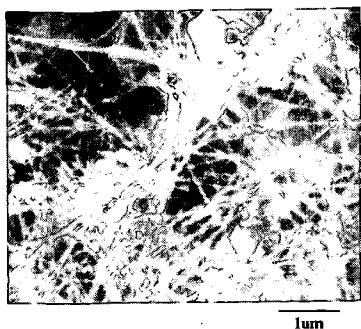
Fig. 3 SEM image of sample
after O_2 gasification at 823K
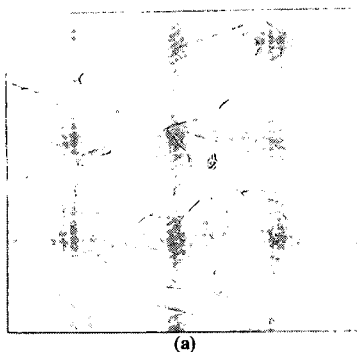
(a)

(a)
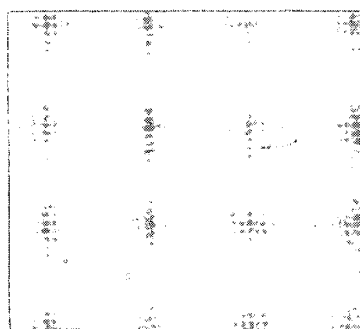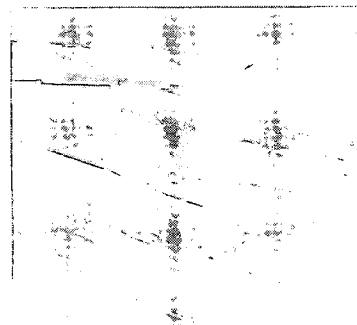

(b)

(b)   20nm

(c)   20nm
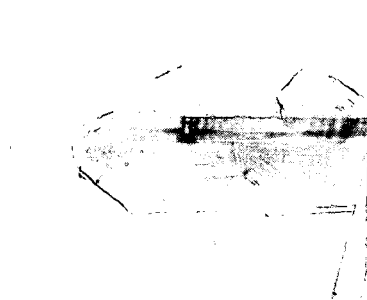
Fig. 4 TEM images before and after
O_2 gasification at 1023K
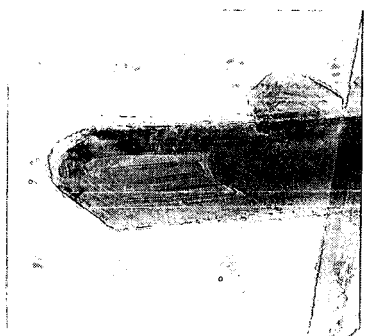
  (a)   raw material
  (b)   reaction time 5 s

Fig. 5 TEM images before and after
O_2 gasification at 1023K

  (a)   raw material
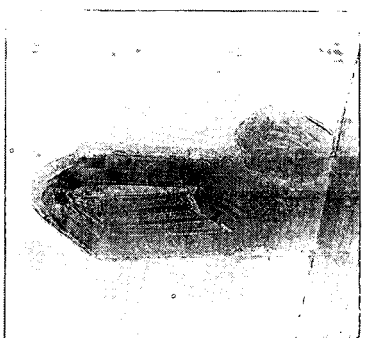 (b)   reaction time 5 s
  (c)   reaction time 10 s

121

(a)

(a)

(b)

(b)

(c)   20nm

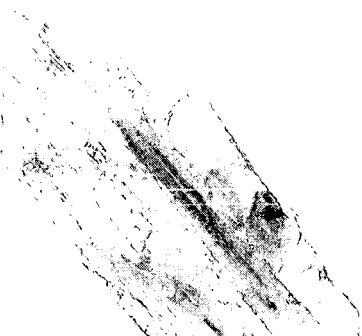(c)   20nm

Fig. 6 TEM images of samples before
and after O$_2$ gasification at 823K
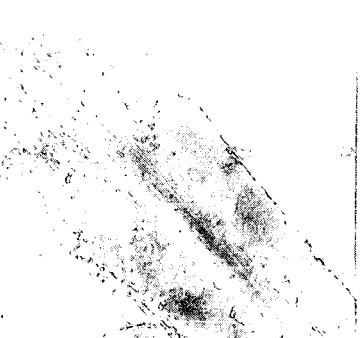
 (a) raw material
 (b) reaction time 20 s
 (c) reaction time 40 s

Fig.7 TEM images of samples before
and after O$_2$ gasification at 823K

 (a) raw material
 (b) reaction time 10 s
 (c) reaction time 30 s

DETERMINATION OF POROSITY AND POROSITY DEVELOPMENT DURING GASIFICATION FROM THERMAL DESORPTION METHODS

L. Zhang and J.M. Calo
Chemical Engineering Program
Division of Engineering
Brown University
Providence, Rhode Island 02912, U.S.A.

Keywords: Char porosity; porosity development; thermal desorption methods.

INTRODUCTION
In the current work, a new approach is explored for the characterization of porosity and porosity development in carbons and chars. It is shown that there exist both qualitative and quantitative relationships between porosity development and post-reaction desorption features of oxygen surface complexes formed during the activation process. It is proposed to exploit these relationships to develop a porosity characterization method based on the interpretation of post-activation temperature programmed desorption (TPD) spectra.

EXPERIMENTAL
The samples used in the experiments were chars produced from Wyodak subbituminous coal obtained from Argonne Premium Coal Sample Bank [1], and from phenol-formaldehyde resin synthesized in our laboratory. The latter material was used as a prototype of a non-mineral matter containing char. The char samples were produced in a tube furnace at 1000°C for 2h in flowing ultrahigh purity helium.

All the oxidation and thermal desorption experiments were carried out in the TPD-MS/TGA apparatus. For gasification, the samples were exposed to one atmosphere of oxygen at a selected temperature, and burned-off to varying extents. The subsequent thermal desorptions were all carried out at a heating rate of 50K/min to 1200°C in ultrahigh purity helium carrier gas, without exposing the previously oxidized samples to ambient air.

Adsorption isotherms for all the char samples were obtained using a Quantachrome Quantasorb surface area analyzer with nitrogen at 77K.

RESULTS AND DISCUSSION
Char Characterization. The total specific surface area, external surface area, and micropore volume of the samples were determined from the nitrogen isotherm data using the so-called α_s-plot method [2]. This technique is based on a comparison of the shape of the adsorption isotherm of a sample with that of a standard nonporous reference material. The α_s-plot method consists of plotting adsorption normalized to a particular point (typically $p/p° = 0.4$; i.e., $\alpha_s = n/n_{0.4}$) for the reference material *vs.* $p/p°$ to obtain a standard α_s curve. This curve is then used to construct the α_s-plot from the isotherm of the test sample. The slope of the resultant plot at low α_s provides the total surface area; the slope of the upper linear branch gives the nonmicroporous surface area; and the extrapolation of this branch of the curve to $\alpha_s = 0$ provides the total micropore volume. α_s-plots were constructed for all the nitrogen adsorption isotherms for the current samples using data for the standard nonporous carbon proposed by Rodriguez-Reinoso *et al.* [3]. Corresponding surface areas and pore volumes were also obtained *via* comparison with the isotherm for the reference adsorbent given in this reference [3], following the data work-up procedures contained therein.

Wyodak Coal Char. Figures 1 and 2 present the thermal desorption spectra for the Wyodak coal char samples as a function of burn-off. In Figures 3 and 4 the total evolved CO and CO_2 obtained from these figures are compared to the micropore volume and the nonmicroporous surface area, respectively, as determined from the α_s-plots, as described above. It is noted that the CO evolution was "corrected" by subtraction of the CO_2 signal, which is explained subsequently. The nitrogen adsorption data indicate that the total surface area (not shown), the nonmicroporous surface area, and the micropore volume all initially increase with burn-off, pass through maxima around 40% burn-off, and decrease steadily thereafter. This behavior is quite typical of carbonaceous materials [4]. As the burn-off proceeds, the nonmicroporous (i.e., the larger porosity) surface area increases continuously but more rapidly prior to 40% burn-off, and less rapidly at higher degrees of burn-off, as shown in Figure 4. This behavior indicates that the microporosity continues to develop up to about 40% burn-off, and decreases thereafter; while, the larger porosity develops continuously with burn-off. These results are consistent with the classical picture of microporosity development at low conversions, followed by pore wall collapse and concomitant surface area loss at higher conversions [5].The principal point of these figures, however, is that the CO and CO_2 evolution correlate quite well with the micropore volume and the nonmicroporous surface area, respectively.

Resin Char. Summaries of the corresponding data for resin char are presented in Figures 5 and 6. As shown, this char behaves somewhat differently than the Wyodak coal char. The nitrogen adsorption data indicate that the micropore volume increases to a maximum at about 45% burn-off, and decreases thereafter. The nonmicroporous surface area, however, increases steadily and monotonically up to 72% burn-off. It is noted that even though the larger porosity increases with extent of burn-off, the majority of the porosity is still microporous over the entire activation

process. That is, even at 72% burn-off, the surface area contribution from the larger porosity is only about 5% of the total surface area. In any case, as for the Wyodak coal char, the CO and CO_2 evolution correlate quite well with the micropore volume and the nonmicroporous surface area, respectively, in spite of the fact that the CO and CO_2 TPD spectra for resin char (not shown) differ considerably from the Wyodak char spectra, both qualitatively and quantitatively.

Starsinic et al. [6] identified carboxylic acid groups on oxidized carbon surfaces using FTIR spectroscopy, and noted that their concentration increases with extent of burn-off. Otake and Jenkins [7] have shown that the CO_2 complexes present on an air-oxidized char are responsible for the acidic nature of the surface, and that the high temperature CO_2 evolution is primarily due to the thermal decomposition of carboxylic acid anhydride surface complexes. Zhuang et al. [8] have also found that CO_2 evolution arises from the decomposition of lactone and/or acid anhydride complexes, whereas CO desorption is mainly from carbonyl and ether type complexes. In a DRIFTS study of the formation of surface groups on carbon by oxygen, Fanning and Vannice [9] also reported that initial exposure to oxygen produces ether structures, and that additional exposure develops cyclic anhydride groups.

Apparently, just like nitrogen, which penetrates practically all the char porosity (i.e., micro-, meso- and macroporosity) during adsorption measurements, oxygen can also penetrate all the porosity under gasification conditions to form surface complexes over the entire carbon surface. The obvious conclusion that one can draw from the results presented here is that CO evolution occurs from the entire apparent specific surface area, but that most of the CO_2-evolving surface complexes are formed only on the surfaces of the larger porosity. In a study of the effect of nonreacting gases on the desorption of reaction-created surface complexes on carbon, Britten et al. [10] concluded that surface transport processes were involved in the desorption of CO, but that no influence of the nonreactive gases on the CO_2 desorption rate was observed. These results support the conclusion that the CO_2-evolving surface complexes are formed on the surface area in the larger porosity.

From the preceding, it is possible that a large portion of the CO_2 evolution derives from carboxylic acid anhydride complexes. Since the stoichiometry for the thermal decomposition of these groups result in one CO_2 and one CO molecule, the CO evolution was "corrected" by subtracting the CO_2 evolution to account for the CO arising from carboxylic acid anhydride complexes. These are the "corrected" CO values which are plotted in Figures 3 and 5. In both cases, this correction improves the correlation between micropore volume and CO evolution. Therefore, it is concluded that there is some justification to this "correction."

Random Pore Model. In addition to the CO and CO_2 evolution data and the nitrogen adsorption data, the reactivities of the samples as a function of burn-off were also obtained. These latter data were used in conjunction with a random pore model [11] to determine the evolution of the microporosity.

According the random pore model [11], the sample burn-off, x_c, vs.time, t, follows the relationship:

$$[(1/4\pi(1-x_c)dx_c/dt]^2 = A_0 \ln[1/(1-x_c)] + A_1^2 \qquad [1]$$

where $A_0 = B_0 v^2/(2\pi)$, and $A_1^2 = (B_1 v)^2$, and B_0 and B_1 are the zeroth and first order moments of the pore number density function, and v is the velocity with which a pore surface element recedes due to reaction. A_0 and A_1 were determined by least squares regression from plots of Eq. [1] derived from the reactivity data. From these values and the surface area at one point (e.g., 5% burn-off), the parameters B_0, B_1, and v were obtained. The apparent total specific surface area, S, was then determined from:

$$S = 4\pi(1-\varepsilon_{T_0})(B_0 v t + B_1) (1-x_c(t)), \qquad [2]$$

where ε_{T_0} is the initial (i.e., zero burn-off) total void fraction. Comparisons of surface areas obtained from the nitrogen BET data with values calculated from Eq. [2] show very good agreement for both chars.

As indicated by the nitrogen adsorption data, both the resin and the Wyodak coal chars are essentially microporous materials at zero burn-off. A Gaussian pore number distribution for the micropore volume was assumed, following Dubinin et al. [12]. It was also assumed, as in the original random pore model development, that the probability density function of pore numbers does not vary with burn-off. With these assumptions, the following relationships were derived:

$$(1- \varepsilon_{micro})/(1- \varepsilon_{micro})_0 = \exp[-2\pi(B_0(\Delta r)^2 + 2 B_1\Delta r)] \qquad [3]$$

$$S_{micro} = d(\varepsilon_{micro})/d(\Delta r) = 4\pi(1- \varepsilon_{micro})(B_0\Delta r + B_1) \qquad [4]$$

where ε_{micro} is the void fraction of the micropores, and Δr is the mean micropore radius change.

For the current data, the micropore void fractions, ε_{micro}, for the two chars as a function of burn-off were determined from nitrogen adsorption data. The mean micropore radius change, Δr, was then determined from Eq. [3], and the total apparent micropore surface area, S_{micro}, was

determined from Eq. [4]. The difference between total surface area and micropore surface area was taken as the nonmicroporous surface area. The agreement between the nonmicroporous surface areas determined in this manner with those obtained from the α_s-plots was quite good. thereby validating this general approach.

Figure 7 shows the results for the mean micropore radius as a function of burn-off for resin and Wyodak coal chars, as determined using this approach. Here the initial mean micropore radius (i.e., prior to gasification) was determined from the zero burn-off nitrogen adsorption data assuming a normal micropore volume distribution. The resultant mean pore radius prior to oxidation was 1.04 nm for Wyodak coal char, and 0.64 nm for resin char. The variance of the normal distribution was 0.24 nm for Wyodak coal char, and 0.18 nm for resin char. These results indicate that the pore size is larger, and the pore distribution is broader for Wyodak coal char than for resin char prior to activation. It is noted that the rate of mean micropore radius decrease with burn-off at high conversion is slower for resin char than for Wyodak coal char. This suggests that the resin char remains more microporous with burn-off. This conclusion is also apparent from the nonmicroporous surface areas for both chars. From these results, it is concluded that the random pore model theory is capable of providing reasonable predictions of microporosity development during gasification for both resin char and Wyodak coal char.

SUMMARY AND CONCLUSIONS
It is concluded that CO-evolving surface complexes are formed over the entire surface area of all the porosity of the two very different chars investigated, and that the total CO evolution upon thermal desorption is well correlated with the total surface area. It is also concluded that the CO evolution "corrected" for the expected contribution from carboxylic acid anhydride surface complexes is well correlated with the microporosity. It is hypothesized that if these observations can be generalized and calibrated, they could be developed into a new method for the characterization of char porosity, in conjunction with the "extended" random pore model.

ACKNOWLEDGEMENT

REFERENCES
1. Vorres, K.S., Users Handbook for the Argonne Premium Coal Samples, ANL/PCSP-93/1, DOE, Argonne, Il, 1993.
2. Gregg, S.J., and Sing, K.S.W., Adsorption, Surface Area, and Porosity, 2nd ed., Academic Press, NY, 1982.
3. Rodriguez-Reinoso, F., Martin-Martinez, J.M., Prado-Burguete, C., and McEnaney, B., *J. Phys. Chem.* **91**, 515 (1987).
4. Walker, P.L. Jr., in *Carbon and Coal Gasification,* Figueiredo, Moulijn, eds., NATO ASI Series, 9.3, 1986.
5. Miura, K. and Hashimoto, K., *IEC Proc. Des. Dev.* **23**, 138-145,1984.
6. Starsinic, M., Taylor, R.L., Walker, P.L., Jr., and Painter, P.C., Carbon 21, 69 (1983).
7. Otake, Y. and Jenkins, R.G., *Carbon* **31**, 109 (1993).
8. Zhuang, Q-L, Kyotani, T., Tomita, A., *Energy and Fuels* **8**, 714, 1994.
9. Fanning, P.E. and Vannice, M.A., *Carbon* **31**, 5, 721, (1993).
10. Britten, J. A., Falconer, J. L. and Brown, L. F., *Carbon* **23**, 627 (1985).
11. Gavalas, G. *AIChE J.* **36**, 577 (1980).
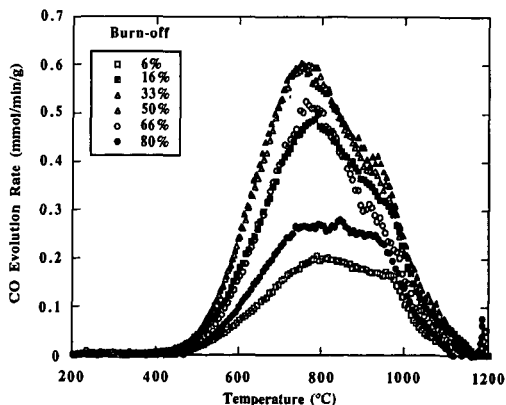12. Dubinin, M. M., *Chemistry and Physics of Carbon*, Vol. 2, Academic, NY, p. 51 (1966).

Figure 1. 50K/min CO TPD spectra from Wyodak char as a function of burn-off in oxygen
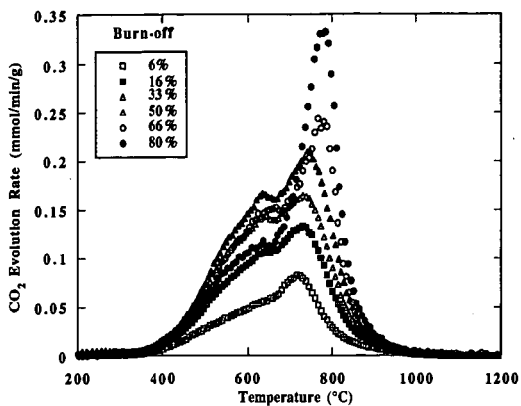
Figure 2. 50K/min CO_2 TPD spectra from Wyodak char as a function of burn-off in oxygen (0.1MPa, 420°C).
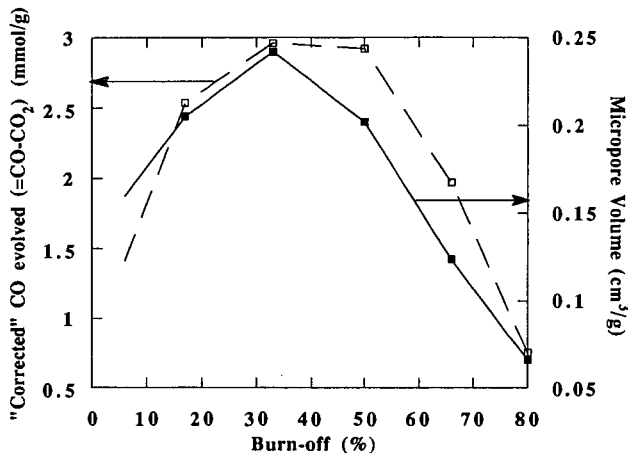

Figure 3. Comparison of total "corrected" CO evolved with micropore volume for Wyodak coal char as a function of burn-off (0.1MPa, 420°C).
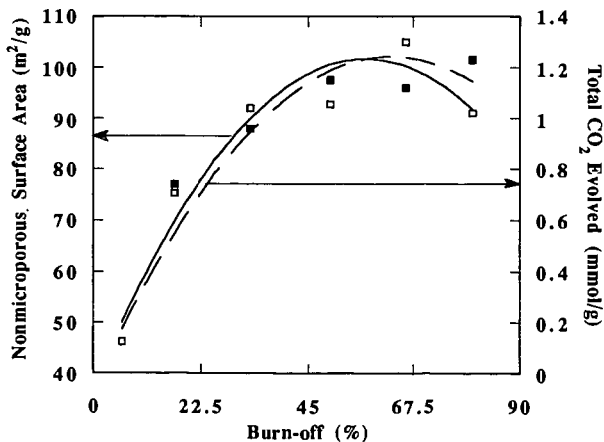

Figure 4. Comparison of total CO_2 evolved with nonmicroporous surface area as a function of burn-off (0.1MPa, 420°C).

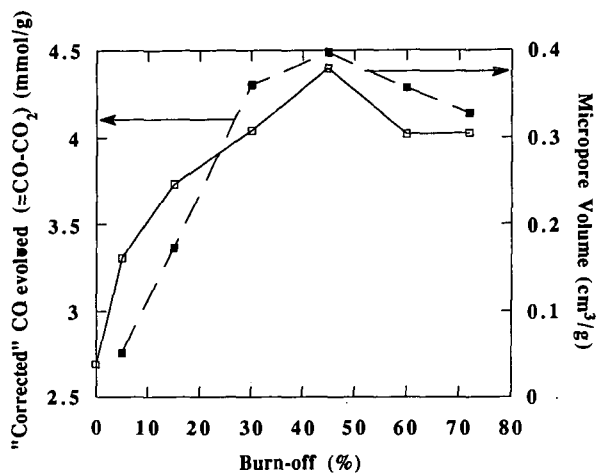Figure 5. Comparison of total "corrected" CO evolved with micropore volume for resin char as a function of burn-off (0.1MPa, 470°C).
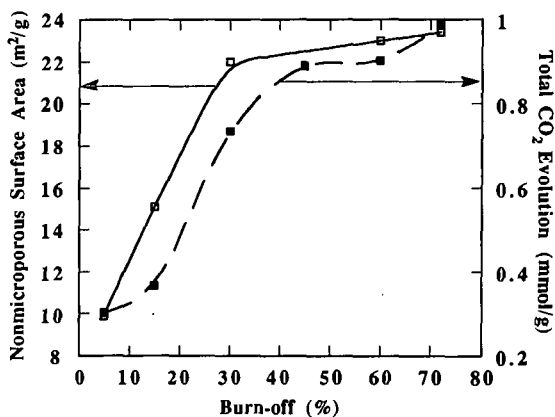

Figure 6. Comparison of total CO_2 evolved with nonmicroporous surface area for resin char as a function of burn-off (0.1 MPa, 470°C).
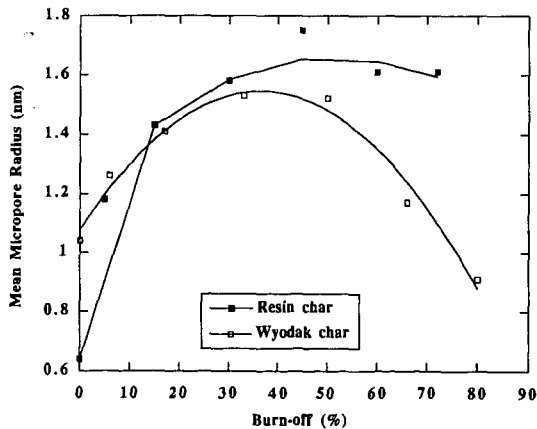

Figure 7. Mean pore radius as a function of burn-off for resin and Wyodak coal char, as determined from the "extended" random pore model.

ANALYSIS OF CARBON-OXYGEN REACTION BY USE OF
A SQUARE-INPUT RESPONSE TECHNIQUE AND ^{18}O ISOTOPE

Kouichi Miura and Hiroyuki Nakagawa
Department of Chemical Engineering, Kyoto University
Kyoto 606, Japan

INTRODUCTION

Carbon gasification reaction has been investigated for decades including the pioneering works of Walker and his co-workers[1], but its mechanism has not been completely elucidated. The concept of the active surface area (ASA) was proposed by them, and its importance has been recognized. However, since ASA was measured by O_2 chemisorption at below 300 °C where carbon loss through gasification is negligible, it does not reflect the actual gasification situation. To overcome this weak point, measurements of ASA in a batch reactor[2-4] and the so-called transient kinetic (TK) method were proposed[5,6]. Ahmed and Back[4] successfully measured the chemisorbed oxygen during the gasification using a batch reactor, and proposed a new mechanistic sequence for carbon-oxygen reaction which stresses the importance of the reaction between the gaseous oxygen and the chemisorbed oxygen. Radovic et al.[7,8] proposed the concept of the reactive surface area (RSA), and reported excellent proportionality between the CO_2 gasification rate and the RSA estimated by the TK and the TPD methods. Kapteijn et al.[9,10] showed that the TK method with labeled molecules is more powerful to examine the mechanism. They found the presence of two types of surface oxygen complexes which desorb at different rates.

Although the TK method is powerful, the method can trace only the desorption phenomena after a step change from an oxidizing gas stream to an inert gas stream. On the other hand, the step response technique changing an isotope stream to another isotope stream step-wisely enables us to observe *in situ* transient behavior without disturbing the reaction system if we can trace the change in all isotope species. This technique has been recently applied to carbon-oxygen reaction by Kyotani et al.[11]

The authors have recently proposed a Square-Input Response (SIR) method as a modification of the step response technique[12]. When we apply the SIR technique to carbon-oxygen reaction, we change the reactant stream containing $^{16}O_2$ step-wisely to the $^{18}O_2$ containing stream at a certain instant, and after a predetermined time interval we change the $^{18}O_2$ stream backwardly to the $^{16}O_2$ stream. This method enables us to observe transient changes on two step changes, to minimize the usage of expensive isotopes, and to facilitate the establishment of the balance of the isotope supplied as the square-input. We have successfully applied this technique to the analysis of a coal char gasification and to the analysis of the stabilization reaction of carbon fiber[13].

In this work the SRI technique was applied to the analysis of carbon-oxygen reaction to examine the reaction mechanism presented by the authors[14], and to determine the rate constants of elementary reactions.

EXPERIMENTAL

A mineral-free carbon black (CB) was used in this study. It was provided by Mitsubishi Chemicals and had the designation CB-30. The ultimate analysis of CB is C: 99.1%, H: 0.8%, and O: 0.1% on weight basis .
Figure 1 shows the apparatus used for the gasification experiments. About 3 to 12 mg of CB were embedded in a reactor made of quartz tube (4mm in ID and 30 cm in length). They were heated to 900 °C in a helium stream and held at this temperature for 10 minutes. Then they were cooled to a constant temperatures of 550, 570, or 600°C. To start the gasification, the helium stream was changed to the $^{16}O_2$ stream diluted by helium (22% conc.), whose flow rate was regulated by a mass flow controller at 50 ml/min. A part of the product gas was introduced to a pressure regulated section *via* a valve (V-2). The pressure of this section was kept at a few mmHg by regulating the opening of the valve V-2. Only a small amount of gas was introduced from this section to a mass spectrometer (MS; Nichiden Anerva, AGS211R), where signals for mass numbers of 28, 30, 32, 36, 44, 46, and 48 were continuously detected. To minimize the delay of the gas analysis from the gas formation, a small tubing (1/16 inch OD) was used and the gas flow in the pressure regulated section was designed as shown in the bottom of Fig. 1. The main flow exiting the reactor was led to a gaschromatograph (GC), where it was analyzed in every 10 minutes to determine precisely the concentrations of CO, O_2, and CO_2. By referring to these concentrations the signals of the MS were calibrated in every 10 minutes. Then the concentration of CO, O_2, and CO_2 in the product gas could be measured continuously and precisely.

The pure ^{18}O isotope (ISOTEC Inc.) containing 99.2 mol % ^{18}O was used for the SIR experiment. The isotope diluted by helium (22% $^{18}O_2$ conc.) was stored in a sample loop of about 50 ml as shown in Figure 1. When the conversion of CB reached 10 %, the 6-way

valve (V-1) was switched. Then the helium stream containing $^{16}O_2$ pushed out the $^{18}O_2$ containing gas in the sample loop to the reactor. The $^{18}O_2$ containing stream was supplied for about 1 min, and then the stream returned again to the stream containing only $^{16}O_2$. After the elapse of 20 min the temperature was raised to 900°C to combust the sample, and the ^{18}O retained in the sample was detected as $C^{18}O$, $C^{18}OO$, and $C^{18}O_2$. Using this technique, the exact ^{18}O balance could be established after changing the $^{18}O_2$ containing stream to the stream containing only $^{16}O_2$. The experiments using 1:1 mixture of $^{16}O_2$ and $^{18}O_2$ as the square-input were also performed to examine probable isotope exchange reactions. The experiments using pure He as the square-input were also performed. The experiments are performed to compare our results with those obtained by the so called TK experiments.
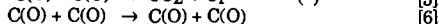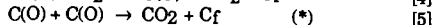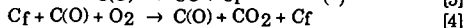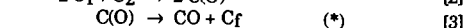
RESULTS AND DISCUSSION

Figures 2a and 2b show typical SIR results, where the formation rates of CO(28), CO(30). CO_2(44), CO_2(46), and CO_2(48) and the flow rate of O_2(36) are shown against the reaction time. Hereinafter, the isotopes are represented by the molecular weights in the brackets following the molecular formula. Figures 2c and 3, respectively, show the results obtained using the square-inputs of the 1:1 mixture of $^{16}O_2$ and $^{18}O_2$ and the pure He under the same experimental conditions as those in Fig. 2b.

First, we consider CO formation in Figs. 2a and 2b. On the step change from the $^{16}O_2$ stream to the $^{18}O_2$ (abbreviated to the $^{16}O_2/^{18}O_2$-step) the CO(28) formation rate decreased rapidly to a half or so, and then decreased gradually. The CO(30) formation rate responded almost instantaneously to the step change to increase a certain level, and increased gradually. On the step change from the $^{18}O_2$ stream to the $^{16}O_2$ (the $^{18}O_2/^{16}O_2$-step) almost reverse responses were observed. The CO(28) formation rate increased rapidly at first, then increased gradually. The CO(30) formation rate decreased instantaneously on the step change to a small value, then decreased gradually. These results clearly show that CO is formed at least two reactions. The gradual formation of CO(28) and CO(30) without the corresponding oxygen isotopes in the gas phase indicates that these are produced from the chemisorbed oxygen. The rapid changes of the formation rates of both CO(28) and CO(30) on the step changes are associated with the reaction between the gas phase oxygen and the active site.

The CO_2 formation rates are considered next. On the $^{16}O_2/^{18}O_2$-step the CO_2(44) formation rate responded almost similarly as the CO(28) formation rate. The CO_2(46) formation rate increased rapidly on the step change, but started to decrease gradually after reaching a maximum. The CO_2(48) formation rate responded slowly to the step change, but it increased monotonously. On the $^{18}O_2/^{16}O_2$-step the CO_2(44) formation rate again responded almost similarly as the CO(28) formation rate. The CO_2(46) formation rate decreased rapidly first, and then decreased gradually. The CO_2(48) formation rate decreased rapidly to a very small value, then decreased gradually. These results indicate that CO_2 is formed by several reaction paths: both the reaction between gaseous oxygen and chemisorbed oxygen and the reaction between chemisorbed oxygens are judged to be significant.

Both the total CO formation rate (the sum of the formation rates of CO(28) and CO(30)) and the total CO_2 formation rate (the sum of the formation rates of CO_2(44), CO_2(46), and CO_2(48))change little during the SRI experiments as shown in Figs. 2a to 2c. This indicates that the SIR experiment using ^{18}O is powerful to examine the reaction mechanism without disturbing the steady state of reaction as expected. This conclusion is further substantiated when comparing Figs. 2b and 3. The response behavior of CO(28) and CO_2(44) in Fig. 3, which is the TK experiment, is significantly different from that in Fig. 2b. The gradual formations of both CO(28) and CO_2(44) observed in Fig.2b were not observed in Fig. 3. This means that the rate parameters determined by the TK method is different from those under the gasification of steady state for at least this reaction system.

We presented the following gasification mechanism for carbon oxidation based on the pulse experiments using $^{18}O_2$ isotope[14].

$$2\,C_f + O_2 \rightarrow C(O) + CO \qquad [1]$$
$$2\,C_f + O_2 \rightarrow 2\,C(O) \qquad [2]$$
$$C(O) \rightarrow CO + C_f \qquad (*) \qquad [3]$$
$$C_f + C(O) + O_2 \rightarrow C(O) + CO_2 + C_f \qquad [4]$$
$$C(O) + C(O) \rightarrow CO_2 + C_f \qquad (*) \qquad [5]$$
$$C(O) + C(O) \rightarrow C(O) + C(O) \qquad [6]$$
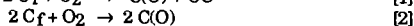
where C_f and C(O) represent the free active site and the chemisorbed oxygen, respectively. We assumed that these reactions proceed only when gaseous oxygen is present. The mechanism is close to that proposed by Ahmed et al.[4] One of the great differences is that we assume the amount of the short-lived oxygen is immeasurably small as Walker et al. assumed in the earlier paper[3]. In other words, we assumed that the short-lived oxygen is formed through Eqs. 1, 2, 4 and 6 only when gaseous oxygen interacted with carbon surface and the oxygen complex. The reactions in which only the short-lived oxygen surface intermediate participates are marked by an asterisk (*).

The validity of the proposed mechanism can be examined in more detail using the results

129

obtained in this work. The balance of the ^{18}O after the $^{18}O_2/^{16}O_2$-step is easily established as stated above, because we analyzed all the ^{18}O containing species including the amount of ^{18}O retained in the sample. Then the amount of chemisorbed oxygen, $n_O(18)$, at a certain time is estimated by summing up the ^{18}O evolved as CO(30), $CO_2(46)$, and $CO_2(48)$ from the end of the reaction. Utilizing the $n_O(18)$ values estimated, the formation rates of CO(30) and $CO_2(46)$were plotted against $n_O(18)$ in Figures 4a and 4b at three reaction temperatures. Both rates increased with the increase of $n_O(18)$ as expected, but linear relationships did not hold. Since CO(30) is produced *via* Eq. 3, the CO(30) formation rate should be directly proportional to $n_O(18)$ if CO(30) was produced from only the stable oxygen complex. However, this was not the case, indicating that the contribution of the short-lived oxygen must be taken into account to explain the CO(30) formation. The relationship between the $CO_2(46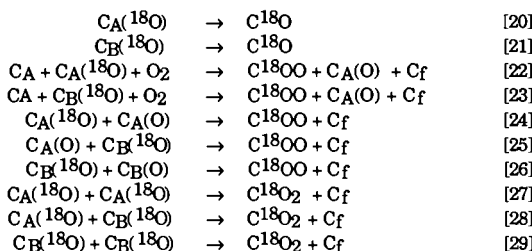)$ formation rate and $n_O(18)$ in Fig. 4b cannot be explained by only Eqs. 4 and 5 as far as we assume only single oxygen complex.

Then the mechanism was rewritten assuming two active sites, C_A and C_B, and in consequence two oxygen complexes, $C_A(O)$ and $C_B(O)$, as follows:

$$
\begin{array}{lll}
C_A + O_2 & \rightarrow & C_A(O) + CO & ; r_{1A} & [7] \\
C_B + O_2 & \rightarrow & C_B(O) + CO & ; r_{1B} & [8] \\
2C_A + O_2 & \rightarrow & 2\,C_A(O) & ; r_{2A} & [9] \\
2C_B + O_2 & \rightarrow & 2\,C_B(O) & ; r_{2B} & [10] \\
C_A(O) & \rightarrow & CO + C_f & ; r_{3A} & [11] \\
C_B(O) & \rightarrow & CO + C_f & ; r_{3B} & [12] \\
C_A + C_A(O) + O_2 & \rightarrow & CO_2 + C_A(O) & ; r_{4A} & [13] \\
C_A + C_B(O) + O_2 & \rightarrow & CO_2 + C_A(O) & ; r_{4B} & [14] \\
C_B + C_A(O) + O_2 & \rightarrow & CO_2 + C_B(O) & ; r_{4C} & [15] \\
C_B + C_B(O) + O_2 & \rightarrow & CO_2 + C_B(O) & ; r_{4D} & [16] \\
C_A(O) + C_A(O) & \rightarrow & CO_2 & ; r_{5A} & [17] \\
C_A(O) + C_B(O) & \rightarrow & CO_2 & ; r_{5B} & [18] \\
C_B(O) + C_B(O) & \rightarrow & CO_2 & ; r_{5C} & [19]
\end{array}
$$
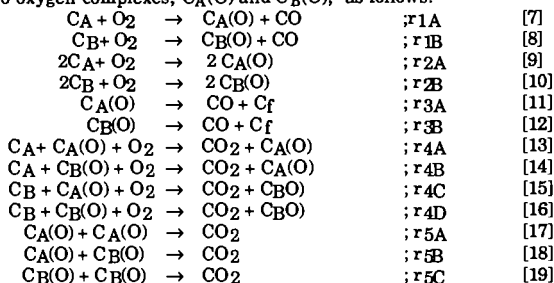
where $C_A(O)$ and $C_B(O)$ represent the short-lived oxygen complex and the stable oxygen complex, respectively. The contribution of Eq. 6 was neglected, because the amounts of $C_A(O)$ and $C_B(O)$ do not change through the reaction. r_{1A} to r_{5C} represent the reaction rates.

The validity of the reaction mechanism was tested using the change in the ^{18}O containing species after the $^{18}O_2/^{16}O_2$-step. The mechanistic sequence for this case is simplified as follows:

$$
\begin{array}{lll}
C_A(^{18}O) & \rightarrow & C^{18}O & [20] \\
C_B(^{18}O) & \rightarrow & C^{18}O & [21] \\
C_A + C_A(^{18}O) + O_2 & \rightarrow & C^{18}OO + C_A(O) + C_f & [22] \\
C_A + C_B(^{18}O) + O_2 & \rightarrow & C^{18}OO + C_A(O) + C_f & [23] \\
C_A(^{18}O) + C_A(O) & \rightarrow & C^{18}OO + C_f & [24] \\
C_A(O) + C_B(^{18}O) & \rightarrow & C^{18}OO + C_f & [25] \\
C_B(^{18}O) + C_B(O) & \rightarrow & C^{18}OO + C_f & [26] \\
C_A(^{18}O) + C_A(^{18}O) & \rightarrow & C^{18}O_2 + C_f & [27] \\
C_A(^{18}O) + C_B(^{18}O) & \rightarrow & C^{18}O_2 + C_f & [28] \\
C_B(^{18}O) + C_B(^{18}O) & \rightarrow & C^{18}O_2 + C_f & [29]
\end{array}
$$

Under the steady state gasification the total amount of chemisorbed oxygen, n_O, is kept constant, and both n_{OA} and n_{OB} would be kept constant. Then the following relationships would hold:

$$
\begin{array}{ll}
n_{OA} + n_{OB} = n_O \quad \text{(constant)} & [30] \\
n_{OA}(16) + n_{OA}(18) = n_{OA} \quad \text{(constant)} & [31] \\
n_{OB}(16) + n_{OB}(18) = n_{OB} \quad \text{(constant)} & [32]
\end{array}
$$

Using the data for the changes in the ^{18}O species after the $^{18}O_2/^{16}O_2$-step and the relationships of Eqs. 30 to 32, we could determine the reaction rate constants, k_{3A}, k_{3B}, $k_{4A}[C_A]+k_{4B}[C_A]$, $k_{4C}[C_B]+k_{4D}[C_B]$, k_{5A}, k_{5B}, and k_{5C}, and the values of n_{OA}, n_{OB}, and n_O which appear in r_{3A}, r_{3B}, r_{4A}, r_{4B}, r_{4C}, r_{4D}, r_{5A}, r_{5B}, and r_{5C}. Then the rate constants, $k_{1A}+k_{1B}$, and $k_{2A}[C_A]+k_{2B}[C_B]$ could be estimated using the change in the formation rate of CO(28), the relationship of Eq. 30 and the parameters determined above. Thus all the rate constants were estimated, although some can not be determined independently. The rate constants at 570°C are shown in Table 2, and the calculated curves using these parameters are compared with the experimental data in Figure 5. Fairly good agreements were obtained between the calculated curves and the experimental data over the whole course of gasification, although most of the parameters were estimated using the changes in the ^{18}O species after the $^{18}O_2/^{16}O_2$-step. We could estimate the amounts of both n_{OA} and n_{OB}, and could clarify that n_{OA} is much smaller than n_{OB}. These results seem to support the validity of the mechanistic sequence given in Eqs. 7 to 19.

At 570°C the ratio of $r_{1A}+r_{1B} : r_{3A} : r_{3B}$ for the CO formation was 4 : 3 : 3, and the ratio of $r_{4A}+r_{4B} : r_{4C}+r_{4D} : r_{5A} : r_{5B} : r_{5C}$ for the CO_2 formation was 4 : 4 : 1 : 2 : 2. These values clearly indicate the importance of the direct reactions between the active site and the gaseous oxygen as well as the desorption and/or reaction of chemisorbed oxygen(s),

supporting the observations given in Figs. 2a to 2c.

CONCLUSION

A square-input response (SIR) technique was applied to analyze the carbon-oxygen reaction. Actual *in situ* transient behaviors of isotopes were successfully traced. Most significant findings are as follows: Existence of two oxygen complexes, one is short-lived and the other is rather stable, was clarified, and their amounts were estimated. The importance of the direct attack of the gaseous oxygen to the active site and/or the chemisorbed oxygen was clarified. In addition, the significant contributions of the desorption of the oxygen complex and the reaction between the complexes to the gasification reaction were notified. The TK method was found not to reflect *in situ* desorption behavior of the oxygen complex at least for the reaction system studied here. Relative importance of elementary reactions was clarified. Further investigation is under way to examine the soundness of the proposed reaction mechanism and the determined rate parameters.

Literatures Cited

1. Laine, N.R.; Vastola, F.J.; Walker, P.L., Jr. J.Phys.Chem. **1963**, 67, 2030- 2034.
2. Tucker, B.G.; Mulcahy, F.R. Trans. Faraday Soc. **1959**, 65, 274-286.
3. Vastola, F.J.; Hart, P.J.; Walker, P.L., Jr. Carbon **1965**, 2, 65-71.
4. Ahmed, S.; Back, M.H.; Roscoe, J.M. ACS Division Fuel Chemistry, **1989**, 34, No.1, 63-70.
5. Freund, H.; Fuel, 1986, 65, 63-66.
6. Nozaki, T.; Adschiri, T.; Furusawa, T. Fuel Process. Techn. **1990**, 24, 277-283.
7. Jiang, H.; Radovic, L.R. ACS Division Fuel Chemistry, **1989**, 34, No.1, 79-86.
8. Lizzo, A.A.; Jiang, H.; Radovic, L.R. Carbon **1990**, 28, 7-19.
9. Kapteijn, F,; Meijer, R.; Moulijn, J.A. Energy & Fuels **1992**, 6, 494-497.
10. Kapteijn, F,; Meijer, R.; Moulijn, J.A.; Cazorla-Amoros, D. Carbon, 1994, 32, 1223-1231.
11. Zhuang, Q.; Kyotanim T.; Tomita, A. Energy & Fuels **1995**, 9, 630-634.
12. Miura, K.; Zha, H.; Hashimoto, K. *Proc. 30th Conf. Coal Sci., Tokyo, Jpan, Oct. 25-26,* **1993**, 63-66.
13. Miura, K.; Nakagawa, H,; Carbon Hashimoto, K. Carbon **1995**, 33, 275-282.
14. Crick, T.M.; Silveston, P.L.; Miura, K.; Hashimoto, K.; Energy & Fuels **1993**, 7, 1054-1061.

Table 1	The Rate Cnstants at 570 °C	
$k_{1A}+k_{1B}$	1.58	$min^{-1} \cdot kg^{-1} \cdot atm^{-1}$
$k_{2A}[C_A]+k_{2B}[C_B]$	1.78	$min^{-1} \cdot kg^{-1} \cdot atm^{-1}$
k_{3A}	1.1	min^{-1}
k_{3B}	0.075	min^{-1}
$(k_{4A}+k_{4B})[C_A]$	4.5	$min^{-1} \cdot atm^{-1}$
$(k_{4C}+k_{4D})[C_B]$	0.35	$min^{-1} \cdot atn^{-1}$
k_{5A}	1.2	$kg \cdot mol^{-1} \cdot min^{-1}$
k_{5B}	0.078	$kg \cdot mol^{-1} \cdot min^{-1}$
k_{5C}	0.01	$kg \cdot mol^{-1} \cdot min^{-1}$
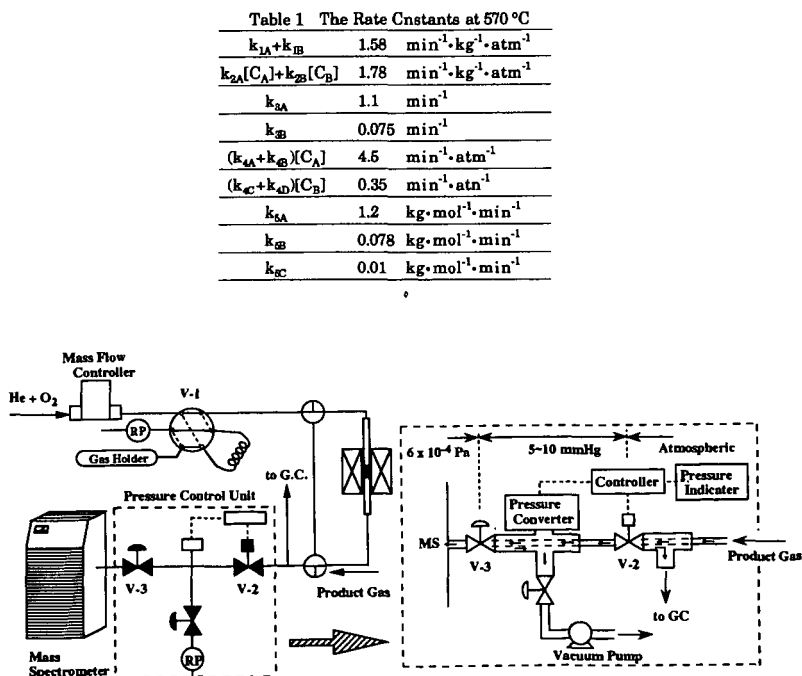
Figure 1 Experimental Apparatus
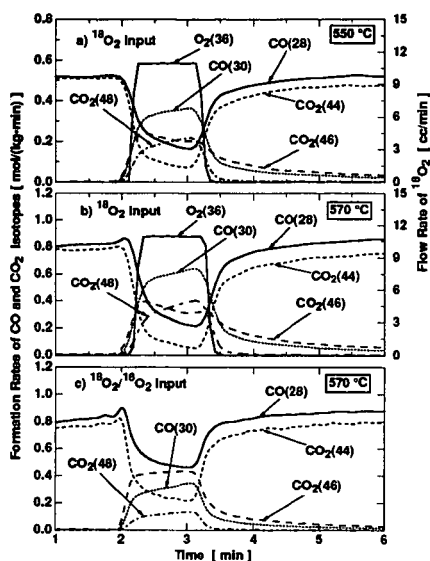
Figure 2 Changes in the formation rates of CO
and CO₂ isotopes of the SIR experiment
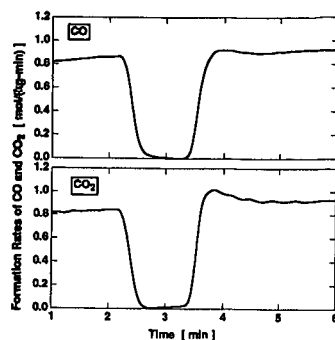

Figure 3 Changes in the formation rates of
CO and CO₂ SIR experiment using
square-input of the He
(Equivalent to the TK technique)
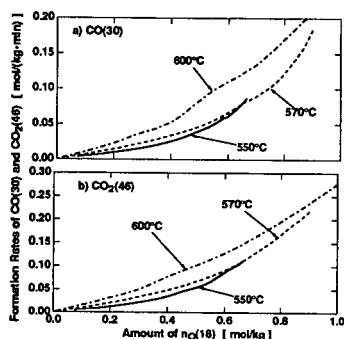

Figure 4 Relationships between formation
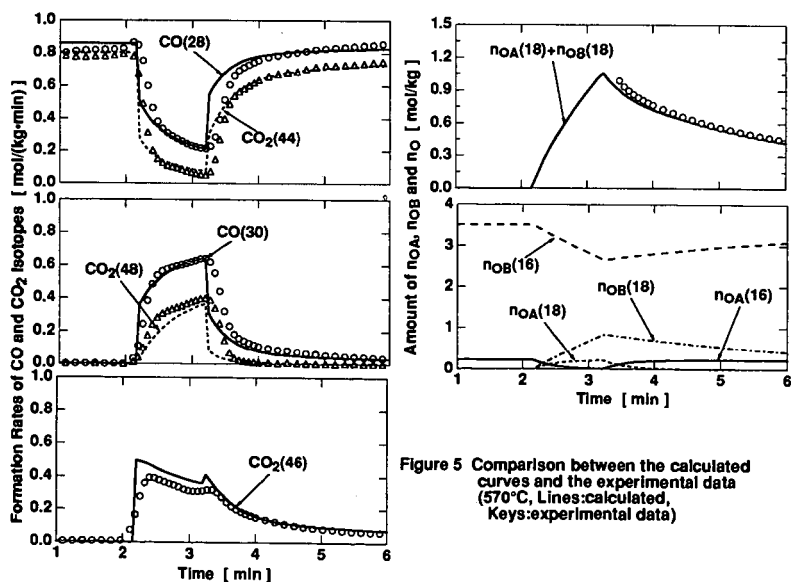rates of CO(30), CO₂(46) and n_O(18)

Figure 5 Comparison between the calculated
curves and the experimental data
(570°C, Lines:calculated,
Keys:experimental data)

132

ADSORBED MOLECULAR OXYGEN AND THE SURFACE BEHAVIOR OF SOOT

D. M. Smith, M. M. O. Atteya, B. K. Konowalchuk,
M. L. Rosenberger, and A. R. Chughtai
Department of Chemistry, University of Denver
Denver, CO 8020B

INTRODUCTION

A role of adsorbed molecular oxygen in surface reactions of black carbon (in the form of n-hexane soot) has been observed. Countless articles on the surface structure and reactivity of solid carbon, including several from this group (1-5), have identified carbon-oxygen surface functionalities as underlying adsorption or reactivity characteristics of specific materials. This paper describes, rather, several cases in which reversibly adsorbed molecular oxygen directly participates in phenomena occurring at the carbon surface.

RESULTS AND DISCUSSION

Hydration

A dependence of the extent of its surface hydration on soot aging was first observed in microgravimetric studies of water adsorption as a function of relative vapor pressure (6). Separate experiments in which freshly-prepared soot samples were exposed to pure O_2 prior to hydration with others evacuated prior to hydration, revealed significantly more and less water adsorption, respectively, compared with the fresh soot itself. Application of a modified Dubinin-Radushkevich (DR) equation (7) to the data enabled the determination of surface coverage and mass adsorbed per gram at limiting adsorption, and also at the point at which activated adsorption is essentially complete (the chemisorption limit).

The adsorption data (mass increase and the relative water pressure, P/P_o) from these measurements were treated with the DR equation to yield the results summarized in Table I.

Table I. Effect of Oxygen Adsorption on Soot Hydration

Soot	Limiting Adsorption $gx10^2/gs$	$\Theta_o{}^*$	Limiting Chemi- sorption $gx10^2/gs$	$\Theta_c{}^*$
24-hours O_2- contacted	1.76 ± 0.01	0.80 ± 0.02	0.507 ± 0.004	0.223 ± 0.004
Fresh	1.26 ± 0.01	0.58 ± 0.01	0.473 ± 0.005	0.217 ± 0.005
Evacuated	0.966 ± 0.006	0.44 ± 0.01	0.440 ± 0.003	0.202 ± 0.005

* Surface coverage using H_2O molecular area as $12.2Å^2$ (8), where Θ_o is at limiting adsorption and Θ_c at the chemisorption limit.

As is evident from these data, adsorption of water by the soot increases with O_2 coverage of the soot surface. For example, the limiting surface coverage (Θ_o) increases from 44% for evacuated fresh soot to 80% for the same material whose surface is saturated with O_2 at ambient temperature. Similarly, by comparing the adsorption of water at the chemisorption limit and at limiting adsorption, it is seen that the fraction of adsorbed water involving chemisorption decreases from about 46% to 29% as the surface O_2 increases. Since a smaller fraction of the (greater) adsorbate is involved in chemisorption on an O_2-saturated surface, a process involving the hydrolysis of

carboxylic functionalities, the adsorbed oxygen appears to be providing adsorption sites for water. A regular decrease in adsorbate affinity coefficient for water (6) with increased O_2 coverage, determined from the DR equation plot, further supports relatively more (weaker) H_2O-O_2 surface interactions.

Although the mechanism by which surface O_2 facilitates increased water adsorption is not yet clear, earlier experiments showed that it is properly described as physisorption (as opposed to activated adsorption). Figure 1 illustrates the effect of the sequential treatment of soot with flowing dry nitrogen, water
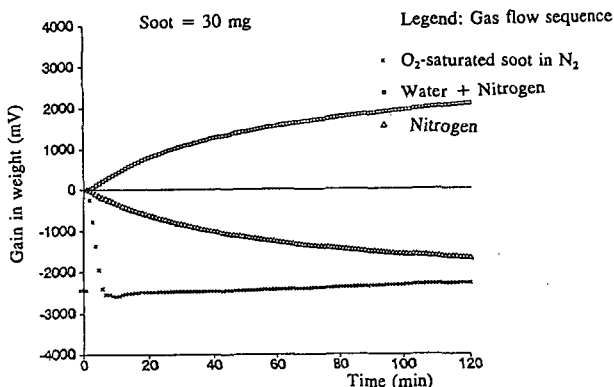

Figure 1.   Study of desorption and adsorption of O_2 and H_2O on soot (6).

vapor plus nitrogen and then nitrogen again. Microgravimetric measurement of mass change reveals a rapid substantial loss when an O_2-saturated sample is subjected to flowing nitrogen, apparently most of it the loss of physisorbed O_2. Subsequent to resetting the microbalance, treatment with water vapor plus nitrogen, and then flowing nitrogen again shows the usual hydration pattern and removal of water adsorbate, respectively. Considerable quantities of molecular oxygen may be adsorbed on freshly-prepared n-hexane soot and are involved in the water adsorption by, and hydration of, the soot surface.

EPR Studies
The observation by EPR of significant concentrations of unpaired electrons in n-hexane soot(1), consistent with their existence in coals and other graphitic carbonaceous materials, suggested the use of spin density as a probe of the behavior of adsorbed molecular oxygen which is paramagnetic. The effect of adsorbed O_2 is to increase the width and to decrease the intensity of the EPR spectrum of soot, changes reflected in an increased peak-to-peak line width, decreased peak height, and decreased normalized integral of the single absorption having a g value of 2.0046. Accordingly, series of replicate measurements using X-band CW EPR on freshly prepared soot samples were carried out. These samples, attached to the vacuum line through a special manifold within a heating mantle, were evacuated at 100°C in the 10^{-6} torr range overnight before exposure to accurately measured pressures of pure O_2. Figure 2A is a plot of the corrected normalized integral (CNI) versus P_{O_2}, where the error bars represent the standard deviation of individual measurements. The CNI for soot evacuated in this manner, before addition of O_2, is (1.62 ± 0.07) x 10^7. The linear relationship between spin density and physisorbed O_2 (assumed proportional to gas phase pressure) over the pressure range from 0 to 35 torr demonstrates not only the interaction between the unpaired electron spins of molecular

134

oxygen and soot, but also provides a means of monitoring the surface behavior of O_2 during adsorption or reaction.
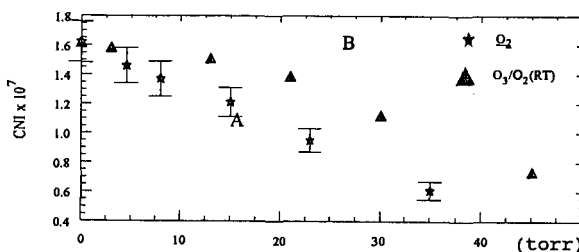

Figure 2. Effect of O_2 on the EPR signal of soot.

The Ozone-Soot Reaction

A detailed study (9) of the reaction between n-hexane soot and ozone at low concentrations has revealed a role of adsorbed molecular oxygen. This complex reaction involves essentially three stages. Following a fast initial catalytic decomposition of O_3, a rapid soot mass increase accompanied by CO_2 and H_2O formation is itself followed by a long period of soot oxidation in which the rate of O_3 loss is second order in O_3 (9). It is during the second stage of this reaction that material balance calculations, based upon careful analysis of products and reactants, reveal an involvement of O_2 in that stage. Expressing the oxygen atom content of reactants and products in micromoles, the overall reaction results in a net loss of O_3 oxygen (as O_2 from catalytic decomposition) in the amount of about 20% which does not yield measurable O-containing product. During this second stage of the reaction, from 2.5 to 30% of reaction, however, the O atom gain in products averages 70%, a gain which is not from O_3 oxygen.

A plot of CNI of the soot EPR spectrum versus gas pressure (1.5% O_3 in O_2) is Figure 2B, to be compared with the same plot for O_2 alone (Figure 2A). At lower pressures, the rate of spin density decrease with increased O_3/O_2 is much less than with O_2 alone, while beyond 20 torr the slopes of the two plots are essentially the same. These data appear to confirm the consumption of a fraction of the O_2 in a reaction which does not leave it for physisorption. A plausible interpretation is that the rapid reaction with O_3, actually probably O atom from its dissociation, yields fragments on the carbon surface which are reactive with O_2. The soot is not similarly reactive with O_2 alone under ambient conditions. We are not aware of other such examples of physisorbed O_2 involvement in surface reactions of black carbon. To the extent that soot " aging" is an annealing of the surface by physisorbed O_2, this effect also must underlie the difference in rate laws for the O_3-soot reaction (9) between freshly prepared and aged soot; for example,

Initial rate = $k[O_3](soot)^{1/2}$ (1)
versus
Initial rate = $k'[O_3] + k''(soot)$ (2)

respectively.

Other Adsorptions
SO_2

Because of the likelihood that adsorbed molecular O_2 plays a role in other soot surface reactions, in the manner discovered for the O_3 reaction, our studies of adsorption on soot also have included O_2 as adsorbate. The rapid oxidation of SO_2 at the soot surface which requires the presence of O_2 and H_2O, for example,

is one important case. The coadsorption of O_2 and SO_2 on n-hexane soot has been examined in detail.

Figure 3 shows the gain in mass of 10 mg soot as a function of
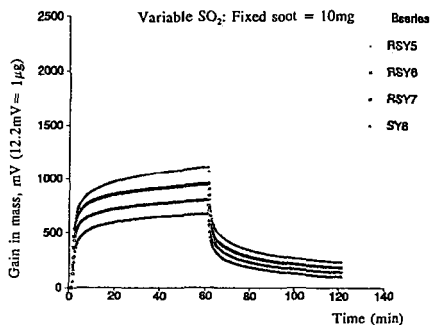
Figure 3. Adsorption of SO_2 on soot.

time in the presence of 606, 1010, 1515, and 2020 ppm SO_2. These were flow experiments in which the medium was zero air. At 60 minutes, the SO_2 flow was stopped and the microgravimetric cell (6) continued to purge with the zero air alone. The rapid loss of SO_2 from the surface follows a pattern which is the inverse of the adsorption, indicating physisorption of SO_2 according to

$$SO_{2\,(g)} + SS \underset{k_{-1}}{\overset{k_1}{\rightleftharpoons}} SS.SO_2(ads) \qquad (3)$$
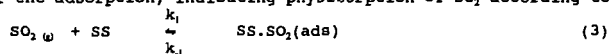
$$K = k_1/k_{-1} = [SS.SO_2(ads)]/[SO_2(g)][SS] \qquad (4)$$

where SS = surface site for SO_2.

From 85 to 79 percent of the SO_2 behaves in this manner, respectively, as indicated by the asymptotic approach of the microgravimetric curve to a limiting mass value greater than the initial. Another pathway, probably surface hydration and possibly oxidation, apparently exists for SO_2 as well; water molecules cannot be rigorously excluded from the surface under these conditions.

The coadsorption of SO_2 and O_2 were studied by EPR, and the results are summarized in Figure 4. No effect of SO_2 on the

Figure 4. Effect of SO_2 on soot.

normalized integral of soot's EPR signal is observed, this lack of effect extending to 10^5 ppm. (The small decline from the 1.62

136

is due to a trace of O_2 in the SO_2 sample). The significance of this study is to be found in the fact that 1) O_2 has the same effect on the spin density of soot on which SO_2 is physisorbed as it does on pure soot, and 2) at a constant O_2 coverage, SO_2 has no effect; no O_2 is displaced by SO_2. This suggests that surface oxida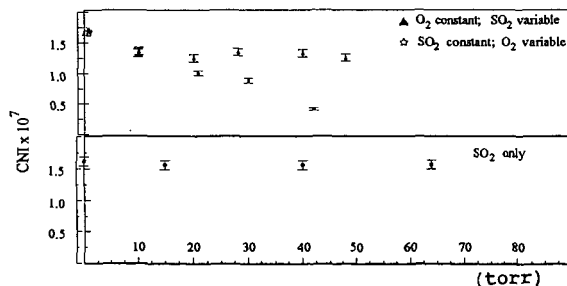tion of SO_2 by O_2 does not occur measurably at these surface coverages. Either O_2 and SO_2 do not compete for the same sites or the soot surface-O_2 interaction is stronger than that between soot and SO_2. Calculations based on the specific surface of n-hexane soot (89m²/g), masses of O_2 and SO_2 adsorbed per gram of soot under the experimental conditions, and established surface areas for the adsorbed molecules (19.2 Å² for SO_2 (10), 14.1 Å² for O_2 (11), indicate that SO_2 occupies nearly the same fraction of the surface (~18%) that O_2 (~20%) does, which means that about 1/3 less SO_2 molecules than O_2 are adsorbed per unit mass of soot under the conditions of zero air (125 torr O_2) and 2000 ppm SO_2. In the case of paramagnetic O_2, the surface coverage is no doubt governed by the surface density of soot's unpaired electrons, where the SO_2 is not influenced by that factor.

NO and NH₃
Evidence of the effect of adsorbed molecular O_2 on the adsorption of both NH_3 and NO has been found as well. These molecules, unlike the reversibly adsorbed SO_2 species, compete with O_2 for surface sites. Microgravimetric studies of NH_3 adsorption at higher concentrations, carried out in a variety of gas phase environments, reveal this competition which probably has its origin in the hydrogen bonding capacity of NH_3. EPR studies of the competition of NO and O_2 for unpaired electron sites on soot clearly show a surface interaction between NO and O_2 as well. Experiments on both of these systems continue.

REFERENCES
1. Akhter, M. S.; Chughtai, A. R. ; Smith, D. M., Appl. Spectrosc. 1985, 39, 143.
2. Akhter, M. S.; Chughtai, A. R. ; Smith, D. M., Appl. Spectrosc. 1985, 39, 154.
3. Chughtai, A. R. ; Jassim, J. A.; Peterson, J. A.; Stedman, D.H.; Smith, D. M., Aersol. Sci. Technol. 1991, 15, 112.
4. Akhter, M. S.; Chughtai, A. R. ; Smith, D. M., Appl. Spectrosc. 1991, 45, 653.
5. Smith, D. M.; Chughtai, A. R., Trends. Appl. Spectrosc. 1993,1, 325.
6. Chughtai, A. R.; Brooks, M. E.; Smith, D. M., J. Geophys. Res., 1995, in press.
7. Kobayashi, M.; Ishikawa, E.; Toda, Y., Carbon 1993,31,990.
8. Harkins, W. D. ; Jura, G. J., J. Am. Chem. Soc. 1944, 66, 1366.
9. Smith, D. M.; Chughtai, A. R., J. Geophys. Res., 1995, in press.
10. Billinge, B. H. M., in Second Conference on Industrial Carbon and Graphite, Society of Chemical Industry, London, 1966; p. 399.
11. Adamson A. W., Physical Chemistry of Surfaces; 5 ed., Wiley, N.Y., 1990; p. 612.

THE EFFECT OF CO_2 PARTIAL PRESSURE ON GASIFICATION REACTIVITY

L. Zhang and J.M. Calo
Chemical Engineering Program
Division of Engineering
Brown University
Providence, Rhode Island 02912, U.S.A.

INTRODUCTION
The mechanisms by which varying partial pressures of oxidant gases affect char reactivity remains a matter of controversy. In the current communication we explore the effect of CO_2 partial pressure on the resultant populations of intermediate oxygen complexes on char surfaces and their relationship to reactivity.

EXPERIMENTAL
The samples used in the experiments were Wyodak subbituminous coal char samples produced from coal obtained from the Argonne Premium Coal Sample Bank [1], and a resin char produced from phenol-formaldehyde resin synthesized in our laboratory. The latter was used as a prototype of a non-mineral matter-containing char. Char samples were produced in a tube furnace in flowing ultrahigh purity helium at 1000°C for two hours.

Partial pressure variation was achieved using CO_2/helium mixtures. All the oxidation and thermal desorption experiments were carried out in the TPD-MS/TGA apparatus. For gasification, the samples were exposed to the CO_2/helium gas mixtures at one atmosphere at a selected temperature to a certain degree of burn-off. The gasification conditions selected for the current work were 825°C, 20% burn-off for Wyodak coal char, and 900°C, 5% burn-off for resin char. The thermal desorptions were all carried out at a heating rate of 50K/min to 1200°C in flowing ultrahigh purity helium carrier gas.

RESULTS AND DISCUSSION
The overall or global reaction order for the char-CO_2 reaction remains a matter of controversy. The typical Langmuir-Hinshelwood-type steady-state rate expressions, as obtained for the Mentser and Ergun [2] oxygen exchange mechanism for example, suggest that the reaction should be first order at low pressures, changing gradually to zeroth order behavior at higher pressures. Turkdogan and Vinters [3] reported half-order dependence at pressures less than 10 atm, and zeroth order behavior at pressures of 10-20 atm. Koenig *et al.* [4] also reported half-order behavior. Blackwood and Ingeme [5] reported that at high pressure, the gasification rate remains dependent on CO_2 partial pressure to a positive order. On the other hand, the gasification data of Johnson [6] for a bituminous coal char in CO/CO_2 mixtures over the range 2-35 atm, showed a decreasing effect of CO_2 pressure on the gasification rate at high pressures. A similar trend was reported by Golovina [7], who reported first order behavior at near-atmospheric pressure, tending to zeroth order over the 3-10 atm range, followed by decreasing gasification rate with CO_2 partial pressure in the 20-40 atm range. In the current work, the apparent reaction orders observed for CO_2 partial pressures of one atmosphere and less, were 0.71 for resin char and 0.60 for Wyodak coal char.

Obviously, the apparent reaction order varies considerably with the nature of the char and gasification conditions, which makes it difficult to compare data from various sources and predict/correlate reactivity. Moreover, most of the interpretive/correlative models are based on one or two-site models which tend to oversimplify the nature of char surfaces and mechanisms. Most chars exhibit distinctly energetically heterogeneous surfaces which can have a significant effect on the behavior of the apparent reaction order. For example, Calo and Perkins [8] demonstrated that surface heterogeneity can result in half-order behavior under certain conditions, and that the observed reaction order depends in a complex manner on the nature of the surface. For these reasons, here we focus on investigations of correlations between reactivity and populations of the intermediate oxygen surface complexes which desorb to gasify the char.

Figure 1 presents CO TPD spectra for resin char samples gasified in various CO_2/He mixtures. As shown, the broad desorption peak is centered at about 1010°C. The total amount of oxygen surface complexes increases with CO_2 partial pressure, but not homogeneously over the entire TPD spectrum. That is, the higher temperature surface complexes fall off more rapidly than the lower temperature complexes. These observations are consistent with those of Kapteijn *et al.* [9] who reported that increasing the CO_2 partial pressure from 0.1 to 1 atm increased the number of stable, higher temperature complexes more than the low temperature, unstable complexes.

Figure 2 presents the corresponding data for Wyodak coal char samples. The same qualitative behavior observed for resin char is readily apparent, although the desorption is peaked at a lower temperature of about 950°C. In addition, the total amount of oxygen surface complexes is about a factor of three or so greater than for the resin char.

The Rate-Controlling Step. It has been concluded by some workers that CO_2 gasification is

desorption rate-controlled [Marchon *et al*. [10]; Cerfontain *et al*. [11]; Chen and Yang [12]; Calo and Hall [13]; and Mentser and Ergun [2]. However, Kapteijn *et al*. [9] contend that for uncatalyzed CO_2 gasification, two processes are operative: (1) the decomposition of semiquinone/carbonyl surface complexes; and (2) the decomposition of an "out-of plane" oxygen complex which can be formed upon oxidation by CO_2 of a saturated carbon atom adjacent to an edge carbon which is already bonded to an oxygen atom. This latter type of oxygen complex has been shown to cause a substantial weakening of neighboring carbon-carbon bonds, and its decomposition results in the formation of a gas phase CO molecule and a semiquinone-type surface complex. This model explained their step-response data quite well, and supports the earlier mechanistic reasoning of Blackwood and Ingeme [5]. It was also concluded that the relative contribution of the two processes to the gasification rate is controlled by the CO_2 partial pressure.

In order to address the issue of the rate-controlling step in the current work, the following types of experiments were performed. Following gasification, samples were rapidly quenched to room temperature in either pure helium or the reactive gas mixture. This was done to assess whether or not the surface was saturated with oxygen surface complexes at gasification conditions. It was reasoned that if the gasification reaction was not controlled by the desorption step, unoccupied active sites would exist which by cooling in the reactant mixture would form additional oxygen surface complexes as the temperature decreased. Consequently, the resultant TPD spectra would differ from those obtained following rapid quenching in helium.

In Figure 3 are presented the corresponding desorption spectra for resin char following gasification in 1 atm of CO_2. As shown, the two spectra are practically identical. This result implies that gasification in pure CO_2 for resin char under these conditions is indeed desorption rate-controlled. However, as shown in Figure 4, the corresponding spectra following gasification in a 60/40 CO_2/He mixture yielded distinctly different TPD spectra. As shown, the principal difference lies in the low temperature surface complex populations. That is, the CO desorption over the temperature range between 600 and 900°C for the sample cooled down in the reaction mixture is greater than that for the sample cooled in He. This result is interpreted to mean that unoccupied active sites exist during the steady-state gasification in the 60/40 CO_2/He mixture under these conditions. These unoccupied active sites remained unoccupied when the samples were cooled down in He, but were populated with oxygen complexes in cooling down in the reaction mixture. Consequently, it is concluded that gasification departs from desorption rate-control as the CO_2 partial pressure decreases from 1 atm.

Distribution of Desorption Activation Energies. The observation that the population of oxygen surface complexes does not decrease evenly over the entire TPD spectrum suggests that the char surface exhibits a distribution of desorption activation energies. Du *et al*. [14] and Calo and Hall [13] have developed distributed activation energy models for the desorption of oxygen surface complexes from carbons following O_2 and CO_2 gasification. In the current work, the distribution of desorption activation energies was calculated using the method described by Calo and Hall [13]. The relationship between the instantaneous CO desorption rate and the distribution of desorption activation energies can be expressed as:

$$d[CO]/dt = [C-O]_0 S(E^*) dE^*/dt \qquad [1]$$

where E^* is the local desorption activation energy, as approximated by an instantaneous step at energy E^*, $S(E^*)$ is the desorption activation energy probability density function, $d[CO]/dt$ is the desorption rate of oxygen surface complexes as CO during TPD, and $[C-O]_0$ is the total initial (i.e. prior to the initiation of desorption) amount of CO-evolving oxygen surface complexes on the surface. Based on the classical work of Redhead [15], the parameters are related by:

$$E^*/RT = \ln [\upsilon_0 T/\beta] - 3.64 \qquad [2]$$

which holds for for $10^8 < \upsilon_0/\beta < 10^{13}$ (K^{-1}), where υ_0 is the pre-exponential factor for the desorption rate constant, T is the temperature, and β is the heating rate. Since a TPD experiment gives the instantaneous desorption rate directly, and dE^*/dt can be obtained from Eq. [2], the distribution of desorption activation energies, $[C-O]_0 S(E)^*$, can be determined from Eq. [1].

The value of the pre-exponential factor, υ_0, was assumed to be a constant. A series of TPD runs was performed at various heating rates from 25K/min to 100K/min for the same oxidized char samples. It was determined that a value of $\upsilon_0 = 10^{10}$ min^{-1} yielded the best fit in that it produced essentially the same energetic distribution for all the heating rates. This proved to be the best value for both resin and Wyodak char. Consequently, this value was used for the determination of the distributions of desorption activation energies.

Figure 5 presents the resultant desorption activation energy distribution for Wyodak coal char gasified in various CO_2/He mixtures. As can be seen, as the CO_2 partial pressure during gasification decreases, the desorption activation energy distribution of the char also changes.

The same trend was also found for resin char samples gasified in various CO_2/He mixtures. In comparison to the results for Wyodak coal char, the energetic distributions of oxygen surface complexes for the resin char samples are shifted to higher energies. It is also noted that mineral matter (most probably calcium) in the Wyodak coal char plays a significant role in determining the population of the low temperature surface complexes which turn over most rapidly during gasification. The absolute amount of the low temperature oxygen surface complexes is much higher for Wyodak coal char than for the resin car, which contains no mineral matter. Therefore the mineral matter in the Wyodak coal char "catalyzes" the formation of low desorption activation energy surface complexes. This represents the basis of the catalytic effect in this char. This is the principal reason that the reactivity of Wyodak coal char is significantly greater than that for resin char even at lower gasification temperatures.

Correlation of Reactivity. For conditions where the gasification rate is desorption rate-controlled, the reactivity can be correlated using the distribution of desorption activation energies. This is accomplished by integrating the desorption rate over the entire distribution:

$$r = \int_0^\infty \upsilon_0 \exp(-E^*/RT) [C-O]_o S(E^*) dE^* \qquad [3]$$

Figure 6 presents a parity plot of predicted *vs.* measured reactivities for Wyodak coal char in one atmosphere of CO_2 as a function of temperature, as determined from Eq. [3] using the desorption activation energy distribution obtained at 825°C. As shown, the agreement is reasonably good. Similar results were obtained for resin char. Therefore, it can be concluded that the correlation of reactivity with the TPD desorption rate is feasible.

SUMMARY AND CONCLUSIONS
The objective of this work was to explore the relationship among reactivity, CO_2 partial pressure, and post-reaction TPD spectra. The results show that CO_2 partial pressure has a significant effect on the population of oxygen surface complexes for both resin and Wyodak coal chars. Generally, the oxygen surface coverage increases with increasing CO_2 partial pressure. It was also determined that gasification reactivity is desorption rate-controlled in 1 atm of CO_2 for both chars. However, as the CO_2 partial pressure decreases, the formation rates of surface complexes become comparable to the desorption rates, and the reaction rate begins to deviate from desorption rate-control.

For heterogeneous char surfaces, the distribution of desorption activation energies can be determined from TPD desorption rates. Prediction/correlation of reactivities from the desorption activation energy distribution is shown to be feasible for the carbon-CO_2 reaction operating under desorption rate-controlled conditions for both resin and Wyodak coal char.

It is possible that the most labile, low temperature oxygen surface complexes that are observed to increase in concentration with increasing CO_2 partial pressure may be of the type hypothesized by Kapteijn *et al.* [9] and Chen *et al.* [16], as being formed by the interaction of CO_2 with existing surface complexes. If this is so, then the thermal desorption methods applied here would reveal a shift or interconversion between labile and stable complexes with increasing pressure. This is a subject of continuing studies.

ACKNOWLEDGEMENT

REFERENCES
1. Vorres, K.S., Users Handbook for the Argonne Premium Coal Samples, ANL/PCSP-93/1, DOE, Argonne, Il, 1993.
2. Mentser, M., and S,. Ergun, *US Bur. Mines Bull.* 644 (1973).
3. Turkdogan, E. T. and Vinters, J. V., *Carbon* 7, 101, (1969).
4. Koenig, P. C., Squires, R. G. and Laurendeau, N. M., *Carbon* 23, 5, 531 (1985); *Fuel* 65, 412 (1986).
5. Blackwood, J.D., and A.J. Ingeme, *Aust. J. Chem.* 13, 194 (1960).
6. Johnson, J.L., *Kinetics of Coal Gasification*, Wiley, NY, 1979.
7. Golovina, E.S., *Carbon* 18, 197 (1980).
8. Calo, J.M. and Perkins, M. T., *Carbon* 25, 395 (1987).
9. Kapteijn, F., R. Meijer, J.A. Moulijn, and D. Cazorla-Amorós, *Carbon* 32, 1223 (1994).
10. Marchon, B., Tysoe, W.T., Carrazza, J., Heinemann, H., and Somorjai, G.A., *J. Phys. Chem.* 92, 5447 (1988).
11. Cerfontain, M.B., Meijer, R., Kapteijn, F., and Moulijn, J.A., *J. Catal.* 107, 173 (1987).
12. Chen, S. G. and Yang, R. T., *J. Catal.* 138, 12 (1992); 141, 102 (1993).
13. Calo, J.M: and P.J. Hall, in *Fundamental Issues in the Control of Carbon Gasification Reactivity*, J. Lahaye and P. Ehrburger, eds, NATO ASI Series, Series E: Applied Sciences, Vol. 192, p. 329, Kluwer Academic Publishers, Dordrecht, 1991.
14. Du, Z., A.F. Sarofim, and J.P. Longwell, *Energy & Fuels* 4, 296 (1990).
15. Redhead, P.A., *Vacuum* 12, 203 (1962).
16. Chen, S.G., R.T. Yang, F. Kapteijn, and J.A. Moulijn, *IEC Res.* 32, 2835 (1993).
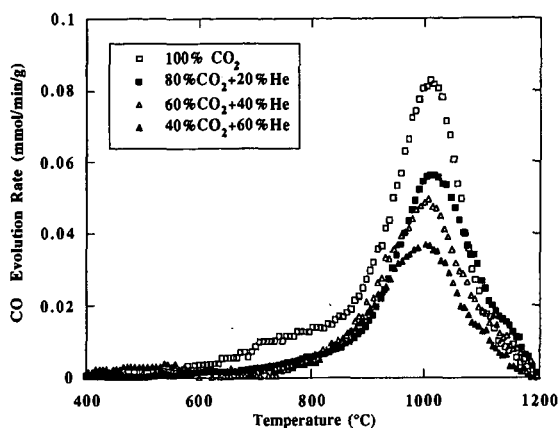
Figure 1. CO TPD spectra from resin char gasified in 1 atm of CO_2/He mixtures at 900°C to 5% burn-off.
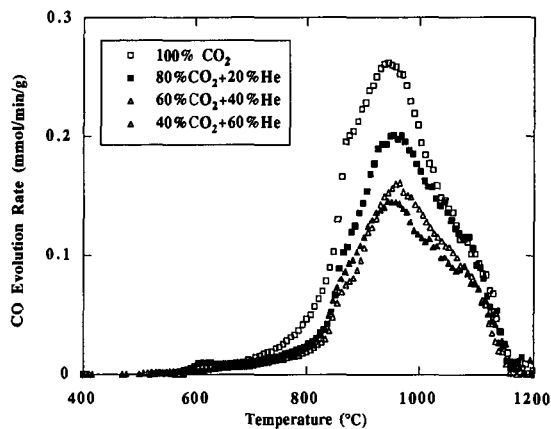
Figure 2. CO TPD spectra from Wyodak coal char gasified in 1 atm of CO_2/He mixtures at 825°C to 20% burn-off.
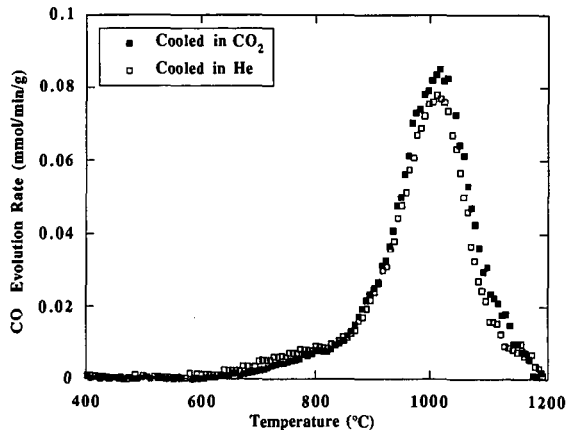
Figure 3. CO TPD spectra from resin char gasified in 1 atm of CO_2 at 900°C to 5% burn-off, following quenching in helium and CO_2.
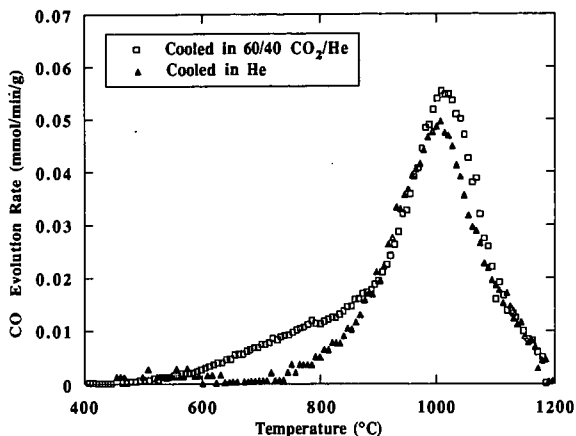
Figure 4. CO TPD spectra from resin char gasified 60/40 CO_2/He at 1 atm, 900°C to 5% burn-off, following quenching in helium and CO_2.
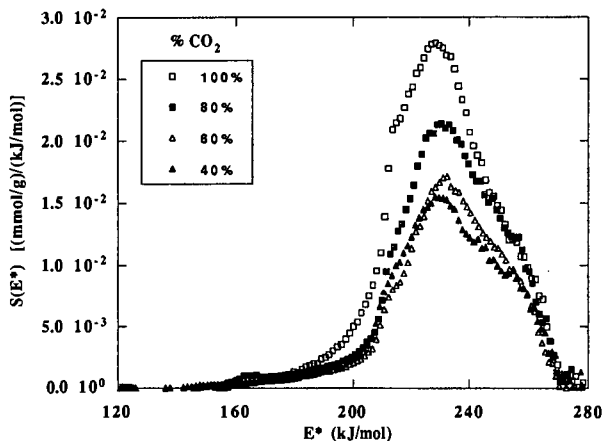
Figure 5. Distributions of desorption activation energies from TPD spectra presented in Figure 2 for Wyodak coal char gasified in CO_2/He mixtures at 825°C, 1 atm to 20% burn-off.
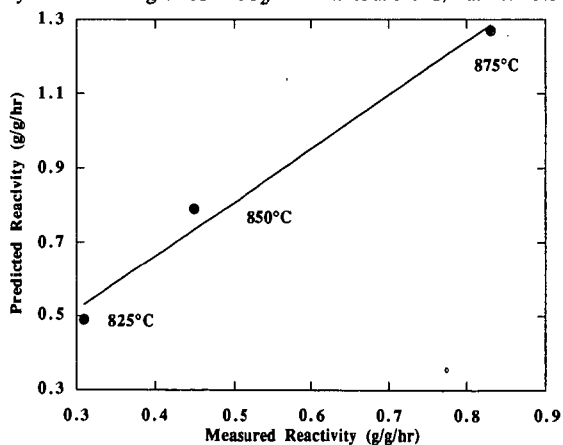
Figure 6. Predicted vs. measured reactivities for Wyodak coal char gasified in 1 atm of CO_2 to 20% burn-off.

ON THE ROLE OF CARBON-OXYGEN SURFACE COMPLEXES
IN THE CARBON/OXYGEN REACTION MECHANISM

K. Skokova and L. R. Radovic
Fuel Science Program
Department of Materials Science and Engineering
The Pennsylvania State University, University Park, PA 16802

KEYWORDS: carbon, gasification, oxygen complexes

INTRODUCTION

In the past, attempts to characterize the reactivity of carbon materials have led to conclusions regarding the importance of active sites and carbon-oxygen (C(O)) complexes in the carbon/O_2 reaction mechanism [1,2]. More recently, questions have been raised concerning the possibility of oxygen presence on the basal plane during gasification. Studies with disordered (turbostratic) carbons (e.g., polymer-derived carbons and coal chars) revealed that the quantity of C(O) complexes on the surface at gasification conditions exceeds significantly the quantities formed during low-temperature chemisorption [3-5]. One of the possible mechanistic explanations for this experimental fact is the so-called "spillover effect" whereby oxygen atoms, chemisorbed on the edge sites of carbon crystallites, migrate ("spill over") from the edges to the basal plane [5]. Spillover is the process that occurs when active species, C(O) complexes, are formed on one type of sites (e.g., edges), and are subsequently transferred to another type of sites (e.g., basal plane). Although the basal plane does not participate directly in carbon gasification, it serves as an additional reservoir of oxygen. A larger quantity of oxygen resides on the surface at higher temperatures, because spillover is an activated process.

Since it is rather difficult (or even impossible) to trace the fate of oxygen atoms on the basal plane by experimental techniques, theoretical molecular orbital calculations seem to be very attractive. Results of such calculations [6-11] have shown that there are no obstacles for the presence of oxygen atoms on the basal plane at temperatures at which gasification of carbon takes place.

Yang and Wong [12] were the first to provide experimental evidence for the presence and mobility of oxygen on the basal plane. Pan and Yang [10] have reiterated that basal-plane oxygen should be taken into consideration in the analysis of high-temperature CO desorption spectra. More recently, Chen et al. [11] showed that an oxygen atom on the basal plane lowers the binding energy of a neighboring C-C bond by 30%; therefore, it is important for the analysis of carbon reactivity. In our previous paper [13], a reaction mechanism was proposed according to which the quantity of basal-plane oxygen determines the CO/CO_2 product ratio.

The objective of the present communication is to pursue a further understanding of the role of basal-plane and edge C(O) complexes in the formation of CO and, especially, CO_2. Both theoretical and experimental techniques were used.

MECHANISM OF CO AND CO_2 FORMATION

The proposed mechanism of CO and CO_2 formation (Figure 1) follows from the reaction mechanism discussed in Ref. [13]. Carbon monoxide forms *via* decomposition of a C(O) complex at the edge of a carbon crystallite. Carbon dioxide, which is known to be a primary reaction product [14], forms by interaction and simultaneous decomposition of adjacent edge and basal-plane C(O) complexes. Formation of CO requires cleavage of two C-C bonds and is straightforward. The transition-state complex for CO_2 formation is more complicated; it requires the simultaneous cleavage of three bonds (two C-C and one C-O bond) and the formation of one C-O bond.
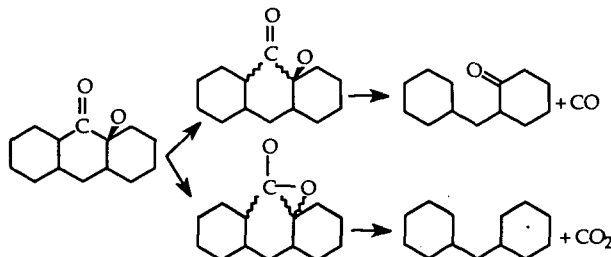

Figure 1. Proposed mechanism for CO and CO_2 formation in the C/O_2 reaction.

MOLECULAR ORBITAL CALCULATIONS

The objective of these computer simulations is to assess how the activation energy for C-C bond dissociation depends on the quantity and nature of surrounding $C(O)$ complexes. The results of such calculations allow us to estimate the relative changes in the rates of CO and CO_2 formation as the concentration of edge and basal-plane oxygen atoms changes. In addition, bond energies for oxygen atoms on the basal plane were calculated in order to show that basal-plane oxygen can indeed exist on the surface at reaction conditions.

The calculations were performed using a molecular orbital theory package (MOPAC 5). The PM3 semiempirical parametric method with unrestricted Hartree-Fock Hamiltonian was used. A seven-ring structure (coronene) was chosen as a model for the carbon surface. The edges were saturated with either hydrogen or oxygen atoms (Figure 2). In addition to the basic structures a, b and c, structures with oxygen on the basal plane in various positions were considered. With the aid of MOPAC, the geometries of each model structure were optimized, and heats of formation of the resulting structures were calculated.

The bond energy of oxygen on the basal plane was calculated as an enthalpy change in the hypothetical reaction of oxygen atom removal from the surface. The resulting bond energies of the basal-plane oxygen in different positions are shown in Table I. It appears that the most stable position of oxygen is between two carbon atoms, rather than right above a carbon atom. This is in agreement with the findings of other authors [6-10]; the absolute values of bond energies are also in agreement with the literature data [7-9]. The rather large bond energies indicate that the basal-plane complex could be present on the surface, and should be included in the reaction mechanism.

Figure 3 shows how the heat of formation of several model structures changes as the distance between carbon atoms 1 and 2 increases and the coordinates of all atoms except 1 and 2 are allowed to relax. The smallest distance corresponds to the unbroken C1-C2 bond, and the largest distance corresponds to the broken C1-C2 bond (zero bond order). The point of maximum energy corresponds to the geometry of a transition-state complex. The difference between the heats of formation of the transition-state complex and the initial structure is equal to the activation energy of the C1-C2 bond cleavage reaction.

As the quantity of both edge and basal-plane $C(O)$ complexes increases, the stability of the C-C bond is seen to decrease. For example, upon addition of a second edge oxygen atom, the activation energy of C1-C2 bond cleavage decreases from 64.7 kcal/mol (structure b) to 48.9 kcal/mol (structure c); similarly, it decreases from 30.7 kcal/mol for structure b_1 to 5.5 kcal/mol for structure c_1. More dramatic changes occur when additional basal-plane oxygen accumulates on the surface. The potential barrier diminishes from 64.7 to 30.7 kcal/mol (structures b and b_1, respectively), and from 48.9 to 5.5 kcal/mol (structures c and c_1, respectively). This result is in agreement with the important experimental fact that the activation energy for oxygen complex removal decreases as the surface coverage increases [15,16].

As it follows form the reaction mechanism shown in Figure 1, cleavage of the C1-C2 bond is a reaction path for CO formation. Therefore, the above results imply that the activation energy for CO formation decreases and the CO formation rate increases with increasing population of both edge and basal-plane oxygen on the surface.

Unfortunately, because of their complexity, no molecular orbital calculations of the potential barrier for CO_2 formation were done to date, and the influence of $C(O)$ complexes on the rate of CO_2 formation was not determined. However, some speculative conclusions can be made on the basis of stability of the C1-C2 bond. Calculations show that for structures with basal-plane oxygen (b_1 and c_1), C1-C2 bond cleavage is an exothermic reaction; therefore, it is probably favored thermodynamically. For structure c_1, the exothermicity of bond cleavage together with a low activation energy (5.5 kcal/mol) implies that this structure is not very stable, and its transition to the structure with the broken C1-C2 bond is more favorable. This in turn suggests that structure c_1 does not give any CO_2 upon its decomposition. This will enhance the above mentioned relative increase in CO formation as the amount of oxygen on the surface increases.

In conclusion, the addition of edge oxygen to structure b_1 and addition of basal-plane oxygen to structure c both lead to an increase in the CO/CO_2 ratio in the products of decomposition of $C(O)$ complexes present on the surface. In the next section, these predictions are compared with experimental results.

EXPERIMENTAL RESULTS AND DISCUSSION

In this section, the relative amounts of CO and CO_2 in the temperature-programmed desorption (TPD) patterns of two different carbon samples are analyzed as a function of the quantity of C(O) complexes on the surface.

Carbon samples were prepared by carbonization of petroleum pitch and cellulose at 1000 °C. Samples were oxidized at 600 °C in a mixture of 20% O_2/80% Ar until ~20% burnoff, and then cooled to room temperature at the fastest possible rate (~100 °C/min in the beginning of cooling) either in O_2 or in Ar. After cooling and without any exposure to air, the samples were analyzed by TPD. The products of surface oxygen complex decomposition were monitored by a quadrupole mass spectrometer.

The procedure of cooling the samples in different atmospheres allows one to prepare samples with different surface concentrations of C(O) complexes, while preserving the same total surface area; so the effect of surface area variations is minimized. During the cooling stage in O_2, chemisorption of oxygen produces additional C(O) complexes on the surface. Since gasification is not taking place, these complexes remain on the surface and are revealed in the subsequent TPD analysis. During the cooling stage in the inert gas, no additional oxygen chemisorption occurs; instead, desorption of the least stable (reactive) C(O) complexes takes place.

The TPD spectra of two pitch-based carbon samples are presented in Figure 4. In agreement with the work of Ranish and Walker [17] and Lizzio *et al.* [4], the sample cooled in O_2 has a much higher amount of oxygen on the surface; it also has a higher amount of CO in the decomposition products. Very similar results were obtained for two cellulose-based samples (Figure 5); although the total amount of C(O) complexes is much less dependent on the manner of cooling, the CO/CO_2 ratio is again higher for the sample that was cooled in O_2.

Therefore, the CO/CO_2 ratio in the products of TPD increases as the quantity of surface oxygen increases. This result is in excellent agreement with the results of molecular orbital calculations. An increasing amount of oxygen on the surface would lead to a larger proportion of structures of type c_1 relative to b, b_1 and c, of structures c relative to b, and of structures b_1 relative to b. According to the molecular orbital calculations discussed previously, all of this would lead to an *increasing quantity of CO in the products of decomposition of these complexes.*

It is important to emphasize that the observed increase in the CO/CO_2 ratio (in the products of TPD) with increasing quantity of C(O) complexes is exactly the opposite to what is commonly observed during carbon gasification in O_2. In agreement with the literature data [2], we have found that the CO/CO_2 ratio decreases as the total amount of C(O) complexes increases during gasification in O_2. In order to explain these different trends, which are thought to contain important mechanistic clues [18], further investigation of the effects of surface oxygen on O_2 chemisorption *vs.* C(O) complex decomposition is needed.

REFERENCES

1. Laine, N. R., Vastola, F. J., and Walker, P. L., Jr., *J. Chem. Phys.* **67**, 2030 (1963).
2. Phillips, R., Vastola, F. J., and Walker, P. L., Jr., *Carbon* **7**, 479 (1969); **8**, 205 (1970).
3. Taylor, R. L., Ph.D. Thesis, Penn State University (1982).
4. Lizzio, A. A., Jiang, H., and Radovic, L. R., *Carbon* **28**, 7 (1990).
5. Walker, P. L., Jr., Taylor, R. L., and Ranish, J. M., *Carbon* **29**, 411 (1991).
6. Bennett, A. J., McCarroll, B., and Messmer, R. P., *Phys. Rev. B* **3**, 1397 (1971).
7. Hayns, M. R., *Theoret. Chim. Acta* **39**, 61 (1975).
8. Barone, V., Lelj, F., Iaconis, E., Illas, F., Nino, R. and Jounou, A., *J. Mol. Struct.* **136**, 313 (1986).
9. Fromherz, T., Mendoza, C., and Ruette, F., *Mon. Not. R. Astron. Soc.* **263**, 851 (1993).
10. Pan, Z., and Yang, R. T., *Ind. Eng. Chem. Res.* **31**, 2675 (1992).
11. Chen, S. G., Yang, R. T., Kapteijn, F., and Moulijn, J. A., *Ind. Eng. Chem. Res.* **32**, 2835 (1993).
12. Yang, R. T., and Wong, C. J., *J. Chem. Phys.* **75**, 4471 (1981).
13. Skokova, K., and Radovic, L. R., Proc. 22nd Biennial Conference on Carbon, 1995, San Diego, CA, p. 608.
14. Hart, P. J., Ph.D. Thesis, Penn State University (1966).
15. Vastola, F. J., Hart, P. J., and Walker, P. L., Jr., *Carbon* **2**, 65 (1964).
16. Ahmed, S., and Back, M. H., *Carbon* **23**, 513 (1985).
17. Ranish, J. M., and Walker, P. L., Jr., *ACS Preprints (Div. Fuel Chem.)* **32**(4), 132 (1987).
18. Ranish, J. M., and Walker, P. L., Jr., *Carbon* **31**, 135 (1993).

Table I. Bond energies of oxygen atom on the basal plane in different positions, in kcal/mol.

Structure	Position of oxygen on the basal plane			
	above C2	between C2 & C3	above C3	between C3 & C4
a	29.0	39.7	25.8	35.9
b	38.6	45.8	26.5	37.1
c	68.6	63.6	37.7	49.3
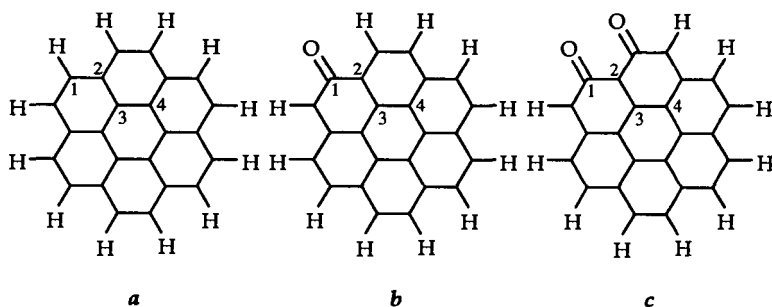
Figure 2. Model carbon structures used for molecular orbital calculations.

structure *b*

structure *b* with oxygen atom attached to carbon atom C2 (structure b_1)

structure *c*

structure *c* with oxygen atom attached to carbon atom C2 (structure c_1)
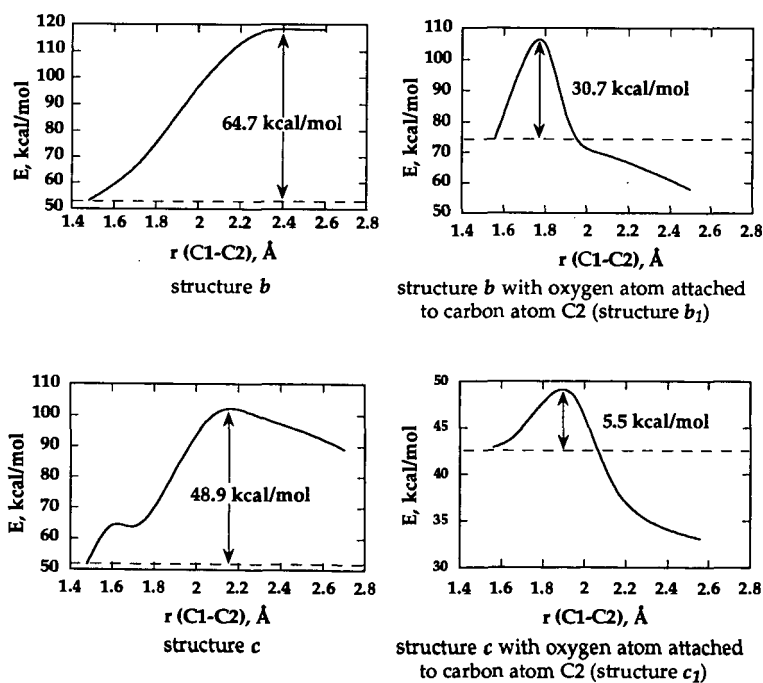
Figure 3. Potential curves for the reaction of C1-C2 bond cleavage.

Figure 4. TPD profiles of petroleum pitch-derived carbon after gasification in O_2 until 20% burnoff followed by cooling in O_2 or Ar.
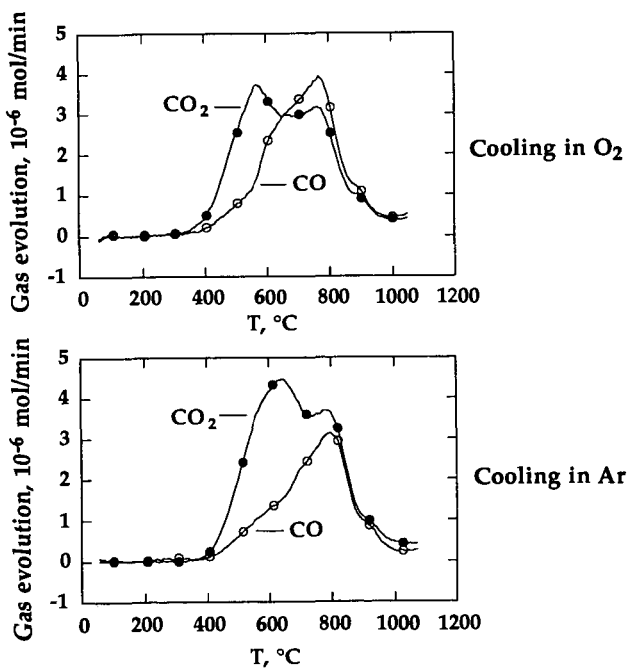
Figure 5. TPD profiles of cellulose-derived carbon after gasification in O_2 until 20% burnoff followed by cooling in O_2 or Ar.

ON THE RELATION BETWEEN STRUCTURE AND REACTIVITY IN THE CARBON OXYGEN REACTION

D. Herein, J. Find, B. Herzog, H. Kollmann, R. Schmidt, R. Schlögl
Fritz Haber Institut der Max Planck Gesellschaft,
Faradayweg 4-6, D- 14195 Berlin, FAX -4930-8413-4401
H. Bartl
Institut für Kristallographie der Universität Frankfurt,
Senckenberganlage 30, D- 60054 Frankfurt,
Ch. Troyer
Institut für Analytische Chemie, Technische Universität Wien
Neubaugeb. 5/11 A-1070 Wien

INTRODUCTION

The oxidation of graphite is a reference process for both generation of energy by combustion and for fundamental aspects of gas-solid interface reactions. The absence of large perfectly ordered crystals of graphite render rigorous model studies under surface science conditions very difficult despite the significant efforts in this area with large synthetic graphite surfaces(1). With integral kinetic techniques such as TPRS and instationary kinetic data a detailed mechanistic picture has been developped in a longstanding effort introducing a fraction of the geometric surface as active surface and the competition of two types of oxygen surface complexes which are either static and hence inhibiting or mobile and hence reactive in gasification(2,3,4). In 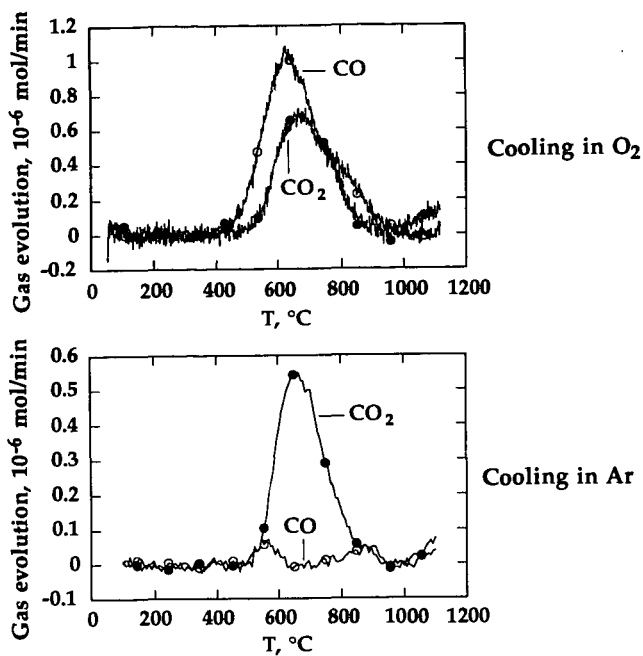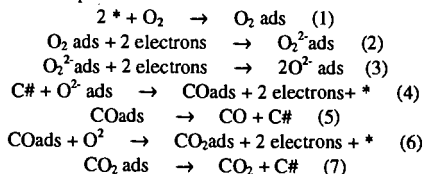addition, the selectivity to CO and CO_2 was traced back to different types of reactive surface intermediates with carbonyl or lactone structures respectively(5). The present contribution is an attempt to investigate the reaction with experiments aimed at selected atomistic aspects of the mechanistic picture. In a previous study the gasification of HOPG was found to procede at low temperatures (200 K) and low oxygen partial pressures (10^{-5} mbar) on suitably prepared surfaces (6). In this work as well as in many other reports(1,2,5) the importance of defects was pointed out which are either present in the substrate or may be created during reaction. In the model experiment (6) self-passivation occured after very little conversion due to the creation of strongly adsorbed oxygen inhibiting low-temperature oxidation. The existence of strongly adsorbed oxygen and weakly adsorbed oxygen (2,3,7) in two different bonding geometrics is a common ingredient to kinetic models of graphite oxidation.

Graphite oxidation is the prototype of a topotactic reaction proceeding only at the prism faces which should lead to a uniform shrinkage of the individual particles in uncatalysed reaction. Parallel to the recession mechanism there are basal plane defects which cause pitting corrosion creating additional prismatic faces during gassification and contribute in a difficult to control way to the overall rate. Other types of defects pin the edge recession e.g. by the occurence of local sp^3 bonding leading to a continous change in the length of the reaction interface and the creation of micro-hills (8) on reacting surfaces.

We used large flakes of RFL (0.5-1.2 mm dia.) and powders AF (3-1-μm dia.) natural graphite from Kropfmühl (Bavaria) which was purified from silicate and metal residues by basic melt and acid leaching. Standard gassification conditions were 20% oxygen in nitrogen and 927 K reaction temperature.

Modelling of the reaction is necessary to link macroscopic rate observations which are often severely affected by mass- and energy transport limitations with a minimum set of elementary step reactions describing the overall process:

$$2 * + O_2 \quad \rightarrow \quad O_2 \, ads \quad (1)$$
$$O_2 \, ads + 2 \, electrons \quad \rightarrow \quad O_2^{2-} ads \quad (2)$$
$$O_2^{2-} ads + 2 \, electrons \quad \rightarrow \quad 2O^{2-} \, ads \quad (3)$$
$$C\# + O^{2-} \, ads \quad \rightarrow \quad COads + 2 \, electrons + * \quad (4)$$
$$COads \quad \rightarrow \quad CO + C\# \quad (5)$$
$$COads + O^2 \quad \rightarrow \quad CO_2 ads + 2 \, electrons + * \quad (6)$$
$$CO_2 \, ads \quad \rightarrow \quad CO_2 + C\# \quad (7)$$

These steps of reductive activation and carbon oxidation at a suitable defect(#) comprise the minimum number of reaction steps for the overall oxidation. It is evident that besides the reaction centre a second type of chemisorption site (*) is required for the reductive activation of oxygen which must exhibit an excess of delocalised electrons such as at the basal planes. These terrace sites are, however, unreactive for the nucleophilic activation product which implies the surface diffusion of the activated species. Some of these steps are different when homolytically activated oxygen from chemical or physical sources is involved (9). In this case, however, the topotactic reaction behaviour is lost. A key issue is the exact chemical nature and the location of the two types of active sites.
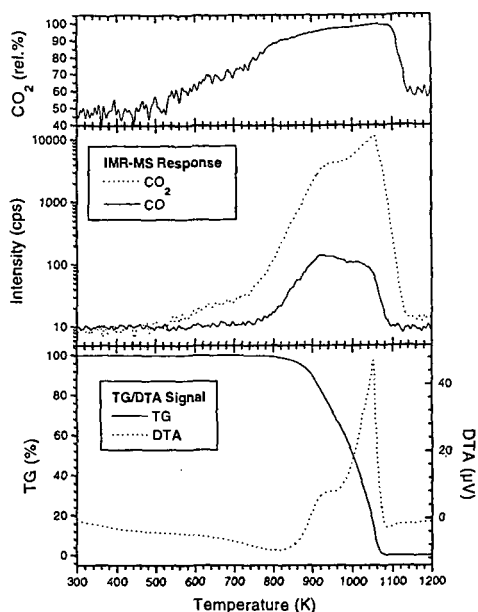
Fig.1: Selectivity, yield and TG/DTA response of an integral reaction experiment at standard conditions of a 0.5 cm bed composed of a 3:1 mixture of AF graphite with SiC powder in a coupled TG-IMR-MS experiment.

In Fig.1 we summarise macroscopic kinetic observations of a gassification experiment of AF graphite in an integral reactor. Sufficient dilution with silicon carbide ensured the presence of molecular oxygen at the reactor outlet at all temperatures applied. A special mass spectrometer of the IMR-MS ionisation type is applied for sensitive detection of CO and CO_2 without fragmentation overlap. Both the changes in selectivity and in rate (proportional to the DTA signal) indicate that the above reaction scheme is insufficient to explain the reaction progress in this case. The increase in CO_2 selectivity in the low-temperature regime complies with the initial removal of pre-formed C-O insertion structures. The second increase in CO_2 at high conversion would mean that the insertion of active oxygen in suitably defective carbon-carbon structures becomes increasingly dominating over the addition of active oxygen onto unsaturated edge sites. This can be seen as consequence of the increasing abundance of mobile surface atomic oxygen (4) creating a high virtual pressure of oxygen. The di-oxygen partial pressure and the increasing abundance of basal plane sites (C*) increase with burn-off in contrast to the decreasing abundance of oxidation sites (C#) due to the recession of prismatic faces.

Changes in rate and selectivity with burn-off were also observed in isothermal macroscopic experiments which were found to be critical in quantitative reproducibility. Thus it was felt that single particle gassification experiments should be useful. The alternative, to use less active reagents or to drastically reduce the temperature, may lead to better kinetic data but may not describe the reaction in the same kinetic state as it is characteristic for a practical combustion, i.e. a different reaction step may be rate-determining at low rates (10) than at higher rates.

RESULTS
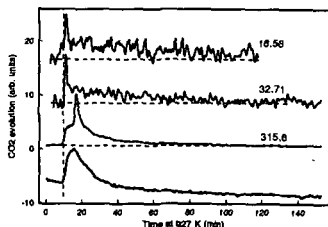
Fig.2: IMR-MS responses for single particle gassifications. The graphite weight in µg is used to designate the experiments. The top two traces refer to AF, the lower trace to RFL gassification. The unassigned trace is the water response for the RFL gassification. The vertical dashed line indicates the first time of constant oxygen partial pressure. At t=0 the heating in nitrogen was started. After reaching 927 K the gas was changed to oxygen in nitrogen. For the RFL experiment the oxygen was admitted in two steps at 11 and 20.5 min.

The simultaneous observation of the weight change and the gas evolution allowed to accurately fix the correct sample weight in single particle gassification experiments displayed in Fig. 2 which are heavily perturbed by bouyancy effects when starting the isothermal reaction after rapid heating in nitrogen. For AF oxidation a portion of the ceramic sample holder was dusted with graphite particles, for RFL single clean flakes (optical microscope) were used. In all cases after reaching a certain threshold partial pressure of oxygen a burst of reactivity occured which was followed by a continous activity at much lower level. For RFL graphite the threshold lies at about 5 vol% oxygen. Associated with the inital gassification is the desorption of water arising from oxidation of OH groups. The burst in reactivity is not connected with the creation of active sites from the OH group desorption as can be seen from the absence of a burst in the water trace. The data imply that an aged graphite surface is particularily reactive as the short duration of the burst excludes a location of the active centres underneath the surface.

The behaviour is reflected in the inital rates of reaction obtained from the weight change data.The observation that within the experimental accuracy both types of graphite with differing geometric surfaces gave comparable results indicates the integral character of the rate integrating over many processes and changes in local surface structure. Unexpected is the shape of the rate curve with time, as the initial gassification of a reactive surface followed by a steady state bulk reaction should not lead to a rate minimum which depends in its shape on type and mass of the graphite used. The characteristic time for reaching a constant rate is with about 120 min so long that a process of surface modification can be excluded. Moreover, comparison with the gas evolution data in Fig.2 reveals that the activity in gassification does not pass through a minimum but follows the expected behaviour. This implies that the weight change not only reflects the weight *loss* from gassification but indicates a simultaneous weight *gain* from the uptake of oxygen. Given that we are dealing with non-porous samples, the increase in weight cannot only be attributed to the formation of unreactive surface oxygen functions which can only cover a fraction of a monolayer (a monolayer of oxygen atoms on the geometric surface of a RFL flake would weigh about 0.002 µg, which is below the detection limit of the present experiment). We attribute the weight gain to the incorporation of oxygen in the bulk of the graphite sample. The effect is strongly dependent on temperature with a significant reduction in the detectable amount of incorporated oxygen with increasing temperature (less than 20% at 977 K compared to the amount at 927 K for RFL, for AF the effect is smaller than for RFL and so is the temperature dependence). The total amount of incorporated oxygen is with about 3 wt% of the RFL sample small enough to leave the question about its location in irregularities of the mosaic structure or as intercalate within the van-der Waals gaps of the regular crystallites. This will be discussed below.

STM can be used to reveal local details of the oxidation mechanism of graphite (8,11) as the reaction does not produce -as in metal oxidation reactions- scales of low electric conductivity. The extra high sensitivity of STM to roughness allows to image deviation from a planar surface with a sensitivity of 2-3 orders of magnitude higher than the lateral resolution of a survey image. This is illustrated in Fig.3 showing a RFL flake before gassification and the same flake after 20 % burn-off. The outer surface of the flake is rather irregular and exposes a high abundance of prismatic faces in form of micro-flakes sitting on top of the main particle. After partial gassification these micro flakes have all disappeared leaving a smooth surface with a considerably lower basal- to prism face ratio. It is noted that none of the steps seen in this image are monosteps. The minimum height is 3 steps and only odd numbers of graphene layers were observed to constitute these stable edges. The impression of the regularity is adventitious, there are many situations with irregular edges on the over 1200 images which were analysed. The different appearance of the steps in different directions is due to the uneven shape of the STM tip used for imaging. These tips have to be extra coarse in order to survive the frequent crashes which are unavoidable in imaging such rough surfaces. From these images it becomes apparent why gassification starts with a high initial rate as the intermixing of the two active centres of planar basal planes for oxygen activation and of rough prism faces for oxidation is much better than after removal of the microflakes. The images fit well to the integral observations of the rate measurements. The triangular rows in image 3C indicate the local interruption of the surface electronic conductivity by firmly held adsorbates such as strongly bound oxygen atoms decorating lines of defects in the partly gassified crystal. Ribbons of dislocations which are normally detected by TEM contrast (12) are exposed to atomic oxygen and provide centres for stable functional group formation. The absence of atomic resolution in oxidised areas can further be seen in image 3D which shows the rare situation (8 out of 1200) of the co-existence of insulating islands of non-graphitic nature such as „carbon oxide" or diamond-like carbon with normal surfaces separated by a double- and single-atomic step structure. These two latter images reveal the presence of lines and areas of basal planes which are non-graphitic in character and provide evidence for a local chemical heterogeneiety.

Imaging monoatomic steps on graphite is rarely possible on cleaved surfaces. On oxidised surfaces it is, however, possible in particular at monoatomic etch pits. Fig.4A shows a situation in which a top crystallite exhibits a 120 deg edge while sitting on a monoatomic step. At this level of resolution the high degree of orientation along crystallographic main directions can be seen in areas with low defect density. Most remarkable is the different appearance of the two prism faces (triatomic step height) in two different directions. The analysis of the effect as function of the STM parameters reveals that the „structure" in one prism face is an artefact caused by the absence of electrical conductivity. This precludes imaging of the atomic arrangement but reveals that the local chemistry of the two prism face orientations is different with the structured face being largely covered by covalently bound oxygen groups. The other edge seems to be free of insulating bonds and may thus represent a more reactive face. These assignments are speculative as the observations are not possible during gassification (4). It remains, however, the evidence for a local difference in chemical interaction of differently oriented prismatic faces.
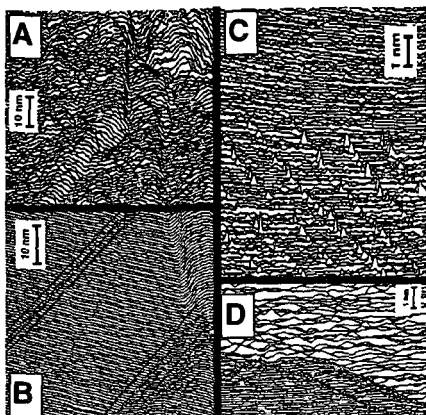
Fig.3: STM wide scans over a flake of RFL graphite before oxidation(A) and after 20% burn-off (B,C;D). A Burleigh ARIS 6000 instrument with a W tip was used: gap voltage + 50 mV, constant current 1.0 nA, raw data as line scans. Scan areas are: A,B: 300x300 nm,C:500x500 nm, D:50x50 nm

In image 4B the atomic resolution is illustrated of oxidised steps near a terminating basal plane defect. Two top graphene layers are sitting in different rotation angles relative to the supporting graphene layer. The fuzzy appearance of the steps is also due to an imaging artefact caused by a low electrical conductivity at the step edges. The striped appearance is a sign of the tip crashing into the step and requiring to travel over several atomic distances behind the steps to reach stable tunnelling conditions again. This is a strong indication of the presence of localised electronic states at the step edges and the absence of radicals or delocalised states at these locations. The presence of carbon-heterobonds (oxygen or hydrogen) is the likely explanation
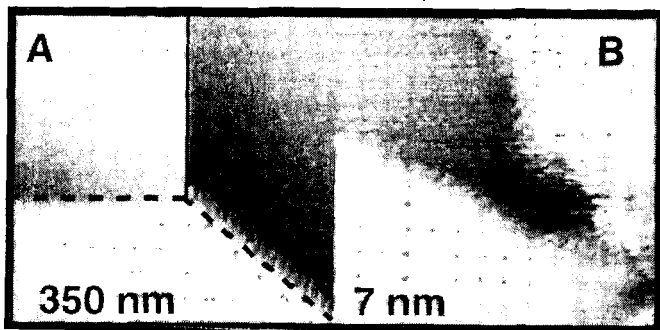

Fig.4: STM images of RFL after 50 % burn-off. In image A the dashed lines denote the contours of a top crystallite sitting over a plane with a monoatomic step (full line). In B the atomic resolution is achieved for oxidised monoatomic steps. The figures denote the lateral image size, the step heights were determined from profile scans (not shown). The imaging conditions were as in Fig.3.

which allows to experimentally support the chemical notion that the terminating graphene edges are the places of interaction between carbon and oxygen. This image reveals a possible zone of reactivity for addition (edges) and insertion (rows of atoms right behind the step) of activated oxygen. The formation of islands of modified carbon atoms within basal plane terraces as a consequence of gassification was not observed indicating that the spontaneous creation of gassification sites within perfect graphene sheets does not occur. This follows also from thermodynamics as the creation of the very first single vacancy requires 676 kJ/mol energy (13) whereas the produced CO_2 molecule contributes only 393 kJ/mole to the energy balance. The creation of vacancies becomes rapidly easier with defects already present (13). The necessity to have already an interruption in the graphene layer for the oxidation to procede, drives the reaction to clean basal planes (11) and to a topotactic progression along prism faces and along „a-priori" defect sites (4,14).

We failed to detect islands of oxygen at the terraces of the basal planes as they are seen in metal-oxygen interaction studies. This implies that the interaction of oxygen with the basal planes which is required for its activation is too weak to allow imaging by STM or that the STM tip field is sufficient to clear the imaging area on the basal planes. We have shown by TDS that both water and oxygen are adsorbed on basal planes and that the failure to see these adsorbates is an STM artefact(8).

X-RAX DIFFRACTION EXPERIMENTS

For the observation of a gas-solid interface reaction the bulk-sensitive technique of X-ray diffraction should not provide any useful data as the reacting surface is not probed by the

151

experiment. In continuation of our single particle analysis of the reaction we studied RFL flakes by Laue photographs as function of burn-off. The results are summarised in Fig.5.
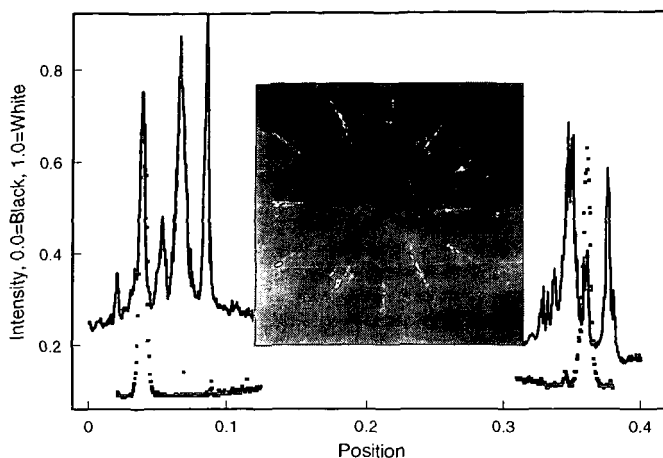

Fig.5. Laue Photographs (Mo kα radiation, beam parallel to the c-axis) of a RFL flake before oxidation (top densitometer trace and photograph) and after 20 % burn-off (bottom densitometer trace). It emerges very clearly that the flake was polycrystalline in (hk) orientation and became almost perfectly single crystalline after partial oxidation.

The data show that the flake was liberated from small crystallites throughout its volume. Moreover, the mosaic crystallites constituing the main part of the flake became better aligned in the basal plane (sharp profile after partial oxidation). This observation is corroborated by the fact that Laue patterns (parallel a,b) showing the stacking order could not be obtained before oxidation but revealed a high degree of AB stacking after partial burn-off. This indicates that partial oxidation causes a kind of „chemical annealing". The most defective crystallites will be burnt away preferentially and so will be interstitial carbon in the interior of the mosaic crystal. This requires the action of oxygen not only on the geometric surface but also at the inner surfaces of defective regions. This is seen in parallel to the small but detectable storage of oxygen in the initial phase of oxidation. We would thus locate the oxygen not as an intercalate in between the graphene galleries but rather as „bubbles" located at defects.

In-situ powder diffraction studies of the (002) reflection under standard gassification conditions were performed in order to support this interpretation. Intercalation, even in small quantities should lead like in residue compounds to a splitting and broadening of the (002) reflection. Initial experiments with HOPG as sample and Si as internal standard seemed indeed to support the notion about the residual intercalation (15). Frequent repetion of the experiment in different diffractometer geometries and with different graphite materials revealed, however, that the observed drastic changes in lineprofiles are diffraction artefacts caused by the uncontrolled sample movement exposing differently misaligned sections of the mosaic crystal to the diffraction condition. The lineprofile became increasingly symmetric and significantly narrower with progressing oxidation after removing this artefact. This is exemplified in Fig.6 The unsteady course of the difference curve at low temperatures indicates the residual positionning problems of the RFL sample. A persistent reduction of the linewidth close to the instrumental limit was observed after oxidation and cooling back to 300 K. The lattice constant was also observed to shrink irrevesibly after oxidation from the value of the Ar experiment which was found to be 340.12 (±0.03) pm at 873 K. The selectivity was also found to change with the structural parameters. The excess of CO_2 formation increased in parallel with the reducing FWHM and with the change in lattice spacing. In particular, the onset of all changes co-incided in all experiments suggesting a correlation of the effects. The defective structural parts gassify preferentially to CO, the better ordered graphitic carbon reacts preferentially to CO_2..

X-RAY ABSORPTION SPECTROSCOPY

The average local electronic structure is an important parameter in the reactivity scenario of the gassification as it provides information about the action of the di-oxygen activation as rate-determining step. XPS was found to be rather insensitive to the variation of carbon-carbon bonding within one type of graphite partly because of the photoemission physics and partly because of the ill-defined surface-sensitivity (16). This fact can be used advantageously in performing photoabsorption experiments at the carbon 1s edge using synchrotron radiation. In this experiment the insensitive photoemission process is the inital state allowing thus to interpret the spectra without having to account for initial state changes. The general shape of the spectra which allow cleary to discriminate π^* states from σ^* states has been discussed elesewhere(16, 17). In Fig.

152

7 some quantitative data about the π^* states are collected. A sample of HOPG was used for the reference experiment shown in the top panel. The changes in the polarisation of the π^* resonance
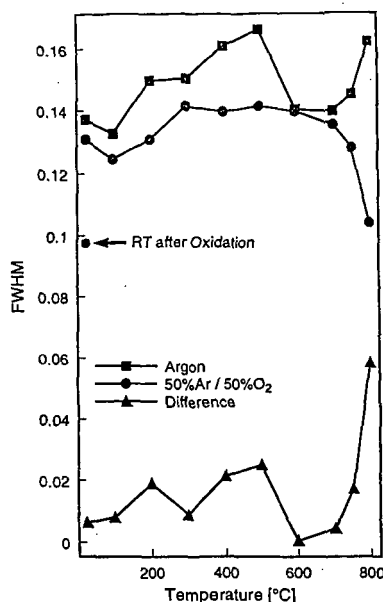

Fig.6: Evolution of the FWHM of the RFL graphite (002) reflection as function of in-situ treatment temperature. The data were obtained from Gaussian lineprofile fits. The difference plot proves the action of oxygen and not of temperature in the annealing procdure. The data were recorded after reaching steady state conversion at each temperature point in the oxidation scan and after 2h waiting under Ar respectively.

are compared for pristine, oxidised and Ar ion sputtered surfaces. Oxidation causes mainly a surface roughening by pitting giving rise to the small loss in polarisation at low angles between the light beam and the sample basal plane. The average electronic structure is, however, not different between pristine and oxidised graphite indicating that oxidation procedes on few sites on the surface and does not cover the surface with intermediate C-O groups. This precludes a significant reaction-induced increase in defect abundance. Sputtering of graphite with Ar ions destroys the surface and breaks many sp^2 bonds leaving a electronically highly disordered surface (18). This can also be seen drastically from the change in polarisation behaviour which indicates the loss of preferred orientation of the π^* orbitals (reduced slope) and the loss in abundance of sp^2 centers (smaller absolute value at high angles). This type of surface serves as model for a type of defects inhibiting oxidation by removing the delocalised electronic states required for the first three steps in the oxidation sequence. The fact that such an isotropic attack of the surface electronic structure does not occur during oxidation is a microscopic confirmation of the topotactic nature of the reaction requiring for its progression minority surface sites which are not located within the basal plane.

This technique is also suited to follow the evolution of the graphitic character with burn-off by examination of the intensity of the π^* resonance normalised to the carbon content as shown in the lower panel of Fig. 7. Changing the detection condition from total Auger yield to partial Auger yield allows to probe non-destructively the electronic structure depth-selective. The data show that with increasing burn-off the degree of graphitic surface increases both at the surface (topmost atomic layer) and in the bulk (some 10 nm). This is full in line with all other observations reported here and shows for a large area the „cleaning" effect detected by STM. It further shows that the oxidative bulk annealing reduces in the inital stage of gasification the abundance of non-graphitic carbon atoms.

CONCLUSIONS

The microscopic informations presented corroborate in general the traditional view about the reaction mechanism as a topotactic gas-solid reaction with two different active sites having to interact for efficient reaction. The prism faces seem to be chemically different according to their crystallographic orientation. They are, however, clearly the sites of carbon-heterobond formation. The consequence of the step is a pronounced modification of the electronic structure of the carbon atoms near the edge. These observations call for a structure-sensitivity of the reaction at different location of the active sites (e.g. variation after equations (5) and (6) of the mechanism). This would be in line with the picture of oxygen addition and insertion as being the elementary steps defining the selectivity. The conjecture that one of these reaction sites would mainly not be located near prism edges or „a-priori" defects is not supported by the data presented. The high thermal stability of the carbon heterobonds on an intact long-range-ordered prismatic edge (see Fig. 4) requires the overall high reaction temperature of the gasification in order to achieve steps (5) and (7) of the reaction sequence. Higher disordered reaction interfaces with an average lower carbon coordination number are benificial for a lower reaction temperature or a higher rate (Fig. 3).
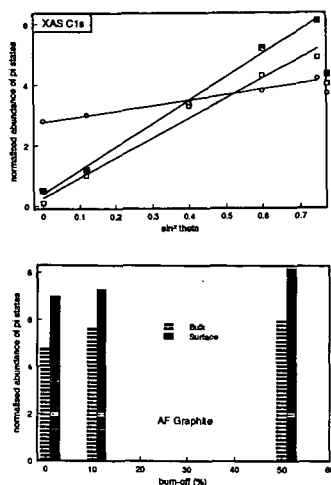
Fig. 7. Top: Angular dependence of the intensity of the 286 eV π* resonance for differently prepared HOPG surfaces. Oxidation was performed in-situ under standard conditions which created a large amounts of etch pits. Ar ion bombardment was carried out at 1 kV and 10-4 mbar Ar for 2 min. XAS data were recorded in the total yield mode at the HE PGM II station at the BESSY synchrotron. The bottom panel shows the evolution of the π* intensity with burn-off for AF graphite (external sample preparation). Surface sensitivity is created by comparison of total yield (0 eV, bulk) and partial yield (150 eV, surface) data.

The single particle experiments further gave evidence for the preferential burn-off of small crystallites with high initial rate covering the individual flakes. This process drives the reaction towards a state in which activation of chemisorbed di-oxygen according to reactions (1)-(3) is not rate-determining despite the overall small sticking coefficient of di-oxygen on graphite (001). This is taken as strong indication that the well-ordered basal planes provide active centers for reductive di-oxygen dissociation and exhibit a function in the gassification mechanism.

Incorporation of oxygen into graphite in weighable amounts was detected which is likely to be located in the voids of the mosaic crystal. It was not possible to produce unambigous structural evidence for regular intercalation of oxygen as islands between graphene layers. At the „internal" surfaces the oxygen removes preferentially lattice defects which allow oxidation-induced low-temperature annealing of the graphite crystal. The effect was detected by X-ray diffraction methods and by the observation of the action of mechanical forces providing activation energy for defect ordering (see Fig. 3 C). Careful oxidation of natural graphite flakes can lead to well-ordered samples.

Defects act on the gassification rate as promoters by interrupting the long-range electronic structure of the graphene edges or within the planes (pitting) without destroying the local electronic structure (Fig. 7) or as inhibitors by pinning the delocalised valence electrons within a few interatomic distances. The counteraction of these irregularities gives rise to an unpredictable rate of individual mosaic flakes. The generation of a sufficient number of defetcs to modify the surface electronic structure as detectable by a (small) change in average hybridisation or structural roughening was not observed.

ACKNOWLEDGEMENTS

REFERENCES
(1) S.R. Kelemen, H. Freund, *Carbon* 23, (1986), 619
(2) P.L. Walker jr., R.L. Taylor, J.M. Ranish, *Carbon*,29, (1991), 411
(3) J.A. Moulijn, F. Kapteijn, *Carbon*,33 (1995), 1155
(4) J.M. Ranish, P.L. Walker jr., *Carbon*, 31, (1993), 135
(5) R.N. Smith, D.A. Young, R.A. Smith, *Trans. Faraday Soc.*, 62, (1966), 2280
(6) R. Schlögl, G. Loose, M. Wesemann, *Solid State Ionics*,43 (1190), 183
(7) B. Henschke, H. Schubert, J. Blöcker, F. Atamny, R. Schlögl, *Thermochimica Acta*,234 (1994), 53
(8) R. Schlögl, F. Atamny, J. Wirth, J. Stephan, *Ultramicroscopy*,42-44, (1992), 660
(9) H. Marsh, T.E. O'Hair, R. Reed, *Trans. Faraday Soc.*, 61, (1965), 285
(10) I.M.K. Ismail, P.L. Walker jr., *Carbon*,27, (1989), 549
(11) L. Porte, D. Richards, P. Gallezot, *J. Microscopy*, 152, (1988) , 515
(12) M.M. Heerschap, P. Delavignette, *Carbon*, 5, (1967), 383
(13) A.P.P. Nicholson, D.J. Bakon, *Carbon*, 13, (1974), 275
(14) C. Roscoe, J.M. Thomas, *Proc. Roy. Soc., A, London*, 297 (1966), 397
(15) B. Herzog, D. Bokern, Th. Braun, R. Schlögl, *Proc. EPDIC-3, European Conf. Powder Diffraction*, (1993), 3
(16) F. Atamny, J. Blöcker, B. Henschke, R. Schlögl, Th. Schedel-Niedrig, M. Keil, A.M. Bradshaw, *J. Phys. Chem.*, 96, (1992), 4522
(17) R. A. Rosenberg, P.J. Love, V. Rehn, *Phys. Rev., B*, 33 , (1986), 4034
(18) R. Schlögl, *Surf. Sci.*, 189, (1987), 861

BEHAVIOR OF HIGHLY POROUS CHARS DURING OXIDATION IN REGIME I

Ezra Bar-Ziv
Department of Mechanical Engineering, Ben-Gurion University of the Negev, and
Nuclear Research Center - Negev, P.O. Box 9001
Beer-Sheva, Israel

Keywords: *Coal Char, Pore Structure, Char Oxidation*

INTRODUCTION

The pore structure and its evolution during burnout are major influence on the mechanism of conversion of highly porous chars. Recently, this topic has been presented in several studies [1-8]. Pore structure, can be studied from macroscopic quantities that can be presently measured routinely. Evolution of the pore structure and its influence on char reactivity can be studied from changes in (1) external dimensions, (2) physical properties, and (3) reaction rate. In this review we concentrate on the role of pore structure for char reactivity and narrowed down to highly porous chars with no volatile or mineral matters. We present an overview, that includes only experimental results, on processes and properties for single particles of highly porous synthetic chars oxidized by oxygen. We will show that there is a general behavior connected to the evolution of the pore structure.

Spherocarb particles (synthetic char) were chosen as a model material because they have relatively well defined and reproducible, are quite spherical and have very close pore structure to certain coal chars. Only results from kinetically controlled conditions (regime I) are included. The particles were with initial total porosities in the range 70-80%, with diameters in the range 150-250 μm, oxidized in air or in pure oxygen, with or without moisture, in the temperature range 700-1200 K. Care was taken to include results that obey the Thiele criterion. Four topics will be discussed: (1) Changes in external shape of particles. (2) Fragmentation. (3) Changes in physical properties. (4) Oxidation rate.

Most of the results presented here were obtained with an electrodynamic chamber (EDC). For details on the EDC see for example in Refs. [5,9-17]. The EDC has been developed and applied for kinetic studies of single particles at high temperatures in many studies. The main advantages of the EDC are: (1) Ability to study the kinetics of a single particle in well controlled conditions. (2) Ability to characterize the particle prior to reaction and monitor the important quantities in real time during reaction. (3) The elimination of heat and mass transfer limitations existing in other methods that restrict kinetic measurements to slow rates. (4) The ability to study particle to particle variations. The quantities that were measured for single particles are: weight, shape and dimensions, density and porosity, temperature, total surface area, thermal conductivity, heat capacity, reaction rate.

OBSERVATIONS AND DISCUSSION

1. Changes in External Shape

Decrease in external dimensions of a particle is referred to as shrinkage. If reaction occurred in external surface, as in regime III and partially in regime II, change in external dimensions are understandable and expected. However, in regime I where oxygen is available to all active sites, the changes in the external dimensions must reflect the changes in the internal morphology. Two types of shrinkage have been observed: uniform and non-uniform shrinkage.

Uniform Shrinkage. Shrinkage has been observed in various studies [15,16,18-20] for highly porous synthetic chars oxidized in regime I. It has been shown [21] that shrinkage is a general phenomenon occurring for a variety of carbonaceous materials at ranges varying from tens of nanometers [22] to 70 mm [23]. Shrinkage factor was defined as the ratio of volume to initial volume. Figure I shows results for the shrinkage factor vs. conversion. The results were gathered from about forty different experiments covering the ranges of diameters, temperatures, and densities mentioned above. The shrinkage factor decreases monotonically with conversion not obeying neither the shrinking sphere model (linear decrease, constant density) nor the hollow sphere model (constant diameter). It was established [19] that shrinkage is not due to external surface reaction, but is a homogeneous reaction-induced densification of the microporous solid phase. Shrinkage is ascribed to rearrangement in the microstructure. Thus, if shrinkage is a result of morphological changes, other properties connected to the pore structure must change accordingly. Porosity (or density) and internal surface area were extensively investigated. Figure 2 presents results for normalized density vs. conversion. Density decreases with conversion to approximately half its initial value at about 85% conversion. Although at high conversion the results are scattered a clear indication of increase in density is seen. This increase may be due to densification of the solid, which is also reflected in the thermal conductivity as will be shown below. The total surface area results are less dramatic, but display the same behavior.

Non-Uniform Shrinkage. Non-uniform shrinkage has been observed [15,17] when a particle was irradiated non-uniformly. It has been quantitatively investigated in a systematic manner [24]. Results

of the shrinkage factor for non-uniform shrinkage from many runs show a similar trend to that seen in Fig. 2, however, with some meaningful differences. The shrinkage factor is equal in the two cases from zero conversion to about 50% conversion, then there is a systematic deviation between the two phenomena. Clearly, the deviation is due to different propagation of the pore structure in the two cases. The important finding is that non-uniform shrinkage is also a general phenomenon that is independent on initial values of porosity and diameter, and reaction rate. The major conclusion from both uniform and non-uniform shrinkage is that the pore structure as represented by shape, external dimension, porosity and total surface area, is undergoing a pattern that is equal to all cases regardless the initial conditions or reaction rates.

2. Fragmentation

Fragmentation is another phenomenon that can shed light on the nature of the pore structure and its evolution. The mechanism that arises from the evolution of the pore structure is usually referred to as percolation fragmentation for oxygen percolates through the porous structure and "erodes" the carbon microcrystals with a possible subsequent fragmentation. Percolation fragmentation of carbon spheres during oxidation was reported in a number of studies [25-28]. A theory for percolation fragmentation was developed and showed that for any homogeneous material, fragmentation will occur at a critical porosity of about 70% [28]. Recent observation [15,24] showed also local percolation fragmentation. These results strengthen the thesis that fragmentation is a threshold phenomenon that occurs above a critical porosity, as predicted in [28]. More than one hundred experiments were carried out up to 80% conversion. None of these showed any fragmentation but a few (two or three) showed formation of a hole in the center of the particle. This was indicative to local percolation fragmentation and was predicted by a recent model [23]. Another twenty-two experiments were conducted up to completion and half of them developed holes in the particle center. Out of these, only a few particles broke into two particles. The formation of holes is resulting from the evolution of the pore structure. In all experiments the particle underwent non-uniform shrinkage, transforming the initially spherical particle into a disk at 50-60% conversion. At higher conversion (above 85%) about half of the particles developed holes in the center. Figure 3 presents a typical conversion vs. time curve with a sequence of shadowgraphs depicting the shape development of a Spherocarb particle of 204 micron diameter at various conversions, oxidized in air at T=920 K. Spatial dimensions of the particle are included in the figure. Three regions of oxidation are observed: (i) at low conversion the particle hardly loses mass; (ii) quick mass loss from about 4% conversion to about 95 conversion; and (iii) very slow mass loss from about 95% up to completion. The initially spherical particle turned into a disk at about 60% conversion.

To conclude, formation of holes is a manifestation of the pore structure evolution displayed more pronouncely in disk-shaped particles, formed due to non-uniform shrinkage. Finally, breaking of the particle is a mere coincidence and a random incident where a particle can break due to growth and overlap of large macropores. The important thing is that in all these experiments, the behavior during oxidation was identical for all particles, regardless of initial conditions and oxidation rate.

3. Changes in Physical Properties

Some physical properties of chars depend on distribution of voids and solid microcrystals. Other properties are the reflection of the details of the pore structure, such as connectivities, microcrystal dimensions. Density, total surface area, and heat capacity, belong to the former and thermal conductivity to the latter. In both groups the behavior of the properties depend on the evolution of the pore structure. Thermal conductivity was systematically studied recently [16,29,30] and was shown to be a very strong tool for details of the pore structure and its evolution.

Thermal conductivity. It has been clearly shown [29] that all previous concepts for highly porous materials cannot explain the strong observed change in thermal conductivity with conversion. The surprising result is that total porosity plays a minor role in the evolution of the thermal conductivity. A model showing that thermal conductivity is a property that is highly capacious of the information on the internal microstructure has been developed [29]. Main conclusions are that thermal conductivity is affected by: (1) Consumption of carbon on the internal surface. (2) Coalescence of microcrystals. (3) Activation of intercrystal joints. The change in thermal conductivity k_p with conversion was found to be similar for all particles, regardless of initial conditions or reaction rate. Figure 4 shows k_p/k_{min} (min refer to minimum) for eleven particles at different temperatures. The value of k_p/k_{min} decreases with conversion by a factor of 5-7 from zero to 30% conversion. k_p/k_{min} remains constant until 80% conversion, then it rises by a factor of 2-3 from about 90% conversion to final burnout. The results from the common models [32] show a very poor match to the experimental data. k_p/k_{min} decreases much slower with conversion at low conversions than observed and it behaves opposite to the observed behavior at high conversions. However, a good fit to the model that includes the features of the micromedium was obtained. The significance of these results is that it is most probable that the main role in the change in thermal conductivity, both at low and high conversion, is the change in the dimensions of microcrystal joints. At low conversion the fast

decrease in k_p can be explained by activation of intercrystal joints, i.e., breaking the joints. The increase of thermal conductivity at high conversion can be ascribed to the increase in the radius of an intercrystal joint. The increase of a joint is a manifestation of better ordering of an individual microcrystal. The abruptness of the increase is likely to reflect the spontaneity of the process. Therefore, we interpret the increase in k_p as an indication of conversion induced graphitization. An indication to graphitization at final burnout stages can be found in a recent study [31] where high-resolution tunneling electron microscopy was used. We should, therefore, conclude that the more likely model to represent thermal conductivity is the one that considers the details of the micromedium structure (including nature of connections between microcrystals) and does not consider the porous structure as a mere two-phase medium -- solid/gas -- as represented in most thermal conductivity models [32]. This conclusion strengthens the importance of thermal conductivity for the understanding of changes in the pore structure of highly porous media in general, and for chars in particular.

4. Mass Transients

Numerous measurements of mass loss were carried out for Spherocarb particles reacting in regime I at the range of conditions specified above. A convenient way of presenting the data is conversion vs. normalized time (by time at half conversion -- $t_{1/2}$), as shown in Fig. 5. The various results fall within one curve, within experimental uncertainty (larger scatter at long time region). Three regions of behavior are observed: (1) slow mass loss with time in the early stages of burnout; (2) fast reaction; and (3) slow reaction at final burnout. Figure 6 shows normalized reaction rate (with $t_{1/2}$) vs. conversion measured from different studies at various temperatures. The fact that all results (transients and rates) can be normalized by one quantity ($t_{1/2}$) has a very strong significance: All three stages of conversion are strongly related to the same mechanism. Note that this mechanism prevails for all conditions of regime I. One can deduce that consumption of carbon is governed by one mechanism. Dividing the consumption process into two stages, one at which reaction sites are activated and the other is the actual gasification (solid carbon turns into gaseous carbon, i.e., CO or CO_2). Clearly, from the results of Figs. 5 and 6, gasification (stage 2) cannot be the rate determining step for it is unlikely that the two mechanisms have the same activation energies. Thus, the only conclusion that one can draw from this behavior is that activation of sites is the dominant mechanism that governs the consumption of carbon. Active sites, however, are a direct consequence of the evolution of the pore structure. Therefore, the reactivity of chars as physical properties discussed above are also a direct consequence of the pore structure.

In light of this conclusion one can draw a picture of the reactivity behavior of highly porous chars. In the early stages of burnout reactive sites are very scarce and reaction is very slow. As reaction proceeds, morphology and crystallinity change, and as a consequence reactive sites start to build up and reactivity increases. At some stage, reaction progressed such that reactive sites start to decline, resulting in decreasing of reaction rate, that occurs at high conversion. In fact from this description one can deduce that the behavior of reaction rate is a consequence of the change in active sites an that the intrinsic reaction rate is constant with conversion.

SUMMARY

The selection of Spherocarb particles has given us the opportunity to examine physicochemical processes under well defined and reproducible conditions. Differences were only on total porosity and diameter. The numerous results obtained in a wide range of conditions has provided a wide-angled view that can help elucidate the governing mechanisms for oxidation. Each of the physical properties studied has behaved in a certain quantitative way equal in all experiments. Similarly, the phenomena of shrinkage and fragmentation showed, each, clear and reproducible pathways. Dependence of reaction rate on temperature, on oxygen concentration, on conversion, on time has shown also a clear pattern regardless of initial conditions. From these observations it is inevitable to reach the conclusion that all these processes and quantities are related to the pore structure and its fine tunes. The most striking evidence is the results of conversion versus normalized time that showed clearly that all stages of conversion must be all connected to one mechanism. This conclusion, however, is only circumstantial. We do not have yet results from direct observation of microscopic changes (morphology and crystallinity) for Spherocarb particles. Still the numerous macroscopic data can serve as strong indication of the microscopic processes. Insights can be gained if a model that includes the microscopic features and can reconstruct the numerous physicochemical experimental data, by minimum parameter fitting.

References

1. Sahimi, A., Gavalas, G.R., and Tsotsis, T.T., Chem. Eng. Sci. **45**:1443 (1990).
2. Hurt, R.H., Sarofim, A.F., and Longwell, J.P., Energy & Fuel **5**:290 (1991).
3. Miccio, F., and Salatino, P., 24th Sym. (Int.) on Combustion, The Combustion Institute, Pittsburgh, 1992, pp. 1145-1151.
4. Salatino, P., Miccio, F., and Massimilla, L., Combust. Flame **95**:342 (1993).
5. D'Amore, M.D., Tognotti, L., Sarofim, A.F., Combust. Flame, **95**:374 (1993).
6. Salatino, P., Miccio, F., 24th Sym. (Int) on Combustion, The Combustion Institute, Pittsburgh, PA, 1994, pp. 1145-1151.
7. Kantorovich, I.I, and Bar-Ziv, E., Combust. Flame **97**:61 (1994).
8. Kantorovich, I.I, and Bar-Ziv, E., Combust. Flame **97**:79 (1994).
9. D'Amore, M., Dudek. R.D., Sarofim, A.F., and Longwell, J.P., Powder Technology **56**:129 (1988).
10. Dudek, D.R., Fletcher, T.H., Longwell, J.P., and Sarofim, A.F., Int. J. Heat Mass Transfer **31**:863 (1988).
11. Bar-Ziv, E., Jones, D.B., Spjut, R.E., Dudek, D.R., Sarofim, A.F., and Longwell, J.P., Combustion and Flame **75**: 81 (1989).
12. Tognotti, L., Longwell, J.P., and Sarofim, A.F., 23rd Sym. (Int.) on Combustion, The Combustion Institute, Pittsburgh, 1990, pp. 1207-1213.
13. Bar-Ziv, E., Longwell, J.P., Sarofim, A.F., Energy and Fuels **5**:227 (1991).
14. Bar-Ziv, E., and Sarofim, A.F., Prog. Energy Comb. Sci. **17**:10 (1991).
15. Weiss, Y., and Bar-Ziv, E., Combust. Flame **95**:362 (1993).
16. Weiss, Y., Ben-Ari, Y., Kantorovich, I.I., Bar-Ziv, E., Krammer, G., Modestino, A., and Sarofim, A.F., 25th Sym. (Int.) on Combustion, The Combustion Institute, Pittsburgh, PA 1994, pp. 519-525.
17. Weiss, Y., and Bar-Ziv, E., Combustion and Flame **101**:452 (1995).
18. Weiss, Y., Ph.D. Thesis, Ben-Gurion University of the Negev, 1995.
19. Hurt, R.H., Dudek, D.R., Longwell, J.P., and Sarofim, A.F., Carbon **25**:433 (1988).
20. Dudek, D.R., Ph.D. Thesis, Massachusetts Institute of Technology, Cambridge, MA, 1988.
21. Hurt, R.H., Sarofim, A.F., and Longwell, J.P., Combust. Flame **95**:430 (1993).
22. Ishiguro, T., Suzuki, N., Fujitani, Y., and Morimoto, H., Combust. Flame **85**:1 (1991).
23. Easler, T.E., Bradt, R.C., and Walker, P.L., Fuel **69**:124 (1990).
24. Zhang, X., Dukhan, A., Kantorovich, I.I., and Bar-Ziv, E., "Bulk Fragmentation of Highly Porous Char Particles in Regime I," Combust. Flame **XX:XXX** (1995).
25. Davis, H., and Hottel, H.C., Ind. Eng. Chem. **26**:889 (1934).
26. Walker, P.L., Jr., Rusino, F., and Austin, L.G., Adv. Catal. **11**:133 (1957).
27. Dutta, S., Wen, C.Y., and Belt, R.J., Ind. Eng. Chem. Proc. Des. Dev. **16**:20 (1977).
28. Kerstein, A.R., and Niksa, S., 20th Sym. (Int.) on Combustion, The Combustion Institute, Pittsburgh, 1984, pp. 941-949.
29. Kantorovich, I.I, and Bar-Ziv, E., "The Effect of Microstructural Transformation on the Evolution of Thermal Conductivity of Highly Porous Chars during Oxidation," Combust. Flame, (1995).
30. Dukhan, A., Zhang, X., Kantorovich, I.I., and Bar-Ziv, E., "Thermal Conductivity and Porosity of Char Particles in Regime I," submitted to 26th Sym. (Int.) on Combustion, The Combustion Institute, Pittsburgh, PA 1996.
31. Davis, K.A., Hurt, R.H., Yang, N.Y.C., nd Headly, T.H., 25th Sym. (Int.) on Combustion, (The Combustion Institute, Pittsburgh, PA 1994), pp. XXX-XXX.
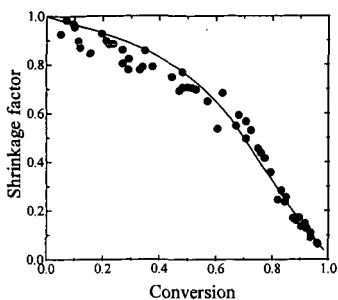32. Hashin, Z. and Shtrinkman, S., J. Appl. Phys. **10**:3125 (1962).

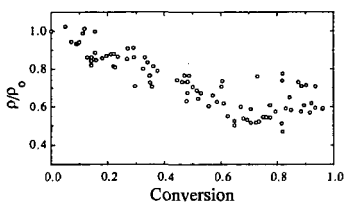Figure 1. Shrinkage factor versus conversion for uniform shrinkage [9,16,19,20].

Figure 4. Ratio of thermal conductivity to its minimum value, k_p/k_{min} as a function of conversion.

Figure 2. Ratio of density to initial density vesrus conversion [7,17,19,20].
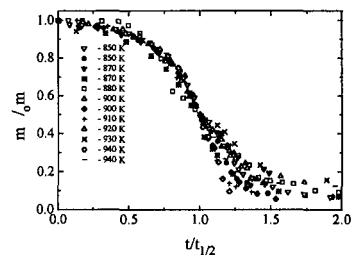
Figure 5. Conversion versus normalized time τ (by time at half conversion -- $t_{1/2}$) for particles oxidized under un-even temperature field.

Figure 3. Conversion versus time and a sequence of shadowgraphs presenting the development of shape of a 204 microns Spherocarb particle vs. conversion oxidized in air at 920 K; C is conversion, l is length, and w is width.

Figure 6. Normalized reaction rate defined as dC/dτ versus conversion [9,12,20].

AN EXAMINATION OF THE TWO KINETIC REGIMES OF THE NITRIC OXIDE-CARBON GASIFICATION REACTION

E.M. Suuberg, H. Teng, and I. Aarna
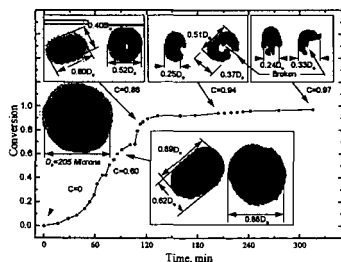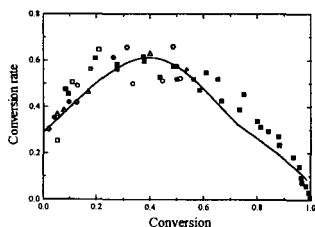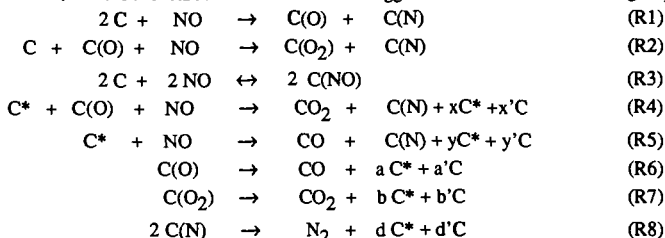Division of Engineering, Brown University,
Providence, RI 02912

Keywords: Nitric Oxide, Carbon, Gasification

INTRODUCTION

The reaction of NO with carbon has been shown by many workers to involve two distinct rate regimes, at temperatures of practical interest [1,2]. Based upon our earlier results, we suggested that the two regimes most likely involve rate control by site creation in the low temperature regime and dissociative chemisorption in the high temperature regime. Further experiments and analysis will be presented here in support of these hypotheses.

The mechanism of the NO-carbon reaction has been suggested to involve the following steps [2]:

$$2\,C + NO \rightarrow C(O) + C(N) \tag{R1}$$
$$C + C(O) + NO \rightarrow C(O_2) + C(N) \tag{R2}$$
$$2\,C + 2\,NO \leftrightarrow 2\,C(NO) \tag{R3}$$
$$C^* + C(O) + NO \rightarrow CO_2 + C(N) + xC^* + x'C \tag{R4}$$
$$C^* + NO \rightarrow CO + C(N) + yC^* + y'C \tag{R5}$$
$$C(O) \rightarrow CO + a\,C^* + a'C \tag{R6}$$
$$C(O_2) \rightarrow CO_2 + b\,C^* + b'C \tag{R7}$$
$$2\,C(N) \rightarrow N_2 + d\,C^* + d'C \tag{R8}$$

The reaction (R3) is only important at quite low temperatures (< 473K) [4]. The reactions (R1) and (R2) are dissociative chemisorption on non-rapid turnover sites [2]. The reactions involving C^* are the rapid turnover site reactions, that yield both CO via (R5) and CO_2 via (R4). The reaction (R2) allows for some small amounts of stable CO_2-forming complex on the surface. The reactions (R6), (R7) and (R8) reflect formation of empty rapid turnover sites C^*, as well as non-rapid turnover sites, C. The exact nature of the C^* sites and C sites, and what makes them different, is unclear. Thus the stoichiometry of their formation is also unclear. The reactions (R6)-(R8) are governed by distributions of activation energies, and (R6) and (R7) make a large contribution to the overall rate at low temperatures [1,2]. In fact, the rapid turnover processes (R4) and (R5) are probably governed by the same continuum of activation energies as are (R7) and (R6), respectively, except that at any given temperature, certain sites are effectively immediately desorbed upon formation.

The low desorption activation energy surface species, for which the rate of desorption is quite fast compared to the rate of their formation by dissociative chemisorption of NO, give rise to surface sites that are normally "empty" (the C^* sites). Again, it is probably impossible at the present time to define a particular reaction pathway for a particular type of site. The concept of a rapid turnover site is largely a bookkeeping construct. Without direct evidence to support the view that there exists a particular carbon structure C^* which will, upon oxidation, immediately desorb as part of CO or CO_2, it is more prudent to adopt a more flexible view of what C^* might represent. It may well be the case that chemisorption on one surface site will tend to destabilize another, neighboring oxide structure. This view is supported by the recent insightful isotope labeling experiments of Orikasa et al. [5] , which suggested that the rate of (R6) might be enhanced by processes involving participation by NO itself (though a thermal artifact was seemingly not ruled out). Kinetically, the transient behavior observed by these workers at 873 K appeared consistent with a rapid turnover process such as (R5), and the isotopic composition showed that some of the oxygen came from oxide on the surface [5]. Thus it might be necessary to define C^* more broadly, so as to include not only a carbon structure that is able to be oxidized, but also possibly neighboring carbon oxide sites. A similar suggestion has been advanced by Tomita and coworkers [6,7]. This represents a considerable step in the direction of increasing complexity of models of the oxidation process.

Here, we consider some new experimental results that help to shed further light on models of NO reaction with carbon. In particular, we explore further the role of surface oxides in determining the rate of the reaction processes in both the high and low temperature regimes. These two regimes have been discussed elsewhere [1,2], and typical two-temperature regime behavior is seen in Figure 1, which will be discussed below.

EXPERIMENTAL

Two different thermogravimetric analyzer (TGA) reactor systems have been used in this study; one from TA Instruments and the other from Cahn Instruments. The TA Instruments TGA has a somewhat smaller enclosed gas volume than does the Cahn system, thus, the experiments in the TA Instruments TGA were performed with a continuous gas flow through the TGA to ensure that depletion of NO was not significant. Apart from this small difference, the TGA work was

performed as earlier described[1,2], and the results indicate no significant differences attributable to the particular TGA system used. As is usual in our TGA work, experiments were performed at quite high NO partial pressures, ranging from about 1 to 10 kPa of NO partial pressure. The reaction has been shown to be first order in NO over a very wide range of pressures [3], and the rates from this range of pressures can be extrapolated with confidence to lower partial pressures.

Some experiments were performed in a packed bed reactor system. This reactor consisted of a 4 mm ID quartz tube packed with around 100-200 mg of char, giving a bed length of order 10-30 mm. The NO concentrations examined in this system were much lower than those in the TGA system, and ranged from about 1 to 20 Pa.

One material selected for study is a char derived from phenol-formaldehyde resin. It has been described before [1,2]. This material has a relatively low impurity content. The material has been heat treated at 1323 K for two hours prior to any experiments. A second material is a char derived from Wyodak coal char. This char was derived from a sample of the Argonne Premium Coal Sample Program [8]. Details of its pyrolysis will be discussed below.

The chars were also subjected to "surface cleaning" in some cases. This procedure involves exposure of the char to high-pressure flowing helium at either 1223 or 1273 K for one to two hours. This results in removal of most, though not all, of the desorbable oxides from the surface. The amount of surface oxides that remains after surface cleaning is difficult to establish, quantitatively. The rate of oxide desorption at the end of the the the surface cleaning process is generally quite low, when the process is stopped.

Results and Discussion
Factors Affecting the Active Site Concentration
Typical results of the experiments on the resin char, at an NO partial pressure of 2 kPa, are shown in Figure 1. The results are shown as first order rate constants for the destruction of NO on the carbon surface. The data show the previously discussed two-temperature-regime behavior. Two different types of experiments are shown and both show the two-regime behavior. One set was performed as previously described [1,2]. Samples were subjected to a sequence of different temperatures, under a constant NO partial pressure. Different temperatures were explored by simply changing the temperature of the reactor. To hasten achievement of pseudo-steady state behavior, these experiments were performed by starting the experimental sequence at high temperatures. No attempt was made to clean the surface of oxides between each temperature step. These experiments will be referred to as those involving an "uncleaned" surface. These experiments gave relatively constant rates of mass loss (the main experimentally measured quantity) over timescales of tens of minutes, and these are what are reported in Figure 1. The approach to apparent steady state was generally faster, the higher the temperature.

A second set of experiments was performed with an identical material, but with a different experimental procedure. The difference had to do with how the surface was prepared for an experiment. Rather than permitting the oxides to remain on the surface throughout the experimental sequence, in this case, each time the temperature was changed, the oxides were desorbed (to a significant extent) by heating the sample at 1223 K for two hours. These experiments are described as involving a "cleaned" surface. This somewhat more tedious experimental procedure had been earlier followed in experiments designed to determine the true order of reaction [1]. In that case, it had been observed that leaving the oxides on the surface gave an apparent non-unity order with respect to NO, particularly in the high temperature regime. This was because the timescale for the oxide population to adjust itself to a different pressure was sufficiently long (many hours) that it was easy to miss this fact in experiments in which the appearance of linear mass loss with time was used to judge approach to pseudo-steady state. In the experiments reported here, the rates were again taken to be those at apparent pseudo-steady state, consistent with how the rates were determined for the uncleaned samples.

Comparison of the results of experiments with cleaned and uncleaned samples shows that in the low temperature regime (below about 1000 K), the rate of the reaction is clearly higher with the surface cleaned samples. In the high temperature regime, no significant differences have been noted between cleaned and uncleaned samples in these, or any other, experiments. Thus there is suggestion that the existence of oxides on the surface can retard the apparent rate of the gasification under certain circumstances, commensurate with the above model in which the C* is viewed as depending upon free sites for rapid turnover [2]. It should be noted that this result is not a consequence of "thermal annealing" [9], in that the more highly heat treated carbon (that with the surface cleaned after each cycle) is more reactive than the sample for which this is not done. These results at first appear to be in direct contradiction to those reported by Suzuki et al. [7], in which oxidation of a carbon surface enhanced the rate of reaction with NO. It is possible that the discrepancy arises from the different degree or nature of oxidation (or surface cleaning) in the two studies. Suzuki et al. used O_2 to oxidize the surface, and the complexes created by oxygen may be different than those created by NO. We have seen evidence of this difference in TPD studies. Further, it has been noted by Tian [10] that addition of H_2 to an NO containing mixture increases the rate of NO destruction. Tian's experiments were conducted at 1073 K, and appeared to be in what we term the high temperature regime, so it is unclear that they can be compared directly with the present results. Nevertheless, they are clearly suggestive of a role of oxide removal in rate

enhancement.'

Similar types of experiments have been performed at significantly lower NO partial pressures in the packed bed reactor. The effect of surface cleaning is barely visible (and of course the overall reaction rates are much lower). This means that the effect of surface oxide population is associated with the partial pressure of NO. The pseudo-steady population of surface oxides increases with increase in NO pressure, though this dependence is very weak at high NO pressures [1], possibly indicating surface saturation. There is, however, evidence that the reaction shows a higher order dependence upon NO pressures when NO pressures become low (of order 1 Pa). This would be expected, as reactions such as (R2) and (R4) become "starved" for surface oxides. The concentration of surface oxides would be expected to become more sensitive to the NO pressure, as the pressure of NO is decreased (as may be reasoned from a simple Langmuir-type adsorption model).

We have also studied the effect of differences in active site density in another way, as shown in Figure 2. This figure illustrates the effect of heat treatment on Wyodak coal char. One char was prepared by heating at 1273 K for a total of four hours, while the other was heated up to a temperature of 1273 K, at a rate of 30 K/min, and then immediately cooled. The results of Figure 2 show one facet consistent with what was seen in Figure 1 - the effects of heat treatment are most notable in the low temperature regime, and largely disappear in the high temperature regime. Here, however, the less highly heat-treated char, which presumably contains more active sites to begin with, was not surface cleaned during the experimental sequence (in fact, each point was obtained with a "fresh" sample). The more highly heat treated char was surface cleaned. The less highly heat treated material would have had more active sites to begin with, and would have retained these, but for filling with oxides. The change in the population of sites with time was not explored. Thus the conclusion from these experiments is that thermal annealing effects can and do play the usual sort of role in influencing reactivity, but the effects are different in the two temperature regimes. It may be further concluded, by comparing with Figure 1, that surface cleaning may affect the extent of annealing, but by the time a sample has already been heat-treated for several hours at 1273 K, the annealing effects become less important than the site-blockage effects.

There are two general conclusions which may be drawn based upon these results. The first is that examination of the rates and dynamics of the NO-carbon reaction must always establish in which temperature regime the processes of interest are occurring. There is no possibility of deriving "general" conclusions concerning mechanism without careful consideration of this point. There is ample evidence of very long timescale dynamics associated with rearrangement of surface oxides, which, in turn, can significantly affect the observed rates. The effects of NO partial pressure must also be taken into account. The second general conclusion is that the rates in the low temperature regime appear to be generally more sensitive to any factors that affect active site populations than are rates in the high temperature regime. It is already clear that the process of NO destruction (or gasification) is somehow different at the higher temperatures. It is possible that a different set of active sites begins to dominate the rate because a different reaction pathway becomes favorable, or it might be that as a result of an increase in available active sites, a second step in a reaction pathway becomes limiting. We have earlier suggested this latter possibility [2].

The Kinetic Role of The Rapid Turnover Active Site Population
The relative roles of the desorption processes such as (R6) compared to the rapid turnover processes such as (R5) has been earlier examined, using the resin char [2]. The rate of carbon gasification is given by the sum of contributions from the desorption processes and the processes such as (R5): $r = r_a + r_d$, where r_d corresponds to (R6) and r_a to (R5). The focus on CO2-yielding reactions is chosen for simplicity; the analysis may be extended to include CO_2 as a product as well, at the expense of greater complexity. The data on the overall rate, r, and the desorption rate in the absence of NO, r_d, have been given elsewhere [2]. Noting that $r_a = k_a[C^*]P_{NO}$ and $r_d = k_d[C(O)]$, then it can be seen that:

$$d[\ln (r_a/r_d)]/d[1/T] = - (E_a-E_d)/R + d \ln [C_{tot}/C^* -1] /d [1/T]$$

where C_{tot} is the total number of sites in either the form C^* or $C(O)$. Working at the limit $C^*/C_{tot} \ll 1$, i.e., most sites are oxide-filled, allows the above result to be approximated as:

$$d[\ln (r_a/r_d)]/d[1/T] = - (E_a-E_d)/R - d \ln [C^*] /d [1/T]$$

The left hand side of the above equation is shown in Figure 3, yielding a slope of - 3969 K. The value of the last term on the right hand side is evaluated from experiments in which the free sites are filled at a temperature below gasification (see ref. 2). The result is also seen in Fig. 3, and define a slope with (1/T) of -7100 K. The rate of desorption of oxides from the surface was tracked in TGA experiments in which the mass loss rate was followed after removal of NO [1,2]. These data are also represented in Figure 3, yielding an apparent $E_d = 89$ kJ/mol. Combining the above values yields $E_a = 181$ kJ/mol, in good agreement with the experimentally determined value for the high temperature range (e.g., Figure 1).

It is noteworthy that the above calculation spanned both the high and low temperature ranges, using data from each. The results of the kinetic calculation are very much in concert with the earlier conclusion, based upon product analyses, that both (R5) and (R6) type reactions occur in both temperature regimes [2]. The fact that reactions of type (R5) appear to play a significant kinetic role

in the low temperature regime cannot be overlooked, even though their inherent activation energy is seen only in the high temperature regime. It is the competition between these reactions, at any particular temperature, that determines the apparent kinetic constants. We have also observed that the shift from low-temperature to high-temperature regimes occurs at widely varying temperatures in different carbons, so it is not possible to make a general statement about which processes may be neglected at what temperatures.

Based upon this analysis, and our earlier results, it is clear that there exists a population of sites that is "empty" (available for reaction) under all reactive conditions, and at which rapid turnover processes occur with an activation energy characteristic of the high temperature regime. The population of such sites appears to increase with increasing temperature. The numbers of such sites depend upon how the sample was prepared (how highly heat treated it was) and how heavily the surface is oxidized. As the temperature of the surface is raised, the population of empty sites increases (due to desorption of oxides) to such an extent that the rate begins to show the thermal dependence of the decomposition of NO on the sites. This defines the high temperature regime. At lower temperatures, the temperature dependence of the overall rate reflects the temperature dependence of desorption processes, since these not only contribute product via reactions such as (R6), but also free up sites for reactions such as (R5). This model will be formalized in a forthcoming paper.

ACKNOWLEDGEMENT

REFERENCES
1. Suuberg, E.; Teng H.; Calo, J. *23rd Symp. (Int.) on Combustion*, The Comb. Inst., Pittsburgh, 1990; p 1199.
2. Teng, H.; Suuberg, E.M.; Calo, J.M. *Energy and Fuels*, 1992, *6*, 398.
3. Aarna, I.; Suuberg, E.M., paper presented at this meeting.
4. Teng, H.; Suuberg, E.M. *J. Phys. Chem.*, 1993, *97*, 478.
5. Orikasa, H.; Suzuki, T.; Kyotani, T.; Tomita, A.; Martin, R., *Proc. Carbon '95*, p 626, American Carbon Society, 1995.
6. Yamashita, H.; Tomita, A.; Yamada, H.; Kyotani, T.; Radovic, L.R., *Energy Fuels*, 1993, 7, 85.
7. Suzuki, T.; Kyotani, T.; Tomita, A., *I&EC Res.*, 1994, *33*, 2840.
8. Vorres, K. *Energy and Fuels*, 1990, *4*, 420.
9. Suuberg, E.M. in *Fundamental Issues in Control of Carbon Gasification Reactivity* (J. Lahaye and P. Ehrburger, Eds.), p. 269, Kluwer, Boston, 1991.
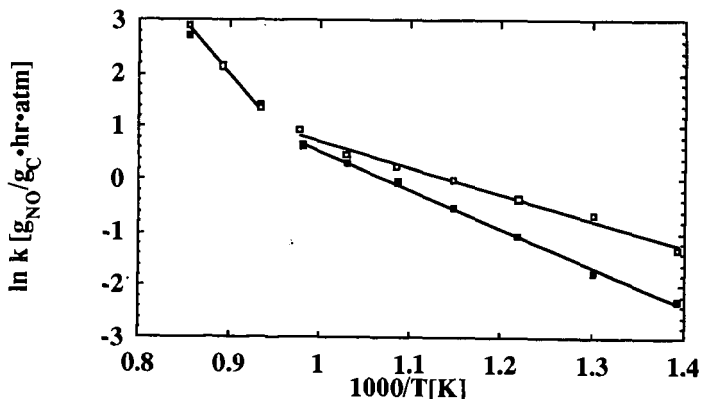10. Tian, Y., Doctoral Dissertation, Chemistry, University of Essen, Germany, 1993.

Figure 1. A comparison of the rate constant for NO reduction by resin char with cleaned surface (open squares) and uncleaned surface (closed squares). The NO pressure was 2 kPa.
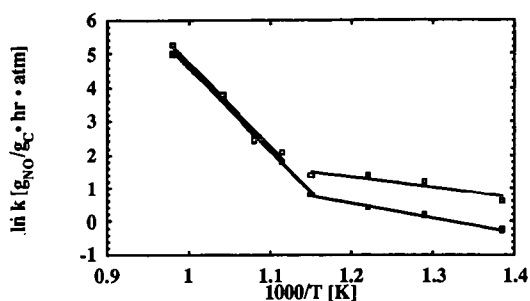
Figure 2. The effect of heat treatment upon the reactivity of Wyodak char. The open points are for a sample heated to 1273 K at 30 K/min, and the closed points are for a sample heated for four hours at 1273 K (see text). The NO partial pressure was 10 Pa.
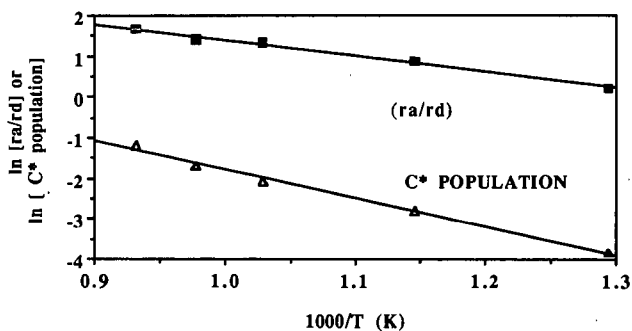

Figure 3. The variation of relative rates of rapid turnover and desorption processes with temperature, and the variation of rapid turnover site population with temperature. Values obtained from TGA experiments at 1 to 10 kPa NO pressure.
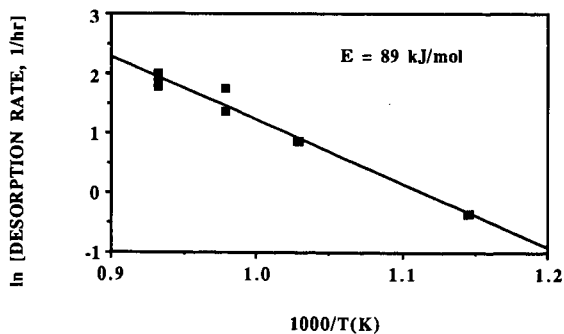

Figure 4. Oxide desorption rate, after removal of NO from the TGA.

NO RELEASE FROM THE ISOTHERMAL COMBUSTION OF COAL CHARS.

A.W. HARDING, S.D. BROWN and K.M. THOMAS.

Northern Carbon Research Laboratories, Department of Chemistry, Bedson Building,
University of Newcastle upon Tyne, Newcastle upon Tyne, NE1 7RU, U.K..

Keywords: Char, combustion, gasification, NOx

Introduction

Coal combustion for power generation has associated environmental problems, in particular, the release of oxides of sulphur and nitrogen which are involved in the formation of acid rain [1,2]. The modification and optimization of the combustion process to minimise the NOx emissions is therefore of considerable interest and importance. The combustion of coal occurs over two stages;

1)   the rapid devolatilisation followed by combustion/ignition of the volatiles *and*
2)   slower gasification of the residual char.

The nitrogen present in the coal is partitioned between the volatile matter and the residual char. Char nitrogen has been identified [3] as the main contributor to NO emissions from low NO_x burners. Previous work on the gasification of char nitrogen [4-6] concentrated on temperature programmed conditions and possible mechanisms of the release of nitrogen. Carbons derived from polynuclear heterocyclic aromatic hydrocarbons with well defined initial functionality [7-10] and isotopic carbon (^{13}C) [11,12] were also used as models for char gasification.

In the present investigation, the release of NO during isothermal combustion of a suite of coal chars produced from a rank series of coals in an entrained flow reactor under conditions similar to those in pulverised fuel combustion systems was studied. The relationships between coal and char structural characteristics and NO release were investigated.

Experimental

Coal Samples

Twenty coals were used in the study, covering a wide range of rank from anthracite to high volatile bituminous coal.

Char sample preparation in an Entrained Flow Reactor(EFR)

Pyrolysis of the coal size fraction (38 - 75μm) to produce char samples was achieved by the injection of coal into an entrained-flow reactor at 1273K in a nitrogen atmosphere. The reactor had a zone length of 1.66m and the particles experienced residence times of ~1s. Char samples were collected using a water cooled probe and a cyclone.

Char characterisation data

Carbon, hydrogen and nitrogen contents were determined using a Carlo Erba 1106 elemental analyser. Proximate analyses of the chars were determined by modified thermogravimetric analysis using a Stanton Redcroft ST780 thermogravimetric analyser. Surface area measurements were obtained from CO_2 adsorption measurements at 273K in a McBain spring gravimetric apparatus.

Combustion measurements

A Thermal Sciences STA 1500 thermogravimetric analysis instrument was connected to a VG quadrupole 300 amu mass spectrometer via a 1mm i.d. silica lined stainless steel probe. The probe was placed directly above the sample at a distance of 10mm from the surface of the sample. Isothermal combustion was carried out by heating the sample to the desired temperature (873 - 1323K) in an atmosphere of argon. After thermal equilibrium was reached, the gas was switched to 20% oxygen/argon. A gas flow rate of 50 cm^3 min^{-1} was used with ~5mg of char sample with particle size 38-75μm. The gaseous species evolved and the weight loss profile were recorded with respect to time. Reactivity measurements were determined from isothermal gasification in 20% O_2/Ar at 773K. The reactivities of the chars during combustion were calculated from the rectilinear region of the weight loss-time curve.

Results

Isothermal Gasification measurements

The gasification rates of the coal chars at various temperatures between 773 and 1323K are shown in Figure 1 as a function of isothermal gasification temperature and volatile matter of the parent coal. It is apparent that there are two regions corresponding to the reaction being under chemical control at temperatures typically less than 973K, while above 973K the reaction is under diffusion control. In the chemical control region (below 973K), the gasification rate increases markedly with temperature. In the diffusion controlled region, above 973K, there is a very slow increase in the rate of gasification with temperature. In the region where the reaction is under chemical control, the gasification rate increases quite sharply with decreasing rank. In the region where the reaction is under diffusion control, there is a slight decrease in the gasification rate with coal rank.

Conversion of char nitrogen to NO

Isothermal Combustion profiles

Figure 2 shows the isothermal combustion profiles for a low rank coal char at 873 and 1273K in 20% O_2/Ar. At 873K, the combustion takes place where the reaction is under chemical control while at 1273K, the reaction is under diffusion control. It is evident that the NO/(CO + CO_2) ratio increases with increasing burn-off for combustion at both temperatures. Similar trends were observed for the combustion of the suite of chars under both chemical and diffusion control.

Gas concentration measurements

The release of nitric oxide from the combustion of the E.F.R. coal chars varied with the rank of the parent coal and the isothermal gasification temperature. In regions of low gasification temperature and for high rank coals, the ratio of nitric oxide released normalised to the initial amounts of nitrogen in the char (NO/char-N), was highest. For low rank coals, the effect of temperature on the NO/char-N ratio was not as great. It was also apparent that there was a dependence of the NO/char-N ratio on coal rank at any given temperature. There was a marked decrease in the NO/char-N ratio with a decrease in coal rank. Again, this was less apparent at the higher combustion temperatures when the reaction was under diffusion control.

The relationships between carbon structural characteristics and the conversion of char nitrogen to NO during combustion are of considerable interest. At low temperatures, gasification rate is governed by chemical control, and therefore the porous and surface structure of the char need to be taken into consideration. Figure 3 shows that there is a correlation between gasification

rate and the evolution of char-N as NO at 873K (chemical control region). At 1273K, when the reaction is under diffusion control, there was no correlation between char gasification rate and NO evolution. The clear correlation of NO/char-N with gasification rate observed for isothermal combustion at 873K was less evident when the rate was normalised by the surface area of the char. This indicates that the porous structure is a factor which influences the gasification of the char under chemical control and also the conversion of char-N to NO during combustion. In diffusion control, the external surface of the char is the important parameter.

Discussion
Char nitrogen conversion to NO

In this study, the gas sampling probe to the mass spectrometer was placed directly above the sample and this has been shown to detect reactive intermediate species before they are converted to equilibrium species (direct sampling) [6,10]. When the sampling probe is moved to the exhaust of the TGA, near equilibrium conditions are obtained (exhaust sampling). At this sampling position, the NO/N ratio increases due to small amounts of reactive intermediate species, such as HCN and $(CN)_2$ produced in the char gasification being converted to NO in the gas phase by reaction with oxygen [10]. NO is the major primary product of char-N gasification. Mass transport effects and reduction of the NO in the carbon bed in the TGA may also modify the conversion of char nitrogen to NO during gasification/combustion. Figure 2 shows that the $NO/(CO + CO_2)$ ratio increases with increasing carbon conversion and similar results were obtained for the combustion of the suite of chars under both chemical and diffusion control conditions. This can be attributed to two reasons; a) the retention of nitrogen in the char and/or b) the lower extent of reduction of the primary char nitrogen oxidation product NO, in the pores or on the surface of the char as the structure changes with carbon conversion.

Tullin *et al* have proposed [13] that char nitrogen reacts with either oxygen to form NO or with NO to form N_2O as the char undergoes gasification. The NO and N_2O are reduced by the char to N_2. Since the diameter of the char particles decreases with increasing carbon conversion there is less opportunity for the NO to be reduced. This explains the increase in $NO/(CO + CO_2)$ with increasing carbon conversion. These authors also observed a decrease in N_2O with carbon conversion. They proposed that there was a decrease in NO concentration in the pores, thus causing a reduction in the formation of N_2O. These authors used modelling studies [14] to support the proposal.

Previous studies of the isothermal combustion of model carbons prepared by the high pressure carbonization of polynuclear aromatic hydrocarbons gave similar results [7-9]. In addition, analytical data showed that the N/C ratio increased with increasing carbon conversion thereby supporting the former explanation. Therefore it is possible that both nitrogen retention and lower NO reduction occur with increasing carbon conversion.

Temperature programmed combustion studies of E.F.R. chars have shown [3,4] that the conversion of char-N to NO increases with rank up to ~ 1.5% vitrinite reflectance before reaching a plateau. High levels of NO release were also associated with lower reactivity chars and it was proposed that the char reactivity, total surface area, and char surface structure are factors which influence the conversion of char nitrogen to NO during combustion.

Previous studies have suggested that NO is reduced on the carbon surface to form N_2 and/or N_2O [4-8, 10, 13,14]. Also the CO reaction with NO may be catalysed by the char

surface [15]. High rank coals have a more ordered structure than the lower rank coals and there are generally fewer active sites available. In addition, the porous structure varies systematically with rank. Coals which develop thermoplasticity give rise to anisotropic chars where there is an increase in the extent of alignment of the carbon lamellae resulting in a low surface area. It is apparent that the coal chars which have the lower surface areas tend to be associated with higher levels of NO release. This indicates that the lower reactivity and available surface area of the high rank coal chars gives rise to higher NO/char-N conversion ratios due to a lower reduction of the primary char oxidation product NO on the surface and/or in the pores of the char. Figure 3 clearly shows that the less reactive chars are associated with high levels of NO release, at low temperatures where the reaction is under chemical control.

Conclusions

The release of nitrogen in the combustion of coal chars derived from a suite of coals covering a wide range of rank has been studied. The $NO/(CO + CO_2)$ ratios increased with increasing burn-off for isothermal combustion in both the chemical and diffusion control temperature regimes. This suggests that the nitrogen is retained preferentially in the char and/or the extent of reduction of NO on the char surface is lower as carbon conversion proceeds. Lower conversions of char nitrogen to NO are observed from low rank coals. Chars with low surface areas and low reactivity have high conversions of char-N to NO. The primary product of char-N combustion, NO, is reduced in the porous structure and/or on the surface of the coal char. The char structure may also catalyse the reaction of CO with NO. The extent of reduction varies with temperature and mass transport limitations as well as the structure of the char.

References

1.   Sloss,L.L.,*NOx Emissions from Coal Combustion,* IEACR/36,1991, IEA Coal Research, London.
2.   Davidson,R.M. *Nitrogen in Coal,* IEAPER/08,1994,IEA Coal Research, London.
3.   Phong-Anant, D., Wibberley, L.J. and Wall, T.F. *Combust. Flame* **62**, 21 (1985).
4.   Wang, W., Brown, S.D., Hindmarsh, C.J. and Thomas, K.M. *Fuel* **73**, 1381 (1994).
5.   Brown, S.D. and Thomas, K.M. *Fuel* **72**, 359 (1993).
6.   Varey, J.E., Hindmarsh, C.J. and Thomas, K.M. *Fuel* accepted for publication.
7.   Wang, W.and Thomas, K.M. Fuel **71**, 871 (1992).
8.   Wang, W. and Thomas, K.M. Fuel **72**, 293 (1993).
9.   Spracklin, C.J., Thomas, K.M., Marsh, H. and Edwards, I.A.S. *International Conference on Coal Science Proceedings,* IEA Coal Research, 1991, p. 343.
10.   Jones, J.M., Harding, A.W., Brown, S.D. and Thomas K.M. *Carbon* **33**, 833 (1995).
11.   Thomas, K.M., Grant, K. and Tate, K. *Fuel* **72**, 941 (1993).
12.   Jones, J.M. and Thomas, K.M. *Carbon* **33**,1129(1995).
13.   Tullin, C.J., Sarofim, A.F. and Beer, J.M. *J. Inst. Energy* **66**, 207 (1993).
14.   Tullin, C.J., Goel, S., Morihara, A., Sarofim, A.F. and Beer, J.M. *Energy and Fuels* **7**, 796 (1993).
15.   Goel,S.K.,Morihara,A. Tullin,C.J. and Sarofim,A.F., 25th Symp.(Int.) on Combustion, The Combustion Institute, Pittsburgh,1051(1994)

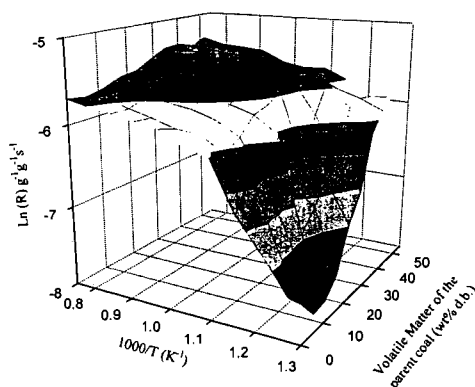Figure 1. The variation of char reactivity with 1/T and volatile matter of the parent coal.

- CO,
- CO_2,
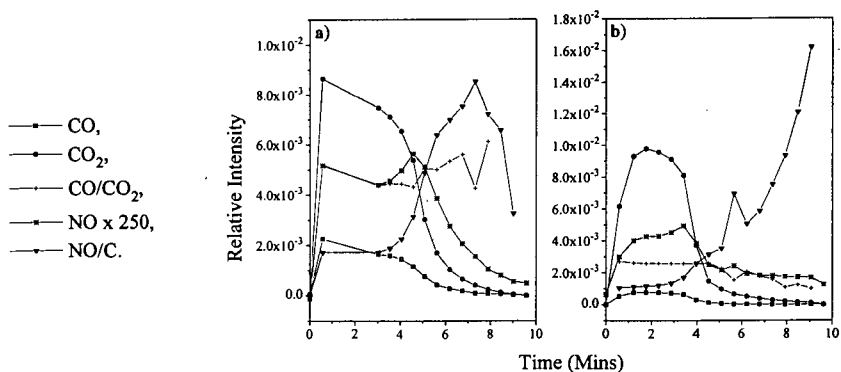- CO/CO_2,
- NO x 250,
- NO/C.

Time (Mins)

Figure 2. Gas evolution profiles from the isothermal combustion in 20% O_2/Ar of a) char-T at 873K, b) char-T at 1273K.
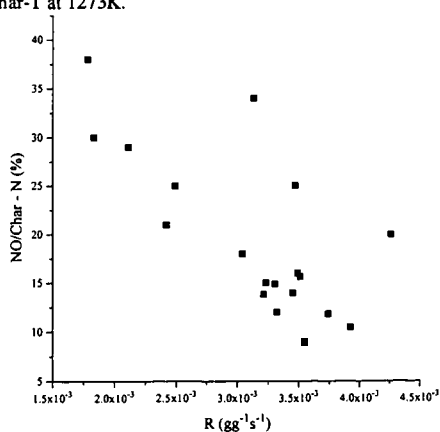

Figure 3. The variation of NO/char-N with gasification rate at 873K.

169

NO REDUCTION WITH CARBON — ANALYSIS OF REACTION MECHANISM BY USING ISOTOPICALLY LABELED NO —

Ph. Chambrion, H. Orikasa, T. Kyotani and A. Tomita
Institute for Chemical Reaction Science,
Tohoku University, Sendai 980, Japan

Keywords: Carbon; NO; Transient kinetics

ABSTRACT

The NO reduction with carbon has been investigated in the presence of oxygen. The use of both mass spectrometer and gas chromatography for gas analysis, together with the use of isotope gas, was quite powerful. It was concluded that N_2 was formed by the reaction between surface nitrogen species and gaseous NO.

INTRODUCTION

Emission of nitrogen oxides is of concern from an environmental point of view as it may be involved in the formation of photochemical smog and acid rain. When they are produced by coal combustion or diesel engines, carbonaceous matter appears to be a good candidate as reducing agent, producing N_2, CO and CO_2[1,2]. However, oxygen is usually present and particular attention was recently paid to the role it plays in the reduction of nitrogen oxides[3,4]. These studies clarified the function of oxygen-containing complexes on carbon as reaction intermediates. The presence of nitrogen-containing species at the surface of carbon was also revealed but the species appear to be stable until 1000°C, at least in the absence of oxygen[2,5].

The purpose of this study is to investigate the role of nitrogen containing species trapped on the carbon surface in the reduction of NO with carbon in the presence of oxygen.

EXPERIMENTAL

Phenol formaldehyde resin (PF) char is used as carbon source throughout this study. Its preparation was described in details in a recent publication[4]. In a typical experiment, about 200 mg of PF char was placed in a fixed bed reactor under He flow and then heat-treated at 950°C for 30 min immediately before use. The concentration of reactant gas was normally around 500 ppm of NO and 5 % of O_2 both diluted in He. $^{15}N^{18}O$ gas was purchased from Isotec Co. and its isotopic purity is 99 % for N and 95 % for O. Neither isotopically labeled carbon nor O_2 were used in this study.

Gases emitted during experiments are identified and quantified simultaneously by mass spectrometer (MS: Anelva AQA 200) and gas chromatography (GC: Area M200). For GC analysis, MS5 and PPQ columns were used for the separation of O_2, N_2 and CO and for CO_2, respectively. Both MS and GC were calibrated by using commercially available standard gases diluted in He.

RESULTS AND DISCUSSION

NO conversion in TPR experiment.

Temperature programmed reactions (TPR) of PF char in the presence of 420 ppm NO were carried out at a rate of 3°C·min^{-1} (Figure 1). Without O_2, the reaction began at about 600°C and almost completed at 950°C. In the presence of oxygen (2 vol%), NO conversion started at 200°C but remained lower than 5 % up to 450°C. Thereafter, it increased to be completed at 700°C. Thus, O_2 shifted the conversion curve of NO by more than 200°C. It should be noteworthy that O_2 conversion curve coincided with that of NO. This coincidence was also observed for other carbon samples, brown coal char, activated carbon and graphite, in spite that the reaction started at quite different temperatures for these four carbons. The reaction with O_2 might create reactive sites which are able to react with NO[2]. In the following experiments 600°C was chosen as the reaction temperature, since this is low enough to avoid an excess reaction of NO in the presence of O_2 and high enough to obtain reasonable conversion rate without O_2.

Reduction of NO at 600°C in the absence of O_2.

Conversion curve in Figure 1 indicates that NO reduction on PF char is almost negligible at 600°C in the absence of O_2. However, since pretreatment by oxygen creates reactive sites available for NO reduction, PF char pretreated by 5 % O_2 at 600°C for 20 min was used to react with 530 ppm NO. Figure 2 shows that before introduction of NO into the reactor, only residual evolution of CO was noticed, indicating the desorption of oxygen complexes from the pretreated char. Introduction

of NO was immediately followed by a dramatic increase of CO production as well as CO_2 and N_2. This indicates the effective reduction of NO even in the absence of O_2. The presence of oxygen-containing sites in char play a key role in this reaction. Thereafter, products concentration decreased to stabilize as NO conversion decreased to a quasi-steady state. After 15 min of the reaction, NO concentration was about 350 ppm in the exhaust gas, corresponding to NO consumption of 180 ppm. N_2 production did not exceed 15 ppm, suggesting the storage of nitrogen species in char. Such compounds are known to be stable, at least under an inert atmosphere to 1000°C[2,5].

Reaction of PF char with NO was immediately followed by its TPR at 10°C·min^{-1} in the presence of 5 % O_2. Figures 3a and 3b show gas evolution during this TPR. The conversion of O_2 started at 500°C (Figure 3a). CO concentration increased first to reach a maximum at 680°C and then decreased while CO_2 reached two maxima at 680 and 830°C and thereafter decreased as the amount of carbon remaining in the reactor became too small. N_2 and NO production profiles were shown in Figure 3b. It seems natural that a part of nitrogen species on PF char, produced in the preceding NO reaction, was oxidized by O_2 and converted to NO. Interestingly, as was reported in the previous paper[4], the formation of N_2 was observed in spite that only O_2 was present as a reactant. Nitrogen containing surface species was liberated as N_2 with the aid of oxygen. It should be noted that the use of both MS and GC made this observation possible.

Reduction of NO at 600°C in the presence of O_2 — Transient kinetics.

In order to clarify whether N-containing species are involved in NO reduction on PF char or not, the following transient kinetic experiment was done: a mixture of 530 ppm $^{14}N^{16}O$ and 5 % O_2 was flowed through the reactor at 600°C for 21 min and then switched to a flow of 530 ppm $^{15}N^{18}O$ and 5 % O_2 for additional 21 min. The main products were CO and CO_2. First, as shown in Figure 4a, their concentrations increased together with O_2 conversion. This may be related to the activation of PF char. Thereafter, concentrations stabilized and later CO and CO_2 production slowly decreased perhaps because of the loss of carbon. Species produced in lower amounts are presented in Figure 4b. First, the conversion of NO to N_2 increased accompanied with the activation of PF char. NO concentration in this steady state was around 370 ppm, which corresponded to disappearance of about 160 ppm. As N_2 concentration did not exceed 35 ppm, some accumulation of nitrogen in PF char might have taken place during this period.

Switching from $^{14}N^{16}O$ to $^{15}N^{18}O$ resulted in a sudden decrease in $^{14}N^{16}O$, and various products were formed. Main products were $C^{16}O$ and $C^{16}O_2$ (Figure 4a) with some $C^{16}O^{18}O$ (Figure 4b). As nitrogen-containing species, m/e of 29, 30, 31 and 33 were observed and they were assigned to $^{14}N^{15}N$, $^{14}N^{16}O$ or $^{15}N_2$ (or $C^{18}O$), $^{15}N^{16}O$ and $^{15}N^{18}O$, respectively. The most important observation here is the formation of $^{14}N^{15}N$. The concentration of $^{14}N^{15}N$ was almost the same as the amount of N_2 determined by GC at least in the initial stage of $^{15}N^{18}O/O_2$ gasification. This indicates that the main N_2 species was $^{14}N^{15}N$, and the formation of $^{14}N_2$ (the same m/e with $C^{16}O$) and $^{15}N_2$ (the same m/e with $C^{18}O$ and $^{14}N^{16}O$) was negligible. In the later stage, however, the discrepancy between $^{14}N^{15}N$ and N_2 (by gas chromatography) became apparent, and therefore $^{15}N_2$ might contribute to some extent in this region. This can be interpreted by the depletion of ^{14}N-species and accumulation of ^{15}N-species on carbon. The above observation suggests that the N_2 formation mechanism can be related to the interaction between ^{14}N-species previously kept in PF char and $^{15}N^{18}O$ in gas phase.

$$C(^{14}N) + {}^{15}NO \longrightarrow {}^{14}N^{15}N + CO_x + C_f$$
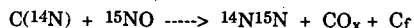
In the previous study[1], it was shown that the possibility of the above mechanism was rather small. However, the previous results were obtained in the absence of oxygen, where the formation rate of N_2 was very low. Moreover, the char was treated for 1 h with He prior to the reaction with NO, and thus the surface nitrogen species was stabilized to some extent. Therefore the present condition is different from that reported earlier and it is more close to the actual gasification condition of interest.

The total NO concentration at 40 min can be expected at around 300 ppm from the extrapolation of the NO concentration between 0 and 21 min, since the reaction itself was continuous before and after gas switching. Unreacted $^{15}N^{18}O$ was 120 ppm and $^{15}N^{16}O$ produced by isotope exchange was 110 ppm. The rest should be $^{14}N^{16}O$ which is the reaction product between surface ^{14}N and gaseous $^{16}O_2$. Gases for m/e of 46, 30 and 31 evolved rather slowly in the beginning, because accumulation of new surface species by the reaction with $^{15}N^{18}O$ was necessary for the formation of these gases.

CONCLUSION

Use of GC and MS enables to show the gas formation behavior in detail during the NO reduction with carbon in the presence of oxygen. Nitrogen-containing species previously trapped on PF char was removed as either N_2 or NO during TPR in O_2. The transient kinetic study where $^{14}N^{16}O$ was switched to $^{15}N^{18}O$ in the presence of $^{16}O_2$ clearly showed the formation of $^{14}N^{15}N$. This is a strong evidence for the proposed mechanism of N_2 formation, which involves one nitrogen from surface nitrogen-containing species and another nitrogen from gaseous NO.

REFERENCES

1. Orikasa, H., Suzuki, T., Kyotani, T., Tomita, A., Martin, R. R. *22nd Biennial Conference on Carbon*, San-Diego, 1995, pp. 626-627.
2. Teng, H., Suuberg, E. M., Calo, J. M. *Energy Fuels* 1992, **6**, pp. 398-406.
3. Yamashita, H., Tomita, A., Yamada, H., Kyotani, T., Radovic, L. R. *Energy Fuel* 1993, **7**, pp. 85-89.
4. Suzuki, T., Kyotani, T., Tomita, A. *Ind. Eng. Chem. Res.* 1994, **33**, pp. 2840-2845.
5. Kapteijn, F., Pels, J.-R., Moulijn, J. A., Zhu, Q., Thomas, K. M. *22nd Biennial Conference on Carbon*, San-Diego, 1995, pp. 548-549.
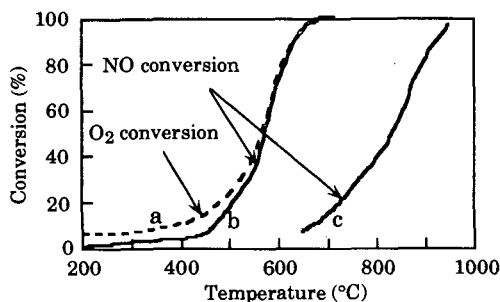
Figure 1 Gas conversion in the presence of PF char.
Reactant gas: (a,b) 420 ppm NO+ 2 % O_2, (c) 420 ppm NO.
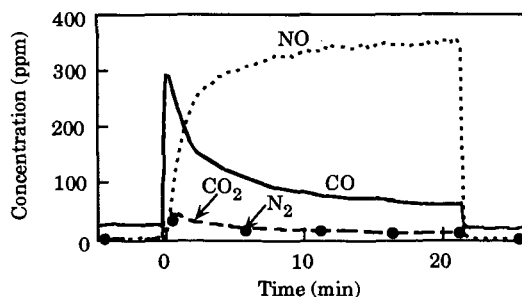
Figure 2 Gas evolution during NO reaction with PF char pretreated with O_2. Solid marks refer to N_2 concentration determined by GC.
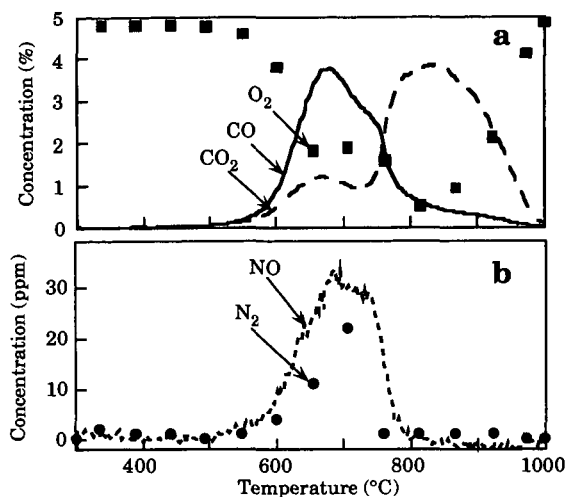
Figure 3 TPR pattern of PF char in the presence of 5 % O_2. (a) O_2, CO and CO_2, (b) NO and N_2. Solid marks refer to concentration determined by GC.
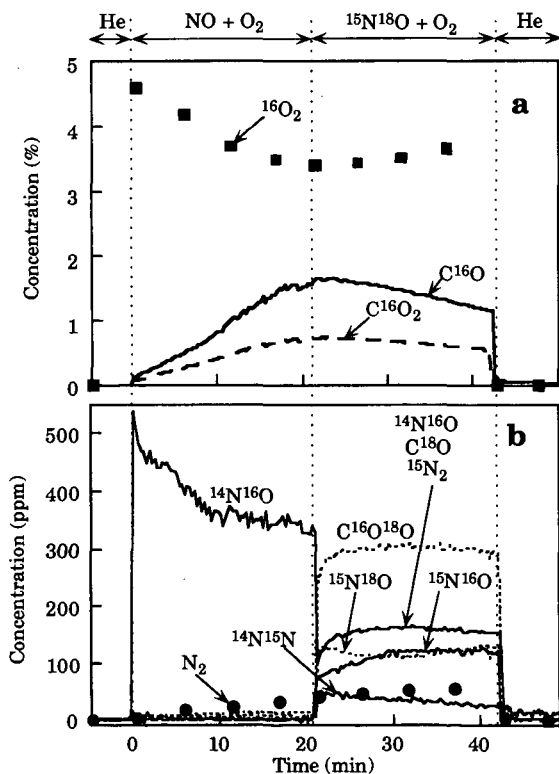
Figure 4 TK pattern on switching from $^{14}N^{16}O$ to $^{15}N^{18}O$ in the presence of 5 % $^{16}O_2$. (a) $^{16}O_2$, $C^{16}O$ and $C^{16}O_2$; (b) N_2, $^{14}N^{15}N$ and other gases. Solid marks refer to concentration determined by GC.

REDUCTION OF NITRIC OXIDE BY LOW-RANK COAL CHARS

M. J. Illán-Gómez, C. Salinas-Martínez de Lecea*, A. Linares-Solano*,
J. Phillips** and L. R. Radovic

Fuel Science Program and **Department of Chemical Engineering
The Pennsylvania State University, University Park, PA 16802
*Departamento de Química Inorgánica, Universidad de Alicante, Spain

KEYWORDS: coal, char, nitrogen oxides, reduction.

INTRODUCTION

The increasingly stringent environmental legislation requires efforts to find more effective and inexpensive pollution control systems. Removal of NO_x from both stationary and mobile sources is the subject of very intense research and development. Selective catalytic reduction (SCR) is commercially available technology [1,2]. However, when excess oxygen is present in the exhaust gases the state-of-the-art catalyst is not effective for removing NO_x [3-5].

Carbon is known to be an effective adsorbent and catalyst in the simultaneous removal of SO_x and NO_x [6-8]. Reducing agents such as NH_3, CO, H_2 or hydrocarbons with an alumina- or titania-supported catalyst are used [3,9-10]. The problem with this technology is the need to introduce a reducing agent to the feed. The use of inexpensive coal-based chars which are gradually consumed can be an interesting solution because no additional reductant is required. Chars produced from lignites are known to exhibit high catalytic activity for the reduction of NO with ammonia [11] and recently a 'calcined' char from a subbituminous coal was used to remove NO_x with the assistance of microwave energy [12].

In this paper, low-rank coal chars are used to remove NO_x from an oxygen-rich atmosphere. The effects of both pyrolysis temperature and inorganic impurities naturally present in coals are studied.

EXPERIMENTAL

Four low-rank coals, two lignites and two subbituminous coals, were selected for direct NO reduction in the presence of O_2. Table 1 shows the PSOC number, the ASTM rank and selected inorganic components in the coals. Eight chars were obtained by pyrolyzing the coals in a tube furnace at 500 and 700 °C (N_2, 80 mL/min, 1h). An additional char was prepared by pyrolyzing one of the lignites at 900 °C.

The kinetics of the $NO+O_2$/carbon reaction was studied at atmospheric pressure in a fixed-bed quartz microreactor connected to a quadrupole mass spectrometer (VG QUADRUPOLE). Temperature-programmed reaction ($^{15}NO+O_2$, 10 °C/min, $T_{max}=500$ °C) and isothermal reaction experiments were carried out in the following environments: (i) 0.5% $^{15}NO/Ar$, (ii) 5% O_2/Ar, and (iii) 0.5% $^{15}NO/5\% O_2/Ar$. Temperature-programmed desorption (TPD) runs were also conducted (He, 20 °C/min, $T_{max}=900$ °C) before and after isothermal reaction in the various mixtures.

RESULTS AND DISCUSSION

Temperature-programmed reaction (TPR) experiments. Figure 1 shows the TPR curves, %NO reduction *vs.* reaction temperature, for the three chars obtained from lignite 1422. Chars 1422/700 and 1422/900 exhibit somewhat different behavior from that of the low-temperature char (1422/500): NO reduction maximum at low temperature (T<200 °C) and a lower NO reduction capacity at high temperature (T>200 °C). As can be concluded from Figure 2, this characteristic low-temperature TPR profile is only exhibited by chars prepared from lignites 1422 and 1548, which have the highest potassium and sodium content (see Table 1). Similar low-temperature profiles were found for activated carbon loaded with potassium [13,14].

The analysis of reaction products evolved during the low-temperature reaction stage reveals some significant differences with respect to the potassium-loaded activated carbons. The quantity of N_2 evolved is much smaller than the quantity of NO retained (~5%); in other words, non-dissociative NO chemisorption seems to be the main phenomenon occurring at the low temperatures [13,14]. Subsequent desorption of thus retained NO gives rise to the negative values shown at intermediate temperatures in Figures 1 and 2.

The fact that the low-temperature TPR behavior described above is observed only for chars pyrolyzed at 700 and 900 °C means that important changes take place during the coal pyrolysis step. The theoretical temperature of reduction of potassium oxide (K_2O) by carbon (graphite) is 825 °C [15]; furthermore, it is well known [16] that reduced potassium species can spread over the surface and thus achieve a high degree of dispersion. Obviously, these two phenomena are more important at higher pyrolysis temperatures; consequently, potassium-catalyzed NO adsorption [17] becomes more pronounced.

In the high-temperature region, where a continuous increase in NO reduction is observed (Figures 1 and 2), pyrolysis temperature has the opposite effect: the low-temperature char exhibits a higher activity for NO reduction than chars pyrolyzed at higher temperatures (1422/700 and 1422/900). Analysis of the reaction products evolved shows that NO reduction is accompanied by evolution of N_2, N_2O and CO_2.

Char 1422/500 thus shows the highest activity for NO reduction. In agreement with the well known effects of pyrolysis temperature on char reactivity [18-20], it also has the highest reactivity in O_2 (see also Table 2). For example, the temperature at which the O_2/C reaction starts (during a TPR experiment) is the lowest. Also, the ignition temperature has been used in the literature as a good index to compare the reactivity of carbons in O_2 [21]; lower ignition temperature was observed for char 1422/500 (~305 °C) than for char 1422/700 (~340 °C). On the other hand, a higher ignition temperature and no substantial difference was observed for the two chars prepared from coal 1547 (~380 °C for both 1547/500 and 1547/700), which has the lowest content of potassium and sodium. This is not a surprising result of course. Alkali metals are very effective catalysts for carbon oxidation reactions [22]. Furthermore, a correlation between the NO reduction capacity of a char and its reactivity in O_2 has been discussed in detail recently [17].

It was thus of interest to monitor the nature and quantity of carbon-oxygen surface complexes formed on the surface of room-temperature-air-exposed coal chars before NO reduction. The CO_2 and CO evolved in a TPD experiment is a convenient measure of surface complexes present on the chars [23]. The quantity of CO_2 and CO evolved by the low-temperature char 1422/500 (1605 and 650 μmol/g C) is higher than that evolved from high-temperature chars 1422/700 and 1422/900 (902 and 963 μmol/g C, and 369 and 113 μmol/g C, respectively); furthermore, the chars obtained from subbituminous coals, 1547/500 and 1547/700, yield less CO_2 and CO (703 and 928 μmol/g C, and 549 and 386 μmol/g C, respectively).

The different effects of pyrolysis temperature in the low-temperature *vs.* high-temperature region imply that different active sites are involved in the two regimes. At low temperatures, the activity for NO reduction is governed by the catalyst active sites; at higher temperatures, the reactivity of the char (i.e., the number of carbon active sites) appears to control the NO reduction behavior. A similar conclusion was reached in our previous TPR study using an activated carbon loaded with different amounts of potassium: the low-temperature profile was determined by catalyst loading and dispersion, but no differences were observed at higher temperatures, where carbon reactivity controls the NO reduction capacity [14].

Isothermal reaction experiments. Isothermal reaction experiments were performed in three different atmospheres: NO+O_2, NO and O_2. After reaction (for ca. 60 minutes), a TPD experiment was also performed.

Figure 3 shows the evolution of the % NO reduction curve with time for all chars pyrolyzed at 500 °C and also for chars 1422/700 and 1422/900. Table 2 summarizes the kinetic data for NO reduction after 1 hour in both atmospheres (NO and NO+O_2), as well as the reactivity in oxygen (5% O_2, balance Ar) and the level of carbon consumption (% burnoff). The isothermal behavior observed supports the conclusions based on the TPR study: (a) chars from lignites 1422 and 1548 have a higher capacity for NO reduction than chars prepared from subbituminous coals, and (b) the low-temperature chars show the highest activity in the NO+O_2/C reaction. Table 2 also reveals that the high NO reduction level is maintained by chars 1422/500 and 1548/500 and that a reasonable carbon consumption level is achieved. The main reaction products are N_2 and CO_2, with some N_2O being evolved (N_2O/N_2=0.15), but CO is not detected.

The activity data in the absence of oxygen confirm the important enhancement of NO reduction capacity in an oxygen-rich atmosphere [24,17]. The degree of enhancement is larger for the 500 °C chars than for the 700 °C chars. It is also more important for chars obtained from the two lignites. The reactivity in O_2 seems to be the key to the understanding of these effects: chars that exhibit the highest increase in NO reduction (1422/500 and 1548/500) also have the highest reactivity in oxygen. Again, the analogy between NO reduction by carbon and the carbon/O_2 reaction is made apparent.

The results discussed above are in agreement with some recent studies of Tomita and coworkers [25] and with our previous proposal about the role of oxygen in NO reduction [17]. This can be summarized succinctly as follows:

$$2C_f + O_2 \longrightarrow 2C(O) \tag{1}$$

$$2C(O) \longrightarrow CO_2 + C_f \tag{2}$$

$$C(O) \longrightarrow CO\ (+ C_f) \tag{3}$$
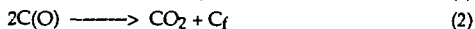
Upon desorption of CO_2 and CO, a larger number of free actives sites (C_f) on the carbon surface is produced than in the absence of O_2; it is these 'nascent' sites which increase char's activity for NO reduction. By comparing columns 3, 5 and 7 in Table 2, we conclude that, despite the much higher propensity of chars to react with O_2, the fraction of carbon consumed by NO (column 8) can be quite high. (It is this number which may require some additional optimization in pursuit of commercial viability of this novel approach to NO_x reduction.) Mochida et al. [26] recently concluded also that the active sites in carbon/NO/O_2 system are created by liberation of CO and CO_2, in contrast to their earlier assumption [7] that the active sites are the carbon-oxygen surface complexes.

Finally, analysis of the species evolved during TPD after isothermal reaction also provides valuable information. Evolution of N_2 is not significant, suggesting both that N_2 is produced primarily according to the reaction $2NO + 2C_f = 2C(O) + N_2$ [17] and that the concentration of C(N) surface complexes is not very high. This conclusion is in agreement with our previous results using activated carbons [13-14,17,27]. In Figure 4, the increase in the amount of CO_2 evolved after the $NO+O_2/C$ reaction indicates that some oxygen is retained on the surface during the NO/C reaction. This surface oxygen (or oxygen-containing species) can be retained by either the catalyst or the char. The fact that the CO_2 desorption curves show a peak with a maximum at ~560 °C suggests that CO_2 is captured by K_2O thus forming a carbonate. The formation of K_2CO_3 has also been suggested by García-García et al. [28] after the $NO+O_2/C$ reaction in similar potassium-loaded char samples; its decomposition, during subsequent TPD, exhibited a maximum at ~600 °C. The CO curves show a maximum at ~700 °C, which can be due to partial reduction of metallic oxides present in the ash (e.g., K_2O, Na_2O, Fe_2O_3) by the char. (CO peaks with maxima at ~750 and ~800 °C were observed during TPD of K- and Fe-loaded activated carbons [13,27].) In support of the above interpretation is the finding that TPD curves for chars 1422/700 and 1422/900 show a better defined CO_2 peak after $NO+O_2/C$ and O_2/C reactions, even though a lower amount of CO_2 is evolved (in agreement with the fact that these chars are less active for NO reduction): a more reduced and better dispersed potassium species seems to be obtained after pyrolysis at 700 and 900 °C. Another interesting result from this series of TPD experiments is that the amount of CO_2 retained by the char after $NO+O_2/C$ reaction increases with increasing pyrolysis temperature: 4% of CO_2 evolved is captured (as K_2CO_3) by char 1422/500, while 18 and 55% are captured by chars 1422/700 and 1422/900, respectively.

ACKNOWLEDGEMENTS

REFERENCES

1. Cho, S.M. *Chem. Eng. Prog.*, January 1994, p. 39.
2. Jüntgen, H.; Kühl, H. In *Chemistry and Physics of Carbon* (P.A. Thrower, Ed.), Marcel Dekker, New York, 1989, Vol. 22, p. 145.
3. Bosch, H.; Janssen, F. *Catal. Today* 1987, 2, 369.
4. Kapteijn, F.; Stegenga, S.; Dekker, N.J.J.; Bijsterbosch, J.W.; Moulijn, J.A. *Catal. Today* 1993, 16, 273.
5. Burch, R.; Millington, P.J.; Walker, A.P. *Appl. Catal. B* 1994, 4, 65.
6. Knoblauch, K.; Richter, E.; Jüntgen, H., *Fuel* 1981, 60, 832.
7. Mochida, I.; Ogaki, M.; Fujitsu, H.; Komatsubara, Y.; Ida, S. *Fuel* 1985, 64, 1054.
8. Kusakabe, K.; Kashima, M.; Morooka, S.; Kato, Y. *Fuel* 1988, 67, 714.
9. Harrison, B.; Wyatt, M.; Gough, K.G. *Catalysis* (London) 1982, 5, 127.
10. Armor, J.N. *Appl. Catal. B* 1992, 1, 221.
11. Lee, J.K.; Suh, D.J.; Park, S.; Park, D. *Fuel* 1993, 72, 935.
12. Cha, C.Y.; Kong, Y. *Carbon* 1995, 33, 1141.
13. Illán-Gómez, M.J.; Linares-Solano, A.; Radovic, L.R; Salinas-Martínez de Lecea, C. *Energy Fuels*, 1995, 9, 97.
14. Illán-Gómez, M.J.; Linares-Solano, A.; Radovic, L.R; Salinas-Martínez de Lecea, C. *Energy Fuels*, 1995, 9, 104.
15. Gilchrist, J.D. "Extraction Metallurgy", 2nd Ed. (Inter. Ser. Mater. Sci. Technol., Vol. 30), Pergamon Press; Oxford, UK, 1980.
16. Pullen, J.R. *Catalytic Coal Gasification*, IEA Report ICTIS/TR26, Coal Research, London, 1984.
17. Illán-Gómez, M.J.; Linares-Solano, A.; Radovic, L.R; Salinas-Martínez de Lecea, C. *Energy Fuels*, in press (to be published in January/February 1996).
18. Jenkins, R.G.; Nandi, S.P; Walker, Jr., P.L. *Fuel* 1973, 52, 288.

19. Radovic, L.R.; Walker, Jr., P.L.; Jenkins, R.G. *Fuel* 1983, *62*, 849.
20. Zhang, L.; Calo, J.M.; Lu, W. This meeting (March 1996).
21. McKee, D.W. In *Chemistry and Physics of Carbon* (P.L. Walker, Jr. and P.A. Thrower, Eds.), Marcel Dekker, New York, 1981, Vol. 16, p. 1.
22. Kapteijn, F.; Moulijn, J.A. *Fuel* 1983, *62*, 221.
23. Otake, Y.; Jenkins, R.G. *Carbon* 1993, *31*, 109.
24. Yamashita, H.; Yamada, H.; Kyotani, T.; Radovic, L.R.; Tomita, A. *Energy Fuels* 1993, *7*, 85.
25. Suzuki, T.; Kyotani, T.; Tomita, A. *Ind. Eng. Chem. Res.* 1994, *33*, 2840.
26. Mochida, I.; Kisamori, S., Hironaka, M.; Kawano, S.; Matsumura, Y.; Yoshikawa, M. *Energy Fuels* 1994, *8*, 1341.
27. Illán-Gómez, M.J.; Linares-Solano, A.; Radovic, L.R; Salinas-Martínez de Lecea, C. *Energy Fuels* 1995, *9*, 112; *9*, 540.
28. García-García, A.; Illán-Gómez, M.J.; Linares-Solano, A.; Salinas-Martínez de Lecea, C., *Proc. 8th Internat. Conf. Coal Science*, Oviedo, Spain, 1995, p. 1787.

Table 1. Properties of Coals

PSOC No.	ASTM rank	ASTM ash yield (wt %)	Inorganic element analysis (wt %)
1422	Lignite	9.49	Na, 0.73; K, 0.11; Ca, 1.4; Fe, 0.81
1548	Lignite A	6.37	Na, 0.66; K, 0.05; Ca, 1.8; Fe, 0.61
1547	Subbituminous	9.85	Na, 0.12; K, 0.05; Ca, 1.3; Fe, 0.85
1546	Subbituminous	4.80	Na, 0.25; K, 0.05; Ca, 0.60; Fe, 0.20

Table 2. NO Reduction Data at 350 °C for Different Coal Chars

Char	Pyrolysis yield (wt %)	% NO reduced		% Burnoff		Reactivity in O_2 (hr^{-1})*	F**
		$NO+O_2$	NO	$NO+O_2$	NO		
1422/500	45	54	12	19.5	0.3	0.20	0.13
1422/700	37	34	18	4.0	0.4	0.06	0.25
1422/900	32	0	-	1.1	-	0.01	0.23
1548/500	47	53	12	21.0	0.5	0.23	0.09
1548/700	40	35	15	4.0	0.4	0.04	0.37
1547/500	54	17	0	3.4	0.3	0.04	0.21
1547/700	52	11	10	2.6	0.2	0.02	0.22
1546/500	52	24	-	11.0	-	0.13	0.20
1546/700	45	11	-	4.3	-	0.05	0.27

*integrated value, based on carbon consumption over the 60-minute period.
**F = fraction of carbon consumed by NO (in the $NO+O_2/C$ reaction).
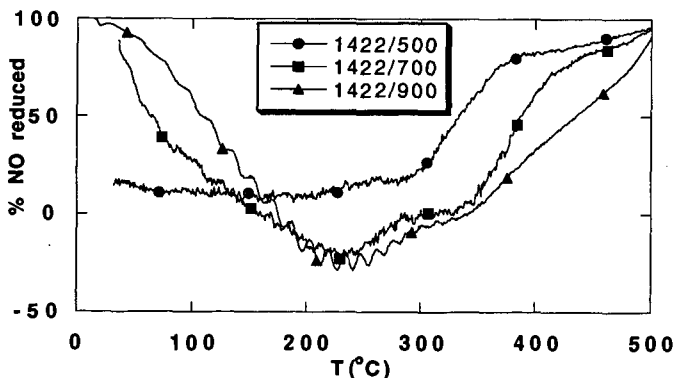
Figure 1. TPR profiles (0.5% NO, 5% O_2, balance Ar) for chars obtained from lignite 1422: effect of pyrolysis temperature.

Figure 2. TPR profiles (0.5% NO, 5% O_2, balance Ar) for chars pyrolyzed at 700 °C: effect of coal rank.

Figure 3. Effect of pyrolysis temperature on the kinetics of the NO+O_2/C reaction (350 °C; 0.5% NO, 5% O_2, balance Ar).

Figure 4. TPD profiles for sample 1422/500 before (He) and after reaction in NO+O_2, NO and O_2.

THE EFFECTS OF CaO CATALYSIS ON THE KINETICS OF
NO REDUCTION BY BEULAH ZAP CHAR

Feng Guo and William C. Hecker *
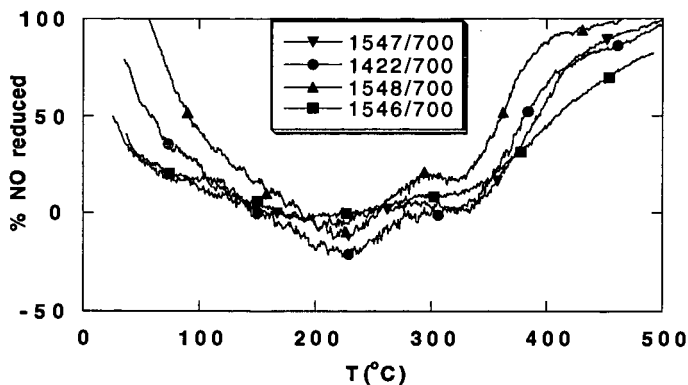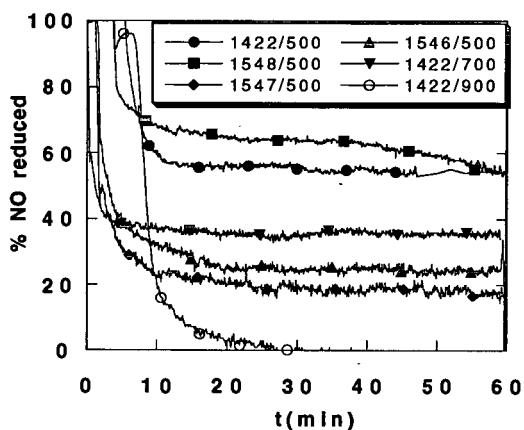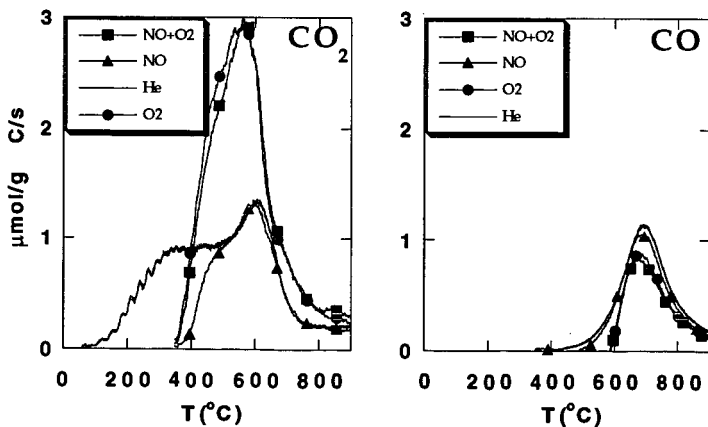*Department of Chemical Engineering and Advanced Combustion Engineering Research Center
(ACERC), Brigham Young University, 350 CB, Provo, Utah 84604*

Keywords: NO/char reaction; Catalysis; Kinetics.

INTRODUCTION

The reduction of NO emissions from combustion processes has become increasingly important in protecting the world's environment. It has been shown that Selective Catalytic Reduction (SCR) with ammonia is an effective commercial technique to remove NO_x from combustion flue gas. However, the implementation of this technique is limited by high investment and operating costs, "ammonia slip", and SO_x poisoning, which motivate the search for alternatives.[1] Carbon (activated carbon or char) is a promising reducing agent for NO_x reduction with many potential advantages, such as low cost, easy availability, high efficiency, simplicity of process, and no secondary pollution.[1-7] Moreover, the heterogeneous reaction of NO with char is very important for the understanding of the formation of NO_x from coal combustion processes. The reaction may significantly destroy the NO_x formed earlier in coal combustion, which partially contributes to low NO emission from fluidized bed combustion.[2,3] Therefore, the reaction of NO with char is receiving significant attention in the literature.

Previous investigations on the reaction of NO with char involve the kinetics and mechanism,[6-23] the effects of char surface area,[24,25] the effects of feed gas composition,[10,7,25] and the catalytic effects of metals.[5,10,22,26-29] The reaction of NO with char has generally been reported to be first order with respect to NO partial pressure,[7,13-16] but reaction orders between 0.42 and 0.73 have also been reported.[30] A sharp shift in the activation energy has been observed in the temperature range of 873~973 K, which suggests a complex reaction mechanism.[6,7,15-18] Several mechanisms have been proposed.[5,6,12,16,18,19,31] However, questions concerning N_2 formation, the surface complexes, the nature of active surface sites, and the effects of minerals in char ash are still not well understood. In most previous studies, chars were taken to be pure carbon, thus the effects of the ash in chars and its composition on the kinetics and mechanism of the reduction reactions are not well known. Although the catalytic effects of certain metals or metal oxides on the reactions have been investigated,[5,10,22,26-29] little is known about their effects on the kinetics of the reaction. Therefore, the objectives of this study are to investigate the kinetics of the reaction of NO with Beulah Zap chars, to study the effects of CaO on the kinetics.

EXPERIMENTAL METHODS

The chars used in this study were prepared from 63 – 74 µm particles of North Dakota Beulah Zap lignite in a methane flat-flame burner (FFB). Parent char (NDL), a portion of NDL *washed* with HCl to remove mineral matter (NDW), and a portion of NDW *reloaded* with calcium oxide (NCa) were used. The CaO contents of NDL, NDW, and NCa are 3.5, 1.1, and 2.4% , respectively. All of these chars were made previously in our laboratory, and details of their preparation were reported elsewhere.[32,33]

The reduction of NO by char was carried out for all chars at 5 – 6 temperatures between 723 and 1073K in a 10 mm ID VYCOR® glass vertical packed bed reactor with a fritted quartz disc of medium porosity as a support. For each run, 0.2 g char mixed with 2 g silicon carbide (inert materials for the reduction of NO) was packed in the reactor, and heated in He to the maximum temperature desired using an electric furnace. NO diluted with He (3130 ppm of NO) was then fed downward through the reactor for about 1 hour, when a pseudo-steady state was reached. Data were subsequently collected at 5 to 6 flow rate settings between 100 and 500 ml/min (NTP) at each of the temperatures studied. For each run, it took about 4 hours to collect all the data, and the burnout of the char was about 10% during that period of time. The inlet gas pressure in the reactor was controlled at 300 kPa (3 atm). The outlet pressure at each condition was also measured to determine the pressure drop cross the packed bed.

The compositions of outlet gases were continuously monitored for N_2 , CO, CO_2, N_2O, and O_2 by a GC (Perkin-Elmer, 3920B) with TCD and two columns (one packed with Chromosorb 106, the other packed with molecular sieve 5A), and for NO and NO_2 by a Chemiluminescence NO_x analyzer (Thermo Environmental, 42H). The variations in nitrogen and oxygen mass balances were determined between inlet and outlet streams for each run and always fell within ±5%.

RESULTS AND DISCUSSION

Pretests and Corrections. A typical plot of NO conversion vs. time shows that decreases from 100% to its pseudo-steady state value after about 1 hour. This probably results from NO adsorption on the sample and/or very active char surface sites that are quickly consumed. Thereafter, the conversion of NO decreases very slowly because of the loss of char mass. In order to account for the effect of the char mass loss in the calculation of kinetic parameters, a correction was made based on a carbon mass balance using the following stoichiometric reaction:

$$C + (1+y) NO = (1-y) CO + y CO_2 + 1/2(1+y) N_2 \qquad (1)$$
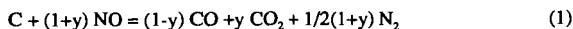
where $y = [CO_2]/([CO]+[CO_2])$, and [CO] and $[CO_2]$ are concentrations of CO and CO_2, respectively. Since [CO] and $[CO_2]$ are measurable quantities, the mass loss of char, ML (g), can be calculated

$$ML = 12 \cdot t \cdot F^0_{NO} \cdot X_{NO}/(1+y) \qquad (2)$$

where t is reaction time elapsed (min); X_{NO} is average conversion of NO in this period; F^0_{NO} is the inlet molar flow rate of NO (mol/min) calculated from the ideal gas law.

Figure 1 shows the variation of char mass (W) with the NO conversion (X_{NO}) in the form of the integrated rate expression, where the char mass has been corrected using Eq. 2, for the beginning and end of run. Since both sets of values fit the same straight line, the effect of the char mass loss on the reaction rate constant has been eliminated.

As mentioned, the inlet reactor pressures was typically 3.0 atm., but the outlet pressures varied with flow rate. In the calculation of concentration used in the kinetic rate expression, an average pressure $P = (P_{in} + P_{out})/2$ was used. Figure 2 shows how using this approach gives kinetic data that all fell on the same straight line for runs in which the pressure was varied (P_{in} from 1.5 to 3.0 atm. and P_{out} from 1.2 to 2.8 atm.) and the total flow rate was varied.

The calculation of film mass transfer and pore diffusion resistances for a worst case scenario (the maximum particle diameter, the minimum flow rate, and the maximum reaction rate observed) indicated that film mass transfer (maximum MT resistance = 2.7%) and pore diffusion (minimum effectiveness factor = 0.99)were negligible in this study.

Kinetics. Because a broad range of NO conversion was observed in this study, the reactor was modeled as an integral plug flow reactor. The reaction rate constants and reaction order were obtained by integral analysis of the experimental data. Briefly, the differential form of the plug flow reactor performance equation is

$$dW/F^0_{NO} = dX_{NO}/ -r_{NO} \qquad (3)$$

If the reaction is first order in NO (as confirmed later), integrating Eq. (3) produces the integrated rate expression as

$$-\ln (1-X_{NO}) = k_1 C^0_{NO} W/F^0_{NO} \qquad (4)$$

where X_{NO} = NO conversion (= (moles NO in - moles NO out) / moles NO in); F^0_{NO} = inlet molar flow rate of NO (moles/s); W = char weight (g); $-r_{NO}$ = NO depletion rate (moles NO reacted/s*g_char); C^0_{NO} = initial NO concentration (moles/L); k_1 = first order rate constant (L/s*g_char).

Thus, if experimental data are plotted as $-\ln(1-X_{NO})$ vs. $C^0_{NO} W/F^0_{NO}$ and a straight line is obtained that passes through the origin, then evidence of 1st order kinetics is obtained and the slope of the line equals the value of the rate constant, k_1.

The experimental data for NDL char plotted as $-\ln(1-X_{NO})$ vs. $C^0_{NO} W/F^0_{NO}$ are shown in Figure 3, indicating that the reaction is first order with respect to NO. Attempts to fit the data to other orders were made, but straight lines were not obtained for all temperatures. Table 1 lists values for the reaction rate constants, their lower and upper 95% confidence limits, and statistical analysis parameters for NDL char data obtained at 6 different temperatures. The correlation coefficients, t-test values, and F-test values all show that the experimental data were excellently fit by first order kinetics under the experimental conditions. The standard error was typically less than 5%. Similar results were obtained for the other two chars, NDW and NCa.

The Effect of CaO. The variations of NO conversion with temperature are shown in Table 2 for three char types at a flow rate of 303 ml/min (NTP) . The results for other flow rates are similar. The conversion of NO increases noticeably in the order NDL > NCa > NDW. This is in the same order as the CaO content of the three chars, 3.5% > 2.4% > 1.1%. Therefore, the effects of CaO on the reaction of NO with chars appear to be significant.

Figure 4 shows the Arrhenius plots of the rate data for NDL, NDW, and NCa chars. The bars around points in the figure show the variation of the reaction rate constants in 95% confidence level. A sharp shift in the apparent activation energy with temperatures was observed, as also reported in literature.[6,7,15-18] The temperatures at which the transition takes place are in the range of 823 ~973 K, and decrease as the CaO content increases. This shift to higher activation energy with increasing temperature is opposite to the expectation if a reaction is changing from chemical rate control to mass transfer control, and suggests different mechanisms or rate determining steps at high and low temperatures. It is also noted that at low temperatures the apparent activation energies for all three char types are essentially the same (22 ~ 26 kcal/mol); at high temperatures, however, the activation energies vary from 45 to 60 kcal/mol, increasing as the CaO content of the

chars decreases. The variation of the NO reduction reactivity, the apparent activation energy, and the transition temperature with the CaO content are summarized in Table 2.

Discussion. The active surface sites of carbon are generally classified as edge sites and basal sites. At low temperatures, the reactivity of the basal sites can be negligible, compared to that of the edge sites.[21] In addition to the active sites of carbon, there exist other active sites, including sites on the surface of CaO, K_2O, CuO, and other potential catalysts. These active sites, as chemical or structural impurities, enhance the carbon edge sites; they can also chemisorb NO dissociatively like the carbon active sites. While chemisorbed oxygen migrates to and reacts with the carbon edge sites around, the chemisorption of NO on the inorganic sites continues. Therefore, CaO, K_2O, CuO etc. may exhibit catalytic effects on the reaction of NO with char.

The reactivity of NO with char increases significantly with increasing CaO content. Such increase involves two aspects. On one hand, an increase in CaO content provides more defects of coal structure, the reactivity of char then increases; on the other hand, the catalytic effects of CaO also increase due to more active CaO sites. The reaction of NO with char may not proceed as a simple catalytic process. Two routes may exist in parallel, which are the direct reduction of NO on active carbon sites and the catalytic reduction of NO through active CaO sites. When there are enough active CaO available, the catalytic reduction route is predominant. On the other hand, when very few active CaO sites exist, the direct reduction route becomes predominant. Between the two extreme cases, which most actual cases may belong to, the reduction of NO may be controlled by the both routes. Therefore, the two parallel processes should be taken into account in the mechanism of the reaction of NO with char. A possible parallel reaction model may be described as follows:

$$NO + 2C^* \rightarrow C^*(O) + C^*(N) \qquad (1a)$$
$$NO + 2C \leftrightarrow C(O) + C(N) \qquad (1b)$$
$$NO + 2S \rightarrow S(O) + S(N) \qquad (1c)$$
$$2C^*(N) \text{ (or } S(N)) \rightarrow N_2 + 2C^* (\text{or } S) \qquad (2)$$
$$S(O) + C^* \rightarrow C^*(O) + S \qquad (3a)$$
$$C(O) + C^* \rightarrow C^*(O) + C \qquad (3b)$$
$$C^* + C^*(O) + NO \rightarrow CO_2 + C^*(N) \qquad (4)$$
$$C^*(O) \rightarrow CO \qquad (5)$$
$$C^*(O) + CO \rightarrow CO_2 + C^* \qquad (6)$$
$$2C^*(O) \rightarrow CO_2 + C^* \qquad (7)$$
$$CO_2 + C^* \rightarrow 2C^*(O) \qquad (8)$$
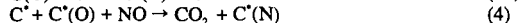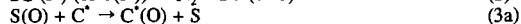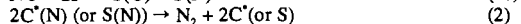
where C^* is the carbon edge sites; C is the basal sites; S is the active sites of catalysts. Reactions 1a, 1b, 1c are parallel processes of the dissociative chemisorption of NO. The desorption of the chemisorbed oxygen involves only the carbon edge sites (C^*) represented by Reaction 4, 5, 7, and 8, which are parallel routes. All oxygen atoms adsorbed on the other active sites (C or S) need to migrate to the carbon edge sites before desorption as described by Reaction 3a, 3b. On the bases of the facts of the delay in CO_2 or CO evolution with respect to N_2 [27-29] and the positive effects of O_2 on the reaction of NO with char,[5] it is reasonable to assume that the desorption of the chemisorbed oxygen is the rate determining steps. At low temperatures, Reactions 5 and 8 may be slow; therefore, the reaction rate of NO with char may depend on Reactions 4, 6, 7 or a combination of these reactions, and CO_2 is a dominant product of C-containing species; at high temperatures, however, Reactions 5 and 8 become fast, and Reaction 5 will be a major pathway of the desorption of the chemisorbed oxygen, so that Reaction 5 controls the reaction rate of NO with char, and CO becomes a dominant product. With the shift in the rate determining step, the apparent activation energy also changes as shown in Figure 4.

Since the reduction of NO by char is composed of two parallel processes, i.e. the direct reduction of NO on active carbon sites and the catalytic reduction of NO through active CaO sites, it seems that the apparent activation energy for the global reaction of NO with char is a combination of the activation energies of the two parallel processes in some way. When the CaO content (actually the CaO surface area) increases, the proportion of the catalytic reduction may increase. If the activation energy for the catalytic reduction is lower than that for direct reduction (a reasonable assumption), the apparent activation energy will decrease as the CaO content increases as listed in Table 2 for the high temperature data.

CONCLUSION

The kinetics of the reaction of NO with char have been determined for three kinds of chars with different CaO contents. The reaction is first order with respect to NO partial pressure, and has a sharp shift in the activation energy with temperature. The shift temperature decreases as the CaO content in the chars increases. At low temperatures, the activation energies for all three char types are essentially the same (22-26 kcal/mol); at high temperatures, however, the activation energies vary in the range of 45 to 60 kcal/mol, and increase as the CaO content decreases. The migration of the chemisorbed oxygen on basal carbon sites to carbon edge sites at high temperatures may result in a shift in the rate determining step, so that a shift in the activation energy takes place . When the CaO content increases, the activation energy of the migration of the chemisorbed oxygen may decrease; hence, the shift temperature decreases.

References

(1) Bosch, H. *Catalysis Today*, **1988**, 2, 1.

(2) Pereira, F. J.; Beer, J. M.; Gibbs, B.; Hedley, A. B. *15th Symposium (International) on Combustion*; The Combustion Institute: Pittsburgh, 1975, p1149.

(3) Johnson, J. E. *Fuels* **1994**, 73, 1398.

(4) Illan-Gomez, M. J.; Linares-Solano, A.; Salinas-Martinez de Lecea, C. *Energy Fuels* **1993**, 7, 146.

(5) Yamashita, H.; Tomita, A., *Energy Fuels* **1993**, 7, 85.

(6) Teng, H.; Suuberg, E. M.; Calo, J. M. *Energy Fuels* **1992**, 6, 398.

(7) Furusawa, T.; Tsunoda, M.; Tsujimura, M.; Adschiri, T. *Fuel* **1985**, 64, 1306.

(8) Furusawa, T.; Kunii, D.; Osuma, A.; Yamada, N. *Int. Chem. Eng.* **1980**, 20, 239.

(9) Wendt, J. O. L.; Pershing, D. W.; Lee, J. W.; Glass, J. W. *17th Symposium (International) on Combustion*; The Combustion Institute: Pittsburgh, 1979, p77.

(10) Levy, J.; Chan, L. K.; Sarofim, A. F.; Beer, J. M. *18th Symposium (International) on Combustion*; The Combustion Institute: Pittsburgh, 1981, p111.

(11) Watts, H. *Trans. Faraday Soc.* **1958**, 54, 93.

(12) Smith, R. N.; Swinehart, J.; Lesnini, D. *J. Phys. Chem.* **1959**, 63, 544.

(13) Richthofen, A. V.; Wendel, E.; Neuschiitz, D. *Fresenius' J. Anal. Chem.* **1993**, 346, 261

(14) Edwards, H. W. *AIChE Symp. Ser. No. 126*, **1972**, 68, 91.

(15) Song, Y. H.; Beer, J. M.; Sarofim, A. F. *Combust. Sic. Technol.* **1981**, 25, 237.

(16) Chan, L. K.; Sarofim, A. F.; Beer, J. M. *Combust. Flame* **1983**, 52, 37.

(17) Radovic, L. R.; Walker, Jr., P. L. *Fuel Process Technol.* **1984**, 8, 149.

(18) Suuberg, E. M.; Teng, H.; Calo, J. M. *23rd Symposium (International) on Combustion*; The Combustion Institute: Pittsburgh, 1990; p1199.

(19) Teng, H.; Suuberg, E. M. *J. Phys. Chem.* **1993**, 97, 478.

(20) Teng, H.; Suuberg, E. M. *ind. Eng. Chem. Res.* **1993**, 32, 416.

(21) Chu, X., Schmidt, L. D. *Ind. Eng. Chem. Res.* **1993**, 32, 1359.

(22) Lai, C.-K. S.; Peters, W. A.; Longwell, J. P. *Energy Fuels* **1988**, 2, 586.

(23) Matos, M. A. A.; Pereira, F. J. M. A.; Ventura, J. M. P. *Fuel* **1991**, 70, 38.

(24) Shimizu, T.; Sazawa, Y.; Adschiri, T.; Furusawa, T., *Fuel* **1992**, 71, 361.

(25) Yamashita, H.; Yamada, H.; Tomita, A. *Applied Catalysis*, **1991**, 78, L1-L6.

(26) Furusawa, T; Koyama, M; Tsjimura, M. *Fuels* **1985**, 64, 413.

(27) Illan-Gomez, M. J.; Linares-Solano, A.; Radovic, L.; Salinas-Martinez de Lecea, C. *Energy Fuels* **1995**, 9, 97.

(28) Illan-Gomez, M. J.; Linares-Solano, A.; Radovic, L.; Salinas-Martinez de Lecea, C. *Energy Fuels* **1995**, 9, 104.

(29) Illan-Gomez, M. J.; Linares-Solano, A.; Radovic, L.; Salinas-Martinez de Lecea, C. *Energy Fuels* **1995**, 9, 112.

(30) Johnson, J. E.; Dam-Johansen, K. *11th International Conference on Fluidized Bed Combustion*, American Soc. Mech. Eng., New York, 1991, p1389.

(31) De Soete, G. C. *23rd Symposium (International) on Combustion*; The Combustion Institute: Pittsburgh, 1990; p1257.

(32) Cope, R. F.; Arrington, C. B.; Hecker, W. C. *Energy fuels* **1994**, 8, 1059.

(33) Cope, R. F. *Dissertation*, Brigham Young University, Provo, Utah, 1995.

(34) Illan-Gomez, M. J.; Linares-Solano, A.; Radovic, L.; Salinas-Martinez de Lecea, C. 8th International conference on Coal Science, Oviedo, Spain, 1995, p1911.

Table 1   The Reaction Rate Constants of NDL Char and Statistical Analysis

T	k_1	k_1	k_1	Std Error	Corr Coef	t Test	t-distrib	F Test	F-distrib
°C	L/sec*g_char	Low 95%	Up 95%		r^2		$\alpha=0.01$		$\alpha=0.01$
650	0.0736	0.0562	0.0909	4.03E-03	0.994	18.2	9.925	333	199
625	0.0353	0.0333	0.0373	7.29E-04	0.998	48.5	4.604	2348	26
600	0.0182	0.0161	0.0202	7.40E-04	0.993	24.6	4.604	457	26
600	0.0181	0.0158	0.0205	8.48E-04	0.991	21.4	4.604	604	26
550	0.0070	0.0063	0.0078	2.66E-04	0.994	26.5	4.604	701	26
500	0.0029	0.0026	0.0032	1.10E-04	0.994	26.2	4.604	686	26
470	0.0016	0.0016	0.0017	2.56E-05	0.999	64.1	4.604	4103	26

Table 2   NO Reduction Reactivity, Apparent Activation Energy and Transition Temperature for Three Char types

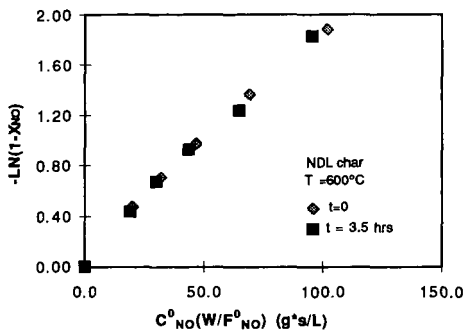|	CaO %	T @50% conv. (Q=303ml/m), K	Transition T K	App. Act. Energy (kcal/mol)	
				High Temp	Low Temp
NDL	3.5	875	853	44.5±5	22.2±3
NCa	2.4	940	893	53.1±5	26.2±3
NDW	1.1	980	953	59.5±5	22.7±3

Figure 1 The effect of run time on the integrated rate expression after the char mass loss correction.
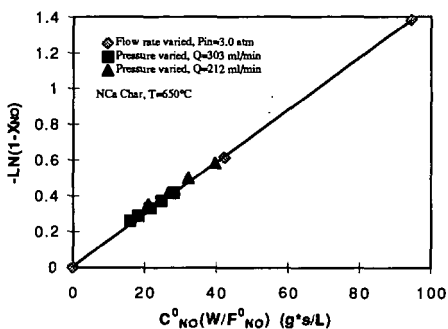

Figure 2 The effect of pressure and flow rate (P_{out}) on the integrated rate expression, using $P_{bed} = 1/2(P_{in} + P_{out})$.
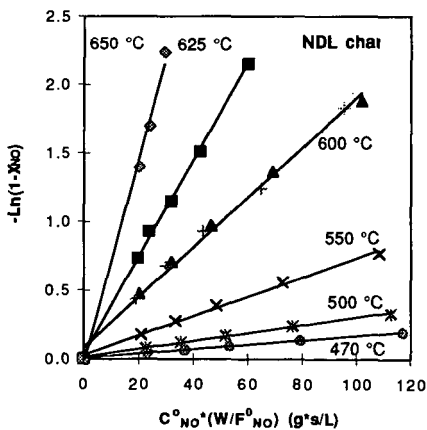

Figure 3 Experimental data for NDL char plotted as $-ln(1-X_{NO})$ vs. $C^0_{NO}W/F^0_{NO}$
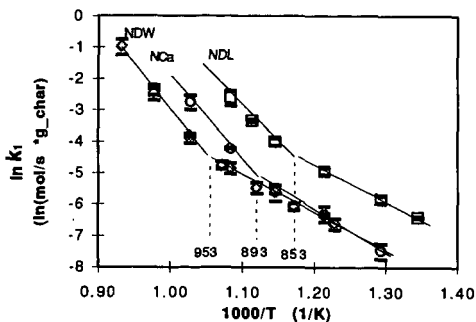

Figure 4 Arrhenius plots of the reaction rate constants for NO reduction with char for three chars.

183

NO_x AND SO_2 ADSORPTION ON CARBON

Aurora M. Rubel and John M. Stencel
Center for Applied Energy Research
University of Kentucky
Lexington, KY 40511-8433, USA

Keywords: NO_x, SO_2, adsorption, carbon

INTRODUCTION

The need to control NO_x emissions from fossil fuel power plants has lead to the development of commercially proven technologies, the best known being selective catalytic reduction (SCR)[1-3]. Because NO_x concentrations are generally at near trace levels and less than 0.3%[4], a number of other potentially more efficient control measures have and are being investigated. One such measure includes the use of adsorbents such as metal oxides[5,6], ion-exchanged zeolites[7], activated carbon fibers with and without modifiers[8-10], and activated carbons[11-15].

Activated carbons can be used effectively for SCR and for the oxidation of SO_2 to SO_3 with the subsequent formation of H_2SO_4[16-19]. The uptake of SO_2 by carbons in the absence of NO_x has been studied extensively[20-26]. Moisture[20-22], O_2 content[22-25], and temperature[24] influence greatly the amount of SO_2 adsorbed onto activated carbons, although agreement is lacking on the synergistic or detrimental effects of co-adsorbed O_2 and H_2O[22-25]. It has been suggested that two different sites on the carbon are involved in SO_2 adsorption and oxidation[26], and that two different SO_2 species are present on the carbon during and after adsorption[22-25].

NO adsorption onto activated carbons over a temperature range of 20-120°C and in the absence of SO_2 have been reported[11-15, 27-29]. Without O_2, a carbon's NO uptake capacities and adsorption kinetics were low[27, 28] in comparison to when O_2 was present as a co-adsorbate[11-13]. These data have shown that the adsorption of NO from a simulated flue gas containing O_2, CO_2, and H_2O involved the catalytic conversion of $NO + \frac{1}{4} O_2 \rightarrow NO_2$ at active site(s) on the carbon[11-13] leading to NO_x adsorption capacities as high as 200 mg NO_2 (g carbon)$^{-1}$. No published work has been found which details adsorption capacities and kinetics during the co-adsorption of NO and SO_2 over activated carbons or other porous materials. However, an understanding of the effects of such co-adsorption is very important because the combustion flue gas from every type of fossil fuel will contain SO_2 and NO_x. Hence, this work was performed to elucidate interactions between NO_x and SO_2 in and over activated carbons during adsorption and desorption cycling.

EXPERIMENTAL

Instrumentation. NO_x/SO_2 adsorption/desorption profiles were obtained using a Seiko TG/DTA 320 coupled to a VG Micromass PC quadrupole mass spectrometer (MS). A heated (170°C) fused silica capillary was used to transfer an aliquot of the atmosphere above the sample pan in the thermogravimetric analyzer (TG) to an inert metrasil molecular leak which interfaced the capillary with the enclosed ion source of the MS. Both instruments were controlled by computers which also provided for programmable control of the furnace, continuous weight measurements, sweep gas valve switching, data acquisition and analysis, review of MS scans and export of data to other computers. The MS has a Nier type enclosed ion source, a triple mass filter, and two detectors (a Faraday cup and a secondary emissions multiplier).

TG-MS procedures. The TG sample pan was loaded with a constant activated carbon volume weighing approximately 20-30 mg. The sweep gas flow rate through the TG was held constant at 200 ml m^{-1} metered at room temperature and pressure. The heating regime of the furnace incorporated segments in the following order for pre-conditioning, cooling, adsorption, reversible desorption, and temperature-induced (irreversible) desorption. Explanations of each step and example programs have been previously published[11,13.] For this study, the pre-conditioning and irreversible desorption heating rate, adsorption time interval, reversible desorption time, and the maximum desorption temperature were 20 °C m^{-1}, 60 m, 30 m, and 350 °C respectively. A He gas sweep was used during pre-conditioning, and reversible and irreversible desorptions. Pre-conditioned carbon was exposed to simulated flue gas only during the adsorption step. Multiple and consecutive adsorption/desorption cycles could be performed by recycling the furnace temperature program.

The MS was used to continuously monitor gases during an experiment. Spectral scans were acquired over a 1-100 a.m.u. range with a total measurement interval of approximately 30 s per 100 a.m.u..

Mass ion identification, analytical procedures, and materials. The identification of desorbed gases detected by the MS was done by using the major mass ions, 64, 44, 32, and 18, for SO_2, CO_2, O_2, and

H_2O respectively. The major mass ion for both NO and NO_2 is 30. The relative abundance of a.m.u. 46 for NO_2 gas is approximately 40 percent, but in mixtures of gases, this value can change. Therefore, NO and NO_2 were identified by comparing the mass ion ratio, 30/46, during desorption with ratios determined using mixtures of NO or NO_2 and all combinations of gases used during our study.

A carbon, commercially produced by physical activation with steam, was used. The carbon had N_2 BET total, meso- and micropore surface areas and pore volumes of 460, 20, and 440 m^2 g^{-1} and 0.69, 0.45, and 0.24 ml g^{-1} respectively. The chemical and physical properties of this carbon, identified as carbon, a, in a previous publication, has been described in detail[15]. Carbon pre-conditioned under a flow of He or SO_2 was used.

Three simulated flue gas mixtures were used during this study. The concentrations of O_2, CO_2, and H_2O were held constant at 5%, 15%, and 0.4-0.6% respectively. The NO and SO_2 composition of the three mixtures were varied as follows: 1% NO with 0% SO_2, 1% NO with 0.025% SO_2, and 0% NO with 0.025% SO_2. He was used as the balance gas. The primary variable studied was the simulated flue gas composition at an adsorption temperature of 70°C.

RESULTS AND DISCUSSION
Adsorption/desorption profiles shown in Figure 1 were generated during each TG/MS experiment. The weight gained, weight lost and an identification of the desorbed gas species were determined using these profiles. Figure 1 shows a profile for the co-adsorption of NO_2 and SO_2 at 70°C. Carbon pre-conditioning is performed up to point a. The weight gained upon exposure of the carbon to the simulated flue gas (points a-to-b) was attributed to the adsorption of gas components. Weight lost at the adsorption temperature after switching from the simulated flue gas to He (points b-to-c) was attributed to "reversibly adsorbed" species. Weight lost as a consequence of increasing the temperature of the carbon (points c-to-d, and beyond), i.e. during temperature programmed desorption (TPD), was attributed to two "irreversibly adsorbed" species which evolved at different temperatures. They were identified by MS as NO_2 and SO_2 and were the only evolved gas species detected. Upon reaching the maximum desorption temperature, the carbon weight returned to the pre-adsorption starting weight.

Weight gain curves during exposure of the activated carbon to the three different flue gas mixtures are presented in Figure 2. The total uptake decreased from 143 mg (g carbon)$^{-1}$ -to- 129 mg (g carbon)$^{-1}$ when SO_2 was a constituent in the gas. Pre-saturating the carbon with SO_2 prior to exposure to gases containing both NO and SO_2 decreased further the total uptake to 109 mg (g carbon)$^{-1}$. In the presence of SO_2 only (no NO), the uptake was only 24 mg (g carbon)$^{-1}$.

The desorption weight loss curves, presented in Figure 3, were defined with respect to reversible and irreversible (TPD) components. Reversible desorption accounted for 18%, 36% and 58% of the total uptake for gases containing both NO and SO_2, NO alone, or SO_2 alone, respectively. Figure 4 shows the DTG curves acquired during TPD and Figure 5 gives the desorption weights which could be attributed to specific evolved gases by MS. For simulated flue gas containing NO and SO_2, two irreversibly adsorbed species desorbed from the carbon and were identified to be NO_2 and SO_2. The temperature of maximum evolution was 145°C for NO_2 and 319°C for SO_2 (also see Figure 1). The adsorption of NO_2 in the absence of SO_2 also gave two irreversibly adsorbed species, having temperatures of maximum evolution at 144°C and 352°C. These two irreversible components were identified as NO_2 and CO_2 respectively. Only one irreversibly adsorbed species, identified as SO_2, was desorbed from the carbon after exposure to gas containing SO_2 (no NO). The maximum evolution of this SO_2 occurred at 302°C.

When SO_2 was present, the amount of irreversibly adsorbed NO $_2$ decreased to 68 mg (g carbon)$^{-1}$ from 87 mg(g carbon)$^{-1}$ when SO_2 was not present (Figure 5). The amount of irreversible NO_2 species further decreased to 59 mg (g carbon)$^{-1}$ when the carbon was pre-saturated with SO_2. However, the amount of irreversibly bound SO_2 was doubled when SO_2 was adsorbed in the presence of NO in comparison to when SO_2 was adsorbed by itself. This enhancement suggests that there is synergistic interaction between NO_2 and SO_2 during adsorption onto the carbon. Another observation was the fact that carbon pre-saturated with SO_2 and then exposed to the NO + SO_2 - containing flue gas (compare Figures 2 and 5) adsorbed more SO_2 than without the pre-saturation. Additionally, the temperature of desorption for the irreversibly adsorbed SO_2 species was increased from 300°C (in the case of SO_2 adsorption without NO) to 320°C when SO_2 and NO_2 are co-desorbed.

We have previously postulated that NO_2 adsorption involved the catalytic conversion of NO + ½ O_2 → NO_2 at an active site(s) on the carbon and that NO_2 then condenses within the micropores of the carbon[13]. It is possible that active sites are created during the co-adsorption of NO_2 and SO_2 that are

not created during the adsorption of SO_2 by itself, or the presence of NO_2 on the surface may assist the oxidation of $SO_2 \rightarrow SO_3$ on the carbon which enhanced the uptake of SO_2. Relative to the effects of SO_2 on the uptake capacity of NO_2, it may bind to or interfere with the sites involved in the catalytic conversion of NO-to-NO_2, thereby resulting in lower NO_2 adsorption.

The temperature of maximum evolution of NO_2 was not altered by the presence of SO_2, indicating that the mechanism of condensation of NO_2 within the micropores was not affected by SO_2 surface species. Because condensation of NO_2 within the micropores would be strongly dependent on van der Waal forces[5,10,12], and because SO_2 and NO_2 have similar van der Waal force constants, it is possible that adsorbed SO_2 would not affect the NO_2 storage mechanism. However, SO_2 has a critical volume 1.5 times that of NO_2 and has stronger bonding to the carbon. Both of these factors would suggest that the adsorbed SO_2 species may concentrate at pore mouths, a location which would limit NO_2 condensation. The slower rate of reversible desorption when $NO_2 + SO_2$ are co-adsorbed (Figure 3) in comparison to adsorption of NO_2 alone may also reflect a physical impediment related to SO_2; for instance SO_2 bound to active sites could limit or block the access of NO_2 to the micropores, thereby affecting not only the storage capacity but also the rate of adsorption/desorption.

In fact, the maximum adsorption rate and the desorption rate for the irreversibly adsorbed NO_2 species were decreased by the co-adsorption of SO_2 (Figure 6). Good correlations ($r^2 = 1.00$) were obtained for the decline in the maximum adsorption rate (second order) and desorption rate (first order) versus the amount of SO_2 adsorbed. We have previously reported that the NO_2 adsorption capacity of different carbons was dependent on the maximum adsorption rate of NO_2, but that the desorption rate of the irreversibly adsorbed NO_2 species was the same for all carbons[15]. For the current study, the amount of NO_2 stored in the carbon versus the maximum adsorption rate, as influenced by SO_2, resulted in a good second order correlation, $r^2 = 0.995$ (Figure 7).

SUMMARY AND CONCLUSION
During the co-adsorption of NO_2 and SO_2 from a simulated flue gas, less NO_2 and substantially more SO_2 was adsorbed in comparison to when either oxide was adsorbed by itself. The adsorption mechanism for NO_2 remained unchanged in the presence or absence of SO_2. When NO_2 and SO_2 were co-adsorbed, a synergism improved the capacity of the carbon for SO_2 uptake. The presence of adsorbed SO_2 in the carbon significantly decreased the rate of adsorption and the rates of both reversible and irreversible desorption of NO_2, indicating the possibility of a physical impediment created by the adsorbed SO_2.

REFERENCES
1. Bosch, H. and Janssen, F. *Catal. Today* 1988, **2**, 369
2. Grzybek, T. and Papp, H. *Appl. Catal. B. Environ.* 1992, **1**, 271
3. Radtke, F., Koeppel, R.A., and Baiker, A. *Appl. Catal.* A 1994, **107**, L125
4. Ritter, J.A. and Yang, R.T. *Ind. Eng. Chem. Res.* 1990, **29**, 1023
5. Arai H. and Machida M., *Catalysis Today* 1994, **22**, 97
6. Stiles, A. B., Klein, M.T., Gauthier, P., Schwarz, S., and Wang, J. *Ind. Eng. Chem. Res.* 1994 **33**, 2260
7. Zhang, W.,Yahiro,H., Mizuno, N., Izumi, J., and Iwamoto, M., *Langmuir* 1993, **9**, 2337
8. Kaneko, K., Shindo, N. Carbon 1989, **27**, 815
9. Knoblauch, K., Richter, E. and Juntgen, H. *Fuel* 1981, **60**, 832
10. Kaneko, K., Nakahigashi, Y. and Nagata, K. *Carbon* 1988, **26**, 327
11. Rubel, A.M., Stencel, J.M., and Ahmed, S.N. *Preprints Symposium on Flue Gas Cleanup Processes* 1993, ACS, Division of Fuel Chem., Denver, CO meeting, 726.
12. Rubel, A.M., Stencel, J.M., and Ahmed, S.N. *Proceeding of the AIChE 1993 Summer National Meeting* 1993, Seattle, WA., paper no. 77b.
13. Rubel, A.M., Stewart, M.L. and Stencel, J.M. *JMR* 1994, **10**, 562.
14. Rubel, A.M. and Stencel, J.M. *Energy and Fuel*, in press
15. Rubel, A.M., Stewart M.L., and Stencel, J.M. In *Reduction of Nitrogen Oxide Emissions, ACS Symposium Series 587*, Ozkan, U.S., Agarwal, S.K., and Marcelin, G. eds., ACS, Washington, D.C. 1995,208
16. Cha, C.Y. *Res. Chem. Imtermed.* 1994, **20**, 13
17. Gangwal, S.K., Howe, G.B., Spivey, J.J., Silveston, P.L., Hudgins, R.R., and Metzinger, J.G. *Environ. Prog.* 1993, **12**, 128
18. Ahmed, S.N., Stencel, J.M., Derbyshire, F.J., Baldwin, R.M. *Fuel Proc. Tech.* 1993, **34**, 123
19. Ahmed, S.N., Baldwin, R.M., Derbyshire, F.J., McEnaney, B., and Stencel, J.M. *Fuel* 1993, **72**, 287
20. Zawadzki, J. *Carbon* 1987, **25**, 43
21. Zawadzki, J. *Carbon* 1987, **25**, 495
22. Tartarelli, R., Davini, P., Morelli, F., and Corsi, P. *Atmosph. Environ.* 1978, **12**, 289

23. Davini, P. *Carbon* 1991, **28**, 565
24. Davini, P. *Carbon* 1991, **29**, 321
25. Carrasco-Marin, F., Uterra-Hidalgo, E., Rivera-Utrilla, J., Moreno-Castilla, C. *Fuel*, 1992, **71**, 575
26. Mochida, I., Hirayama, T., Kisamori, S., Kawano, S., and Fujitsu, H. *Langmuir* 1992, **8**, 2290
27. Teng, H. And Suuberg, E.M. *J. Phys. Chem.* 1993, **97**,478
28. DeGroot, W.F., T.H. Osterheld, G.N. Richards. *Carbon* 1991, **29**,185
29. Richter, E., R. Kleinschmidt, E. Pilarczyk, K. Knoblauch, and H. Juntgen. *Thermochimica Acta* 1985, **85**,311
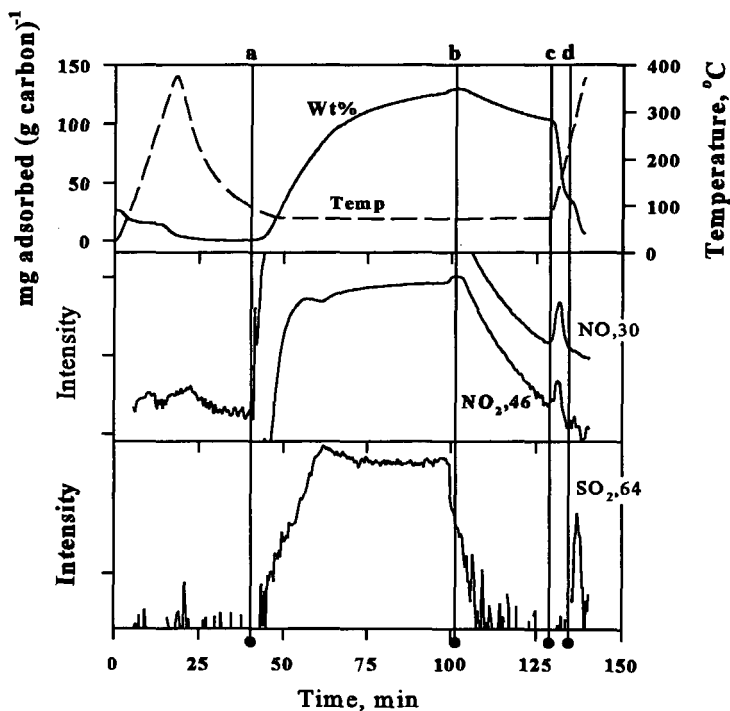
Figure 1. Adsorption-desorption profile from TG-MS for adsorption of NO_2 and SO_2 at 70°C.
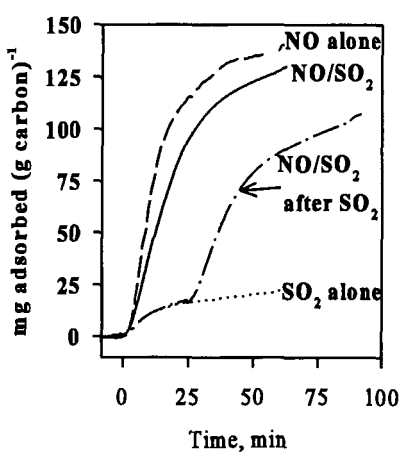
Figure 2. Weight gain curves during adsorption.
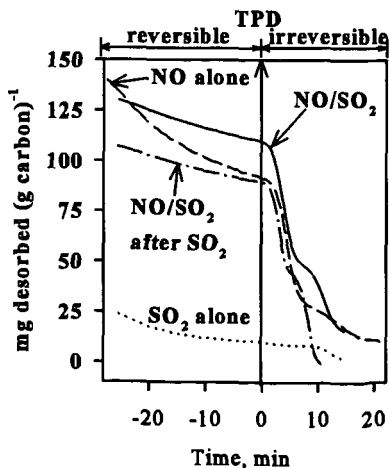
Figure 3. Weight loss curves during TPD.
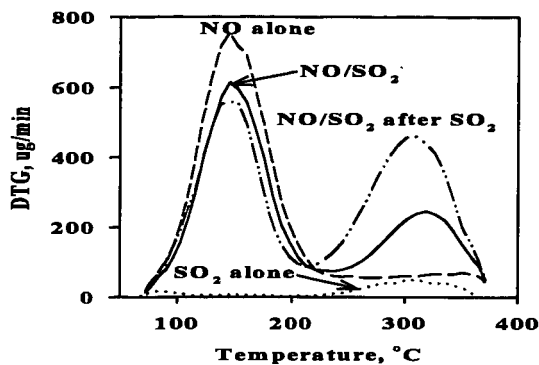
Figure 4. DTG curves during irreversible desorption.
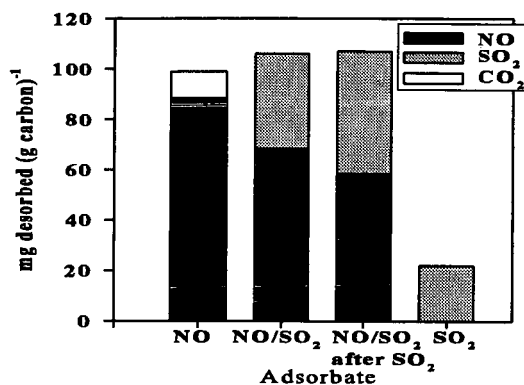
Figure 5. Evolved gases during irreversible desorption.
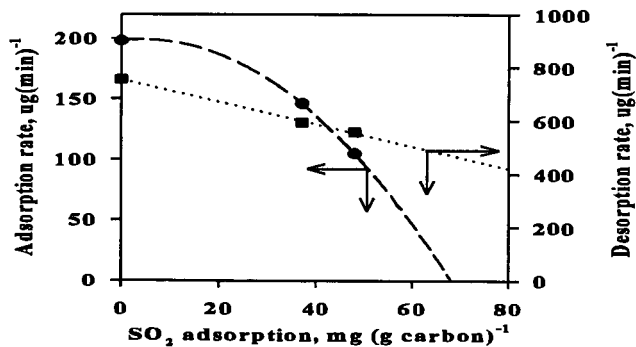
Figure 6. Influence of adsorbed SO_2 on adsorption and desorption rates.
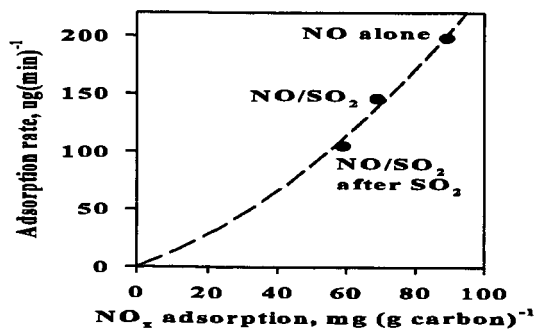
Figure 7. Correlation between NO_x adsorption capacity and total adsorption rate.

188

INTERACTION OF SO_x AND NO_x WITH SOOT

A. R. Chughtai, M. M. O. Atteya, B. K. Konowalchuk,
M. L. Rosenberger, and D. M. Smith
Department of Chemistry, University of Denver
Denver, CO 80208

INTRODUCTION

As part of a continuing study of the heterogeneous reactions of black carbon with gas phase oxidant species, the adsorption of low concentrations (30 - 2000 ppm) of SO_2 and NO_2 individually, together, and in the presence of other adsorbates have been studied by spectroscopic and microgravimetric techniques. Previous work in this study has revealed a dual path mechanism for the reaction of NO_2/N_2O_4 with n-hexane soot over concentration range 9 ppm - 200 torr (1,2). (This soot has been used throughout these investigations as a model for fossil fuel-produced black carbon). The effect of simulated solar radiation on the reaction at lower pressures (9-35ppm) is in the diminution of the NO_2 reactant through its photolytic dissociation (2). An FT-IR study of the reaction of various nitrogen oxides with black carbon showed the only reactive species at 298K to be NO_2, with NO and N_2O unreactive (3). A spectroscopic examination of the gaseous products of the soot-oxides of nitrogen-water vapor reaction has revealed the formation of CO, CO_2, and N_2O, along with NO, from a redox reaction between NO_2/N_2O_4 and the most reactive components of soot during the reaction's early stages (4). At higher temperatures and NO_2/N_2O_4 pressures, n-hexane soot undergoes chemisorption and two types of redox reaction depending upon the conditions (5). The major redox reaction, for which an intermediate $C-(NO_2)x$ complex has been identified, is precluded by prior chemisorption but, if initiated, results in brisk oxidation of the carbon to CO and CO_2 (5). Previous studies of black carbon-SO_2-H_2O-O_2 reaction systems in these laboratories include the effect of simulated solar radiation in the formation of surface sulfate (6) and the effect of metal oxides with carbon on sulfate formation (7). Interaction of SO_2 and carbon represent the most intensively studied of the heterogeneous systems containing carbon. An attempt to understand the molecular dynamics involved in the reactions of carbon in the presence of multiple reactants, such as SO_2 and NO_2, underlies the present work.

RESULTS AND DISCUSSION

SO_2 Adsorption

Because those reactions of SO_x and NO_x in the presence of and with black carbon which are of interest to us occur in air, all adsorption studies were carried out in the presence of zero air (compressed air with CO_2 and H_2O removed). This immediately raises the question of any role of O_2 in SO_2 adsorption, one addressed in our other paper in this symposium (8), involving competition for adsorption sites. That work demonstrates no such direct competition, or at least weaker adsorption of SO_2, the presence of SO_2 showing no effect on the corrected normalized integral of soot's EPR signal (8).

Microgravimetric experiments in which 10 mg n-hexane soot was exposed to 600-2000 ppm SO_2 show a depletive adsorption as illustrated in Figure 1. At 60 min., just prior to the purge with zero air, the surface coverages (θ) by SO_2 were calculated from soot mass increase, its specific surface area of 89 ± 2 m^2/g, and a molecular area for SO_2 of 19.2 Å^2(9), for each replicate run. A plot of θ versus P_{SO_2} shows a linear dependence, Figure 2, for which the relationship

$$\theta = (5.06 \pm 0.07) \times 10^{-5} \ P_{SO_2} + (18.16 \pm 0.08) \times 10^{-2} \qquad (1)$$

obtains. A linear relationship between θ and P is expected at low pressures for adsorption systems obeying the Langmuir isotherm (10)

$$\theta = kP/(1+kP) \tag{2}$$

The intercept in this case suggests a second mode of SO_2 adsorption which may be determined by some surface
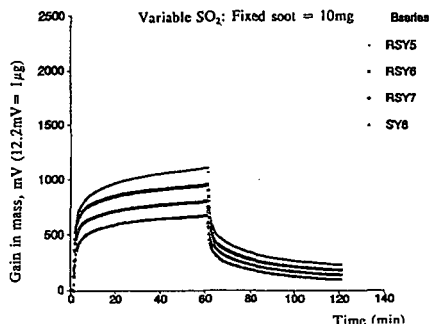
Figure 1.   Adsorption of SO_2 on soot

characteristic. Independent evidence of another mode comes from Figure 1 in which the desorption of SO_2 by zero air asymptotically approaches a limiting mass reflecting retention of as much as 20% of the total adsorbed. A likely candidate for
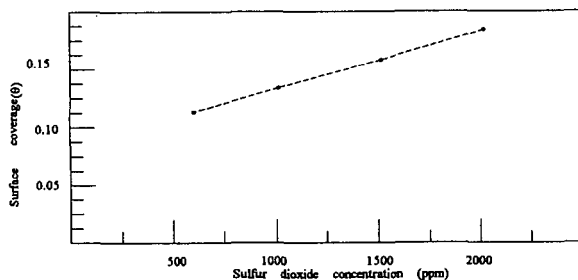
Figure 2.   Plot of surface coverage (θ) as a function of P_{SO2}

this adsorption pathway is the surface hydrolysis of SO_2 to $SO_2 \cdot H_2O$ (H_2SO_3). The resulting reaction scheme

$$SO_2 \text{ (g) } + SS \overset{k_1}{\underset{k_{-1}}{\rightleftharpoons}} SS \cdot SO_2 \text{ (s)} \tag{3}$$

$$SS \cdot SO_2 \text{ (s) } + H_2O.ads \overset{k_2}{\rightarrow} SS \cdot H_2SO_3 \text{ (s)} \tag{4}$$
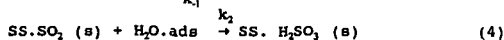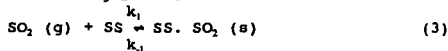
where SS = surface site, could be followed by oxidation to sulfate

$$SS \cdot H_2SO_3 + 1/2O_2 \overset{k_3}{\rightarrow} SS \cdot H_2SO_4 \tag{5}$$
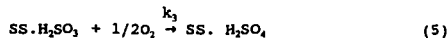
Small amounts of adsorbed water cannot be excluded from the soot surface under these conditions.

The effect of temperature on SO_2 adsorption was examined with a soot mass of 15 mg at 1010 ppm SO_2 by the same microgravimetric technique.   Figure 3 shows a family of mass gain versus time curves over the temperature range 22°C to 66°C for the first 5

minutes of the adsorption experiment. These data represent surface coverages ranging from 8.6 to 2.2 percent, respectively, which exhibit a linear relationship to temperature. Utilizing microgravimetric data such as those of Figure 1, it is possible to estimate the fraction of adsorbed SO_2 which is irreversibly bound to the surface, as represented by equation 4,
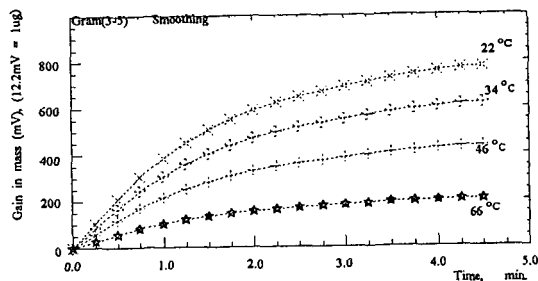
Figure 3. Mass gain versus time curves as a function of temperature.

at each temperature. From the total number of adsorbed molecules per gram, then, the reversibly adsorbed (physisorbed) SO_2 and a set of equilibrium constants for equation 3 have been calculated. These data are summarized in Table I.

Table I. Effect of Temperature on SO_2 Adsorption

Temperature, °C	SO_2 Surface Coverage, θ	Fraction of SO_2 physisorbed, f	$K_{eq} \times 10^{-16}$, molecules per g-ppm
22	0.0858	0.823	3.24
34	0.0684	0.810	2.54
46	0.0479	0.772	1.74
66	0.0225	0.763	0.79

Plots of $\log K_{eq}$ versus $1/T$ show some curvature reflecting the apparent fact that the enthalpy of physisorption for SO_2 on n-hexane soot is a function of surface coverage. Over the temperature range 22-66°C, this value averages 26.8 kJ/mol-K, a figure within the range of 20-27 kJ/mol found by Davini (11) for SO_2 adsorption on three oxidized carbons at 20°C and 1 atmosphere. By comparison, the molar heat of vaporization of SO_2 also is 26.8 kJ/mol at 22°C.

Coadsorption of SO_2 and NO_2
Spectroscopic and microgravimetric data from the NO_2/N_2O_4-soot system (1,2) over a wide concentration range conform to the Elovich equation, an isotherm for activated adsorption or chemisorption. The principal products at low concentration of NO_2 at laboratory temperatures are such functional groups as $-NO_2$, $-ONO$, $-NNO_2$. As noted above, on the other hand, SO_2 adsorption is primarily reversible, involves a low heat of adsorption and is more properly termed physisorption; however, up to 20% appears to be surface reactive or undergoes some type of chemisorption. Of interest in this work have been the molecular mechanisms of coadsorption of SO_2 and NO_2, given the different natures of their adsorption.

Figure 4 is a composite of microgravimetric curves of soot which summarizes its behavior during a series of SO_2 and NO_2 exposures.

Figure 4. Adsorption of SO2 and NO2 on soot.
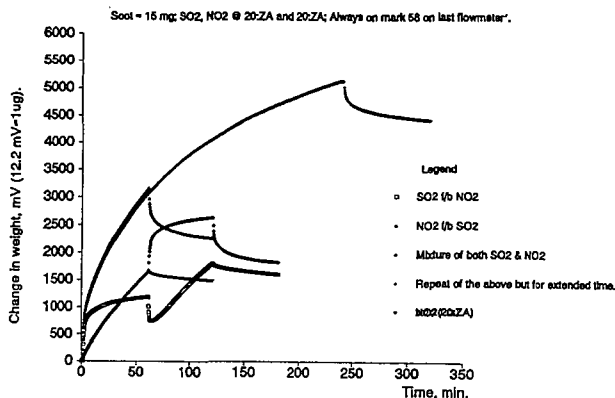
Each experiment was carried out with 15 mg soot and 1010 ppm of SO_2 and \ or NO_2 in zero air at 22°C. This sequence of curves reveals the following:

    1. the typical SO_2 adsorption curve is interrupted by a flow of NO_2 at 60 min, the SO_2 desorption (as P_{SO2} --> 0) followed within 4 minutes by the increase in mass accompanying NO_2 chemisorption;

    2. the inverse order of flow shows an adsorption of SO_2 following NO_2 of about 16% less than untreated soot; because NO_2 is mostly chemisorbed, the SO_2 flow does not result in visible mass loss.;

    3. a flow of SO_2 and NO_2 together yields an increase in mass 11% higher than separately; this curve is reproduced over the longer term, with the loss of mass (mostly SO_2) about the same in each case when the same zero air purge is used;

    4. small amounts of NO_2 are lost through zero air purge, indicating a small amount (9.7%) of NO_2 is loosely bound (physisorbed) under these conditions.

EPR measurements of spin density, the principles of which are discussed in our first symposium paper (8), have been carried out on this system as well, and the results are summarized in Figure 5. The decrease in corrected normalized integral (CNI) of soot's EPR signal with the pressure of paramagnetic NO_2 is evident as is the lack of effect of diamagnetic SO_2. When experiments in which SO_2 adsorption is followed by NO_2 adsorption and vice-versa are carried out, there clearly is no effect of the presence of SO_2 on the interaction of NO_2 with the unpaired electrons of soot. These data are consistent with the displacement of some adsorbed SO_2 by NO_2, however, as indicated by the microgravimetric data of Figure 4. This does not account for any presence of O_2 in zero air and its occupation of free radical sites, which would be reflected microgravimetrically in changes in capacity for SO_2 under some conditions.

Separate experiments have shown that soot treated with 140 torr NO_2, resulting in a reduction of CNI from 1.62×10^7 to 0.61×10^7, undergoes an increase of 10% in unpaired spins upon exposure to air. Evacuation at 10^{-6} torr further increases the CNI to 1.05×10^7 while the addition of air returns it to 0.67×10^7, the cycle continuing to change the spin density of carbon in this manner. It appears that O_2 does compete effectively with the small physisorbed fraction (~10%) of adsorbed NO_2 for

unpaired electron sites.
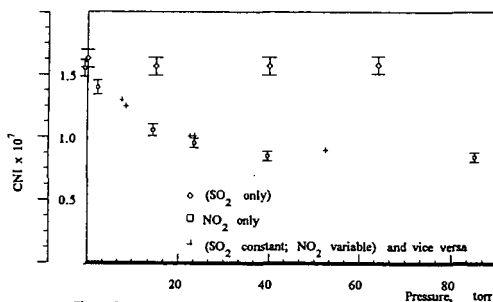
Figure 5. CNI against gas pressure

NO Adsorption

The FT-IR evidence presented for the lack of NO reactivity with soot at ambient temperatures (3) is supported by EPR studies of NO and NO + O_2 adsorption. Figure 6 shows the effects of O_2 and
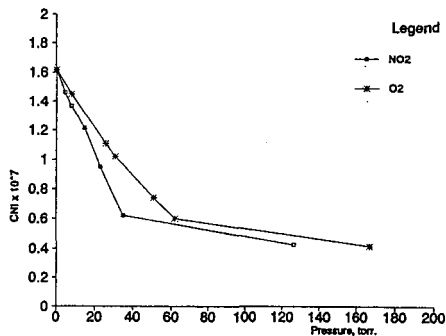
Figure 6. Effects of oxidants on the normalized integral of soot.

NO adsorption on the CNI of soot beyond a linear range below 50 torr to pressures of nearly 170 torr. The similar but slightly lesser effect of NO on spin density, as compared with that of O_2, forms the basis for the experiments summarized in Figure 7. Exposure of the soot to air following adsorption of NO at 8 and 62 torr shows the effect on CNI expected below and at / or above surface saturation by NO, respectively. The surprising effect is the more complete removal of paramagnetic species NO + O_2 to yield a higher CNI than the initial. This consistent result shows NO-assisted removal of that O_2 still remaining on the soot surface following the initial evacuation and mild thermal treatment. It is to be contrasted with the similar experiment with NO_2 described above. NO apparently is reversibly adsorbed and, probably through formation of a complex (or reaction) with pore O_2, even raises the spin density of the soot though its evacuation.

193
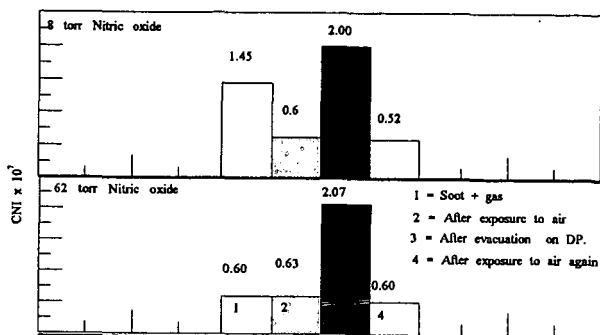
Figure   7 . Plot of CNI for Soot/gas-Air exposure-Evacuation-Exposure to air sequence .

REFERENCES

1. Akhter, M. S.; Chughtai, A. R. ; Smith, D. M., J. Phys.
    Chem., 1984, 88, 5334.
2. Chughtai, A. R. ; Gordon, S. A.; Smith, D. M., Carbon
    1994, 32,405.
3. Smith D. M.; Welch, W. F.; Graham, S. M.; Chughtai, A. R.;
    Wicke, B. G.; Grady, K. A., Appl. Spectrosc. 1988, 42,674.
4. Chughtai, A. R.; Welch, W. F.; Akhter, M. S.; Smith, D. M.,
    Appl. Spectrosc. 1990, 44, 294.
5. Chughtai, A. R.; Welch, W. F.; Smith, D. M., Carbon 1990,
    28, 411.
6. Smith D. M.; Keifer, J. R.; Novicky, M.; Chughtai, A. R.,
    Appl. Spectrosc. 1989, 43, 103.
7. Chughtai, A. R.; Brooks, M. E.; Smith, D. M., J. Geophys.
    Res., 1995, in press.
8. Smith D. M.; Atteya, M. M. O; Konowalchuk, B. K.;
    Rosenberger, M. L.; and Chughtai, A. R., Symposia
    Preprints, Div. Fuel Chemistry, Am. Chem. Soc., New
     Orleans, 1996.
9. Billinge, B. H. M., in Second Conference on Industrial
    Carbon and Graphite, Society of Chemical Industry, London,
    1966; p. 399.
10. Hayward, D. O.,; Trapnell, B. M. W., Chemisorption, 2nd
    ed., Butterworths, London, 1964, p. 167.
11. Davini, P., Carbon, 1994, 32, 349.

TPD STUDY ON SO₂ GASIFICATION OF COAL CHAR

T. Takarada and Y. Suzuki
Faculty of Engineering, Gunma University
1-5-1 Tenjin-cho, Kiryu, Gunma, Japan 376

INTRODUCTION

Elementary sulfur can be recovered from SO₂-containing gas by a gasification reaction between carbon and SO₂. Limited studies on the reaction of coal with SO₂ have been reported[1], [2]. Works on the mechanism of gasification of coal chars with oxygen-containing gases such as O₂, H₂O, CO₂ have been carried out for a long time. Recently, many temperature-programed desorption (TPD) studies on the surface complexes formed by the chemisorption of oxygen-containing gases on carbon have been performed, because the technique is very useful to evaluate the surface active sites in detail. We already investigated the effects of coal type, mineral matter and catalyst addition on the SO₂ gasification rate of coal chars[3]. In this study, nine coal chars derived from coals ranging from brown coal to anthracite, three demineralized coal chars and catalyst-loaded coal chars were chemisorbed with SO₂. TPD patterns of samples were obtained and the relationship between the reactivities of chars and the TPD patterns was discussed. The comparison of TPD pattern of SO₂-chemisorbed char with that of O₂-chemisorbed char was also performed.

EXPERIMENTAL

Sample

Nine coals were used in this study. Carbon contents of nine coals are as follows; Loy Yang (LY) 65.1, Yalloum (YL) 66.1, Morwell (MW) 67.9, Sufco (SF) 73.9, Taiheiyo (TH) 77.0, Leopold (LP) 79.9, Liddell (LD) 83.5, Smokyriver (SR) 90.6, Kuznetsky (KN) 90.7 (wt%, daf). The analyses of these coals have been described elsewhere[3]. The particle size of coal was 32-60 mesh. To examine the effect of the inherent mineral matter on the reactivity and TPD pattern of char, YL, MW and TH coals were treated with a dilute HCl solution for 2 h.

Method of catalyst addition

Yalloum coal, Australian brown coal, was used for catalytic gasification experiments. Potassium carbonate, sodium hydroxide, calcium hydroxide, magnesium hydroxide and iron nitrate were used as the starting materials for catalyst impregnation. Yalloum coal treated with a dilute HCl solution was impregnated with an aqueous solution of catalyst salt and dried at 107°C. The metal to coal ratio was ranged from 1:10 to 1:200 by weight.

Reactivity measurement

The gasification reaction was conducted in a thermo-balance (Shinku-Riko, TGD-7000). The temperature was raised to the gasification temperature at a rate of 60 °C/min after evacuation and substitution with nitrogen gas. After a stationary condition was established, SO₂-N₂ gas (SO₂ concentration:5.2vol%) was introduced and the gasification of char was initiated. The isothermal reaction was allowed to continue for 2 - 10 h.

TPD experiment

TPD experiments were carried out in a fixed bed reactor with gas analysis systems. About 100mg of coal sample was placed in the fixed bed reactor and heated up to 950°C at a heating rate of 60°C/min with flowing Ar gas. The devolatilization of sample was allowed to continue for 30min. Then, two kinds of chemisorption procedures were performed as follows. Procedure 1: samples were cooled down to 150°C and then exposed to either SO₂ (5.2vol%) or O₂ (20vol%) for 60min. Procedure 2: the sample was cooled down to 800°C. Then, SO₂ gas was introduced in the reactor and the sample was cooled down to 500°C at a cooling rate of 60°C/min with flowing SO₂/Ar gas. During the adsorption stage, a part of char (less than 10% of conversion) was gasified. After evacuation and substitution with Ar gas, the samples were heated up to 900°C

or 950°C at a heating rate of 5°C/min or 10°C/min under Ar flow. The gases desorbed during the heat-treatment were continuously analysed with quadrupole mass spectrometer (Nichiden Anelva AQA-200) and the total amounts of CO and CO_2 gases evolved were analysed with a gas chromatography and IR gas analysers.

RESULTS AND DISCUSSION

TPD patterns of SO_2- and O_2-chemisorbed MW chars

The TPD patterns of SO_2- and O_2-chemisorbed MW char prepared by procedure 1 are shown in Figures 1 and 2. The TPD pattern strongly depended on the type of adsorbed gas. A broad desorption of CO_2 for O_2-chemisorbed char was obtained in the range from 150°C to 650°C as previously reported by Zhang et al.[4]. On the other hand, a sharp desorption peak of CO_2 for SO_2-sorbed char appeared at around 700°C. Relatively broad desorption of CO for O_2-sorbed char was observed, while CO gas was evolved at higher temperature range for SO_2-sorbed char. It is noteworthy that no desorptions of both CO_2 and CO for SO_2-sorbed char were detected at a low temperature range below 450°C.

Reactivities and TPD patterns of raw coal chars

Figure 3 shows TG curves obtained for nine coal chars. The sample weight gradually increased in the earlier gasification stage, and then decreased. The increase in weight may be due to the adsorption of SO_2 gas to char surface and to the reaction between mineral matter in char and SO_2. The weight decrease is due to the SO_2 gasification of coal char. The reactivity and the gasification profile strongly depended on coal type. The reactivities of chars derived from coals with carbon content >80 wt% were small and those of lower-rank coal chars were high and widely spread. These results are quite similar to those obtained in the study on the steam gasification of coal chars[5]. The TPD patterns for nine coal chars prepared by procedure 2 were obtained . Four examples are shown in Figure 4. The TPD pattern depended on the coal type. A large and sharp CO_2 peak at around 700°C for MW char and YL char was observed. TH char gave a small CO_2 peak. Little CO_2 gas desorption for LP char was obtained. The TPD patterns for higher rank coal chars such as KN, SR and LD were quite similar to that of LP char. A broad desorption of CO was observed for all coal chars examined. The correlation between the reactivity and the amount of gases desorbed was examined. It was found that the amount of CO desorbed shows a good correlation with the gasification reactivity.

Effect of mineral matter on reactivity and TPD pattern

The effect of acid treatment on the reactivity and TPD profile was examined. The results are shown in Figures 5 and 6. Extraction of coal samples with HCl solution caused appreciable decrease in gasification rate, almost complete disappearance of CO_2 desorption peak and considerable decrease in CO desorption peak. Ratcliffe et al. have reported that acid treatments of lignite caused a decrease in SO_2 gasification rate of char[1]. It is well known that exchangeable cations such as Na and Ca show high activity for steam gasification of low rank coal chars[5]. The decreases in the rate and the amount of gases desorbed may be due to the removal of catalyst metals in mineral matter.

Effect of catalyst addition on reactivity and TPD pattern

The effect of catalyst addition on the reactivity and TPD pattern was investigated (Figures 7 and 8). The gasification profile and TPD pattern was strongly affected by the catalyst addition. The addition of alkaline metals such as K and Na enormously enhanced not only the gasification rate but also the amount of gases desorbed. Relatively sharp desorption peaks of CO_2 and CO for alkaline metal-loaded chars were observed at around 780°C and 830°C, respectively. Both the reactivity and the amount of gases evolved depended on the potassium loading (Figures 7 and 9). In the case of Ca catalyst, although the CO_2 desorption peak at 700°C was increased, the effectiveness of Ca as catalysts for SO_2 gasification of char was quite small. The results show that all CO_2 evolved are not responsible for the gasification rate. XRD measurements of Ca-loaded char showed that Ca catalyst was gradually transformed to CaS during SO_2 gasification of char. The TPD results obtained in this study give the information of initial reactivity of Ca-loaded char. Further investigations are needed to reveal the relationship among the TPD pattern of Ca-loaded char, the activity and chemical form of Ca catalyst.

CONCLUSIONS

The TPD patterns of coal chars chemisorbed with SO_2 gas were determined. The TPD pattern depended on the coal type, mineral matter and catalyst type. Alkaline metals such as Na and K enormously enhanced the gasification rate and the amount of CO_2 and CO evolved. A relatively good correlation was obtained between the reactivity of char and the amount of CO gas desorbed during TPD.

REFERENCES

1. Ratcliffe, C. T. and Pap, G., FUEL, 59, 244 (1980)
2. Abramowitz, H. et al., Carbon, 14, 84 (1976)
3. Takarada, T. et al., Proceedings of the 7th ICCS, p.170 (1993)
4. Zhang, Z.-G. et al., Energy & Fuels, 2, 679 (1988)
5. Takarada, T. et al., FUEL, 64, 1438 (1985)
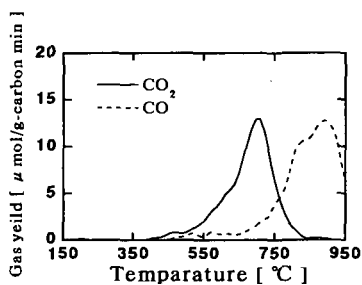
Fig.1 TPD pattern of SO_2-chemisorbed MW char.
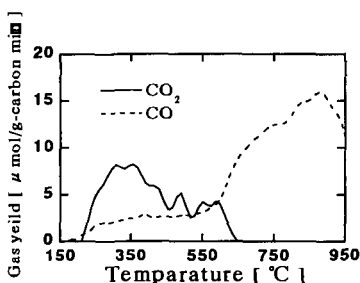
Fig.2 TPD pattern of O_2-chemisorbed MW char.
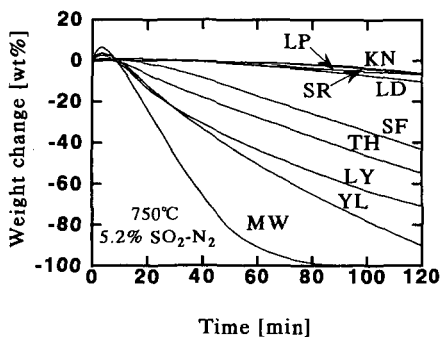
Fig.3 SO_2 gasification profiles of raw coal chars at 750°C.

Fig.4 TPD patterns of raw coal chars.
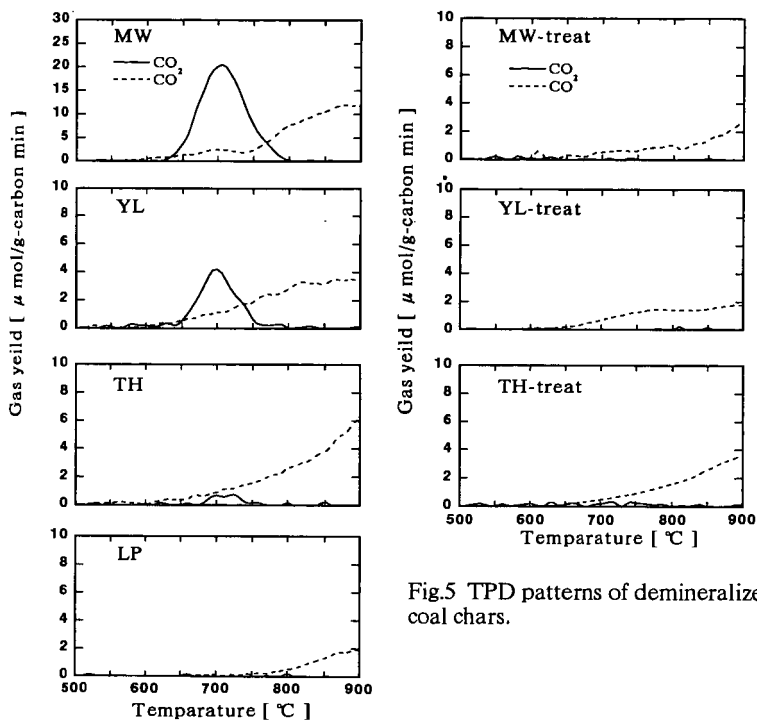
Fig.5 TPD patterns of demineralized coal chars.
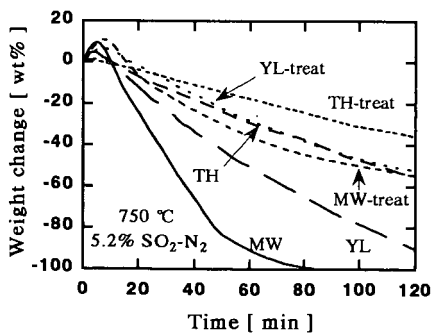
Fig.6 Effect of acid treatment on SO_2 gasification profile at 750°C.
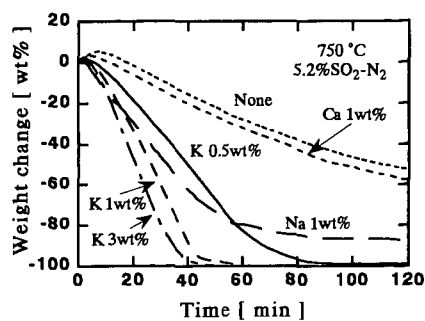
Fig.7 Catalytic SO_2 gasification of YL char at 750°C.
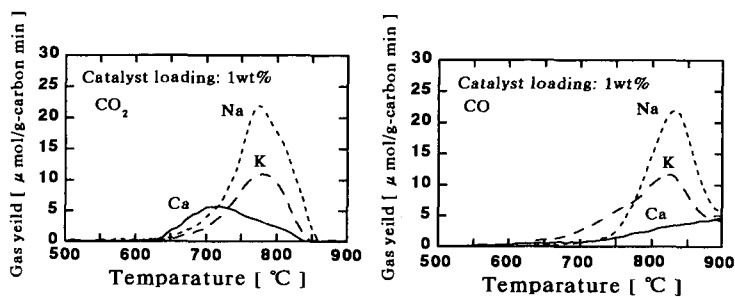
Fig.8 TPD patterns of catalyst-loaded YL chars.
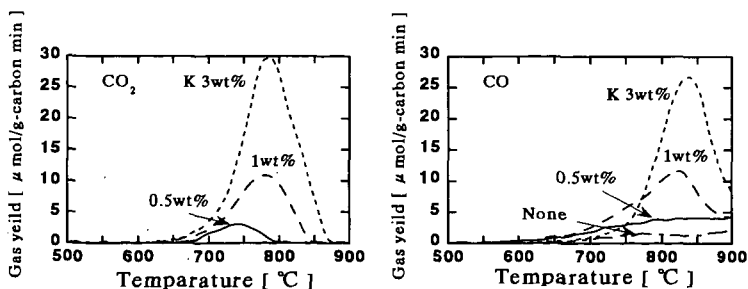
Fig.9 TPD patterns of K-loaded YL chars.

199

This page left intentionally blank.

THE MECHANISM OF SO$_2$ REMOVAL BY CARBON

Anthony A. Lizzio[1] and Joseph A. DeBarr[1,2]

[1]Illinois State Geological Survey, 615 East Peabody Drive, Champaign, IL 61820
[2]Environmental Engineering and Science Program, University of Illinois, Urbana, IL 61801

Keywords: activated char, sulfur dioxide, temperature programmed desorption.

INTRODUCTION

There are a number of research groups currently involved in the development of novel carbon-based processes and materials for removal of SO$_2$ from coal combustion flue gas [1-16]. The type of carbon used more often than not dictates the economic viability of a given process. A high quality carbon adsorbent for SO$_2$ removal should have a high adsorption capacity, rapid adsorption kinetics, low reactivity with oxygen, minimal loss of activity after regeneration, low pressure drop, high mechanical strength, and low cost. The objective of this study [17-23] has been to produce activated char from Illinois coal with optimal SO$_2$ removal properties, and to gain a better understanding of SO$_2$ removal by carbon.

The reaction of SO$_2$ with carbon in the presence of O$_2$ and H$_2$O at relatively low temperatures (80-150°C) involves a series of reactions that leads to the formation of sulfuric acid as the final product. The overall reaction is SO$_2$ + 1/2 O$_2$ + H$_2$O + C -----> C-H$_2$SO$_4$. Most studies that have sought to maximize the SO$_2$ removal capabilities of a carbon only assume a certain mechanism for SO$_2$ adsorption and conversion to H$_2$SO$_4$ is operable. In the literature [1-5,8,10,24], the following reaction sequence has usually been presented before beginning any discussion on SO$_2$ removal by carbon.

$$C + SO_2 -----> C\text{-}SO_2$$
$$C + 1/2\ O_2 -----> C\text{-}O$$
$$C + H_2O -----> C\text{-}H_2O$$
$$C\text{-}SO_2 + C\text{-}O + C\text{-}H_2O -----> C\text{-}H_2SO_4$$

It implies that SO$_2$, O$_2$ and H$_2$O are all adsorbed on the surface of the carbon in close enough proximity and in the proper steric configuration to react and form H$_2$SO$_4$. A clearer understanding of this sequence of reactions will no doubt lead to the development of activated carbons better suited for adsorption of SO$_2$ and its conversion to H$_2$SO$_4$. In this paper, we examine the effect of surface area and chemisorbed oxygen on the SO$_2$ adsorption capabilities of chars prepared from a bituminous coal. Using temperature programmed desorption, we titrate the carbon sites responsible for adsorption of SO$_2$ and its conversion to H$_2$SO$_4$, and based on the experimental results, we propose a more detailed mechanism for SO$_2$ removal by carbon.

EXPERIMENTAL

Activated chars were prepared from a sample of Illinois Colchester (No. 2) hvC bituminous coal (IBC-102) obtained from the Illinois Basin Coal Sample Program. A 2 in. ID batch, fluidized-bed reactor was used to pyrolyze 200 g of 48x100 mesh coal (N$_2$, 900°C, 0.5 h) and activate the resultant char (H$_2$O, 860°C, 30% conversion). The steam activated char was treated with nitric acid (10 M HNO$_3$, 80°C, 2 h) to modify its pore structure and surface chemistry. The HNO$_3$-treated char was heated in nitrogen to various temperatures (200-925°C) and held there for 1 h to desorb carbon-oxygen (C-O) complexes formed during the HNO$_3$ treatment. A commercial activated carbon (Calgon F400) was also studied. SO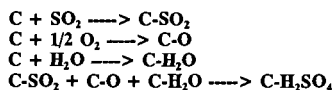$_2$ adsorption capacities of prepared carbons were determined by thermogravimetric analysis using a simulated flue gas containing 2500 ppm SO$_2$, 5% O$_2$ and 7% H$_2$O. Temperature programmed desorption (TPD) experiments (N$_2$, 25-1000°C, 5°C/min, 1 h at 1000°C) were performed to determine the amount of oxygen adsorbed on the char surface. Further details of the experimental equipment and procedures used in this study are provided elsewhere [19-21].

RESULTS AND DISCUSSION

Table 1 shows how poor the correlation is when SO$_2$ adsorption capacities of chars are normalized with respect to their surface areas or oxygen contents. It is interesting to note that the steam activated IBC-102 char (H$_2$O, 860°C) and untreated Calgon F400 carbon have comparable SO$_2$ adsorption capacities despite a large difference in N$_2$ BET (77 K) surface area; their CO$_2$ BET (195 K) surface areas seem to correlate better with SO$_2$ adsorption capacity. Table 1 also shows that the SO$_2$ adsorption capacity of the nitric acid treated, thermally desorbed chars increases with increasing thermal desorption temperature. A similar effect of heat treatment (at 800°C) on the SO$_2$ adsorption capacity of polyacrylonitrile-based activated carbon fibers was recently reported by Mochida and his research group [7,11,12], and attributed to an increase in the number of active sites generated by the evolution of CO and CO$_2$ during decomposition of C-O functional groups. Davini [25,26] ascribed enhanced SO$_2$ adsorption on oxidized activated carbon to the presence of basic C-O groups on the carbon surface. Most recently, Kim et al. [13] and Fei et al. [14] proposed that the inherent nitrogen in polyacronitrile and shale oil derived activated carbon fibers, respectively, increases their catalytic activity for SO$_2$ adsorption and conversion to H$_2$SO$_4$.

The TPD profiles of thermally desorbed, nitric acid treated IBC-102 chars shown in Figure 1 indicate
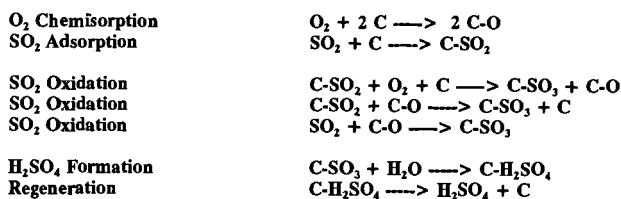
that the absence of oxygen on the carbon surface results in a char with highest SO_2 adsorption capacity (e.g., HNO_3-925°C char). Apparently, carbon atoms, which are not tied up by an adsorbed oxygen atom, have valence electrons that are more available, and are more reactive towards SO_2 adsorption. We, therefore, postulate that the unoccupied or free sites control the uptake of SO_2. It is well known that once carbon is evolved as CO or CO_2 during carbon gasification, a new carbon atom of equal or greater reactivity will be exposed. These newly exposed carbon atoms, coined nascent sites by Phillips et al. [27], in many cases define the surface chemistry of a carbon [28,29]. It is these nascent sites, made active by the thermal desorption treatment at 925°C, that we believe are responsible for enhanced SO_2 adsorption on the HNO_3-925°C char. Nitric acid, being a very strong oxidant, oxidizes the surface of the carbon so that even carbon atoms that would otherwise not react with the oxygen in air are oxidized. Upon thermal desorption treatment, a once relatively unreactive carbon atom is released as CO or CO_2 leaving behind a carbon atom which is then primed *to react with SO_2. The evolution of CO or CO_2 also serves to activate the pore structure* thereby widening the pores making them more accessible to reactant gases; this could also increase SO_2 adsorption. A parallel study with activated carbon fibers (ACF) in our laboratory [30], however, has shown that ACF with smaller pores (9 Å) and lower surface areas (600 m²/g) actually adsorb more SO_2 than higher surface area ACF (1900 m²/g) having larger pores (18 Å). This increase in SO_2 adsorption for low surface area fibers is presumably due to enhanced adsorbent-adsorbate interactions caused by the smaller average pore size [31].

To test our hypothesis that free sites are primarily responsible for SO_2 adsorption, the TPD profiles of the nitric acid treated, thermally desorbed IBC-102 chars of Figure 1 were utilized. We defined the free sites for this series of chars as being those sites that were once occupied by oxygen because of nitric acid treatment, but now, because of the thermal desorption treatment, had become unoccupied or free. To quantify the CO free sites for a given char, say, the HNO_3-725°C char, we subtracted its CO evolution profile from the one of the original nitric acid treated char (Figure 2). The unshaded region in Figure 2 represents the number of free sites that are created by CO evolution during the thermal desorption treatment at 725°C. Table 2 lists the number of both the CO and CO_2 free sites calculated for each of the nitric acid thermally desorbed IBC-102 chars. The last two columns show the SO_2 adsorption capacities normalized with respect to the CO and CO_2 free sites. The SO_2 adsorption capacity is seen to vary by a factor of 1.6 and 2.8 when normalized with respect to CO and CO_2 free sites, respectively. This is an excellent correlation compared to those we found for surface area or adsorbed oxygen (Table 1). To the best of our knowledge, this type of quantitative approach has never before been used to explain SO_2 removal by carbon. The concept of free or unoccupied sites was first postulated and utilized by Laine et al. [32] to explain the gasification reactivity of carbon in oxygen. Our new approach for analyzing TPD data shows that it may be possible to titrate directly the free sites responsible for SO_2 adsorption and conversion to H_2SO_4. A slight variation in this same approach could be used to explain results in other studies that have examined SO_2 removal by carbon. For example, Davini [25,26] found that the SO_2 adsorption capacity of a commercial grade carbon increased with an increase in activation temperature. The activation conditions he used ranged from 300°C in air to 800°C in 2% O_2. Char gasification reactivity studies have shown that less oxygen will adsorb on the carbon surface at higher temperatures and in lower pressures of an oxidizing gas [28,33,34]. The higher temperature used by Davini during activation is likely to have deposited less oxygen on the carbon surface, thus preserving more free sites for reaction with SO_2. In fact, further analysis of his SO_2 and O_2 adsorption data [26] using our concept of free sites shows that the SO_2 adsorption capacities of two groups of carbons that each varied by more than a factor of three, could be made to vary by less than a factor of 1.2 when normalized to the total number of free sites.

This procedure for assessing free adsorption sites was also applied to the Calgon F400 carbon (also a steam activated bituminous coal char). Table 2 shows that there was no significant improvement in the SO_2 capacity of this carbon with our nitric acid, thermal desorption treatment, perhaps because its pore structure was already optimized for adsorption of contaminants. Table 2 shows that the SO_2 adsorption capacity of the Calgon F400 carbons normalized with respect to the number of CO and CO_2 free sites also varies by less than a factor of 2 and 3, respectively. It is interesting to note the almost one to one ratio of SO_2 adsorption capacity to CO free sites for both the IBC-102 and Calgon F400 carbons.

Based on these experimental results, we propose the following sequence of reactions to explain the mechanism of SO_2 removal by carbon.

O_2 Chemisorption	$O_2 + 2\ C \longrightarrow 2\ C\text{-}O$
SO_2 Adsorption	$SO_2 + C \longrightarrow C\text{-}SO_2$
SO_2 Oxidation	$C\text{-}SO_2 + O_2 + C \longrightarrow C\text{-}SO_3 + C\text{-}O$
SO_2 Oxidation	$C\text{-}SO_2 + C\text{-}O \longrightarrow C\text{-}SO_3 + C$
SO_2 Oxidation	$SO_2 + C\text{-}O \longrightarrow C\text{-}SO_3$
H_2SO_4 Formation	$C\text{-}SO_3 + H_2O \longrightarrow C\text{-}H_2SO_4$
Regeneration	$C\text{-}H_2SO_4 \longrightarrow H_2SO_4 + C$

Adsorption of SO_2 and O_2 occurs in parallel on the free carbon active sites (denoted by C). Molecular oxygen dissociates on two free sites to form a pair of C-O complexes. SO_2 competes with O_2 for free sites. The reaction of oxygen with carbon produces a stable C-O complex, which apparently inhibits

SO_2 adsorption. The next step is the oxidation of SO_2 to SO_3. Conceivably, three reactions are possible. The $C-SO_2$ complex can react directly with molecular oxygen in the vicinity of a free site to form a $C-SO_3$ intermediate and stable C-O complex. SO_2 oxidation could also be accomplished by the reaction of either the $C-SO_2$ complex or SO_2 with the C-O complex. However, the occurrence of these two reactions is less likely since we observed an inverse correlation between SO_2 adsorption and stable C-O complex. The conversion of stable C-O complex into a reactive C(O) intermediate, as proposed in recent carbon gasification studies [33-36], may also influence SO_2 adsorption and conversion to H_2SO_4 [19].

According to the SO_2 removal mechanism often presented in the literature (see Introduction), one could assume that the more oxygen adsorbed on the carbon surface, the more SO_2 will be adsorbed. In this study, we have seen that the formation of stable C-O complex during char preparation serves only to occupy otherwise reactive free adsorption sites, and that the C-O complex probably is not an essential reaction intermediate in the conversion of SO_2 to H_2SO_4. It may also be that our TPD method did not titrate those C-O complexes responsible for catalytic oxidation of SO_2 to SO_3, and that a fleeting C(O) complex, formed contemporaneously with SO_2 adsorption and/or by transformation of stable complex into reactive intermediate, acts as the "catalyst." Isotope labelling studies could be useful in determining if such an intermediate exists [37]. Another question is whether SO_2 removal would occur if there was no oxygen in the flue gas and/or adsorbed on the carbon surface. This was resolved by using two of the IBC-102 chars, one with some adsorbed oxygen (HNO_3-525°C) and one with essentially no adsorbed oxygen (HNO_3-925°C). Figure 3 shows that, with 5% O_2 in the flue gas, the HNO_3-925°C char adsorbs the most SO_2. With no oxygen in the flue gas, this char still adsorbs SO_2, but in this case, it is not converting $C-SO_2$ to H_2SO_4 due to a lack of oxygen. SO_2 adsorption is enhanced for both chars when oxygen is present in the flue gas (compare 0 and 5% O_2 plots in Figure 3). The adsorption of SO_2 on a free site is seen to account for nearly 50% of the weight gain for both chars. This data seems to support the first SO_2 oxidation mechanism, i.e., the one involving the reaction of adsorbed SO_2 with O_2 and a free site to form $C-SO_3$.

Hartman and Conghlin [38] found the catalytic oxidation of SO_2 to SO_3 by carbon to be the rate determining step in the overall reaction. If the rate determining step is, indeed, catalytic oxidation of SO_2 to SO_3, and assuming that the first SO_2 oxidation reaction is operable, the overall rate of reaction could be expressed as

$$\text{rate} = k_2 \, [C] \, [C-SO_2] \, [O_2]$$

where k_2 is a fundamental rate constant. The unknowns in this expression are k_2 and the concentration of $C-SO_2$ complex. At steady state, the rates of each of the reactions in the mechanism presented above are equal to that of the rate determining step, and by definition, the concentration of each of the intermediate species does not change with time. Thus,

$$\frac{d[C-SO_2]}{dt} = 0 = k_1 \, [C] \, [SO_2] - k_2 \, [C] \, [C-SO_2] \, [O_2]$$

Solving for $[C-SO_2]$,

$$[C-SO_2] = \frac{k_1 \, [C] \, [SO_2]}{k_2 \, [C] \, [O_2]} = \frac{k_1 \, [SO_2]}{k_2 \, [O_2]}$$

and substituting this into the rate expression,

$$\text{rate} = k_1 \, [C] \, [SO_2]^n$$

where n is the order of reaction with respect to SO_2. The rate is then only a function of the concentration of free sites and the partial pressure of SO_2, a departure from the more elaborate rate expressions recently proposed by others (see, for example, refs. [2] and [24]). For concentrations of SO_2 less than 1500 ppm, we found values of n between 0.5 and 1, and for concentrations of SO_2 greater than 1500 ppm, the value of n approached zero (Figure 4). Nevertheless, at a constant partial pressure of SO_2, the rate of SO_2 adsorption and conversion to H_2SO_4 should be directly proportional to the number of free adsorption sites as confirmed by our TPD experiments. It remains to be determined whether this TPD method can be applied to adsorption of other contaminants in flue gas. If so, it could facilitate preparation of activated char optimized for removal of SO_2 as well as other air toxics (e.g., nitrogen oxides, mercury) from combustion flue gas. Recent studies suggest that adsorption of NO_x and reduction to N_2 is more or less controlled by free sites on the carbon surface [39-41].

In the above mechanism, the $C-SO_3$ intermediate reacts with water to form sulfuric acid. The free site returns to its original state after regeneration. The water adsorbed in the pores may act as a regeneration medium. The acid adsorbed on the carbon surface will be continuously removed by a reservoir of water adsorbed in the pores. As the acid goes into solution, the free site once again becomes reactive towards SO_2 adsorption. Thus, the site can undergo numerous cycles of adsorption/desorption without any external means of regeneration. The production of H_2SO_4 proceeds indefinitely until water adsorbed in the pores becomes saturated with H_2SO_4 and/or the free sites

become occupied with oxygen, at which point the spent carbon needs to be regenerated, e.g., thermal treatment or flushing with water or dilute acid. (The latter treatment will not remove any of the C-O complex). Thus, it can be expected that the amount of water retained in the pore volume of the carbon should determine its equilibrium SO_2 adsorption capacity, which may require more than 40 h to attain (Figure 4); whereas, the rate (or kinetics) of SO_2 adsorption, say, in the first 6 h of adsorption, will be controlled by the number of free sites. In an earlier paper, Jungten and Kuhl [3] hypothesized that the active sites would control the rate of SO_2 adsorption, but this was never verified experimentally. The observed increase in the SO_2 adsorption capacity of nitric acid treated chars with increasing thermal desorption temperature is probably due to both an increase in the concentration of free active sites and in the accessible pore volume of the char. The latter leads to a greater reservoir for storage of dissolved H_2SO_4 and an increased ability to regenerate the active sites for additional SO_2 adsorption.

CONCLUSIONS

In this study, we found the SO_2 adsorption capacity of a coal char to be inversely proportional to the amount of oxygen adsorbed on its surface. Temperature programmed desorption was used to titrate those sites responsible for adsorption of SO_2 and conversion to H_2SO_4. Based on these results, a detailed mechanism for SO_2 removal by carbon was proposed. The derived rate expression shows SO_2 adsorption to be dependent only on a fundamental rate constant and concentration of carbon atoms we designate as free sites. The results obtained here are analogous to those of a recent study [33] which found that a similar relationship exists between the specific rate (R_{sp}) of carbon gasification in carbon dioxide and the number of reactive sites measured initially by transient kinetics (TK) experiments and later confirmed by TPD, i.e., $R_{sp} = k [C]$. In that study, TK and TPD were used to titrate those occupied sites or $C(O)$ intermediates responsible for controlling the rate determining desorption step in CO_2 gasification of carbon. The results of both studies seem to support a unified approach to the reactions between carbon and oxygen-containing gases, as most recently proposed by Chen [42] and Moulijn and Kapteijn [43].

ACKNOWLEDGEMENTS

REFERENCES

1. Richter, E., Knoblauch, K. and Jungten, H., Proc. 1st Int. Conf. on Processing and Utilization of High Sulfur Coals, 1985, p. 563.
2. Richter, E., Knoblauch, K. and Jungten, H., Gas Separation and Purification 1, 35 (1987).
3. Jungten, H. and Kuhl, H., Chem. Phys. Carbon 22, 145 (1989).
4. Richter, E., Catalysis Today 7, 93 (1990).
5. Tsuji, K. and Shiraishi, I., Proc. Electric Power Research Institute SO_2 Control Symposium, Washington, D.C., 1991, p. 307.
6. Lu, G.Q. and Do, D.D., Carbon 29, 207 (1991).
7. Mochida, I., Hirayama, T., Kisamori, S., Kawano, S. and Fujitsu, H., Langmuir 8, 2290 (1992).
8. Gangwal, S.K., Howe, G.B, McMichael, W.J. and Spivey, J.J., Final Report to U.S. DOE (1993).
9. Gangwal, S.K., Howe, G.B., Spivey, J.J., Silvestou, J.J., Hudgins, R.R. and Metzinger, J.G., Envir. Prog. 12, 128 (1993).
10. Lu, G.Q. and Do, D.D., Gas Separation and Purification 8, 17 (1994).
11. Kisamori, S., Mochida, I. and Fujitsn, H., Langmuir 10, 1241 (1994).
12. Kisamori, S., Kurado, K., Kawano, S., Mochida, I., Matsumura, Y. and Yoshikawa, M., Energy and Fuels 8, 1337 (1994).
13. Kim, J.-Y., Hong, I. and Lee, J.G., Proc. 22nd Biennial Conf. on Carbon, San Diego, CA, 1995, p. 534.
14. Fel, Y., Sun, Y.N., Givens, E. and Derbyshire, F., ACS Preprints, Div. Fuel Chem. 40 (4), 1051 (1995).
15. Vladea, R.V., Hinrichs, N., Hudgins, R.R., Suppiah, S. and Silveston, P.L., ACS Preprints, Div. Fuel Chem., New Orleans, LA, 1996 (in press).
16. Mochida, I., Kuroda, K., Yasutake, A., Yoshikawa, M., Matsumura, Y., ACS Preprints, Div. Fuel Chem., New Orleans, LA, 1996 (in press).
17. Lizzio, A.A., DeBarr, J.A., Kruse, C.W., M., Donnals, G.L. and Rood, M.J., "Production and Use of Activated Char for Combined SO_2/NO_x Removal," Final Technical Reports to the Illinois Clean Coal Institute (1994, 1995).
18. DeBarr, J.A. and Lizzio, A.A., Proc. Int. Conf. on Carbon, Granada, Spain, 1994, p. 268.
19. Lizzio, A.A. and DeBarr, J.A., Fuel 1995 (in press).
20. DeBarr, J.A., "The Role of Free Sites in the Removal of SO_2 from Simulated Flue Gases by Activated Char," M.S. Thesis, University of Illinois at Urbana-Champaign (1995).
21. DeBarr, J.A., Lizzio, A.A. and Rood, M.J., Proc. 88th Annual Air and Waste Management Assoc. Meeting, San Antonio, TX (1995).
22. DeBarr, J.A. and Lizzio, A.A., Proc. 22nd Biennial Conf. on Carbon, San Diego, CA, 1995, p. 562.
23. Lizzio, A.A. and DeBarr, J.A., Proc. 12th Int. Annual Pittsburgh Coal Conf., Pittsburgh, PA, 1995, p. 652.
24. Gail, E. and Kast, W., Chem. Eng. Sci. 45, 403 (1990).
25. Davini, P., Fuel 68, 145 (1989).
26. Davini, P., Carbon 28, 565 (1990).
27. Phillips, R., Vastola, F.J. and Walker, P.L., Jr., Carbon 8, 197 (1970).
28. Boehm, H.P. and Bewer, G., Proc. 4th London Int. Conf. on Carbon and Graphite, 1974, p. 344.
29. Leon y Leon, C.A. and Radovic, L.R., Chem. Phys. Carbon 24, 213 (1994).
30. DeBarr, J.A., Lizzio, A.A. and Daley, M.A., ACS Preprints, Div. Fuel Chem., New Orleans, LA, 1996 (in press).
31. Foster, K.L., Fuerman, R.G., Economy, J., Larson, S.M. and Rood, M.J., Chem. Mater. 4, 1068 (1992).
32. Laine, N.R., Vastola, F.J. and Walker, P.L., Jr., Phys. Chem. 67, 2030 (1963).
33. Lizzio, A.A., Jiang, H. and Radovic, L.R., Carbon 28, 7 (1990).
34. Radovic, L.R., Jiang, H. and Lizzio, A.A., Energy and Fuels 5, 68 (1991).
35. Back, M.H., Carbon 29, 1290 (1991).
36. Radovic, L.R., Karra, M. and Skokova, K., Proc. 22nd Biennial Conf. on Carbon, San Diego, CA, 1995, p. 636.
37. Kapteijn, F., Meijer, R. and Moulijn, J.A., Energy and Fuels 6, 494 (1992).
38. Hartman, M. and Coughlin, R.W., Chem. Eng. Sci. 27, 867 (1972).
39. Teng, H., Snuberg, E.M. and Calo, J.M., Energy and Fuels 6, 398 (1992).
40. Yamashita, H., Tomita, A., Yamada, H., Kyotani, T. and Radovic, L.R., Energy and Fuels 7, 85 (1993).
41. Mochida, I., Kisamori, S., Hironaka, M., Kawano, S., Matsumura, Y. and Yoshikawa, M., Energy and Fuels 8, 1341 (1994).
42. Chen, S.G., Yang, R.T., Kapteijn, F. and Moulijn, J.A., Ind. Eng. Chem. Res. 32, 2835 (1993).
43. Moulijn, J.A. and Kapteijn, F., Carbon 33, 1155 (1995).

Table 1. Correlation of SO₂ adsorption capacity with surface area and adsorbed oxygen.

Sample	SO₂ Capacity[1] (mg SO₂/g char)	N₂ BET (m²/g)	CO₂ BET (m²/g)	SO₂/N₂ (mg/m²)	SO₂/CO₂ (mg/m²)	O₂ (wt%)	SO₂/O₂
IBC-102, 900°C, 0.5 h	7	1.2	98	5.8	0.07	0.5	1.40
IBC-102, 900°C; H₂O, 860°C	176	220	613	0.80	0.29	1.1	16.0
IBC-102, 900°C; H₂O, 860°C; HNO₃	...[2]	400	585	0.06	0.04	16.4	...[2]
IBC-102, 900°C; H₂O, 860°C; HNO₃, 525°C	91	460	693	0.20	0.13	5.9	1.54
IBC-102, 900°C; H₂O, 860°C; HNO₃, 725°C	241	500	727	0.48	0.33	1.6	15.0
IBC-102, 900°C; H₂O, 860°C; HNO₃, 925°C	287	550	726	0.05	0.39	0.5	57.4
Calgon F400	206	1000	1000	0.21	0.21	0.5	41.2
Calgon F400, HNO₃	...[2]	...[2]	...[2]	...[2]	...[2]	15.7	...[2]
Calgon F400, HNO₃, 200°C	46	600	...[2]	0.08	...[2]	14.3	0.32
Calgon F400, HNO₃, 525°C	117	456	...[2]	0.26	...[2]	5.6	2.09
Calgon F400, HNO₃, 725°C	156	533	...[2]	0.29	...[2]	3.4	4.59
Calgon F400, HNO₃, 925°C	214	463	...[2]	0.46	...[2]	1.7	12.6

[1] SO₂ capacity determined after 6 h.
[2] not determined.

Table 2. Correlation of SO₂ adsorption capacity with free adsorption sites.

Sample	SO₂ capacity[1]	Adsorbed oxygen[1]	CO/CO₂	CO free sites[1,2]	CO₂ free sites[1,2]	SO₂ capacity (CO free sites)	SO₂ capacity (CO₂ free sites)
IBC-102, HNO₃	...[3]	5.12	1.4	0	0	...[3]	...[3]
IBC-102, HNO₃, 525°C	0.142	1.84	6.7	1.37	2.59	1.04	0.55
IBC-102, HNO₃, 725°C	0.376	0.50	12.8	3.35	2.94	1.12	1.28
IBC-102, IINO₃, 925°C	0.448	0.16	---[4]	3.90	3.01	1.15	1.49
Calgon F400, HNO₃	...[3]	4.91	1.4	0	0	...[3]	...[3]
Calgon F400, HNO₃, 200°C	0.072	4.47	0.8	0.86	0.34	0.84	2.12
Calgon F400, HNO₃, 525°C	0.183	1.75	7.6	1.28	2.52	1.43	0.73
Calgon F400, HNO₃, 725°C	0.244	1.06	5.5	2.26	2.56	1.08	0.95
Calgon F400, HNO₃, 925°C	0.334	0.53	5.4	3.28	. 2.75	1.02	1.22

[1] moles/kg char.
[2] calculated-assuming that 1 chemisorbed O₂ evolved as 2 CO during TPD is equivalent to 2 CO free sites, and 1 chemisorbed O₂ evolved as 1 CO₂ is equivalent to 1 CO₂ free site.
[3] not determined.
[4] CO₂ concentration below detectable limits.
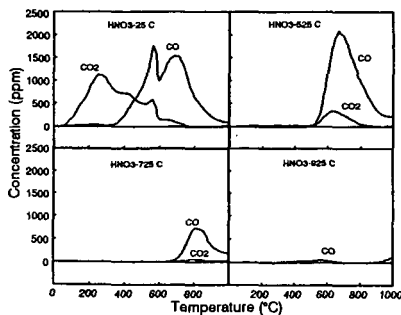
Figure 1. TPD profiles of nitric acid/thermally desorbed IBC-102 chars.
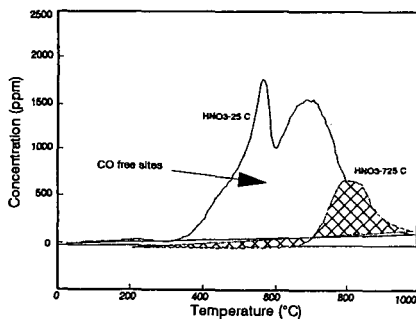
Figure 2. Subtraction of CO evolution profiles to determine CO free sites.
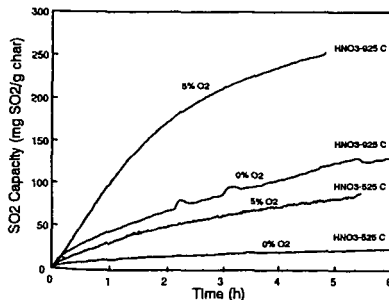
Figure 3. Effect of oxygen on SO2 adsorption.
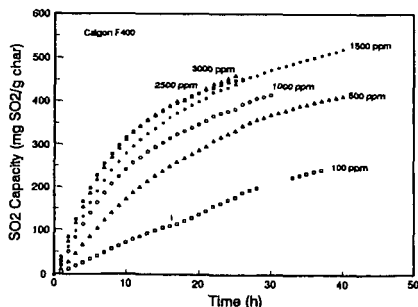
Figure 4. Effect of SO2 concentration.

CHARACTERIZING RATE INHIBITION IN H_2O/H_2 GASIFICATION VIA MEASUREMENT OF ADSORBED HYDROGEN CONCENTRATION

M. G. Lussier, Z. Zhang, and D. J. Miller

Department of Chemical Engineering
Michigan State University
East Lansing, MI 48824

Keywords: Gasification, Kinetics, Rate Inhibition

INTRODUCTION

Gasification of coal for fuels production is not currently used on a wide scale because extreme conditions are needed to achieve reasonably fast reaction rates. One reason for these extreme conditions is the inhibition of gasification by hydrogen in the reacting gas phase. For example, gasification rate decreases by an order of magnitude with the addition of only 1 ppm hydrogen to steam [1], and rate has been shown to decline significantly with conversion in hydrogen and steam/hydrogen mixtures [2,3]. Hydrogen dissociatively chemisorbed onto carbon is very stable, generally accepted as dissociative in nature, and requires temperatures approaching 1800 K to completely desorb [4].

The three possible modes of hydrogen inhibition in steam gasification are as follows [3]:

Reverse oxygen exchange: $\quad C(O) + H_2 \rightarrow C_f + H_2O \qquad$ (1)

Dissociative hydrogen adsorption: $\quad C_f + \frac{1}{2}H_2 \rightarrow C(H) \qquad$ (2)

Associative hydrogen adsorption: $\quad C_f + H_2 \rightarrow C(H)_2 \qquad$ (3)

Selection of any of the possible inhibition modes gives the following basic rate expression [3,5]:

$$rate_{co} = \frac{C_A K_1 P_W}{1 + K_2 P_W + K_3 P_H^n} \qquad (4)$$

Dissociative adsorption gives a value of 0.5 for n [3], which has been found to be the case for low hydrogen pressures [6] and subatmospheric steam pressures [7]. Reverse oxygen exchange and associative hydrogen adsorption both give values of one for n, as reported in earlier studies [5,8,9]. Associative adsorption has been found to contribute to inhibition at higher pressures, but dissociatively bound hydrogen still dominates char surfaces [10].

EXPERIMENTAL

A char of Dow Saran Resin (MA 127) was prepared in a quartz tube reactor at 1173 K in flowing nitrogen for 0.5 hr., ground and sieved to -60+100 mesh, then annealed in an alumina reactor at 5 K/min to 1773 K in flowing argon for 6 hr.

Chars were gasified inside a quartz lined Inconel 625 differential packed bed microreactor which was housed inside a larger pressure vessel capable of simultaneous operation at 1273 K and 6.6 MPa. The entire system was designed to have absolute minimal internal volume to facilitate accurate measurement of transient species. After gasification in 40% steam and various proportions of argon and hydrogen at 1123 K and pressures ranging from 0.3 to 3.3 MPa, rapid switching to pure argon was done and transients monitored. The inherent system transient response was accounted for by using 1% krypton as a tracer in the reactant gas argon.

After gasification, chars were removed, weighed, and placed inside the alumina reactor for temperature programmed desorption (TPD) to measure the quantity of adsorbed hydrogen. Samples were outgassed in argon at 10 K/min to 1773 K in a Mellen split tube furnace with a programmable temperature controller. Effluent species from both reactors were analyzed with an Ametek M100M Quadrupole Mass Spectrometer, which is interfaced with a personal computer for data collection and deconvolution.

RESULTS

Figures 1 and 2 show rate curves for steam/hydrogen gasification of annealed Saran char at 1.0 MPa and 3.1 MPa total pressure, 1123 K, 40% steam, and varying concentrations

of hydrogen balanced with argon. The CO + CO_2 formation rate is independent of steam partial pressure at these conditions when no hydrogen is present in the reactant gas, and hydrogen inhibition of CO + CO_2 formation is clearly observable with increasing hydrogen partial pressure. Methane formation rate is approximately first order in hydrogen partial pressure and independent of steam partial pressure. A decline in rate is also observed over the first 1% conversion when hydrogen is present in the reactant gas for both CO + CO_2 formation and methane formation; this decline becomes more pronounced under higher hydrogen partial pressures. In the most extreme case, CO + CO_2 formation rate approaches zero at 1.0 MPa total pressure and 0.6 MPa hydrogen partial pressure. All rate curves gradually increase with conversion after the first 1%, which follows the increase in char surface area. Figure 3 shows char surface areas as determined by N_2 BET analysis, indicating a very highly porous material is formed with conversion.

Figure 4 shows adsorbed hydrogen on a per unit weight basis as a function of char conversion following gasification. Surprisingly, adsorbed hydrogen concentration is only a function of conversion and not reactant gas composition. There appears to be two zones of adsorption behavior. The first is an initial rapid adsorption to almost 30 ccH$_2$(STP)/g up to 1% conversion, and the second is a more gradual but steady increase in adsorbed hydrogen to 100 ccH$_2$/g at 70% conversion. The hydrogen peak maximum is at 1500 K during TPD, indicating that hydrogen is dissociatively adsorbed on the char surface.

Figure 5 shows adsorbed hydrogen concentration following gasification on a per unit area basis. The increase in adsorbed hydrogen with conversion after the initial rapid adsorption stage is partially accounted for by the increase in char surface area with conversion; however, the gradual increase in adsorbed hydrogen concentration per unit area indicates that hydrogen continues to adsorb onto the char throughout the entire course of gasification.

Figure 6 shows CO + CO_2 formation rate during a reaction in which hydrogen fraction of the reactant gas is cycled between 0% and 60%. A rate curve from a steam only gasification has been included for reference. Rate reversibly changes from a value close to that of the reference curve to a very low value as hydrogen is added and excluded from the reactant gas. This indicates that steady state rate is only a function of reactant gas composition.

DISCUSSION

Our results support both reverse oxygen exchange and dissociative hydrogen adsorption as modes of inhibition in steam/hydrogen gasification of chars, with reverse oxygen exchange acting throughout the course of reaction and dissociative hydrogen adsorption inhibiting rate only upon initial exposure to hydrogen. Temperature programmed desorption studies show that dissociative hydrogen adsorption occurs throughout gasification, most rapidly during the first 1% conversion. There may be a relationship between this initial rapid adsorption and the rate decline over the same initial 1% conversion for chars exposed to hydrogen-containing reactant gases; however, the same initial rapid hydrogen adsorption is not accompanied by a decline in rate when there is no hydrogen present in the reactant gas. Conversion beyond the first 1% is also marked by an increase in adsorbed hydrogen, albeit much less rapidly, but not by a decline in rate. Step changes in reactant gas compositions result in gasification rates that reach steady-states which are similar to those achieved with unchanging reactant gas compositions.

This leads to the conclusion that, at high conversions (>1%) the adsorbing hydrogen does not compete for the same active sites at which gasification occurs. If the dissociative hydrogen adsorption measured by TPD has blocked sites active in gasification, the increase in surface hydrogen concentration would lead to a corresponding decrease in the total number of active sites and thus a decrease in gasification rate regardless of reactant gas composition. This does not occur.

At low conversion, however, dissociative hydrogen adsorption may play a role. At high hydrogen partial pressures, reverse oxygen exchange cannot be solely responsible for hydrogen inhibition because it is driven by hydrogen partial pressure which is not changing during the initial rapid decline in rate. It appears that dissociative hydrogen adsorption contributes to rate inhibition by competing with oxygen exchange for active sites. Upon initial exposure of the char to a reactant gas with a high hydrogen partial pressure, a greater proportion of active sites become blocked with dissociatively adsorbed hydrogen over the course of 1% conversion. Once the rapid transient adsorption is complete, an

equilibrium is established in which there are fewer active sites and steady-state rate is achieved.

The fact that methane formation rate is approximately first order in hydrogen partial pressure may appear to be contradictory to a reduction in the number of active sites upon an increase in hydrogen partial pressure; however, the mode by which methane is formed makes a higher steady state rate with fewer active sites possible. Both $CO + CO_2$ and methane formation rates decrease simultaneously over 1% conversion upon exposure of chars to hydrogen, indicating that sites active for both must be affected. Unlike oxygen exchange, methane formation must be preceded by hydrogen adsorption, so an unsaturated carbon site is not always needed to form methane. Oxidation does require an unsaturated site, of which there are fewer under higher hydrogen partial pressure.

Our findings lead us to conclude that annealed Saran char is covered with two types of active sites. The most abundant are those that acquire dissociatively adsorbed hydrogen from the gas phase to cover much of the char surface, achieving a bulk H/C ratio as high as 0.1 at about 70% conversion. The second type of sites are active for gasification, with competition between oxidation and methane formation reactions. Under low hydrogen partial pressure the driving force for reverse oxygen exchange is small, as is the driving force for methane formation. Thus, C(O) formation at active sites dominates and CO is the primary product, with CO_2 subsequently formed via the shift reaction. As hydrogen partial pressure is increased the case is reversed. The reverse oxygen exchange driving force is increased as is methane formation. The total number of unsaturated surface carbons is reduced over 1% conversion by adsorbing hydrogen until an equilibrium is reached with active site competition. Methane formation includes hydrogen adsorption onto the char surface, while oxygen exchange requires unsaturated active sites. The oxygen exchange reaction will always have to compete with the methane formation reaction for unsaturated active sites, while the methane formation reaction does not have to compete with the oxygen exchange reaction since methane formation can occur at sites that have been saturated with hydrogen.

CONCLUSIONS

Reverse oxygen exchange and dissociative hydrogen adsorption both inhibit steam gasification of annealed Saran char, which is covered with two major types of active sites. The first and most abundant type of site dissociatively adsorbs hydrogen throughout the course of reaction, and is inactive for gasification. The second type of site is active in gasification to form CO and methane, but can become blocked with dissociatively adsorbed hydrogen upon exposure to increased hydrogen partial pressure. Reverse oxygen exchange, however, always influences CO formation. The total concentration of sites which are active towards gasification, as well as the equilibrium at these sites between oxidation, methane formation, and site blockage determines char gasification rate.

ACKNOWLEDGMENT

REFERENCES

1. Montet, G.L. and Myers, G.E., Carbon 9, 673 (1971).
2. Toomajian, M.E., Lussier, M.G., and Miller, D.J., Fuel 71, 1055 (1992).
3. Huttinger, K.J. and Merdes, W.F., Carbon 30(6), 883 (1992).
4. Redmond, J.P. and Walker, P.L.Jr., J. Phys. Chem. 64, 1093 (1960).
5. Gadsby, J., Hinshelwood, C.N., and Sykes, K.W., Proc. Royal Soc. London A187, 129 (1946).
6. Giberson, R.C. and Walker, J.P., Carbon 3, 521 (1966).
7. Yang, R.T. and Duan, R.Z., Carbon 23(3), 325 (1985).
8. Blackwood, D.J. and McGrory, F., Aust. J. Chem. 11, 16 (1958).
9. Mims, C.A. and Pabst, J.K., ACS Div. Fuel Chem. Prepr. 25(3), 263 (1980).
10. Huttinger, K.J., Carbon 26(1), 79 (1988).
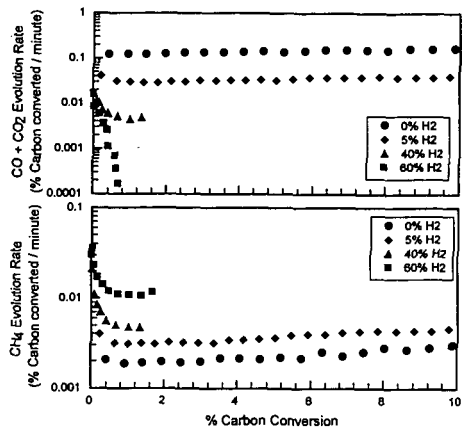
Figure 1: H$_2$O/H$_2$ Gasificaiton Rate
of Annealed Saran Char at 1.0 MPa
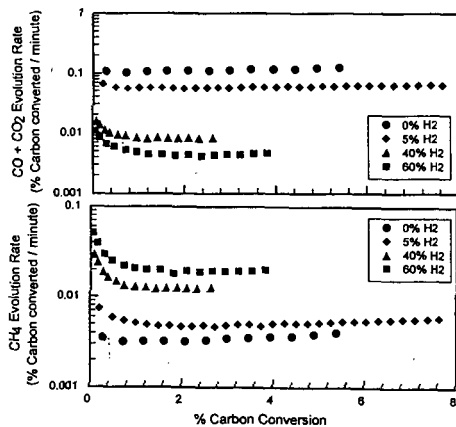
Figure 2: H$_2$O/H$_2$ Gasification Rate
of Annealed Saran Char at 3.1 MPa
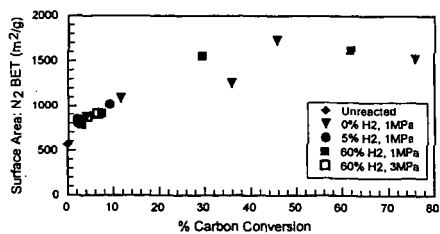
Figure 3: Surface Area (N$_2$ BET) of Annealed
Saran Char Following H$_2$O/H$_2$ Gasification
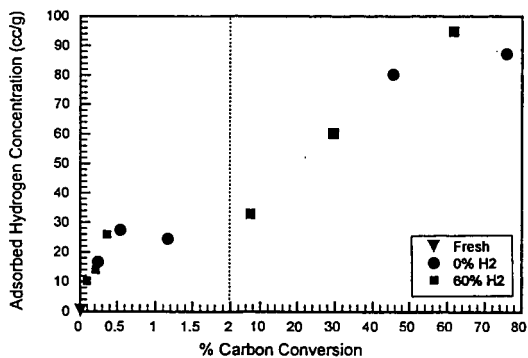
Figure 4: Adsorbed Hydrogen Concentration per Unit Weight on Annealed Saran Char Following H_2O/H_2 Gasification at 1.0 MPa
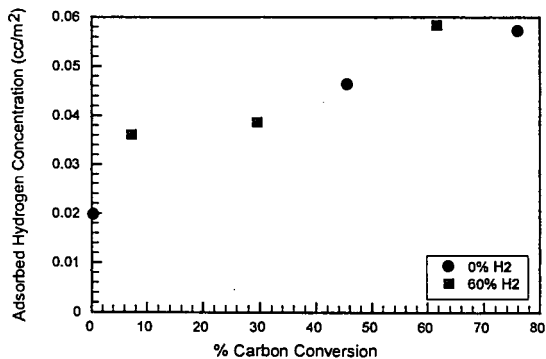
Figure 5: Adsorbed Hydrogen Concentration per Unit Surface Area on Annealed Saran Char Following H_2O/H_2 Gasification at 1.0 MPa
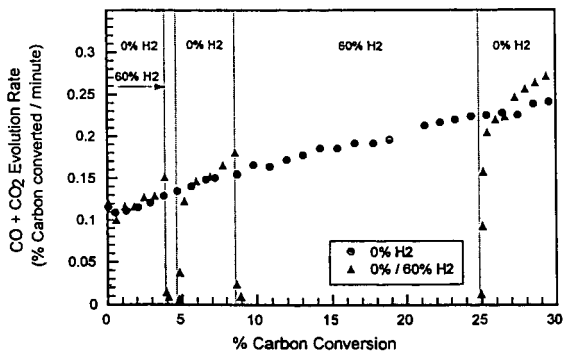
Figure 6: H_2O/H_2 Gasification Rate of Annealed Saran Char at 1.0 MPa, Step Changes in Reactant Gas Composition

210

THE ROLE OF SUBSTITUTIONAL BORON IN CARBON OXIDATION: INHIBITOR *AND* CATALYST!

M. Karra, P. A. Thrower and L. R. Radovic

Fuel Science Program
Department of Materials Science and Engineering
The Pennsylvania State University, University Park, PA 16802

INTRODUCTION

Carbon oxidation has been very thoroughly investigated. It is a reasonably well understood heterogeneous gas/solid reaction [1-4]. Yet there are many practical and fundamental 'details' that need to be sorted out. There are also some very important fundamental issues that are not understood. Others may want to add (or subtract?) some issues, but here is our list of key outstanding questions in the C/O_2 reaction:

(a) What is the exact nature of the relation between 'reactive' $C(O)$ intermediates and 'stable' C-O complexes on the carbon surface?

(b) What is the reason for the commonly observed "compensation effect" in both uncatalyzed and catalyzed carbon gasification?

(c) Which structural features of the carbon surface govern the magnitude of the CO/CO_2 ratio in the products of oxidation and, in particular, how is CO_2 formed?

(d) Is it possible that, when carbon is doped with boron, both a catalytic and an inhibiting effect can be observed?

A companion paper presented at this symposium [5] addresses issue (c). The present communication deals with issue (d). Reference 6 had roughly the same title as this paper, but it ended with a question mark. In the macroscopic world, in contrast to the quantum world [7], mutually exclusive phenomena are not commonly thought to coexist. So boron is considered to be either an inhibitor or a catalyst of carbon oxidation, but not both. Here we provide additional arguments for this remarkable influence of boron on the oxidation of a wide range of carbonaceous solids (and we thus replace the question mark with an exclamation point). Elsewhere [7] we address issues (a) and (b); in particular we argue that both the elusive concept of the compensation effect and the intriguing balance between reactive and stable carbon-oxygen surface complexes may have an analogous explanation to the one offered here for the role of boron in carbon oxidation.

Boron is considered to be one of the very few promising candidates for chemical protection of carbon/carbon composite materials against oxidation. Oxidation protection is of paramount importance for the use of these strategic materials in demanding (e.g., structural) aerospace applications. (Most ceramic coatings have a thermal expansion mismatch with carbon and thus develop cracks which lead to carbon exposure to high-temperature O_2.) The conventional wisdom is that boron inhibits carbon oxidation. Its inhibiting effect can be manifested in three different ways: (a) Substitutional boron enhances the graphitization of carbon [8-10]. (b) As the surface carbon atoms are consumed, substitutional boron forms an oxide surface film, which acts as an O_2 diffusion barrier and an active site blocker [9,11-14]. (c) Substitutional boron redistributes the π electrons in the basal plane (graphene layer), lowers the Fermi level of carbon, and hence presumably inhibits the desorption of CO and CO_2 [9,11,14]. This last mode of inhibition is of great fundamental interest; it had not been verified in the past. As a consequence of our recent results [6], and upon closer examination of some early studies, its closer scrutiny is warranted. We provide such a scrutiny in the present communication.

EXPERIMENTAL

Three widely differing carbon materials were used: a heat-treated ('graphitized') carbon black (Graphon, Cabot Corp.), Saran char (produced by pyrolysis of a PVC/PVDC copolymer manufactured by Dow Chemical Co.) and a glassy carbon (a phenolic-resin-derived material, Alfa-Aesar). Boron was introduced substitutionally into the quasi-graphitic lattice by heating these carbons, physically mixed with boron powder (99.999%, Alfa-Aesar) at different levels (1, 2 and 5 wt % B), to ~2450 °C in Ar [6,15]. Some loss of boron occurred during this treatment (see Results).

Isothermal carbon oxidation experiments (~10 mg samples; 1 atm; 21% dry O_2, 99.994%; 250 cc/min) were performed with these samples in a Mettler TGA. The reaction temperature was achieved after heating the sample in N_2 at 25 °C/min; negligible gasification occurred during this nonisothermal period [15]. In selected cases, the reactive surface area (RSA) [16] of the carbons was determined using a commercial transient kinetics apparatus (SSITKA 2000, Altamira Instruments). The

integrated area under the transient decay curves for CO and CO_2, after switching from O_2 to inert gas at different conversion levels, was used as a first approximation to true RSA values.

RESULTS

Figure 1 shows that boron acts as a catalyst of oxidation of glassy carbon. Figure 2 summarizes the kinetic data (at the same carbon conversion level) for the boron-doped polymer-derived carbons. In agreement with the behavior observed for boron-doped Graphon [6], boron is seen to act as a catalyst at low boron loadings and as an inhibitor at higher boron loadings. The global activation energy does not seem to depend in a consistent way on boron content. It is governed rather by the nature of the carbon: as almost invariably reported in the literature, it increases as the degree of crystalline perfection of the carbon increases (33±3 kcal/mol for undoped and boron-doped Saran char vs. 44±5 kcal/mol for undoped and boron-doped Graphon).

Figure 3 shows the x-ray diffraction profiles for undoped and boron-doped Saran chars. At the highest boron loadings, the signature of enhanced graphitization - splitting of the {10} turbostratic peak (at ~43 °2θ) into {100} and {101} graphitic peaks (at ~42 °2θ and ~44 °2θ) - is observed.

Figures 4 and 5 summarize the catalytic and/or inhibiting effects of boron in carbon oxidation as a function of the reaction temperature and the extent of reaction (percent carbon conversion). In agreement with the data shown in Figure 2 and in our earlier work [6], the net effect depends on the concentration of boron in the carbon. It is surprising that boron, present presumably as substituent atoms in the carbon lattice, acts as a catalyst at low loadings and as an inhibitor at higher loadings. This is in contrast to all other reports in the literature [11,12,14], where an inhibiting effect was found at all boron concentration levels when dry O_2 was used as the reactant. Interestingly, Thomas and Roscoe [17] observed a catalytic effect in moist oxygen. More recently, Rodriguez and Baker [18] confirmed the inhibiting effect of the boron oxide, but reported a catalytic effect of boron carbide.

In summary then, all our experimental results obtained to date show that boron inhibits carbon oxidation at high initial boron loadings, high temperatures and high carbon conversion levels. In contrast, boron catalyzes carbon oxidation at low initial loadings, low temperatures and low conversion levels. Additional results [15] suggest that boron is an inhibitor of oxidation at low O_2 partial pressures and a catalyst at higher pressures.

DISCUSSION

In light of the foregoing results, the premises on which some of the earlier work was based [9,11,14] need to be reexamined.

There is no doubt that boron catalyzes the graphitization of a wide range of carbons. (Figure 3 and our other results [15] confirm this well known effect.) This in turn leads in general to a decrease in carbon reactivity [19] and thus, effectively, to oxidation inhibition.

On the basis of results shown in Figures 4 and 5, there is no compelling reason to doubt either that B_2O_3 is formed upon oxidation of boron-doped carbons [17]. It is worth noting, however, the recent work by Cermignani et al. [20] in which X-ray photoelectron spectroscopy was used to identify the boron-containing species after heat treatment and oxidation of boron-doped CVD carbon films. After oxidation at 600 °C for 4 h, they saw no clear evidence that B_2O_3 was the predominant species formed; instead, they identified boron oxycarbides as the dominant surface species.

What needs reevaluation is the proposed [9] electronic effect of boron (mechanism (c) in the Introduction). Its origin lies in the electronic effect of a carbon gasification catalyst which, upon oxygen adsorption, induces type (b) distribution of the π electrons in the graphene layer [21]:
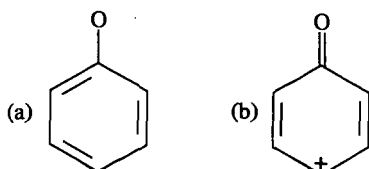
By accepting electrons from the graphene layer (e.g., into unfilled d bands of a transition metal), a catalyst is thought to facilitate both O_2 adsorption (by increasing the C-O bond strength) and product desorption (by weakening the adjoining C-C bonds, as illustrated above).

In contrast to the oxygen-transfer theory [22], the electron-transfer theory of catalysis [23] has not found much support in the carbon gasification literature and had not been confirmed experimentally. Nevertheless, a recent theoretical study of potassium-catalyzed graphite oxidation [24] does indicate that this electron-donating catalyst lowers the work function of graphite and thus enhances the dissociation probability of O_2 on the surface. This is opposite to the well known electronic effect of substitutional boron, which does not contribute electrons to the delocalized π system of the graphene layer and lowers the Fermi level of graphite [12]. Boron would thus be expected to decrease, to some extent at least, the dissociation (chemisorption) probability of O_2. Indeed, Allardice and Walker [12b] concluded that boron inhibits the chemisorption of CO_2 in the C/CO_2 reaction.

This redistribution of π electrons in the presence of substitutional boron results not in the weakening of C-O bonds and strengthening of C-C bonds [9], but in exactly the opposite effect (see figure above): being essentially an electron 'acceptor', as discussed above, boron is predicted to induce type (b) distribution of π electrons and thus weaken C-C bonds and strengthen C-O bonds. This trend was confirmed by a straightforward application of Hückel molecular orbital theory [15]. In fact, Allardice and Walker [12a] used this argument, together with the observed decrease in the activation energy for oxidation of graphite, to anticipate the *catalytic* effect of substitutional boron (even though in their study this effect was masked and overwhelmed by the inhibiting effect of B_2O_3).

Substitutional boron thus emerges as *both* a catalyst and an inhibitor of carbon oxidation. The catalytic effect is clearly observed for the first time; this is attributed to the fact that samples possessing relatively high surface areas were used, and the catalytic effect was not masked by the ubiquitous inhibiting effect of B_2O_3. The fact that boron is a catalyst under conditions favoring desorption control (low temperature and high oxygen partial pressure) and inhibitor under conditions favoring adsorption control (high temperature and low oxygen partial pressure) is quite intriguing. It suggests that this phenomenon is yet another example of the well known 'compensation effect', which we tentatively interpreted [7] as a 'macroscopic complementarity principle': in the presence of substitutional boron the turnover frequency for carbon atom removal increases (due to the catalytic effect of C-C bond weakening), but the number of reactive sites decreases (due to the inhibiting effect on O_2 adsorption). The latter point is illustrated in Figure 6.

ACKNOWLEDGMENTS

REFERENCES

1. R. H. Essenhigh, in "Chemistry of Coal Utilization", 2nd Suppl. Vol. (M. A. Elliott, Ed.), Wiley, New York, 1981, p. 1153.
2. N. M. Laurendeau, *Prog. Energy Combust. Sci.* **4**, 221 (1978).
3. P. L. Walker, Jr., R. L. Taylor and J. M. Ranish, *Carbon* **29**, 411 (1991).
4. J. Lahaye and P. Ehrburger (Eds.), *Fundamental Issues in Control of Carbon Gasification Reactivity*, Kluwer, Dordrecht, The Netherlands, 1991.
5. K. Skokova and L. R. Radovic, this symposium, March 1996.
6. M. Karra, R. J. Zaldivar, G. S. Rellick, P. A. Thrower and L. R. Radovic, in *Proc. 22nd Biennial Conf. Carbon*, San Diego, CA, July 1995, p. 646.
7. L. R. Radovic, M. Karra and K. Skokova, in *Proc. 22nd Biennial Conf. Carbon*, San Diego, CA, 1995, p. 636.
8. S. Marinkovic, C. Suznjevic and I. Dezarov, *Carbon* **7**, 185 (1969).
9. L. E. Jones and P. A. Thrower, *J. Chim. Phys.* **84**, 1431 (1987).
10. R. J. Zaldivar, R. W. Kobayashi and G. S. Rellick, *Carbon* **29**, 1145 (1991).
11. D. W. McKee, in *Chem. Phys. Carbon* (P. A. Thrower, Ed.) **23**, 173 (1991).
12. D. J. Allardice and P. L. Walker, Jr., (a) *Carbon* **8**, 375 (1970); (b) ibid. **8**, 773 (1970).
13. P. Ehrburger, P. Baranne and J. Lahaye, *Carbon* **24**, 495 (1986).
14. W. Kowbel, Y. Huang and H. Tsou, *Carbon* **31**, 355 (1993).
15. M. Karra, M. S. Thesis, The Pennsylvania State University, 1996.
16. A. A. Lizzio, H. Jiang and L. R. Radovic, *Carbon* **28**, 7 (1990).
17. J. M. Thomas and C. Roscoe, in *Proc. 2nd Conf. Ind. Carbon Graphite*, London, 1965, p. 249.
18. N. M. Rodriguez and R. T. K. Baker, *J. Mater. Res.* **8**, 1886 (1993).
19. L. R. Radovic, P. L. Walker, Jr. and R. G. Jenkins, *Fuel* **62**, 849 (1983).

20. W. Cermignani, T. E. Paulson, C. Onneby and C. G. Pantano, *Carbon* **33**, 367 (1995).
21. P. L. Walker, Jr., M. Shelef and R. A. Anderson, in *Chem. Phys. Carbon* (P. L. Walker, Jr., Ed.) **4**, 287 (1968).
22. D. W. McKee, in *Chem. Phys. Carbon* (P. L. Walker, Jr. and P. A. Thrower, Eds.) **16**, 1 (1981).
23. T. J. Long and K. W. Sykes, *Proc. Royal Soc.* **A215**, 100 (1952).
24. C. Janiak, R. Hoffmann, P. Sjövall and B. Kasemo, *Langmuir* **9**, 3427 (1993).
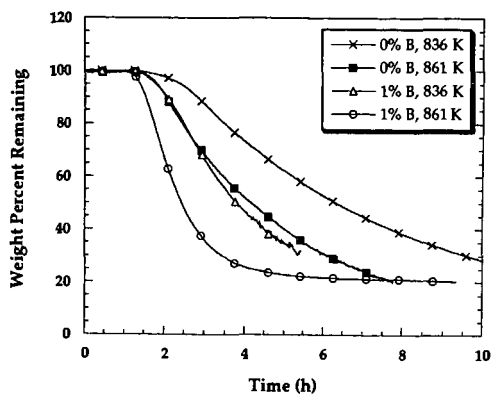
Figure 1. Typical TGA plots for boron-free and boron-doped glassy carbon.
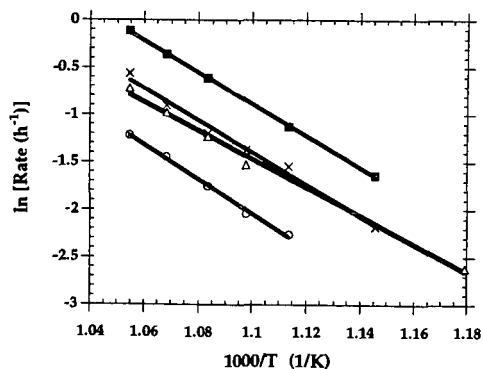
Figure 2. Arrhenius plots for Saran char doped with different amounts of boron and gasified at 1 atm (21% O_2): x, 0% B, 33 kcal/mol; ■, 1.1% B, 33 kcal/mol; Δ, 1.9% B, 30 kcal/mol; O, 3.8% B, 36 kcal/mol.
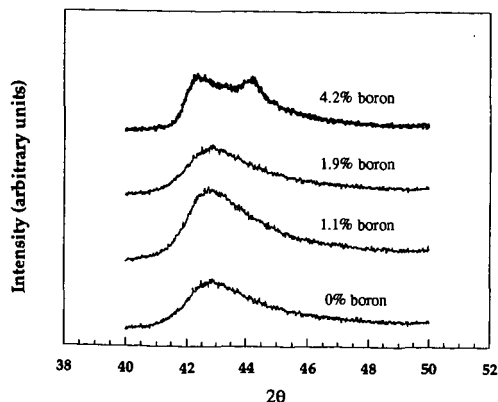
Figure 3. X-ray diffraction patterns for Saran char doped with different concentrations of boron.

214
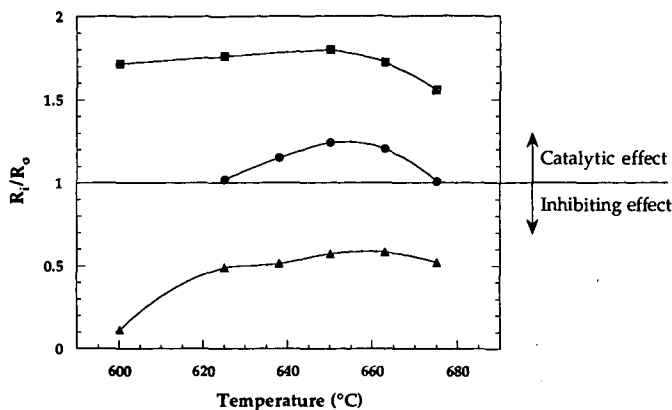
Figure 4. Effect of reaction temperature on the inhibition effect of boron-doped Saran char for various levels of initial boron concentration: ■, 1.1% B; ●, 1.9% B; ▲, 3.8% B. (R_i and R_o are the reaction rates for doped and undoped samples.)
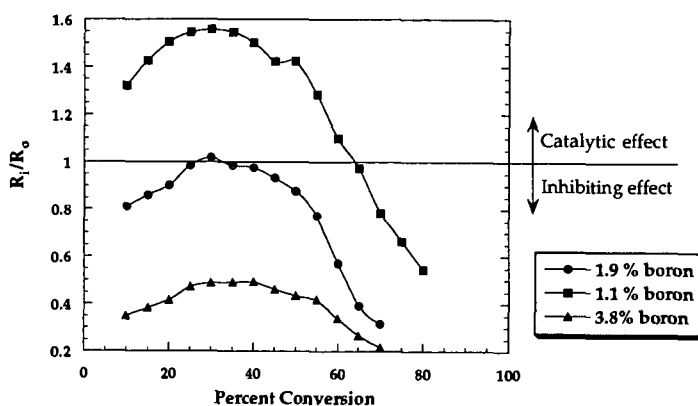
Figure 5. Effect of conversion level on the inhibition effect of boron-doped Saran char for various levels of initial boron concentration.
(R_i and R_o are the reaction rates for doped and undoped samples.)
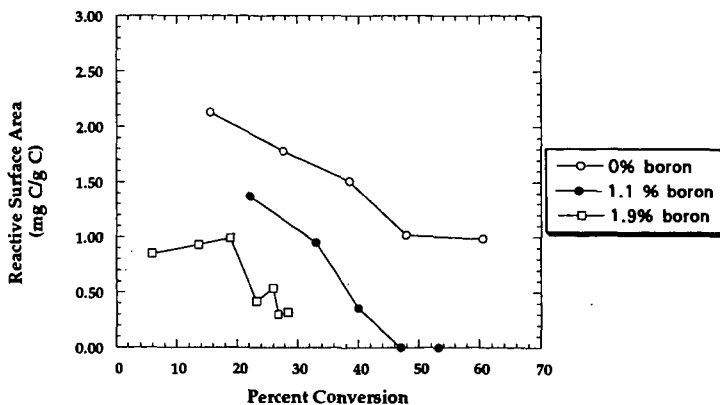
Figure 6. Reactive surface area vs. conversion for Saran char doped with boron: ○, 0% B; ●, 1.1% B; □, 1.9% B. (RSA estimated at 700 °C and 1 atm, 5% O_2.)

LOW TEMPERATURE STEAM-COAL GASIFICATION CATALYSTS

Edwin J. Hippo and Deepak Tandon
Department of Mechanical Engineering and Energy Processes
Southern Illinois University
Carbondale, IL 62901

INTRODUCTION

Shrinking domestic supplies and larger dependence on foreign sources have made an assortment of fossil fuels attractive as possible energy sources. The high sulfur and mineral coals of Illinois would be an ideal candidate as possible gasification feedstock.

Large reserves of coal as fossil fuel source and a projected shortage of natural gas (methane) in the US, have made development of technology for commercial production of high Btu pipeline gases from coal of interest. Several coal gasification processes exist, but incentives remain for the development of processes that would significantly increase efficiency and lower cost. A major problem in coal/char gasification is the heat required which make the process energy intensive. Hence, there is a need for an efficient and thermally neutral gasification process.

At the present time, natural gas (methane) reserves are sufficient to meet the demands but projections indicate a dwindling supply in the future. There is a need to develop an economical process for production of methane to ensure a steady supply. Direct methanation of high sulfur and mineral coals would not only utilize this important fossil fuel feedstock but would also be inexpensive as compared to other energy intensive gasification processes. Direct formation of methane in the gasifier would also increase the efficiency of the combined cycle power generation plant over that of an integrated gasification combined cycle (IGCC) process, producing CO and H_2 only.

Catalytic steam methanation of coal is an almost thermoneutral process:

$$2C + 2H_2O \leftrightarrow CO_2 + CH_4 \qquad \Delta H = 8 \, kJ \, mol^{-1} \qquad (1)$$

The role of the catalyst in coal/carbon gasification has been to reduce the reaction temperature and increase the rate of reaction. The main objective of these studies has been to improve the production of water gas, producer gas, or hydrogen as sources for ammonia production. Most of these works were carried out at lower pressures and have little qualitative value in assessing the catalytic effects on coal/char gasification for methane production.

Catalytic gasification of coal/carbon has attracted much attention recently. A majority of the elements in the periodic table have been tested as potential gasification catalysts and a number of leading candidates have been identified. Catalyst that are active at low temperatures would favor the process of direct gasification for methane production, since low temperature and high pressure favors the formation of methane.

Various oxides, halides and carbonates of both alkali and alkaline earth metals, along with transition metals have been surveyed as possible char gasification catalysts. Some of the general conclusions drawn are as follows:
(1) Catalytic effect decreases with increasing temperature;
(2) Catalysts are more effective in gasification processes if steam is present in the gasification gases;
(3) There usually is an optimum catalyst loading, beyond which either negligible or negative effects are observed;
(4) Relative effects of catalysts can differ under different reaction conditions;
(5) Gasification reactivity can be effected significantly by the method /condition of catalyst impregnation; and
(6) Catalyst impregnation is more effective than physical mixing with the carbon.

Methane cannot be produced by the reaction of $C(H)_2$ complex with hydrogen, if no catalyst is present. Therefore, incentives exist to explore the thermoneutral catalytic steam methanation (reaction 1) of coals to produce methane economically and in a single reaction.

Catalytic effects on gasification of carbon materials have been studied for last several decades. The mechanisms of catalytic gasification are still not completely understood and are not the same for all catalysts systems and reactions. In general, reactivity of catalyzed carbons is at least one order of magnitude higher than those of uncatalyzed carbons. A majority of the elements in the periodic table have been tested as potential gasification catalysts. The main objective of these studies have been to improve the process for production of water gas or producer gas. Outside of the work at Exxon, these work, have little qualitative value in assessing the catalytic effects on coal/char gasification for production of methane from steam.

Thermodynamically, high pressure and low temperature shift the reaction towards methane formation. It was the aim of this research to study the catalytic steam gasification of high sulfur, high mineral, agglomerating coals at elevated pressures and lower temperatures for production of methane. This research focused mainly on prevention of catalyst deactivation and coal char agglomeration. A study of pure catalysts was performed at various temperatures (773 to 973 K) and pressures (0.1 to 3.5 MPa). These catalysts were also used in various combinations to determine any synergistic effects on the methanation reaction. At High pressures alkali metals such as potassium, kept transition metal catalyst(s) reduced, mobile, and activated for longer time periods. The alkali metals and Mo also helped in the penetration of transition metals and thus provided a better contact with the carbon matrix.

The ultimate goal of this research was to develop a low temperature sulfur resistant catalyst system that would not only be efficient and economic but would also produce methane in a single step. The single-reaction process would eliminate the cost of separation, compression and recycling of hydrogen gas. Developing a low temperature catalyst system should also help reduce catalyst recycle costs. At low temperature operations, interaction of catalyst with the coal mineral phases are less likely.

BACKGROUND
The mechanism of gasification is not the same for all the catalysts systems and reactions. The catalyst basically works through a redox cycle, and dissociates molecular oxygen into atomic oxygen much faster than the uncatalyzed carbon surface. It is these mobile oxygen atoms that migrate to the carbon surface, thereby, generating oxides of carbon (CO and CO_2). This effect is called the _Spill-over effect_.

Recently it has been established that oxygen transfer plays a major role in catalysis. For transition metal salts (e.g. Fe, Ni) the catalyst oscillates between two oxidation states, on the other hand alkali metal salts (e.g. Na, K) during catalysis involve a carboxylic, phenolic or a completely reduced structure.

The catalytic effects of a catalyst system depends on; (i) activation of the catalyst, (ii) intrinsic activity of the active species, and (iii) inactivation of the active species [1]. During activation of the catalyst the metal salt reacts and decomposes to the elemental state or any other intermediate state that is catalytic. The dispersion and adhesion of such species on the carbon surface is extremely important. The catalyst looses its activity due to agglomeration, volatilization, inclusion in micropores, poisoning or interaction with the mineral matter of the coal. Catalyst mobility is important for its effectiveness. If the catalyst is in the molten phase, diffusion will depend on the temperature difference between the melting point and gasification temperature [2-5].

Single catalyst (one metal element) gasification has several limitations: (i) the rate of gas production is very slow, (ii) reduced active surface area by pore blockage, (iii) rapid deactivation of the catalyst by poisoning and sintering, (iv) low gas production, (v) loss of contact of catalyst and reactant, and (vi) volatilization of catalyst, and catalyst encapsulation by carbon deposition [6-12].

Exxon catalytic gasification process produces substitute natural gas (SNG) by catalytic steam gasification of coal [13]. The process operates at 700°C and 3.5 MPa and uses potassium carbonate as the catalyst. The catalyst plays three important roles:
(1)   It enhances the rate of gasification and lowers the reaction temperature thereby favoring methane production.
(2)   Favors gas phase methanation equilibrium.
(3)   Inhibition of swelling and caking of coals.
In this process calcium performed better at lower loadings because it does not interact

preferentially with the mineral matter. Since calcium is not as mobile as potassium its impregnation was very critical.

Iron is one of the desired catalysts for steam gasification of coal. The cheap availability of iron and its salts (mainly sulfate) make it even a more promising catalyst than the alkali metals. Commercially, it is one of the best catalysts for about 10 wt.% char conversion. The problem in using iron is that it deactivates (oxidizes) very rapidly. Nickel is another good catalyst, but it also deactivates fast and the gas production stops after about 10% graphite conversion [14]. Calcium deactivates because of sintering as a result of particle growth but remains active for longer burnoff times than iron and nickel. Abel et al. [2] found that reaction rate falls as a result of pore blockage by the catalyst which results in the reduction of accessible surface area. The catalytic activity of iron has been described by various mechanisms: electron transfer, oxygen transfer, carbide mechanism [15-17].

Bimetallic catalysts have addressed some of the limitations of single catalyst gasification. Gas production increases with the use of bimetallic catalyst. The catalyst remains active for a longer duration and is more resistant to poisoning. A catalyst that is not deactivated by sulfur would enable the gasification of high sulfur coals. Synergetic effects have been observed by the use of bimetallic catalysts [18].

Bimetallic catalysts not only increase the activity and selectivity towards desired products, but are also more resistant towards catalyst deactivation by poisoning or carbon deposition. Researchers have performed both experimental and theoretical analysis for bimetallic catalyst systems and have found significant differences in the surface and bulk compositions, as a result of one component of the catalyst system segregating preferentially to the surface. Also, an adjuvant gas can influence the segregation process [19-20].

EXPERIMENT
The coal used in this study was IL. No. 6 coal. This coal was selected because of its high sulfur content. Both the raw and demineralized coal samples were gasified in this study. Gasification of all samples was conducted in an electric furnace. The reactor, was a stainless steel tube, mounted vertically in the furnace. A high pressure pump was employed to pump water at the rates of 30 ml hr^{-1} gm^{-1} of coal. All the experiments were performed at 500 and 700°C and 500 and 1000 psig. Samples were placed in the reactor in a wire mesh bucket. The glass wool at the top of the reactor was used to trap any tarry material that might tend to escape. The system was purged with argon and pressurized with steam. Gas samples were collected at regular time intervals (5, 15, 30, and 60, min.) in gas bags and gas chromatography was performed on each gas bag. Product gas composition and concentration were monitored by gas chromatography. From the gas yield and composition, the carbon conversion in each interval and the accumulated carbon conversion were calculated. The experiments were terminated when the rate of gas production diminished significantly.

RESULTS AND DISCUSSION
At 500°C and both 500 and 1000 psig, negligible amount of raw coal was gasified. This suggested that the activation energy barrier cannot be crossed at 500°C for the raw coal alone. The unreacted steam would condense at the bottom of the reactor. Even when the flow rate of water was reduced to 0.25 ml min^{-1} similar problems were encountered. At 700°C there was a substantial increase in the amount of coal gasified. Almost 36-39 wt.% (assuming 100% carbon) coal was gasified at 500 psig. At 5 minutes the analysis of the gas at 500 psig showed CO_2 as the main gas (77%), there was significant amount of CH_4 (18%) and minute quantities of CO and H_2. Gas production was observed till 15 minutes but at this time CO_2 was the primary gas (89%). No gas production was observed at 30 minutes. At 700°C and 1000 psig there was a slight increase in the amount of coal gasified (43 wt.%). The gas analysis at 5 min showed 61% CO_2, 28% CH_4, 5% H_2, and 6% CO. At 15 min the gas composition was 79% CO_2, 16% CH_4, 3% H_2, and 2% CO. Once again no gas production was observed at 30 min. This high jump in coal conversion at 700°C suggested that at this temperature the energy was sufficient to clear the activation barrier and a portion of the char formed was also gasified. Demineralized coal gasified almost like raw coal with 38 wt.% conversion at 700°C and 500 psig. The gas analysis at 5 min showed 88% CO_2, 0% CH_4, 6% H_2, and 6% CO. At 15 min the gas composition was 96% CO_2, 0% CH_4,

4% H_2, and 0% CO.   Once again no gas production was observed at 30 min. Conversion numbers and gas analyses are presented in Table 1.

In presence of the catalyst significant gasification was observed at 500°C and 500 psig. Both the raw and demineralized coal samples were gasified in presence of the catalyst. Catalysts studied thus far are salts of potassium, iron, nickel, and molybdenum. For the single catalyst experiments of potassium salts (hydroxide and carbonate) increasing the catalyst loading from 5 to 10% had little effect on coal conversion. For KOH catalyzed raw coal experiments the coal conversion was around 28-35 wt.%. Similarly increase in temperature had very little effect on conversion. Gas production was observed till 30 min.   Increase in pressure resulted in increased methane formation.   For 10% potassium loading (KOH) the gas analysis at 5 min showed 55% CO_2, 32% CH_4, 7% H_2, and 6% CO. At 15 min the gas composition was 61% CO_2, 29% CH_4, 6% H_2, and 4% CO. At 30 min the gas composition was 66% CO_2, 26% CH_4, 5% H_2, and 3% CO. No gas production was observed at 45 min. For potassium carbonate, however, the conversion went down from 40 to 33% with increase in the loading from 5 to 10%. This could be due to interaction of potassium carbonate with the mineral of coal at higher loadings. The gas analyses were comparable to the KOH experiments. Conversion numbers and gas analyses are presented in Table 1.

Salts of transition metals behaved like potassium salts. The conversion numbers were comparable but the methane concentration was slightly lower. In some cases the gas production stopped after 15 min. At 500°C and 500 psig almost 30% conversion was achieved with 10% loading of iron chloride. The gas analysis at 5 min showed 64% CO_2, 27% CH_4, 5% H_2, and 4% CO. At 15 min the gas composition was 68% CO_2, 26% CH_4, 5% H_2, and 1% CO. At 30 min the gas composition was 74% CO_2, 23% CH_4, 3% H_2, and 0% CO. No gas production was observed at 45 min. At the same conditions 37% conversion was achieved with nickel hydroxide. The gas analysis at 5 min showed 59% CO_2, 30% CH_4, 7% H_2, and 4% CO. At 15 min the gas composition was 67% CO_2, 26% CH_4, 5% H_2, and 2% CO. At 30 min the gas composition was 72% CO_2, 24% CH_4, 4% H_2, and 0% CO. No gas production was observed at 45 min. Conversion with molybdenum oxide was lower (22%) under same conditions. No gas production was observed after 15 min. The conversion numbers and the gas analyses for the demineralized coal samples were comparable to the raw coal conversions. Conversion numbers and gas analyses are presented in Table 1.

When potassium hydroxide was used with transition metals significant increases in the conversions were obtained and also the concentration of the methane in the product gas increased substantially. As shown in Table 1 at 500°C and 500 psig when iron chloride and potassium hydroxide are used together at 5% each loading the conversion increased to 42% with an increase in methane concentration in the product gas. The gas analysis at 5 min showed 56% CO_2, 35% CH_4, 7% H_2, and 2% CO. At 15 min the gas composition was 59% CO_2, 34% CH_4, 6% H_2, and 1% CO. At 30 min the gas composition was 69% CO_2, 27% CH_4, 4% H_2, and 0% CO. No gas production was observed at 45 min. At 10% each loading the conversion went up to 53%. The gas analysis at 5 min showed 47% CO_2, 39% CH_4, 9% H_2, and 5% CO. At 15 min the gas composition was 52% CO_2, 37% CH_4, 7% H_2, and 4% CO. At 30 min the gas composition was 58% CO_2, 33% CH_4, 6% H_2, and 3% CO.   No significant gas production was observed at 45 min. This shows some synergistic effects. Possibly potassium helps keep iron reduced for longer duration and thus the conversion and methane formations are increased. Conversion numbers and gas analyses are presented in Table 1.

When nickel hydroxide and potassium hydroxide are used together at 500°C and 500 psig and at 5% each loading the conversion was 39%. The gas analysis at 5 min showed 60% CO_2, 33% CH_4, 5% H_2, and 2% CO. At 15 min the gas composition was 69% CO_2, 27% CH_4, 3% H_2, and 4% CO. No significant gas production was observed at 30 min. At 10% each loading the conversion went up to 55%. The gas analysis at 5 min showed 58% CO_2, 35% CH_4, 7% H_2, and 0% CO. At 15 min the gas composition was 67% CO_2, 28% CH_4, 5% H_2, and 0% CO. At 30 min the gas composition was 76% CO_2, 21% CH_4, 3% H_2, and 0% CO. No significant gas production was observed at 45 min.   At 700°C and 1000 psig and 5% each loading of nickel and potassium a conversion of 74% was achieved. The gas had increased concentration of carbon monoxide and lower methane production. Experiments performed with demineralized coal samples resulted in slightly lower conversions but similar gas analyses.

CONCLUSIONS

1. Significant amounts of hydrogen can be produced at moderate gasification conditions.
2. Low to negligible CO concentrations and ratios of H_2/CO is at synthesis gas stoichiometry.
3. Steam reforming of methane is avoided at 3-6 MPa range.
4. The combination of alkali and transition metals gave significant synergistic effects.

Table 1.
Carbon Conversion and Gas Analyses of Various Steam-Coal Gasification Experiments

Run	Temp (°C)	Pres (psig)	Catalyst	Loading (Wt.%)	Conv. %	$H_2/CO_2/$ CH_4/CO 5 Min	$H_2/CO_2/$ CH_4/CO 15 Min	$H_2/CO_2/$ CH_4/CO 30 Min
Raw	700	500	None	None	37	2/77/18/3	1/89/8/2	-------
Raw	700	500	None	None	39	2/76/18/4	0/91/7/2	-------
Raw	700	500	None	None	36			
Raw	700	1000	None	None	43	5/61/28/6	3/79/16/2	-----
Demin	700	500	None	None	38	6/88/0/6	4/96/0/0	-------
Raw	700	500	K_2CO_3	5	36.4			
Raw	700	1000	K_2CO_3	5	39.9	6/53/35/6	5/59/32/4	4/68/26/2
Raw	700	1000	K_2CO_3	10	33.1	7/54/32/7	5/66/26/3	-------
Raw	500	500	KOH	10	28.4	6/61/29/4	6/61/29/4	5/66/26/3
Raw	500	1000	KOH	10	36.4	6/52/35/7	5/59/31/5	4/64/28/4
Raw	700	750	OH	5	34.6	7/54/33/6	5/60/30/5	5/65/26/4
Raw	500	500	KOH	10	28.4	7/55/32/6	6/61/29/4	5/66/26/3
Raw	500	500	$FeCl_2$	10	29.7	5/64/27/4	5/68/26/1	3/74/23/0
Raw	500	500	$KOH/FeCl_2$	5 each	42.16	7/56/35/2	6/59/34/1	4/69/27/0
Raw	500	500	$KOH/FeCl_2$	10 each	53	9/47/39/5	7/52/37/4	6/58/33/3
Raw	500	1000	NiOH	10	37	7/59/30/4	5/67/26/2	4/72/24/0
Raw	700	1000	KOH/NiOH	5 each	74	8/53/32/7	4/82/11/3	4/72/24/0
Raw	500	500	KOH/NiOH	10 each	55	7/58/35/0	5/67/28/0	3/76/21/0
Raw	500	500	KOH/NiOH	5 each	39	5/60/33/2	3/69/27/1	-----
Raw	500	500	MoO_3	10	22	1/71/28/0	0/83/17/0	----

REFERENCES

1. J. Alder, K.J. Huttinger, and R. Minges, Fuel, 63, 1397, 1984.
2. D.A. Fox and A.H. White, Ind. Eng. Chem., 23, 259, 1931.
3. D.W. McKee and D. Chatterji, Carbon, 13, 381, 1975.
4. D.W. McKee and D. Chatterji, Carbon, 16, 53, 1976.
5. T. Wigmans, H. Haringa, and J.A. Moulijn, Fuel, 62, 185, 1983.
6. J. Carrazza, W.T. Tysoe, H. Heinemann and G.A. Somorjai, J. Catal., 96, 234, 1985.
7. J.S. Binford and H. Eyring, J. Am. Chem. Soc., 60, 486, 1956.
8. R.G. Jenkins, S.P. Nandi, and P.L. Walker, Jr. Fuel, 52, 288, 1973.
9. E.J. Hippo and P.L. Walker, Jr., Fuel, 54, 245, 1974.
10. K.J. Huttinger and W.F. Merdes, Carbon, 30(6), 883, 1992.
11. J.L. Johnson, Fuel Chem. Div. Prepr., 170th ACS national meeting, Chicago, IL. Aug. 24-29, 1975.
12. J.W. Patrick and F.H. Shaw, Fuel, 51, 69, 1972.
13. W.R. Epperly and H.M. Siegel, Proc. of the 11th Intersociety Energy Conversion Conference, Nevada, USA, 1976.
14. T. Wigmans, A. Hoogland, P. Tromp, and J.A. Mouljin, Carbon 21(1) 13, 1983.
15. F.W. Long and K.W. Sykes, J. Chem. Phys., 47, 361, 1950.
16. Y. Tamai, H. Watanabe, and A. Tomita, Carbon, 12, 453, 1974.
17. W.L. Holstein and M. Boudart, Fuel, 62, 162, 1983.
18. Y. Nishiyama, Fuel Processing Technology, 29, 31, 1991.
19. V. Ponec, Surf. Sci., 80, 352, 1979.
20. M.F.L. Johnson and V.M.J. Leroy, J. Catal., 35, 434, 1974.

CATALYSIS OF PETROLEUM COKE GASIFICATION
BY CALCIUM HYDROXIDE AND CARBONATE

Yasuo Ohtsuka, Atsuko Yamauchi and Qianlin Zhuang
Research Center for Carbonaceous Resources
Institute for Chemical Reaction Science, Tohoku University
Sendai 980-77, Japan

ABSTRACT

Catalysis of petroleum coke gasification in pure CO_2 by $Ca(OH)_2$
or $CaCO_3$ has been investigated with a thermobalance.   The reac-
tivity of the original coke is very low. $Ca(OH)_2$ kneaded with
the carbon in water enhances the reactivity drastically, and thus
realizes complete gasification at 900°C within 25 min. $CaCO_3$
shows almost the same catalytic activity as $Ca(OH)_2$ except for
the initial stage of gasification.   The X-ray diffraction meas-
urements and X-ray photoelectron spectroscopy of partly gasified
samples reveal that the calcium promotes remarkably the formation
of non-crystalline carbon, in other words, surface oxygen com-
plexes, during gasification.   The temperature programmed deso-
rption shows that there are strong interactions between calcium
and carbon, which contributes to the creation of reactive sites.

1. INTRODUCTION

Petroleum coke as a byproduct in coking processes of residual
oils is used partly as an energy source [1].   Since it is com-
posed of graphitized carbon, however, the gasification reactivity
is low compared with coal.   It may be interesting from a practi-
cal point of view if the reactivity is enhanced by catalyst
addition and consequently petroleum coke can be employed as a
feedstock for the production of hydrogen and syngas.   However,
no successful approach has been reported so far.

In earlier publications we have found that inexpensive $Ca(OH)_2$
and $CaCO_3$ are the most promising gasification catalysts [2-4], as
long as water slurry of $Ca(OH)_2$ or $CaCO_3$ is mixed with low rank
coals with large amounts of oxygen functional groups as ion
exchangeable sites.   Whereas, recent dynamic studies on the
catalysis of carbon gasification by Ca have shown that the cata-
lyst can create surface oxygen complexes, that is, reactive
sites, even on well-ordered graphite [5,6].

It may be expected from these observations that graphitized
carbon in petroleum coke is also activated during gasification by
the calcium from $Ca(OH)_2$ or $CaCO_3$.   Therefore the present work
focuses on making clear catalyst effectiveness of these compounds
for the gasification of petroleum coke and on elucidating the
catalysis by the calcium.

2. EXPERIMENTAL

Petroleum coke of size fraction 75-150 μm was used.   The prox-
imate and ultimate analyses are shown in Table 1.   The ash and
oxygen contents were very low.   The X-ray diffraction (XRD)
analysis revealed the presence of graphitized carbon, but the
degree of graphitization was not so developed, as shown by the
XRD parameters of interplanar spacing (d_{002}) and average crystal-
line height (L_c) in Table 1.   Powdery $Ca(OH)_2$ or $CaCO_3$ was
loaded onto the carbon by simply kneading them in water, Ca
loading in the dried sample being 3 wt% as metal.   The $Ca(OH)_2$-
loaded carbon was used unless otherwise described.

About 20 mg of the sample was heated quickly up to 800-1000°C in
a stream of pure CO_2, and the weight loss during the isothermal
gasification was monitored with a thermobalance [3,4].   The XRD,
X-ray photoelectron spectroscopy (XPS), and temperature pro-
grammed desorption (TPD) of partly gasified samples were carried
out to characterize the catalyst state and reactive sites.   In
the TPD runs, the sample after gasification at 850°C followed by
cooling to room temperature was heated in He up to 1000°C, and CO
and CO_2 released were determined with a gaschromatograph.

3. RESULTS AND DISCUSSION

Rate Enhancement by Calcium Catalyst

The profiles for the CO_2 gasification of petroleum coke are shown in Figure 1, where conversion is calculated on a basis of fixed carbon after devolatilization. The reactivity of the original coke was quite low at 800-900°C, and fixed carbon conversion at 900°C was < 20 wt% after 2 h. On the other hand, $Ca(OH)_2$ enhanced the reactivity dramatically; the conversion at 800°C reached 65 wt% after 2 h, and at 900°C the carbon was gasified completely within 25 min. Our previous studies have shown that the Ca cations in saturated $Ca(OH)_2$ solution can readily be ion-exchanged with COOH groups when mixed with low rank coals at room temperature [7], and the exchanged Ca is very active for the steam gasification [2,3,7]. No exchange reactions would take place significantly in the present work, however, since there are almost no oxygen functional groups as exchangeable sites in petroleum coke, as is expected by very low content of oxygen (Table 1). It should therefore be noted that $Ca(OH)_2$ loaded on the carbon by simple kneading shows the high catalytic activity for the gasification.

The specific rate of carbon, defined as the gasification rate per unit weight of remaining carbon, is plotted as a function of conversion in Figure 2. The rate of the $Ca(OH)_2$-loaded coke at 800°C was independent of the conversion, and it was comparable to the rate at 1000°C without catalyst. This observation means that the use of $Ca(OH)_2$ can lower the temperature by 200°C. The rate of the Ca-catalyzed gasification at 850 or 900°C changed as fixed carbon conversion increased, and seemed to have minimum at the conversion of around 50 wt%. Since such the change would be determined by the balance between catalyst agglomeration and enrichment due to the consumption of carbon [8], the decreased rate observed in the conversion range of less than 50 wt% suggests that the agglomeration of Ca catalyst may be dominant at the initial stage of reaction. At 900°C the initial rate of the catalyzed gasification was 90 times as large as that of the uncatalyzed one.

As is seen in Figure 2, $CaCO_3$ also promoted the gasification remarkably. The initial rate at 850°C was lower than that with $Ca(OH)_2$, but it increased gradually with increasing conversion, and both rates were almost the same at the latter part of reaction. The use of $CaCO_3$ as alternative to $Ca(OH)_2$ is interesting from a practical point of view, since limestone and seashell wastes as received can be used as catalyst sources.

Catalyst State and Reactive Sites

Strong, sharp diffraction lines of $Ca(OH)_2$ were observed on the $Ca(OH)_2$-loaded coke. When the coke was devolatilized in pure N_2, these lines disappeared and CaO peaks with very weak intensities appeared. These observations show that $Ca(OH)_2$ loaded is transformed mostly to non-crystalline species, which suggests catalyst redistribution on devolatilization, possibly the formation of finely dispersed Ca species. The surface of petroleum coke might be mildly oxidized in the kneading process, and the preoxidation and/or mechanochemical effects during kneading, if any, might affect the dispersion of Ca catalyst.

Figure 3 shows the XRD patterns after gasification of petroleum coke with and without $Ca(OH)_2$ to 50 wt% conversion. $Ca(OH)_2$ was transformed mainly to $CaCO_3$ and partly to CaS during gasification. Since CaO was stable in the devolatilization step preceding carbon gasification, as mentioned above, $CaCO_3$ was formed by the reaction of CaO with CO_2. The presence of CaS may mean the catalyst deactivation by the sulfur evolved, which may be one reason for the decrease in specific rate with conversion at the initial stage of reaction (Figure 2). Figure 3 also revealed lower diffraction intensities of C(002) lines than those from the corresponding original carbon. Higher d_{002} and lower L_C were observed in the Ca-bearing sample. These observations point out the formation of non-crystalline carbon in the presence of the catalyst.

When the XPS spectra of these gasified samples were measured, the C 1s peak of the Ca-bearing carbon was broad compared with the

original carbon, and the intensities of the spectra at 286-288 eV, attributable to ether and carbonyl bonds, were higher in the presence of the catalyst. Further, the atomic ratio of O/C, determined by the O and C 1s spectra, with Ca was about 5 times as that without Ca. It is evident from the XPS observations that surface oxygen complexes are formed on the carbon to a larger extent during the Ca-catalyzed gasification.

In order to characterize surface oxygen complexes, the TPD runs of gasified samples were carried out, and the results are summarized in Table 2. No significant amount of CO_2 was detectable without Ca catalyst, and CO alone was released with the largest rate at around 950°C, where the CO_2 gasification of the original coke proceeded at an appreciable reaction rate.

On the other hand, CO_2 desorbed in the presence of Ca catalyst. The desorption started at about 550°C, showed a maximal rate at 700°C, and completed at around 750°C. Since the catalyst was present in the form of $CaCO_3$ after gasification (Figure 3), it is no doubt that CO_2 desorption comes mainly from the decomposition of $CaCO_3$. However, the peak temperature of CO_2 desorption was much lower than the decomposition temperature of $CaCO_3$ bulk, and the TPD pattern was broad. Further, as is seen in Table 2, CO desorption occurred significantly at 700°C where CO_2 desorbed at the largest rate. These observations point out strong interactions between $CaCO_3$ and carbon surface. The CO evolved at 700°C may originate partly from the formation of $CaCO_3$-C intermediate and subsequent CO desorption [9,10]. The promotion of $CaCO_3$ decomposition by carbon has been confirmed by the high temperature XRD technique [2]. The total amount of CO_2 released was larger than Ca loading onto petroleum coke, which suggests that surface complexes such as lactone and acid anhydride formed during the Ca-catalyzed gasification may be decomposed into CO_2 [11,12].

Most of CO desorbed in the wide temperature range of 750-1000°C, where the calcium showed high catalytic activity. The total amount of CO released with Ca catalyst was two times as that without Ca (Table 2). Consequently, the presence of the catalyst lead to about four-fold oxygen uptake on carbon. This is in good agreement with the oxygen increase determined by XPS measurements. Since the sample after gasification of the $CaCO_3$-loaded coke showed almost the same TPD profiles as in the case of $Ca(OH)_2$, $CaCO_3$ also enhanced the number of reactive sites. It is probable that the increased sites are responsible for large reactivity of petroleum coke in the presence of $Ca(OH)_2$ and $CaCO_3$.

4. CONCLUSION

$Ca(OH)_2$ or $CaCO_3$ showed high catalytic activity for the CO_2 gasification of petroleum coke at 800-900°C when loaded by simple kneading. The calcium promoted the formation of surface oxygen complexes on the carbon during gasification.

REFERENCES

1) Dymond, R.E. *Hydrocarbon Processing* 1991, September, 162-C.
2) Ohtsuka, Y.; Tomita, A. *Fuel* 1986, 65, 1653.
3) Ohtsuka, Y.; Asami, K. *Energy Fuels* 1995, in press.
4) Ohtsuka, Y.; Asami, K. *Energy Fuels* in press.
5) Martin, R.R.; Macphee, J.A.; Kyotani, T.; Hayashi, S.;
   Tomita, A. *Carbon 29*, 475.
6) Kyotani, T.; Hayashi, S.; Tomita, A. *Energy Fuels* 1991, 5,
   683.
7) Nabatame, T.; Ohtsuka, Y.; Takarada, T.; Tomita, A. *J. Fuel
   Soc. Japan* 1986, 65, 53.
8) Asami, K.; Ohtsuka, Y. *Ind. Eng. Chem. Research*, 1993, 32,
   1631.
9) Cazorla-Amorós, D.; Linares-Solano, A.; Salinas-Martinez de
   Lecea, C.; Joly, J.P. *Carbon* 1991, 29, 361.
10) Cazorla-Amorós, D.; Linares-Solano, A.; Salinas-Martinez de
    Lecea, C.; Kyotani, T.; Yamashita, H.; Tomita, A. *Carbon*
    1992, 30, 995.
11) Koenig, P.C.; Squires, R.G.; Laurendeau, N.M. *Carbon* 1985,
    23, 531.
12) Zhuang, Q.; Kyotani, T.; Tomita, A. *Energy Fuels* 1995, 9,
    630.

Table 1 Analysis of petroleum coke used

Ash	V.M.	C	H	N	S	O	d_{002}	L_c
(wt%, dry)				(wt%, daf)			(nm)	
0.3	11.2	89.4	4.0	2.5	2.1	2.0	0.348	2.5

Table 2 Desorption of CO_2 and CO from the samples gasified at 850°C

Catalyst	Peak temperature (°C)		Total amount released (mmol/g)	
	CO_2	CO	CO_2	CO
None	n.d.[a]	950	n.d.[a]	7
Ca(OH)$_2$	≈700	700[b], 900–1000	8	14

[a]Not detectable. [b]Shoulder peak.
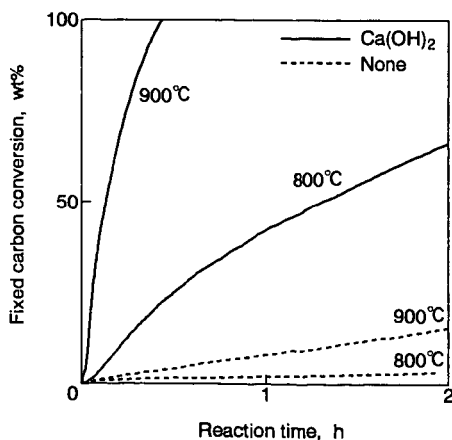
Figure 1. Profiles for the gasification of petroleum coke with CO_2.
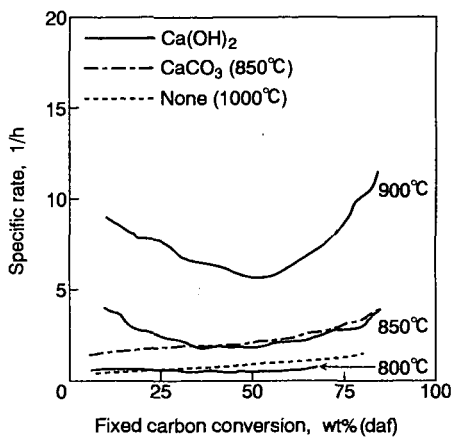
Figure 2. Relationship between specific rate and fixed carbon conversion.
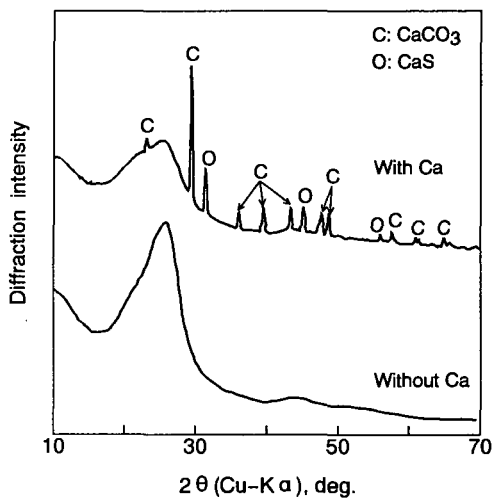
Figure 3. X-ray diffraction patterns of gasified samples with and without Ca catalyst.

LOW TEMPERATURE CATALYTIC COMBUSTION OF CARBON
BY ALKALI METAL SALT/PEROVSKITE TYPE OXIDE MIXTURE

Tatsuro Miyazaki, Masahiro Inoue, and Isao Mochida*
Material&Component Research Laboratory, Kyushu Matsusita Electric
Co.,Ltd. Minosima, Hakata-ku, Fukuoka 812 Japan,
*Institute of Advanced Material Study, Kyushu University
Kasugakoen, Kasuga-shi, Fukuoka 816 Japan

Key words : Catalytic combustion, Alkali salt, Perovskite type oxide

Introduction

Alkali metal salts have been reported the best catalysts for the carbon combustion.[1,2] However, their active species have been recognized to vaporize out from the combustion zone.[3] Some transition metal oxides has been reported active to catalyze the combustion and gasification of carbon.[4,5] However, their intimate contact with the carbon substrate should be assured for the catalysis. Enhancement of catalytic activity has been examined by increasing dispersions and controlling composition.[6,7] However, maintenance of contact with the separate carbon grains to increase the conversion has not been attempted.

In the present study, catalytic activity of alkali metal salts supported on γ -Al$_2$O$_3$ and perovskite type oxide for the combustion of active carbon was studied, to find a way to realize the repeated contact of alkali metal species with carbon through their sublimation and precipitation over the surface of the perovskite type oxide. Influence of anions of salts, mixing procedures of the catalyst, support and carbon as well as the reaction temperature, were examined. The elution of active species was also estimated to observe the combustion of carbon placed at the down-stream of the catalyst bed.

Experimental

Activated carbon (AC) (Nacalai tesque inc.; surface area 370 m^2/g) was used, after washing with hydrochloric acid aq. to remove ash and heat treated at 973K for 8h in nitrogen. Ultimate analysis showed that resulting AC carried small amount of mineral matter (0.01wt%), being free from any detectable hydrogen, oxygen, nitrogen or sulphur. Supported catalysts were prepared by the impregnation. A prescribed amount of potassium metal salts (K$_2$CO$_3$, KCl, K$_2$SO$_4$) were dissolved in deionized water.

The AC, Al$_2$O$_3$ (Nikkei Kinzoku Co. ,Ltd.), perovskite type oxide used as carrier material was dispersed in the solution and then heated to dryness at 363K for 12h. The catalyst loading was adjusted to 1.3$\times$10^{-3} atom alkali per total amount of carrier and reactant (AC) (g).

Perovskite type oxide was prepared from the mixture of component metal nitrates or acetates, through vigorous mixing in water, freezed-dry and calcined at 1123K for 5h. X-ray diffraction analyses showed perovskite type structure of mixed oxide. Examined composition of perovskite was La$_{0.8}$Sr$_{0.2}$Cr$_{0.5}$Mn$_{0.45}$Pt$_{0.05}$O$_3$ (LSCMP).

A continuous flow reactor apparatus was operated under atmospheric pressure. In order to prevent local accumulation of heat, an initial ratio of AC to catalyst was 0.1. The mixture of AC and catalyst was dispersed on a ceramic foam (Brigestone Co. Ltd.). A thermocouple was located at the end of catalyst bed. N$_2$ was flowed during the heating to the reaction temperatures and the oxidant gas (N$_2$ containing 4% O$_2$) was introduced for the combustion. The gaseous products were analyzed by IR-spectrometer (Simadzu Co. ,Ltd.). The amount of AC consumed was determined by the product gas analysis.

Results
Catalytic activity of supported potassium carbonate catalysts

Figure 1 shows AC combustion catalyzed by supported K2CO3 as function of time at 723K. The activity of supported K$_2$CO$_3$ catalysts used in this study increased in the order; K$_2$CO$_3$/γ -Al$_2$O$_3$< K$_2$CO$_3$/Pt- γ -Al$_2$O$_3$ < K$_2$CO$_3$/ AC < K$_2$CO$_3$/γ -Al$_2$O$_3$ blended with LSCMP < K$_2$CO$_3$/LSCMP. The activity of supported K$_2$CO$_3$ catalysts was significantly influenced by the supports;

particularly, K_2CO_3 supported on LSCMP catalyst showed the largest activity among the catalysts tested. Because the activity of LSCMP was not so high, K_2CO_3 supported LSCMP performed the catalysis of very rapid combustion within 500 sec, increasing the conversion upto 100%. K2CO3/γ-Al$_2$O$_3$ physically blended with LSCMP showed high activity than K_2CO_3/γ-Al$_2$O$_3$, giving c.a.100% conversion within 2000 sec. K_2CO_3 supported on AC, Pt-γ-Al$_2$O$_3$, and γ-Al$_2$O$_3$ showed rapid combustion at low conversion level, however the conversion was saturated at 60%.

Catalytic activity of supported potassium salts

Figure 2 summarizes the activity of potassium salts supported on γ-Al$_2$O$_3$ blended with or without LSCMP at 723K. First of all, KCl/γ-Al$_2$O$_3$ showed the largest activity among the salts supported on γ-Al$_2$O$_3$, obtaining nearly 100% combustion by 3000 sec. The K_2SO_4/γ-Al$_2$O$_3$ exhibited the lowest activity .

The effectiveness of the blended catalysts with LSCMP depended very much on the type of potassium salts. The blended catalysts of K_2CO_3/γ-Al$_2$O$_3$ with LSCMP exhibited the strongest synergistic effect to show the largest activity among the potassium salts tested. KCl blended with LSCMP exibited lower activity than KCl/γ-Al$_2$O$_3$.

Analysis for disappearance of potassium on catalysts

In order to estimate potassium amount on carriers after the combustion reaction, the catalytic combustion was repeated three times, using the same catalyst. K_2CO_3/γ-Al$_2$O$_3$ and K_2CO_3/LSCMP were mixed with carbon respectively, and then were heated to 873K under air flow (700 ml/min.). The potassium element remaining on these catalysts was extracted with HCl aq., and analyzed by capillary zone electrophoresis(SZE). Table 1 showed the diminution ratio of the potassium amount before and after reactions. K_2CO_3/γ-Al$_2$O$_3$ lost significant amount of K after the reaction, but less loss of potassium was detected on K_2CO_3/LSCMP.

And then to estimate outflow of potassium element from catalyst bed to down-stream, the combustion reactions were executed at 723K. AC was mixed with K_2CO_3/LSCMP and K_2CO_3/γ-Al$_2$O$_3$ respectively in the same way as mentioned above. Then AC was placed at the down-stream of the catalyst bed.

The results are shown in Figure 3. The activities of K_2CO_3/LSCMP and K_2CO_3/γ-Al$_2$O$_3$ are in it for references. The conversion(X) in this figure is defined as

$$X=(Wo-W-Wb)/(Wo-Wb)$$

where Wo is the initial amount of AC, which was mixed with catalyst, W is the combustion amount of AC at reaction time, Wb is the combustion amount of AC without catalyst at reaction time.

The combustion profiles over K_2CO_3/LSCMP were similar regardless of the down flow carbon. In contrast, K_2CO_3/γ-Al$_2$O$_3$ increased the conversion of AC when the AC free from catalyst was placed at the down stream. Some catalysts may be transferred bed carrying the catalyst to the down stream.

Influence of reaction temperature

Figure 5 shows the catalytic activity of K_2CO_3/γ-Al$_2$O$_3$, K_2CO_3/LSCMP, and blended K_2CO_3/γ-Al$_2$O$_3$ with LSCMP at 623~723K.

K_2CO_3/LSCMP exhibited the highest activity of these three catalysts at this temperature range. Although the activity of K_2CO_3/γ-Al$_2$O$_3$ blended with LSCMP was same to that of K_2CO_3/γ-Al$_2$O$_3$ at 423 K, the blended catalyst exhibited the higher activity at higher temperatures.

Discussion

Potassium salts have been reported to catalyze the combustion of the carbon through their reduction into metal to activate oxygen[8]. The alkali metal can sublime to be mobile over the carbon substrates, maintaining the intimate contact for the catalytic activity. On the other hand, sublimed metal may flow out from the carbon bed, no catalytic activity being maintained. Thus, the sublimation and precipitation of the metal should be

balanced in the carbon bed for the maintenance of the catalytic activity.

LSCMP appears a unique support to perform such sublimation and precipitation for catalytic activity. Another role of the support is to influence the decomposition of potassium salts into active species, LSCMP appears to have such a role. Questions why LSCMP performs such roles are not answered in this paper. Further research is attempted.

KCl/γ -Al_2O_3 exhibited a unique activity to show stable activity, achieving nearly 100% conversion. Active species for KCl/γ -Al_2O_3 is now studied.

References
1) Walker,Jr.,P.L., Shelef,M., Anderson,R.A., "Chemistry and physics of carbon" ,ed.by walker,Jr.,P.L.,vol.4, marcel Dekker, New York 1986, 287.
2) Mckee,D.W., Chatterji,D., Carbon,1975,13,381.
3) Marsh,H.,Mochida,I., ECSE Report , 1978.
4) Backer,R.T., Chludzinski,Jr., Carbon, 1981,19,75.
5) Carrazza,J., Tysoe,W.T.,Heinemann,H., Somorjai,G.A., J.Catal.,1985,96,234.
6) Mochida,I.,Gao,Y.-Z., Fujitsu,H., Sekiyu Gakkaisi, 1991,34,178.
7) Mckee,D.W., "Chemistry and physics of carbon" ,ed.by walker,Jr.,P.L., vol.16, marce Dekker, New York 1981, 1.
8)Frinks,I.L.C.,vanWechem,H.M.H.,Stuiver.J.C.M.,Bouwman,R.,Fuel, 1981,60,463.

Table1 Potassium diminution ratio of K
before and after reaction by CZE

Catalyst	Diminution ratio
K_2CO_3/γ -Al_2O_3	55.5%
K_2CO_3/LSCMP	8.0%

o :K_2CO_3/γ -Al_2O_3
▲ :K_2CO_3/Pt- γ Al_2O_3;
□ :K_2CO_3/AC
● :K_2CO_3/LSCMP
▲ :K_2CO_3/γ -Al_2O_3+LSCMP
+ LSCMP
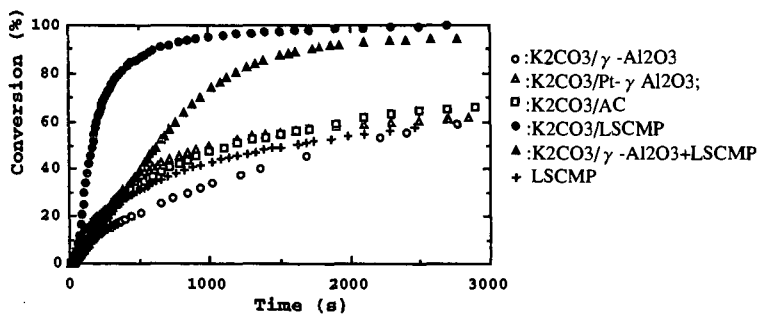
Fig.1 Conversion of carbon catalyzed by supported potassium carbonate

o :K_2CO_3/γ -Al_2O_3
■ :KCl/γ -Al_2O_3
▲ K_2SO_4/γ -Al_2O_3
● :K_2CO_3/γ -Al_2O_3+LSCMP
■ :KCl/γ -Al_2O_3+LSCMP
▲ :K_2SO_4/γ -Al_2O_3+LSCMP
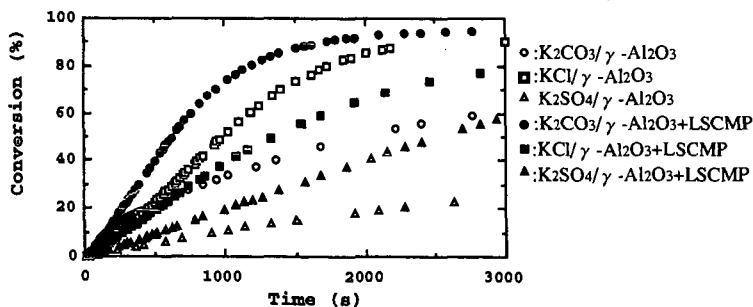
Fig.2 The activity of potassium salts supported on γ -Al_2O_3
blended with or without LSCMP
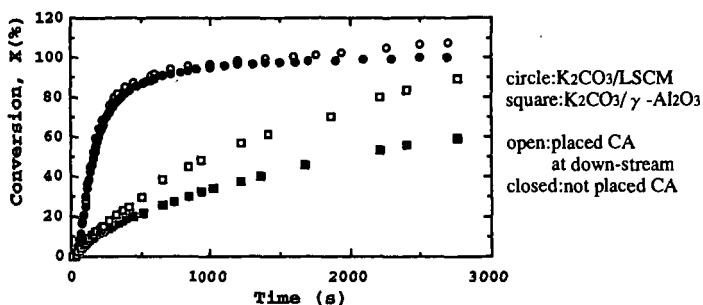
Fig.3 The combersion of carbon placed at down-stream
of carbon/supported potassium carbonate bed
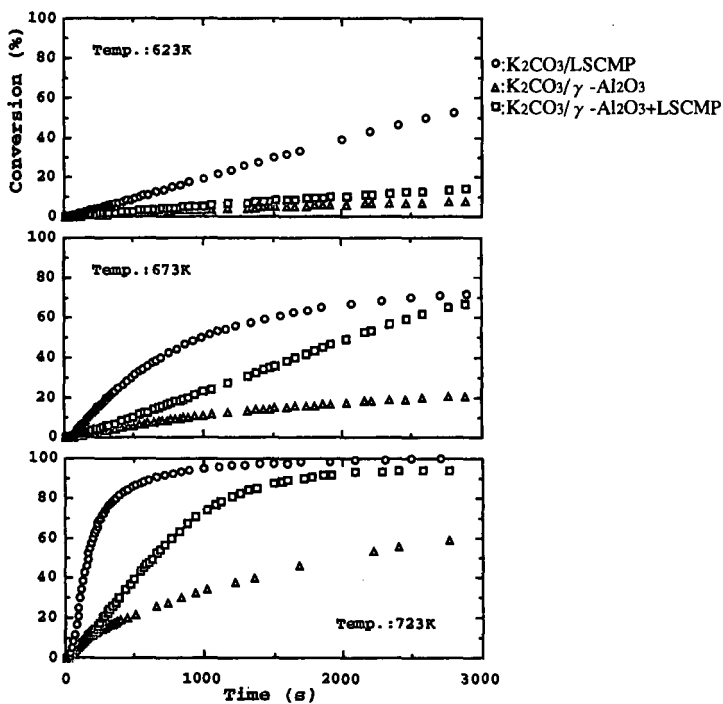
Fig.4 The activity of supported K2CO3 catalysts at some temperatures

DRIFT ANALYSIS OF SURFACE OXYGEN COMPLEXES ON SOOT FORMED BY METAL OXIDES

G. Mul, F. Kapteijn and J.A. Moulijn

Delft University of Technology, Section Industrial Catalysis,
Julianalaan 136, 2628 BL Delft, The Netherlands.

INTRODUCTION

At the Delft University of Technology a project concerning the catalytic removal of soot from diesel exhaust gases is being carried out. We are interested in a catalyst for the oxidation of soot particulates because: *(i)* diesel engines can no longer meet the requirements of the particulate (soot) emission standards, and *(ii)* collection of soot in a monolithic filter and simultaneous oxidation at diesel exhaust gas temperatures (600 K) is considered to be the best option to abate the emission of soot.

The mechanism of catalytic oxidation reactions of carbonaceous materials has been the subject of many researchers over the last decades. Although it has been generally exepted that Surface Oxygen Complexes (S.O.C.) play an essential role in these reactions, their chemical nature, and interaction with catalysts and the oxidant (CO_2, H_2O or O_2) have hardly been reported. A powerful tool in analyzing carbonaceous materials is Fourier Transformed Infrared spectroscopy and in particular Diffuse Reflectance Infrared Fourier Transformed (DRIFT) spectroscopy. Several research groups have analyzed coal of several ranks using this technique *e.g.* (*1-3*). Also *in situ* studies regarding the oxidation of coal have been performed (*4-6*), as well as DRIFT studies on oxidized soot (*7,8*) and PF chars (*9*). Very few reseachers have used DRIFT spectroscopy to analyze the catalytic oxidation of carbon or soot. Cerfontain has studied the alkali carbonate catalyzed carbon oxidation by CO_2 by means of FT-IR (*10*), but carbon oxidation involving O_2 and (transition) metal oxides have only been reported by us (*11*). It has been shown that during burn-off certain metal oxides enhance the amount of S.O.C. on the soot surface, while others do not. This observation has been explained by two different reaction mechanisms: *(i)* a redox mechanism and *(ii)* a spill-over mechanism (*11*). However, these results were obtained with catalyst/soot mixtures with a high catalyst to soot ratio (1:1, *i.e.* 50 wt%). In this paper DRIFT analyses of partially converted soot by impregnated Fe-, Co-, Cr-, K-, and Ca- oxides (10 wt%) are presented, which validates a comparison of these analyses with literature data on catalyzed carbon and coal gasification.

EXPERIMENTAL

Printex-U (a model soot, purchased from Degussa) was used to perform the oxidation studies. This soot has a BET surface area of 96.0 m^2g^{-1} and contains approximately 5 wt% of adsorbed hydrocarbons and only 0.2-0.4 wt% sulfur (*12*).

Analytical grades of the (transition) metal nitrates were used to impregnate the soot. An amount of the nitrate, corresponding with 10 wt% of the most stable oxide (Fe_2O_3, Co_3O_4, Cr_2O_3, K_2O, and CaO) was dissolved in 200 ml ethanol, followed by addition of 200 mg soot to the solution. The ethanol was removed at 325 K under reduced pressure in a rotating evaporator. The black powder could be recovered by scratching it from the glass wall of the flask with a spatula.

Partial conversion of the soot was accomplished in a so-called six-flow reactor. A six-flow experiment was carried out by packing five quartz reactors (one reactor was used as a blank) with approximately 25 mg of the impregnated soot/metal nitrate mixture, sandwiched between two layers of SiC. A controlled flow of 150 ml/min. 10 vol% O_2 in Ar was led through the reactors. A non dispersive infrared detector (Hartmann & Braun Uras 10 E) was used to measure CO, CO_2 and NO concentrations. These concentrations were measured alternately every 90 seconds in each reactor. A multiposition valve (Valco) selected the reactor for analysis. The partial conversions were obtained isothermally @ 575 K (K, Co) and @ 585 K (Ca, Fe, Cr). The final temperature was reached with a ramp of 5 K/min. The amount of soot converted was determined by integrating the CO and CO_2 concentrations with time. After reaction SiC was separated from the soot sample before analysis.

DRIFT spectra were recorded on a Nicolet Magna 550 spectrometer equipped with a DTGS detector and a Spectratech DRIFT accessory. KBr was used as a diluent. Spectra are displayed in 8 cm^{-1} resolution in absorbance reflectance mode against a (*non*-converted) soot in KBr background.

RESULTS & DISCUSSION

Transition metal nitrates

A typical result of the analysis of one reactor in a sixflow measurement is shown in figure 1. The variations in the CO, CO_2 and NO concentrations as a function of time are given for the $Fe(NO_3)_3$/soot sample. Decomposition of $Fe(NO_3)_3$ into N_2O, NO and NO_2 (the concentrations of N_2O and NO_2 were not determined) occurs at approximately 450 K. As NO_2 is a strong oxidant, reaction of NO_2 with soot results in NO, CO and CO_2 formation (13). The reaction of NO_2 with soot is reflected by high NO, CO and CO_2 concentrations in the first 6 ks of the reaction, when the temperature is still increasing with time. After the temperature has become constant @ 585 K (the temperature was isotherm between the verticle dashed lines), the CO and CO_2 concentrations decrease exponentially with time. A similar trend was obtained for the $Co(NO_3)_2$/soot sample @ 575 K (not shown). By integration of the CO and CO_2 concentrations, soot conversion was calculated to be 20% for the $Fe(NO_3)_3$/soot, and 50% for the $Co(NO_3)_2$/soot mixture respectively.

Variations in the CO, CO_2 and NO concentrations @ 585 K for the impregnated $Cr(NO_3)_3$/soot mixture are shown in figure 2. Similar to the $Fe(NO_3)_3$ measurement, a rapid decomposition of the nitrate into (presumably) Cr_2O_3 can be observed at 400 K, accompanied by high NO, CO and CO_2 concentrations. In the isothermal part, the development of the CO and CO_2 concentrations is quite different from the $Fe(NO_3)_3$ sample. Instead of a decay, a slow increase in the CO and CO_2 concentrations can be observed. A similar result has been obtained for a mechanical mixture of Cr_2O_3 and soot (14). The soot conversion was calculated to be 50%. Another six-flow experiment was performed upto a conversion level of 20%.

The DRIFT spectra of the partially converted $Fe(NO_3)_3$/soot (20% (A)), $Co(NO_3)_2$/soot (50% (B)) and $Cr(NO_3)_3$/soot (20% (C) and 50% (D)) samples are shown in figure 3. Infrared absorptions which are typical for compounds containing (hydrated) nitrato groups (1560-1540, 1020-1070, 800 and 760 cm^{-1}) (15) are not present in the spectra. The absorptions located @ 665 and 578 cm^{-1} (spectrum B) can be ascribed to the spinel vibrations of Co_3O_4. The broad absorption band @ 549 cm^{-1} is ascribed to Cr_2O_3 (spectra C and D). Hence, confirming the six-flow analysis, the transition metal nitrates were completely converted into their oxides. Generally three types of Surface Oxygen Complexes (S.O.C.) can be identified with DRIFT on soot (or carbon) surfaces: (i) ethers (1250-1275 cm^{-1}), (ii) quinones (1600-1620 cm^{-1}), and (iii) lactones (1730-1740 cm^{-1}) (9). On the surface of the partially converted soot by $Cr(NO_3)_3$ (Cr_2O_3) large quantities of these S.O.C. were formed. The spectra of the Fe_2O_3 and Co_3O_4 samples show approximately the same amount of S.O.C. as were formed non-catalytically on soot under similar conditions. These results are in agreement with the results obtained for mechanical mixtures of Cr_2O_3, Fe_2O_3 and Co_3O_4 with soot (11).

Potassium nitrate

The activity in the soot oxidation of KNO_3 is shown in figure 4. KNO_3 decomposition is not as fast as the decomposition of the transition metal nitrates. Moreover, the maxima in the CO and CO_2 concentrations do not coincide with the maximum in the NO concentration. Apparently the peculiar "peaks" in the CO and CO_2 concentrations are not entirely explained by the NO_2/soot reaction. After the "peaks", the CO and CO_2 concentrations decay linearly in time. The calculated conversion was 75%.

DRIFT spectra of KNO_3/soot samples at conversion levels of 0% (A), 50% (B), 75% (C), and >90% (D) are shown in figure 5. Spectrum A corresponds quite well with the spectrum of pure KNO_3 (the 1383 cm^{-1} vibration can be assigned to a nitrato vibration (15)). After 50% soot conversion, the 1383 cm^{-1} vibration is no longer present. Hence, the nitrate has decomposed. Although ether-like species are not so clearly present (@ 1250-1300 cm^{-1}), the absorptions located @ 1721 cm^{-1} and 1595 cm^{-1} indicate that (a) potassium oxide catalyzes the formation of S.O.C. These absorptions are increasing with the conversion level, and shifted to somewhat lower wavenumbers, compared to the spectra shown in figure 3. This might indicate that a potassium oxide is in the vicinity of the S.O.C.

Carbonate formation is witnessed by broad absorption bands @ 1456 cm^{-1} and 871 cm^{-1} (15,22), which are clearly present in the spectrum of the sample converted to >90% (spectrum D). Other absorption bands, @ 1118 cm^{-1} and 620 cm^{-1}, are increasing with conversion. Also impregnated Rb and Cs oxides cause the formation of these absorptions during burn off. We are still speculating on the nature of the (potassium) compound responsable for these absorptions. The assignment of these bands to potassium sulfate, which has vibrations in the 1100-1200 cm^{-1} region, is not likely, because the amount of sulfur initially present in the soot (Printex-U) is low and the sulfate-ion has a more complex IR pattern than shown in figure 5 (15). The 1118 cm^{-1} band has been observed by other authors in the K_2CO_3 catalyzed carbon gasification with CO_2 (10) and steam (16). Cerfontain (10) and Freriks (16) did not detect the 620 cm^{-1} band, because they did not record their spectra below 1000 cm^{-1}. In our opinion this absorption is related to the 1118 cm^{-1} one. The 1118 cm^{-1} band has been assigned to a potassium phenolate (10). However,

the carbon-oxygen vibration of potassium phenolate (or phenoxide) occurs at much higher wavenumbers (around 1300 cm^{-1} (17), verified by ourselves). The mass difference of a phenoxide and a poly-aromatoxide ion can only partly account for a red shift of 150 cm^{-1}. Unless the frequency of C-OK vibrations is strongly influenced by the vicinity of other C-OK groups (e.g. in the compound proposed by Freriks (16)) or other oxygenated species, the assignment of the 1118 cm^{-1} vibration to phenolate species is not very likely. A second proposition for the assignment of the 1118 cm^{-1} band is based on the following: the structure of alkali metal catalysts under gasification conditions is thought to be a potassium oxide (K$_2$O) cluster attached to the carbon surface (18). It has been shown that CO$_2$ adsorption on the potassium oxide cluster is very strong (18,19). Therefore, the 1118 and 620 cm^{-1} absorptions might be the result of CO$_2$ (formed during soot oxidation) strongly interacting with a potassium oxide cluster. Interestingly, similar absorptions have been reported in studies on CO$_2$ adsorption on Cu$_2$O (20) and CuO (21).

Calcium nitrate

Decomposition of calcium nitrate is less rapid than decomposition of the transition metal nitrates (figure 6). Although some NO (and CO and CO$_2$) production takes place during the temperature ramp, a considerable amount of nitrate decomposes in the isothermal stage. For some reason, the decomposition rate increases with time. The NO, CO and CO$_2$ concentrations run parallel, indicating that the primary product of nitrate decomposition is NO$_2$, which subsequently oxidizes the soot, resulting in the observed products. After complete decomposition of Ca(NO$_3$)$_2$, a second increase in reaction rate can be observed. The measurement shown in figure 6 resulted in 50% soot conversion.

DRIFT spectra of Ca(NO$_3$)$_2$.4H$_2$O/soot samples (0% (A), 20% (B), 50% (C) and >90% (D) soot conversion) are shown in figure 7. After preparation several absorptions occur in the 500-2000 cm^{-1} region of the spectrum, due to nitrate vibrations (@ 1384, 1046 and 838 cm^{-1}). The absorption band @ 1635 cm^{-1} can be ascribed to the O-H bending mode of water of crystallization in Ca(NO$_3$)$_2$.4H$_2$O (23). The broad band located @ 1433 cm^{-1} is also present in the DRIFT spectrum of pure Ca(NO$_3$)$_2$.4H$_2$O. After 20% soot conversion @ 575 K, the nitrato vibrations are still present, which is in agreement with six-flow data. The 1433 cm^{-1} band has broadened and a new vibration, located at approximately 1579 cm^{-1}, can be observed. At higher conversions (spectra C and D) the vibrations due to the nitrato group have disappeared and are replaced by the vibrations ascribed to the carbonato group (CaCO$_3$ (14,23,24)) @ 712 cm^{-1}, 875 cm^{-1}, centred @ 1436 cm^{-1}, and 1795 cm^{-1}). The 1579 cm^{-1} band has shifted somewhat to 1587 cm^{-1}. Also a broad absorption band starts to develop @ 1142 cm^{-1}. This band is clearly visible in the spectrum of the >90% soot conversion. In the latter spectrum, the 1587 cm^{-1} vibration is no longer present.

Absorptions due to regular lactone, quinone and ether like complexes are hardly visible. However, the 1587 cm^{-1} absorption is related to the presence of soot, because this absorption frequency is not visible after 90% soot conversion. Probably this band is due to quinone species. The shift of approximately 20 cm^{-1} might be caused by some kind of interaction with a Ca-ion. The broad 1142 cm^{-1} absorption might be related to the 1118 cm^{-1} absorption band observed in the KNO$_3$/soot spectra.

Mechanistic considerations

The investigated metal nitrate precursors show an increasing reactivity in the order K > Co > Cr > Fe = Ca. The activities of the impregnated samples are higher than the activities found for the mechanical mixtures of the metal oxides and soot (11). Especially the activity of the impregnated chromium nitrate is much higher than the activity of bulk Cr$_2$O$_3$. The differences in reactivity might be explained by a better dispersion of the oxides formed after decomposition of the impregnated nitrates. X-Ray Diffraction and Transmission Electron Microscopy studies are currently being performed to determine the particle size of the various impregnated nitrates and oxides.

The DRIFT spectra shown in this paper indicate that the formation of S.O.C. is dependent on the catalyst used. In the presence of K, Ca and Cr catalysts, S.O.C. are catalytically formed. The differences in CO and CO$_2$ concentration profiles shown in figures 1,2,4 and 6, are very likely related to this formation of S.O.C. Catalysts which do not enhance the formation of S.O.C., show an exponential decay, while catalysts which increase the amount of S.O.C. show a less pronounced activity loss (K), or even an activity increase (Cr, Ca). The differences in reactivity profiles is discussed in more detail elsewhere (14).

A redox cycle is often proposed as the most likely mechanism by which metal oxides operate in the oxidation of carbon (e.g. (25,26)). Other authors mention spill-over of oxygen to explain catalytic carbon oxidation. Baker et al. (27) argued, explaining their Controlled Atmosphere Electron Microscopy (CAEM) studies, that Cr$_2$O$_3$ was able to dissociate molecular oxygen and to transfer the activated oxygen to the carbon surface. Eventually, reaction occurred

at the graphite edges. This might indicate that the enhanced formation of S.O.C. is related with oxygen spill-over.

Oxygen spill-over has never been proposed for alkali metal carbon gasification reations (28-31). However, the mechanism proposed by Meijer and Moulijn (21) involves the transfer of oxygen from a K-oxide cluster to an active carbon site, which could be interpreted as spill-over. Reaction of this transferred oxygen results in the formation of S.O.C. Kapteijn et al. (32), discussing a transient isotopic CO_2 gasification study, describe several kinds of S.O.C., which they indicate as $C(O)C_f(O)$ (lactone) and $C_f(O)$ (semi-quinone). The DRIFT spectra presented in this paper show, in agreement with the literature data, that upon carbon (soot) oxidation several S.O.C. are formed, probably in the vicinity of a potassium oxide cluster.

The spill-over effect was also mentioned by Kyotani and Tomita et al. in relation with Ca catalyzed graphite oxidation (33-36). Although Martin and Kyotani et al., using SIMS and TPD, did not reveal the nature of the S.O.C. formed after Ca catalyzed oxidation (35), they indicated that the distribution of the S.O.C. corresponded to the distribution of the Ca catalyst. This is in agreement with the fact that we observe a shift of the 1605 cm^{-1} quinone band to lower wavenumbers, which could be induced by the presence of Ca ions. The fact that we were unable to detect lactone species (or C(O.O) (33)), formed by reaction of a C(O) complexes with an activated oxygen atom, might be due to a very fast, Ca induced, desorption of those complexes (as CO_2). The nature and role of the species absorbing @1142 cm^{-1}, is not clear at this moment.

Evaluating the presented DRIFT spectra and literature mentioned, we believe that the catalytic formation of S.O.C. must be related to some kind of oxygen spill-over mechanism. The intensity and frequency of the absorptions of the S.O.C. might be indicative for the stability and the vicinity of a metal oxide. Catalysts which do not enhance the amount of S.O.C. are thought to be active according to a redox-mechanism (11,14).

CONCLUSIONS
- The transition metal nitrates decompose in air at approximately 450 K. DRIFT analysis revealed that metal oxides are formed upon decomposition.
- The results of the DRIFT analyses of impregnated samples are in agreement with the results presented earlier (11) for mechanically mixed soot/transition metal oxide mixtures. Cr_2O_3 causes an enhancement of the amount of S.O.C. (compared to non-catalytic oxidation), whereas Co_3O_4 and Fe_2O_3 do not.
- Alkali metal nitrates are less easily converted into their corresponding oxides. After decomposition an alkalimetal oxide attached to the carbon surface is being formed. The exact nature of this compound remains to be illucidated.
- Alkali metal oxides enhance the amount of S.O.C. The IR absorption band of the quinone species is shifted from 1605 cm^{-1} to 1585 cm^{-1}. Also the lactone vibration (1735 cm^{-1}) is shifted to lower wavenumbers, indicating the vicinity of a potassium ion.
- $Ca(NO_3)_2$ is the most stable of the nitrates investigated, and decomposes into $CaCO_3$ upon soot oxidation. Also an "alkali metal like" complex on the soot surface is eventually being formed. $CaCO_3$ probably generates quinone species, whereas lactones are not formed.
- The catalytic formation of S.O.C. by Cr, K, and Ca, as shown by the DRIFT spectra presented in this paper, is tentatively explained by "spill-over" of activated oxygen. This is in reasonable agreement with data reported in the literature.

REFERENCES
1.   Smyrl, N.R. and Fuller, E.L. Appl. Spectrosc. 41, 1023 (1987).
2.   Fuller, E.L. and Smyrl, N.R. Appl. Spectrosc. 44, 451 (1990).
3.   Meldrum, B.J. and Rochester, C.H. J.Chem.Soc.Faraday Trans. 86, 1881 (1990).
4.   Meldrum, B.J. and Rochester, C.H. J.Chem.Soc.Faraday Trans. 86, 2997 (1990).
5.   Rochester, C.H. and Meldrum, B.J. J.Chem.Soc.Faraday Trans. 86, 861 (1990).
6.   Meldrum, B.J., Orr, J.C., and Rochester, C.H. J.Chem.Soc.Chem.Commun. 1176 (1985).
7.   Jassim, J.A., Lu, H.P., Chughtai, A.R., and Smith, D.M. Appl.Spectrosc. 40, 113 (1986).
8.   Akhter, M.S., Chughtai, A.R., and Smith, D.M. Appl.Spectrosc. 45, 653 (1991).
9.   Zhuang, Q.-L., Kyotani, T., and Tomita, A. Energy & Fuels 714 (1994).
10.   Cerfontain, M.B., Moulijn, J.A. Fuel 62, 256 (1983).
11.   Mul, G., Kapteijn, F., and Moulijn, J.A. Proc. 22nd Biennal Conf. on Carbon, San Diego 554 (1995).
12.   Neeft, J.P.A., "Catalytic oxidation of soot-Potential for reduction of diesel particulate emissions", PhD Thesis, TU Delft, p. 71 (1995).
13.   Cooper, B.J. and Thoss, J.E. SAE Paper 890404, 171 (1989).
14.   Neeft, J.P.A., "Catalytic oxidation of soot-Potential for reduction of diesel particulate emissions", PhD Thesis, TU Delft, p. 165 (1995).
15.   Ross, S.D. "Inorganic Infrared and Raman Spectra" McGraw-Hill Book Company, London, 1972.

16. Freriks, I.L.C. *Fuel* **60,** 463 (1981).
17. Davies, M. and Jones, R.L. *J. Chem. Soc.* **42,** 121 (1954).
18. Moulijn, J.A. and Kapteijn, F. *Carbon* **33,** 1155 (1995).
19. Meijer, R., van der Linden, B., Kapteijn, F., and Moulijn, J.A. *Fuel* **70,** 205 (1991).
20. Busca, G. *J. Mol. Catal.* **43,** 225 (1987).
21. Davydov, A.A. and Budneva, A.A. *React. Kinet. Catal. Lett.* **25,** 121 (1984).
22. Schutte, C.J.H. and Buijs, K. *Spectrochim. Acta* **17,** 921 (1961).
23. Nyquist, R.A. and Kagel, R.O. "Infrared Spectra of Inorganic Compounds" Academic Press, New York, 1971.
24. Sterzel, W. and Chorinsky, E. *Spectrochim.Acta* **24A,** 353 (1968).
25. McKee, D.W. *Fuel* **62,** 170 (1983).
26. McKee, D.W. *J. Catal.* **108,** 480 (1987).
27. Baker, R.T.K. and Chludzinski, J.J. *Carbon* **19,** 75 (1981).
28. Yuh, J.Y. and Wolf, E.E. *Fuel* **62,** 252 (1981).
29. Mims, C.A. and Rose, K.D. *J.Am.Chem.Soc.* **104,** 6886 (1982).
30. Silva, I.F. and Lobo, L.S. *Fuel* **65,** 1400 (1986).
31. Meijer, R., Kapteijn, F., and Moulijn, J.A. *Fuel* **73,** 723 (1994).
32. Kapteijn, F., Meijer, R., Moulijn, J.A., and Cazorla-Amoros, D. *Carbon* **32,** 1223 (1994).
33. Kyotani, T., Hayashi, S., and Tomita, A. *Energy and Fuels* **5,** 683 (1991).
34. Kyotani, T., Hayashi, S., Tomita, A., MacPhee, J.A., and Martin, R.R. *Fuel* **71,** 655 (1991).
35. Martin, R.R., MacPhee, J.A., Kyotani, T., Hayashi, S., and Tomita, A. *Carbon* **29,** 475 (1991).
36. Martin, R.R., MacPhee, J.A., Kyotani, T., Hayashi, S., and Tomita, A. *Proc. 20th Biennal Conf. on Carbon, Santa Barbara,* 490 (1991).

ACKNOWLEDGEMENT
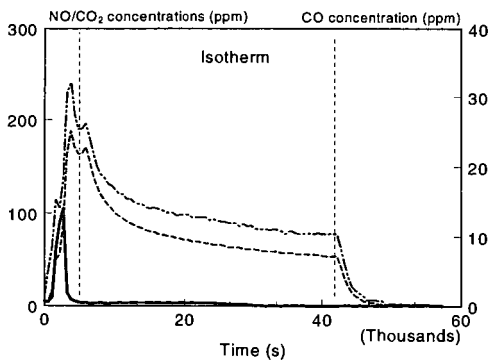
Figure 1. Fe(NO₃)₃ catalyzed soot oxidation. Development of NO (solid), CO_2 (dash) and CO (alternating dash) concentrations in time.
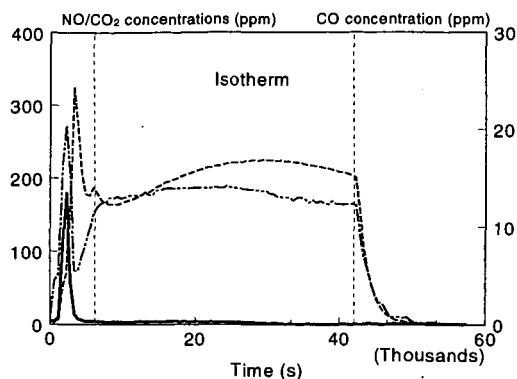
Figure 2. Cr(NO$_3$)$_3$ catalyzed soot oxidation. Development of NO (solid), CO$_2$ (dash) and CO (alternating dash) concentrations in time.
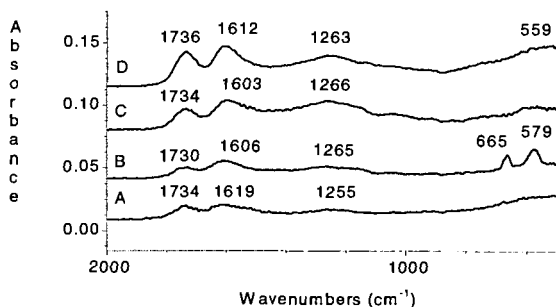
Figure 3. DRIFT spectra of partial converted soot by transition metal oxides: **A.** Fe$_2$O$_3$-20%, **B.** Co$_3$O$_4$-50%, **C.** Cr$_2$O$_3$-20%, **D.** Cr$_2$O$_3$-50%.
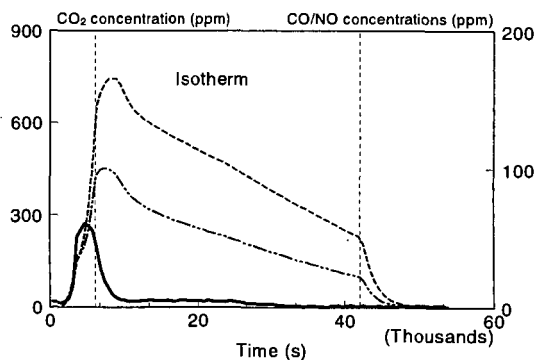
Figure 4. KNO$_3$ catalyzed soot oxidation. Development of NO (solid), CO$_2$ (dash) and CO (alternating dash) concentrations in time.

235
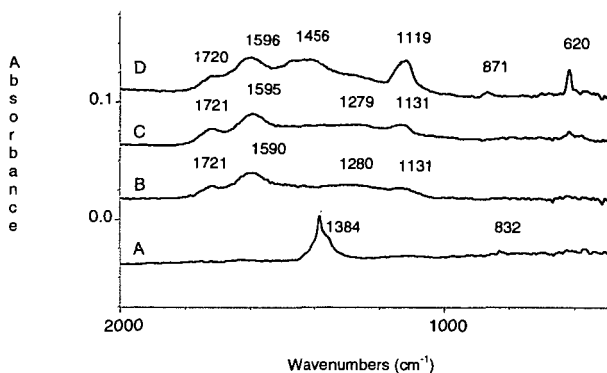
Figure 5.   DRIFT spectra of partial converted KNO_3 impregnated soot :
A. 0%, B. 50%, C. 75%, D. >90%
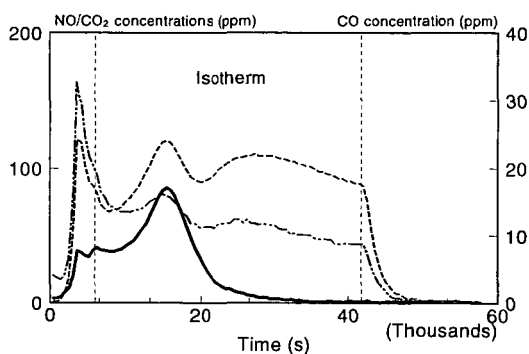
Figure 6. $Ca(NO_3)_3$ catalyzed soot oxidation. Development of NO (solid), CO_2 (dash) and CO (alternating dash) concentrations in time.
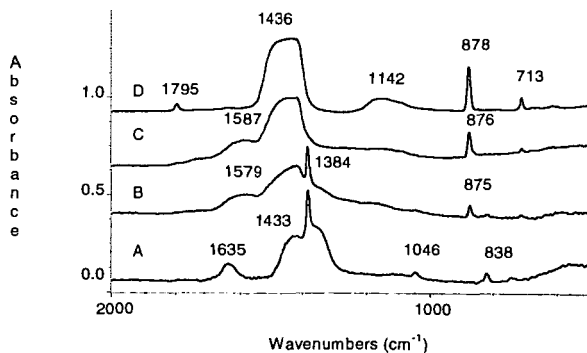
Figure 7.   DRIFT spectra of partial converted $Ca(NO_3)_2$ impregnated soot :
A. 0%, B. 20%, C. 50%, D. >90%

STEAM GASIFICATION OF COAL — THE EFFECTS OF ACID- AND ALKALI-LEACHING OF COAL ON ITS GASIFICATION RATE —

Satoru Murata, Akira Murakami, and Masakatsu Nomura
Department of Applied Chemistry, Faculty of Engineering, Osaka University
2-1 Yamada-oka, Suita, Osaka 565, Japan

INTRODUCTION

The conversion reaction of coal to synthesis gas ($CO + H_2$) is one of the most significant coal utilization processes because a wide range of coals could be applied in this process and the resulting gases are available as valuable feedstocks of chemical industry. One of the drawbacks of coal gasification is the presence of inorganic materials in coal, which cause fouling or slugging phenomena by producing scale during the gasification. Consequently, "deashing of coal" is a technically very important pretreatment for gasification. In this study we conducted acid- (HF or HNO_3) and alkali-leaching of five coals, Australian Yallourn (YL), Indonesian South Banko (SB), US Illinois NO. 6 (IL), Japanese Akabira (AK), and Australian Newstan coals (NS), the treated coals of which were submitted to steam gasification.

EXPERIMENTAL SECTION

Coal Samples

Illinois No. 6 coal was purchased from Argonne national laboratory. Newstan original and alkali-leached coals were presented by CSIRO. Other coals were our samples and stored in a glass vessel, respectively, under nitrogen atmosphere. Reagents and solvents were commercially available and used without further purification.

Leaching of coal with HNO_3

Pulverized coal (100 mesh under, 1.5 g) and 1N HNO_3 (300 mL) were stirred magnetically in a 1 L flask at 130 °C for 3 h. The products were poured into a 2 L beaker containing 100 g of ice. The resulting mixture was filtered, the filter cake being washed with water until the filtrate became neutral.

Leaching of coal with HF

A platinum crucible containing pulverized coal (100 mesh under, 2.5 g) and 46% HF (5 mL) was heated on an oil bath (90 °C) for 7 h. After the end of reaction, the resulting mixture was filtered and washed with deionized water.

Gasification reaction

Coal (*ca.* 10 mg, daf base) was put on a platinum cell in the heating zone of TG apparatus (Shimadzu TF-50H), being heated from room temperature to 900 °C at a heating rate of 50 K/min. Then, steam was introduced to the system at 900 °C, being kept for about 2 h. The resulting gases were analyzed by a Shimadzu GC-8A gas chromatograph (Polarpack Q column, 6mm diameter x 3m long) connected to the TG apparatus. Using the same apparatus, pyrolytic experiments were conducted for the original and treated coals (heating from room temperature to 900 °C, 5 K/min).

Heat treatment of the sample coals

The sample coals (1 g) were heated up to 900 °C with a heating rate of 30 K/min under a nitrogen stream (100 mL/min) by using an Isuzu DKRO-14K type tubular electric furnace. The resulting semicokes were submitted to specific surface area-measurement. Their specific surface area was measured by using argon adsorption method on a Shimadzu 2205 type analyzer.

RESULTS AND DISCUSSION

Deashing of the sample coals

In order to remove inorganic materials (IOM) in coal, five coals were treated by HF or HNO3, the results being shown in Figure 1. Treatment of coal with HF resulted in removal of IOM in 36-96%, while HNO_3 treatment resulted in 33-46% removal. It should be noted that HNO_3 treatment could remove sulfur in these coals, especially, in the case of IL coal known as a high-sulfur coal, where 67% of sulfur could be removed. Huffman *et al.* had reported that sulfur in IL coal composed of 37% of inorganic form (mainly pyrite) and 63% of organic form (thiophenic and sulfidic).[1] The result indicates that HNO_3-treatment could remove organic sulfur in the coal.

As to nitrogen and oxygen, N/C and O/C atomic ratios were increased by treatment with HNO_3. FT/IR spectra of the original and treated coals revealed that nitration of aromatic rings and oxidation of alkyl side chains to carboxylic groups occurred to some extent during the treatment.

237

Steam gasification of the original and treated coals

The original and treated coals were submitted to steam gasification. The reaction was conducted at 900 °C under steam flow (75.7 mmHg). Figure 1 shows a time profile for conversion of char. The order of gasification rate obeyed the following sequence: YL > SB > IL > NS > AK, this indicating that lower rank coals have higher reactivity than higher rank ones. These results agree well with the results reported by Hashimoto et al.[2] and Tamai et al.[3] In the case of the lower rank coals (YL and SB), HF-treatment lead to decrease their reactivity, on the other hand, HF-treatment of the higher rank coals (IL, AK, and NS) resulted in the increase of their reactivity (Figure 2). YL and SB coals contain CaO and Fe_2O_3, these are known to act as gasification catalysts. This might suggest that HF-leaching remove these catalyst species. As to HNO_3-leaching of coal, this pretreatment could improve their reactivity to a small extent (in the case of IL, AK, and NS coals). The NaOH soaked NS coal (provided by CSIRO) was found to have higher reactivity than that of the HF- or HNO_3-leached coals.

Catalytic gasification of the original and treated coals

Catalytic gasification of the sample coals was conducted. Potassium carbonate (3 wt%) was impregnated from its aqueous solution. The results of catalytic gasification are shown in Figure 3. The catalyst increased the rate of gasification as 2-4 times. In the all coals employed, HF treated coals showed higher reactivity than those of the original coals. These are different from the results of non-catalytic reaction of the lower rank coals (YL and SB).

Pyrolytic behavior of the sample coals

In order to examine the pyrolytic behavior of the sample coals, their TG/GC analyses (sample ca. 10 mg) were conducted (heating from room temperature to 900 °C at 5 K/min). TG curves are shown in Figure 4, the order of the rate of devolatilization obeying the following sequence; NS < IL < AK < SB < YL. Figure 4 also shows the time profiles for gas evolution (CO_2 and CH_4). The peak of the evolution of CO_2 was observed at 400 °C for SB and YL coals and at 700 °C for all coals, the former peak corresponding decarboxylation. On the other hand, the peak of CH_4 evolution was observed at around 600 °C. The order of its rate obeyed the following sequence; YL < SB < IL < NS < AK, this corresponding the reversed sequence for the gasification rate. Solomon et al. had stated that lighter hydrocarbon gas evolution during pyrolysis results in formation of crosslinking.[4] The reaction described in the following equation might occur and this might cause deactivation of char.

$$ArH + Ar'CH_2R \rightarrow Ar\text{-}CH_2\text{-}Ar' + RH$$
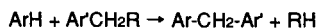
Specific surface area (SA) of pyrolytic residues from the sample coals was measured. SA was increased according to the sequence; IL (160 m^2/g) < AK (235) < NS (275) < SB (713) < YL (870). This order does not agree with rank (carbon contents) or gasification rate of the sample coals. The lower rank coals have relatively larger SA value, this being resulted from decarboxylation reaction at around 400-500 °C.

Now, we are conducting TG/GC analyses of the acid- or alkali-leached coals and investigating a relationship between their pyrolytic behavior and reactivity.

SUMMARY

In this study, we examined the effects of acid- or alkali-leaching of five coals (from brown to bituminous coal range) on the rate of catalytic and non-catalytic steam gasification. The results obtained were summarized bellow.

1) HF- and NaOH-leaching of coal could remove 60-90 % of inorganic materials in it. In the case of HNO_3-leaching, degree of deashing was somewhat small, but this treatment could remove both inorganic and a part of organic sulfur.

2) Acid- and Alkali-leaching of coal could enhance the rate of non-catalytic and catalytic steam gasification to some extent.

3) TG/GC analyses of the sample coals showed the presence of some relationships between reactivity of char and amount of CH_4-evolution during pyrolysis (related to formation of cross-linking).

REFERENCES

1) Taghiei, M. M.; Huggins, F. E.; Shah, N.; Huffman, G. P. Energy Fuels 1992, 6, 293.
2) Hahimoto, K.; Miura, K.; Ueda, T. Fuel, 1986, 65, 1516.
3) Takarada, T.; Tamai, Y.; Tomita, A. Fuel, 1985, 64, 1438.
4) Solomon, P. R.; Fletcher, T. H.; Pugmire, R. J. Fuel 1993, 72, 587.

Table 1. Elemental analyses and ash contents of the original and treated coals

Samples	Atomic ratio			Ash (Wt%)	Degree of deashing (%)
	O/C	N/C	S/C		
NS coal					
Original	0.079	0.022	0.003	9.2	-
HNO$_3$-leached	0.295	0.064	0.002	6.3	33.4
NaOH-leached	0.087	0.022	0.004	0.6	93.9
HF-leached	0.102	0.021	0.003	0.4	96.4
AK coal					
Original	0.090	0.023	0.008	8.0	-
HNO$_3$-leached	0.280	0.060	0.006	4.5	46.1
HF-leached	0.101	0.023	0.008	2.7	68.8
IL coal					
Original	0.103	0.016	0.030	16.0	-
HNO$_3$-leached	0.364	0.065	0.010	8.6	50.8
HF-leached	0.150	0.016	0.025	4.7	74.3
SB coal					
Original	0.269	0.017	0.002	2.4	-
HF-leached	0.275	0.015	0.002	1.1	54.4
YL coal					
Original	0.310	0.006	0.001	1.6	-
HF-leached	0.360	0.009	0.001	1.0	36.4

Table 2. Composition of inorganic materials in the sample coals

Coals	Na$_2$O	MgO	Al$_2$O$_3$	SiO$_2$	CaO	Fe$_2$O$_3$
NS coal	0.7	0.8	25.7	62.4	1.9	5.1
AK coal	1.6	2.0	26.1	55.2	2.2	6.7
IL coal	0.9	0.7	19.4	35.4	10.0	27.3
SB coal	1.3	2.1	20.0	12.8	16.6	11.5
YL coal	6.0	19.5	1.4	12.6	14.4	33.6
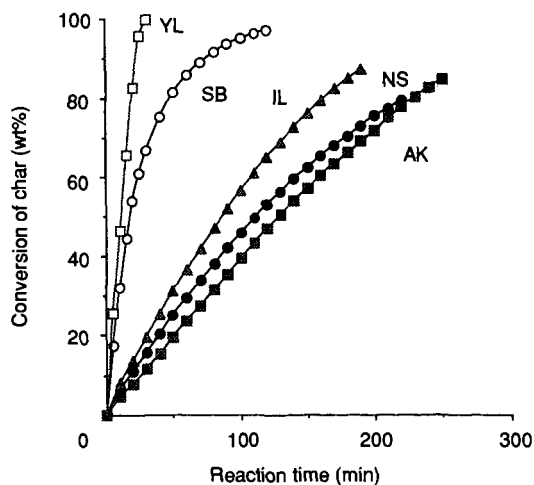
Figure 1. Time profile of steam gasification of sample coals
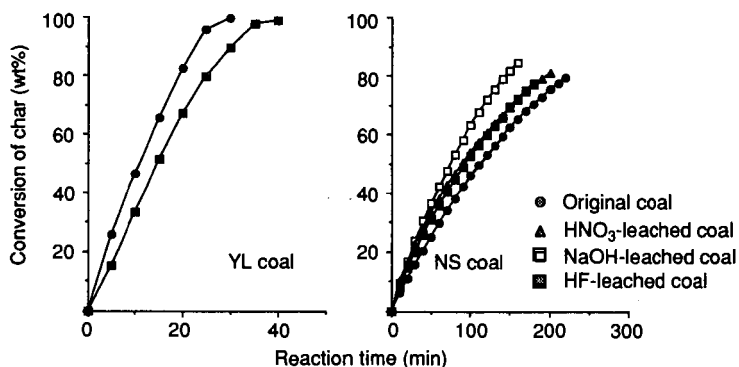
Figure 2. Steam gasification of the original and treated coals
Catalyst K_2CO_3 3wt%, 1173 K, steam flow
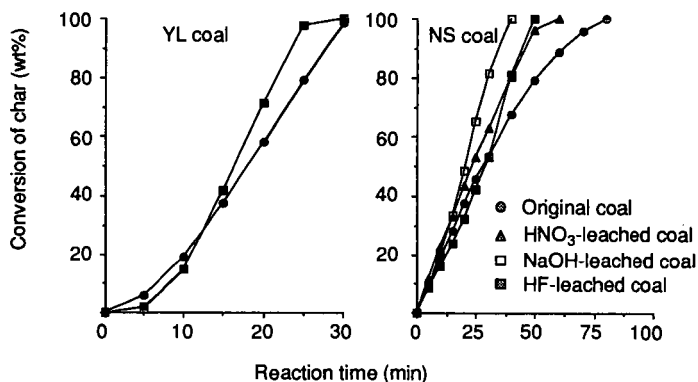
Figure 3. Catalytic gasification of the original and treated coals
Catalyst K_2CO_3 3wt%, 1173 K, steam flow
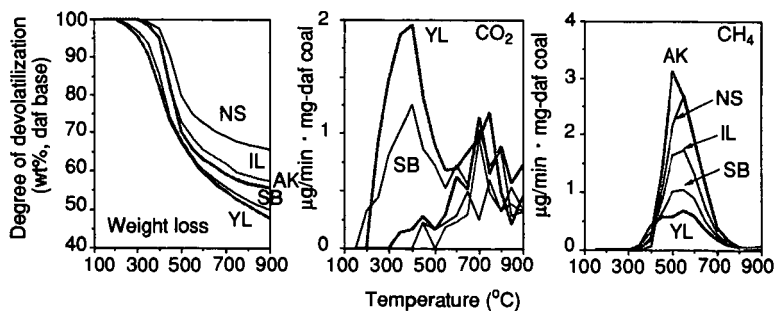
Figure 4. TG/GC analyses of the sample coals

PRODUCTION OF ACTIVATED CARBONS FROM ILLINOIS COALS

Edwin J. Hippo AND William S. O'Brien
Department of Mechanical Engineering and Energy Processes
Southern Illinois University at Carbondale
Carbondale, IL 62901-6603

Jian Sun
Department of Civil Engineering
University of Illinois
Champaign, IL 61802

Keywords: Activated Carbons from Coal, Preoxidation, Surface Area of Chars

INTRODUCTION

Although the predominant use of coal is for combustion applications, more beneficial, reasonable and profitable uses may be as a resource for the production of chemicals, and materials, including activated carbon. Activated carbons represent a family of carbonaceous substances manufactured by processes that develop the carbon's adsorptive properties (1). They are highly disorganized, aromatic lamellae which stack in 3-dimensional space to form porous solids (2-4). They normally have a high surface area, high adsorption capacities, and high surface reactivities. They are widely used in waste water treatment processes and are gaining increasing popularity for adsorbing vaporous organic molecules from gases and liquid phases. They are often the material of choice for many environmental applications and can also be used as a catalysts support.

Coals are a popular parent material for the production of activated carbons. Many workers have reported the production of high grade activated carbons from coal (5-17).

Several problems have kept coals from becoming dominant parent materials. One problem is the inherent mineral content of coals. Second, high and low rank coals are thermosetting solids which means that the microstructure of the activated carbon produced from these coals is relatively fixed. Only minor changes in microstructure can be made by controlling the weight loss during the activation process. This phenomena allows for consistency in the product but the quality of the product is not optimal. The opposite problem exists for bituminous coals. Bituminous coals melt during pyrolysis and the inherent pore structure collapses. The char must be heavily activated in order to produce a high grade of product. This can be circumvented by oxidation in air prior to the devolatilization step. However, the preoxidation step is difficult to control and the consistency of the end product is poor. Thus, bituminous coals give higher grade product than the lower or higher rank coals but the product consistency is poorer for the bituminous rank coals. Other chemical methods have also been used to prevent pore collapse. All of these processes are costly. Besides these problems, little is understood in terms of the basic fundamentals that produce a carbon of desired microstructure from a given parent coal. Thus, for a given feedstock many tests must be conducted to properly optimize both yield and product quality. This paper discusses the production of activated carbon from an Illinois coal with a two- and a three-step process.

EXPERIMENTAL

The primary objective of this study was to demonstrate that an activated carbon with acceptable commercial properties could be made from a -20x100 mesh fraction of an Illinois Basin coal (IBC 106). This sample was chosen for its low ash yield and represents a major coal producing seam in Illinois. The analysis of the whole coal can be found elsewhere (18). Pretreatment time and temperature, devolatilization temperature, and activation time and temperature were studied as production variables. The carbon products were characterized by CO_2 single point BET, helium density, bulk density, pore volume, and a dynamic toluene adsorption test.

Figure 1 illustrates the three-step process for producing activated carbon from bituminous coal. Direct activation of two oxidized coals was also applied in order to reduce the total production time. The figure lists the various conditions for which samples were prepared.

The oxidation step for pretreating the raw coal was performed in an auto-programmable ashing furnace. Approximately 40 grams of coal sample was scattered as a 3 mm thick layer onto a 200 mesh sieve, and air was passed through the sieve screen at temperatures ranging from 150°C to 250°C.

The devolatilization and activation steps were carried out in a reaction system arranged as shown in Figure 2. The apparatus consists of a nitrogen and air supply system, a metering pump, a steam generating unit, a vertical reactor system, and a reaction flue gas cleanup unit. An annular sample basket was used in the experiment. To monitor the sample (reaction) temperature, a thermocouple (chromel-alumel) was inserted in the center of sample. Approximately 40 grams of preoxidized coal was used for each devolatilization step and 10 gm of char during each activation step. The air supply and the steam generating unit were used only during the activation reactions. The flow rate of nitrogen (for devolatilization) or steam, air and nitrogen mixture (for activation) were one liter/min.

A "Quantasorb" solids surface analyzer was used to measure the carbon surface area using carbon dioxide single point BET method (19). The helium density measurements were carried out in a "Stereopycnometer", as described by Lowell and Shields (19). The bulk density was calculated using the mass of an activated carbon sample and the volume of this sample measured in a 5 ml cylinder after 10 tapping times.

241

To evaluate the practical adsorption capacity of the products, a mini-column adsorption system was constructed as shown in Figure 3. A saturated toluene water mixture was pumped through the column. A data logger was used to record the percentage transmittance (%T), after passing the mixture through the column. The mini-column was made of stainless steel, about 8.7 cm in length, 3.5 mm I.D. and 6.35 mm O.D. Both ends of the column was plugged with a small wad of glass fiber to contain the sample. A charge of 0.2 gm of activated carbon was used for each test.

RESULTS AND DISCUSSION

The first try at oxidation of the coal was carried out at 150°C following the studies reported by Maloney and Walker (9,10). The criterion for oxidation success was to treat the coal with air at 150°C until the coal lost its caking property (did not melt or agglomerate) during a 730°C heat treatment in a nitrogen atmosphere. An oxidation reaction at 150°C for 40 hours in flowing air converted the raw coal into the first non-caking, oxidized coal (CxOy 1). The coal gained 1.9 wt.% during this oxidation step. The oxidation temperature was then increased to 225°C and to 250°C, in an attempt to produce the oxidation treatment in a shorter time. The criterion for oxidation success was to oxidize the coal until it reached 1.9 wt.% weight gain (dry). The coal was weighed periodically. It took 6 hrs to reach the 1.9 wt.% gain target at 225°C and only 2 hours to reach the target at 250°C.

The 250°C reaction temperature was the highest on a practical basis, since the coal ignition temperature in this reactor was around 275°C (coal becoming ashed at 275°C in the furnace). The three oxidized coals (CxOy 1, CxOy 2, CxOy 3) were used for carbon production. The reactivity of the chars largely depends on the temperature of the char preparation step and the activation-gas composition. It was found in the earlier SIUC study [7] that a 1000°C devolatilization totally destroyed the original micropores in the unoxidized coal. Char devolatilized at 500°C seemed to be more reactive than the char devolatilized at 750°C. Since time of activation is an important economic factor, a more reactive char is desirable, provided that the char produces the desired quality of carbon.

In this work, Char 1 was gasified at 730°C to produce the first set of carbon products, C1/730/730. The rate of char weight loss is fast during the first several hours of reaction. Afterwards, the weight loss rate becomes linear. The carbon surface area develops gradually as the weight loss increases. The maximum surface area was reached at 60 hours, with a 63.73 wt.% weight loss. Activation for more than 60 hours resulted in a decrease in the surface area due to the destruction of the walls between micropores inside the particles.

The gasification temperature was increased to 780°C during the making of the second set of carbon products from Char 2. Both Char 2 and Char 1 were made from CxOy 1, while Char 2 was devolatilized at 500°C in an attempt to preserve the reactive sites in the char. The overall reaction rate at 780°C for Char 2 was much faster than that of Char 1 at 730°C. The maximum carbon surface area were reached after 17 hours of activation with a 70.93 wt.% weight loss. It is noticed in Figure 4 that the maximum surface areas in the production of C1/730/730 and C1/500/780 are not on the same point of char weight loss, because their gasification reactions were based on the different chars. But the surface area development is similar in both cases.

CxOy 2 was devolatilized at 500°C to make Char 3, on which activation tests at 780 to 880°C were performed. Surprisingly, regardless of the activation temperature, the maximum surface (about 1070 m^2/g) developed at about 73% burnoff. At higher temperature, it became more difficult to obtain the target burnoff.

The specific surface areas were measured or calculated on a dry basis, which is conventionally used in industry. It is of interest to also calculate the carbon surface area on the basis of dry ash free (daf). In the production of C1/730/730, the value of the maximum surface area (1058 m^2/g, dry) became 1464 m^2/g (daf). The surface area value of the carbon after 96 hour activation jumped up from 872 m^2/g (dry) to 1638 m^2/g (daf).

The pore volume of a carbon adsorbent is one of the major factors that influence the carbon adsorption behavior. This property should normally increase step by step as more and more surface area is developed while the coal converts to form porous carbon. As a result, the carbon bulk or apparent density should decrease, and the helium (or true) density should increase. Figure 5 illustrates the change of pore volume during the gasification step.

The measurement of each carbon's capacity for toluene adsorption was the major method used in this study to evaluate the applied performance of the carbon adsorbents. These experiments were run in a mini-column adsorption system. Toluene is considered as a practical adsorbate which represents potential industrial solvents and domestic organic pollutants.

A UV spectrophotometer was used to monitor the percentage transmittance of the effluent stream coming from the column, yielding a time history of percentage transmittance of the flow stream. The toluene adsorption capacities of all the carbon products produced in this work are summarized in Table 1.

Darco coconut charcoal (Fisher Scientific), a commercial activated carbon, was chosen as the reference adsorbent for this study. The "raw" adsorbent with an "as-received" commercial size (-6+14 mesh) demonstrates very poor adsorption behavior, probably because of the small ratio of particle diameter to tube diameter. The commercial carbon was then ground into the -20+100 mesh size-range, the same as that of the coal-carbons made during this study, in order to reduce

the diffusion distance and improve the adsorption efficiency.

The toluene "adsorption capacity" of the carbon is defined as the amount of toluene removed from the water stream by each gram of carbon. The adsorption capacity in this study is defined by the amount of toluene adsorbed before the 5% level (break point) was reached on the break-through curve. It took 200 minutes for the concentration ratio to reach the break point with the C1/730/730 carbon, which is about 140 minutes longer than with the commercial carbon.

The C1/500/780 carbon shows the highest adsorption capacity (1.57 g/g) that is consistent with its highest surface area. The C2/500/780 carbon also demonstrates a very high adsorption capacity, only second to the C1/500/780 carbon. While the C2/500/800, C2/500/840, and C2/500/860 carbons have about same high surface area values as the C2/500/780 carbon, they exhibit smaller adsorption capacities.

In consideration of the mass diffusion behavior during adsorption, the C1/500/780 and C2/500/780 carbons may have a size-range of micropores that would cause slower toluene mass transfer inside carbon particles. This is depicted by the small slopes of the respective break-through curves. Another two products, the C2/None/860 and C3/None/860 carbon, made by direct gasification at 860°C on oxidized coals were also produced. They demonstrated quite similar adsorption behavior to that of carbon made by char gasification at the same temperature.

CONCLUSIONS

It can be concluded from the results of this study that activated carbon adsorbents with accept-able commercial properties can be produced from an Illinois Basin coal. A total of nine carbon products were produced, seven of these having carbon dioxide specific surface area greater than 1000 m^2/g (dry), as compared with the surface area of 547 m^2/g (dry) measured for a commercial activated coconut carbon. All the SIUC products demonstrated better toluene adsorption. The adsorption capacity of the carbon with the largest pore surface area of 1114 m^2/g (dry), corre-sponding to 1560 m^2/g (daf), is four times greater than that of commercial carbon. The highest daf surface area value was 1638 m^2/g, corresponding to 872 m^2/g (dry). Devolatilization at lower temperatures is preferred for the conservation of the reactivity of resultant char. The successful production of carbons by direct gasification on oxidized coals indicates that the devolatilization process might be ignored if the oxidized

There have been three pretreatment oxidation temperatures tested in this study. Oxidation at 150°C probably takes too long (40 hours) to be practical in industry. Oxidation at 250°C seems to be too strong, causing partial damage of aromatic structure of the carbon. The oxidation pretreatment at 225°C seems to be the most feasible oxidation temperature of those evaluated in this study.

REFERENCES

1. 1991 Annual Book of ASTM Standards, Vol. 15.01, pp. 362.
2. Marsh, H. and Menendez, R., Chapter 2 in Introduction to Carbon Science, Butterworths, 1989.
3. Marsh, H. and Kuo, K., Chapter 4 in Introduction to Carbon Science, Butterworths, 1989.
4. Stoeckli, H.F., Carbon, 1990, 28, 1.
5. Juntgen, H., Jurgen, K., Knoblauch, K., Schroter, H. and Schulze, J., Chapter 30 in Chemis-try of Coal Utilization, John Wiley & Sons, Inc., New York, 1981, pp. 2141-2153.
6. Bansal, R.C., Donnet, J. and Stoeckli, F., Active Carbon, Marcel Dekker, Inc., New York and Basel, 1988.
7. O'Brien, W., Hippo, E. and Crelling, J., Products of Activated Carbons from Illinois Coals, Final Technical Report to Center for Research on Sulfur in Coal (now Illinois Institute for Clean Coal), Carterville, IL, July 6, 1992.
8. McEnaney, B. and Mays, T.J., Chapter 5 in Introduction to Carbon Science, Butterworths, 1989.
9. Walker, P.L., Coal-Derived Carbon, Materials Technology Center, SIUC, Carbondale, IL, 1987.
10. Maloney, D.J. and Jenkins, R.G., Fuel, 1982, 61, 175.
11. Bend, S.L., Edwards, I.A. and Marsh, H., Chapter 22 in Coal Science II, Academic Press, New York, 1991.
12. Derbyshire, F. and McEnaney, B., Energeia, 1991, 2, 1.
13. Joseph, J.T. and Mahajan, O.P., Chapter 23 in Coal Science II, Academic Press, New York, 1991.
14. Wachowska, H., Pawlak, W. and Andrzejak, A., Fuel, 1983, 62, 85.
15. Clements, A.H., Matheson, T.W. and Rogers, D.E., Fuel, 1991, 70, 215.
16. Ehrburger, P., Addoun, A., Addoun, F. and Donnet, B., Fuel, 1986, 65, 1447.
17. Khan, M.R. and Jenkins, R.G., Fuel, 1986, 65, 1203.
18. Harvey, R.D. and Kruse, C.W., Journal of Coal Quality, 1988, 7, 109-113.
19. Lowell, S., Introduction to Powder Surface Area, John Wiley & Sons, New York, 1979.

Oxidation	Devolatilization	Activation

```
                           730°C              730°C
          150°C                   ┌──Char 1──────────C1/730/730
                  ─CxOy 1─┤ 500°C │                  780°C
                          │       └──Char 2──────────C1/500/780
                                                     780°C
                                            ┌────────C2/500/780
                                            │ 800°C
                                            ├────────C2/500/800
          225°C          500°C              │ 840°C
 Coal ─┤  ─CxOy 2────────────Char 3─┤      ├────────C2/500/840
                                            │ 860°C
                                            ├────────C2/500/860
                                            │ 880°C
                                            └────────C2/500/880
                    860°C Activation of CxOy 2
                                                 ────C2/None/860
          250°C         860°C Activation of CxOy 1
                  ─CxOy 3────────────────────────────C3/None/860
```

↑	↑	↑	↑
Coal	**Oxidized coal**	**Char**	**Activated carbon**

Reaction	Condition
Oxidation	oxidized at 150, 225, or 250°C in flowing air with unlimited supply for 40, 6 and 2 hours.
Devolatilization	devolatilized at 500 or 730°C in nitrogen for 1 hour.
Activation	activated (gasified) at 730-880°C in 45% steam, 4% oxygen in nitrogen for 3-96 hours.

Figure 1. Production Procedures for Making Activated Carbon from IBC-106 Coal

Figure 2. Vertical Tube Furnace Reactor System

Figure 3. Mini-Column Adsorption System

Carbon surface area, m^2/g

Figure 4: Relationship Between Surface Area and Weight Loss

Pore volume, cm^3/gm
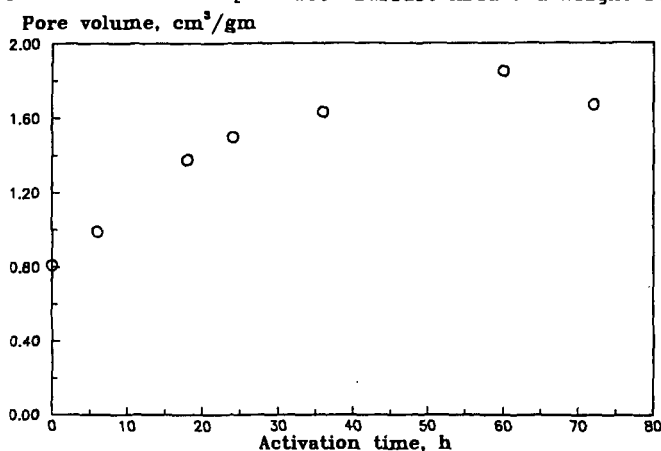
Figure 5: Pore Volume Developes During Activation

TABLE 1
TOLUENE ADSORPTION CAPACITIES OF CARBONS
WITH MAXIMUM SURFACE AREA

Carbon	Carbon surface area m^2/g	Toluene adsorption capacity g/g
Darco	547	0.31
C1/730/730	1058	1.05
C1/500/780	1114	1.57
C2/500/780	1054	1.36
C2/500/800	1076	1.00
C2/500/840	1031	0.74
C2/500/860	1050	0.89
C2/500/880	968	0.89
C2/None/860	1040	0.84
C3/None/860	852	0.84

ADSORBED NATURAL GAS STORAGE WITH ACTIVATED CARBON

Jian Sun, Todd A. Brady and Mark J. Rood
Department of Civil Engineering, University of Illinois
205 North Mathews Ave., Urbana, IL 61801

Massoud Rostam-Abadi and Anthony A. Lizzio
Illinois State Geological Survey
615 East Peabody Dr., Champaign, IL 61820

INTRODUCTION

Despite technical advances to reduce air pollution emissions, motor vehicles still account for 30 to 70% emissions of all urban air pollutants.[1] The Clean Air Act Amendments of 1990 require 100 cities in the United States to reduce the amount of their smog within 5 to 15 years. Hence, auto emissions, the major cause of smog, must be reduced 30 to 60% by 1998.[2] Some states like California have set stringent laws to clean up severe air pollution. Beginning in 1997, 25% of all cars sold in California must qualify as low emissions vehicles (LEVs). By 2005, 75% of the cars sold in California must be LEVs.[3] This situation has spurred interest in research and development of alternative fuels.

Alternative fuels
Electricity: Although electric vehicles (EV) do not produce tailpipe emissions, pollution is produced at power plants that generate electricity to charge the vehicles' batteries. If 50% of the electricity is produced from coal, 20% from natural gas, and the remaining 30% from nuclear or hydro power, then EVs will produce 99% less hydrocarbons, 99% less CO and 60% less NOx, compared with conventional gasoline fueled vehicles. However, SOx and particulate emissions could increase by a factor of five.[4] Other pollutants can also result from the use of batteries in vehicles. Water quality and solid waste disposal could be additional environmental problems. EV can be used to reduce local air pollution in specific markets such as vehicles for public services or urban use where speed and range are not limitations. EVs are also recommended for those regions where fossil fuels are not the primary fuel used to produce electricity.

Methanol, liquefied petroleum gas and hydrogen: Vehicles operating with M85 (85% methanol/15% gasoline) or M100 (pure methanol) have similar CO and NOx emissions to conventional gasoline fueled vehicles.[5] The largest emission benefit from methanol (M100) fueled vehicles is their reduced ozone-producing potential (Table 1).[6] Emissions from liquefied petroleum gas (LPG) fueled vehicles are comparable to gasoline fueled vehicles except for ozone formation. Hydrogen fueled vehicles theoretically produce no pollutants except NOx, which can be further reduced by lowering combustion temperature.[7] However, it is important to consider that hydrogen is made by coal gasification or water electrolysis, and these processes generate air pollutants directly or indirectly.

Natural gas: Natural gas can be used as a fuel for vehicles and offers many environmental benefits. A natural gas vehicle (NGV) uses a conventional spark ignition engine with only minor modifications. Natural gas burns more completely and produces less air pollutants than gasoline. There are three technologies for on-board natural gas storage: liquefied natural gas (LNG), compressed natural gas (CNG) and adsorbed natural gas (ANG). CNG has been commercialized worldwide. ANG uses adsorbents and operates at a much lower storage pressure (500 psig) than CNG (3,000 psig), thus has relatively lower capital and maintenance costs.
   There are about 40,000 NGVs in the US and about one million worldwide.[5] Emission data (Table 2) show that NGVs, compared with conventional vehicles, have significantly lower CO emissions due to better mixing of the gaseous fuel, lean fuel to air ratio and lack of fuel enrichment to start.[5,6], Carcinogenic pollutant (e.g., benzene and 1,3-butadiene) emissions are effectively eliminated.[6] Because the hydrocarbon constituent in NGV exhaust is dominantly methane, which has insignificant photochemical reactivity, emissions from NGV are expected to contribute the least to ozone formation (Table 1).[6,8]
   Natural gas, as an automobile fuel, has emerged as a leading alternative to conventional fuels. In the short term, depot-based commercial fleets (e.g., buses and taxis) will be the first beneficiaries of NGV because of limited range and lack of fuel-service infrastructure.

Improvement in the technologies for adsorbed natural gas (ANG) storage will offer significant opportunities for reducing capital and operating costs.[7,9,10]

Adsorbed natural gas

The key ingredient for successful commercialization of ANG is the adsorbent. The natural gas storage capacity of an adsorbent is usually evaluated in terms of its volumetric methane storage capacity (Vm/Vs), where Vm is the volume of stored methane at standard temperature and pressure, and Vs is the volume of the storage container. Commercial development of ANG requires adsorbents with low costs (< $2.00/lb) and high gas storage capacities (> 150 Vm/Vs).[9] Activated carbons have the most favorable gas storage density.[7,11] This paper describes some methods for producing adsorbent carbon from an Illinois bituminous coal and scrap tires. The potential application of these low cost adsorbents in low pressure ANG vehicles is also evaluated.

Coal and scrap tire as parent materials

Because combustion of Illinois coals is increasingly restricted due to their higher sulfur contents, they are being studied as potential precursors for commercial activated carbon production.[14] The US has large stockpiles of waste tires, growing at a rate of approximately 280 million tires per year.[12] Currently over 80% are landfilled, constituting a loss of significant resources and creating environmental problems. If some of these tires are converted into activated carbons, millions of tires would be diverted from the nation's landfills. Carbons from these sources may meet the cost and adsorption capacity requirements for ANG adsorbents.

EXPERIMENTAL

Sample preparation

Adsorbent carbons were produced from an Illinois coal, IBC-106 (Free Swelling Index: 4.5[13]). The raw coal, provided by the Illinois Basin Coal Sample Program[13], was ground and sieved from -8 mesh to -20+100 mesh and to -100 mesh. The -20+100 mesh portion was used as feedstock for physical activation and the -100 mesh portion was used for chemical activation. Shredded automotive tires used in this study were obtained from three vendors: Atlas (Los Angeles, CA), National Tire Services (Chicago, IL), and Baker Rubber (South Bend, IN). Their nominal particle diameters were 3, 1 and 0.4 mm, respectively. Results from proximate and ultimate analyses of the IBC-106 coal and a typical tire sample are listed in Table 3.

Adsorbent production

Carbon adsorbent production by both physical and chemical activation techniques was carried out in a bench scale tubular reactor with a horizontal tube furnace (Lindberg; Type 54232). For physical activation, a three-step process was applied: coal oxidation in air at 225°C for 2 or 4 h; devolatilization of oxidized coal in nitrogen at 400°C for 1 h; and steam activation of the resulting char in 50% steam in nitrogen at 800-850°C for 0.5-5.5 h. The air oxidation step was performed in an auto-programmable ashing furnace (Fisher Scientific, Model 495A) with unlimited air supply. About 12 g of sample was used during oxidation and devolatilization while 1 to 2 g of sample was used during steam activation. The gas flow rate during devolatilization and steam activation was 1 L/min. For chemical activation, about 2 g of the coal (-100 mesh) was mixed with granular KOH (coal/KOH mass ratio 1:1) and ground into a gel-like solid using a mortar and pestle. This mixture was then activated at 800°C in 100% nitrogen for 0.5 and 1.25 h. After chemical activation, the sample was immediately submerged in deionized water, filtered, crushed, and then washed again in deionized water to remove KOH derivatives which may have been on the surface of the particles.

Physical activation of the tires was carried out by a two-step process: devolatilization of about 5 g sample tire in nitrogen at 600°C for 45 min; and then steam activation of the resulting char in 50% steam in nitrogen at 850-900°C for 0.5-3 h. Chemical activation of the tires with KOH was performed in a similar manner to that of coal, except tires were chemically activated at 900°C for 0.5 to 1.5 h.

Adsorbent characterization

BET surface areas and t-plot micropore volumes (micropore volume is defined as the volume of pores < 17 Å) were calculated based on the nitrogen adsorption isotherms (relative pressure P/P_0: 0.001-1) measured with a volumetric adsorption apparatus (Micromeritics ASAP2400). Methane adsorption capacity, on a mass basis (g/g), at pressures up to 500 psig was determined with a pressurized thermogravimetric analyzer (Spectrum Research and Engineering Model TL-TGA

1900/600 PTGA). Buoyancy correction was performed for coal-derived carbon when calculating the methane adsorption capacity (g/g). The true density of activated carbons produced from Illinois coal was taken as 2.2 g/cm^3.[14] Vm/Vs values (cm^3/cm^3) were determined from the experimental data obtained with a custom built 4.92 cm^3 pressurized vessel at 500 psig.

Pelletization

Select tire-derived carbons were made into pellets using a 1/4 in. (6.35 mm) diameter cylindrical die and manual press. Samples of 100-200 mg were prepared by mixing the carbon with a liquid 1-step phenolic resin (Durez 7347A, Occidental Chemical) binder. The resin was used at a mass ratio of 5-20%. The mixture was then placed in the die and compressed. The die and pellet were subsequently heated at 165°C in an oven (Precision Scientific, Model 17) for 5 min to insure proper setting of the binder. The die was then removed from the oven and allowed to cool to room temperature before removing the pellet.

RESULTS AND DISCUSSION

Physical activation

Properties of several carbon samples produced by physical activation of the IBC-106 coal are presented in Table 4. Properties of a commercial activated carbon, BPL manufactured by Calgon Carbon Corp., are included in the table for comparative purposes. Vm/Vs values of coal-derived carbons range from 54 to 76 cm^3/cm^3. These values are comparable to that of BPL. The measured Vm/Vs value for BPL is consistent with values reported by other researchers.[15-17] Select sample products were then ground to minimize their inter-particle space and increase their bulk density. Bulk densities of select carbons with initial Vm/Vs values of 70 cm^3/cm^3 increased by 35% when the -20+100 mesh granular products were ground to -325 mesh. Using this revised bulk density and a Vm/Vs value of 76 cm^3/cm^3 provides a Vm/Vs value of 103 cm^3/cm^3.

Tire-derived carbons were produced from each of the parent tire samples. The tire samples from Atlas and National Tire Services were activated with steam. Production conditions and properties of tire-derived carbons are also listed in Table 4. Tire-derived carbons have lower micropore volumes and methane storage capacities than coal-derived carbons, possibly due to their lower bulk densities. For the highly activated samples (TA2), 10% by mass of the original tire sample remains. Steam activation probably leads to broadening of pores in the tire-derived carbons. Theoretical models have predicted an optimum pore width of 11.4 Å for methane storage. Even deviations of 2-3 Å from this optimal pore size significantly reduces the ability of the pore to adsorb methane.[18] Therefore, it is possible that the highly activated tire carbons have micropores which have broadened so that many pores are larger than ideal. Pore size distributions of sample products have yet to be determined.

Chemical activation with KOH

BET surface areas and micropore volumes of the chemically activated carbons from coal (0.5 h activation) are significantly higher than those of physically activated carbons. However, the Vm/Vs value for the KOH-activated carbon is lower (Table 4). This is attributed to the resulting lower bulk density. Chemical activation of the coal appears to be an effective method for producing carbon adsorbents for gas storage, provided that the carbon's bulk density can be increased. The methane adsorption capacity (g/g) for KOH-activated carbon is 50% higher than that of BPL at 500 psig (Table 4). Carbon sample C1 was prepared from the coal without pre-oxidation. Its methane adsorption capacity (g/g) is 15% lower than that of BPL at 500 psig. This is most likely due to its lower micropore volume. Carbon sample C2 was prepared by pre-oxidation for 4 h resulting in a surface area of 1037 m^2/g. Pre-oxidation of the coal causes increased methane adsorption capacity at 500 psig when compared to BPL or the activated carbons prepared without pre-oxidation.

Tire samples from Baker Rubber were chemically activated since it was closest in size (0.4 mm) to the crushed KOH. It is desirable to have as much direct contact as possible between the KOH and the tire since the reaction involves two solid materials. KOH-activated tire-derived carbons have much higher bulk densities than the steam-activated tire-derived carbons, most likely due to the chemical reaction between the two solids resulting in the realignment of carbon structure. As a result of their increased bulk density, methane storage capacities of the KOH-activated carbons are 40-50% higher than the physically activated carbons.

Pelletization

Pellets were formed from select tire-derived carbons and chars. In all cases, the bulk density of the material increased over 100%. The changes of adsorbent bulk density, micropore volume and

Vm/Vs values are summarized in Table 5. Efforts to make pellets with < 10% binder were unsuccessful. The unactivated char was mixed with binder at a mass ratio of 5% (of the char). Although pelletization of the TA3 carbon increased bulk density by about 160%, the micropore volume was reduced by 50%, resulting in no effective change in Vm/Vs values (Table 5). The loss of micropore volume is most likely due to the large amount of binder (11%) required to make the pellet. The binder may block access to the micropores by covering or filling the pores. A micropore volume reduction of about 20% has been reported.[19] Micropore volume did not seem to be impeded when making a pellet from the TA4 char prior to activation. This result cannot be attributed to the amount of binder used with the char. Since significant mass loss occurs during activation, the amount of binder in the final activated pellet is roughly the same as the TA3 pellet. Instead, the binder does not limit micropore development during activation and may actually contribute to the total micropore volume by developing micropores during activation. Similar results were observed for the KOH-activated tire-derived carbons.

CONCLUSIONS

Activated carbons for natural gas storage were produced by physical and chemical activation of an Illinois coal and scrap tires. Volumetric methane storage capacities (Vm/Vs) were measured at pressures up to 500 psig. Vm/Vs values of 76 cm^3/cm^3 are achievable when physically activating the coal. This value is comparable to that of 70 cm^3/cm^3 for BPL, a commercial granular activated carbon. Vm/Vs values exceeding 100 cm^3/cm^3 were achieved by grinding the granular coal-derived products. The increase in Vm/Vs is due to the increase in bulk density. KOH-activated coal-derived carbons have higher surface area, micropore volume, and methane adsorption capacity (g/g), but lower volumetric methane storage capacity, than the physically activated carbons. The lower volumetric methane storage capacity is due to the lower bulk density of KOH activated carbon. Tire-derived carbons have lower methane storage capacity due to their lower bulk density, when compared to the coal-derived carbons. Forming pellets from tire-derived carbons increases bulk density by as much as 160%. However, this increase was offset by a decrease in the micropore volume of the pelletized materials due to the amount of binder required in the process. As a result, Vm/Vs values were about the same for granular and pelletized tire-derived carbons. Carbon obtained by activating a pelletized tire-derived char increased storage capacity by about 20 %.

REFERENCES

1. DeLuchi, M.A. and Ogden, J.M. *Transpn. Res.* **27** 255 (1989)
2. *USA Today* Oct. 23 (1990)
3. Keller, M.N. *Cars* pp.59 March (1992)
4. Johannson, L. *ENVIRO* **13** 11 (1992)
5. Alson, J.A., Adler, J.M. and Baines, T.M. in *Alternative Transportation Fuels* Quorum Books, New York (1989)
6. Carslaw, D.C. and Fricker, N. *Chemistry & Industry* August 7 (1995)
7. Golovoy, A. *Proceedings: Compressed Natural Gas* Soc. Auto. Eng., Pittsburgh PA (1983)
8. Seinfeld, J.H. *Air Pollution: Physical and Chemical Fundamentals* McGraw Hill (1975)
9. Nelson, C.R. "Physical Sciences NGV Gas Storage Research," Gas Research Institute, Chicago IL (1993)
10. Wegrzyn, J., Weismann, H. and Lee, T. *Proceedings: Annual Automotive Tech. Develop.* Dearborn MI (1992)
11. Quinn, D.F., McDonald, J.A. and Sosin, K. 207th ACS National Mtg, San Diego CA (1994)
12. *New York Times* p. D1 May 9 (1990)
13. Harvey, R.D. and Kruse, C.W. *Journal of Coal Quality* **7** 109 (1988)
14. Sun, J. MS thesis, Southern Illinois University, Carbondale IL (1993)
15. Innes, R.A., Lutinski, F.E., Occelli, M.L. and Kennedy, J.V. *Report AC 01-84CE50071* Washington, DC: US DOE (1984)
16. Parkyns, N.D. and Quinn, D.F. in *Porosity in Carbons* John Wiley & Sons, Inc. (1995)
17. Quinn, D.F. and McDonald, J.A. *Carbon* **30** 1097 (1992)

18. Matranga, K., Stella, A., Myers, A., and Glandt, E. *Sep. Sci. and Tech.* **27** 1825 (1992)
19. Kimber, G. Workshop on Adsorbent Carbon, Lexington KY, July 12-14 (1995)

Table 1. Equivalent ozone-producing potential for select vehicular fuels

Fuels	g of O_3/mile
Gasoline	3.8
M85 (85% methanol in gasoline)	4.7
M100 (100% methanol)	1.8
CNG	0.2
LPG (Liquefied petroleum gas)	0.7

Table 2. Reduction of emissions from NGV when compared to gasoline fueled vehicle

Pollutants	% Reduction
CO	76
NOx	75
HCs (Non-methane)	88
Benzene	99
1,3-butadiene	100

Table 3. Proximate and ultimate analyses of IBC-106 coal (-20+100 mesh) and Atlas scrap tire

	Coal [wt%]	Tire [wt%]
Proximate analysis (as received)		
Moisture	8.3	0.9
Volatile matter	37.9	3.2
Fixed carbon	45.9	69.8
Ash	8.0	26.2
Ultimate analysis (dry)		
Carbon	70.3	86.2
Hydrogen	5.2	7.4
Nitrogen	1.5	0.1
Sulfur	3.7	1.5
Oxygen	11.3	1.7

Table 4. Type of treatment and properties of resulting activated carbons that are produced from Illinois coal, scrap tires and BPL

Sample ID	Pre-oxidation [°C, h]	Activation conditions [°C, h]	Surface area BET (dry) [m^2/g]	Micropore volume [cm^3/g]	CH$_4$ adsorption at 500 psig [g/g][d]	Bulk density [g/cm^3]	Vm/Vs [cm^3/cm^3]
C1[a]	None	850, 1.5	897	0.330	0.0525	0.33	54
C2[a]	225, 4	850, 2	1037	0.370	0.0643	0.44	73
C3[a]	225, 4	825, 3	1056	0.410	0.0610	0.44	76
C4[a,c]	None	800, 0.5	1478	0.620	0.0903	0.27	68
TA1[b]	None	850, 3	888	0.254	0.0540	0.15	44
TA2[b]	None	900, 1	1031	0.278	0.0530	0.13	41
TB[b]	None	850, 2.5	420	0.131	-	0.24	38
TC[b,c]	None	850, 1.5	820	0.274	-	0.33	53
BPL	unknown	unknown	1000	0.430	0.0606	0.46	72

[a] produced from Illinois coal (IBC-106)
[b] produced from tire samples from Atlas, National Tire Services and Baker Rubber, respectively
[c] activated with KOH
[d] Sample weight at 1 atm CH$_4$ used as starting weight for calculation; Data for tire-derived carbon obtained without buoyancy correction

Table 5. Effect of pelletization on bulk density, micropore volume and Vm/Vs of select tire-derived carbons

Sample ID	Bulk density [g/cm^3]	Micropore volume [cm^3/g]	Methane storage Vm/Vs, [cm^3/cm^3]
TA3	0.16	0.25	43
TA3 pellet	0.42	0.13	44
TA4 activated pellet	0.37	0.23	51

Carbon TA3 and TA4 produced from Atlas scrap tire samples

ISOBARIC ADSORPTION AND DESORPTION OF HYDROCARBONS FOR THE DETERMINATION OF A WIDE RANGE OF PORE ENERGY DISTRIBUTIONS

W.G. Tramposch

Calgon Carbon Corporation

P.O. Box 717

Pittsburgh, PA 15230

INTRODUCTION

Several standard methodologies are employed to determine the adsorptive properties of activated carbon.[1] These methodologies have, as a common goal, the generation of isotherm data. The isotherm data collected, in concert with any of the methodologies, can be used to calculate pore radius distributions using the Kelvin Equation,[2] surface areas using B.E.T.[3] and Langmuir Theories,[4] spreading pressures from the Gibb's Equation,[5] and adsorption potential distributions using Polanyi Theory.[6]

Gas phase isotherm data is typically collected by either of two methods.[1] In the first, the concentration of the adsorbate is varied while maintaining the temperature and total pressure of the system constant. This method is limited by difficulties in controlling both temperature and adsorbate concentration over the time period required to reach equilibrium. In the second method, the pressure of the adsorbate is varied while maintaining the temperature of the system constant. This method is limited mainly by the achievable system pressures and diffusional constraints.

Carbon capacities can also be measured by maintaining the adsorbate pressure at some constant value and varying the temperature to several known values.[1] Such isobaric data can easily be collected if the system pressure is selected at some convenient value such as atmospheric pressure. Using the undiluted adsorbate gas at atmospheric pressure, mass transfer is rapid, especially at high temperatures, and equilibrium is quickly achieved. The isobaric data can then be converted into the more useful isothermal result using Polanyi Adsorption Theory. Alternatively, the Dubinin-Radushkevich Equation[7] can be used for the same purpose. In the following sections a method is presented which provides a fast, convenient means for collection of isobaric carbon adsorption data. The isobaric data is correlated with isothermal data using Polanyi Adsorption Theory.[8]

EXPERIMENTAL

System Description

Isobars were determined using a customized instrument fabricated by George Associates (Berkeley, Ca.). The instrument was able to attain temperatures of -150°C to 600°C with positive and negative temperature ramping capabilities.

Procedures

Isobars - All isobars were performed at atmospheric pressure. Gravimetric determinations were performed once the system had reached both thermal and mass equilibria as indicated by no more than a 0.1°C change in temperature over one minute and no more than a 0.2 mg weight change over the same period. Samples were conditioned at 250°C in nitrogen prior to the determinations. Pure methane or ethane was adsorbed onto the sample in a series of 10 individual steps which were accomplished by incrementally decreasing and holding the temperature at each of several levels. After completing the adsorptive process, the methane or ethane was desorbed in a similar manner by increasing the temperature step-wise to the starting value. The amount of adsorbate loading was calculated as the mass difference between the equilibrated and the conditioned sample after making corrections for buoyancy effects.

Isotherms - Ethane isotherms were determined using granular material that had been previously dried in air at 150°C for three hours. Isotherms were performed at 25.0 ± 0.1°C in a water bath. The adsorbate gas was passed through a copper heat exchanger prior to contacting the carbon which was contained in a glass u-tube in the water bath. Gas flow was maintained until the mass change of the sample was less than 5 mg over an eight-hour period.

Methane isotherms were performed by the volumetric expansion method. A known volume and pressure of methane was allowed to expand into a vessel containing the activated carbon under vacuum. The amount of methane adsorbed was determined from the change in pressure of the system taking into account the void volume of the vessel containing the activated carbon. Void volumes were determined using helium expansion. The system was thermostatted at 25.0 ± 0.1°C. Samples were conditioned at 100°C under vacuum for 6 hours. No difference in adsorption capacity was observed when the samples were conditioned at 250°C.

RESULTS AND DISCUSSION

Methane and ethane were chosen as the adsorbate compounds. These molecules lack any significant dipole or induced dipole characteristics[9] such that only van der Waals interactions with the carbon are important. Within the temperature bounds of the isobars, both methane and ethane are stable with the exclusion of oxygen and the avoidance of catalytic metals.

Isobars can be presented as a plot of adsorbate capacity versus adsorption energies by employing Polanyi Theory. Following Polanyi Theory, the energy of adsorption, ϵ, is equal to the work required to take a molecule from the bulk phase to the adsorbed phase according to the following relationship:

$$\epsilon = \int_{Bulk}^{Ads} \overline{V} dp = RT \ln \frac{f_s}{f} \tag{1}$$

where f_s is the saturation pressure fugacity of the adsorbate at temperature $T(°K)$, f is the vapor fugacity of the adsorbate, and R is the gas constant. For isotherms, T is held constant while f is varied either by changing the concentration of the component in a diluent stream or by varying the absolute pressure of the adsorbate. For isobars, the temperature of the adsorbate or probe gas is varied thereby changing the value of f_s.

f_s can be calculated at any temperature below the critical temperature by use of the Antoine Equation and Peng-Robinson EOS. Above the critical temperature, the following expression was used to calculate the saturation pressure:[10]

$$P_s = \left(\frac{T}{T_c} \right)^2 P_c \tag{2}$$

Adsorbed phase densities were calculated according to the following equations:[11,12]

$$V_A = V_m \, e^{\Omega (T - T_b)} \tag{3}$$

$$\Omega = \frac{\ln \left(\frac{b}{V_m} \right)}{T_c - T} \tag{4}$$

Where V_A and V_m are the adsorbed phase molar volume and molar volume of the adsorbate liquid at the normal boiling point temperature, respectively. b is the van der Waals volume.

The isobar adsorption and desorption loadings for a single adsorbate onto a specific carbon are plotted as a function of ϵ as shown in Figure 1. As can be seen, the data points define a smooth curve that is typical for all carbons examined to date. The regularity of these data can be easily described by fitting the data to a polynomial of seventh order or less. The curves which can be described by the adsorption and desorption polynomials, are essentially collinear. This result clearly shows that equilibrium conditions were established at each isobaric point. No adsorption-desorption hysteresis has, as yet, been observed for any activated carbon using this technique with methane or ethane as probe gases. The smooth isobaric curves illustrate why it is not necessary to collect large numbers of adsorption and desorption isobaric points or to collect isobaric points at corresponding temperatures. This not only simplifies the method for generation of the isobaric data but also provides a significant advantage over isothermal techniques where temperatures need to be accurately known and precisely controlled. For the case of the isobaric techniques, the carbon and adsorbate gas need only to be in thermal equilibrium at a precisely known temperature. The Dubinin-Radushkevich Equation provides an alternate means of describing the data. The form of this equation is the logarithm of the volume adsorbed versus the square of ϵ.[7,13]

Correlation of Isobars with Isotherms

By use of Equation 1, ϵ values can be calculated from isotherm data as well as from isobar data. This provides a convenient way of reducing the data for comparative purposes. For example, Table 1 presents the ϵ values for each isotherm concentration as well as the temperature of the pure component isobar at equivalent ϵ values. Once the data have been reduced to a common scale, with reference to the ϵ-parameter, comparisons can be made between the techniques. A graphical representation of this comparison is given in Figure 2 for a single carbon. As can be seen, the isobar and isotherm data are essentially interchangeable at the individual ϵ-values. Therefore, this technique provides a convenient method to generate simple isotherms from isobaric data. Table 1 also illustrates the advantage of the isobar technique to generate adsorbate loadings at various pore energies. In the case of ethane, an increase in temperature from 25°C-to-220°C is equivalent to reducing the concentration or partial pressure of the adsorbate by two orders of magnitude. The operating temperature range for isobar determinations for ethane from -76 to 250°C is equivalent to greater than a three order of magnitude change in isotherm concentration. When utilizing the isotherm technique, this reduction in concentration to the resulting low adsorbate concentration levels requires the consumption of large quantities of adsorbate gas and extended time periods in making isotherm determinations.

The average relative standard deviation for the isobaric technique was 8.7% versus 4.3% for the isotherms. A statistical comparison of the variances of the isotherms versus isobars was made using the F-test at the 0.05 statistical level. The variance of the methane and ethane isobars versus the respective isotherms was found to be equal. This analysis was based upon the use of three replicates for both of the experimental techniques for the six carbons investigated.

Table 1 presents a summary of the average errors between the isotherms and isobars. No systematic errors were observed between the two techniques. Differences were examined using the student's T-test at the 0.05 statistical level. The methods were found to produce equivalent results over the adsorption energy range studied.

CONCLUSIONS

A method has been demonstrated that permits the generation of isotherm data from isobaric data. The method is rapid and generates estimates of isotherms with an accuracy and precision comparable to those generated by traditional means. The principal advantage of the isobar procedure

is that equilibration is rapid as higher temperatures and neat adsorbates are used. A span of greater than three orders of magnitude in f_s/f can be attained by varying the temperature of the system by several hundred degrees. The time required for the analysis is typically about four hours, whereas the time to perform isotherms which span the same energy region would require days-to-weeks to gain an equivalent amount of information.

Future directions in our research program will include the correlation of the isobar data with isotherm results from other classes of compounds. The achievement of such correlations will greatly enhance the utility of a variety of carbon performance predictive models. The models that would benefit most from this method are those that depend upon the determination of single component isotherms over a wide adsorbate concentration range for a specific carbon.

REFERENCES

1. S. Brunauer, The Adsorption of Gases and Vapors, Vol. 1, Princeton University Press, Princeton, New Jersey, 1945.

2. Halsey, G. D. *J. Phys. Chem.*, 1948, *16*,931.

3. Brunauer; S., Emmett, P. H.; Teller E. *J. Amer. Chem. Soc.*,1938, *60*,309.

4. Langmuir, I. *J. Amer. Chem. Soc.*,1918, *40*,1361.

5. Sircar, S.; Myers, A. L. *A.I.CH.E. Journal*, 1971, *17*, 186.

6. Polanyi, M. *Verh. Deut. Phsik. Ges.*, 1914, *16*,1012.

7. Dubinin, M. M.; Radushkevich, L. V. *Comp. Rend. Acad. Sci.* (U.S.S.R.), 1947, *55*, 327.

8. Semonian, B. P.; Manes, M. *Anal. Chem.*, 1977, *29*, 991.

9. Smyth, C. P. Dielectric Behavior and Structure, McGraw-Hill, New York, 1955.

10. Dubinin, M. M. *Chem. Rev., 1960, 60*, 235.

11. Ozawa, S.; Kusumi, S.; Ogino, Y. *J. Coll. Int. Sci.*, 1976, *56, 83*.

12. Dubinin, M.M. Prog. Surface and Membrane Science, Chapter 1, Academic Press, New York: 1975.

13. Ruthven, D. M.; Principles of Adsorption and Adsorption Processes, John Wiley & Sons, New York, 1984.

Table 1

Equivalence in Adsorption Energies for Isotherms and Isobars

	Methane			Ethane		
ε (Kcal/mole)	1.83	2.14	2.90	1.95	3.31	4.68
Temperature of Pure Component Isobar (°C)	-40.7	-15.1	28.5	25.0	103.7	222.2
Isotherm Partial Pressure of Adsorbate (mm Hg)	5500	3137	782	745	74.5	7.5
Average Error Between Isotherms and Isobars (%)	1.6	-2.2	· 5.5	-3.3	-5.1	11.9
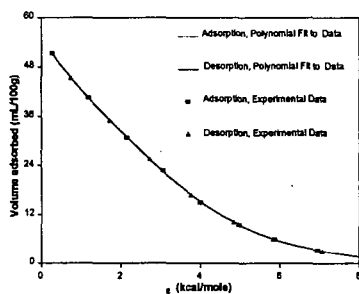
Figure 1
Adsorption and Desorption Isobars
Ethane Adsorbed on Xtrusorb 700 Carbon
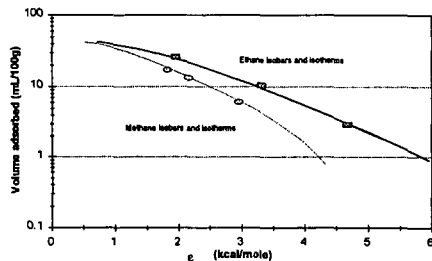
Figure 2
Comparison of Isotherms and Isobars
Methane and Ethane Adsorbed on PCB Carbon

255

GAS-SOLID EQUILIBRIA IN POROUS MATERIALS: A NEW MODEL

Russell S. Drago, J. Michael McGilvray, and Wm. Scott Kassel
Department of Chemistry, University of Florida
Gainesville, FL 32611-7200

INTRODUCTION

A new model for analyzing gas-solid equilibria in porous materials has been developed. Adsorption experiments with several probe gases and a commercial carbonaceous adsorbent have been analyzed using a multiple process adsorption model in which the capacity of each process, i, is calculated in millimoles per gram of adsorbent ($n_{i,ads}$) and the equilibrium adsorption constant for each process i is given as $K_{i,ads}$. The associated enthalpies of adsorption ($-\Delta H_{i,ads}$) were determined from adsorption measurements conducted at multiple temperatures via the van't Hoff equation. Since the values of $n_{i,ads}$ for each process are temperature independent, adsorption at other temperatures introduces only new $K_{i,ads}$ values.

The effects of porosity and surface area on the adsorptive properties of porous materials should be considered when selecting a porous material as an adsorbent. Work in our laboratory has shown that in catalyst doped adsorbents, small pores tend to concentrate reagents providing for better catalytic activity. An understanding of the pore size distribution and accessible surface area of solids is useful in selecting a suitable porous material for the adsorption of gaseous and liquid substrates. The BET equation has been the standard for many years in the determination of the surface area of porous materials. Although generally accepted, the BET equation has limitations, and as a result, has received some criticism in recent years. Our research efforts have been focused on developing a new gas-solid equilibrium model which is capable of providing information into the adsorption capacity of porous materials as well as thermodynamic data corresponding to the enthalpies of adsorption and equilibrium constants for adsorption of various sorptives.

EXPERIMENTAL

Approximately 0.3g of Ambersorb®572, a commercially available carbonaceous adsorbent, was degassed ($<10^{-4}$ torr) for a minimum of 8 hours at 200°C prior to each adsorption experiment. The sorptives chosen were selected to encompass a wide range of properties. Nitrogen, CO, and CH_4 are non-condensible adsorptives at the temperatures examined and are non-polar, polar and polarizable sorptives, respectively. Propane, SO_2, and NH_3 are condensible sorptives at the temperatures studied and are polarizable, acidic, and basic, respectively. All gases were of 99.99% purity and required no further purification. Gaseous uptake measurements were performed on a Micromeretics ASAP 2000 analyzer using a 36 point pressure table ranging from 1 torr to 760 torr. Low temperature adsorption measurements were performed with the aid of solvent / liquid N_2 baths to give the desired temperature.

RESULTS AND DISCUSSION

Adsorption measurements to determine porosity and surface area of porous materials have long been evaluated by the BET equation [4](Equation 1)

$$\frac{x}{n(1-x)} = \frac{1}{CN_m} + \frac{(C-1)x}{CN_m} \qquad (1)$$

where n = moles of gas adsorbed, N_m = total moles adsorbed, and x = P/P° with P = equilibrium pressure in torr and P° = 760 torr. The values N_m and C are obtained from a linear plot of x/n(1-x) vs x. The equation is only applicable in a pressure range of 0.05 to 0.3 torr. The BET C constant (Equation 2) is a complex quantity related to the equilibrium constant for monolayer adsorption ($K_{i,ads}$) and multilayer adsorption ($K_{j,ads}$) along with

$$C = \frac{K_{i,ads}}{K_{j,ads}} \exp\left(\frac{Q_{mono} - Q_{multi}}{RT}\right) \qquad (2)$$

contributions from the enthalpy of adsorption of the monolayer (Q_{mono}) and multilayer (Q_{multi}). The components of Equation 2 are not resolved, so C is difficult to interpret.[2,3]

Our research has focused on the development of a multiple process adsorption model[1] which is applicable over a wider pressure range and is presented in Equation 3. The adsorption isotherm is resolved into individual adsorption processes (n_i) and equilibrium constants for adsorption $(K_{i,ads})$ for those processes using Equation 3.

$$N_{total} = \sum_i \frac{niKi[P]}{1+Ki[P]} \qquad (3)$$

Here N_{total} = total moles adsorbed per gram of solid, P = relative equilibrium gas pressure in torr, n_i = number of millimoles of process i, and $K_{i,ads}$ = the equilibrium constant for adsorption for process i. From the equilibrium constants calculated from multiple temperature adsorption experiments, a direct thermodynamic measure of the enthalpy of adsorption , $-\Delta H_i$, for each process can be calculated. Table 1 lists the $n_{i,ads}$ values and corresponding equilibrium constants $(K_{i,ads})$ that have been calculated from our multiple process adsorption model. One can see in the values for $K_{i,ads}$, that as the polarizabilty of the sorptive increases so does the affinity for adsorption. Table 2 lists the enthalpies for the adsorption processes, $-\Delta H_{i,ads}$ that have been calculated based on the temperature dependency of $K_{i,ads}$. One can see that the calculated enthalpies are greater than the reported heats of vaporization of the gases and that they fall within the accepted range for physisorption processes (2-12 kcal/mol).

Once the best n_i and K_i values for each process have been determined by a modified Simplex fitting routine capable of fitting multiple temperature adsorption data, the adsorption isotherm can be separated into the individual adsorption processes. Figures 1 and 2 show the individual adsorption processes for propane and methane adsorption by Ambersorb® 572 at 25°C. Three adsorption processes were found to be occurring at the same time, however, process 1, which corresponds to filling the smallest accessible pores, finishes before the entire adsorption process is complete. It should be clarified that the pores accessible to the sorptives will depend on the size of the probe, and that not all of the pores accessible to CH_4 will be accessible to propane.

In contrast, standard N_2 porosimetry analysis at 77K reports a micropore volume of 0.45 ml for A-572. If one multiplies the $n_{i,ads}$ values obtained for propane and methane adsorption by the corresponding molar volumes of the sorptives, one gets 0.41 ml for the total adsorption process for propane, and 0.25 ml for the total adsorption process of methane. The results indicate that the multiple process adsorption model may be able to distinguish pore size distributions in the reported micropore region of porous materials.

CONCLUSIONS

A multiple process adsorption model has been developed to analyze gas-solid equilibria in porous materials. From this model, one is able to calculate the number of millimoles $(n_{i,ads})$ and the corresponding equilibrium constants $(K_{i,ads})$ for each adsorption process. Enthalpies of adsorption $(-\Delta H_{i,ads})$ for each process can be calculated from the temperature dependency of $K_{i,ads}$. In contrast to the standard BET approach, this multiple process adsorption model has the potential for distinguishing the micropore distribution in porous materials as well as providing important thermodynamic data not readily obtainable from the BET method.

ACKNOWLEDGMENTS

REFERENCES

1. Drago, R.S., Burns, D.S., Lafrenz, T.J. J. Phys. Chem., **1995**, accepted.
2. Gregg, S.J., Sing, K. S. W. "Adsorption, Surface Area, and Porosity," **1967**, Academic Press: London.
3. Adamson, A.W. "Physical Chemistry of Surfaces," 5th Ed., **1990**, John Wiley & Sons, Inc.: New York.
4. Brumauer, S.; Emmett, P.H.; Teller, E. J. Am. Chem. Soc. **1938**, *60*, 309.

Table 1: Equilibrium Adsorption Parameters for A-572						
T(°C)	n_1	n_2	n_3	K_1	K_2	K_3
		(mmol/g)				
			N_2			
-93	0.322	1.68	5.38	124.5	11.46	0.8587
-42				5.739	.9214	.1213
0				1.068	0.2065	0.0423
25				0.6992	0.045	0.045
			CO			
-93	0.5138	1.934	5.325	204.9	16.53	1.169
-42				8.448	1.112	0.1455
25				0.4704	0.058	0.058
			CH_4			
-43	0.17750	1.427	5.037	153.4	13.71	0.996
0				15.98	2.07	0.238
25				4.91	0.876	0.111
40				3.24	0.563	0.0803
			C_3H_8			
25	1.02	2.46	2.008	2704	62.5	3.3
40				947	29	1.75
55				410.6	15.2	0.97
75				158.4	7.12	0.48
			SO_2			
25	0.932	4.75	6.21	364.6	11.83	2.81
40				136.2	6.15	1.42
55				66.3	3.44	0.81
75				29.4	1.6	0.416
			NH_3			
40	0.2389	0.800	1.410	1903	17.51	0.3193
55				581.6	8.339	0.2048
75				143.4	3.237	0.1214

Table 2: Enthalpies of Adsorption for A-572 (kcal/mol ± 0.5 kcal/mol)			
	H_1	H_2	H_3
N_2	-4.78	-4.74	-2.82
CO	-5.48	-5.08	-2.74
CH_4	-6.74	-5.51	-4.37
C_3H_8	-11.68	-8.96	-8.05
SO_2	-10.32	-8.22	-7.83
NH_3	-14.14	-6.43	-6.16

Figure1: Propane Adsorption by A-572
25oC
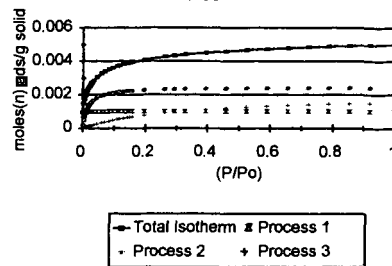
Figure 2: CH4 Adsorption by A-572
25oC
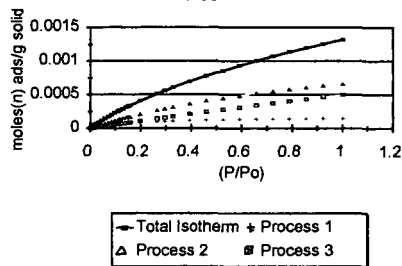
PRODUCTION AND CHARACTERIZATION OF ACTIVATED CARBONS FROM CEREAL GRAINS

A. Venkatraman, W. P. Walawender, and L. T. Fan
Department of Chemical Engineering, Kansas State University, Manhattan, KS 66506-5102

INTRODUCTION

The term, activated carbon, is a generic name for a family of carbonaceous materials with well-developed porosities and consequently, large adsorptive capacities. Activated carbons are increasingly being consumed worldwide for environmental applications such as separation of volatiles from bulk gases and purification of water and waste-water streams. The global annual production is estimated to be around 300 million kilograms, with a rate of increase of 7% each year [1].

Activated carbons can be prepared from a variety of raw materials. Approximately, 60% of the activated carbons generated in the United States is produced from coal; 20%, from coconut shells; and the remaining 20% from wood and other sources of biomass [2]. The pore structures and properties of activated carbons are influenced by the nature of the starting material and the initial physical and chemical conditioning as well as the process conditions involved in its manufacture [3].

The conventional method of manufacturing activated carbons involves two steps. In the first step, the raw material, usually of lignocellulosic origin, is carbonized in an inert atmosphere. The second step entails the physical activation of the resulting char of a low adsorptive capacity with either steam or carbon dioxide at a temperature usually exceeding 800° C [4]. The significance of these two steps have been described in detail elsewhere [5].

Although the general two-step procedure for generating activated carbons from lignocellulosic precursors has been well documented in the literature, knowledge of the specific variables involved is essential for a particular feedstock for developing the porosity and adsorptive capacity sought in a given application. In this sense, the current work investigates the evolution of the porosity of activated carbons generated from the pyrolysis and physical activation of novel feedstocks with a very low content of ash - kernels of cereal grains such as corn and hard red winter wheat (HRW). These grain kernels, either edible or off-grade are abundant and relatively inexpensive. The porous structures of both non-graphitizable charcoals obtained by the carbonization of the kernels and those of the resulting activated carbons have been characterized by the methods of physisorption. Specifically, the total micropore volumes and surface areas have been determined at various temperatures of carbonization and degrees of activation. Furthermore, an investigation of the probable fractal nature of the pore interfaces of a representative sample of HRW charcoal has been conducted through small-angle X-ray scattering.

THEORETICAL
Small Angle X-ray Scattering

X-rays are scattered primarily by the electrons of an irradiated material. The distribution of electrons throughout the material is not homogeneous, and the electronic density (number of electrons / unit volume) varies in different regions of the sample. Small-angle X-ray scattering (SAXS) by a material occurs as a consequence of this inhomogeneity in the electron density existing on length scales appreciably larger than the normal distances between atoms [6, 7]. As a result, the structures of various disordered materials can be investigated by SAXS over length scales varying from 5 to 4000 Å [8]. A schematic of a typical SAXS system is shown in **Figure** 1. Conventionally, small angles imply that the values of the scattering angle, 2θ, are no greater than 6 degrees.

The relationship between the intensity of the scattered X-rays, $I(q)$, and the scattering wave-vector, q, for a porous material has been described in detail elsewhere [9, 10]. Of relevance to this work is the scattering from systems of isotropic, i.e., randomly oriented, independent scatterers, with an average particle or pore dimension, d, wherein $I(q)$ can be approximated by the Guinier equation

$$I(q) = I(0) \exp [- (qR_g)^2 / 3] \tag{1}$$

for values of qd not appreciably greater than 1.0 [6]. The mean radii of gyration of the scatterers, R_g, can be evaluated in this regime from the slope of a plot of the natural logarithm of $I(q)$ versus q^2. An order-of-magnitude estimate of d is obtainable from R_g if the shape and charge distribution of the scatterers are known; usually, $2R_g < d < 3.5 R_g$ [11]. Specifically, if the system of scatterers can be assumed to be composed of identical, spherical pores of radius r_0, then the relation, $r_0 = 1.3 R_g$, can be applied to obtain r_0 [6].

The scattered intensity has been shown to be proportional to q^{-4} or θ^{-4} [6, 12] when the boundaries of the pores can be considered as smooth, i.e., free from irregularities. When the surfaces of the pores are fractal [13 -15], the scattered intensity takes cognizance of the surface irregularities, and can be described by the following relationship for values of qd far greater than 1.0 [10, 16]

$$I(q) = \pi I_e \delta^2 N_0 \lceil (5\text{-}d_{SF}) \sin [0.5 \pi (d_{SF}\text{-}1)] / q^{(6\text{-}d_{SF})} \tag{2}$$

or equivalently,

$$I(q) = I_0 q^{-\alpha} ; \alpha = 6 - d_{SF} \tag{3}$$

where I_0 is a constant, and d_{SF} is the surface fractal dimension. Since d_{SF} is bounded in the interval between 2.0 and 3.0, it is obvious from Eq. 3 that α can take on values between 3.0 and 4.0. When d_{SF} approaches 3.0, however, $I(q)$ vanishes according to Eq. 2; this apparent dilemma has been discussed at length elsewhere [9,10,17].

EXPERIMENTAL
Treatment of Raw Material

Whole grain kernels of corn and hard red winter wheat (HRW) were procured from a local source. The hull, i.e., the outer portion or the pericarp, constitutes a very small fraction of the total weight of the kernel, especially for corn. The moisture content in the grains, as determined by air-drying, was around 10%. The kernels were carbonized batchwise in 2-3 gram lots in an inert atmosphere of nitrogen flowing within a bench-scale tubular furnace [18]. Each batch of kernels was placed in a vertical, cylindrical wire-guaze reactor suspended inside the tubular reactor. The retention time of the kernels in the reactor was sufficient to allow complete devolatilization at a specified temperature of carbonization or pyrolysis; hence, the resultant charcoals were deemed terminal. These charcoals were obtained from the pyrolysis of the kernels in a single-stage as well

as a two-stage process. The single-stage process carbonized the kernels in one single step at a specified temperature. The two-stage process carbonized the kernels at a low temperature in the range from 250 to 300° C followed by that at a specified temperature. The kernels were pyrolyzed over a temperature range of 250 to 850° C. The charcoals generated by both processes were rapidly cooled to room temperature by quenching in a stream of nitrogen gas of 99.99% purity.

Physical Activation

The experimental set-up for the physical activation of the ensuing charcoals with CO_2 gas of 99.5% purity, was similar to that for carbonization. The vertical configuration of the reactor ensured that the reactant gas was forced directly through the char bed, thus minimizing the influence of film mass transfer resistances during activation. The charcoals after activation for the desired period of time, deemed as activated carbons, were purged in a stream of nitrogen of 99.99% purity. The activation was performed at a temperature of 850° C, for durations ranging from 0.5 to 6 hours.

Characterization of Charcoals and Activated Carbons

Both charcoals and activated carbons obtained were characterized by nitrogen adsorption at 77.4 K. A fully automated Nova-1200 instrument manufactured by Quantachrome Corporation determined the volumes adsorbed at various relative pressures. The duration of adsorption for each data point was approximately one hour in all the measurements. The surface areas were calculated by the BET method while the total micropore volumes were estimated by applying the D-R equation [19].

Small Angle X-ray Scattering

The X-ray scattering data were obtained with the aid of the SAXS system at the National Center for Small-Angle Scattering Research, Oak Ridge, Tennessee. The wavelength associated with the X-ray measurements was 1.54Å. The data on the scattered intensities were corrected for the effects of background scattering, slit-length collimation, and photoelectric absorption by the sample [11, 22].

RESULTS AND DISCUSSION

Pyrolysis

The elemental compositions of the two grain kernels are compared in **Table 1**; they are similar in that their contents of ash, i.e., mineral matter, are low. **Table 2** lists the terminal yields of the charcoals obtained from the single-stage pyrolysis of the grain kernels at various temperatures. The yield for HRW is always higher than that for corn at each temperature of carbonization. This may be attributable to a higher weight ratio of the hull to the kernel in HRW than in corn.

The yields of charcoals obtained from the single-stage process and the corresponding two-stage process are compared in **Table 3.** It is evident that the yield of each species obtained from the former is lower than that from the latter, particularly for HRW. Note that the temperature of pyrolysis for the first stage of the two-stage process has been optimized to maximize the surface areas of the resultant charcoals as determined by the BET method. This optimum temperature is approximately 270 ° C.

The surface areas of charcoals obtained from the two kernels by both processes are displayed in **Table 4** for various temperatures of carbonization. The table indicates that the surface areas increase sharply at temperatures ranging between 650° C and 700° C. This increase corresponds to the complete breakdown of the initial cellulosic skeleton of the grains and the formation of a three-dimensional network composed of subunits known as elementary crystallites [20]. A distinct reduction in the surface areas, however, is observable when the temperature of pyrolysis exceeds 750° C; this is attributable to the effects similar to those involved in graphitization [20]. Also note that the surface area of the HRW charcoal by the two-stage process is nearly twice as high as that by the corresponding single-stage process, while that of the corn charcoal is not affected as much. Further work is anticipated to facilitate the rationalization of this observation.

The experimentally obtained adsorption isotherms are shown in **Figure 2** for the charcoals generated by both processes at different temperatures of carbonization. The isotherms are clearly of Type I [21], typical of microporous materials. The enhancement of the microporous nature of the HRW charcoal from the single-stage process with an increase in the temperature of carbonization from 700 to 750° C is evident. Furthermore, the volumes adsorbed by the charcoals produced by the two-stage process are considerably higher than those by the corresponding single-stage process at all relative pressures. Note, however, that these volumes have been determined under conditions of pseudo-equilibrium. The drawbacks of nitrogen adsorption to characterize microporous solids are well known [3, 21]; nevertheless, the volumes adsorbed by the charcoals at a given relative pressure can be compared with one another, since the duration of adsorption in each case is identical and sufficiently long.

Physical Activation

The BET surface areas of activated carbons obtained from the physical activation of the two charcoals generated by both processes, are presented in **Table 5** for various degrees of burn-off. The maximum value attained for the surface area is 1750 m²/ g, corresponding to a HRW activated carbon with a burn-off of approximately 60%, as shown in the table. This carbon has been obtained from the HRW charcoal generated by the two-stage process at 700° C. The total micropore volume, W_o, estimated from the D-R equation [19] for each activated carbon is also listed in **Table 5**. The general trend exhibited by the surface areas and W_o's of most commercial activated carbons with an increase in the degree of burn-off [3] is clearly discernable. However, the maximum surface area of activated carbons produced from corn charcoals generated by both processes does not exceed 700 m² /g. The limiting factor in enhancing the development of their surface areas is the low density and hardness of the feedstock. The loss of strength and hardness experienced by the corn charcoals is appreciable, especially when the degree of burn-off exceeds 30%. Consequently, there is a constraint for developing the microporous nature of these activated carbons.

The nitrogen adsorption isotherms of the aforementioned activated carbons of HRW are shown in **Figure 3**; similar isotherms have been obtained for those of corn and hence, have not been illustrated. Note that the volumes adsorbed near the vicinity of the "knee" of the isotherm are considerably higher than those for the corresponding charcoals shown in **Figure 2**. This effect is expected as the purpose of physical activation is to remove tarry deposits generated by the carbonization process from the entrances of narrow pores as well as to widen existing pores, thereby increasing the accessibility of the finer pores to molecules of adsorbate. Consequently, an appreciably larger internal surface area is "seen" by nitrogen in these activated carbons.

Small-Angle X-ray Scattering

The corrected scattering curve for a HRW charcoal generated by the single-stage process at 700° C is depicted in **Figure 4**. The charcoal sample has been chosen to illustrate its unique scattering behavior. Note

that the intensities are expressed in dimensionless units, i.e., relative to an arbitrary system of measurement in terms of counts per second. Thus, the plot involves the relative rather than the absolute intensity since the latter requires determining the cross-sectional areas of the scattering medium, a task not done in the present work.

A prominent power-law regime is discernable in **Figure 4** over an interval spanning nearly three orders of magnitude in values of q ranging from $3.7 \times 10^{-4} \text{ Å}^{-1}$ to $9.3 \times 10^{-2} \text{ Å}^{-1}$. This large range in q or equivalently, nine orders of magnitude in I(q), is unprecedented and rarely encountered in SAXS analysis. To date, the only other material that has exhibited a similar scattering behavior over a comparable range in either q or I(q) is Beulah lignite coal [8, 16]. This type of scattering is yet to be fully understood; it is plausible that the average size of the macropores in this charcoal is so large that it satisfies the condition, qd being far greater than 1.0, even near the smallest values of q resolvable by experiment [8]. Accordingly, the minimum value of d for this sample is 2500 Å.

In the outer part of the curve, the intensity is observed to decay much more slowly relative to the power-law region. This slowly-decaying outer part is ascribed to the scattering from the micropores [22, 23]. Hence, the porous structure of the HRW charcoal can be characterized by two different length scales corresponding to the macropores and micropores. Therefore, the total intensity scattered can be considered to be the sum of the intensities from the two types of pores provided that they scatter independent of each other.

Surface Fractal Dimension from SAXS

The exponent, α, in Eq. 3 has been recovered from weighted, first-order least-square fit of the data [24], over the range of q shown in **Figure 4**. This procedure assigned a weight to every data point of the corrected intensity that is inversely proportional to the square of the calculated statistical uncertainty in the value of the corrected intensity [10]. The value of α thus obtained for the HRW charcoal is 3.55 ± 0.10, over the interval, $3.7 \times 10^{-4} \text{ Å}^{-1} < q < 9.3 \times 10^{-2} \text{ Å}^{-1}$. The non-integral value of α implies that the interfaces of the pores of the charcoal, producing the scattering in this range of q, can be considered to exhibit fractal properties, or alternatively, the power-law distribution of these pores can be associated with a non-integral dimension [14, 23]. Consequently, the d_{SF} for this sample evaluated on the basis of Eq. 3 is 2.45 ± 0.10.

The length scales, ξ's, corresponding to the power-law regime can be estimated from the approximate Bragg relation, $\xi = \pi / q$ [25]; hence, the property of geometrical self-similarity is satisfied over yardsticks ranging from approximately 35 Å to 8500 Å. From this size range, it is evident that the interfaces of the macropores as well as those of the mesopores of the HRW charcoal are surface fractals [9]. This fact is yet to be verified by other techniques such as scanning electron microscopy and atomic force microscopy. Nonetheless, marked increases are expected in the values of d_{SF}'s for the grains upon carbonization [10]; the degradation and subsequent rearrangement of the carbon skeleton combined with the violent release of the volatile matter are likely to generate rough interfacial surfaces. Considering the unusually large span of the length scales associated with the self-similar behavior of the pores, however, the results of the present investigation should be interpreted with discretion until it is fully corroborated by evidence from independent techniques. We are in the process of analyzing the SAXS behavior of other charcoals and activated carbons obtained from the grains under different process conditions. It is desirable to compare and contrast the scattering behavior of these charcoals and activated carbons and interpret the results based on similarities / differences expected in their pore structure.

Mean Radii of Gyration

The mean radii of gyration, R_g, of the micropores of the HRW charcoal has been obtained by applying the Guinier equation, Eq. 1, to the outer portion of the curve shown in **Figure 4**. Note that this equation is valid only when the product, qR_g, is not appreciably greater than 1.0. Furthermore, the scattering system must be composed of randomly oriented, independent scatterers [11]. The R_g thus obtained for the HRW charcoal is approximately 6.7 Å. The intricacies involved in the procedure for computing R_g from the Guinier plot have been expounded elsewhere [10]. This value of R_g or equivalently, the average pore size d, compares favorably with the characteristic average dimension of the micropores, B, computed from the D-R equation [19]. Hence, the analysis has revealed that the results from SAXS are consistent with those obtained from adsorption data.

SUMMARY

Whole grain kernels of HRW and corn are potentially viable feedstocks for producing activated carbons with high surface areas. These activated carbons have been obtained by the physical activation of charcoals generated by a single-stage as well as a two-stage pyrolytic process at 850° C in an atmosphere of CO_2. For both kernels, the terminal yield of charcoals and the surface areas of the corresponding activated carbons obtained by the two-stage process at various temperatures of carbonization are appreciably higher than those by the single-stage process. Moreover, the surface areas and the total micropore volumes of the HRW activated carbons, produced from charcoals generated by the two-stage process at an optimum temperature of 700° C, are comparable to those of commercial carbons. The investigation has also shown that whole grains of HRW are preferable to those of corn, on account of the superior textural characteristics of the resulting charcoals and their greater resistance to abrasion during the activation process. The SAXS analysis has revealed the fractal nature of the interfaces of pores over unexpectedly large length scales in a HRW charcoal chosen for illustration as a representative surface fractal system. In addition, the SAXS analysis has confirmed the existence of two independently scattering entities of vastly different dimensions in this sample. These results obtained from the pyrolysis of a naturally occurring product may prove to be beneficial for investigating the influences of fractal surfaces on the rates of heterogeneous gas-solid reactions.

ACKNOWLEDGEMENT

LITERATURE CITED

1. Peaff, G., C & EN, November 14, 15-19 (1994).
2. Lussier, M. G., J . C. Shull, and D. J. Miller, Carbon, 32, 1493-1498 (1994).
3. Rodriguez-Reinoso, F., in "Carbon and Coal Gasification," pp. 601-641, J. L. Figueiredo and J. A. Moulijn, eds., NATO ASI Series, Series E: Applied Sciences 105, Martinus Nijhoff, Dordrecht (1986).
4. Rodriguez-Reinoso, F., and M. Molina-Sabio, Carbon, 30, 1111-1118 (1992).
5. Gonzalez, M. T., M. Molina-Sabio, and F. Rodriguez-Reinoso, Carbon, 32, 1407-1413 (1994).
6. Guinier, A., G. Fournet, C. B. Walker, and K. L. Yudowitch, Small-Angle Scattering of X-rays,

pp. 3-4, 17, 24-28, 80, Wiley, New York (1955).

7. Glatter, O., and O. Kratky, Small-Angle X-ray Scattering, pp. 126-146, 167-188, Academic Press, New York (1982).
8. Schmidt, P. W., Proceedings of the XVIth Conference on Applied Crystallography, Cieszyn, Poland, August 22-26 (1994).
9. Schmidt, P. W., in The Fractal Approach to Heterogeneous Chemistry, pp. 67-78, D. Avnir, ed., John Wiley, Chichester (1989).
10. Venkataraman, A., A. A. Boateng, L. T. Fan, and W. P. Walawender, "An Investigation of the Surface Fractality of Wood Charcoals through Small-Angle X-ray Scattering", Accepted for Publication in the AIChE J (1995).
11. Schmidt, P. W., D. Avnir, H. B. Neumann, A. Hoehr, M. Steiner, D. Levy, J. Lin, Y. M. Kapoor, and J.S. Lin, pp. 1-34, Unpublished research (1995).
12. Porod, G., Kolloid Z., 124, 93-99 (1951).
13. Mandelbrot, B. B., The Fractal Geometry of Nature, pp. 25-83, Freeman, San Francisco (1982).
14. Pfeifer, P., and D. Avnir, J. Chem. Phys., 79, 3558-3564 (1983).
15. Fan, L. T., D. Neogi, and M. Yashima, An Elementary Introduction to Spatial and Temporal Fractals, pp. 1-10, Springer-Verlag, Berlin (1991).
16. Bale, H. D., and P. W. Schmidt, Phys. Rev. Lett., 53, 596-599 (1984).
17. Pfeifer, P., and P. W. Schmidt, Phys. Rev. Lett., 60, 1345 (1988).
18. Boateng, A. A., L. T. Fan, W. P. Walawender, and C. S. Chee, Fuel, 70, 995-1000 (1991).
19. Dubinin, M. M., and H. F. Stoeckli, J. Col. Interf. Sci., 75, 35-42 (1980).
20. Wigmans, T., in "Carbon and Coal Gasification," pp. 601-641, J. L. Figueiredo and J. A. Moulijn, eds., NATO ASI Series, Series E : Applied Sciences 105, Martinus Nijhoff, Dordrecht (1986).
21. Gregg, S. J., and K. S. W. Sing, Adsorption, Surface Area and Porosity, pp. 193-195, Academic Press, London (1982).
22. Kalliat, M., C. Y. Kwak, P. W. Schmidt, in "New Approaches in Coal Chemistry," p. 3, B. D. Blaustein, B. C. Bockrath, and S. Freidman, eds., ACS Symposium Series 169, Washington, D.C. (1981).
23. Bale, H. D., M. L. Carlson, M. Kalliat, C. Y. Kwak, and P. W. Schmidt, in "The Chemistry of Low-Rank Coals," pp. 79-94, H. H. Schobert, ed., ACS Symposium Series 264, Washington, D.C. (1984).
24. Bevington, P. R., Data Reduction and Error Analysis for the Physical Sciences, pp. 106-108, McGraw-Hill, New York (1969).
25. Hohr, A., H. Neumann, P. W. Schmidt, P. Pfeifer, and D. Avnir, Physical Review B, 38, 1462-1467 (1988).

Table 1. Elemental Analysis of Grains

Element	Corn (%)	HRW (%)
Carbon	48.4	45.3
Hydrogen	7.2	6.6
Oxygen	43.1	45.1
Nitrogen	0.1	0.1
Ash	1.5	1.6

Table 2. Effect of Temperature on Charcoal Yields from the Single-Stage Process

Temperature ($^{\circ}$C)	Corn (%)	HRW (%)
270	44.2	47.6
350	32.9	34.3
450	18.2	20.8
650	13.7	17.7
700	12.2	15.6
750	10.4	13.5

Table 3. Comparison of Charcoal Yields from the Single-Stage and Two-Stage Processes

Temperature ($^{\circ}$C)	Corn (%)		HRW (%)	
	Single-Stage	Two-Stage[δ]	Single-Stage	Two-Stage[δ]
650	13.7	18.5	18.3	24.9
700	12.2	17.2	15.6	22.7
750	10.4	14.8	13.5	20.3

δ : Temperature of the first stage was 270° C

Table 4. BET Surface Areas of Charcoals

Temp. ($^{\circ}$C)	Corn (m^2/g)	HRW (m^2/g)
575[α]	15	13
650[α]	37	57
700[α]	72	110
750[α]	70	84
800[α]	16	14
850[α]	5	8
700[β]	109	200
850[β]	24	25

α : Single - stage process
β : Two-stage process

Table 5. Textural Characteristics of Activated Carbons[δ]

Burn-off (%)	Temp. of Pyrolysis	Corn		HRW	
		BET(m^2/g)	W_0 (cm^3/g)	BET(m^2/g)	W_0 (cm^3/g)
10	700° C[β]	325	0.10	190	0.03
20	700° C[β]	390	0.12	434	0.11
30	700° C[β]	525	0.19	600	0.23
50	700° C[β]	695[τ]	0.24	1350	0.51
60	700° C[β]	—	—	1750	0.68
20	700° C[α]	303	0.08	333	0.07
30	700° C[α]	407	0.14	435	0.10
20	300° C[α]	375	0.11	405	0.10
30	300° C[α]	500	0.18	564	0.19

α : Single-stage process
β : Two-stage process
δ : Activation at 850 C with CO_2
τ : Condition of carbon was fragile
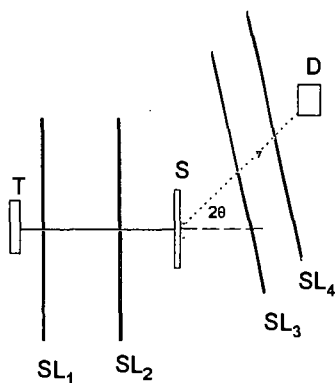
Figure 1. Schematic representation of a SAXS system:
T is the X-ray tube; SL₁, SL₂, SL₃, and SL₄, the
collimating slits; S the sample holder; and D the detector.
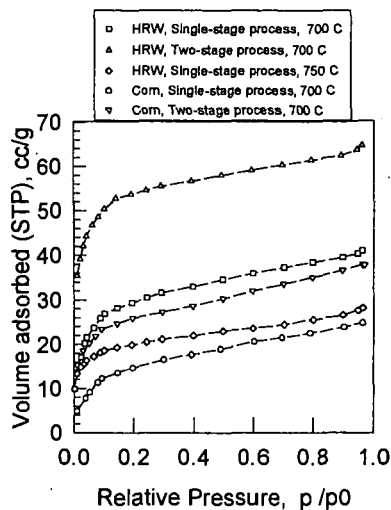
Figure 2. Adsorption isotherms for the charcoals
obtained by both single-stage and two-
stage processes at various temperatures.
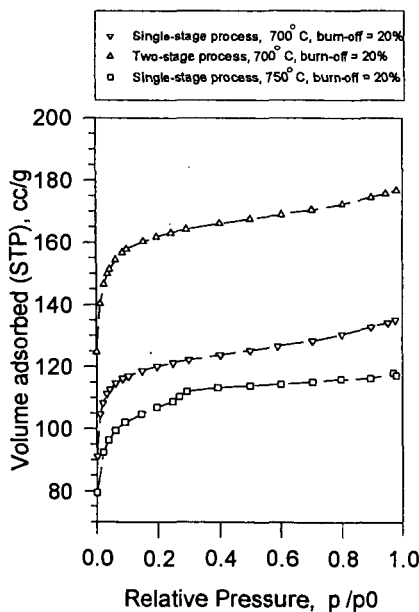
Figure 3. Adsorption isotherms of HRW activated
carbons obtained from charcoals genera-
ted by both single-stage and two-stage pro-
cesses at various temperatures.
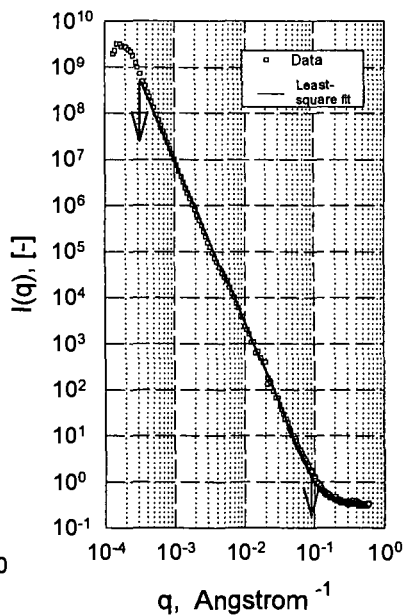
Figure 4. Relative scattered intensity versus the
scattering wave vector for a charcoal
of hard red winter wheat pyrolyzed
at 700 C.

ADSORPTIVE PROPERTIES OF FLY ASH CARBON

U.M. Graham, T.L. Robl, R.F. Rathbone
Center for Applied Energy Research, 3572 Iron Works Pike,
University of Kentucky, Lexington, Kentucky 40521l-8433
and and C.J. McCormick
Advanced Pozzolan Technologies, Inc.,
175 West Wieuca Rd., NE, Atlanta, Georgia 30342

Keywords: Fly ash, adsorbents, pore structures, activation mechanism

INTRODUCTION
The driving force behind the development of this research project has been the increasing concerns about the detrimental effects of high carbon carryover into combustion ash. Without the carbon, combustion ash can be utilized in cement industry avoiding environmental implications in landfill operations. Because the carbon surfaces have been structurally altered while passing through the combustor, including the formation of a macro-porous surface, fly ash carbons, after separation from the ash, may constitute a unique precursor for the production of adsorbents. This paper discusses a novel approach for using fly ash carbons in the cleanup of organic pollutants.

Fly Ash Carbon
Fly ash carbon may take a special place amongst the carbon materials that are produced either as a major co-product (e.g. in the pyrolysis of different starting materials for the production of liquids and gases) or processed primarily for the manufacture of active carbons and carbon-carbon composites. The fly ash carbons occur in the residual coal ash as a result of the incomplete combustion process. Due to the increasing applications of activated carbons [1,2], this study has been focused on the preparation of cost-effective adsorbents as a substitute for activated carbon materials. Today, only few efforts have been made to investigate the advantages of fly ash carbons as a starting material to produce a powerful adsorbent [3,4]. The main objective of this study, therefore, has been to explore the possibility of using fly ash carbon as an adsorbent for the removal of organic pollutants including phenols.

Manufacturing and commercialization have not yet been considered for the fly ash carbons, mainly because there still prevails a number of problems related to fly ash carbons. A critical impediment to the utilization of fly ash carbon is the fact that these particles need to be recovered from the ash. Recently the removal of the carbons from fly ash has received major attention, because the mandated lowering of NO_x emissions as a consequence of the Clean Air Act, resulted in an overall increase of unburned coal particles in the ash [5,6]. This has significant consequences in terms of utilization potential of the ash. Carbon separation allows the recovery of a low LOI (loss on ignition) ash suitable for cement applications [5-7], but also entails the concentration of unburned carbon particles that have undergone partial carbonization in the combustion furnace. Once the carbons are recovered the topics that are focused on in this study are (1) what controls the optimum amount of pores in the fly ash carbons, (2) what influences surface morphologies and surface functional groups, and ultimately (3) what controls the potential of fly ash carbons to be activated and upgraded to a commercial product. It should be recognized in this paper that the word carbon is used interchangeably with unburned coal particles.

MATERIALS AND PROCEDURES
Combustion Char Characteristics
The concentration of unburned carbon particles in fly ash varies greatly among ashes produced by different utilities, and the nature of the microscopic carbon forms can also be distinct [7-10]. The fly ash carbons are composed of three petrographically distinguishable types, namely, inertinite, isotropic coke and anisotropic coke; the absolute quantities of which may vary depending on feed stock and boiler conditions [9]. Both coke forms are most likely derived from vitrinite macerals and are artifacts of incomplete combustion. Inertinite is relatively unreactive in the thermal processing of coal and occurs essentially unaltered in the fly ash, while "coke" is produced from melting, devolatilization, swelling, and resolidification of the reactive macerals vitrinite and liptinite. Samples were derived from Midwestern power stations after NO_x conversion. The proportions of isotopic : anisotropic coke: inertinite in 21 fly ashes are shown in Figure 1, indicating that petrographically fly ash carbon fits into three broad ranges.

The residence time of the fly ash carbons in the furnace causes the particle surfaces and in some types of coal particles the entire grains to be perforated with submicron-sized pores. Extensive parallel orientation of individual crystallites in the carbonaceous matrix relates to the porosity of the fly ash carbons, leaving few micro-voids between the crystallites and low micro-porosity in the

precursor phase. For the purpose of this study it was of paramount importance to select a carbon concentrate with a high isotropic carbon fraction as preliminary tests indicated a preferential adsorption capacity for samples enriched in the isotropic "coke". The adsorptive properties of the fly ash carbon may be
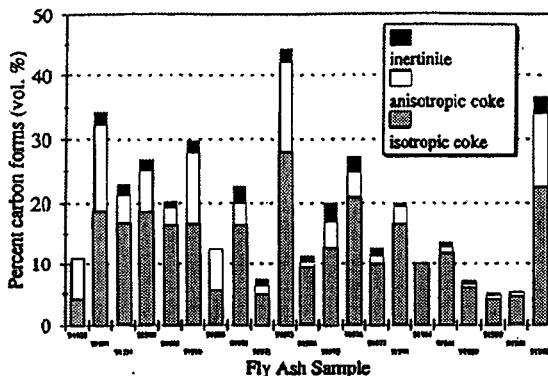

Figure 1   Variations in carbon forms and centent of 21 coal combustion fly ash samples. The samples are ASTM C618 Class F (1992 -1994 CAER survey data).

enhanced in physical and/or chemical treatment if the structural order of the individual crystallites and their mutual orientation may be affected by the treatment. Structural differences among the two types of fly ash carbon (isotropic vs. anisotropic coke) were studied using SEM applications and are illustrated in Figures 2 and 3.

Figure 2

SEM image of isotropic carbon grain. Effect of combustion is clearly visible on the surface with process induced macro-porosity. The irregularity of the char surface suggests that partial oxidation must have occurred with increased surface areas and perforated structures at the outside layer of the carbon grains. This porosity may serve as infrastructure for steam and catalysts during activation.
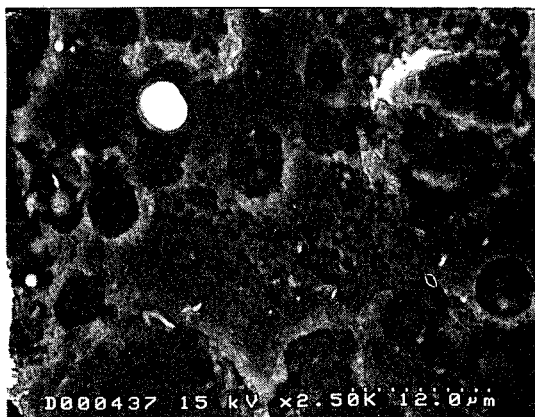
The pore sizes among different isotropic grains vary immensely. During combustion the isotropic char particles were observed to form a macro-porous network of carbonized material. The remaining coke between large pores was subsequently observed at higher magnification. Its surface is irregular and is characterized by the presence of numerous smaller (10^1 nanometer) pores. Intercalated Si-Al-rich fly ash spheres occur in the larger pores within the carbonaceous matrix and aid to stabilize the macro structure of the particles. Figure 3 shows the structural alignment observed in the anisotropic char particles.

Carbon Concentrates
The sample chosen for study for preparing an effective adsorbent from fly ash carbon was focused on a material with a relatively high ratio of isotropic to anisotropic coke. After separation of the fly ash carbon a concentrate sample composed of 81.9 wt % carbon was prepared. Chemical analysis of the carbon concentrate sample is given in Table 1.

TABLE I

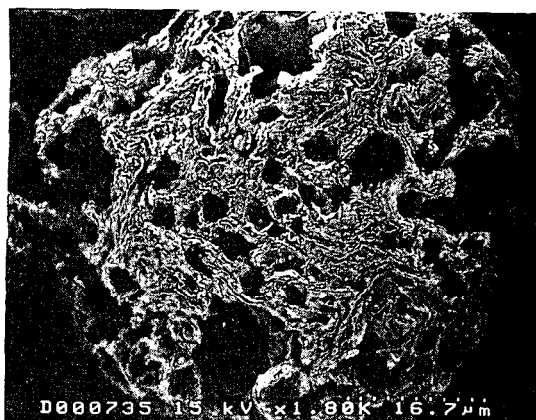| Concentrate Sample:	81.9 % C	9.3 % SiO$_2$	8.6 % Al$_2$O$_3$

Figure 3

SEM image of anisotropic char particle. The structure clearly indicates structural alignment within the anisotropic particle and less process induced porosity compared to the isotropic coke particle illustrated in Figure 1. The alignment is expected to affect the particle's capacity to be activated.

The manufacture of activated carbons typically involves two main stages, the carbonization of the precursor, and the activation of the resulting char. During carbonization, carbon atoms group themselves into sheets of condensed aromatic ring systems, with an irregular and often bent arrangement. It becomes quite obvious that within the combustion chamber of a coal utility boiler a combination of these processes takes place, affecting each coal particle. Therefore, the experimental part will not involve a separate carbonization step.

EXPERIMENTAL
The carbon concentrate sample (81.9 % C) was used in two types of activation experiments involving (a) physical activation using steam and CO$_2$ mixture at 900°C, and (b) chemical activation with potassium hydroxide with a 4:1 ratio of carbon : KOH. The synthesis procedure involved dehyration of the concentrate sample at 300°C followed by activation at 900 C for one hour. Activated products were cooled, washed with nitric acid (2mol/ml) and analysed using thrmogravimetric analysis (TGA). N$_2$ adsorption isotherms were analysed for activated and starting materials using an Auatosorb-1-MP (QUANTACHROME) instrument to determine changes in surface areas and pore volumes after activation. Surface areas were calculated using the BET equation[11].

CHARACTERISTICS OF ACTIVATED FLY ASH CARBON
The macro-porosity of the precursor carbon concentrate was observed to be 19 m^2/g. The macropore framework constitutes an infrastructure that may readily allow steam/CO$_2$ to infiltrate the fly ash carbon during activation, and the intercalation of KOH catalyst, facilitating the development of higer surface areas. The SEM investigations of the activated materials revealed a much rougher surface than that of the precursor, with corresponding increases in BET surface areas. Physical activation for one hour resulted in chars with corresponding BET surface areas ranging from 310 to 380 m^2/g for three experiments. Chemical activation for the same amount of time resulted in an enhanced pore development with higher BET surface areas corresponding to 730 to 840 m^2/g for four experiments (Table 2). Chemical activation improves not only the total surface area of the fly ash carbon materials, but greatly increases the number of micropores in the processed materials as indicated by differences in micro and meso pore volumes (Table 2).

TABLE 2	Surface Area	Pore Volume [cc/g]
Precursor Fly Ash Carbon	19 m^2/g	-
Physically Activated Precursor	310 - 380 m^2/g 4 samples	Micro=0.18 Meso=0.33
Chemically Activated Precursor	730 - 840 m^2/g 3 samples	Micro=0.41 Meso=0.13

The adsorption capacity of the activated fly ash carbons will depend on the surface area and porosity

of the carbonaceous material as well as the hydrophobicity of the substituent.

Phenol Adsorption Potential
The presence of phenolic compounds and other organic pollutants typically present in water is of paramount concern to health departments. In past efforts the adsorption of these compounds from aqueous solutions, essentially that of phenol and p-nitrophenol, has been studied [12-14], and major findings indicated that the adsorption of phenols not only depends on the porosity of the adsorbent, but was significantly influenced by surface oxygen complexes present on the activated carbons used. The fact that the fly ash carbons spent a short residence time in an oxidizing furnace at combustion temperatures led to the hypothesis that the process induced surface chemistry of the fly ash carbons may help create a unique precursor material for carbons with affinity to adsorb phenolic compounds.

The experiments included adsorption of phenol (dissolved in aqueous solution) on (a) physically activated fly ash carbon, (b) chemically activated fly ash carbon and (c) commercial carbon (NORIT). Adsorption isotherms were determined for solutions containing 100 mg of dispersed carbon at 298 K. Samples were obtained for different time intervals with a maximum exposure time of 3×10^3 minutes. Phenol adsorption potential was determined spectrophotometrically using maximum UV absorbance wavelength for phenol (269 nm). Results are illustrated in Figure 4.
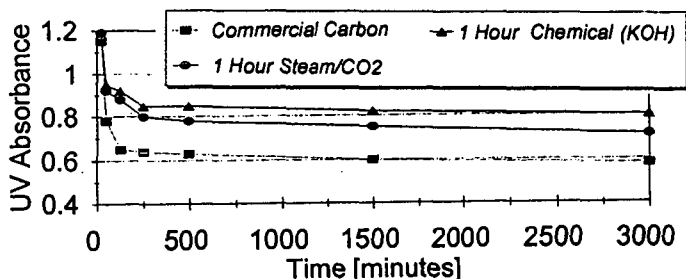
Figure 4   Illustration of the phenol adsorption capacities of (a) physically activated fly ash carbon, (b) chemically activated fly ash carbon and (c) commercial carbon

Results suggest that although chemically activated fly ash carbon has higher surface areas and greater micropore volumes, its adsorption potential for phenol is not much superior over that of the physically activated material. Both physically and chemically activated fly ash carbons exhibit excellent potential for phenol adsorption compared with a commercially available carbon (NORIT).

SUMMARY
Fly ash carbons constitute the char particles that are left in fly ash after the incomplete combustion of coal in the furnace, rendering fly ash above spec for ASTM C618 applications for cement. A beneficiation process allows the selective separation of unburned carbon from fly ash to be used for upgrading into a higher value product. The porosity, surface area, and surface chemistry of fly ash carbons before and after activation were characterized using mercury porosimetry, BET analysis, and liquid-phase adsorption of phenolic compounds

The results of the study underline that adsorbents produced from fly ash carbon as precursor matrix exhibit a remarkable developmental potential. It has been demonstrated in two different ways, by physical activation using a steam/CO$_2$ treatment and chemical activation using KOH, that activation of the fly ash carbon plays a key role in improving the adsorptive properties. The adsorptive capacity of the fly ash carbon produced either by steam activation and/or chemical treatment with KOH lead to the production of active carbons with an optimal range of micropores and adsorption activity towards phenolic compounds. These observations lead to the conclusion that the maximum capacity and the optimum potential of the fly ash carbons may be improved by applying controlled

experiments that help evaluate the optimum activation temperature, activation time and activation environment. In practical manufacturing and commercialization have not yet been considered for the fly ash carbons, mainly because there still remains a number of problems related to carbonaceous fly ash particles that must be solved in order to achieve high enough performance.

REFERENCES

1   Juntgen, H., Carbon, **15**, 273, 1977
2   Peaff, G., C&EN, Nov. 14, 15-19, 1994
3   Zhonghua, H. and Vansant, E.F., Carbon, **33** (9), 1293-1300, 1995
4   Zhonghua, H., Zhu, H. and Vansant, E.F., Separation Technology (Edited by E.F. Vansant) p. 895, Elsevier Science B.V., Amsterdam (1994).
5   Groppo, J.G., Robl. T.L. and McCormick, C.J., Proceedings of 1995 International Ash Utilization Symposium, Lexington, Kentucky, October 1995
6   Robl, T.L., Hower, J.C., Graham, U.M., Rathbone, R.F., and Medina, S.S., Proceedings of 12th Annual International Pittsburgh Coal Conference, 121, 1995
7   Hurt, R.H. and Gibbins, J.R., Fuel, **74** (4), 471, 1995
8   Bailey, J.G., Tate, A., Diessel C.F.K., and Wall, T.F., Fuel, **69**, 225, 1990
9   Hower, J.C., Rathbone, R.F., Graham, U.M., Groppo, J.G., Brooks, S.M., and Robl., T.L., 11th International Coal Testing Conference, p. 49, 1995
10   Vleeskens, J.M., Haasteren van, T.W.M.B., Roos M., and Gerrita, J., Fuel, 67 (3), 427, 1988.
11   Brunauer, S., Emmett, P.H. and Teller, E., *J. Amer. Chem. Soc.*, **60**, 309, 1938
12   Moreno-Castilla C., Rivera-Utrilla, J., Lopex-Ramon, M.V., and Carrasco-Marin, F., Carbon, Vol 33 (6) 845, 1995.
13   Mattson J.S. and Mark, H.B., Activated Carbon, Surface Chemistry and Adsorption form Solution, Marcel Dekker, New York (1971).
14   Moreno-Castilla, C., Carrasco-Marin, F., and Lopez-Ramon, M.V., Langmuir 11, 247, 1995.

PREPARATION OF ACTIVATED CARBONS WITH MESOPORES BY USE OF ORGANOMETALLICS

Yoshio Yamada, Noriko Yoshizawa, Takeshi Furuta and Minoru Shiraishi
National Institute for Resources and Environment,
Tsukuba, Ibaraki 305 JAPAN
Shigeyuki Kojima, Hisashi Tamai and Hajime Yasuda
Department of Applied Chemistry, Hiroshima University,
Higashi-Hiroshima 739 JAPAN

INTRODUCTION

Activated carbons are commercially produced by steam or CO_2 activation of coal, coconut shell and so on. In general the carbons obtained give pores with a broad range of distribution. Recently, Matsumura[1] and Jagtoyen et al.[2] have reported that chemical activation with KOH or H_2PO_3 provides microporous carbons with high surface area. These activated carbons are suitable for separation of molecules with small size i.e., removal of pollutant gases from exhausted substances. For applications to adsorption of macromolecules in a liquid media, however, it is important to prepare activated carbons having meso- or macropores.

Tamai et al. have found that steam activation of coal tar pitch homogeneously mixed with rare earth metal complexes brings about mesoporous carbons[3]. Also, the carbons thus obtained were confirmed to be very effective to selective adsorption of giant molecules such as humic acids and dextrans.

This study aims to provide mesoporous activated carbons from coals by use of various organometallic compounds. The carbons prepared are characterized by nitrogen adsorption to evaluate the pore size, and the crystal forms and size of metal compounds on the carbons are investigated by means of X-ray diffraction and transmission electron microscopy. The formation mechanism of the mesopres is also discussed on the basis of the results.

EXPERIMENTAL

Three kinds of coals different in rank, i.e., Miike, Taiheiyo and Morwell coals were used for this study. The analytical data of the coals are summarized in Table 1. Each coal with particle size of minus 100 mesh was dispersed in tetrahydrofuran(THF) in Ar atmosphere. Al, Y, Ti, or Zr acetylacetonate(Al(acac)$_3$, Y(acac)$_3$, TiO(acac)$_2$, Zr(acac)$_4$) solution of THF was added to the coal dispersion and the mixture was stirred at room temperature for 1h under Ar gas. Thereafter, THF solvent was removed from the mixture by flash distillation under vacuum at room temperature and then 100℃. The weight percent of each metal added to the coal was adjusted to 2.5wt% before activation. Steam activation was carried out at 900℃ for various times(3～25min).

Nitrogen adsorption isotherms at 77K were obtained by Quantachrome Autosorb-6. The X-ray diffraction measurement and transmission electron microscopic observation were performed using Rigaku RU-300 with a CuKα radiation and Philips CM30 equipments, respectively.

RESULTS AND DISCUSSION

<u>Surface area and mesopore ratio.</u> Figure 1 shows the change in BET surface area of various activated carbons obtained from Miike coal against activation time at 900℃. The data of the carbons from the coal alone are also added for comparison in this figure. When Al(acac)$_3$ was loaded on the coal and activated, the surface area increases with the time. On the other hand, the coal containing TiO(acac)$_2$ results in the carbon with an approximately constant surface area (ca.500m²/g) over these activation times. The pore size distribution and mesopore(2～50nm) area of each sample were obtained from nitrogen desorption by using BJH method[4]. Mesopore

ratio is given by dividing the mesopore area by the BET one. The ratios obtained were plotted against activation time(Fig. 2). The result shows that the mesopore ratios in the carbons increase with activation time. It is noteworthy that addition of the Ti chelate enhances mesopore ratio. The similar behavior was observed in the case of Taiheiyo and Morwell coal. The results are summarized in Table 2 and 3. The $TiO(acac)_2$ compound promotes to develop mesopores also in both cases and, especially in the activated carbons from Taiheiyo coal ca. 90% of total pores are consisted of mesopore structures, as can be seen in Table 2. Brown coals such as Morwell easily produce micropore structures with heat-treatment. Therefore, the mesopore ratio of the activated carbons from Morwell coal with or without metal is not so high compared with those from other coals, but it is obvious that the Ti complex contributes to the development of mesopore.

<u>X-ray diffraction and TEM observation.</u> As described above, it was found that $TiO(acac)_2$ dispersed on coals enhances the formation of mesopores. In order to understand the formation mechanism of these carbons, it is necessary to examine the form and size of Ti compounds on the activated carbons. Thus, the species of the compounds on the carbons were determined by X-ray diffraction. A profile of the carbon from Taiheiyo coal with $TiO(acac)_2$ is given in Fig. 3, together with that from the coal without metal. Several strong peaks due to metal compounds in Taiheiyo coal which contains a high amount of ash(Table 1) appear in Fig.3(a). When $TiO(acac)_2$ loaded on the coal was activated with steam, the chelate is considered to decompose and form the cluster of the Ti oxides. The TiO_2 crystals with rutile and brucite structures can be evidently identified from the lattice constants of the profile indicated in Fig. 3(b). The same results were obtained in the case of Miike and Morwell coal.

The transmission electron photomicrographs of the activated carbons from Taiheiyo coal are shown in Fig. 4. Whereas a typical amorphous structure due to carbon layers was observed in the activated carbon from the coal alone, there are some voids and TiO_2 crystals with the size of few nm in the carbon with the metal(Fig. 4(b)) and at the same time these are closely present each other. Such a morphology was seen also in the carbons from the other coals. The particle size distribution of the crystals was estimated by an image analyzing technique(Fig. 5). Although the distribution is somewhat different in coal rank, most of the particles are ranging from 2 to 12 nm in diameter. Taking into account that the size of the mesopores in the activated carbons is comparable to that of TiO_2 crystals, the behaviors of the metal oxides, such as migration or lacking may cause the generation of these mesopores.

CONCLUSION
Mesoporous carbons were prepared by steam activation of metal acetylacetonates dispersed on Miike, Taiheiyo and Morwell coal. The $TiO(acac)_2$ complex was effective for the occurrence of these carbons. The surface areas and mesopore ratios were evaluated by analyzing the nitrogen adsorption isotherms. In addition, the size distribution of TiO_2 crystals present on the carbons was examined by transmission electron microscopic observation. As a result it was found that the development of the mesopores is associated with the formation of TiO_2 crystals on the carbons.

REFERENCES
1. Matsumura,Y., *Chem. & Chem. Ind.*,1990,43(3),358-360.
2. Jagtoyen,M.,Thwaites,M.,Stencel,J.,MacEnaney,B.and Derbyshire,F., *Carbon*,1992,30(7),1089-1096.
3. Tamai,H.,Kakii,T.,Hirota,Y.,Kumamoto,T. and Yasuda H., *Chem.Mater.*, in press.
4. Barrett,E.P.,Joyner,L.G. and Halenda,P.P., *J.Am.Chem.Soc.*, 1951, 73,373-380.

Table 1 Analysis of coals

Coal	C	H	N	S + O(diff)	Ash
	(wt%, daf)				(wt%, dry)
Miike	83.8	6.8	1.0	8.5	8.7
Taiheiyo	75.7	6.3	1.3	16.7	14.2
Morwell	65.0	4.8	0.6	29.5	1.6

Table 2 Pore characteristics of activated carbons(AC) from metal/Taiheiyo coal

Sample	Time * (min)	Yield (%)	BET surface area (m^2/g)	Mesopore surface area (m^2/g)	Mesopore ratio (%)	Average pore size (nm)
Blank/AC	6	16.3	134	72	54.0	6.24
$Y(acac)_3$ /AC	6	16.9	70	50	71.8	10.39
$Al(acac)_3$ /AC	6	20.6	347	112	32.3	3.84
$TiO(acac)_2$/AC	6	20.9	174	156	89.7	7.06
$Zr(acac)_4$ /AC	6	18.8	163	80	48.9	5.15

* at 900℃

Table 3 Pore characteristics of activated carbons(AC) from metal/Morwell coal

Sample	Time * (min)	Yield (%)	BET surface area (m^2/g)	Mesopore surface area (m^2/g)	Mesopore ratio (%)	Average pore size (nm)
Blank/AC	3	20.8	888	269	30.3	3.72
$Y(acac)_3$/AC	6	14.0	729	186	25.5	3.73
$Al(acac)_3$/AC	6	20.9	791	162	20.5	3.24
$TiO(acac)_2$/AC	6	15.6	806	431	53.6	4.73
$Zr(acac)_4$/AC	3	24.5	794	118	14.9	2.99

* at 900℃
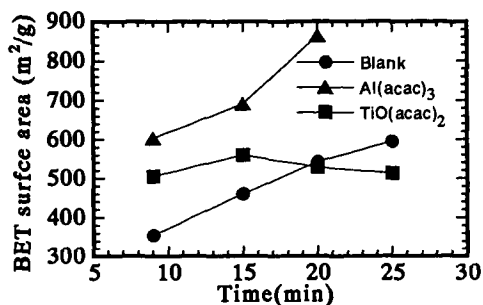
Fig. 1 BET surface area of activated carbon
from metal/Miike coal
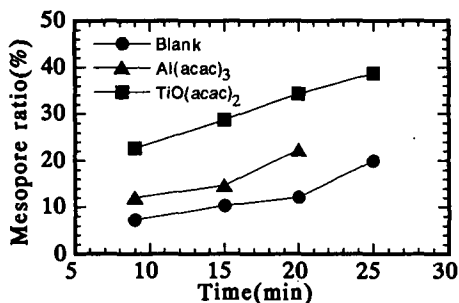
Fig. 2 Mesopore ratio of activated carbons
from metal/Miike coal
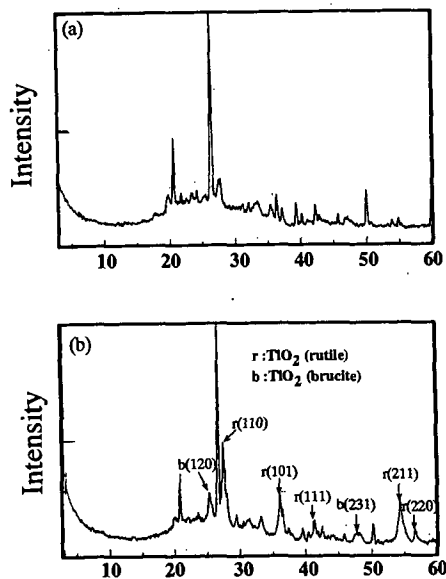
Fig. 3 X-ray diffraction profiles of AC from (a)Taiheiyo coal
and (b)Taiheiyo coal/TiO(acac)$_2$

Pore →

(b)

AC from Taiheiyo /TiO(acac)$_2$

10 nm

AC from Taiheiyo coal

(a)
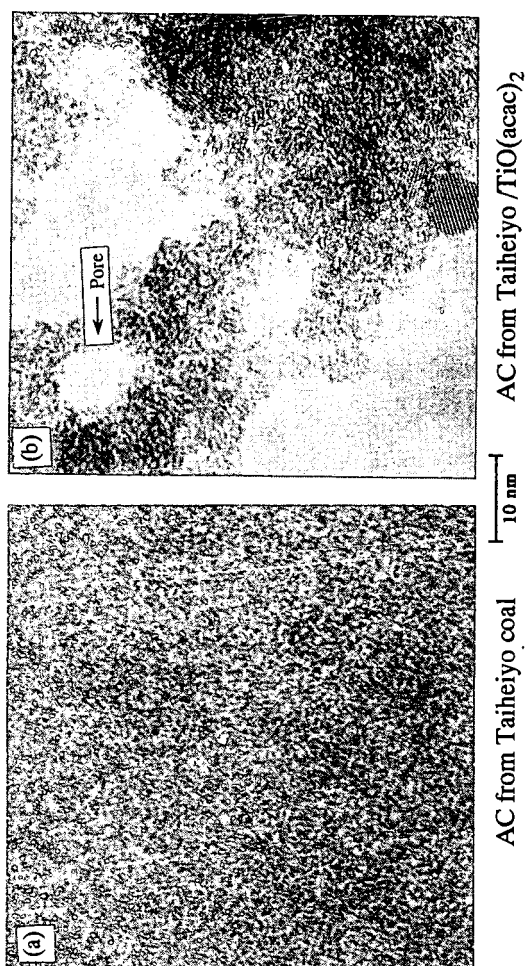
Fig. 4 Transmission electron photomicrographs of AC from
(a) Taiheiyo coal and (b) Taiheiyo coal/TiO(acac)$_2$

Miike
Taiheiyo
Morwell

Frequency (%)

Diameter (nm)
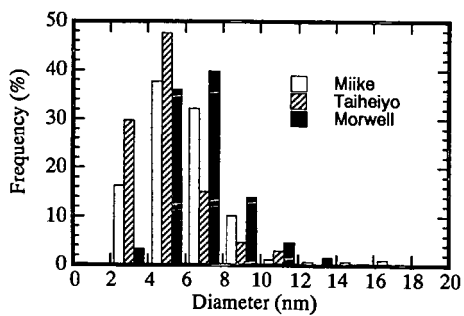
Fig. 5 Histogram of particle size of TiO$_2$ on
activated carbon from coal/TiO(acac)$_2$

GASIFICATION CHARACTERISTICS OF AN ACTIVATED CARBON CATALYST DURING THE DECOMPOSITION OF HAZARDOUS WASTE MATERIAL IN SUPERCRITICAL WATER

Yukihiko Matsumura, Frederick W. Nuessle, and Michael J. Antal, Jr.
Hawaii Natural Energy Institute
University of Hawaii at Manoa, Honolulu, HI 96822

Key Words -- Carbon gasification, activated carbon, supercritical water

INTRODUCTION

Recently, carbonaceous materials including activated carbon were proven to be effective catalysts for hazardous waste gasification in supercritical water [1]. Using coconut shell activated carbon catalyst, complete decomposition of industrial organic wastes including methanol and acetic acid was achieved. During this process, the total mass of the activated carbon catalyst changes by two competing processes: a decrease in weight via gasification of the carbon by supercritical water, or an increase in weight by deposition of carbonaceous materials generated by incomplete gasification of the biomass feedstocks. The deposition of carbonaceous materials does not occur when complete gasification is realized. Gasification of the activated carbon in supercritical water is often favored, resulting in changes in the quality and quantity of the catalyst. To thoroughly understand the hazardous waste decomposition process, a more complete understanding of the behavior of activated carbon in pure supercritical water is needed.

The gasification rate of carbon by water vapor at subcritical pressures was studied in relation to both coal gasification and generating activated carbon [2]. It is known that carbon reacts with water vapor via:

$$C + H_2O \rightarrow CO + H_2 \tag{1}$$

$$CO + H_2O \rightarrow CO_2 + H_2 \tag{2}$$

A reaction mechanism which considers the competitive adsorption of water and hydrogen molecules to the same active sites was proposed [3-5]:

$$H_2O \rightleftarrows (OH)(H) \rightleftarrows (O)(H_2) \tag{3}$$

$$H_2 \rightleftarrows (H_2) \tag{4}$$

$$C + (O) \rightarrow CO, \tag{5}$$

in which parentheses indicate the adsorbed species. Long and Sykes [5] assumed a steady state for the adsorbed molecules and succeeded in explaining results for subatmospheric conditions, using the rate equation:

$$r = \frac{k_1 p_{H2O}}{1 + k_2 p_{H2} + k_3 p_{H2O}} \tag{6}$$

where k_1, k_2, and k_3 denote reaction rate constants, and p_{H2O} and p_{H2} are the partial pressure of water and hydrogen, respectively. This equation correctly predicts the inhibition by hydrogen observed in the experiment.

At elevated pressures, the generation of methane becomes more important. Gasification at steam pressures as high as 4.7 MPa was conducted by Blackwood and McGrory [6]. They proposed that the reaction between adsorbed hydrogen and water vapor for methane formation should be included with the reactions given by Eqs. 3 to 5, and correspondingly obtained the following rate equations:

$$r = \frac{k_1 p_{H2O} + k_4 p_{H2} p_{H2O} + k_5 p_{H2O}^2}{1 + k_2 p_{H2} + k_3 p_{H2O}} \tag{7}$$

$$r_{CH4} = \frac{k_2}{k_4} p_{H2O}, \tag{8}$$

where r_{CH4} denotes the methane generation rate. These rate equations satisfactorily explained their results. Later, Van Heek et al. [7] found two mechanisms of methane generation: pyrolysis

coal at higher temperatures (higher than 600°C) for coal gasification in steam up to 7.1 MPa. Methane formation by pyrolysis was not intensified by pressure, but the rate of reaction between steam and char was clearly increased with pressure.

In spite of this accumulation of reaction data, we were unable to find measurements of the gasification rate of carbon in supercritical water. Data of this kind is needed to predict the lifetime of the catalyst and its contribution to the gas yields observed during biomass gasification. Consequently, the effects of temperature and pressure on the gasification rate and gas composition were measured and interpreted in relation to the previous research on carbon gasification under subcritical conditions. The change in iodine number of the carbon catalyst during supercritical water treatment was also measured.

EXPERIMENTAL

Experiments were conducted using a packed bed reactor [1] as shown in Fig. 1. The reactor was fabricated from Inconel 625 tubing, with a 9.53 mm OD and a 4.75 mm ID. Granular activated carbon (coconut shell based, 14-30 US mesh) was packed with a length of 406 mm in the reactor. Water was pressurized by an HPLC pump (Waters, Model 510) and fed to the reactor at 1.0 g/min. The temperature of the water flow was rapidly raised to the desired value by an entrance heater. The reactor was maintained at isothermal conditions by the furnace and a down-stream heater. The axial temperature profile along the reactor wall was measured using 11 type K thermocouples; another retractable type K thermocouple was placed inside the annulus of the reactor at the entrance of the packed bed. The pressure in the reactor system was measured by a pressure transducer. The reactor temperature was set at 600°C or 650°C, and the pressure was set at 25.5 MPa, 29.9 MPa, or 34.5 MPa.

After being cooled, the reactor effluent was sent to a sampling system principally composed of two three-way valves and a sampling loop. The effluent was discharged into the sampling loop for a defined duration, after which the contents were released into a pre-evacuated sampling tube. In the actual system, these two three-way valves were incorporated into one ten-port valve, enabling simultaneous switching of these valves. Effluent bypassing the sampling loop was delivered to an accumulator, where liquid and gas were separated and the gas was released through a pressure regulator, thus maintaining constant system pressure.

The gas generation rate was calculated from the pressure rise in the sampling tube, using the equation of state for an ideal gas. The change in gasification conversion with time was calculated using this measured gas generation rate and gas composition as determined by a gas chromatograph. Iodine tests (ASME D4607) were conducted to estimate the specific surface area of the residual carbons. BET surface area analysis was also conducted for a limited number of samples.

The iodine number of the virgin activated carbon was 1050. The ultimate analysis of this carbon showed the presence of hydrogen at 0.88 wt%.

RESULTS AND DISCUSSIONS
1. *Total gasification rate*

The composition of the product gas was similar for all the experimental conditions: hydrogen, 64%; carbon dioxide, 33%; methane, 2%; and carbon monoxide, 1% by mole. This composition was steady throughout the gasification. The ratio of hydrogen to carbon dioxide is close to 2, which is expected from the reactions shown in Eqs. 1 and 2.

It is known that the curves of carbon gasification conversion versus time can be often expressed by a single cubic equation in a normalized dimensionless plot using reduced time based on the time to attain a gasification conversion of 0.5 [8]. Although activated carbon is a partly gasified carbonaceous material, the normalized plot was drawn using conversion based on the initial activated carbon weight. In this work, the normalized plot was drawn using the reduced time τ based on the time needed for increasing conversion from 0.075 to 0.1 because the highest conversion was 0.25.

$$\tau = \frac{t - t_{0.075}}{t_{0.1} - t_{0.075}} \tag{9}$$

Here, t, $t_{0.075}$, and $t_{0.1}$ denote the time to be reduced, and times at which conversions of 0.075 and 0.1 were attained, respectively. The plots shown in Fig. 2 show good agreement for all the gasification experiments. This agreement indicates the possibility of using a single cubic equation to express the reaction rate change during gasification. It is also to be noted that the relation between conversion and reduced time is basically expressed by a linear function for the conversion range observed in this work.

From this graph of generalized conversion change, the dimensionless gasification rate at zero conversion is 0.0278. Dividing this value by the time needed to change conversion from

0.075 to 0.1 for each experiment gives the gasification rate at zero conversion for each experiment. These zero conversion values are used for the following data analysis, because they are not affected by the surface area change which occurs during gasification.

No clear trend with pressure was established, in agreement with the results from Long and Sykes [5]. (See Eq. 6, which shows that the effect of water vapor pressure becomes negligible at high pressures.) On the other hand, the earlier experiments by Blackwood and McGrory [6] predict a 20% increase in reaction rate with increasing pressure from 25.5 to 34.5 MPa at 600°C. Thus, the extrapolation of the results of Blackwood and McGrory [6] does not predict the effect of pressure within this pressure range.

The effect of temperature is shown in Fig. 3 in the form of an Arrhenius plot. Carbon gasification rates at 34.5 MPa, projected using the rate equations of earlier workers, are also shown in the figure. Extrapolation of the results from Long and Sykes [5] predicts our result accurately. From the results of our work, the activation energy was found to be 166 kJ/mol, which is in good agreement with 176 kJ/mol observed by Long and Sykes [5]. This agreement suggests that the fundamental mechanism of gasification does not change under high pressures such as the supercritical condition. The prediction using the rate equation by Blackwood and McGrory [6] presents a quite different dependence of the reaction rate on temperature.

2. *Methane generation rate*

No clear dependence of the methane generation rate on total pressure is observed, which suggests that methane generation occurs by pyrolysis [7]. The ratio of the methane generation rate to the total gasification rate is thus constant, showing a value around 3%. Assuming that all hydrogen in the original activated carbon turns into methane by pyrolysis, the ratio should be 2.8%, in agreement with the observed value. The prediction of this value using the rate coefficients determined by Blackwood and McGrory [6] gives 0.03%, which indicates reaction of steam with carbon at this temperature is very slow. Thus, it should be concluded that the methane generation observed here is due to pyrolysis of activated carbon.

3. *Iodine number*

The iodine number is a crude measure of the surface area of an activated carbon, obtained by analyzing its capacity for iodine adsorption. The relation between the iodine number and the conversion (see Fig. 4) shows at first an increase in the iodine number with increasing conversion, then maximum iodine number from 0.05 to 0.2, and finally a decrease in the iodine number at conversions above 0.2. The early increase in the iodine number is because of gasification accompanied with the development of the microporous structure. In the middle flat region, the microporous structure is maximized, and there is a equilibrium between creation of new pores and destruction of the walls between them. The decrease at high conversion indicates when the burn-off of the walls between the pores dominates over creation of new pores. Thus, short-term treatment in supercritical water effectively develops the microporous structure of the carbon. BET analysis showed a similar increase in surface area from 809 m²/g to 1011 m²/g after 6-hour reaction in supercritical water at 600°C and 34.5 MPa. No significant influence of pressure on the iodine number after a 6-hour treatment was observed.

4. *Activated carbon production in supercritical water*

This increase in the iodine number of carbon by treatment in supercritical water can be utilized for activated carbon production. A series of experiments were conducted to activate charcoals in supercritical water. Charcoals produced in-house (14-30 US mesh) were packed in the reactor in place of activated carbon, and after treatment in supercritical water at 600°C, 34.5 MPa, the iodine numbers of the product activated carbon were measured. Table 1 shows the results of these iodine tests. Large increases in the iodine number from the initial values of less than 50 are observed for each treatment. Thus, treatment of carbonaceous materials in supercritical water can be a novel approach for producing activated carbon production at lower temperatures than conventional activation methods.

CONCLUSION

The gasification rate of activated carbon in supercritical water is unaffected by variations in total pressure above the critical pressure of water, and is predictable by previous gasification measurements made at subatmospheric pressure, indicating the same gasification reaction mechanism. The methane generation characteristics indicate that methane is produced by the pyrolysis of the activated carbon itself. Short-term gasification in supercritical water increases the specific surface area of activated carbon, and thus its adsorbent capabilities. Supercritical water treatment can be a novel technique of activated carbon production at lower temperature than conventional activation methods.

REFERENCES

1. X. Xu, Y. Matsumura, and M. J. Antal, Jr., submitted to *Ind. Eng. Chem. Res.* (1995).
2. J. L. Johnson, in *Chemistry of coal utilization, 2nd suppl. volume* (Edited by M. A. Elliot) p.1491. John Wiley & Sons, Inc., New York (1981).
3. J. Gadsby, C. N. Hinshelwood, and K. W. Sykes, *Proc. R. Soc. (London)*, A187, 129 (1946).
4. R. F. Strickland-Constable and D. Phil, *Proc. R. Soc. (London)*, A189, 1 (1947).
5. F. J. Long and K. W. Sykes, *Proc. R. Soc. (London)*, A193, 377 (1948).
6. J. D. Blackwood, and F. McGrory, *Aust. J. Chem.*, 11, 16 (1958).
7. K. H. Van Heek, H. Juntgen, and W. Peters, *J. Institute Fuel*, 46, 249 (1973).
8. P. L. Walker, Jr., in *Fundamentals of Thermochemical Biomass Conversion* (Edited by R. P. Pverand, T. A. Milne, L. K. Mudge) p.485. Elsevier, London (1985).
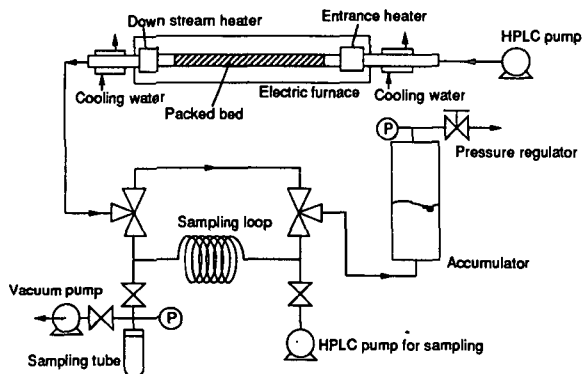
Fig. 1. Supercritical flow reactor scheme
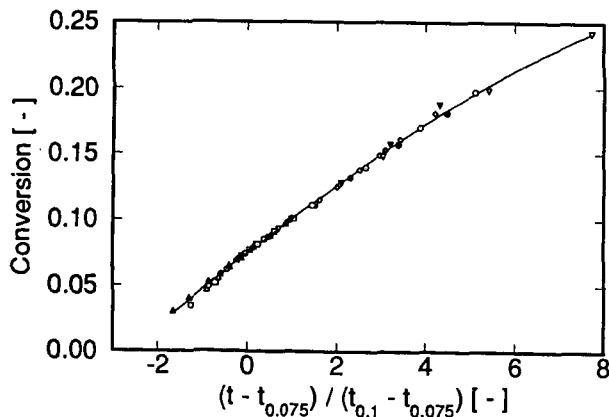
Fig. 2. Normalized plot for the gasification of activated carbon in supercritical water
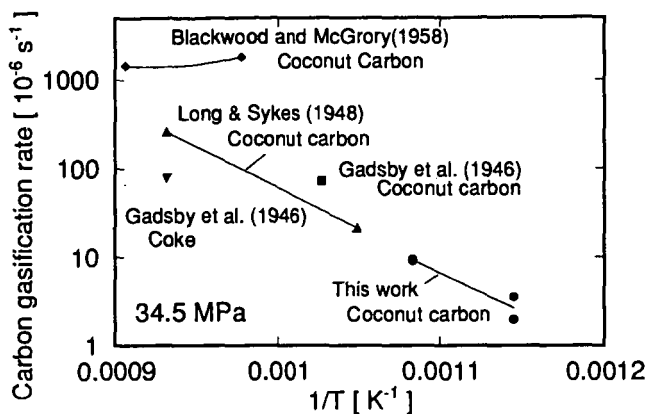
Fig. 3. Arrhenius plot for the gasification rate of carbon in water at 34.5 MPa
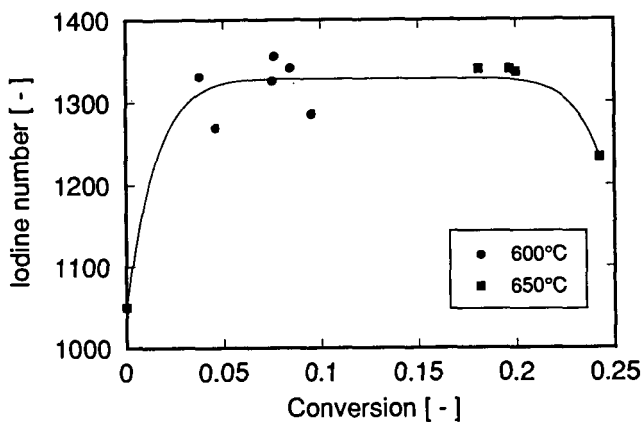
Fig. 4. Relationship between conversion and iodine number

Table 1. Increase in iodine numbers after treatment of charcoal in supercritical water at 600°C, 34.5 MPa.

Charcoal	Time	Iodine number	Conversion
	[h]	[-]	[-]
Macadamia nut shell	2	498	0.47
Macadamia nut shell	6	622	0.68
Macadamia nut shell (650°C)	6	689	0.49
Coconut husk	6	512	0.42
Coconut shell	6	450	0.22

DEVELOPMENT TECHNIQUE IN THE ACTIVATION PROCESS OF PETROLEUM COKE

Theresia I. Pudiyanto and S. Nurlatifah
PERTAMINA
Petrochemical and Non Fuel Product
Jalan Raya Bekasi KM 20, Jakarta 13920, INDONESIA

1. INTRODUCTION

The manufacture of activated carbon involves two main stages, the carbonization of the carbonaceous precursor and the activation of the resulting char. Process activation is to enhance the pore structure by the partial gasification of the char in steam, carbon dioxide, air or a mixture of these; this is the so-called "physical activation". The term "chemical activation" refers to the carbonization of the precursors after addition of substances that restrict the formation of tar (H_3PO_4, KOH, etc); in this way, a carbonized product with a well developed porosity (after appropriate washing) may be obtained in a single operation. There is, of course, the possibility of combining these two activation processes. In our experiments, the two principal methods of activation, i.e., that which uses CO_2 and that which uses KOH were chosen and treated to green petroleum coke as starting materials. The properties such as surface area and Iodine adsorption were relatively low in the physical activation. The surface area was reached in the range of 27 to 79 m^2/g and Iodine adsorption 59 to 85 mg/g. The adsorptive power in Iodine solutions increased to the value of approximate 600 mg/g for physical activation of green coke binded with tar pitch. Further more, a well developed in pore, surface area and Iodine adsorption was achieved using KOH activant with appropriate process condition.

2. EXPERIMENTAL

a). Green petroleum coke was obtained from Dumai oil refinery. The size of particle was +4 mesh. The raw material was carbonized at 400 – 500°C for 2 hours and then proceed to activation process. For activation, temperature was increased to 600 – 700°C and flow of CO_2 after reaching the temperature. After activating with CO_2 for 3 hours, cooling to room temperature was carried out naturally before taking the sample for further analysis.

b). The green petroleum coke was ground and sieved to sizes of 200 mesh. Afterwards this material was mixed thoroughly with coal tar pitch of known percent weight. The mixed petroleum coke is then extruded to form discontinuously tube in a cylinder press. These moulded forms are then broken into short lengths and sieved to size between 8 – 4 mesh for further carbonization and CO_2 activation. During carbonization, the sample was shielded by calcined coke with size 16 – 14 mesh and gradually heated to 110°C for 2 hours and proceed to temperature 500 – 600°C for 3 hours and cooled to ambient temperature. Before activation, the carbonized material was separated from calcined coke by sieving in order to obtain the required size (2.5 – 4.5 mm). The activation carried out at temperature 900 – 1000°C for

3 hours under flowing of CO_2. For comparison, green coke with the same size was treated directly in the same process condition as mentioned above.

c). Green coke was ground to -50 mesh and the process under investigation in this study involves the reaction of coke with a substantial proportion of solid KOH (KOH : coke varied from 1 to 4 parts weight). Reactions took place in a nickel boat, within a reaction furnace tube under nitrogen. Reaction mixtures were heated 600 - 900°C for periods up to 1 hour and after reaction the furnace was withdrawn and cooled to ambient temperature. The reaction products were removed from the container and washed with distilled water to remove soluble salts. Other samples were reacted at 450°C for 1 hour and then subjected to thermal treatment up to 850°C and held at this temperature for 1 hour. Each of the solid products was leached with distilled water and vacumm dried at 110°C.

3. RESULTS AND DISCUSSION

Table 1 : Typical Properties of Green Petroleum Coke

Moisture, wt %	0.62
Volatile matter, wt %	14.54
Ash content, wt %	0.34
Fixed carbon, wt %	84.50
Sulphur content, wt %	max 0.5

Table 2 : Preparation Condition of 2 a and Its Properties

Sample	Carbonization & Activation, °C	Iodine Adsorption, mg/g	Surface Area, m²/g
C1	400	59.73	47
C2	500	59.34	42
C3	400 ; 600	72.52	28
C4	400 ; 700	85.69	79
C5	500 ; 600	69.12	54
C6	500 ; 700	69.59	33
C7	Reference		588

Table 3 : Preparation Condition of 2 b and Its Properties

Sample	Carbonization & Activation, °C	Iodine Adsorption, mg/g		Ash, wt %	
		With binder	Non binder	With binder	Non binder
A1	600 ; 1000	674.76	669.42	0.18	0.19
A2	600 ; 900	698.82	645.72	0.07	0.08
A3	500 ; 1000	662.13	637.36	0.10	0.12
A4	500 ; 900	656.24	626.11	0.04	0.06
A5	Referene	850.23		1.03	

Table 4 : Preparation Condition of 2 c and Its Properties

Sample	$\dfrac{KOH}{Coke}$	Reaction Temperature °C/time, hour	Heat Thermal Treatment °C/time, hour	Surface Area, m^2/g
B1	1:1	600/1	-	439
B2	4:1	600/1	-	50
B3	1:1	900/1	-	416
B4	4:1	900/1	-	34
B5	1:1	450/1	850/1	177
B6	1:2	450/1	850/1.5	1190
B7	1 3	450/1	850/1.5	1404
B8	1:4	450/1	850/1.5	2054

The activation technique process that was chosen in the experiment 2 a did not indicate the development of adsorptive properties and surface area as can be seen from Table 2. The gasification of carbonaceous materials with CO_2 at 600 and 700°C have no influences to Iodine adsorption and surface area improvement. Its value range from 59.34 to 85.69 mg/g and highest surface area was achieved max 79 m^2/g. These value was below expectation compare to the required properties of an adsorbent materials. The obtained surface area was 1/10 from 588 m^2/g of reference.

To improve the adsorptive properties, next sample binded with coal tar pitch, moulded and shielded with calcined coke during carbonization up to 600°C. The aim of using calcined coke was to avoid rapid decreasing of particle size due to oxidation. The CO_2 activation which subjected to carbonized product have increased drastically the Iodine solution adsorption and the highest value was 698.82. On the other hand, the non binder activated samples seems to have nearly same value as the binded one. The use of calcined coke in the second experiment act as an inert media during process operation and the higher temperature chosen for activation (900 – 1000°C) lead to the surface affinity improvement of the green petroleum coke.

The Iodine adsorption in the range from 626.11 to 698.82 mg/g for binder and non binder materials. Although these obtained value were less than reference (850 mg/g), this technique reveals that inert condition facilitate the activation process of green petroleum coke. The lower ash content in both samples reflex the higher quality of the starting material and binder. The ash content of reference 1.03 wt % indicated that difference carbon precursor was being used. Since the two previous physical activation techniques did not indicate good results, so the further experiment was carried out by chemical activation. The carbonization of coke with potassium hydroxide is expected to destroy the coking and coking capacities of green coke and to produce a char of high surface area and showed increase in adsorptive capacity. The progress of activation involves the reaction of coke with a substantial proportion of solid KOH from 1:1 up to 4:1 at reaction temperature 450°C for times 1 hour and subjected to

heat treatment at 850°C for times of 1 hour to 1.5 hours could produce an active carbon of high surface area up to 2054 m^2/g as can be seen from Table 4 and suitable for further application analysis.

The reaction temperature carried out at 600 and 900°C results nearly same surface area namely 439 and 416 m^2/g. On the other hand, the least introduce reactant tend to decrease the surface area of activated carbon to value 34 - 50 m^2/g. The process conditions and amount of KOH have influenced the surface area formation of carbon, an important property for adsorbent.

4. Conclusions

- Different preparation technique of activation were greatly influence the pore structure enhancement of green petroleum coke.
- Formation of high surface area active carbon from green petroleum coke was obtained effectively by using KOH activant.

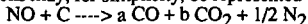# A COMPARISON OF THE REACTIVITIES OF DIFFERENT CARBONS FOR NITRIC OXIDE REDUCTION

Indrek Aarna and Eric M. Suuberg
Division of Engineering
Brown University
Providence, RI 02912

Keywords: Nitric Oxide, Carbon, Gasification

INTRODUCTION

Carbon has been recognized to play a significant role in reducing NO in some combustion systems (e.g., fluidized beds) and offers the potential as a reducing agent in other, new applications. In order to more fully appreciate this potential, it is useful to explore what factors influence the reactivity of carbons (and, more generally, chars) towards NO. This paper summarizes what is known about the reactivity of different carbons, and examines some questions raised by the comparison, in light of new experimental results.

The reduction of NO by carbons may, for simplicity, be represented by the general reaction:
$$NO + C \longrightarrow a\ CO + b\ CO_2 + 1/2\ N_2$$
Other products (for example, N_2O) are possible under certain specific conditions. Likewise, other reaction pathways (involving carbon catalyzed NO reduction by CO) are also possible. Still, the main carbon reduction route involves the products as indicated. Many aspects of this reaction system have been reviewed in recent years [e.g., 1-4]. Many of the published data on the NO-carbon reaction are summarized in Figures 1 and 2. A more complete summary of the available data is in preparation, and will be presented shortly. This summary is intended to convey the essential features of what is known about the kinetics of the reaction.

Figure 1 presents the data on the rate constant for the reaction, expressed as an NO consumption rate, on a per unit mass of carbon basis. The assumption has been made, consistent with most reports in the literature, that the reaction is first order with respect to NO [1,2, 5- 8]. Several features are immediately apparent. First, there is a significant spread in the rates of reaction. The variation is of two to three orders of magnitude, which may not initially be surprising inasmuch as the data were not normalized based on surface areas, *vide infra*. It is apparent that there is quite commonly a shift in apparent activation energy of the rate constant. The "breaks" occur at temperatures ranging from about 900 to 1050 K, and always involve an increase in activation energy with increasing temperature. This break has been earlier noted by several groups. It must involve a change in mechanism, as opposed to an encroachment of heat and/or mass transfer effects, since the shift is in the direction of higher activation energies with increasing temperature. A hypothesis to explain the two regimes has been previously advanced [2]. The individual studies offer a wide range of activation energies, with some sets showing no evidence of the "break". There are surprisingly few clear trends with the nature of the carbon. For example, a highly pyrolyzed resin char exhibits a lower reactivity than does a graphite. De-ashing of a lignite char shows only a modest effect on reactivity. A cellulose char with low inorganic impurity content is seen to have a higher reactivity than coal chars.

Figure 2 presents a comparison of literature data on a surface area-normalized basis. The surface areas were taken as reported by the investigators themselves, and include some measured by nitrogen sorption and others with carbon dioxide. It should be noted that the data sets represented in Figures 1 and 2 are not identical, because the data were not always available to include results on both plots. It is perhaps surprising that converting data to a surface area basis does little to reduce the amount of scatter in the data. It is worth noting that the degree of scatter is not unlike that observed in similar summary plots of data on the oxygen-carbon reaction [9]. Thus it appears as though there is a high degree of variability of carbon reactivity towards NO, just as there is towards oxygen. This has been attributed to differences in the numbers of active sites per unit surface area. It is not yet possible to predict this value. It is interesting to note that the graphites exhibit relatively high reactivities per unit surface area. There is, however, no clear trend in reactivity with the nature of the carbon.

The results of Figures 1 and 2 present a confusing picture of the factors that influence the reactivity of carbons towards NO. While small subsets of the data can be compared and logical hypotheses drawn regarding the influence of certain variables, there is not yet an ability to predict reactivity to better than orders of magnitude uncertainty. The problem with an approach based upon comparing reactivities from literature accounts is that there are a number of experimental variables that may have had an influence on reactivity, and these are never completely controlled or reported. Most of these variables have to do with how the carbon is prepared, but some might also have to do with how the reactivities were determined. The remainder of this paper will explore how measured reactivities can be influenced by a number of experimental factors.

EXPERIMENTAL

Two different reactor systems were selected for study, in order to represent the two most widely employed techniques for study of this reaction. The first reactor system was a thermogravimetric

analyzer (TGA). In this case, a TA Instruments TGA was employed. As compared with the Cahn TGA system in which we had performed most of our earlier work [1,2], the TA Instruments TGA has a somewhat smaller enclosed gas volume. Thus, the experiments were performed with a continuous gas flow through the TGA to ensure that depletion of NO was not significant. The TGA work was performed, as earlier [1,2] , at quite high NO partial pressures, ranging from about 1 to 10 kPa of NO partial pressure.

Many of the studies reported in the literature have employed packed bed reactors. One of the advantages of these systems is that they more realistically simulate possible "end-of-pipe" reduction systems. They also tend to be less complicated to operate, allowing for a steady flow of NO-containing gas which is continuously analyzed using an NO_x analyzer. Operation at lower, more realistic, NO concentrations is also possible. Operation of a TGA at low NO concentrations is often considered impractical, because of the long times needed to achieve significant burnoff (weight loss).

In our case, we employed a 4 mm ID packed tubular reactor, made of quartz. A bed of between 20 and 200 mg of carbon (char) was packed into a predetermined length of between 1 and 30 mm, depending upon the conditions to be studied. The bed was held in place with quartz wool. Blank runs indicated no significant NO reduction in the absence of carbon (this was not the case if ordinary glass wool was employed). A carrier flowrate between 70 and 125 cc/min of helium was passed through the reactor. In the work considered here, the only other component in the inlet gas was NO. The inlet NO concentration ranged between 100 and 300 ppm. The particle size in the bed was approximately 200 µm in all cases. Before all runs, the surface of the char was cleaned of oxides by heating at 1173 K for one to two hours.

RESULTS AND DISCUSSION
Several different carbons were tested in the TGA, using a consistent protocol. The samples examined were a resin char (ex-phenolformaldehyde) that we had studied extensively [1,2], a graphite powder (from AESAR/Johnson Matthey Company), a coconut char (from Fisher Scientific), and a Wyodak coal char, prepared from a sample obtained from the Argonne Premium Coal Sample Program. The results are shown in Figure 3.

The results of Figure 3 show that this wide range of carbons gives fairly consistent rates, when the results are represented on a unit surface area basis. The one exception is the rates from our earlier work [1,2], and the reasons for this will be discussed below. It should be noted that the carbons range from those of quite high purity (the phenolic resin char and the graphite) to a mineral-containing coal char. The good agreement between the carbons and chars might be attributable to the fact that an effort was made to compare highly heat treated materials, in this case. The coconut char and graphite were used as-received (apart from surface cleaning at 1273 K for one hour). The phenolic resin char and the Wyodak char were prepared by a two-hour pyrolysis at 1223 K, and then surface cleaned prior to use. Thus for carbons and chars which may be considered as "old" there is quite good agreement in reactivity. Further tests, which will be reported separately, have not surprisingly indicated that the "age" of a char (i.e., how severely it is heat treated) does indeed have some effect on its reactivity. Here, however, it came as a surprise that the aging seems to lead to similar reactivities towards pure NO, despite significant differences in contents of impurities.

Figure 3 also indicates that the "break" in the Arrhenius plots depends upon the type of carbon. It can be seen that the break occurs at a much higher temperature in the graphite than in the other carbons. The agreement between the reactivities of the different carbons, on a per unit mass basis, was not nearly as good. In fact, the results gave a spread similar to that seen in Figure 1. Thus it appears that the reactions occur in Zone I, and that the micropore area of the carbons is significant.

When our earlier TGA results on the same resin char are compared with those from the present study, there appears to be a significant difference (see Figure 3). This turned out to be a consequence of how the sample was prepared, and indicates an important consideration in developing experimental testing procedures. The extent to which the resin char surface was cleaned of oxides was responsible for the differences in the observed rates. In our earlier work [1,2], the reactivity of the resin char was established as a function of temperature, merely by varying temperature and recording what appeared to be pseudo-constant rates. This might be considered a "normal" experimental procedure. In this more recent work, it was learned that by cleaning the surface of oxides, by heating at 1273 K for an hour between each temperature to be studied, the resulting pseudo-steady mass loss rate was significantly higher. This means that the oxide population on the char surface is a function of the reaction history of the sample, and that this, in turn, influences the observed rate. What may appear to be a pseudo-steady state rate might actually be slowly evolving, as the oxide population readjusts on a timescale longer than that used to obtain the rate. We had actually noted the same problem earlier, in connection with determination of the reaction order with respect to NO [1]. Failure to clean the surface between different partial pressures gave an apparently less than unit order with respect to NO, since the surface oxide population could only very slowly adjust to the new NO partial pressure. Thus it is essential to report how kinetic experiments are performed, in order to establish a sample reaction history. Without this information, comparison of rate data from the literature may be quite misleading. Once this aspect of the process was noted, all our experiments were performed on a self-consistent basis, with surface oxide cleaning between each temperature step. Because we are measuring rates

on a virgin surface in each case, issues related to the influence of remaining oxides on rate are minimized. Further experiments in the TGA again established that the reaction is unequivocally first order with respect to NO partial pressure, validating the form of the rate constant used in Figures 1 through 3 (see Figure 4).

Generally, good agreement was obtained between the rate constants from the TGA and packed bed experiments, despite the fact that there was about a two order of magnitude difference in the concentrations of NO in the two reactor systems (around 2% in the TGA vs. 200 ppm in the packed bed reactor). Results for the coconut char in Figure 5, illustrate this conclusion. Further discussion of the small differences will be presented elsewhere. Thus apparently large differences in reactivity in Figures 1 and 2 are not attributable to what type of reactor system is used for testing, nor to the concentration level of NO employed. It is clear that the purity of the gas feed is important in determining the apparent reactivity; small amounts of oxygen affect rates significantly. This will be reported on elsewhere. We have further established, consistent with an earlier presented hypothesis [10], that it is difficult to obtain reliable reaction order information from packed bed experiments. This will also be reported elsewhere.

ACKNOWLEDGEMENT

REFERENCES

1. Suuberg, E.; Teng H.; Calo, J. *23rd Symp. (Int.) on Combustion*, The Comb. Inst., Pittsburgh, 1990; p 1199.
2. Teng, H.; Suuberg, E.M.; Calo, J.M. *Energy and Fuels*, 1992, 6 , 398.
3. de Soete, G.G., *23rd Symp. (Int.) on Combustion*, The Combustion Institute, Pittsburgh, 1990; p 11257.
4. de Soete, G.G., *Pulverized Coal Combustion: Pollutant Formation and Control 1970-80*, Chapter 8, EPA Monograph, 1991.
5. Watts, H., *Trans. Faraday Soc.*, 1985, 54, 93.
6. Smith, R.N.; Swinehart, J.; Lesnini, D., *J. Phys. Chem.*, 1959, 63, 544; 1956, 60, 1063.
7. Chan, L.K.; Sarofim, A.F.; Beer, J.M., *Comb. Flame*, 1983, 52, 37.
8. Furusawa, T.; Kunii, D.; Osuma, A.; Yamada, N., *Int. Chem. Eng.*, 1980, 20, 239.
9. Smith, I.W., *19th Symp. (Int.) on Comb.*, The Combustion Institute, 1982, p. 1045.
10. Calo, J.M.; Suuberg, E.M. *Proc. 22nd Biennial Conf. on Carbon*, p. 618, American Carbon Society, 1995.
11. Degroot, W. F. ; Richards, G. N., *Carbon*, 1991 29, 2, 179.
12. Matos, M.A.A.; Pereira, F.J.M.A.; Ventura, J.M.P., *Fuel*, 1991, 70, 38.
13. Song, Y. H.; Beer, J. M.; Sarofim, A. F., *Comb. Sci. and Tech.*, 1981, 25, 237.
14. Johnsson, J.E., *Fuel*, 1994, 73, 1398.
15. Edwards, H. W., *AIChE Symp. Ser. No. 126*, 1972, Vol. 68, p. 91.
16. Bedjai, G.; Orbach, H.K.; Reisenfeld, F.C., *I&EC*, 1958, 50, 1165.
17. Chu, X.; Schmidt, L.D., *Ind. Eng. Chem. Res.*, 1993, 32, 1359.
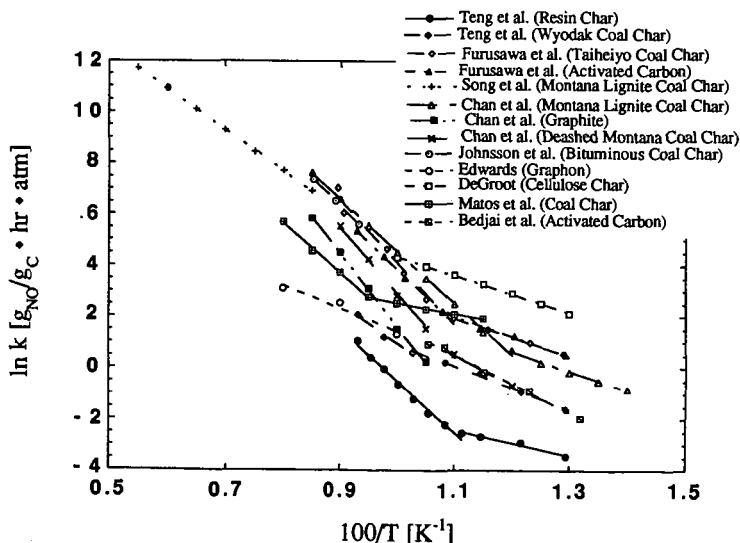18. Illán-Gómez, M.; Linares-Solano, A.; Salinas-Martinez , C.; Calo, J.M., *Energy and Fuels*, 1993, 7, 146.

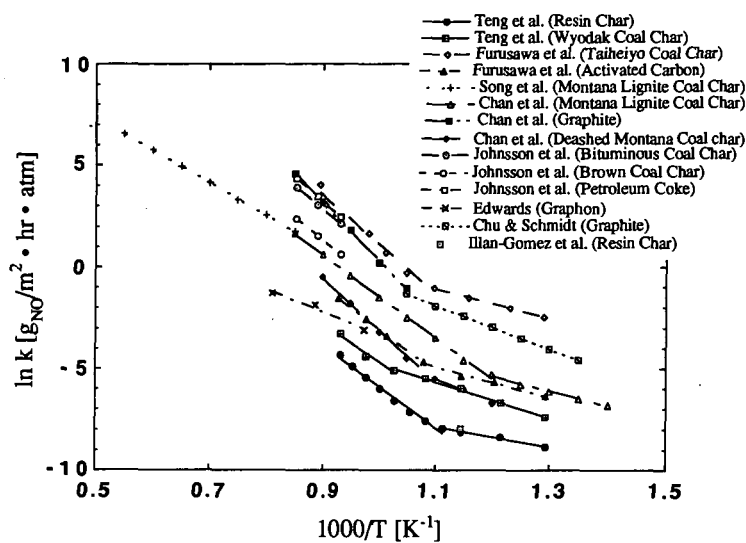Figure 1. NO-carbon reaction rate constant, per unit mass of carbon reactant.

Figure 2. NO-carbon reaction rate constant expressed on a surface area basis

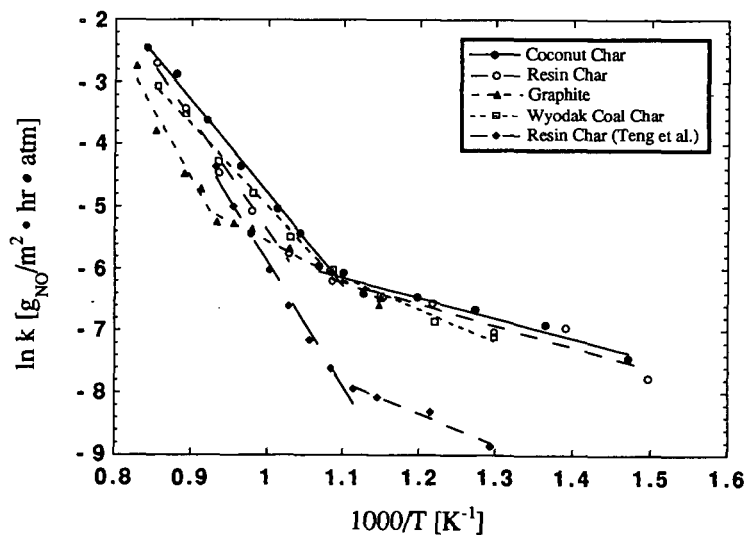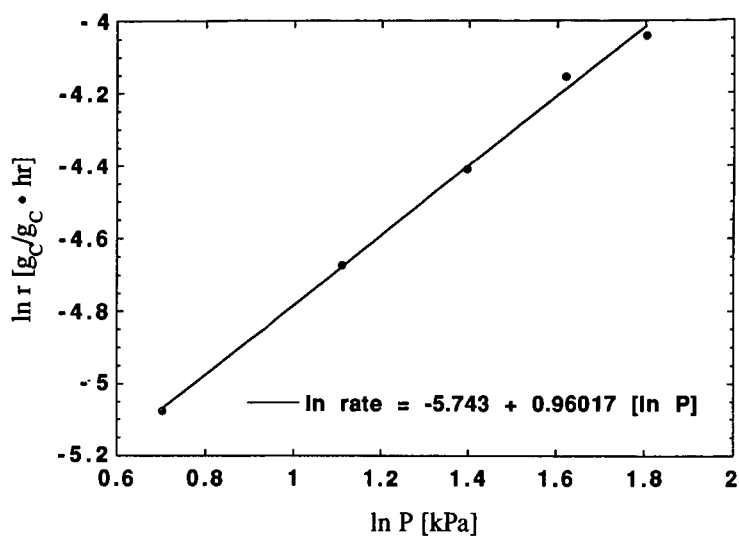

Figure 3. NO-carbon reaction rates from TGA experiments.

287

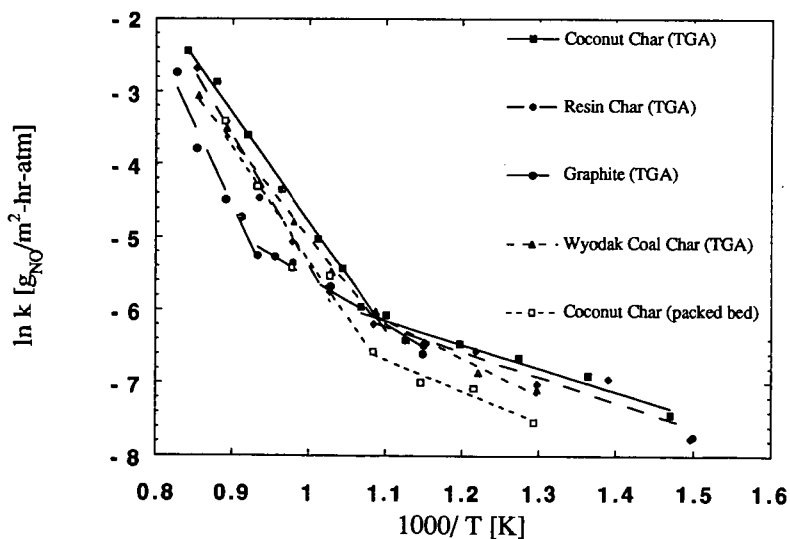Figure 4. Reaction rate of resin char in the TGA, showing first order rate. (T=600°C)

Figure 5. Comparison of rates obtained on various samples, in the TGA and packed bed reactor.

REMOVAL OF NOx OR ITS CONVERSION INTO HARMLESS GASES BY CHARCOALS AND COMPOSITES OF METAL OXIDES

Shigehisa Ishihara and Takeshi Furutsuka
Wood Research Institute, Kyoto University,
Uji, Kyoto 611, Japan

Keywords: adsorption, charcoal, metal oxide

Introduction

In recent years, much attention has been devoted to environmental problems such as acid rain, photochemical smog and water pollution. In particular, NOx emissions from factories, auto mobiles, etc. in urban areas   have become worse. To solve these problems on environmental pollution on a global scale, the use of activated charcoal to reduce air pollutants is increasing. However, the capability of wood-based charcoal materials is not yet fully known. The removal of NOx or its conversion into harmless gases such as N_2 should be described.[1] In this study, the adsorption of NO over wood charcoal or metal oxide-dispersed wood charcoal was investigated.

In particular, carbonized wood powder of Sugi (Cryptomeria japonica D. Don) was used to study the effectivity of using these materials in adsorbing NOx. Since wood charcoal is chemically stable, metal oxide with the ability of photocatalysis was dispersed into wood charcoal to improve its adsorption and capability to use the light energy effectively.

Experimental method

1. Carbonization method
Wood meal of Sugi (Cryptomeria japonica D. Don) was carbonized in electric furnace with the desired carbonization temperatures of 300, 400, 500, 600, 700 and 800°C. The temperature was increased at the rate of 4 °C/min , and then kept constant for 1 hour after reaching the desired temperature.

2. Metal oxide-dispersed wood charcoal
·   Wood charcoal with a weight of 0.5 g was soaked in solution of Titanium (IV) alkoxide dissolved in about 5 ml 1-propanol . The charcoal was then ovendried at 105 °C for 24 hours.

3. Adsorption method

NOx gas of about 100 ppm was passed through the reaction tube with 0.5 g of wood charcoal or metal oxide-dispersed wood charcoal. The concentration of NOx gas was measured by gas detectors. During measurement, the reaction tube was lighted up or covered by black shield.

Results and Discussion

The relationship between carbonization temperature and adsorption of NO in light and dark reactions is shown in Fig. 1. Based from the results, the adsorption was highest in 600°C. It was previously thought that in using wood charcoal, there will be no difference between light reaction and dark reaction. However, based from the results, adsorption was better in dark reaction than light reaction. As reflected, higher adsorption is observed in all the carbonization temperatures in the light reaction.

As shown in Fig. 2, adsorption of NO is different when charcoal is soaked in titanium oxide. Adsorption is better in light reaction when greater amount of titanium oxide is used as observed in all the carbonization temperatures studied. It seems that titanium oxide oxidized NO gas by light energy. However, in this study the source of light reaction was a fluorescent light. If the light with the suitable wavelength is irradiated to the titanium oxide-dispersed wood charcoal, the adsorption ability may be better.

Fig. 3 shows the relationship between carbonization temperature and adsorption of NO in light and dark reaction using the same percentage of titanium oxide. It is clear that adsorption is better in light reaction than dark reaction in the all the carbonization temperatures. This is because titanium oxide plays an important role in the light reaction. Further, higher adsorption is observed in high temperature carbonized materials.

Conclusion

The adsorption of NO over wood charcoal was better in dark reaction than light reaction. Higher adsorption is observed in all the carbonization temperatures in the dark reaction although the highest adsorption is observed in 600 °C.

On the other hand, 800 °C was observed to adsorb more when soaked in titanium oxide. It can be concluded that the use of titanium oxide is very effective in improving the adsorption of NO especially in light reaction. Further, adsorption is better in light reaction when greater amount of titanium oxide is used as observed in all the carbonization temperatures studied. It seems that titanium oxide oxidized NO gas by light energy.

Reference

1) Imai, J. et al. 1993. N_2 formation from NO over metal oxide-dispersed microporous carbon fibers. Catalysis Letters 20, 133.

NO (ppm)

C_0=96ppm

Carbonization temperature (°C)
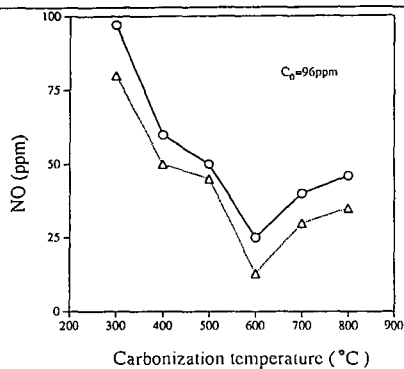
Fig.1   Adsorption of NO over charcoal

Notes: C_0 : Initial concentration of NO

—O—   in light reaction

---△---   in dark reaction

NO (ppm)

C_0=96ppm

Carbonization temperature (°C)
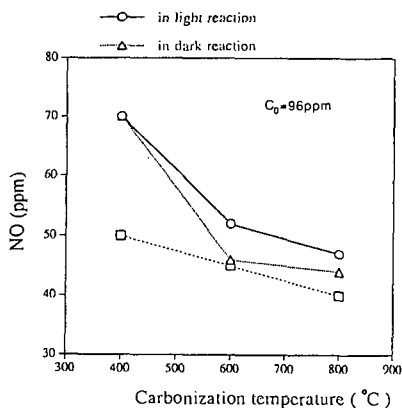
Fig.2   Adsorption of NO over charcoal materials in light reaction

Notes: C_0:Initial concentration of NO

—O—   charcoal+titanium oxide (10%)

---△---   charcoal+titanium oxide (30%)

····□····   charcoal+titanium oxide (50%)

NO (ppm)

C_0=96ppm

Carbonization temperature (°C)
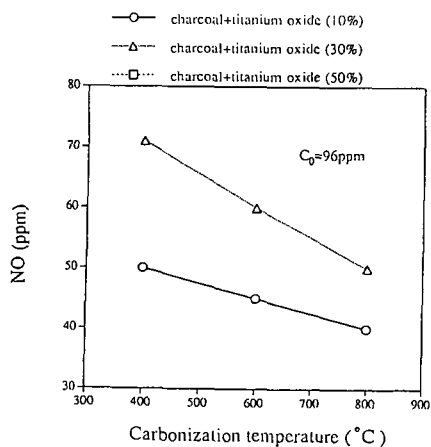
Fig. 3   Adsorption of NO over charcoal materials

Notes: C_0:Initial concentration of NO

—O—   charcoal+titanium oxide (50%) in light reaction

---△---   charcoal+titanium oxide (50%) in dark reaction

292

NO REDUCTION BY POTASSIUM CONTAINING COAL BRIQUETTES. EFFECT OF MINERAL MATTER CONTENT AND COAL RANK

A. García-García, A. Linares-Solano and
C. Salinas-Martínez de Lecea
Departamento de Química Inorgánica. Universidad de Alicante.
Alicante. Spain

INTRODUCTION

Carbons and activated carbons have been proposed as reducing agents for NO removal from exhaust gases as well as for applications to vehicles and other small sources[1-3]. The use of carbon for NO reduction could present advantages over gaseous reactants used in conventional technologies[4]. Moreover, coals could be bindered and pyrolized in order to obtain carbon briquettes with good mechanical strength that will resist abrassion[5].

Recently, a method for briquette preparation and its use as NOx reducing agent has been presented[6]. This novel manufacture method presents the advantage of using a binder agent which inherently contains potassium. Illán et al.[7,8] found that potassium acts as catalyst of the NO-carbon reaction. In a previous paper[9], it was found that potassium containing coal briquettes have an activity similar to that of activated carbons with potassium remaining from the preparation method although, they were not as active as activated carbon oxidized with HNO_3 and ion exchanged with potassium acetate[8]. The study[9] was conducted using only one type of coal precursor but, as the NO-carbon reaction is a gasification reaction, it is expected that both the coal rank and the mineral matter content affect the NO reduction[10].

The objective of this study is to analyze the effect of coal rank and mineral matter content in the NO reduction activity of potassium containing coal briquettes.

EXPERIMENTAL

Four coals of different rank have been selected as raw material for the briquette preparation. An anthracite (UA1), a high volatile A bituminous (A3), a high volatile C bituminous (P) and a lignite (LY). To study the effect of mineral matter content, two fractions of coal A3 with very different ash content (8% and 25%), denoted as A3 and A3′respectively, have been used. These fractions were obtained using two portions of the raw coal with different particle size (0.71 < ϕ <1.40 and ϕ < 0.71 mm, respectively). To prepare the briquettes raw coals were grounded and sieved to a particle size of 0.1 < ϕ < 0.2 mm.

Commercial humic acid (liquid with a density of 1.12 g/cm^3 and a potassium content of 0.049 g/cm^3) has been used as binder agent for briquette preparation. The method was previously described[6,9]. In summary, a coal sample is impregnated with a variable binder volume depending on the humic acid/coal ratio desired, mixed for 30 min, dried at 110°C, pressed (1-2 Kg/cm^2) and pyrolyzed in N_2 for 2 h at 700°C. Potassium content was determined after the pyrolysis step by atomic absorption spectroscopy by AES-ICP.

After pyrolysis, a test was conducted to determine mechanical

strength of the briquettes. The impact strength test was previously described[9]. All the briquettes described in this papers have satisfactory values, independently of the humic acid/coal ratio.

The kinetics of the NO-carbon reaction were studied at atmospheric pressure in a fixed-bed flow reactor (15 mm, i.d.; ca. 300 mg sample) connected to a gas chromatograph (Hewlett Packard, Model 5890A. The reactant mixture used was: 0.5% NO in He using a 60 ml/min flow rate, which resulted in a bed residence time of 0.56 s. NO, N_2, N_2O, CO_2 and CO were analyzed using a Porapak Q 80/100 column and a thermal conductivity detector. Briquettes were ground to < 1.5 mm to introduce them in the microreactor.

Two types of experiments were performed: i) a temperature programmed reaction (TPR) at a linear heating rate of 5°C/min up to a maximum temperature of 900°C; and ii) an isothermal reactions at 300, 400, 500 and 600°C for 120 minutes. The samples were treated in helium at 50°C/min, up to 900°C for 10 minutes prior the reaction. In case i), the temperature is lowered to ambient temperature and He replaced by the reactant mixture. In case ii), the temperature is lowered to the desired level and the isothermal experiment is initiated by substituting He by the NO/He mixture. The reaction products were monitored in both cases, thus allowing detailed oxygen and nitrogen balances to be determined.

RESULTS AND DISCUSSION

Table 1 presents the results for sample preparation, consisting of coal precursor, humic acid to coal ratio (HA/C), yields of the pyrolysis process and sample nomenclature including final potassium content. It is interesting to note that samples prepared, with the same HA/C (1.20), using the different coal precursors present a very different potassium content which is higher as coal rank decreases. This fact must be due to two phenomena, the increase in weight lost during pyrolysis from the anthracite to the lignite, as observed in the values of pyrolysis yield (Table 1) and the higher oxygen surface groups as coal rank decreases[11], that are mainly responsible for potassium anchorage[12].

For a fixed coal, an increase in HA/C produces an increase in potassium content up to a limit value, this could be observed in the series prepared from coals P and LY (Table 1). For coal P, an increase from 0.8 to 1.2 in HA/C only produces a 20% increase in potassium content while from 0.4 to 0.8 it increases in 100%. The specific activity (per gram of potassium) decreases, for a given coal precursor, with increasing potassium content. This behaviour was previously observed and explained for potassium impregnated activated carbons[8].

To study the effect of coal rank, briquettes with similar potassium contents have been prepared from coals UA1, P and LY. Figure 1 presents the results of specific activity determined at steady state conditions, at different temperatures, as a function of percentage of fixed carbon in the coal precursor. It is clearly observed a decrease in activity as the coal rank increases. Briquettes prepared from lignite (LY) has a much higher activity. It may be observed that the same value is found for sample LY-1.9 at 400°C and for sample P-1.5 at 600°C. A reduction of 200°C in the process temperature is very important for a practical point of view. It is also interesting to note that the ash content of coal LY is very low (0.5 wt%) in comparison to UA1 (7.0 wt%) or P (16.7 wt%). Both low rank and low ash content could be responsible for

the high activity, as we will discuss later. Sample LY-1.9 has an activity as high as that of an activated carbon, oxidized with HNO_3 and ion-exchanged with potassium acetate[13]. The behaviour of both samples for NO reduction in the temperature range studied (300-600°C) is very similar. These results confirm that, if very reactive low rank coals are used as precursors, the briquetting process can produce very active samples, with the advantage of higher mechanical strength and in a very simpler procedure.

Figure 2 shows the activity plots for briquettes A3-4.7 and A3´-3.6. As already mentioned in the experimental section, these samples were prepared from two portions of coal A3 containing different ash content. At 600°C the behaviour is not very different for the two samples although, at steady state conditions the activity level is more constant for the sample prepared with low ash content coal. At 500°C, the difference is dramatic. Sample A3´-3.6 very much deactivates presenting a very low activity at steady state conditions.

To explain these results, the analysis of reaction products, mainly N_2O, N_2, NO, CO_2 and CO, during TPR experiments are presented in Figures 3 and 4. Similar results were obtained for potassium containing activated carbons[8]. The profiles can be described as follows:

i) An initial period from 100 to 300°C with NO uptake reaching a maximum about 150°C. In this zone N_2O and N_2 are the only products.

ii) A second period from 300 to 600 °C, where NO reduction activity increases with temperature. In this zone N_2 and CO_2 are the main products.

iii) Above 600°C, N_2 becomes constant, the 100% NO reduction is reached and CO begins to evolve being the majority product at about 800°C. The CO appearance coincides with the complete disappearance of NO.

However, an important difference is observed in these plots in comparison to those of potassium containing activated carbons. The CO_2 evolution reaches a maximum at 620-650°C that is typical of most of the briquette samples[9].

For potassium containing activated carbons[8], an excess CO_2 in relation to N_2 (both the main reaction products at this temperature range) was observed forming a broad band but, no single peak appeared. In a previous study[9], the CO_2 peak, appearing in the TPR of coal briquettes has been attributed to K_2CO_3 decomposition, considering the temperature range of appearance. The area under the peak allows to calculate the carbonated potassium during TPR experiment. This portion of the metal will be inactive as catalyst for the reaction[8]. The results in Figures 3 and 4 explain the large difference in activity at 500°C for samples A3-4.7 and A3´-3.6. For the second one (Figure 4) an 88% of the catalyst is in the carbonated form while only 25% for the former one (Figure 3). At 600°C, the K_2CO_3 decomposition starts and the activity is very similar for both samples.

At present, it is not probed the origin of the negative effect of mineral matter, present in the raw coal, that produces an increase in the K_2CO_3 formation. The hypothesis that is being investigated,

it is that mineral matter acts as a sink for potassium, producing a lower dispersion and consequently larger particles that will be easier carbonated in the reaction conditions since most part of the catalyst is not in contact with the carbon substrate.

CONCLUSIONS
NO reduction activity of potassium containing coal briquettes depends on coal precursor rank. Regarding samples with similar potassium content the activity increases with decreasing coal rank. Coal rank also affects potassium content of the briquettes. Using a similar humic acid to coal ratio the lower the coal rank the higher the potassium content. Briquettes prepared from low rank coals are as active as potassium ion-exchanged activated carbons which need a much more complicated preparation method. Mineral matter in the coal precursor produces deactivation of potassium catalyst, favoring the K_2CO_3 formation in reaction conditions.

REFERENCES
(1) Mochida, I., Ogaki, M., Fujitso, H., Komatsubara, Y. and Isa, S. *Fuel* 1985, **64**, 1054
(2) Teng, H., Suuberg, E., Calo, J. and Hall, P. In Proceedings of the 19th Carbon Conference, Pennsylvania State University 1989, p.574
(3) Yamashita, H., Yamada, H. and Tomita, A. *Appl. Catal.* 1989, **78**, L1
(4) Illán-Gómez, M.J., Linares-Solano, A., Radovic, L.R. and Salinas-Martínez de Lecea, C. *Energy Fuels,* in press.
(5) Wen, W. W., Bergman, P. D., and Dembrouck, A. W. In Proceeding of the 10th International Coal Preparation Congress, Edwonton, Canada, 1986, p.119
(6) García-García, A., Illán-Gómez, M.J., Linares-Solano, A.and Salinas-Martínez de Lecea, C. Spain Patent P9400104, 1994
(7) Illán-Gómez, M.J., Linares-Solano, A., Radovic, L.R. and Salinas-Martínez de Lecea, C. *Energy Fuels* 1995, **9**, 97
(8) Illán-Gómez, M.J., Linares-Solano, A., Radovic, L.R. and Salinas-Martínez de Lecea, C. *Energy Fuels* 1995, **9**, 104
(9) García-García, A., Illán-Gómez, M.J., Linares-Solano, A. and Salinas-Martínez de Lecea, C. *Fuel* submitted.
(10) Van Heek, K. H., and Mühlen, H-J. *Fuel* 1985, **64**, 1405
(11) Hessley, R. K., Reasoner, J. W., Riley, J. T. "Coal Science", Ed. Wiley-Interscience, 1986
(12) Meijer, R., Weeda, M., Kapteijn, F., and Moulijn, J. A. *Carbon* 1991, **29**, 929
(13) Illán-Gómez. Ph.D. Thesis. University of Alicante 1994

TABLE 1. Briquette preparation

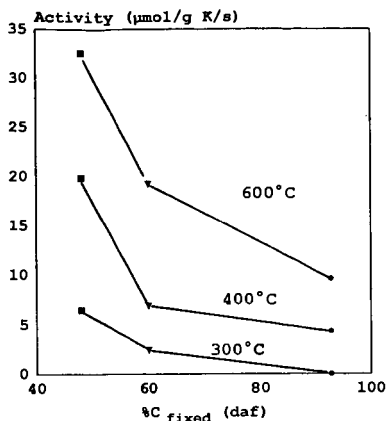| Coal precursor	Humic acid/ coal ratio	pyrolysis yield (%)	Briquette nomenclature
UA1	1.20	88.1	UA1-1.3
A3	1.20	72.0	A3-4.7
A3´	1.20	---	A3´-3.6
P	0.40	---	P-1.5
P	0.80	---	P-3.2
P	1.20	65.2	P-3.9
LY	0.25	52.1	LY-1.9
LY	0.78	53.4	LY-6.0
LY	1.20	53.4	LY-7.2

Figure 1. Briquette specific activity for NO reduction versus fixed carbon of coal precursors.(● UA1-1.3, ▼ P-1.5, ■ LY-1.9)
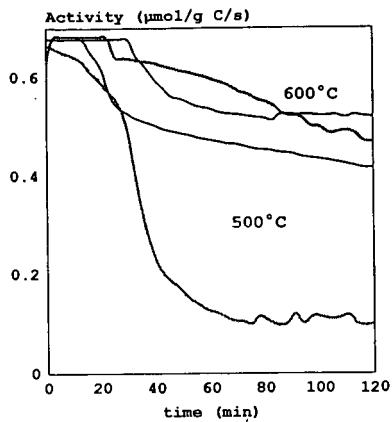
Figure 2. NO reduction activity curves. (── A3-4.7, ──── A3'-3.6)

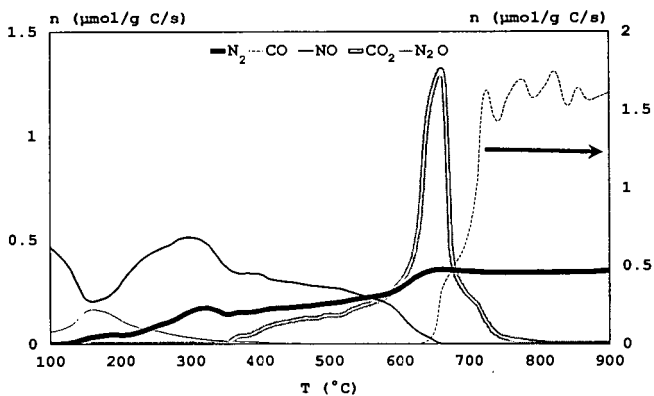

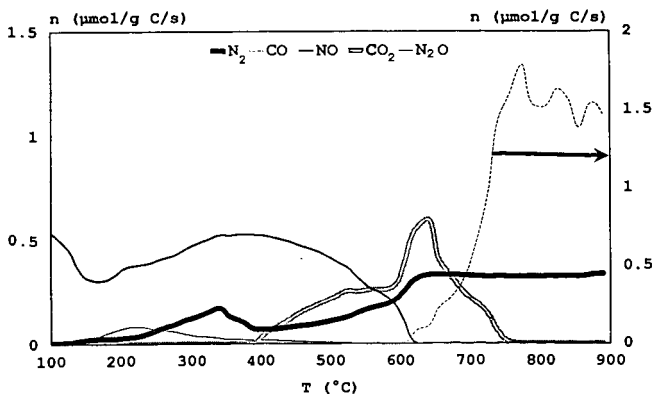Figure 3. TPR gas composition profiles for briquette A3'-3.6.

Figure 4. TPR gas composition profiles for briquette A3-4.7.

ACTIVATED CARBON USE IN TREATING DIESEL ENGINE EXHAUSTS

Sidney G. Nelson and Rick A. Babyak
Sorbent Technologies Corporation
1664 East Highland Road
Twinsburg, OH   44087

Keywords: Diesel engines; NOx control

INTRODUCTION

Diesel engines, both stationary and mobile, are major sources of air pollution. Pollutants of concern are solid and liquid particulates, nitrogen oxides (NOx), toxic hydrocarbon gases, and, in some cases, sulfur dioxide (SO_2). Approaches considered in the past to reduce these pollutants have included modifying the engine design, modifying the fuel composition, recirculating the exhaust gases, and installing a device or system on the exhaust gas stream to remove or modify the undesirable constituents. Of particular concern to the U.S. Air Force are the high levels of NOx that are present in their diesel engine exhaust gases. Sorbent Technologies Corporation (Sorbtech) engineers, during the past two years, have been examining and developing ways to remove NOx from these exhaust gases.

The principal NOx species in diesel engine exhaust gases is nitric oxide (NO). Typical NO levels range from 100 to 1200 ppm. Higher NO levels generally occur with higher engine loads that result in higher engine temperatures.

Both stationary and mobile diesel engines are employed at Air Force sites. Typical stationary engines produce back-up electrical power at critical sites, such as at computer or hospital locations. Mobile diesel engine applications include portable or mobile generators, air heaters, air-conditioners, and incinerators, small and large trucks, and buses. Each engine application presents its own problems because each has different space constraints and each produces gases with different characteristics of temperature, flow rates, and composition.

At least four different methods have been used in the past to remove nitrogen oxides (NOx) from waste gases. These methods include (1) selective catalytic reduction, (2) selective non-catalytic reduction, (3) reaction of the oxides with water or alkali solutions, and (4) sorption by a solid sorbent. The first two methods are receiving most attention today. In selective catalytic reduction, ammonia is commonly injected into the waste gas stream and the combination is passed across a catalyst to reduce nitrogen oxides to nitrogen and water. Disadvantages of this approach include high cost, narrow temperature range of applicability, and ammonia emissions into the atmosphere. In selective non-catalytic reduction, ammonia or urea is injected into the engine or combustor itself or into the gas leaving the engine where temperatures are very high. Disadvantages of this approach are low NOx removals and the problems associated with the handling of ammonia or urea. Reaction of the oxides with water or alkali has seen only limited success because of NO, the principal NOx species in most gases, does not readily dissolve in water or react with alkali in aqueous solutions.

APPROACH

Sorbtech engineers have adopted two separate approaches in treating exhaust gases from stationary diesel sources and from mobile diesel sources. Each approach involves the use of activated carbon, but in different manners.

Few materials sorb NOx well. An exception is activated carbon under certain conditions. Specially prepared activated carbons can sorb 10 percent or more of their weight in NOx under ideal conditions. After NOx is sorbed at a low temperature, heating the carbon to a higher temperature can release it. This process of sorbing NOx at a low temperature with activated carbon and releasing it at a high temperature has been used commercially in the past. This approach was pursued in treating exhaust gases from mobile sources.

An observation by Sorbtech engineers made possible a second approach for use with stationary sources. It was found that certain activated carbons, when saturated with NOx, act as a catalyst for the rapid conversion of NO to NO_2, in the presence of oxygen. The resulting gas stream containing principally NO_2, instead of NO, was then observed to be readily treatable with water alone or with alkali solutions. This approach was pursued in treating exhaust gases from stationary sources.

MOBILE DIESEL-ENGINE APPLICATIONS

System Design

The concept for mobile applications consists of two steps: (1) capture of NOx with an activated carbon filter; and (2) regeneration of the filter after it is saturated. The concept is shown schematically in Figure 1. For mobile applications, Steps 1 and 2 are generally performed at two separate locations. In Step 1, the use of a prefilter is recommended to remove particulates before the saturated carbon bed. Diesel engine exhaust gases usually contain huge amounts of particulates. Not only do large puffs of black particulates occur during engine start-up and during power changes, but smaller, PM-10 particles are emitted during all running conditions. Particle traps can be employed to effectively remove these particulates. A special vermiculite-based filter developed by Sorbtech likewise does an effective job in reducing particulates, particularly PM-10 particles. In Step 2, the carbon bed is regenerated by simply heating the bed. The NOx released during regeneration is destroyed by reaction with natural gas over a special catalyst developed by Sorbtech. The products of reaction are nitrogen, CO_2 and H_2O.

Figure 2 shows a mobile filter cart designed and constructed by Sorbtech to control emissions from Air Force mobile diesel generators. The cart was designed to be attached to the portable generator unit and to move with it to the usage location. Twenty-four separate activated carbon filters are employed on this cart. When saturated, the individual filters are removed from the cart and are processed in a separate regeneration/NOx-destruction unit.

Experimental Studies

The effectiveness of activated carbon filters in reducing the levels of NOx and CO in exhaust gases from a mobile diesel generator was examined in studies at Wright Patterson AFB, Ohio. The results of these studies are listed in Table 1. Two filter designs were considered, one consisting of 9 inches of activated carbon alone and a second consisting of 6 inches of a vermiculite-based sorbent followed by 6 inches of activated carbon. The supplier of the carbon was Calgon Carbon Corporation. The exhaust gas was cooled to 60°-100°F before entering the beds. During each run, the activated carbon bed temperatures increased to 110°-120°F due to heat of adsorption. The total run time was several hours. The residence time and flow rate of gas through the filters were 1.0 second and 40 SCFM, respectively.

The results of these runs showed that average NOx removals of 54 to 64 percent were achieved. These results agreed well with earlier laboratory results. Laboratory results showed that NOx removals were a strong function of space velocity. Because lower overall gas velocities will occur with the mobile filter cart, higher NOx removals with this unit can be expected.

STATIONARY DIESEL-ENGINE APPLICATIONS

System Design

The system developed to cleanse NOx and other contaminants from stationary diesel-engines exhaust gases is shown schematically in Figure 3. This system consists of four components: a prefilter (to remove particulates); a gas cooling means; an activated carbon bed; and a NO_2 scrubber. The key component in this system is the activated carbon bed that converts NO to NO_2.

Experimental Studies

A number of carbons were examined for their ability to first sorb NOx and then convert NO to NO_2. Two materials, one supplied by Calgon Carbon Corporation and one, an experimental char, supplied by the Illinois State Geological Survey proved to be particularly effective.

In one test, for example, an 8.0 gram bed of activated carbon was exposed at 26°C to a simulated exhaust gas having the composition: 460 ppm NO, 50 ppm NO_2, 10 wt% oxygen, and balance nitrogen at a flow rate of 4 liters per minute. The bed was exposed for 60 hours. Figure 4 shows the levels of NO and NO_2 entering and exiting the bed during the 60-hour exposure. In this figure, it can be seen that during an initial period, both NO and NO_2 were sorbed. After this period, however, NO ceased to be sorbed, but instead the NO partially passed through the bed and partially was converted to NO_2. After a time, about 15 hours in this case, an equilibrium occurred in the ratio of NO converted to NO_2 and the level of NO passing through the bed. In this run, a conversion of NO to NO_2 of over 75 percent was achieved.

In separate experiments, the ability of water and alkali solutions to scrub NO_2 and NO from gas streams was studied. Water alone was not effective in removing NO from gas streams, and concentrated alkali solutions were only partially effective. Water alone, however, was effective in removing the majority of the NO_2 present, and alkali solutions removed NO_2 almost completely.
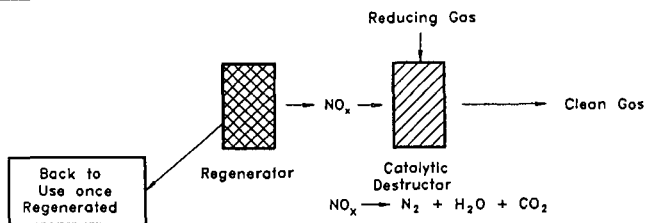
SORPTION
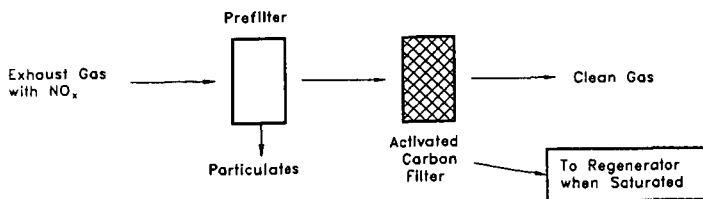
REGENERATION

Figure 1. Two-Step Process for NOx-Control-
Mobile Applications
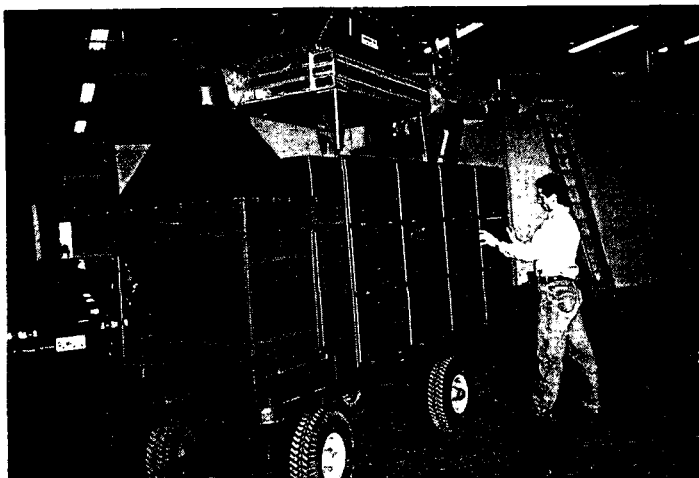
Figure 2. Activated Carbon Beds on a Mobile Filter
Cart for Controlling NOx Emissions

**TABLE 1. TEST RESULTS AT WRIGHT PATTERSON AFB
ON MOBILE DIESEL-ENGINE
EXHAUST GASES**

Gas Composition

	Entering Filter	Leaving Filter	Average Removal Rate
9" Activated Carbon			
NO	1000 ppm	320 ppm	68%
NO_2	200 ppm	120 ppm	40%
NOx	1200 ppm	440 ppm	63%
CO	200 ppm	200 ppm	0%
O_2	15%	15%	0%
6" Vermiculite Sorbent + **6" Activated Carbon**			
NO	800 ppm	345 ppm	57%
NO_2	300 ppm	205 ppm	32%
NOx	1100 ppm	550 ppm	50%
CO	100 ppm	100 ppm	0%
O_2	16%	16%	0%

Figure 3. Single-Step Process for NOx Control-
Stationary Applications

Figure 4. NO to NO_2 Conversion at Room Temperature

301

PRESSURE ENHANCED REVERSIBLE ADSORPTION
OF NO$_x$ BY ACTIVATED CARBONS

Aurora M. Rubel and John M. Stencel
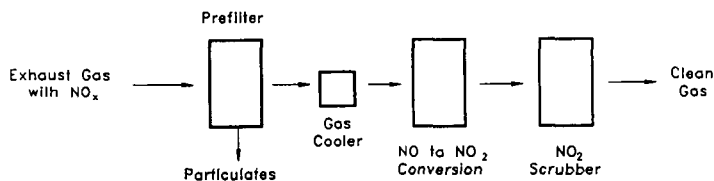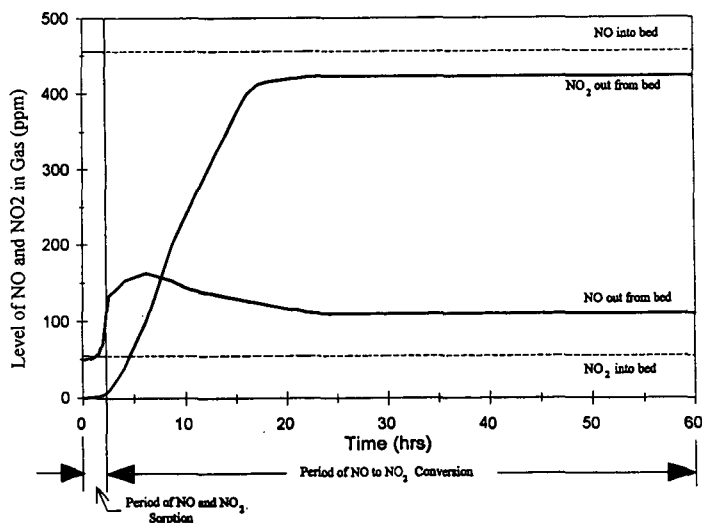Center for Applied Energy Research
University of Kentucky
Lexington, KY 40511-8433, USA

Keywords: NO$_x$, pressure, adsorption, carbon

INTRODUCTION

Although a tremendous amount of research has been and continues to be performed on the catalytic reduction of NO$_x$[1,2], the development of selective adsorbents for NO$_x$ could provide a chemically benign option for the control of these emissions through a process which sequesters and then concentrates NO$_x$. One requirement for an adsorption/desorption process is a material with a high, reversible adsorption capacity. A number of potential adsorbents have been examined, including metal oxides[3,4], zeolites[5,6], activated carbons[7-11], and carbon fibers[12,13] Activated carbons in the absence of O$_2$ have slow NO adsorption kinetics and low NO adsorption capacities[14,15]. However, at temperatures between 20-120°C and in the presence of O$_2$, recent studies has shown that both the kinetics and capacities are enhanced dramatically[7-11]. The research suggested that activated carbon catalytically converted NO + ½ O$_2$ → NO$_2$, which then condensed within the micropores of the carbon. At atmospheric pressure and 70°C, the NO$_x$ adsorption capacities were as high as 150 mg NO$_2$ (g carbon)$^{-1}$. Other coreactants such as CO$_2$ and H$_2$O did not inhibit nor were significantly adsorbed.

Our data suggested that the site(s) of NO → NO$_2$ conversion was different from the micorpores in which the NO$_2$ condensed[10]. Therefore, it may be possible to pressure enhance micropore filling and improve the overall kinetics and capacities of NO$_x$ adsorption over a greater temperature range. Such pore filling is influenced by a gas' van der Waals attractive force constant, a[3,13]. For example, the a constant for NO$_2$ is 25 times greater than that for NO[16], making NO$_2$ the preferred adsorbate. However, increased temperature has a disordering effect, decreasing the van der Waals attraction[17] and impacting negatively the overall adsorption capacity.

Since no work has been reported for pressurized adsorption-desorption of NO$_x$ over activated carbons, this study was initiated. In the current paper, the effects of pressure on the NO$_x$ adsorption capacity and kinetics over an activated carbon were studied, with specific attention to the effect of pressure on the storage of irreversible versus reversible NO$_x$ species.

EXPERIMENTAL

A Cahn C1100 high pressure microbalance and accompanying reactor was used for this study. The balance controls were interfaced to a personal computer for data acquisition. A cylindrical porous (100 m) stainless steel bucket, 10 mm O.D., 8 mm I.D. and 20 mm in length, was used as the sample holder. This bucket when loaded was suspended by a platinum wire and hook from the balance beam to a position within the heated portion of the high pressure cell. The reactor was enclosed within a vertical, split tube, furnace which was regulated by a programmable temperature controller. Pressure in the reactor was maintained by a back pressure regulator. Gases flowing into the reactor were controlled by high pressure mass flow controllers.

A VG Micromass quadrapole MS was used to monitor the gases leaving the reactor immediately down stream from the back pressure regulator. A heated (170°C) fused silica capillary was used to transfer a small aliquot of the gases leaving the pressure cell to an inert metrasil molecular leak which interfaced the capillary with the enclosed ion source of the MS. The MS has a Nier type enclosed ion source, a triple mass filter, and two detectors (a Faraday cup and a secondary emissions multiplier). The MS was controlled by a dedicated personal computer which was also used to acquire and review scans.

The identification of desorbed gases was done by using the major mass ions, 44, 32, and 18, for CO$_2$, O$_2$, and H$_2$O respectively. The major mass ion for both NO and NO$_2$ is 30. The relative abundance of mass 46 for NO$_2$ gas is approximately 40% but in mixtures of gases this value can change. Therefore, NO and NO$_2$ were identified by comparing peak intensities of the mass ion ratio, 30/46, during desorption and relating these intensities to those obtained using mixtures of NO or NO$_2$ and all combinations of gases used during our study.

Approximately 0.6 to 0.7 g of carbon were loaded in the zeroed sample bucket. The weight of the carbon was monitored continuously. Each batch of carbon was subjected to several adsorption and

desorption cycles. The flow rate through the reactor was measured at room temperature and pressure and was maintained at 100 ml/m during the entire experiment which involved gas switching between He and the combustion gas mixture. The sample was first pre-conditioned by heating to 180-200°C in a flow of He to remove any pre-adsorbed NO_x. The carbon was then cooled to the desired adsorption temperature before the first exposure to the simulated combustion flue gas.

As the carbon approached saturation with adsorbate, the gases flowing through the reactor were switched to He and reactor pressure was lowered to atmospheric beginning a pressure release desorption step. Weight loss was monitored until no further changes were observed. The weight loss during this period was attributed to reversibly adsorbed species. System pressure was then re-established with flowing combustion gas mixture and another adsorption cycle was begun. The amount of irreversibly adsorbed material was determined by temperature induced desorption after reversible desorption was complete during some experiments. The adsorption variables studied were temperature (70 and 100°C) and pressure (14.7, 150, 250, and 400 psi).

A commercially produced activated carbon was used in this study. The carbon was physically activated using steam and had N_2 BET total, mesopore and micropore surface areas of 460, 20, and 440 m²/g, and volumes of 0.69, 0.45, and 0.24 ml/g, respectively. The NO_x adsorption capacity of this carbon determined by thermal analysis-mass spectrometry was 120 mg NO_2 (g carbon)$^{-1}$ at atmospheric pressure and 70°C when a simulated flue gas, containing 2.0% NO, 5% O_2, 15% CO_2, 0.4% H_2O and He as the balance, was used. The reactant gas used for this work had the same composition. The gases were added simultaneously except during experiments where the carbon was presaturated with CO_2/O_2 before NO was added to the reactant mixture.

Control adsorption experiments were performed to determine the contributions of He and CO_2/O_2 to the total weight gained by the carbon. The gases and gas mixtures used during these experiments were: He alone; NO in He; O_2/CO_2 in He; and O_2/NO in He.

RESULTS
Figure 1 shows results of an experiment with three consecutive adsorption - reversible desorption steps at a pressure up to 250 psi (points a-to-b) which followed a pre-conditioning step (up to point a), and one temperature induced desorption of the irreversibly adsorbed species (from point c). The mass uptake of NO_2 was 200 mg (g carbon)$^{-1}$ at a temperature of 70°C. The weight loss following pressure release at point b was attributed to a reversibly adsorbed species. After pressure release (to point c) approximately 40 mg (g carbon)$^{-1}$, or 20% of the weight gain, remained on the carbon even after 1700 minutes of purging with He at 70°C. This more strongly bound adsorbate, considered as the irreversibly bound species, required temperature induced desorption to 180-200°C to be completely removed. The adsorption capacity associated with the reversibly adsorbed species was not affected by repeated adsorption - desorption cycles; as many as 10 cycles were performed using the same sample without loss of capacity.

The effect of pressure on the adsorption of combustion flue gas components was studied using the adsorption - desorption profiles just described. Figure 2 is a plot of the amount of total, reversibly, and irreversibly adsorbed NO_2 verses pressure at a temperature of 70°C. Pressure improved total adsorption and increased the amount of reversibly adsorbed material while reducing the amount of irreversibly adsorbed species. Plotting the reversible adsorption data as the ratio of NO_2 volume adsorbed (carbon microporous volume)$^{-1}$, V_{NO2}/V_μ, verses the total pressure, P, results in a typical Type I isotherm[18]. This type of isotherm suggested that micropore volume filling is important for NO_2 uptake, with the formation of a monolayer at pressures near 150 psi (Figure 3).

Figures 4a, 4b and 4c show the weight loss and intensities of mass spectral peaks as a function of time during pressure release to atmospheric from either 400 psi or 250 psi, and during temperature induced desorption. For simplicity, only trends for masses 30, 32 and 44 are displayed. The mass ion ratio, 30/46, for the data in Figure 4 was compared to the mass ion ratio obtained from standard mixtures. This comparison defined NO_2 as the only detectable nitrogen oxide species evolved during pressure release and thermal desorption.

Increasing the adsorption pressure from 250 to 400 psi caused increased intensity for ion mass 30 (NO_2) and decreased or held constant the intensity for ion masses 32 (O_2) and 44 (CO_2) during pressure release desorption. The data in Figure 4a and 4b, when compared to the data in Figure 3, indicate that O_2 and CO_2 may be important components of the reversibly adsorbed species (see below). Subsequent to eliminating the reversibly adsorbed species, the temperature induced desorption data in Figure 4c show that very little O_2 evolved from the carbon, whereas significant amounts of CO_2 and NO_2 were present.

303

The time sequence by which NO_2, O_2 and CO_2 were desorbed was different during pressure release versus temperature induced desorption. During pressure release, the evolution of O_2 and CO_2 began immediately and maximized at approximately 115 s before the peak in the NO_2 desorption. During a thermal desorption cycle, the peak for NO_2 occurred 150 s before the CO_2 desorption peak; the temperatures of these maxima were 140 and 155°C for NO_2 and CO_2, respectively. It is likely that, whatever the source of the CO_2 in the mass spectral data, the origin of the CO_2 detected during pressure release was different than the origin of CO_2 during temperature induced desorption. Because only a trace amount of O_2 was detected during temperature induced desorption, its evolution time was not quantified.

A comparison of desorption spectra from 150, 250, and 400 psi experiments clearly demonstrated that the amount of NO_2 released from the carbon increased with increasing adsorption pressure. In contrast, the amounts of stored O_2 and CO_2 did not appear to be uniformly affected by pressure. To quantify the relative contribution of NO_2, CO_2, and O_2 to the total mass uptake, control experiments were used to provide the relative amount of weight gain which could be related to each of these adsorbates. For example, data in Figure 5, for experiments performed at 250 psi, confirmed our previous findings at atmospheric pressure that less than 10 mg NO_2 (g carbon)$^{-1}$ was adsorbed if O_2 was not present in the reactant gas[7-11]. This value is approximately 2% of the mass uptake for the case of simultaneous exposure to $NO + O_2$. During the CO_2/O_2 adsorption displayed in Figure 5, the mass uptake was as great as 78 mg (g carbon)$^{-1}$, or about 36% of the total uptake when NO is also present in the reactant stream. In addition, Figure 6 shows that the relative contributions of the reactants to the total mass uptake were sensitive to temperature with less than 10% of the total uptake at 100°C resulting from CO_2/O_2. The remainder of the mass uptake for the carbons was the result of $NO + \frac{1}{2} O_2 \rightarrow (NO_2)_{adsorbed}$.

The relative percent of reversibly and irreversibly adsorbed NO_2 removed from the sample is given in Figure 7. At 70°C and atmospheric pressure, approximately 65% of the NO_2 in the carbon was reversibly desorbed; this percentage increased to 80% at 250 psi. At 100°C and atmospheric pressure, approximately 75% of the NO_2 in the carbon was reversibly desorbed; this percentage increased to greater than 95% at 250 psi. Hence, increased pressure decreased the relative amount of NO_2 which was irreversibly adsorbed at each temperature.

DISCUSSION
The Type I isotherm in Figure 3 suggests micropore filling. We have applied both Langmuir theory and BET adsorption theory to these data with the identical conclusion that the NO_2 adsorbed within the carbon was primarily located within the micropores and that a monolayer capacity within these pores was reached at total pressure near 150 psi[19]. Other work has shown that micropore filling is not effective for gases which have critical temperatures less than the temperature used during adsorption[3]. NO_2 is the only gas in this study with a critical temperature (158 °C) that is greater than the adsorption temperatures which were used. Hence, the amounts of NO, O_2, and CO_2 adsorbed in the micropores should be expected to be small in comparison to the amount of NO_2 (see Figure 6). However, at 250 psi and 70°C, the amount of CO_2 adsorbed was 78 mg (g carbon)$^{-1}$, a value representing 36% of the total uptake of the carbon. This uptake was possibly a consequence of the increased pressure affecting CO_2 condensation since the critical temperature for CO_2 is 31°C which is close to the adsorption temperature, 70°C. The low value of the critical temperature for NO (-93°C) also indicates that it would not be a stable, adsorbed species in the carbon's micropores.

Another factor which favors NO_2 adsorption is its high van der Waals force constant, a, which is 1.5 times greater than the a constant for CO_2. Therefore, the attractive force between NO_2 molecules upon entering the pores would be greater than for CO_2. This difference may account for the desorption of CO_2 before NO_2 during pressure release. During temperature induced desorption, the evolution of CO_2 subsequent to NO_2 desorption may be related to the gasification of carbon at C-O bonds.

The total amount of gaseous NO_2 (at STP) adsorbed into the activated carbon at 400 psi and 70°C is approximately 70 ml (g carbon)$^{-1}$. This value is significantly larger than the amount of NO reported to occupy the microporosity of cation-exchanged zeolites[2]. In addition, the amount of irreversibly adsorbed NO_2 in the activated carbon at 250 psi and 100°C is less than 5% of the total amount of adsorbed NO_2. Such a value is as good as or less than values reported for the cation-exchanged zeolites.

SUMMARY AND CONCLUSIONS
The amount of NO_2 reversibly adsorbed on activated carbons increased with pressure over a range of pressures from 15-400 psi. At 100°C and 250 psi pressure, the amount of NO_2 adsorbed was nearly the same as at 70°C and atmospheric pressure and 3 to 4 times greater than at 100°C and

atmospheric pressure. The NO_2 adsorption Type I isotherm suggested that the reversible NO_2 adsorption mechanism involved micropore filling. The time profiles during pressure release and temperature programmed desorptions were consistent with important roles for critical temperature and pressure and van der Waals forces in the adsorption and condensation of NO_2, CO_2, and O_2 within the micropores of the carbon.

REFERENCES

1. Bosch. H. and F. Jansen *Catal. Today* **1988**, *2*, 369
2. Ritter, J.A. and R.T. Yang *Ind. Eng. Chem. Res.* **1990**, *29*,1023
3. Arai H. and M. Machida *Catalysis Today* **1994**, *22*, 97
4. Stiles,A.B., M.T.Klein, P.Gauthier, S.Schwarz, J.Wang *Ind. Eng.Chem. Res.* **1994** ,*33*, 2260
5. Zhang, W., H. Yahiro, N. Mizuno, J. Izumi, and M. Iwamoto *Chem. Lett* **1992**, 851
6. Zhang, W., H. Yahiro, N. Mizuno, J. Izumi, and M. Iwamoto *Langmuir* **1993**, *9*, 2337
7. Rubel, A., J.Stencel, and S.Ahmed *Proc.AIChE Summer Nat. Meeting* **1993**, Seattle, WA, 77b
8. Rubel, A.M., M.L. Stewart, and J.M. Stencel *Preprints Sym.NO$_x$ Reduction*, ACS, Div. Pet.Chem., San Diego **1994**, *39(1)*, 137
9. Rubel, A.M., M.L. Stewart, and J.M. Stencel *Preprints Sym. on Appl.Fuel Chem. to Other Areas*, ACS, Div. of Fuel Chem., Washington, DC **1994**, *39(3)*, 879
10. Rubel, A.M., M.L. Stewart, and J.M. Stencel *JMR* **1994**,*10(3)*562
11. Stencel, J.M.,A.M. Rubel *8th ICCS Conf.Proceedings*, Elsevier Science B.Y. **1995**, in press
12. Kaneko, K., N. Shindo *Carbon*, **1989**, *27,6*, 815
13. Kaneko, K., Y. Nakahigashi, and K. Nagata *Carbon* **1988**, *26,3*, 327
14. Teng, H., and E.M. Suuberg *J. Phys. Chem* **1993**, *97*, 478
15. Teng, H., E.M. Suuberg, and J.M. Calo *Proc. 19th Conf. on Carbon* **1989**, 574
16. *CRC Handbook of Chemistry & Physics*, *55*, D157
17. Sienko, M.J. and R.A. Plane *Chemistry*, McGraw Hill, **1976**, 138
18. Brunauer, S., L.S. Deming, W.E. Deming, E. Teller *J. Amer. Chem. Soc.* **1940**, *62*, 1723
19. Rubel, A.M. and J.M. Stencel, *Energy and Fuel*, in press
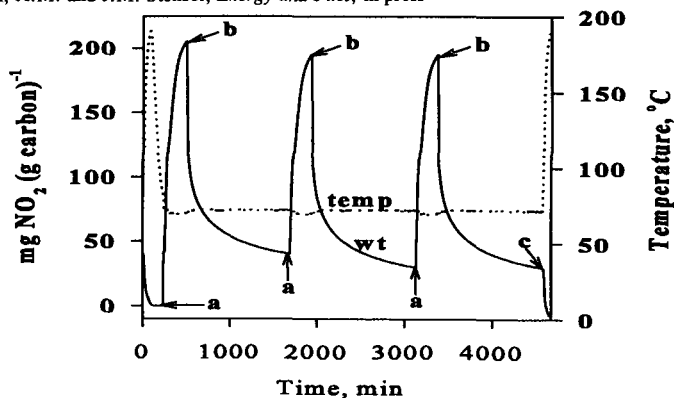
Figure 1. Adsorption - desorption profile for activated carbon.
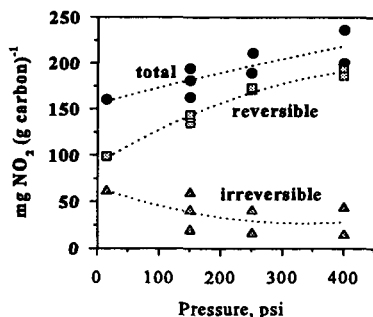
Figure 2. Plot of total, irreversible, and reversible adsorption versus pressure.
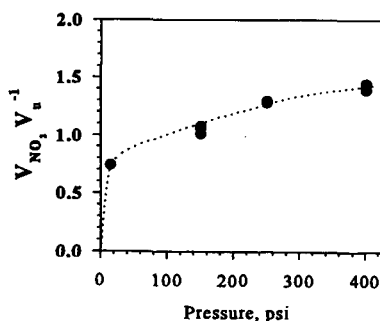
Figure 3. The type I adsorption isotherm for 70°C adsorption on activated carbon.
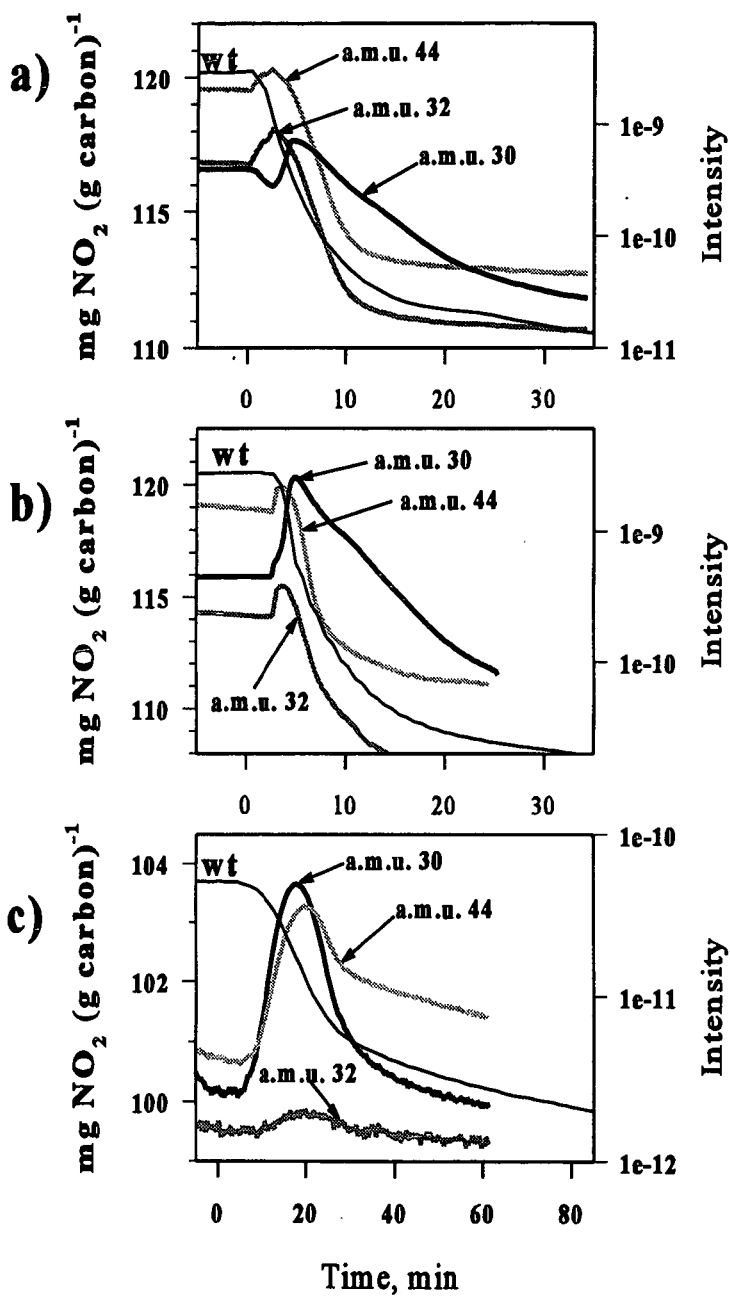
Figure 4a, b, c. Integrated weight loss - mass spectral data for pressure-release and thermal-induced desorptions; **4a)** pressure-release from 250 psi; **4b)** pressure-release from 400 psi; **4c)** thermal-induced desorption.
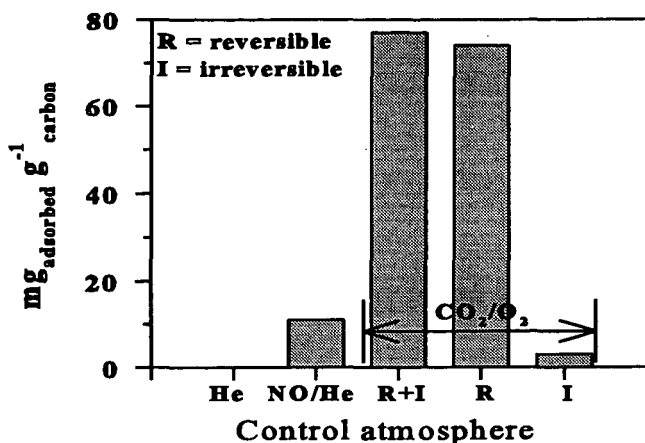
Figure 5. Contributions of He, NO, and CO_2/O_2 to total adsorption.
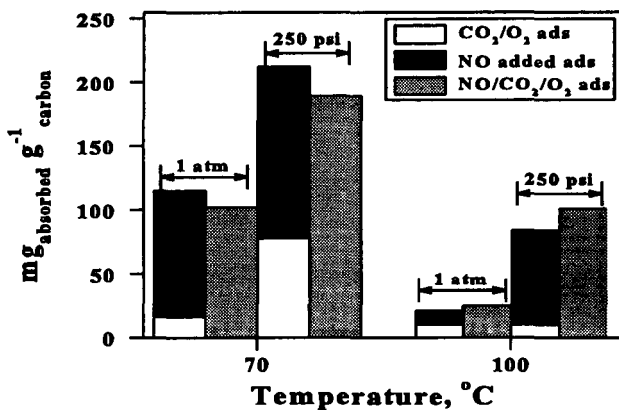
Figure 6. Effect of temperature on the relative contribution of CO_2/O_2 to total uptake.
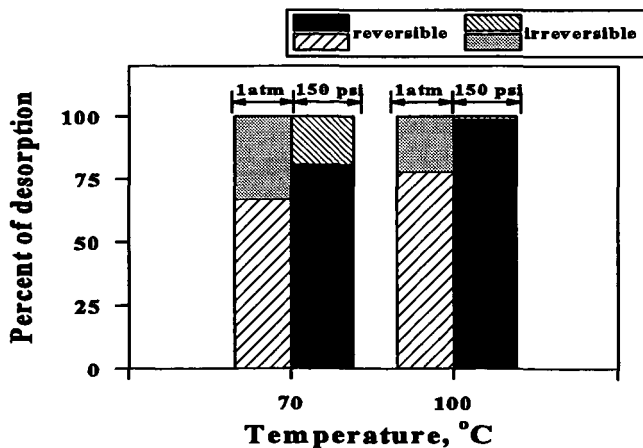
Figure 7. Effect of temperature and pressure on the relative percentage of reversibly and irreversibly adsorbed NO_2 removed from the carbon.

LOW-TEMPERATURE NO$_x$ REMOVAL FOR FLUE GAS CLEANUP

Ben W.-L. Jang[1], James J. Spivey[1], Mayfair C. Kung[2], and Harold H. Kung[2]

[1]Center for Engineering and Environmental Technology
Research Triangle Institute
Research Triangle Park, NC 27709
[2]Department of Chemical Engineering
Northwestern University, Evanston, IL 60208

Key Words: NO$_x$ reduction, NO oxidation, carbons

INTRODUCTION

A wide range of NO$_x$ control processes for electric utilities are under investigation to compete with the current processes such as selective catalytic reduction (SCR). Although SCR using NH$_3$ is effective for NO reduction, the process suffers from many disadvantages [1]. In addition, current SCR processes must be located at places within the flue gas treatment process where temperatures are near 400 °C. Retrofitting SCR into these locations in the plant is costly because space and access in many power plants are extremely limited [2]. Therefore, there is a need to develop NO$_x$ control technologies that can be located downstream of the particulate control device, near the stack, where temperatures are around 150 °C.

This study investigates the low-temperature selective reduction of NO with hydrocarbons under simulated flue gas conditions over carbon and carbon-supported catalysts. NO oxidation to NO$_2$ was also investigated as a way of making NO more reactive with hydrocarbons or easier to be removed by absorption at these temperatures.

EXPERIMENTAL

Four active carbon samples including type GI of Barnebey & Sutcliffe Corp. (GI), GmbH from Carbo-Tech (GmbH), PCB from Calgon (PCB), and Rheinbraun AG (AG) and one active carbon fiber (Osaka) provided by Professor Machida (Kyushu U.) were used in this experiment. All the granules were broken into 16/30 mesh particles followed by drying at 120 °C overnight. The carbon-supported catalysts were prepared by pore volume impregnation. The impregnated catalysts were first dried under vacuum at room temperature for 2 h, then at 60 °C for 2 h and 80 °C overnight. All catalysts were treated with 150 cm^3/min of helium at 400 °C for 1 h before reaction. The schematic of the experimental system used in this study is the same as shown in the authors' previous report [3]. NO reduction was tested with 400 cm^3/min of 0.1% NO, 4% O$_2$, 8% H$_2$O, and hydrocarbons in He over 7 g of catalysts. NO oxidation was carried out with 400 cm^3/min flow of 0.1% NO, 4% O$_2$, and balance He over 4 g of catalysts.

RESULTS AND DISCUSSION

NO Reduction

Supports. Four carbon-supported Cu catalysts were tested for the selective reduction of NO at 150 °C. BET surface area measurement was carried out for those carbons. The surface areas ranged from 90 m^2/g to 943 m^2/g. The activities for NO selective reduction with acetone were investigated in the presence of O$_2$. The activity over Rheinbraun AG, with the lowest surface area (90 m^2/g), was the lowest among the carbons tested. The activity for NO conversion was much better for GmbH from Carbo-Tech with surface area of 440 m^2/g. The initial NO conversion for Carbo-Tech carbon was high, but decreased to ~20% after 5 h. PCB from Calgon (927 m^2/g) and GI of B&S (943 m^2/g) carbons were the two best catalysts for NO reduction with acetone in the presence of O$_2$. The NO conversions were 26% and 32% after 5 h for GI and PCB, respectively. The results indicate that carbon materials with higher surface area would be better for NO selective reduction with acetone in the presence of O$_2$. Although the surface area of GI was about the same as PCB, the activity of PCB was somehow more stable than GI. This result suggests that the surface area was not the only factor affecting the activity of carbon catalysts for NO reduction. Factors such as pore size and Cu dispersion could influence the catalytic activity and the stability of reaction.

Reductants. Because the NO reduction activity of PCB was the best among the carbon materials tested, further investigation was focused on supported PCB catalysts. The NO conversion over 5%Cu-2%Ag/C with various hydrocarbons as reductants in the presence of O$_2$ and H$_2$O is shown in Table 1, along with the results in the absence of any hydrocarbon. The efficiency order of reductant was acetone>2-propanol>isobutanol>ethyl ether>propene, ethanol> methanol. The major NO reduction product was N$_2$ with >99% selectivity. Acetone was the most active reductant for NO selective reduction in the presence of O$_2$ and H$_2$O over the 5%Cu-2%Ag/C catalyst at 150 °C. The NO conversion with acetone was 35% with 3,000 h^{-1} space velocity after 5 h on stream. Interestingly, the NO conversion without any reductant was higher than the conversion using propene, ethanol, or methanol as reductant. The results suggest

that propene, ethanol, and methanol inhibit the direct reduction of NO with carbon which is known as catalyzed by Cu in the presence of O_2.

The necessity of oxygen to promote the reduction of NO by acetone is shown in Figure 1. The NO conversion was low in the beginning and decreased to ~10% after 20 min on stream for the reaction without the presence of O_2. With 1% of O_2, NO conversion was high and slowly decreased to a steady level. With O_2 concentration of 4%, the reduction activity followed the same trend except with higher NO conversion. This shows that the reaction of NO directly with acetone is not significant in comparison with the NO selective reduction in the presence of O_2. Under the reaction conditions, the fast decrease of NO conversion during the first hour is not due to the NO adsorption on carbons since the conversion is also low in the absence of O_2. It is also unlikely that the decrease of NO conversion is caused by the adsorption of NO_2 since NO_2 decomposes quickly to NO on the surface of carbons.

Effect of H_2O and SO_2. Most literature shows an inhibiting effect of H_2O on NO reduction over various catalysts, e.g., Cu-ZrO_2 [4] and Co-ZSM-5 [1]. In contrast, results on 5%Cu-2% Ag/C showed that H_2O had no effect on NO reduction. The conversion of NO with 8% H_2O or without H_2O was essentially the same. Probably the highly hydrophobic property of carbon material surface prevents the interference of H_2O. SO_2, on the other hand, has a large negative effect on NO selective reduction with acetone. As shown in Figure 2, the catalyst deactivated very fast with 0.1% of SO_2. It is suspected that the presence of SO_2 poisons the metals by the formation of metal sulfates which deactivate the NO reduction activity.

Effect of Metals. Carbon alone is known as a catalyst for the selective reduction of NO with ammonia [5]. Figure 3 shows the NO conversion versus time for the carbon alone and for the 5%Cu-2%Ag/C catalyst. The enhancing effect of Cu+Ag on the activity of active carbon for NO reduction can be clearly seen with acetone as a reductant. The NO conversion decreased rapidly on active carbon alone (without Cu+Ag) with acetone in the presence of O_2 and H_2O. NO conversion was negligible after 1 h of reaction. On the other hand, the NO conversion over 5%Cu-2%Ag/C slowly decreased to 35% after 5 h. The results show that acetone in the absence of oxygen is not an effective reductant for NO reduction and it suggests that the function of Cu+Ag is to promote the oxidation of acetone for the selective reduction of NO. All experiments, with one exception, over 5%Cu-2%Ag/C in the presence of O_2 showed nearly 100% N_2 selectivity, i.e., no N_2O was formed. The only exception was the NO reduction with acetone in the absence of O_2, which showed >80% N_2O selectivity, suggesting that the NO reduction pathway in the presence of O_2 is different from the pathway in the absence of O_2. The formation of N_2O is probably from the direct reaction between NO and acetone or from the disproportionation of NO [6]. The high selectivity of the 5%Cu-2%Ag/C catalyst may be related to low catalyst activity for the activation of molecular oxygen, as observed on some solid acid catalysts [7]. Other metals supported carbon catalysts, such as Pt and Pd, were also tested for NO selective reduction with acetone. However, the NO reduction activity over Pt and Pd supported catalysts was much lower than the activity with Cu+Ag. Besides lower NO reduction activity with Pt and Pd, lower selectivity to N_2 was also noticed.

NO Oxidation
Active Carbon Fibers vs Active Carbon. Both the activated carbon fibers (ACFs) and PCB active carbon showed high NO oxidation activities at low temperature. The results are summarized in Table 2. At 30 °C with 400 ppm NO, 4% O_2, and balance He, NO conversions are 90% and 82% over ACF and active carbon, respectively. The activity, however, decreases with the temperature. At 75 °C, the NO oxidation conversion decreased to 51% and 42% on active carbon fibers and active carbon, respectively. Negligible oxidation was observed at 120 °C. This is consistent with results reported by Machida et al. [8]. The oxidation activity of both active carbon fibers and active carbon are interesting. Figure 4 shows the NO_x concentration versus time during NO oxidation reaction over active carbon at 30 °C. In the beginning, the adsorption of NO_x is severe. The concentration of NO increased with time and no NO_2 was detected for the first 7 h. After 7 h, NO_2 adsorption sites were saturated and as a result NO_2 breakthrough was observed. This suggests that NO_2 is adsorbed more strongly than NO on carbon materials.

Effect of Pretreatment. Three different pretreatments were tested to increase the NO oxidation activity of active carbons including heat treatment at 800 °C in N_2, reduction with H_2 at 800 °C, and oxidation using HNO_3. The results are shown in Table 3. None of the pretreatments increased NO oxidation at 120 °C. As reported by Machida et al. [8], the heat treatment increased the oxidation activity of active carbon fibers for NO to NO_2 in the presence of H_2O. It is speculated that the increased oxidation activity of fibers is from the formation unsaturation of carbon surface by the liberation of CO and CO_2 with the heat treatment in N_2. The removal

of the oxygen functional group, which increases the hydrophobic nature of the carbon, also contributes to the increase in NO oxidation activity of carbons in the presence of H_2O. However, as shown in Table 3, the heat treatment actually slightly decreased the oxidation activity of the PCB active carbon at 75 °C. The NO oxidation activity decreased from 42% to 35% at 75 °C after the heat treatment.

It was reported that H_2 reduction at high temperature was able to reduce the oxygenated functional groups on carbons [9]. The active carbon pretreated with H_2 was then tested for NO oxidation. The activity, also shown in Table 3, was negligible at 120 °C. The oxidation activity at 75 °C was close to the activity after the heat treatment and was lower than the catalyst without pretreatment. Both heat treatment and H_2 reduction treatment were intended to remove the oxygenated functional groups on carbon and to improve the oxidation activity. However, the results showed a negative effect on NO oxidation to NO_2. The results of active carbon for NO oxidation after the HNO_3 treatment are also included in Table 3. The activity was negligible at 120 °C and was only 28% at 75 °C.

All pretreatments resulted in some negative change of the activity of activated carbons for NO oxidation, indicating that the functional groups alone do not play the major role in the NO oxidation reaction. It is possible that the cooperative relationship between oxygenated functional groups and nonoxygenated functional groups is important for NO oxidation to NO_2.

Effects of SO_2 and H_2O. The effect of SO_2 on NO oxidation activity over heat-treated PCB active carbons was studied by adding 0.1% SO_2 to the inlet gas. The results are also shown in Table 3. The NO oxidation activity was negligible in the presence of SO_2 over the catalyst at 120 °C. When the reaction temperature was further decreased to 75 °C, no oxidation activity was observed as compared to 35% NO oxidation conversion in the absence of SO_2. The result suggests that the presence of SO_2 poisoned the oxidation activity of carbon catalysts, which is similar to the results reported in the literature [10-12]. The competitive adsorption of NO and SO_2 on carbon surfaces is possibly the cause.

We also tested the combined effect of SO_2 and H_2O on the active carbon for NO oxidation. As reported earlier [13], SO_2 greatly promotes the NO oxidation reaction in the presence of H_2O over Co/Al_2O_3. However, the NO oxidation activity was negligible over the active carbon in the presence of SO_2 and H_2O at 120 °C.

Active Carbon Supported Catalysts. Five percent cobalt oxide and 1% iron oxide supported on active carbons were tested for NO oxidation. The results are summarized in Table 4 to compare with the NO oxidation activity of unsupported active carbon. Again, both active carbon-supported catalysts showed negligible activity at 120 °C. It is believed that the decomposition activity of carbons for NO_2 to NO is too fast at 120 °C to be overcome by the oxidation activity of metal oxides. The activities at 75 °C were obtained followed by the tests at 120 °C. The NO oxidation activities were 26% and 24% over 1% iron oxide/A.C. and 5% cobalt oxide/A.C., respectively. The activities of active carbon-supported catalysts were lower than the unsupported catalyst at 75 °C.

CONCLUSIONS

Acetone was the most active reductant for NO selective reduction over 5%Cu-2%Ag/C among the hydrocarbons tested. Acetone, oxygen, and carbon-supported Cu+Ag catalyst are all required to maintain high NO conversion and high N_2 selectivity at these low temperatures. Although 35% NO conversion is relatively high at 150 °C in the presence of O_2 and H_2O, further improvement is needed for the process to be competitive with other processes. The NO reduction activity of Cu-Ag/carbon with acetone was also greatly decreased by the presence of 0.1% SO_2, which may be present even downstream of some flue gas desulfurization systems.

Both active carbon fibers and active carbon are active for NO oxidation to NO_2 at low temperature. At 30 °C and 0.01 g·min/cm^3 space velocity, the NO conversions to NO_2 were 90% and 82% on active carbon fibers and active carbon, respectively. However, the activity decreased with the temperature, becoming negligible at 120 °C on both active carbon fibers and active carbon. Different treatments (heat treatment at 800 °C, reduction in H_2, and oxidation with HNO_3) and additional metals did not improve the NO oxidation activities of carbons at 120 °C. With the addition of 0.1% SO_2, the NO oxidation activity of activated carbon was poisoned and the conversion was negligible at 75 °C.

ACKNOWLEDGMENTS

LITERATURE CITED

1. Li, Y., Battavio, P.J., and Armor, J.N. *J. Catal.* 142:561-571, 1993.
2. Wood, S. C. *Chem. Eng. Prog.* 37, 1994.
3. Jang, B.W.-L., Spivey, J.J., Kung, M.C., Yang, B., and Kung, H.H. ACS Symposium Series 587, p. 83, 1995.
4. Kung, H.H., Kung, M.C., Yang, B., Spivey, J.J., Jang, B.W.-L. Technical report for March-May/1994 to the Illinois Clean Coal Institute under ICCI contract 93-1/3.1A-3P: Urbana, IL, 1994.
5. Spivey, J.J. *Annual Rep. Prog. Chem., Part C*, Royal Society of Chemistry: Cambridge, UK, 1994.
6. Li, Y., Armor, J.N. *Appl. Catal.* 76, L1, 1991.
7. Hamada, H., Kintaichi, Y., Yoshinari, T., Tabata, M., Sasaki, M., Ito, T. *Catal. Today*, 17:111-120, 1993.
8. Machida, I., Kisamori, S., Hironaka, M., and Kawano, S. *Energy and Fuels*, 8(6), 1994.
9. Avgul, N.N., Kisele, A.V., Kovalyova, N.V., and Khrapova, E.V. Proc. 2nd Intern. Congress on Surface Activity, ed., J.H. Schulman, Vol. II, Academic Press, New York, 1957, p. 218.
10. Karisson, H.T., and Rosenberg, H.S. *Ind. Eng. Chem. Process Des. Dev.* 23:808-814, 1984.
11. Takayasu, M., An-Nen, Y., and Morita, Y. *Rikogatu Weseda Daigaku*, 72:17-21, 1976.
12. Arai, H., Tominaga, H., and Tsuchiya, J., *6th Int'l Cong. on Catalysis*, pp. 997-1006, 1977.
13. Kung, H.H., Kung, M.C., Yang, B., Spivey, J.J., Jang, B.W.-L. Technical report for Sept.-Nov./1994 to the Illinois Clean Coal Institute under ICCI contract 93-1/3.1A-: Urbana, IL, 1994.

Table 1. NO Selective Reduction by Hydrocarbons over 5%Cu-2%Ag/C (1,000 ppm NO, 4% O_2, and 8% H_2O, 3,000 h^{-1}, 150 °C)[a]

Reductant	NO Conversion (%)	N_2 Selectivity (%)
0.13% acetone	35	>99
0.13% 2-propanol	31	>99
0.10% isobutanol	25	>99
0.08% ethyl ether[b]	18	>99
0.20% ethanol	<10	>99
0.11% propene	<10	>99
0.40% methanol	negligible	>99
none	11	>99

[a] All catalysts subjected to He treatment at 400 °C for 1 h before reaction. The conversion and selectivity was taken after 5 h on stream.
[b] The concentration of ethyl ether was limited by its solubility in water.

Table 2. NO Oxidation to NO_2 over Active Carbon Fibers (ACF) and PCB Active Carbon (A.C.)

Carbon	Temperature		
	30 °C	75 °C	120 °C
ACF	90%	51%	negligible
PCB A.C.	82%	42%	negligible

Note: Activities were obtained after 40 h on stream. Reaction conditions: 400 ppm NO, 4% O_2, and balance He; 400 cm^3/min over 4.0 g of catalysts.

Table 3. NO Oxidation to NO_2 over PCB Active Carbon (A.C.)

PCB A.C.	Temperature	
	120 °C	75 °C
Fresh	negligible	42%
Heat treatment	negligible	35%
H_2 reduction	negligible	31%
HNO_3 oxidation	negligible	28%
With 0.1% SO_2	negligible	negligible
With 0.1% SO_2 + 10% H_2O	negligible	not available

Note: Activities at 120 °C were obtained after 24 h on stream and the activities at 75 °C were obtained after 24 h at 120 °C and 40 h at 75 °C. Reaction conditions: 400 ppm NO, 4% O_2, and balance He; 400 cm^3/min over 4.0 g of catalysts.

Table 4. NO Oxidation to NO_2 over PCB Active Carbon (A.C.) and Active Carbon-Supported Catalysts

Catalyst	Temperature	
	120 °C	75 °C
Fresh A.C.	negligible	42%
1% iron oxide A.C.	negligible	26%
5% cobalt oxide A.C.	negligible	24%

Note: Activities at 120 °C were obtained after 24 h on stream and the activities at 75 °C were obtained after 24 h at 120 °C and 40 h at 75 °C. Reaction conditions: 400 ppm NO, 4% O_2, and balance He; 400 cm^3/min over 4.0 g of catalysts.
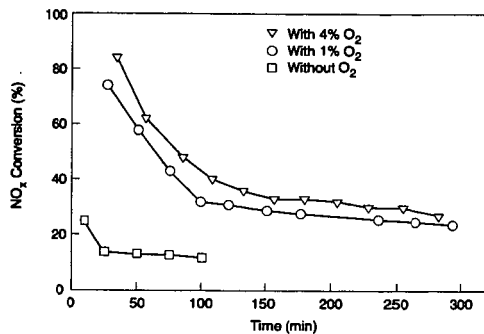
Figure 1. NO conversion over 5%Cu-2%Ag/C as function of time with different O_2 concentration. Reaction conditions: 0.1% NO, 0.13% acetone, 8% H_2O at 150 °C with 3,000 h^{-1} space velocity.
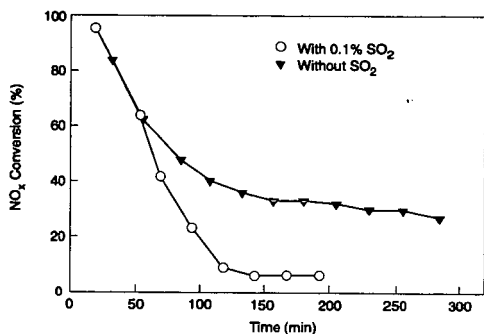
Figure 2. The effect of SO_2 on NO reduction with acetone over a Cu supported carbon catalyst at 150 °C; 0.1% NO, 0.13% acetone, 4% O_2, and 8% H_2O; 3,000 h^{-1}.
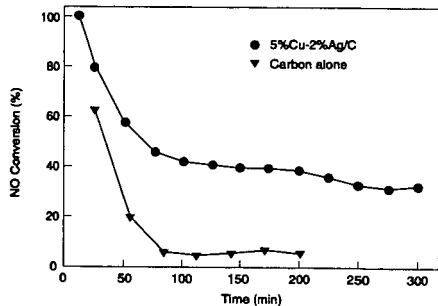
Figure 3. NO conversion versus time over 5%Cu-2%Ag/C and carbon only. Reaction conditions: 1,000 ppm NO, 8% H_2O, 3,000 h^{-1}, 150 °C.
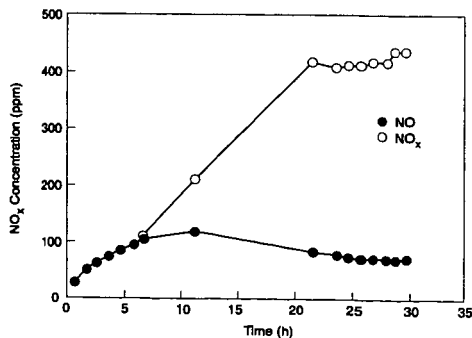
Figure 4. NO and NO_x concentrations as function of time during NO oxidation over activated carbon at 30 °C; 400 ppm NO, 4% O_2, and balance He; 400 cm^3/min over 4.0 g of catalysts.

312

STATE OF NOx OVER PITCH BASED ACTIVE CARBON FIBER AT THE INITIAL STAGE OF NO-NH3 REACTION

Isao Mochida*, Shizuo Kawano*, Akinori Yasutake[†], Masa-aki Yoshikawa[††],
and Yuji Matsumura[††]
*Institute of Advanced Material Study, Kyushu University,
6-1 Kasugakoen, Kasuga, Fukuoka 816, Japan
[†]Nagasaki R. and D. Center, Mitsubishi Heavy Industry,
5-717-1 Fukabori, Nagasaki 851-03, Japan
[††]Research & Development Center, Osaka Gas Co., Ltd.,
6-19-9 Torishima, Konohana, Osaka 554, Japan

INTRODUCTION

Removal of NO in the atmosphere as well as the flue gas is still an objective to increase the efficiency. The present authors have reported a significant catalytic activity of pitch based active carbon fiber for the reductive[1,2] and oxidative[3] removal of NO at room temperature, especially after the ACF was heattreated at a proper temperature.[4,5] The problem to be solved is the inhibition of humidity above 70% relative humidity (rh).[6,7] Hence the enhancement of the activity in the humid area is the major target be explored.

In the present study, adsorption and reduction of NO over pitch based active carbon fiber (ACF) was analyzed especially at the initial stage of NO-NH3 reaction where the high rate of NO removal was observed ever the ACF in the humid air, although the activity decreased gradually to the stationary level. The analyses of NO adsorption and reduction over the ACF may suggest plausible ways how to maintain or regenerate such an activity for more efficient process of NO removal.

EXPERIMENTAL

The ACF examined in the present study was a pitch based active carbon fiber supplied by Osaka Gas Co. (OG-8A, surface area 800m^2/g). The ACF was heattreated at 850°C to develops the highest activity for NO reduction with NH3 (OG-8A-H850).

The reactivity and adsorption of NO-NH3 (200 and 300ppm respectively in air) was studied by a conventional flow reactor at 25 to 70°C. The ACF of 0.5g (8cm length) was packed in the reactor. The flow rate of the total gas was fixed at 100 ml/min. Humidity of air was controlled by feeding H2O in the reactor.

By analyzing the outlet NO and NH3 concentrations by NOx meters (NH3 was oxidized before the analysis), the removal and desorption of NO were quantified to calculate the adsorption and the reduction of NO.

The desorption of NO and NH3 adsorbed on the ACF during the NO-NH3 reaction and their single flow was performed by program heating up to 300°C the ACF bed in the flowing He of 100ml. The heating rate was 3.3°C/min.

RESULTS
Removal of NO in the reactor with NH3 over OG-8A-H850

Figure 1 illustrates the removal of NO in the presence of NH3 in dry and humid (80%rh) airs over OG-8A-H850 at 25 to 70°C by W/F : 5x10^{-3}g·min/ml. NO was completely removed for initial 20min at 25°C in dry air and then its removal decreased gradually for 120min to give a stationary removal of 98%. The higher temperature shortened the periods of complete removal and gradual reduction, reducing the stationary removal. Thus the stationary removal obtained at 40, 55 and 70 was 85, 75 and 50%, respectively.

Relative humidity of 80% eliminated the period of complete removal under the present conditions and reduced the stationary removal to 20, 60, 50 and 40%, respectively, at 25, 40, 55 and 70°C. It should be noted that an intermediate temperature of 40°C allowed the largest removal of NO in humid air of 80%rh, being very contrast to the reaction in dry air.

Adsorption of NO and NH3 at the early stage of the reaction

Figure 2 illustrates the temperature programmed desorption of adsorbed NO and NH3 over OG-8A-H850 after for the NO-NH3 reaction at 25°C for 3h.

NO started to desorb at 30°C, slowly up to 60°C, after which the desorption became may rapid to reach a maximum at 80°C. Further heating provide another maximum at 180°C. The total amount of desorbed NO was 7x10^{-2}mmol/g ACF.

Ammonium started to desorb immdiately after the switch of carrier gas and increased rapidly its concentration to the maximum at 40°C. The second maximum of small concentration was found at 230°C.

Figure 3 summaries the amounts of adsorbed NO after 3h reaction at several reaction temperatures, as measured by the procedure described in Figure 2, . The amount under dry conditions decreased monotonously at higher temperatures. In contrast, the amount at 80%rh showed the maximum at 40°C where the inhibition of H2O may be reduced.

The conversion of NO by 3h shown in Figure 1 includes the amounts of reduced as well as adsorbed NO. The amounts of reduced NO thus calculated are plotted also in Figure 3. The amount of NO by 3h under dry conditions was much the same up to 55°C, then decreased sharply. Hence the conversion decreasing at the higher reaction temperature shown Figure 1 decreases reduction of NO reduction as well as adsorption.

In contrast, the amount of NO reduction was much higher at 40 - 70°C than at 25°C in humid air. Inhibition by H2O on reduction and adsorption of NO is reduced at higher temperature where the adsorption of H2O is minimized.

313

Figure 4 shows the adsorption amount of NO alone over OG-8A-H850 for 3h where adsorption appeared saturated. The amount of NO adsorption were very similar to those during NO-NH3 in the same temperature range, indicating that the adsorption of NO is saturated regaredless of NH3 presence.

Reactivity of NO adsorbed during the NO-NH3 reaction

Figure 5 illustrates the description profiles of NO during the NO-NH3 reaction over OG-8A-H850 after the reaction with 300ppm NH3 alone for 3h at 25 - 55°C. Desorption amount of NO was markedly reduced by the reaction with NH3. NO desorbing at the lower temperature was reduced more readily by the reaction. The higher temperature reduced more NO of desorption.

DISCUSSION

The present study focussed the early stage of NO-NH3 reaction over a pitch based active carbon fiber of fairly large surface heattreated at 850°C. At the initial stage, NO was completely removed by adsorption and reduction over the ACF. The adsorption took place rapidly to contribute principally to the removal at the very initial stage, however its contribution decreases as the progress of run because the adsorption approaches the saturation. After the saturation of the adsorption, the NO removal becomes stationary. Although humidity reduces both adsorption and reduction, the situation of the NO removal over the ACF was basically common.

The higher reaction temperature reduces the adsorption of NO to decrease its reduction in dry air as previously reported and hence NO removal decreases. In contrast, the higher reaction temperature up to 40°C increased both adsorption and reduction in humid air because the inhibition of H2O due to its adsorption decreases markedly up to 40°C. A particular temperature of 40°C allows the highest removal by compromising adsorptions of NO and H2O.

The adsorbed NO at the early stage stayed unreduced while NO and NH3 are fed. However NH3 alone can reduce NO, the higher temperature up to 45°C accelerating the reduction. It should be noted that two adsorbed species of NO are present on the ACF, of which desorption temperatures are very different and that the NO species desorbing at the lower temperature is more reactive with NH3. It is also worthwhile to note that the stationary reduction of NO does not appear to reflect such adsorbed species. More details of NO adsorbed species are of value to be analyzed. The lower stationary removal of NO in humid air is a task to be overcome for the practical application. The removal of NO at early stage which includes both adsorption and reduction can be applied for the complete removal where the regeneration of adsorption ability by reducing adsorbed NO and NO removal can be practically cycled. The optimization is the next target of the study.

REFERENCE
1 I.Mochida, S.Kawano, S.Kisamori, H.Fujitsu, T.Maeda, *Nippon Kagaku kaishi*, **6**, 694, (1993).
2 I.Mochida, S.Kawano, S.Kisamori, H.Fujitsu, T.Maeda, *Carbon*, **32**, 175, (1994).
3 I.Mochida, S.Kisamori, M.Hironaka, S.Kawano, Y.Matsumura, M.Yoshikawa, *Am. Chem. Soc., Eng. & Fuels*, **8**, 1341, (1994).
4 I.Mochida, S.Kawano, M.Hironaka, S.Yatsunami, Y.Korai, Y.Matsumura, M.Yoshikawa, *Chem. Lett.*, 385, (1995).
5 I.Mochida, S.Kawano, S.Yatsunami, M.Hironaka, Y.Matsumura, M.Yoshikawa, *Am. Chem. Soc., Eng. & Fuels*, **8**, 659, (1995).
6 I.Mochida, S.Yatsunami, M.Hironaka, S.Kawano, Y.Matsumura, M.Yoshikawa, *J. Petrol. Inst. Jpn.*, in press.
7 I.Mochida, S.Kawano, Y.Kawabuchi, Y.Korai, Y.Matsumura, M.Yoshikawa, *Langmuir*, in submission.
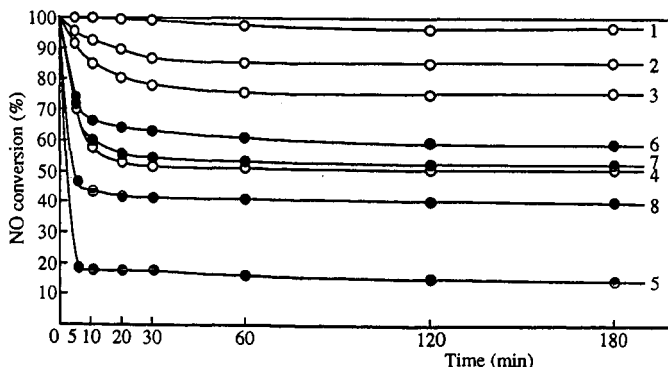
Fig.1   NO-NH3 reaction profile over ACF OG-8A-H850 in dry and wet air
NO : NH3 = 1:1.5 (NO = 200ppm), O2 = 10%, N2 balance
W/F = 5 × 10⁻³g · min · ml⁻¹, W = 0.5g, Time : 180min
Dry (r.h. = 0%) : O   1. 25°C,   2. 40°C,   3. 55°C,   4. 70°C
Wet (r.h. = 80%) : ●   5. 25°C,   6. 40°C,   7. 55°C,   8. 70°C
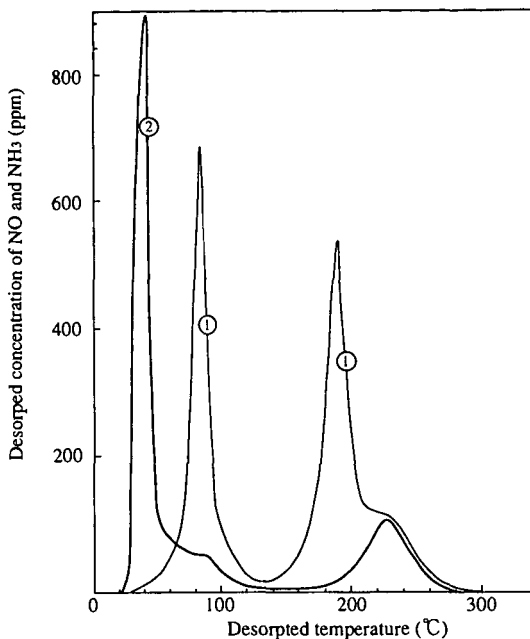
Fig.2 Desorption profile of NO and NH₃ after NO-NH₃ reaction over OG-8A-H850

Reaction : NO : NH₃ = 1 : 1.5 (NO = 200 ppm), O₂ = 10%, N₂ balance
W = 0.5g, W/F = 5×10⁻³g · min · ml⁻¹, Temp. = 25℃
r.h = 0%, Time = 180 min
Desorption : Flow gas (He) = 100 ml/min, Temp. : 25 - 300℃
H.R. = 3.3℃/min
① NO, ② NH₃
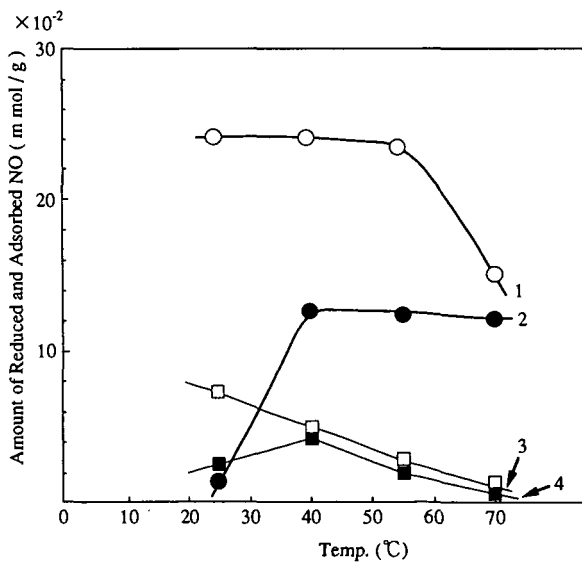
Fig. 3 NO reduction and adsorption over OG-8A-H850

NO : NH₃ = 1 : 1.5 (NO = 200 ppm), N₂ balance, O₂ = 10%
W/F = 5×10⁻³ g · min · ml⁻¹ , W = 0.5, F = 100 ml/min, Time : 180min
O :1. Reduction (Dry, rh = 0%)   □:3. Adsorption (Dry, rh = 0%)
● :2.   〃   (Wet, rh = 80%)   ■:4.   〃   (Wet, rh = 80%)
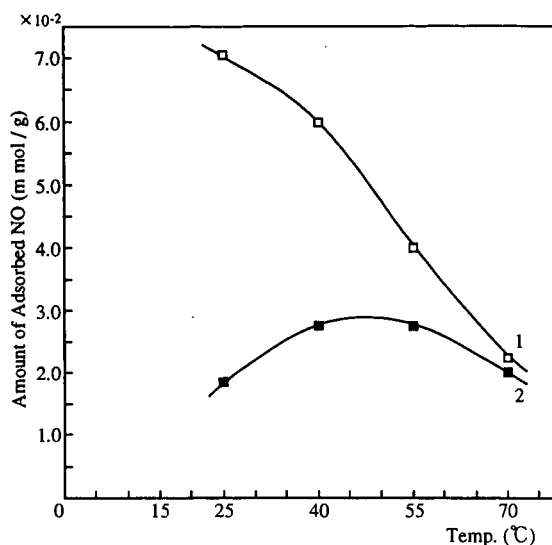
Fig. 4 Adsorption amount of NO alone over OG-8A-H850

NO : 300ppm, W/F = 5×10⁻³g · min · ml⁻¹, W = 0.5g, Time : 180min
1 : Dry (r.h. = 0%),   2 : Wet (r.h. = 80%)
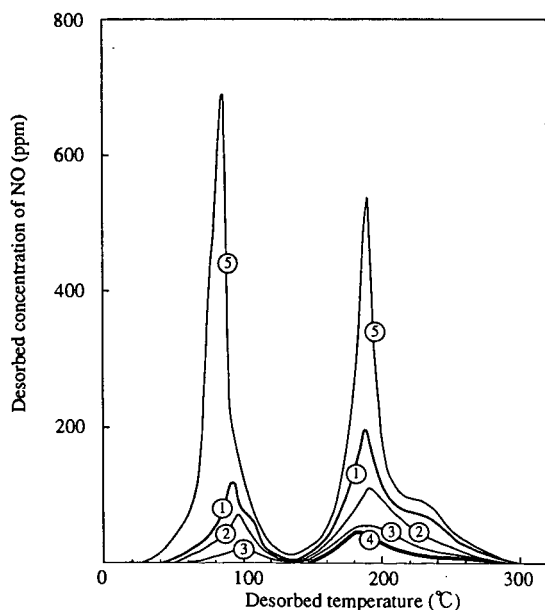
Fig.5 Desorption after regeneration with NH₃ of adsorbed NO
       during NO-NH₃ reaction

ACF : OG-8A-H850 (Pitch based)
Reaction : NO : NH₃ = 1 : 1.5 (NO = 200ppm), O₂ = 10%, N₂ balance,
         W / F = 5×10⁻³ g · min · ml⁻¹, r.h. = 0%, Time : 180min
Regeneration : NH₃ = 300 ppm, O₂ = 10%, N₂ balance
         W/F = 5×10⁻³ g · min · ml⁻¹, W = 0.5g
         r.h. = 0%, Temp. : 25 - 55℃, Time : 180min
Desorption : Flow gas (He) = 100 ml/min, Temp. : 25 - 300℃, H.R. = 3.3℃/min
① Regen. Temp. = 25℃   ④ Regen. Temp. = 55℃
② 〃   〃   = 35℃   ⑤ Non-Regen.
③ 〃   〃   = 45℃

316

EFFECT OF PRESSURE ON THE HEATS OF SORPTION AND DESORPTION OF O_2, NO AND N_2, ON AN ACTIVE CARBON AND A CARBON MOLECULAR SIEVE

A. J. Groszek,

Microscal Ltd. 79 Southern Row, London W10 5AL U.K.

Keywords: carbon molecular sieve :   pressure :   heat of adsorption.

Introduction

Pressure swing adsorption techniques with the use of carbon molecular sieves (CMS) are now all established for the separation of individual components of gas mixtures. One important example of such a separation is the isolation of pure oxygen and nitrogen from air.   Recently K.M. Thomas, M.L. Sykes and H. Chagger have shown that the heat evolution which accompanies the adsorption of O_2 and N_2 on various CMS's from a stream of helium, takes place at rates which are closely similar to the heats of adsorption, with nitrogen adsorbing much more slowly than oxygen (1).   The work was carried out at room temperature and at atmospheric pressures. Pressure swing separation processes which are used industrially, employ adsorption pressures that can vary from atmospheric pressure to 20 barg. The application of pressure increases the adsorption of individual components of gas mixtures and generates heat evolution due not only to adsorption of the first layer of molecules, but also to the pore filling phenomena which densify the gas contained in micropores. The heats evolved or absorbed during pressure swing operations are important parameters which affect the efficiency of gas separation operations as indicated recently by Sircar (2). But so far experimental determination of the heats of pore filling and gas adsorption on molecular sieves have not received much attention. This work was carried out, therefore, to determine experimentally the effect of pressure on heat evolution during adsorption of O_2 and N_2 on a commercial molecular sieve and an active carbon using a Microscal Flow Microcalorimeter (FMC) modified for use at high pressures under static conditions.

The pressures of oxygen and nitrogen in contact with the adsorbent were increased in steps from 1 to 20 barg and decreased back to atmospheric pressures and the resulting heats of sorption determined together with the duration of each heat effect. A limited amount of work was also carried out on nitric oxide.

Experimental

A schematic diagram of Microscal's Flow Microcalorimeter (FMC) which can be used under static conditions at pressures up to 50 barg is shown in Figure 1. In the procedure used, the calorimetric cell which had a volume of 0.17 cc was filled with accurately weighed adsorbent, with outlet tube in position, and the cell closed by a tightly fitting stainless steel inlet tube. The inlet tube is connected to a gas cylinder via a Druck pressure regulator capable of increasing or decreasing the gas pressure inside the cell in steps determined by the operator. The heat effects produced by the increasing or decreasing pressures are measured by the thermistors and calibration is effected by generating heat effects inside the cell electrically, as described previously for a Flow Microcalorimeter (3). The cell in the high pressure instrument is made from MACOR (glass reinforced with mica flakes) giving high temperature and pressure capability and very low time constant. With the inlet open and the outlet tube closed, the pressure was changed in a stepwise fashion resulting in the generation of heat effects. A typical record of one such measurement series is shown in Figure 2 for O_2 and N_2 adsorbed sequentially on a 0.095 g sample of Bergbau molecular sieve. The carbon adsorbents used in this study were Chemviron BPL active carbon and a commercial sample of a Bergbau molecular sieve. Gases were Aldrich materials with purities exceeding 99%. All the work was carried out at 20°C ± 1°C.

Figure 2

HEAT EFFECTS PRODUCED BY PRESSURE CHANGES OF O_2 AND N_2 IN CONTACT WITH BERGBAU MS AT 20°C

Heat Effects, Jg^{-1}

Pressure, Barg
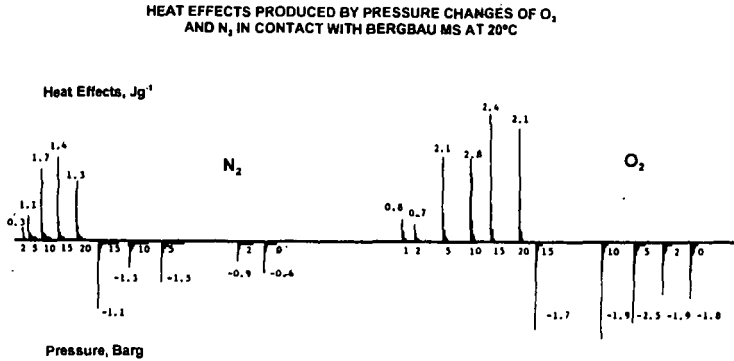
Results and discussions

A plot of differential heat effects represented in Figure 2 for the adsorption of O_2 and N_2 on the carbon molecular sieve is shown in Figure 3. There is a clear difference between the two gases with the ratio of the heats for O_2 and N_2 diminishing as the pressure increases. This suggests that the efficiency of gas separation would be somewhat higher for pressure swings of 0 - 2 barg than it would be for the swings of 18 - 20 barg, notwithstanding the greater amounts of gas throughput at the higher pressures. The heat effects plotted in Figure 3 do not take into account the rates of heat evolution which are very different for O_2 and N_2, as illustrated by the heat evolution peaks shown in Figure 4. It appears, however, that the differences in the rates of heat evolution under a pressure swing regime are smaller than those reported by K.M. Thomas et al for the adsorption at atmospheric pressure (1).

Figure 1

SCHEMATIC DIAGRAM OF MICROSCAL MICROCALORIMETER FOR THE DETERMINATION OF THE HEATS OF ADSORPTION AT HIGH PRESSURES

Figure 3

CUMULATIVE HEATS OF ADSORPTION/DESORPTION OF O_2 AND N_2 ON BERGBAU MS CAUSED BY PRESSURE CHANGES BETWEEN 0 AND 20 barg AT 20 °C.
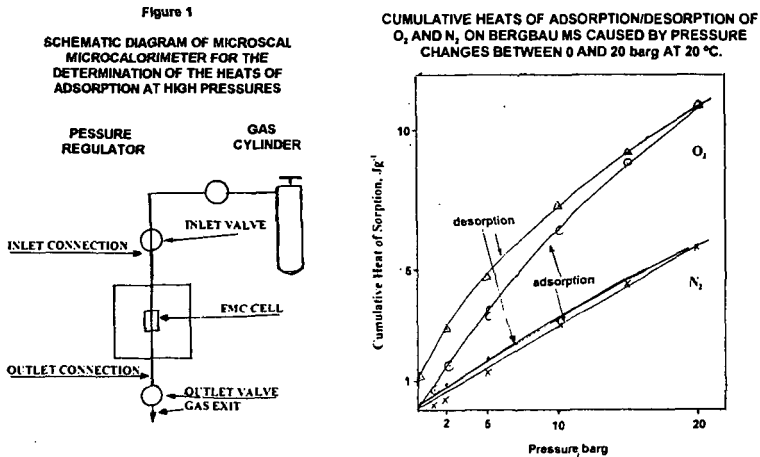
Figure 4

EVOLUTION AND ABSORPTION OF HEAT DURING A
PRESSURE SWING OPERATION WITH O, AND N,
ON BERGBAU CARBON MOLECULAR SIEVE
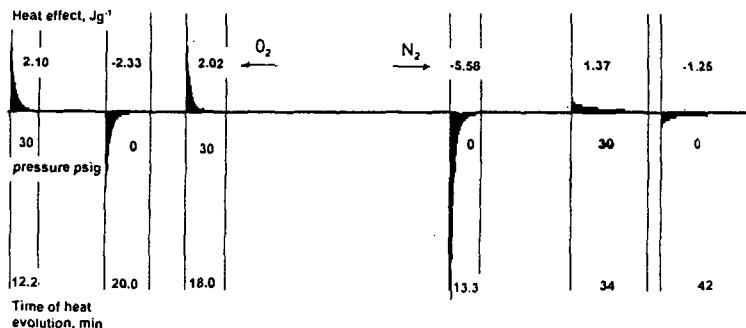
The differences between the heats adsorptions of O_2 and N_2 on CMS and active carbon BPL are shown in Figure 5 for pressure changes between 0 and 2 barg. As can be seen, the active carbon, as expected, shows very different behaviour from the CMS and gives slightly higher heats of adsorption for O_2 than for N_2. The active carbon does not show any significant difference between the rates of heat evolution. However, for CMS it is evident that the periods of heat evolution for N_2 are longer than they are for O_2. If it is assumed that the rates of heat evolution are directly related to the rates of adsorption, the differences between the rates can be used to optimise the gas separation efficiency over the whole range of the pressures investigated.

A brief investigation of the effect of pressure on the heat of adsorption of NO shows that this gas is very strongly adsorbed on both carbons and that the adsorption that occurs initially at low pressures is to a large extent irreversible. However, after saturation of the surface sites on the carbon with the chemisorbed NO, the additional more weakly adsorbed gas gives much higher increases in the heats of adsorption to those shown by nitrogen or oxygen. This is shown in Figure 6 in which the heats of adsorption after the initial contact of NO with the carbon molecular sieve are monitored during pressure changes between 0 and 2 barg. The first adsorption cycle gives a higher heat of adsorption than the following two cycles for which the heats of adsorption continue to be higher than the heats of desorption. The rates of heat evolution for NO are even slower than those shown by N_2, indicating that even the weaker more reversible adsorption of NO is still much stronger than that of N_2 and O_2. The rates of heat evolution are also relatively low for NO indicating a difficulty that the molecule has in entering and leaving the micropores modified by chemisorption after several cycles of NO adsorption. The subsequent adsorption cycles of O_2 give much higher heats of adsorption and are of longer duration than those obtained on CMS before contact with NO. Clearly the interaction of CMS surface within the pores with NO changes fundamentally the nature of the interaction between the O_2 molecules and the micropores in the CMS.

Figure 5

**EFFECT OF PRESSURE ON THE HEAT OF ADSORPTION OF
O_2 AND N_2 ON CHEMIVRON BPL AND BERGBAU MS**
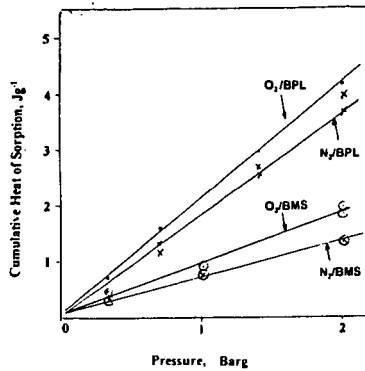
Figure 6

**EFFECT OF PRESSUE CHANGES ON THE HEAT EVOLUTION
OF NO IN CONTACT WITH BERGBAU MOLECULAR SIEVE
AFTER INITIAL IRREVERSIBLE ADSORPTION**
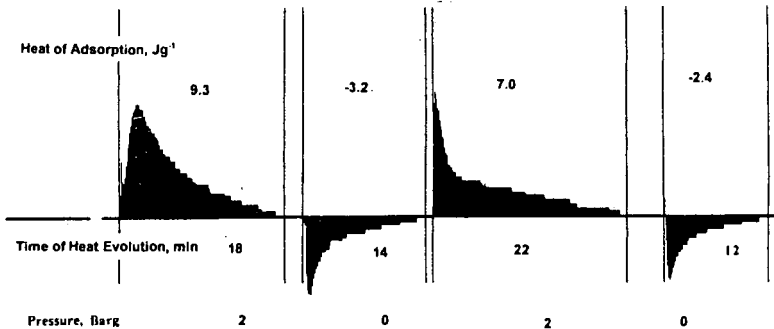
Conclusions

The heats of adsorption and desorption of O_2 and N_2 change significantly when the pressure is varied between 0 and 20 barg at room temperature. The changes are much greater for O_2 than for N_2 on carbon molecular sieve, but this effect is not observed for a typical active carbon which adsorbs both O_2 and N_2 with similar intensity and similar rates of adsorption. The work indicates that apart from the sieving action the pore filling mechanism may play an important role in the separation of gases on carbon molecular sieves. The adsorption of NO on microporous carbons is very intense and is partly irreversible. NO modifies the nature of the adsorbing sites in the carbon molecular sieve investigated and makes the adsorption of O_2 on such a modified adsorbent much stronger and apparently more extensive.

References

1. M.L. Sykes, H. Chagger and D.K. Thomas, Carbon, 31 pp 827-832; 1993.

2. S. Sircar, Proceedings 2nd ISSHAC Symposium, Poland, Sept 4-10 1995, p169

3. A.J. Groszek and S. Partyka, Langmuir, 9, 1993, p 2721-2725.   6802vf

ACTIVATED CARBON FIBERS - PAST, PRESENT, AND FUTURE

by
J. Economy, M. Daley, C. Mangun
1304 West Green Street
Materials Science and Engineering
University of Illinois
Urbana, IL 61801

Introduction

In this paper the background to the development of activated carbon fibers (ACFs) is reviewed, and then some of the recent progress of the past several years is discussed. Finally, a glimpse of the future for this field is provided which builds on some very recent results produced in our group.

The ACFs were first developed in the period of 1969-72 and made available in developmental quantities at that time. Since then, Nippon Kynol, the current manufacturer, has developed a number of niche markets which today have resulted in a multi-million dollar industry. Surprisingly, it is only in the last several years that a number of researchers have begun to examine this very interesting family of materials as witness the number of papers on ACFs in this Symposium.

It should be noted that the ACFs are currently priced in the range of $100/lb and hence hardly compete with the activated carbon granules (ACGs) which are available for $1.00/lb. and less. Hence, the ACFs only find commercial application in those areas where the unique textile forms of the ACFs permit use based on the greatly improved contact efficiency of the fibers. For the future, we have recently shown that we can prepare ACFs at a cost much closer to that of ACGs. Hence, one would anticipate a major market opportunity not only as a replacement of ACGs, but also from the creation of many new markets which are not available to ACGs because of the need for containment.

Past (1963 - 1975)

In 1963, at the Carborundum Co. we first showed that we could prepare crosslinked phenolic (phenol formaldehyde) fibers by spinning from a Novolac melt and then curing with $HCl + CH_2O$.[1] This fiber could be processed into a wide range of textile forms by conventional methods. It also displayed an outstanding flame resistance. In 1969 we commercialized this fiber under the trade name Kynol as a potentially low cost textile for use in highly aggressive environments.

More pertinent to this article, we showed in ~1968 that we could produce a range of high surface area ACFs by heating the Kynol in steam 700 - 900°C (See Figure 1).[2] By 1971 we began to make developmental quantities available commercially in the USA and also a joint venture company in Japan, Nippon Kynol Inc. In 1974, commercial development was transferred to Nippon Kynol and the program was terminated at the Carborundum Company.

During the period of 1968 - 74, we made considerable progress in developing and characterizing the ACFs. Thus, we were able to finalize on three ACFs with nominal surface areas of 1500, 2000 and 2500m^2/g. The 2500m^2/g ACF was shown to have the highest capacity, but was also the

most brittle. Considerable work was carried out to determine possible
advantages over ACGs. It was found that for similar surface areas the
ACFs displayed an almost 2x increase in breakthrough times over ACGs for
removal of phenol or butane.[3] The ACFs could be reactivated in situ by
electrical resistance heating at 100 - 200°C (See Table 1). It was also
shown that the modestly acidic pore surface of the ACFs could be
converted to a basic surface by heating in ammonia at 600 - 900°C.[4]
Finally, it was found that high surface fibers (600m^2/g) could be obtained
by etching at much lower temperatures of 450°C to produce an activated
phenolic fiber (APF).[4] These fibers appeared to have a smaller pore size
distribution, but could be made at somewhat lower cost
that the ACFs.

Present   (1990 - 94)

Starting in about 1990 we initiated a program at the University of
Illinois to develop a far better understanding of the nature of activated
carbons. Our intent was that we would not only develop a more predictive
capability concerning the adsorption characteristics of ACFs, but that this
could also lead to design of much lower cost fiber based systems that
would be cost competitive to ACGs. Our expectation was that with a
greatly improved understanding of the kinetics of adsorption and of
contact efficiencies we would be able to design low cost systems that
would be capable of removing trace contaminants in the low parts per
billion (ppb) range.
Initially our efforts focused on pursuing possible leads from the
work of the early 1970's. Thus we found that we could chemically convert
the pore surface of the ACFs to a much wider range of chemistries (See
Figure 2).[5] As a result of these studies it became apparent that we could
tailor the pore surface chemistry to be much more acidic or basic or more
polar or relatively neutral. Several papers have already been published
showing the utility of chemically tailored surfaces for selective removal of
VOCs[6] and of H$_2$O.[7] The role of surface area and pore size and shape
has also been examined in far greater depth particularly with respect to
the dramatic changes in separation of contaminants at high versus low
concentrations.[8] A critical component of this study has been our ability
to directly access the porosity in ACFs using Scanning Tunneling
Microscopy (STM).[9] As a result of these studies we are now able to
directly measure the microporosity dimensions and correlate these
measurements with the adsorption characteristics of the ACFs. All of these
issues are discussed in far greater detail in the ensuing paper by Daley, et.
al.
The earlier work on the APFs has also been reexamined during the
last several years and the conditions for reproducible manufacture have
been identified. (See Figure 3) We have also shown that the APFs have
modestly improved wear resistance over the ACFs.[4] As might be
expected the microporosity is smaller (in the range of 5 - 7Å as compared
to 10 - 13Å for ACF 1500). The potential for design of molecular sieve-like
carbon is clearly a possibility from this work.

Future   (1996 -)

One of the most exciting aspects of our program has been the recent
announcement that we had developed a low cost alternative to ACFs.[10]

This was accomplished by coating glass fibers with a phenolic resin. Activation of the phenolic coating can be carried out by any one of a number of techniques normally used for ACFs. Thus, for the first time one has access to a very low cost activated fiber assembly. Typically, phenolic resins are available for 60 - 70¢/lb while the glass fiber, depending on its product form, can cost well under a dollar for non-wovens and somewhat higher for woven textiles. In order to maintain flexibility of the final textile we limit the percentage of phenolic resin to ~30% by volume in the case of woven textiles. With non-woven textiles, paper or felt we can go to much higher loadings of phenolic resin. This may appear to be a limitation in terms of the amount of activated material for a given volume. However, we find that the contact efficiency is greatly improved compared to ACFs which of course are significantly better than ACGs (See Figure 4). Obviously reactivation of the spent assembly would be much faster than with ACFs. From preliminary tests the glass fibers coated with activated carbon can be reactivated by electrical resistance heating at 100 - 200°C or by use of steam at 120 - 170°C.

An important advantage of the activated, glass coated textile is the greatly improved wear resistance of this material. We believe that this arises from the fact that the coating provides protection to the glass fiber surface, which otherwise would be very sensitive to damage.

As a result of our recent announcement concerning this development we have had a number of inquiries from industry concerning commercial availability and utility. Currently, we have identified a number of companies that would be interested in participating in those aspects of the manufacture of this new product where they have a core competency. We are also starting to talk to companies that would be interested in acting as product form assemblers. In the new environment in industry, which requires focusing on one's core business, few companies appear willing to embrace the entire spectrum of activities required for commercial development of a new product. On the other hand, this product appears to lend itself to the establishment of a virtual business involving 3-4 companies to manufacture the product. With such an approach, only a minimal investment in manufacturing and scale-up would be required. A similar argument can be made for product assembly.

One area that we are examining carefully is that of chemical warfare including nerve gases. Up to now, gas masks that depend on ACGs have been in use for the past 50 years. However they are cumbersome and expensive and because of the acidic nature of the pore surface are not as effective against most of the toxic agents which are also acidic. It would seem that fabric which is easily deployed as a hood over the head and shoulders would provide very low cost protection against most all of the chemical warfare agents. To further enhance the adsorption capacity it would be important to activate in such a way that the pores are basic and would bind the toxic chemicals more tightly. If indeed all this proves to be correct, we may have available for the first time the ultimate defense against chemical warfare and one that would discourage future use of such methods by terrorists.

Other directions that we are now beginning to pursue is the use of these new activated assemblies as catalyst supports. We also plan to revisit some of our earlier work of 28 years ago on hyperfilters based on activated membranes[11] and on ion exchange fibers[12] which are tailored to remove specific metal contaminants.

References

1. Economy, J., Flame-Retardant Polymeric Materials, Vol. 2, 1978, Plenum Publishing Corporation, p. 203-226.

2. Lin, R.Y., Economy, J., Applied Polymer Symposium, 1973, 21, p. 143-152.

3. Economy, J., Lin, R. Y., Applied Polymer Symposium, 1976, 29, p. 199.

4. Andreopoulos, A. G., Economy, J., Chemistry of Materials, 1991, Vol. 3, No. 4, p 594.

5. Economy, J., Foster, K. L., Andreopoulos, A. G., Jung, H., ChemTech, October 1992, p. 597.

6. Dimotakis, E. D., Cal, M. P., Economy, J., Rood, M.J., Larson, S. M., Environmental Science and Technology, 1995, Vol. 2, Issue 7.

7. Dimotakis, E. D., Cal, M. P., Economy, J., Rood, M.J., Larson, S. M., Chemistry of Materials (in press).

8. Foster, K. L., Fuerman, R. G., Economy, J., Larson, S. M., Rood, M. J., Chemistry of Materials, 1992, Vol. 4, No. 5, p. 1068.

9. Economy, J., Daley, M., Hippo, E. J., Tandon, D., Carbon, 33, 1995, No. 3, p. 344-345.

10. Mangun, C. L., Daley, M. A., Economy, J., 88th Annual Meeting of Air & Waste Management Association, San Antonio, TX, June 18-23, 1995.

11. Economy, J., Lei, G. IR 100 Award, 1975, Carbon Film Hyperfilter.

12. Economy, J., CHEMTECH, 1980, Vol. 10, p. 240.

Fig. 1
Steam Activation of Carbonized Kynol Fibers
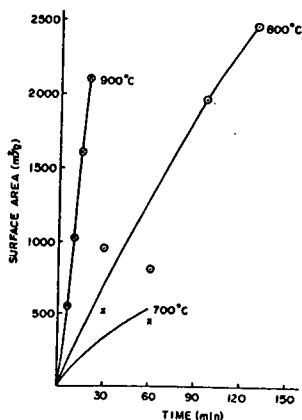
Sample	PAC Before Adsorption (mg/g)	Reactivation Time (min)	Reactivation Current (amp)	PAC After Reactivation (mg/g)	Capacity Regain (%)
1	139	10	3	88	66.5
2	140	10	4	--	--
3	153	10	5	46	38.0
4	131	10	2	113	86.0
5	160	10	1	94	52.5

Table 1
Effect of Current Strength on Phenol Adsorption
Capacity Regain in Electrical Reactivation
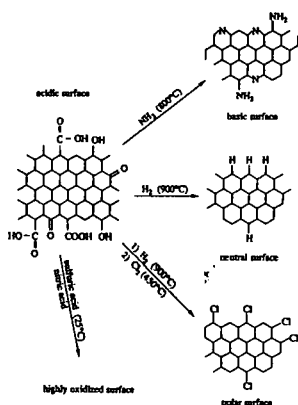
Fig. 2
Chemical Treatment of ACFs Produces a
Number of Different Surface Chemistries
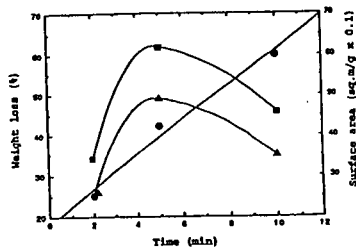
Figure 3
Heating Phenolic on Hot Plate at
450°C for Increasing Times
circle-wt loss (%)
square- Langmuir S.A.
triangle- B.E.T. S.A.
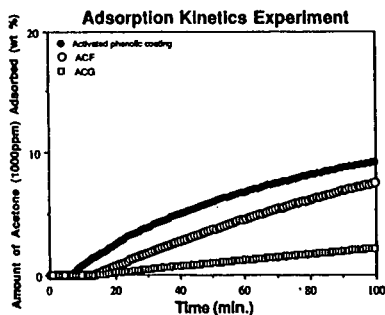
Figure 4
Comparison of Adsorption Kinetics of
ACG, ACF, and Activated Phenolic Coating

325

PREDICTING ADSORPTION PROPERTIES FOR ACFS

M. A. Daley, C. L. Mangun, and J. Economy
1304 West Green Street
Materials Science and Engineering
University of Illinois
Urbana, IL   61801

Introduction

Activated carbon fibers (ACFs), and activated carbon granules (ACGs) have been available for about the past 25 and 50 years, respectively. However, selection of the appropriate activated carbon to remove specific contaminants is still very much an empirical process. The problem that exists in creating a more fundamental understanding of these processes is the fact that up to now there has been no direct method for measuring the key parameters. In this paper data are presented which begin to lay the foundations for understanding the adsorption capabilities of ACFs essential to establishing a predictive model.

Factors that Control Adsorption in the Micropore

Many factors control the adsorption in the micropores of the ACFs including the pore size distribution, the pore shape, the pore surface chemistry, the fiber diameter, the adsorbent form, the adsorbate size and shape, the adsorbate chemistry, the physical properties of the adsorbate, the adsorbate concentration, the adsorbate environment, and other adsorbates which may compete for similar sites. In our laboratory, many factors are being examined systematically in great detail. The present status of our work is best summarized by considering the following four questions:

1.) How do pores initially form in the ACFs?
2.) What is the structure of high surface area ACFs?
3.) What is the role of pore size in adsorption?
4.) What is the role of pore surface chemistry in adsorption?

How do Pores Initially Form in the ACFs?

The origin of pore formation has recently been elucidated for ACFs (1).   This discovery came about when it was observed that high surface area carbon fibers were produced during activation of phenolic fiber precursors under inert conditions.   Presumably, the microporous structure was created by the evolution of volatile by-products at temperatures as low as 400-500°C and its persistence during further heating must be due to the presence of a stable crosslinked structure. Images of this microporous structure were obtained from scanning tunneling microscopy (STM) which provided direct insight into the size and shape of these initial pores.   From cross-sectional images of the fiber, a remarkably homogeneous microporous structure was observed in which pores measured from several tenths of nm up to 1.1 nm in diameter with the majority of pores measuring less than 0.6 nm in diameter.   At the fiber

surface, the pores were less than 5 nm in diameter and are larger than those in the bulk due to the rapid evolution of volatiles near the carbonization temperature. The initial pores which were observed from STM were not slit-shaped as originally proposed by Dubinin (2) but were ellipsoidally shaped. Thus for the first time an unambiguous interpretation now exists as to the origin of micropores in the ACFs.

What is the Structure of High Surface Area ACFs?

The phenolic fibers can be further activated using an etchant or oxidizing agent. Commercially, the ACFs are activated in a mixture of CO_2 and steam at high temperatures (600 -800 °C) to produce a family of materials with controlled surface area ranging from 700 to 2800 m^2/g (3). In practically all cases there is 2-5 % oxygen present in the ACF with a considerable percentage at the pore surface in the form of phenolic and carboxylic units.

The porous structure of the ACFs has been examined at great length using a number of indirect techniques such as fundamental adsorption theory (4), x-ray and neutron scattering (5), and adsorption of different size and shaped molecular probes (6). The greatest progress has been made with STM and we now have a database of over 800 images (7). The initial pores which were formed during carbonization begin to widen when exposed to steam/carbon dioxide due to diffusion of these etchants into the fiber bulk. Throughout activation the pores in the fiber bulk remain homogeneous and average pore sizes measure between 1 and 2 nm depending on the duration of activation (Fig. 1). Again, in contradiction to Dubinin (2), the pores remain ellipsoidally shaped in the bulk of the fiber and do not take on a slit-shaped character. Compared to the homogeneous micropores in the bulk of the fiber, the surface porosity was more heterogeneous and large mesopores and micropores were observed from the extensive reaction at the fiber surface (Fig. 2). A significant decrease in fiber diameter with increasing duration of activation was also noted where the fiber diameter decreases from 15 um to 9-12 um. The transition between the surface porosity and that in the bulk occurs in a region less than 32 nm and in this region a narrowing of the pores might lead to wedge-shaped pores.

What is the Role of Pore Size in Adsorption

Pore size is one of the most important factors affecting adsorption. In order for adsorption to occur, the adsorbate must fit into the pore. Foster showed a cross-over regime for the adsorption of butane where lower surface area ACFs adsorb better at low concentrations due to a higher overlap in potential which binds the adsorbate more tightly (4). At higher concentrations the higher surface area ACFs adsorbed larger amounts due to a larger pore volume (8). From recent studies, we have observed that the cross-over regime shifts to higher concentrations with lower boiling point adsorbates and to lower concentrations with higher boiling point adsorbates (9). The APFs which have a much smaller pore size in the bulk permit enhanced adsorption of contaminants at ppm levels to ppb levels (Fig. 3). The equilibrium amount adsorbed and its dependence on adsorbate size and boiling point has been related to physical constants using fundamental adsorption theory.

The adsorption kinetics or the rate at which equilibrium adsorption is approached at a given concentration is strictly dependent on the diffusion pathlength. This property is also a function of the adsorbent size and shape, the number and size and shape of pores at the fiber surface and the number and size and shape of pores in the bulk and their

interconnectivity. Our basic studies using ACFs have shown that the rate of adsorption/desorption is faster for materials with larger pores and broader pore size distributions (Fig. 4). The larger pores facilitate fast diffusion to the smaller pores which bind the adsorbate more tightly allowing it to be adsorbed.

Therefore it becomes important to have a good distribution of large and small pores. One reason why the adsorption kinetics of the ACFs is much faster than the granules is because the ACFs have many large mesopores at the fiber surface which permits rapid access to the homogeneous microporous structure in the bulk. ACGs can not usually be tailored in this manner since they contain far fewer pores than the ACFs at their surface and typically they have a much broader pore size distribution in the bulk. One dimension for control of adsorption kinetics in ACGs is the particle diameter. Generally, as the particle diameter decreases the adsorption kinetics increase because the diffusion pathlength decreases.

As the adsorbate size decreases or the concentration decreases, materials with a larger concentration of pore sizes closer to the adsorbate size will have a higher equilibrium adsorption.

Based on these fundamental studies and others it has been possible to design/tailor adsorbents to remove contaminants from air and water to below several ppb level with little increase in estimated cost.

What is the Role of Pore Surface Chemistry in Adsorption

The pore surface chemistry plays an equally critical role in adsorption and can be tailored through chemical activation or through posttreatment. The advantages of chemical activation are that a single step treatment is all that is required to control the surface chemistry and pore size and this can lead to higher reaction yields.

Activation of the phenolic precursors in air results in a high surface area fiber with acidic surface chemistry. When this fiber is activated below the carbonization temperature a unique material is formed which has higher activation yields and better wear properties (10). Under these conditions a family of adsorbents has been developed with as much as 30% oxygen in the form of phenolic hydroxyls. Based on a molecular probe study, these materials have a pore size distribution which is less than 7Å and may be tailored by controlling the activation conditions. Through control of pore size and acidic surface chemistry, small molecules such as ammonia may be removed to low concentrations (< ppm).

Surprisingly, ammonia will etch the phenolic precursors and may be used to activate them to create high surface area carbon fibers at temperatures as low as 500°C. These materials are basic containing as much as 10 wt% nitrogen usually in the form of pyridine-like groups and aromatic amines depending on the activation conditions. Yields are much higher than that of ACFs that are posttreated in ammonia. Preliminary results have indicated that a large number of acidic contaminants can be selectively removed from air and water.

The ACFs have also been posttreated (8) in chlorine, ammonia, oxidizing agents, or hydrogen to create an ACF with a polar, basic, (basic, polar, or acidic surface chemistry depending on agent used), or neutral surface chemistry, respectively. Depending on the chemistry of the adsorbate, the ACFs can be tailored for selective removal of an adsorbate. For example, ammonia activation of a phenolic precursor permits enhanced adsorption of acidic contaminants such as HCl from air or paranitrophenol from water (Fig. 5). A post-treatment of an ACF with strong acid will produce a number of surface functionalities such as carboxylic acids, phenolic hydroxyls, and quinones. The surface of this material is therefore both acidic and polar thus enhancing the adsorption of both polar (i.e.

acetone) and basic (i.e. ammonia (11)) contaminants (Fig. 6). To date we have developed and characterized approximately 75 different materials with various surface chemistries and pore sizes (12). From these materials we have developed an extensive data base which relates the synthesis conditions to the number and type of functional groups and subsequently relates the effects of these groups to adsorption.

Conclusions/ Future Work

Some of the key parameters important for controlling adsorption have been described in this paper. Selective adsorption of specific adsorbates has been indicated. This work provides the necessary foundation for the next step which is to establish a predictive capability. We are now in the process of relating these material features to the key engineering parameters.

References

1. Economy, J., Daley, M., Hippo, E. J., Tandon, D., *Carbon*, 33, 3, 344-345 (1995).
2. Dubinin, M. M., Plavnik, G. M., Zaverina, E. D., *Carbon*, 2, 261-268 (1964). Stoekli, H. F., *Carbon*, 28, 1, (1990).
3. Lin, R. Y., Economy, J., *Applied Polymer Symposium*, 21, 143-152, (1973).
4. Foster, K. L., Fuerman, R. G., Economy, J., Larson, S. M., Rood, M. J., *Chemistry of Materials*, 4, 5, 1068, (1992).
5. Kieffer, J., *J. Appl. Phys.*, 72, 12, (1992).
6. Kasaoka, S., Sakata, Y., Tanaka, E., Naitoh, R., *International Chemical Engineering*, 29, 4, 734-742 (October 1989).
7. Daley, M., Tandon, D., Economy, J., Hippo, E., submitted to Carbon.
8. Economy, J., Foster, K. L., Andreopolous, A. G., Jung, H., *Chemtech*, 597, (October 1992).
9. Daley, M., Mangun, C., Economy, J., in preparation.
10. Andreopoulos, A. G., Economy, J. , *Chemistry of Materials*, 3, 4, 594, 1991.
11. Mangun, C., Daley, M., Economy, J., in preparation.
12. Daley, M., Mangun, C., Economy, J., in preparation.
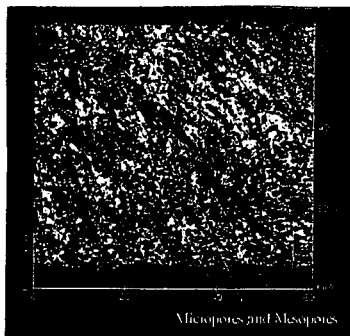
Fig. 1
STM image of the cross-section of an ACF
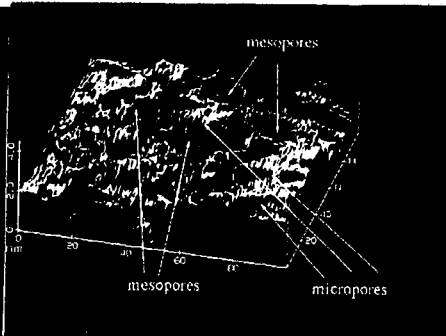
Fig. 2
STM image of the surface of an ACF

Adsorption of Methane on APFs

- □ 545 m2/g
- • 356 m2/g
- △ 60 m2/g
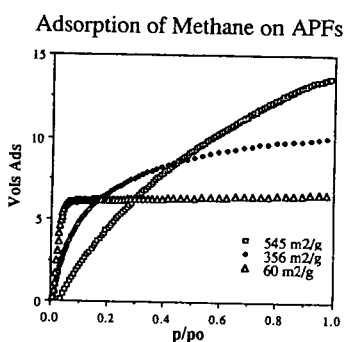
Fig. 3
Lower surface area APFs have smaller average pore sizes which adsorb larger amounts of methane at lower concentrations

Desorption of Freon from ACFs

- • ACF-25
- • ACF-20
- • ACF-10
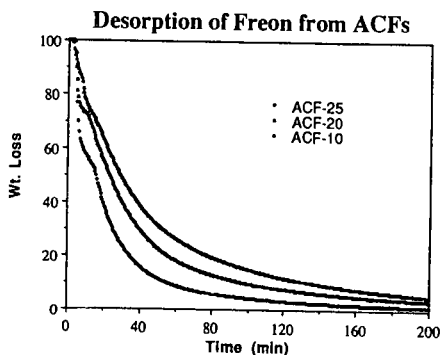
Fig. 4
The larger number ACFs have broader pore size distributions which permits for faster desorption

Activated Carbon Fibers
- ● Basic (10%N)-1400 m^2/g
- △ Basic (5.9%N)-2200 m^2/g
- ■ Basic (1.8%N)-1900 m^2/g
- ▲ Acidic (5%O)-1600 m^2/g

Fig. 5
As the basic character of the ACF increases (wt% N increases), the amount of HCl adsorbed increases proportionally

Activated Carbon Fibers
- ● Highly Oxidized (32%O)-1200 m^2/g
- ■ Untreated-1600 m^2/g
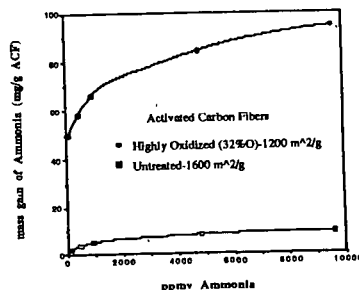
Fig. 6
As the ACF becomes more oxidized, the amount of ammonia adsorbed increases.

330

HIGH PRESSURE CO_2 ADSORPTION ON ACTIVATED CARBON FIBERS

J. Alcañiz-Monge, D. Cazorla-Amorós and A. Linares-Solano
Dept. Inorganic Chemistry. U. Alicante.
Apt² 99, Alicante 03080. Spain

INTRODUCTION

Physical adsorption of gases is the most employed technique for the characterization of porous solids [1-3]. N_2 adsorption at 77 K is the more used and, usually, has a special status of recommended adsorptive [4]. The advantage of N_2 adsorption is that it covers relative pressures from 10^{-8} to 1, what results in adsorption in the whole range of porosity. The main disadvantage of N_2 adsorption at 77 K is that when used for the characterization of microporous solids, diffusional problems of the molecules inside the narrow porosity (size < 0.7 nm) occur [5].

CO_2 adsorption, either at 273 K or 298 K [5,6], and He adsorption at 4.2 K [7] are two alternatives to N_2 adsorption for the assessment of the narrow microporosity. He adsorption at 4.2 K has been proposed [7] as a promising method for the accurate determination of the microporosity. However, the experimental conditions used (adsorption at 4.2 K) makes this technique not so available as CO_2 adsorption. In the case of CO_2 adsorption the high temperature of adsorption used for CO_2 results in a large kinetic energy of the molecules that can enter into the narrow porosity. In this way, CO_2 adsorption has been proposed as a good complementary technique, not alternative, for the analysis of the porous texture as it could be used to assess the narrow microporosity (size <0.7 nm).

A confirmation of the reliability of the method for essentially microporous materials, makes necessary the comparison of both N_2 and CO_2 adsorptions at comparable relative pressures where N_2 adsorption has not diffusional limitations. This requires the performance of CO_2 adsorption at high pressures. This type of comparison of both adsorptives has not been performed in the literature through the use of high pressure adsorption experiments.

According to all this, the objectives of this work are the following: i) to cover the lack of studies on CO_2 adsorption at high pressures; ii) to analyze the adsorption of this gas at relative pressures similar t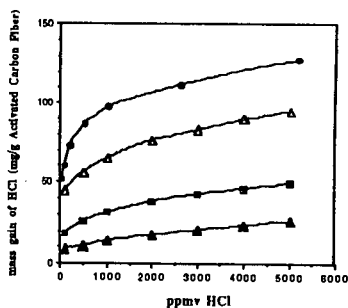o those used with N_2; iii) to show the problems of the use of N_2 adsorption at 77 K specially at low relative pressures. All these objetives can be summarized in confirming of the validity of CO_2 adsorption to characterize microprous carbon materials.

MATERIALS AND METHODS

A series of activated carbon fibers (ACF) obtained from CO_2 (series CFC) activation has been used in this study. The mechanical properties and porosity of these materials have been already analyzed [8]. In summary, the samples are essentially microporous, with a negligible volume of mesopores (only mesoporosity of size larger than 7.5 nm is only observed in samples with high burn-off). Samples with burn-off lower than about 40% have a DR (Dubinin Radushkevich) N_2 volume lower than the DR CO_2 one, what indicates the existence of narrow microporosity where N_2 adsorption has diffusional limitations. The ACF with higher burn-off have some amount of supermicroporosity, as reflected by the larger value of the DR N_2 volume compared to the DR CO_2.

CO_2 adsorption isotherms at 298 K and at high pressures have been carried out in a DMT high pressure microbalance

(Sartorius 4406) connected to a computer for data acquisition. The maximum pressure reached is 4 MPa. Additionally, CO_2 adsorption at 298 K and N_2 adsorption at 77 K up to 0.1 MPa have also been performed with an Autosorb-6 and Omnisorp equipments, respectively, to cover lower relative pressures.

RESULTS AND DISCUSSION
High pressure CO_2 adsorption isotherms at 298 K.
Figure 1 shows CO_2 adsorption isotherms obtained for the samples CFC14 and CFC54, plotted versus the relative fugacity. Each isotherm contains the experiment obtained at sub-atmospheric and at high pressures. It is important to note, by its relevance in the content of the paper, that there is a good continuation in both measurements performed up to sub-atmospheric and high pressures in spite of the different experimental systems used. CO_2 adsorption isotherms can be compared with those obtained from N_2 adsorption at 77 K previously described [8]. The evolution of the isotherms with burn-off is similar for both adsorbates. In fact, several common features can be noted from these experiments: i) the adsorption capacity increases with burn-off and ii) as burn-off increases, the knee of the isotherm widens, showing an increase in microporosity distribution. These results indicate that, due to the range of relative fugacities covered in the high pressure CO_2 adsorption isotherms, this molecule also adsorbs in the supermicroporosity (pore size 0.7-2 nm).

Characteristic curves for N_2 and CO_2 adsorptions.
The characteristic curves that are presented in the following discussion have been obtained by applying the DR equation to the different adsorption measurements performed. The characteristic curves obtained for N_2, correspond to the experiments performed with an Omnisorp apparatus that cover relative pressures from 10^{-7} to 1. The affinity coefficient used in this case is 0.33 [9]. The characteristic curves for CO_2 adsorption contain the isotherms obtained up to sub-atmospheric and up to high pressures. The affinity coefficient for CO_2 has been calculated to have coincident characteristic curves for CO_2 and N_2 adsorptions, in those samples where the adsorption of this gas is not kinetically restricted. From this approach, the coefficient affinity calculated for CO_2 is 0.35, value similar to that proposed by Dubinnin [9].

Figures 2 and 3 include two examples of characteristic curves obtained for samples CFC14 and CFC54 (plots of lnV vs $(A/\beta)^2$). These samples cover the different type of porosity found for the ACF studied. Sample CFC14 has a quite narrow porosity and N_2 adsorption has important diffusional problems. The porosity of sample CFC54 is well developed and contains some amount of supermicroporosity.

There are several relevant points that must be emphasized from Figures 2 and 3. In all the cases, the overlapping and continuation of the CO_2 characteristic curves obtained at low and high pressures is very good. For sample CFC14, the characteristic curve for N_2 adsorption remains always below that for CO_2, in agreement with the kinetically restricted adsorption for N_2 in this sample. With increasing the burn-off, the characteristic curve has not a unique slope and deviates upward. This reflects the development of porosity and the widening of the pore size distribution. This is clearly observed in Figure 3 that corresponds to sample CFC54. In this case, the characteristic curve for N_2 adsorption is very similar to the one for CO_2 obtained at high pressures (see the zone between 0-500 $(kJ/mol)^2$ in Figure 3). This indicates that CO_2 also fills the supermicroporosity that exists in this sample.

Finally, the characteristic curves for N_2 adsorption show in

all the samples a large deviation with respect to the one for CO_2 for values of $(A/\beta)^2$ higher than about 300 $(kJ/mol)^2$. In this zone, the volume of N_2 adsorbed by the sample is lower than the volume of CO_2 and decreases with increasing $(A/\beta)^2$. The adsorption potential, $(A/\beta)^2$, at which this deviation finishes depends on the burn-off of the sample. So, with increasing the burn-off, the recovery of the curve happens at higher $(A/\beta)^2$. This deviation, that happens at low relative pressures of N_2 (lower than 10^{-5} for sample CFC54 and lower than 10^{-4} for sample CFC14), shows that N_2 adsorption in the narrow microporosity is influenced by diffusional limitations. These experimental results are important by their relevance in the use of N_2 adsorption for the characterization of the porosity. As a consequence of the diffusional limitations, N_2 adsorption cannot be used to determine the micropore volue of the narrowest porosity, what makes necessary the use of other adsorptive to analyze this range of porosity. Hence, as already proposed [5], N_2 adsorption, complemented with CO_2 adsorption is an adequated procedure to determine the porosity of an activated carbon from the narrowest to the widest.

CONCLUSIONS
The results commented up to now show that CO_2 adsorption up to sub-atmospheric pressures can be used to calculate the volume of the narrow microporosity and that it is a convenient technique to complement the characterization of porosity through N_2 adsorption. CO_2 adsorbs in the super-microporosity when CO_2 pressures of about 4 MPa are used. The adsorption of N_2 at 77K is limited by diffusional problems that happen in the narrow porosity. For this reason, N_2 adsorption cannot be used to characterize this range of porosity that can be estimated by CO_2 adsorption.

REFERENCES
1. S.J. Gregg and K.S.W. Sing, *Adsorption, Surface Science and Porosity.* Academis Press (1982).
2. *Characterization of Porous Solids II,* (Eds. F.Rodrigue z-Reinoso et al.) Elsevier Science Publishers B.V., Amsterdam (1991).
3. *Characterization of Porous Solids III,* (Eds. J.Rouquerol et al.) Elsevier Science Publishers B.V., Amsterdam (1994).
4. J. Rouquerol et al; *Characterization of Porous Solids III,* pp 1 (Eds. J.Rouquerol et al.) Elsevier Science Publishers B.V., Amsterdam (1994).
5. F.Rodriguez-Reinoso and A.Linares-Solano; *Chemistry and Physics of Carbon,* (Ed. P.A.Thrower) Vol. 21, 1. MARCEL DEKKER, NEW YORK (1988).
6. J. Garrido, A. Linares-Solano, J.M. Martín-Martínez, M. Molina-Sabio, F. Rodríguez-Reiono and R. Torregrosa; *Langmuir,* 3, 76 (1987).
7. K. Kaneko, N. Setoyama and T. Suzuki; *Characterization of Porous Solids III,* pp.593 (Eds. J.Rouquerol et al.) Elsevier Science Publishers B.V., Amsterdam (1994).
8. J. Alcañiz-Monge, D. Cazorla-Amorós, A. Linares-Solano, S. Yoshida and A. Oya; *Carbon,* 32, 1277 (1994).
9. M.M. Dubinin; *Chemistry and Physics of Carbon,* (Ed. P.L. Walker) Vol. 2, 1. Marcel Dekker, New York (1966).
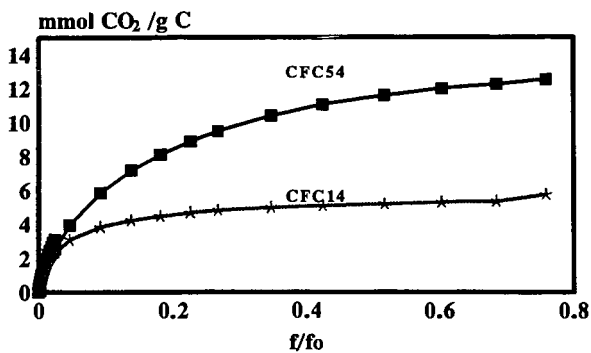
Figure 1. CO_2 adsorption isotherms.
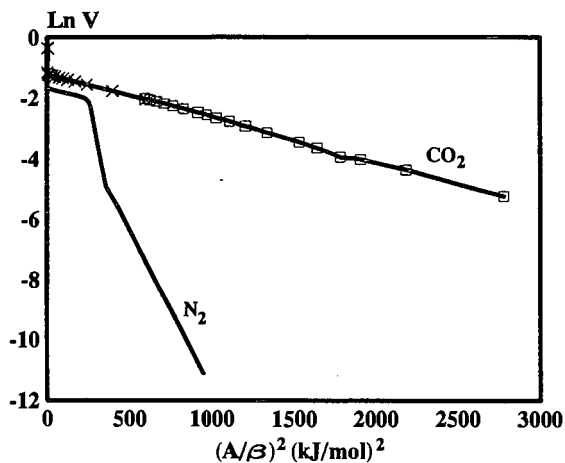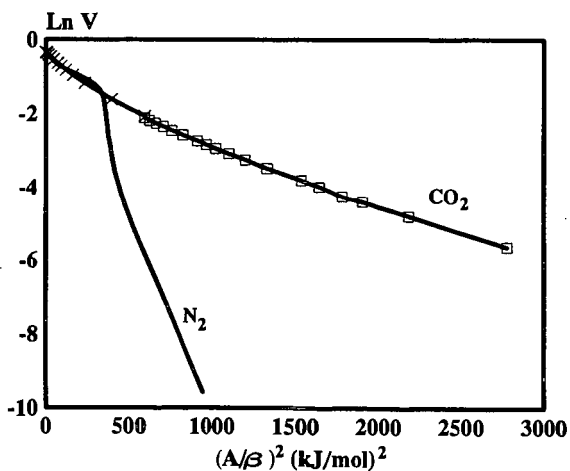

Figure 2. Characteristic curve of sample CFC14

Figure 3. Characteristic curve of sample CFC54

OXIDATION OF SO2 INTO RECOVERABLE AQ.H2SO4 OVER PITCH BASED ACTIVE CARBON FIBERS

Isao Mochida*, Keiichi Kuroda*, Yuji Kawabuchi*, Shizuo Kawano*, Akinori Yasutake[†]
Masaaki Yoshikawa[††], and Yuji Matsumura[††]
*Institute of Advanced Material Study, Kyusyu University,
6-1 Kasugakoen, Kasuga-shi, Fukuoka 816, Japan.
†Nagasaki R and D Center, Mitsubishi Heavy Industry,
5-717-1 Fukabori, Nagasaki, 851-03, Japan.
††Research & Development Center, Osaka Gas Co., Ltd.,
6-19-9 Torishima, Konohana-ku, Osaka 554, Japan.

KEYWARDS : SO2 removal, Active carbon fiber, Catalytic oxydation.

INTRODUCTION

The present authors have proposed a novel base for the removal of SO2 in the flue gas where SO2 is adsorbed, oxidized and hydrated over PAN-ACF to be continuously recovered in the form of aq. H2SO4.[1-3] Higher activity of ACF and less amount of humidity are wanted for smaller volume of the reactor, recovery of more concentrated H2SO4 and less consumption of water to reduce the cost of flue gas cleaning.

The present authors have found significant enhancement of the catalytic activity of PAN-ACF by the heat-treatment at 800°C.[4.5]

In the present study, catalytic activities of pitch based ACFs of high surface area were examined for the oxidative removal of SO2. Pitch based ACF of as-received form has been reported to be inferior to PAN-ACF in the oxidative adsorption of SO2.[5] However the heat-treatment is expected to enhance its catalytic activity. Hence the heat-treatment at rather high temperatures above 1000°C was examined to find higher activity. The hydrophobic surface of pitch based ACF can be expected to require smaller amount of H2O for the complete removal of SO2.

EXPERIMENTAL

OG series of pitch based ACF were supplied by Osaka gas Co.. It was heat-treated in nitrogen gas at several temperatures. Some of their properties are summarized in Table 1. SO2 removal was carried out at 30°C, using a fixed bed flow reactor. Weights of ACF were 0.1 and 0.25g. The total flow rate was 100ml/min. The model flue gas containing SO2 of 500-1000ppm, O2 of 5vol% and H2O of 5-20vol% in nitrogen was used. Aq.H2SO4 was recovered at the outlet of the reactor. SO2 concentrations in the inlet and the outlet gases were observed continuously by a flame photometric detector (FPD) and NOx gases were analyzed by NOx meter (ECL-88US, Yanagimoto Co.,Ltd.).

Temperature programmed decomposition (TPDE) spectra of the ACFs were measured by using a quartz-glass apparatus equipped with a mass spectrometer (AQA-200, ANELVA INC.) The sample of 0.1g was heated in helium flow up to 1100°C with 10°C/min increments and the evolved gases such as CO and CO2 were analyzed by the mass spectrometer.

RESULTS

The effects of heat-treatment temperature

Figure 1 illustrates the effects of heat-treatment temperature for SO2 removal over pitch based ACFs. Stationary removal of SO2 over all fibers was enhanced by the heat-treatment above 800°C. The activity was enhanced at higher temperature up to 1100°C. Complete removal was achieved for at least 15h with ACFs heat-treated above 900°C on OG-20A of the largest surface area. The ACF heat-treated at 1100°C removed completely SO2 at W/F of 1×10^{-3} g min ml^{-1}. The Activity enhancement is remarkable. The large surface area provided the large activity after the heat-treatment among the ACF.

The activity of pitch based ACF OG-20A of the largest surfase area

Figure 2 illustrates the desulfurization profiles of 1000ppm SO2 by as-received and heat-treated OG-20A at W/F (Weight/Flow) = 1×10^{-3} g·min ·ml^{-1}, 10% humidity and 30°C. The favorable influences of the heat-treatment at higher temperature up to 1100°C were definite. The heat-treatment at 900°C and 1000°C increased the removal up to 40 and 80%, respectively. A further higher temperature of 1100°C removed completely SO2 of 1000ppm for at least 15h. High temperature of 1200°C decreased the activity to 40% removal. There is certainly an optimum temperature of the heat-treatment with this particular OG-20A of very large surface area.

The effects of H2O

Figure 3 illustrates the effects of H2O in the SO2 removal over OG-20A-H1100 by W/F of 1×10^{-3} g·min ·ml^{-1} at 30°C. Lower concentration of H2O decreased the extent of SO2 removal , providing 100% removal at 10% H2O, 96% at 7.5% H2O, and 55% at 5% H2O. Larger W/F of 5×10^{-3} g·min ·ml^{-1} allowed complete removal with 5% H2O.

The influence of NO

Figure 4 illustrates the influence of NO of 500ppm at SO2 of 500ppm removal over pitch based ACFs by W/F of 2.5×10^{-3} g min ml^{-1} at 30°C. Without NO, SO2 was removed completely for longer than 20h. While a concentration of NO of 500ppm reduced the stationary removal of SO2 to 35%. More H2O and a larger W/F increased SO2 removal in the presence of NO. NO leaked freely without any removal except for the initial 1h while its outlet concentration increased very sharply from 0 to 100%. No reaction of NO was estimated at the stationary state while NO

certainly inhibited the SO2 removal by requiring larger H2O concentration or W/F for the complete removal of SO2.

TPDE spectrum of pitch based ACFs

Figure 5 shows the profiles of CO and CO2 evolution from OG-20A, OG-15A, and OG-10A. CO2 began to be evolved at about 180°C giving a highest evolution at 300°C, and then gradually decreased its amount to become null at 900°C regardless of the extent of activation of the fibers. CO began to be evolved at about 200°C and its amount increased gradually upto 500°C and then rapidly to 900°C where the maximum was observed. The amount of evolved CO increased with the increasing extent of activation and surface area. Significant retardation of NO without its stationary conversion should be studied in more details for scientific as well as technical view points.

DISCUSSION

The present study reported a remarkably high activity of a pitch based active carbon fiber of very large surface area after the heat-treatment at unusually high temperature of 1100°C. The activity observed in the present study allowed the complete removal of 1000ppm SO2 at room temperature over OG-20A-H1100. A very small volume of reactor is designed by such a high activity. The active site for SO2 removal is not identified. Large surface area and deoxygenated surface may provide more active sites of SO2 oxidation and accelerate the elution of aq.H2SO4 with minimam H2O from the active site because of high hydrophobicity.

REFERENCES

1 I. Mochida, S. Kisamori, S. Kawano, and H. Fujitsu, *Nippon Kagaku Kaishi*, **12**, 1429, (1992).
2 I. Mochida, T. Hirayama, S. Kisamori, S. Kawano, and H. Fujitsu, *Langmuir*, **8**, 2290, (1992).
3 S. Kisamori, I. Mochida, and H. Fujitsu, *Langmuir*, **10**, 1241, (1994).
4 S. Kisamori, S. Kawano and I. Mochida, *Chem. Lett.*, **11**, 1899, (1993).
5 S. Kisamori, K. Kuroda, S. Kawano, I. Mochida, Y. Matsumura and M. Yoshikawa, *ENERGY & FUELS*, **8**, 1337 (1994).

Table 1. Some Properties of Pitch Based Active Carbon Fibers.

ACFs	Ultimate analysis (wt%)					Surface area (m²/g)
	C	H	N	O	Ash	
OG-5A	89.6	1.1	0.7	8.2	0.3	480
OG-15A	92.5	0.9	0.4	5.8	0.4	1550
OG-20A	93.9	0.9	0.3	4.6	0.5	1860
OG-20A-H900 [a]	95.8	0.6	0.3	2.8	0.5	1690
OG-20A-H1100 [a]	97.5	0.1	0.2	1.6	0.6	1570
OG-20A-H1200 [a]	98.0	0	0.2	1.2	0.6	1420

a) Calcination temperature (°C)
OG-series : Pitch based active carbon fiber
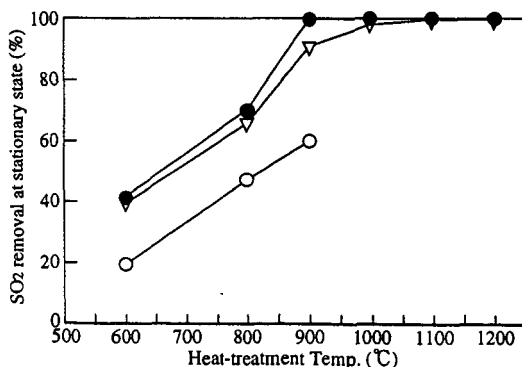
Figure 1 The effects of heat-treatment temperature for SO2 removal over Pitch-ACFs
  SO2 1000ppm, O2 5 vol%, H2O10 vol%
  W/F = 2.5 × 10⁻³ g min mL⁻¹, Reaction Temp. 30°C
  O: OG-5A (S.A. 480m²/g)
  ▽: OG-15A (S.A. 1550m²/g)
  ●: OG-20A (S.A. 1850m²/g)
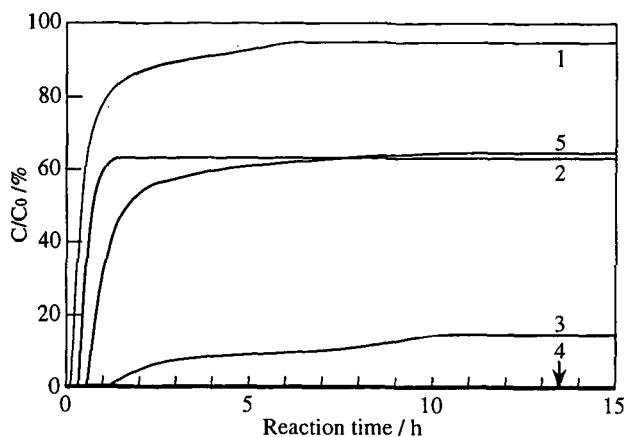
Figure 2 Breakthrough Profiles of SO₂ over Pitch-ACFs at 30℃
SO₂ 1000ppm, O₂ 5 vol%, H₂O 10 vol%
W/F : 1.0×10 g min mL
1: OG-20A
2: OG-20A-H900
3: OG-20A-H1000
4: OG-20A-H1100
5: OG-20A-H1200
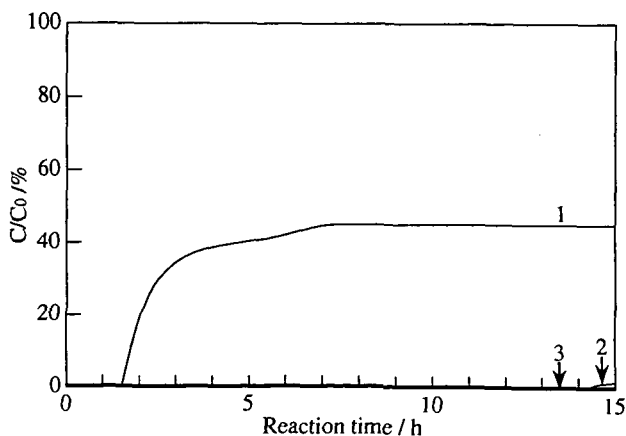
Figure 3. Breakthrough Profiles of SO₂ over Heat-treated Pitch-ACF
at several H₂O concentration at 30℃
SO₂ 1000ppm, O₂ 5 vol%, H₂O 10 vol%
W/F : 1.0×10^{-3} g min mL⁻¹
ACF : OG-20A-H1100
H₂O   1 : 5vol%,   2 : 7.5vol%,   3 : 10vol%
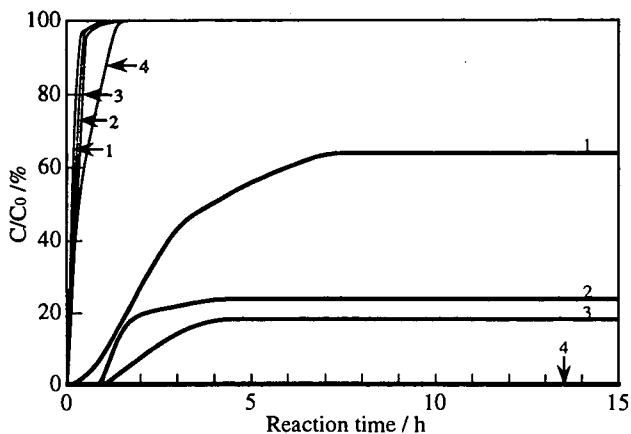
Figure 4　Breakthrough profiles of SO₂ and NO over
　　　　　 OG-20-1100 at 30℃
　　　　　 SO₂ : 500 ppm, NO : 500 ppm, O₂ : 5 vol%,
　　　　　 W/F = 1.0×10^{-3} g $\cdot$ min $\cdot$ ml^{-1}
　　　　　 H₂O　1 : 10 vol%,　2 : 15 vol%,　3 : 20 vol%

　　　　　 4 : W/F = 2.5×10^{-3} g $\cdot$ min $\cdot$ ml;^{1} H₂O : 10%

　　　　　 SO₂ : ——
　　　　　 NO : ——
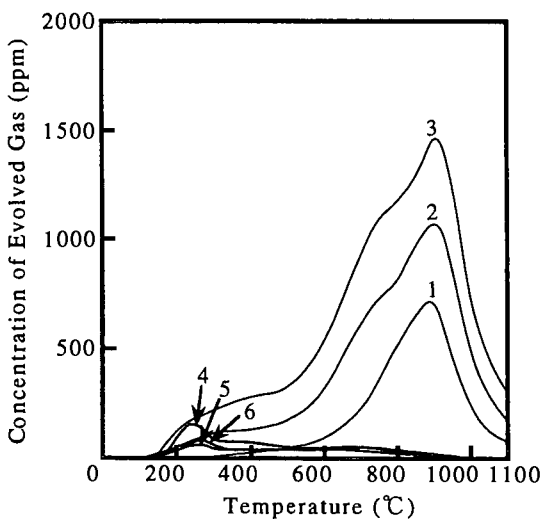
Figure 5　TPDE spectra of CO and CO₂ evolution
　　　　　 from Pitch Based ACF
　　　　　 Weight : 100mg
　　　　　 Carrier gas : Helium
　　　　　 Flow rate : 100ml/min

　　　　　 Sample
　　　　　　 CO　　　　　　　CO₂
　　　　　 1 : OG-5A　　　　 4 : OG-5A
　　　　　 2 : OG-15A　　　　5 : OG-15A
　　　　　 3 : OG-20A　　　　6 : OG-20A

338

ADSORPTION OF SO$_2$ ON BITUMINOUS COAL CHAR AND ACTIVATED CARBON FIBER PREPARED FROM PHENOL FORMALDEHYDE

Joseph A. DeBarr[1,2], Anthony A. Lizzio[1] and Michael A. Daley[3]
[1]Illinois State Geological Survey, 615 E. Peabody Dr., Champaign, IL 61820
[2]University of Illinois, Environmental Engineering and Science Program, Urbana, IL 61801
[3]University of Illinois, Materials Science and Engineering Department, Urbana, IL 61801

Keywords: Activated carbon fiber, coal char, SO$_2$ adsorption

INTRODUCTION

Carbon-based materials are used commercially to remove SO$_2$ from coal combustion flue gases. Historically, these materials have consisted of granular activated carbons prepared from lignite or bituminous coals [1-3]. Recent studies have reported that activated carbon fibers (ACFs) may have potential in this application due to their relatively high SO$_2$ adsorption capacity [4-6]. In this paper, a comparison of SO$_2$ adsorption for both coal-based carbons and ACFs is presented, as well as ideas on carbon properties that may influence SO$_2$ adsorption.

EXPERIMENTAL

Sample Preparation

The chars used in this work were prepared from an Illinois No. 2 hvCb coal, sample IBC-102 of the Illinois Basin Coal Sample Program [7]. A physically cleaned 48x100 mesh sample having 3.6% mineral content was prepared from the parent coal and used throughout as the feedstock for activated char. Chars were prepared at 900°C for 0.5 h in a 5 cm ID batch fluidized-bed reactor (FBR). In each run, 200 g IBC-102 coal was fluidized in flowing N$_2$ (6 L/min) and heated to the desired pyrolysis temperature. A multistep heating procedure was used to minimize agglomeration of coal particles in the FBR. Steam activation was done to develop microporosity and increase surface area further. Typically, 50 g of char was placed in the FBR and heated to 860°C in flowing N$_2$. The N$_2$ flow was replaced by 50% H$_2$O/50% N$_2$ (6 L/min) for 0.75 h to achieve 30% carbon conversion. In some cases, the H$_2$O-activated char was treated with nitric acid (HNO$_3$). Typically, 10 g of the char was added to 0.2 L 10 M HNO$_3$ solution, and refluxed at 80°C for 1 h. The HNO$_3$-treated carbon was washed with distilled H$_2$O to remove excess acid and vacuum dried overnight at 25°C. In some cases, the HNO$_3$-treated char was heated in N$_2$ to 525, 725, or 925°C and held for 1 h to remove oxygen placed on the carbon by the HNO$_3$ treatment.

ACFs with surface areas and oxygen contents ranging from 700 to 2800 m^2/g and 0 to 5 wt%, respectively, were prepared commercially by reacting phenol formaldehyde fiber precursors (Kynol) in a steam/carbon dioxide mixture at temperatures between 700 and 900°C. ACFs with acidic and basic surface chemistry were prepared using methods described elsewhere [8,9].

Sample Characterization

The SO$_2$ adsorption capacities of samples were determined by thermogravimetric analysis (Cahn TG-131). In a typical run, a 30-50 mg sample was placed in a platinum pan and heated at 20°C/min in flowing N$_2$ to 360°C to remove moisture and impurities. The sample was cooled to 120°C. Once the temperature stabilized, the N$_2$ was replaced by a mixture of gases containing 5% O$_2$, 7% H$_2$O and the balance N$_2$. Once there was no further weight gain due to adsorption of O$_2$ and H$_2$O, SO$_2$ was added in concentrations representative of a typical flue gas from combustion of high sulfur coal (2500 ppmv SO$_2$). The weight gain was recorded versus time by a computerized data acquisition system.

Temperature programmed desorption (TPD) experiments were done in a flow-thru, 2.5 cm ID stainless steel fixed-bed reactor system. In a typical run, 0.5 g of sample was heated in flowing nitrogen (0.5 L/min) at 5°C/min to a final temperature of 1000°C and held for 1 h to achieve nearly complete desorption of CO and CO$_2$ from the carbon surface. Non-dispersive infrared analyzers (Rosemount Model 880) were used to monitor the concentrations of CO and CO$_2$ in the effluent gas continuously.

N$_2$ BET surface areas of chars were determined using a single point BET adsorption equation with N$_2$ (77 K) adsorption data obtained at a relative pressure (P/P$_o$) of 0.30 with a Monosorb flow apparatus (Quantachrome Corporation). Surface areas were determined for ACFs with a Micromeritics analyzer using nitrogen adsorption at 77K. Average pore sizes of ACFs were calculated using the Dubinin-Radushkevich equation and the nitrogen adsorption isotherm measured using a Coulter Omnisorb.

RESULTS AND DISCUSSION

Coal Chars

The results presented in Figure 1 suggest a lack of correlation between SO$_2$ adsorption and N$_2$ BET surface area. Two steam activated carbons prepared from IBC-102 with intermediate surface areas (200 and 360

m^2/g) and a commercial activated carbon, Calgon F400 (1000 m^2/g), adsorbed similar amounts of SO_2 (between 15 and 20 wt% SO_2) after about 4 hours. The Centaur carbon, which had the highest SO_2 adsorption capacity, had an N_2 BET surface area of only 360 m^2/g. This carbon catalyst was developed by Calgon for both liquid and vapor phase applications, including removal of SO_2 and NO_x from flue gas. Figure 1 also shows that an activated carbon prepared from IBC-102 coal by steam activation, HNO_3-treatment and subsequent heat treatment to 925°C exhibited SO_2 adsorption behavior similar to the Centaur carbon. One study [10] showed that there was no correlation between the SO_2 adsorption capacity and surface of a coal-based carbon, while another [11] has maintained that "surface area is the most important parameter in order to predict the behavior of a char in the abatement of SO_2 from exhaust gases."

A better understanding of SO_2 adsorption behavior may require more detailed information about the carbon-oxygen (C-O) complexes formed during char preparation and SO_2 adsorption. The authors showed previously a poor correlation between SO_2 adsorption capacity and the total amount of chemisorbed oxygen for chars prepared under a wide range of conditions [12-14]. Davini [15] also observed no correlation between SO_2 adsorption and chemisorbed oxygen. He found a better correlation between SO_2 capacity and the basic (or high temperature) C-O functional groups. In the current study, the steam activated char was found to have a surface populated predominantly by high temperature C-O complexes. To increase the number of high temperature C-O complexes, and presumably SO_2 capacity, the H_2O-activated char was treated with HNO_3 and thermally desorbed at temperatures ranging from 200 to 1075°C. Figure 2 presents the TPD profiles of the HNO_3-treated char and those thermally desorbed at 525, 725 and 925°C. The CO and CO_2 evolution profiles of the original HNO_3-treated char showed only slight overlap. Conceivably, this char could be heated in inert gas to a certain temperature, e.g., 525°C, to remove only the CO_2-forming functional groups and retain the CO-forming ones. Figure 3 shows that the SO_2 adsorbed increased with increasing thermal desorption treatment. A three-fold increase in SO_2 adsorption is observed with the relatively small increase in thermal desorption temperature from 525 to 725°C, and the char with the smallest amount of C-O complex (925°C) adsorbed the largest amount of SO_2. This suggests that sites that form a stable C-O complex during char preparation are made available by the thermal desorption treatment, and that adsorption of SO_2 may preferentially occur at these free adsorption sites. Using TPD, the authors previously measured the number of free adsorption sites for several carbons; a direct relationship was found between SO_2 capacity and free sites [12,14,16]. Based on these results, a reaction scheme was recently proposed to explain SO_2 removal by carbon whereby the free sites control the rate of adsorption of SO_2 and conversion to H_2SO_4 [17,18].

ACFs

Figure 4 shows that the SO_2 adsorbed varies inversely with surface area for the ACFs studied. The pore volumes of these ACFs are known to increase from about 0.3 (ACF-10) to 0.8 cm^3/g (ACF-25) [19]. Others have also observed a decrease in adsorption of SO_2 with increasing surface area and micropore volume of ACF (polyacrylonitrile fibers) [4,6]. The oxygen and nitrogen ($< 0.05\%$) content, although not measured directly for this series of ACF, should not have varied much among these four samples; although, the oxygen content of ACF-10 and 15 may have been slightly greater than that of ACF-20 and 25 [19,20]. Excluding the idea of free sites for now, the results presented in Figure 4 suggest that pore size was the most important factor for determining the SO_2 adsorption properties of these ACFs. These ACFs are known to have relatively narrow pore size distributions [20,21]. In this study, we calculated the average pore sizes of ACFs 10, 15, 20 and 25 to be 9.4Å, 11.7Å, 13Å and 17.5Å, respectively. Foster et al. [19] studied a series of ACF similar to those used in this study and found that for ppm levels of n-butane, benzene or acetone, low surface area ACF adsorbed more than high surface area ACF. It is well known that smaller pores are preferentially filled at low relative pressures (concentrations) of adsorbate due to the overlap of attractive forces of opposite pore walls. If a similar adsorption mechanism occurs in the SO_2-ACF system as in the n-butane-ACF system, this would explain the behavior observed in Figure 4, and help explain the lack of correlation between N_2 BET surface area and SO_2 capacity observed for the coal chars. Ultimately, the number of free sites as well as pore size distribution and pore volume of an activated carbon should define its SO_2 adsorption behavior. The relative importance of each remains to be determined.

Figure 5 shows that the ACF-10 treated with both sulfuric and nitric acids (H_2SO_4/HNO_3) and thermally desorbed to 400 and 700°C exhibits SO_2 adsorption behavior similar to that of the HNO_3-treated, thermally desorbed coal chars (Figure 3). The SO_2 adsorption capacity of the H_2SO_4/HNO_3 treated carbon thermally desorbed at 700°C is much greater than that of the original ACF-10. The presence of adsorbed O_2 on ACF may serve only to block access of SO_2 to free active sites, similar to the behavior we have observed for Illinois coal char. Heating the H_2SO_4/HNO_3-treated ACF to 700°C would gasify part of the ACF, evolving oxygen as CO or CO_2, thus increasing the average pore size. If the average pore size of ACF increases with oxidation/thermal desorption, the results shown in Figure 4 would predict a decrease in the SO_2 capacity of H_2SO_4/HNO_3 treated ACF thermally desorbed at 700°C, if pore size was the only controlling factor. The fact that there was an increase in SO_2 adsorption despite an increase in pore size suggests the strong influence of free sites in controlling SO_2 adsorption behavior. It remains to be determined whether the free site concentration of these ACFs can be measured. It is interesting that the thermal desorption treatment applied to both the H_2SO_4/HNO_3-treated ACF and the HNO_3-treated coal char serves to increase not only the SO_2 adsorbed, but also the initial rate of SO_2 adsorption (Figures 3 and 5); this behavior has been attributed to an increase in the number of active sites [22].

Modifying the surface chemistry of ACFs by incorporating different functional groups has been shown to improve adsorption of various adsorbates [8,9,19,20,23,24]. ACFs with both acidic and basic surfaces, and an average pore size smaller than the original ACF-10, were prepared using methods described in previous work [8,9]. Since SO_2 is an acid gas, a carbon with basic surface characteristics would be expected to exhibit enhanced SO_2 adsorption. Indeed, Figure 6 shows that a basic ACF adsorbs more SO_2 than an acidic ACF. Others have also suggested that the presence of small amounts of nitrogen in ACF can markedly improve its SO_2 removal capabilities [4,6,25,26]. Work is in progress to learn how the interrelationships among number of free sites, pore size distribution and types of functional groups may control a carbon's SO_2 adsorption behavior [27].

CONCLUSIONS

Coal-based activated carbons and ACFs, prepared by a novel oxidation/thermal desorption treatment, had SO_2 adsorption capacities approaching that of a commercial carbon catalyst. The current price of ACFs, about $10/lb., may limit their use in SO_2 removal applications, however, some recent work suggests that ACFs can be prepared for $1- $2/lb. [28]. Further work is needed to characterize these less expensive ACF systems for SO_2 removal. The results obtained in this study suggest that pore size as well as the number of free active sites play important roles in determining a carbon's SO_2 adsorption capacity. The complete pore size distributions of the treated coal-based carbons and ACFs remain to be determined; these should provide additional insight into the relative importance of pore size and free sites in controlling SO_2 adsorption behavior. The use of functional groups, e.g., nitrogen-containing ones, to modify a carbon's surface to improve SO_2 adsorption appears promising, and is also an area for further investigation.

ACKNOWLEDGMENTS

REFERENCES

1.   Richter, E., Knoblauch, K., Jungten, H., 1987, *Gas Sep. Purif.* 1, p. 35.
2..   Tsuji, K., Shiraishi, I., 1991, "Mitsui-BF Dry Desulfurization and Denitrification Process using Activated Coke," Proceedings of the EPRI SO_2 Control Symposium," Washington, D.C., p. 307.
3.   Brueggendick, H., Pohl, F.G., 1993, "Operating Experience with STEAGs Activated Carbon Processes - a/c/t™ - In European Waste Incinerator Plants," Proceedings of Tenth Annual International Pittsburgh Coal Conference, p. 787.
4.   Mochida, I., Hirayama, T., Kisamori, S., Kawano, S., Fujitsu, H., 1992, *Langmuir* 8, p. 2290.
5.   Kisamori, S., Mochida, I., Fujitsu, H., 1994, *Langmuir* 10, p. 1241.
6.   Kim, J.Y., Hong, I., Lee, J.G., 1995, "Influences of Preparation Conditions of ACF on Catalytic Activity for SO_2 Removal," Proceedings of 22nd Biennial Conference on Carbon, San Diego, CA, p. 534.
7.   Harvey, R.D., Kruse, C.W., 1988, *J. Coal Qual.* 7, p. 109.
8.   Economy, J., Foster, K, Andreopoulos, A. and Jung, H., 1992, "Tailoring Carbon Fibers for Adsorbing Volatiles," Chem Tech, p. 597.
9.   Economy, J., Daley, M.A. and Mangun, C.L., 1996, "Activated Carbon Fibers - Past, Present and Future," ACS Preprints, Fuel Chem. Div., New Orleans, LA
10.   Davini, P., 1989, *Fuel* 68, p. 145.
11.   Rubio, B., Izquierdo, M.T., Mastral, A.M. and Mayoral, C., 1994, " Proceedings of International Conference on Carbon, "Use of Low Rank Coal Chars in the Abatement of SO_2 from Flue Gases," Granada, Spain, p. 402.
12.   Lizzio, A.A., DeBarr, J.A., Donnals, G.L., Kruse, C.W., Rood, M.J., Gangwal, S.K., 1995, "Production and Use of Activated Char for Combined SO_2/NO_x Removal," Final Technical Report, Illinois Clean Coal Institute, Carterville, IL.
13.   DeBarr, J.A. and Lizzio, A.A., "Production of Activated Char for Combined SO_2/NO_x Removal," Proceedings of International Conference on Carbon, Granada, Spain, 1994, p. 268.
14.   Lizzio, A.A. and DeBarr, J.A., "Effect of Surface Area and Chemisorbed Oxygen on SO_2 Adsorption Capacity of Activated Char," Fuel 1996 (in press).
15.   Davini, P., 1990, *Carbon* 28, p. 565.
16.   DeBarr, J.A., 1995, "The Role of Free Sites in the Removal of SO_2 from Simulated Flue Gases by Activated Char," M.S. Thesis, University of Illinois, Urbana, IL.
17.   DeBarr, J.A. and Lizzio, A.A., 1995, "New Insights on the Mechanism of SO_2 Removal by Carbon," Proceedings of 22nd Biennial Conference on Carbon, San Diego, CA, 1995, p. 562.
18.   Lizzio, A.A., DeBarr, J.A., 1996, "The Mechanism of SO_2 Removal by Carbon," ACS Preprints, Fuel Chem. Div., New Orleans, LA.
19.   Foster, K.L., Fuerman, R.G., Economy, J., Larson, S.M., Rood, M.J., 1992, *Chem. Mater.* 4, p. 1068.
20.   Cal, M.P., 1995, "Characterization of Gas Phase Adsorption Capacity of Untreated and Chemically Treated Activated Carbon Cloths," Ph.D. Thesis, University of Illinois, Urbana, IL.
21.   Lin, R.Y., Economy, J., 1973, *Applied Polymer Symposium* 21, p. 143.
22.   Jungten, H. and Kuhl, H., 1989, *Chem. Phys. Carbon* 22, p. 145.

23. Cal, M.P., Dimotakis, E.D., Economy, J., Larson, S.M. and Rood, M.J., 1996, "The Effect of Chemcial Modification of Activated Carbon Cloth on the Adsorption Capacity of Organics and Water Vapor," ACS Preprints, Fuel Chem. Div., New Orleans, LA.

24. Daley, M.A., Mangun, C.L., Economy, J., 1996, "Predicting Adsorption Properties for ACFs," ACS Preprints, Fuel Chem. Div., New Orleans, LA.

25. Nishijima, A., Kurita, M., Kiyozumi, Y., Kobayashi, R., Hagiwara, H., Ueno, A., Sato, T., Todo, N., 1980, *The Chemical Society of Japan* **53**, p. 3356.

26. Fei, Y., Sun, Y.N., Givens, E., Derbyshire, F., 1995, "Continuous Removal of Sulfur Oxides at Ambient Temperature, using Activated Carbon Fibers and Particulates," ACS Preprints, Fuel Chem. Div., **40** (4), p. 1051.

27. DeBarr, J.A., 1996, Ph.D. Thesis, University of Illinois, Urbana, IL.

28. Daley, M., 1996, Ph.D. Thesis, University of Illinois, Urbana, IL.
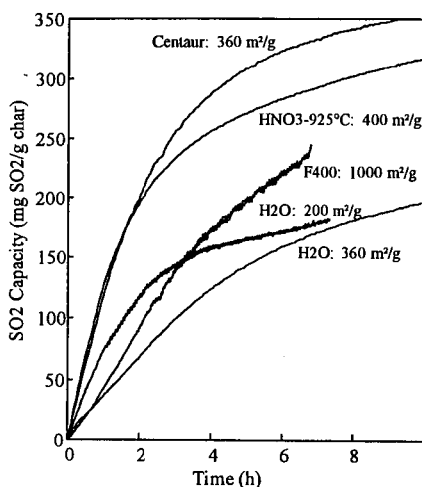
Figure 1. Effect of N2 BET surface areea on SO2 adsorption capacity of selected IBC-102 chars and commercial carbons.

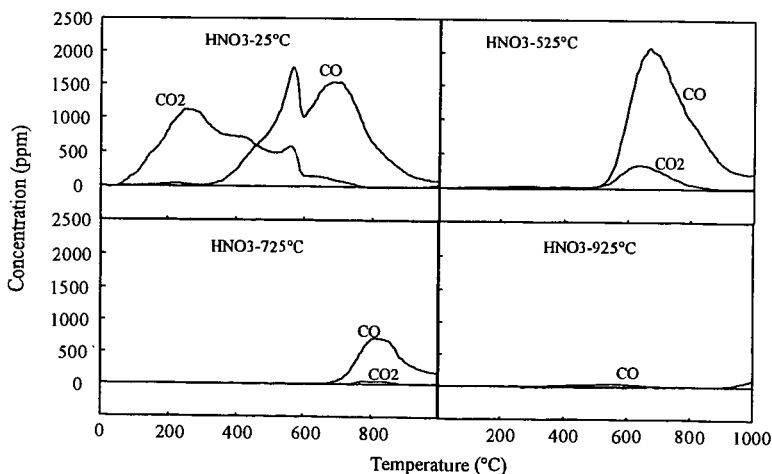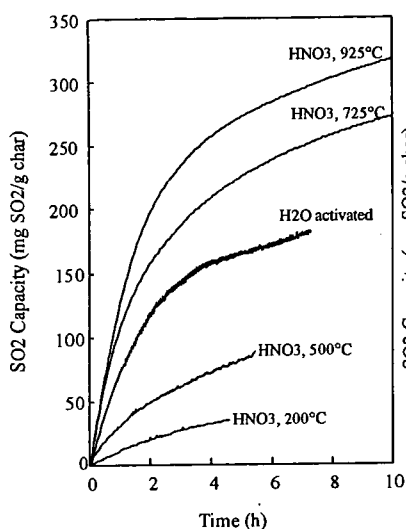Figure 2. TPD profiles of nitric acid treated/thermally desorbed IBC-102 chars.

Figure 3. SO2 adsorption for HNO3-treated
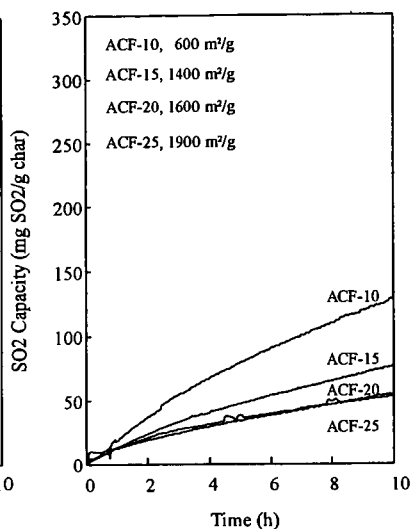chars desorbed to different temperatures.
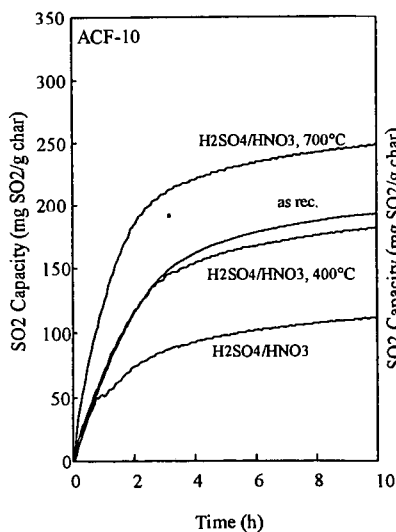

Figure 4. SO2 adsorption for ACFs.

Figure 5. SO2 adsorption for oxidized ACFs
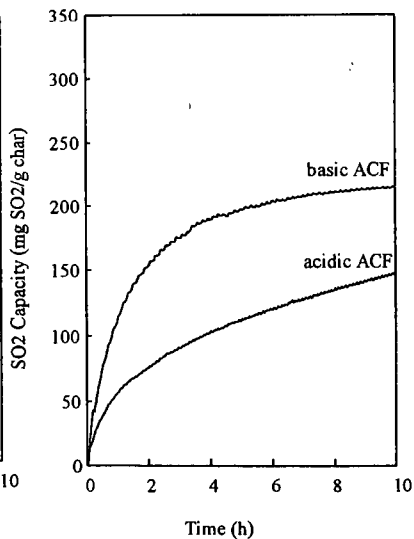desorbed to different temperatures.

Figure 6. SO2 adsorption for acidic and basic ACF.

THE EFFECT OF CHEMICAL MODIFICATION OF ACTIVATED CARBON CLOTH ON THE ADSORPTION CAPACITY OF ORGANICS AND WATER VAPOR

Mark P. Cal[1], Emmanuel D. Dimotakis[2], James Economy[2], Susan M. Larson[3], and Mark J. Rood[3]

University of Illinois at Urbana-Champaign, Urbana, IL 61801

[1]P.O. Box 70400, Reno, NV, e-mail: markc@sage.dri.edu

[2]Department of Materials Science and Engineering

[3]Environmental Engineering and Science Program, Department of Civil Engineering

Keywords: adsorption, activated carbon, chemical treatment.

INTRODUCTION

In an effort to maximize VOC adsorption, particularly in the case of compounds which are not readily adsorbed on activated carbon cloth (ACC), e.g., acetaldehyde, and to minimize the adsorption of water vapor, several chemical treatments were performed on virgin ACC-20. A sulfuric/nitric acid treatment produced a highly oxidized surface; chemical treatment with NH_3 produced a basic surface and increased the nitrogen content of the ACC; and finally, Cl_2 was used to produce a polar surface. Adsorption isotherms were measured for acetaldehyde, benzene, and water vapor to observe the effect on adsorption capacity for chemically treated ACC-20.

EXPERIMENTAL PROCEDURES

The starting material, ACC-20, was obtained from Nippon Kynol, Inc. Characteristics of the untreated and chemically modified ACC-20 samples are presented in Table 1. A brief summary of the experimental procedures used in this research is presented below. For a more detailed description of experimental procedures, please consult Dimotakis et al., 1995 and Cal, 1995.

Modification of ACC-20 with Ammonia or Chlorine

About 1.0 g of ACC-20 was placed in a 5-cm i.d. temperature-controlled quartz tubular furnace. The tube was purged with N_2 for 5 min, the temperature was increased to 180°C for 15 min, and then at the desired reaction temperature NH_3 or Cl_2 were introduced for the necessary reaction period. After completion, the gas was replaced with nitrogen, and the sample was cooled to room temperature. The samples were stored in closed vials prior to analysis.

Oxidation of ACC-20

The oxidations reactions were performed by immersing 1.45 g of ACC-20 in 100 ml of 1/1 (v/v) HNO_3/H_2SO_4 solution for two time periods: 10 min and 4 days. Gas evolution was observed during treatment. After the treatment, the product was washed with distilled water and left to dry overnight. Twelve hours later, it was dried at 150°C with N_2 for 30 min and then was stored in closed vials.

X-Ray Photoelectron Spectroscopy (XPS) Measurements

XPS was used to determine the elemental content (O, N, Cl and C) of the surface of the treated and untreated ACC samples (Briggs and Seah, 1983). The work was carried out at the Materials Research Laboratory of the University of Illinois at Urbana-Champaign, using a PHI 5400 (Perkin-Elmer, Physical Electronics Inc.) instrument. Mg-Ka radiation and a power of 400 Watts at 15 kV were used. The samples were dried at 150°C for 30-45 min prior to analysis since the technique requires ultrahigh vacuum (10^{-8} to 10^{-10} torr). To analyze for the surface groups the carbon region of the XPS spectrum was deconvoluted to individual peaks (Table 2). XPS techniques were used to characterize the chemical changes on the surface of the fiber down to about 30 Å to 100 Å which is the maximum depth that the emitted photoelectrons can escape and be detected (Briggs and Seah, 1983). XPS can identify the N, Cl or O groups present based on their binding energy values. It was assumed that the chemical nature of the surface is similar to that of the core of the sample. Table 2 describes the percent of total carbon area of each group as a function of the binding energy (variations within 0.7 eV are observed for the treated samples): phenol or ether (285 eV), carbonyl (287 eV), carboxylic (288.8 eV) and unsaturated bond transitions (291.1 eV, also known as shake-up peaks) (Foster, 1993).

Organic and Water Vapor Adsorption Isotherms

Acetaldehyde, benzene, and water vapor adsorption isotherms for the ACC samples were measured gravimetrically using a Cahn microbalance (Model C-2000). The gas stream for the organic compound of interest was generated using a certified gas cylinder of known organic concentration, diluted with hydrocarbon-free air using mass flow controllers (Tylan Model FC-280) to obtain the desired concentrations. To generate gas streams with different relative humidities, a membrane humidifier was used in combination with a dew-point hygrometer (Cal, 1995). The adsorption isotherms were measured at 25°C and a total pressure of about 1 atm. ACC sample masses were between 10 and 20 mg and the total gas flow rate through the gravimetric balance was 0.1 to 0.25 L/min.

Acetaldehyde Adsorption

Acetaldehyde typically has a low adsorption capacity on activated carbons, including ACC. Therefore, any chemical treatment that could substantially enhance the adsorption of acetaldehyde (and similar compounds, such as formaldehyde) could be potentially useful. Comparison of the adsorption capacities (at 25°C and 1 atm total pressure) for a series of chemically modified ACC-20 samples that were untreated, oxidized, nitrided and chlorinated as described by Table 2 are presented in Figure 1.

The largest gas-phase acetaldehyde concentration in air examined was 500 ppmv, while 1000 ppmv was the highest concentration of acetone and benzene studied. It was observed that acetaldehyde undergoes conversion to acetic acid at higher concentrations, making the adsorption capacity measurements invalid (Venugopal et al., 1967; Matheson Gas, 1993). The highly oxidized sample, ACC20-(32% O), exhibits a much higher adsorption capacity for

acetaldehyde in the 50 to 500 ppmv concentration range when compared to untreated ACC-20. At 50 ppmv ACC20-(32% O) adsorbs 400% more acetaldehyde than untreated ACC-20 and at 500 ppmv it adsorbs 130% more acetaldehyde. The less oxidized sample, ACC20-(21% O), also shows enhanced acetaldehyde adsorption similar to that of ACC20-(32% O).

The increase in acetaldehyde adsorption capacity on oxidized ACC is theorized to be due to an increase in dipole interactions and hydrogen bonding that occurs between the acetaldehyde molecules and the additional carboxylic groups present on the oxidized ACC-20 (Table 1). This effect appears to most pronounced at lower adsorbate concentrations, and diminishes at higher adsorbate concentrations, when the larger adsorbent pores begin to fill. It has been reported in the literature that surface oxygen groups can affect adsorption (Zawadski, 1981; Boehm, 1966; Szymanski and Rychlicki, 1991).

Nitridated ACC20-(4% N) shows improved acetaldehyde adsorption capacity over untreated ACC-20 of 51% at 50 ppmv and 9% at 500 ppmv. This increase in adsorption capacity may be due to interaction with the basic surface or may be due to the change in pore structure of the ACC. Finally, in the case of the chlorinated ACC20-(7.8% Cl) a slight decrease in the adsorption capacity is observed compared to the untreated ACC. The decrease in adsorption capacity appears to be related to the ACC surface chemistry instead of physical properties because the pore volume is similar to that of ACC20-(21% O) (Table 1).

Benzene Adsorption

Adsorption isotherms for benzene and the series of chemically modified ACC are presented in Figure 2. Since benzene is nonpolar and essentially immiscible in H_2O, a hydrophilic surface should result in decreased adsorption (Puri et al., 1973). Oxidation of the ACC resulted in a 34% decrease in adsorption capacity for 1000 ppmv benzene in air, which is the same as the observed decrease in surface area (Figure 2 and Table 1). Therefore, oxidation had little or no effect on benzene adsorption, but rather the difference in adsorption capacity is due to changes in surface area and/or pore volume between ACC20-(3.9% O) and ACC20-(32% O). The nitrided (basic) surface shows a slight increase in benzene adsorption capacity, while the chlorinated ACC20-(7.8% Cl) showed a slight decrease in adsorption capacity as compared to ACC20-(3.9% O). This decrease in adsorption capacity may be attributable to the decrease in micropore volume observed on the chlorinated ACC samples or may also be attributed to experimental error in the measurements (Table 1).

Water Vapor Adsorption on Chemically Modified ACC

The adsorption of water vapor on ACC20-(32% O) differs significantly from the usually observed type V isotherm, and more closely resembles a type II isotherm (Figure 3). ACC20-(32% O) is expected to have many more oxygenated or hydrophilic sites than any of the other ACC due to its high oxygen content. The XPS data in Table 2 shows a higher number of carboxylic bonds than the untreated ACC-20, confirming that some of the hydroxyl and carbonyl bonds were oxidized to carboxylic bonds. The XPS data also shows that more carbon-oxygen (hydrophilic) bonds were formed during oxidation compared to untreated ACC-20. The increase in carboxylic groups may be responsible for the enhanced water vapor adsorption at low relative humidities (RHs). From Table 2 and the adsorption isotherm data, it appears that carboxylic groups have the most influence on water vapor adsorption at low RH. The difference between the adsorption and desorption curves (hysteresis) is not as pronounced here, as it is for the untreated ACC. This may be due to the increase in hydrogen-bonding between water and the oxidized carbon, allowing removal of water molecules in a more continuous manner.

Adsorption-desorption isotherms for nitridated ACC20-(4.1% N) are presented in Figure 3. ACC20-(4.1% N) exhibits an increase in water vapor adsorption capacity (200 to 600%, depending upon the RH) in the lower RH range (RH < 50%). This may be due to the increase in carboxylic sites compared to untreated ACC20-(3.9% O), as represented in the XPS data in Table 2. It has also been suggested that nitrogen can also constitute polar sites for $H_2O_{(g)}$ adsorption (Bradley and Rand, 1993; Tomlinson, et al., 1993), thereby increasing $H_2O_{(g)}$ adsorption at low RH. ACC20-(4.1% N) exhibits about a 10% higher water vapor adsorption capacity than ACC20-(3.9% O) at high RHs. This is due to the increased total pore volume of ACC20-(4.1% N) observed in Table 1. The widening in the adsorption hysteresis curve in for ACC20-(4.1% N) in Figure 3 is most likely due to a change in pore size distribution.

Adsorption isotherms for water vapor and chlorinated ACC are presented in Figure 4. Table 1 shows a decrease in BET surface area, a decrease in carbon content (in wt%), and a slight increase in oxygen content with increasing chlorination. The decrease in surface area may be due to chlorine atoms limiting or closing off access to the smaller micropores present on the ACC. Water vapor adsorption was decreased at RHs < 60% and where capillary condensation occurred (the step rise in the adsorption curve) was shifted to higher RHs for the chlorinated ACCs. The amount of water vapor adsorbed at saturation was decreased to a due to a decrease in pore volume (Table 1). While chlorination increases the amount of polar sites present on the ACC due to the addition of chlorine atoms, these sites do not appear to be favorable for water adsorption, as are carboxylic sites. Chlorination appears to increase the hydrophobicity of ACC.

SUMMARY

ACC-20 was chemically modified, producing oxidized, chlorinated, and nitrated samples. Adsorption capacities for VOCs in the 10 to 1000 ppmv concentration and water vapor from 0 to 95% RH were measured. Oxidized ACC-20 showed an enhanced physical adsorption for acetaldehyde and water vapor, probably due to increased dipole-dipole interactions and hydrogen bonding. Oxidation of ACC-20 changed the shape of the water vapor adsorption isotherm, so that it no longer resembles a Brunauer type V. Benzene showed a decreased adsorption capacity (about 20 to 30% less, depending upon concentration) on oxidized ACC-20, which may be due to and increase in hydrophilicity of ACC-20, or a change in pore size distribution. Nitridation of ACC showed little effect on organic adsorption capacity, but increased the saturation adsorption capacity for water vapor by 10% on ACC-20 and increased the breadth of its hysteresis loop. These changes were the result of changes in the pore size distribution of ACC-20.

ACKNOWLEDGEMENTS

REFERENCES

Boehm, H.P., *Adv. Catal.*, **16**:179, 1966.

Bradley, R.H., and Rand, B., "The Adsorption of Vapours by Activated and Heat-Treated Microporous Carbons. Part 2. Assessment of Surface Polarity Using Water Adsorption," *Carbon*, **31**(2): 269-272, 1993.

Briggs, D., and Seah, M.P., *Practical Surface Area Analysis by Auger and X-ray Photoelectron Spectroscopy*, John Wiley and Sons, New York, 1983.

Cal, M.P., "Characterization of Gas Phase Adsorption Capacity of Untreated and Chemically Treated Activated Carbon Cloths," Doctoral Dissertation, University of Illinois at Urbana-Champaign, Environmental Engineering and Science Program, UMI Press, 1995.

Dimotakis, E.D., Cal, M.P., Economy, J., Rood, M.J., Larson, S.M., "Chemically Treated Activated Carbon Cloths (ACCs) for Removal of VOCs from Gas Streams: Evidence for Enhanced Physical Adsorption,"*Environmental Science and Technology*, **29**(7): 1876-1880, 1995.

Dimotakis, E.D., Cal, M.P., Economy, J., Rood, M.J., Larson, S.M., "Water Vapor Adsorption on Chemically Treated Activated Carbon Cloths," accepted for publication to *Chemistry of Materials*.

Foster, K.L., "The Role of Micropore Size and Chemical Nature of the Pore Surface on the Adsorption Properties of Activated Carbon Fibers," Doctoral Dissertation, University of Illinois at Urbana-Champaign, Department of Material Science and Engineering, 1993.

Gregg, J. and Sing, K.S.W., *Adsorption, Surface Area and Porosity, 2nd ed.*, Academic Press, London, 1982.

Matheson Gas, personal communication, 1993.

Puri, B.R., Kaistha, B.C., Vardan, Y., and Mahajan, O.P., *Carbon*, **11**: 329-336, 1973.

Syzmanski, G. and Rychlicki, G., "Importance of Oxygen Surface Groups in Catalytic Dehydration and Dehydrogenation of Butan-2-ol Promoted by Carbon Catalysts," *Carbon*, **29**(4/5): 489-498, 1991.

Tomlinson, J.B., Freeman, J.J., and Theocharis, C.R., "The Preparation and Adsorptive Properties of Ammonia-Activated Viscose Rayon Chars," *Carbon*, **31**(1): 13-20, 1993.

Venugopal, B., Kumar, R., and Kuloor, N.R., "Oxidation of Acetaldehyde to Acetic Acid in a Sparger Reactor," *I&EC Process Design and Development*, **6**(1): 139-146, 1967.

Zawadski, J., "IR Spectroscopy Investigations of Acidic Character of Carbonaceous Films Oxidized with HNO_3 Solution," *Carbon*, **19**:19-25, 1981.

Table 1. Physical Characteristics and Elemental Composition of ACCs.

ACC-20 Chemical Treatment	BET Surface Area [m²/g]	Total Pore Volume [cm³/g]	Micropore Volume [cm³/g]	C [wt%]	H [wt%]	N [wt%]	O [wt%]	Cl [wt%]
3.9% O/untreated	1550	0.74	0.61	95.40 95.97[a]	0.68	0.05	3.92 4.03[a]	0
4.1% N (nitridated)	1738	0.84	0.59	91.96 94.34[a]	0.27	4.50 4.06[a]	3.23 1.60[a]	0
7.8% Cl (chlorinated)	1523	0.73	0.54	87.71	0.06	0.27	4.15	7.8
16% Cl (chlorinated)	1374	0.66	0.51	77.93 88.94[a]	0.01	0.06	6.00 3.27[a]	16 7.8[a]
21% O (oxidized)	1409	0.66	0.55	76.26 85.53[a]	1.41	1.49	20.84 13.84[a]	0
32% O (oxidized)	1105	0.47	0.35	64.76 76.60[a]	1.55	0.72	32.32 23.39[a]	0

a. % Elemental as determined by XPS. Difference in Cl values between the two methods may be due to uncertainty in the calibration standard used.

Table 2. XPS Deconvolution of the Carbon 1s Peak Area for Chemically Modified ACC-20.

Binding Energy [eV]	Percentage of Total Area of Carbon Peak					
	3.9% O (untreated)	21% O	32% O	12.3% Cl	16% Cl	4.1% N
285 (C-C, C-H)	50.94	55.9	46.86	57.28	42.08	48.43
286 (phenol, hydroxyl, C-OH)	27.87	14.92	24.68	21.00	31.12	24.20
287 (carbonyl, C=O)	9.29	13.03	7.64	8.12	8.23	8.14
289 (carboxylic, C=OOH)	5.58	9.99	14.59	7.16	8.56	7.90
291 (shake-up band, $\Pi \to \Pi^*$)	6.32	6.15	6.23	6.43	10.00	11.35
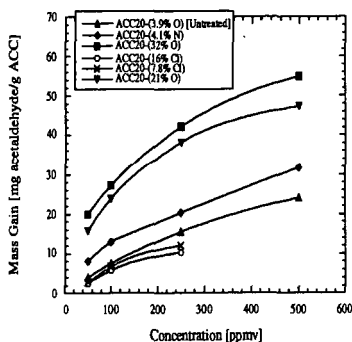
Figure 1. Adsorption of Acetaldehyde on Chemically Modified ACC.
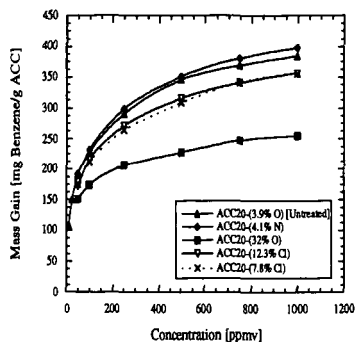
Figure 2. Adsorption of Benzene on Chemically Modified ACC.
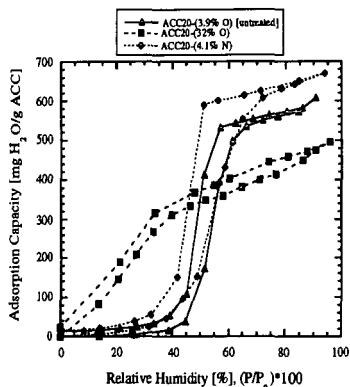
Figure 3. Adsorption and Desorption of Water Vapor on Oxidized and Nitrated ACC-20.
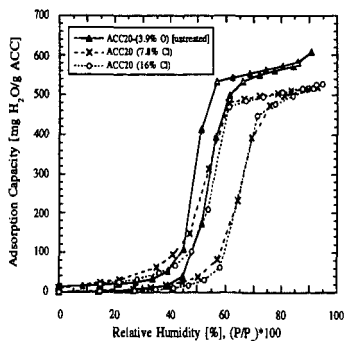
Figure 4. Adsorption and Desorption of Water Vapor on Chlorinated ACC-20.

PRODUCTION OF VAPOR GROWN CARBON FIBER
WITH COAL FINES WITHOUT SO$_2$ EMISSIONS

D. Burton, M. Lake, and R. Alig
Applied Sciences, Inc.
P.O. Box 579
Cedarville, OH 45314

ABSTRACT
Each year millions of tons of low-cost hydrocarbons in the form of
coal fines are impounded. One potential application would be
utilization in a unique process capable of converting the carbon
into a highly graphitic vapor-grown carbon fiber (VGCF). This
process currently produces vapor-grown carbon fiber from the vapor
phase using natural gas, hydrogen sulfide and iron particles. The
iron particles initiate the growth of the carbon fibers while the
hydrogen sulfide enhances the yield, allowing the process to be
economically feasible. Previous demonstrations involving
pulverized coal have proven that coal can be used as an alternative
source of carbon and sulfur in the production of VGCF.
Furthermore, there is evidence that the sulfur from the coal
remains with the carbon fiber catalyst during the reaction and does
not exhaust as SO$_2$ into the atmosphere. It is the object of this
research to determine if coal fines pulverized to -325 mesh are
also a viable source of carbon and sulfur for VGCF production.

INTRODUCTION
Currently, commercial carbon fibers possessing a wide range of
properties are formed from precursors of polyacrylonitrile (PAN) or
petroleum pitch. Generally, these types of fibers have common
methods of synthesis and handling, the latter of which is similar
to textiles. Commercial fibers are made by extruding or spinning
a continuous filament or thread from a polymer. The continuous
filament is subsequentially oxidized under tension to 200^{0}C then
carbonized by slowly heating it in the absence of air to 1000^{0}C.
Additional heating up to 3000^{0}C provides higher degrees of
graphitization necessary for ultra-high strength and/or stiffness
applications. The cost of multi-step production for commercial
carbon fibers limits their application to reinforcements in
aerospace composites, golf clubs, fishing poles and other high
performance products.

The production method of vapor grown carbon fibers is in sharp
contrast to the production method of commercial carbon fiber. The
one-step process, shown in Figure 1, has no involved extrusion or
spinning operations allowing VGCF to be produced at a significantly
lower cost. One type of vapor grown carbon fiber produced in our
laboratory, and designated as PYROGRAF III, is initiated with iron
particles which catalyze the growth of partially graphitic
filaments in the presence of hydrocarbons at 1000-1100^{0}C. Such
fibers have diameters on the order of nanometers. Pyrocarbon
subsequently deposited on the walls of the filament thickens the
diameter of the fiber with the basal planes of the deposited carbon
preferentially oriented parallel to the filament surface[1]. Recent
studies have shown significant enhancement of fiber nucleation
efficiency by the addition of sulfur into the reaction[2]. The
sulfur reacts with the catalyst and becomes overcoated by the
fiber. Although H$_2$S is beneficial to the efficiency of fiber
production, it is used with great reluctance since it is expensive,
highly corrosive to rubber seals and metal fittings, flammable, and
as toxic as hydrogen cyanide. Therefore, coal fines are being
trialed as the source of sulfur to eliminate the hazards and high
cost of hydrogen sulfide.

Figures 2 and 3 show scanning electron micrographs of PYROGRAF III
and typical continuous commercial carbon fibers. The diameter of
PYROGRAF III generally averages 0.2μm as produced while commercial
fibers are 8μm in diameter. Unlike commercial fibers, PYROGRAF III
are not continuous but are an entangled mass resulting from the

turbulence of their gas phase generation. The length/diameter ratio for PYROGRAF III ranges from 40 to 200. However, due to the purity with which carbon is incorporated into the fiber, VGCF has a highly graphitic structure which results in higher values of physical properties than are realized in commercial carbon fibers, as shown in Figure 4.

Currently, PYROGRAF III production uses iron pentacarbonyl, natural gas and hydrogen sulfide as the sources of iron, carbon, and sulfur respectively. An economic scale-up analysis on the PYROGRAF III process performed by Battelle showed that the VGCF can be produced for under 5 $/lb using the aforementioned feedstocks. Additional cost reduction would result from using coal fines as shown in Table 1. Reduction in the cost of the feedstocks is vital for allowing PYROGRAF III to be considered for automotive applications, such as in sheet molding compounds and numerous low strength components such as motor housings, interior panels, and other low-cost applications.

EXPERIMENTAL
A reactor used in PYROGRAF III production (Figure 1) was modified to allow the introduction of pulverized coal into the reactor. The reactor normally uses a feedstock mixture of natural gas, iron pentacarbonyl particles transported into the reactor by a helium stream, and 99.3% pure H_2S gas simultaneously injected into the 2000^0 F reactor. A typical control formulation that would produce a 25% yield is shown in Table 2. The apparatus to feed the coal fines is a Vibra Screw® Mini Feeder driven by a variable speed motor. The hopper is sealed to prevent the influx of oxygen which could cause immediate combustion of any fiber or hydrocarbons at the process temperature. The coal feeder transports the coal dust directly into the main gas feed to be carried into the reactor.

In the coal trials, the hypothesis is that sulfur-bearing coal can replace H_2S as the source of sulfur in the reaction. A combination of coal and methane were used as the hydrocarbon feedstock. The formulation was chosen such that the percentage of sulfur in the reactor derived exclusively from coal is equivalent to the "control" formulation of sulfur in the process when using methane only. Ohio #8 Coal from CONSOL Inc., at 4.71% total sulfur and 46.6% total carbon, was pulverized to less than 63μm. Methane was used as the carrier gas in Trial 1 at the rate required to balance the sulfur/carbon ratio to the control value. To determine the material balance, it was assumed that all the sulfur in the coal exists as hydrogen sulfide. In fact, the compounds of sulfur in coal vary extensively; however, as shown elsewhere[2], the sulfur level can vary and still produce acceptable vapor grown carbon fiber.

RESULTS
Figure 5 is a micrograph of fiber produced from a mixture of coal and methane in which all of the sulfur was supplied by the coal. It is inferred from this micrograph that the sulfur contained in the coal plays an active role in the catalytic process, similar to the case where H_2S is used. The morphology of the fiber product and the absence of soot in this trial indicates comparable quality to the best material which can be produced by this method. Coal also contributes carbon to the process as can be inferred from Figure 6 in which fiber was produced using coal as the sole source of sulfur and carbon. In this micrograph the presence of soot is evident indicating that the sulfur to carbon ratio is unbalanced.

The degree of graphitic ordering is the crucial property that causes the wide range of strength and conductivity of carbon fibers. To estimate the degree of graphitization of the fiber produced with coal, X-Ray diffraction was used. Table 3 shows that the "as grown" samples using coal has graphitization in a range typical of a low modulus commercial fiber.

In the control process, which relies on H_2S introduced to a pure methane feedstock, periodic analysis has been made of the exhaust

emissions during trials. In the tests to date, sulfur has not been detected in the exhaust. During the present experimentation, the exhaust was sampled using gas chromatography, with a similar result. While the current GC analysis is relatively insensitive with respect to measurements on the control process, the detectability limit implies a sulfur concentration less than 1%.

Since the sulfur content in coal exceeds the control balance, such a result implies an optimistic consequence to a balanced sulfur content. These data taken together offer incontrovertable proof that VGCF can be generated from high sulfur coal. Furthermore, effort to optimize the formulation should result in carbon fiber generated from high sulfur coal with quality and efficiency comparable to processes using other hydrocarbon sources, and at costs enabling economic viability. Although further work is needed to assess the effects of the organics and ash content variation in coal, their presence does not prevent the growth of a carbon fiber with graphitic ordering, and would be acceptable in applications such as reinforcements for cement and rubber.

While these studies indicate the viability of using high sulfur coal as the hydrocarbon feedstock in the production of VGCF, in practice, the high percentage of sulfur in various coals, as well as the variability of the percentage of sulfur in coal, will most likely mandate a combination of hydrocarbon feedstocks in order to maintain the process balance needed for optimum production. The role of coal particulate in contributing both to the hydrocarbon balance and sulfur balance, is significant in any event.

CONCLUSIONS
It has been demonstrated that coal particulate can be used to produce VGCF, contributing both carbon and sulfur to the reaction. Work is in progress to optimize the process for conversion of coal fines to carbon fiber. Viability of the process will depend on the conversion efficiency, degree of graphitization of the fiber, percentage of ash in the product, and whether the process can be sustained on a continuous basis with an environmentally-benign exhaust. This work suggests an economical and ecologically safe process for the utilization of coal fines as the source material for carbon fiber reinforcements in rubber, cement, as well as composites for automobiles, electronics, and aerospace components.

ACKNOWLEDGEMENT

REFERENCES
1. J.L. Kaae, Carbon 23, 665 (1985).
2. G.G. Tibbetts, C.A. Bernardo, D.W. Gorkiewicz, and R.A. Alig, "Effect of Sulfur on the Production of Carbon Fibers in the Vapor Phase" CARBON, 32, no. 4, pp.569-576, (1994).

Table 1. PYROGRAF III Material Cost Comparison

	High Purity Methane Only ($/lb)	Natural Gas Only ($/lb)	Coal Only @ $30/ton ($/lb)	Coal Fines Only @ $23.50/ton ($/lb)
Sulfur Source	0.189	0.194	0	0
Carbon Source	69.83	0.44	0.023	0.016
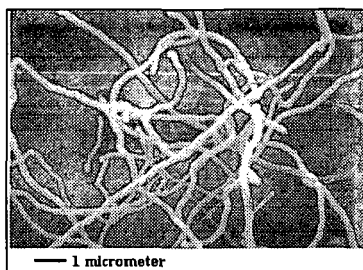
Figure 2. As-grown PYROGRAF III Produced with Methane.
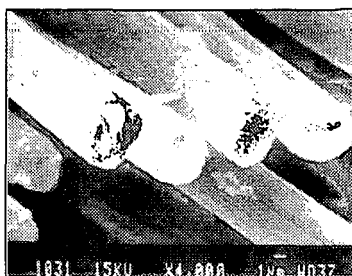
Figure 3. Commercial Carbon Fiber.
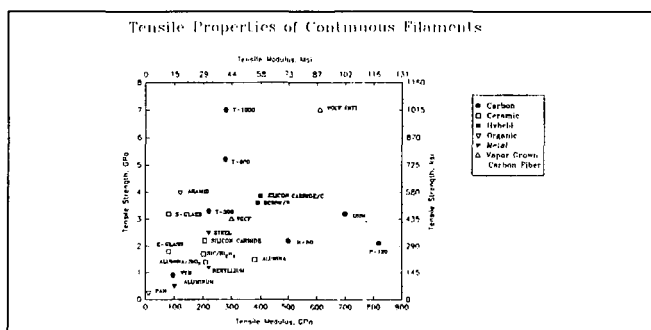
Figure 4. Tensile-Modulus Properties of VGCF.
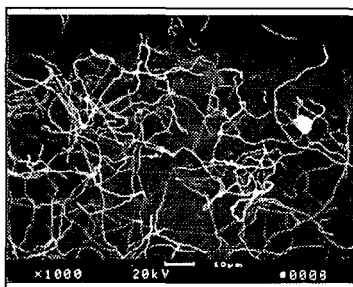
Figure 5. As-grown PYROGRAF III Produced with Coal Replacing H2S.
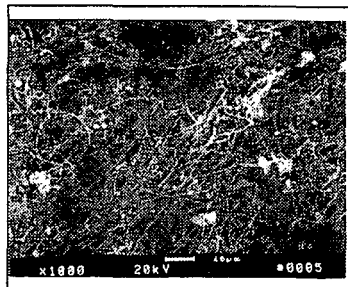
Figure 6. As-grown PYROGRAF III Produced with Coal as Sole Source of Carbon and Sulfur

TABLE 2. Control Formulation for PYROGRAF III Production[*]

	CONTROL	TRIAL 1
Natural Gas	96.9	87.58
Coal	None	9.33
Sulfur	0.47	0.44
Helium	0.96	0.96
Fe(CO)$_5$	1.68	1.69

* Formulations are in per cent by weight

Table 3. X-Ray Diffraction Analysis[*]

Heat Treat (C)	Fiber	D-spacing (nm)	g_p* (%)
As-grown	VGCF	.34490	--
1300	ex-PAN	.354	--
As-grown	ATrial (coal)	.3459	--
2200	VGCF	.34206	23
2500	VGCF	.33770	73
2500	ex-PAN	.342	23
2700	VGCF	.33697	82
2800	VGCF	.33663	86
As-grown	PYROGRAF III	.3385	64
--	P-120	.3392	56
--	P-120	.3378	72

*g_p=(.3440-D-spacing)/(.3440-3354)
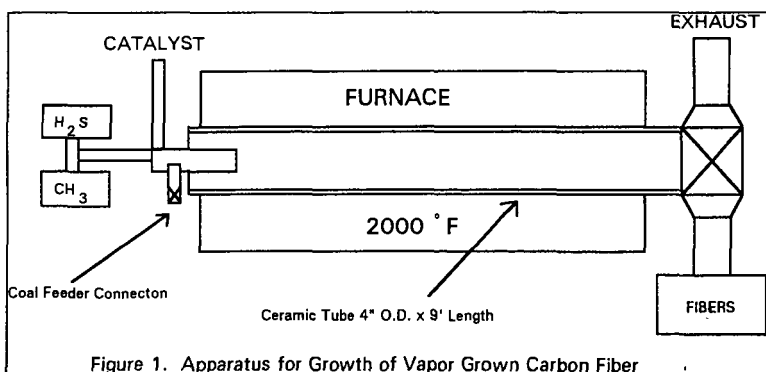
Figure 1. Apparatus for Growth of Vapor Grown Carbon Fiber

MECHANICAL PROPERTIES OF CARBON FIBER COMPOSITES FOR ENVIRONMENTAL APPLICATIONS.

Rodney Andrews and Eric Grulke, Chemical and Materials Engineering Department, University of Kentucky, Lexington, KY 40506-0046.
Geoff Kimber, Center for Applied Energy Research, University of Kentucky, Lexington, KY 40511-8433.

Keywords: carbon fiber composite, activated carbon, mechanical properties, permeability

Abstract:

Activated carbon fiber composites show great promise as fixed-bed catalytic reactors for use in environmental applications such as flue gas clean-up and ground water decontamination. A novel manufacturing process produces low density composites from chopped carbon fibers and binders. These composites have high permeability, can be activated to have high surface area, and have many potential environmental applications. This paper reports the mechanical and flow properties of these low density composites. Three point flexural strength tests were used to measure composite yield strength and flexural moduli. Composites containing over 10 pph binder had an adequate yield strength of about 200 psi at activations up to 40% weight loss. The composites were anisotropic, having along-fiber to cross-fiber yield strength ratios between 1.2 and 2.0. The pressure drop of air through the composites correlated with the gas velocity, and showed a dependence on sample density.

Introduction:

The use of activated carbons for waste stream clean up is well known. However, the costs of using beds of adsorptive carbons are prohibitive in many cases. The uptake of chemicals into beds of granular carbon can be slow, and the pumping cost for beds of powdered carbons can be prohibitively high. The carbon fiber composites studied here have the advantages of high mass transfer rates inside the fibers, good mechanical strength, and high permeability to liquids and gases.

The composites were manufactured using a novel process developed at the University of Kentucky. ACFC's are made from amorphous carbon fibers which are "glued" together using a variety of binder systems. The binder works by cementing together fibers at their points of intersection. Binder may also adhere to the fiber surface, and can be activated as well.

These materials, which can be described as a highly porous solids, can be machined or formed to fit in many existing systems, and will act as fixed bed catalytic reactors for chemical removal or adsorption. Specific applications of these materials will result in different static and dynamic loadings. The composite parts must be able to withstand the loads seen during installation as well as operation and exhibit low pressure drop characteristics.

Mass Transfer Inside the Fibers

Reactants need to move from the bulk gas stream to the fiber surface, and then diffuse to reaction or sorption sites inside the fiber interior. One critical step in this sequence is the diffusion of the reactants inside the fibers. Because of the small diameter of the fiber, the rate at which this step takes place will be rapid compared to other factors in the process. The fibers have small pores through which gases and liquids can diffuse to the interior. The Fourier number for diffusion can be used with various unsteady state solutions to the cylindrical diffusion equation (Newman, 1931) in order to estimate the time needed to accomplish 90% of a step change in the gas phase concentration at the fiber surface. The diffusion coefficient of the solute is taken to be appropriate values for gas or liquid solutes, and the average fiber diameter was less than 25 microns. The Fourier numbers for the two types of carbons show that the diffusion time for a fiber is several orders of magnitude shorter than for a granular carbon particle (Table 1). The fibers used in the ACFC's studied here have intrinsically rapid uptake rates for both gas and liquid systems.

Mechanical Strength

The activated carbon fiber composites would be used either as flat filters treating the entire gas flow, or as annular (candle) filters arranged in a bag house type system. In either case, the filter unit would require good flexural strength. It also must withstand installation, cyclic loading, and, for some applications, regeneration. These criteria have led us to evaluate the mechanical performance of the composites using flexural tests. In addition, some applications will require complex composite shapes which are expected to be anisotropic due to the nature of the forming operation. Therefore, measurements in the machine and transverse directions are compared.

Permeability to Gases and Liquids

Activated carbon fiber composites (ACFC's) can be used in gas phase processes because of their low pressure drops and high internal mass transfer rates. Possible uses include low temperature removal of sulfur dioxide and nitrogen oxides from flue gas streams. The flue gas velocities are on the order of 3 meters per second, requiring high reaction rates, high mass transfer rates, and low pressure drop operation for economic treatment. The pressure drop for a fluid flowing through the composite can be compared to that of a fluid in a packed bed. The commonly used model for flow in a packed bed is the Ergun equation:

$$\frac{\Delta P}{L} = \frac{150\mu U}{D_p^2} \cdot \frac{(1-\varepsilon)^2}{\varepsilon^3} + \frac{1.75\rho U^2}{D_p} \cdot \frac{1-\varepsilon}{\varepsilon^3},$$

where ($\Delta P/L$) is pressure drop per length, U is the superficial velocity, D_p is the effective fiber diameter, μ is the fluid viscosity, ρ is the fluid density, and ε is the composite void fraction. As the system studied does not follow the

assumptions necessary for use of the Ergun equation, a modified form of the equation was used in this study. This is equation is

$$\frac{\Delta P}{L} = K \cdot (U^*)^n,$$

with K being a parameter dependent on the fluid properties, and n is between one and two. U*, the corrected velocity, is defined by

$$U^* = \frac{(1 - \varepsilon)^2}{\varepsilon^3} \cdot U.$$

Objectives

This study measures the failure strength and the permeability of a novel activated carbon fiber composite. The mechanical properties of these materials were studied using modified ASTM flexural testing methods. Pressure drop was correlated with gas velocity and the density of the composite.

Experimental:

The composites were tested to determine flexural strength at break, maximum strain, and the elastic modulus of the material. Samples were formed in 4 inch diameter cylinders, about 4 inches in height. ASTM standard C203-92 (3 point bend flexural testing of block type insulation) was followed. The samples were cut from the block in two directions. The cross direction is the plane parallel to the direction of composite formation. The along direction is the plane perpendicular to the direction of formation. The samples were tested using a three point apparatus on an Instron.

Scanning electron micrographs were taken of the fracture plane of the samples. SEM analyses were used to identify failure mechanisms and binder distribution in the samples. In most cases, the samples were sputtered with gold and then analyzed at 600x magnification.

Pressure drop measurements were made using an Omega DP41-E High Performance Process Indicator and 0 - 2 psi microtransducer. Nitrogen at controlled volumetric rates was passed through composite samples until a constant pressure drop was determined for each flow rate.

The variables effecting the flexural strength of the composites were: fiber length, binder content, thermal treatments, and preactivation of the fibers before formation. The binder used in composite formation is a phenolic thermoset. All fibers used were obtained from Ashland Chemical and have an average diameter of 17 microns. Samples were made which contained differing binder quantities: 5, 10, 20 and 40 parts per hundred. Each of these samples were also tested under all of the activation phases: cured, baked, and activated at 10%, 20% and 40% weight loss.

Several different thermal treatments were studied: curing, baking, and activation. During curing, the composite is held at 150 °C to completely cure the binder resin. The composite is baked in an inert atmosphere at > 650 °C. Activation is done by heating the composite at temperatures greater than 750 °C in a carbon dioxide or steam atmosphere.

Results:

Composite Morphology

The 5 pph binder composites were found to be too weak for practical application, and friable during handling for all thermal treatments. Because of this poor sample integrity, the 5 pph samples were difficult to test, and had low reproducibility. SEM analysis of these composites showed binder wicking at the fiber contact points during the curing process. Some of the fiber contact points were not wetted with binder, and the fiber surfaces were not been coated with binder.

The 10 pph binder composites exhibited much higher strength than the 5 pph samples. In the SEM analysis of the 10 pph binder composites, most of the fiber contact points are wetted with binder. Some of the excess binder wicks onto the fibers, completely covering the fibers in samples containing 20 pph binder. This wicking of binder to cover the fibers continues at the 40 pph binder content level and gives a thick coating.

Mechanical Strength

The flexural strength at break of standard samples made with P400 fibers and cured only were compared in the cross- and along-fiber directions. These samples were found to exhibit anisotropy. The yield strengths of these samples are adequate in all samples except the 5 pph binder content sample. The yield strength increases with increasing binder weight fraction. The level of anisotropy is 1.1 to 2.0 based on cross- to along-fiber strengths. (Figure 1).

More thermal processing reduces yield strength and elastic modulus. This trend is true for samples with differing binder contents as well (Figure 2). The effect of thermal processing can also be seen in the SEM analysis. Composite samples containing 40 pph binder before curing were activated to 13, 19, and 35 % weight loss. At 13%, binder completely coats the fibers. At 19%, binder still coats the fibers, although not as thickly. At 35 % weight loss activation the fibers are no longer coated with binder. At each activation level, evidence of binder failure, fiber pullout, and flaking of the binder away from the fibers can be seen. This indicates a failure mechanism of fiber pullout, or, failure of the fiber binder interface.

Fiber length has a significant effect on composite strength. The shortest fibers, P200's with a length of 350 microns, result in the composite with the highest flexural strength at break. The longest fiber, at 10,000 microns, has the longest span between binder contact points, resulting in the weakest composite. See Table 2.

Composite mechanical properties decrease with increasing thermal processing. Cured composites are the strongest, have the highest modulus, and have the highest density. Baked samples have a lower density, but also have lower strength and modulus. Activated samples have the lowest strength, the lowest modulus, and the lowest density (Table 3). This could be a result of the binder coating acting to stiffen the fiber-binder piece. At higher stages of thermal processing, excess binder is burned away, and the strength of the composites decrease. This trend of decreasing modulus and strength with increasing thermal processing is seen in composites made from medium and long fibers as well.

355

Higher amounts of binder in the composite make it stronger, but increase the density. Normalized moduli (E/ρ) increase directly with binder content, suggesting that the binder contributes directly to material strength (Table 4).

Composite Flow Characteristics

Pressure drop per unit length increases with composite density, and with increasing fluid superficial velocity (Figure 3). The data is fitted by the modified Ergun equation: K equals 288 for nitrogen and n is 1.168 (Figure 4). Ninety-eight percent of the data fall within two standard deviations of this fit. Thermal processing has no significant effect on pressure drop. The composites are isotropic with respect to pressure drop.

Conclusions:

Variables which effect the strength and modulus of activated carbon fiber composites are fiber length, binder content, and level of thermal processing. The composites show strength anisotropy, 1.1 to 2.0, between the cross- and along-fiber alignment directions.

SEM micrographs show that the failure mechanism for these composites is fiber pullout. Increasing binder content leads to thicker layers of wicked binder coating the fibers. Thermal processing burns away the binder, resulting in a weaker composite with lower density.

For most applications, the strength of composites with 10 parts per hundred binder and higher composites would have adequate strength for low pressure drop systems at activations up to 40% weight loss. This implies great flexibility in application and tailoring of the composite morphology for different catalytic systems.

The effect of fiber length was as expected. Composites made with shorter fibers have higher densities, higher yield strengths at break, higher elastic moduli, and a lower elongation at break. Thermal processing reduces the composite strength and moduli because the wicked binder is burned away.

The composite is highly permeable to gas flows, and has a low pressure drop at industrial flue gas velocities. The pressure drop in the composites can be accurately predicted using a modified form of the Ergun equation. Pressure drop is proportional to the corrected velocity to the 1.168 power, and K, the proportionality constant, is 288 for nitrogen.

Table 1: Time to accomplish 90% of a step change in the surface concentration.

Carbon Form	Length Scale, cm	Gas Phase (90%), s	Liquid Phase (90%), s
fiber	0.0025	0.000005	0.05
granule	0.10	0.032	320

Table 2: Effect of fiber length on strength.

Fiber	Length, microns	Strength, psi
P200	350	324
P400	700	215
P3200	10,000	8.5

Table 3: Effects of thermal processing on short (P200) fiber composites.

Thermal Stage	Dry Density, g/cc	Strength, psi	Modulus, psi
cured	0.330	324	39,000
baked	0.309	249	14,200
activated	0.261	157	9,870

Table 4: Effect of binder content on normalized modulus. P400 fibers.

Binder Content, part per hundred	Modulus, psi	Dry Density, g/cc	E/ρ
10	6,430	0.210	30,600
20	10,300	0.220	˙46,800
40	22,000	0.237	92,800
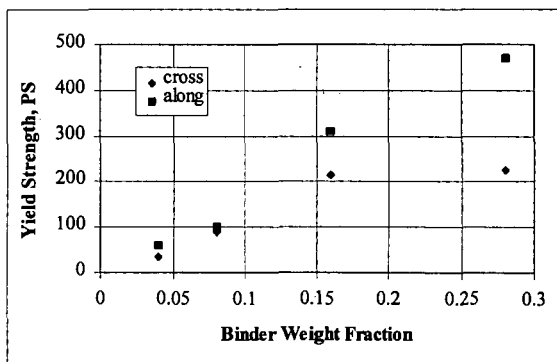
Figure 1. Effect of binder weight fraction on Yield Strength. P400 fibers, cured.
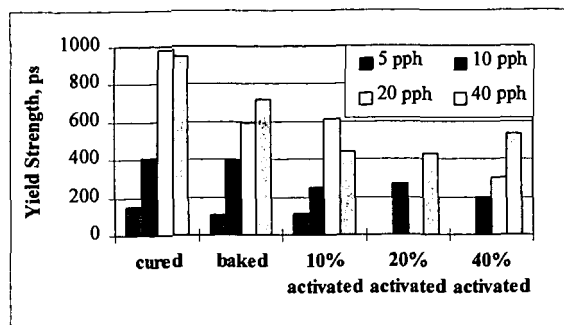
Figure 2. Yield strength over the processing lifecycle.
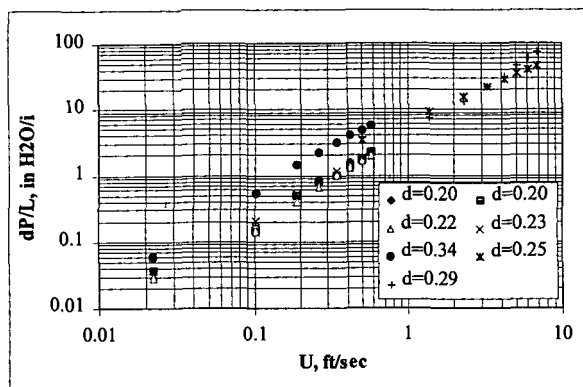
Figure 3. Pressue Drop versus Superficial Velocity.
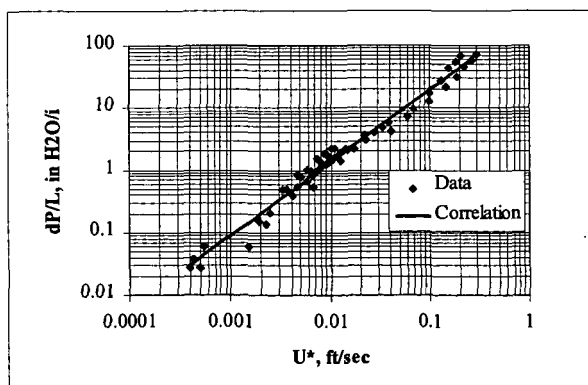
Figure 4. Pressure drop versus corrected velocity. K = 288, n = 1.168.

STATE-OF-THE-ART IN PREDICTING ACTIVATED CARBON PERFORMANCE

Mick Greenbank
Calgon Carbon Corporation
P.O. Box 717
Pittsburgh, PA 15230-07171

Abstract:
Adequate theories of multicomponent gas and liquid phase adsorption have been available for 10 to 15 years. Yet the ideal of using computer simulations to determine treatment costs and to aid in design of real-world environmental systems has never fully materialized. However, current adsorption theories are accurate enough, and quite useful, for making relative comparisons of performance of different carbons and for looking at adsorption versus other technologies for new applications. The use of a gas- and liquid- phase adsorption model is evaluated for predicting performance, optimizing carbon selection, and designing systems for environmental applications.

I. MODELING ENVIRONMENTAL APPLICATIONS - DEFINITION OF THE PROBLEM

The ideal situation would be to have a computer program that instantly predicts the capital and operating cost of an optimized activated carbon system that solves a specific environmental problem in both the gas and liquid phase. In addition, the program would need to be able to account for variability in conditions and stream composition. This algorithm would allow 'what-if' type analyses to aid in design of an optimal system and account for upsets and shutdowns. Also, in the activated carbon design, the algorithm rhythm would provide instant feed back on performance leading to better activated carbon processing schemes and products. We are not there in 1996, but have made progress.

This is not a statistical error analysis or a review of existing adsorption theories. Instead it is a description of what the most practical theoretical approaches can and cannot do with environmental applications. The discussion is less mathematical and more problematical.

A. APPLICATION DEFINITION - COMPUTATIONAL PERSPECTIVE

To do a computation of performance of an adsorption system, we need to know each adsorbable component present, including water. Any background components may be important, even if nondetectable using current techniques. For each component we need concentrations and variations in concentration over the life of the system. Also the treatment objective (acceptable effluent composition) should be defined in similar terms. The required system variables are temperature of each carbon particle (Usually approximated as a simple linear or a radial temperature profile through the adsorber) and gas-phase or liquid-phase linear velocity between the particles. The stream must be a single phase, to have effective contact of the contaminants with the carbon particles and to avoid any unpredictable decay in performance. This means that for the gas phase there must be no particulate matter or freely condensed material, for the liquid phase there must be no suspended solids or precipitation within the column.

B. APPLICATION DEFINITION - REAL WORLD PERSPECTIVE

This ideal of an application description satisfying requirements for computation is rarely, if ever, obtained. Differences between the information required for computation and what is provided by the application definition are listed below.

1. Stream composition

Generally the best case scenario is a stream analysis using a gas chromatograph/mass spectrometer (GCMS) and is usually a first step for both gas and liquid phase applications. This gives a list of compounds and concentrations for a sample taken usually at one moment in time. The GCMS analysis is relatively expensive. Consequently, time averaged values and histories of stream composition are generally not available, and thus variability of composition is not well defined. The major problem with GCMS analysis is that the largest, most adsorbable molecules are also not volatile, and thus are difficult to detect with GCMS. Test methods that are less specific, such as gas or liquid chromatography (GC or LC), measure the major or critical components and give little information on background components. Nonspecific tests such as total organic carbon (TOC), chemical oxygen demand (COD), biological oxygen demand (BOD), color, odor give no useful information and only hint at the composition. However, comparing the results of one of these nonspecific tests to the sum of the concentrations of the known components can be useful to find how much background material is not accounted for in the calculation. Sometimes, this background material can be approximated by substituting model compounds.

2. Carbon temperature
The temperature critical to the calculation is the temperature of the carbon where the adsorption is occurring, not the ambient or stream temperature (when gradients are present). Fortunately the carbon temperature profile in the adsorber is usually known or can be approximated.

3. Linear velocity or flow rate and its variability
Assuming no flow complication such as plugging or wall effects, the activated carbon is only concerned with the instantaneous linear velocity in the voids between it and its neighbors. This generally can be determined from the mass flow rate, void fraction, and dimensions for a given carbon system design. What generally is not included in the calculations are the fluctuations in the flow rate, or stoppage of flow due to shutdowns.

4. Variability of concentration and composition.
Variability in stream compositions involves probability of upsets or spills and their magnitude, equipment operating schedules and flow rate changes, and the reliability of the sources of contamination. Few streams are consistent, but many streams that involve a leaching phenomenon, and where the equipment follows a regular routine schedule can become predictable with experience. Unfortunately this experience is generally not available during the design or evaluation stages of a project.

5. Other variables affecting performance
Other factors that can affect performance for gas-phase systems are: relative humidity, presence of condensables (including water), dusts or particulate matter (particulate size and amount). Other factors affecting performance of liquid-phase systems are: pH, conductivity, suspended solids (particulate size and amount). For humidity and pH, the effects can be estimated over a range of conditions and the performance detriment determined. Then an economic decision can be made for humidity or pH control or adjustment. The inlet end of a carbon adsorber will act as a particulate filter for dust and suspended matter, with the ability to filter material with diameters greater than one tenth of the smallest carbon particle diameter. However, operation of a carbon adsorber as a particulate filter is awkward and can be more expensive. The decision on whether to use prefilters for particulates is economical and depends on the severity of the problem. Unfortunately the adsorptive performance decay resulting from the lack of a prefilter for particulates can only be approximated crudely.

6. Defining treatment objectives
Performance is usually defined by the point at which the treatment objective is exceeded. Although objectives are usually defined, the exact point at which a treatment objective is exceeded sometimes adds uncertainty. For example, predicting the point at which a treatment objective is exceeded can be complicated when the objective is a nonspecific test result such as total hydrocarbon, TOC, BOD, COD, color, or odor, and a wide variety of components are present in the effluent of the carbon system. When the objective is cumulative mass over a time period (for example, kilograms of hydrocarbon per month), determining the calculated point at which the carbon system is exhausted and should be replaced is difficult. Percentage removal objectives for individual components can be difficult due to the potential variability of the influent stream and the time lag of a change in the influent to a change in the effluent. From a computational point of view, the simplest treatment objectives are concentration limits for individual components.

7. Regeneration (thermal or extraction)
Incorporation of a regeneration scheme, whether thermal (Steam or hot air), vacuum, or extraction (using a solvent or a pH shift) adds many more variables and uncertainty to the calculations. For example, a correlation of isotherm data as a function of temperature is required for thermal regeneration. Generally the approach is to measure several regeneration cycles and look for the system to reach a steady state. This approach is generally adequate, but does not predict the eventual exhaustion of the carbon with nonregenerable components or other operating inefficiencies that occur later in the life of the carbon bed (such as degradation of the particle to a smaller particle size or slow oxidation of the carbon structure).

II. THEORETICAL APPROACH TO ADSORPTION
A few computational approaches can be used to approximate adsorptive performance, even within the limitations of the real world descriptions of environmental applications mentioned above. In order to select an adsorption theory for predicting performance in environmental applications, the following criteria must apply. The theory must be applicable: for systems with an unlimited number of components, for use with any of the wide variety of commercial activated carbons, and for the range of system variables present such as temperature, pressure, and pH or humidity. These are not trivial requirements because they imply that a multicomponent isotherm capacity can be determined for any component for any activated carbon over a range of concentrations and temperatures, pressures, pH, or humidity. With all these variables, measuring enough points to define the multicomponent isotherm surfaces is not practical. Therefore, the theoretical approach must predict multicomponent isotherms from single component isotherm data. Also isotherm data on one

activated carbon must generalize to all other commercialized carbons (Libraries of empirical isotherms will not be available for all commercial carbons). At least two approaches can satisfy these computational requirements and the practical limitations on the amount of empirical data required. The Ideal Adsorbed Solution Theory[1] (IAS) incorporating a generalized characteristic curve[2], and the Polanyi Adsorption Potential Theory[3] incorporating the Hansen-Fackler Modification[4] (Polanyi). The remainder of the discussion on performance prediction will be limited to the use of these two approaches.

A. THEORETICAL APPROXIMATIONS AND ASSUMPTIONS

1. Physical adsorption predominates

The adsorbates exhibit no specific interactions with the surface or each other, including chemical reactions on other nonideal behavior. This is a good assumption for most adsorbates on activated carbons. Specific interactions do occur, for example dipole-dipole and dipole-surface oxide interactions, but they are generally less significant than the nonspecific physical attractions. If this is not the case, then a polar adsorbent like Silica gel or alumina should be used instead of a nonpolar activated carbon. If the specific interaction between adsorbates is strong, such as with dimerization, then treat the dimer as the adsorbate.

2. Bulk behavior is observed in the pores

What happens outside the particle happens inside the pores of the activated carbon. In other words, the adsorbates exhibit lateral interactions, bulk solubility limits, and melting points. The carbon structure does not alter the physical properties of the adsorbate. This is a good approximation on nonimpregnated activated carbons.

3. No molecular sieving

All adsorbates have equal access to all portions of the carbon pore structure. Generally this is a good assumption. Molecular sieving or exclusion of large or bulky molecules does occur in activated carbons in specific instances, but it is the exception and not the rule. Also, on commercial activated carbons, the pore structure is purposefully open to provide easy access. Adsorbates excluded are generally so large that they are adsorbed in another part of the structure. When exclusion does occur, accounting for it with mathematical corrections to the single component isotherm is a possibility.

4. Volume-based competition

Application is based on pore filling, and adsorbates compete on a volume basis. An adsorbate with twice the molar volume will compete with two of the smaller molecules. This is a good assumption and is why molar volume is one of the most important properties in determining adsorbability of a molecule.

B. STEPS IN THE COMPUTATION

1. Generate single component isotherms

The first step is to generate a set of single component isotherms on a carbon of interest over the range of temperatures and stream conditions. An empirical approach would require a handbook of adsorption isotherms to be determined for each contaminant, on every carbon, over the range of temperatures and pH. The solution is to generate the single component isotherms using a generalized characteristic curve for the carbon and set of specific characteristics for each adsorbate determined on a standard carbon. The IAS theory can also incorporate a generalized characteristic curve[5] to generate the single component isotherms that are very similar to this classic Polanyi approach.[6]

First assume a pair of adsorbate properties, independent of the carbon, which can be used to scale adsorption isotherms to a single characteristic curve. One property is related to relative strength of the adsorptive interaction (Polanyi polarizability), and the other is related to the efficiency of filling the pore structure (molar volume in the pore determined from the maximum adsorption capacity at near saturated conditions). Next assume that the characteristic curve is a function of the carbon pore structure and therefore is a property of the adsorbent and independent of the adsorbate. The characteristic curve is generally presented as a distribution of pore volume over different adsorptive forces, corresponding to different pore sizes. The assumption is that the carbon pore structure is constant and fills on a volume basis and interacts with molecules in the same manner. Differences are in the number of molecules that fit into a pore and the relative strength of the interaction with the carbon structure.

With these assumptions, only one isotherm for a standard adsorbate (for example propane) is required on each carbon to determine the characteristic curve. Several simple techniques are available to generate these data easily.[7] Then one isotherm for each contaminant is required on a standard and well-defined activated carbon to determine the adsorbate molar volume and relative

adsorption strength in the pores. The database of published isotherms on well-defined standard carbons is growing, but is still inadequately small.

2. Calculate the multicomponent isotherms

The thermodynamics of adsorption of multicomponent systems on activated carbons, both from the gas-phase and liquid-phase, has been defined by several models,[8] but the most popular have been the Polanyi and IAS theories. Both approaches are thermodynamically consistent[9], and calculation algorithms are available which can handle a large number of carbons and adsorbates efficiently.[10] The computation determines the partial occupation of the different regions of the pore space (adsorption sites) by the different contaminants. By summing the occupation of all sites by all contaminants, under the stream conditions, a multicomponent loading on the carbon particle is determined.

3. Incorporate a kinetic model for mass-transfer resistance

Once the multicomponent thermodynamics has defined the equilibrium state, a kinetic model can be incorporated to account for the diffusion of the adsorbate into the carbon pore structure. The adsorption kinetics has been most often modeled using an approach that incorporates three or four diffusion steps: the interparticle mass transfer (bulk diffusion), intraparticle mass-transfer (pore diffusion), and finally adsorption/reorganization (surface diffusion).[11]

The interparticle step is dependent on flow rates and column packing efficiencies. It is independent of carbon structure except its particle size and shape, and has been adequately modeled using columns of glass beads. Some modelers also add a boundary layer or film diffusion step as a second step in the interparticle (or bulk) diffusion process. The Interparticle diffusion process is readily handled mathematically with few empirical parameters.

Intraparticle diffusion is independent of the flow rate or column dimensions but is highly dependent on carbon transport pore structure, often called the macropores and mesopores. Because this transport structure is specific to the carbon pore size distribution and how the pores are connected, the intraparticle diffusion coefficient can only be determined empirically. Unfortunately for nearly all 'well-designed' systems this is the slowest and thus the rate-controlling step in the adsorption process. The surface diffusion or rearrangement steps are independent of the transport pore structure but are dependent on the carbon and processes that are occurring. It also is only modeled empirically.

One goal in commercial adsorption systems design is to ensure the mass transfer zone is less than 20% of the column length to use the capacity of the activated carbon efficiently. For gas-phase adsorption systems it is generally much less than 20%. Therefore, the accuracy of the kinetic model is less critical when dealing with well-designed adsorption systems, especially in the gas-phase. Consequently, crude approximations for the interparticle, intraparticle, and surface diffusion coefficients are often used and are adequate.

4. Representation of the adsorbent column

Once the kinetics and thermodynamics are described, then a model is needed to represent the adsorption system. The column dynamics can be represented several different ways,[12] from theoretical plate (or stage-wise equilibrium) approximations, that resemble distillation column models, to calculation of widths of adsorption bands which resemble chromatography approaches. More rigorous approaches using coupled partial differential equations for heat and mass balance can also be used, but are generally not justified unless the system is complex, for example involving a complicated regeneration scheme.

Errors are also introduced when simplifying assumptions are made, like treating nonisothermal column profiles as isothermal or ignoring heat losses and treating the column as adiabatic. The other complications that can be over simplified are competitive displacement resulting in a rollover of displaced component, and concentrations within the column that are higher than the influent. Rollover increases column efficiency, but this increase is often ignored by models.[11] Finally, complications are added by the regeneration process, which is almost always a partial regeneration, and usually runs counter current to the adsorption flow. This results in complicated temperature and loading profiles in the carbon column and broader mass transfer zones. Simplifying approximations for regenerable systems are the same as the ones mentioned above, but are more significant and thus result in larger errors.

C. RESULTS OF THE COMPUTATION

The results of the computation describe the column performance as order of elution, adsorption band widths, rollover or displacement, mass transfer zone size, and carbon exhaustion rate to a percentage breakthrough or to an effluent concentration limit. The order of elution shows which compounds elute first and will be key in exceeding the treatment objective. The adsorption band widths define

the segregation or chromatographic separation of components on the carbon column that can be important in some purification and separation processes. Rollover or displacement behavior can be important when dealing with separation using desorption processes or adsorbate recovery processes. A mass-transfer zone is predicted for each component present, but only the early eluting components are of interest. The mass transfer zone size of these components dictates the adsorber size and is the key to the system balance between the capital cost of the adsorption system and operating cost for the replacement activated carbon. (Utility costs, for energy and water, are an additional consideration for regenerable systems.)

Finally the predicted exhaustion rates are usually in units of bed volumes treated to an effluent treatment objective, which can be a percentage of the influent concentration or it can be an absolute concentration level. This exhaustion rate determines the absolute operating cost of the system and the change-out or replacement frequency of the activated carbon in the column. The operating cost derived from the exhaustion rate, can be compared directly to costs of alternate technologies.

III. SOURCES OF ERROR

Accuracy of these methods is highly dependent on complexity and consistency of the stream, the ideality of the components, and the definition of the treatment objectives. The following discussion is not a statistical error analysis, but the relative assessment of the greatest sources of error based on experience running performance prediction calculations for general gas-phase and liquid-phase environmental applications. Table 1 lists a description of the various sources of uncertainty, and the relative importance of the contribution to the overall error of the performance predictions.

A. SINGLE COMPONENT ISOTHERM MEASUREMENT AND PREDICTION

The multicomponent adsorption models must also predict the original single component isotherms. Any errors due to oversimplification, when approximating single component behavior are incorporated in the single component prediction and carried over to the multicomponent case. Several examples of the levels of errors for single component predictions are listed in Table 2 for the Polanyi approach.

Major sources of error for the single component predictions are as follows.
1. Inaccuracies in the isotherm test or measurement - equilibrium was not attained, the carbon temperature was not controlled or measured, or the analytical errors were magnified by calculating the adsorption as a small difference between two large measurements.
2. Carbon samples were not representative - samples were contaminated (solvent vapors from the lab), out-of-date and no longer representative of the commercial activated carbon, or highly oxidized which can modify the pore structure.
3. A known isotherm was substituted for an unknown component - using an isotherm for an isomer of the adsorbate, for an adsorbate with similar molecular structures, or for an adsorbate with similar molecular formula and weight.
4. Selection of a single component adsorption theory - Polanyi and IAS can both assume a characteristic curve shape, necessary to be practical, but significantly decreases the accuracy of the predictions.

B. MULTICOMPONENT ISOTHERM PREDICTION THEORY

Most of the errors are due to the inherent assumptions of the theories.[13] Typical errors for common components are smaller than the single component values in Table 3, but exceptional errors can magnify theoretical shortcomings and become quite large. Thus, the multicomponent errors primarily reduce the reliability of the performance prediction.

Major sources of error for the multicomponent predictions are as follows.
1. Choice of the multicomponent theory - in some simple cases the Polanyi and IAS theories are mathematically identical, but for the general case the simple Polanyi approach is less accurate than the IAS, which is less accurate than the Polanyi with the Hansen-Fackler modification.[14]
2. Breakdowns of the basic assumptions (sometimes the effects can be corrected for by adjusting the single component isotherm[15]), for example:
Volume-based competition - in rare instances molecular shape can affect the volume competition.
Molecular sieving - becomes significant specifically with large molecules and can affect competition in the smaller pores.
Chemisorption - nonideal systems involving highly polar or reactive species can have additional specific interactions, such as hydrogen bonding, polar interactions, dimer formation, etc.
Bulk behavior in the pores - unique characteristics observed only when the molecule is an adsorbate, usually due to a configuration or interaction due to the carbon structure.

C. Problem Definition

The two biggest concerns for accurate performance prediction are a precise identification of the background components and definition of the treatment objective. Vaguely defined background components (TOC, BOD, COD) and unknown or nondetectable compounds would add uncertainty to the prediction even if the calculation method was perfect. Empirical means of classifying the competitive effects of background components exist, even when the components are not well defined or detectable.[16] However, these methods can be difficult to carry out and are only approximations.

The definition of the treatment objective also can contribute to uncertainty in the performance prediction when defined vaguely using terms like TOC, BOD, COD, non detectable, color, or odor. To compute adsorptive performance, all treatment objectives must be translated to absolute concentration levels for specific individual components for computation. Occasionally, the computation is run once just to learn the order of elution of the contaminants, which is used to decide which eluting component exceeds the treatment objective. The objective is redefined as an absolute concentration of that critical component and the computation is repeated. Table 2 lists treatment objective definitions and how to convert them to a usable form, and their effect on the accuracy of the results.

D. Modeling the Adsorption System

Other inaccuracies in the predictions are modeling of the adsorption kinetics and choice of models for the column dynamics (adsorbent bands, theoretical plates, etc.). These errors are not as critical for well designed commercial adsorption systems, where the carbon utilization is greater than 80% (the mass transfer zone of the early eluting components is less than 20% of the column). Consequently, the error contribution due to the kinetic model or the column dynamics is generally less than that of the single component isotherm approximations. The exception is for poorly designed systems with shallow beds and high linear velocities, or systems that involve a complex regeneration scheme.

IV. State-of-the-Art of Adsorptive Performance Prediction

We should neither be satisfied nor be despondent over the previous discussion of current performance prediction methods. The methods are useful evaluation tools, although they fall short of our goals for environmental applications, and the situation can only improve to the future.

A. What Currently Can Be Done Accurately

The existing techniques have inherent errors due to simplifying assumptions that are necessary to make them easier to use. However, these techniques are adequate for making gross comparisons of technologies or relative performance comparisons for activated carbon product selection.

1. Relative comparison of different carbons

Many major errors in predicting adsorption isotherms cancel when making relative performance comparisons under identical conditions and stream compositions. This is often the case when trying to identify the optimal activated carbon for a specific application. Performance of several different carbon structures can be compared to select the activated carbon product with the optimum performance or price-performance ratio. The absolute performance may not be accurate, but if the same errors were reproduced for each carbon, then selecting the best performing carbon is still possible.

2. Comparison of carbon adsorption to alternative technologies

When comparing activated carbon adsorption to alternative technologies for environmental cleanups, generally differences in performance are large, or gross assumptions had to be made to equate the dissimilar systems. Consequently, the size of these errors is insignificant compared to the differences in performance or the errors introduced by the gross assumptions. When the performance (or price-performance ratio) of carbon adsorption and another technology are similar, the prediction errors can become significant. In this situation, however, the proper conclusion should be that both technologies are equal and no real performance differentiation exists. In these cases, the selection of the best technology will usually be dictated by capital-operating cost ratios, system size, available utilities, or engineering preferences.

3. Describing general behavior of activated carbon columns

The existing models are also useful in "what if" scenarios. Because the Polanyi and IAS approaches have a basis in thermodynamics, many fundamental principals are incorporated in the computations. Consequently, the methods will extrapolate to extreme conditions and predicted behavior of the system under upset conditions.

For example, they can approximate the effects of spikes in the influent concentration during upsets, or spills and dips in concentration during shutdowns (loss of the contaminant source). The bed volumes a carbon system can treat during a spike are always greater than the bed volumes that would

have been treated if the same amount of contaminant had been introduced at the average influent concentration. In terms of mass of contaminant removed per mass of carbon, the spike improved performance. However, the benefit of the spike, a band within the column with more heavily loaded carbon, decreases with additional bed volumes treated after the spike occurs due to dilution and spreading of this band. Thus the benefit of a spike is least for a fresh column and greatest for a column that was nearing exhaustion.

The situation is different for dips in concentration (disappearance of contaminants). The bed volumes a carbon system can treat during a dip are greater than the bed volumes that would have been treated if the dip had not occurred. As for bed volumes treated, the dip improves performance and the life of the carbon. Desorption of the contaminant-loaded carbon does occur, but this is less important than the decrease in influent concentration. With a dip in concentration, contaminants were removed or not added upstream, which reduces the requirements on the carbon system more than the negative effects of extraction or desorption. However, the benefit of the dip is not realized unless the influent returns to its previous concentrations and the carbon system has the opportunity to treat additional bed volumes of contaminated influent. Thus the benefit is greatest for a fresh column and is least for columns nearing exhaustion.

B. WHAT CURRENTLY CANNOT BE DONE

For most all real-world environmental applications, today's performance prediction techniques are inadequate for making cost guarantees or for determining minor improvements due that would result from evolutionary changes in equipment design.
1. Cost guarantees
The average error levels are small enough, and their effect could be incorporated into cost guarantees by conservatively adjusting the specified performance by several standard deviations. Problems arise due to the uncertainty of when the basic assumptions of the theories breakdown. The effects of these breakdowns can be large errors and represent an incalculable risk to business. Rough cost estimates can be made for comparison purposes, which are generally useful for making a decision to investigate carbon adsorption further.
2. Engineering design
For engineering design, the computations are useful only for relative sizing or selecting equipment from a catalog list. The computational errors are simply too large to measure improvements in performance due to refinements in designs, for example improved adsorbers flow patterns, optimal height to diameter (H/D) ratios, or inlet/outlet nozzle patterns. In these situations the design changes will only slightly affect performance and the effect is often less than the error in the calculations. Also effects of particulate and suspended matter cannot be considered, which often dictate design.
3. Replacing pilot-scale column simulations
Computations with theoretical models are not yet substitutes for on-site, pilot-scale, column simulation tests. This is especially true when the stream and the treatment objectives, or even the background components, are defined vaguely (using color, odor, TOC, BOD, COD, or nondetectable).

C. WHAT CAN BE DONE TO IMPROVED THE PREDICTION OF ADSORPTIVE PERFORMANCE?
The simplest way to improve the accuracy of any computational method is to incorporate more empiricism or empirically derived variables. However, the approach must also be practical as for data required. Some errors are inherent in the simplifying assumptions required to reduce the amount of empirical data required for performance prediction. For example, the presumption of a characteristic curve greatly reduces the amount of single component isotherm data required, but also is a major contributor to error. The following are several things that could be done now to improve the accuracy of the predictions in a practical manner.
1. Standardized activated carbon samples
Isotherms/adsorption data needs to be generated on standard carbons - even commercial carbons of one name change over the years. Carbons should have published carbon characterization curves or an isotherm with a single known component with data ranging more than five orders of magnitude in concentration or in partial pressure.
2. A handbook on adsorption characteristics
Accurate single component isotherm data on a wider variety of contaminants over a broader range of temperatures is needed on standard activated carbon samples with known characteristic curves. With this data the empirical adsorbate characteristics can be determined and then assembled in a handbook.
3. Additional real-world experience
Comparing more results from real world adsorption systems versus the best theoretical predictions increases the confidence in the reliability of the basic assumptions of the adsorption theories.

Eventually we may learn how to approximate backgrounds empirically and predict the breakdown of theories. We may reassess the relative importance of sources of error of existing models and direct the theoretical and empirical work being done on adsorption on activated carbon to improve the current situation.

V. REFERENCES

1. A. L. Meyers and J. M. Prausnitz, A.I.Ch.E. Journal, 11, 121(1965) and C. J. Radke and J. W. Prausnits, A.I.Ch.E Journal, 18, 761 (1972).

2. J. A. O'Brien, A. L. Myers,"Physical adsorption of gases on heterogeneous surfaces. Series expansion of isotherms using central moments of the adsorption energy distribution", J. Chem. Soc., Faraday Trans. 1 (1984), 80(6), 1467-77

3. A. Wohleber and M. Manes, J. Phys. Chem., 75, 61 (1971).Theory of the Structure of Activated Carbon - Relationship to Adsorption Properties, and Manes and M. Greenbank, In "Treatment of Water by Granular Activated Carbon", M. J. Mcguire and I. H. Suffet, Eds., American Chemical Society, Washington, D.C. 1983, p9.

4. R.S. Hansen and W. V. Fackler, J. Phys. Chem., 57, 634 (1953).

5. D.P. Valenzuela, A. L. Myers,O. Talu,I. Zwiebel, "Adsorption of gas mixtures: effect of energetic heterogeneity", AIChE J. (1988), 34(3), 397-402

6. R. J. Grant and M. Manes, Ind. Eng. Chem. Fundamentals 5, 490 (1966) and M. R. Rosene, M. Ozcan, and M. Manes, J. Phys. Chem., 80, 2586 (1976) and R. J. Grant, M. Manes, and S. B. Smith, A.I.Ch.E. Journal, 8(3), 406 (1962).

7. B. P. Semonian and M. Manes, Anal. Chem., 49, 991 (1977) and M. Greenbank, T.M. Matviya, W.G. Tramposch, "Rapid Carbon Adsorption Characterization using Temperature Programmed Adsorption and Desorption", presentated at the AICHE Meeting in Los Angeles,CA, November 17, 1991.

8. C. Malara, G. Pierini, A.Viola, "Correlation, analysis and prediction of adsorption equilibria" Jt. Res. Cent., Comm. Eur. Communities, Ispra, I-21020, Italy, Report to Comm. Eur. Communities, [Rep.] EUR (1992), EUR 13996, 47 pages.

9. S. Sircar and A. L. Meyers, A.I.Ch.E. Journal, 17, 186(1971), and M. Greenbank and M. Manes, J.Phys.Chem., 85, 3050 (1981).

10. J. A. O'Brien, A. L. Myers, "Rapid calculations of multicomponent adsorption equilibria from pure isotherm data", Ind. Eng. Chem. Process Des. Dev. (1985), 24(4), 1188-91,and M. Greenbank, Ph. D. Dissertation, Kent State University (1981).

11. J. C. Crittenden, G. Friedman, D.W. Hand, J. Berrigan, T. Speth, "Design of fixed-beds to remove multicomponent mixtures of volatile organic chemicals",Proc. - AWWA Annu. Conf. (1985) 1327-46 and J. C. Crittenden, D. W. Hand, "Modeling of adsorption , desorption and displacement in fixed-bed adsorbers", Fundam. Adsorpt., Proc. Eng. Found. Conf. (1984), Meeting Date 1983, 185-94. Editor(s): A. L. Myers,G. Belfort, Publisher: Eng. Found., New York, N. Y.

12. M. D. LeVan, D. K. Friday, "Models for thermal regeneration of adsorption beds", Fundam. Adsorpt., Proc. Eng. Found. Conf. (1984), Meeting Date 1983, 295-304. Editor(s): A. L. Myers, G.Belfort, Publisher: Eng. Found., New York, N. Y.

13. E. Richter, W. Schuetz, A. L. Myers, "Effect of adsorption equation on prediction of multicomponent adsorption equilibria by the ideal adsorbed solution theory", Chem. Eng. Sci. (1989), 44(8), 1609-16

14. M. Greenbank and M. Manes, J.Phys.Chem., 86, 4216 (1982) and M. Greenbank and M. Manes, J.Phys.Chem., 88, 4684 (1984).

15. T. W. Schenz and M. Manes, J. Phys. Chem., 79, 604 (1975) and M. R. Rosene, M. Ozcan, and M. Manes, J. Phys. Chem., 80,2586 (1976).

16. M. R. Rosene, R. T. Deithorn, J. R. Lutchko, and N. J.Wagner, "High pressure Technique for Rapid Screening of Activated Carbons for use in Potable Water", Activated Carbon Adsorption of organics from the Aqueous Phase, Vol. 1, I. H. Suffet and M. J. McGuire editors, Ann Arbor Science, Ann Arbor, Chaper 15 (1980).

Table 1   Relative Importance of the Different Sources of Errors

Sources of Error in Adsorption Calculations	Typical Error Contribution	Potential for Large Error in Special Cases
Single component isotherm prediction/measurement		
Analytical Errors in measurement	<10%	No
Carbon sample not representative	<20%	Yes
Substitution of an known isotherm for an unknown component	10 to 100%	Yes
Selection of theory/technique	0 to 100%	Slight
Multicomponent isotherm prediction theory		
Choice of theory IAS vs. Polanyi	0 to 100%	Yes
Volume-based competition	<10%	Slight
Interactions and accessability	0 to 100%	Yes
Bulk behavior in the pores	<10%	Slight
Modeling adsorption system		
Selection of the Kinetic approaches	<20%*	No
Choice of Models for Column dynamics	<20%*	No
Problem Definition		
Stream Composition - critical and background components and concentration	10 to 100%	Yes
Background components and nondetectable compounds	50 to 500%	Yes
Treatment Objectives defined vaguely (nondetectable)	<20%	Slight
Nonspecific Test Objective (TOC, BOD, COD, etc.)	10 to 100%	Slight
Temperature - (within each carbon particle - through-out the bed)	<20%	No
Flow rate - Linear velocity/mass flow and its variability	<10%*	No
Variability of concentration and composition,	10 to 100%	No
Complex Schemes-Regeneration processes	20 to 200%	Yes

* For well-designed adsorption systems with MTZ<20% of column

Table 2   Errors in Single Component Predictions

	Average Deviation %	Range of Errors* High % Error	Range of Errors* Low % Error	Concentration High ppm	Concentration Low ppm	Loading Range High cc/100g.carbon	Loading Range Low	No. of Points	Probable Cause of Error
Gas-phase Adsorption Isotherms (ref.15)									
Methanol @ 22C,60C	275.6%	1082%	-11.1%	3461	387	7.4	0.146	6	Chemisorption at low loadings
Toluene @ 121C	6.7%	34.7%	-6.4%	45	0.066	5.24	0.494	5	Fitting characteristic curve
Trimethyl pentane @ 117C	-61.5%	5.2%	-94.2%	50	0.068	9.36	0.153	16	Molecular sieving
Liquid-phase Adsorption Isotherms (ref.14)									
Pentanol @ 25C	4.9%	21.6%	-19.2%	13800	11	46.8	8.44	14	Fitting characteristic curve
Benzamide @ 25C	1.0%	12.0%	-10.1%	9970	160	34.5	18.1	6	Analytical (random)
o-Phthalic acid @ 25C	-0.5%	8.2%	-14.0%	1990	3.9	19.6	7.22	6	Hydration effects at high loadings

* negative error means the actual measurement was less than the predicted value

Table 3   Contributions to Errors in Computing Breakthrough Limits

Breakthrough Criterion	Example of Criteria	Sources of Additional Computation Error
Specific Objectives - Effluent Level is an Identified Key Component		
1 Absolute concentration	5ppm CHCl3	Analytical accuracy/reproducibility
2 % Breakthrough/removal	99% removal of CHCl3	#1 + Inaccuracy of influent level Determination
3 Non Detectable	Nondetectable CHCl3	#1+Analytical Sensitivity/background interferences
Grouped Objectives - Effluent Level is a Sum of Several Key Components		
4 Class of Compounds	5ppm Chlorinated Hydrocarbons	#1,2,or 3 + know order of elution and sum breakthrough conc.
5 lb.emissions per month	10 lb.hydrocarbons per month limit	#4+Integrate breakthrough curves and sum over several events
Nonspecific Objectives - Effluent Level is a Response of a Detector or Test		
6 TOC	100 ppm TOC	#4 + relative weighting factors for sensitivity to test(TOC)
7 Total Combustibles (by FID)	1 ppm Hydrocarbon as propane	#4 + relative weighting factors for FID sensitivity
8 Nonmethane hydrocarbon	1 ppm nonmethane hydrocarbon	#7 + inaccuracy of methane determination
9 COD	100 ppm COD	#6 + COD interferences (Ex. Inorganic reductants)
10 BOD		#6 + BOD interferences (Ex. Low BOD due to toxics present)
11 Color		#6 + Complex formation, color shifts, turbidity corrections
12 Taste or Odor		#6 + T/O panels problems (Ex. Odor interactions,desensitizers)

SEPARATION AND CONCENTRATION OF VOLATILE ORGANIC CONTAMINANTS BY ACTIVATED CARBON CLOTH FOR CRYOGENIC RECOVERY

Mehrdad Lordgooei, Kelly R. Carmichael, Terrance W. Kelly,
Mark J. Rood, and Susan M. Larson

Environmental Engineering & Science Program, Department of Civil Engineering
University of Illinois at Urbana-Champaign, Urbana, IL, USA 61801-2352

Keywords: activated carbon cloth, gas purification, electrothermal desorption

Introduction

New air quality control regulations and economics are causing the development of new devices or the optimization of existing technologies for control of toxic emissions from industrial sources. Toxic chemicals are emitted into the atmosphere from facilities within the United States at a rate of 1.1×10^9 kg/year [1]. Volatile organic contaminants (VOCs) account for 47%, and non-halogenated VOCs account for 36% of these toxic emissions [1]. For these emissions, under the 1990 Clean Air Act Amendments (CAAA), the United States Environmental Protection Agency (USEPA) should establish maximum achievable control technology (MACT) standards. MACT standards are based on best control technologies that offer the maximum degree of emission control [2]. MACT will have important effects on specific VOC sources within the next eight years because all MACT standards are required to be promulgated by 15 November 2000, and a source subjected to MACT standards must achieve compliance within three years of promulgation of the standards. Sources that must comply with the new VOC standards are related to food processing, wastewater treatment, electronic manufacturing, petroleum refining, petrochemical manufacturing, asphalt production, pharmaceutical industry, polymer and resin manufacturing, solvent production, and dry cleaning industry.

Based on an economic and engineering study about VOC control technologies [3], if the VOCs have a value > $0.66/kg then carbon adsorption and vapor recovery should be considered. Dyer and Mulholland [3] indicated that carbon adsorption is the most cost effective technology for gas flow rates > 1,000 scfm and VOC concentrations > 500 ppmv. Moreover, variable flow rates and variable VOC concentrations are not disruptive for carbon adsorber performance [4], and they do not produce secondary pollutants. But, conventional carbon adsorbers can achieve recovery efficiencies up to 98% which may not be sufficient for MACT standards.

New carbon adsorption recovery systems can be developed that achieve higher recovery efficiencies while providing better economical and technical advantages over existing ones. For this purpose, we have developed a new activated carbon cloth (ACC) adsorption system that has been integrated with electrothermal desorption and cryogenic condensation to reduce the amounts of VOC emissions to MACT standards and provide for reuse of the VOCs that are recovered.

In this system liquid nitrogen (LN2) is used as the required refrigerant. LN2 can reduce VOC emission concentrations to ppbv levels due to its high cooling capacity and low temperature. One advantage of the LN2 system compared to other refrigeration systems is the multiple use of LN2. First, the cooling capacity of LN2 is used to condense VOCs. Then, the evaporated N_2 can be used for other process needs such as inerting and safety blanketing. Another advantage of LN2 refrigeration over conventional mechanical condensation systems is the absence of moving parts such as compressors. But, LN2 consumption rate is high for typical industrial effluent concentrations. The effluent VOC concentrations are typically <1% by volume due to the limitations caused by their lower explosion limits. Ideal LN2 consumption (minimum mass of LN2 required per unit mass of VOC recovered in an isolated thermodynamical system) is linearly related to the inverse of the VOC concentration (Figure 1). If the VOC concentration can be increased, then LN2 consumption can be decreased. This is due to the fact that some portion of the cooling capacity transfers to the noncondensible carrier gas. Therefore, ACC adsorption technology is used to pre-concentrate the effluent VOCs for an efficient vapor recovery.

In the developed system, ACC adsorption is followed by electrothermal regeneration resulting in formation of a concentrated organic vapor which is cryogenically condensed from the gas phase. Electrothermal desorption allows for optimizing the desorption time and the concentration profile of the desorbed VOC to allow minimal use of cryogen. This system can enable VOC sources to meet air quality control regulations while providing a high quality liquid VOC product for reuse.

Description of the laboratory scale system

The laboratory scale ACC adsorption-cryogenic vapor recovery system is presented in Figure 2. Sample gas is generated by passing ultra-high purity (UHP) N_2 gas through VOC liquid and saturating the gas stream. The saturated stream is then mixed with the second pure N_2 stream to produce a gas sample with desired VOC concentration and total flow rate. The sample gas generation system is calibrated using a gas chromatograph/mass spectrometer (GC/MS, Hewlett Packard GC 5890 and MS 5971), a gas chromatograph/flame ionization detector (GC/FID, Hewlett Packard GC 5830A), UHP N_2 gas and a Matheson calibrated VOC gas mixture. The calibrated gas stream passes through the fixed bed of ACC, where the organic material is separated from the carrier gas by adsorption. After breakthrough of VOC from the fixed bed, pure N_2 gas is passed through the adsorption bed and electrical power is supplied to the ACC. Electrical energy regenerates the adsorption capacity of the ACC and provides a N_2 gas stream containing desorbeded VOC. VOC concentration in the N_2 carrier gas is controlled by the supplied electrical power and the flow rate of the carrier gas. The concentrated vapor stream is then directed to a custom shell-and-tube cryogenic condenser where the VOC is condensed on the condenser's internal cold surfaces. The condensed VOC is transferred from the bottom of the condenser into an Erlenmeyer flask.

Activated Carbon Cloth Adsorbent

ACC, which is made of woven activated carbon fibers (ACFs), is an efficient adsorbent to separate VOCs from gas streams. Compered with activated carbon pellets (ACPs), granular activated carbons (GACs) or powder activated carbons (PACs), ACCs have a higher contact efficiency, higher specific surface area for a higher specific pore volume, 10 to 100 times faster adsorption and desorption rates [5]. These properties are mainly due to the existence of no macropores, no or little mesopore volume, and more uniform desorption of micropores from the external surface to the core of fiber [6]. ACC's rapid adsorption and desorption rates can reduce the required process cycle time and increase the bed adsorption capacity by reducing the length of mass transfer zone (MTZ). Due to its cloth form, ACC can be installed in different configurational forms inside fixed beds providing different adsorption and desorption performance as well as specific pressure drop (Pa/gm adsorption). Suitability for in-situ electrothermal regeneration and easy handling are other advantages of ACC.

ACC samples were obtained from American Kynol, a subsidiary of Nippon Kynol, located in Pleasantville, NY. Kynol's ACCs are made of novoloid fibers (polymerized cross-linked phenolic-eldehyde fibers). Novoloid fibers have an amorphous network structure containing 76% carbon, 18% oxygen, and 6% hydrogen [9]. These fibers are woven by conventional textile techniques to produce a novoloid cloth. The cloth is then carbonized and activated in an O_2 free atmosphere using steam or CO_2 at 900 °C in a one step process to produce ACC. Carbon content of ACC is typically 95% with oxygen and hydrogen contents of 4% and 0.7%, respectively [10]. Pore volume and pore size of the ACC increase with increasing duration of activation. The resulting micropores are slit shaped and remain uniform from the external surface to the core of the fiber [6].

Kynol™ ACC-5092-20 was identified as e suitable ACC adsorbent for the VOC concentration range of industrial emissions (in the order of 1% by volume). ACC-5092-20 have a higher adsorption capacity than the other Kynol's ACCs for 1% by volume concentration of the VOCs considered for the system evaluation tests (acetone, methyl ethyl ketone and toluene). This is mainly due to the existence of a high specific pore volume and high volume ratio for pore widths in the supermicro, transitional rang, and mesopores close to the transitional range. SEM micrographs of the ACC sample are provided in Figure 3. Mesopores and transitional micropores can be seen from the SEM micrograph of the ACC's fiber cross section. The cumulative pore size distribution of the ACC sample in comparison with some other adsorbents is given in Figure 4. Specific surface area and micropore volume of ACC-5092-20 were measured with a Micromeritics ASAP 2400 using nitrogen at liquid nitrogen temperature. The BET specific surface area of the sample was 1592 m^2/g. The specific micropore volume was 0.69 cm^3/g.

Fixed Bed of Activated Carbon Cloth

In the fixed bed ACC layers are installed in parallel to each other in a cross flow fashion. This allows for flexibility in effective adsorption bed length and apparent ACC density. With a 1.14 mm separation distance between each layer, an apparent ACC bed density of 94.5 mg/cm^3 results. The bed packing density can be increased to 800 mg/cm^3 (0.47 total porosity). In the fixed bed, the ACC layers are connected electrically in parallel in three separate modules. The modules are connected electrically in series. The resulting circuit is connected to electrodes of a 120 V a.c. source controlled by a Variac. This arrangement is expected to result in uniform electrical heating and carefully controlled VOC desorption.

Electrothermal Regeneration of Activated Carbon Cloth

In electrothermal regeneration process an electric current is passed through the fibers. Electrical work due to phonon and defect scattering [11] in ACC is directly transformed to thermal energy in the ACC and the adsorbed VOC. By the continuous flow of electric current, the thermal energy of the adsorbed molecules increase to a level that overcome the surface bonding energy, and the VOC desorbs from the ACC. Since electrical work is transformed to desorption energy directly, the carrier gas temperature can be substantially lower than the ACC temperature. The temperature gradient along the bed is positive, and along the fiber radius is negative (or zero, depending on the value of fiber Biot number). In conventional thermal desorption methods, the temperature gradient along the bed is negative and along the fiber radius is positive. These effects cause positive desorption rate contributions for electrothermal desorption due to the heat transfer, Soret effect and pore effusion. While, mass transfer contributions are negative for conventional thermal desorption methods. Therefore, electrothermal regeneration should have higher energy efficiency compared to conventional thermal regeneration methods. Another advantage of electrothermal desorption is that the energy transfer rate can be very high and controlled easily. This enables careful control of desorption time and effluent VOC concentration profile for a better cryogenic recovery.

Results and Discussion

The laboratory-scale fixed bed configuration was used to measure breakthrough curves. For each breakthrough test, total gas flow rate through the bed was 5 slpm. VOC concentration of the inlet gas stream was measured before passing through the fixed bed. Gas phase VOC in the bed was sampled from the sampling ports along the bed's length and analyzed intermittently using the GC/MS and continuously using GC/FID (Figure 2). Sample results for MTZ distribution curves describing how acetone concentration changed with time and location within the bed are presented in Figures 5. Breakthrough time was 75 min when using three ACC modules containing 27.05 g ACC and a packing density of 94.5 mg/cm^3. Breakthrough was followed by a saturation time of 58.5 min. Saturation time is defined as the time required for the effluent concentration (C_{out}) to increase from 5% to 95% its inlet concentration (C_{in}).

The breakthrough curve for the bed outlet exhibit an standard diffusion mass transfer limited behavior in the form of: $C_{out} = C_{in} (1 + exp[K(t^* - t)])^{-1}$ where t^* is the stoichiometric time (time for $C_{out} = 1/2 \, C_{in}$ or $t^* = W_e/C_{in} F$, where W_e is bed VOC adsorption capacity at C_{in} and F is the total gas flow rate), and K is a constent that depends on the effective diffusion resistanca of the MTZ. From these results, dynamic adsorption capacity of the ACC for 1% by volume acetone is 456 mg/g or 0.581 cm^3/g. Equilibrium isotherm for adsorption and

desorption of acetone and ACC-5092-20 can be classified as BDDT type IV isotherm. Due to capillary condensation in mesopores, the isotherm has a hysteresis region at high concentration values. The equilibrium micropore adsorption and capillary condensation capacities of the ACC for 1% by volume acetone were measured to be 401 mg/g and 93.6 mg/g, respectively.

Effect of packing density on adsorption dynamic is presented in Figure 6. An smaller packing density results a shorter breakthrough time and a larger MTZ due to axial dispersion and mixing effects. Increasing packing density from 94.5 mg/cm^3 to 450 mg/cm^3 increases the breakthrough time from 75 min to 91.7 min. Since a higher packing density produces e larger pressure drop, it is possible to find an optimum set of packing density and pressure drop for a minimum cost.

Regeneration tests for a saturated fixed bed of ACC were performed to evaluate the effect of applied electrical power (Figure 7). N$_2$ gas flow rate through the bed was controlled at 1 slpm for three tests and 0.5 slpm for two tests. Electrical voltage for each test was set at select values to observe the effect of applied electrical power profile on the resulting effluent VOC concentration and bed temperature profiles. Effluent maximum VOC concentrations during desorption range from 18% to 63% by volume. VOC concentration profile and desorption time is readily controlled by carrier gas flow rate and applied electrical power. Increasing VOC concentration was observed with decreasing carrier gas flow rate and increasing applied power. In all five tests, more than 75% of the adsorbed acetone was regenerated at a bulk gas temperature of < 60 °C and an effluent concentration of > 10% by volume. Low resulted bulk gas temperature is indicative of an efficient energy transfer. Effect of generated high effluent concentration values on improvement of LN2 consumption and amount of vapor recovery can be examined from Figure 1. Moreover, the high effluent concentrations enable the cryogenic condenser to operate at warmer temperatures while achieving high recovery efficiencies.

Cryogenic vapor recovery efforts are discussed in the next paper [12].

Conclusions

A novel activated carbon cloth (ACC) adsorption/electrothermal regeneration/cryogenic system was developed to separate, concentrate and recover volatile organic contaminants from industrial gas streams. ACC demonstrates good performance characteristics due to its high contact efficiency, high adsorption capacity, and ease in handling. Electrothermal regeneration provided fast desorption rates and efficient energy transfer. Electrothermal regeneration concentrated VOC vapors up to 63% by volume without optimization. Concentrating the gas stream, drastically reduces the amount of cryogen required to condense the VOC from the gas stream end enables the condenser to operate at warmer temperatures while achieving a high recovery efficiency.

References

1   United States Environmental Protection Agency, *Toxics in the Community, National and Local Perspectives*, USEPA, USA (1991)
2   Majumdar, S. *Regulatory Requirements for Hazardous Materials*, McGraw-Hill, Inc., New York, USA (1993)
3   Dyer, J. A. and K. Mulholland Toxic Air Emissions: What is the Full Cost to Your Business, *Environmental Engineering, A special supplement to February 1994, Chemical Engineering*, pp. 4-8
4   Ruddy, E.N. and L. A. Carrol Select the Best VOC Control Strategy, *Chemical Engineering Progress*, July 1993, pp. 28-35
5   Ermolenko, I. N., I. P. Lyubliner, and N. V. Gulko *Chemically Modified Carbon Fibers and Their Applications* p. 62 & 212
6   Fujii, R. Kynol™ Novoloid Fibers, Nippon Kynol, Inc., Osaka, Japan p. 14
7   Cal, M. P. Characterization of gas phase adsorption capacity of untreated and chemically treated activated carbon cloths, PhD Thesis, University of Illinois at Urbana-Champaign, Illinois (1995)
8   Yang, R. T. *Gas Separation by Adsorption Processes*, Butterworths Publishers, Stoneham, MA (1987)
9   Hayes, J. S. JR. Novoloid Fibers, *Kirk-Othmer: Encyclopedia of Chemical Technology*, 3rd Edn, Vol 16, John Wiley & Sons, Inc. (1981)
10   Foster, K. L., R. G. Fuerman, J. Economy, S. M. Larson, and M. J. Rood Adsorption Characteristics of Trace Volatile Organic Compounds in Gas Streams onto Activated Carbon Fibers *Chem. Mater.* (1992) Vol 4, No. 5
11   Donnet, J. B., and R. C. Bansal *Carbon Fibers*, 2nd Edn, Marcel Dekker, Inc., New York (1990
12   Carmichael, K. R., M. Lordgooei, T. W. Kelly, M. J. Rood, and S. M. Larson, Desorption and Cryogenic Recovery of Volatile Organic Compounds for Re-Use, 1996 ACS National Meeting, New Orleans, Louisiana, March 24-28, 1996
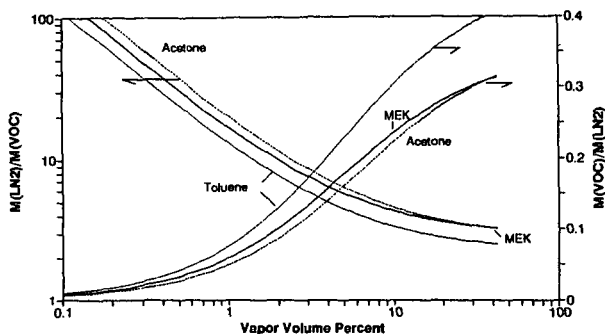
Figure 1. Ideal mass of LN2 required per unit mass of VOC recovered and ideal mass of VOC that can be recovered per unit mass of LN2.
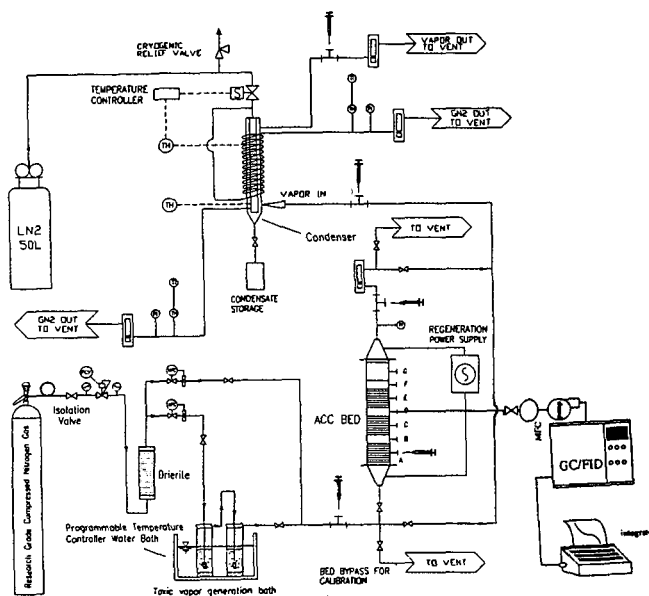
Figure 2. Integrated adsorption/electrothermal regeneration/cryogenic vapor recovery system.
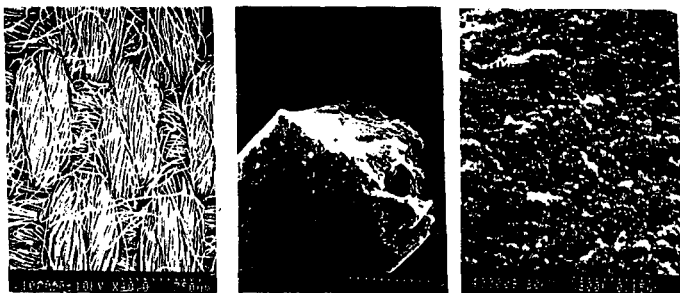
Figure 3. SEM micrograph of ACC-5092-20 and fiber cross section.
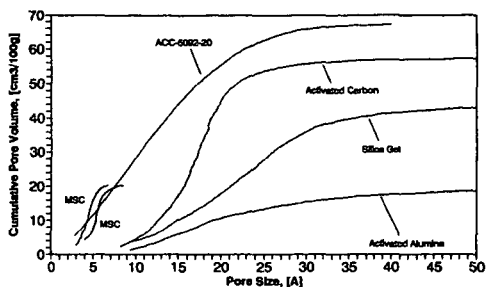
Figure 4. Cumulative pore-size distribution for ACC-5092-20 [7] compared with some other adsorbents [8]
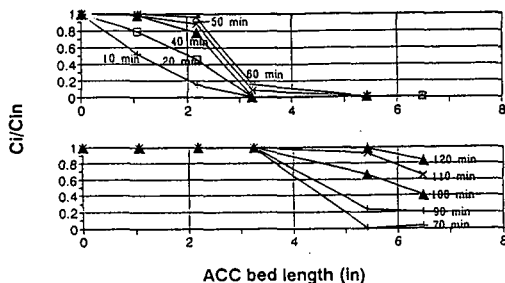
Figure 5. Mass transfer zone movement through the ACC bed. Inlet concentration: 1% acetone in N_2. Total gas flow rate: 5 slpm.
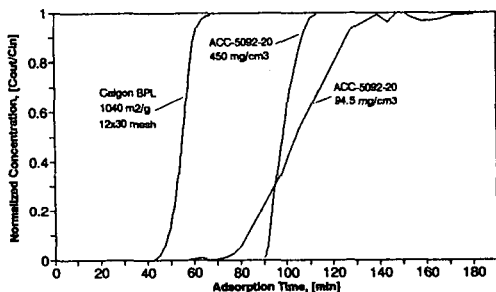
Figure 6 Effect of packing density on the dynamic characteristics of breakthrough.
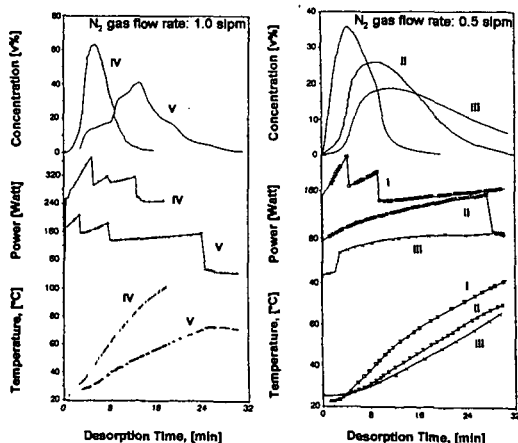
Figure 7. Electrothermal regeneration test results.

DESORPTION AND CRYOGENIC RECOVERY OF VOLATILE ORGANIC COMPOUNDS FOR RE-USE

K.R. Carmichael, M. Lordgooei, T.W. Kelly, M.J. Rood, S.M. Larson
Department of Civil Engineering / Environmental Engineering Program
University of Illinois at Urbana-Champaign
205 N. Mathews St.
Urbana, Illinois U.S.A.   62801-2352

Keywords: VOC Recovery, Cryogenic Condensation, Gas Cleanup

Introduction

Both the magnitude and toxicity of emissions of volatile organic compounds (VOCs) have led to public health concern and recent government regulations to reduce VOC emissions. VOCs are a part of the 1.1×10^9 kg of toxic chemicals released into the atmosphere from point sources within the United States in 1990 [1]. VOCs appearing on the list of 189 hazardous air pollutants (HAPs) accounted for 4.5×10^8 kg/yr of emissions to the atmosphere [1]. Many of these toxic chemicals cause chronic and acute health effects, including cancer [2].

The 1990 Clean Air Act Amendments (CAAAs) established technology-based guidelines for the reduction of VOC emissions to the atmosphere from point sources [3]. Under Title I of these amendments, USEPA is required to establish reasonable achievable control technology (RACT) standards for point source VOC emissions in ozone related non-attainment areas. Furthermore, Title III requires USEPA to establish maximum achievable control technology (MACT) standards for point source emissions of 189 HAPS, many of which are considered VOCs. HAP emission standards for point sources based on MACT must be promulgated by November 15, 2000. Sources regulated under Title III must meet permit requirements within three years of promulgation.

Point source VOC emission reduction is generally accomplished by process modification and/or utilization of ancillary control devices [4]. Process modification is generally the most economical method of reducing VOC emissions. Further reduction of VOC emissions require the addition of control devices along the waste stream.

The seven most widely used control devices that remove VOCs from gas streams are: 1) thermal incinerators, 2) catalytic incinerators, 3) flares, 4) boilers/process heaters, 5) carbon adsorbers, 6) absorbers and 7) condensers [5] (Table 1).

Table 1. Control devices commercially available for VOC removal from effluent gas streams [4].

Control Device	VOC Content (ppmv)	Flow Rate (acfm)	Capital Cost 1993	Annual Cost 1993	Removal Efficiency	Advantages	Disadvantages
Thermal Incinerator	100-2000*	1000 to 500,000	$10 to 450/cfm	$15 to 150/cfm	95-99+%	Up to 95% energy recovery	Halogenated compounds may require additional control
Catalytic Incinerator	100-2000*	1000 to 100,000	$20 to 250/cfm	$10 to 90/cfm	90-95%	Up to 70% energy recovery	Catalyst poisoning
Flare [5]		<2,000,000			>98% Steam-assisted	VOC destruction of variable emission conditions	Low heating value VOC requires auxiliary fuel
Boiler [5]		Steady			>98%	Supplement fuel	Variations may affect process
Carbon Adsorber	20-5000*	100 to 60,000	$15 to 120/cfm	$10 to 35/cfm	90-98%	Vapor recovery, Pre-Concentrator	High RH may lower capacity, Pore fouling
Absorber	500-5000	2000 to 100,000	$15 to 70/cfm	$25 to 120/cfm	95-98%	Vapor recovery	Scale build-up, Liquid waste
Condenser	>5000	100 to 20,000	$10 to 80/cfm	$20 to 120/cfm	50-90%	Vapor recovery	Scale build-up, Liquid waste

* <25% of lower explosion limit; RH is relative humidity

In this paper, discussion will primarily pertain cryogenic condensation of VOCs during regeneration of a carbon adsorber used to concentrate VOCs in effluent gas streams. Condensation of VOCs is especially applicable when recovery and reuse of the VOC in the process stream is economically beneficial. Recovery should be considered when a relatively pure condensate with a monetary value > $0.66/kg can be recovered [6].

Adsorption has been used often as a pre-concentrator in conjunction with other control devices. This is especially applicable to condensers as will be discussed here. Carbon adsorbers can remove VOCs from relatively low vapor concentration and high flow rate gas streams and desorb at high vapor concentration and low gas flow rates, where condensers operate more efficiently. High inlet VOC concentrations for condensers yield higher removal efficiencies and require lower refrigerant flow rates, thus lowering operating costs. Low gas flow rates require less condensable surface by increasing residence time, again lowering capital costs. Lower gas flow rates also require less refrigerant to cool the carrier gas.

Design of Contact Condensers

Two general types of condensers are commercially available, direct contact and indirect contact [7]. Direct contact condensers mix the refrigerant with the process gas stream. Heat is more efficiently exchanged due to the intimate contact between the refrigerant and VOC. Direct contact condensation is typically simpler, less expensive to install and requires less auxiliary equipment [7]. However, the refrigerant is

mixed with the process stream. This may prevent refrigerant recycling and/or cause contamination of the refrigerant. Indirect contact condensers utilize a physical barrier across which only heat is exchanged between the refrigerant and the process gas stream. Heat exchange is therefore less efficient in indirect methods. Keeping the refrigerant separate from the process gas stream allows for refrigerant re-use. This is beneficial if the refrigerant undergoes a cyclic mechanical refrigeration process. Indirect contact condensers typically cost more and are more complicated to design and operate [7]. Because of the indirect contactor's advantages, however, it is the most common type of condenser in air pollution control applications [5].

Refrigerants

The most common refrigerant used in pollutant removal condensers is water [5]. Water is inexpensive and easy to handle. However, because the condenser temperature is limited by the refrigerant temperature, cooling water results in low removal efficiencies for many VOCs (Table 2). Removal efficiencies were determined from the reduction of a 10% acetone stream to the equilibrium saturation vapor concentration. For applications where the process stream needs to be cooled below ambient temperatures, the use of cooling water typically requires auxiliary equipment to chill the water prior to use.

Ethylene glycol and water mixtures are also commonly used refrigerants [8]. Lower operating temperatures can be achieved with this mixture than for pure water, thereby lowering the effluent VOC concentration and recovering more condensate. Ethylene glycol water mixtures are exclusively used with indirect contact condensers to prevent ethylene glycol losses to the effluent gas stream [8]. Auxiliary equipment is needed to cool the mixture to temperatures below the ambient temperature.

Liquid nitrogen (LN2) refrigerant can provide a wide range of condenser temperatures because a controlled LN2 flow rate can be delivered to the condenser. Furthermore, because LN2 undergoes a phase change in the condenser, both the enthalpy of vaporization and specific heat change provide cooling capacity. The use of LN2 as a refrigerant generally requires a vacuum jacketed storage vessel and well insulated or vacuum jacketed delivery lines. However, auxiliary cooling equipment is not necessary, as the refrigerant is available in liquid form from commercial sources. The LN2 can be used in direct or indirect contactors. After it passes through the condenser, the vaporized nitrogen refrigerant can be used as a blanket gas in process streams or as a purge stream during desorption if an adsorber is used as a pre-concentrator. The gaseous nitrogen refrigerant waste stream can be used during desorption as a purge stream to prevent explosive hazards and reduce moisture levels, normally present in air purge streams, that may foul the condenser.

By operating the condenser near the freezing point of the organic, very low effluent VOC vapor pressures can be achieved while still producing a liquid condensate. In high humidity process streams two condensers can be used in series. The first condenser can operate at temperatures above the freezing point of water to remove water vapor from the stream. The second condenser can then be operated at temperatures below the freezing point of water to achieve greater removal efficiencies of the organic and reduce condenser fouling from frozen water vapor.

Table 2. Theoretical removal efficiencies for three refrigerants and three VOCs with a 10% by volume inlet gas stream.

Refrigerant	Operating Temperature (K)	Acetone Saturation[a] Vapor Concentration (ppmv)	Acetone Removal Efficiency (%)	Methyl Ethyl Ketone Saturation[a] Vapor Concentration (ppmv)	Methyl Ethyl Ketone Removal Efficiency (%)	Toluene Saturation[a] Vapor Concentration (ppmv)	Toluene Removal Efficiency (%)
Water	278	102,000	0	40000	60	5500	94
60% Ethylene Glycol + H20	240	15000	85	3800	98	420	99+
LN2	200	300	99+	70	99+	2	99+

[a] determined from the Wagner equation [9]

Experimental Design

Our research efforts have focused on developing, testing and evaluating the integration of cryogenic condensation with carbon adsorption. Regeneration of the carbon adsorber provides a concentrated vapor stream at a low gas flow rate which is then sent to the condenser. Using the adsorber as a pre-concentrator improves the operating efficiency of the condenser by increasing removal efficiency and decreasing refrigerant consumption. LN2 was used as the refrigerant due to its' low achievable temperature range and possible re-use capabilities.

A 1% by volume acetone in nitrogen gas stream was passed through an activated carbon cloth fixed bed at 5 slpm (Figure 1). The adsorbent ACC-5092-20 was manufactured by American Kynol™. Nitrogen BET specific surface area is 1592 m^2/g, and its' micropore volume is 0.69 cm^3/g [10]. Apparent ACC bed density is 94.5 mg/cm^3. Equilibrium adsorption capacity of the ACC was found to be 456 mg/g for 1% acetone in nitrogen [10].

The ACC was electrothermally regenerated by applying an a.c. voltage across the cloth. The temperature of the ACC surface was controlled by the voltage. Acetone concentration in the adsorber's effluent was controlled by the bed's temperature and flow rate of nitrogen carrier gas. During regeneration, acetone concentrations greater than 60% by volume were achieved at nitrogen gas flow rates of 0.5 slpm [11].

A copper shell-and-tube indirect contactor was used to condense the concentrated acetone onto the surface walls. The concentrated vapor stream was passed between the condenser tube and the outside shell. The total condensing surface area was 1241 cm^2. LN2 was introduced at the condenser tube inlet

counter current to the vapor laden gas stream. LN2 was also circulated through an 1/8 in. copper tube coil jacket wound around the outside shell of the condenser. LN2 was delivered with a Cryofab self-pressurizing dewar model CFPB25-115. The temperature of the condenser was controlled by the liquid flow rate of LN2. The flow rate of LN2, in turn, was controlled by the pressure of the dewar and by an Asco Red-Hat cryogenic solenoid valve. The vapor laden gas stream temperature was monitored using type T thermocouples at the condenser inlet, mid-point and outlet. The nitrogen refrigerant flow rate was also monitored at the outlet of the condenser using a BIOS DC-2 DRY CAL in continuous operation. Inlet and outlet vapor concentrations were monitored by analyzing 150 µl syringe samples with a Hewlett-Packard GC/MS (GC 5890 Series II, 5971 MS).

Results and Discussion

The ACC fixed bed was integrated with the cryogenic condenser to test acetone removal with condensation. A 1% acetone in nitrogen vapor stream at 5 slpm was passed through the bed at ambient temperatures. At breakthrough, the acetone was desorbed at 1 slpm nitrogen purge stream. The desorbed stream was sent directly to the pre-cooled condenser at ambient temperature and ambient pressure. The condenser log-mean operating temperature was 220 ± 9 K and was at ambient pressure. The acetone vapor concentration at the condenser outlet remained low and fairly constant throughout the desorption cycle (Figure 2). At desorption times between 150 sec. and 1000 sec., the desorbed acetone concentration was greater than the equilibrium vapor saturation concentration. As the vapor cooled in the lines to the condenser, the acetone condensed to the equilibrium vapor concentration of 24% at an ambient temperature of 296 K. The condenser further cooled the vapor to the equilibrium concentration of approximately 0.2 % by volume at 220 K. A removal efficiency of 99.0% was found for the integrated test. During the adsorption/desorption cycle, the acetone in the 1% by volume and 5.0 slpm challenge stream was concentrated up to 60%, and the flow rate was decreased by an order of magnitude [10].

Condenser outlet concentrations were also measured for inlet concentrations ranging from 0.25% to 18.3% by volume (Figure 3) to determine VOC removal efficiencies. The acetone in nitrogen challenge gas stream was generated by passing nitrogen gas through liquid acetone in a dual bubbler set-up. The challenge gas flow rate was 0.5 slpm and at ambient temperature. The condenser was pre-cooled to an equilibrium log-mean temperature of 215 ± 10 K for each experiment. Over the entire range, outlet acetone concentrations remained fairly constant near the equilibrium vapor concentration of 0.17% at 215 K as predicted by the Wagner equation. Removal efficiencies are therefore higher for higher inlet concentrations. For instance, the removal efficiency found for an acetone inlet concentration of 18.3% was found to be 98.8%. However, the removal efficiency for at an inlet of 0.6% was only 70.5%.

Theoretical and experimental LN2 refrigerant requirements were also evaluated (Figure 3). The theoretical mass of LN2 per unit mass of acetone condensed was determined from thermodynamic calculations. At low inlet concentrations, more LN2 is required to condense a unit mass of acetone. For instance, at an inlet concentration of 2.5% by volume acetone, 10 kg of LN2 is theoretically required to condense 1 kg of acetone. However, at an inlet concentration of 20% by volume acetone, only 2 kg of LN2 is required to condense 1 kg of acetone. Experimental results showed the same general trend with deviations from the theoretical curve resulting from heat loss from the condenser. This supports the earlier statement that higher concentration vapor streams result in more efficient recovery of VOC vapor. Therefore at high concentrations the removal efficiency is maximized and the mass of refrigerant per unit mass of acetone condensed is minimized.

The condenser was also evaluated for acetone removal performance at various condenser equilibrium temperatures (Figure 4). A 10% by volume acetone challenge gas stream at 0.5 slpm was sent through the condenser at log-mean temperatures ranging from 209 K to 271 K. The measured outlet concentrations closely approximated the theoretical equilibrium vapor concentration as predicted by the Wagner equation. This indicates that the acetone bulk vapor concentration reached equilibrium with the acetone vapor concentration at the condenser's surface. This would also exist during scale-up if adequate condensing surface is available for the given process stream's vapor concentration, temperature and flow rate.

A model was developed to predict the axial concentration of a vapor along the condenser length. Radial mass transfer was incorporated with the thermodynamic characteristics of the heat exchange between the VOC gas stream and LN2 refrigerant. For a condenser surface area of 1241 cm^2 and process conditions similar to the experimental conditions, equilibrium concentration is predicted at approximately 30 cm for an inlet concentration of 15% acetone (Figure 5). The laboratory condenser is 62.2 cm long. The model can also be used for designing condensers for a specific process gas stream.

Condenser design can be carried out by first determining the process gas stream characteristics such as VOC vapor concentration, temperature and flow rate. By assuming equilibrium conditions, the desired condenser temperature can be determined from the vapor concentration dependence on temperature at the desired outlet concentration. Once the temperature is known, an appropriate refrigerant can be selected. Then by modeling the axial concentration profile, the appropriate surface area and length can be determined from the condensing surface required to reach the desired outlet vapor concentration.

Summary and Conclusions

Integration of a carbon adsorber with cryogenic condensation provides a method to recover VOCs from gas streams in a laboratory scale set-up. Experimental results showed that removal efficiencies of >98% can be achieved for acetone in nitrogen gas streams. Modeling and experimental results also show that condensers operate more efficiently at high VOC concentrations and low gas flow rates. Carbon adsorption can remove relatively low concentration VOCs in high flow rate gas streams and desorb at relatively high concentrations and low flow rates. Carbon adsorption/desorption concentrated a 1% gas stream by over an order of magnitude and decreased flow rates from 5.0 slpm to 0.5 slpm. Condenser removal efficiencies increased from 70.5% to 98.8% for inlet acetone concentrations between 0.6% and 18.3% by volume. The mass of LN2 required to condense a unit mass of acetone was also found to decrease as inlet concentration increased. The Wagner equation proved to be valid for determining the outlet concentration of acetone vapor given the condenser temperature. Cryogenic recovery of VOCs is more efficient when the condenser was integrated with a carbon adsorber.

References

[1]   United States Environmental Protection Agency, *National Air Quality and Emissions Trends Report*, EPA 454/R-93-031, USEPA, 1992.
[2]   McIlvaine, R., Halderman, S. and J. Schwartz *Pollution Engineering*, February 15, 1992, pp. 54-57.
[3]   United States Environmental Protection Agency, 1990 Clean Air Act Amendments, USEPA, 1990.
[4]   Ruddy, E.N. and L.A. Carrol *Chemical Engineering Progress*, July 1993, pp. 28-35.
[5]   United States Environmental Protection Agency, *Control Technologies for Hazardous Air Pollutants*, EPA/625/6-91/014, USEPA, 1991.
[6]   Dyer, J.A. and K. Mulholland *Chemical Engineering*, February 1994, pp. 4-8.
[7]   Buonicore, A.J. and W.T. Davis, Air and Waste Management Association, *Air Pollution Manual*, New York, 1992.
[8]   American Society of Heating, Refrigeration and Air-Conditioning Engineers, *1983 Equipment Volume*, 1983.
[9]   Reid, R.C., Prausnitz, J.M. and T.K. Sherwood *The Properties of Gases and Liquids*, New York, 1977.
[10]   Lordgooei, M., Carmichael, K.R., Kelly T.W., Rood, M.J. and S.M. Larson, Activated Carbon Cloth Adsorption-Cryogenic System to Recover Toxic Volatile Organic Compounds, submitted to Gas Separation and Purification, 1995.

Acknowledgments
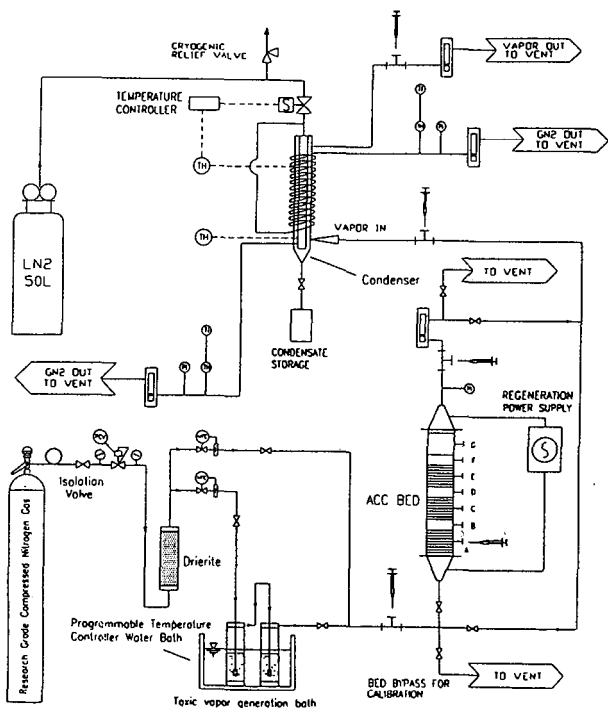
Figures

Figure 1. Laboratory condenser set-up integrated with a fixed carbon adsorber.
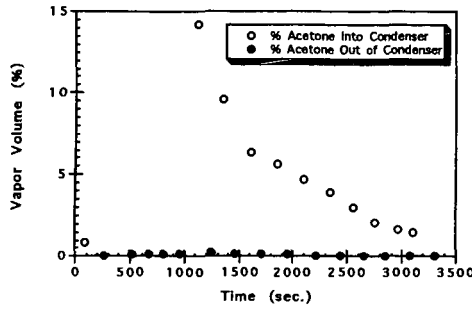
Figure 2. Acetone outlet concentrations from desorption and condensation.
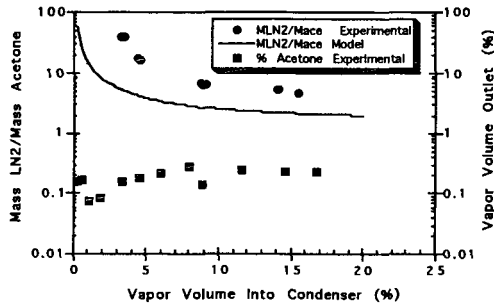
Figure 3. LN2 requirements and condenser acetone outlet concentrations versus inlet concentrations.
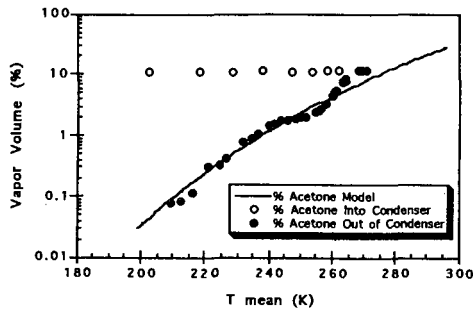
Figure 4. Acetone outlet concentrations versus condenser equilibrium temperature.
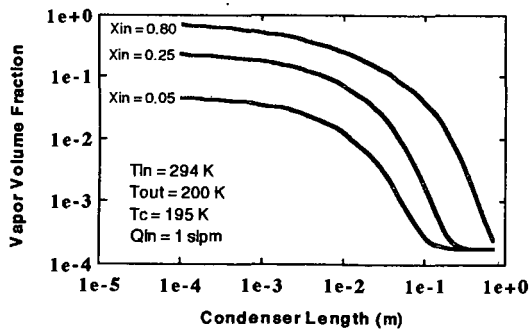
Figure 5. Modeled outlet acetone volume fractions for various condenser lengths. Xin is the inlet vapor volume fraction and Tc is the condensate film temperature.

THE ADSORPTION ONTO FIBROUS ACTIVATED CARBON
APPLICATIONS TO WATER AND AIR TREATMENTS

Pierre Le Cloirec[1], Catherine Brasquet [1] and Etienne Subrenat[2]
(1) UMR Subatech, Ecole des Mines de Nantes, 4 rue Alfred Kastler
44070 Nantes Cedex 03, France
(2) Actitex, 16 rue Trézel, 92309 Levallois Cedex, France

Keywords : Fibrous activated carbon, adsorption, water, air

Abstract :
        The adsorption of polluted fluids is performed by fiber activated carbon (FAC).The adsorption is carried out in a batch or dynamic reactor. Classic models are applied and kinetic constants are calculated. Results showed that the performances of FAC are significantly higher than that of granular activated carbon (GAC) in terms of adsorption velocity and selectivity. The breakthrough curves obtained with FAC adsorbers are particularly steep, suggesting a smaller mass transfer resistance than GAC. The adsorption zone in the FAC bed is about 3.4 mm and is not really dependent on the water flow rate within the studied range. Applications are developped in water and air treatments. Examples are given in the micropollutants removal of an aqueous solution. Air loaded with VOC or/and odorous molecules is treated by fibers. Regeneration of this material is performed by heating by joule effects or electromagnetic induction. Theses original approaches to water or air treatment processes are successfully put to use.

INTRODUCTION

        The removal of organic matter in aqueous or gas phases with granular activated carbon (GAC) is commonly performed for the treatment of waters or VOC (Cheremisinoff and Ellerbush, 1978; Schulhof, 1979; Bansal et al. 1988). GAC adsorbers have been proved effective in removing a large number of organic molecules (Clark and Lykins, 1989).
        Fibrous activated carbon (FAC) has received increasing attention in recent years as an adsorbent for purifying water. The raw materials of FAC are polyacrylonitrile (PAN) fibers, cellulose fibers, phenol resin fibers or pitch fibers and their cloths or felts. They are first pyrolysed and then activated at a temperature of 700-1000°C in an atmosphere of steam or carbon dioxide (Seung-Kon Ryu, 1990).
        The main objectives of the present paper is to assess the performance of the FAC adsorbents in water and air treatments. Phenol and its derivatives are the basic structural unit of a wide variety of synthetic organics including many pesticides. Then, phenol was the model compound used throughout the adsorption studies in aqueous solutions. The Volatil Organic Compounds (VOC) are well adsorbed on FAC, an exemple is schown. Two new regeneration method are proposed.

MATERIALS AND METHODS

Activated Carbon Materials

        Activated carbon materials are commercial products proposed by the PICA Company and Actitex Company (France). The main characteristics of the materials used in the present investigations are presented in Table 1. Scanning electronic microscopy pictures of the different adsorbants have been shown elsewhere (Le Cloirec et al., 1990 b)

Water treatments

        Kinetic and equilibrium studies. Activated carbon (about 0.6 g) in the form of GAC or FAC was continuously stirred with 1 liter of an aqueous solution at 20 ± 1°C containing initially 100 mg.l⁻¹ as micropollutants. Samples were withdrawn at regular times and then filtered for analysis until a steady state was obtained, up to 300 minutes for GAC. For the equilibrium studied, the activated carbon mass was varied from 0.05 to 0.5 g in 250 ml of solution. The final solution was then filtered and analysed.
        Continuous Flow Reactor. A laboraty pilot unit was set up for the continuous flow study (Figure 1). The raw water contained 50 mg.l⁻¹ of micropollutant and was pumped to the adsorption line which was composed of four similar stages. Just one stage is shown on the figure 1. The modules have a diameter of 2.5 cm. The dead volume inside and between the FAC modules was negligible. The water flowed through each FAC module with a given velocity of 0.67 to 2.07 m h⁻¹. Samples were taken at regular times in the outflow of the FAC modules in order to determine the corresponding breakthrough times.

Air treatments

        Adsorption procedure. A laboraty pilot unit was set up for the continuous flow study. The raw air contained 50 mg m⁻³ to 50 g VOC m⁻³ and was sent to the adsorption line. The air velocity through the FAC was in a range between 50 and 1000 m h⁻¹. Samples were taken at regular times in the outflow of the FAC modules in order to determine the corresponding breakthrough times.
        Regeneration. Two kinds of regeneration were tested. The heating of FAC was developped by joule effect (Figure 2) or by electromagnetic induction (Figure 3).

RESULTS AND DISCUSSION

Water treatments

The results are presented in terms of adsorption velocity and selectivity compared to activated carbon grains.

Adsorption velocity. The kinetic cœfficients were calculated for the two activated carbon materials into account the initial slopes of the curves. The Freundlich or Langmuir's models are applied (Table 2) the values of initial velocities are shown in Table 3. Adsorption isotherms were performed for the adsorption of phenol from synthetic solutions. All the isotherms demonstrated a favorable adsorption (Weber and Smith, 1987). The Freundlich equilibrium constants were higher for FAC than for GAC probably because of the higher specific surface area and the microporous structure of the activated carbon fibers. Therefore the FAC materials are more interesting than GAC from the standpoint of adsorption capacities. Therefore FAC was used for the breakthrough experiments. The kinetic cœfficient for the FAC was found more than 50 times greater than that for GAC. Suzuki (1991) measured similar intraparticular diffusion cœfficients with GAC and FAC. On the other hand, Seung-Kon Ryu (1990) came to the conclusion that the superposition of the adsorption forces generated by the opposite walls of the micropores causes an increase in the adsorption potential inside them. FAC seems to have only micropore which are directly connected to the external surface of the fibers (Le Cloirec et al., 1990; Suzuki, 1991; Abe et al., 1992)). The pore size distribution for PAN-based activated carbon fibers concentrate around 2.5 to 2.6 nm (Tse-Hao Ko and co-workers, 1992). Thus adsorbates reach adsorption sites through micropore without additional diffusion resistance of macropore which usually is the rate-controlling step in the case of granular adsorbents (Suzuki, 1991). Moreover, the small diameter of the fibers results in the large external surface area exposed to the flowing fluid. Thus FAC adsorbents provide much faster adsorption kinetics compared with GAC (Baudu and co-workers, 1990, 1991).

Selectivity. In order to approach the selectivity of the two adsorbents, adsorptions in bactch reactor were performed with a mixture of commercial humic substances and phenol. The results are presented in Figure 4. Similar curves are obtained for the two experiments. The FAC presents a selectivity for the low molecular weight molecules (Phenol) compared to macromolecules (Humic Substances). The adsorption capacities are found to be very closed for different waters as shown in Table 4. The micropore distribution coud explain this selectivity.

Dynamic adsorptions. Breakthrough experiments were carried out for the adsorption of phenol onto FAC material with different flow rates through the FAC modules. Typical breakthrough curves for a given flow rate of 2.07 m.h^{-1} are presented in Figure 5. Very steep breakthrough curves were obtained for all the flow rates used in the present investigation. This characteristic shape has already been mentionned in the review by Seung-Kon Ryu (1990). Again, Suzuki (1991) showed drastic differences between the breakthrough curves obtained in the same experimental conditions with GAC and packed FAC. The sharper breakthrough curves observed for the FAC suggested smaller mass transfer resistance than for the GAC. Similarly, Seung-Kon Ryu (1990) concluded that the adsorption rates of FAC are much higher than those of GAC. Therefore the mass transfer zones are much smaller in the case of adsorption onto FAC. The breakthrough times were measured when the phenol concentration (C) reached 0.05 Co (initial concentration). The breakthrough time values obtained for the various thicknesses and flow rates used in the study were introduced into the Bed Depth Service Time (BDST) relation developed by Hutchins (1973) and currently used. Parameters of the BDST relation are shown in Table 6. The N_0 (adsorption capacity) and Z_n (adsorption zone) values were not really strongly dependent on the flow rate within the range 0.62 - 2.07 m.h^{-1}. One might hypothesize that the adsorption reaction was not significantly influenced by the external mass transfer of the solutes through the hydrodynamic boundary layer. The main resistance to the mass transfer might be due to the diffusion through micropores inside the activated carbon fibers. The adsorption capacities (No) were recalculated as a function of the activated carbon weight (Table 5). A good adsorption capacity (about 130 mg/g), close to the maximum surface concentrations determined in the batch reactor, is found with this dynamic system.

Air treatments

VOC adsorption. A large number of works were published on the air treatment with activated carbons. Volatil Organic Compounds (VOC) were found to be well adsorbed onto GAC or FAC. During this study, adsorption onto FAC were performed with different VOC. An exemple is proposed on the figure 6. In this case, the dynamic adsorption capacity is found about 30 %. In order to recover the solvent, an "in situ" regeneration is required.

Regeneration of FAC. Two conventionnal methods are currently used to desorbe VOC from activated carbon by hight pressure steam or preheating fluid (air, nitrogen...). In order to overcome problems found with conventionnal methods, new processes usefull with FAC were considered.

Regeneration by joule effect. Recently, a new thermal regeneration process has been used. It consists of submitting the carbon to the passage of an electric current. the carbon can be either granular (Baudu et al., 1992) or fibrous (Le Cloirec et al., 1991). the activated carbon structure is akin to a semi-conductor. Laboratory scale experiments on solvent desorption are very promising. The advantage of such a process is that it can be easily implemented in-situ. Examples of regeneration by joule effect on fibrous carbon is given in the Table 6.

The regeneration by induction heating (Le Cloirec, 1993; Mocho, 1994). Induction heating can be used to regenerate activated carbon for the purpose of recycling volatil organic carbon. As he technological possibilities offered by induction on an industrial scale have to be taken into account, the FAC was presented as cylinders. Figure 4 shows the activated carbon heating equipment. Experiments developped with ethyl acetate show the best the frequency is in a range of 1 to 100 kHz. A regeneration rate of 100% is reached for the activated carbon at the end of an hour. At this time, this kind of regeneration is developped at a laboratory scale for a treatment by FAC of air loaded by solvents.

CONCLUSIONS

The objective of this study was to determine the efficiency of adsorption of fibrous activated carbon in water and air treatments. Results showed that performance of FAC is significant. FAC have a fast adsorption kinetics and selectivity. Thus, FAC well adsorbed VOC and new regeneration processes were proposed. For air and water treatments new reactors could be developped.

ACKNOWLEGMENT

BIBLIOGRAPHY

Abe, M., Y. Kaneko, W. Agui, and K. Ogino (1992). Removal of humic substances dissolved in water with carbonaceous adsorbents. *Sci. Tot. Environ.*, 117/118, 551-559.

Bansal, R.C., J.B. Donnet, N. Stoeckli (1988) Active Carbon, *Marcel Dekker Inc*, N.Y., USA.

Baudu, M., P. Le Cloirec, and G. Martin (1991). Pollutant adsorption onto activated carbon membranes. *Wat. Sci. Technol.*, 23, 1659-1666.

Baudu M., Le Cloirec P., Martin G. (1992) Thermal regeneration by joule effect of activated carbon used for air treatment, *Environ. Technol.*, 13, 423-435

Cheremisinoff P.M., F. Ellerbush (1978), Carbon adsorption Handbook, *Ann Arbor Sci*, Ann Arbor, Mi, USA.

Clark, M. K.,B. W. Lykins (1989). Control of trihalomethane and synthetic organics. In R. M. Clark (Ed.), *Granular activated carbon*, Lewis Publ., Michigan. pp.257-293.

Hutchins, R. (1973). New method simplifies design of activated carbon systems - Water bed-depth service time analysis. *Chem. Eng.*, 20, 133-138.

Le Cloirec P., M. Baudu, G. Martin, G. Dagois (1990 b), Membrane, toiles, fibres ou feutres : des charbons actifs d'utilisations prometteuses, *Rev. Sci. Tech. Défense*, 2, 111-123.

Le Cloirec P. Baudu M., Martin G. (1991) Dispositif de traitement de fluide, au moyen d'une structure d'adsorption à couches superposées espacées, et régénération par effet joule. Brevet Européen n° 91460043.2 Dépôt le 20/09/91

Mocho P., Le Cloirec P. (1994) Regeneration of granular activated carbon by inductive heating. Application in the elimination and recycling of air-born solvent, Vigneron S., Hermia J., Chaouki J. Ed, Studies in Environmental Science 61, Elsevier, Amsterdam, 251-262.

Seung-Kon Ryu (1990). Porosity of activated carbon fibre. *High Temp.- High Pressures*, 22, 345-354.

Schulhof P.(1979), An evaluating approach to activated carbon treatment, *J. Am. Water Works Ass.*, 71, 648-661.

Suzuki M. (1991), Application of fiber adsorbents in water treatment, Water Sci. Technol, 23, 1649-1658

Tse-Hao Ko, P. Chiranairadul, Chung-Hua Lin (1992). The study of polyacrylonitrile-based activated carbon fibres for water purification: Part I. *J. Materials Sci. Letters*, 11, 6-8.

	GAC	FAC
Commercial name	Pica NC 60	Actitex 1501
Size (mm)	3	-
Origin	coconut	viscose
Porosity	microporous	microporous
Specific area ($m^2.g^{-1}$)	1200	1550

Table 1 : Main Characteristics of Activated Carbons
(PICA Company, Levallois France for GAC and Actitex, Levallois, France for FAC)

	GAC	FAC
1/n	0.39	0.428
k	0.06	27.7
qm	117	183
b	0.03	0.083

Table 2 : Langmuir and freundlich model parameters of phenol adsorption

	GAC	FAC
γ (l. $mg^{-1}.min^{-1}$)	$5.8 \ 10^{-6}$	$4.5 \ 10^{-5}$

Table 3 : Initial adsorption velocity for phenol removal

Water	Phenol only	HS only	Phenol in the mixture	HS in the mixture
Deionised	40.1	1	34.3	0
Drinking Water	40.3	0.5	32.6	0
River water	44	0	40.2	0

Table 4 : Adsorption capacity (mg g-1) of phenol and humic substances (HS) in different waters

U (m/h)	Z_o (mm)	N_o ($mg.l^{-1}$)	N_o ($mg.g^{-1}$)
0.62	3.5	9210	134
1.02	3.3	8925	130
2.07	3.4	8625	126

Table 5 : Adsorption zone and capacity at different flow velocities

Experiment	P (w)	Time to be at 100°C	Regeneration yield (%)
1	240	3 min 45 s	95
2	340	1 min 20 s	100
3	440	55 s	100

Table 6 : Thermal regeneration of fibrous activated carbon by joule effect (Baudu et al., 1992)
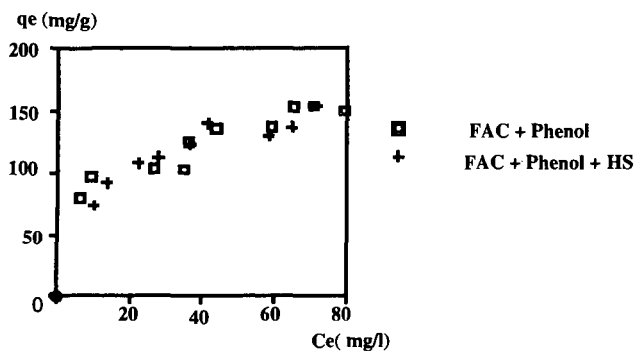
Figure 4 : Adsorption of mixture of humic substances (HS) and Phenol onto FAC
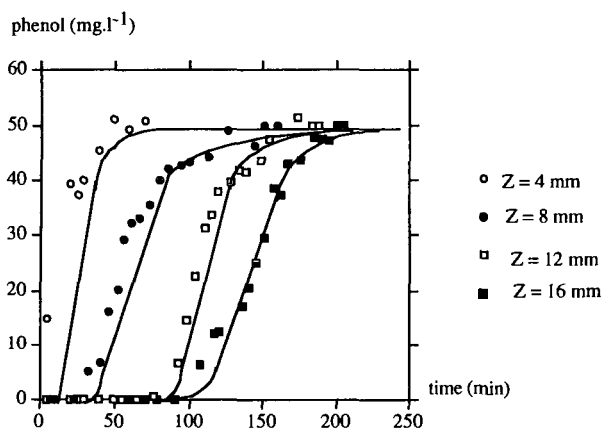
Fig.5 : Breakthrough curves for different thicknesses of FAC (flow rate: 2.07 $m.h^{-1}$;. raw water concentration: 50 mg $phenol.l^{-1}$).
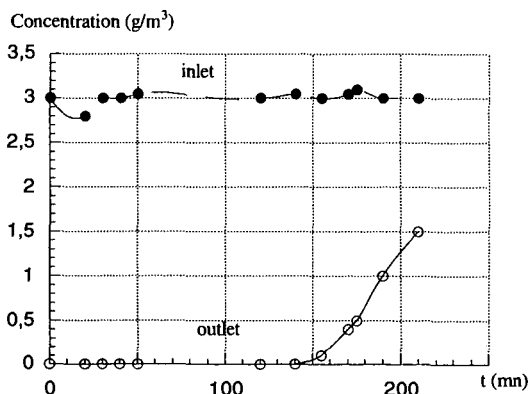
Figure 6 : Breakthrought curve on FAC. Air loaded with perchlorethylene, Velocity : 522 m/h; FAC weight : 7 kg (Baudu et al., 1992)
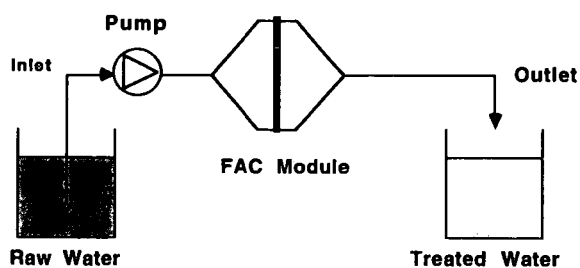
Figure 1 : Continous flow reactor used in water treatment
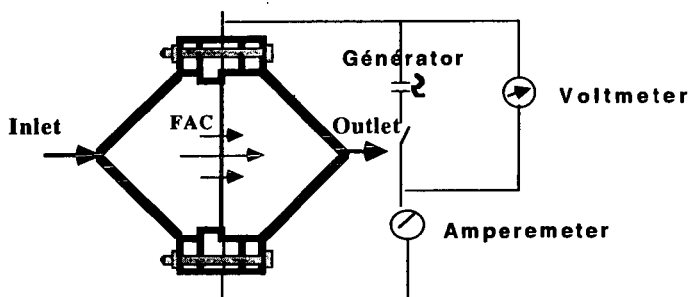
Figure 2 : Heatin by joule effect, experimental equipment
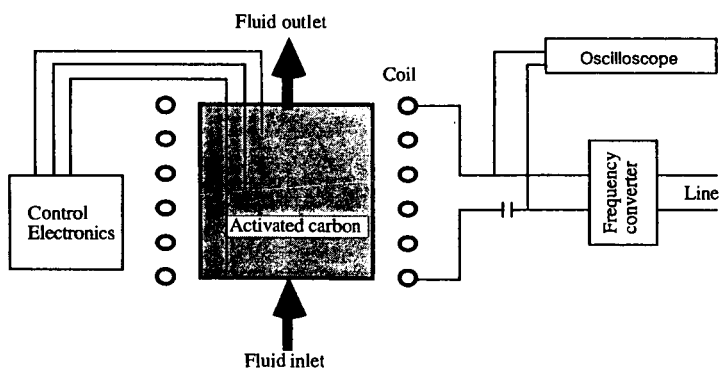
Figure 3 : Heating by electromagnetic induction. Experimental equipment

THE USE OF CARBON FIBER COMPOSITES AS SUBSTRATE FOR A ZERO VALENT METAL DECHLORINATION SYSTEM.

Rodney Andrews, Billy Spears, and Eric Grulke. Department of Chemical and Materials
Engineering, University of Kentucky, Lexington, KY, 40506-0046.

Chris Lafferty. Center for Applied Energy Research, University of Kentucky,
Lexington, KY, 40511-8433.

Abstract
The use of zero valent metals is known to successfully degrade chlorinated hydrocarbons.
The use of zinc metal to decholorinate trichloroethene (TCE) in contaminated groundwater sources
has been limited by metal surface area for reaction. A highly porous carbon fiber composite substrate
for the zinc metal provides a much higher surface area for reaction in a decholorination system. The
zinc coating applied to the carbonaceous fibers provides higher reaction rates than traditional
powdered metal systems. Added advantages of using the zinc coated carbon substrate for ground
water clean up are low pressure drop, easy removal and emplacement of composites, and the ability
to recharge the zinc coating *in situ*. The novel zinc impregnation method results in a uniform coating
of zinc throughout the composite and a greatly increased area for reaction.

Introduction
The dehalogenation of hydrocarbons by zero-valent metals offers many attractive features for
environmental application. The relatively high reaction rates, low cost of the metal catalyst, and
non-contaminating nature of the catalyst all make this an attractive system for ground water clean-
up. The limiting factor for the dehalogenation reaction is the surface area of the metal available for
reaction. Large metal pellets offer slow reaction rates, while fine metal particles lead to faster
reaction rates. In this study, a carbon fiber composite is used as a support for zinc plating; producing
a supported zinc catalyst with very high surface area for reaction and low resistance to flow. The
zinc plated composite system also has the advantage of being regenerable after metal depletion. This
regeneration could be performed *in situ*.
The decholorination of trichloroethene (TCE) by zero-valent zinc is demonstrated with both
supported and unsupported zinc systems. Initial rate constants for this reaction are reported. The zinc
was placed onto the carbon composite using electrochemical reaction at low current densities and the
resistance to flow through the composite was measured and compared to uncoated composite.

Literature Review
The use of zero-valent metals, mainly iron, tin and zinc, to remediate water containing
chlorinated hydrocarbons has been proposed by several researches. The emphasis of most research in
this area has been on the use of iron as the metallic catalyst or a modified iron, such as the palladium
plated iron granules used by Korte et. al. (1-7) Boronina et. al. (8) have demonstrated the efficacy of
using Zn or Sn as the catalytic metal, showing the relatively fast reaction rates obtained using very
fine Zn particles in an inert atmosphere.
The destruction of chlorinated species into metal salts and dechlorinated byproducts has been
shown to occur at reaction rates ranging from 5 to 15 orders of magnitude faster than that observed
for natural abiotic processes. (6) O'Hannesin et. al. have shown that a reactive bed containing Fe
filings was able to remove 90% of the trichloroethene (TCE) from groundwater at the Canadian
Forces Base, Borden, Ontario site. They concluded that the reaction rate was independent of TCE
concentration . In further studies, this group found chlorinated species destruction by granular iron of
13 out of 14 halogenated methanes, ethanes and ethenes. (6)
In building a pilot scale operation for the reduction of TCE using iron filings, MacKenzie et.
al. (7) determined several factors controlling the process. The alkalinity of the ground water being
treated as well as the amount of dissolved oxygen in the water effect catalytic bed lifetime. The
presence of carbonate or oxide forming species in the water leads to a inert layer of metal oxide or
metal carbonate forming on the metal surface. This layer greatly reduces the overall reaction rate.
(1,5,7,8). MacKenzie et. al. found that a 10 fold increase in aqueous alkalinity reduced the reaction
rate by three fold.
Metallic surface area is a controlling factor in the rate of reaction. (1, 8) Boronina et.al. (8)
have shown that cryo-particle Zn with a surface area of >65 m²/g reduced the concentration of CCl_4
in water by over 90% in three hours, while granular Zn, having a surface area < 1 m²/g, achieved a

reduction of only 25%. A similar correlation between surface area and dechlorinating ability was seen in studies using Sn metal.

Objectives

This paper describes a novel process for supporting zero-valent zinc on a carbon fiber composite. The study also reports some preliminary rate constants for unsupported and supported zinc dechlorination of TCE.

Experimental

Unsupported Zinc Powder

Zinc powder was reacted with an aqueous solution of 1000 ppm TCE under a nitrogen atmosphere. The zinc (from J.T. Baker Chemical) was 60 to 200 mesh in size, and was washed in 0.01 M HCl to eliminate any oxide coating. A vacuum tight reaction vessel was charged with 100 ml of nitrogen saturated water and 10 grams of the washed zinc powder were added. A vacuum was drawn on the system and held for 15 minutes to remove any remaining oxygen. The vacuum was broken by introduction of a nitrogen gas stream. The reactor was kept under a constant positive pressure of nitrogen, and 100 µl of TCE was added. High agitation rates were used to insure uniformity of composition. The concentration of chloride ions was measured using a chloride selective electrode.

Supported Zinc

Carbon fiber composite was manufactured using the process described earlier at this conference at CAER, UK. The composite was carbonized at 600 °C to improve the conductivity of the material. A 10 cm long composite sample with 2.54 cm diameter was placed in the holder of the plating apparatus (Figure 1). This sample was immersed in a chloride zinc bath (Table 1) and a plating fluid at 100 ml/min was passed through the sample. A solid zinc electrode was immersed in the bath and an electrode with 2.5 cm diameter was contacted with the carbon composite. A 10 volt, 0.1 ampere current was applied to the composite. This low current density was allowed to flow until a 2 micron layer of zinc was deposited on the composite which had 17 µm diameter fibers.

Scanning electron microscopy and elemental analysis were used to determine the uniformity of zinc coating on the composite support. This composite was then cut and the composite samples used as paddles for agitation in a reactor system as described above in place of the zinc powder.

Results

Zinc Plating

SEM showed that the zinc layer was uniform through out the 10 cm length of the composite and had no radial variation. The zinc layer was 2 µm in thickness. This ease of control of the plating process would allow the composite plating to be regenerated as needed by flowing a zinc-chloride solution through the composite and applying a current as needed *in situ*.

Reaction Rates

To determine if TCE decholorination was occurring, the reaction was monitored for chloride ion concentration in solution using a chloride selective electrode. A typical reaction profile is shown in Figure 2. For this initial study, first order kinetics and total reaction were assumed. Reaction rate constants were determined based on the amount of chloride not released into solution, and are reported on a per gram of zinc basis. The zinc powder was shown to degrade the TCE and the rate of degradation increases with temperature (Table 2).

The reaction rate for the zinc plated composite system is an order of magnitude faster than for the powdered zinc system, indicating that the surface area for reaction of the metal controls the reaction rate. The pressure drop through the zinc plated composite was measured and compared to that of the untreated composite. These values were found to be the same indicating that no increase in pressure drop results from the zinc plating. This pressure drop is low, and the zinc plated composite would be ideal for use in a fixed-bed flow system.

Conclusions

Zero-valent zinc metal has been shown to successfully decholorinate TCE in aqueous solution. The rate of this reaction is determined by the surface area of metal available for reaction. A novel process for depositing zinc metal onto a carbon fiber composite produces a reaction system with high surface area of metal. This zinc plated composite has a reaction rate an order of magnitude higher than that of powdered zinc.

References

[1] Sivavec, Horney and Baghel. "Reductive Rechlorination of Chlorinated Ethenes by Iron Metal and Iron Sulfide Minerals.", Emerging Technologies in Hazardous Waste Management VII, Special Symposium, Atlanta, Georgia, Industrial and Engineering Chemistry Division, American Chemical Society, Sept. 17-20, 1995.

[2] Liang and Goodlaxson. "Kinetics and Byproducts of Reductive Dechlorination of Ground Water TCE with Zero-Valence Iron", Emerging Technologies in Hazardous Waste Management VII, Special Symposium, Atlanta, Georgia, Industrial and Engineering Chemistry Division, American Chemical Society, Sept. 17-20, 1995.

[3] Orth and McKenzie. "Reductive Dechlorination of Chlorinated Alkanes and Alkenes by Iron Metal and Metal Mixtures.", Emerging Technologies in Hazardous Waste Management VII, Special Symposium, Atlanta, Georgia, Industrial and Engineering Chemistry Division, American Chemical Society, Sept. 17-20, 1995.

[4] Korte et. al. "The Use of Paladized Iron as a Means of Treating Chlorinated Contaminants.", Emerging Technologies in Hazardous Waste Management VII, Special Symposium, Atlanta, Georgia, Industrial and Engineering Chemistry Division, American Chemical Society, Sept. 17-20, 1995.

[5] Agrawal, Liang and Tratnyek. "Phenomena Affesting Remediation of Organic Groundwater Contaminants with Iron Metal at Solid-Water Interface.", Emerging Technologies in Hazardous Waste Management VII, Special Symposium, Atlanta, Georgia, Industrial and Engineering Chemistry Division, American Chemical Society, Sept. 17-20, 1995.

[6] O'Hannesin, Gillham and Vogan. "TCE Degradation in Groundwater Using Zero-Valent Iron.", Emerging Technologies in Hazardous Waste Management VII, Special Symposium, Atlanta, Georgia, Industrial and Engineering Chemistry Division, American Chemical Society, Sept. 17-20, 1995.

[7] MacKenzie et. al. "Pilot-Scale Demonstration of Chlorinated Ethene Reduction by Iron Metal: Factors Affecting Iron Lifetime.", Emerging Technologies in Hazardous Waste Management VII, Special Symposium, Atlanta, Georgia, Industrial and Engineering Chemistry Division, American Chemical Society, Sept. 17-20, 1995.

[8] Boronina, Klabunde and Segeev. "Destruction of Organohalides in Water Using Metal Particles: Carbon Tetrachloride/Water Reactions with Magnesium, Tin, and Zinc.", Environmental Science & Technology, vol. 29, no. 6, pg. 1511, June, 1995.

Table 1: Chloride Zinc Bath

$ZnSO_4 \cdot 7H_2O$, g/L	240
zinc, g/L	55
NH_4CL, g/L	15
$Al_2(SO_4)_3 \cdot 18H_2O$, g/L	30

Table 2: First order reaction rate constants for decholorination of TCE by zero-valent zinc.

Type of Zinc	Temperature (°C)	k $(min^{-1} g^{-1})$
Unsupported Zinc Powder	25	0.000007
Unsupported Zinc Powder	30	0.00001
Unsupported Zinc Powder	40	0.00002
Supported Zinc on Composite	25	0.00025

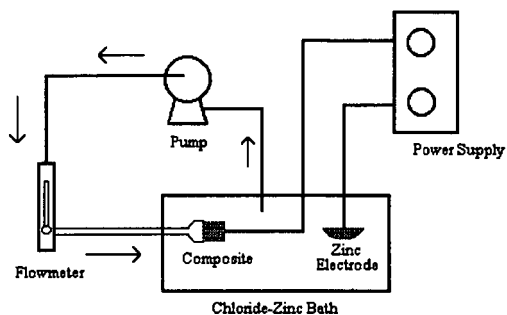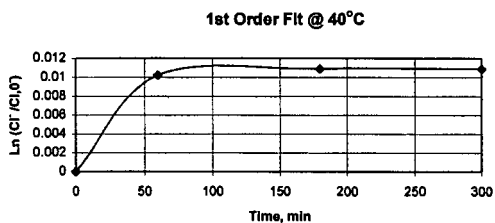Figure 1: Diagram of composite plating apparatus.

Figure 2: Typical reaction profile for powdered zinc degradation of aqueous TCE. Temperature = 40 °C, Initial rate constant, k, = 0.00002 $min^{-1} g^{-1}$.

IMPREGNATED CARBONS FOR THE
ADSORPTION OF H$_2$S AND MERCAPTANS

Stephen Boppart
Norit Americas Inc.
1050 Crown Pointe Pkwy, Suite 1500
Atlanta, GA 30338

Keywords:　　　　H2S, Oxidation, Activated Carbon, Potassium Iodide

Introduction:

Activated carbon has been used for many years for the adsorption of H$_2$S and Mercaptans from natural gas streams, carbon dioxide, and sewage vents. It is widely thought that the carbon pore surface catalyses the oxidation of H$_2$S to elemental sulfur and higher oxidized forms of sulfur[1,2]. However, due to the poor loading capacities achieved at ambient conditions, most commercial activated carbon employed for H$_2$S adsorption contain some sort of impregnant, such as NaOH, KOH, or KMnO$_4$, to enhance the loading capacity on the carbon.

By far the most widely used impregnated carbons used for H$_2$S adsorption has been NaOH and KOH impregnated carbons. These carbons show greatly increased Sulfur loading capacities, however due to high heats of reactions involved, are prone to bed fires. Non-impregnated carbons, which have undergone pore surface modification are also commercially available. These carbons fail to meet the same high loading capacities as caustic impregnated carbons, however it's manufacturer claims that that simple water wash is all that is required to achieve partial regeneration of the carbon.

A relatively new carbon type, NORIT ROZ 3, has been developed, which not only increases the Sulphur loading capacity significantly over caustic impregnated carbons, but it is not as susceptible to bed fires. This carbon differs from caustic impregnated carbons commercially available in two distinct ways. First the base carbon used has a higher pore volume, especially in the meso and macro pore range. Secondly, Potassium Iodide, is used as an impregnant.

This paper will present laboratory and field data of both caustic impregnated carbons and NORIT ROZ 3, as well as laboratory data of a surface modified carbon, Calgon Centaur™ HSV.

Laboratory studies:

Carbon types:
Three commercially available carbons were tested for their ability to adsorb H$_2$S. These were Calgon IVP, Centaur HSV and NORIT ROZ 3. In table 1, the carbon characteristics are listed. All three carbons vary significantly.

NORIT ROZ 3 is a highly activated peat based carbon which has a high degree of macro and mesopores. It is impregnated with minimum 2 % potassium iodide.

Calgon IVP is a bituminous based activated carbon typical for vapor phase applications. It has been impregnated with Sodium Hydroxide.

Calgon HSV is a non-impregnated bituminous coal product which has been treated to enhance its catalytic activity.

™ TM of the Calgon Corporation, Pittsburgh, PA

Reaction Mechanism:
For the oxidation of H_2S, a certain amount of water vapor must be present. Hedden et al[3] have proposed the following mechanism. Water is adsorbed, forming a film of water on the pore surface. H_2S and O_2 diffuse down into the carbon pores and are dissolved in the water. The O_2 is adsorbed on the carbon surface and breaks down into radicals. These oxygen radicals then react with the dissolved hydrosulfide ions, forming elemental sulfur and water (figure 1).

Since the radical formation occurs on the pore surface of the carbon, it might be concluded that surface area would be a predominant factor in this reaction.
T.K Ghosh et al[1] found however, that the amount of surface area of a carbon has no effect on the oxidation of H_2S. Ghosh concluded that carbons which had high pore volumes, not high surface areas, achieved higher rates of conversion of H_2S.

Further oxidation to sulphur dioxide and sulfuric acid can occur. In the presence of NaOH, Na_2SO_4 and Na_2SO_3 can also be formed. Klein et al[2] suggest that the addition of KI as a catalyst not only increases the reaction velocity, but also limits the formation of sulfuric acid.

Test description:
The standard test used to measure the performance of carbon for H_2S adsorption is a dynamic test. Humidified air (RH 75 %, 20°C) containing 1 % vol. (10,000 ppm) of H_2S is passed through a column of carbon (diameter 3.9 cm, bed height 22.9 cm) at a linear velocity of 8.8 cm / second (6350 ml/min.). This results in a contact time of 2.7 seconds. The test is stopped at breakthrough concentrations of 50 ppm.

The adsorptive capacity of a carbon is given in g/ml, which is calculated as follows:

Adsorption capacity = $(H_2S)*F*T_{BT} / V_C$

Where: (H_2S) = Concentration, in g/ml
  F = Flow, in ml / min.
  T_{BT} = Break through time, in minutes
  V_C = Volume of carbon, in ml

Lab results:
The results of the tests are given in table 2. Of all three carbons tested, only NORIT ROZ 3 achieved the 0.14 g/ml which has become the standard in the odor control market. After breakthrough, the carbon in the top, middle and bottom of the column were analyzed for total sulfur content and the results were corrected back to % sulfur adsorbed per ml of virgin product. The results are presented in table 3.

With Calgon Centaur HSV, the mass transfer zone is very long, as it can be observed that the middle of the bed had much lower loading capacities than the bed inlet (0.06 vs 0.11 g/ml). This was also the case with NORIT ROZ 3, although not as dramatic as with the Calgon Centaur HSV. Curiously, with the caustic impregnated carbon, the bed inlet has a lower Sulfur loading capacity than the middle of the bed. This could possibly be due to high heats of reaction drying the bed, limiting the amount of H_2S which could react.

Previous tests carried out NORIT ROZ 3 resulted in an equilibrium loading capacity of approximately 120 wt. % (0.54 g/ml). These tests were done with an humidified air stream (20°C, RH 80%), with a H_2S concentration of 0.5 vol. % (5,000 ppm) for 450 hours.

This clearly shows that this accelerated test, lasting only a few hours, does not allow sufficient time for the H_2S to oxidize to maximum loadings. It can be argued that the accelerated H_2S oxidation test has limited relevance to actual field performance due to the high H_2S loadings, short run time and that no other organic compounds are co-adsorbed. Questions have also been raised about the reproducibility of this test. In addition, Koe et al.[4] found that, for caustic impregnated carbons, the actual field trials show Sulphur loadings which are only 30 % that of laboratory loadings. A detailed discussion of this is

beyond the scope of this paper, however it is evident that actual field data will give a much better understanding of the relative performance of carbons.

Field Data:

Two case studies were conducted with NORIT ROZ 3.

Case 1:
A single adsorber containing 7,000 lbs of NORIT ROZ 3 was installed at a sewage odor filter in the Netherlands. The size and conditions of the installation are listed in Table 4. After odor breakthrough, carbon from various depths within the bed was analyzed, the results appearing in Table 5.

It can be clearly seen from the carbon analysis, that the odor was due to organic compounds breaking through the bed. The upper 1/2 of the carbon bed did in fact not even have any sulphur loading on the bed. The inlet portion of the bed did achieve very high Sulphur loadings in addition to high organic loadings. It can be assumed that if the bed had been run until H_2S breakthrough, that the average sulphur loadings would have been much higher.

Case 2:
At a sewage discharge station, a small adsorber was filled with 1764 lbs of NORIT ROZ 3. Previously this adsorber was filled with KOH impregnated bituminous based carbon. After odor breakthrough, both carbons were sampled from the top, middle and bottom portions of the bed and analyzed with the following results:

A marked difference in bed life and loading capacity was noticed between the KOH impregnated carbon and the NORIT ROZ 3. In fact the NORIT ROZ 3 lasted 275 % longer than the KOH impregnated carbon. This was in spite of the fact that the bed containing the caustic carbon had 13.4 % more carbon on a % wt basis.

It is interesting to note that even after 11 months of adsorption, the middle of the bed containing NORIT ROZ 3 did not reach equilibrium loadings, with S loadings of 47.1 wt % for the bottom vs, 25.5 wt % for the middle. The KOH impregnated carbon on the other hand seemed to have reached its maximum loading at 12 % loading in both the top and middle sections of the bed. This would suggest that the reaction rate of a caustic impregnated carbon is more rapid than that of the KI impregnated carbons.

Bed Fires:

NORIT ROZ 3 has been installed in over 70 installations world wide in addition to over 100 sewage gas breathing filters. In all of these installations, no bed fire has ever occurred. Caustic impregnated carbons do have somewhat higher heats of reaction, however this alone fails to explain why so many bed fires have occurred in the field with caustic impregnated carbons.

Conclusion:
The accelerated oxidation test does not give a representative view of activated carbons field performance. This is primarily due to the short test period which would not allow sufficient time for the oxidation reaction to go to completion. It appears that the KI impregnated carbons and the surface modified carbons have a slower rate of reaction than caustic impregnated carbons and thus would be negatively biased in such a test.

In both long term laboratory tests and actual field cases, NORIT ROZ 3 achieved very high loading capacities for both organic and sulphur bearing compounds. This can be attributed to the high pore volume and KI impregnant.

[1] "Catalytic oxidation of low concentrations of Hydrogen Sulfide", T.K Ghosh and E. Tollefson Presented at the meeting of the Canadian Gas Processors Associations, March 14, 1985.
[2] "Catalytic oxidation of hydrogen sulfide on activated carbons", J. Klein & K-D Henning, Bergbau-Forshung GmbH, Essen, FRG. Carbon and Catalysis conference, London, December 19, 20, 1983
[3] "Adsorptive Reinigung von Schwefelwasserstoffhaltigen Abgasen", K. Hedding and B.R. Rao. VDI-Bericht Nr.253 S.37/42, Duesseldorf, VDI-Verlag, 1976.
[4] "Comparisons of field and laboratory loading capacity of activated carbon." L.C.C. Koe & N.C. Tan. Department of Civil Engineering. National University of Singapore. Water, Air, and Soil Pollution 50:193:203, 1990

Table 1: Carbon Characteristics.

Carbon Type	NORIT ROZ 3	Centaur HSV	Calgon IVP
Bulk Density, g/L	0.450	.600	.530
Micropore volume, ml/g	0.32	0.25	.031
Mesopore volume, ml/g	0.11	-	0.06
Macopore volume, ml/g	0.41	0.14	0.21
Total pore volume, ml/g	0.84	-	0.58

Mesopore volume not available for Centaur HSV

Table 2: Results of accelerated H_2S Oxidation test

Carbon type	Adsorptive capacity (g/ml)
NORIT ROZ 3	0.15
Calgon Centaur HSV	0.06
Calgon IVP	0.11

Table 3: Sulfur analysis of spent carbon from table 2

Carbon Type (g/ml)	Bottom (g/ml)	Middle (g/ml)	Top (g/ml)
NORIT ROZ 3	0.16	0.14	0.02
Calgon Centaur HSV	0.11	0.06	0.02
Calgon IVP	0.07	0.12	0.01

Table 4: Process conditions (Case 1)

Carbon Bed Height	2 m
Carbon Bed Diameter	2.1 m
Flow Rate	2400 m^3/hr
H_2S Concentrations	15-40 ppm
Breakthrough	Odor
Contact Time	10.4 seconds
Relative Humidity	70-80 %

Table 5: Sulfur loading as a function of bed depth (case 1)

Bed Height	55 cm	115 cm	170 cm	190 cm
H_2O loading (wt %)	39.3	9.6	12.7	2.7
Organic loading (wt %)	42.1	22	2.4	4.1
Sulphur loading (wt %)	25.5	5.9	<1	<1

Table 6: Process Conditions (Case 2):

	NORIT ROZ 3	KOH \carbon
Carbon Bed Height	3.4 ft	2.83 ft
Carbon Bed Diameter	5 ft	5 ft
Flow direction	up	down
Flow Rate	1200 cfm	1200 cfm
H_2S Concentrations	10-25 ppm	10 - 25 ppm
Carbon Quantity	1764 lbs	2000 lbs
Contact Time	3.3 s	2.8 s

Table 7 Sulfur loading capacities, (Case 2):

	NORIT ROZ 3	KOH carbon
Top of Carbon bed, S loading, wt %	26.2 %	12.9%
Middle of bed, S loading, wt %	25.5%	11.8%
Bottom of bed, S loading, wt %	47.1%	5.4%
Average Sulfur loading, wt % dry basis	32.9%	10.0%
Bed life	11 months	3-4 months

Figure 1: Proposed reaction mechanism for the oxidation of H_2S

Novel Nanoporous Carbon Membranes for Recovery of Hydrogen from Refinery Waste Gas
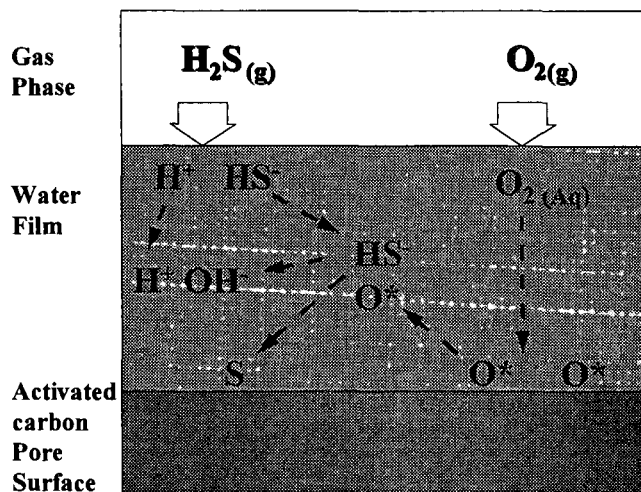
M. B. Rao and S. Sircar
Air Products and Chemicals, Inc.
7201 Hamilton Boulevard
Allentown, PA 18195-1501

1. Introduction

Petroleum refineries are among the largest users of hydrogen in the chemical industry. Hydrogen is used in hydrogenation, desulfurization and denitrogenation processes and a large source of hydrogen in refining operations is the production of aromatic compounds which are used as octane enhancers in gasoline. Environmental regulations are requiring refiners to reduce the amount of aromatic compounds in transportation fuel and, thus, the total amount of hydrogen produced in dehydrogentation processes is being reduced. In addition, refineries are being forced to use crudes which are higher in sulfur which further increases the total H_2 needs. This requires refiners to make or buy hydrogen by conventional methods such as Steam-Methane Reforming or to recover hydrogen from their processes. The purpose of this paper is to describe the preparation and performance of a new carbon-based gas separation membrane and its application in two new processes for hydrogen recovery from refinery waste streams.

2. Selective Surface Flow ™ Mechanism

Surface diffusion on nanoporous membranes is an attractive choice for practical separation of gas mixtures because the separation selectivity is determined by preferential adsorption of certain components of the gas mixture on the surface of the membrane pores, as well as by selective diffusion of the adsorbed molecules [1]. The Selective Surface Flow (SSF™) mechanism is shown schematically in Figure 1 for a mixture of hydrogen and hydrocarbons. The hydrocarbons are more strongly adsorbed on the pores than hydrogen on the high-pressure side of the membrane. These adsorbed components diffuse along the pore surface to the low-pressure side of the membrane where they desorb into the permeate stream. If the pores of the membrane are made small, the adsorbed layer of hydrocarbons serves to block the gas phase flow of hydrogen across the pore. Thus, the feed gas is depleted in the hydrocarbons and an enriched hydrogen stream is withdrawn at feed pressure. This is in contrast to typical polymeric membranes which selectively permeate hydrogen. Permeation selectivities of these membranes can be very high because the adsorption selectivity is high even at low feed pressure. The hydrocarbon permeability across the membrane will be high because the diffusivity for surface diffusion is orders of magnitude higher than typical diffusivities for these components through a polymeric matrix. This allows the membrane thickness to be 1-3 microns rather than the submicron membrane thicknesses typically needed for polymeric membranes. We have developed a novel nanoporous carbon-based membrane which exhibits these properties and shows very attractive gas separation properties for hydrogen/hydrocarbon and carbon dioxide/methane/hydrogen mixtures.

3. Membrane Preparation

We have prepared very thin, defect-free, nanoporous carbon membranes by converting a thin-film of polyvinylidene chloride polymer to carbon by pyrolysis. A polyvinylidene chloride (PVDC) latex (55 wt% solids) was cast on a porous graphite support; the film thickness was estimated to be between 5 and 10 microns. The coated support was then carbonized to temperatures between 600 and 1000C under nitrogen to convert the PVDC to carbon. This coating and carbonizing procedure was repeated up to five and the resultant carbon layer had a thickness of 1-3 microns.

Permeation properties of the carbon membrane were measured using a plate and frame membrane module. A schematic representation of the module is shown in Figure 2. It can hold 6 flat sheet carbon membranes to provide a total membrane area of ~0.5 ft². The purge gas passed through the module countercurrent to the feed direction. The module was instrumented to allow measurement of feed and effluent gas flows and compositions.

The pore size of the membrane was estimated by comparing the pure methane diffusivity through the membrane to the methane diffusivity through zeolites of known pore structure [1]. It was found that methane diffusivity through the carbon membrane is in the activated diffusion regime

and the mean pore size is ~ 5.5A. This suggests that these membranes will exhibit the Selective Surface Flow properties.

4. Practical Applications of SSF™ Membranes

4.1 Recovery of Hydrogen From Refinery Fuel Gas

Refinery waste streams are typically used as fuel within the plant. They contain 20-50% H_2 and C_1-C_4 hydrocarbons are available at pressures of 50 to 150 psig. Conventional separation methods are not amenable to hydrogen recovery from these streams because of low hydrogen recovery efficiency or high energy of separation. Pressure swing adsorption (PSA) process are commonly used in hydrogen separation and purification, however, the overall hydrogen recovery is low when the feed gas contains hydrogen concentrations less than ~50-60% [2]. Additionally, hydrogen PSA systems cannot handle C_4+ hydrocarbons because these constituents are not easily desorbed from the adsorbent. Polymeric membranes are used in refineries for hydrogen recovery however they typically require high feed gas pressure (>300 psig) and they produce hydrogen at the low pressure side which requires recompression before being fed to a PSA system [3]. The use of two compression steps (feed and permeate) make this process very energy intensive.

A process to recover a good portion of the H_2 from such mixtures without further compression of the feed gas while rejecting a substantial portion of the hydrocarbons and has been patented by Air Products and Chemicals, Inc. [4]. The refinery waste gas is fed to an SSF™ carbon membrane module at the available pressure. The H_2-enriched stream on the high pressure side of the membrane can then be compressed and separated in a conventional pressure swing adsorption (PSA) process to produce ultra-pure H_2. The waste gas from the PSA system containing some H_2 and lower hydrocarbons can be used to provide the low-pressure purge stream for the membrane. Figure 3 shows a schematic flow sheet for such a membrane-PSA hybrid scheme.

The performance of the carbon membranes for separation of a multicomponent H_2-hydrocarbon mixture was tested in plate-and-frame membrane module. A gas mixture containing 40.9% H_2, 20.2% CH_4, 19.8% C_2H_6, 9.2% C_3H_8 and 9.9% C_4H_{10} (mole %) at 50 psig was used as the feed gas and a purge gas consisting of H_2, CH_4 and C_2H_6 mixtures (typical PSA waste of Figure 3) was passed through the module in a countercurrent direction to the feed gas flow. The module was operated at -11.0°C and 25°C. It was found that the membrane could be used to produce a H_2-enriched gas containing 56.0% H_2 while rejecting (to the lower pressure side) 100.0% C_4H_{10}, 92.0% C_3H_8, 67.5% C_2H_6 and 36.0% CH_4. The H_2 recovery in the membrane was 63.0%. The H_2-rich gas was produced at 48 psig from the membrane unit (see Figure 3). These membrane clearly show Selective Surface Flow properties --- high rejection of heavier hydrocarbons and high hydrogen recovery at feed pressure.

The hydrocarbon-rich membrane reject gas could be used as fuel. The recovered H_2-rich gas from the membrane could be further compressed to a pressure of 200 psig and fed to a conventional PSA system in order to produce a 99.99+% H_2 product with an overall H_2 recovery of ~43.0% from the waste feed gas. Thus, the nanoporous membrane can be used to recover a valuable chemical (H_2) from a waste gas using only one compressor between the high pressure effluent and the PSA system.

A comparison of the relative energy requirement for recovering H_2 by this process and to make hydrogen using conventional Steam-methane reforming shows that the membrane/PSA hybrid process requires 15% energy less than reforming [6].

4.2 Enhanced Hydrogen Recovery in Hydrogen Manufacture

Steam Methane Reforming (SMR) followed by separation of the reformer product (typically 75% H_2, 20% CO_2, 4% CO, and 1% CH_4) in a pressure swing adsorption (PSA) system is the method of choice for H_2 manufacture today. The reject stream from the PSA (5 psig) contains a significant amount of hydrogen (approximately 20% of the PSA feed) which is used as fuel for the reformer (See Figure 4). The H_2 in PSA reject stream cannot be economically recovered by conventional technology because the hydrogen concentration and pressure are low.

SSF™ membranes have the advantage of operating very efficiently even at low pressures. These membranes can be used to increase the overall hydrogen recovery of the SMR/PSA process by recovering and recycling part of the hydrogen from PSA reject gas. A schematic diagram of the process patented by Air Products and Chemicals, Inc. [5] is shown in Figure 5. The reject of the PSA is compressed from 5 to 30 psig. An SSF™ membrane module is then used to selectively remove CO_2, CO and CH_4 and enrich the hydrogen. The enriched hydrogen product from the membrane can be compressed and recycled to the PSA unit. A countercurrent CH_4 sweep gas is used on the low-pressure side of the membrane at 3 psig.

The performance of the SSF™ membranes for separation of CO_2 and CH_4 from H_2 was measured at 294K using a feed gas containing 35% H_2, 55% CO_2, and 10% CH_4. It was assumed that CO behaves similar to CH_4. The feed pressure was maintained at 30 psig and a low-pressure CH_4 sweep gas used at a flowrate of 15% of the feed flowrate and pressure of 3 psig. Under these conditions, the membrane was able to reject 87.5% of the CO_2, 64.3% of the CH_4 while recovering 55% of the H_2.

The overall hydrogen recovery from a SMR/PSA system shown in Figure 5 was calculated using the above membrane performance. The membrane selectively rejects the CO_2, CO and CH_4 thereby reducing the flow of the recycle stream to the PSA feed and enriching the H_2 concentration. The addition of the recycle does not significantly change the PSA feed composition so that the PSA H_2 recovery remains constant. The overall hydrogen recovery for this process was 89.9% compared to a hydrogen recovery of 80% for the base case without the SSF membrane. This significant improvement in H_2 recovery is only possible because the SSF™ membrane can be operated efficiently at such low feed-gas pressure.

5. Summary

A novel microporous carbon membrane has been developed that uses adsorption and surface flow as the means of gas separation. These membranes have significant advantages in terms of energy efficiency and overall process performance for the separation of H_2 from refinery waste gas streams compared to conventional methods.

6. References:

1.M. B. Rao and S. Sircar, " Nanoporous Carbon Membranes for Separation of Gas Mixtures by Selective Surface Flow," J. Membrane Sci., 85, 253 (1993).

2.L. Lancelin, E. Rudelstrofer, M. A. Scholler, "Hydrogen Purification by Pressure Swing Adsorption," Hydrogen Symposium of the French Association of Petrochemicals Engineers, Feb. 26, 1976.

3 K. J. Doshi, U.S. Patent 4,460,695 (1987).

4. M. B. Rao, S. Sircar, J. M. Abrardo, and W. F. Baade, U. S. Patent 5,447,559 (1995).

5. M. Anand, M. B. Rao, and S. Sircar, U. S. Patent 5,435,836 (1995).

6. DOE Report, "Novel Selective Surface Flow Membranes for Recovery Of Hydrogen From Was Gas Streams," Work performed under Co-operative Agreement No. DE-FC04-93AL94461, August 1995.
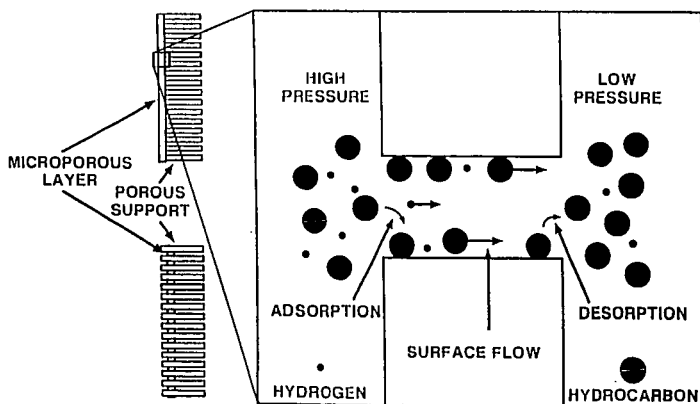
Figure 1: Mechanism of Gas Separation by Selective Surface Flow
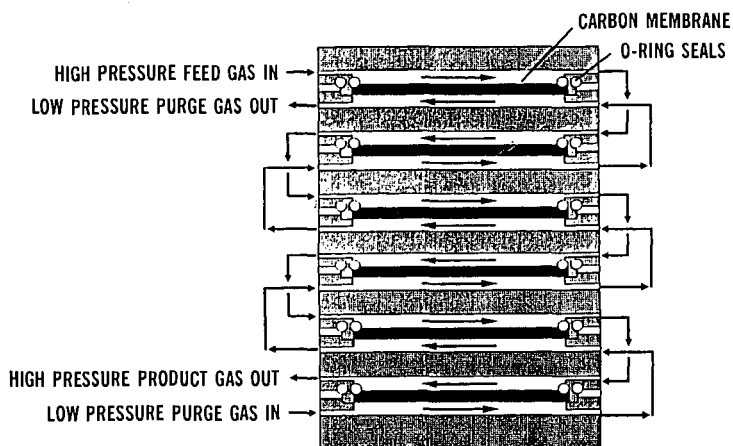
Figure 2: Plate-and-Frame Membrane Module

REFINERY WASTE GAS

50 psig
-11.0°C

40.9% H_2
20.2% CH_4
19.8% C_2H_6
9.2% C_3H_8
9.9% C_4H_{10}

MEMBRANE

250 psig
56.0% H_2

4.0A
COMPRESSOR

H_2 PSA SYSTEM

H_2 PRODUCT
99.99+% H_2

TO FUEL

5 psig
MEMBRANE PERFORMANCE

100.0% C_4H_{10} REJECTION
91.1% C_3H_8 REJECTION
67.5% C_2H_6 REJECTION
36.0% CH_4 REJECTION
H_2 RECOVERY = 63.0%
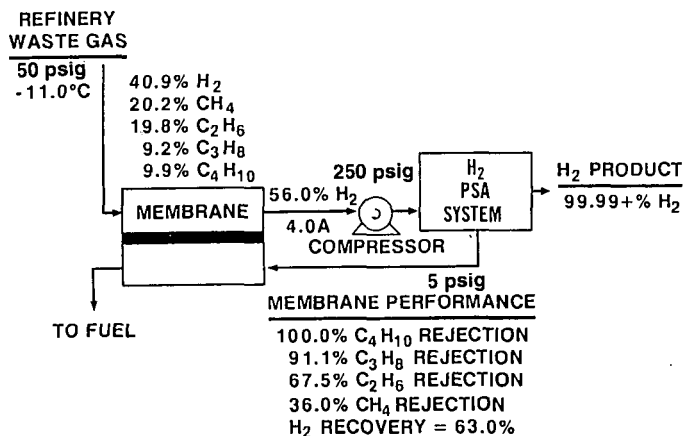
Figure 3: Process for Recovery of H_2 from Refinery Waste Streams

SMR PRODUCT
75% H_2 20% CO_2
4% CH_4 1% CO

P = 250 psig

H_2 PSA

H_2 Recovery = 80%
99.9+% H_2 Product

250 psig

P = 3 psig
PSA Reject to SMR Fuel

Figure 4: Conventional Process for H_2 Production

397

Figure 5: Enhanced H_2 Production using SSF Membranes

ADSORPTION TECHNOLOGY BRINGS WASTE INCINERATORS INTO COMPLIANCE
- STEAG'S /a/c/t™-PROCESS IN EUROPEAN FACILITIES -

Hermann Brüggendick, Ralf Gilgen
STEAG AG
Ruettenscheider Strasse 1 -3
45128 Essen, Germany

ABSTRACT

Due to the stringent emission limits for waste incinerators in Europe, the use of activated carbon technology became necessary.
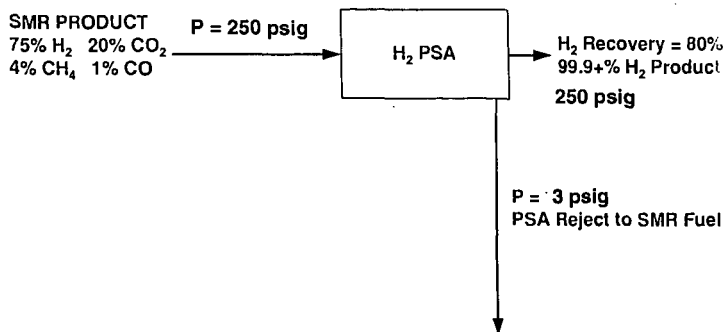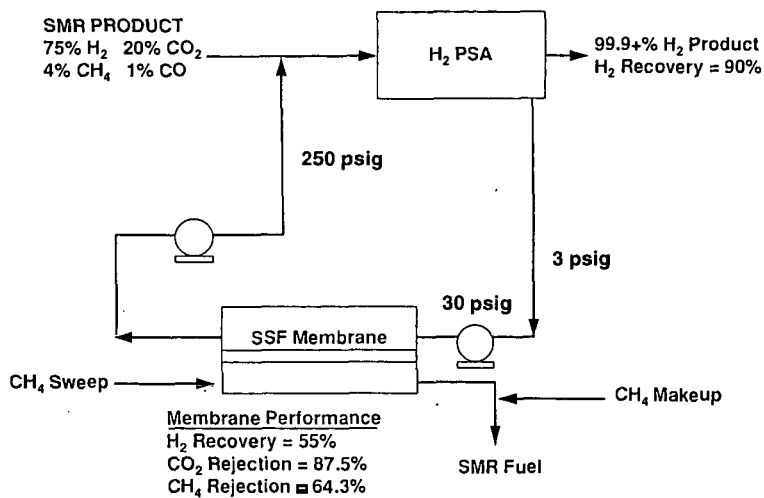STEAG is a licensor for the design and construction of an activated carbon fixed bed adsorber , the so called /a/c/t™-process with licensees in Europe and the United States.
The following paper provides a short desription of this technology and experience in commisioning and operation of the system.
The effectiveness of the /a/c/t™-process is demonstrated.

Emission control is an issue affecting many different sectors of industry. Some of the most stringent regulations apply to waste incinerators and Waste-to-Energy facilities.

Activated carbon technology is used in Europe to comply with these regulations. This technology makes it possible to reduce dioxin, furan, heavy metal, sulfur and acid emissions far below the required limits. Activated carbon processes are installed in Europe downstream of the flue gas desulfurization at medical, hazardous and municipal waste incineration plants.

The development of this technology occurred when the legal emission limits in Germany, the Netherlands, and Austria were tightened significantly.

Table 1 shows a comparison of the current legal emission limits in Europe and the United States.

STEAG has nearly 20 years experience in carbon technology. Since 1978 STEAG operates pilot plants to investigate the efficiency of this technology and to optimize the process. This resulted in the the "know-how" needed to design a cost effective adsorption system with guaranteed safe operation. Although STEAG has licensee AE&E (Austrian Energy and Environment), K+L (Kessler and Luch, Germany), and Black & Veatch (Kansas City, USA), STEAG has been involved in the design and commissioning of all /a/c/t™ facilities.

The proprietary fixed bed design is shown in figure 1. It is a cross flow fixed adsorber system. The flue gas flows horizontally through it. The bed consists of three vertical layers of activated carbon. Each layer is subdivided by perforated plates and each layer has it own coke discharge equipment so it can be moved and extracted separately and independently from the others. The first layer - the inflow layer - removes particulates, gaseous heavy metals and dioxins and furans, the second layer removes sulfur oxides ($SO_2/SO3$) and the third layer halogenated hydrogen (acid gases). The adsorbent in each layer can be replaced according to its capacity, providing the most efficient use of the carbon. The adsorption unit is designed to hold a supply of fresh carbon in a hopper at the top of the bed, which continually replenishes the supply. Each layer can be replenished individually, based on the conditions at the gas inlet. The carbon supply hopper needs to be filled only periodically. The unit's unique, patented features ensure the safe and efficient use of activated carbon while operating at temperatures between 215 to 300 F.

Since 1990, when the first contract was signed, STEAG and their licences have installed /a/c/t™-systems at 8 different sites in Europe with a total flue gas volume of more than 2.2 million dscm. Black & Veatch signed a contract to construct the first carbon adsorber of its kind in the United States. This was a team effort between Black & Veatch and STEAG.

In table 2 a reference list of the /a/c/t™--systems installed downstream of Waste Incineration plants in Europe is shown.

Following is a brief description of the operating experience at three of the European sites.

THE MUNICIPAL WASTE INCINERATOR AT AVR ROTTERDAM

This facility is the largest municipal waste incineration plant in Europe. It consists of 7 independent units, all equipped with roller grate incinerators, electrostatic precipitators, two-stage wet scrubbing systems, /a/c/t™-systems, and a low temperature SCR-DeNO$_x$. This facility has a total capacity of over 1,000,000 tons of waste per year (20 to/hr per unit).

Each unit has an a/c/t™-system consisting of two beds, which are installed parallel to the flue gas flow. The main dimensions of the adsorber are 52 ft (length), 16 ft (width), and 88 ft (height). The total filter surface is approximately 5340 sqft.

The guarantee measurements were carried out separately for each unit between April and October 1994. Table 3 presents actual measured emission values.

It can be seen, that all the emissions are clearly far below the legal emission limits and the specified levels. The carbon consumption is about 1.65 lbs/t of burned waste.

This state-of-the-art flue gas cleaning system shows impressive results, proving it is possible to operate even an old incinerator while protecting the people and the environment most effectively from air pollution.

THE HAZARDOUS WASTE INCINERATOR AT AVR ROTTERDAM

At the same site there are three rotary kilns for incineration of industrial and chemical wastes with a total capacity of approx. 80,000 tons per year of hazardous waste.

The relevant main components of this hazardous waste incineration plant are as follows: rotary kilu, waste heat boiler, spray quencher, electrostatic precipitator, two stage wet scrubbing system, /a/c/t™-system.

Trial operation of this hazardous waste incineration plant ended in October 1992, the results are shown in table 4. Several series of emission measurements have shown that the actual levels are clearly far below the emission standards and the specified levels.

400

The /a/c/t™-system is not only able to clean flue gases but also any other gases containing air pollutants.

The HCl-production facility consists of a combustor, which burns liquid chlorinated hydrocarbons. In a two stage wet scrubber with acid recirculation a purchasable hydrochloric acid is formed. The gas cleaning system consists of two-stage neutralization and an /a/c/t™-system in order to remove dioxins, furans, and other organic substances.

The /a/c/t™-system is a single bed adsorber with a height of 63 ft, a width of 17 ft, and a length of 8 ft. The total filter surface is approximately 360 sqft.

Table 5 shows a comparison of the legal emissions limits, the guaranteed values and the results of the emissions measurements

The /a/c/t™-system removes the air pollutants with a very high efficiency and helped to increase the acceptance of this facility in the surrounding region.

CONCLUSION

With the /a/c/t™-system STEAG and their licensees can provide a state-of-the-art flue gas cleaning technology with the highest removal efficiency available. This system can clean all kinds of gases containing air pollutants or odorous substances and can be operated safely and with minimum maintenance.

TABLE 1:   Legal Emission Limits for Waste Incinerators

Substance	Unit [1]	Germany[6]	Netherlands[7]	Austria[8]	European Union [3][6]	USA [4]
Total dust	mg/dscm	10	5	15	10	12
HCl	mg/dscm	10	10	10	10	32
HF	mg/dscm	1	1	0.7	1	-
SO_2	mg/dscm	50	40	50	50	67
NO_x	mg/dscm	100 [2]	70	100	-	288
Hg	mg/dscm	0.05	0.05	0.05	0.05	0.06
Cd, Tl	mg/dscm	0.05			0.05	0.01
Dioxins, Furans	mg/dscm	0.1 [5]	0.1 [5]	0.1 [5]	0.1 [5]	0.16

[1] related to 11 % oxygen, dry at 273 K and 1 atm   [2] general value-depending on local standards
[3] guideline   [4] municipal waste incinerators only   [5] corrected by toxic equivalent factors
[6] one day mean value   [7] one hour mean value [8] half hour mean value

TABLE 2: Reference list of the /a/c/t™--systems installed downstream of Waste Incineration plants in Europe.

Type	Location	Owner/Operator	Commissioning	Flue gas Volume/dscm
Medical waste	Heidelberg, Germany	University	Oct 1991	2 x 6,500
Hazardous waste	Rotterdam, Netherlands	AVR Chemie	Oct 1992	1 x 77,000
Industrial flue gas	Freiberg, Germany	NE-Metall GmbH	Jun 1993	1 x 1,500
Municipal waste	Rotterdam, Netherlands	AVR	Nov 1993	6 x 155,000
Municipal waste	Essen, Germany	RWE-Energie AG	May 1995	4 x 168,000
Municipal waste	Wels, Austria	WAV	Jul 1995	1 x 55,000
Municipal waste	Mannheim Germany	RHE	Jun 1995	1 x 295,000
Municipal waste	Rotterdam, Netherlands	AVR	Aug 1995	1 x 155,000
Industr. flue gas	Rheinberg, Germany	Solvay GmbH	Apr 1995	1 x 15,380
Crematory	Gießen, Germany	Stadt Giessen	Dec 1993	1 x 1,500
Liq. hazard. waste	Southeast, USA	Commercial Fac.	N/A	1 x 28,000

TABLE 3: Results of the Emission Measurements at AVR Rotterdam (unit 1 to 6, unit 7 under construction)

Substance	Unit	RV[1] 1989	Unit 1	Unit 2	Unit 3	Unit 4	Unit 5	Unit 6
Dust	mg/Nm³	5	< 1.0	< 1.0	< 1.0	< 1.0	< 1.0	< 1.0
HCl	mg/Nm³	10	0.9	< 0.7	1.0	1.8	< 0.5	< 0.6
HF	mg/Nm³	1	< 0.4	< 0.2	< 0.4	< 0.4	< 0.1	< 0.1
SO_x (as SO_2)	mg/Nm³	40	12	< 5	23	11	< 5	< 5
SO_x (as NO_2)	mg/Nm³	70	36	32	36	41	23	26
Cd	mg/Nm³	0.05	< 0.003	< 0.001	< 0.003	< 0.003	< 0.001	< 0.001
Hg	mg/Nm³	0.05	0.03	0.003	0.002	0.004	0.001	0.001
As, Co, Cu, Cr, Mn, Ni, Pb, Sb, Se, Sn, Te, V	mg/Nm³	1	0.030	< 0.050	0.03	0.04	< 0.050	< 0.050
PCDD/F (TEQ)	ng/Nm³	0.1	0.01	0.030	0.01	0.015	0.013	0.009

[1] RV means: Dutch legal emission limits   All values refer to standard condition (273 K, 1013 hPa dry) and 11 % O_2

TABLE 4: Emission Measurements at AVR Rotterdam Hazardous Waste Incineration Plant

	Unit	RV 1989	Results of the accept. measurements Dec. 1992
Dust	mg/Nm³	5	< 0.5
HCl	mg/Nm³	10	0.19
HF	mg/Nm³	1	0.05
SO_2	mg/Nm³	40	6
Cd	mg/Nm³	0.05	< 0.0001
Hg	mg/Nm³	0.05	0.0022
Sb, As, Pb, Cr, Co, Cu, Mn, Ni, V, Sn, Se, Te	mg/Nm³	1	< 0.025
PCDD/PCDF in TEQ	ng/Nm³	0.1	0.03

RV means: Dutch legal emission limits

TABLE 5: Comparison of the legal emissions limits, the guaranteed values and the results of the emissions measurements

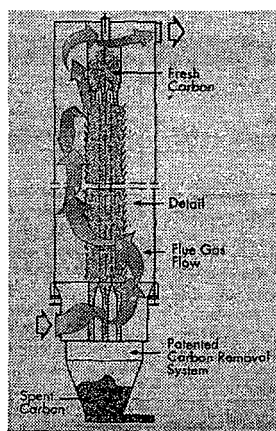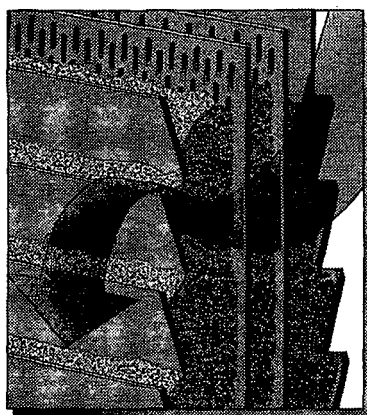| Chemical Compounds	Unit	Emission Standards as per Clean Air Act 17. BImSchV	Guaranteed Emissions	Measured Emissions Mean values over the sampling time
Total Dust	mg/dscm	10	5	< 1
HCl	mg/dscm	10	10	4
HF	mg/dscm	1	0.1	not detected
SO_2	mg/dscm	50	5	not detected
Hg	mg/dscm	0.05	0.03	not detected
Dioxins, Furans	ng/dscm TE	0.1	0.05	not yet measured

Figure 1: STEAG's /a/c/t™-process

THE COMBINED SOX / NOX / AIR TOXICS REDUCTION PROCESS USING ACTIVATED COKE FOR FLUE GAS CLEANUP

Kazuhiko Tsuji   and   Ikuo Shiraishi
Mitsui Mining Company Ltd.,
1-3 Hibikimachi, Wakamatsu Ward
Kitakyusyu City, Fukuoka,808 JAPAN

INTRODUCTION

The dry desulfurization and denitrification process using activated coke(AC) as a dry type flue gas cleanup technology was originally researched and developed during the nineteen-sixties by Bergbau Forschung(BF) [1] , now called Deutsche Montan Technologies.   Mitsui Mining company(MMC) concluded a licensing agreement with BF in 1982 to investigate, test and adapt the system to the facilities in Japan where the regulations are stricter towords SOx/NOx pollutants, as well as dust emissions from utility industries, oil refineries, and other industries.   There are three commercial plants of this process installed to coal fired boiler, FCC units, and incinerator in Japan and two plants in Germany(the latter two plants were constructed by Uhde GmbH).   Recently, the capability of AC process to adsorb and reduce toxic trace materials, such as Hg vapor and dioxines, is attractive for flue gas cleanup of waste incinerators or coal combustion boilers.   General Electric Environmental Services, Inc.(GEESI) signed a license agreement in 1992 with MMC.   Under this agreement, GEESI will market, design, fabricate and install the AC process for flue gas cleaning applications in North America.

MMC also developed a technology to produce activated coke to be used in the DeSOx/DeNOx process, based on our own metallurgical coke manufacturing technology.   The commecial plant with the capacity of 3,000tons per year to produce MMC's activated coke has been in operation.

We have a plan to construct a larger plant of activated coke production in Japan preparing for the increase of demands for AC process in the near future.

In this paper,we would like to present some data of DeSOx, DeNOx and toxic removal with MMC's AC, which include basic data from laboratory tests, characteristic data of sampled AC from test plants, and performance data of commercial plants.   Furthermore, we will put a focus on the relationship of the DeSOx and DeNOx activities of AC to the surface functionalities of chemically modified AC in both labo. tests and pilot tests.

MMC's ACTEVATED COKE AND GE-MITSUI-BF PROCESS

Activated coke(AC) is a formed carbonaceous material designed for dry DeSOx/DeNOx and Toxic removal process of flue gas cleanup.   For this purpose, we selected a suitable raw coal from bituminous coals and investigated an appropriate process for production [2] , which include a pretreatment of raw coal, blending of raw materials, briquetting, carbonization and activation, to give AC high DeSOx/DeNOx activities and high mechanical strength against abrasion and crush during circulation and handling in the flue gas cleanup process.

There are several differences in characteristics of MMC's AC compared to an activated carbon using criteria such as gas recovering or deoderizing processes.   BET surface area of MMC's AC is 150-250m^2/g, which is less than one-third that of activated carbon.   BET surface area of the carbon materials represents their micro-porous structure, which becomes larger during the manufacturing process where the chemical activation condition is severe.   As the activation becomes more severe, the yield of the product decreases and the mechanical strength of the product falls.   A decrease in yield results in increased product cost and a decrease in mechanical strength causes greater material loss during the flue gas cleanup process.   As MMC's AC is processed with a temperate activation procedure, it is one-fourth to one-third the price and has a higher mechanical strength compared to activated carbon.   MMC's AC also has advantages in its abilities to remove SOx and NOx as compared with activated carbon.

Figure 1 illustrates a schematic of the GE-Mitsui-BF DeSOx/DeNOx/Toxic removal process, which is designed for SOx/NOx containing flue gas treatment system consisting of twin AC beds and an AC regenerator.   In this system, AC moves continuously from top to bottom through the AC beds.   The regenerated AC with some part of fresh make-up AC enters in DeNOx zone(I) at first, where NOx reduction occurs with the addition of NH₃.   The discharged AC from I enters into DeSOx zone(II), where the majority of the SOx and air toxics adsorption and the minor NOx reduction without NH₃ (we call now non-SCR DeNOx) occur.   The SOx/air toxics-loaded AC discharged from II is sent to the regenerator by backet conveyers.   In the case of NOx with low-SOx or SOx with low-NOx containing flu gas treatments, single AC bed system can be designed.   Table 1 summarizes a designed system, efficiencies and applications of GE-Mitsui-BF process.

DESULFURIZATION (DESOX) WITH ACTIVATED COKE

Figure 2 shows the SO$_2$ adsorption capacity of activated coke and a commercial activated carbon with fresh one and used one. With fresh one, the SO$_2$ adsorption capacity becomes higher as surface area of adsorbent increases. On the other hand, with used one, which has experienced four times of desulfurization−regeneration cycle of labo. test, SO$_2$ adsorption capacity of the used activated carbon drastically decreased to about one−third of the fresh one, while the used activated cokes, having lower surface area and still less micro−porous than activated carbon, are less influenced. There has been several observations [3, 4] of the similar phenomenon with activated carbons of those surface area ranging 300−900m^2/g, where a marked decrease in adsorbed SO$_2$ amount along with cycle has been explained due to the increase in the amount of acidic groups on the surface of activated carbons. It is supposed that there is an appropriate activation level where the SO$_2$ adsorption capacity is less influenced with the cycle of SO$_2$ adsorption−desorption. MMC's activated coke seems to be on a such level. It has been confirmed that MMC's activated coke keeps a stable deSOx performance during the process [5].
Table 2 shows the characteristics and the deSOx activities measured in labo. test with MMC's activated coke, fresh one and used ones, which were sampled from two test plants under operation. Used ones are characterized with an enlarged surface area, an increased O/C and N/C values, and an enhanced deSOx activity than fresh one. These changes in characteristics are derived from operation conditions, such as the molar ratio of adsorbed NH$_3$ −SOx species on AC and the types of reactions(oxidation−reduction) between NH$_3$ −SOx species and AC surface in regenerator. It is noticiable that the surface area and O/C value are higher in used I (the adsorbed NH$_3$/SOx molar ratio is approx. 0.2) and N/C value is higher in used II (the ratio is approx. 1.5). The increased deSOx activities(η SOx %) of used AC to fresh one relate to both the surface area enlargement and the modified surface functionality. It is supposed that k(rate constant) especially correlates to N/C and q$_0$ (adsorption capacity) relatively correlates to surface area. η SOx is the highest in used II , supporting that N/C is the most influencing factor to deSOx rate.
It has been reported that nitrogen−containing activated carbon [6] and activated carbon fiber [7] from PAN and brown coal char via sulfuric acid activation followed by ammonia treatment [8] show the remarkable high deSOx activities.

DENITRIFICATION (DENOX) WITH ACTIVATED COKE

Figure 3 shows the profiles of two types DeNOx(SCR and non−SCR) reactions in labo. tests with the used II AC(Table 2), which exhibited a high non−SCR DeNOx activity. Non−SCR DeNOx proceeds without NH$_3$ in gas phase and an active N−species on AC surface seems to react with NOx, because non−SCR activity is deactivated along with reaction time. NH$_3$ treatment at 400−500 ℃ is effective to reactivate AC for the non−SCR reaction. There has been several observations of the effects of NH$_3$ treatment to the preoxidized activated carbon [9] and brown coal char [8] on the enhancement of their SCR DeNOx activities. Now, we would like to put attention upon the non−SCR DeNOx activity of AC and have interest in the effect of NH$_3$ treatment on the non−SCR DeNOx activity of AC, because the non−SCR DeNOx is useful as a no NH$_3$ leakage process for flue gas cleanup with AC. We can expect to remove approx. 10−20% of inlet NOx concentration with non−SCR DeNOx in the DeSOx zone, where no NH$_3$ is added in gas phase, under coexisting of high SOx concentration in the DeSOx/DeNOx proces(Figure 1).
The efficiency of non−SCR DeNOx becomes higher in proportion with lowering of inlet NOx concentration. Figure 4 shows approx. 60−70% high efficiencies of non−SCR DeNOx with 24ppm of inlet NOx concentration. Figure 4 also shows the increasing non−SCR DeNOx efficiency along with a cycle testing, where simultaneous deSOx/deNOx run, regeneration after the run and NH$_3$ treatment at 500 ℃ to the regenerated AC were cycled 10 times, showing the effect of NH$_3$ treatment. DeSOx efficiency is also increasing with this cycle test, supporting the effect of NH$_3$ treatment on the DeSOx activity of AC(former discussion). Figure 5 shows the increasing non−SCR DeNOx efficiency with increase of NH$_3$ treatment amount. Although we scarcely have informations to identify an active N−species on AC surface, it is probably thinkable that an active N−species being produced by NH$_3$ treatment contributes to the non−SCR DeNOx reaction.

TOXIC REDUCTION WITH ACTIVATED COKE

The AC process can also remove trace toxic compounds such as mercury and dioxines that are present in waste incinerator flue gas. Several pilot and demonstration tests [10, 11] have been done to confirm the ability of the AC process to remove NOx and trace toxic compounds with AC from waste incinerator flue gas at low temperature, where the mercury removal efficiencies of approx. 80−90% at 150−180 ℃ and the dioxines removal efficiencies of approx. 90−98% at the same temperature range were observed.
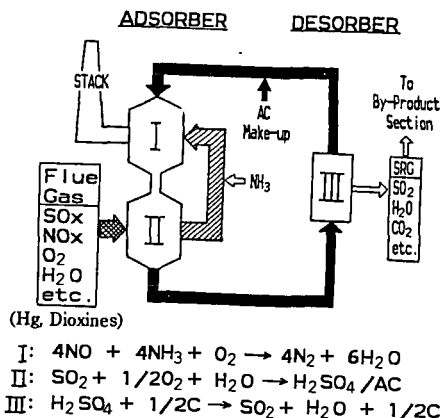
CONCLUSION

- The dry DeSOx/DeNOx/Toxic removal process with activated coke is applicable for various flue gas cleanup with high efficiencies(Table 1).
- Activated coke has an appropriate activation level where the SO_2 adsorption capacity is less influenced with the cycle of SO_2 adsorption—desorption. It has been confirmed that MMC's activated coke keeps a stable deSOx performance during flue gas cleanup process.
  It is supposing that N/C value of AC is influencing factor to the deSOx activity.
- Activated coke has non—SCR DeNOx activity, which proceeds without NH_3 in the gas phase. The non—SCR DeNOx is useful as a no NH_3 leakage process for flu gas cleanup.
  It is supposing that an active N—species being produced by NH_3 treatment at 400—500 °C contributes to non—SCR DeNOx reaction.
- Activated coke can also remove trace toxic compounds such as mercury and dioxines with high efficiencies from flue gases of waste incinerators and coal combustion boilers at low temperature.

REFERENCES

*1) Knoblauch,K., Richter,E., Juntgen,H. Fuel 1981, 60, 832.
*2) Komatsubara,Y., Yano,M., Shiraishi,I. and Ida,S.
   Proceedings of 16th Biennial Conference on Carbon 1983, 325.
*3) Davini,P. Carbon 1991, 29, 321.
*4) Carrasco—Marin,F., Utrera—Hidalgo,E., Rivera—Utrilla,J. and Moreno—Castilla,C.
   Fuel 1992, 71, 575.
*5) Tsuji,K. and Shiraishi,I.
   Proceedings of the 1991 SO2 Control Symposium 1991, 307.
*6) Nishijima,A., Hagiwara,H., Kurita,M., Ueno,A., Sato,T., Kiyozumi,Y. and Todo,N.
   Bull.Chem.Soc.Jan. 1982, 55, 2618.
*7) Mochida,I., Kisamori,M,. Hirayama,T., Kawano,S. and Fujitsu,H.
   65th CATSJ Meeting Abstructs 1990, 105.
*8) Fujitsu,H., Mochida,I., Verheyen,T.V., Perry,G.J. and Allardice D.J.
   Fuel 1993, 72, 109.
*9) Kuhl,H., Richter,E., Knobrauch,K. and Juntgen,H.
   Reprints Carbon '86, 4th Int. Carbon Conference 1986, 351.
*10)Kimura,T., Kawamoto.K. and Satoh.M.   Proceedings of the 2nd Annual Conference of the
   Japan Society of Waste Management Experts,1991.
*11)Kimura,T., Nishihara.M., Fujinaka.K., Satoh.M. and Hamada,T. Proceedings of the 5th Annual
   Conference of the Japan Society of Waste Management Experts,1994.

I: $4NO + 4NH_3 + O_2 \rightarrow 4N_2 + 6H_2O$
II: $SO_2 + 1/2O_2 + H_2O \rightarrow H_2SO_4 /AC$
III: $H_2SO_4 + 1/2C \rightarrow SO_2 + H_2O + 1/2CO_2$

Figure 1 : The combined SOx/NOx/Air toxics reduction process using AC
(GE—Mitsui—BF Process / Schematic flow diagram with twin AC beds)

Table 1 : A designed system and efficiencies of GE−Mitsui−BF process applications

Flue Gas	Designed system	Efficiencies	Applications
SOx and NOx	Twin AC beds	· η SOx $\geq$ 98% · η NOx $\geq$ 80%	· Utility boilers · RFCC Units · Other industries
NOx 　with−low SOx	Single AC bed	· η NOx $\geq$ 80% · η SOx $\geq$ 98%	· FBC boiler · Waste incinerator (After pre−scrubber)
SOx 　with low−NOx	Single AC bed	· η SOx $\geq$ 98% · non−SCR DeNOx 　expected	· Combination with other DeNOx system

All systems can remove trace toxic materials such as Hg vapour and dioxines with high
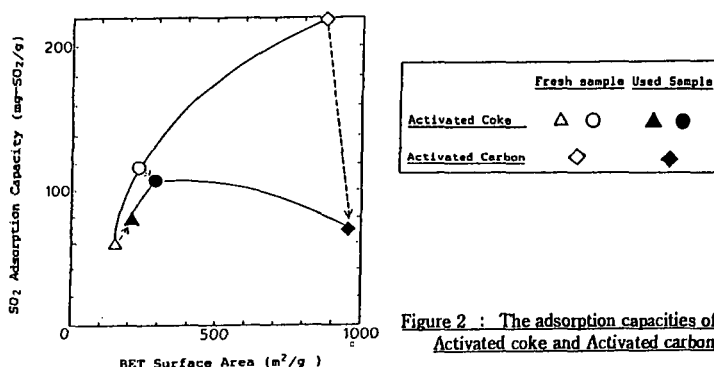efficiencies.

Figure 2 : The adsorption capacities of
Activated coke and Activated carbon

· Used samples are those after the 4th cycle of deSOx
　(SO ₂ 2000ppm, O ₂ 5%, H ₂ O 10%) at 130 ℃ and regeneration under N ₂ at 400 ℃ .
· SO ₂ adsorption capacity was measured by contacting 10cc of AC sample
　with SO ₂ containing gas flow(SO ₂ 2%, O ₂ 5%, H ₂ O 10%) at 100 ℃ for 3hours.

Table 2 : The characteristics and DeSOx activities of sampled AC from test plants

AC sample	Surface area(m ^{2} /g)		Elemental analysis		DeSOx Activity [labo. test]		
	S(CO ₂)	S(N ₂)	O/C	N/C	η SOx(%)	k(10^{-4})	q₀(10^{-2})
Fresh	150	150	0.019	0.012	64.7	3.87	0.87
Used I	300	500	0.073	0.034	91.3	4.62	2.15
Used II	230	270	0.046	0.040	98.3	5.82	1.78

· Used I and II were sampled at the operation time of approx. 4000hours from the outlet
　of regenerator of test plant I and II , respectively.
· Test plant I was a DeSOx/DeNOx plant with twin AC beds as illustrated in Figure 1.
　NH ₃ was added after DeSOx zone(II). The adsorbed NH ₃ /SOx molar ratio was approx.
　0.2 [SOx rich] with AC of the inlet of regenerator.
· Test plant II was a DeNOx plant with single AC bed, which is almost equivalent to the
　DeNOx zone(I) in Figure 1. The adsorbed NH ₃ /SOx molar ratio was approx.
　1.5 [NH ₃ rich] with AC of the inlet of regenerator.
· DeSOx activity was measured by contacting 4.3 liters of AC sample with 28.7 liters of
　SO ₂ containing gas flow (SO ₂ 2000ppm, O ₂ 5%, H ₂ O 10%) at 130 ℃ .
　η SOx is the DeSOx efficiency(average of integration during 25 hours reaction)
　k is the deSOx reaction rate constant.
　q ₀ is the amount of adsorbed SO2 at equilibrium condition.
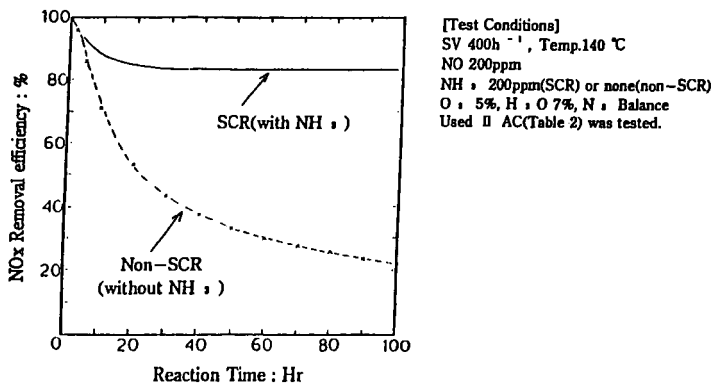
Figure 3 : The DeNOx profile of SCR and
Non−SCR reactions on Activated coke
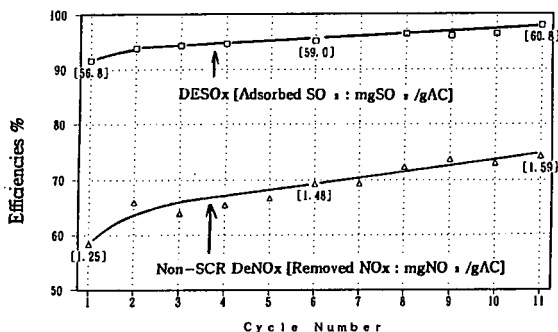
Figure 4 : The effect of NH ₃ treatment on Non−SCR DeNOx and DeSOx activities of AC

- DeSOx/DeNOx Run Conditions : SV 400h $^{-1}$, Temp.140 ℃ , Time 70Hr
  NO 24ppm, SO ₂ 500ppm, NH ₃'' 250ppm, O ₂ 5%, H ₂ O 7%, N ₂ Balance
  ")NH ₃ will react with SO ₂ almost selectively. SCR DeNOx can't proceed.
- Efficiencies denotes an average of integration during 70 hours reaction.
- NH ₃ leakage was not detected during the DeSOx/DeNOx test run.
- NH ₃ treatment (1.48ccNH ₃ /ccAC) was done at 500 ℃ to the regenerated AC
- Testing AC is a used AC sampled from another test plant differing from Ⅰ , Ⅱ (Table 2).
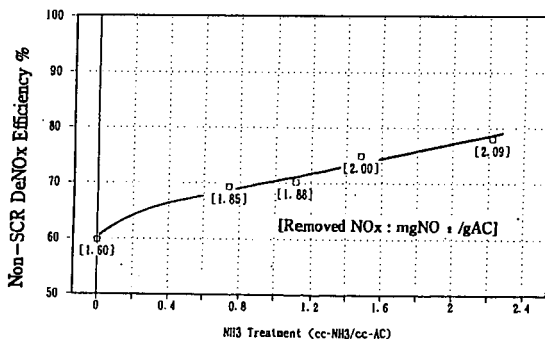
Figure 5 : Increasing Non−SCR DeNOx activity with increase of NH ₃ treatment amount

- Test conditions is the same as Figure 4.
- Used Ⅱ AC(Table 2) was tested.

The Use Of Activated Char For Flue Gas Polishing In Municipal And Hazardous Waste Combustors

Hans-Ulrich Hartenstein
L. & C. Steinmüller GmbH, Gas Cleaning Division
Fabrikstrasse 1, 51643 Gummersbach, Germany

INTRODUCTION

During the late 1980's and the early 1990's legislation on emissions from waste combustors were tightened drastically [1, 2]. Also emission limits on „new" pollutants like dioxins and furans were introduced. Since the flue gas cleaning equipment commonly used before was not designed to meet these emission limits, new technologies had to be developed. Most of these new technologies rely on the use of activated carbon or char for the adsorption of the pollutants [3].

Due to the fact that the amount of activated char used is directly proportional to the mass flow rate of pollutants entering the adsorber, the bulk part of the pollutants has been removed in the preceeding gas cleaning stages. Thus the activated char adsorption reactor is employed as a flue gas polishing stage at the end of the APC-train.

In 1984 Steinmüller and its 100 % subsidiary, Hugo Petersen, began to develop flue gas filters for large volume flow rates based on the use of activated carbon. The original goal of development was the removal of residual SO_2 left after the FGD-scrubber, in order to eliminate the problem of ammonia sulfate formation in low-dust SCR-DeNO$_x$-systems. Shortly after that the catalytic capability of activated carbon to reduce NO_x in the presence of NH_3 was recognized; as well as the suitability of this technology for the flue gas polishing of waste incinerators. In the latter case the removal capability of activated char for a wide range of different pollutants, mainly organics, like PCDD/F's, PCB's, PAH's, etc., highly toxic heavy metals such as Hg, Cd, Pb, etc. and acid gases was of primary interest.

ADSORBER DESIGN

The Steinmüller / Hugo Petersen ACR-technology follows the crossflow principle. Where as the char migrates through the ACR-adsorber vertically from top to bottom, the flue gas flows through the activated char bed horizontally. Figure 1 shows the concept of the adsorber providing a vertical cross section of an activated char bed. Each bed consists of 3 individual layers separated by a perforated shroud. Each layer can be extracted independently, according to its pressure drop, saturation or other guiding parameters. As described in previous papers [4, 5, 6] especially designed cellular discharge cylinders at the bottom of each bed allow the extraction of a precisely defined amount of activated char from each layer individually. Besides a minimization of char consumption, this multilayer design allows for the adaptation of the discharge program to the well known selective adsorption characteristics of the various pollutants [6, 7]. Figure 2 shows how the multilayer design is matched to the characteristic concentrations of adsorbed pollutants within the char bed. The fresh char is conveyed to, and evenly distributed within, the bed by screw conveyors on the top of the bed. The flue gas inlet as well as the outlet of the bed perform important tasks for the correct operation of the filters. The gas outlet insures the retention of even small char particles within the bed. The compounds with a high molecular weight are adsorbed quickly within the first few inches of the activated char, thus pushing the lower molecular weight compounds towards the end of the bed. Due to this reason HCl leaves the bed first, indicating an approaching break-through.

The size of a bed is limited due to specific restrictions, such as the height of the bed, the lengths of the screw conveyors and the discharge cylinders. In order to allow the treatment of large volume flow rates one adsorber unit can be expanded to contain 2, 4, 6 or 8 beds. In this case each bed acts as an individual module within the ACR-unit. Figure 3 shows such an arrangement. ACR's built by Steinmüller / Hugo Petersen treating volume flow rates between 5.000 and 250.000 m³/h and containing up to 8 modules are in operation in power plants as well as in municipal and hazardous waste combustors.

ACR PERFORMANCE

Extensive measurements of the performance of the ACR-technology were obtained at various full scale installations. Among those were municipal as well as hazardous waste combustors in Holland as well as in Germany.

Table I presents a summary of the emission data collected at these facilities. It has to be pointed out that the extremely low emission values reported were measured over a longer period of time, thus accounting for the fluctuations in the inlet pollutant concentration.

The removal efficiency for acid gases, heavy metals and high molecular weight organics was determined to range in the 99.9 % to + 99.99 % region. Especially for acid gases the buffering capacity of the ACR-plant is remarkable. The outlet value of below 1 mg/m^3 @ STP for SO_2, for example, remained unaffected even by extremely high peak inlet concentrations of up to 700 mg/m^3 @ STP.

Due to the very low outlet concentrations of the various pollutants, significant difficulties were encountered concerning sampling and analysis. Very much care has to be taken regarding the stack sampling and analytical procedures in the lab in order to ensure a reasonable accuracy and precision of the results.

ACR-RETROFITS TO EXISTING MWC'S AND HWC'S

During the early 1980's a significant number of MWC's and few HWC's were built using an APC-train comprised of an ESP, a spray dryer and a baghouse. Representing the state-of-the-art technology 10 to 15 years ago, these APC-trains are unable to meet the stringent emission limits introduced in the early 1990's. Therefore those plants had to be retrofitted. A spray dryer / baghouse combination is capable of removing 90 to 95 % of the pollutants. However, it usually fails to meet the required emission limits by a factor of 1.5 to 2 for the acid gases, and by a factor of 2 to 4 for the heavy metals and the organics. Even though these factors seem high, they represent only a rather small mass flow rate of pollutants. Combined with the fact that the flue gas temperature at the outlet of the spray dryer / baghouse system is commonly adjusted to around 140°C, this makes an excellent basis for a retrofit using the ACR-technology. Figure 4 shows a process flow scheme of such a retrofit at a MWC. The temperature of 140°C is ideally suited for the ACR by being low enough for enhanced adsorption and high enough to avoid any condensation of moisture and/or acids. In most cases a Low Temperature SCR (LTSCR) DeNO$_x$ plant is added at the end of the train. Due to the virtual absence of any pollutants after the ACR, the SCR operational temperature can be reduced to as low as 150 -170°C. This makes the use of SCR a very economical alternative to SNCR, avoiding NH$_3$-contamination of the fly ash and the spray dryer/baghouse residue. NH$_3$-contents typically found after SNCR increase the disposal cost of these residues significantly.

Most HWC's built in Europe were equipped with wet scrubbers, even before 1990. The most common APC-train used on HWC's was an ESP followed by a one or two stage HCl-scrubber operated at a pH below 2 and a SO$_2$-scrubber operated of a pH of around 5 to 6. These systems are better suited to handle the significantly higher pollutant concentrations of HWC's at the inlet of the APC-train. Besides the possibility of retrofitting these facilities with an ACR / LTSCR combination as described above, another option is to add an ACR / ACCR combination as presented in Figure 5. This 125 tpd HWC was retrofitted with an ACR and the ACCR-DeNOx system [8]. Both the ACR and ACCR are combined in one reactor with the NH$_3$-injection system upstream of the ACR. In the ACR lignite based hearth oven char (HOC) is used, whereas the ACCR utilizes the catalytic capabilities of hard coal based form activated carbon (FAC). The plant has been in operation since 1991 and NO$_x$ emission values of less than 100 mg/m^3 @ STP, 11 % O$_2$ have been obtained continuously. The advantage of ACCR is its low operating temperature of between 120°C and 140°C. Its disadvantage is that high NO$_x$-removal efficiencies (> 85 %) cannot be realized due to the catalytic limitations of the activated carbon [8].

ACR FOR NEW MWC'S and HWC'S

In new installations, the ACR forms an integrated part of the APC-train. As presented in Figure 6 such a modern five-stage gas cleaning system is designed to achieve the lowest possible emission limits. Thus a baghouse is employed to insure the best possible removal of particulate matter.

It is followed by a multi-stage wet scrubbing system designed to recover hydrochloric acid from the removed HCl and wall board quality gypsum from neutralized SO_2 [9]. The heat losses through evaporation in the scrubbers are minimized by employing a cross-flow heat exchanger. It cools the flue gas before entering the first scrubber and then reheats the flue gas after leaving the second scrubber. Thus the flue gas is prepared for the final polishing by the ACR before it enters the stack via a LTSCR-DeNO$_x$ plant. To adjust for the appropriate LTSCR-temperature the compression heat liberated in the fan is utilized. The remaining heating is done by a low pressure steam heater. The specific advantages of LTSCR as described elsewhere [10] are ideally enhanced in combination with an ACR.

CONCLUSION
Today, little over 5 years after the introduction of new and stringent emission regulations for MWC's and HWC's, ACR ist a well proven, accepted technology. Table II provides a list of installations of new and retrofitted MWC's and HWC's in Holland, Germany and Austria employing ACR. In these countries the market share of the ACR-technology with respect to other technologies ist about 35 % in the retrofit market and about 65 % in the market for new facilities. The ACR-technology developed by Steinmüller / Hugo Petersen was not only the first of its kind but still leads the way. As can be seen in Table III, Steinmüller / Hugo Petersen holds about 50 % of the ACR-market for power plants and municipal and hazardous waste combustors. The ACR-technology integrated in a modern state-of-the-art multi-stage APC-train represents the leading edge of pollution control for HWC's and MWC's. The fast increasing interest in this technology, especially in environmentally aware countries like Japan, South Korea, Taiwan and the US-leads to the expectation that ACR will soon be considered the best available control technology not only in Europe but all over the world as well.

REFERENCES
[1] „Siebzehnte Verordnung zur Durchführung des Bundes-Immissionsschutzgesetztes (Verordnung über Verbrennungsanlagen für Abfälle und ähnliche brennbare Stoffe - 17. BlmSchV) vom 23. November 1990", Bundesgesetzblatt Nr. 64, Teil 1, FRG 1990

[2] „Planfeststellungsbeschluß für das Restmüllheizkraftwerk Böblingen des Zweckverbandes Restmüllheizkraftwerk Böblingen", Regierungspräsidium Stuttgart, Breitscheidstraße 4, 70174 Stuttgart, FRG 1994

[3] H.-U. Hartenstein, B. Söhndel, „The Status of the Waste-to-Energy Technology in Central Europe", presented at the 3rd International Conference on Municipal Waste Combustion, Williamsburg VA, USA 1993

[4] H.-U. Hartenstein, H. Hemschemeier, „Retroffitting of an Existing Hazardous Waste Incineration Plant With an Activated Carbon Filter for Removal of Dioxins and other Air Toxics", presented at the Dioxin 1991/EPRI-Seminar, North Carolina, USA 1991

[5] H.-U. Hartenstein, „Fixed Bed Activated Coke Filters for the Control of Toxic Metals and Organics from Waste Incinerators - the Second Generation", presented at the 86th Annual AWMA Meeting, Denver CO, USA 1993

[6] H.-U. Hartenstein, „Activated Carbon Filters for Flue Gas Polishing of MWI's" presented at the 3rd International Conference on Municipal Waste Combustion, Williamsburg VA, USA 1993

[7] H.-U. Hartenstein, „The retrofit of the MWC ROTEB in Rotterdam, Holland with a modern flue gas cleaning system including an activated char adsorption unit", presented at ASME 16th National Waste Processing Conference & Second Annual North American Waste-to-Energy Conference, Boston MA, USA 1994

[8] H.-U. Hartenstein, „A Fixed Bed Activated Coke/Carbon Filter as a Final Gas Cleaning Stage Retrofitted for a Hazardous Waste Incineration Plant - The First 6 Months of Operation Experience", presented at the 5th Annual AWMA Meeting, Kansas City MO, USA 1992

[9] H.-U. Hartenstein, „Recycling of Residuals from Flue Gas Treatment of Municipal and Hazardous Waste Incinerators", presented at the 86th Annual AWMA Meeting & Exhibition, Denver CO, USA 1993

[10] H.-U. Hartenstein, A. Licata. „The Application of Low Temperature SCR for Municipal and Hazardous Waste Combustors", presented at ASME 17th Biennial Waste Processing Concerence & Nawtec-IV: North American Waste-to-Energy Conference, Atlantic City NJ, USA 1996

Table I Emission Data Obtained at Various Full-Scale MWC's and HWC's

Group	Compound	Data- 1	2	Points 3	4	Unit
Acid Gases	SO₂	0.11	0.20	0.47	0.14	mg/m³
	SO₃	0.04	0.07	0.03	0.06	mg/m³
	HCl	0.84	0.45	0.63	0.79	mg/m³
	HF	0.03	0.02	0.03	0.02	mg/m³
	HBr	0.07	0.15	0.13	0.07	mg/m³
	HJ	0.10	0.19	0.22	0.10	mg/m³
Heavy Metals	Sb	< 3	< 6	< 4	< 4	µg/m³
	As	< 5	< 7	< 8	< 7	µg/m³
	Cd	< 0.5	< 0.9	< 0.8	< 0.7	µg/m³
	Co	< 3	< 4	< 4	< 4	µg/m³
	Cr	< 3	< 4	< 4	< 4	µg/m³
	Cu	< 4	< 5	< 5	< 15	µg/m³
	Pb	< 5	< 8	< 8	< 7	µg/m³
	Mu	< 3	< 8	< 5	< 4	µg/m³
	Hg	< 0.9	< 1.1	< 0.7	< 0.9	µg/m³
	Ni	< 3	< 4	< 4	< 4	µg/m³
	Te	< 0.3	< 0.4	< 0.4	< 0.4	µg/m³
	Sn	< 3	< 8	< 4	< 8	µg/m³
	V	< 3	< 4	< 4	< 4	µg/m³
Other Elements	Al	257	97	278	93	µg/m³
	Ba	6	11	15	10	µg/m³
	Be	< 0,5	< 0.7	< 0.8	< 0.7	µg/m³
	B	52	27	46	48	µg/m³
	Fe	22	41	120	52	µg/m³
	Mg	16	29	36	29	µg/m³
	K	52	104	99	60	µg/m³
	Se	< 5	< 7	< 7	< 8	µg/m³
	Si	78	45	34	80	µg/m³
	Ag	< 3	< 4	< 4	< 4	µg/m³
	Na	279	665	405	321	µg/m³
	Te	< 9	< 15	< 14	< 13	µg/m³
	Zn	10	23	19	26	µg/m³
Organics	PCDD			0.0238	0.0261	ng/m3
	PCDF			0.0222	0.0223	ng/m3
	TEQ (NATO CCMS incl ½ the detection limits)			0.0009	0.0014	ng/m3
	PBrDD			< 0.760	< 0.815	ng/m3
	PBrDF			< 0.760	< 0.815	ng/m3
	PAH (E/PA/ 610)			6.282	4.146	ng/m3
	PCB₂ (Di-Hexa)			3.2	1.8	ng/m3
	PCP₁			12.3	9.2	ng/m3
	PCB (Ballschmiter)			10.4	10.4	ng/m3
	Benzene			< 95	< 90	µg/m³
	Toluene			< 95	< 90	µg/m³
	Ethylbenezne			< 95	< 90	µg/m³
	p- and m-Xylene			< 95	< 90	µg/m³
	O-Xylene			< 95	< 90	µg/m³
	Dichloromethane			< 160	< 150	µg/m³
	1-1, Dichloroethane			< 265	< 250	µg/m³
	Trichloromethane			2	2	µg/m³
	1-1-1, Trichchloromethane			< 1.1	< 1	µg/m³
	Tetrachloromethane			< 1.1	< 1	µg/m³
	Trichloroethene			< 1.1	< 1	µg/m³
	Tetrachloroethene			< 1.1	< 1	µg/m³
	1-1-2, Tetrachloroethane			< 1.1	< 1	µg/m³
	1-1-2-2, Tetrachloroethane			< 11	< 1	µg/m³
	trans-1-2, Dichloroethene			< 160	< 150	µg/m³
	cis-1-1, Dichloroethene			< 160	< 250	µg/m³
	Dichlorobromomenthane			< 1.1	< 1	µg/m³
	Dibromochloromethane			< 1.1	< 1	µg/m³

< means that the actual value is below the given number, which represents the dection limit

Table II — List of Installations equipped with activated char adsorbers in Austria, Germany and the Netherlands

Name of Plant	Country	Operator / Consultants	Employed APC-train	Volume Flow Rate	Type of waste	ACR supplier / Lizensor	Start-up
AVR RO-0 - RO 6	NL	AVR / Tebodin	ESP-HCl-SO$_2$-ACR-LTSCR	7 x 155.000	MW	AE / STEAG	1993
AVR RO-0	NL		ESP-HCl-SO$_2$-ACR-LTSCR	1 x 155.000	MW	STEAG	1995
AVR DTO-9	NL	AVR / Tebodin	Q-ESP-HCl-SO$_2$-ACR	1 x 77.000	HW	AE / STEAG	1992
AVR DTO-8	NL	AVR / AVR	ESP-HCl-ACR	1 x 77.000	HW	LCS / HP	1994
RZR Herten IM 1	D	STEAG / STEAG	ESP-HCl-SO$_2$-ACR-ACCR	1 x 70.000	HW	LCS / HP	1991
RZR Herten IM 2	D	STEAG / STEAG	ESP-HCl-SO$_2$-ACR-LTSCR	1 x 70.000	HW	LCS / HP	1995
RZR Herten SM 1/2	D	STEAG / STEAG	SD-ESP-HCl-SO$_2$-ACR-LTSCR	2 x 120.000	MW	LUT / WKV	1994
RZR Herten SM 3/4	D	STEAG / STEAG	FF-HCl-SO$_2$-ACR-LTSCR	2 x 157.000	MW	LCS / HP	1999
MVA Düsseldorf-Flingern	D	SWD / SWD	ESP-SD-ESP-ACR-LTSCR	4 x 160.000	MW	LUT / WKV	1993
	D	SWD / SWD	ESP-SD-ESP-ACR-LTSCR	1 x 180.000	MW	LUT / WKV	1997
MHKW Hameln	D	EWAG / VGU	SNCR-DIP-FF-ACR-LTSCR	3 x 60.000	MW	LUT / WKV	1993
EBS Wien	A	EBS / Fichtner	ESP-HCl-SO$_2$-ACR	2 x 68.500	HW	INT / WKV	1992
		EBS / Fichtner	ESP-HCl-SO$_2$-ACR	2 x 126.500	SS	INT / WKV	1992
		EBS / Fichtner	ESP-HCl-SO$_2$-ACR	1 x 74.000	HW	INT / WKV	1992
		EBS / Fichtner	ESP-HCl-SO$_2$-ACR	1 x 15.000	CW	INT / WKV	1990
Hoechst-Frankfurt	D	Hoechst / Hoechst	ESP-HCl-SO$_2$-ACR	1 x 75.000	HW	LUT / WKV	1994
AVG Hamburg	D	AVG / VKR	ESP-HCl-SO$_2$-ACR-LTSCR	2 x 78.000	HW	LUT / WKV	1996
MVA II Stellinger-Moor	D	Hamburg / GRP	ESP-HCl-SO$_2$-ACR-LTSCR	2 x 131.000	MW	LUT / WWK	1995
AWG Wuppertal	D	AWG / AWG	ESP-HCl-SO$_2$-ACR-LTSCR	3 x 135.000	MW	LTU / WKV	1995
MHKW Essen-Karnap	D	RWE / RWE	ESP-HCl-ACR-LTSCR	4 x 168.000	MW	AE / STEAG	1995
MVA Wels	A	WAV / GRP	ESP-HCl-SO$_2$-ACR-LTSCR	1 x 62.000	MW	AE / STEAG	1995
KVA Uni Heidelberg	D	Hospital / ECH	ESP-HCl-SO$_2$-ACR-LTSCR	2 x 65.000	CW	AE / STEAG	1991
AVI ROTEB	NL	ROTEB / Tebodin	HCl-SO$_2$-ACR-LTSCR	4 x 75.000	MW	LCS / HP	1993
MVA Kassel	D	Stadtreiniger / GRP	ESP-SD-FF-ACR-LTSCR	2 x 70.000	MW	LCS / HP	1996
MVA Stapelfeld 1+2	D	MVA Stapelfeld GmbH / MVS	ESP-HCl-SO$_2$-ACR-LTSCR	2 x 120.000	MW	LCS / HP	1996
MVA Stapelfeld 3+4	D		FF-HCl-SO$_2$-ACR-LTSCR	2 x 157.000	MW	LCS / HP	
MWA Weissenhorn	D	County / AEW	DIP-FF-SO$_2$-ACR-LTSCR	2 x 51.000	MW	LCS / HP	1996
AEZ Kreis Wesel	D	STEAG / STEAG	ESP-SD-ESP-HCl-SO$_2$-SCR-Oc-ACR	2 x 120.000	MW	LCS / HP	1997
RVA Böhlen	D	BAS / STEAG	ESP-SD-FF-HCl-SO$_2$-ACR-LTSCR	1 x 40.000	HW	LCS / HP	1997
MVA Köln	D	AVG / ITG	SD-FF-HCl-SO$_2$-ACR-Oc-SCR	4 x 95.000	MW	LCS / HP	1998
RMHKW Böblingen	D	ABB / GRP	FF-HCl-SO$_2$-ACR-LTSCR	2 x 62.000	MW	LCS / HP	1999
TAD Dortmund		ABB / GRP	ESP-Q-HCl-SO$_2$-ACR-LTSCR	2 x 63.000	MW	LCS / HP	2003

ESP	= electrostatic precipitator	FF	= fabric filter
SD	= spray dryer	HCl	= HCl-scrubber
SO$_2$	= SO$_2$-scrubber	DIP	= direct injection process
ACR	= activated char reactor	ACCR	= activated carbon catalytic reduction
SNCR	= selective non catalytic reduction	SCR	= selective catalytic reduction
LTSCR	= low temperature selective catalytic reduction	SCR-Oc	= SCR + oxidation catalyst
MW	= municipal waste	HW	= hazardous waste
SS	= sewage sludge	CW	= clinical waste
AE / STEAG	= Austrian Energy & Environment / STEAG AG	LUT / WKV	= Lentjes Umwelttechnik / Grochowski
INT / WKV	= Integral Engineering / Grochowski	LCS / HP	= L. & C. Steinmüller GmbH / Hugo Petersen

Table III   Market Share of Steinmüller / HP of ACR for Power Plants and
                       Waste Combustors in January 1996

Total Number of Plants (larger than 5.000 m^3/h) : 84
delivered by

LCS/HP	50.0 %
LUT/INT	22.6 %
AE/STEAG	21.0 %
Uhde*	3.6%

Total Volume Flow Rate treated : 11.045.000 m^3/h net @ STP in ACR's by

LCS/HP	47.2 %
LUT/INT	22.6 %
AE/STEAG	21.0 %
Uhde*	9.2 %

LCS/HP	= Steinmüller / Hugo Petersen
LUT/INT	= Lentjes Umwelttechnik / Integral Engineering
AE/STEAG	= Austrian Energy & Environment / STEAG
Uhde	= Uhde Engineering GmbH

* Uhde gave up the ACR product line in 1990 after delivering only 3 ACR units for
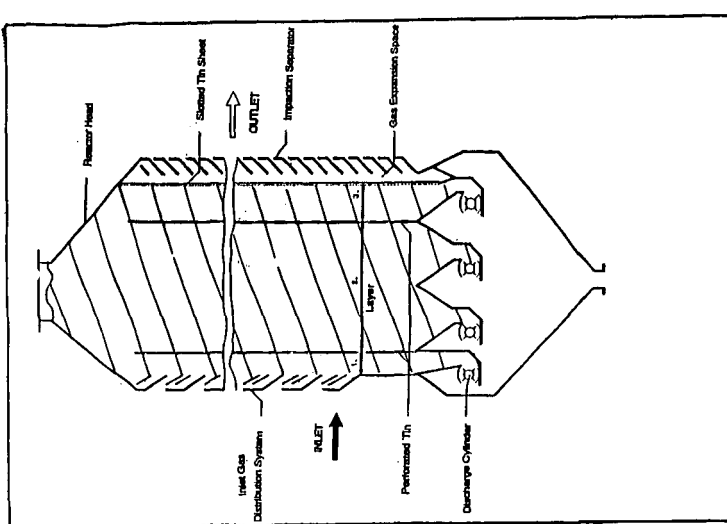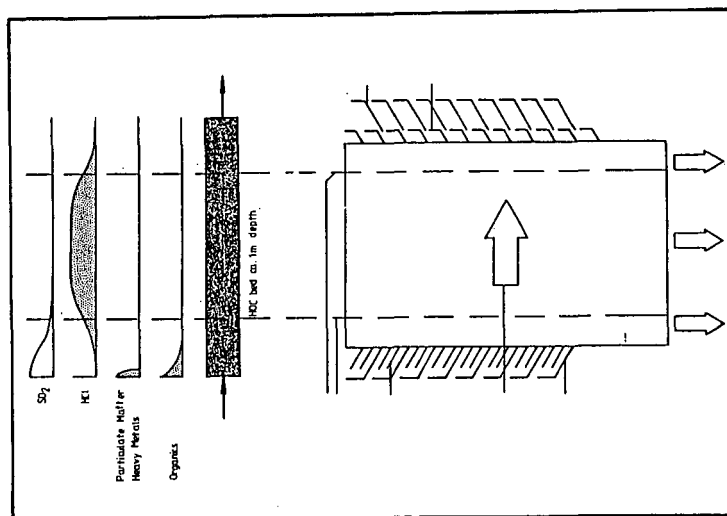 power plants

Figure 1 ACR Adsorber Concept

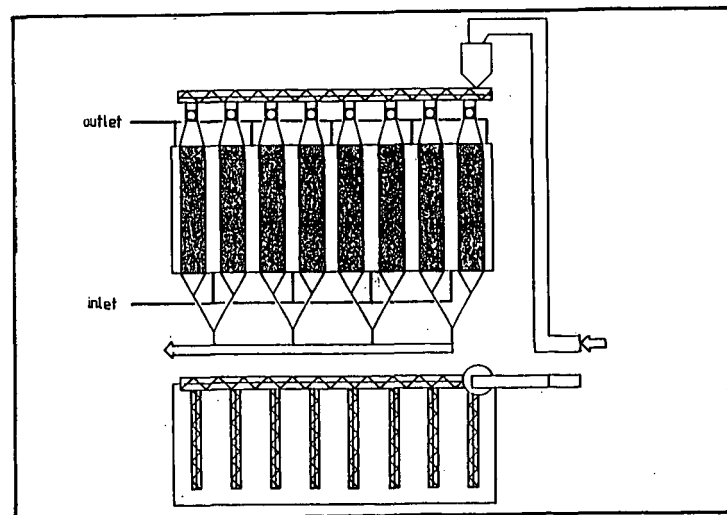Figure 2 Adsorption Characteristics Adapted by the Adsorber Design
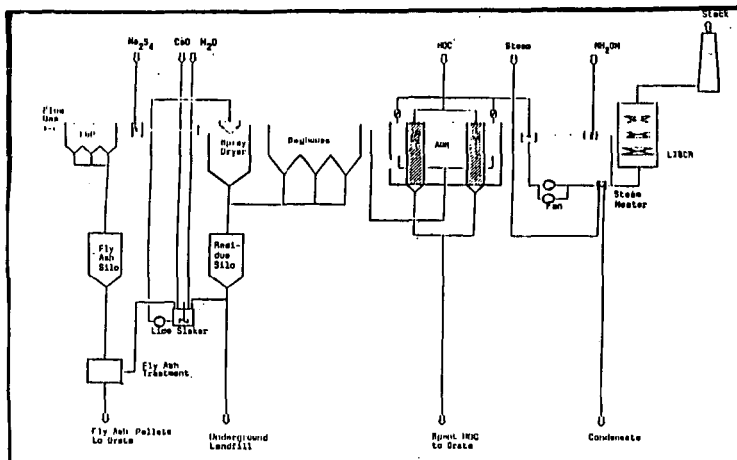

Figure 3 Modular Arrangement Within the ACR Adsorber

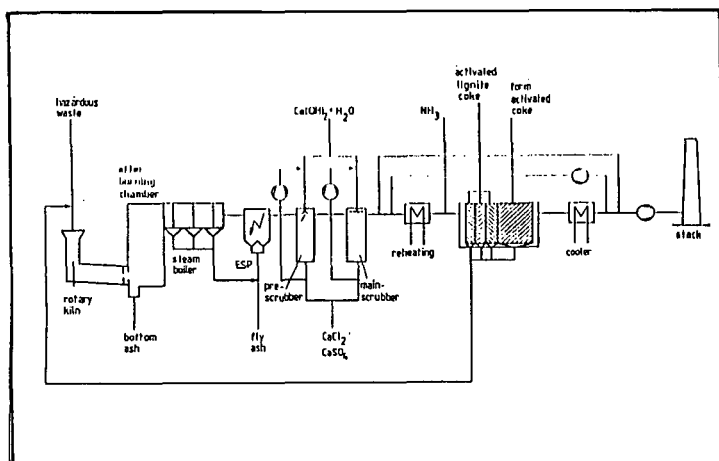Figure 4 17. BImSchV Retrofit of an Existing MWC

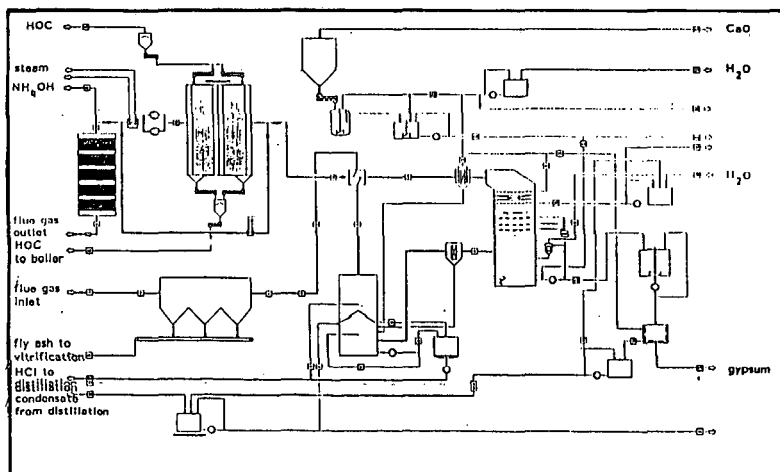Figure 5 17. BImSchV Retrofit of an Existing HWC

Figure 6 Modorn 5-stage APC-Train for MWC's ona HWC's

THE APPLICATION OF ACTIVATED CARBON ENHANCED LIME FOR CONTROLLING ACID GASES, MERCURY, AND DIOXINS FROM MWCs

Anthony Licata
Licata Energy & Environmental Consultants, Inc., Yonkers, NY

Manyam Babu and William Carlson
Dravo Lime Company, Pittsburgh, PA

Key Words: Activated Carbon, Dioxins, Mercury

INTRODUCTION
Environmental control agencies have sought to reduce Municipal Waste Combustor (MWC) emission rates by the implementation of new regulations. Examples of these regulations are Germany's 17th *Federal Regulation on Emission Protection; the Clean Air Act Amendments of 1990;* EPA's New Source Performance Standards (NSPS) and Emission Guidelines; and recent regulatory actions in Minnesota, New Jersey, and Florida to adopt Hg standards for MWCs.

Sorbalit® is an activated carbon enhanced lime process that reduces MWC emissions and has been successfully demonstrated in Europe and the U.S. The process consists of two components: 1) a specially developed agent characterized by a high adsorption material capable of adsorbing toxic elements and acid gases, and 2) highly efficient air pollution control systems used by MWCs and various other types of combustion sources, which provide through agitation, a vortexing of the adsorbing agent mixture in a collection device, usually a fabric filter or ESP.

This paper presents the theoretical design of the Sorbalit technology. Actual field test results illustrate applications that reduce the concerns related to mercury and dioxin emissions based on practical experience. The adsorbing agent is described in detail and results obtained in various types of air pollution control systems which are applicable to the U.S. are presented.

THE SORBALIT SYSTEM
Sorbalit is a patented system for controlling emissions of acid gases, mercury, and organics in a single application. The sorbent component of the technology is produced by mixing lime, either calcium hydroxide or calcium oxide, with surface-activated substances such as activated carbon or lignite coke and sulfur-based components in a proprietary process. Sorbalit can be produced with carbon contents ranging from 4% to 65% depending on the operational requirements of each project.

The Sorbalit process produces a homogeneous formulation containing calcium, carbon, and sulfur compounds that will not dissociate (demix) when used, either in a slurry or dry form. It is particularly important to avoid flotation or separation of the carbon and sulfur substances that have been added to the lime. To maintain product quality and effective levels of air pollution control, the components must stay as a uniform mix from the manufacturing process through transportation and use in the air pollution control system.

Theory of Lime Adsorption
Lime is the largest component of Sorbalit and has the primary role of adsorption of the acid gases present in the flue gas such as SO_2, HCl, and HF. Calcium oxide (CaO) is called "pebble lime" or "quicklime". Hydrated lime [$Ca(OH)_2$] is made from CaO by adding 32% by weight of water in a hydrator. CaO is not very reactive with acid gases for scrubbing at the temperatures and conditions that exist in MWC facilities and has to be converted into the hydrate form to be reactive in scrubbing systems. CaO converts to $Ca(OH)_2$ in the slaking process in which four parts of water are added to one part CaO to form $Ca(OH)_2$ in a slurry that has about 25% solids. This conversion requires two phases that takes place in a slaker. The first phase converts the CaO into $Ca(OH)_2$. The second phase is to convert the hydrate by mixing 3.96 lbs of free water with one part hydrate that results in a 25% solids slurry.

Theory of Carbon Adsorption
The adsorption of mercury and organics such as dioxin into activated carbon and coke is controlled by the properties of both the carbon and the adsorbate, and by the conditions under which they are contacted. This phenomenon is generally believed to result from the diffusion of vapor molecules into the surface of the carbon. These molecules are retained at the surface in the liquid state because of intermolecular or Van der Waals forces.

As the temperature falls, or as the partial pressure of the vapor above the carbon rises, the average time that a molecule resides on the surface increases. So does the fraction of the available surface covered by the adsorbate. However, the carbon surface is not uniform and consists of sites whose

activities vary. More active sites will become occupied first and, as the activity of the remaining available sites decreases, the adsorption energy will change.

The physical structure of activated carbon and coke is not known in detail, but it is believed to contain randomly distributed pores in the carbon, between which lies a complex network of irregular interconnected passages. Pores range in diameter down to a few angstroms, and provide a internal surface area from 300 to 1,000 m²/gram of carbon. The volume of pores at each diameter is an important variable that directly affects carbon performance. Diagrams illustrating the structure of carbon particles and the adsorption of dioxin and mercury are presented in Figures 1 and 2.

Since adsorption takes place at the carbon-gas interface, the surface area of the carbon is one of the most important factors to consider. The second factor is the pore radius distribution. Laboratory bench scale tests have shown that both increasing the surface area and the addition of sulfur compounds result in higher adsorption rates of elemental mercury (Hg°). Most of the laboratory work on carbon adsorption has been done on Hg°, not with the Hg compounds we normally see in MWC emissions and without humidification.

Field tests at MWCs injected with carbon products with a wide range of surface areas have shown that there is not a significant improvement in Hg (total) capture based on the increased carbon surface area. It is important that laboratory programs be developed that simulate field conditions to consider the effects of the surface area of various products. Since high surface area products are more expensive, their performance advantages and cost trade-offs have to be demonstrated.

However, the surface area must be available in the proper range of pore sizes. If too much of the area is available in pores smaller than 5 Å, many molecules will be unable to penetrate the pores and that area of the carbon will essentially be unavailable for adsorption. For most pollution-control applications, the surface areas of pores whose diameters range between 5 and 50 Å yield good efficiency rates because the relative pressure of the vapor is usually too low for the larger pores to become filled. At high relative pressures, however, the total pore volume becomes important because the macropores also become active.

The adsorption of benzene, for example, has been shown to be affected by pore size distribution. At high benzene concentrations, carbons in which large pores predominate have higher capacities than those in which medium or small pores predominate. But at low concentrations, the large-pore carbon has a lower capacity.

The size of the Hg° molecule is approximately 4.5 Å and the dioxin molecule is 10 Å x 3 Å. Both molecules are adsorbed in different parts of the carbon particle. In theory, dioxins are collected in the macropores while the mercury is collected in the micropores. Dioxin, being larger, blocks the passages, preventing mercury from entering the micropores. To increase the mercury capture rate, the amount of carbon used must be significantly increased, the surface area of the carbon must be increased, or sulfur added.

The carbon/mercury balance has been established through laboratory experiments where they found that under ideal conditions, three grams of carbon will adsorb one gram of mercury. However, in operating facilities, considerably more carbon is required to reduce Hg emissions from 600 μg/Nm³ to 70 μg/Nm³; approximately 300 grams of carbon per gram of Hg are used in MWC applications with a baghouse operating at 135°C.

The actual adsorption capacity of carbon is affected by:
- Gas temperature
- Flue gas moisture
- Inlet concentrations of Hg
- Species of Hg
- Acid content of the flue gas
- Concentration of organics such as dioxin
- Type of carbon used and surface area
- Contact time

The effects of each of these variables has not been quantified. However, field test programs have demonstrated the relative effect that flue gas temperature has on Hg adsorption as follows:
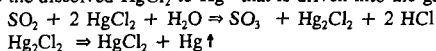
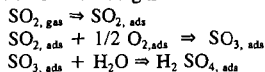| Carbon/Coke Adsorption	
Flue Gas °C	gC/ gHg
135 - 145	300 - 400
145 - 165	400 - 500
165 - 185	500 - 600
185 - 200	600 - 800

Theory of Sulfur Adsorption

The addition of sulfur compounds to the process plays a major role in the adsorption of mercury but not in the adsorption of dioxin. Sulfur's role in the adsorption is two fold, first the sulfur compounds maintain the active state of the carbon. Activity is defined as the amount of open pores in the carbon. Sulfur's role is to keep these pores open and to allow the mercury to get into the sub-structure pores. The exact process in which the sulfur keeps the pores open has not been defined. One theory is that the sulfur reacts with water which is adsorbed or is on the surface of the carbon particles to form an acid that penetrates the pores. No measurable acids have been observed when applying Sorbalit, most likely because any excess acids would react with the lime.
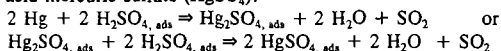
The second role for sulfur is converting Hg° to a sulfate. Hg° is more difficult to capture than Hg_2Cl_2, which is the predominant species in MWC emissions or Hg_2SO_4. Hg° accounts for only 5% to 10% of the total mercury emissions from an MWC. Flue gas constituents such as SO_2 can reduce the dissolved $HgCl_2$ to Hg° that is driven into the gas stream due to its poor solubility.

$$SO_2 + 2\ HgCl_2 + H_2O \Rightarrow SO_3 + Hg_2Cl_2 + 2\ HCl$$
$$Hg_2Cl_2 \Rightarrow HgCl_2 + Hg\uparrow$$

The adsorption capacity of carbon is affected by formation of sulfuric acid on the carbon owing to adsorption of the flue gas constituents SO_2 and H_2O:

$$SO_{2,\ gas} \Rightarrow SO_{2,\ ads}$$
$$SO_{2,\ ads} + 1/2\ O_{2,ads} \Rightarrow SO_{3,\ ads}$$
$$SO_{3,\ ads} + H_2O \Rightarrow H_2SO_{4,\ ads}$$

Hg° then reacts with the sulfuric acid to form mercurous sulfate (Hg_2SO_4) or in the presence of excess acid mercuric sulfate ($HgSO_4$):

$$2\ Hg + 2\ H_2SO_{4,\ ads} \Rightarrow Hg_2SO_{4,\ ads} + 2\ H_2O + SO_2 \qquad \text{or}$$
$$Hg_2SO_{4,\ ads} + 2\ H_2SO_{4,\ ads} \Rightarrow 2\ HgSO_{4,\ ads} + 2\ H_2O + SO_2$$

Since the lime component of Sorbalit removes the SO_2 from the flue gas, some adsorption capacity of the carbon for Hg° is diminished. The sulfur component in Sorbalit added during manufacturing, replaces the missing SO_2 and enhances the adsorption of Hg°. Mercuric chloride does not react with the sulfuric acid, but is dissolved in sulfuric acid.

Recent tests have demonstrated the significance that sulfur plays in capturing Hg. The test program conducted at the Marion County, OR MWC showed Sorbalit captured more Hg (total and vapor phase) than dry carbon injection. To determine the equivalent performance of carbon and Sorbalit, both were injected at the same carbon feed rate of 5 lbs/hr. Sorbalit captured 87.7% of the total Hg while carbon injection captured 84.2%. More importantly, Sorbalit captured 83.2% of the vapor phase Hg while carbon collected 77.6%.

Hg emissions from coal fired plants are significantly different in two ways from those of MWCs. First, the uncontrolled Hg emissions from U.S. eastern coal ranges from 8 to 30 μg/dscm while a typical mass burn MWC would emit 600 μg/dscm. Secondly, since there is a relatively low chlorine content in coal, the percentage of vapor phase Hg is much higher than in a MWC. As a result, the capture of Hg emissions is more difficult via dry injection. In a test program on a coal fired plant, Sorbalit captured between 44% to 55% of the vapor phase Hg while carbon injection only captured 10% to 15%. These tests were conducted under difficult Hg capture conditions: high temperatures and low moisture.

AREAS OF APPLICATION

In its simplest form, the air pollution control system consists of a duct or pipe, through which Sorbalit is injected into the flue gas, and a fabric filter or ESP located down stream. This simple solution has an economic advantage because it is easily integrated into existing plants without having to expend significant capital for new equipment.

This Section deals with the applications for the air pollution control systems employed in various waste treatment plants. Systems which are typically used in MWCs include dry injection, water conditioning followed by dry injection, and spray dryer technologies. Since spray dryer application will become standard practice in the U.S. we will only present data on this technology. Data on other technologies has been previously published.

MWC Marion County, OR

In July of 1992 Sorbalit was tested at an MWC in Marion County, Oregon. Tests were conducted on Unit #1 which is rated at 10.4 Mt/h (275 T/D) of MSW. The air pollution control system consists of a spray dryer and a fabric filter. During the test program, up to .75 Mt/h (20 T/D) of medical waste was also combusted in the units.

419

Sorbalit was injected dry after the spray dryers in the dry venturi feed duct and before the pulse jet fabric filter at a flue gas temperature of 148°C (300°F). Seven efficiency tests were performed over the four day test program. The inlet concentration averaged 935 μg/dscm^3 @ 12% CO_2 and ranged from 508 to 2,695 μg/dscm^3 @ 12% CO_2. The outlet emissions averaged 131 μg/dscm^3 @ 12% CO_2 and ranged from 10 to 465 μg/dscm^3 @ 12% CO_2. The average Hg removal efficiency for the test program was 87.7%.

Hazardous Waste Incineration Plant Schöneiche/Berlin

The incineration plant at Schöneiche near Berlin, in the former GDR, has a hazardous waste capacity of 2.3 Mt/h (60 T/D). Flue gases down stream of the boiler are cooled to a temperature of 140°C (284°F) by water sprays. The gas volume rate during the test was 31,000 Nm^3/h (19,657 scfm). The plant decided to use the carbon enhanced lime technology because it was the only way in which the approved limits for mercury could be achieved without the addition of new control equipment. Before the use of Sorbalit, hydrated lime was employed as the adsorbing agent.

Mercury test measurements made in January 1990, on the untreated flue gases before and after the injection of Sorbalit are shown Table 1. The measurements showed that reductions in Hg emissions were in excess of 88%. These figures represent values well below the maximum emission limit for mercury as stipulated in the German's 17th Federal Pollution Control Directive (17.BimSchV). Since the initial test, over 80 measurements for mercury have been made, confirming the initial test results.

The Table 1 shows the respective levels of the dioxin and furan concentrations in the untreated and in the cleaned flue gases. The dioxin concentration in the Sorbalit treated flue gas was undetectable in some cases.

Concentrations of polychlorinated biphenyls (PCBs) in the untreated and in the cleaned flue gas were also measured. The values are shown in Table 1. The level of PCB content in the untreated flue gas was 130 ng/Nm^3. Various types of PCBs were no longer detectable in the cleaned flue gas. The high rate of removal of the PCBs also leads us to the assumption that additional heavy superchlorinated compounds such as hexachlorobenzene and hexachlorocyclohexane are removed from the flue gases. Separation rates for the polyaromatic hydrocarbons cannot be established until the relevant measurements are available, however, high levels of removal are expected.

It should be emphasized again that these levels for the treated cleaned flue gases were attained without any modifications to the plant or the air pollution control system. The viability of the concept of improving a flue gas cleaning system via the use of modified hydrated lime with carbon is thus confirmed. The air pollution control system at the Schöneiche hazardous waste incineration plant has been using Sorbalit since December 1989. About 50 dioxin measurements have been taken since; never have the limits been exceeded.

Hazardous Waste Incineration Plant Schweinfurt

At the hazardous waste plant at Schweinfurt 2.5 Mt/h (66 T/D) of hazardous waste are converted to energy. The flue gas volume rate is 28,000 Nm^3/h (17,755 scfm). The original plant consists of a pebble lime slurry preparation plant (slaker) with a spray dryer and a pulse jet fabric filter. In the retrofit, instead of the traditional lime slurry, a Sorbalit with 3% carbon suspension was employed, with no further modifications to the plant being employed. Test results showing the range of emission reductions for dioxin and mercury are presented in Table 1. Based on these results, the test program was immediately followed by continuous operation.

CONCLUSIONS

When an activated carbon enhanced lime product such as Sorbalit is employed, the following emission values have been reliably attained:

- < 50 μg Hg/Nm^3 for mercury at 11% O_2 (70 μg/Nm^3 at 7% O_2)
- < 0.1 ng TEQ/Nm^3 for dioxin and furans at 11% O_2
- Reduction to the detectable limit for PCBs
- EPA's NSPS and Emission Guidelines for SO_2 and HCl

Furthermore, the use of this technology in waste combustion processes obtains a number of advantages in process engineering and modification to the facilities involved. Sorbalit can be stored and added using standard lime and hydrated lime handling equipment. In retrofit applications where lime or hydrated lime is used, no new equipment may be required. Material handling equipment in most facilities, from the supply silo through conveying and dosing equipment to the mixing lines, filters, and flow controllers, all remain in use.

The gas cleaning process, that is, the injection of Sorbalit into the flue gas flow, followed by vortexing of the flow and subsequent separation on the fabric filter or ESP, can be installed as a

"Sorbalit System" downstream of any combustion plant. Many areas of application are envisioned for Sorbalit in the field of flue gas cleaning, some of which have already been put into practice. Activated carbon enhanced lime technology used for separating volatile inorganic and organic substances can be integrated into the flue gas cleaning systems of the following processes:

- Solid & hazardous waste incineration plants
- Sewage/sludge incineration plants
- Coal fired power plants
- Aluminum smelting plants
- Wood drying plants
- Steel mills
- Glass/ceramic furnaces
- Wood fired boilers

Sorbalit is effective in removing mercury over a wide range of operating conditions and applications. The test data indicates that two of the key parameters in deciding the overall removal efficiency of mercury are the inlet concentration and the temperature of the flue gas.

The data in this paper have demonstrated that Sorbalit has the flexibility to be integrated into many existing U.S. applications and systems. Additional information on new systems and wet scrubbers will be published in the near future.

Table 1

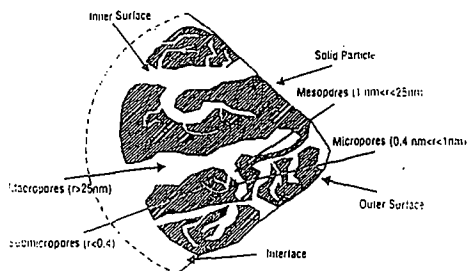| Pollutant		Schöneiche Test			Schweinfurt Test		
		Inlet	Outlet	% Removal	Inlet	Outlet	% Removal
Total PCBs	ng/Nm³	130	>1 (nd)	N/A	-	-	-
Dioxins ITEQ	ng/Nm³	1.74	0.02	98.8	11.59	0.085	99.2
Dioxins ITEQ	ng/Nm³	0.34	nd	N/A	6.79	0.06	91.1
Hg	μg/Nm³	250.9	29	88.4	765	47	93.8
Hg	μg/Nm³	180	2.5	98.6	40	8	80.0

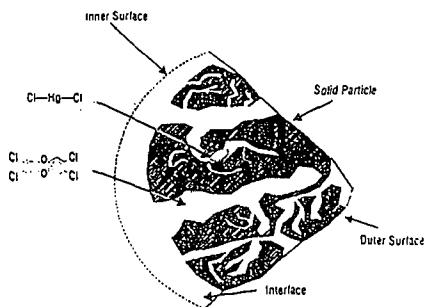Figure 1: Distribution of pores in a grain of activated carbon

Figure 2: Structure of pores in a lignite coke particle

LOW TEMPERATURE SO_2 CAPTURE BY CALCIUM BASED SORBENTS: CHARACTERIZATION OF THE ACTIVE CALCIUM.

M.C. Macías-Pérez, C. Salinas-Martínez de Lecea, M.J. Muñoz-
Guillena and A. Linares-Solano
Departamento de Química Inorgánica. Universiad de Alicante
Alicante. Spain

Keywords: SO_2 retention, CO_2 chemisorption, calcium sorbents, calcium supported on carbon.

INTRODUCTION
Well dispersed CaO particles play an important role in some heterogeneous solid-gas reactions. Examples are the carbon-gas reactions catalyzed by calcium and the SO_2 retention by calcium-based sorbents. In these solid-gas reactions the characteristics of the CaO particles (i.e., dispersion, available surface area, etc.) have to be known to understand their behavior and their catalytic activity. Unfortunately, the characterization of well dispersed CaO particles by XRD does not give valuable information[1-3].

Selective CO_2 chemisorption has been deeply analyzed to characterize both CaO and CaO-carbon samples; thermodynamic arguments and details of the method have been discussed elsewhere[3-5]. The results show that CO_2 chemisorbs on CaO in an irreversible manner, and is restricted to the surface of the CaO particles, provided that the chemisorption temperature is lower than 573K. Therefore, this technique allows to assess the available surface area of the particles (active calcium) and consequently CaO dispersion. These two parameters were used to interpret the catalytic activity of calcium in different carbon-gas reactions. The usefulness of the method has been shown, gasification rate shows a close relationship with the area of the CaO particles[3,6,7]. Based on the above results, and considering that the SO_2-CaO interaction might depends on the surface of CaO, the CO_2 chemisorption has been used to characterize the SO_2 retention by CaO prepared from thermal decomposition of several limestones[8-10]. The observation that SO_2 retention at 573K depends strongly on the dispersion and surface area of the CaO particles leads us to propose the use of carbon supports to improve the dispersion of the CaO particles[11,12]. In this context, this paper extends and analyzes the usefulness of the CO_2 chemisorption method to characterize the active calcium in a wide variety of CaO-carbon samples. Several parameters, preparation conditions, nature of the calcium compounds, porosity of the carbons, etc. have been used to vary the available surface of the CaO particles.

EXPERIMENTAL
CaO samples. CaO samples were prepared by thermal decomposition of commercially available $CaCO_3$ and several limestones of very different origins. Decomposition was carried out in a thermobalance (Stanton-Redcroft) as described elsewhere[10].

CaO-carbon samples. A large number of samples of calcium containing carbon have been selected for this study. The samples have been prepared varying calcium precursors, calcium content, carbon support properties (porosity, surface area, surface chemistry, etc.), and preparation methods (impregnation, ion-exchange).

<u>CO_2 chemisorption</u>. As described elsewhere[3,4] the sample (CaO or CaO-carbon) is heated in N_2, at 20K/min, up to 1173K, subsequently it is cooled to 573K and then N_2 is switched to CO_2. From the CO_2 uptake, and assuming that one CO_2 molecule chemisorbs on one CaO site (1:1 stoichiometry), the number of calcium atoms, the available surface area and dispersion can be estimated[3,4].

<u>SO_2 retention experiments</u>. Isothermal SO_2 retention measurements of calcium-based samples were mainly performed by TG at 573K (other temperatures have also been tested). Details of the procedure used are described elsewhere[10,12]. Prior the retention run, the sample was heated, at 20K/min, up to 1173K, in a N_2 flow (60 mL/min), for 10 min. Subsequently, the sample was cooled to 573K and N_2 flow was changed to a gas mixture containing 0.3 vol% SO_2 in He. The amount of SO_2 retained by the sample, after 1.5-2 h of reaction, was determined by the increase in weight.

RESULTS AND DISCUSSION
The retention of SO_2 by CaO has been analyzed in our laboratory in a wide range of reaction temperatures (298-1173K)[8-10]. At temperatures lower than 673K the interaction of SO_2 with CaO forms $CaSO_3$[8-10,13,14], being this compound an intermediate of the formation of $CaSO_4$ at higher temperatures[8-10,14,15]. Depending on the reaction temperature considered (T< 673K) two processes are distinguished during the formation of $CaSO_3$. For higher temperatures than 573K the formation of $CaSO_3$ occurs through a bulk process, however at temperatures below 573K, the SO_2 retained produces surface $CaSO_3$[10], both in presence and in the absence of O_2, through the reaction[9]:

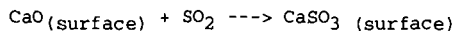$$CaO_{(surface)} + SO_2 ---> CaSO_3 \text{ (surface)}$$

Figure 1 presents the isothermal retention of SO_2 at 573K, expressed as mol of SO_2 retained per gram of sample, versus time. After a period slightly over 1h, the uptake of SO_2 is practically constant. The SO_2-CaO surface reaction is confirmed on a large number of CaO by the observation that the ratio between mol of SO_2 (obtained from runs like that of Figure 1) per mol of CaO on the surface (determined from CO_2 chemisorption) is very close to one (see Figure 2). The extend of this surface reaction can not be explained by referring to any "classical" textural parameter of the limestones (N_2 (BET) surface area, pore volume, etc.) or those of CaO[10]. On the contrary, an interesting correlation between the SO_2 retention degree and the surface CaO is obtained, as shown in Figure 2. From this correlation, that shows the importance of the CaO surface area, it follows that the higher the dispersion of CaO, the higher the retention of SO_2. By selecting systems with high CaO dispersion[12], the efficiency to retain SO_2 can be increased. Activated carbons can act as dispersing agent as it is shown next.

A large number of CaO containing activated carbons prepared with different type of activated carbons, calcium compounds, calcium loadings and method of preparation have been selected for this study. Figure 3 compiles the SO_2 retention by these CaO-carbon samples which have been determined at 573K from runs similar to

that of Figure 1. It is interesting to note that samples containing less than 15% in weight of calcium exhibit retentions similar to those of bulk CaO (Figures 2 and 3).

The SO_2 retention (Figure 3) shows a marked dependence on the calcium content. Increasing the calcium content, the available CaO surface will increase, if there is not an important loss of dispersion. Figure 4 presents the CO_2 chemisorption data plotted versus calcium content of the supported samples. The results show that activated carbons act as good dispersing agents, they allow to increase the available CaO surface in respect to unsupported CaO.

Despite some data dispersion, both Figures 3 and 4 indicate that correlations between the calcium content and the CaO surface or the SO_2 retention exist. Figure 5, that presents the SO_2 retention per gram of sample versus the CaO surface, confirms the existence of a correlation among SO_2 retention and CaO surface as observed for unsupported CaO (Figure 2). Nevertheless, two aspects of Figure 5 need to be pointed out: 1) the ratio mol SO_2/mol CaO_s is usually higher than unity, contrary to that found on Figure 2 for unsupported CaO. It means that the SO_2 retention by CaO-carbon is not restricted to the CaO surface and that some bulk $CaSO_3$ occurs. 2) this behaviour is more pronounced in highly dispersed CaO (high CaOs values).

To prove the formation of bulk $CaSO_3$, SO_2 retentions have been conducted at different temperatures. Figure 6 presents the results obtained on two CaO samples (unsupported and supported one). An important shift to lower temperatures (about 200K) is observed in the transition from surface to bulk $CaSO_3$ formation, in the case of carbon supported CaO. For practical applications of these supported CaO samples to remove SO_2, the observation that in the temperature range of 573-673K the CaO conversion is almost 100% is very interesting. It has to be noted that the application of these results is based on the fact that CaO can be regenerated, and hence reused for SO_2 removal, by thermal decomposition (873-973K) of $CaSO_3$[9,10,16,17].

The most serious challenge at this moment is to be able to increase the amount of CaO supported on a given activated carbon. In fact, the maximun SO_2 retention reached with these supported CaO, expressed per gram of sample, is comparable to those obtained with some bulk CaO, as can be seen comparing Figures 2 and 5.

CONCLUSIONS
SO_2 retention by CaO and CaO-carbon depends very much on the CaO surface area which can be determined by CO_2 chemisorption. For unsupported CaO the retention is a surface process whereas for carbon supported CaO both surface and bulk reaction take place. Activated carbons act as good dispersing agent enhancing the SO_2 retention. The usefulness of the SO_2 removal at low temperatures by CaO supported on carbon appears to be limited by the amount of CaO that can be loaded on the carbon. This point needs further studies.

REFERENCES
(1) Linares Solano, A., Almela Alarcón, M., Salinas Martínez de

Lecea and Cazorla Amorós, D. *Am. Chem. Soc., Division of Fuel Chemistry*, 1989, **34** (1), 136.

(2) Cazorla Amorós, D., Linares Solano, A., Salinas Martínez de Lecea, C.; *An. Quim.* 1991 **87**, 995.

(3) Salinas Martínez de Lecea, C., Almela Alarcón, M.and Linares Solano, A.; *Fuel* 1990, **69**, 21.

(4) Linares Solano, A. Almela Alarcón, M.and Salinas Martínez de Lecea; *J.Catal.*,1990, **125**, 401.

(5) Cazorla Amorós, D., Joly, J.P., Linares Solano, A.,Salinas Martínez de Lecea, C. and Marcilla Gómiz, A. ; *J. Phys. Chem.* 1991, **95**, 611.

(6) Linares Solano, A., Salinas Martínez de Lecea, C.,Cazorla Amorós, D. and Joly, J.P. In *Fundamental Issues in Control of Carbon Gasification Reactivity* 1991, (Edited by J. Lahaye and P. Ehrburger), p.409. Kluwer Academic Publishers, Dordretch, Netherlands: NATA ASI Series E192.

(7) Cope, R.F., Arrington, C.B. and Mecker, C.W. *Energy Fuels*, 1994, **8**, 1095.

(8) Muñoz-Guillena, M.J., Linares-Solano, A. and Salinas-Martínez de Lecea, C. *Appl. Surf. Sci.*, 1994, **81**, 409.

(9) Muñoz-Guillena, M.J., Linares-Solano, A. and Salinas-Martínez de Lecea, C. *Appl. Surf. Sci.*, 1994, **81**, 417.

(10) Muñoz-Guillena, M.J., Linares-Solano, A. and Salinas-Martínez de Lecea, C. *Appl. Surf. Sci.*, 1995, **89**, 197.

(11) Macías-Pérez, M.C., Linares-Solano, A. and Salinas-Martínez de Lecea, C. *Coal Sci. Technol.* 1995, **24**, 1831.

(12) Muñoz-Guillena, M.J., Linares-Solano, A. and Salinas-Martínez de Lecea, C. *Fuel.*, submitted.

(13) Elfving, P., Panas, I. and Lindqvist, O. *Appl. Surf. Sci.*, 1994, **74**, 91

(14) Bhatia, S.K. and Perlmutter, D.D. *AIChE J.*, 1983, **29**, 79

(15) Ghardashkhani,S. and Cooper, D.A., *Thermochimica Acta* 1992, **195**, 113

(16) Marsh, D.W. and Ulrichson, D.L. *Chem. Eng. Sci.* 1985, **40**, 423.

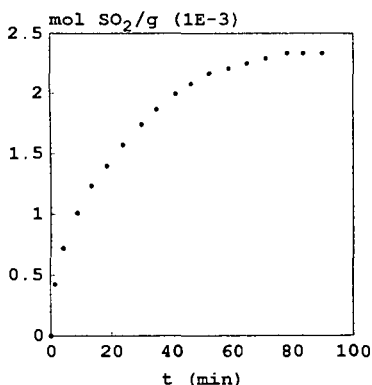(17) Gopalakrishnan, R. and Seehra, M.S. *Energy Fuels* 1990, **4**, 226.

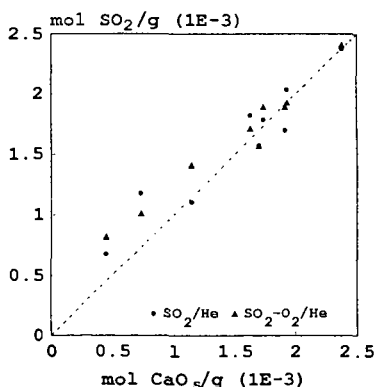Figure 1. Sulfur dioxide retention by CaO at 573K versus time.
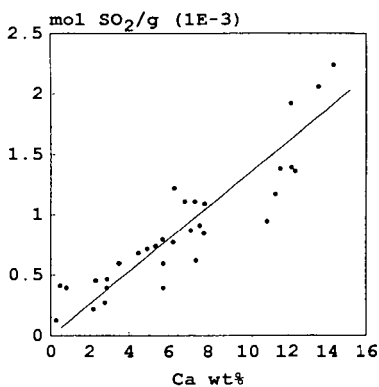

Figure 2. SO_2 retention versus surface CaO (unsupported CaO).

Figure 3. SO$_2$ retention versus Ca wt% (CaO/activated carbon samples).

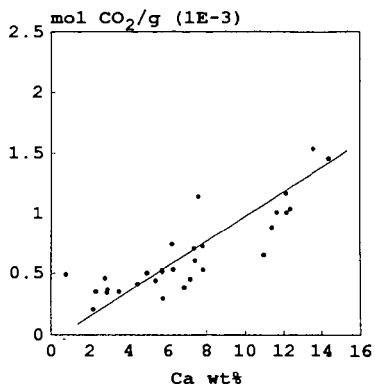

Figure 4. Chemisorbed CO$_2$ versus Ca wt% (CaO/activated carbon samples).

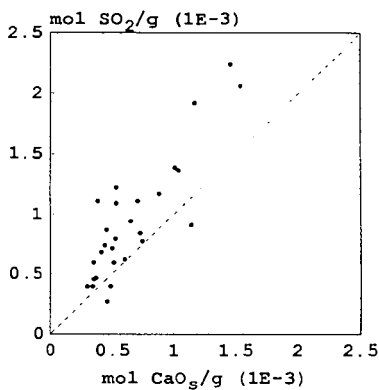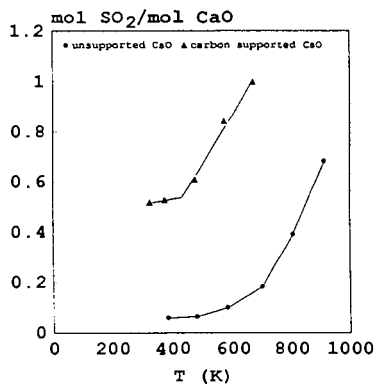Figure 5. SO$_2$ retention versus surface CaO (CaO/activated carbon samples).

Figure 6. SO$_2$ molar conversion versus temperature.

PRODUCTION OF ACTIVATED CHAR FROM ILLINOIS COAL FOR FLUE GAS CLEANUP

Anthony A. Lizzio[1] and Joseph A. DeBarr[1,2]

[1]Illinois State Geological Survey, 615 East Peabody Drive, Champaign, IL 61820
[2]Environmental Engineering and Science Program, University of Illinois, Urbana, IL 61801

Keywords: coal, activated char, flue gas cleanup.

INTRODUCTION

One of the unique properties of activated carbon is that it can remove nearly every impurity found in flue gas including SO_2, NO_x, particulates, mercury, dioxins, furans, heavy metals, volatile organic compounds, and other trace elements [1-6]. No other existing sorbent has that capability. An activated carbon-based process, typically placed after the precipitator and just before the stack, can be used alone or in conjunction with other control methods to remove SO_2 and NO_x from flue gas [7-10]. This technology has been used in Europe and Japan for cleanup of flue gas from both coal combustion and waste incineration. Currently, no U.S. utility employs a carbon-based process to clean flue gas. An ongoing research program [10-19] at the Illinois State Geological Survey (ISGS) has as one of its principal objectives the development of activated char from Illinois coal suitable for cleaning flue gas. This paper summarizes some of our recent efforts to produce activated char for several flue gas cleanup applications, including coal-fired utilities, diesel engine exhaust and waste incinerators.

RESULTS AND DISCUSSION

SO$_2$ Removal

The initial aim of this study was to identify process conditions for production of activated char with optimal SO_2 removal characteristics [10-16]. Chars with varying pore structure and surface chemistry were prepared from an Illinois hvC bituminous coal (IBC-102) under a wide range of pyrolysis and activation conditions, and tested for their ability to remove SO_2 from simulated flue gas (2500 ppm SO_2, 5% O_2, 10% H_2O, balance He). Table 1 summarizes the results. A novel char preparation method, involving nitric acid treatment followed by thermal desorption of carbon-oxygen (C-O) complexes, was developed to produce activated chars with SO_2 adsorption capacities comparable to those of commercial activated carbons. An attempt was made to relate the observed SO_2 adsorption behavior to the physical and chemical properties of the char. There was no correlation between SO_2 capacity and N_2 BET surface area. A TPD method was used to determine the nature and extent of C-O complexes formed on the char surface. TPD data revealed that SO_2 adsorption was inversely proportional to the amount of stable C-O complex. The formation of stable C-O complex may have served only to occupy carbon sites that were otherwise reactive to SO_2 adsorption. TPD data also revealed that SO_2 adsorption was directly proportional to the number of free adsorption sites on the carbon surface [12-15]. Based on these results, a detailed mechanism for SO_2 removal by carbon has been proposed [19].

NO$_x$ Removal

Carbon can also be used to remove NO_x from flue gas at temperatures between 80 and 150° C. Carbon may act as both a sorbent [20-22] and a catalyst [23-25]; the extent of each depending on the physical/chemical properties of the carbon and flue gas conditions. Sorbent Technologies Corporation (STC) is presently developing a carbon-based process for low-temperature (20-100°C) removal of NO_x from exhaust streams from jet engine test cells and other combustion sources such as diesel engines that would not require the use of ammonia [22]. The carbon filter being developed is a relatively simple NO_x control device that is placed directly into the exhaust duct path. There it substantially removes the NO_x as well as other contaminants such as SO_2, HCl and organics.

The ISGS and STC are working together to develop a carbon for this process. Several carbons prepared at the ISGS were tested by STC. The experimental conditions used were: 10 g of carbon, 1 in. ID fixed bed reactor, 500 ppm NO in air, and a flow rate of 4 L/min. Figure 1 shows that a steam activated Illinois coal char treated with HNO_3 and thermally desorbed at 925°C for 1 h in flowing N_2 (IBC-102,-HNO_3-925°C) removed 100% of the NO_x during a one hour test. Recall that this char also adsorbed the greatest amount of SO_2 (Table 1). The NO_x removal efficiency of a similarly treated Calgon F400 carbon (Calgon, HNO_3, 925°C) decreased from 100% to 70% after 1 h. The HNO_3-treated Calgon carbon that was not heat treated at 925°C (Calgon, HNO_3) removed only 10% of the NO_x after 60 minutes illustrating the importance of the thermal desorption step in our char preparation method. Thermal desorption of C-O complexes opens closed porosity and widens pores, but more importantly, creates nascent sites on the carbon surface that react vigourously with NO_x. Figure 2 shows that the NO_x removal performance of the IBC-102, HNO_3-925°C char decreases as flue gas temperature increases from 22°C to 150°C. The NO_x removal efficiencies of IBC-102, HNO_3-treated chars thermally desorbed at 525°C, 725°C and 1075°C were all less than that of the IBC-102, HNO_3-925°C char. It was interesting that the NO_x removal efficiencies of the KOH activated chars listed in Table 1 were comparable to those of the IBC-102, HNO_3-925°C char. These chars contained some leftover potassium, about 0.5% by weight. Potassium has been found to be an excellent catalyst for NO reduction [26-29].

Figure 3 compares the NO_x removal behavior of the IBC-102, HNO_3-925°C char and the Centaur carbon, a catalytic carbon manufactured by the Calgon Carbon Corporation. The HNO_3-925°C char

achieves nearly 100% NO_x removal for the first 8 h compared to only 4 h for the Centaur carbon. For the HNO_3-925°C char, the concentration of NO in the effluent increases from about 3% to 80% between 8 and 15 h, while the Centaur carbon continues to remove 50% of the NO after 20 h. It is interesting to note that NO_2 is generated by both carbons, and that its onset occurs at 15 h (50% of maximum breakthrough). The formation of NO_2 during the low temperature reaction of activated carbon fibers with NO was recently observed [30,31]. It seems that once the carbon surface becomes saturated with C-O, C-N and C-NO functional groups, NO_2 formation is initiated. Eventually, a char would require regeneration as these functional groups accumulate on the carbon surface and block the sites responsible for NO reduction. Preliminary tests suggest that the NO_x removal activity of the spent HNO_3-925°C char can be partially restored by thermal regeneration. Further work is needed to determine the mechanism by which this high activity carbon removes NO_x from flue gas.

Combined SO_2/NO_x Removal

The Research Triangle Institute (RTI) in conjunction with the University of Waterloo developed a low temperature process capable of removing more than 95% of the SO_2 and 75% of the NO_x from coal combustion flue gas [32,33]. The flue gas is cooled to 100°C and the SO_2 is catalytically oxidized to SO_3 by one type of carbon and converted to medium strength H_2SO_4 in a series of periodically flushed trickle-bed reactors. The SO_2 free gas is reheated to 150°C and NH_3 is injected over a different carbon to reduce NO_x to N_2 and H_2O.

In this study, RTI performed SO_2 removal tests on five ISGS chars under conditions simulating those used in the RTI-Waterloo process: 100°C, 2500 ppm SO_2, 5% O_2, 10% H_2O, balance helium, space velocity of 1400 h^{-1}. Each adsorption cycle was followed by a 0.2 L wash with 4.32 N H_2SO_4. The results of nine adsorption/desorption cycles performed with the HNO_3-925°C char are summarized in Table 5. After the first cycle, the 20% breakthrough time (BT), i.e., when 20% of inlet concentration of SO_2 is measured in the effluent, was extended from 3 to 80 minutes, however, BT decreased steadily thereafter. Also, the lowest emission (LE), i.e., the minimum SO_2 concentration detected in the effluent, increased with each subsequent cycle. It should be mentioned that the NO_x removal tests for the HNO_3-925°C char were performed prior to these SO_2 removal tests. The poor performance of this char may be attributed to adsorbed NO, NH_3 and O_2 poisoning SO_2 adsorption sites. Commercial processes typically remove SO_2 before NO_x to avoid production of ammonium sulfate, which can also reduce catalytic activity [3,8]. All subsequent SO_2 removal tests were performed on carbons that were not previously exposed to NO or NH_3. The KOH activated char was also tested (Table 5). A relatively low concentration of SO_2 in the effluent was achieved and the 20% BT was 45 minutes, but after the first cycle, performance decreased dramatically.

Table 6 shows that the SO_2 removal performance of the Centaur carbon was superior to all other carbons tested. Its 5% BT, however, also decreased after the first cycle. The IBC-102, HNO_3-725°C char performed best among the ISGS chars tested. Its initial LE was 10 ppm SO_2 (equivalent to 99% removal efficiency), but this increased to 1200 ppm SO_2 after just the first acid wash. An RTI carbon (not listed in Table 6) showed similar deactivation after the first cycle. The integral feature of the RTI-Waterloo process is its regeneration step involving a water wash with dilute H_2SO_4. One important advantage of doing this instead of thermal regeneration is that it does not consume carbon. Thus, a carbon catalyst in this process could last for many years without having to be replaced. The SO_2 removal performance of all the carbons tested by RTI in this study decreased markedly after the first cycle. Whether a low cost carbon having a high concentration of free sites resistant to poisoning by the dilute acid wash can be developed for this process remains to be determined.

The NO_x removal capabilities of these chars in the presence of ammonia were also tested. The following reaction conditions were used: 40 cm^3 carbon, 130-160°C, 500 ppm NO, 690 ppm NH_3, 5% O_2, 10% H_2O and 1400 h^{-1} space velocity. Table 4 shows that the NO_x removal activity of the HNO_3-925°C char, although highest among the ISGS chars tested, was still significantly lower than that of the carbon catalyst developed and tested by RTI (commercial activated carbon impregnated with a metal catalyst). The RTI carbon, although it achieved better than 99% conversion of NO to N_2, remains quite costly to produce. Table 4 also shows that the five ISGS samples responded differently to variations in reaction temperature. The NO removal activity of the HNO_3-925°C char went through a maximum at 150°C. NO_x conversion with the air-925°C char decreased with increasing temperature, while the steam activated char maintained essentially the same level of activity between 130 and 160°C. The NO_x reduction activity of the HNO_3-725°C char increased from 3% to 22% between 130 and 160°C, whereas that of the KOH activated char decreased from 22% to 7%. The Centaur carbon performed rather poorly at the two temperatures studied. Note that the ISGS chars tested were not representative of chars optimized for this application. Typically, commercial selective catalytic reduction (SCR) processes use higher surface area (1000-1500 m^2/g) activated carbons made from bituminous coal. Carbo Tech (Essen, Germany) presently manufactures ton quantities of this carbon for carbon-based SCR processes operating in Europe. Singoredjo et al. [34] recently noticed that NO_x removal with carbon in the presence of ammonia was influenced by a number of factors including the number and type of C-O complexes on the carbon surface, nitrogen content of the char, and accessibility of the pores. The oxygen contents of most of our chars were minimized due to the steam activation or thermal desorption treatments used in their preparation.

Incinerator Flue Gas

Incinerator flue gas typically contains much lower concentrations of SO_2 (20-100 ppm) compared to

those found in coal combustion flue gas (500-3000 ppm), but also contains much higher levels of other pollutants such as mercury, dioxins, furans, heavy metals, and hydrochloric acid. STEAG Aktiengesellschaft (Essen, Germany) has pioneered the cleanup of incinerator flue gas using their patented /a/c/t™ process and a low cost (< \$300/ton), low surface area (< 300 m²/g) activated carbon made from German brown coal [1,2]. A U.S. source of this carbon is currently needed for their processes soon to be installed on waste incinerators in the U.S. A market potential of 80,000 tons/year of activated char (160,000 tons of coal) has been estimated, assuming 10% of U.S. incinerators adopt their technology to meet needs emanating from anticipated regulation of emissions from existing incinerators. This potential market for Illinois coal was of interest to us, so we agreed to produce this type of carbon for STEAG.

The laboratory conditions needed to produce a suitable sorbent from a Colchester (Illinois No. 2) hvC bituminous coal were first identified. Char production runs were performed at the ISGS using a 2 in. ID horizontal tube furnace, 4 in. ID, 4 ft. heated zone, continuous feed rotary tube kiln, and a continuous feed charring oven. With the assistance of Allis Mineral Systems (Milwaukee, WI), the production steps were carried through two levels of scale up, culminating in the production of 610 pounds of activated char in an 18 in. ID, 10 ft. heated zone, externally fired rotary tube kiln. A 1500 pound sample of size-graded bituminous coal having a free swelling index of 4.5 was used as feedstock for the production run. A three-step process, which included preoxidation, pyrolysis and activation, was necessary to process this coal. Details of the conditions used in the production runs are described elsewhere [10,16,17]. Table 7 compares the properties of the ISGS char and the char presently used by STEAG (hereafter referred to as Herdofenkoks). It shows that ISGS char had a N₂ BET surface area of only 110 m²/g, but an SO₂ capacity after 4 h greater than that of the Herdofenkoks. The iodine number of the Herdofenkoks was about three times greater than that of ISGS char. (This number relates to the surface area contained in pores greater than 10 Å.) The mechanical strength of ISGS char, although not as good as Herdofenkoks, was still considered satisfactory for this application. Note that the carbon tetrachloride activity of ISGS char is 51 mg/100 g char, about three times that of the Herdofenkoks. The carbon tetrachloride activity is used as an indicator of carbon performance in vapor phase applications, e.g., VOC removal. Normally, one would not expect a carbon tetrachloride activity to be this high given the N₂ BET surface area of the char (110 m²/g). The observed value of 51 is more typical of carbons having surface areas of 800-1200 m²/g. Evidently, the ISGS char (bituminous coal char activated in CO₂ for 2 h) developed a more extensive microporosity than the Herdofenkoks (brown coal pyrolyzed at 950°C for 0.75 h).

Commercial activated carbons available in the U.S. are believed to be too reactive due to their relatively high surface area (> 600 m²/g) and propensity to adsorb and react with NO$_x$. The reaction of carbon with adsorbed NO$_x$ is exothermic and can ignite the carbon bed under certain conditions, e.g., in the absence of gas flow. The STEAG /a/c/t™ process requires the use of a low activity char having a surface area less than 300 m²/g. A 550 pound sample of low surface area activated char produced in this study was shipped to Essen, Germany where it was installed in a pilot plant unit and subjected to a NO$_x$ self heating test. This involved adsorbing NO$_x$ on the carbon until saturated, shutting off the flow of gas to the adsorber, and measuring the temperature rise of the char bed. The ISGS char passed the test and is the only U.S. material known to have done so. (Figure 1 also shows that the NO$_x$ removal efficiency of this char was less than that of the Herdofenkoks.)

The test unit containing ISGS char was then installed on a slipstream of flue gas from a commercial waste incinerator in Germany. Flue gas velocity through the 800 mm char bed was 0.15 m/s. The ISGS activated char removed more than 99.7% of the dioxins and furans from the incinerator flue gas (Table 8). Also, the mercury, which was present in the inlet gas, was not detected in the exit gas. The removal efficiencies achieved by ISGS char were at least as good as, if not better than, those achieved with Herdofenkoks. The two-week test, however, was not of ample duration to observe complete breakthrough of any of the pollutants listed in Table 8, so there was no information on total adsorption capacity. Typically other pollutants do not breakthrough the bed before SO₂, so the SO₂ capacity is considered a good measure of the total adsorption capacity of the char. An economic analysis indicates that it would cost between \$325 and \$400 to produce one ton of ISGS char with a plant designed and constructed to produce 80,000 tons per year, assuming a 20% rate of return on initial investment.

Another potential market for low cost char is the cleanup of coal combustion flue gas. The Mitsui Mining Company Limited (Tokyo, Japan) has developed a combined SO₂/NO$_x$ removal process featuring a two stage adsorber in which flue gas is contacted with activated coke at temperatures between 100 and 200°C [3]. Sulfur oxides are adsorbed onto the activated coke in the first stage resulting in the formation of sulfuric acid. The flue gas moves into the second stage where NO$_x$ reacts with NH₃ to form N₂ and H₂O. The coke from the first stage is thermally regenerated at temperatures between 300 and 500°C. Mitsui has licensed their technology to General Electric and both are working together to develop new markets in the U.S. for their process. (They have also developed a process to clean incinerator flue gas [4].) A carbon having a selling price less than \$600/ton is needed.

Our low cost char was tested by Mitsui Mining under the following conditions: 140°C, 1000 ppm SO₂, 200 ppm NO$_x$. Table 9 compares the properties of ISGS char and Mitsui Mining activated coke. The N₂ BET surface area and SO₂ adsorption capacity of ISGS char is less than that of Mitsui coke. Also, the NO$_x$ removal efficiency of Mitsui coke is significantly greater than that of ISGS char. The surface of the Mitsui coke is said to contain functional groups (C-O, C-N and C-OH) that react more effectively with SO₂ and NO$_x$. Note that the ISGS char tested by Mitsui Mining was not optimized for this process. These tests were performed only to evaluate the potential of our low cost char in other applications.

429

SUMMARY

Activated chars were produced from Illinois coal and tested in various flue gas cleanup applications. A low cost, low surface area char was developed for cleanup of incinerator flue gas. Five hundred pounds of the char was tested on a slipstream of flue gas from a commercial incinerator. The char was effective in removing more than 97% of the dioxins and furans present in the flue gas; mercury levels in the effluent were below detectable limits. Higher activity chars that showed excellent potential for both SO_2 and NO_x removal were also produced. The performance of one char compared favorably with that of a commercial carbon catalyst.

ACKNOWLEDGEMENTS

REFERENCES

1. Brueggendick, H. and Pohl, F.G., Proc. 10th Annual Int. Pittsburgh Coal Conf., 1993, p. 787.
2. Brueggendick, H. and Gilgen, R., ACS Preprints, Div. Fuel Chem., New Orleans, LA, 1996.
3. Tsuji, K. and Shiraishi, I., Proc. Electric Power Research Institute SO_2 Control Symposium, Washington, D.C., 1991, p. 307.
4. Tsuji, K. and Shiraishi, ACS Preprints, Div. Fuel Chem., New Orleans, LA, 1996.
5. Hartenstein, H.-U., Proc. 85th Annual Air and Waste Management Assoc. Meeting, Kansas City, MO (1992).
6. Hartenstein, H.-U., ACS Preprints, Div. Fuel Chem., New Orleans, LA, 1996.
7. Richter, E., Knoblauch, K. and Jungten, H., Proc. 1st Int. Conf. on Processing and Utilization of High Sulfur Coals, 1985, p. 563.
8. Richter, E., Knoblauch, K. and Jungten, H., Gas Separation and Purification 1, 35 (1987).
9. Jungten, H. and Kuhl, H., Chem. Phys. Carbon 22, 145 (1989).
10. Lizzio, A.A., DeBarr, J.A., Kruse, C.W., M., Donnals, G.L. and Rood, M.J., "Production and Use of Activated Char for Combined SO_2/NO_x Removal," Final Technical Reports to the Illinois Clean Coal Institute (1994, 1995).
11. DeBarr, J.A. and Lizzio, A.A., Proc. Int. Conf. on Carbon, Granada, Spain, 1994, p. 268.
12. Lizzio, A.A. and DeBarr, J.A., Fuel 1995 (in press).
13. DeBarr, J.A., "The Role of Free Sites in the Removal of SO_2 from Simulated Flue Gases by Activated Char," M.S. Thesis, University of Illinois, Urbana, IL (1995).
14. DeBarr, J.A., Lizzio, A.A. and Rood, M.J., Proc. 88th Annual Air and Waste Management Assoc. Meeting, San Antonio, TX (1995).
15. DeBarr, J.A. and Lizzio, A.A., Proc. 22nd Biennial Conf. on Carbon, San Diego, CA, 1995, p. 562.
16. Lizzio, A.A., DeBarr, J.A. and Kruse, C.W., Proc. 22nd Biennial Conf. on Carbon, San Diego, CA, 1995, p. 744.
17 Kruse, C.W., Lizzio, A.A., DeBarr, J.A. and Bhagwat, S.B., ACS Preprints, Div. Fuel Chem. 40 (4), p. 838.
18. Lizzio, A.A. and DeBarr, J.A., Proc. 12th Int. Annual Pittsburgh Coal Conf., Pittsburgh, PA, 1995, p. 652.
19. Lizzio, A.A. and DeBarr, J.A., ACS Preprints, Div. Fuel Chem., New Orleans, LA, 1996.
20. Rubel, A.M. and Stencil, J.M., ACS Preprints, Div. Fuel Chem., New Orleans, LA, 1996.
21. Groszek, A.J., ACS Preprints, Div. Fuel Chem., New Orleans, LA, 1996.
22. Nelson, S.G. and Bayak, R.A., Div. Fuel Chem., New Orleans, LA, 1996.
23. Jungten, H., Richter, E., Knoblauch, K. and Hoang-Phu, T., Chem. Eng. Sci. 43, 419 (1988).
24. Ahmed, S.N., Stencel, J.M., Derbyshire, F.J. and Baldwin, R.M., Fuel Processing Technology 34, 123 (1993).
25. Spivey, J.J., Catal. Today 18, 155 (1994).
26. Illan-Gomez, M.J., Linares-Solano, A., Salinas-Martinez de Lecea and Calo, J.M., Energy and Fuels 7, 146 (1993).
27. Illan-Gomez, M.J., Linares-Solano, A., Radovic, L.R. and Salinas-Martinez de Lecea, C., Energy and Fuels 9, 97 (1995).
28. Illan-Gomez, M.J., Linares-Solano, A., Radovic, L.R. and Salinas-Martinez de Lecea, C., Energy and Fuels 9, 104 (1995).
29. Garcia-Garcia, A. Linares-Solano, A., and Salinas-Martinez de Lecea, C., Div. Fuel Chem., New Orleans, LA, 1996.
30. Mochida, I., Kisamori, S., Hironaka, M., Kawano, S., Matsumura, Y. and Yoshikawa, M., Energy and Fuels 8, 1341 (1994).
31. Jang, B.W.-L., Spivey, J.J., Kung, M.C. and Kung, H.H., ACS Preprints, Div. Fuel Chem., New Orleans, LA, 1996.
32. Gangwal, S.K., Howe, G.B, McMichael, W.J. and Spivey, J.J., Final Report to U.S. DOE (1993).
33. Gangwal, S.K., Howe, G.B., Spivey, J.J., Silveston, P.L., Hudgins, R.R. and Metzinger, J.G., Envir. Prog. 12, 128 (1993).
34. Singoredjo, L., Kapteign, F., Moulijn, J.A., Martin-Martinez, J.M. and Boehm, H.-P., Carbon 31, 213 (1993).

Table 1. Correlation of SO_2 adsorption capacity with surface area and chemisorbed oxygen.

Sample	SO_2 Capacity[1] (mg SO_2/g char)	N_2 BET (m^2/g)	CO_2 BET (m^2/g)	SO_2/N_2 (mg/m^2)	SO_2/CO_2 (mg/m^2)	O_2 (wt%)	SO_2/O_2
Calgon F400	206	1000	1000	0.21	0.21	0.5	41.2
Calgon Centaur	327	360	...[2]	0.91	...[2]	...[2]	...[2]
IBC-102, N_2 500°C, 0.5 h	19	1.2	270	15.8	0.07	8.8	0.22
IBC-102, N_2 700°C, 0.5 h	33	10	315	3.3	0.10	1.5	2.20
IBC-102, N_2 900°C, 0.5 h	7	1.2	98	5.8	0.07	0.5	1.40
IBC-102 + KOH, N_2 600°C, 0.5 h	157	500	725	0.31	0.22	7.4	2.12
IBC-102 + KOH, N_2 800°C, 0.5 h	176	800	1155	0.22	0.15	5.6	3.14
IBC-102, 500°C; 10% O_2 390°C	13	220	422	0.06	0.03	8.6	0.15
IBC-102, 700°C; 10% O_2 440°C	37	320	490	0.11	0.08	8.9	0.42
IBC-102, 900°C; 10% O_2 500°C	42	230	395	0.18	0.11	5.2	0.81
IBC-102, 900°C; H_2O, 860°C	176	220	613	0.80	0.29	1.1	16.0
IBC-102, 900°C; H_2O, 860°C; 45% HNO_3, 2.5 h, 25°C	...[2]	400	585	0.06	0.04	16.4	...[2]
IBC-102, 900°C; H_2O, 860°C; 45% HNO_3, desorbed at 525°C	91	460	693	0.20	0.13	5.9	1.54
IBC-102, 900°C; H_2O, 860°C; 45% HNO_3, desorbed at 725°C	241	500	727	0.48	0.33	1.6	15.0
IBC-102, 900°C; H_2O, 860°C; 45% HNO_3, desorbed at 925°C	287	550	726	0.05	0.39	0.5	57.4

[1] SO_2 capacity determined after 6 h.
[2] not determined.

Table 2. SO₂ removal tests.

Cycle	Low Emission (ppm SO₂)	20% BT (min)
HNO₃-925°C		
1	80	3
2	100	80
3	80	60
4	150	25
5	160	35
6	240	30
7	300	20
8	350	15
9	400	10
KOH activated		
1	25	45
2	1800	----

Table 3. SO₂ removal tests.

Cycle	Low Emission (ppm SO₂)	5% BT (min)
HNO₃-725°C		
1	10	60
2	1200	----
Centaur		
1	0	725
2	10	40

Table 4. NOₓ reduction with ammonia.

Sample	130°C	140°C	150°C	160°C
HNO₃-925°C	20	29	33	30
air-925°C	14	8	3	0
H₂O activated	16	14	14	14
HNO₃-725°C	3	6	----	22
KOH activated	22	8	7	----
Centaur carbon	0	----	----	4
RTI carbon	99	99	99	99

Table 7. Comparison of Mitsui coke and ISGS char.

Property	Mitsui coke	ISGS char
N₂ BET surface area (m²/g)	200	105
CO₂ BET surface area (m²/g)	---	142
SO₂ capacity (mg SO₂/g)	100	27.1
DeNOx efficiency (%)	55	18.8
Bulk density (g/ml)	0.60	0.39
Micro strength (%)	70	48
Ignition point (°C)	420	468

Table 5. Comparison of Herdofenkoks and ISGS char.

Property	Herdofenkoks	ISGS char
N₂ BET Surface Area (m²/g)	275	110
Iodine Number	349	137
SO₂ Capacity (wt%, 120°C, 4 h)	2.8	4.2
SO₂ Capacity (wt%, 120°C, 15 h)	7.6	5.8
Bulk Density (lb/ft³)	29.8	23.8
Carbon (wt%)	83.1	87.0
Volatile Matter (wt%)	7.7	4.7
Ash (wt%)	8.7	8.3
Mechanical Strength	98.8	78.3
Ignition Point (°C)	405	395
Carbon Tetrachloride Activity (mg/100 mg char)	17	51

Table 6. Pilot plant tests with ISGS char.

Pollutant	Inlet	Outlet	Efficiency (%)
Dioxins, Furans			
Test 1 (ng/m³)	333.3	0.062	99.98
Test 2 (ng/m³)	337.9	0.052	99.98
Test 3 (ng/m³)	282.3	0.789	99.72
Cadmium, Titanium			
Test 1 (mg/m³)	0.0140	0.0012	91
Test 2 (mg/m³)	0.0062	0.0012	81
Test 3 (mg/m³)	0.0052	0.0004	92
Mercury			
Test 1 (mg/m³)	0.0177	----[1]	----[1]
Test 2 (mg/m³)	0.0384	----[1]	----[1]
Test 3 (mg/m³)	0.0223	----[1]	----[1]
Sb, As, Pb, Cr, Co, Cu, Mn, Ni, V, Sn			
Test 1 (mg/m³)	0.2698	0.0744	72
Test 2 (mg/m³)	0.0805	0.0347	57
Test 3 (mg/m³)	0.0634	0.0185	71

[1] below detection limits.
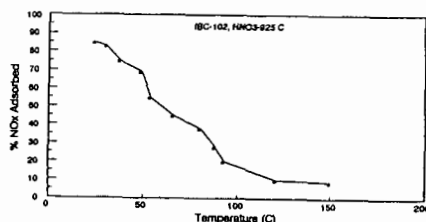
Figure 2. Effect of temperature on NOx removal efficiency.

Figure 1. NOx removal efficiency at 22 C.
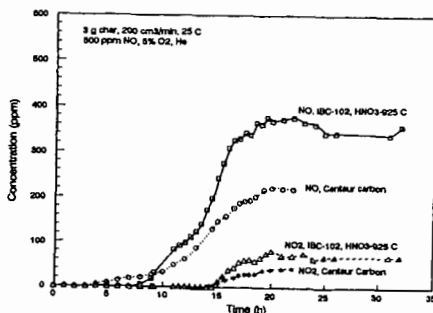
Figure 3. NOx removal with Centaur carbon and IBC-102, HNO3-925 C char.

431

HIGH EFFICIENCY, STRUCTURED-PACKING CATALYSTS WITH ACTIVATED CARBON FOR SO_2 OXIDATION FROM FLUE GAS

Radu V. Vladea[1], Natalia Hinrichs[2], Robert R. Hudgins[1], Sam Suppiah[3], Peter L. Silveston[1]
[1]Chemical Engineering Department, University of Waterloo, Waterloo, Ontario, Canada N2L 3G1
[2]Chemical Engineering Department, University of Erlangen - Nürenberg, Germany
[3]Chemistry and Chemical Engineering Division, Chemical Engineering Branch, AECL, Chalk River, Ontario, Canada K0J 1J0

ABSTRACT
Monolithic or Sulzer CY gauze structured packings were loaded with hydrophobized activated carbon. Studies of their activity for SO_2 conversion to sulfuric acid were carried out with respect to principal scale-up variables of the process: temperature, pressure drop, periodic vs. continuous operation, gas and liquid flow rates. High conversions, high catalyst efficiency, and low pressure drops, long catalyst lifetime, easy of handling catalyst packings are some of the outstanding features of the system.

INTRODUCTION
Environmental regulations impose a removal of at least 85 - 90% of sulfur from fuel. Huge volumes of flue gases (e.g., that of a 700 MW oil-fired power station is equivalent to ca. 2 million cubic meters per hour) containing up to 0.3% SO_2, impose severe requirements on industrial flue gas clean-up plants: low pressure drops at high gas flow rates (>10,000 h^{-1}), sulfuric acid solutions of at least 15 wt% concentration, small volume, easy-to-handle catalysts, long catalyst lifetimes, no waste products generated by the exhausted catalyst, almost constant temperature profiles.

One of the most attractive method is to use activated carbon catalyst to oxidize SO_2. Over the last three decades, numerous studies have described the oxidation of SO_2 on activated carbon catalysts either in gas-solid system when H_2SO_4 is thermally desorbed, or in gas-liquid-solid systems (trickle-bed or slurry) when H_2SO_4 is washed with water [1-10]. As the gas-solid system involves catalyst reheating to accomplish desorption in which the adsorbed sulfuric acid reacts with carbon to form CO_2, H_2O and SO_2, the three phase system seems to be more attractive. Use of large-scale trickle-bed reactors is still hindered by some specific drawbacks: very low effectiveness factor (0.021 for 2.59 mm particle diameter, and 0.45 for 99 μm) , high pressure drops over the catalyst bed, maldistribution of various kinds (including a non-uniform access of reactants to the catalytic surface), rapid SO_2 breakthrough due to sulfuric acid entrapped in pores, and very low concentrations of the sulfuric acid in the effluent. Recognizing that reaction in dumped catalysts is controlled by mass transfer to and from the catalyst, we have studied a three-phase reactor in which the catalyst is deposited as a thin layer (micrometers) on screens of appropriate hydrophobicity. Either monolithic or static mixers configurations, known for their low pressure drops, are used. Their hydrophobic-hydrophilic characteristics determine the distribution of dry and wet zones that spontaneously change with time ensuring both higher access for gaseous reactants to the catalyst and more efficient removal of product from it. The frequency of shifting depends on the gas and liquid flow rates and the catalyst geometry which determines the flow pattern. Because of this dynamic alternation, almost the entire catalytic surface is involved in the oxidation process.

SO_2 oxidation on activated carbon involves a reaction among three species: SO_2, O_2, and H_2O adsorbed on the carbon surface. A reaction of three adsorbed species simultaneously is, statistically speaking, possible but quite unlikely. Nevertheless, activated carbon has an affinity for molecular SO_2, 2.7 times larger than for oxygen [13]. As the solubility of SO_2 in water is more than 10 times larger than for oxygen, O_2 is the thus limiting reactant despite a 100 fold larger partial pressure than that of sulfur dioxide. It is thus intuitive that carbon surfaces are readily populated with SO_2, so that the rate of uptake of oxygen on the active sites is almost certain to be rate-limiting. Infrared analysis demonstrated that in the presence of water vapor and oxygen, sulfuric acid is formed on

carbon. In addition to sulfuric acid, a small quantity of chemisorbed SO_2 was found, as well as some residual water [11]. Once H_2SO_4 is formed, it becomes a competitor for active sites, along with SO_2, O_2, and H_2O. Meanwhile, sulfuric acid decreases SO_2 and O_2 solubilities but not in the intrinsic rate of surface reaction itself, within reasonable limits (up to 30 wt% H_2SO_4).

Sulfuric acid formation is ensured by the water vapor present in flue gas, liquid water only playing the role of product carrier from the catalyst pores. Therefore water flow rate affects the liquid film resistance to the reactants transferring from gas onto the active catalyst sites. The preparation method of our catalysts ensures a hydrophobic catalytic surface still keeping a polar character inside the pores. As was shown [16], pyrone and pyrone-like structures are responsible for the catalytic activity. The presence of hydroxyl groups on the activated carbon provides an additional opportunity for controlling the hydrophobicity inside the pores in order to obtain a controlled wet-proofing.

EXPERIMENTAL
Catalyst
Two basic types of structured packings were used: monoliths and static mixers (Sulzer CY) gauze. Monoliths were built up by rolling together a corrugated gauze, on which activated carbon was loaded using a hydrophobic binder, with a flat screen which was either hydrophilic or hydrophobic. Monolithic catalysts were supplied by Atomic Energy of Canada Limited (AECL). Static mixers were supplied by Sulzer Chemtech, Winterthur, Switzerland, and loaded with activated carbon by AECL. Properties of activated carbon and catalyst beds are given in Table 1. Centaur^{TM} activated carbon (Calgon Carbon Corp.) with an average particle diameter of 0.3 μm has been used for loading the screens in all runs. BET surface areas of the bound carbon were determined at -195.5°C by nitrogen adsorption using a Quantachrome Autosorb Automated Gas Sorption System, Micropore Version 2.44. Typical values were 139.9 m^2/g for overall surface area, 95.7 m^2/g for mesopore area, and 44.2 m^2/g for micropore area.

Table 1. Properties of activated carbon and catalyst beds.

Catalyst	Type	Carbon type/weight (g)	Height cm	Cross-section area cm^2	Volume cm^3
QA 95-8	Monolith-hydrophilic sep. screen, 120 mesh	Centaur/ 10.23	3x10	19.63	589.1
QA 95-9-0	Monolith-hydrophilic sep. screen, 20 mesh	Centaur/ 23.43	3x10	19.63	589.1
QA 95- 9-1	Monolith-hydrophilic sep. screen, 20 mesh	Centaur/ 22.52	3x10	19.63	589.1
QA 95-11-0	Monolith-hydrophilic sep. screen, 28 mesh	Centaur/ 28.44	1x10	19.63	196.3
QA 95-11-1	Monolith-hydrophobic sep. screen, 28 mesh	Centaur/ 28.44	1x10	19.63	196.3
QA 95-12	Static mixers CY	Centaur/ 23.28	2x15	15.90	476.8

Apparatus
The SO_2 oxidation was carried out in a glass reactor of 600 mm length and 50 mm id. Gaseous reactants and water were fed concurrently in the top of reactor. Water was supplied by a micropump Gear Pump - Model 130/150, (Micropump Corporation, Vancouver, WA), after preheating (as needed) and saturation with oxygen in a saturation column filled with static mixers Sulzer Mellapak 125.Y of polypropylene. An adjustable height spray nozzle was used to distribute washing liquids evenly over the cross section of the reactor. Periodic liquid interruptions were achieved by means of a solenoid valve in the feed line to the reactor vessel. The valve was controlled by a microcomputer through a D/A interface. Feed gas with a volumetric composition of 10% CO_2, 5% O_2, and 0.3 % SO_2 was preheated (as needed) and saturated with water at 45°C correspondent to 10% H_2O in the gas mixture, the balance being N_2. Flow rates of the individual gaseous streams were controlled by mass flowmeters Unit (Unit Instruments, Inc., Orange, CA). The reactor was heated using three heating tapes, and temperatures were measured by 0.2 mm o.d. type K thermocouples and recorded by the data acquisition system. Pressure drop in the catalytic bed was measured with a water-filled manometer connected to taps located above and below the bed. The reactor effluent

was cooled and liquid and gas phases were separated. SO_2 concentration in the gaseous effluent was continuously monitored by a UV spectrometer (Western Research, model 721 AT) and recorded by the data acquisition system. The liquid phase was analysed for H_2SO_4 by titration with 0.1 N solution of NaOH. Sulfur dioxide dissolved in liquid effluent was determined by means of a conventional iodine titration. Typical operation conditions are summarized in Table 2.

Table 2. Operating conditions for the reaction studies.

Temperature, $^{\circ}C$	23 to 80
Pressure, MPa	1.013 E - 01
Liquid phase	Deionized water (DI), DI + Tween 20 (4 E - 07 mol/l), DI + acetone (20 wt %)
Gas flow rate, m^3/s, at $25^{\circ}C$	(5.5 to 33) E - 05
Liquid flow rate, m^3/s	(5.3 to 55) E - 09

RESULTS AND DISCUSSIONS

The exploratory investigations were carried out on three main catalytic configurations: monoliths with hydrophilic separation screens (QA 95-9 and QA 95-11-0), monoliths with hydrophobized catalyst and separation screen (QA 95-11-1), and hydrophobized static mixers CY (QA 95-12).
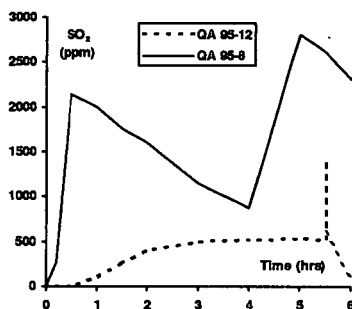

Figure 1. Concentration Profiles of Free SO $_2$ in the Reactor Effluent for Different catalysts

Monoliths with hydrophilic-hydrophobic screens (QA 95-9 and QA 95-11-1) give rise to high liquid static hold-up over the catalyst bed (equivalent to 20 wt% of catalytic stack weight). With these stagnant columns of liquid in each channel, there was poor reproducibility of data preventing a clear conclusion. Obviously, a higher contact time between liquid and catalytic surface improves sulfuric acid removal but, on the other hand, reduces the mass transfer rates of gaseous species onto the catalytic surface. Both periodic operation (flushing periods of 30 to 45 seconds followed by "dry" periods of 255 to 270 seconds) and continuous flushing, gave non-reproducible results. Periods of high conversions alternate with lower removal of SO_2 in a random way due, probably, to a very complex hydrodynamic regime in the channels which creates a "storage effect" of SO_2. A typical concentration profile for the "free" SO_2 released in the effluent is shown in Figure 1 (QA 95-8). In spite of high conversions periods - especially in forced periodic operation - the system didn't permit further studies of the influence of other process variables, because

Figure 2. Conversion to H $_2SO_4$ vs. Superficial Liquid Velocity

of high oscillations in SO_2 conversions during the same run.

Initially with low temperature runs, negligible H_2SO_4 is formed in the micropores because of low reaction rate; the diffusing species (SO_2, O_2, and H_2O) fill the micropore volume taking up the available vacant sites. However, beyond this initial period, reaction occurs on a time-scale longer than the adsorption time-scale, the product H_2SO_4 forms and displaces other molecules (SO_2, O_2, H_2O) until a new steady-state between sorption and reaction prevails.

The influence of liquid flow rate on the SO_2 conversion is shown in Figure 2. An increase in conversion is expected due to the improvement of sulfuric acid removal. Obviously, better contact between catalyst surface and washing liquid will facilitate efficient cleaning of the catalyst. Runs with a mixture of deionized water and 20 wt% acetone or with a wetting agent (Tween 20, 10^{-6} M) which facilitate penetration in the meso- and micro-pores and faster removal of sulfuric acid, led to an increase of conversion with 10 to 18%. This is contrary to the contention [8]

that the higher the liquid flow rate the lower is the fraction of SO_2 oxidized to sulfuric

Figure 3. Conversion to H ₂SO₄ vs. Superficial Gas Velocity

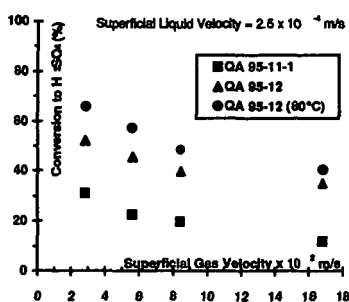acid. In the range of interest, due to the hydrophobicity of the catalyst surface, reactants are mainly supplied directly from the gaseous phase.

Meanwhile, at temperatures higher than 80°C, sulfuric acid present in catalyst pores has such high concentrations as to allow the use of sulfuric acid solutions (7 to 15%) as washing liquids. In this way it is possible to use optimum flow rates of liquid, without an undesirable dilution of the solution. On the other hand, preliminary tests done with an organic substrate (dodecylbenzene) gave very promising results in a reactive removal of sulfuric acid with production of surfactants, which might be a novel route for

SO_2 removal.

Increasing the gas flow rate cause a decrease in conversion (Figure 3). The oxidation rate lagged behind the adsorption step rate [16]. As expected, shorter contact time
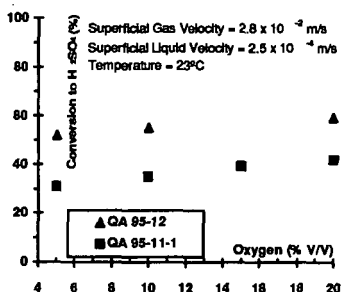

Figure 4. Conversion to H ₂SO₄ vs. Oxygen Concentration in the Feedstock

between reactants and catalyst reduced conversions. The most likely reasons for this are correlated with the efficiency of sulfuric acid removal and/or oxygen activation rate. An enhance of catalytic activity has been achieved by doping the internal surface with typical oxidation catalysts, e.g., oxides of cobalt, chromium, and vanadium, or phthalocyanines [14,15].

It is important to mention that even at the highest gas and liquid flow rates, the pressure drops over the catalytic bed were less than 25×10^{-2} kPa.m^{-1}. The lowest values were achieved with hydrophobic monoliths.

One of the most important requirements in the oxidation process is to supply sufficient amounts of oxygen onto the active sites. The oxygen adsorption onto the catalytic surface follows a Henry type isotherm; hence an increase in its partial pressure will increase the available active oxygen and will provide an increase in conversion. As shown in Figure 4, an increase in the range of 5 to 20 % O_2, led to higher conversion. Further investigations are necessary to develop a better correlation of oxygen concentration with temperature and nature and size of liquid flow rate.

Temperature has a complex effect on the oxidation process. An increase in temperature leads to higher reaction rates and higher concentrations of the sulfuric acid loaded in the
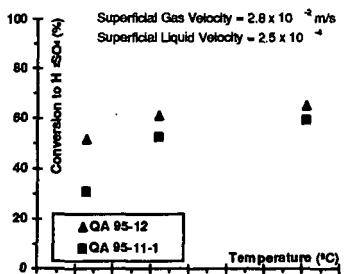

Figure 5. Conversion to H ₂SO₄ vs. Temperature

pores. However, temperature also determines lower solubilities of reactants in the liquid inside and outside the pores with a subsequent decrease of reaction rate. In our situation, experimental data confirm an enhancement of conversion to sulfuric acid with temperature increase. Values as high as 92% were achieved at 80°C. Experiments in the range of 90 to 120°C are now in progress. The hydrophobic character of the catalytic surface and the continuous alternation of dry and wet surfaces permits easier transfer of reactants to the catalyst surface directly from the gaseous phase, making the contribution of dissolved species less important (Figure 5).

CONCLUSIONS

Centaur activated carbon bound in a thin layer on monolithic or static mixer packings has been used with very good results for SO_2 oxidation. Conversions of 92% and productivities relative to a unit weight of carbon were achieved. The high catalytic activity shown by the hydrophobic thin layer catalyst appears to benefit from its hydrophobicity to water and short diffusional paths. Investigations on catalytic system behaviour at higher temperatures (100-120°C), using either sulfuric acid solutions or organic substrates, as washing liquids are now in progress. As a consequence of the system features, the use of periodic flushing is expected to enhance catalyst productivity. Very low pressure drops over the catalyst bed, and production of either concentrated solutions of sulfuric acid or sulfated/sulfonated organic substrates make the process very attractive for commercial plants.

REFERENCES

1. H. Komiyama and J. M. Smith, AIChE J., 21 (1975) 664
2. N. E. Amadeo, M. A. Laborde and N. O. Lemcoff, Chem. Eng. J., 41 (1989) 1
3. G. Q. Lu and D. D. Do, Sep. Technol. 1993, 106
4. P. M. Haure, R. R. Hudgins and P. L. Silveston, Chem. Eng. J., 43 (1990) 121
5. J. V. Metzinger, A, Kühter, P. L. Silveston and S. K. Gangwal, Chem. Eng. Sci., 49 (1994) 4553
6. P. M. Haure, R. R. Hudgins and P. L. Silveston, AIChE J., 35 (1989) 1437
7. H. Jüngten, Carbon, 15 (1977) 273
8. E. Richter, K. Knoblauch and H. Jüngten, Gas Separation & Purification, 1, (1987) 35
9. P. Davini, Carbon, 29 (1991) 321
10. M. Hartman and R. W. Coughlin, Chem. Eng. Sci., 27 (1972) 867
11. E. Richter, Catal. Today, 7 (1990) 93
12. G. Q Lu, P. G. Gray and D. D. Do, Chem. Eng. Comm., 96 (1990) 15
13. X. Py, C. Roizard and N. Midoux, Chem. Eng. Sci., 50, (1995) 2069
14. M. Vassileva, A. Andreev, G. Schulz-Ekloff and D. Wohrle, React. Kinet. Catal. Lett., 50 (1993) 139
15. H. Jüngten and H Kühl in P. A. Thrower (Ed.), Chemistry and Physics of Carbon, vol.22, Marcel Dekker, 1989, p.145-193
16. C. Moreno-Castilla, F. Carasco-Marin, E. Utrera-Hidalgo and J. Rivera-Utrilla, Langmuir, 9 (1993) 1378

CONTROL OF MERCURY EMISSIONS IN FLUE GASES BY ACTIVATED CARBON ADSORPTION

Radisav D. Vidic
Department of Civil and Environmental Engineering
University of Pittsburgh, Pittsburgh, PA 15261

ABSTRACT

The adsorptive capacities of virgin and sulfur impregnated activated carbons (GAC) for gas-phase mercury were evaluated as a function of temperature and influent mercury concentration. The virgin activated carbon showed little adsorptive capacity, especially at temperatures above 90 °C. The pronounced effect of temperature on the adsorptive capacity evidences a physical adsorption mechanism between the mercury and virgin GAC. Sulfur impregnated activated carbons exhibited enhanced mercury removal efficiency over the non-impregnated varieties due to formation of mercuric sulfide on the carbon surface. This chemisorption process is enhanced with increased temperature between 25 and 90 °C. However, at 140 °C a decrease in adsorptive capacity occurs, indicating reduced formation of mercuric sulfide. The method used for impregnating GAC with sulfur had a pronounced effect on mercury removal capacity. The chemical bonding of sulfur and carbon surface at 600 °C provides a more uniform distribution of sulfur throughout the GAC pore structure than achieved by conventional condensation techniques, yielding improved performance.

INTRODUCTION

Numerous studies have documented the pathways of trace contaminants through coal-fired power plants[1-4]. Lack of mass closure for Hg, Se, Cl, and Br indicates that these elements exist entirely in the gas phase upon exiting the combustion zone, and pass unaffected to the smokestack[1]. Numerous studies have shown that the best available control technology for particulate pollution abatement (high-efficiency electrostatic precipitator) has virtually no impact on the release of vapor-phase trace elements to the atmosphere[1,3-5]. The estimated quantity of mercury released globally from coal combustion is 3000 metric tons per year[5]. Gaseous mercury emissions exist in both the elemental and oxidized (Hg^{2+}) forms. Chu and Schmidt[6] have determined that the percent of oxidized mercury in flue gases is a function of the coal type and composition. By quantifying the speciation of mercury in flue gases Prestbo and Bloom[7] reported that particulate forms of mercury generally constitute less than 5% of the total mass of mercury emitted.

The deposition of mercury following discharge to the atmosphere causes some local, but mostly regional impacts. Klein and Russel[8] showed that the soil around a Michigan power plant was enriched with Cd, Co, Cr, Hg and Ni, with contaminant concentration gradients reflecting the prevailing wind patterns. Hall et al.[9] found that the elemental Hg^0 will add to the atmospheric background concentration, while the divalent gaseous and particle-associated mercury will have a tendency to deposit within the region where it is emitted.

Increased levels of mercury in the environment are of particular concern due to well documented food chain transport and bioaccumulation of mercury and its forms[10]. Mercury is highly toxic to algae, fungi and seed plants. Mercury tends to accumulate in the lower stem areas rather than in the upper photosynthetic areas. Mercury is a cumulative poison in animals since there is no known homeostatic mechanism for regulating mercury concentration in tissues. Mercury is also a potent neurotoxin that is capable of causing irreversible damage to the central nervous system, or even death. Metabolism and degree of toxicity of mercury to animals is a function of several factors: chemical form, route of entry, duration of exposure, and dietary content of interacting elements, especially selenium. Mercury vapors can cause bronchitis, interstitial pneumonia, circulatory collapse, renal failure and dermatitis, while mercury salts can cause anorexia, memory loss, weight loss and gingivitis. Methylmercury causes paresthesia, hearing loss, ataxia, peripheral vision loss and cerebral disease[11].

Regulatory initiatives and increased public concern regarding elevated levels of mercury in the environment have stimulated research efforts to develop technologies for mercury emission control. Although there are currently no regulations for mercury emissions from electric utilities, the Clean Air Act Amendments of 1990 (Title III, Section 112[b][1]) (CAAA) require major sources to use the best available control technology (BACT), and require the U.S. Environmental Agency (EPA) to perform a study of mercury emissions.

Activated carbon adsorption is a technology that offers great potential for the control of gas-phase mercury emissions. Sinha and Walker[12] demonstrated that the capacity of sulfur impregnated carbons greatly surpassed the virgin carbons at 150 °C due to chemical adsorption of mercury

(through formation of mercuric sulfide) on the carbon surface. Matsumura[13] found that iodized and oxidized activated carbons adsorb 20-160 times more mercury than the untreated variety. Metzger and Braun[15] determined that 5% iodine impregnated activated carbon was an excellent adsorbent for elemental mercury, with the adsorptive capacity greater than 5 mg/g at temperatures ranging from 20 to 180 °C. Otani et al.[14] found that increased sulfur impregnation up to 13.1 wt. %, did not have a detrimental effect on elemental mercury adsorption at low temperatures (36 °C), as reported by Sinha and Walker[12]. Otani et al.[14] suggested that the contradicting results are related to surface area reduction resulting from different impregnation methods and activated carbon types. They also found that a portion of the sulfur impregnated on the activated carbon surface is chemically adsorbed, and not available to react with mercury to form mercuric sulfide. Krishnan et al.[15] demonstrated that the virgin activated carbons adsorbed less mercury with increased temperature, and that heat pretreatment with clean nitrogen at 140 °C destroyed active sites, reducing the adsorptive capacity further still. Livengood et al.[16] showed that the adsorption capacity of sulfur impregnated carbon decreased with an increase in temperature from 55 to 90 °C.

MATERIALS AND METHODS
Three types of activated carbons were used in this study. Two of the carbons, Filtrasorb-400 (F-400) and HGR were supplied by the manufacturer (Calgon Carbon Corporation, Pittsburgh, PA) in 12x40 and 8x12 U.S. Mesh sizes, respectively. The third type, F-400S, was produced by contacting F-400 carbon with excess amount of sulfur in a pure nitrogen atmosphere at 600 °C. The sulfur contents of F-400, F-400S, and HGR were 0.76, 7.61, and 9.24 wt. %, respectively. The particle size used in this study was 60x80 U.S. Mesh size.

A schematic representation of the experimental setup is shown as Figure 1. By varying temperature of mercury permeation cell and nitrogen flow rate, a wide range of mercury concentrations were generated. The impinger solution used for absorbing gas-phase mercury was prepared with 1.5% potassium permanganate in 10% sulfuric acid as described by Shendrikar et al.[17] Quantification of elemental mercury in the gas phase was performed at a wavelength of 253.7 nm using a Perkin-Elmer Model 403 atomic absorption spectrophotometer (AAS) (Perkin-Elmer, Norwalk, CT) fitted with 18-cm hollow quartz gas cell (Varian Australia Pty. Ltd., Mulgrave, Victoria, Australia). Vapor-phase mercury detection limit for the analytical system used in this study was 1.8 μg/m³.

Breakthrough curves were generated using a 3/16 inch stainless steel column charged with 100 mg of activated carbon. The bed was secured in the adsorber by two 200 U.S. Mesh size stainless steel screens. The adsorber was operated in the downflow mode to minimize the potential for fluidization of the packed bed. The influent gas and activated carbon temperatures were regulated by placing the adsorber in a temperature controlled oven. With both the mercury generation device and adsorber off-line, clean nitrogen was passed through the AAS cell for 30 minute warm-up period. Once the lamp output was stabilized and AAS zeroed, the mercury generation device was placed on-line, and the oil bath temperature adjusted to generate the desired mercury concentration. The gas flow rate was adjusted to 0.97 L/min and the absorbance from the AAS was recorded following a 2 hour equilibration period. The adsorber was then placed on-line and the effluent mercury concentrations were continuously monitored until complete breakthrough. Several blank runs with no carbon in the adsorber that were performed at temperatures ranging from 25 -140 °C using an influent mercury concentrations in the range of 25-115 μg/m³ revealed that no uptake or transformation of elemental mercury was facilitated by the stainless steel reactor or support screens.

RESULTS AND DISCUSSION
Figure 2 summarizes the adsorptive capacities measured for F-400 activated carbon at different temperatures. The increase in the slope of the isotherm lines with an increase in temperature shows that bonding of mercury to the carbon surface decreases with an increase in temperature. Only a single data point is shown at 200 °C because no adsorptive capacity was detected at the next lower influent concentration increment of 55 μg/m³. The pronounced effect of temperature on the adsorptive capacity of F-400 GAC for elemental mercury indicates that the adsorption mechanism is physical in nature.

A series of experiments was conducted to determine the adsorptive capacity of sulfur impregnated (HGR) activated carbon as a function of adsorber temperature. The influent mercury concentration was maintained at 55 μg/m³ in all cases while the adsorber temperature was 25, 50, 90, and 140 °C. Figure 3 indicates that the adsorptive capacity of HGR carbon for mercury increases with an increase in temperature. However, this figure accounts only for the elemental form of mercury in the adsorber effluent as detected by the AAS. A separate experiment was performed to simultaneously monitor the effluent from an adsorber maintained at 90 °C for elemental and total mercury. The elemental form (Hg⁰) was constantly monitored by AAS output, and the total mercury concentration was determined by trapping the gases in an impinger train at various time increments. As illustrated in Figure 4, complete breakthrough was achieved for total mercury, while

elemental mercury reached equilibrium effluent concentration at C/C_0 equal to 0.6. The difference is attributed to the presence of mercuric sulfide in the adsorber effluent. Once a critical concentration of mercuric sulfide is formed on the surface of the GAC, desorption of mercuric sulfide occurs, forcing the product (HgS) into the effluent gas stream with the desorption process being more pronounced at 90 °C than at 20 or 50 °C.

Figure 5 compares the breakthrough characteristics of HGR GAC at 25 and 140 °C. As is apparent from this figure, after 8 hours into the experiment, the effluent from the adsorber operated at 140 °C reached complete breakthrough, while the effluent from the adsorber operated at 25 °C reached equilibrium at C/C_0 equal to 0.75. Experimental investigations of sulfur loss from the carbon surface upon exposure to nitrogen gas at various temperatures revealed that the low adsorptive capacity of HGR GAC exhibited at 140 °C can not be the result of sulfur loss form the carbon surface. However, this difference in behavior may be attributed to the fact that both physisorption and reaction with sulfur contribute to mercury uptake at 25 °C while only the reaction with sulfur could be occurring at 140 °C. Another possible explanation for the observed behavior is that the rate of HgS formation on the surface of the sulfur impregnate is much higher at 140 than 25 °C so that the HgS would quickly blind the sulfur surface and prevent any further mercuric sulfide formation, which results in complete breakthrough.

Figure 6 compares the adsorptive characteristics of F-400S to that of HGR and F-400 at 25 °C and an influent mercury concentration of 115 $\mu g/m^3$. As is apparent from this figure, F-400S performed much better than HGR and F-400. The superior adsorptive capacity of F-400S over HGR can not be explained by sulfur content on the GAC surface since F-400S contained 7.61 wt. % sulfur while HGR contained 9.24 wt. % sulfur. It is hypothesized that the higher adsorptive capacity of F-400S is the result of improved sulfur distribution throughout GAC surface. The sulfur in the HGR pore is most likely deposited by condensation as a slug deeply imbedded in the pore. Since the sulfur in the case of F-400S carbon is chemically bonded to the surface, it is more evenly distributed over the entire surface area. Although HGR carbon has higher sulfur content as compared to F-400S, the mercury-sulfur reaction on the surface of the HGR carbon is limited by the rate of diffusion of mercuric sulfide from the surface into the sulfur mass.

REFERENCES
1. Klein, D.H.; Andren, A.W.; Carter, J.A.; et al. *Environ. Sci. & Technol.*, 1975, 9, 973-979.
2. Kaakinen, J.W.; Jorden, R.M.; Lawasani, M.H.; West, R.E. *Environ. Sci. & Technol.*, 1975, 9, 862-869.
3. Germani, M.S.; Zoller, W.H. *Environ. Sci. & Technol.*, 1988, 22(9), 1079-1085.
4. Meij, R. *Water, Air, and Soil Pollution*, 1991, 56, 21-33.
5. Billings, C.E.; Sacco, A.M.; Matson, W.R.; Griffin, R.M.; Coniglio, W.R.; Harley, R.A. *J. of the Air Pollution Control Association*, 1973, 23, 773-777.
6. Chu, P.; Schmidt, C. Proceedings of the 1994 Pittsburgh Coal Conference, 1994, 1, 551-556.
7. Prestbo, E.M.; Bloom, N.S. Proceedings of the 1994 Pittsburgh Coal Conference, 1994, 1, 557-562.
8. Klein, D.H.; Russel, P. *Environ. Sci. & Technol.*, 1973, 7, 357-358.
9. Hall, B.; Schager, P.; Lindqvist, O. *Water, Air, and Soil Pollution*, 1991, 56, 3-14.
10. Langley, D.G. *J. Water Pollution Control Federation*, 1973, 45, 44-51.
11. Westoo, G. *Science*, 1973, 181, 567-568.
12. Sinha, R.K.; Walker, P.L. *Carbon*, 1972, 10, 754-756.
13. Matsumura, Y. *Atmospheric Environment*, 1974, 8, 1321-1327.
14. Metzger, M.; Braun, H. *Chemosphere*, 1987, 16, 821-832.
15. Otani, Y; Emi, H.; Chikao, K.; Uchijima, I.; Nishino, H. *Environ. Sci. & Technol.*, 1988, 22, 708-711.
16. Krishnan, S.V.; Gullett, B.K.; Jozewicz, W. *Environ. Sci. & Technol.*, 1994, 28, 1506-1512.
17. Livengood, C.D.; Huang, H.S.; Wu, J.M. Proceedings of the 87th Annual Meeting of the Air & Waste Management Association. 1994, reprint , 14 p.
18. Shendrikar, A.D.; Damle, A.; Gutknect, W.F. *Collection Efficiency Evaluation of Mercury-Trapping Media for the SASS Train Impinger System*, U.S. Environmental protection Agency. U.S. Government Printing Office: Washington, DC, 1984, EPA-600/7-84-089.
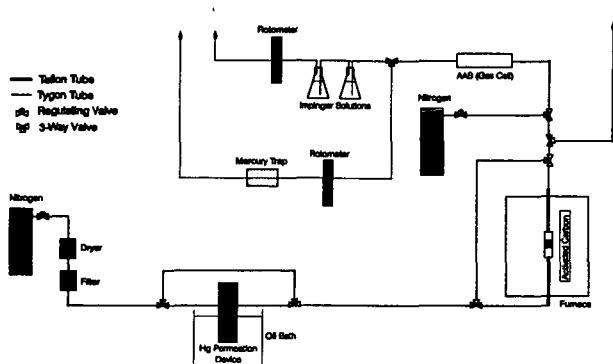
Figure 1. Schematic representation of the experimental system

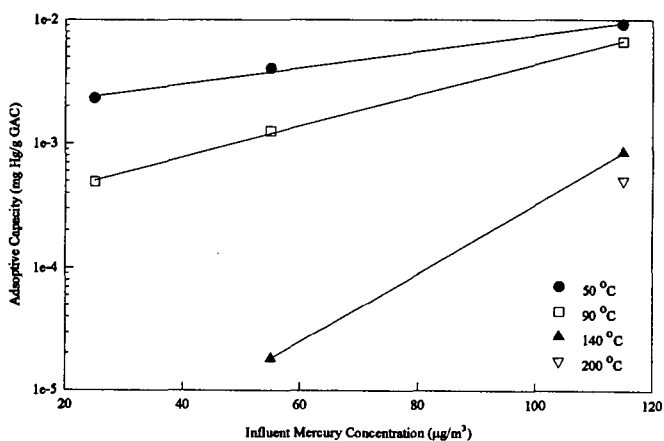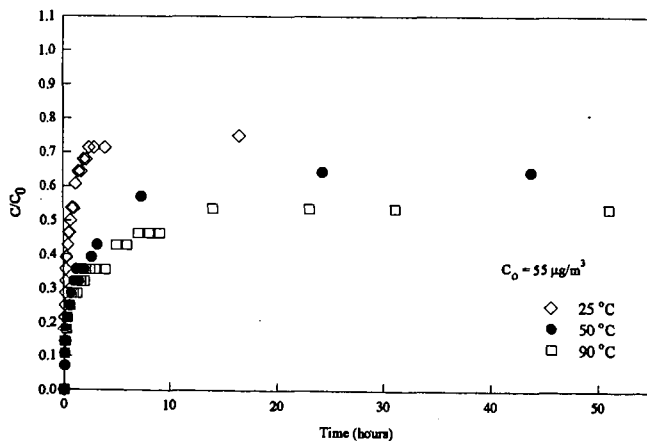**Figure 2.** Adsorptive capacity of F-400 GAC for vapor-phase mercury

Figure 3. Effect of temperature on mercury breakthrough from HGR adsorber

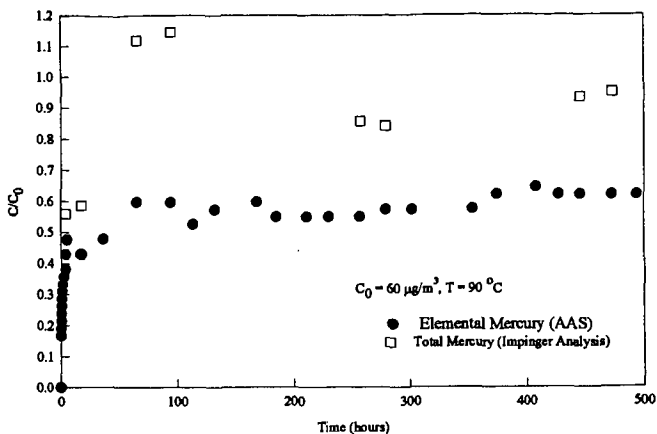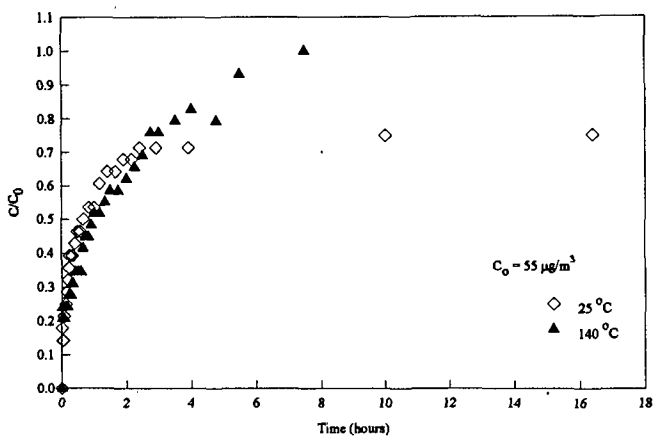**Figure 4.** Elemental and total mercury breakthrough from HGR adsorber

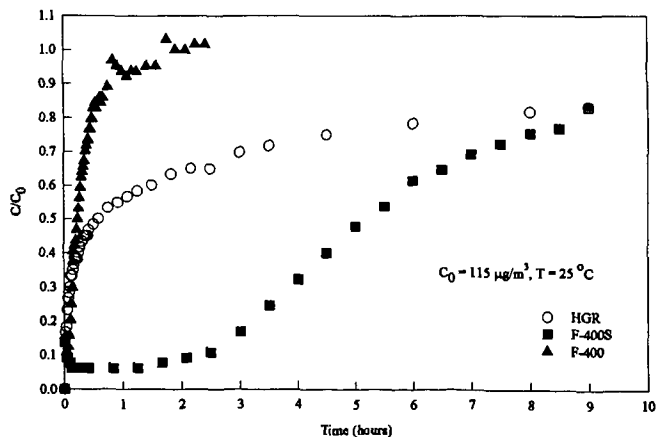**Figure 5.** Breakthrough of mercury from HGR adsorber at 25 and 140 $^{\circ}$C

Figure 6. Removal of mercury by F-400, HGR and F-400S activated carbons

441

MERCURY REMOVAL FROM COMBUSTION FLUE GAS BY ACTIVATED CARBON INJECTION: MASS TRANSFER EFFECTS

Shiaoguo Chen and Massoud Rostam-Abadi
Illinois Geological Survey, Champaign, IL 61820
Ramsay Chang
Electric Power Research Institute, Palo Alto, CA 94304-1395

Keywords: Mercury, Activated Carbon, Flue Gas and Mass Transfer

INTRODUCTION

The Clean Air Act Amendments of 1990 listed 189 substances as hazardous air pollutants, of which 37 substances have been detected in power plant emissions. Of the 37 hazardous air pollutants, 11 are trace metal species. Mercury is trace metal species of greatest concern because of perceived risks from its environmental release and because it is present mainly in the vapor form and is not captured effectively by existing particulate removal systems.

Carbon-based processes (both direct injection and fixed-bed) have been developed for control of mercury emission from municipal- and hazardous-waste incinerators. Existing data from the incinerators provide some insight on mercury control, but these data cannot be used directly for coal-fired utilities because mercury concentration, species, and process conditions differ greatly[1]. For example, municipal solid waste (MSW) mercury concentrations (200 to 1000 $\mu g/m^3$) are one to two orders of magnitude higher than that for coal combustion sources which contains typically 5 to 10 $\mu g/m^3$.

Injection of activated carbon upstream of a particulate control has the potential of providing a low-cost option for control of mercury emissions from utility flue gas[1]. In several bench[2-7] pilot and full-scale tests[8-10] of the method, the influence of carbon type[2-4,10], carbon structure[3-4] and carbon surface chemistry[2,4,5,7], injection methods (dry or wet)[10], amount of carbon injected[8-10], and flue gas temperatures[8-10] on mercury removal have been examined. The low concentrations of mercury in the flue gas, and limited exposure time (3 seconds) of the sorbent, generally required large amounts of activated carbons in these sorbent injection tests. To achieve high Hg removal (>90%), the required ratio of carbon to mercury (C/Hg) in the flue gas has generally (on weight basis) been found to be 3,000-20,000, depending on the process conditions. Tests have shown that the carbon to mercury ratio in MSW incinerators is more than an order of magnitude lower than that necessary to achieve similar mercury removal in coal combustors.

The high C/Hg ratio could be a result of either mass transfer limitation or low mercury capacity of carbon due to the extremely low concentration of mercury in the flue gas, or the low reactivity of the carbon. To reduce the operating cost of the carbon injection process, either a more efficient sorbent that can operate at a lower C/Hg ratio, or a lower-cost sorbent, or both is required. An understanding of physical and chemical processes that affects mercury removal from flue gas and a systematic sorbent development study would be required to develop an efficient, cost effective carbon injection process for removal of mercury from coal-fired utility flue gas.

The work presented here represents phase 1 of an ongoing EPRI and Illinois Clean Coal Institute funded research program to develop a low-cost, high efficiency sorbent for mercury removal. In this paper the influence of both film and intraparticle mass transfer on mercury removal in the carbon injection process are described.

MASS TRANSFER CALCULATIONS

Film Mass Transfer,

In absence of internal (intraparticle) diffusion, the equation describing the transfer of mercury molecules from the bulk flue gas to the surface of carbon per unit interfacial area is:

$$N = k_g (C_g - C^{'}) \tag{1}$$

where N=mass flux (g/cm^2*s); k_g is mass transfer coefficient (cm/s); C_g are the mercury concentration (g/cm^3) in the bulk flue gas and and C* is the mercury concentration in equilibrium with the adsorbed mercury on the carbon surface. Assuming the interfacial area per unit volume in the duct is a/V, the flux per volume of the duct will be:

$$N = k_g \frac{a}{V} (C_g - C^{'}) \tag{2}$$

where a is the total interfacial area in the duct (cm^2/cm^3) and V is the total volume of the duct (cm^3) and Cg-C* is considered as the driving force for mass transfer.

The typical mercury concentration in the utility flue gas is about 10 $\mu g/Nm^3$ and usually 90% removal is required. Typically, the particle size of powdered activated carbon ranges between 1 and

60 μm. When injected into the flue gas, the fine carbon particles will suspend and flow with the gas stream. The relative velocity between the particles and the flue gas is practically zero. If the carbon particles are well dispersed and do not agglomerate during the process, the mass transfer coefficient at the gas-solid interface could be calculated by the following equation:

$$\frac{k_g d_p}{D_{Hg}} = 2 \tag{3}$$

where d_p = particle size (cm) and D_{Hg} = diffusivity of the mercury molecule in flue gas (cm²/s). Equation (3) shows that the mass transfer coefficient k_g increases with decreasing carbon particle size. Any attempts to introduce turbulence to the flow may not have any significant effects on the mass transfer coefficient.

The value reported in the literature for the diffusivity of mercury in air at 341 °C is D_{Hg}= 0.473 cm²/s which can be corrected to the flue gas temperature (140 °C), D_{Hg}= 0.261 (cm²/s). Substituting this value into equation (3) gives :

$$k_g = \frac{2D_{Hg}}{d_p} = \frac{2 \times 0.261}{d_p} = \frac{0.522}{d_p} \quad (cm/s) \tag{4}$$

If no strong turbulence or back mixing occurs in the duct, the gas-solid phase can be modeled as a plug flow system. The mass balance equation for a plug flow system is:

$$k_g \frac{a}{V}(C_g - C^*)Sdz = -F_g dC_g \tag{5}$$

where S is the cross section area of the duct (cm²), F_g is the flue gas flow rate (Nm³/s) and dz is the differential length of the duct (cm).

To examine the role of film mass transfer (the maximum mass transfer flux), assume $C^* << C_g$ at all positions in the duct (this means that mercury adsorption capacity of the carbon and the carbon reactivity are not limiting the mass transfer rate). Equation (6) is obtained by integrating equation(5) using the following boundary conditions:

At the entrance: z=0, C_g=C_0

At the outlet: z=L, C_g=C_g

$$\ln(\frac{C_0}{C_g}) = k_g \frac{a}{V} \frac{SL}{F_g} \tag{6}$$

where L is the length (cm) of the duct and SL/F_g=t is the residence time of carbon particles in the duct. For 90% mercury removal, C_g=0.1C_0 and Equation (6) can be rearranged to solve for the minimum interfacial area:

$$\frac{a}{V} = \frac{2.303}{k_g} \frac{F_g}{SL} = \frac{2.303}{0.522} \frac{d_p}{t} = 4.412 \frac{d_p}{t}(cm^2/cm^3) \tag{7}$$

This relationship provides the minimum activated carbon interfacial area required by film mass transfer to remove 90% of the mercury from one Nm³ of utility flue gas.

Because only the external surface area of carbon particles serves as the gas-solid interfacial area the minimum interfacial area needed for mass transfer implies that a certain minimum amount of carbon is required to achieve the desired mercury removal. The minimum amount of carbon and thus the minimum ratio of carbon/mercury can be calculated as follows.

For spherical particles the external surface area per gram of activated carbon is:

$$\frac{\pi d_p^2}{\frac{1}{6}\pi d_p^3 \rho_c} = \frac{6}{d_p \rho_c} \tag{8}$$

443

where ρ_c is the carbon particle density in g/cm^3. The amount of carbon required for mercury removal from one Nm^3 of utility flue gas therefore is:

$$(4.412\frac{d_p}{t})/(\frac{6}{d_p\rho_c})=0.7353\frac{d_p^2\rho_c}{t} \qquad (9)$$

The carbon /mercury ratio can be calculated from the following relationship:

$$\frac{Carbon}{Mercury}=0.7353\frac{\rho_c d_p^2}{t\ (C_0-C_g)} \qquad (10)$$

Assuming carbon particle size of 10 μm, residence time of 3 seconds, carbon particle density of 0.5 g/cm^3, inlet mercury concentration of 10 $\mu g/Nm^3$, and outlet mercury concentration of 1 $\mu g/Nm^3$, the carbon/mercury ratio is:

$$\frac{Carbon}{Mercury}=0.7353\times\frac{0.5\times(10\times10^{-4})^2}{3\times(10\times10^{-12}-1\times10^{-12})}=13611$$

This analysis indicates that a high C/Hg ratio is required when the carbon particle size is larger than 10 μm.

Equation (10) shows that the C/Hg ratio depends strongly on the particle size. Table 1 represents the carbon/mercury ratios required for 90% mercury removal under mass transfer limited conditions with activated carbon ranging in size from 1 to 10 μm (particle density of activated carbon ρ_c= 0.5g/cm³ and contact time of 3 seconds were used).

Table 1 Carbon/mercury ratios for different carbon particle sizes

Particle size (μm)	k_g (cm/s)	Interfacial area (m²/g)	Ratio of C/Hg *	
			Utility Flue Gas	MSW Flue Gas
10	522	1.2	13611	227
5.5	949	2.18	4117	68
5	1044	2.4	3402	57
3	1740	4.0	1224	20
1	5220	12.0	136	2.3

* The inlet mercury concentrations for utility flue gas and MSW flue gas are 10 and 600 μg/Nm³, respectively.

Equation (10) also shows that the C/Hg ratio depends on the mercury concentration in the flue gas (C_0-C_g). Usually, MSW incinerator flue gas has a mercury concentration of around 200-1000 $\mu g/Nm^3$ which is almost two orders of magnitude higher than that of utility flue gas. The C/Hg ratio, according to equation (10), for the MSW flue gas will be about two orders of magnitude lower than that of the utility flue gas. The last column of Table 1 lists the C/Hg ratios required for MSW flue gas. For example, the theoretical C/Hg ratio required for a MSW flue gas containing 600 $\mu g/Nm^3$ mercury is about 60 times lower than that of a utility flue gas containing 10 $\mu g/Nm^3$ mercury for the same level of mercury removal .

These calculated C/Hg ratios are the minimum needed and assumes mass transfer limitations. At low C/Hg ratios (such as for the MSW flue gas at a C/Hg ratio of 2.3), it is possible that the carbon will actually have reached its equilibrium capacity. Also at higher temperatures, most sorbents have very low capacity for mercury. Under these conditions much more sorbent than that predicted by mass transfer limitation will be needed.

Intraparticle Diffusion

Because diffusivities in mircroporous materials vary broadly, depending on the pore structure and pore size, it is difficult to estimate diffusivity when the diffusion is in the configurational range. Configurational diffusion only occurs when the micropore size is comparable to the molecular size of the adsorbate. In this study, calculations were made for a single spherical carbon particle dispersed in a flue gas. The carbon particle is exposed to a step change in mercury concentration at its external surface at t = 0 (corresponding to the injection location). The diffusion of mercury molecules into the carbon, assuming a constant effective diffusivity, can be described by:

$$\frac{\partial q}{\partial t} = D_{Hg}(\frac{\partial^2 q}{\partial r^2} + \frac{2}{r}\frac{\partial q}{\partial r}) \tag{11}$$

where D_{Hg} is the mercury effective diffusivity in carbon particle and q(r,t) is the adsorbed phase concentration of mercury at position r (inside the carbon particle) and time t. If the mercury concentration at the external surface of the particle remains constant, the following initial and boundary conditions apply:

$$q(r_c = \frac{1}{2}d_p, t) = q_0 \tag{12}$$

$$q(r,0) = 0, \tag{13}$$

$$(\frac{\partial q}{\partial r})_{r=0} = 0 \tag{14}$$

The solution to this problem is given by[11]:

$$\frac{\bar{q}}{q_0} = \frac{m_t}{m_\infty} = 1 - \frac{6}{\pi^2}\sum_{n=1}^{\infty}\frac{1}{n^2}\exp(-\frac{4n^2\pi^2 D_{Hg}t}{d_p^2}) \tag{15}$$

where $\bar{q}$, the average concentration of mercury inside the particle, is defined by:

$$\bar{q} = \frac{3}{r_c^3}\int_0^{r_c} qr^2 dr \tag{16}$$

and m_t and m_∞ are the uptakes of mercury at time t and t= ∞. When the fractional uptakes, m_t/m_∞, are larger than 70%, the following simplified equation can be used:

$$\frac{m_t}{m_\infty} = 1 - \frac{6}{\pi^2}\exp(-\frac{4\pi^2 D_{Hg}t}{d_p^2}) \tag{17}$$

For a particle size of d_p=10 μm, t=3 s, and 90% mercury uptake (m_t/m_∞=0.90), the mercury diffusivity in activated carbon can be calculated using Equation (17):

$$D_{Hg} = -\frac{d_p^2}{4\pi^2 t}\ln(\frac{\pi^2}{6}(1 - \frac{m_t}{m_\infty})) = -\frac{(10\times10^{-4})^2}{4\times\pi^2\times3}\ln(\frac{\pi^2}{6}\times0.1) = 1.52\times10^{-8}(cm^2/s) \tag{18}$$

This value of diffusivity is in the range of configurational diffusion. The above calculations indicate that with a 10 μm activated carbon particle, the intraparticle diffusion will be important only when the pore diameter is about 3 Å, i.e., the molecular diameter of mercury.

It should be noted that in the above calculations it was assumed that the mercury concentration at the external surface of the particle remains constant. In the actual process, however, the mercury concentration in the flue gas decreases as the particles flow along the duct. If other conditions remain same, the diffusivity calculated under this situation is 1.32×10^{-8} cm²/s which is comparable to the value calculated using Equation (17).

From the above calculations, it can be concluded that intraparticle diffusion is unlikely to be the controlling step in the carbon injection process so long as the micropore size of the activated carbon is larger than around 3 Å, which is true for most of activated carbon.

DISCUSSION

Assuming that the adsorption of mercury from flue gas is mass transfer limited provides an indication of the maximum mercury efficiency possible for a specific amount of sorbent injected or an indication of the minimum amount of sorbent needed to achieve a specific mercury removal efficiency. The analysis presented in this paper indicates that under certain carbon injection conditions, mercury removal from coal-fired flue gas is film mass transfer controlled. For example,

Miller et al.[5] used a C/Hg ratio greater than 3000 for an activated carbon with a weight-averaged particle size of 5.5 μm, to remove about 90% mercury from a flue gas. In the same study, for an iodine-impregnated activated carbon with a weigh-averaged particle size of 3 μm, the C/Hg ratio was about 1000. Such C/Hg ratios are comparable to those listed in Table 1.

Full-scale tests of carbon injection process in MSW flue gas also confirm the results shown in Table 1. Licata et al.[9] reported that the equilibrium mercury capacity of an activated carbon used in their tests was about 0.33 gHg/gAC which corresponds to a C/Hg ratio of 3 (temperature was not mentioned). However, in full-scale MSW tests with the same carbon, a C/Hg ratio of more than 300 was used to reduce mercury concentration in the flue gas from 600 to 70 μg/Nm³ at 135 °C. This ratio corresponds to 0.0033 gHg/gAC which is only 1% of the equilibrium capacity of the carbon. In still another field test, White et al.[10] found that carbon injection methods (dry or wet) had a significant effect on the mercury removal while the type and surface chemistry of the activated carbon had not. These data suggested that mass transfer was controlling the mercury removal.

For conditions where mercury adsorption is mass transfer limited, measures should be taken to increase the mercury mass flux (from the bulk gas to the surface of carbon) rather than using a carbon with high capacity. To increase the mass transfer, either the mass transfer coefficient, k_g, or the interfacial area, a/V, should be increased. According to equation (3) the mass transfer coefficient increases with decreasing carbon particle size. Reducing carbon particle size also increases the interfacial area, without increasing carbon dosage. The most effective way to reduce the C/Hg ratio is therefore to decrease the carbon particle size. This is clearly shown in Table 1; when the carbon particle size is reduced from 10 μm to 1 μm, the C/Hg ratio is reduced from 13,611 to about 136.

Mass transfer limits only apply when the carbon has sufficiently high reactivity and capacity. When the operating temperature of the process is high, e.g. >180 °C, and the level of mercury removal is high, e.g. 95%, then the mercury capacity of carbon may become limiting. In this case, significantly larger amounts of carbon may be needed unless better carbon (larger capacity and high reactivity) can be produced.

CONCLUSIONS

- The minimum amount of carbon needed to achieve a specific mercury removal efficiency via sorbent injection can be predicted by assuming mass transfer limitations.

- Mercury removal effectiveness can be increased by decreasing the size of the carbon injected, increasing the residence time, or the amount of carbon injected.

- Intraparticle diffusion is not important because of the small carbon sizes normally used for injection.

- If mercury removal is limited by the reactivity and capacity of the carbon (i.e. not mass transfer limited), then significantly more carbon than predicted by mass transfer limitations may be needed for effective mercury removal unless the reactivity and capacity of the carbon can be improved through structural and surface chemistry changes.

ACKNOWLEDGEMENT

REFERENCES

1. Chang, R.; and Offen, G., "Mercury Emission Control Technologies: An EPRI Synopsis," Power Engineering ,Volume 5, November, 1995.
2. Teller, A. and Quimby, J. M., In Proc. of 84th Annual Meeting & Exhibition of the Air & Waste Management Association, Vancouver, British Columbia, June 16-21, 1991.
3. Krishnan, S. V.; Gullett, B. K. and Jozewicz, W., Environ. Sci. Technol. 1994, 28, 1506
4. Gullett, B. K. and Jozewicz, W., Presented at 1993 International Conference on Municipal Waste Combustion, Williamsburg, VA, 1993.
5. Miller, S. J., Laudal, D. L.; Chang, R. and Bergman, P.D., In Proc. of 87th Annual Meeting & Exhibition of the Air & Waste Management Association, Cincinnati, Ohio, June 19-24, 1994.
6. Maskew, J. T.; Rosenhoover, W. A.; Stouffer, M. R.; Vargo, F. R. and Withum, J. A., Preprint ACS Fuel Division, 40(4), 843, 1995.
7. Young, B. C. and Musich M. A., Preprint ACS Fuel Division, 40(4), 833, 1995.
8. Felsvang, K., Gleiser, R.; Juip, G. and Nielsen, K. K., Fuel Proc. Technol., 1994, 39, 417.
9. Licata, A.; Babu, M.; and Nethe, L.; Proceedings of the 1994 National Waste Processing Conference. Boston, Massachusetts, June 1994.
10. White, D. M.; Kelly, W. E.; Stucky, M. J.; Swift, J. L.; and Palazzolo, M. A., US EPA, EPA/600/SR-93/181. January, (1994).
11. Ruthven, D. M., "Principles of Adsorption & Adsorption Processes", John Wiley & Sons, New York, 1984.

CARBON CATALYSTS FROM COAL FOR ENVIRONMENTALLY RELEVANT REACTIONS

Phillip B. Kaufman, Edward P. Ladner and Malvina Farcasiu
U.S. Department of Energy, Pittsburgh Energy Technology Center
P.O. Box 10940, Pittsburgh, PA 15236

Marit Jagtoyen and Frank Derbyshire
University of Kentucky, Center for Applied Energy Research
3572 Iron Works Pike, Lexington, KY 40511-8433

INTRODUCTION

Activated carbons can be produced from coals by a variety of thermal and chemical-thermal methods. A method related to the present paper is the chemical treatment of coal with aqueous KOH first at relatively low temperature (315-482 °C), followed by carbonization at higher temperatures in the range of 704-982 °C (1). In previous publications (2-4) we have shown that temperatures as low as 75 °C in the first step, followed by carbonization at 600-900 °C gave good quality, high surface area, active carbons.

Activated commercial carbons produced from coal are used for water purification, solvent recovery, supports for catalysts (5) and for SOx and NOx removal from gas streams (6).

Another important use of carbon catalysts for environmental cleaning is the removal of halogen from halogen-containing compounds. Two basic approaches could be used: 1. gas phase catalyzed oxidation of the halogen-containing compounds to carbon dioxide and the corresponding halogen-containing acid (7) and 2. catalytic dehalogenation. The case of carbon catalyzed dehalogenation of an alkyl chloride was studied in detail by Sohr and Boehm (8). The case of liquid-phase carbon black catalyzed hydrodehalogenation of halogenated aromatic compounds was studied by Farcasiu et. al (9,10). An important difference between the oxidative dehalogenation and hydrodehalogenation is that in the oxidative method the carbon in the halogen-containing compounds is transformed into carbon dioxide, while in hydrodehalogenation the halogen removal from an aromatic hydrocarbon is selective and the hydrocarbon skeleton is maintained. The two methods address two different environmental situations, i.e. the removal of a high concentration contaminant (oxidation), or the selective removal of halogen from a hydrocarbon mixture containing some halogen compounds.

The use of carbon materials such as some carbon blacks, for hydrodehalogenation and hydrodehydroxylation of condensed polyaromatic compounds has been reported (9,10). Very good activities and selectivities have been observed with some carbon blacks for the hydrodehalogenation of halogenated condensed polyaromatic compounds such as halogenated naphthalenes, phenanthrenes, and pyrenes. Only very modest dehalogenation was observed for compounds, such as 4-chlorobiphenyl, containing halogen substituted at benzenic rings.

When carbon materials are used as catalysts for specific reactions, the preparation of the carbon material could be customized to substantially increase in the catalytic activity. The role of the carbonization temperature on the catalytic activity (for hydrocracking of alkyl substituted condensed polyaromatics) of resorcinol-formaldehyde aerogel-based materials has been reported (11). In that work it was shown that the catalytic activity of the carbonized aerogels increases with the carbonization temperature, reaches a maximum around 1050 °C and then decreases dramatically. Graphite is not active catalytically in such hydrocracking reactions.

We have found that under very defined preparation conditions, carbon materials prepared from coal could be very active hydrocracking and hydrodehalogenation catalysts for aromatic compounds. We reported recently (12) the influence of the method of preparation on the catalytic activity of coal-derived carbon catalysts for hydrocracking and hydrodehydroxylation reactions.

In the present publication, we will discuss how various parameters could be varied during

the preparation of coal-based catalysts to optimize their activity for the dehalogenation reaction of halogenated aromatic compounds.

EXPERIMENTAL

Various coals were activated using a two step procedure at the Center for Applied Energy Research (2). The first step involved the mixing of a solution of potassium hydroxide with -100 mesh cleaned coal (KOH to coal weight ratio 1.42:1). This mixture was heated at 75 °C for two hours under nitrogen. The heat treatment temperature (HTT) at 800 °C or 900 °C for one hour is the second step, followed by leaching to remove KOH.

Indiana VII is a hvC bituminous coal and was cleaned at Entech Global, Inc, using two different methods. Selective agglomeration (SA) is a method for rejecting mineral impurities from ground coal using pentane and heptane as reusable bridging liquids. Microcel™ Column (MC) is a column flotation method. Wyodak Black Thunder is a subbituminous coal, and Illinois Basin hvC coal (IBC) is a high volatile, bituminous coal.

The surface areas of these activated carbons were measured by nitrogen adsorption at 77 K using the BET method.

Two activated carbons, WS 4 and Centaur™ HSV, were donated by Calgon Carbon Corporation. The WS 4 carbon is prepared from dense wood and thermally activated, while Centaur™ HSV is prepared from bituminous coal. A carbon black, Black Pearls 2000 (BP2000), was donated by Cabot Corporation.

The dehalogenation activity of various carbon catalysts was tested for the debromination of 1-bromonaphthalene in the presence of a hydrogen donor, 9,10-dihydrophenanthrene (9,10-DHP). The reaction conditions were in all cases: 350 °C, 1 hour, wt. ratio 1-bromonaphthalene : 9,10-DHP : catalyst 1 : 4 : 0.1. The experimental procedure is explained elsewhere (9).

Gas chromatographic analysis of the product was carried out on a Hewlett Packard 5890A Series II, equipped with a JW-SE-42 column and a FID.

RESULTS AND DISCUSSION

We observed previously (9,12) that the reaction-specific catalytic activity of some synthesized carbon catalysts could be optimized by varying the preparation conditions. We observed that the preparation is reaction-specific and chemical reactions with various mechanisms could require quite different carbon materials to achieve optimum catalytic activity. We believe this fact is related to the presence of several types of active sites on the surface of the catalyst and to their relative concentration and/or strength, as a function of the preparation conditions. We will discuss how such a preparation could be optimized for the dehalogenation of halogenated condensed polyaromatic hydrocarbons. The method for the synthesis of coal-based carbon catalysts is described in the experimental part. Several parameters are very important in the preparation of coal based catalysts according to this method:
    1. the temperature of step 2 (HTT)
    2. the rank of coal
    3. the method of coal preparation/cleaning prior to activation

1. Influence of the temperature in step 2 (HTT)

We have found that catalysts for hydrodebromination and hydrodehydroxylation reactions can be made by chemically activating coals (Table 1). These activated carbons perform better than commercially available carbon materials such as BP2000 (Cabot), WS 4 and Centaur™ HSV (Calgon). As shown in Table 1, the extent of the hydrodebromination of 1-bromonaphthalene is greatest when the heat treatment temperature (HTT) in step 2 reaches 800 °C. At this temperature, surface area is at a maximum, but as can be observed from the conversion data, the increase in surface area alone cannot explain the difference in reactivity. In the case of the hydrodehydroxylation of 2-naphthol, the maximum conversion is reached at 700 °C and appears to become steady above that temperature. For comparison we show data (Table 1) on the catalytic activity of some commercial active carbons. BP2000 and WS 4 are nearly the same for both reactions. However taking into account the higher surface area of BP2000, WS 4 appears to be a

slightly more active catalyst. Centaur™ HSV, which is made from bituminous coal, is the least active in our reactions.

The products in the hydrodebromination reaction are tetralin, naphthalene, and 2-bromo-5,6,7,8-tetrahydronaphthalene. The hydrodehydroxylation reaction yields tetralin, naphthalene, naphthalone, and 2-hydroxy-5,6,7,8-tetrahydronaphthalene.

The influence of HTT in step 2, was also observed for Indiana VII activated carbons in Table 2.

2. Influence of coal rank

We found that a HTT of 900 °C is optimal for both Indiana VII bituminous coal and Black Thunder subbituminous coal in the hydrodehalogenation of 1-bromonaphthalene. However, if we compare the highest hydrodehalogenation values, the catalyst prepared from subbituminous coal is better than the catalyst prepared from bituminous coal. Under our test conditions, the best catalyst obtained from Indiana VII gave a conversion of 1-bromonaphthalene of 62% as compared with 76% for the best preparation from Black Thunder subbituminous coal. Whether these results represent the general case, and better catalysts for the debromination can be obtained from subbituminous coals, is far from being proven and therefore more cases should be studied.

3. Influence of the method of coal cleaning on the catalytic activity of the carbon catalysts

To avoid a large concentration of mineral matter in the activated carbons prepared from coals, the coal mineral matter should be substantially removed prior to activation. We started a systematic study in this area using Indiana VII precleaned by Entech to about 2.6 % ash by two different cleaning methods: solvent agglomeration and column flotation (see the experimental section). Cleaning the same coal using a dry separation method (tribo-electrostatic separation) is in progress, and the coal obtained by this method will be also used to prepare carbon catalysts. The results obtained to date are given in Table 2.

The data (Table 2) seem to indicate that coal cleaning by aqueous flotation (MC) in the presence of low amounts of surfactants is a preferred method to clean coals prior to synthesis of the catalysts. It may be that the coal cleaning method influences the types of active sites present on the surface of carbon catalysts, and therefore it may be possible to control the selective catalytic properties by choosing the conditions of the catalyst preparation.

CONCLUSIONS

Carbon materials prepared from coals could be used as active and selective catalysts for reactions of interest in environmental chemistry, such as the dehalogenation of halogenated condensed polyaromatics and the dehydroxylation of phenols or condensed polyaromatics. We have identified three important parameters to be considered in the catalyst preparation: 1. the temperature of step 2 (HTT); 2. the rank of coal; 3. the method of coal preparation/cleaning prior to activation.

DISCLAIMER

Reference in the paper to any specific commercial product, process, or service is to

facilitate understanding and does not necessarily imply its endorsement by the United States Department of Energy.

REFERENCES

1. U.S. Patent 4,082,694, Apr. 4, 1978.
2. Jagtoyen, M., Toles, C., and Derbyshire, F., ACS Preprints Division of Fuel, 1993, 38(2), 400.
3. Jagtoyen, M., Derbyshire, F., Proceedings Ninth Annual Pittsburgh Coal Conference, 1992, October 12-16, p.483.
4. Jagtoyen, M., Derbyshire, F., Rimmer, S., and Rathbone, R., Fuel, 1995, 74(4), 610.
5. Baker, F.S., "Activated Carbons" in Kirk-Othmer Encyclopedia of Chemical Technology, 4th Ed., John Wiley & Sons, Inc. 1992, Vol.4, p.1016.
6. Tsjui, K., Shirashi, I., and Dague, R.F., Proceedings Sixth International Symposium Integrated Energy and Environment Management, New Orleans, LA, U.S.A., 1993, March 10-12.
7. Petrosius, S.C., and Drago R.S., J. Chem. Soc. Chem. Commun. 1992, 344 and references therein.
8. Stohr, R; Boehm, H.P. in "Proceeding, Carbon 1986, International Carbon Conference", Baden-Baden, 1986, p.334, and references therein.
9. Farcasiu, M; Petrosius, S.C.; Ladner, E.P., J. Catal, 1994, 146, 313.
10. Farcasiu, M.; Petrosius, S.C., U.S. Patent 5,369,214, Nov. 29, 1994.
11. M. Farcasiu, C. Smith, A.P. Sylwester and E.P. Ladner, "Carbon Materials - Activity and Selectivity in Hydrocracking Reactions" ACS Preprints, Division of Fuel Chemistry, 202nd ACS Meeting, New York (Fall 1991), 36(4), 186
12. M. Farcasiu, P.B. Kaufman, E.P. Ladner, F. Derbyshire and M. Jagtoyen " Carbon Catalysts for Reactions Relevant to Coal Liquefaction" Coal Science, 1995 Conference on Coal Science Proceedings, J.A. Pajares and J.M.D. Tascon Editors, 1995 Elsevier Vol II, p.1303.

Table 1. Effect of Heat Treatment Temperature (HTT) on Hydrodehalogenation and Hydrodebromination Reactions.

CATALYST	HTT °C	SURFACE AREA m^2/g	% CONVERSION[1.]	
			1-Br-naphthalene	2-Naphthol
IL #6 IBC 106	600	835	26	35
IL #6 IBC 106	700	1081	40	48
IL #6 IBC 106	800	1583	72	48
BP-2000	-----	1475	25	36
WS4	-----	1300	22	34
CENTAUR™ HSV	-----	-----	8	20

1. Wt ratio Catalyst:1-Br-naphthalene or 2-naphthol:9,10-DHP = 1:10:40; reaction temperatures for 1-Br-naphthalene or 2-naphthol are 350 °C and 410 °C, respectively , for 1 hour.

Table 2. Effects of Coal Cleaning Methods on the Conversion of 1-Br-naphthalene.

COAL[1.]	HTT °C	SURFACE AREA m^2/g	% CONVERSION[2.]
Indiana VII-SA	800	1602	50
Indiana VII-SA	900	2180	59
Indiana VII-MC	800	1790	57
Indiana VII-MC	900	1997	69

1. SA = Selective Agglomeration; MC = Microcel™ Column.
2. Catalyst:1-Bromonaphthalene:9,10-DHP = 1:10:40 at 350 °C for 1 hour.

THE POTENTIAL FOR INCREASING THE USE OF
CATALYTIC CARBONS IN COMMERCIAL APPLICATIONS

Carl W. Kruse, Illinois State Geological Survey,
615 E. Peabody Drive, Champaign, IL 61820

ABSTRACT
A carbon catalyst, prepared either by oxidizing activated carbon with air at 500-700°C or by oxidizing activated carbon with boiling nitric acid followed by heating it to 500-700°C, is the subject of this paper. This catalyst, designated $OAC_{500-700}$, catalyzes the removal of hydrogen chloride from alkyl halides. Because $OAC_{500-700}$ retains adsorptive properties of an activated carbon it can be used both to adsorb pollutants from liquid or gaseous streams and to convert them to recyclable products. A highly-developed micropore structure is not required for all uses of activated carbon or a catalyst produced from it. A comparatively inexpensive ($325/ton projected) low surface area (<300 m^2/g) carbon has been developed at the Illinois State Geological Survey (ISGS) for cleaning incinerator flue gas. This grade of activated carbon is widely used in Europe for flue gas cleaning and for other applications. Activated carbon adsorbers of some type are required by recently passed U.S. Environmental Protection Agency (EPA) regulations for municipal waste combustors to control emission of cadmium, mercury, lead, dioxins, furans and acid gases (U.S. EPA, 1995). Similar regulations are expected for hospital and hazardous waste incinerators. The marketing of less costly activated carbons of the type used widely in Europe is expected in the United States. Low cost $OAC_{500-700}$ made from less expensive grades of activated carbon may become available for large scale adsorbent/catalyst systems designed to both remove and decompose toxic pollutants found in liquid and gaseous streams, chlorinated organic compounds in particular.

INTRODUCTION
$OAC_{500-700}$ has the potential to solve a number of environmental problems associated with misplaced organic chlorides. Chlorinated compounds in drinking waters and aquatic environments have become a significant topic for study by scientists concerned about effects of direct toxicity and/or carcinogenicity on human and aquatic life (Hanson, 1994). A correlation between surface water chlorination and cancer mortality rates in humans has been shown to be statistically significant (Kalmaz and Kalmaz, 1981). The chlorination of surface waters has been shown to produce high levels of trihalomethanes (THMs) (Bellar et al., 1974). Roughly 98% of this nations drinking water systems use chlorination. More than 300 chlorinated organic compounds have been identified in chlorinated potable waters, cooling waters, and sanitary effluents (U.S. Environmental Protection Agency (EPA), 1975). Activated carbons are needed to capture, concentrate, and decompose pesticides and THMs that are formed when the water is chlorinated (Graham and Ramaratnam, 1993). Regeneration with steam or superheated steam in the field is practical with low molecular weight volatile organic compounds (VOCs), but less volatile organics may require high temperatures (750-850°C) if regeneration of the expensive types of activated char now available is required.

The destruction of halogenated organics in wastes is another potential use of $OAC_{500-700}$. Halogenated organic compounds account for a major portion of toxic and persistent hazardous wastes. In Illinois, the General Assembly in 1981 passed a bill which prohibits landfill disposal of hazardous wastes effective January 1, 1987, unless the generator and disposal site operator can demonstrate that no reasonable alternative is available. In 1983, this schedule was accelerated for liquid hazardous wastes; P.A. 83-1078 prohibits landfill disposal of liquid hazardous wastes unless there is no reasonable alternative. A November 7, 1986, rule on solvents and dioxins began the phasing out of all landfill disposal of halogenated solvents. Methods which will convert some of this hazardous waste into recyclable chemical compounds are high priorities for the Illinois Hazardous Waste Research and Information Center (Miller, 1990).

The destruction of halogenated waste compounds is also a goal of the US EPA. A US EPA report describes an experimental project at Radian Corporation, Research Triangle Park, North Carolina, to validate the effectiveness of a treatment of halogenated waste compounds with a reagent composed of potassium hydroxide in a relatively small quantity of polyethylene glycol (Harden & Ramsey, 1986). It was effective in destroying the organic compounds chosen as being representative of low molecular weight compounds encountered in hazardous wastes including CCl_4, $CHCl_3$, CH_2Cl_2, $C_2H_4Br_2$, and CCl_3NO_2.

Potential uses of $OAC_{500-700}$ go beyond the problem of chlorinated organics. $OAC_{500-700}$ has recently been shown to catalyze other elimination reactions including the dehydration of alcohols, the deamination of amines and the dehydrosulfurization of mercaptans (Kruse et al., 1991).

BACKGROUND

Oxygen complexes control many of the properties of activated carbons (Boehm and Bewer, 1976; Leon y Leon D. and Radovic, 1994). An oxidized carbon catalyst of a type first described in the patent literature (Kruse and Ray, 1966) is the focus of this paper. It was initially produced by air oxidation of carbon blacks and activated carbons in the 500-700°C temperature range and is now designated $OAC_{500-700}$. It was effective for the dehydrochlorination of alkyl halides and promoted polymerization of chloromethyl aromatics (Kruse, 1969a). Incorporating potassium salts into the catalyst inhibited skeletal rearrangements of olefins produced from monochloro n-alkanes (Mahan et al., 1967). Continuous vapor phase dehydrochlorination of mixed linear C_{13}-C_{14} monochlorides gave >95% conversion for 690 hours (73.5 g of alkyl chlorides/gram catalyst) with $OAC_{500-700}$ produced from Darco activated charcoal (Kruse, 1969b). Engineers advising the inventors of this catalyst believed the costs would be too high for one-time use in a commercial plant. Regeneration was achieved with a steam-nitrogen mixture at 750°C but predicting the time needed to attain the desired precise amount of burn-off was difficult. Too much gasification shortened catalyst life. The regeneration method and the projected catalyst cost were among the factors that frustrated commercial development in the late 1960s. The commercial price of activated carbons marketed in the United States remains high today, at approximately $0.40 to dollars/pound (one to a few dollars/kg) and $OAC_{500-700}$ manufactured from them will bear the same high cost liability of the 1960s.

Not all processes require the expensive, high surface area adsorbents that dominate the U.S. domestic market. STEAG's a/c/t™ process is one of the processes being offered for licensing in the United States to clean incinerator flue gas. It does not require a sorbent with a N_2 BET surface area greater than 300 m^2/g (Bruggendick, 1993). The spent sorbent from STEAG's process is not regenerated, and regeneration may not be necessary with other processes using lower cost, lower surface area activated carbon. The state of Illinois through its Illinois Clean Coal Institute has demonstrated that an activated carbon satisfactory for use in STEAG's process can be produced from Illinois coal (Kruse et al., 1995b). The projected price by the ISGS for this sorbent, if produced in a dedicated plant having an 80,000 tons/year capacity, is $325/ton ($0.35/kg).

The price of the adsorbent (herdofenkoks) used by STEAG's European licensees is about $0.15/lb ($0.33/kg). This less costly activated carbon adsorbent has been available in Europe for several decades. Adsorbents of this type, made from brown coal, are known in Germany as F-coal and in Russia as S-coal (Smisek, 1970). They are used in technical applications for which cost and not adsorption capacity is the primary concern. This is the case when the active life of the material is for some reason low and replacement is not dictated by inadequate adsorption capacity. For example, the desulfurization of industrial gases using activated carbon is effective because activated carbon catalyzes the reaction

$$2 H_2S + O_2 \text{ --> } 2 H_2O + 2 S + 106 \text{ kcal}$$
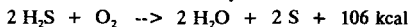
The sulfur, deposited in the pores of the active carbon, is extracted when the hydrogen sulfide in the gas exceeds a prescribed limit. Gas-adsorption active carbons are not suitable for this purpose. For this use, the important factor is not a highly developed microporous structure, but the number of macropores. The best results are obtained with F-coal.

DISCUSSION

A two step method for producing $OAC_{500-700}$ is a recent development (Kruse, 1995). The discovery that the oxidation of an activated carbon with boiling nitric acid followed by desorption of most of the CO_2-forming oxygen complexes in an inert atmosphere produces $OAC_{500-700}$ was a by-product of other research. During a study to determine the effect of oxygen complexes on the selective adsorption of targeted compounds from water, a series of carbons having differing levels of oxygen complexes was prepared by thermally desorbing CO_2 and CO from oxygen complexes introduced by nitric acid oxidation (Feizoulof et al., 1993). Adsorption isotherms for p-nitrophenol (PNP) were determined for the series of carbons and plots were made of the data using the Freundlich equation. The slope of the line generated in these plots is a measure of the strength of adsorption. The strength of the adsorption of PNP went through an unexpected maximum between desorption temperatures of 425°C and 725°C; material desorbed at 525°C had the highest slope (figure 1a). The adsorption tests were then repeated with carbons produced by desorption at 475°C, 525°C, 575°C and 625°C. The strongest adsorption was at 575°C (figure 1b).

Initial catalyst work by the author in the 1960s showed that the oxygen complexes put on below about 300-400°C did not produce dehydrohalogenation catalysts. Heating to 800°C destroyed the catalyst properties. A temperature of 600°C was an ideal mid range temperature for producing the active catalyst. Because temperature programmed desorption (TPD) in the recent studies showed the oxygen complexes on materials produced by the two methods, i.e., air (or dilute oxygen) oxidation (figure 2 e,f) and the two step oxidation/desorption method (figure 2 b,c) were similar and the strength of the adsorption of PNP went though a maximum at the preferred temperature (600°C) for producing the catalyst with air, comparisons of catalyst

452

activity were made. The percent conversion in a vapor phase dehydrochlorination of 1,1,2,2-tetrachloroethane at 450°C over a bed of the test material was the measure of catalyst activity (Fatemi et al, 1993). The material produced by desorption of oxygen complexes at 500-700°C was indeed a good catalyst (Kruse et al., 1995a). It appears that CO-producing oxygen complexes are essential and that the CO_2-producing complexes that are desorbed by heating to 500°C reduce catalyst activity. A similar effect for catalyzing oxidation reactions was stated by Boehm et al. (1984), "enhancement could sometimes also be observed after chemisorpiton of oxygen. There was no clear-cut picture in this case, however, the general impression is that catalytic activity is enhanced by basic surface oxides, whilst acidic surface oxides are inhibitory".

The adsorption properties of the starting activated carbon are modified but not lost by making it a catalyst. Most of the initial carbon's adsorption capacity is available to remove a variety of pollutants from liquid and gas streams and, in addition, $OAC_{500-700}$ has the potential to convert many classes of pollutants to recyclable compounds (Kruse et al., 1992; Beaulieu et al., 1992; Fatemi et al., 1993; Feizoulof et al., 1993).

COMMERCIALIZATION

Important factors for future commercial development of $OAC_{500-700}$ include (1) how it ranks in competing tests with other catalysts, (2) comparative disposal costs and (3) availability and pricing. Porous glass (unglazed porcelain) (Lycourghiotis, 1976), silica gel, (Misono, 1973, Lycourghiotis et al., 1981; Mochida et al., 1981; Suarez and Mazzieri, 1987), B-18 crown ether-potassium chloride on silica gel (Fujitsu et al., 1985), alcoholic potassium hydroxide, and the new Calgon carbon catalyst, Centaur, are among its rivals. Extensive comparative tests of $OAC_{500-700}$ and other catalysts will be necessary to determine the strengths and weaknesses for specific applications. The disposal costs must be weighed against regeneration costs. Incineration appears an option for $OAC_{500-700}$ and Centaur not available to other catalysts. It remains to be seen how much the price of Centaur (about $2.50/pound today) will decrease with large scale production.

The estimated production capacity of activated carbon in the United States, which currently has N_2 BET surface areas from 500-2500 m^2/g, was estimated in 1990 to be 146,000 metric tons (Baker et al., 1992). Retrofitting only a fraction of the existing incinerators with carbon-based systems would create a demand greater than exists today for all types of activated carbon. Because of the number of grades of activated carbon marketed today, the prices reflect fine chemicals prices, often in dollars per pound. With the arrival of dedicated facilities for producing 80,000 ton/year or more of one type of activated carbon, the prices can be expected to decline, whatever the grade of activated carbon marketed. The future cost of $OAC_{500-700}$ should parallel the decreasing prices of activated carbon marketed in the Unied States.

CONCLUSIONS

The high cost of many technically feasible systems for protecting the environment prevents serious consideration of their use. Providing the data base on lower cost adsorbents and catalysts will promote their commercial availability in the future. A low temperature oxidation/desorption sequence has been developed; this process is not only more readily managed than air oxidation at 500-700°C for producing $OAC_{500-700}$ dehydrochlorination catalyst but may also be adaptable to regenerating the catalyst activity of fixed beds in place. The projected availability of lower cost activated carbons means lower cost $OAC_{500-700}$ produced from them. There are many areas where organic halide capture and destruction can be tested for addressing environmental pollution problems. The recycling of hydrocarbons that are produced by removing hydrogen chloride, water and hydrogen sulfide from a host of organic compounds would support the growing emphasis on recycling misplaced and spent materials.

REFERENCES

Baker, F.S., C.E. Miller, A.J. Repik, and E.D. Tolles 1992 *Kirk-Othmer Encyclopedia of Chemical Technology 4th. Ed.* Vol 4 pp 1015-1037 (1022-1023 for production figures).

Beaulieu, P.L., S.M. Fatemi, J.B. Tumidalsky, C.W. Kruse, M. Chou, and C. Feizoulof 1992 *Use of activated coal char for removal of volatile organic compounds from water* Preprints of Papers Presented at the Washington D.C. ACS Div. of Fuel Chemistry, 37 (4) 1965-1991.

Bellar, T.A., J.J. Lichtenberg, and R.C. Droner, 1974 *J. Am. Water Works Assoc.* 71, pp 40-42.

Boehm, H.P., G. Mair, T. Stoehr, R.R. De Rincon, and B. Tereczki 1984 *Carbon as a catalyst in oxidation reactions and hydrogen halide elimination reactions* Fuel 63:8 pp 1061-3.

Boehm, H.P. and G. Bewer 1976 *The role of surface oxides in the gasification of carbon and the thermal stability of functional groups* 4th London International Conference on Carbon and Graphite, pp 344-360.

Bruggendick, H. 1993 *Operating experience with STEAG's activated carbon processes - a/c/t^{TM} - in European waste incineration plants* Proceedings of the Tenth Annual International Pittsburgh Coal Conference, Pittsburgh, PA, September 20-24 pp 787-794.

Fatemi, S.M., C.W. Kruse, and R.T. Lagman 1993 *Oxidized activated char as an adsorbent and catalyst* Abstract of papers presented at the 21st Biennial Conference on Carbon, State University of New York at Buffalo, June 13-18 pp 505-506.

Feizoulof, C., V. Snoeyink, and C.W. Kruse 1993 *The effect of carbon surface chemistry on enhanced adsorption of a targeted compound from water* Abstracts of papers at 21st Biennial Conference on Carbon, State University of New York at Buffalo, June 13-18 pp 367-368.

Fujitsu, H.; T. Takagi and I. Mochida 1985 *Influences of supporting silica gel on the catalytic activity of B-18 crown ether-potassium chloride complex for the selective dehydrochlorination of 1,1,2-trichloroethane* Bull. Chem. Soc. Jpn. 58 pp 1589-90.

Graham, J. R., and M. Ramaratnam 1993 *Recovering VOCs using activated carbon*, a special supplement to Chemical Engineering 100 (2) pp 6-12.

Hanson, D. 1994 *EPA study points to health risks of dioxins and similar compounds* C&EN May 30 pp 13-14.

Harden, J. M. and G.G. Ramsey 1986 *Catalytic dehydrohalogenation: A chemical destruction method for halogenated organics* Report (EPA/600/2-86/113; Order No. PB87-133104/GAR).

Kalmaz, E.V. and G.D. Kalmaz 1981 *The health effects and ecological significance of chlorine residuals in water* Chemosphere, 10 (10) pp 1163-1175.

Kruse, C.W., G.C. Ray 1966 *Dehydrohalogenation of hydrocarbon halides* US Patent 3,240,834 March 15.

Kruse, C.W. 1969a *Polymerization* US Patent 3,437,695 April 8.

Kruse, C.W. 1969b Unpublished Phillips Petroleum Company report, used by permission.

Kruse, C.W., J.M. Lytle, M. Rostam-Abadi, M .Chou, C. Feizoulof, S.M. Fatemi, J. Schreiner, R. Roginski, and G. Zajac 1991 *Upgrading mild gasification char: Evaluation of oxidized char as a catalyst* Final Tech. Report, Illinois Clean Coal Institute, August 31.

Kruse, C.W., M.I.M. Chou, C. Feizoulof, M. Fatemi, and P. Beaulieu 1992 *Oxidized coal char as a catalyst: Characterization* Preprints of Papers Presented at San Francisco, CA ACS Div. of Fuel Chemistry, 37 (2) pp 556-563.

Kruse, C.W., A.A. Lizzio, C.A. Feizoulof, J.A. DeBarr, S.M. Fatemi 1995a *Oxidation/Desorption Treatment of Carbon to Enhance its Adsorptive/Catalytic Properties* Proceedings of the 22nd Biennial Conference on Carbon, San Diego, C.A. July pp 538-539.

Kruse, C.W., A.A. Lizzio, M. Rostam-Abadi, J.A. DeBarr, and J.M. Lytle 1995b *Producing activated char for cleaning flue gas from incinerators* Final Technical Report to the Illinois Clean Coal Development Institute, Subgrant 22CRGTSK592C December.

Kruse, C.W. 1995 *A review of research on non-fuel applications of coal at the Illinois State Geological Survey: Oxidized activated carbon* in Proceedings of the Twelfth Annual International Pittsburgh Coal Conference September 11-15 pp 364-369.

Leon y Leon D., Carlos A. and L.R Radovic 1994 *Interfacial chemistry and electrochemistry of carbon surfaces* Chapter 4 in Chemistry and Physics of Carbon Ed. by Peter A. Thrower, Marcel Dekker, Inc. N.Y. Vol 24 pp 213-310.

Lycourghiotis, A., 1976, *A first approach to the catalytic properties of porous glass* React. Kinet. Catal. Lett. 5:4 pp 453-7.

Lycourghiotis, A., D. Vattis and N.A. Katsanos 1981 *Catalytic deamination on solid surfaces. Part 3. Kinetics of deamination of aminocyclohexane on silica gel* Z. Phys. Chem. (Wiesbaden) 126:2 pp 259-267.

Mahan, J.E., R.E.Reusser and C.W. Kruse 1967 *Dehydrohalogenation process* US 3,352,935 November 14.

Misono, M. 1973 *Stereoselectivity of the elimination reactions of alkyl halides over silica gel and alkali-treated silica gel* J. Catal. 30:2 pp 226-34.

Miller, G.D. 1990 personal communication.

Mochida, I., H. Watanabe, A. Uchino, H. Fujitsu, K. Takeshita, M. Furuno, T. Sakura, and N. Nakajima 1981 *Selective dehydrochlorination of 1,1,2-trichloroethane into 1,1-dichloroethylene catalyzed by DBU-hydrochloride on silica* J. Mol. Catal. 12:3 pp 359-64.

Smisek, M. 1970 *Manufacture of active carbon; Applications of active carbon* Chapters 2 and 5 in Active Carbon Milan Smisek and Slovoj Cerny, Editors Elsevier Amsterdam-London-New York pp 42 & 256-257.

Suarez, A.R. and M.R. Mazzieri 1987 *Dehydrohalogenation of vic-dihaloalkanes over silica gel* J. Org. Chem. 52:6 pp 1145-7.

U.S. EPA 1995 *Standards of performance for new stationary sources and emission guidelines for existing sources* U.S. Environmental Protection Agency 40 CFR Part 60, October 31.

U.S. EPA 1975 *Preliminary assessment of suspected carcinogens in drinking water* Report to Congress p 3.

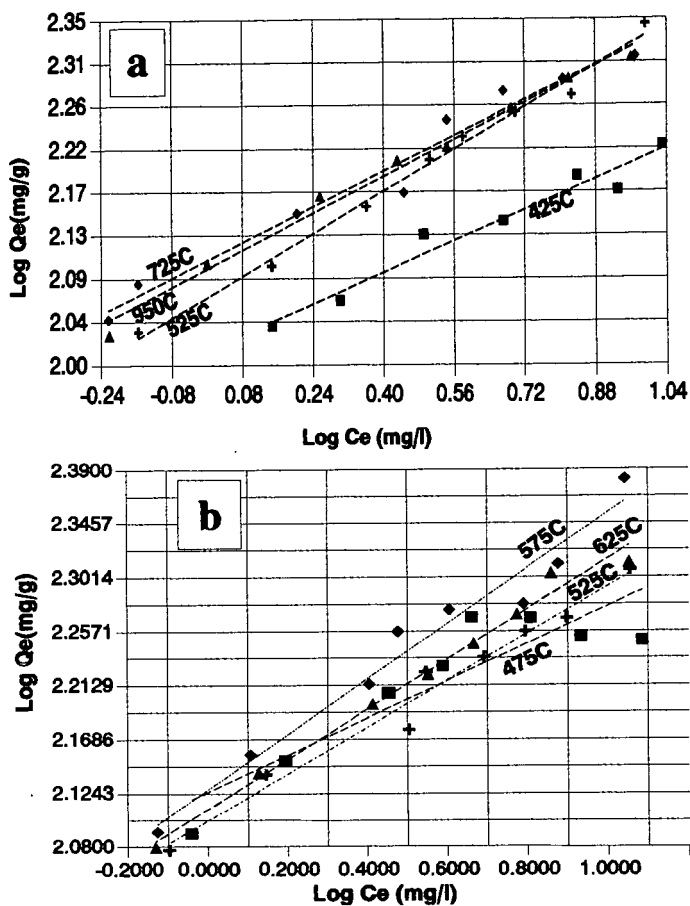Figure 1. Freundlich equation plots for p-nitrophenol on HNO₃-oxidized activated carbon desorbed to the temperature shown.
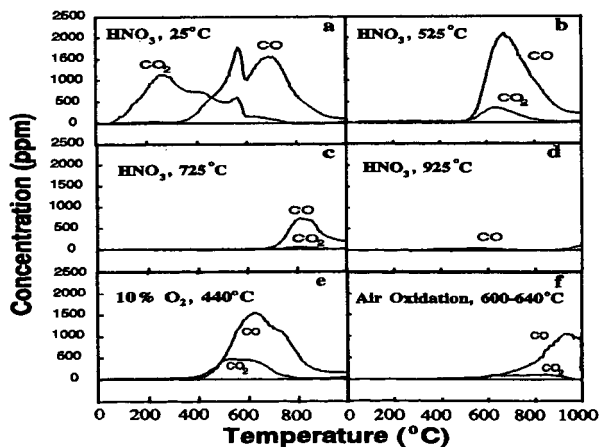

Figure 2. TPD profiles of HNO₃-oxidized chars desorbed at 25°C to 925°C and oxygen oxidized samples.

IMPROVED GRANULAR ACTIVATED CARBON FOR THE STABILIZATION OF WASTEWATER PH

Richard W. Farmer, Bertrand W. Dussert, and Susan L. Kovacic
Calgon Carbon Corporation
500 Calgon Carbon Drive
Pittsburgh, PA 15205

Keywords - pH stabilization, Granular activated carbon, Carbon oxidation

ABSTRACT
Laboratory studies have identified the cause of the pH rise, which occurs during water treatment with activated carbon, as an interaction between the naturally occurring anions and protons in the water and the carbon surface. The interaction can be described as an ion exchange type of phenomenon, in which the carbon surface sorbs the anions and corresponding hydronium ions from the water. These studies have shown that the anion sorption and resulting pH increase is independent of the raw material used for the activated carbon production, e.g. bituminous or sub-bituminous coal, peat, wood or coconut. Also, the pH excursions occur with virgin, reactivated, and acid washed granular carbons. Current pH control technologies focus on adjustment of the wastewater pH prior to discharge or recycle of the initial effluent water until the pH increase abates. However, improved water pH control options have been realized by altering the carbon surface through controlled oxidation rather than the water chemistry or extended preprocessing at the treatment site.

INTRODUCTION
Many times, the start up of granular activated carbon adsorption systems for the control of organic contaminants in wastewater exhibits unacceptable increases in the adsorber effluent pH. This increase can result in an effluent pH exceeding NPDES permits. Experience shows that the duration of the pH increase ranges from several hours to several days, during which time several hundred bed volumes of water can be discharged with a pH in excess of 8.5 to 9, which are typical high limits on discharge pH.

Historically, the methods used in the remediation of the high pH effluent were to treat the effluent with acid to lower the pH, to backwash the system for extended periods of time, or to recirculate the water until the pH rise naturally abated. Obviously, an incentive exists to remediate the problem with methods other than the extensive and expensive ones mentioned here. As a result, a program was begun to identify the cause of the pH excursions and provide a cost effective remediation to the problem.

EXPERIMENTAL
The activated carbons used in this experimentation were both virgin and reactivated, acid washed and non acid washed, and produced from a wide variety of raw materials. The water used in the experimentation was either tap water from the Robinson Township Municipal Authority, a suburb of Pittsburgh, or ultra pure Milli-Q Plus water (Millipore Corp. Bedford, MA). Additionally, when examining specific anion effects, the sodium salt of sulfate, chloride, or nitrate was added to the Milli-Q water. These salts were Fisher ACS grade or equivalent.

pH measurements were performed following Standard Methods[8]. Anion analyses were performed with a Dionex Model 14 Ion Chromatograph (Dionex Corp. Sunnyvale, CA). Cation analyses were performed using atomic absorption spectroscopy.

The experimental apparatus consisted of a one inch ID x 12 inch L Pyrex glass column through which the water was pumped upflow with a Masterflex peristaltic pump and tygon tubing. Each carbon was boiled in Milli-Q water for 15 minutes, cooled to room temperature, and then transferred to the column. The water flow rate provided approximately 7.5 minutes empty bed contact time (EBCT), and discrete samples were collected for analysis. For the anion specific experiments, the water was prepared in a seven gallon, glass carboy.

The oxidized carbons were prepared at both high and low temperature with air as the oxidant.[4,5,6] Carbon pH measurements on both oxidized and non-oxidized carbons were performed by gently stirring 25 g of carbon in 100 mL of a sodium sulfate solution (80 mg sulfate/L) for 30 minutes. This procedure is referred to as the modified contact pH.

RESULTS AND DISCUSSION

Effect of Water Quality
The extent and duration of the pH excursion depends upon the water quality. Using Filtrasorb 200 as the test carbon in this simulation, the water was varied from tap to Milli-Q water. Figure 1 shows that tap water from Robinson Township, PA yields a pH rise up to 10. With the Milli-Q water, the excursion is very limited, i.e. 40 bed volumes when the pH drops below 8.5. However, the pH excursion can occur with Milli-Q water through the introduction of any of a number of anions. Shown in Figure 1 is the effect of sulfate addition on the pH spike. Adding 80 mg/L of sulfate causes the pH spike to return and the pH profile closely matches that of tap water. (Throughout this discussion, 8.5 pH is chosen as the reference point for a pH excursion.)

The type of anion does not have a significant effect on the excursion, and concentration only affects the pH profile at low anion concentrations. Table 1 highlights the excursion that occurs as the anion concentration and anion changes. When the anion changes from sulfate to chloride to nitrate, the impact of the anion is negligible with the pH peak occurring around 10 and the excursion lasting about 400 BV. Only at very low concentrations does the pH spike become muted. The loading of the anions ranges from 3.3 to 4.3 mg/L after treating 400 bed volumes of water. Cations were not removed by the carbon.

Effect of Carbon Type
A pH excursion has been shown to be independent of the raw material and whether or not the carbon is acid washed. Figure 2 shows that whether the carbon is prepared from bituminous or sub-bituminous coal, coconut, wood, or peat each carbon exhibits an increase in pH when the carbon is brought on line. This same conclusion results when the carbon is acid washed and also following reactivation.

Hypothesized Mechanism
It is believed that the pH excursions are a function of the activated carbon surface that results from the high temperature activation or reactivation process. Huang[1] broadly classifies activated carbons as H or L types of carbon. In these broad categories, an H-type carbon, produced at high temperature in a reducing atmosphere, adsorbs strong acids while L-type carbons, produced by surface oxidation, adsorb strong bases. Thus, adsorption of "acid groups" as witnessed by Snoeyink[2] may be responsible for upsetting the water equilibrium. This adsorption may actually be protonation of pyrone type surface oxides (Leon y Leon[3]) or other structures on the carbon surface. Following protonation, the surface is charge neutralized with the sulfate, chloride, or other anions which may be present in the water. In absence of these ions, the neutralization of the surface occurs with the hydroxide ions that result from hydrolysis of water which initially yielded the protons. It may actually be more accurate to say that the anions (sulfate, chloride, etc.) exchange with the hydroxide ions following protonation; however, additional testing will be required to conclusively determine the mechanism.

pH Stabilization with Oxidized Carbons
An effective remediation of the pH increases is accomplished through the controlled oxidation of the activated carbon surface, prior to treating the water, which alters the carbon surface to stabilize the effluent water pH. Two methods have been developed to achieve this. First, an elevated temperature oxidation[4,5] provides surface oxides that inhibit the ion exchange phenomenon and stabilize the pH. Likewise, a low temperature oxidation also effectively stabilizes the water pH[6].

When carbon prepared by either of these methods is exposed to water, the excessive pH rise in the effluent water is eliminated. Figure 3 shows that both the high temperature and low temperature oxidized pH stable carbons can keep the effluent water pH at or below the target pH of 8.5. Further, effluent water pH stabilization can be accomplished for both the synthetic water prepared with Milli-Q water plus sulfate and also tap water, which had an initial pH of 7.8. The two stabilized pH profiles were developed with virgin carbon (Milli-Q plus 80 mg/L sulfate) and reactivated carbon (tap water) which demonstrates that the oxidation processes are applicable to both virgin and reactivated carbons. The modified contact pH of the oxidized virgin carbon was 7.4 while the oxidized reactivated carbon had a modified contact pH of 8.5. Finally, Carr and Farmer[7] demonstrated that pH stabilized carbons can be implemented easily in full scale systems.

Surrogate pH Stable Carbon Test
A modification has been made to a standardized pH test to predict whether a carbon will exhibit a significant pH rise. The standard test contacts carbon with deionized water. With this test, most carbons will have a contact pH between 6 and 8. However, by adding sulfate to the deionized water, greater pH changes can occur, and the test can be used to predict whether the carbon will

cause a rise in the effluent water pH. Table 2 shows that carbons with a modified contact pH above about 9 will exhibit a pH increase. Also, with the exception of the wood base carbon, as the modified contact pH decreases, the duration of the pH increase generally decreases.

SUMMARY AND CONCLUSIONS
Stabilization of the effluent water pH has been demonstrated through the use of oxidized granular activated carbons. This oxidation can be accomplished at both low and elevated temperatures through the use of air, oxygen, or other suitable oxidants and is applicable to both virgin and reactivated carbons. Prediction of the ability of a carbon to stabilize the effluent water pH is also possible through the use of the modified contact pH test.

REFERENCES

1. Huang, C. P., "Chemical Interactions Between Inorganics and Activated Carbon," Carbon Adsorption Handbook, Ann Arbor Science, Ann Arbor, MI 1978 pp 281-329.

2. Snoeyink, V., "Adsorption of Strong Acids, Phenol, and 4-nitrophenol from Aqueous Solution by Active Carbon in Agitated Non-flow Systems," Ph.D. Thesis, University of Michigan, 1968.

3. Leon y Leon, C. A., J. M. Solar, V. Calemma, and L. R. Radovic, "Evidence for the Protonation of Basal Plane Sites on Carbon," Carbon 30 (5), 797 1992.

4. Dussert, B. W. and R. A. Hayden, "Oxidized Activted Carbon for the Control of PH and Alkalinity in Water Treatment Applications," U. S. Patent 5,368,738, November 29, 1994.

5. Dussert, B. W., R. W. Farmer, and R. A. Hayden, "Oxidized Activated Carbon for the Control of pH and Alkalinity in Water Treatment Applications," U. S. Patent 5,466,378, November 14, 1995.

6. Dussert, B.W., et. al., "Activated Carbon Oxidized by Air at Near Ambient Temperatures for the Control of pH in Water Treatment Applications," U. S. Patent 5,368,739, November 29, 1994.

7. Carr, S. L. and R. W. Farmer, "React-pH Improves pH in Carbon Effluent," The National Environmental Journal, March/April 1995.

8. "Standard Methods for the Examination of Water and Wastewater", 17th Edition, Clesceri, L., A. Greenberg, and R. R. Trussel eds. 1989.

Table 1. Effect of Anion and Anion Concentration on Effluent pH Profile

Anion	Concentration mg/L	Maximum pH	pH Excursion Duration Bed Volumes	Anion Loading mg/g GAC
Sulfate	80	10.5	360	4.3
Chloride	18	10.2	420	3.3
Nitrate	5.3	9.8	>410	3.9
Sulfate	1	9.4	220	0.73

Duration of the pH spike represents volume of water treated until pH ≤ 8.5
Water used was Milli-Q water spiked with the referenced amount of anion
Anion loading is represented as mg anion/g GAC after treating 400 bed volumes

Table 2. Modified Contact pH and Extent of pH Excursion

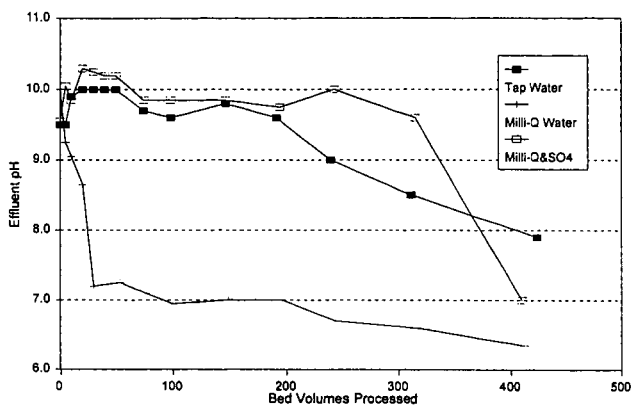| Activated Carbon	Modified Contact pH	pH Excursion Duration (Bed Volumes)
Bituminous	10.4	350-400
Sub-bituminous	10.4	350
Peat	11.1	460
Coconut	10.3	200-250
Bituminous-acid washed	9.8	200-250
Wood	9.6	550
Reactivated bituminous	10.6	400
pH Stable	8.2	0

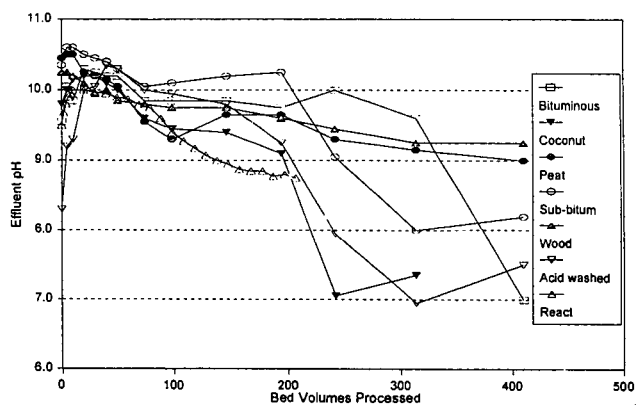Figure 1. Effect of Water Quality on pH Profile - Bituminous Carbon

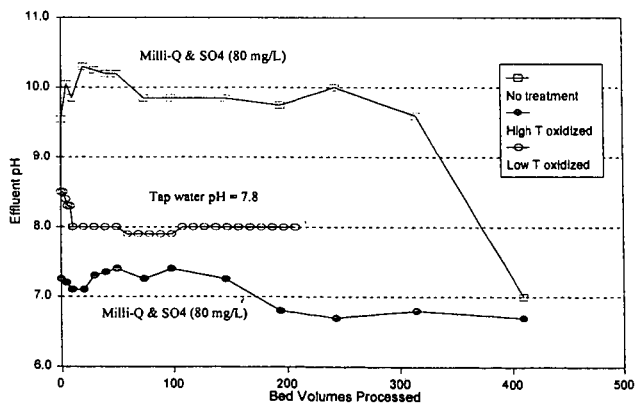Figure 2. Effect of Carbon Raw Material on pH Profile - Milli Q Water & Sulfate (80 mg/L)

Figure 3. Effect of Oxidized Carbon on pH Profile - Bituminous Carbon

EFFECTS OF SURFACE CHEMISTRY OF ACTIVATED CARBON ON THE ADSORPTION OF AROMATICS CONTAINING ELECTRON-WITHDRAWING AND ELECTRON-DONATING FUNCTIONAL GROUPS

I. F. Silva, J. I. Ume, A. W. Scaroni and L. R. Radovic

Fuel Science Program
Department of Materials Science and Engineering
The Pennsylvania State University, University Park, PA 16802

KEYWORDS: activated carbon, adsorption, organics, surface chemistry.

INTRODUCTION

Adsorption of organic water pollutants onto activated carbon surfaces has been studied extensively and a voluminous literature is available on this increasingly important practical problem [1,2]. There are many well established facts; there are also some conflicting data. More importantly, conflicting interpretations have been offered and no attempt seems to have been made to reconcile them. Because many of the pollutants are weak electrolytes, the central fundamental issue is how to account for the well documented importance of (a) the pH of the aqueous solution, and (b) the surface chemistry of the adsorbent.

In an early study, Getzen and Ward [3,4] presented a Langmuirian theoretical framework for the adsorption of both ionic and molecular adsorbate species as a function of pH. Their approach provided an explanation for the often observed maximum in adsorbate uptake at pH = pK_a, without explicitly taking into account the changes in the surface chemistry with pH. The explanation for an acid adsorbate is as follows: as pH decreases toward the pK_a value, H^+ ions as well as organic anions are adsorbed on the surface. Since the concentration of H^+ rapidly exceeds that of the weak electrolyte anions, the former adsorb on the carbon surface far in excess of the anions and subsequently enhance anion adsorption. However, because the concentration of anions decreases as pH increases, a point of diminishing returns is eventually reached and a maximum in adsorption uptake is observed.

In another milestone study, Müller et al. [5-7] used the same approach based on Langmuirian competitive adsorption of ionic and molecular species, but accounted explicitly for the pH-induced variations in the adsorbent surface charge. This allowed them to provide a more rigorous explanation of the adsorption maximum at pH = pK_a in terms of both adsorbate and adsorbent properties. It is necessary that considerable ionization of the adsorbate (solute) take place while the surface still possesses a charge that is opposite to that of the ionic solute. In particular, for an acidic solute, it is necessary that, for a given pH increment, the magnitude of the slope of the solute dissociation curve be larger than that of the surface potential curve.

Our interest in this topic [8,9,10] stems from the realization [11,12] that the lack of understanding of adsorption of inorganic solutes on carbons has suffered for many years from a lack of appreciation of the amphoteric nature [13] of carbon surfaces. Based on intriguing results for adsorption of benzoate, oxalate and fumarate anions on chemically modified (oxidized vs. nitrided) activated carbons [14], we proposed the following mechanisms of adsorption: (a) adsorption of benzoate (aromatic) anions occurs primarily on the basal plane of carbon and the electron-withdrawing effects of nitrogen and carboxyl functional groups suppress the interaction of the basal planes with the adsorbate's aromatic rings; (b) adsorption of aliphatic anions occurs also predominantly on the basal plane and the same electron-withdrawing effects enhance its interaction with the carboxyl anions. More recently, we have begun to study in some detail the relative importance of dispersion and electrostatic adsorbate/adsorbent interactions as we examined the uptake of methylene blue and p-nitrophenol, as well as benzoic acid and oxalic and fumaric acids [15]. We concluded that, while electrostatic interactions are important, π-π dispersion interactions appear to be dominant in the adsorption of aromatic solutes. On the other hand, electrostatic repulsion appears to be much more important for the adsorption of aliphatic anions. These are important and arguably novel findings, and their further investigation (and substantiation) is of interest.

In the present study, we contrast the behavior of chemically different carbons in adsorbing two vastly different aromatic solutes: nitrobenzene is a very weak Lewis acid that possesses the electron-withdrawing NO_2 group, while aniline is a predominantly cationic species at pH < 4.6 which also possesses the electron-donating NH_2 group.

461

EXPERIMENTAL SECTION

Two commercial granular carbons, NORIT GCW and Calgon BPL, were used as the adsorbents. Oxidation of GCW was performed by contacting the sample with concentrated HNO_3 at 363 K for 6 h. The sample was washed until neutral pH was achieved, and dried at 380 K before use. The reaction with NH_3 (nitriding) was carried out in a tubular furnace flushed at a flow rate of 30 cc/min. The temperature was kept constant for 3 h. Prior to use, the sample was washed and dried. Devolatilization of the carbon was achieved by heat treatment in inert atmosphere at 1173 K. Elemental analysis of the samples was performed using LECO CHN-600. Maximum nitrogen incorporation was observed at 673 K.

The isoelectric point (IEP) and the point of zero charge (PZC) were measured by electrophoresis and mass titration, respectively. The IEP was determined with a Zeta-Meter System 3.0+ apparatus, using 10^{-3} M KNO_3 as the indifferent electrolyte; the plateau in the plot of equilibrium pH of the slurry vs. solid weight fraction identified the PZC of a carbon. Additional chemical surface characterization of the as-received and modified carbons was attempted briefly using XPS (ESCALAB 200A-VG). Physical surface properties of the carbons were determined using an Autosorb adsorption apparatus (Quantachrome).

Adsorption isotherms were obtained by adding different amounts of carbon to Nalgene flasks containing 0.1 g/L of aniline or nitrobenzene. The pH was adjusted with NaOH or HCl. The suspensions were shaken until equilibrium was reached (ca. 24 h), and the residual adsorbate concentrations were measured by uv spectroscopy.

RESULTS AND DISCUSSION

Table 1 summarizes the physical and chemical characteristics of the GCW samples used. For both nitrided and oxidized samples no drastic changes in surface area or micropore volume were observed, in agreement with our previous studies [12,14]. Curiously, for a nitrided sample that had been oxidized previously, a higher N incorporation (~7 wt%) was achieved (at 658 K for 3 h) at the expense of a drastic decrease in BET surface area (~300 m^2/g).

The values of PZC were consistently higher than those of IEP, in agreement with previous studies [12,14]. They indicate surface charge inhomogeneities within the carbon particles [12,14]. More recently, this difference between IEP and PZC values, i.e., the combination of electrophoresis and mass titration, was shown to be a powerful tool for the analysis and design of surface chemistry of active carbons, especially for determining the spatial (radial) distribution of the acidic oxygen functional groups within carbon particles [16].

Deconvolution of the broad and complex N1s XPS peaks of nitrided carbon [10] suggests the presence of pyridine (or nitrile groups), as well as amide, amine and pyrrole groups.

Figures 1-3 show the behavior of the different carbons in adsorbing aniline under widely varying solution chemistry conditions. A significant effect of solution chemistry (pH) on the uptake is observed for both as-received and modified carbons. The effect of carbon surface chemistry is seen to depend on pH. The uptakes at pH≤PZC are enhanced by surface oxidation; at pH=11 the effect is much less pronounced.

Figures 4-6 show the behavior of the different carbons in adsorbing nitrobenzene. In contrast to the findings for aniline, solution chemistry (pH) had little effect on the equilibrium uptakes. The effect of surface chemistry is seen to be much more important. The as-received and devolatilized carbons had the highest uptakes, while adsorption was suppressed for both nitrided and oxidized carbons.

Some of the phenomena observed in the present work were observed in the published literature. Some of them were also misinterpreted, as argued in more detail elsewhere [2,10]. The principal reason for these misinterpretations is the failure to recognize the amphoteric nature of carbon surfaces and its effects on electrostatic adsorbate/adsorbent interactions. For example, in a large number of studies it is assumed that the carbon surface acquires a net negative charge over a very wide range of pH conditions [17]. A typical example of the resulting inconsistencies is a discussion of phenol adsorption by Grant and King [18]. They observed a significant increase in reversible phenol uptake as the pH was reduced from 12.1 to 8.0, and then to 1.8. This was tentatively attributed to changes in phenol activity with decreasing pH. A more straightforward explanation (apparently discarded by the authors) - which is thought to explain the vast majority of phenol adsorption data [2] - is the one based on the work of Müller et al. [5-7]. At the high pH of 12.1 ($pH>pK_a$, $pH>PZC$), the low uptake is due to the electrostatic repulsion between the negatively charged carbon surface and phenolate anions. At pH=8.0

(pH<pK$_a$), 99% of the adsorbate exists as phenol molecules, and 1% as phenolate anions; at the same time, the degree of dissociation of acidic groups decreases and there is a better balance between positively and negatively charged sites on the surface. At low pH (e.g., pH<3), most carbons are positively charged, at least in part as a consequence of donor/acceptor interactions between the graphene layers and the hydronium ions [19]. In agreement with these arguments, for BPL carbon we observed similar uptakes of aniline at pH>PZC (pH=6.0-10.8) and a drastic decrease at pH=1.5.

The importance of dispersive interactions is also apparent in Figures 1-6. For example, aniline is much more soluble in water than nitrobenzene (35 vs. 2 g/L at 25 °C); yet its uptake does not reflect this. This is attributed to the beneficial effect of the electron-donating NH$_2$ group. Enhanced adsorption of aniline is due to the resulting increase in the negative charge density on the graphene layers of the adsorbent. Similarly, both oxidation and nitriding of the carbon (which have opposite electrostatic effects) reduce the π electron density on the graphene layers and have a negative effect on the uptake of nitrobenzene, in agreement with our results with benzoic acid [14]. Furthermore, neutralization of oxygen functional groups produced no significant effect on the uptake of nitrobenzene [10].

REFERENCES
1. A. Derylo-Marczewska and M. Jaroniec, *Surf. Colloid Sci.* 14, 301 (1987).
2. L. R. Radovic, C. Moreno-Castilla and J. Rivera-Utrilla, in preparation.
3. T. M. Ward and F. W. Getzen, *Environ. Sci. Technol.* 4(1), 64 (1970).
4. F. W. Getzen and T. M. Ward, *J. Colloid Interf. Sci.* 31, 441 (1969).
5. G. Müller, C. J. Radke and J. M. Prausnitz, *J. Phys. Chem.* 84, 369 (1980).
6. G. Müller, C. J. Radke and J. M. Prausnitz, *J. Colloid Interf. Sci.* 103, 466 (1985).
7. G. Müller, C. J. Radke and J. M. Prausnitz, *J. Colloid Interf. Sci.* 103, 484 (1985).
8. J. M. Solar, Ph.D. Thesis, The Pennsylvania State University, 1991.
9. G. M. K. Abotsi, Ph.D. Thesis, The Pennsylvania State University, 1990.
10. I. F. Silva and L. R. Radovic, in preparation.
11. J. M. Solar, C. A. Leon y Leon, K. Osseo-Asare and L. R. Radovic, *Carbon* 28, 369 (1990).
12. C. A. Leon y Leon, Ph.D. Thesis, The Pennsylvania State University, 1992.
13. C. A. Leon y Leon and L. R. Radovic, in *Chem. Phys. Carbon* (P. A. Thrower, Ed.), Vol. 24, 1994, p. 213.
14. J. I. Ume, A. W. Scaroni and L. R. Radovic, Proc. 21st Biennial Conf. Carbon (Buffalo, NY), July 1993, p. 468.
15. L. R. Radovic, J. I. Ume and A. W. Scaroni, in "Fundamentals of Adsorption" (D. M. LeVan, Ed.), Elsevier, Amsterdam, in press (1996).
16. J. A. Menendez, M. J. Illan-Gomez, C. A. Leon y Leon and L. R. Radovic, *Carbon* 33, 1655 (1995).
17. K.-S. Ha, H. Hinago, A. Sakoda and M. Suzuki, in "Fundamentals of Adsorption" (M. Suzuki, Ed.), International Adsorption Society, 1993, p. 251.
18. T. M. Grant and C. J. King, *Ind. Eng. Chem. Res.* 29, 264 (1990).
19. C. A. Leon y Leon, J. M. Solar, V. Calemma and L. R. Radovic, *Carbon* 30, 797 (1992).

Table 1
Characteristics of GCW Carbons Used

Sample	C (wt%)	H (wt%)	N (wt%)	O (wt%)	S$_{N2}$* (m^2/g)	V$_{mi}$** (cc/g)	IEP	PZC
As received	96.5	0.57	1.29	1.64	859	0.62	4.0	8.0
Devolatilized	98.0	0.41	1.46	0.13	858	0.58	5.5	10
Oxidized	82.9	1.30	1.60	14.2	807	0.55	1.5	2.6
Nitrided	90.5	0.47	5.81	3.22	869	0.59	5.2	8.9

*BET surface area;
**micropore volume obtained from the Dubinin-Radushkevich equation applied to the N$_2$ adsorption isotherm.

Figure 1. Aniline adsorption isotherms at pH=2 for different carbons: ■ , as-received(1); □ , as-received(2); ▲ , devolatilized; ○ , nitrided; △ , oxidized.

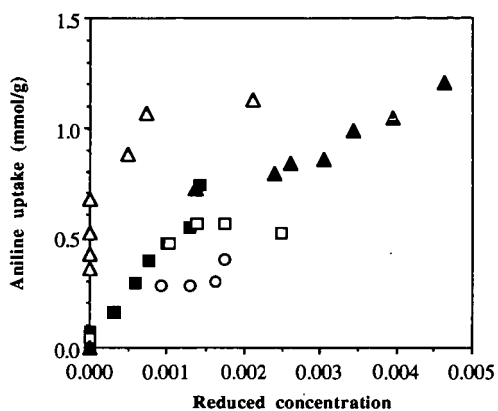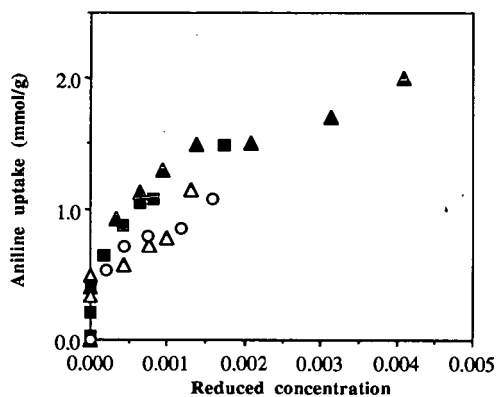**Figure 2.** Aniline adsorption isotherms at pH=11 for different carbons: ■ , as-received; ▲ , devolatilized; ○ , nitrided; △ , oxidized.

Figure 3. Aniline adsorption isotherms at pH=PZC for different carbons: ■ as-received; ▲ , devolatilized; ○ , nitrided; △ , oxidized.

Figure 4. Nitrobenzene adsorption isotherms at pH=2 for different carbons: ■ , as-received; ▲ , devolatilized; O , nitrided; Δ , oxidized.

Figure 5. Nitrobenzene adsorption isotherms at pH=11 for different carbons: ■ , as-received; ▲ , devolatilized; O , nitrided; Δ , oxidized.

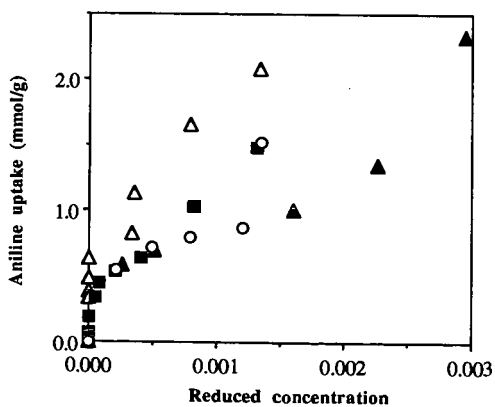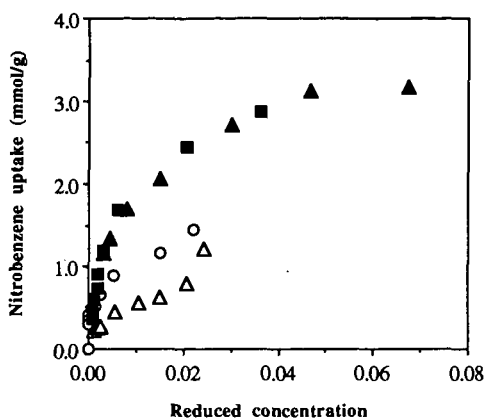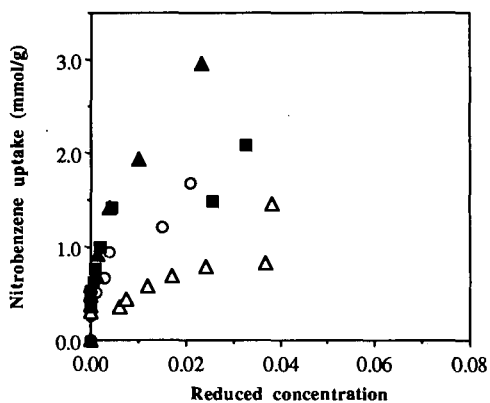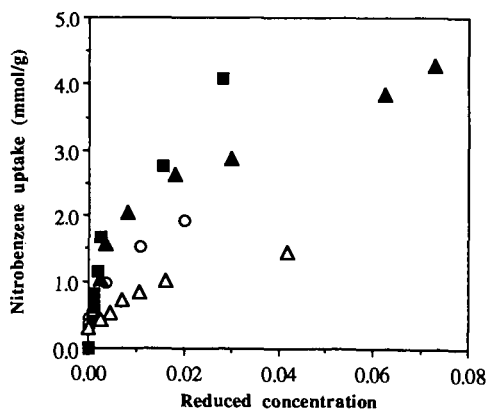**Figure 6.** Nitrobenzene adsorption isotherms at pH=PZC for different carbons: ■ , as-received; ▲ , devolatilized; O , nitrided; Δ , oxidized.

GRANULAR ACTIVATED CARBON AS A TOXICITY REDUCTION TECHNOLOGY FOR WASTEWATER TREATMENT

Steven L. Butterworth
Calgon Carbon Corporation
P.O. Box 717
Pittsburgh, PA 15230

Keywords: toxicity reduction, activated carbon, use rate

Introduction

The Clean Water Act governs the discharge of wastewater to all navigable waterways in the U.S. It is the explicit purpose of this Act to prevent the discharge of "toxic pollutants in toxic amounts" to the nation's surface water supplies. To achieve this goal, the National Pollutant Discharge Elimination System (NPDES) was established, whereby a facility wishing to release wastewater to a surface water system must obtain a permit to do so. This NPDES permit contains the wastewater quality criteria that must be met before the wastewater can be legally discharged.

Historically, specific chemical limits have been used for establishing the quality of a wastewater discharged from a facility. The EPA developed a list of priority pollutants for which maximum discharge concentration limits were established. This regulatory approach had the advantage that straightforward protocols with clearly defined quantification limits were available for compliance and testing purposes. However, it became increasingly apparent that there were weaknesses with this approach when it was used exclusively. Many chemicals not included in the priority pollutant list will produce toxic responses from indigenous biota when released to a surface water. Therefore, the EPA developed methods for directly assessing the potential toxicity a discharge may generate in a receiving stream. The protocols and techniques for performing toxicity tests have been refined to the point the EPA is comfortable including them as another method for regulating the quality of a permitted discharge [1,2,3].

As a result, there is now increased attention on quantifying the toxicity, or potential toxicity, of wastewaters from industrial facilities and publicly owned treatment works (POTWs). Therefore, as these facilities renew their NPDES permits, toxicity testing and/or toxicity limits are being increasingly introduced. Since biological systems are often more sensitive to pollutants than can usually be quantified by conventional analytical methods, dischargers are faced with achieving more stringent water quality goals.

This paper will present several case studies to illustrate how certain facilities have used granular activated carbon (GAC) to achieve compliance with these more stringent regulations.

What Is Toxicity?

Toxicity is operationally defined as any adverse biological effect [4]. It is classified as either acute or chronic in nature. The adverse effect monitored for acute toxicity is organism death, while chronic toxicity can be any deviation from normal growth or behavior for an organism. Toxicity may be reported as a concentration (or the percent solution of wastewater mixed with a control water), as Toxicity Units, or as "% Survival." Tests for determining acute toxicity are usually shorter in duration than those for chronic toxicity. Acute tests are typically completed within 48 hrs, while chronic tests may last much longer (full chronic tests could last a year or more). Table 1 presents a comparison of acute and chronic testing. Dischargers that have acute tests in their current permits may have more sensitive species or chronic tests included when their permits are renewed. Chronic criteria are often more difficult to satisfy than acute criteria. Thus, the inclusion of a more sensitive specie or a chronic test means the discharger is again faced with a more stringent effluent quality requirement.

Resolving Toxicity Problems

A facility that expects to receive toxicity limits or toxicity test requirements may do preliminary testing to determine whether they will have a compliance problem. If the results indicate the presence of unacceptable levels of toxicity, a "Toxicity Reduction Evaluation" (TRE) must be completed to determine how to eliminate or reduce the toxicity to acceptable levels. A TRE can be very time consuming and costly, particularly if a complex wastewater is involved. Figure 1 presents a schematic of the steps involved in a TRE.

Included in the TRE is a systematic attempt to identify the chemical(s) causing the toxicity. This so-called "Toxicity Identification Evaluation" (TIE) can have one of three outcomes [5]; 1.) a specific chemical is identified, 2.) a particular wastewater fraction is consistently identified as toxic, or 3.) no specific chemical or fraction is consistently identified as causing the toxicity.

If (1) is the outcome, it is a straightforward matter to design treatment systems to remove specific contaminants. If (2) or (3) is the outcome, it becomes more difficult to choose an appropriate

treatment technique and considerable effort will be required to prove the best alternative(s). However, if organics are implicated as a source of toxicity, activated carbon should be considered as a toxicity reduction technology.

To illustrate this point, several case studies will be reviewed below. These studies include three oil refineries and a chemical manufacturing facility. In some cases, studies were not optimally designed, while others were. Also, one of the examples is of a successful program that subsequently required optimization.

CASE STUDY 1 - REFINERY A

Refinery A treats a sour crude oil. It became apparent that toxicity testing using Daphnia would be included when they renewed their NPDES permit. Their treatment system consisted of pH adjustment and a equalization/bio-treatment pond and would not produce an effluent complying with the new permit. A series of toxicity reduction treatability studies were begun, rather than a systematic TRE, to determine what methods might remove the toxicity. The technologies tested as tertiary treatments to Activated Sludge (AS) processes were ClO_2, H_2O_2, O_3, and GAC. Table 2 presents the results of the batch tests completed with these technologies. The results indicated that AS and or Activated Sludge-Powdered Activated Carbon (AS-PAC) followed by ClO_2 or H_2O_2 actually increased their toxicity. However, tertiary treatment with O_3 or GAC reduced the effluent toxicity to satisfactory levels. Unfortunately, because a treatability-based toxicity reduction approach was used rather than an organized TRE which included a TIE, the presence of NH_3 excursions in the refinery caused inconsistent results in some aspects of the study. Thus, it was decided that an AS system with PAC addition could provide sufficient performance during the interim while sources of NH_3 were traced and reduced. The addition of GAC polish would be considered if operational experience showed that it was needed to ensure compliance. GAC was chosen over O_3 due to its cost effectiveness.

CASE STUDY 2 - REFINERY B

Refinery B processes heavy crudes. The wastewater treatment system consisted of API separators, DAF units, an aerated bio-pond and clarification pond. This refinery was informed that a sensitive toxicity test (a 96 hr flow through trout test) was going into their renewed permit. Due to the timing of the permit renewal, the refinery did not attempt to evaluate any toxicity reduction technologies. Instead, a survey of similar facilities with similar permits was made and GAC was found to be the preferred technology. Thus, while installation of a full scale GAC system proceeded, a pilot study was conducted to prove GAC worked and to determine the GAC use rate. Table 3 provides a description of the pilot system and Figure 2 presents the study results. A GAC use rate of 0.4 lb/1000 gal was determined in the pilot study for this refinery. Due to improved performance from their bio-treatment system over time, the full scale system has operated at an even lower use rate.

The refinery did not stop at this point. In anticipation of stricter limits in the future, a TIE is underway at the refinery to determine what the toxicants are and where they are generated. The plan now is to reduce the toxicity at the source an improve the GAC use rate further. An optimization of the GAC system may occur in the future, as a result.

CASE STUDY 3 - REFINERY C

Refinery C treats heavy crudes. The wastewater system included API separators, DAF units, coagulation and biological treatment. However, a polish operation was needed to achieve compliance with the refinery's acute toxicity limits for 3-spined stickleback. After some preliminary screening studies, GAC was chosen as the technology for achieving compliance and a custom system was successfully installed and operated for the life of the permit.

When the refinery renewed its permit, after five years of compliance, a more sensitive specie (trout) was required for toxicity testing. As a result, the refinery had to re-evaluate the current system for compliance with new criterium, >95% survival for a 96 hr flow through trout test. An optimization study was initiated to determine whether the system could be operated more economically while still satisfying the new permit. Table 4 provides the operating conditions for the tests and Figure 3 illustrates the results of this optimization study. Result for the full-scale system under normal operation are included in Figure 3. A change in the operation of the full scale system was recommended to satisfy the new permit and provide a more cost effective use rate. The carbon use rate could be reduced from >2.5 lb/1000 gal to 1.7 lbs/1000 gal.

CASE STUDY 4 - SPECIALTY CHEMICAL PLANT

A chemical plant had to meet toxicity limits for two species, Daphnia and fathead minnows. Its wastewater treatment system consisted of pH adjustment, activated sludge, and clarification. The expected toxicity limits were exceeded for both species. A thorough TRE was completed and several treatment technologies were evaluated for toxicity reduction, as a result. However, only GAC consistently reduced the toxicity to acceptable levels. An extensive pilot study was completed to determine optimal operating conditions and other design information for a GAC system. Table 5 presents a summary of the pilot test conditions that evaluated performance at 30 and 40 gpm. Figures 4 and 5 present results for tests completed at 30 gpm.

The use rate for the 30 gpm test averaged 3.02 lb/1000 gal and the use rate for the 40 gpm averaged 1.62 lb/1000 gal. The apparent discrepancy between these two use rates is reflected by two differences between the tests. First, the activated sludge plant did a much better job removing toxicants during the 40 gpm tests. Second, a sand filter for solids removal was included in the 40 gpm study, which reduced backwash frequency and removed some toxicity which was attributable to the solids in the wastewater.

It was of interest to note in these case studies that toxicity breakthrough could not be unequivocally correlated to any of the routine monitoring parameters used at the facilities. Also, toxicity breakthrough did not correlate with specific chemical breakthrough. Thus, one of the challenges in operating a GAC system for toxicity reduction is deciding upon a monitoring method to determine change out. With flow through toxicity tests, monitoring between GAC vessels in series can be done and change outs based on a certain percentage of toxicity breakthrough in a lead bed. In other cases, a global parameter such as TOC or COD may consistently achieve 100% breakthrough before toxicity breakthrough. In these cases, the global parameters may be useful monitoring tools. Some facilities have successfully based change outs strictly on a timed schedule.

Table 6 summarizes the use rate information for the studies reported here by providing an estimate of the cost for treating the specific wastes. Overall, these results were such that they provided attractive economics, compared to other technologies, for the facilities that have installed or will install GAC for toxicity reduction.

Summary

The case studies presented have served to illustrate that GAC provides an effective, yet flexible means for reducing the toxicity of wastewater where organics are a source for at least some of the toxicity. Compared to alternate technologies, GAC has been shown to be cost effective in achieving compliance goals. It also offers the opportunity for further optimization should GAC be installed to achieve one toxicity goal and another more stringent goal is introduced at a later date.

References

1. Peltier, W.H., and Weber, C.I., EPA Report No. 600/4-85/013, March, 1985.
2. Weber, C.I., et. al., EPA Report No. 600/4-89/001, March, 1989.
3. National Resources Defense Council v. EPA, No. 80-1607, slip op. at 61-62 (D.C. Cir. Sept. 20, 1988).
4. Chapman, P.M., Water Poll. Res. J. Canada, 24, 425. 1989.
5. Vigon, B.W., et. al., Proc. 44th Purdue Ind. Waste Conf., 97, 1990.

TABLE 1
Comparison of Acute and Chronic Toxicity Tests

Acute Toxicity	Chronic Toxicity
Effect observed is organism death. Usually is a short term test (<96 hr).	Effect observed can be growth inhibition, reduced reproduction, behavioral changes, or other life cycle changes. Full chronic tests may last 30 days - 1 yr. EPA subchronic tests usually last 4-8 days.

Advantages
  Standardized protocols
  Relatively rapid and less expensive
  Endpoint easy to identify
	Advantages
	  More sensitive than acute tests
	  Assess parameters other than death

Disadvantages
  Indicates only fatal concentrations
  Assumes fast acting toxicants
  May not reflect real world exposure
	Disadvantages
	  More costly and time intensive than acute
	  End points more difficult to recognize
	  More difficult protocols

TABLE 2
Results of Tertiary Treatment Technologies After AS for Refinery A

Treatment	Average % COD Removal	Effect on Toxicity Chronic	Acute
O_3	5.8	decreased	decreased
H_2O_2	-13.1	increased	increased
ClO_2	n/a	increased	increased
GAC	80.3	decreased	decreased

TABLE 3
Pilot Test Unit Description and Testing Conditions for Refinery B

Flow Velocity (gpm/ft^2)	4.2
Adsorber Diameter (ft)	4.0
Weight GAC/vessel (lbs)	2000
Average TOC (mg/l)	- (range 13-105)
Average COD (mg/l)	63
Average TSS (mg/l)	6 (range 2-45)

TABLE 4
Pilot Test Unit Description and Testing Conditions for Refinery C

Flow Velocity (gpm/ft^2)	5.4
Adsorber Diameter (ft)	0.125
Weight GAC/vessel (lbs)	0.45 (6 columns in series)
Average TOC (mg/l)	53
Average COD (mg/l)	162

TABLE 5
Pilot Test Unit Description and Testing Conditions for Chemical Plant A

Flow Velocity (gpm/ft^2)	2.39/3.18
Adsorber Diameter (ft)	4.0
Weight GAC/vessel (lbs)	2000
Average TC (mg/l)	95
Average TOC (mg/l)	48
Average TSS (mg/l)	25

TABLE 6
Treatment Costs for Toxicity Reduction Using GAC

Site	$/1000 gal
Refinery A	n/a
Refinery B	0.5
Refinery C	1.4
Chemical Plant A	1.4

Figure 1: Schematic of a systematic TRE.

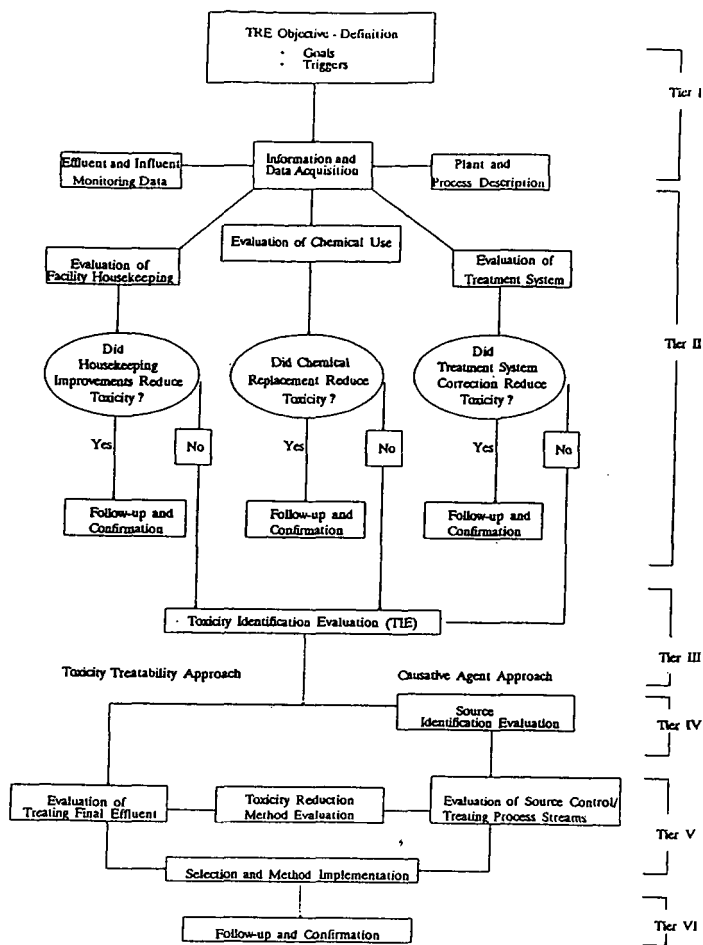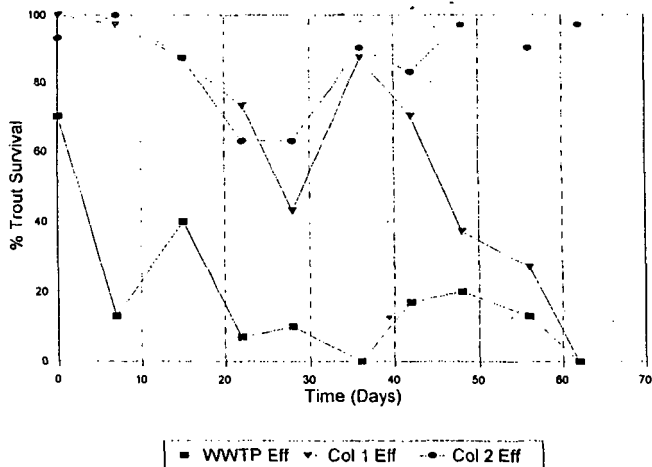**Figure 2:** Toxicity data from the pilot study for Refinery B.

Figure 3: TOC breakthrough data with toxicity data superimposed for the Refinery C optimization study. Data for toxicity breakthrough from the commercial system is also included.
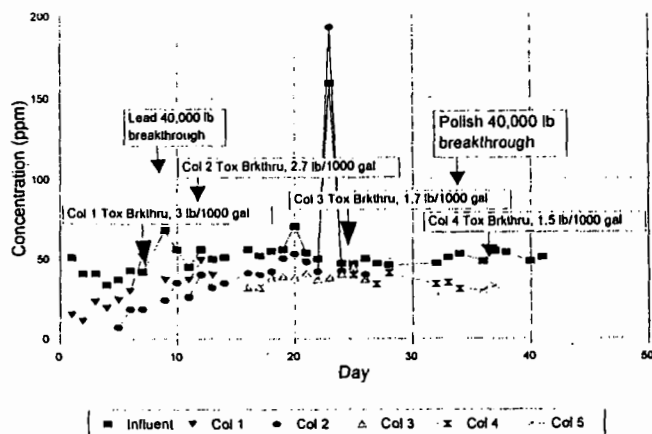

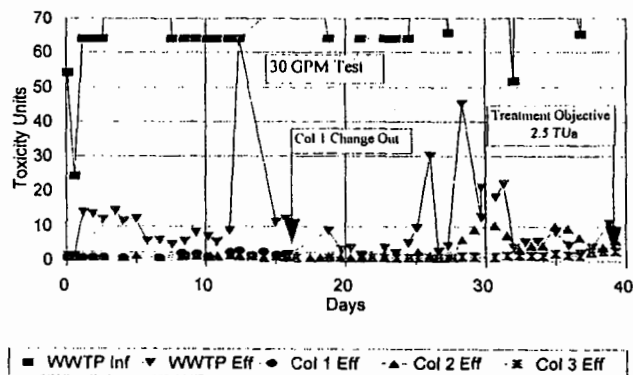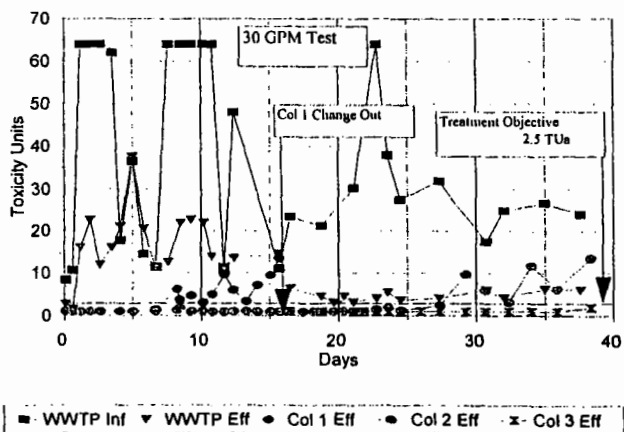**Figure 4:** Daphnia toxicity data from the Chemical Plant A pilot study.

Figure 5: Fathead minnow toxicity data from the Chemical Plant A pilot study.

ADSORPTION OF HERBICIDES USING ACTIVATED CARBONS

F. Derbyshire, M. Jagtoyen, C. Lafferty, and G. Kimber
Center for Applied Energy Research, University of Kentucky,
3572 Iron Works Pike, Lexington, KY 40511-8433, USA.

INTRODUCTION

This paper describes the results of research in which novel activated carbons have been examined for their efficacy in water treatment and, specifically, for the adsorption of a common herbicide and wood preservative, sodium pentachlorophenolate. To place this work in context, the introduction will discuss first some of the considerations of using activated carbons for water treatment, and then certain aspects of the authors' research that has led to this particular topic.

Activated Carbons for Water Treatment
One of the largest uses of activated carbons lies in the treatment of domestic and industrial water supplies. Activated carbons in various physical forms, have been used for more than 50 years to treat public water supplies for the removal of organic compounds that adversely affect taste, odor, and toxicity. Powdered activated carbons are used on a once-through basis, while granular activated carbons (GAC) possessing high surface areas, coupled with high attrition resistance, are used in packed bed applications.

Rising concern about the quality of drinking water supplies as well as the increased awareness of pollution from industrial waste waters have led to a significant growth in the activated carbon market. Demand for ion exchange resins and activated carbons for water treatment reached 200 million lb in 1992 and is expected to grow 4.6% per year to 251 million lb by 1997, mainly due to increased demand for activated carbons. The corresponding market value for these materials reached $271 million in 1992 and it is expected to rise to $376 million by 1997[1]. A small but ever-increasing market for activated carbons is also developing in the area of household water filtration systems for improving the quality of drinking water.

The surfaces of most commercial activated carbons are hydrophobic, which means that they are very effective for the adsorption of non-polar organic molecules. Activated carbons are less effective for the removal of polar compounds, and still less useful for the adsorption of ionic species (e.g. metals). For this reason, household treatment systems use activated carbon in multi-component filters that may also include materials such as ion-exchange resins. The high cost of ion-exchange media excludes their use in large-scale water treatment processes, where activated carbon is the preferred choice. However, there is a need to develop activated carbons that can be comparably effective for the adsorption of a wide range of pollutants.

Granular activated carbons have gradually replaced powdered activated carbons in water treatment and are now used on a much larger scale than ever before. In 1986 the Amendments to the Safe Drinking Water Act specified adsorption with GAC as the benchmark technology for organic chemical removal[2]. Alternative technologies must be at least as effective in controlling synthetic organic chemicals. Municipal water plants traditionally incorporate fixed beds of GAC as part of the filtration system, the carbon bed acting as a physical filter, as well as an adsorbent. The high attrition resistance of GAC is important to water treatment applications in that it allows for the carbons to be backwashed, pumped, excavated and recycled through regeneration units without suffering excessive material loss due to mechanical abrasion[3]. Although granular carbons are generally more expensive than powdered carbons, they have been found to be more cost-effective when their overall usage rate is high. Pressure drop, containment, and other considerations make powdered carbons impractical for use in adsorber beds.

Activated carbon fibers have recently started to attract interest as adsorbents for a number of applications, including water treatment[4]. Among other factors, the narrow fiber diameters (typically 10 to 30 microns) allow rapid rates of adsorption and desorption - a characteristic that also applies to fine particle powdered carbons. However, cost has so far presented one of the major obstacles to wide-scale development (over $20/Kg for carbonized fibers, i.e. before activation). In addition, to surmount problems in handling and utilization, it will be necessary to incorporate the fibers into some type of structure.

Current Research
Over the past few years, research at this Center has been involved with investigations of the synthesis of activated carbons by different methods and from a range of precursor materials[5-10]. The general objectives are to develop a basic understanding of the mechanisms leading to the formation of an extensive pore structure, and ultimately to be able to produce activated carbons with controlled porosity and surface chemistry, as well as other properties. These investigations have included: the formation of activated carbon particles and extrudates by the phosphoric acid activation of hardwoods and blends of hardwood with other materials [5,6]; activated carbon particles by the KOH activation of bituminous coals [7]; activated carbon extrudates by the KOH activation of lignite and oxidized bituminous coal [8]; activated carbon fibers from isotropic pitch precursors [9];

and the development of rigid, monolithic activated carbon composites [10].

The present work is related primarily to activated carbon composites. These are strong, highly permeable materials that can be produced in almost any size or shape, and are particularly suitable for applications where it is desirable to achieve high rates of throughput with minimum pressure drop. Moreover, the use of an immobilized bed can eliminate the attrition that would occur with a granular bed. Emanating from this work, we have found that it is possible to alter the pore structure of the activated carbon, and to introduce heteroatoms, such as nitrogen, into the structure by altering the method of synthesis. These attributes are germane to water treatment applications in two respects. First, the effectiveness of activated carbons in any particular application is dependent upon the pore size distribution: generally, for water treatment, a proportion of wider pores is desirable, both to facilitate diffusion of the adsorbate through the liquid phase, and to be able to accommodate large adsorbate molecules, such as color bodies and humic acids. Second, as already noted, activated carbons are typically hydrophobic. A number of studies has shown that the deliberate introduction of surface species, such as oxygen-containing groups, can enhance the ability to remove contaminants such as polar compounds and metals [11-13]. However, the necessary treatments can be expensive, and it is difficult to control the type and distribution of the surface groups. By the introduction of heteroatoms directly during the synthesis process, it should be possible to provide specific surface functionalities that are uniformly distributed over the adsorbent surface, and that may enhance the adsorptive capacities for non-polar species. In the research described here, we have conducted preliminary experiments to assess the potential of different formulations of activated carbon composites for the removal of a representative polar contaminant of groundwaters.

EXPERIMENTAL

In their original form, activated carbon composite materials have been prepared in collaboration with the Oak Ridge National Laboratory [10,14]. These composites are made from water slurries containing chopped carbonized pitch based fibers (~ 15 - 20 μm diameter x ~ 0.35 mm length, supplied by Ashland Carbon Fibers Division, Ashland Inc.) and a phenolic resin. The slurry is vacuum molded into tubular or plate configuration, followed by drying, curing and carbonization to 650°C. The composite is activated in steam or CO_2 at temperatures from 800-900°C to introduce porosity. The method of preparation of the other composites that have been prepared for this work is proprietary and will not be described here.

Some properties of the activated carbon composites are presented in Table 1, together with data for a commercial granular activated carbon that was used for comparison. Composite J was prepared by the method described above. It can be seen that these adsorbents possess quite different pore structures. The BET surface areas range from 660 to 1940 m^{2}g^{-1}, and have very different pore size distributions: some are predominantly microporous (pores < 2 nm diameter) and some have very high mesopore volumes (pores 2 - 50 nm diameter). The commercial water treatment carbon has a BET surface area at the low end of this range, but possesses an appreciable mesopore volume.

To measure the adsorptive capacities of the activated carbon composites for sodium pentachlorophenolate (PCP), 1.3 cm diameter plugs were cut from 1.5 cm blocks of activated monolith using a hole-saw. Three such plugs were lain end to end to form a column of total length 4.5 cm and volume 6 cm^3. The column was then sealed into a water-tight assembly using heat-shrink tubing (Markel Corporation, polyolefin tubing), by heating to approximately 180°C using a heat gun. The ends of the column were fitted with plastic barbed connections enabling Tygon tubing to be attached.

Comparable columns of granular activated carbon were prepared by sealing 2.0 g samples of carbon into polyolefin tubing, using the same technique, to create a column of volume 8 cm^3 and length 6 cm. Plugs of quartz wool were fitted at the column ends to contain the bed. A peristaltic pump, Pulsafeeder - Mec-o-matic VSP-20, located downstream of the column continuously drew a 40 ppm solution of sodium pentachlorophenolate (NaC_6Cl_5O) from a reservoir and through the column. The concentration of PCP in the column effluent stream was monitored via a UV-Vis spectrophotometer (Varian, Series 634) fitted with a 10 mm path length flow-through quartz cell, at a wavelength of 317.5 nm. Column breakthrough was determined as the point where the ratio of effluent to inlet PCP (C/Co) was equal to 0.3. The flow rate of PCP solution through each of the columns was held constant at 1 ml.min^{-1}.

RESULTS AND DISCUSSION

At the time of writing, adsorption data for PCP are available for the composite J and the commercial carbon. A plot of C/Co is shown as a function of the number of column volumes of PCP solution that have been processed in Figure 1. The breakthrough time for composite J was found to be almost 1400 column volumes, whereas it was closer to 150 column volumes for the granular carbon - a factor of about nine. It should also be noted that both columns continued to adsorb PCP after breakthrough and never reached saturation.

At first sight, the difference in the performance of these carbons is surprising, since they are of comparable surface area (see Table 1), and the commercial product has a much greater total pore volume (0.76 vs 0.39 cc/g) and, therefore, expected adsorption capacity. It is possible that part of

the difference may be attributable to the way in which the two columns are formed. As the activated composite is a monolith, the composition of the column is uniform over its cross section and length, and all of the solution has to pass through the interior of the composite before emerging: the monolithic form effectively ensures that the fluid feed is distributed uniformly through the column. With any granular bed, inefficiencies in packing can lead to channeling, allowing some of the feed to experience shorter contact times than the average that is calculated over the whole column: this phenomenon is more likely to occur in shallow packed beds.

At the same time, it is interesting to find that, at a similar overall space velocity (the volume feed rate per weight of carbon is 33.3 h^{-1} for the composite and 30.0 h^{-1} for the granular carbon), the column of composite is much more effective in adsorbing PCP. This observation indicates that the rate of adsorption is faster over the composite than the granules, which is consistent with other observations. The narrow diameter of the fibers (15 - 20 μm) essentially minimizes mass transfer limitations, and allows much faster rates of adsorption (and desorption) than is possible over large granules, as illustrated by an example obtained by a TGA study of the gas phase adsorption of NO, Figure 2. The rate of NO uptake is found to be higher by as much as three orders of magnitude for an activated carbon fiber composite than for 2 mm granules. Only when the granules are reduced to a size comparable to that of the fiber diameter, do the rates correspond. Thus, powdered carbons could be used with comparable effectiveness if the practical difficulties of containment, and the penalty of the pressure drop over a column of fine particles could be surmounted.

A second factor is that the composites have a very open architecture (approximately 90% is free volume), which means that the contacting fluid enjoys free access to the adsorbent surfaces. Essentially, the composite can be viewed metaphorically as a situation in which the granules have been "peeled open" to allow the adsorbent to readily access all of inner adsorbent surface, which can otherwise only be approached by diffusion through an extensive pore network.

REFERENCES

1. Peaff, G., C&EN, November 14, 15-19 1994.
2. Clark, R. M. And Lykins, B. W. Jr., "Granular Activated Carbon, Design, Operation and Cost", MI: Lewis, Chelsea, 1989.
3. Hutchins R.A., in "Activated Carbon Adsorption in Wastewater Treatment", Perrich J.R. Ed., CRC Press, 1981.
4. Suzuki, M., Proc. Biennial Carbon Conference, Buffalo, 1993.
5. Jagtoyen, M. and Derbyshire, F.J., Carbon, **31** (7), 1185-1192, 1993 .
6. Jagtoyen, M., Black, H. and Derbyshire, F., in Proceedings CARBON '95, San Diego, CA, 16-21 July, 1995, pp 398-9.
7. Jagtoyen, M., Toles, C. and Derbyshire, F., American Chemical Society, Fuel Division Preprints, **38** (2), 400-407, 1993.
8. Verheyen, V., Rathbone, R., Jagtoyen, M. and Derbyshire, F., Carbon, **33** (6), 763-772, 1995.
9. Fei, Y. Q., Derbyshire, F., Jagtoyen, M. and Kimber, G., in Proceedings of CARBON'94, 3-8 July, 1994, Granada, Spain, pp 664-5.
10. Jagtoyen, M., Derbyshire, F., Custer, N, Burchell, T., 1994 Spring Meeting, Materials Research Society, San Francisco, April 4-8, 1994 in Symposium Proceedings, **344,** 77-81, 1994..
11. Rivera-Utrilla, J. and Ferro-Garcia, M.A., Adsorption Science and Technology, 3, 293-302 1986.
12. Reed, B.E. and Arunachalam, S., Environmental Progress, **13** (1), 60-64 , 1994.
13. Reed, B.E. and Matsumoto, M.R., J. Environmental Engineering, **119**(2), 332-348 , 1993.
14. G. C. Wei, and J. M. Robbins, Ceramic Bull., **64** (5), 691-699 (1985).

ACKNOWLEDGEMENTS

Table 1: Properties of activated carbon adsorbents

Sample	BET surface area (m^2/g)	Pore volume (cc/g) micro	meso	Bulk Density (g/cc)
A	870	0.42	0.03	-
E	1140	0.43	0.87	-
F	1940	0.76	0.73	-
I	1930	0.61	1.10	-
J	790	0.38	0.01	0.30
Granular carbon*	660	0.29	0.47	0.25

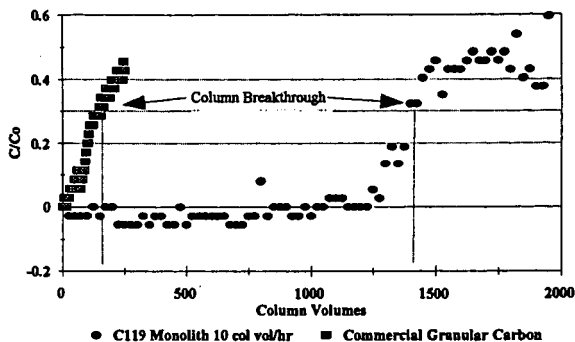* commercial water-treatment carbon, 1-2 mm granules

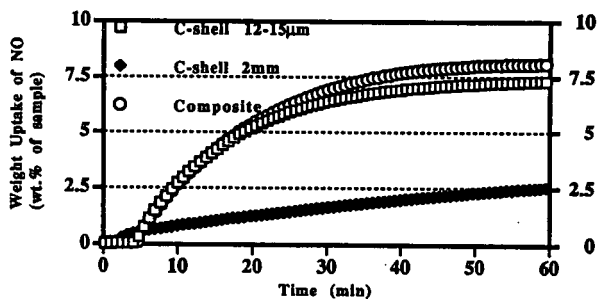Fig. 1. Adsorption of Na-PCP by Carbon Columns

Figure 2: Adsorption rate of NO on activated carbon composite compared with a commercial granular activated carbon at two average particle sizes; 2mm, and finely ground to 14µm.
(c-shell= coconut shell)

CARBONIZED MATERIAL ADSORBENTS FOR THE REMOVAL OF MERCURY FROM AQUEOUS SOLUTIONS

Shigehisa Ishihara, Lilibeth L. Pulido
Wood Research Institute, Kyoto University
Uji, Kyoto 611, Japan
and
Takeshi Kajimoto
Wakayama Industrial Technology Center
Wakayama, City 649-62, Japan

Introduction

Although wood has essentially been excluded as a starting material for the production of granular activated carbon because of the poor strength and friability of the products [1], powdered wood based activated carbons are still being used in water treatment and other liquid phase applications. However, the capability of powdered wood-based charcoal which in itself porous has not been fully known. Few studies have been conducted in harnessing its potential for adsorption purposes especially in water treatment.

This study was conducted to investigate the possibility of using wood based carbonized materials from Sugi (Cryptomeria japonica D. Don) as adsorption materials in aqueous solutions of heavy metals like mercury, zinc, lead, cadmium and arsenic. However, of all the heavy metals investigated, mercury is considered to be the most toxic so this paper describes only the adsorption ability of the carbonized materials in adsorbing this metal from aqueous solutions of different concentrations.

Materials and Methods

A. Materials

The raw materials used in this study were Sugi , activated carbon from coconut shell and Mercuric chloride ($HgCl_2$) as heavy metal.

B. Methods

1. Preparation of Materials: Small diameter logs of Sugi were cut into flakes and made into powder. Wood powder was passed through a 20-mesh size sieve. The wood powder was ovendried at 105± 2 °C prior to carbonization.

2. Carbonization Process: Wood powder was carbonized in a furnace with the desired temperatures of 200, 400, 600, and 1000 °C. Nitrogen (N_2) gas of 1500 ml/min. was flowed in a heating rate of 4 °C/min. After getting the desired temperature, it was kept for one hour and then turned it off. The charcoal was cooled naturally before it was taken out of the furnace.

3. Adsorption Experiment: Aqueous solutions of 5, 50 & 100 ppm $HgCl_2$ were prepared. Each of the carbonized materials with a weight of 0.5 g was mixed with 50-ml $HgCl_2$ solution and continuously stirred in a hotting bath at 30± 2 °C for 1, 4, 8 and 24 hours of soaking time. The mixtures were filtered with ADVANTEC Toyo glass fiber filter paper. The concentration of the filtered solution was determined using an Inductively Coupled Plasma machine.

4. Determination of Acidity and Dissolved Oxygen of the Solute: The acidity of the solution was measured using a pH meter while that of the dissolved oxygen was measured using a COD meter.

Results and Discussion

1. Adsorption ability of carbonized wood materials

Figures 1-3 show the relationship between total soaking time and adsorption of carbonized materials. Based from Fig. 1, similar adsorption behavior was observed in all the carbonized materials. The adsorption was highest in 1000 °C in all the total soaking times, and then followed by 600 °C and 200 °C. It can be observed that the adsorption in activated carbon is not comparable with the high temperature carbonized materials. Further, adsorption in 1000 °C was almost the same in all the total soaking times.

In Fig.2, adsorption was still highest in 1000 °C in all the soaking times and then followed by 600 °C and activated carbon. However, it can be observed that 105 °C and 200 °C had a remarkable adsorption compared when soaked at 5 ppm solution and even comparable with the high carbonized materials (8 & 24 hours).

Different results were observed in 100 ppm solution (Fig.3). Although the adsorption trend of all the carbonized materials in all the total soaking hours was the same with that of 5 and 50 ppm, it can be observed that at higher concentrations of $HgCl_2$ solution, higher adsorption is observed not only at 1000 °C but also in activated carbon. Moreover, it can be noticed that activated carbon adsorbed almost the same as the high carbonized materials unlike in the low concentrations.

Generally, the extent of adsorption depends mainly on the surface area and the chemical nature of the adsorbents.[2] Based from the preliminary measurement of the specific surface area of the adsorbents, high carbonized materials have higher specific surface areas. However, in this study, it is clear that surface area was independent of the adsorption. The higher temperature carbonized materials with a high specific surface area performed almost the same with the low temperature materials. The chemical properties which can be a source of explanation on certain extent seem not to have any effect especially on lower concentrations of $HgCl_2$ solutions. The elemental analysis results of the carbonized materials [3] revealed that the carbon contents increases with the increase of temperatures. Consequently, carbonized materials with high carbon content adsorbs more than those with low carbon content materials. However, in higher concentrations of $HgCl_2$, higher carbonized materials adsorbs more than those of low carbonized materials.

According to Lee, et al.[4], in general, adsorption capacity can be influenced both by the microspore structure and also by the surface chemistry interactions. Carbon surfaces are covered with chemisorbed oxygen species which have a profound influence on surface properties.[5] In a study conducted on the removal of chromium (metal) from aqueous solutions by activated carbon adsorbents, it has been observed that not only the microporous structures and the surface area but the chemical structure of the carbon surface plays an important role in the adsorption. In particular, the nature of the surface-oxygen chemical structure present in the carbon surface, not the total amount of oxygen determines the adsorption of chromium. [6] The addition of oxygen-containing functional groups to the carbon surface caused by the exposure in the atmospheric thus altering its adsorptive properties [7] is a probable source of change in the surface oxygen chemical structure which in turn affects its adsorption capability.

In another study conducted on the lightest metal, Lithium(Li), diffusion is the main parameter in controlling the adsorption of this metal. Interaction of Li with surface groups may also play an important role in the adsorption process. [8]

2. Water purification ability of carbonized materials

In connection with the pollution of water, the content of dissolved oxygen in water is of prime concern. The overuse of water systems for disposal purposes in many instances had almost fully depleted the dissolved oxygen available for life support.

In this study, the amount of COD was monitored with soaking time. Table 1 shows the decrease in the amount of COD of the $HgCl_2$ solution

after 24 hours of soaking the carbonized materials. Rate of decrease is somewhat higher for the high carbonized materials and activated carbon. The decrease in the COD values through time can be observed through a sample graph as shown in Fig.7.

The pH values after treating the carbonized materials in 24 hours is shown in Table 2. The original $HgCl_2$ solutions which was acidic was made close to neutral or neutral for 600 °C and 1000 °C, and activated carbon after it was treated with carbonized materials. However, at 105 °C and 200 °C, the pH values also increased but at low concentrations only. Fig. 9 shows the behavior of pH value with total soaking time.

Conclusion

Wood based carbonized materials can be used as adsorption materials in treating aqueous solutions of heavy metals like mercury. However, the behaviour of the adsorption of carbonized materials in $HgCl_2$ solutions cannot still fully explained because of lack of basic information on the nature of the adsorbent materials. Microporous structure and surface-oxygen chemical structure present in the carbon surface will be investigated in future studies to further explain the adsorption ability of this heavy metal.

Reference

1) Jagtoyen, M.H. Black and F. Derbyshire. 1995. Carbon '95-22nd Biennial Conference on Carbon. Extended Abstracts and Program. p. 398.
2) Fundamentals of Physical Chemistry. 1964. H.B. Crockford and S.B.Knight. A. Wiley International Ed. 2nd ed. Chapter 17.
3) Nishimiya, K. et al.1995. Mechanism and Clarification of Electrical Conduction through Wood Charcoal. Wood Research. Bulletin of the Wood Research Institute. Kyoto University. p. 34-36.
4) Lee, W.H. et al.1995. Adsorption of Inorganic Vapors on Coal and Wood-Based Chemically Activated Carbons. Carbon'95 - 22nd Biennial Conference on Carbon. Extended Abstracts and Program. pp. 486-487.
5) Barton, S.S. et al. 1995. Surface Oxide Structures on Porous Carbon. Carbon '95 - 22nd Biennial Conference on Carbon. Extended Abstracts and Program. pp. 436-437.
6) Bansal, R.C. et al. 1995. Activated Carbon Adsorbents for the Removal of Chromium from Aqueous Solutions. Carbon '95 - 22nd Biennial Conference on Carbon. Extended Abstracts and Program. pp.452-453.
7) Barton, S. S. et al. 1995. The Influence of Surface Modification of BPL Carbons on Aging. Carbon '95 - 22nd Biennial Conference on Carbon. Extended Abstracts and Program. pp.438-439.
8) Seron, A. et al. 1995. Electrochemical and Chemical Sorption of Lithium Ions Onto Activated Carbons from Aqueous Solutions. Carbon '95 - 22nd Biennial Conference on Carbon. Extended Abstracts and Program. pp.454-455.
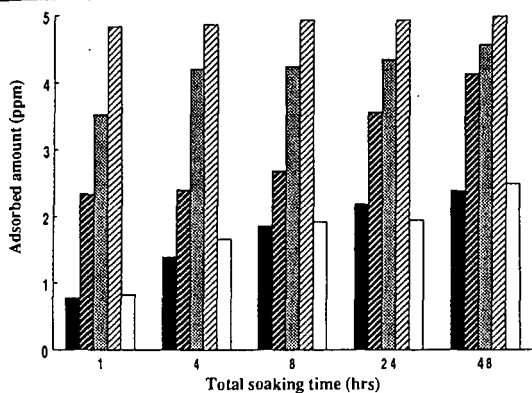
Fig. 1. Relationship between total soaking time and adsorbed amount of HgCl in 5 ppm aqueous solution.
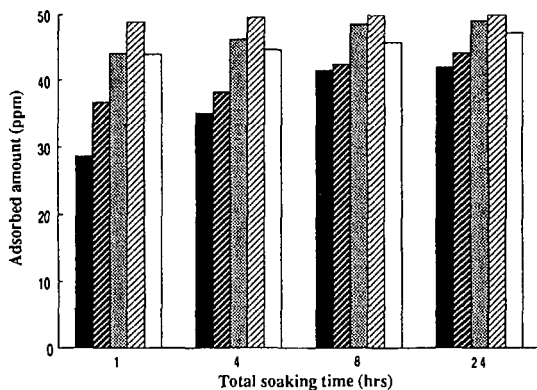

Fig. 2. Relationship between total soaking time and adsorbed amount of HgCl in 50 ppm aqueous solution.
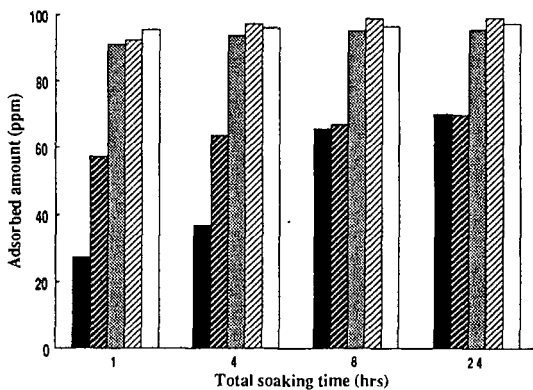

Fig. 3. Relationship between total soaking time and adsorbed amount of HgCl in 100 ppm aqueous solution.

Legend: ■ Control
▨ 200°C
▨ 600°C
▨ 1000°C
□ Activated charcoal

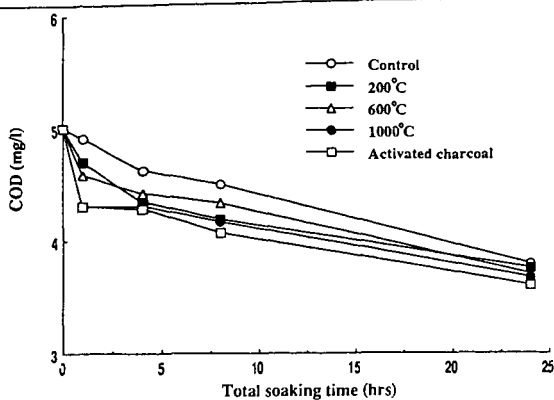Note: Control - wood powder ovendried at 105°C

479

Fig. 4. Relationship between total soaking time and COD in 100 ppm aqueous solution.
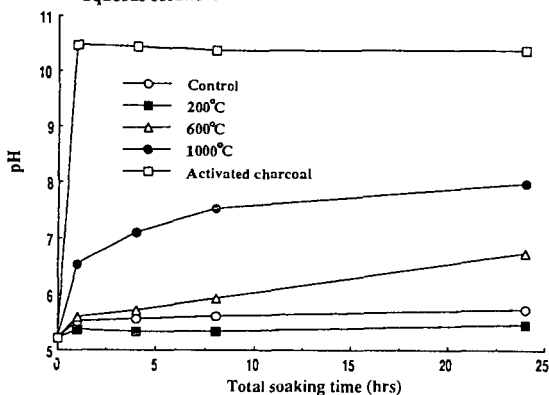

Fig. 5. Relationship between total soaking time and pH in 5 ppm aqueous solution.

Table 1. Effects of carbonized materials on the COD of HGCl$_2$ aqueous solutions after 24 hours.

| | COD (mg/l) | | | Rate of decrease (%) | | |
	1	2	3	1	2	3
Original HgCl$_2$ solution	5.600	5.050	5.000	-	-	-
Carbonized materials						
Control	3.570	3.650	3.790	36	28	24
200 °C	3.520	3.620	3.750	38	28	25
600 °C	3.460	3.600	3.100	38	29	38
1000 °C	3.460	3.500	3.070	38	31	39
Activated charcoal	3.390	3.450	3.000	39	32	40

Legend: 1 - 5 ppm; 2 - 50 ppm; 3 - 100 ppm

Table 2. pH values of HgCl$_2$ aqueous solutions treated with carbonized materials after 24 hours.

| | pH | | |
	1	2	3
Original HgCl$_2$ solution	5.21	4.92	5.23
Carbonized materials			
Control	5.72	5.12	4.45
200 °C	5.45	4.88	4.69
600 °C	6.73	5.98	5.79
1000 °C	7.96	7.56	7.34
Activated charcoal	10.35	9.60	9.11

Legend: same as in Table 1.

THE ION EXCHANGE PROPERTIES OF LOW RANK COALS
ON ACTINIDES AND OTHER HEAVY METALS

A. S. Wong[1], N. D. Stalnaker[1]

[1]CST-8, MS G740, Los Alamos National Laboratory, Los Alamos, NM 87545

C. J. Lafferty[2] , J. D. Robertson[2,3] , and J. H. Kuhr[3]

[2]Center for Applied Energy Research, University of Kentucky, 3572 Iron Works Pike,
Lexington, KY 40511. [3]Department of Chemistry, University of Kentucky, Lexington KY 40506.

Keywords: actinides, ion exchange, lignite

ABSTRACT

The removal of heavy metal and low-level radioactive wastes from the environment and their subsequent immobilization in an appropriate repository is one of the major environmental challenges facing our nation. The scope and magnitude of the contamination at many DOE and Superfund sites are such that successful remediation will require the development of new, inexpensive technologies which remove, in an environmentally acceptable manner, the heavy metal and radioactive wastes from contaminated soil and water. In this paper, we will present the preliminary data on the viability of using low rank coals or lignites as a novel, inexpensive material to remove actinides and other metals from the aqueous system, and the effects of high radiation on ion-exchange properties of lignites.

INTRODUCTION

After more than a half a century of nuclear processing activities by DOE and its predecessors, a wide range of wastes and environmental problems exists at more than 100 contaminated installations in 36 states and territories.[1]   Uncontained hazardous and radioactive contaminations in soil and ground water exist throughout the DOE complex.   The calls for developing cost-effective technologies to remove radioactive and toxic metal contaminants from the waste processing streams and ground water, and to reduce secondary waste volumes are the top priority for environmental restoration at the DOE sites.

In groundwater, the most common binary contaminant found in the DOE sites is a mixture of radionuclides, metals, and chlorinated hydrocarbons. The most important metal contaminants identified are lead, chromium, arsenic and zinc; radionuclide contaminants are tritium, uranium, strontium, plutonium, cesium, cobalt, technetium, and iodine.[2] At the Waste Treatment Facility at Los Alamos National Laboratory (LANL) and Rocky Flat Plant (RFP), the principle metal contaminants found in these processing streams are plutonium (Pu) and americium (Am). Waste water streams generated from the research operations, reactors, and radiochemical production facilities such as Savannah River Site, Oak Ridge Y-12 Plant, Fernald Plants, and Hanford Site contain a wide spectrum of radionuclides (e.g., strontium, cesium, technetium, nickel, uranium, thorium, and radium), heavy metals, reactive chemicals, and organic solvents.[1]

Clearly the scope and magnitude of the contaminations at various DOE sites require the development of new, inexpensive technologies which would remove, in an environmentally acceptable manner, the heavy metal and radioactive wastes from contaminated soil and water. Conventional treatments of radioactive waste water at the DOE sites are the precipitation methods, which generate large volumes of secondary radioactive sludge waste. The other common technologies for removal of heavy metals from ground water and waste water are ion exchange resin based processes; however, these commercial resins are usually very costly (> $10/lb) and generate secondary acid waste from the regeneration process.

In the past few years, the University of Kentucky Center for Applied Energy Research (CAER) and Department of Chemistry have developed a system based on the unique ion exchange properties of low rank coals for the treatment of large volumes of water containing low to moderate levels of metal contaminations.[3],[4],[5] Because of the cationic selectivity of lignites

on a high charge density metal, a collaborative effort between the University of Kentucky and Inorganic Elemental Analysis group (CST-8) at LANL will attempt to address the needs of DOE environmental cleanup of actinides and other heavy metals from the aqueous system, and reduce the generation of secondary sludge waste from the waste water treatment process. Our goals are (1) to develop a novel, inexpensive material to remove actinides (Pu, Np, Am, and U) and heavy metals from the waste water streams and ground waters, (2) to understand the ion exchange mechanism of actinides with low rank coals, and (3) to study the effect of radiation on ion exchange properties of lignites.

ION-EXCHANGE PROPERTIES OF LIGNITES

Low rank coals, brown coals or lignites are characterized by low specific energy, high oxygen and moisture contents and poor internal strength (the latter excludes underground winning of low rank coals). The high moisture content of the coal retards efficient combustion and must be removed by energy consuming processes prior to combustion. An economical use of brown coal for power generation is feasible only when the combustion process is located close to the coal supply, minimizing the amount of transport required between coal source and power station. The high oxygen contents of low rank coal does however impart one unique property to these coals, that of the ability to remove cations from solution via ion exchange with carboxylic acid and phenolic hydroxyl functional groups on the coal surface. These functional groups undergo dissociation in solution to form a negatively charged site upon the coal surface which is subsequently capable of complexing cationic species from solution to form a stabilized coal-metal structure. The dominant functional group responsible for the ion exchange process has been shown to be the carboxylic acid group. These weak acid sites are virtually completely dissociated at solution pH's greater than 4, and would therefore be ideal for the treatment of most natural water samples which routinely display pH values between 4 and 9. The coal however, would not be suitable for treating many industrial waste streams which have pH values often less than 1. Slight adjustment of pH to the waste streams may be required.

Table I gives the typical cation exchange capacities of various North American lignites. The cation exchange capacities of these coals are considerable lower than those measured for commercially available synthetic ion exchange resins ($\sim$ 0.4-1.0 meq/g c.f. 7-10 meq/g for commercial resins) however the lower cost of the coal ($\sim$ \$10/ton) compared to the commercial resins ($\sim$\$10/lb) makes the cost per unit volume of solution treated significantly lower for the coal based process. Table II shows the calculated cost per liter for both a brown coal and synthetic resin based process treating several different 100 ppm solutions. The processing costs listed in Table II show that the lignite based process is cheaper than a resin based system by a factor of 170, although the total mass of adsorbent used in the coal based process is 18 times that of the resin. However, for the proposed solutions to be treated, e.g. groundwater containing low to moderate levels of contamination, processing costs are envisaged to be the main criteria in determining which process would be used, and would therefore favor the implementation of a coal based system.

TABLE I.   Cation Exchange Capacities (meq/g) measured for North American Lignites
(1000 ppm solution, 5 g coal/100 mL solution)

Metal	West Kentucky	North Dakota	East Texas
Cd	.35	.38	.37
Pb	.20	.22	.21
U	.16	.17	.17
Hg	-	.22	

TABLE II.   Cost per Liter (cents) to treat 100 ppm Solution of Divalent Metal.
Using Brown Coal and Resin Based Systems

Metal	Brown Coal @ \$10/ton 0.4 meq.g^{-1}.	Ion Exchange Resin @ \$30/kg 7.0 meq.g^{-1}.
Cu^{2+}	7.88×10^{-3}	1.351
Cd^{2+}	4.44×10^{-3}	0.763
Hg^{2+}	2.49×10^{-3}	0.427
U^{2+}	2.10×10^{-3}	0.360

APPROACH

A series of standard adsorption experiments, principally in batch mode, will be conducted on the Western Kentucky lignites with solutions containing actinides (e.g., ^{239}Pu, ^{241}Am, ^{237}Np, and ^{234}U). Some of the key variables that are known to effect lignite exchange capacity, which will be investigated as initial part of the study include:

- Cation exchange capacity as a function of solution pH.
- Cation competition effects.
- Effect of multiple low loading contacts compared to single high loading contacts.

Quantitation of radionuclide adsorption will be performed using a combination of liquid scintillation and alpha spectroscopy. The experiment will be conducted in a wide range of radioactivity (from several hundred pCi/L to mCi/L level) in order to simulate the radioactive contaminants present in the ground water to the waste processing streams.

In addition to adsorption study, a sample of Western Kentucky lignites is currently exposed to a ~ 2.5 rem per hour gamma-radiation source (radiation dose = ~2.5 rads per hour). We plan to expose this sample to the radiation source with several thousand rads (> 2 months) and examine the structure of functional groups in the lignites after irradiation. This will give us some opportunities to compare the ion exchange capacities of lignites before and after exposing to relatively high radiation field.

EXPECTED RESULTS

The analytical results from the proposed experiment are not available at the time of publication. From the previous work,[3],[4],[5] a single 5% loading w/v (2.5 grams of coal dry weight per 50 mL of solution) of Western Kentucky and East Texas lignite removed greater than 99% of the uranium from a 1000 ppm uranium (uranyl nitrate) solution. We anticipate that the other highly charged actinide species (Pu, Am, Np) will interact with lignites similar to uranium in the aqueous system.

CONCLUSION

The success of developing a system, which utilizes low-rank coals as an ion-exchange media for removals of radionuclides and heavy metals in environmental cleanup and waste water treatment, would dramatically reduce the cost of expensive environmental remediation and industrial waste stream treatments.

REFERENCES

(1) "Efficient Separations and Processing Crosscutting Program," Office of Environmental Management Technology Development, U. S. Department of Energy, Washington, DC, June 1995, DOE/EM-0249.
(2) R. G. Riley and J. M. Zachara, "Nature of Chemical Contaminants on DOE Lands and Identification of Representative Contaminant Mixtures for Basic Subsurface Science Research,", Office of Energy Research, U.S. Department of Energy, Washington, D. C., 1992, DOE/ER-0547T.
(3) C. J. Lafferty, J. D. Robertson, J. Kuhr, J. Emley, and E. McGonigle, Proc. Am. Chem. Soc., Emerging Technologies in Hazardous Waste Management, VII, Atlanta, Ga, 1995.
(4) C. J. Lafferty, J. D. Robertson, J. Kuhr, J. Emley, and E. McGonigle, Am. Chem. Soc., Emerging Technologies in Hazardous Waste Management, VI, Atlanta, Ga, 1994.
(5) J. D. Robertson, C. J. Lafferty, and K. Burberry, Am. Chem. Soc., Emerging Technologies in Hazardous Waste Management, V, Atlanta, Ga, 623, 1993.

THE USE OF CARBON AEROGEL ELECTRODES FOR ENVIRONMENTAL CLEANUP

Joseph C. Farmer, David V. Fix,
Richard W. Pekala, Jacquelyn K. Nielsen, Alan M. Volpe, and Daniel D. Dietrich
Lawrence Livermore National Laboratory
Livermore, CA 94550

INTRODUCTION
An electrochemical cell with a stack of carbon aerogel electrodes has been used to remove a variety of contaminants from aqueous waste streams and natural waters. In the case of non-reducible and non-oxidizable salt solutions, the cell is operated in a capacitive mode [1-7]. Electrolytic or electrophoretic deposition is used for the removal of heavy metals. The removal of $NaNO_3$ from water with subsequent concentration is an example of capacitive operation. Electrodialysis with bipolar membranes can be used to separate neutral salt solutions into their acid and base components so that recycle is possible, thereby lowering risk to the environment [8]. However, the electrodialysis process is not 100% efficient and generates a dilute waste stream of $NaNO_3$ in addition to the HNO_3 and $NaOH$ product streams. Carbon aerogel electrodes can be used to remove $NaNO_3$ from the effluent, concentrating it for recycle to the electrodialysis cell. Solutions are passed through a stack of carbon aerogel electrodes, each having a very high specific surface area (400 to 1100 m^2 g^{-1}) and very low electrical resistivity (less than 40 mΩ-cm). After polarization, Na^+ cations and NO_3^- anions are removed from the electrolyte by the imposed electric field and held in electric double layers formed at the surfaces of electrodes. Two streams are produced, pure water and $NaNO_3$ concentrate. This process is also capable of removing other impurities such as dissolved heavy metals and suspended colloids. In these cases, contaminants are removed by electrodeposition and electrophoresis, respectively. The carbon aerogel cell has been used for the separation of copper, zinc, cadmium, and lead from 0.1 M KNO_3 solutions, as well as for the separation of cobalt, chromium, manganese, lead, and uranium from sea water. Treatability tests on ground water at LLNL have shown that chromium contamination can be reduced from 32 to 2 ppb, well below the acceptable level of 11 ppb. Previously, other types of porous carbon electrodes have been used for the removal of heavy metals from water. These electrolytic separation processes have several potential advantages over other more conventional technologies. Unlike ion exchange, no acids, bases, or salt solutions are required for regeneration of the system. Regeneration is accomplished by either electrical discharge or reverse polarization. Therefore, no secondary waste is generated. In contrast to thermal processes such as evaporation, such processes are more energy efficient. Since no high pressure pumps are required, these electrolytic separation processes offer operational advantages over reverse osmosis (RO).

ELECTROCHEMICAL CELL WITH CARBON AEROGEL ELECTRODES
A typical double-sided electrode is made by gluing two sheets of a carbon aerogel composite (CAC) to both sides of a titanium plate that serves as both a current collector and a structural support for the CAC. Conductive silver epoxy is used for gluing. Carbon aerogels were developed at Lawrence Livermore National Laboratory and are synthesized by the polycondensation of resorcinol and formaldehyde in a slightly basic medium, followed by supercritical drying and pyrolysis in an inert atmosphere. Sheets of CAC are made by impregnating carbon cloth with the resorcinol-formaldehyde solution and then carbonizing. This fabrication process results in unique open-cell carbon foams that have high specific surface areas (400 to 1100 m^2 g^{-1}), optimal pore sizes (~50 nm), and a monolithic structure composed of interconnected colloidal-like particles or fibrous chains with characteristic diameters of 10 nm. This structure results in exceptionally low electrical resistivity (40 mΩ-cm). The porosity and surface area of aerogels can be controlled over a broad range, while the pore size and particle size can be tailored at the nanometer scale. Each sheet of CAC used in the experiments described here is 6.86 cm x 6.86 cm x 0.0125 cm, has a total active surface of approximately 2.8×10^6 cm^2, and a through resistance of about 10 $\mu\Omega$. Two orifices are located along one side of the carbon aerogel electrode and admit water to the electrode gap. A pattern of holes are located around the perimeter of the titanium plate and accommodate 12 threaded rods that hold the cell stack together. Even electrodes serve as cathodes while odd electrodes serve as anodes. The electrodes and headers are aligned by the threaded rods. An electrode separation of 0.05 cm is maintained by cylindrical nylon spacers concentric with the threaded rods and a rubber

compression seal. Since the orifices in each electrode alternate from one side of the stack to the other, the flow path through the stack is serpentine. Flow through the cell is generated by a programmable, magnetically-coupled, screw pump with a 304 stainless steel head. The maximum flow rate that can be achieved with this pump is 3.5 L/min. The differential pressure across a stack of 48 electrodes is only 5 psi at a flow rate of 1.7 L/min. All lines are made of Teflon and have a nominal diameter of 1/4 inch. The cells are polarized by programmable power supplies that have a voltage range of 0 to 12 V or a current range of 0 to 60 A. Sensors are placed on the inlet and outlet lines of the cell. Electrical conductivity, pH, individual ion concentrations, and temperature are continuously monitored. A computerized data acquisition system logs important operating parameters such as voltage, current, conductivity, pH, and temperature. Data acquisition system is based on an Intel 486DX-33 microprocessor, a National Instruments 8-channel A/D converter, and LabTech Notebook data acquisition software for Microsoft Windows. X-ray fluorescence is used off line for the quantitative measurement of heavy metals.

REMOVAL OF NITRATE SALTS

The removal $NaNO_3$ from a fixed 4000 ml volume of water by a stack of 192 carbon aerogel electrodes is illustrated by Fig. 1. The circulation rate through the stack was approximately 1000 ml/min. After application of a voltage between two adjacent electrodes, Na^+ cations and NO_3^- anions are drawn towards the cathode and anode, respectively. These ions are held in the electric double layers formed at the extensive surface of the carbon aerogel electrodes until the voltage is reduced. Tests demonstrated that CDI with carbon aerogel can effectively remove $NaNO_3$ from water. Deionization was accomplished during charging, while regeneration was accomplished during discharge. The concentration and conductivity was cycled up and down numerous times by charging and discharging the stack. The ability of the CAC electrodes to remove ions from water, i.e., the electrosorption capacity, had a strong dependence on cell voltage. The best results were achieved at 1.2 V, with relatively poor performance below 0.6 V. During experiments without recycle, a characteristic breakthrough curve (not shown) was observed. Deionization of more concentrated solutions requires more carbon aerogel electrodes.

REMOVAL OF HEAVY METALS

Two carbon aerogel electrodes polarized at 1.2 V can remove copper, zinc, cadmium, and lead from a fixed, 500 ml volume of a 0.1 M KNO_3 solution (Fig. 2). The electrolyte was circulated through the electrochemical cell at a rate of 50 ml/min. The concentration of lead dropped from an initial level of approximately 1 ppm to less than 0.2 ppm after 4 hours of polarization. The concentration of copper dropped from 1 ppm to less than 0.05 ppm. At such low concentrations, one would expect rates of removal to be mass transfer controlled, similar in magnitude, and independent of the standard electrode potentials of the ions being deposited. However, the rates for several of the ions appear to be correlated to some extent with their standard electrode potentials, indicating that process efficiency may not be governed by mass transport alone. Forty carbon aerogel electrodes polarized at 1.2 V were able to remove trace quantities of cobalt, chromium, manganese, lead, and uranium from a fixed, 1000 ml volume of sea water (Fig. 3). Here too the electrolyte was circulated through the electrochemical cell at a rate of 50 ml/min. The initial concentration of each contaminant was 100 ppb. After 5 hours of polarization, the concentrations of cobalt, chromium, manganese, and uranium dropped to levels of about 5 ppb or less. The concentration of lead dropped to about 15 ppb. The slow increases in concentration observed between 5 and 25 hours are probably due to some combination of redissolution and particle entrainment. Such difficulties can be avoided by periodic regeneration of the carbon aerogel electrodes. No electrode separator was used in the experiments represented by Figs. 2 and 3. By incorporating an anion exchange membrane between anodes and cathodes, electrode regeneration by stripping is possible.

SUMMARY

In summary, it has been shown that capacitive deionization with carbon aerogel electrodes can be used to remove salts such as $NaNO_3$ from water. It has also been shown that electrolysis with carbon aerogel electrodes can be used to effectively remove a variety of heavy metals from process streams and natural waters. The exceptionally low electrical resistivity of the monolithic carbon aerogel electrodes, due to their unique interconnected nanostructure, has made it possible to eliminate metal substrates such as titanium in more recent cell designs. Recent cell designs use only carbon aerogel and a plastic such as polycarbonate. Disposable cells made of carbon aerogel and plastic are now being made and operated.

REFERENCES

1. D. D. Caudle, J. H. Tucker, J. L. Cooper, B. B. Arnold, A. Papastamataki, "Electrochemical Demineralization of Water with Carbon Electrodes," Research and Development Progress Report No. 188, United States Department of Interior, May 1966, 190 p.

2. A. M. Johnson, J. Newman, "Desalting by Means of Porous Carbon Electrodes," J. Electrochem. Soc., 118 3 (1971) 510-517.

3. Y. Oren, A. Soffer, "Electrochemical Parametric Pumping," J. Electrochem. Soc. 125 6 (1978) 869-875.

4. J. C. Farmer, D. V. Fix, G. W. Mack, R. W. Pekala, J. F. Poco, *Capacitive Deionization of Water: An Innovative New Process*, Proc. Fifth Intl. Conf. Rad. Waste Mgmt. Environ. Remediation, Berlin, Germany, Sept. 3-9, 1995, ASME, New York, NY, Vol. 2, pp. 1215-1220, 1995.

5. J. C. Farmer, D. V. Fix, G. W. Mack, R. W. Pekala, J. F. Poco, *Capacitive Deionization with Carbon Aerogel Electrodes: Carbonate, Sulfate, and Phosphate*, Proc. 1995 Intl. SAMPE Tech. Conf., Albuquerque, NM, Oct. 9-12, 1995, SAMPE, Covina, CA, Vol. 27, pp. 294-304, 1995.

6. J. C. Farmer, D. V. Fix, G. W. Mack, R. W. Pekala, J. F. Poco, *Capacitive Deionization of NaCl and NaNO₃ Solutions with Carbon Aerogel Electrodes* J. Electrochem. Soc., Ms. No. 95-05-098, in press.

7. J. C. Farmer, *Method and Apparatus for Capacitive Deionization, Electrochemical Purification, and Regeneration of Electrodes*, U. S. Pat. No. 5,428,858.

8. J. C. Farmer, D. V. Fix, R. G. Hickman, V. M. Oversby, M. G. Adamson, *Regeneration of Acids and Bases by Electrodialysis*, Proc. Symposium on Water Purification by Photocatalytic, Photoelectrochemical, and Electrochemical Processes, 185th Electrochem. Soc. Meeting, San Francisco, CA, May 22-27, 1994, T. L. Rose, O. Murphy, E. Rudd, B. E. Conway, Eds., Electrochem. Soc., Pennington, NJ, Vol. 94-19, pp. 184-190, 1994.
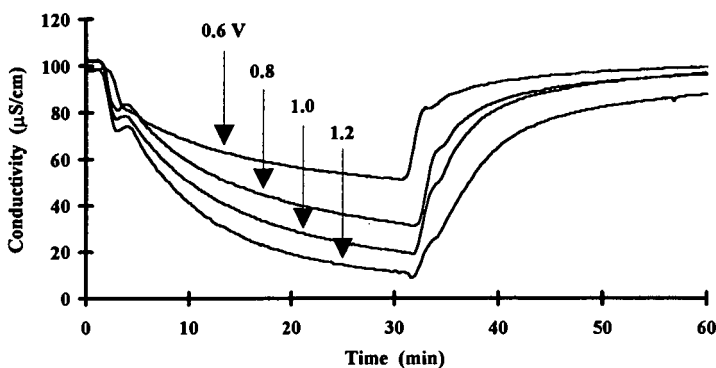
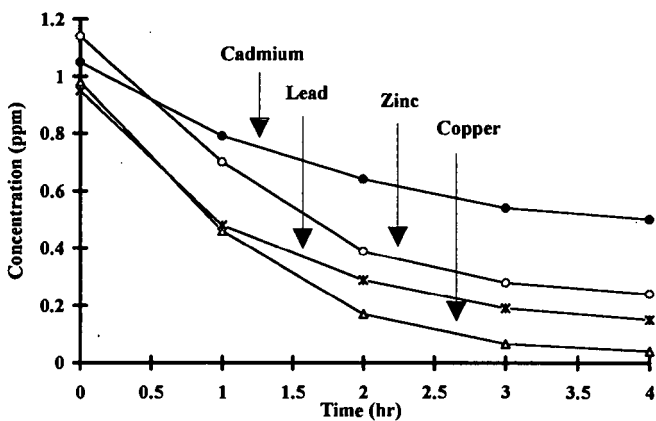Fig. 1. Use of carbon aerogel electrodes in capacitive mode to remove $NaNO_3$ from fixed volume of electrolyte.

Fig. 2. Use of two carbon aerogel electrodes polarized at 1.2 V to remove copper, zinc, cadmium, and lead from a fixed 500 ml volume of a 0.1 M KNO_3 solution.
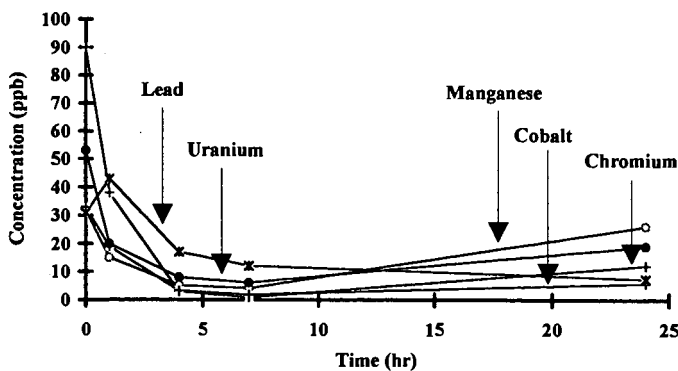

Fig. 3. Use of forty carbon aerogel electrodes polarized at 1.2 V to remove cobalt, chromium, manganese, lead, and uranium from fixed 1000 ml volume of sea water.

487

ENVIRONMENTAL POLLUTION CONTROL DEVICES BASED ON NOVEL FORMS OF CARBON

Albert Brennsteiner, John W. Zondlo, Alfred H. Stiller
Department of Chemical Engineering, P.O. Box 6102
West Virginia University
Morgantown, WV 26506

Keywords: Electrochemistry, Trace Metals, Remediation.

Introduction

The purpose of this research was to assess the feasibility of using carbon devices for the electrochemical removal of heavy metal contaminants from aqueous streams. The ability of several carbonaceous materials to remove metal ions was evaluated using a porous flow-through electrochemical cell. The resulting effluent was monitored downstream using Anodic Stripping Voltammetry (ASV) to determine the decrease in analyte concentration and hence the electrode efficiency.

A schematic diagram of the apparatus used to carry out these experiments is shown in Figure 1. It is a two-cell system. The upstream working cell removes metal ions from the flowing stream, and the downstream analytical cell is used to measure the metal ion concentration in the resulting effluent.

The upper cell is used to test the various carbonaceous electrode materials for their ability to remove certain heavy metal ions from an aqueous stream. The cylindrical body is made of Lexan™. A solution flow channel is drilled through the Lexan™ body. The carbonaceous working electrode material to be tested is placed in the flow channel.

The analyte solution is pumped into the upper working cell and through the carbonaceous working electrode material. A peristaltic pump is used to control the flow rate for all experiments. For the cathodic removal of metal ions, a potential more negative than the standard reduction potential of the metal ion of interest is applied to the working electrode. This applied potential forces the plating of the metals onto the electrode surface thus removing the contaminants from solution. Various carbonaceous materials were obtained to assess their ability to operate as the cathode material. Reticulated Vitreous Carbon (RVC), a graphite fiber mat, a graphite felt and a proprietary carbon material were analyzed. The surface area of these materials was increased via a proprietary alteration technique. This increased surface area improves the ability of the carbon to remove metal ions from solution. Experimental parameters require optimization to maximize the removal of these metals. These parameters include pH, buffer concentration, solution flow rate, applied potential and carbon bed thickness. Conversion efficiency, long-term stability and loading capacity require appraisal. Finally, the pressure drop through the cell and flow characteristics of the solution flowing through the upper cell also need to be evaluated.

EXPERIMENTAL

The surface areas of the carbonaceous samples have been determined and the data are shown in Table 1. These surface areas were obtained using a Gemini III 2375 Surface Area Analyzer (Micrometrics Instrument Corporation, Nocross, GA). Standard operating procedures were followed as outlined in the operator's manual.

The cylindrical body of the upstream metal removal cell was made of Lexan™ (5.0 cm diameter, 6.0 cm length). The flow channel (1.6 cm i.d.) was drilled through the Lexan™ body. The Ag/AgCl reference electrode (3M NaCl, Model RE-4, BioAnalytical Systems, Inc. (BAS), West Lafayette, IN) was introduced into the flow channel through a Lexan™ sleeve positioned 90 degrees to the flow channel. Leakage was prevented using an o-ring and compression fitting. A piece of coiled platinum wire at the outlet of the cell was used as the auxiliary electrode. Contact to the working electrode was established via a platinum mesh positioned through the cell wall and sealed with an o-ring. The potential of the flow-through cell was controlled using a BAS Model PWR-3 Power Module.

The downstream, thin-layer flow cell (Model LC-44-01000, BAS) was used to measure the metal ion concentration before and after the solution is passed through the metal removal cell. The working electrode was a glassy carbon disk (0.3 cm diameter) over which the solution flowed. Two 50 μm spacers were used to produce the flow channel and direct the solution flow across the carbon disk. Prior to use, the glassy carbon disk was polished using successive slurries of 1.0, 0.3, and 0.05 μm alumina until a mirror-like surface was obtained. The glassy carbon electrode was then thoroughly washed with deionized water. A thin mercury film was plated onto the glassy carbon surface. The metal ions to be analyzed were accumulated into the mercury film. Following accumulation, the metal ions were electrochemically stripped from the mercury film and the measured current used to calculate the metal ion concentration. All potentials were measured relative to the Ag/AgCl reference electrode (BAS). Stripping voltammograms at the thin-layer flow cell were obtained using the

BAS Model CV-27 Voltammograph in conjunction with a Hewlett Packard Model 7044B X-Y recorder.

Stock solutions of metal ions were prepared using AA standard solutions (Fisher Scientific, Fair Lawn, NJ) and deionized water. The deionized water was further purified using a NANOpure™ ultrapure water purification system (Barnstead/Thermolyne, Dubuque, IA). These solutions were stored in Nalgene™ containers to avoid contamination. The 1×10^{-4} M Hg(II) solution for mercury plating was prepared from $Hg(NO_3)_2$ as needed. The mercury ion solution and sample solutions were prepared in 0.1M KNO_3 supporting electrolyte. The pH was adjusted to 3.5 using nitric acid. All chemicals were certified ACS grade purchased from Fisher Scientific unless otherwise noted.

PROCEDURE

The carbon material to be studied was pretreated to oxidize it and assist in the wetting of the carbonaceous surface. This was accomplished by placing the carbon material in a dilute solution (10%) of nitric acid over night in a covered beaker. The material was then thoroughly washed using deionized water. The carbonaceous material was then positioned into the metal removal cell. A threaded plug was used to press the material between a platinum mesh and a piece of filter paper. The pressure on the carbonaceous material can be easily adjusted by turning the threaded plug. This was important because it established contact between the carbon cathode material and the platinum mesh. A 0.1M KNO_3 electrolyte solution was pumped through the cell. In order to remove air bubbles and wet the electrode surface, a mild electrochemical pretreatment was used. The cell potential was held at +1.00 V for 10 minutes followed by -1.00 V for 10 minutes. The performance of the carbonaceous material under study was tested by placing a solution containing a known concentration of metal ion into the sample reservoir. The solution was then allowed to pass through the metal removal cell at a known flow rate and applied potential. The performance was assessed by measuring the metal ion concentration in the effluent and comparing it to the initial ion concentration. The percentage efficiency of the cell is equal to the percentage of metal ions removed from the solution by the electrolytic cell.

A pre-plated mercury film was used for downstream anodic stripping voltammetric (ASV) detection of the metal ion in the effluent stream. A 1×10^{-4} M Hg(II) solution in 0.1M KNO_3 was purged with nitrogen for 20 minutes to remove any oxygen. The mercury film was produced by applying a potential of -1.00 V at the glassy carbon electrode while passing the Hg(II) solution through the cell at 0.87 mL/min for 5 minutes. After this period, the potential was held at +0.05 V for 90 seconds. Following this conditioning, the stopcock was turned to stop the flow of mercuric ions and allow the flow of the deaerated sample solution through the cell. This flow was continued for 3 minutes to flush any mercuric ions from the system and replace all of the solution in the system with the sample to be measured. While the solution was flowing at a known flow rate (0.87 mL/min), the ASV deposition potential was applied to the thin-layer flow cell (usually for 1 minute) and the metal ions accumulated. At this point, the solution flow was stopped and after a 30 second equilibrium period, a potential ramp was initiated (-1.00 V to +0.20 V) and the stripping voltammogram recorded. The scan was terminated at +0.20 V. Solution flow was renewed and the electrode cleaned at +0.50 V for 90 seconds to prepare the system for the next determination. The mercury film was removed at the end of a series of experiments using a moist Kimwipe. The electrode was subsequently polished for the next series of studies.

RESULTS and DISCUSSION

The effectiveness of commercially available Reticulated Vitreous Carbon (RVC) was examined for its performance as the cathode material of the upstream metal removal cell. Minimal removal of ions was observed for the RVC via adsorption (no applied potential). Upon the application of a potential negative enough to reduce the metal ions, removal efficiencies of 10.2% and 50.0% were observed for Pb and Cd, respectively. In order to improve these efficiencies, several parameters must be addressed. By increasing the ratio of cathode surface area to electrolyte solution volume, increasing the time that the solution remains in the electrode material and/or by optimizing the potential applied to the cell, greater efficiencies can be obtained. This work examined the ability to improve removal efficiencies via greatly increasing the surface area either by altering the surface of the cathode material or by utilizing a proprietary high surface area carbonaceous material.

Two samples of the proprietary carbon material were received from an independent laboratory. Of the two, the more conductive and graphitic sample (Sample A) was used for analysis. The surface area of this material was measured to be 115 m^2/g. This surface area is 1000 times greater than that of the RVC. This large surface area should enhance the removal efficiencies of the working cell over those seen using planar cathodes or the RVC. The material was pretreated as described above. The pretreatment improved the wetting ability of the carbon surface and it also increased the measured surface area to 228 m^2/g. Good electrical contact was easily established between the carbonaceous cathode material and the platinum mesh lead. The ability of this material to remove cadmium and lead was addressed.

489

No effect was observed for the removal of the metal ions due to adsorption alone (i.e. no applied potential). Application of a negative potential greatly improved this material's ability to remove the metal ions. Figure 2 shows the effectiveness of this carbon material to remove cadmium and lead. The stripping voltammograms are shown for the metal ion solution (1) prior to being passed through the metal removal cell (FEED), (2) after the solution is passed through the cell with no applied potential (0.00 V) to assess adsorption and (3) after the solution was passed through the cell with an applied potential sufficient to reduce the metal ions at the cathode surface (-1.00 V). Minimal removal was observed due to adsorption. Efficiencies of 91% for cadmium and 95% for lead were obtained for the reductive removal of the metal ions. These large removal efficiencies show great promise for the use of high surface area carbonaceous materials for the cathodic removal of metal ions from aqueous streams.

A graphite fiber mat was assessed for it's ability to remove metal ions. Following the employment of the graphite mat to remove metal ions, the mat's surface was altered in a proprietary manner to increase the surface area. Prior to altering the surface, the mat had a surface area of 0.59 m^2/g. The surface area of the graphite fiber mat following alteration was 99.9 m^2/g. This was 167 times greater than that of the graphite fiber mats alone. The performance of the graphite fiber mats before and after alteration was assessed. The removal via adsorption alone resulted in the minimal removal of metal ions from solution. Upon the application of a sufficiently negative potential, improved removal was obtained. For the unaltered mat, virtually no removal was noted. However, when the altered mat was tested, removal efficiencies of 99%, 91% and 88% were accomplished respectively for Cu, Pb and Cd using an applied potential of -1.00 V. At a potential of -1.20 V, an effluent concentration of zero was measured for each of the metals.

A conductive graphite felt was analyzed in the next study. Both unaltered and altered graphite felt were utilized. Surface area measurements demonstrate the ability to increase the surface area by alteration. Prior to alteration, the surface area of the graphite felt was 0.17 m^2/g. Upon altering the surface, this was increased to 55.41 m^2/g, over a 300-fold increase. The performance of the bare graphite felt was first assessed. Minimal removal was seen due to adsorption. Upon applying a potential of -1.00 V, most of the lead (97%), but only 22% of the cadmium was removed. Solutions treated under the same conditions using the altered graphite felt removed the lead below detectable limits, as well as improved the removal of cadmium (46%). Application of a more negative potential and optimization of experimental parameters can be employed to improve these efficiencies.

To confirm minimal contribution from the platinum mesh, the system was tested in the absence of any carbonaceous cathode material. It was found that the platinum mesh does not contribute significantly (<2%) to the removal of the metal ions from solution.

Continuous removal of lead from an aqueous stream using electroplating on the proprietary carbon material was used to demonstrate the long-term effectiveness of the carbonaceous cathode. The lead solution was passed through the remediation cell and the ions were removed by applying the desired potential. A potential of -1.00 V was applied to remove lead via electroplating. Over a continuous period of 72 hours, a removal efficiency of 89% or greater was achieved for an inlet lead concentration of 100 ppm. Calculation of the lead removed over this period demonstrates a capacity of 0.90 g_{Pb}/g_{carbon}, but it should be stressed that even at 72 hours, the carbon showed no signs of saturation (see Figure 3).

The final desire is the recovery of the metals once they have been removed from the aqueous stream. It is possible to recover the metal ions plated onto the cathode surface simply by reversing the potential. This was demonstrated using a feed solution concentrated 100 ppm in lead ions. The lead ions were removed at a potential of -1.00 V for 3 hours. Subsequent recovery of the lead at a potential of +1.00 V produced an effluent stream more concentrated in lead. This concentration was 331 ppm lead, which demonstrated a 3:1 concentration of the waste stream. For mixed metal streams, individual metal ions can be selectively removed and recovered by these means.

A summary of the removal efficiencies for all of the carbonaceous cathodic materials is given in Table 2. As can be seen, some of these devices are extremely effective for the removal of heavy metal contaminants from aqueous streams.

CONCLUSION

The use of carbonaceous cathodes is an effective means to remove heavy metal contaminants from aqueous streams. By increasing the surface area of existing cathode materials or by using new high surface area materials, improvements in the removal efficiencies are obtained without the vast increase in the electrode volume. By careful selection of the appropriate experimental parameters, the selective removal and recovery of these metal ions is feasible.

PROPERTIES of CARBON MATERIALS

Surface Areas

Material	Surface Area (m²/gram)	
	BET	Langmuir
Proprietary Carbon Cathode		
Sample A	115.13 (227.8)*	186.78
Sample B	182.77 (192.3)*	286.03
Graphite Fiber Mats		
Untreated	0.59	-
Treated	99.92 (112.8)*	-
Graphite Felt		
Untreated	0.17	-
Treated	55.41	-
RVC		
100 ppi	0.092	-
80 ppi	44.80	-

Table 1: Surface Areas of the Various Carbonaceous Cathode Materials.

REMOVAL EFFICIENCIES (%)
[ion concentration, ppb (% removed)]

Metal ion	Feed	Applied Potential	
		0.00 V	-1.00 V
Cd	100	100 (0%)	9 (91%)
Pb	100	100 (0%)	5 (95%)

Figure 2: Metal ion Removal Using the Proprietary Carbon Cathode.
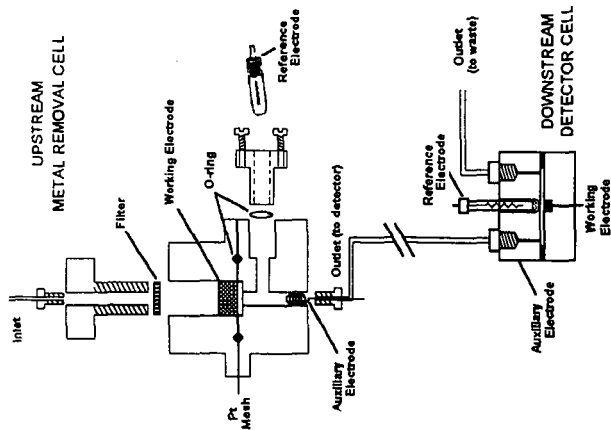
Figure 1: Schematic of Metal Removal Cell and Detector.

TABLE OF REMOVAL EFFICIENCIES

Cathode Material	Cathode Potential, V	Metal Ion Removed Cd	Pb
RVC	0.00	16%	0%
	-1.00	50%	8%
Sample A	0.00	0%	0%
	-1.00	91%	95%
Untreated Graphite Mat	0.00	0%	0%
Treated Graphite Mat	-1.00	5%	17%
	0.00	0%	0%
Untreated Graphite Felt	-1.00	90%	92%
	0.00	13%	7%
Treated Graphite Felt	-1.00	22%	97%
	0.00	0%	0%
Platinum Mesh	-1.00	46%	99%
	0.00	0%	0%
	-1.00	0%	9%

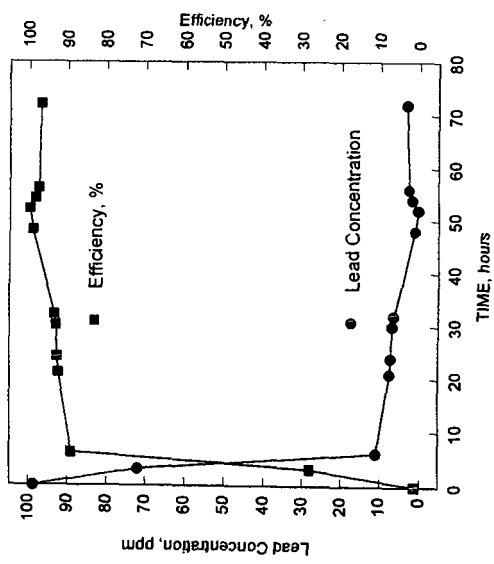**Table 2: Removal Efficiencies of Various Carbon Cathodes.**

Figure 3: Long-term (72 hour) Removal of Lead via Electroplating.

ELIMINATION OF COPPER ION FROM ITS DILUTE AQUEOUS SOLUTION BY VARIOUS CARBON FIBERS UNDER APPLIED CATHODIC POTENTIALS

I.TOMIZUKA, A.MIYAZAKI, M.OKAMOTO AND T.MEGURO*
National Research Institute for metals,
Sengen Tsukuba, Ibaraki, Japan.
*Faculty of Engineering, Yokohama National University
Tokiwadai, Hodogaya, Yokohama, Japan.

SYNOPSIS

A series of carbon fibers were dipped in an acidic aqueous solution containing copper ion. Cathodic potentials were applied to them. Chronological variation of residual concentration was observed. The behavior was discussed based on electrochemical impedance spectrometry. The ultrahigh modulus carbon fiber performed the best under the condition most favorable for it. Poorly crystallized activated carbon fiber was not much behind. A carbon fiber with a high electro–conductivity and covered with prism planes of the graphitic layer over the surface would perform much better, if such a fiber were available.

INTRODUCTION

Elimination of copper ion from acidic waste water is a problem to be solved for manufacturers of print–circuit boards. The ion is eliminated by non–recycling processes or by recycling ones. Non–recycling ones are cheaper but dubious from environmental point of view. The reverse is the case for the recycling ones. This research is intended to develop a new, more economical recycling process on the basis of electrochemical deposition of the metal.

The material for the electrode for this purpose must be electro–conductive, chemically stable and of a large surface area. Carbon fibers are considered to satisfy these requirements to a reasonable extent. In order to specify the most appropriate fiber, we compared performance of a series of carbon fibers and discussed the behavior based on electrochemical impedance spectrometry (EIS).

EXPERIMENTAL

Employed carbon fibers are tabulated in Table 1. They cover fibers of a wide range of crystallinity, starting from a virtually–amorphous fiber from phenol resin, terminating at an ultrahigh modulus fiber (UHMF) from pitch. They include an activated carbon fiber from phenol–resin based carbon fiber (ACF). A wire of fine copper filaments was also used as a reference. This wire comprises 45 filaments of 170micrometers in diameter. Any fiber carries no coating and no sizing except for ACF, whose surface treatment in not disclosed.

Chronological variation of residual concentration of copper ion was observed with use of a cell depicted in Fig.1, together with details of the connecting section from the metallic terminal pipe to carbon fiber. The free length of the fiber was 40mm. Bottom 35mm of the fiber was dipped in a 15ml of 0.5M of sulfuric acid containing 124wppm of copper ion. A potential of –180mV or –100mV was applied to the terminal (as measured against an Ag/AgCl reference electrode. Also –200mV, 0mV and +100mV for ACF). Separate experiments were performed for each intended time of dipping. Neither mechanical stirring nor gas–bubbling was performed, because these actions might cause detachment of once–deposited metallic copper, which was weakly bonded to a fiber. Numbers of monofilament were approximately 3000 – 4500. Exact number varied depending on the specimen, because some fibers were in a form of yarn, and because their exact counting was not practical. Residual concentration was determined by an atomic absorption spectrum.

EIS was observed in an ordinary cell containing 500ml of the solution. The free length of the fiber was 25mm, and its bottom 5mm was dipped in the solution. The number of monofilament was approximately 2100 for ACF and 2000 for UHMF. Impedance was observed at in the frequency range between 100kHz through 100mHz at each increment of 0.2 of its logarithmic value. A bias voltage was selected from –200mV, –180mV, –100mV, 0mV and +100mV, as appropriate. Perturbation voltage was 10mV(0–p value). The impedance was calculated from integrated values of 1000cycles.

RESULTS AND DISCUSSION
Variation of the residual concentration

In the case of ACF, a nominal potential more cathodic than –100mV was required for elimination of copper ion. Variations of residual concentration of the ion at nominal potentials of –100mV and –180mV are illustrated in Fig. 2 for selected fibers. Tentatively the data are cited in as–observed values, not normalized by the surface area or another, because it is not certain what type of normalization makes sense. Amount of deposited metal varied along the fiber axis and/or among filaments. UHMF performed the best (whether normalized or not). But the other fibers, including those not shown here, were not much behind it.

The trends of the variation were almost identical for most of the cases. The variation in the first 12 hours (the initial period) was more or less different from what followed thereafter(the later period). The amount of the variation in the initial period varied considerably with fibers and applied potentials. For poorly–crystallized fibers it was almost always nil or a moderate decrease. For well–crystallized one, it was a drastic decrease at –180mV, while it was almost nil at –100mV. In the later period, logarithm of the residual concentration decreased almost linearly against time for most fibers, especially at –180mV. In the other words, the variations

were reasonably approximated with an equation of the type

$$\log(C) = p \cdot t + \log(q) \qquad (1)$$

C: residual concentration, t: time, p,q: constants.

This means that the rate of the elimination is roughly proportional to the residual concentration. The values of p were not much different among most of the fibers for a given potential. As the pattern of the variation was such that the performance of a fiber was controlled largely by the value of q, especially at −180mV.

A taper−off of the rate of the elimination or even an increase in the residual concentration was observed for certain high−performance fibers in a very later stage of their dipping. A likely cause for it is that some of excessively−grown metallic copper particles detached off the fiber and re−dissolved into the solution. They were found to be bonded to a fiber very weakly.

Electrochemical Impedance Spectrometry (EIS)

Shape of the Cole−Cole plots varied considerably from one fiber to another. Most of them were composed of two arcs, although some appeared to comprise a single arc or three arcs. Three cases of two fibers are discussed in this preprint.

Cole−Cole plots for ACF, one of the most poorly crystallized fibers, are shown in Fig.3. They are typical of two arc plots. They contain a large (apparent) solution resistance and two arcs, respectively of various sizes. The right arc, which is made from impedance seen in the lower frequency side (less than 1Hz) is understood to come solely from reaction(s) across the fiber/solution interface. The left arc, made from impedance in the region larger than 1kHz, is difficult to handle, because a signal of impedance was observed even when EIS was observed in air in this frequency range. It is understood to include impedance with the fiber.

Characteristic values of the right arcs of the plots shown in Fig.3 were evaluated by assuming an equivalent circuit shown in Fig. 4. R_{sol}, C_h & R_h, and C_l & R_l stand for (apparent) solution resistance, characteristic values for the left arc and those for the right one.

Results of the right arcs are shown in Fig. 5 (the values are based on the values of impedance observed at 0.25Hz). The values of charge transfer impedance are low. Both C_l and R_l decreased with time until a considerable amount of solid copper deposited on the fiber in the cases of the copper−containing solution, while only C_l decreased to come in cases of copper−free solution. This implies deposited copper making an active center. The values of R_{sol}, R_h, R_l and their sum (which would be an approximate value of resistance when direct potential is applied) are summarized in Fig. 6. This chart reveals that a significant part of the total resistance goes to R_{sol}. The values of R_{sol} increased with time. Copper ion in solution diminishes R_h even when metallic copper does not deposit.

Fig. 7 illustrates Cole−Cole plots of UHMF, the most crystallized fiber, at a nominal potential of −100mV. Although they appeared to be composed of two arcs, they are of three. This is revealed from the plots of impedance against frequency (not shown). An arc at the high frequency end is too small to be seen in Fig. 7. This fiber shows a very small solution resistance. This chart includes plots for a copper wire observed when it was dipped in the same solution and in the copper−free sulfuric acid of the same molality. Although a chart like Fig. 5 or 6 cannot be prepared since the arcs are not well resolved, two facts are easily noticed. The first is that the initial impedance of UHMF in the copper containing solution is far higher than that of the copper wire. This means that UHMF is initially a semiconductor, if not an insulator. The second is that the shapes of the plots of UHMF approach with time to those of the copper wire in the copper−free solution.

Model of the Behavior of the Two Fibers.

ACF: Smaller value of R_l estimated from EIS for the fiber suggests that a large number of active sites are present over the fiber surface. That is an advantage of poorly crystallized fiber. That will be the reason why poorly−crystallized fibers perform not far behind the well−crystallized fibers. Most of high R_{sol} of poorly crystallized fibers is considered to emanate, not from genuine solution resistance, but from resistance of the carbon fiber, because it is much smaller for UHMF. This means that the potential difference across the fiber/solution interface is considerably lower than the nominal voltage applied by the potentiostat, (especially when current is large i.e. in the initial period), now that cathodic nature wanes along the fiber axis towards the free end of the fiber. This will be the reason why the performance is not so excellent in spite of the large number of active sites over the surface of this fiber. The larger values of R_{sol} result in a lower power efficiency.

UHMF: The initial high impedance across the fiber/solution interface of UHMF suggests that the surface acts initially as a capacitor. The large decrease in residual concentration seen in the initial period for this fiber at −180mV is likely due to enrichment of copper ion in or near the electrochemical double layer. The enrichment will be high, because the potential difference across the fiber/solution interface is large. The large potential difference over the whole interface is enabled by a low electric resistance along the fiber axis, which is evident from the low (apparent) solution resistance. This effect is small at a lower cathodic potential, say at −100mV.

After finishing the initial period, main mechanism of the elimination shifts from a capacitative nature to a depositing nature. Metallic copper will deposit and grow on the active sites, now possibly on the already−deposited copper particles. This will make the mechanism of the elimination more akin to that for the copper wire. This will be the reason why the EIS of UHMF approaches to that of copper wire (in the copper−free solution, because the solution

is diluted with time). The initial high impedance of UHMF suggests also that only a limited number of active sites are present over the surface. This is a disadvantage in terms of electric deposition. This will be the reason why UHNF performs not far ahead of the other fibers in the later period in spite of its high potential difference across the fiber/solution interface.

Conclusions

A pitch-based ultrahigh modulus (and some other high modulus) fiber performed better in the condition most favorable for it. But poorly crystallized (activated or ordinary) fiber performed not too bad. Their mechanisms appear to be based on different advantages. The advantage of the former group is their high electrical conductivity along the fiber axis. This makes whole surface evenly effective. Low electrical conductivity across their surface is advantageous in the initial stage at a deep cathodic potential, but it is rather disadvantageous otherwise, especially when the cathodic potential is shallow. Directions of the high and the low electrical conductivity are mutually replaced for the latter group. The low conductivity along the fiber axis and high conductivity across the surface are their disadvantage and advantage, respectively. It is likely that a carbon fiber with a high electrical conductivity covered by prism layers of graphitic layer over the surface would perform better than those examined in this work, when such a fiber is materialized.

Table 1. Employed carbon fibers.

Code	In Fig.2	Manufacturer	Features
Activated C.F.	ACF	Toyo Boseki	Commercial product.
Ex–Kynol		Home–made	Virtually amorphous.
Ex–Kevlar		Home–made	Poorly crystallized, but oriented.
Ex–lignin	GLY	Nippon Chemicals	Poorly crystallized.
PAN High–strength		Toho–Rayon	Commercial grade.
PAN High–modulus	No.2	Toho–Rayon	Commercial grade.
Ex–Pitch 70ton	UHMF	Petca	Ultrahigh modulus, well–crystallized
Ex–pitch 50ton		Petca	High modulus, next to above.
Copper wire	Wire	-----	Commercial wire with vinyl cover.

a) b)

Glass tube
Copper tube
Copper rod
Epoxy resin
Activated carbon fibre

0.5 MH$_2$SO$_4$
+
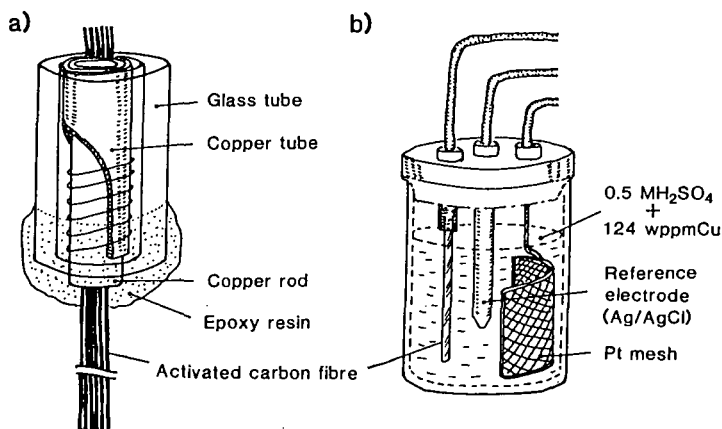124 wppmCu

Reference electrode (Ag/AgCl)

Pt mesh

Fig. 1 Schematic illustration of the cell used for observation of residual concentration of copper ion.
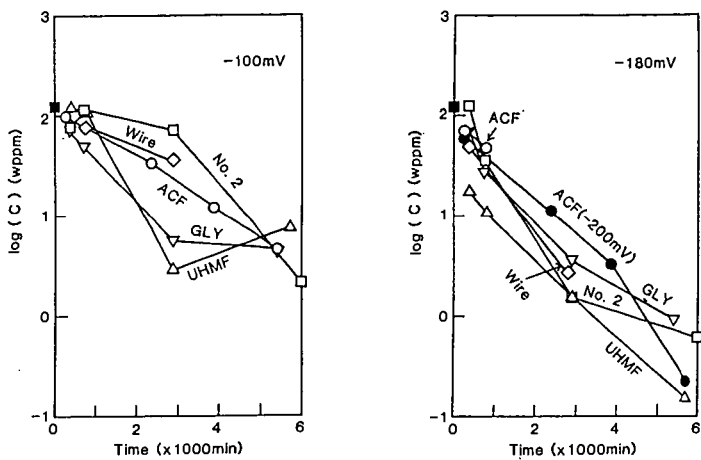
Fig. 2 Chronological variations of residual concentration of copper ion for ACF.
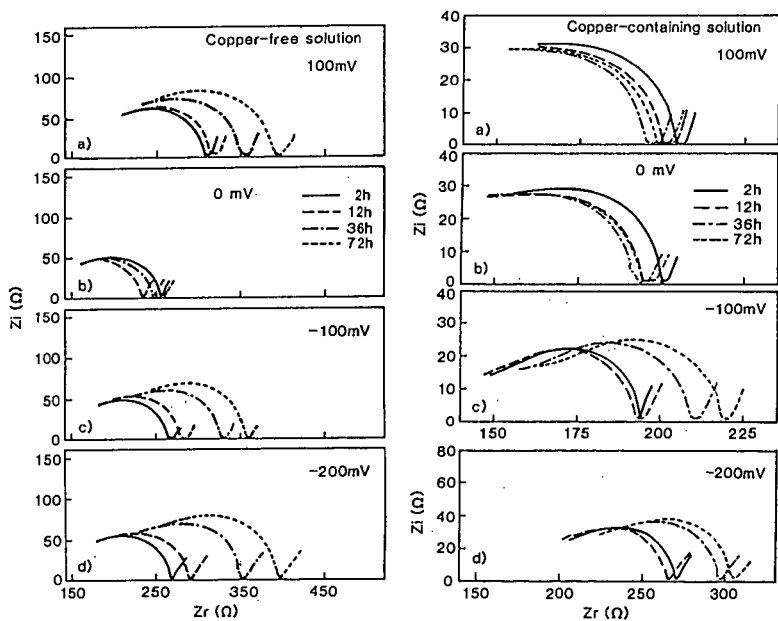

Fig. 3 EIS for ACF

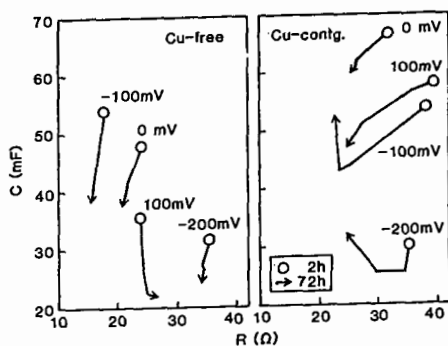Fig. 4 Equivalent circuit used for
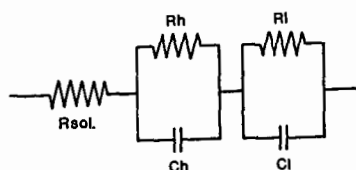analysis of EIS of ACF

Fig. 5 Values of C_1 and R_1 for the right arcs shown in Fig. 3.
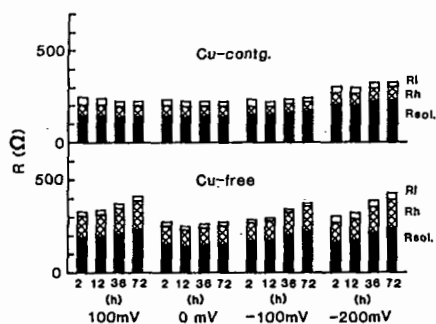

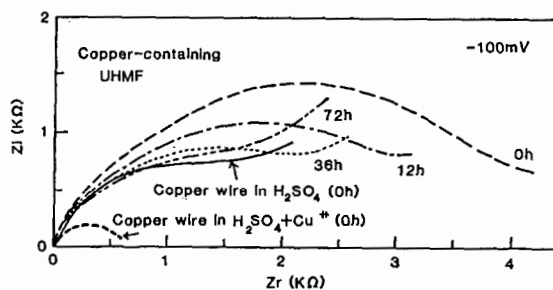Fig. 6 Estimated contents of resistances under direct current for ACF

Fig. 7 Cole-Cole plots of UHMF together with those of copper wire.

CARBON BLACK AND CARBON BLACK-CONDUCTING POLYMER COMPOSITES FOR ENVIRONMENTAL APPLICATIONS

Krishnan Rajeshwar
Department of Chemistry and Biochemistry
The University of Texas at Arlington
Arlington, Texas 76019-0065

Wesley A. Wampler, Scott Goeringer and Michel Gerspacher
Sid Richardson Carbon Co.
Fort Worth Research Center
Fort Worth, Texas 76106

INTRODUCTION

A large fraction of the carbon black commercially produced in the U. S. and other parts of the world goes into the automobile tire industry and other rubber applications. However, specialty applications of this material are expected to grow in the future. The present study explores the applicability of composites of carbon black and an electronically conductive polymer, polypyrrole, in environmental pollution abatement scenarios.

Chromium was used as a model environmental pollutant for demonstration of our approach. Chromium occurs in two common oxidation states in nature, Cr(III) and Cr(VI). Because it is only weakly sorbed onto inorganic surfaces, Cr(VI) is notoriously mobile in nature. On the other hand, Cr(III) is readily precipitated or sorbed on a variety of inorganic and organic surfaces at near neutral pH. The properties of Cr(III) and Cr(VI) have been reviewed with respect to acute and chronic toxicity, dermal toxicity, systemic toxicity, toxicokinetics, cytotoxicity, genotoxicity and carcinogenicity [1]. The hexavalent chromium compounds appear to be 10-100 times more toxic than their Cr(III) counterparts when both are administered by the oral route. The toxicology of chromium does not reside with the elemental form but varies greatly among a wide variety of many different chromium compounds. Oxidation state and solubility appear to be crucial factors in the regard [1]. Other aspects of chromium toxicity and carcinogenesis have been reviewed [2].

Reduction of Cr(VI) to Cr(III) followed by a pH adjustment to form the highly insoluble $Cr(OH)_3$ species would clearly be an effective means to counter the harmful effects of this element on the environment. It is worth noting that a wide variety of anthropogenic sources generate Cr(VI) in effluent streams: Chrome plating, electronic, metallurgical, timber, and leather tanning industries to name a few. Chemicals such as SO_2, $FeSO_4$ or sodium metabisulfite are currently used for Cr(VI) reduction. However, these chemicals are consumed in the process which also generates sludge and consequent solid waste handling problems.

We demonstrate herein a new electrochemical strategy for the environmental remediation of Cr(VI) that is based on *spontaneous* electron transfer to Cr(VI) from a pre-reduced conducting polymer (polypyrrole)-carbon black composite thus reducing Cr(VI) to the trivalent form. In doing so, the composite itself is oxidized, and can be *electrochemically recycled* back to the reduced state for a fresh treatment cycle. The present work builds upon an earlier effort [3] in these laboratories that utilized polypyrrole as the active material.

EXPERIMENTAL

The carbon black-polypyrrole composites and the parent conducting polymer were chemically synthesized. Polypyrrole was chemically synthesized from an aqueous 0.1 M pyrrole solution using potassium persulfate as the oxidant. Further details of the preparation procedure and characterization are contained elsewhere [4].

The polypyrrole-carbon black composite was prepared in a similar manner except that the polymerization medium contained in addition, the requisite amount of the N135 black [4]. Nominally, a composite containing ~43% (by wt.) of carbon black was utilized. In other experiments, the relative amount of polypyrrole and carbon black in the composite was varied by correspondingly varying the carbon black content of the polymerization medium [3]. For preparation of PVC-polypyrrole and PVC-carbon black composite, appropriate quantities of the two components were thoroughly mixed together (in a mortar and pestle) to afford ~43 wt.% of the active material (polypyrrole or carbon black). A similar procedure was also adopted in one instance for preparation of the polypyrrole-carbon black composite.

In all the experiments for this pilot study, pelletized rectangular-shaped samples were used. The pellet dimensions were chosen to fit inside a 1 cm path length quartz optical cuvette. The Cr(VI) solution comprised 1 mM of $K_2Cr_2O_7$ in 0.1 M H_2SO_4 yielding an initial concentration of Cr(VI) of 104 ppm. In a typical experiment, 2 mL of this solution were pipetted into the cuvette. Chromium (VI) has an optical absorption band at 350 nm that can be used to monitor its concentration. The optical absorbance of the solution in contact with the pelletized active material, was monitored at requisite time intervals after initial contact. All tests were performed at the laboratory ambient temperature.

The efficacy of the polypyrrole-carbon black composite for Cr(VI) reduction was compared against three reference samples: polypyrrole, and composites of polypyrrole or carbon black with an *inert* matrix polymer, namely polyvinylchloride (PVC). The carbon black used in this study (N135) was made by a furnace process.

RESULTS AND DISCUSSION

In a related study [3] we showed that spontaneous electron transfer occurs from an electrochemically pre-reduced polypyrrole sample to Cr(VI) consistent with a reaction scheme as follows:

$$Cr_2O_7^{2-} + 6\,PPy^0 + 14\,H^+ \rightarrow 2\,Cr^{3+} + 6\,PPy^+ + 7\,H_2O \qquad (1)$$
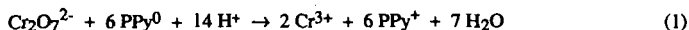
In the above equation, PPy denotes polypyrrole and the superscripts "0 " and "+" correspond to the reduced and oxidized states of the redox polymer respectively. Taking values for the standard reduction potential of –0.20V and +1.16V [3] respectively for the two redox couples in the above scheme, namely $PPy^{+/0}$ and $Cr^{6+/3+}$, the process represented by Reaction 1 has a standard free energy change of - 787 kJ/mol. One potential advantage of this approach (over currently-used chemical treatment schemes) is that the active material, polypyrrole, can be repeatedly shuttled back and forth between its two redox states (Figure 1). On the other hand, for a heterogeneous process (such as ours), very high surface dispersion of the active material obviously is desirable, and carbon black can serve this function as a "surface modifier" component. Figure 2 contains data showing the ability of chemically synthesized polypyrrole to reduce Cr(VI). Half of the original Cr(VI) is reduced after ~ 35 min. in contact with polypyrrole as illustrated in Figure 2b. We presume (as verified by atomic absorption spectroscopy experiments in the previous case, Ref. 3) that most of the chromium resides in the solution phase as Cr(III). The solid line in Figure 2b is an exponential decay model fit to the data, consistent with first-order kinetics (see below).

Carbon black by itself can be compacted into a pellet; however it is much too fragile for routine handling and use in this form. Thus, PVC was chosen as an inert polymeric "binder." A pelletized sample of PVC alone gives no reduction of Cr(VI) during a 60 min. exposure. Next, a 40% (w/w) carbon black in PVC was prepared as described in the Experimental Section. The sample was first electrochemically pre-reduced (at –0.9 V, all potentials herein quoted with respect to Ag/AgCl reference) in 0.1 M H_2SO_4 prior to contact with the Cr(VI) solution; Figure 3 contains the results from this experiment. The lower Cr(VI) reduction rate in this case (relative to Figure 2) could be either a manifestation of the lower surface coverage of the active (carbon black) material, or an intrinsic difference between polypyrrole and carbon black. Nonetheless, the high activity of carbon black toward Cr(VI) was a bonus in terms of our new approach (see below). Again, the solid line in Figure 3b is an exponential decay model fit to the data.

Figure 4a contains data from an experiment wherein the potential of a carbon black-PVC composite electrode was continuously monitored during contact with Cr(VI). As before, the electrode was pre-reduced at –0.9V. On opening the circuit in 0.1 M H_2SO_4, the electrode potential gradually relaxes to the "rest" value. When the solution is subsequently dosed with Cr(VI), the potential undergoes a sharp excursion in the positive direction prior to attainment of a plateau. This excursion is symptomatic of the oxidation of the electrode surface by Cr(VI).

In order to examine whether the oxidation resulted in introducing oxygen functionalities at the carbon black surface, XPS spectra of the carbon black samples were compared before and after Cr(VI). No change in the C1s binding energy was noted. The lack of adsorption of chromium onto carbon black was also signaled by the absence of the chromium peaks at 44 eV (3 p), 576 eV (2 p3/2) and 586 eV (2 p1/2) in the XPS data. Similarly, experiments on samples before and after Cr(VI) contact show no significant change in Lc and La from the initial values of 11.10 Å and 23.50 Å, indicating that the material removal (by oxidation) occurs without alteration of the carbon black crystallite size within the matrix.

The driving force for electron transfer from carbon black to Cr(VI) can be tuned by controlling the potential of the former. This is shown in Figure 4b wherein three types of samples, namely a "neutral" (electrochemically untreated) specimen, a sample pre-oxidized at +0.9 V and one pre-reduced at –0.9 V, are compared in terms of their relative efficacy for Cr(VI) reduction. Electrochemical reduction raises the electron energy levels in the carbon black whilst the corresponding electronic states in the untreated and oxidized samples lie at lower energy levels. Stated in alternative terms, the reduction capacity of carbon black can be electrochemically tuned.

The PVC-carbon black composite exhibits classical electronic percolation behavior [21]. That is, there is a critical carbon black concentration in the matrix at which particle connectivity is established. Beyond this threshold (which occurs at ~ 20% (w/w) of the black), rapid increase in the electronic conductivity occurs with further carbon black loading, quickly obtaining a plateau [4]. Figure 5 contains Cr(VI) conversion data for four different PVC-carbon black samples. Samples containing carbon black at levels below the percolation threshold exhibit negligible activity toward Cr(VI). Interestingly, there is an abrupt increase in the activity at the threshold beyond which only a modest increment occurs for the 40% (w/w) black PVC-carbon black sample.

Figure 6 contains a comparison of the relative efficacy of polypyrrole and carbon black for Cr(VI) reduction. These data were generated on three types of samples: a polypyrrole-carbon black composite, a reduced PVC-carbon black composite and a polypyrrole-PVC composite. The polypyrrole-carbon black composite contained ~ 43% (w/w) of carbon black. To facilitate the

comparison, all these samples were "diluted" to the same extent with the PVC binder to afford 40% (w/w) of the active material. That is, the polypyrrole-carbon black composite in this particular experiment had a composition of 22.8% (w/w) polypyrrole, 17.2% (w/w) carbon black and 60% PVC in the final pelletized sample.

Interestingly, the composite containing *both* polypyrrole and carbon black as the active material exhibits the highest activity for Cr(VI) reduction. Further, carbon black (at least the grade used in this study) outperforms polypyrrole in its ability to reduce Cr(VI). The conversion data in Figure 7 can be fitted to a pseudo first-order kinetics scheme.

The influence of carbon black level in the polypyrrole-carbon black composite on the ability of the latter to reduce Cr(VI) was also considered. Contrary to the experiments considered earlier in Figure 6, the composite samples in this case were prepared *without* the PVC binder. A systematic improvement in the composite performance is noted with an increase in the carbon black content although the rate of improvement tends to saturate at the higher loadings.

SUMMARY

This study has shown that the composites outperform both polypyrrole and carbon black in terms of their ability to reduce Cr(VI). It is worth nothing that in the composite, both redox (polypyrrole) and oxidizable (carbon black) functions are built into the material framework. The former is reversible and the latter is irreversible. This is fortuitous in an economic sense in that carbon black is the less expensive of the two components, and can be periodically replenished. The stability of polypyrrole in repeat use cycles was also briefly explored in this study. No appreciable and systematic loss of conversion efficiency was noted over three Cr(VI) conversion cycles as long *as the electrochemical regeneration (reduction) step was essentially complete.* This latter process is a function of the polypyrrole morphology and the reduction potential used, and could encompass a time period anywhere from a few seconds to a few minutes. In our hands, a regeneration potential of –0.9 V in 0.1 M H_2SO_4 and a reduction time of 30 minutes were effective in restoring the activity of the sample.

We have used compacted samples for the active material in this study, merely for experimental convenience. A practical Cr(VI) treatment system can be envisioned to consist of a *packed bed* through which the effluent stream could be recirculated. This bed would comprise fine (μm size) particles of the polypyrrole-carbon black composite. Electrical contacts could be introduced via procedures routinely adopted for packed-bed electrochemical flow reactors (c.f. Ref. 5). Ideally, the charge-transfer kinetics at the active material/solution interface must be fast enough such that the system is under mass-transport control. Further efforts will focus on optimizing the Cr(VI) conversion kinetics at the polypyrrole-carbon black particle/solution interface. The fact that the reaction half-life is independent of the initial Cr(VI) concentration is encouraging in this regard.

A practical system would also require a pH adjustment step to immobilize the reduced Cr(III) onto the sample bed. The immobilized Cr(OH)$_3$ could be reoxidized and released in a subsequent back-flushing cycle so that the Cr(VI) treatment system also regenerates Cr(VI) for fresh reuse. Further development of our Cr(VI) pollution abatement approach and the implementation of a practical system along the lines outlined in the previous paragraphs, are continuing in these laboratories.

REFERENCES

1. S. A. Katz and H. Salem, *J. Appl. Toxicol.* **13**, 217 (1993).
2. J. A. Alcedo and K. E. Wetterhann, *Int. Rev. Exptl. Path.* **31**, 85 (1990).
3. C. Wei, S. German, S. Basak, and K. Rajeshwar, *J. Electrochem Soc.* **140**, L60 (1993).
4. W. A. Wampler, K. Rajeshwar, R. G. Pethe, R. C. Hyer, and S. C. Sharma, *J. Mater. Res.* **10**, 1811 (1995).
5. K. Rajeshwar, *J. Appl. Electrochem.* **24**, 1077 (1994).
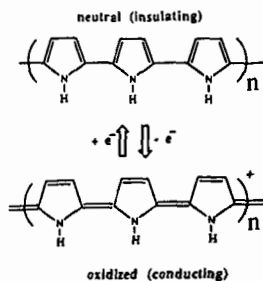
ACKNOWLEDGMENTS

Figure 1.   Neutral and oxidized redox states of polypyrrole and their inter-convertible nature.
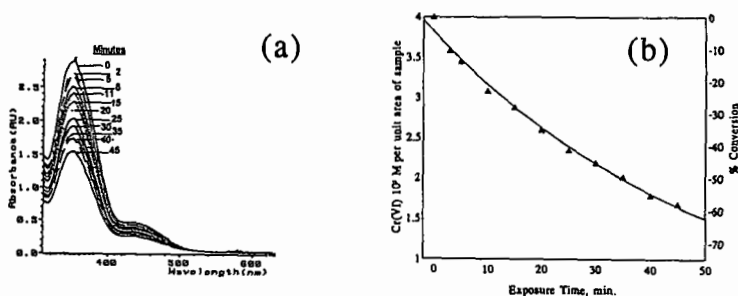

Figure 2.

Data illustrating the ability of chemically synthesized polypyrrole to reduce Cr(VI).
UV-VIS spectra are shown in Figure 2a, and the Cr(VI) conversion vs. time computed
from these spectral data are contained in Figure 2b. The numbers on the spectra in
Figure 2a show the contact time with Cr(VI). The initial Cr(VI) solution composition is
specified in the Experimental Section. The solid line in Figure 2b is a least-squares fit
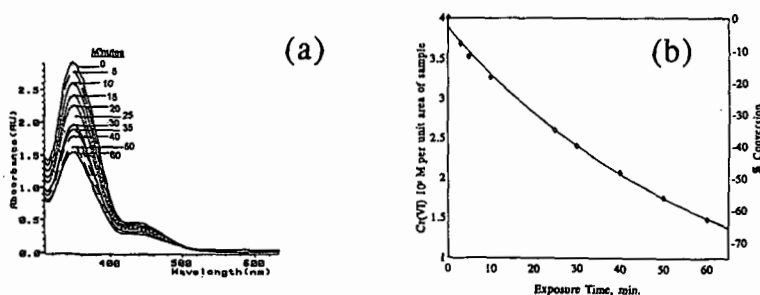of the data (see text).

Figure 3.

Data illustrating the ability of carbon black to reduce Cr(VI). UV-VIS spectra are
shown in Figure 3a, and the Cr(VI) conversion vs. time computed from these spectral
data are contained in Figure 3b. The spectral notation in Figure 3a as in Figure 2a. The
carbon black was dispersed in PVC to yield a composite containing 40% (w/w) of the
black. The sample was first reduced at -0.9 V in 0.1 M H_2SO_4 prior to Cr(VI) contact.
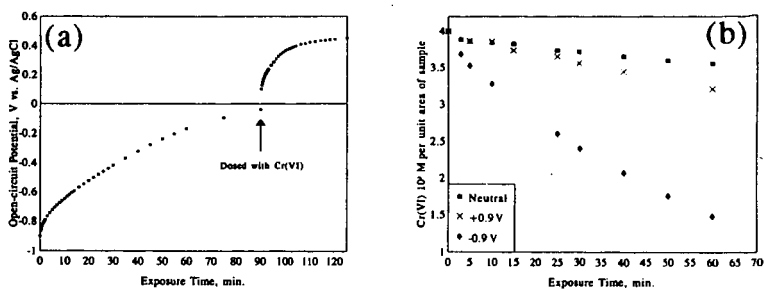
Figure 4.   (a) Variation of the open-circuit potential of a PVC-carbon black composite electrode (30% w/w of carbon black) before and after contact with the Cr(VI) solution. The electrode was pre-reduced at -0.9V in 0.1 M H_2SO_4 prior to opening the circuit and monitoring the potential. (b) Effect of electrochemical pre-treatment (in 0.1 M H_2SO_4) on the ability of a PVC-carbon black composite (30% w/w of carbon black) to reduce Cr(VI).
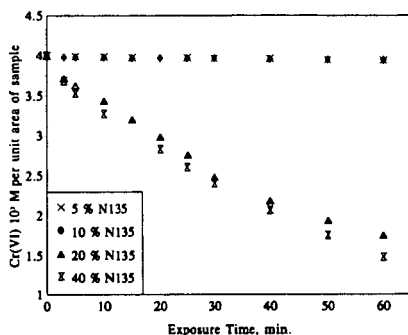

Figure 5.   Influence of carbon black level (in the PVC-carbon black composite) on the Cr(VI) reduction ability of the composite. The percolation threshold in the composite occurs at ~20% (w/w) of the black (refer to text).
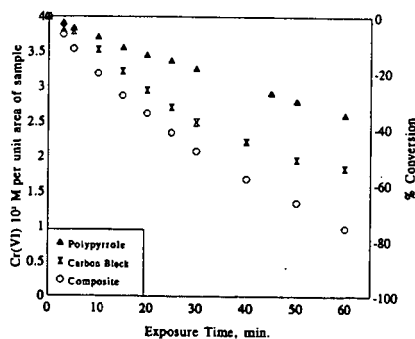

Figure 6.   Comparison of the relative efficacy of polypyrrole, carbon black and the polypyrrole-carbon black composite for Cr(VI) remediation. The composite contained ~43% (w/w) of the black. In all the three cases, the active material was diluted to 40% by mixing with the inert PVC (refer to text).

DESULFURIZATION STUDY OF HYDROCARBON MOLECULES
BY PLASMA PROCESS FOR GASOIL APPLICATIONS

Mohammedi. M.N. , Leuenberger. J.L. & Amouroux. J.,
Université Pierre et Marie Curie, Laboratoire de Génie des Procédés Plasmas
11, rue Pierre et Marie Curie
75231 Paris Cedex 05, France.

ABSTRACT

During these last years, many investigations have been made on sulphur elimination processes from hydrocarbon feedstocks because of environmental regulations which are more and more strict. This is a study on a plasma process dedicated to heavy hydrocarbon hydrotreatment and hazardous substances removing such as sulphur compounds. It is a co-processing of a fluidized spouted bed and an inductively coupled plasma working at atmospheric pressure. A high flow of hydrogen radicals is generated and a rapid quench of the plasma leads to an increase of hydrogen radical lifetime and promotes chemical reactions of desulfurization at low temperature (700-900 K).
The primary objective of this work is to understand the cleavage of C-S bond under these plasma conditions. To this end, thermodynamic calculations are done and preliminary experiments are carried out with different mixtures where n-hexadecane is chosen as the model molecule in hydrocarbon hydrocracking, and sulphur compounds are added in small amounts (0-1 % S wt). Compounds such as dimethyl sulphide, 2-butanethiol, benzothiophene and thiophene are currently studied. The influence of $CH_3°$, $H°$, $HS°$ and $PhS°$ ($C_6H_5S°$) is also considered.

INTRODUCTION

The development of upgrading processes in order to convert heavy feeds to lower boiling products, have to take into account the presence of components which make processing difficult, such as sulphur compounds. Besides, one of the operational problems of upgrading heavy feeds is the formation of undesirable high amounts of coke, which represent losses in hydrocarbonaceous materials and also need a costly separation step [1].
The development of such processes requires improvement of certain properties, especially H/C ratio. This is equivalent to adding hydrogen or rejecting carbon. For this reason, considerable attention is given to hydrogen addition technologies (hydrocraking) as opposed to carbon rejection technologies (thermal processes).
It has been revealed that hydrogen plays an important role in the activation and control of conversion of heavy feeds into marketable products [2,3]. However, high conversion of heavy feeds into distillate products require an efficient hydrogen activation, which can be promoted by adding a suitable catalysts. Nowadays many new and hydrotreatment catalysts are entering the market and their evaluation in terms of activity and stability is the subject of many recent works [4]. However, their use presents also inconvenients which are mainly reliable to deactivation phenomenon - due to the coke deposition and sintering of the active sites [5,6] - and also to the high cost of the active metal species.
Our approach in this paper is to present briefly a new upgrading thermal inductively coupled plasma process working under atmospheric pressure and dedicated to heavy hydrocarbon hydrocracking. The plasma produces a high flow of hydrogen radicals and a spouted bed is used for the plasma quenching in order to avoid coke formation. The coupling of the plasma and the spouted bed provides a non equilibrium system where hydrogen radicals amounts are 1000 times greater than those in an equilibrium system [7]. The use of such a process seems to be suitable since the high temperature and the high flow of radicals provide high efficiency of molecule decomposition such as sulphur compounds. In fact, plasma may operate by providing a source of hydrogen radicals through the dissociation of molecular hydrogen and then these radicals can promote the bond cleavage reactions.
Since many years, investigations have been made on sulphur compound addition effects on various hydrocarbons such as methane [8], propane [9], heptane, n-nonane [10], and in petroleum fractions such as naphtha [11]. Sulphur compounds, like thiophenics have long been known to be fairly stable thermally and relatively unreactive. At this end, the behaviours of compounds such as thiophene, in n-hexadecane is investigated in this paper. The studies are also directed towards extending these experiments to industrial feed stocks like gas oil. The analytical results are obtained by off-line gas chromatography.
Moreover, the reactor parameters have to be taken into account, so as to point out the properties of the plasma phase (H° and CH$_3$° radicals) and those of the solid phase (Al$_2$O$_3$, CaO, CaCO$_3$).
In the same aim, a preliminary and predictive study had been realized on C-H-S-O system, and thermodynamic calculations permitted to determine the gas phase evolution: the stable species versus the temperature, the pressure and the initial composition of the gas mixture, and then optimal reactor parameters.

PREDICTIVE CALCULATIONS

Thermodynamic evolution of the gas phase. Thermodynamic calculations for C-H-S-O system give information about stable species in function of temperature, pressure and initial composition of the gas mixture. Moreover, these calculations lead to the prediction of optimal reactor parameters towards the distribution of molecules in the gas phase at the equilibrium state.
The principle of calculations is based on the Gibbs free energy minimization of the studied mixture using a second order Taylor method [12].

The calculation parameters are:
— thermodynamic parameters: pressure, temperature and free enthalpy versus temperature,
— different species considered at the equilibrium (molecules, atoms, ions, radicals),
— initial composition of the chemical mixture. Thermochemical data are taken from Janaf tables [13].

The computational program can only consider homogeneous phase cases. So, phenomena involved in solid phase interaction could not be taken into account. Besides, this method does not predict the kinetic evolution of the physicochemical system.

In order to study the desulfurization of sulphur containing hydrocarbons, a first simulation was made, it is intended to represent the decomposition of an average petroleum section $(C/H/O/S = 1/1.4383.10^{-3}/3.10^{-3}/1.7.10^{-2})$ [14]. This result shows the important role of temperature and initial composition in C-S bond cleavage.

The major products obtained (fig.1) are light hydrocarbons (CH_4, C_2H_2..), aromatic hydrocarbons (C_6H_6), and sulphide molecules such as H_2S and CS_2. We observed that the effect of hydrogen addition (fig.2) is to eliminate progressively sulphur from hydrocarbon chains by formation of hydrogen sulphide which can easily be trapped by inert solids. The decomposition of sulphide hydrocarbons must be carried out at temperatures under 2000 K, because of the growth of their stability with temperature elevation. Besides, the increase of oxygen amount in those systems leads to the apparition of toxic molecules such as SO_2, CSO and CO (fig.3).

Thermodynamic study of the heterogeneous phase. One of the main objectives of this study in using a solid phase in the plasma post-discharge is to keep toxic molecules level in gas effluents under the ppm value. The toxic elements such as H_2S can be eliminated from the gas phase by trapping on solid particles and producing an inert solid [15]. The possibility of using alkaline earth oxides in such heterogeneous systems was demonstrated by means of free energy diagram of sulphur compounds (fig.4). This diagram represents the thermodynamical stability of solids versus temperature and it suggests that using a spouted bed of alkaline earth oxide, like calcium oxide, seems to be suitable for trapping toxic sulphur containing gas by calcium sulphide formation. These can be possible at temperature up to 1170 K where calcium dioxide is able to react with toxic gases.

EXPERIMENTS AND RESULTS

Experimental equipment. The reactor (fig. 5) is composed of a double-flow inductively coupled plasma torch made of quartz and working with an argon-hydrogen mixture. The inductor is made of four water cooled copper coils. The double flow torch, supplied with up to 20% hydrogen in argon, is injected laterally in a two dimension spouted bed reactor. The inductively coupled plasma (5.4 MHz, 18 kW) is characterized by a global efficiency of 50%. The bed is a parallelepipedical refractory reactor with a regime of a jet spouted bed [16], where particles - Al_2O_3, $CaCO_3$ or CaO, (250-350 μm) - are fluidized by argon or hydrogen. The formed particle fountain divided the bed in two parts :
— the region in front of the plasma with temperatures in the range of 2500-1800 K,
— and the region behind the fountain with temperatures in the range of 700-1100 K.
The hydrocarbon feedstocks are injected in the latter region.

Hydrocracking experiments. The decomposition of n-hexadecane was investigated in the presence and absence of sulphur compounds which are introduced into the reaction system together with the feed. The purpose of this work is to study the influence of dimethyl sulphide, 2-butanethiol and methyl-phenyl sulphide on the conversion rate of n-hexadecane and on yields of products. Hydrogen sulphide produced is measured for each experiment by way of tube gas (Prolabo). The bed particles used are alumina particles (350 μm). All sulphur compounds are added in the mixture at the same content: 1 % wt of sulphur, in order to achieve comparable experiments. The hydrocarbon composition of gaseous and liquid product mixtures was determined by gas chromatography.

The qualitative and quantitative composition of the sulphur products are still not possible at this time for analytical problems, nevertheless their effects on n-hexadecane decomposition are observed.

Gaseous products are analysed by gas chromatography (Girdel 30, flame ionization) with ST104 column, and liquid ones by Shimadzu GC-9A chromatographe (flame ionization) with an SE 30 non polar column. Carbon black quantification is done thanks to reflectance measurements on normalized filters.

Mass balance and conversion rate. The mass balance is realized for gases and liquids. Analysis lead to mass balance in term of conversion as follows:
Conversion C (% mass) = mass flow n-C_{16} initial/mass flow n-C_{16} after reaction
Two samples are taken on the effluent gas: one in a glass gas sampling bulb (for gases C_1-C_4) and an other one in a liquid nitrogen trap (for liquid compounds C_5-C_{16}) (fig.5).

Experimental conditions. Pressure: 1 atm, power : 4.16 kW, plasmagen gases: argon and hydrogen : 27l/min and 3l/min respectively, fluidization gas: argon: 42.9 l/min, total hydrocarbon flow: 0.4 kg/h, particles used: alumina 350 μm.

Hydrocracking of n-hexadecane. Previous works on n-hexadecane hydropyrolysis in plasma spouted bed reactor at atmospheric pressure and realized in the laboratory are summarized in the following conclusions:

— linear light α—olefins are principally obtained where ethylene and propylene are the major products,
— the carbon black formation can be neglected,

504

— the residence time is very short about 0.3 seconds,
— n-hexadecane conversion rate increases while hydrogen flow increases,
— hydrogen radicals produced by the plasma and quenched by the fluidized bed are involved in radical reaction processes, especially in initiation ones.

Under these conditions, at 973 K, with a residence time of 0.3 second, the cracking yield obtained is 37.4 % (wt). The major products are ethylene (33.45 %), propylene (11.81 %) and CH_4 (6.8 %). Olefins represents about 90 % (wt) of the cracking products, and the coke less than 0.5 % (wt).

Effects of sulphur compounds on n-hexadecane hydrocracking. The addition of sulphur compounds leads to an increase of gas and n-hexadecane conversion rate (table 1). Experimental conditions are on the whole similar, except for the fourth experiment (Me-Ph-sulphide) where the temperature is higher and the process is more a thermal one, but on the whole the conversion rate increase by 8 % for thiophene addition, 18 % for dimethyl sulphide and 2-butanethiol. The hydrocarbon product (without sulphurs) distribution is not really affected in these operating conditions in terms of quality, nevertheless, an increase of olefins of 2 % is observed (fig.6). Besides, C_2H_4 and C_2H_2 decrease while an increase of C_4H_6 can be noted.

Hydrogen sulphide amount for thiophene mixture is the lowest one (5 ppm) because this compound is thermally stable and relatively unreactive. These properties have been attributed to its conjugated structure which allows the free electron to be largely delocalized. The highest value is for 2-butanethiol mixture (140 ppm), and for sulphides : dimethylsulphide and methyl-phenyl sulphide, hydrogen sulphide emission is at about the same.

These results suggest that under plasma conditions, the cleavage of hydrocarbons is intimately related to the appearence of highly reactive light radicals such as $CH_3°$, $H°$, $HS°$ and $PhS°$ and which influence the course of radical reactions and the rate of hydrogen transfer is one of the main factors to be considered in mechanism understanding. Thus, the fact that thiols have the ability of accelerating H-transfer reaction by a factor of 200 [17] might be explain at least in part the increase of n-hexadecane conversion for 2-butanethiol mixture.

Cracking of gas oil feedstock. The behaviour of a classical industrial feedstock (<150-$450°C>$; $S = 1.5$ % wt) has been studied in the plasma spouted bed reactor. This oil product was characterized before and after the treatment (fig. 7).

The effect of this treatment is to reduce heavy hydrocarbons ($>300°C$) from 60 to 18 %, while conserving the middle product (<150-$300°C>$) up to 40 %.

Sulphur compounds of the considered petroleum fraction have also been analyzed before and after plasma treatment [18] on SPB sulfur column (Supelco) with chemiluminescence detector. The preliminary observations were the followings:
— presence of sulphur compounds in the gas-oil : aliphatics and cyclics,
— hydrogen sulphur emission during plasma treatment, testifying to C-S bond cleavage,
— reduction of mercaptans and sulphides amounts,
— dealkylation of substituted benzothiophene,
— thiophene production after treatment which is testimony to ring opening.

Alkylated sulphur compounds in gasoline feedstock are sources of $CH_3°$ radicals which have an effective influence on reactions occurring during hydrocarbon plasma pyrolysis. This is validated by the increasing of the conversion rate in case of aliphatic hydrocarbons such as n-hexadecane.

CONCLUSION

Sulphur compounds under plasma conditions, introduced into the reaction system together with the feed, catalyses the rate of n-hexadecane decomposition and influence the selectivity especially in terms of coke precursors during hydropyrolysis. Compared to the pure n-hexadecane, the decomposition rate increases by 8 to 18% depending on the nature of added sulphur compounds which are effective H-transfer catalysts and improve the yield of α-olefins. The decomposition increase as the amount of thiyl radicals is increased. In case of gas oil feedstock, a dealkylation of substituted sulphur compounds and ring opening in aromatic ones are observed

ACKNOWLEDGEMENTS

REFERENCES

1. Del Bianco. A., Panariti. N., Di Carlo. S. , Elmouchnino. J., Fixari. B. and Le Perchec.P., Applied Catalysis A: General, 94 (1993) 1-16.
2. Beret. S and Reynolds. J.G, Am.Chem.Soc., Prep., Div. Petrol. Chem., 30 (4), 664, (1985).
3. Bunger. J.W., Am.Chem.Soc., Prep., Div. Petrol. Chem., 30 (4), 658, (1985) .
4. Panarello. F. and Guanziroli. S., Intern. Symp. on Deactivation and Testing of Hydrocarbon Catalysts, 210th National Meeting, Am. Chem. Soc., Chicago, IL, August 20-25, 542-546, (1995).
5. Masaomi Amemiya and Kyuji Yano, Intern. Symp. on Deactivation and Testing of Hydrocarbon Catalysts, 210th National Meeting, Am. Chem. Soc., Chicago, IL, August 20-25, 636-639, (1995).
6. Ushio. M., Waku. T., Akiyama. M., Okamoto. Y., and Inoue. A., Intern. Symp. on Deactivation and Testing of Hydrocarbon Catalysts, 210th National Meeting, Am. Chem. Soc., Chicago, IL, August 20-25, 537-541, (1995).

7. Leuenberger. J.L., Mohammedi. M.N., Al Ayoubi. S., Francke. E., and Amouroux. J., 3rd European Congress on Thermal Plasma Processes, Aachen, Germany, September 19-21, (1994).
8. Szymansky. A. and Podgorsky. A., Z.phys.Chemie, Lieipzig 256,4,S.765-769, (1975).
9. Trimm . D.L. and Turner. C.J., J.Chem.Tech.Biotech. 31, 285-289, (1981).
10. Depeyre. D.,.Flicoteaux. C., Ind. Eng.Chem.Process.Des.Dev. 24, 920-924, (1985).
11. Sahu .D. and Kunzru. D. , Can.J.Chem.Eng. vol 66, Oct 1988.
12. Amouroux. J., Rapakoulias. D., Ann.Chim, vol 1, 227, (1976).
13. Janaf Thermochemical Tables, American Chemical Society.
14. Raymond. B., Pétrole et Techniques n°360- novembre-decembre 1990.
15. Leuenberger. J.L., Mohammedi. M.N., Francke. E. and Amouroux. J.,.Proceeding of Fluidization VIII International Symposium of the Engineering Foundation, Tours, 14-19 Mai 1995.
16. Le Perchec. P., Fixari. B., Vrinta.M., Morel. F., 210th National Meeting, Am. Chem. Soc., Chicago, IL, August 20-25, 747-751, (1995).
17. Al Ayoubi. S., Mohammedi. M.N., Francke. E., Gonnord. M.F.and Amouroux. J., 3rd European Congress on Thermal Plasma Processes, September 19-21, 1994, Aachen, Germany.
18. Mohammedi. M.N., Leuenberger. J.L., Amouroux. J., 12th International Symposium on Plasma Chemistry, Minneapolis, Minnesota, USA, August 21-25, (1995).
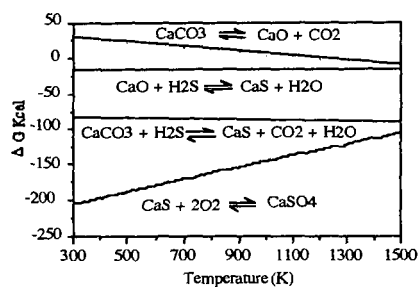
Compounds added to n-hexadecane (1%S wt)	T_b (K) (bed temperature)	T_{inj} (K) (injector temperature) ·	% Gases	Conversion rate (%)	Hydrogen sulfur (ppm)
n-hexadecane	973	483	62	37.4	0
Thiophene	993	803	58	45.2	5
(Me)2S	993	803	67	55.3	60
2-Butanethiol	1028	872	79	55.4	140
Me-Ph-S	1123	871	88	84.3	65

Table 1: sulfur compound effects

Figure 1: Complex Equilibrium of the system: C:H:O:S = 1 : 1.438 : 3.10^{-3} : 1.7.10^{-2} at P=1atm.

Figure 2: Complex equilibrium of the system: C:H:S = 4 : 4 :1, at P=1atm

Figure 3: Complex equilibrium of the system: C:H:S = 4 : 12 : 1, at P=1atm

Figure 4: Free energy of different heterogeneous reactions versus temperature
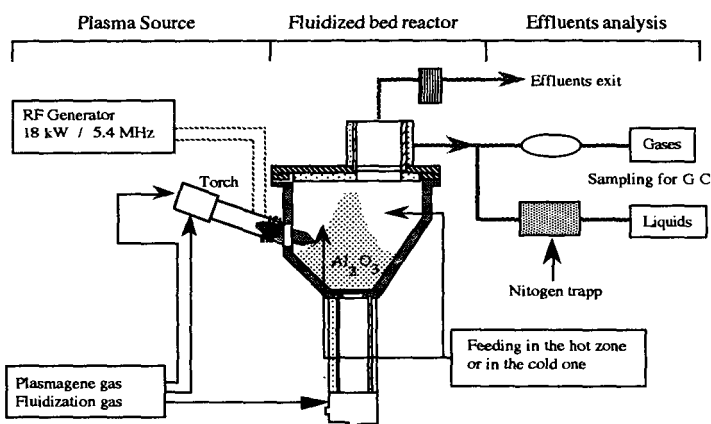
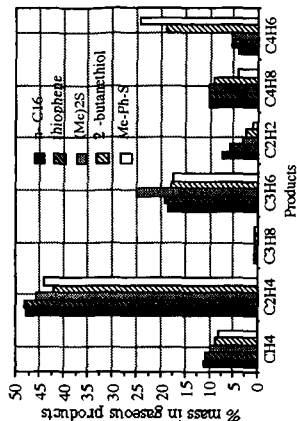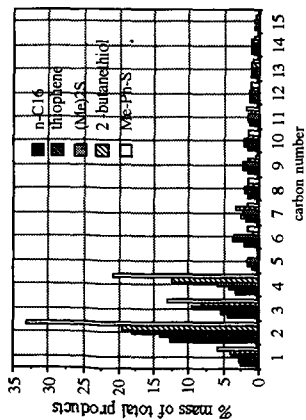Figure 5 : General flow sheet of the plasma fluidized bed reactor

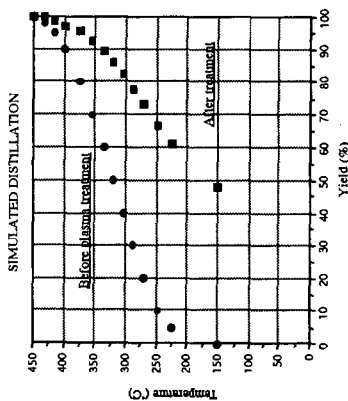Figure 6: Products distribution for different mixtures with n-hexadecane (1% S

Figure 7 : Results of gasoline hydropyrolysis